



ANNUAL REPORT OF NATIONAL INSTITUTE FOR FUSION SCIENCE

April 2004–March 2005

November 2005

NATIONAL INSTITUTE FOR FUSION SCIENCE

Address : Oroshi-cho, Toki-shi, Gifu-ken 509-5292, JAPAN

Phone : +81-572-58-2222

Facsimile : +81-572-58-2601

Homepage on internet : URL = <http://www.nifs.ac.jp/>

Editorial Board

Isobe, M., Murakami, I., Muroga, T., Tanaka, M. Y., Toda, S., Namba, C.

<Editorial Office Staff> Kohmoto, Y., Hashimoto, K.

Inquiries about copyright should be addressed to the Research Information Center,
National Institute for Fusion Science, Oroshi-cho, Toki-shi, Gifu-ken 509-5292 Japan.
E-mail: bunken@nifs.ac.jp

<Notice about photocopying>

In order to photocopy any work from this publication, you or your organization must obtain permission from the following organization which has been delegated for copyright clearance by the copyright owner of this publication.

Except in the USA

Japan Academic Association for Copyright Clearance (JAACC)
6-41 Akasaka 9-chome, Minato-ku, Tokyo 107-0052 Japan
Phone: 81-3-3475-5618 FAX: 81-3-3475-5619 E-mail: jaacc@mtd.biglobe.ne.jp

In the USA

Copyright Clearance Center, Inc.
222 Rosewood Drive, Danvers, MA 01923 USA
Phone: 1-978-750-8400 FAX: 1-978-646-8600

Contents

I.	National Institute for Fusion Science in April 2004 – March 2005.....	1
II.	Research Activities	3
1.	Large Helical Device (LHD) Project	3
1-1.	LHD Experiment	3
(1)	Overview of LHD Experiment	3
(2)	LHD Physics Experiments	5
§1.	Half Hour Plasma Discharge.....	5
§2.	Plasma Collapse in the Long Pulse Plasma Discharge	6
§3.	Termination of Steady State Plasmas Caused by Penetration of Impurity Metal Flakes	7
§4.	Control of Divertor Heat Load by Real-time Magnetic Axis Swing in Steady State Operation.....	8
§5.	Sustainment of keV-order Stable Plasma by ECH Over One Hour on LHD.....	9
§6.	Dynamic and Static Properties of Wall Recycling in the Long Duration Discharges.....	10
§7.	Characterization of Energy Con nement Using Extended International Stellarator Con nement Database.....	11
§8.	New Global Con nement Scaling for High-Density LHD Plasmas.....	12
§9.	Global Energy Con nement Properties in LHD High Beta Plasmas.....	13
§10.	Features of Non-Local Electron Heat Transport in LHD.....	14
§11.	Heat Pulse Propagation across the Rational Surface in Large Helical Device Plasma with Counter Neutral Beam Injection	15
§12.	Edge Transport Barrier Extended to Ergodic Field Layer in a Low Density Plasma of LHD.....	16
§13.	Comparison of Con nement Degradation in High Density and Particle Transport between Tokamak and Helical	17
§14.	Experimental Study of Turbulence and Particle Transport in LHD	18
§15.	Investigation of Micro-turbulence and Particle Transport in LHD from 2d CO ₂ Laser Phase Contrast Imaging.....	19
§16.	Observation of Energetic Particle Mode Fluctuation by Using Microwave Re ectometer	20
§17.	Scattering Measurement from Gyrotron	21
§18.	Control of the Radial Electric Field Shear by Modi cation of the Magnetic Field Con guration in LHD	22
§19.	Formation of the Radial Electric Field Shear at the Boundary of Magnetic Island with Repetitive Pellet Injection in LHD	23
§20.	Characteristics of High -Te Plasmas Related to NBI-Beam-Driven Current.....	24
§21.	Recent Progress on High Ion Temperature Experiment with High-Z Discharge in LHD	25
§22.	Con nement Improvement in High-Ion Temperature Plasmas in LHD	26
§23.	Toroidal Rotation in Ar Discharges	27
§24.	Estimation of the Particle Con nement Time of the Helium Ash in LHD...	28
§25.	Parameter Dependence of Particle Transport in LHD	29
§26.	Three-dimensional Observation System for Pellet Ablation in LHD Plasmas.....	30
§27.	Estimation of the Effect of Fast Ions on Pellet Ablation	31
§28.	Injection of Repetitive Ice Pellet during ICRF Heating.....	32

§29.	Measurement of Inhomogeneous Poloidal Distribution of He Neutral Atom Flux	33
§30.	High-resolution Measurements of $H\alpha$ Line Spectral Profiles in LHD Steady State Plasmas.....	34
§31.	High-beta Experiments in LHD	35
§32.	Observed Pressure Gradients at a Peripheral Rational Surface in LHD High Beta Plasma.....	36
§33.	Onset of Pressure Driven Mode	37
§34.	Transport Analysis of High β Plasmas on LHD	38
§35.	Observation of Internal Structure of Edge MHD Modes in High Beta Plasmas on LHD	39
§36.	Spatial Structure of the MHD Events Observed in LHD.....	40
§37.	MHD Stability of the Current Carrying Plasma with Finite β in LHD.....	41
§38.	Experiment Study of Current Driven MHD Mode in LHD Plasma.....	42
§39.	Comparative Study of MHD Instability in LHD and JT-60U.....	43
§40.	Quantitative Evaluation of Pressure Anisotropy by Magnetic Measurements	44
§41.	The Effect of the Rotational Transform on Shafranov Shift.....	45
§42.	Effective Plasma Boundary Behavior in Finite Beta Plasma of LHD	46
§43.	Effects of Magnetic Axis on Formation and Healing of Magnetic Island	47
§44.	The Local Island Divertor Experiment	48
§45.	Edge Transport Study of LID Configuration in LHD	49
§46.	Titanium Tracer Impurity Behavior in the LHD Plasma with a Plasma Detachment	50
§47.	Study of ECRH Effect on Impurity Behavior with Tracer-Encapsulated Solid Pellet Injection on LHD.....	51
§48.	A New Method on Recycling Coefficient Measurement Using Impurity Pellet Injection in LHD	52
§49.	Forbidden M1 Transitions Emitted from Argon Discharges in LHD	53
§50.	Sustained Detachment - Serpens Mode.....	54
§51.	Time Evolution of Divertor Particle Flux during Serpense-mode	55
§52.	Observation of Rotating Radiation Belt in LHD.....	56
§53.	Behavior of Impurity Radiation and Edge Plasma during Radiative Collapse at the LHD Density Limit	57
§54.	Temperature Measurement of a Vertically Installed Divertor Plate with an Infrared Radiation Thermometer in Self-sustained Detachment Plasmas	58
§55.	CH Band Emission Profile Measurement in Self-sustained Detachment Plasmas in LHD	59
§56.	Heat and Particle Deposition Profiles on the Helical Divertor during Magnetic Axis Swing Operation.....	60
§57.	Transport Analyses of Carbon Atoms in the LHD Divertor Region	61
§58.	Edge Plasma Measurement with Fast Scanning Langmuir Probes.....	62
§59.	Characterization of the LHD Edge & Divertor Plasma by Ion Sensitive Probe Measurement (II)	63
§60.	Measurement of Two Dimensional Electron Density Profile in Edge Plasma Region by Thermal Lithium Beam Sheet.....	64
§61.	Evaluation of Heating Efficiency of EC Waves for Discharges of LHD 8th Experimental Campaign.....	65
§62.	Electron Bernstein Heating Experiment in LHD	66
§63.	Study on Electron Heating and Current Drive by Electron Bernstein Waves.....	67
§64.	Electron Cyclotron Current Drive Experiment in LHD.....	68

§65.	Investigation of Polarization and Deposition of EC Wave Beams	69
§66.	Development of High Beta Plasma Production by Using Higher Harmonic Fast Wave in ICRF.....	70
§67.	Dependence of Magnetic Axis on Neutral Beam Driven Current in LHD ...	71
§68.	Neutral Beam Attenuation Measurement in the High Temperature Plasma	72
§69.	Doppler Shift Spectra of H α Lines from Negative Ion Based Neutral Beams.....	73
§70.	Study of the Loss Cone Feature Using Neutral Particle Analyzer in Large Helical Device.....	74
§71.	Local Measurements of Neutral Particle Spectra on LHD by PCX Method	75
§72.	Observation of Clump and Hole Pair Creations with TAE-bursts on LHD.....	76
§73.	Excitation of High Frequency Fluctuations and Their Effects on High Energy Ions in LHD.....	77
§74.	Erosion of Plasma Facing Materials by Charge Exchange Neutrals.....	78
§75.	Study on Erosion Mechanism of Materials by High Flux Divertor Leg Plasma	79
§76.	Study on Generation Mechanism of Particles in LHD.....	80
§77.	Initial Wall Conditioning in LHD	81
§78.	The Study of Hydrogen Retention and Existence States in Boron Thin Film Exposed to Hydrogen Glow Discharge	82
§79.	The Effect of Helium Glow Discharge on Boronized Surface in LHD	83
§80.	Surface Analysis for Boronized Wall During 7 th Experimental Campaign ...	84
§81.	ICRF Wall Conditioning.....	85
§82.	Development of Integrated Simulation Code for LHD Plasma Experiments.....	86
(3)	LHD Device Engineering Experiments.....	87
§1.	Observation of Coupling Currents with Very-Long Time Constants in LHD Poloidal Coils Using Hall Sensors.....	88
§2.	Evaluation of Residual Magnetic Field by Superconducting Coils of the LHD.....	89
§3.	Acoustic Emission (AE) Measurement of the LHD Helical Coils	90
§4.	Monitoring of the Superconducting Coil System Using Fuzzy Theorem for the Large Helical Device.....	91
§5.	Strain Measurement of Cryogenic Support Structure of LHD.....	92
§6.	Advanced Current Control Scheme Using H-in nity Design for LHD Superconducting Coils	93
1-2.	Device Engineering and Cooperative Development Research.....	94
(1)	Physics and Engineering of LHD Torus System.....	94
§1.	Studies on Behavior of Solid Hydrogen Pellets in a Drift Tube	95
§2.	Characteristics of Hydrogen Absorption in Vanadium Pumping Panel.....	96
§3.	In-situ Measurements of Secondary Electron Emission Coef cient in Plasma-Surface Interaction	97
§4.	Behavior of Rhenium Interface on Tungsten Coated Carbon by Heat Load.....	98
(2)	Applied Superconductivity and Cryogenics.....	99
§1.	Study on Long Loops with Long Time Constants in Cable-in-Conduit Superconductor	100
§2.	Experimental Plan of a 7-T Force-Balanced Helical Coil	101
§3.	Study on Electrical Insulation Characteristics of Super uid Helium	102

§4.	Database Development for He II-cooled Superconducting Magnet System Design	103
§5.	Studies on the Mechanical Properties and Fracture Mechanisms of Single Crystal RE High T_c Bulk Superconductors.....	104
§6.	Development of a Current-Feed System with Low Heat Load Using a Pulse Tube Cooler.....	105
§7.	Fundamental Study on Application of Magnetic Levitation Using YBCO Bulk Superconductor to Fusion Research.....	106
§8.	Fundamental Study on Cryogenic Characteristics of SiC Power Device and Its Application to AC/DC Converter.....	107
§9.	Research and Development of Small General-purpose Pressure Sensor in Cryogenic Environment	108
§10.	Development of Observation and Diagnosis Systems for Superconducting-coil Operations Using the Poynting Vector Method.....	109
§11.	Basic Research on the Oxide Superconductors for Fusion Reactors	110
§12.	Effect of the Phase Transition on Heat Transfer in He II	111
§13.	Composite Electrical Insulation and its Reliability at Cryogenic Temperature for LHD	112
§14.	Design and Optimization of High T_c Superconductors for Current Lead Application.....	113
§15.	Development of Conduction-Cooled LTS Pulse Coil.....	114
§16.	Cryogenic Stability of the Model Coil of the LHD Helical Coil in Saturated Helium.....	115
§17.	Elimination of Variable Harmonics on Motor Generator Circuit	116
§18.	Thermal Contact Conductance between the Bundle and the Conduit in Cable-in-Conduit Conductors	117
§19.	Effective Resistivity of HTS Tapes with Shielding Currents	118
§20.	SMES System Designed to Protect from Momentary Voltage Drop.....	119
§21.	Development of a Pulse Tube Current Lead	120
§22.	HTS Conical Bulk for Current Lead Use.....	121
§23.	Cooldown Performance of the Cryogenic System Applied for the Cryogenic Target of the FIREX Project.....	122
§24.	Performance of Cold Compressors in the Cooling System for the R&D Coil Cooled by Subcooled He I	123
§25.	Simulation of Electromagnetic Behaviors of Lap Joints for Fusion Magnet Systems	124
§26.	Interaction between the Transport Current and Shielding Currents in Bi-2223/Ag HTS Tapes.....	125
(3)	RF Heating Technologies	126
§1.	CW Gyrotron Operation.....	127
§2.	Improvement of ECH Transmission Line for CW Experiments.....	128
§3.	Workshop on Generation, Application and Measurement of High Power Millimeter Waves.....	129
§4.	Temperature Measurement of ICRF Antennas in LHD.....	130
§5.	Impedance Matching during Long Pulse Discharge in LHD.....	131
§6.	Liquid Stub Multi-computer Control System for ICH on LHD.....	132
§7.	Power Circulation System on LHD Combine Antenna	133
§8.	Study on High Energy Particles Escaped from LHD Using Lost Ion Probe	134
(4)	High Energy Beam Technology	135
§1.	Operational Status of Negative-Ion-Based Neutral Beam Injection System in LHD	136

§2.	Correction of Beam Profile by Modifying Aperture Shape of Steering Grid II.....	137
§3.	Doppler Shift Spectra of $H\alpha$ Lines from Negative Ion Based Neutral Beams.....	138
§4.	Fundamental Processes in H^- Ion Source Plasma	139
§5.	Plasma Injection from Several Cesium-Hollow Cathodes into the Large H^- Ion Source	140
§6.	Rf Power Performances for Ring Shaped and New Parallel Rod Multi-antenna Systems of Rf Ion Source	141
§7.	Development of RF Plasma Source for Negative Ion NBI.....	142
(5)	Diagnostic Systems	143
§1.	A Convenient Method of Calibrating Relative Sensitivity of Multi-Channel Thomson Scattering Diagnostic System	144
§2.	An Estimation of Uncertainties in Electron Density Measurements due to the Beam Spatial Variations in the LHD YAG Thomson Scattering.....	145
§3.	Development of Ka -band Ultrashort Pulsed Radar Reflectometer for Electron Density Profile Measurement	146
§4.	The First Detection of the Secondary Beam of the 6 MeV Heavy Ion Beam Probe on LHD	147
§5.	Confirmation of Beam Orbit of the Heavy Ion Beam Probe on LHD	148
§6.	Performance and Development of Au^- Beam Source for a Heavy Ion Beam Probe of the LHD.....	149
§7.	Measurements of Rotational Transform Due to Non-inductive Toroidal Current Using Motional Stark Effect Spectroscopy in Large Helical Device	150
§8.	Argon Transport Obtained with an Assembly of Pulse Height Analyzer in LHD.....	151
§9.	Microwave Imaging Reflectometry for the LHD Edge Plasma.....	152
§10.	Application of Ultrashort-Pulse Reflectometer to LHD.....	153
§11.	Study of High-performance Array Antennas for Millimeter-wave Imaging Array	154
§12.	A New Tracer-encapsulated Pellet Injector for Plasma Diagnostics	155
§13.	Ultra-Wideband Data Acquisition and Real-Time Data Streaming in LHD Steady-State Experiments	156
§14.	Enhancement of the Experimental Database.....	157
§15.	Development of a New Two Color FIR Laser Interferometer (II).....	158
§16.	Two Dimensional Ion Temperature and Velocity Measurements by Use of Visible Light Tomography Technique.....	159
§17.	Image Reconstruction by Hopfield Neural Network for Bolometer Tomography of LHD Plasma	160
§18.	Bench Testing of New Polarimeter with Use of Photo Elastic Modulator for 57 & 48 Micron Laser	161
§19.	Research and Development of an Extremely Compact Fusion Neutron Source by Spherically Converging Ion Beams	162
§20.	On the Construction of Databases of Experiment Data	163
1-3.	Theoretical Study.....	164
§1.	Effects of Self-Consistent Flow on Island Generation in Interchange Mode	165
§2.	Effects of the Resistive Wall on the Growth Rate of Weakly Unstable External Kink Mode in General 3D Configuration.....	166
§3.	Properties of the Compressible Pressure-driven Perturbations.....	167
§4.	Nonlinear Simulation of Edge-Localized Mode in Spherical Tokamak	168

§5.	New Theoretical Approach to 3D Equilibrium of the LHD	169
§6.	The Configuration Dependence of Ripple Transport in LHD.....	170
§7.	Impact of Ion Species on Ambipolar Radial Electric Field in LHD	171
§8.	Transport Analysis of Radial Electric Field in Helical Plasmas	172
§9.	Non-local Neoclassical Transport Simulation in LHD	173
§10.	Particle Drift in Static Magnetic Fields.....	174
§11.	Strike Point Patterns on the LID Head in Various LHD Configurations	175
§12.	Development of a Monte-Carlo Simulation Code for Radial Profiles in Magnetic Island.....	176
§13.	Self-consistent Model for Two-dimensional Structures in Tokamak H Modes.....	177
§14.	Two-dimensional Structure and Particle Pinch in Tokamak H Mode	178
§15.	Coherent Structure of Zonal Flow and Nonlinear Saturation	179
§16.	Excitation of Geodesic Acoustic Mode in Toroidal Plasmas.....	180
§17.	Periodic Change of Solar Differential Rotation	181
§18.	Life Time of Plasma States Near Transition Boundary	182
§19.	A Novel Turbulence Trigger for Neoclassical Tearing Modes in Tokamaks	183
§20.	Collisionless Damping of Geodesic Acoustic Modes.....	184
§21.	Dynamics of Zonal Flows in Helical Systems	185
§22.	A Variational Analysis of Flow-reversal Condition in a Turbulent Swirling Pipe Flow Using the Bulk-helicity Concept.....	186
§23.	Effect of Flow Shear on Temperature Gradient Driven Short Wavelength Modes.....	187
§24.	Short Wavelength Ion Temperature Gradient Instability in Toroidal Plasmas.....	188
§25.	Short Wavelength Electron Temperature Gradient Instability in Toroidal Plasmas.....	189
§26.	Emission of Electromagnetic Pulses from Laser Wake fields through Linear Mode Conversion.....	190
§27.	An Equilibrium Equation of a Magnetized Rotating Plasma.....	191
§28.	Dust Plasma Experiments and Collisional Oscillations	192
1-4.	LHD Project Research Collaboration	193
§1.	Experiment on Charge Separation in a Small-Scale CUSPDEC	194
§2.	Experiment on Direct Energy Conversion in a Small-Scale CUSPDEC Device	195
§3.	Characteristics of Single Slanted Cusp-DEC	196
§4.	Numerical Simulation of Large-Scale TWDEC and HelmholtzDEC Devices.....	197
§5.	Suppression of Harmonic Frequencies of Induced Voltages in a Decelerator of a TWDEC Simulator	198
§6.	Active Deceleration Experiments in TWDEC Simulators.....	199
§7.	Development of High Beta Plasma Formation Using ICRF High Harmonic Fast Wave.....	200
§8.	Experimental Study of Compatibility of a Transport Barrier and Energetic Ion Confinement.....	201
§9.	Study of the Repetitive Fueling Pellet Transportation in the Guiding Tube.....	202
§10.	Quasi-Optical Analysis of Output Beam from Remote Steering Antenna ...	203
§11.	Production Mechanism of D ⁻ Ions and Evaluation of D ⁻ Ion Current Extraction	204

§12.	Analysis of a Graphite Plate Interacting with a High-density Hydrogen Plasma	205
§13.	Development of Continuously Size-Controllable Pellet Injector and Detailed Study of Passage Properties in Drift Tube.....	206
§14.	Temperature Dependence of Optical Constants of Silicon for 48- and 57- μ m FIR Lasers	207
§15.	Anisotropy of Proton Velocity Distribution Function in Argon Plasma Analyzed by Means of Plasma Polarization Spectroscopy	208
§16.	Spectroscopy and Atomic Modeling of EUV Light from LHD Plasmas.....	209
§17.	Development of Wide Band and Compact X-ray Spectrometer	210
§18.	Development of Laser Thomson Scattering System Applicable to Low Temperature Recombining Plasmas in Divertor Simulator MAP-II in the Univ. Tokyo	211
§19.	Diagnostics of Plasma with Negative Ions Using the Eclipse Laser Photodetachment Method in Divertor Simulator MAP-II in the Univ. Tokyo	212
§20.	Study on Effects of Bending Strain to Critical Current Characteristics of Nb ₃ Al CIC Conductors.....	213
§21.	Change in Properties of Superconducting Magnet Materials by 14 MeV Neutron Irradiation under Cryogenic Temperature	214
§22.	Development of New High Field and High Current Density Superconductors for Fusion Devices	215
§23.	Stability of Superconducting Coil with Various Surface Conditions in Pressurized He II	216
§24.	Suitability of Boron-titanium as First Wall Material	217
§25.	Measurement of the Negative Ion and Control of Recombination Plasma in the LHD Divertor	218
§26.	Kinetics of Hydrogen Isotopes at Surfaces and Bulks of Plasma Facing Materials Based on Group 5 Metals.....	219
§27.	Heat Removal Enhancement of Plasma-Facing Components by Using Nano-Particle Porous Layer Method.....	220
§28.	Investigation of Tritium Behavior and Tracability in In-vessel Systems of LHD during D-D Burning.....	221
§29.	Assessment Study on Biological Effects of Radiation in LHD	222
§30.	Study on Environmental Behavior of Tritium	223
2.	Collaboration on Fusion Engineering	224
(1)	Fusion Engineering Studies	224
§1.	In uence of Inner Surface Roughness on Subcooled Flow Boiling Critical Heat Flux in a Short Vertical Tube	226
§2.	Development of Low Activation Compound Superconducting Wires for Fusion Reactor	227
§3.	Development of Strength Evaluation Methods of Cryogenic Material Systems	228
§4.	Development of the Fracture Toughness Test Method by Round Bar with Circumferential Notch.....	229
§5.	Examination of Materials Irradiation Test Program Using Intense Neutron Source (IFMIF)	230
§6.	Thermal and Mechanical Properties of Composite Materials for Superconducting Coils	231
§7.	Development of Fine-Grained, Particle-Dispersed Vanadium Alloys with Improved Resistances to High-Temperature Deformation and Embrittlement by Neutron and Helium Irradiations	232

§8.	Development of Simulation Models for Irradiation Performance of Fusion Materials.....	233
§9.	Evaluation of MHD Pressure Drop in Multi Layer Wall Channel.....	234
§10.	Preparation of Cylindrical Superconductor Composed with Ni Mesh for Current Lead.....	235
§11.	Dynamic Behavior of He-vacancy Complex in Highly-purified Vanadium Alloys.....	236
§12.	Joining and Heat Load Test of Tungsten Divertor.....	237
§13.	Overall Characterization of High Purity Reference Vanadium Alloys NIFS-HEATs.....	238
§14.	Environmental Effects on Radiation Effects in V-4Cr-4Ti Alloys.....	239
§15.	Measurements of Radiation Induced Conductivity of Ceramic Insulators for Fusion Blanket.....	240
§16.	Examination of Electrical Degradation of Ceramic Coating Materials Using Ion Beam Irradiation.....	241
§17.	Development of Joint Technique of SiC/SiC Composites.....	242
§18.	Development of Reduced Activation Ferritic Steels with Improved Heat Resistance and Elemental Property Characterization for High Cycle Efficiency Steel-based Blankets.....	243
§19.	Crack Length Measurement in Cryogenic Environment Using Unloading Elastic Compliance.....	244
§20.	Lithium Compatibility of MHD Coatings Fabricated by Arc Source Plasma Deposition Method.....	245
§21.	Creep Mechanism of NIFS-Heat2 Alloys by Using Pressurized Creep Tubes.....	246
§22.	Negative Longitudinal Magnetoresistance of Bulk Bismuth in Low Temperature.....	247
§23.	Development and Synthetic Evaluation of High-Z Plasma Facing Materials.....	248
§24.	Transmutation of High-level Waste in a Spherical-tokamak Reactor.....	249
(2)	Helical Reactor Design.....	250
§1.	Modification of Design Parameters on LHD-type Reactor FFHR2.....	250
§2.	Design Studies on Long-life Breeder Blanket for LHD-type Reactors.....	251
§3.	Study of the Burning Plasma Physics Issues in Helical Reactors.....	252
§4.	Design Study of Magnets for Heliotron Type Fusion Reactor FFHR.....	253
§5.	Effect of Surface Angle on Mechanical Jointing of HTS.....	254
§6.	System Design Study of Hydrogen Isotope Recovery from Molten-Salt Blanket of Fusion Reactor.....	255
§7.	Study on Heat Transfer Region for Fluid System in a Liquid Blanket.....	256
§8.	Development of Heat Transfer Enhancement Technique in High Pressure Number Fluid Blanket.....	257
§9.	Feasibility of Helium Gas Turbine System for Molten Salt Blanket.....	258
§10.	Design on New Type First Wall under High Temperature and Particles for Nuclear Fusion Reactor.....	259
(3)	Fusion Reactor System and Safety.....	260
§1.	Investigation of Tritium Behavior and Tracability in In-vessel Systems of LHD during D-D Burning.....	261
§2.	Studies of Interaction between Cooling Pipe Materials and Tritium, and Their Chemical Behavior.....	262
§3.	Advancement of Water-Hydrogen Chemical Exchange Apparatus by Introducing Trickle Bed Reactor.....	263

§4.	Development of High-power Adsorbents for Hydrogen Isotope Separation by Pressure Swing Adsorption Method.....	264
§5.	Studies of Tritiated Water Vapor Removal with a Hollow-fiber Type Polyimide Membrane Dehumidifier.....	265
§6.	Development of Advanced Catalyst for Oxidation of Tritium and Quantification of Mass Transfer Coefficient.....	266
3.	CHS Experiments.....	267
§1.	Study on Parameter Dependences of Power Threshold for Edge Transport Barrier Formation.....	268
§2.	Power Threshold for ETB Transition Based on NBI Power Deposition Calculation	269
§3.	Dependence of Power Threshold on Magnetic Field Configuration.....	270
§4.	Time Evolutions of the Ion Temperature in the Edge Transport Barrier (ETB) Operations in CHS	271
§5.	Comparison of Impurity Poloidal Rotations in Recent Improved Modes in CHS	272
§6.	Radiation Profile Measurements for Edge Transport Barrier Discharges in the Compact Helical System Using AXUV Photodiode Arrays.....	273
§7.	EHO-like Density Fluctuations Measured Using Beam Emission Spectroscopy in ETB Discharge on CHS.....	274
§8.	Statistical Analysis of Peripheral Plasma with Edge Transport Barrier in CHS	275
§9.	Measurement of Edge Transport Barrier Structure by Langmuir Probe in the Compact Helical System	276
§10.	Discharge Aiming at High Stored Energy in Compact Helical System (CHS)	277
§11.	Efficient Heating of High Density Plasmas Up to Cut-off Density of 106.4 GHz ECH Power on CHS	278
§12.	Confinement of Perpendicularly Injected Energetic Ions on Different Magnetic Configurations in CHS	279
§13.	Wavelet Analysis on Density and Potential Fluctuation on Internal Transport Barrier	280
§14.	Magnetic Field Fluctuation Measurement with Heavy Ion Beam Probe in CHS	281
§15.	Consideration of a Necessary Condition for Local Density Fluctuation Measurements with Heavy Ion Beam Probe	282
§16.	A Method to Infer Internal Mode Structure with HIBP and Magnetic Probes.....	283
§17.	Measurements of Electron Density Fluctuations in CHS Plasmas by Using YAG Laser Imaging Method	284
§18.	HCN Laser Scattering Measurement on CHS.....	285
§19.	2nd and 3rd Harmonic ECE Measurement on CHS.....	286
§20.	Fast Ion Measurement Using the Hybrid Probe in CHS.....	287
§21.	MHz Range Fluctuation Measurements in Electron Cyclotron Resonance Heating Plasmas on Compact Helical System	288
§22.	Lithium Beam Probe for Edge Plasma Diagnostic in CHS.....	289
§23.	Lithium Beam Probe (LiBP) Imaging Using CCD Camera.....	290
§24.	Neutral Particle Transport in CHS Edge Region	291
§25.	Detailed Dynamics of Internal Transport Barrier Formation in Low Temperature CHS Plasmas	292
§26.	Electron Heating of an Over-Dense Plasma by 2.45 GHz Microwaves in CHS	293

§27.	Hot Cathode Biasing Experiment in CHS.....	294
§28.	Radial Electric Field Control by Electron Injection in CHS.....	295
§29.	Radial Density Profiles of Microwave and Whistler Wave Discharges	296
§30.	Observation of Space Potential Variation on Magnetic Surfaces on CHS ...	297
§31.	Extreme Ultraviolet Spectroscopy of CHS Plasma for Use in Detailed Atomic Modeling	298
§32.	Trial Production of a Simple Neutral Particle Analyzer	299
§33.	CHS Data Acquisition and Analysis System	300
4.	Basic Research and Development	301
§1.	High Density Plasma Experiment HYPER-I	302
§2.	Observation of Plasma Hole Transition Induced by Microwave Power Modulation	303
§3.	Measurements of Neutral-gas Flow in High-density Plasma Using a Tunable Laser Diode	304
§4.	Measurement of Rotational Flow Velocity Using Laser-Induced Fluorescence Spectroscopy	305
§5.	Observation of Neutral Particle Distributions in a Plasma Vortex Using a Few Lines of Sight of Visual Light.....	306
§6.	Spontaneous Magnetic Fluctuation in HYPER-I Plasma.....	307
§7.	A Study of Charge Exchange Processes by Collision with Excited Atoms	308
§8.	Ejected Electron Spectroscopy in Electron-Ion Collisions	309
§9.	Isotope Effect on Charge Transfer by Slow Hydrogen Ions from Hydrogen Molecules	310
§10.	Laser Thompson Scattering Measurement of High Density Plasma Produced by TPD-II	311
§11.	Period of the Macroscopic Oscillation of Detached Plasma in the TPD-II	312
§12.	The Role of H^- Energy and Electric Field in the Extraction Region for H^- Extraction Probability of a Negative Ion Source	313
§13.	Determination of Plasma Temperature and Density in Laser Produced Tin Plasmas.....	314
§14.	Ion Heating in a Supersonic Plasma Flowing through a Magnetic Nozzle...	315
§15.	Physical Mechanism of Self-organization of Novel Density Distribution in a Pure Electron Plasma Driven by Rotating Wave Field	316
§16.	Dynamic Control of Bifurcated Transition in Magnetized Plasma.....	317
§17.	Basic Process of Solid Hydrogen Ablation by Plasma	318
§18.	Plasma-quenching Efficiency of CO_2 by Estimation of C_2 Rotational and Vibrational Temperatures in High-pressure High-power Ar- CO_2 Induction Plasmas.....	319
§19.	Transient Response of the Induction Coil Loading in the Initial Startup Phase of rf Induction Thermal Plasmas	320
§20.	Experimental Study of Current Drive Using Nernst Effect	321
§21.	A Solar Wind Simulator Using An Intensive Arc-Jet System	322
§22.	Spatial Distribution of Losses of Neutral Beam-injected Fast Ions in Quasi- axisymmetric System	323
§23.	Consideration on Scale-up of Quasi-axisymmetric Stellarator with Low Aspect Ratio	324
§24.	Preliminary Investigation of a Quasi-Axisymmetric Configuration Optimized for Contours of the Second Adiabatic Invariant.....	325
§25.	The Trial Modular Coil Design for a N=2 Quasi-isodynamic Stellarator	326

§26.	A Numerically Robust Formula for Bootstrap Current Coefficients in the Banana Regime in Boozer Coordinates	327
§27.	A Method to Eliminate the Logarithmic Singularity in Fourier Series, Which Appear in Parallel Viscosity Calculations in the Banana Regime	328
5.	Theory and Computer Simulation Project.....	329
§1.	Boundary Modulation by the Finite β Free Boundary Equilibrium Motion in Heliotrons.....	331
§2.	Significant Stabilization of Ideal MHD Instabilities by the Boundary Modulation in Heliotrons	332
§3.	The Second Stability of the High- n Ballooning Modes in Heliotrons	333
§4.	Fourier Mode Analysis of Numerical Results Obtained by Direct Numerical Simulation of MHD Under LHD Inward-shifted Configuration.....	334
§5.	Nonlocal Energetic Particle Mode in a JT-60U Plasma.....	335
§6.	Simulation of Alfvén Eigenmodes and Energetic Particles in an LHD Plasma	336
§7.	Nonlinear Evolution of the Fishbone Instability	337
§8.	Velocity-Space Structures of Distribution Function in Toroidal Ion Temperature Gradient Turbulence	338
§9.	Linear Analysis of Resistive Wall Mode with Poloidal Rotation	339
§10.	Effect of Poloidal Rotation on Nonlinear Resistive Wall Mode.....	340
§11.	Study of Energy Transport of External MHD Modes in a Cylindrical Tokamak.....	341
§12.	Motion of Ablation Cloud in Torus Plasmas	342
§13.	Three-Dimensional Particle-In-Cell Simulation of Scrape-off-Layer Plasmas.....	343
§14.	Core-SOL-Divertor Model and Application to Operation Space of EAST	344
§15.	Edge Plasma Simulation of Stellarator System with UEDGE.....	345
§16.	The Strike Point Pattern on Local Island Divertor in LHD	346
§17.	3-D Rayleigh-Taylor Instability in Spherically Stagnating Systems	347
§18.	Laser Fusion Research	348
§19.	Research on High Energy Density Laser Plasma Physics	349
§20.	Structure of Thin Current Layer in Two-dimensional Open System.....	350
§21.	Collisionless Driven Reconnection in Three-dimensional Thin Current Sheet.....	351
§22.	Three Dimensional Particle Simulation on Collisionless Driven Reconnection.....	352
§23.	Suppression of Hall Term Effects by Gyroviscous Cancellation in Collisionless Magnetic Reconnection.....	353
§24.	Plasma Instabilities and Anomalous Resistivity in the Current Sheet	354
§25.	Simulation Study of Nonlinear Dynamics in Plasmas with Flows	355
§26.	Simulation Study of the Formation Mechanism of Sigmoidal Structure in the Solar Corona.....	356
§27.	Study on MHD Wall Shear Turbulent Flow on High Reynolds Number via Paralleled Direct Numerical Simulation	357
§28.	Low-Frequency Instabilities Due to Flow Velocity Shear in Magnetized Plasmas.....	358
§29.	Self-Organization of Large-Amplitude Waves and Associated Particle Acceleration	359
§30.	Holistic Simulation – Auroral Arc Formation as the First Trial –	360
§31.	Intermittency and Transfer Phenomena in NS and MHD Turbulence.....	361

§32.	Orthonormal Divergence-free Wavelet Analysis of Nonlinear Interactions between Coherent Structures.....	362
§33.	Yin-Yang Grid and Geodynamo Simulation.....	363
§34.	Development of Exact Charge Conservative Particle Simulation Code with High Performance Fortran.....	364
§35.	Development of an Electromagnetic Particle Code for Space Propulsion Application Using ECR Discharge	365
§36.	Dissipative Particle Dynamics Simulation on Self-assembly of Amphiphilic Molecules.....	366
§37.	Molecular Dynamics Simulation of Collision between Graphite and Hydrogen.....	367
§38.	Molecular Dynamics Simulation of Micelle Formation in Amphiphilic Solution	368
§39.	Construction of Collaborative and Seamless Virtual Environment for Numerical Simulation	369
6.	Personal Interchange Joint Research Program.....	370
§1.	Life Time of Plasma States Near Transition Boundary	372
§2.	Higher-Harmonic Oscillation of Peniotron.....	373
§3.	Clarification on Cooling Mechanism of Stirling Type Pulse Tube Cryocooler.....	374
§4.	Ion Heating in a Supersonic Plasma Flowing Through a Magnetic Nozzle	375
§5.	Electron Bernstein Wave Heating by Long Wavelength Microwave in a Spherical Tokamak and a Helical Device	376
§6.	Assessment on Fusion Energy Development from the Socio-Economic Viewpoint.....	377
§7.	Magnetic Island Effect on Radial Particle Flux in TU-Heliac.....	378
§8.	Heating and Current Drive Experiments on the TST-2 Spherical Tokamak.....	379
§9.	ECH Plasma Experiments of an Internal Ring Device with HTS Coil.....	380
§10.	Experimental and Theoretical Studies of Startup Methods for Spherical Tokamak Plasmas.....	381
7.	Collaborations Using Super SINET	382
§1.	Network Reconstruction of LHD Experiment Remote Participation System	383
§2.	Millimeter-Wave Remote Experiment System Using Super-SINET.....	384
§3.	Statistical Analysis of Density Fluctuation in SOL/Divertor Plasmas of the LHD with Super-SINET	385
§4.	Emission Locations and Influx of Hydrogen Atoms on the Basis of Zeeman Profile	386
§5.	Two Dimensional Ion Temperature and Velocity Measurements by Use of Visible Light Tomography System and Super SINET.....	387
§6.	Remote Participation for Plasma Experiments on the Mini-RT Device by Use of SuperSINET System.....	388
8.	Coordination Research Center	389
§1.	Particle Control by Moving-surface PFCs	391
§2.	Activities on ITER Collaboration	392
§3.	Theoretical Investigation of Molecular Dynamics in Intense Laser Fields.....	393
§4.	First-Principles Molecular Dynamics Studies of Plasma-Surface Interactions.....	394

§5.	DNA in Nanopores: Strong Electrostatic Interactions in Cellular Dynamics Processes	395
§6.	High-Performance Cluster Computer by means of Linux PCs and Low-Latency (GAMMA) Communication Software	396
§7.	Microwave Heating of Liquid Water and Ice: Molecular Dynamics Study	397
§8.	Microscopically In-situ Investigation for Microwave Processing of Metals.....	398
§9.	Time Dependent Electron Temperature and C^{2+} Ion Density Derived from CIII Spectra	399
§10.	EUV Spectra of Xe Ions Measured from LHD	400
§11.	X-ray Spectral Analysis on Electron Interatcion with Highly-Charged Xe Ions.....	401
§12.	Dielectronic Recombination of Xe^{10+} Ions	402
§13.	Satellite line of Xe^{9+} Ions	403
§14.	Radiative Recombination of Xe^{10+} Ions	404
§15.	Dielectronic Recombination Rate Coef cients to Excited States of Carbonlike Oxygen and Dielectronic Satellite Lines.....	405
§16.	Ion Source Development for the Research of High Z Impurity Ions.....	406
§17.	Time-dependent Density Functional Study on Excited Hydrogen Atom Formation via Non-resonant Electron Capture by a Proton from Refractory Metal Surfaces.....	407
§18.	Charged and Neutral Particle Behavior at and near Plasma Facing Material Surfaces.....	408
§19.	Cross Section Database for Carbon Ions: Electron-impact Excitation, Ionization, and Charge Exchange in Collisions with Hydrogen Atoms	409
§20.	Network of Atomic and Molecular Database Related to the Processing Plasmas.....	410
§21.	Study of Evolutional Data Collecting System for the Atomic and Molecular Databases.....	411
§22.	LAMP Prototype Bibliography Databases.....	412
§23.	Simulation Experiment of Con nement Improvement of Plasmas for Super Science Highschool (SSH) Program (Fluid Dynamics Experiment in Kitchen).....	413
§24.	Evaluation of Fusion R&D — Cost Reduction of Fusion Plants —.....	414
§25.	Archival Studies on the Nuclear Fusion Research at Universities in Japan — Inter-University Collaboration System in Early Days of Fusion Science —	415
§26.	Complementary Study of Nuclear Fusion Archiving by Means of Oral History	416
§27.	Foundation of Fusion Science Archives	417
9.	Fusion Engineering Research Center	418
§1.	Neutronics Investigation into a Test Blanket Module with Li and V alloys	419
§2.	Development of 14 MeV Neutron Irradiation Test System for Superconducting Magnet Materials	420
§3.	Tensile Properties of Low Activation Vanadium Alloy after Liquid Lithium Exposure.....	421
§4.	Fabrication and Superconductivity of V-based Laves Phase Compound Multi lametary Wires Synthesized by a RHQ Process to PIT Precursors Using a V Tube	422
§5.	Neutronics Investigation of Self-cooled Liquid Blanket Systems for Modi ed FFHR2 Design.....	423

§6.	Development of Tantalum Matrix RHQT Processed Nb ₃ Al Superconductors	424
§7.	Helium Retention and Thermal Desorption Properties of V-4Cr-4Ti Alloy (NIFS-HEAT2)	425
§8.	The Growth and Resistivity of In-situ Er ₂ O ₃ Coating on V-4Cr-4Ti	426
§9.	Study on Low Cycle Fatigue Behaviors of JLF-1 Steel	427
§10.	Experimental Study on Liquid Lithium Flow for IFMIF Target	428
§11.	Control of Nitrogen Concentration in Liquid Lithium by Iron-Titanium Alloy	429
§12.	An Experimental Study to Recover Tritium by Yttrium from IFMIF Li Loop	430
§13.	Design Activity of High Flux Irradiation Test Module of IFMIF	431
§14.	Evaluation of Validity of Master Curve Method to Measure the DBTT Shift of Ferritic Steels for Blanket Structural Components	432
§15.	Experimental Studies on the Neutron Emission Spectra and Activation Cross-section in IFMIF Accelerator Structural Elements	433
10.	Safety and Environmental Research Center	434
§1.	Design of a Portable Directional Neutron Source Finder	435
§2.	Environmental Atmospheric Tritium Monitoring with Automatic Discriminate Sampling of Different Chemical Forms	436
§3.	A Simplified Method for Tritium Measurement in the Environmental Water Samples	437
§4.	Isotopic Separation Analysis Using Improved Hydrogen Analyzer	438
§5.	Development of Exhaust Gas and Effluent Liquid Treatment System for LHD	439
§6.	Water-Vapor Decomposition by Using Zirconium-Nickel Alloy	440
§7.	Performance of Honeycomb Type Catalysts for Oxidation of Tritiated Hydrogen and Methane Gases	441
§8.	Field Measurement in Hi-Level Multiple Source EM Environment	442
§9.	Measurements of Static and Variable Magnetic Fields in a Large Plasma Experimental Facility	443
11.	Computer and Information Network Center	444
12.	Bidirectional Collaborative Research Program	448
§1.	ICRF Wave Excitation and Propagation in the Axisymmetrized Tandem Mirror GAMMA 10	449
§2.	Study of Impurity Ion Radiation Intensity in the GAMMA 10 Plasma	450
§3.	Anisotropic Electron Velocity Distribution Function in GAMMA10 Tandem Mirror Plasma Analyzed by Means of Plasma Polarization Spectroscopy	451
§4.	Development of High Performance Antennas for Electron Heating in GAMMA 10	452
§5.	Investigation on Applicability of a CUSPDEC to the GAMMA 10 Tandem Mirror	453
§6.	Magnetic Configuration of Kobe-Cusp DEC in GAMMA 10	454
§7.	Excitation of RF Waves in GAMMA 10 and in the Local Magnetic Mirror Configuration on LHD	455
§8.	ICRF Heating and Ion Acceleration at the Open End in GAMMA 10	456
§9.	Propagation and Radiation of Cyclotron Waves and Excitation of Fluctuations Due to High Power Plug ECRH	457
§10.	Study of Radial Transport of Bounce Ions by Means of Control of Radial Potential Profile of Core Plasma	458

§11.	Study of Potential Confinement Mechanism via Plasma Visualization Technology	459
§12.	Analysis of Neutral Particle Transport and Recycling Behavior in Open Magnetic Field Configuration Plasmas	460
§13.	Analysis of Edge Fluctuation with ICRF in a Tandem Mirror for the Purpose of Radial Transport Control	461
§14.	Progress in Potential Formation and Findings in the Associated Radially Sheared Electric-Field Effects on the Suppression of Intermittent Turbulent Vortex-like Fluctuations and Transverse Losses	462
§15.	Study of Relations between the Spatial Structure of Potential-Trapped Electron Distribution Functions and the Physics Scaling Law of Plasma Confining Potentials.....	463
§16.	Study of Heliotron J Peripheral Plasma Using Fast Camera.....	464
§17.	ICRF Heating Experiment in Heliotron-J	465
§18.	Study on Neutral Hydrogen and Impurity Behavior in Heliotron J Plasmas.....	466
§19.	Hard X-ray Diagnostic System Intended to Study Effect of Bumpy Ripple Control on Plasma Confinement in Heliotron J	467
§20.	Dependence of Poloidal Viscosity on Magnetic Configuration in Heliotron J and its Implication to H-Mode Quality.....	468
§21.	Optimization of Helical System Concept.....	469
§22.	Study of the Driving Mechanism of Toroidal Current in Heliotron-J	470
§23.	Interaction of Intense Femtosecond Laser Pulses with Clusters.....	471
§24.	X-ray Imaging in Fast Ignition Fusion Experiments — Poisson Noise Reduction by ICA Filter —	472
§25.	X-ray Penumbra Imaging for Laser-produced Plasma — Uniformly Redundant Penumbra Array —	473
§26.	Compression and Fast Heating of Liquid Deuterium Targets and Related Research	474
§27.	Simulation Study of Chamber Evacuation Dynamics of Laser Fusion Reactor	475
§28.	Evaluation of the Stability of SiC/SiC Composites for Inertial Fusion Dry Wall Chamber to High Temperature Irradiation and Design Study Based on the Material Properties	476
§29.	Study on Tritium Behavior in Liquid Blanket System of Laser Inertial Fusion Reactor.....	477
§30.	Design Study on Foam-cryogenic Targets by Integrated Simulations.....	478
§31.	Innovative Concepts of Free Surface Cooling System on First Wall of Fusion Reactor.....	479
§32.	Measurement of Particles Ablated by Intense Laser Irradiation.....	480
§33.	Research on Target Heating Processes Using PW-Laser-Driven Intense Proton Beams.....	481
§34.	Physics of High Energy Density Plasma driven by Fast Pulse Power Discharges.....	482
§35.	Measurement of Bremsstrahlung Emission Using SX-CCD Camera.....	483
§36.	Natural Diamond Detector for Neutron and γ -ray Measurements in Laser Fusion Experiments.....	484
§37.	Aerosol Formation and Its Effects on the Chamber Wall Lifetime and Operation of IFE Power Reactors	485
§38.	Application of a Fast Video Camera for Study on Triam-2M Peripheral Plasma and Plasma-surface Interactions	486

§39.	Application of the Zeeman Patterns to the Local Plasma Diagnostics in the TRIAM-1M Tokamak (NIFS04KUTR001).....	487
§40.	Design and Fabrication of Compact Plasma Wall Interaction Experimental Device (CDP)	488
§41.	Current Startup/Current Drive and Heating Experiments Using RF/mm-Waves on the TRIAM-1M Tokamak	489
§42.	Modeling of Particle Balance in Steady State Plasma Confinement Device: TRIAM-1M.....	490
§43.	Measurement of Two Dimensional Image of Hard X-ray in TRIAM-1M ...	491
§44.	Integration of PWI Experiments, Diagnostics, Simulation and Modeling in Steady State Plasma	492
13.	Research Information Office	493
III.	International Collaboration	494
1.	US - Japan (Universities) Fusion Cooperation Program.....	496
2.	TEXTOR Collaboration	499
3.	International Collaboration on Helical Fusion Research — IEA Stellarator Agreement —.....	501
4.	JSPS-CAS Core-University Program on Plasma and Fusion	511
IV.	Department of Engineering and Technical Services.....	518
V.	Department of Administration	530
APPENDIX 1.	Organization of the Institute.....	533
APPENDIX 2.	Members of Committees	534
APPENDIX 3.	List of Staff	535
APPENDIX 4.	List of Publications I (NIFS Series)	541
APPENDIX 5.	List of Publications II (Journals, etc.)	543
	Author Index	562
	How to Reach National Institute for Fusion Science.....	569

I. National Institute for Fusion Science in April 2004 – March 2005

On April 1, 2004, 5 major leading inter-university research institutes in the natural sciences, i.e., the National Astronomical Observatory, the Institute for Molecular Science, the National Institute for Basic Biology, the National Institute for Physiological Sciences and NIFS (the National Institute for Fusion Science) were consolidated and realigned into the National Institutes for Natural Sciences (NINS). NIFS continues to enhance its competence for scientific fusion research and also is becoming responsible for the exploration of much broader areas of scientific research beyond the boundaries of the existing fusion field through cooperation with universities.

This annual report summarizes the research activities at NIFS between April 2004 and March 2005. To promote mutual interaction with annexed research institutes of universities on an equal footing, the framework for bilateral coordinated collaboration research has been formed. A synergetic effect with the existing frameworks of general collaboration research and the Large Helical Device (LHD) program collaboration research is anticipated. About 400 collaborating studies have been implemented during the covered period.

The major programs at NIFS are (i) the experimental study of toroidal plasma confinement using the Large Helical Device (LHD) and (ii) theoretical research and computer simulations for study of the complex state and the nonlinear dynamics such as those seen in high temperature plasmas. These major projects are accompanied by unique supporting research. Advanced engineering and fusion reactor design studies are also strongly promoted.

The LHD is a heliotron type device with an intrinsic divertor. It is the largest superconducting fusion device in the world. The major goal of the LHD experiment is to demonstrate the high performance of helical plasmas in a reactor relevant plasma regime. The thorough exploration should lead to the establishment of not only a prospect for a helical fusion reactor but also a comprehensive understanding of toroidal plasmas. We completed the 8th experimental campaign in FY2004.

The plasma parameters as well as physical understanding have been progressing steadily since the beginning. The highlight achievement in the last experimental campaign in FY2004 is the long pulse operation by means of ion cyclotron resonant heating (ICRH). The pulse length has been prolonged to more than 30 minutes (precisely 1905 s) with the heating power of 680 kW. The total input energy for this discharge reached 1.3 GJ which is a world record in magnetic confinement experiments. This achievement can be attributed to physics optimization of the magnetic configuration to confine high-energy trapped particles and operational optimization to reduce accumulated heat flux by real time control of the plasma position. With a lower power using electron cyclotron heating alone (110kW), the pulse length exceeded 1 hour (3900s). Also, a steady extension of the operational envelope has been realized in plasma beta (4.3%) and ion temperature (13.5keV) by applying our knowledge to date. Diversified studies in LHD have elucidated the broad scope of steady-state high temperature plasmas. In particular, the issues of high density, particle control and its related confinement improvement, and particle & impurity transport have been highlighted in the last

experimental campaign.

LHD produced 7398 plasma discharges in FY2004, which verifies its potential to provide plentiful opportunities for scientific research. The reason of this high availability of operation is mainly attributed to the advantage of LHD plasmas without disruption. Infrastructure such as remote branches of the LHD control room using Super SINET has been developed steadily to facilitate collaboration. The logistics are methodically supported by three kinds of collaboration frameworks.

Experimental approaches to basic plasma physics have been continued in CHS and HYPER-I by putting emphasis on the clarification of structural flows such as zonal flows and viscous eddies.

Simulation studies in NIFS are oriented towards the exploration of “Simulation Science” while remaining founded in the large-scale simulation of fusion plasmas such as LHD. Activity in simulation is organized into three categories, i.e., complex fusion plasmas, basics processes in plasmas and simulation technology. Two examples among many interesting achievements are referred to here. In order to understand high beta discharges in LHD, the effect of the modification of the plasma boundary due to finite pressure has been discussed very rigorously, which has developed a system of MHD stability together with a fully 3-D nonlinear compressible MHD simulation. Also, global simulation by the high-accuracy gyrokinetic-Vlasov code is highlighted as a challenge to the problem of infinitesimal structure.

The reliability and robustness of the LHD superconducting magnet system has been confirmed by routine investigations over a 7-year long operation. In order to improve the cryostability of the LHD helical coil, application of subcooled helium by an additional cooler has been achieved in an R&D coil test and design study. The operating currents of the helical coils are expected to increase up to 12kA from 11.2kA by lowering the temperature to 3.5K.

The fusion engineering research center has extended the key-technology for an advanced blanket system. For example, FLiBe blanket technology has been developed under the US-J collaboration. Each key-technology is being integrated into the design of the LHD-type demonstration reactor FFHR (Force Free Helical Reactor).

A variety of coordinated research is managed by the coordinated research center. The three major activities are coordinated research with industries and with other institutions in NINS, and an atomic and molecular database. In addition, microwave sintering technology has been successfully applied to an industrial continuous kiln.

Finally, the Office of Fusion Science Archives has been organized as an official division in NIFS in view of the importance of historical documentation as well as experience in fusion research.



Osamu Motojima

Director-General

National Institute for Fusion Science

II. Research Activities

1. Large Helical Device (LHD) Project

1-1. LHD Experiment

(1) Overview of LHD Experiment

The main goal in the 8th experimental campaigns is to achieve long pulsed discharges with temperatures greater than 1 keV. In December 2004, a steady state plasma was successfully sustained for 31 min and 45 sec and the total injected heating energy was 1.28 GJ. Time evolutions of the plasma parameters are plotted in Fig. 1. The average input power was 680 kW (ICRF [38.47MHz] 520 kW, ECH 100 kW and NBI 60 kW. Note that the NBI heating is intermittent). The central temperature was around 2 keV and the line-averaged density was around $0.7 \sim 0.8 \times 10^{19} \text{ m}^{-3}$. The line average electron density was controlled with a He gas puffing rate using a measured microwave interferometer signal. But the electron density decreased by $\Delta n_e = 0.25 \times 10^{19} \text{ m}^{-3}$ during the NBI heating phase in spite of the gas puff feedback control. Before the 2003 campaign, the plasma duration time of the ICRF long-pulse experiment was limited by local temperature rise of the divertor carbon plates near the ICRF antenna section, and gradual increase of out-gassing from the wall finally terminated the plasma operation. Since then, a new mechanical structure and new carbon material sheets were added to suppress the temperature rise and the out-gassing rate. The hardware of ICRF heating was also improved. The LHD vacuum chamber was conditioned by boronization, which seemed to be effective in suppressing the impurity influx to a low level during the steady-state operations. The long-duration operation was made possible by introducing a sweeping technique for the magnetic axis position between 3.6 m and 3.7 m for spreading the heat load, resulting in lower temperature of the divertor plates.

Attempts to achieve higher beta plasma have been made. Capability to change the current center of the helical coil, the effective coil pitch allows us to change the minor radius and the iota profile. We find that the optimum coil pitch for high beta is around 1.2. (1.254 for the standard configuration). A beta value of 4.3 % has been maintained in

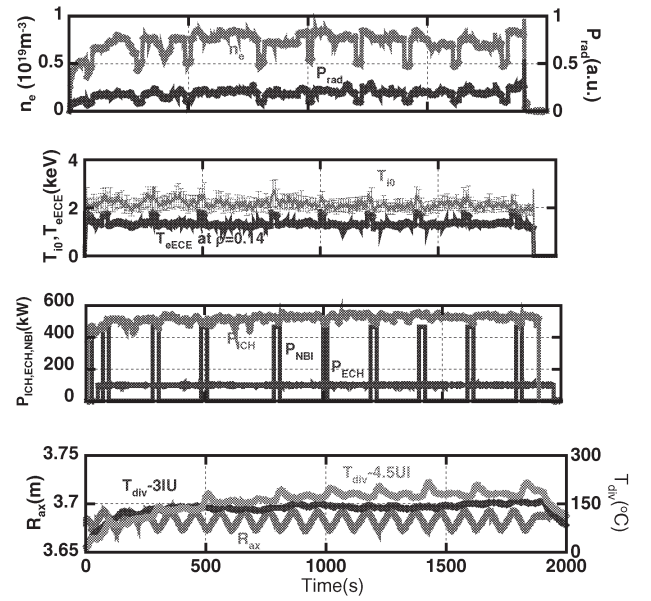


Fig.1 Time evolutions of plasma parameters and heating Power in the long-pulse plasma discharge of 1905s.

a nearly stationary discharge, in which the plasma density is maintained simply by the gas puff. With increasing β , the mode amplitude with $n/m = 1/1$ generally increases. It is intriguing that at $\beta \geq 3.0 \%$, the mode disappears, seemingly caused by a natural flattening of the electron temperature profile at $\iota/2\pi = 1$. The mode number ratio (n/m) of the observed magnetic fluctuation mode with the highest amplitude increases with increasing beta.

The basic divertor functions of the Local Island Divertor (LID) have been confirmed. Plasmas flowing outwards are found to be guided along the island separatrix to the divertor plates mounted on the divertor head. The particle pumping is so effective that the required gas puffing rate is an order of magnitude higher compared with non-LID discharge with the same density. One of the major objectives

is to achieve confinement improvement. There are a few promising observations. e.g., (i) The LID discharges with pellet fuelling exhibit density ITB (internal transport barrier) at $\iota/2\pi = 1/2$, leading to very high central density and high pressure plasma (ii) The electron temperature profile in LHD is generally characterized by a broad shape (close to parabolic). For low density (around $2 \times 10^{19} \text{m}^{-3}$) operation with the LID, the shape becomes even broader. In the edge region ($0.75 < \rho < 1.0$), the edge electron temperature gradient is higher by a factor of ~ 3 , compared with non-LID discharges.

We observed a bifurcation between equilibria with a large island (its width of up to 17 % of the minor radius) and without. A large island ($n/m=1/1$) generated by the external resonant field disappears suddenly when the beta at the rational surface exceeds a critical value, which is proportional to the applied resonant field strength.

A central ion temperature of 13 keV was obtained with good reproducibility by following a guiding principle that maximizing the absorbed power per ion results in the maximum ion temperature. High Z gas, i.e. neon and/or argon, was employed in such experiments.

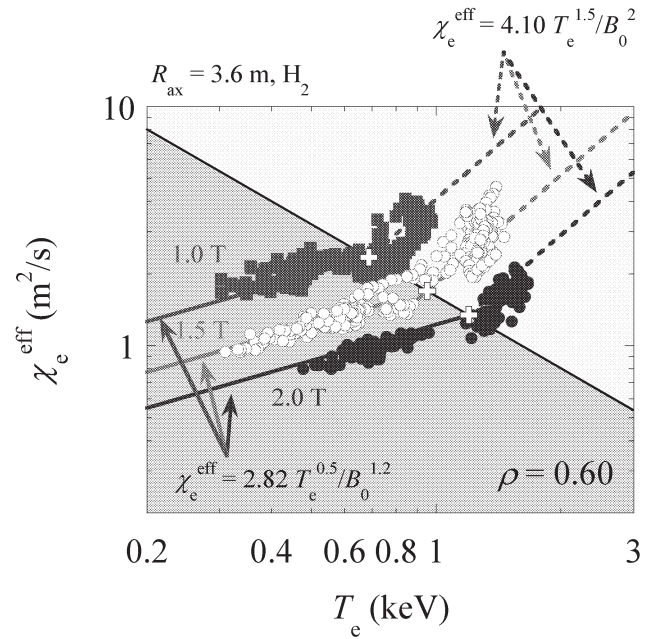
In the LHD discharges, it is difficult to maintain the detached plasma state. The plasma either becomes attached or shrinks and subsequently collapses. Under the certain conditions with $R_{\text{ax}} = 3.65\text{m}$, however, detached state of the plasma is triggered by massive gas puff and maintained for 2 seconds.

Systematic density and power scan experiment has been done to find out parametric (n , T_e , B) dependences of the effective thermal diffusivity (χ_e^{eff}) for hydrogen discharges with R_{ax} (the magnetic axis)=3.6m. Figure 2 depicts the temperature dependence of the χ_e^{eff} for fixed B (1, 1.5, 2T). There seems to exist two scalings for high and low temperature regimes respectively. For high temperature regime ($T_e > T_{\text{el}}$), gyro-Bohm type transport dominates, i.e., $\chi_e^{\text{eff}} = 4.10 \cdot T_e^{1.5} / B_0^2$. For low temperature regime ($T_e < T_{\text{el}}$), the thermal diffusivity has a weak temperature dependence, $\chi_e^{\text{eff}} = 2.82 \cdot T_e^{0.5} / B_0^{1.2}$.

Finally we summarize the maximum plasma parameters achieved in the LHD experiment.

PLASMA PARAMETERS ACHIEVED at LHD

Fusion triple product	$2.3 \times 10^{19} \text{keV m}^{-3} \text{s}$
Central electron temperature	10 keV at $n = 5 \times 10^{18} \text{m}^{-3}$
Central ion temperature	13.5 keV at $n = 3 \times 10^{18} \text{m}^{-3}$
Beta	4.3 % at $B = 0.45 \text{T}$
Pulse length	1 hr 5 min at $P = 110 \text{kW}$ 31 min 45 sec at $P = 680 \text{kW}$
Average density	$2.4 \times 10^{20} \text{m}^{-3}$



(Komori, A.)

(2) LHD Physics Experiments

§1. Half Hour Plasma Discharge

Kumazawa, R.

In the 8th LHD experimental campaign (2004), the steady-state discharge was selected as the main object of experiment and many trials were carried out.

Time evolutions of the plasma parameters of a typical long-pulse plasma discharge (#53776) are plotted in Fig.1; this is the discharge accompanying the largest input heating-energy so far achieved in the LHD. A plasma with an electron density $n_e=8 \times 10^{18} \text{ m}^{-3}$, an electron temperature at $\rho=0.14$ of $T_{eECE}=1.5 \text{ keV}$ and an ion temperature on the magnetic axis of $T_{i0}=2.0 \text{ keV}$ was produced with $P_{ICH}=0.51 \text{ MW}$, $P_{ECH}=0.1 \text{ MW}$ and averaged $P_{NNBI}=0.063 \text{ MW}$ (a ten times intermittent NNBI heating, i.e., $P_{NNBI}=0.45 \text{ MW}$ for 20-30s). The intermittent NNBI heating was done because when the magnetic axis was moved to the outside, the energy confinement time was deteriorated a little. Such long-pulse plasma discharges lasting a half hour were obtained in three successive discharges, i.e., #53775~#53777 with intermissions of about half an hour to cool down plasma-facing components. The key factor which led to the success of the long-pulse discharge was a swing of the magnetic axis, i.e., $R_{ax}=3.67 \text{ m} \sim 3.70 \text{ m}$ in the period of 100sec as shown in Fig.1. The dispersion of the plasma heat load to the divertors decreased the temperature to less than 250°C as shown in Fig.1. The line average electron density was controlled with a He gas-puffing rate using a measured micro-wave interferometer signal. The He gas-puffing rate was $0 \sim 0.5 \text{ Pam}^3/\text{s}$ depending on the electron density. The electron density decreased by $\Delta n_e=2.5 \times 10^{18} \text{ m}^{-3}$ during NNBI for 20~30s in spite of the He gas-puffing feedback control, which must be improved in the 9th experimental campaign. The plasma duration was 1905s, and the total injected heating energy was $W_h=1.29 \text{ GJ}$, which consisted of $W_{ICH}=0.98 \text{ GJ}$, $W_{ECH}=0.19 \text{ GJ}$ and $W_{NNBI}=0.12 \text{ GJ}$ in the discharge as shown in Fig.1. W_h exceeded 1GJ in the other two successive discharges.

Here an experimental method for achieving a long-pulse plasma discharge, i.e., 1905s is described. The temperature increase in the divertor plates was thought to be the main cause limiting the long-pulse plasma discharge. Therefore the method of reducing the temperature increase in divertor plates was employed. The magnetic axis affects the local plasma heat load to the divertor plates. The precise calculation suggests that the local heat load becomes broader when R_{ax} is located at $R_{ax} > 3.65 \text{ m}$. The average magnetic axis R_{axav} and the swing width ΔR_{ax} are important key factors in reducing the temperature increase, prolonging the pulse duration and subsequently increasing the heating energy W_h , as shown in Fig.2. R_{axav} was changed from $R_{ax}=3.55 \text{ m}$ to $R_{ax}=3.685 \text{ m}$. However R_{axav} and ΔR_{ax} were determined by the appearance of the hot spot observed at the side protector of the ICRF antenna. Therefore the outermost edge of the magnetic axis was limited to $R_{ax}=R_{axav}+\Delta R_{ax}=3.70 \text{ m}$. The further the magnetic axis is shifted outward within the

experimental range of R_{ax} , the larger is the total heating energy which can be input, as shown in Fig.2. At the beginning of the 8th experimental campaign a long-pulse plasma discharge was tried employing the fixed and the inward shifted R_{ax} because of the improved confinement. At this time the pulse duration was limited to 150sec and the input heating energy W_h was less than 0.2 GJ . When R_{axav} was located at more than $R_{axav}=3.65 \text{ m}$, the pulse length exceeded 10min. and W_h exceeded 0.4 GJ . Finally the pulse length and W_h exceeded 30min. and 1 GJ , as shown in Fig.2. W_h exceeded 1GJ in three discharges, which were the sequential discharges, i.e., #53775~53777 as already described.

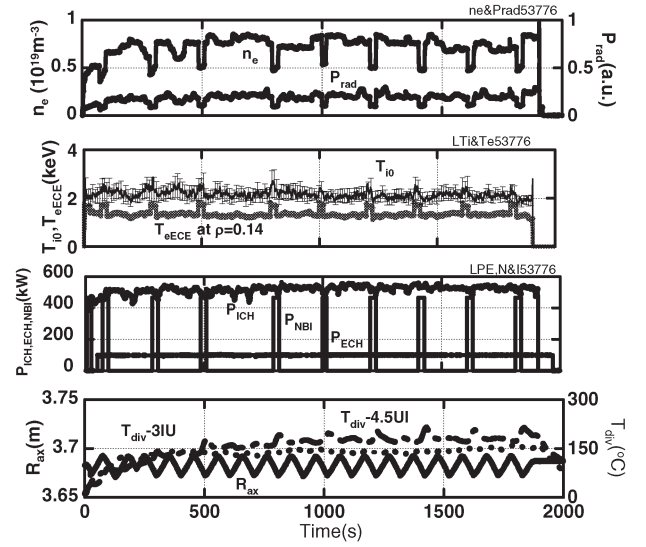


Fig.1 Time evolutions of plasma parameters and heating power in the long-pulse plasma discharge of 1905s.

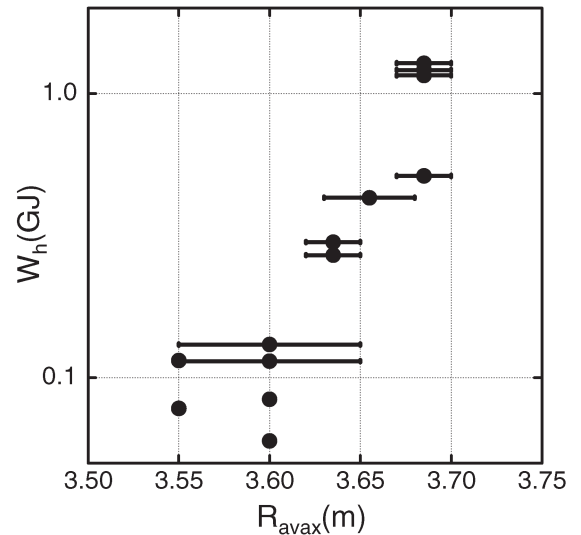


Fig.2 Total heating energy vs. average magnetic axis with the swing width.

§2. Plasma Collapse in the Long Pulse Plasma Discharge

Kumazawa, R.

The duration of the plasma discharge is limited by several factors including; 1) the work of the interlock systems, 2) the gradual increase in the uncontrollable density. Two abovementioned causes could be eliminated, by employing the feedback control in the liquid impedance matching systems and by reducing the out-gassing from the divertor plates employing a method of the magnetic axis swing.

At the present time the steady-state plasma discharge operation is confronted with the penetrated heavy impurities in the 8th experimental campaign, though a long-pulse discharge of more than 30min. was achieved. A typical example is shown in Fig.1, which was obtained at almost the end of the plasma discharge, i.e., at the time between 1640 and 1645sec. This discharge was one of three successive long-pulse discharges for half an hour within a few hours. A TV camera viewing through 6-T port projected an arcing at 7-I port on the time of 1641.34sec, as shown in Fig.2(a). After the arcing intensities of FeX (174.52nm), n_e and P_{rad} suddenly increase as shown in Fig.1. At the time of 1641.60sec (0.24sec after the arcing) the intensity of FeX showed its maximum, as shown in Fig.1. Then the plasma was judged extraordinary from the TV screen as shown in Fig.2(b). An increase in CIII (977.02nm) followed them at the time of the lower electron temperature. Although the reflected power did not exceed the interlock level, i.e., the reflected power fraction of 20% (as seen in the bottom of Fig.1), the RF power generator was turn off manually after the plasma, shown on a TV screen, was judged abnormal. The arcing was not found in the other two discharges among the successive three half-hour discharges. However the increase in n_e , P_{rad} and CIII were similarly found.

We examined the LHD vacuum wall and the divertor plates specially near the 7-I port. However we could not find any serious damage on the surface of the plasma facing components. However many thin stainless flakes were found at the 4.5 U & L ICRF heating antennas, which were not used in the 8th experimental campaign. It was thought that the thin stainless flake penetrated into the plasma and became a cause of the increase in the intensity of FeX. However it was not understood why the thin stainless flakes were produced in the unused ICRF heating antennas.

We propose a method to continue the long-pulse discharge even in penetrating the heavy impurity and increasing P_{rad} : An additional ECH power can be injected triggered by a sudden increase in plasma signal, e.g., P_{rad} and n_e etc.. The plasma will be restored by an additional ECH power, e.g., 0.5MW for 0.5s. This trial will be tried in the next 9th experimental campaign.

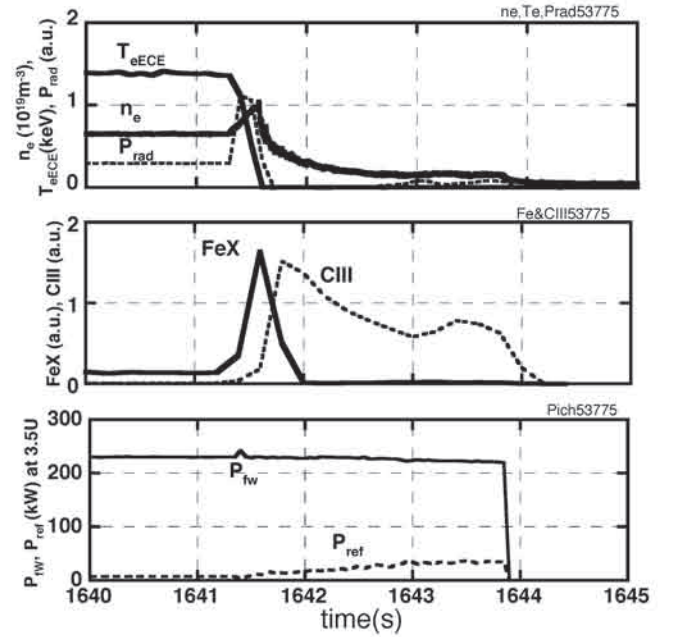


Fig.1 Time evolution of plasma parameters, and P_{fw} and P_{ref} in the plasma collapse due to penetrated Fe ions.

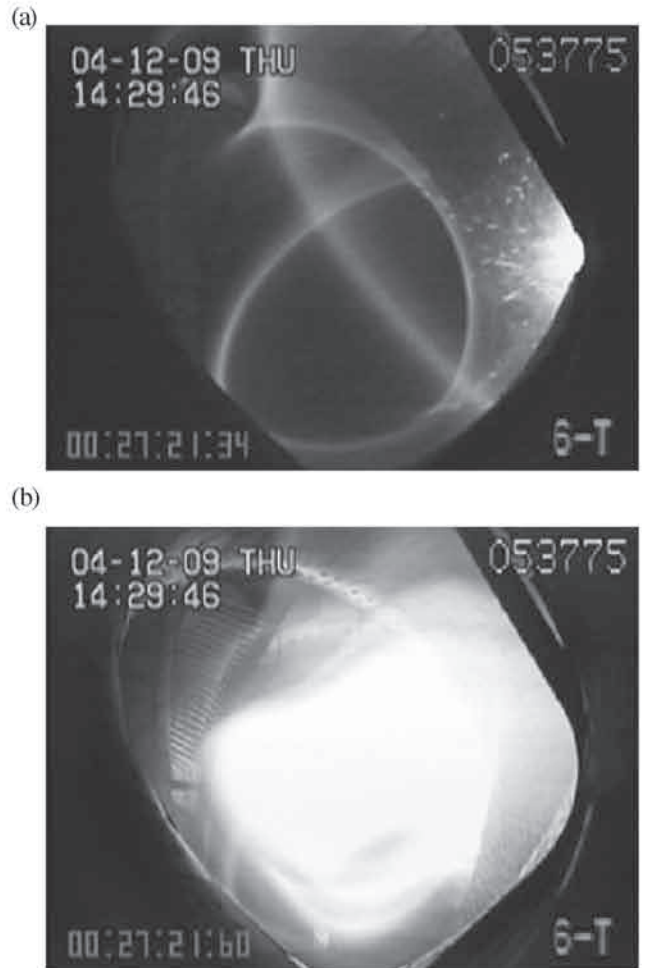


Fig.2 (a) Observed arcing at 1641.32s.
(b) Maximum intensity of Fe X at 1641.60s.

§3. Termination of Steady State Plasmas Caused by Penetration of Impurity Metal Flakes

Nakamura, Y., Sato, K., Mutoh, T., Kumazawa, R., LHD Experimental Group

Steady state divertor operation with high performance plasmas ($n_e \sim 0.7 \times 10^{19} \text{ cm}^{-3}$, $T_i \sim 2 \text{ keV}$) was demonstrated for half an hour in the superconducting helical device LHD. The high performance plasmas have been sustained with an averaged heating power of 680 kW and achieved an injected energy exceeding 1.3 GJ. Long pulse experiments so far have been performed in the magnetic configuration with $R = 3.6 \text{ m}$ for NBI and ICH discharges. In the last experimental campaign, the optimum operational regime for long pulse ICH discharges was investigated by changing the magnetic axis during the discharge. As a result, we found the best operational regime in a magnetic configuration with $R = 3.67 \sim 3.7 \text{ m}$ as shown in Fig. 1. In the inward shifted magnetic configuration ($R = 3.55 \sim 3.6 \text{ m}$), the discharge duration was limited to 160 s without any gradual density increase, which was observed in the previous experiments. As the magnetic axis moves outward, the discharge duration was extended, and then thirty minutes discharges were achieved by using a real-time magnetic axis swing with $R = 3.67 \sim 3.7 \text{ m}$. In course of this experiment, we observed an abrupt termination of steady state plasmas without any trouble in the heating system. Therefore, we investigate the reason why the plasma is terminated unexpectedly.

Figure 2 shows a time history of steady state plasma just before the unexpected discharge termination. Unlike a normal discharge, the abrupt increase of density and radiation was observed in spite of constant heating power input. At this timing, there is no such a large increase of helium and hydrogen particle influx. The plasma temperature extremely decreases with increasing the radiation and it leads to a radiation collapse. After that, an extremely low temperature plasma was sustained for about 1 s. On the other hand, we observe the plasma with TV cameras at various positions and more frequently we can see something like a flake heated in the plasma just before the termination of the discharge. Therefore, in order to investigate which material comes into the plasma, spectroscopic measurements are carried out by observing visible lines and vacuum ultra violet (VUV) lines. As indicated in the last column in Fig. 2, it is found that the metallic impurity (mainly iron) line intensities not but light impurity ones increase suddenly at the same time as the increase of density and radiation. The spectral analysis indicates that highly ionized iron lines (FeXXIII etc.) are prominent in the steady state phase and low ionized lines (FeX etc.) explosively appear in the plasma termination phase. The penetration of metallic flakes makes a dramatic

change in the profiles of electron temperature and density as shown in Fig. 3. The steady state plasma has a relatively smooth profile for temperature and density, respectively. However, a step-wise sharp density profile and a fast shrinking of temperature profile appear by penetrating the metal flake into the plasma. These events can be seen in most of long pulse discharges terminated unexpectedly. Most probably, steady state discharges are limited by the penetration of metal flakes into the plasma.

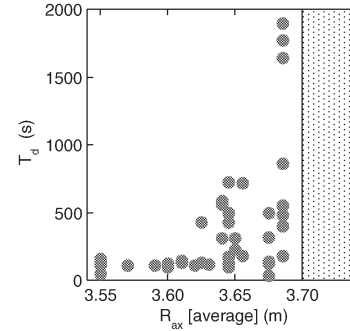


Fig. 1. Dependence of discharge duration on operational regime (magnetic axis)

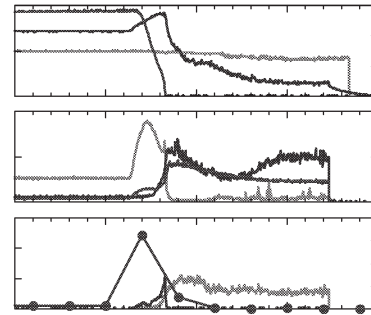


Fig. 2. Time history of long pulse discharge just before unexpected plasma termination

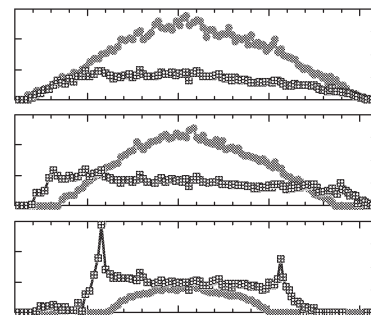


Fig. 3. Radial profiles of temperature and density before and after the abrupt increase of radiation

§4. Control of Divertor Heat Load by Real-time Magnetic Axis Swing in Steady State Operation

Nakamura, Y., Masuzaki, S., Chikaraishi, H., Kumazawa, R., Mutoh, T., LHD Experimental Group

Significant progress has been recorded at LHD. In high power operation with a combination of ICH, ECH and intermittent NBI, the plasma with the temperature of more than 1 keV has been sustained over 31 min 45 sec. Steady-state divertor operation unlike limiter discharges in TRIAM and Tore Supra has been achieved.

Long pulse discharges with the heating power of less than 1 MW have been successfully achieved over 2 min. However, an uncontrollable density increase due to outgassing from divertor components was observed, when the injected energy exceeded about 75 MJ. As a result, the plasma was terminated by a radiation collapse. Strong nonuniformity in divertor heat flux distribution along divertor leg trace was observed. Such a toroidal nonuniformity is connected with the existence of ergodic region just outside the last closed flux surface (LCFS), which depends on the magnetic configuration (magnetic axis). Therefore, in 2004 experimental campaign, an optimum toroidal repartition of divertor heat flux has been attempted by changing the magnetic axis and it has enabled us to access a steady-state regime with a safety level for actively cooled divertor plates.

Figure 1 shows the dependence of divertor heat flux on the magnetic axis. We measured the temperature increase of divertor plates located at the inboard and top of the torus for the discharges with the same plasma parameters in different magnetic axis. In the inward shifted configuration ($R = 3.6$ m), the divertor flux is concentrated on the inboard side as expected by calculation. As the magnetic axis is moved outward, the concentrated location changes from inboard side to top one. From this figure, it is found that it might be reasonable to operate in the magnetic configuration with $R = 3.65 - 3.7$ m from the view point of non-localization of divertor heat flux. The optimum operational regime for steady state operation was explored by changing the magnetic axis during the discharge. As a result, thirty minutes discharges were achieved by using a new technique of real-time magnetic axis swing within $R = 3.67-3.7$ m. In those discharges, the divertor heat flux was dispersed along the divertor leg trace as shown in Fig. 2. The concentration of heat flux observed on the inboard side of the torus, in particular, near the ICRF antennas, was evaded and all measured divertor temperatures were reduced within 200°C , which is a safety level of actively cooled divertor plates. Power balance in the divertor was also analyzed by using a calorimetric method, in which the exhaust power is measured with the difference between the input and output water temperatures and the flow rate. The

cooling channel is divided into ten sections along the divertor trace and passes through the inboard and the outboard sides of the torus alternately. Figure 3 shows the distribution of divertor heat load along each divertor leg trace. We can find that there is still a nonuniformity in the divertor heat flux. This may be related to the loss of high-energy ions accelerated at the ion cyclotron resonance layer near ICRF antennas. The particle orbit calculation is now under investigation. The total power exhausted in the divertor is 310 kW and the radiation power is 102 kW. The averaged injection power can be estimated to be 425 kW from the absorption efficiency for each heating method. The energy flow through the plasma is almost completely accounted.

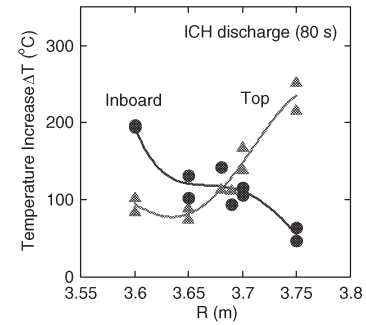


Fig. 1. Dependence of divertor heat flux on Magnetic axis

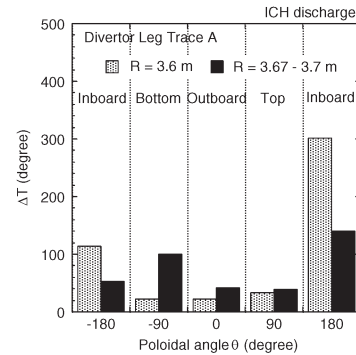


Fig. 2. Repartition of heat flux along a divertor leg trace

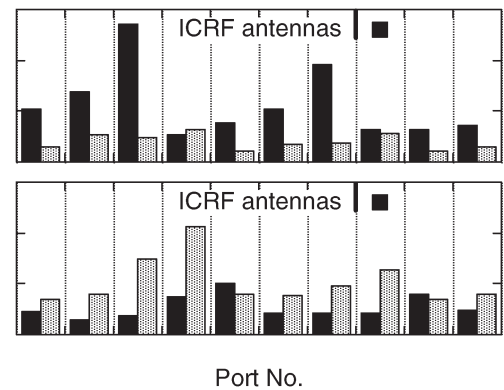


Fig. 3. Distribution of divertor heat load along each divertor leg trace

§5. Sustainment of keV-order Stable Plasma by ECH Over One Hour on LHD

Yoshimura, Y., Kubo, S., Shimosuma, T., Igami, H., Kobayashi, S., Ito, S., Mizuno, Y., Takita, Y., Notake, T., Ohkubo, K., Mutoh, T., Nakamura, Y., Inagaki, S., Kojima, M., Tokuzawa, T., Nakanishi, H., Miyazawa, J.

Stable and continuous plasma sustainment is one of the main goals of LHD project. So far long-pulse operation has been tried and a 756 second plasma sustainment was achieved in the 7th experimental campaign in F. Y. 2003. In that case, the pressure inside the evacuated waveguide gradually increased during the power transmission up to the interlock threshold level 1.3 Pa so that the power transmission was terminated. The temperature all over the transmission line was much increased up to 100 degrees by transmission loss.

During the maintenance period between the 7th and 8th campaigns, two major modifications on the transmission line were performed. To enforce evacuation, straight waveguides were replaced by pumpout-tees at eight positions. Each new pumpout-tee was connected to an common evacuated duct or turbo pumps. To remove the transmission loss energy on the waveguides, almost all the surface of the waveguides and their couplings were covered with water cooled thin copper jackets except supported positions.

Previous to a trial of the long pulse discharge, magnetic axis position scanning experiment was performed to search an optimized experimental configuration. Referring to the result of the configuration optimizing experiment shown in Fig. 1, the trial of the CW plasma sustainment was performed with $R_{ax}=3.6$ m and $B_{ax}=1.5$ T. For the long pulse discharge, data acquisition settings such as sampling time were changed so that the data could be processed for 3932 seconds (30 ms sampling, 128 kword).

At first, using several shots of duration up to a few hundred seconds, optimized gas flow rate was searched and gradual increase with an increment step of 0.0002 Pam^3/s for every 5 seconds up to 0.003 Pam^3/s was determined. Then the discharge #56068 was started with this gas fueling scenario. Plasma start up was supported by 82.7 GHz power of total 420 kW, 300 ms pulses and the CW power sustained the plasma. Waveforms of ECH power monitor output, gas flow rate, line averaged electron density and electron temperature measured with ECE system are plotted in Fig. 2. Until about 1900 seconds, density was kept nearly constant at $1.5 \times 10^{18} / \text{m}^3$ though the gas flow rate was controlled sometimes to compensate gradual decrease of the density.

At about 1900 seconds, gas flow rate was increased for trial of plasma sustainment at higher density. However, increase of gas flow rate up to 0.006 Pam^3/s caused uncontrollable density increase up to $3.2 \times 10^{18} / \text{m}^3$ and the flow rate was decreased again. Three more times increasing the density was tried. However at each trial rapid density increase occurred and keeping the density at moderate level could not accomplished with the ECH power of 110 kW.

Excluding those density increases by high-density trials the plasma could be much stable, and except for the limitation on data acquisition the discharge could be continued longer.

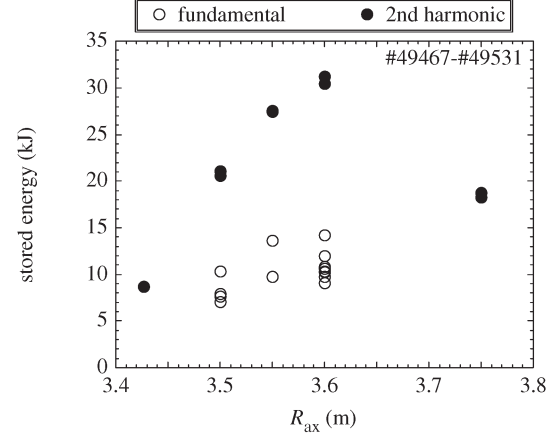


Fig. 1. Result of magnetic axis scanning experiment searching the optimized configuration for CW-ECH experiment. Closed circles denote the maximum stored energy at each magnetic axis position with on-axis 2nd harmonic resonance conditions, and the open circles with higher field conditions.

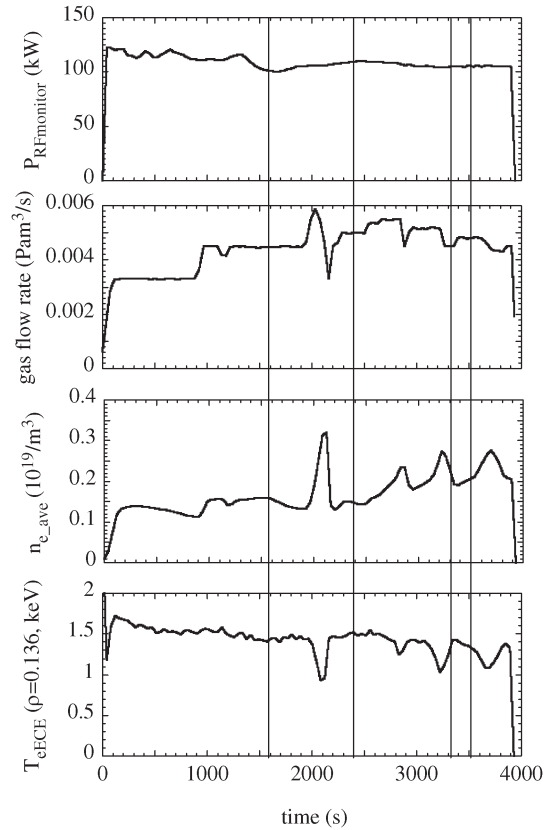


Fig. 2. Waveforms in the 3900 second discharge. Top column is a plot of injection power evaluated from power monitor on a miterbend, the second: gas flow rate, the third: line averaged electron density and the bottom: electron temperature measured with ECE system.

§6. Dynamic and Static Properties of Wall Recycling in the Long Duration Discharges

Sakamoto, M., (Advanced Fusion Research Center,
Research Institute for Applied Mechanics,
Kyushu Univ.)
LHD Experimental Group

The achievement of the stable long pulse operation is one of the requirements for the future fusion reactor. The global particle balance in the main chamber and its control are critical in achieving the steady state operation. The control of the global particle balance depends on the wall recycling. The wall recycling changes with a long time constant depending on the wall condition. However, not only the wall condition but also plasma condition (e.g., particle flux out of the plasma) influences the wall recycling property. In such transient phenomena as edge localized modes or the pellet injection, the wall would considerably contribute for pumping the particle flux out of the plasma. In TRIAM-1M, it has been observed that there exists a quite large difference between properties of wall recycling in the static condition (i.e. the continuous gas feed case) and the dynamic condition (i.e. the additional gas puff case) [1]. In this time, similar experiments were carried out on LHD to promote better understanding of the wall recycling.

Figure 1 shows the time evolution of the line averaged electron density \bar{n}_e in the cases of additional gas puffs and gas feed termination in plasmas heated by NBI of which beam direction is CCW. The additional gas puffs were carried out five times at the interval of 5 s as shown by the arrows in the figure. The gas feed was stopped at $t \sim 5$ s, 15 s and 25 s in separate discharges. The decay time of \bar{n}_e after the gas puff (i.e. dynamic condition) and the termination of the gas feed (i.e. static condition) means the effective particle confinement time τ_p^* and it is a good scale for the evaluation of the wall recycling, since it is defined as $\tau_p^* / (1 - R)$, where τ_p is a particle confinement time and R is a recycling coefficient. Figure 2 shows the density decay time in the dynamic and static conditions as a function of the discharge duration. Clear difference can be seen between both conditions. The decay time in the static condition increases with the discharge duration and it seems to saturate after $t \sim 15$ s. That in the dynamic condition slightly increases with the discharge duration. The large difference of the density decay time between both conditions is similar to the result of TRIAM-1M.

On the other hand, when another NBI system of which beam direction is CW is used, no clear difference between both conditions can be seen as shown in Fig.3. In this case, the density decay time of the static condition is almost the same as that of CCW NBI plasma. However, that

of the dynamic condition is larger than that of the CCW NBI plasma. It may suggest that the behavior of the particle confinement time against the gas puff is different between CW and CCW NBI plasmas.

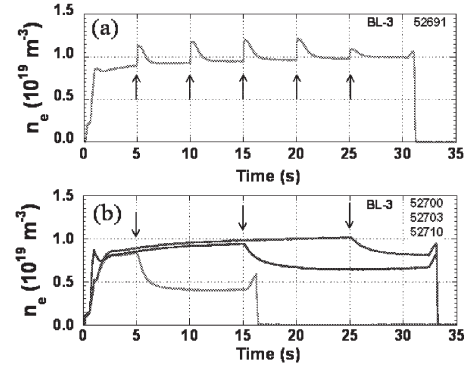


Fig.1 Time evolution of the line averaged electron density in the cases of the gas puffs (a) and the gas feed termination.

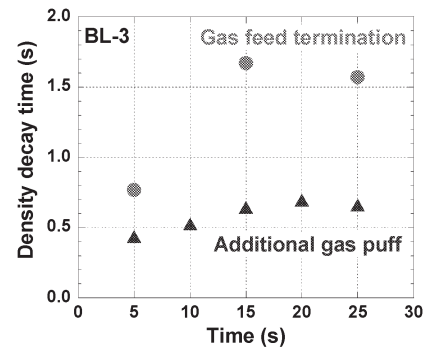


Fig.2 Density decay time in cases of the gas puff and the gas feed termination. The plasma is heated by NBI of which beam direction is CCW.

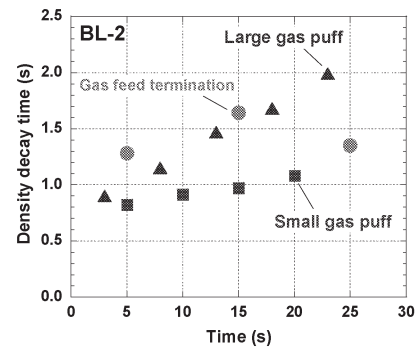


Fig.3 Density decay time in cases of the gas puff and the gas feed termination. The plasma is heated by NBI of which beam direction is CW.

Reference

- 1) Sakamoto, M. et al., J. Nucl. Mater. 313, (2003) 519.

§7. Characterization of Energy Confinement Using Extended International Stellarator Confinement Database

Yamada, H., Yokoyama, M., Watanabe, K.Y., Suzuki, Y., Harris, J.H. (Australian National Univ., Australia)
Dinklage, A., Beidler, C.D., Kus, A. (Max-Planck-Institut für Plasmaphysik, EURATOM Association, Germany)
Ascasibar, E., Tribaldos, V. (CIEMAT, Spain)
Sano, F., Murakami, S. (Kyoto Univ.)

International collaboration on development of a stellarator confinement database has progressed. More than 3000 data points from major 9 stellarator experiments have been compiled. In order to express the energy confinement in a unified scaling law, systematic differences in each subgroup are quantified (see Table 1). An a posteriori approach using a confinement enhancement factor on ISS95 as a renormalizing configuration-dependent parameter yields a new scaling expression ISS04 (see Fig.1);

$$\tau_E^{ISS04} = 0.134 a^{2.28} R^{0.64} P^{-0.61} \bar{n}_e^{0.54} B^{0.84} \epsilon_{2/3}^{0.41}.$$

Gyro-Bohm characteristic similar to ISS95 has been confirmed for the extended database with a wider ranger of plasmas parameters and magnetic configurations than in the study of ISS95.

It has also been discovered that there is a systematic offset of energy confinement between magnetic configurations and its measure correlates with the effective helical ripple of the external stellarator field. Another potential geometrical parameter related to a renormalization factor is that given for the neoclassical flux in the plateau regime. This plateau factor corresponds to the effect of elongation in tokamaks. Lackner-Gottardi scaling, which is close to ISS95, was derived from this theoretical approach. An equivalent formulation covering stellarator geometry is available in Ref.[1]. Here the geometrical factor characterizing a particular stellarator is the ratio of the dimensionless fluxes for the multi-harmonic stellarator field to that for tokamaks with only toroidal ripple of a/R , expressed as $\Gamma_{stell}/\Gamma_{tok}$.

Figure 2 shows the correlation of this plateau factor $\Gamma_{stell}/\Gamma_{tok}$ with the enhancement of confinement times with respect to the unified scaling law ISS04. There seems to be a correlation. However, the plateau factor is closely related to plasma elongation and an elongation scan in LHD ($\kappa=0.8-1.4$) has excluded this collinearity, which has not indicated significance of dependence (compare closed and open diamonds in Fig.2). Therefore, ϵ_{eff} is more likely to be the essential configuration factor than is the plateau factor. It should be noted that both ϵ_{eff} and $\Gamma_{stell}/\Gamma_{tok}$ are measures of the difference between drift surfaces and magnetic flux surfaces.

Full documentation of the international stellarator confinement database is available at <http://iscdb.nifs.ac.jp/> and <http://www.ipp.mpg.de/ISS>.

Device	f_{ren}
ATF	0.43 ± 0.09
CHS	0.43 ± 0.08
Heliotron-E	0.44 ± 0.09
ATF/CHS/Heliotron E	0.43 ± 0.09
Heliotron-J	0.58 ± 0.23
LHD $R_{ax} = 3.6$	0.93 ± 0.15
LHD $R_{ax} = 3.75$	0.67 ± 0.06
LHD $R_{ax} = 3.9$	0.48 ± 0.05
LHD $\kappa = 0.8$	0.71 ± 0.05
LHD $\kappa = 1.4$	0.70 ± 0.11
TJ-II	0.25 ± 0.04
W7-A	0.71 ± 0.19
W7-AS $\epsilon_{2/3} < 0.48$	1.00 ± 0.27
W7-AS $\epsilon_{2/3} \geq 0.48$	0.79 ± 0.19
W7-AS high β	0.92 ± 0.18

Table 1 Renormalization factors

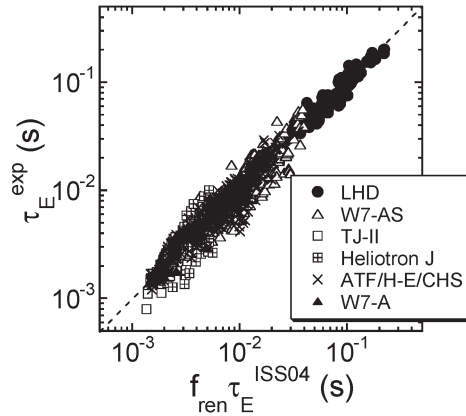


Fig.1 Comparison of energy confinement times in experiments with prediction from ISS04

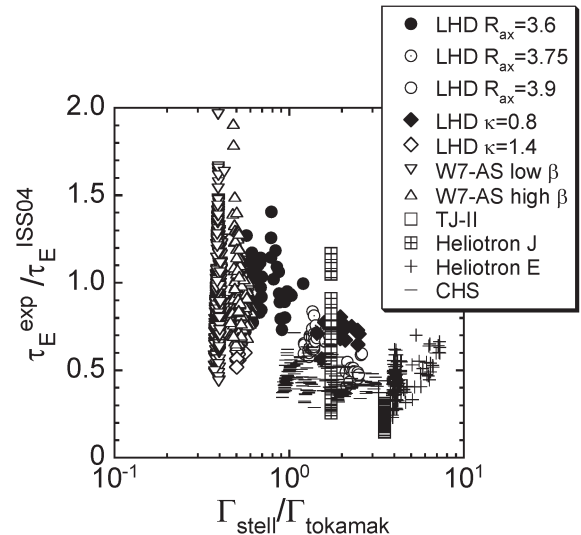


Fig.2 Confinement enhancement factors on ISS04 as a function of $\Gamma_{stell}/\Gamma_{tok}$ at $r/a=2/3$.

Reference

- 1) Rodriguez-Solano, R., Shaing, K.C., Phys. Fluids **30** (1987) 462.

§8. New Global Confinement Scaling for High-Density LHD Plasmas

Miyazawa J., Yamada H., Funaba H.
Murakami S. (Kyoto Univ.)

Systematic density and power scan experiment has been carried out at various magnetic field strength, to investigate the temperature and magnetic field dependences of the thermal diffusivity. In the experiment discussed here, B_0 is varied as 1.0, 1.5, and 2.0 T, while the magnetic configuration is fixed to $R_{ax} = 3.6$ m. Plasmas are heated by negative-ion based neutral beam (NB) injection. One or two tangential beam lines are used in the B_0 scan experiment and the total heating power is varied from 2 to 5 MW. The density is scanned by hydrogen gas puffing.

In Fig. 1, depicted are the effective electron thermal diffusivity, χ_e^{eff} , versus T_e , obtained after the B_0 scan experiment. The weak ($\chi_e^{\text{eff}} \propto T_e^{0.5}$) and gyro-Bohm like ($\chi_e^{\text{eff}} \propto T_e^{1.5}$) temperature dependences are recognized for each datasets at different B_0 . To estimate the inflection temperature, T_{e1} , where the temperature dependence of χ_e^{eff} changes from $\chi_e^{\text{eff}} \propto T_e^{0.5}$ to $\chi_e^{\text{eff}} \propto T_e^{1.5}$, a set of models below is assumed;

$$\chi_e^{\text{eff}} = C_1 T_e^{0.5} / B_0^\alpha \quad (T_e \leq T_{e1}), \quad (1)$$

$$\chi_e^{\text{eff}} = C_2 T_e^{1.5} / B_0^2 \quad (T_e > T_{e1}). \quad (2)$$

Below the inflection temperature, χ_e^{eff} increases with $C_1 T_e^{0.5}$ and decreases with an unknown B_0 dependence of an index α . Note that $\alpha = 1.0 \pm 0.2$ was obtained in the former study [1]. Above the inflection temperature, we simply assume the gyro-Bohm model with a factor C_2 . Three parameters of C_1 , C_2 and α are determined at each $\rho (= r/a)$, to give the minimum standard deviation, σ , of the experimental χ_e^{eff} compared with the model. From the fitting results, we conclude $\alpha = 1.2 \pm 0.1$, which is consistent with the former result of $\alpha = 1.0 \pm 0.2$, while the ambiguity is reduced. Examples of the fitting are also shown in Fig. 1, by solid and broken lines.

To obtain a dimensionally correct expression, another dependence on the minor radius of $\chi_e^{\text{eff}} \propto a^{-0.5}$ should be introduced to Eq. (1) as below;

$$\chi_e^{\text{eff}} \propto (T_e/a)^{0.5} / B_0^{1.2}. \quad (3)$$

Assuming $\tau_E^{\text{HD}} \propto a^2/\chi_e^{\text{eff}}$, Eq. (3) is transformed to

$$\tau_E^{\text{HD}} \propto P_{\text{tot}}^{-1/3} \langle n_e \rangle^{1/3} B_0^{4/5} a^{7/3} R^{1/3}. \quad (4)$$

where P_{tot} , $\langle n_e \rangle$, and R denote the total heating power, the volume-averaged electron density, and the plasma major radius, respectively.

According to Eq. (4), the plasma stored energy should be expressed by the HD (High-Density) scaling below;

$$W_p^{\text{HD}} = C \langle P_{\text{dep}} \rangle^{2/3} \langle n_e \rangle^{1/3} B_0^{4/5} a_{\text{eff}}^{7/3} R_{\text{ax}}^{1/3}, \quad (5)$$

where units of W_p^{HD} , $\langle P_{\text{dep}} \rangle$, $\langle n_e \rangle$, B_0 , a_{eff} , and R_{ax} are kJ, MW, 10^{19} m^{-3} , T, m, and m, respectively. To include the NB deposition profile effect, which becomes shallower in the

high-density regime, the volume average of the NB deposition profile, $\langle P_{\text{dep}} \rangle$, is adopted as an index of the heating power. An effective minor radius, a_{eff} is defined by a product of a and $\rho_{100\text{eV}}$, where $\rho_{100\text{eV}}$ is the average of ρ where T_e ranges from 50 to 150 eV. This T_e range is chosen because the reliability of our Thomson scattering system is assured at $T_e > 30$ eV. In our database, the effective minor radius is distributing within roughly $\pm 5\%$ of 0.64 m, which corresponds to a in the vacuum configuration. As for the major radius, we adopt R_{ax} for simplicity. This scaling is compared with the datasets of B_0 scan experiment in Fig. 2. The factor $C = 140$ is determined by the least square method using this data. As seen in the figure, the HD scaling well matches with the experiment.

Compared with ISS95 ($\tau_E^{\text{ISS95}} \propto n^{0.51} P^{-0.59}$), the HD scaling has weaker density dependence ($\tau_E^{\text{HD}} \propto n^{1/3}$). However, it should be noted that the HD scaling is still favorable since the density dependence is positive and, especially, the power degradation is weak ($\tau_E^{\text{HD}} \propto P^{-1/3}$).

Reference

- [1] J. Miyazawa *et al.*, Plasma Phys. Control. Fusion **47**, 801 (2005).

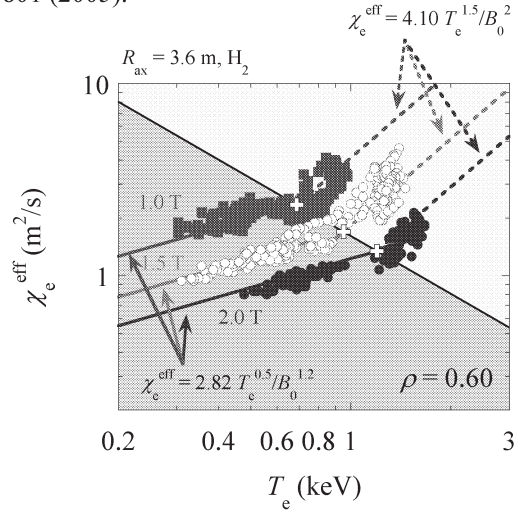


Fig. 1. T_e dependence of χ_e^{eff} at various B_0 . Solid and broken lines show fitting results with $\alpha = 1.2$.

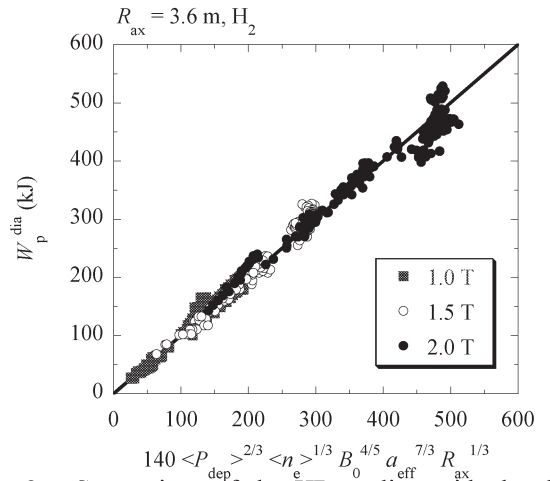


Fig. 2. Comparison of the HD scaling with the data from the B_0 scan experiment.

§9. Global Energy Confinement Properties in LHD High Beta Plasmas

Watanabe, K.Y., Funaba, H., Yamada, H.

In recent LHD experiments, the highest operational averaged beta value has been expanded up to 4.3% by increasing the heating capability and exploring a new magnetic configuration with a high aspect ratio. Although the MHD stability properties are considered to be unfavourable in the new high aspect configuration, the heating efficiency due to neutral beams and the transport properties are expected to be favourable in a high beta range. Here we study the global energy confinement properties in LHD high beta plasmas.

Figure 1 shows the improvement factor (H_{ISS}) of the global energy confinement time with respect to the ISS95 (International Stellarator Scaling 1995) empirical scaling in the new high aspect configuration ($R_{ax}^V=3.6m/A_p=6.3$) as a function of $\langle\beta_{dia}\rangle$. Here $H_{ISS-dia}$ and $H_{ISS-kin}$ are based on the diamagnetic flux measurement and the electron temperature and density profile measurements under the assumption of $Z_{eff}=1$ and $T_i=T_e$, respectively. Z_{eff} , T_i and T_e are the effective electric charge, the ion and the electron temperature, respectively. The $\langle\beta_{dia}\rangle$ is estimated based on the diamagnetic energy. A disruptive degradation of both global energy confinement times based on the diamagnetic flux measurement and the profile measurements have not been observed up to $\langle\beta_{dia}\rangle \sim 4\%$. However, the enhancement factors are gradually reduced as beta increases. In Fig.1, $H_{ISS-dia}$ is better than $H_{ISS-kin}$, especially in high beta range. One of the reasons is why the beam contribution to the beta value.

As shown in Fig.1, though a gradual degradation of a global energy confinement on beta value is observed based on the ISS95 transport model, the disruptive degradation of the global confinement has not been observed around $\langle\beta_{dia}\rangle=3-4\%$, where the global ideal MHD modes is predicted to be marginally unstable. Figure 2 shows the electron density normalized by a density limit scaling proposed by Sudo et al. [1], H_{Sudo} , as a function of the beta value. High beta discharges are done in a high collisionality range close to the density limit, $H_{Sudo} > 0.5$ in $\langle\beta_{dia}\rangle > 2\%$ and $H_{Sudo} \sim 1$ in $\langle\beta_{dia}\rangle \sim 4\%$. According to a recent LHD transport scaling analysis at high collisionality [2], the dependence of the global energy confinement time on the electron density changes from the ISS95 scaling, $\tau_E \sim n_e^{0.51}$ in the low collisionality range to $\tau_E \sim n_e^{0.28}$ in the high collisionality range. Figure 3 shows the results when the above new scaling law is applied to $H_{ISS-kin}$ (closed squares) in Fig.1 for the data with $H_{Sudo} > 0.5$. Closed squares, open squares and open triangles correspond to $H_{Sudo} < 0.5$, $0.5 < H_{Sudo} < 0.7$ and $H_{Sudo} > 0.7$, respectively. The scatter of data in the low beta range becomes smaller than that in Fig.1. However, the degradation in the high beta range, $\langle\beta_{dia}\rangle = 2-4\%$, is still observed, where the beta gradients in the peripheral region are in the Mercier unstable region ($\langle\beta_{dia}\rangle > 2\%$). The above suggests the possibility that the high

mode number ideal MHD instabilities affects the global confinement. As other explanations of the degradation, the high number resistive MHD instabilities and the invasion of stochastic region are considered. Further study on the degradation mechanism is also one of our important future subjects.

[1] Sudo S. et al 1990 Nucl. Fusion 30 11

[2] Miyazawa J. et al 2005 J. Plasma and Fusion Res. 81 302

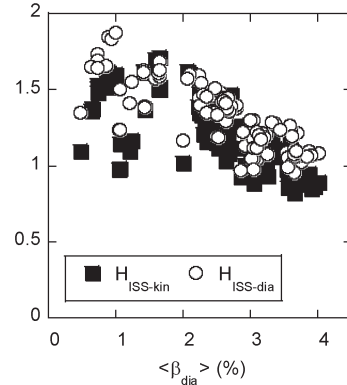


Fig.1 The beta dependence of the improvement factor of the global energy confinement time with respect to the ISS95 empirical scaling.

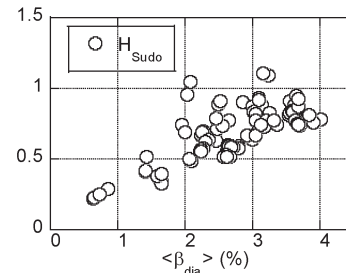


Fig.2 The electron density normalized to a density limit model proposed by Sudo et al. as a function of the beta value.

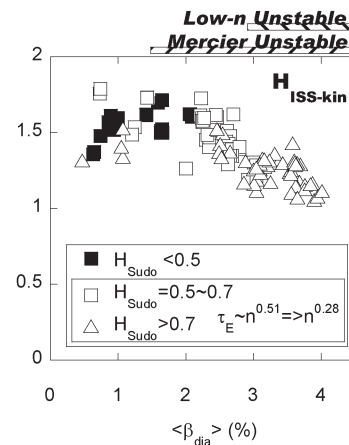


Fig.3 The modified beta dependence of the improvement factor of the global energy confinement time based on a new scaling in the high collisionality regime.

§10. Features of Non-Local Electron Heat Transport in LHD

Inagaki, S., Nagayama, Y., Kawahata, K.

It is presumed that local turbulence led by local microinstability drives local transport. Several recent experiments in LHD, however, point to the importance of non-local effects in the turbulent-induced transport. It has been observed that the non-local response to edge cold pulses often have reversed polarity, with the core T_e increasing in response to edge cooling as well as in tokamaks. The reported features of the non-local T_e rise observed in LHD are, (1) This phenomenon is observed in plasmas sustained by ECH, NBI and NBI+ECH, (2) The non-local response is also observed in the e-ITB plasmas. In this report, the newly obtained features of non-local transport in LHD are described.

The strong non-local effect is usually observed by TESPEL injection in LHD. The similar improvement of confinement induced by pellet or impurity injection (e.g. PEP-mode RI-mode) has been observed in tokamaks. Similarities and differences between these modes and the non-local phenomena will help to make a physical picture of the turbulence. The non-local T_e rises are observed not only by TESPEL injection but also by shallow pellets injection as shown in Fig. 1. The TESPEL contains impurity (e.g. C and Ti) but pellet is consists of pure H, and thus little importance of impurity is suggested. The particle source profile and/or density profile is also considered to be irrelevant to the non-local transport mechanism because the change in density induced by TESPEL or shallow pellet injection is negligible small ($< 10\%$).

The non-local T_e rises are observed in low collisionality (high T_e and low n_e) plasmas in LHD as shown in Fig. 2. This result is qualitatively consistent with TFTR scaling. There are no qualitative differences of non-locality between Co- and Ctr-NBI plasmas in LHD. The similarities of non-locality between tokamaks and LHD and Co- and Ctr-NBI plasmas allow us to conclude that the magnetic shear is not important in the non-local transport. There are some differences of non-locality between tokamaks and LHD and they are important for understanding non-local transport. The non-local effect is unclear in the auxially heated tokamak plasmas, while it tend to be strong in high power density (low collisionality) LHD plasmas. It has been observed that the non-local effect takes place more easily in small rather than large tokamaks. In helical systems, however, no observation has been reported in small devices.

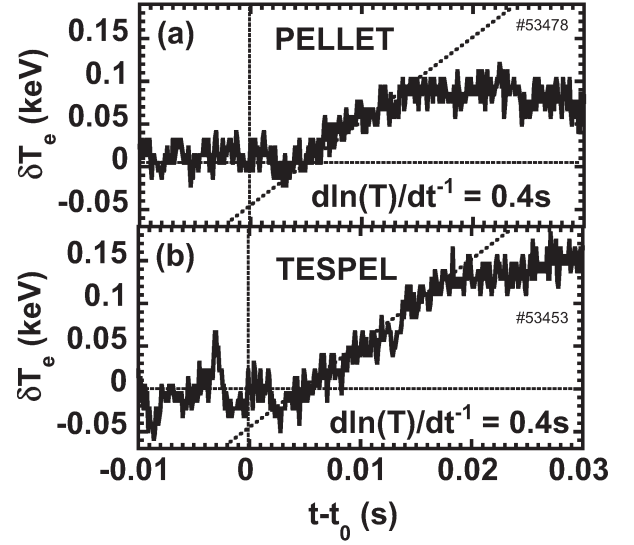


Fig. 1: Time evolution of T_e perturbation in core region ($\rho = 0.3$) induced by (a) a pellet and (b) a TESPEL injection. The pellet and TESPEL are injected to the edge of ECH+NBI plasmas at $t = t_0$. The typical experimental conditions are $R_{ax} = 3.6\text{m}$, $B_{ax} = 2.75\text{T}$, $\bar{n}_e = 1 \times 10^{19}\text{m}^{-3}$.

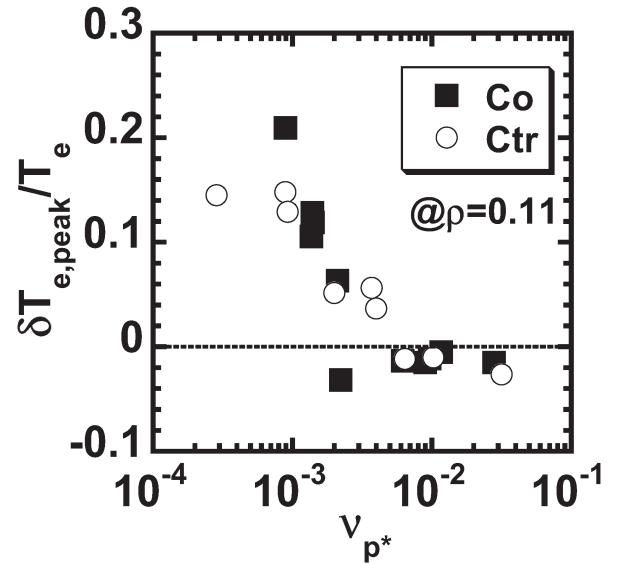


Fig. 2: Collisionality dependence of the normalized T_e perturbation peak. The $\delta T_e/T_e > 0$ indicates the non-local T_e rise. Experiments has been performed in a magnetic configuration of $R_{ax} = 3.5\text{m}$, $B_{ax} = 2.829\text{T}$.

§11. Heat Pulse Propagation across the Rational Surface in Large Helical Device Plasma with Counter Neutral Beam Injection

Yakovlev, M., (Graduate University for Advanced Studies)
Inagaki, S., Shimozuma, T., Kubo, S., Morisaki, T.,
Nagayama, Y., Kawahata, K., Komori, A.

The core electron temperature flattening ($\rho < 0.3-0.4$) is observed in the LHD inward shifted plasma with counter neutral beam injection (Ctr-NBI) as shown in Fig.1(a). To study this phenomenon the heat pulse experiments are performed by modulated on-axis ECH. Typical parameters in these experiments are following: a major radius of 3.5m, an averaged minor radius of 0.6m and magnetic field at axis of 2.83T, line averaged density of $2.0 \times 10^{19} \text{ m}^{-3}$, injected neutral beam power of 1-6MW. The phase delay and amplitude profiles of heat pulse indicate the monotonic heat pulse propagation from core to edge in Co-NBI plasmas, where T_e flattening has not been observed, as it shown in Fig.1. A unique feature of heat pulse propagation is observed near the $m/n = 2/1$ rational surface in Ctr-NBI plasmas. The simultaneous response of temperature perturbation on the radially separated flux surfaces is observed. The non-monotonous heat pulse propagation can not be explained by any one-dimensional heat transport models. The change in topology due to the presence of a magnetic island structure is used to explain this non-monotonous heat pulse propagation. In fact, the $m/n = 2/1$ natural island has been observed in the electron beam mapping experiments on LHD. The ECE system views the region near the O-point of the $m/n = 2/1$ natural island. Thus, the growth of $m/n = 2/1$ natural island can explain the non-monotonous heat pulse propagation in the Ctr-NBI plasmas.

A heat transport model based on the magnetic island structure is shown in Fig.2. The one-dimensional heat transport inside the island, i.e. presence of nested closed flux surfaces and $\chi_{\perp} \ll \chi_{\parallel}$ are assumed inside the magnetic island, where χ_{\perp} and χ_{\parallel} are heat diffusivity perpendicular and parallel to magnetic field, respectively. The simultaneous response of T_e perturbations on radially separated flux surfaces (i.e. $\rho \sim 0.2$ and $\rho \sim 0.5$) can be explained by parallel heat transport on the separatrix of the island due to the large parallel heat diffusivity. The phase delay behaviour from $\rho = 0.2$ to $\rho = 0.33$ and from $\rho = 0.5$ to $\rho = 0.33$ indicates heat pulse propagation from island edge to O-point. The estimated O-point location from the position of the local peak in phase delay profile is in agreement with the $m/n=2/1$ rational surface location. The large difference in phase delay between O-point and edge of the island discloses that there are nested closed flux surfaces inside the island. The clear structure of the $m/n = 2/1$ island showed by phase delay means that the $m/n = 2/1$ island does not rotate, otherwise the phase delay inside of island must to have same values due to averaging of sampled data from ECE.

The magnetic island enlargement is considered to be related to direction and profile of plasma current mainly driven by NBI. In Co-NBI plasmas, the beam-driven

current increases the rotational transform, thereby the $m/n = 2/1$ rational surface will be vanish. No evidence for the presence of $m/n = 2/1$ MHD activity in Co NBI plasmas is observed by the magnetic measurement system.

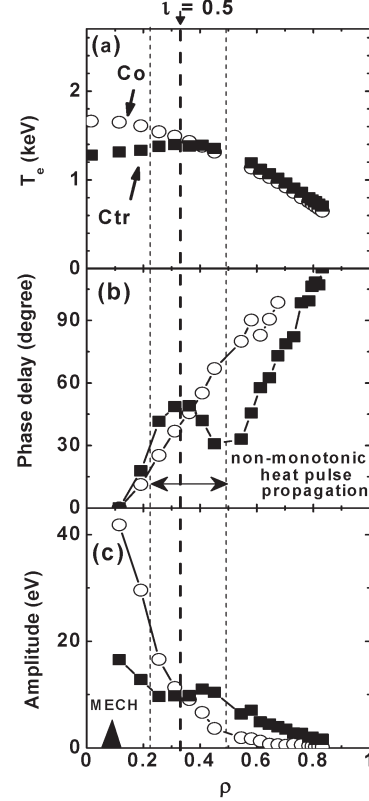


Fig. 1. Comparison of (a) T_e profiles just before MECH injection, (b) phase delay of heat pulse and (c) amplitude of heat pulse between Co- and Ctr- NBI plasmas

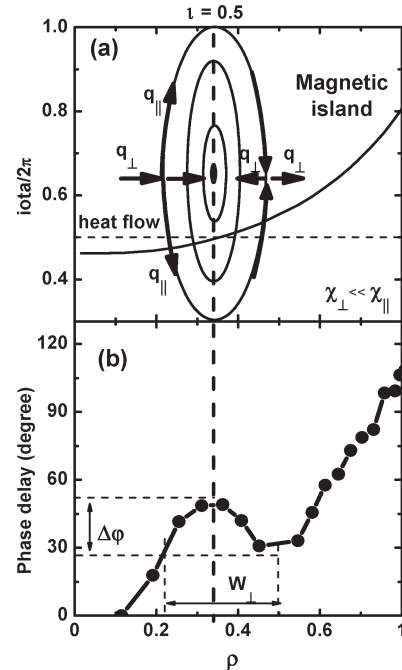


Fig. 2. Two-dimensional heat transport model based on growth of $m/n = 2/1$ island structure. The nested closed flux surfaces and $\chi_{\perp} \ll \chi_{\parallel}$ are assumed inside the island.

\$12. Edge Transport Barrier Extended to Ergodic Field Layer in a Low Density Plasma of LHD

Toi, K., Ohdachi, S., Watanabe, F. (Dep. Energy Eng. Sci., Nagoya Univ.), Narihara, K., Morisaki, T., Sakakibara, S., Morita, S., Goto, M., Ida, K., Yoshinuma, M., Tanaka, K., LHD Experimental Group

In a tokamak with axisymmetric poloidal divertor, regions of closed magnetic surface and open field line are clearly separated by the separatrix. In the poloidal divertor tokamak, H-mode with edge transport barrier (ETB) is easily achieved and its confinement improvement is high. However, small misalignment of poloidal coils and/or edge MHD instabilities could generate magnetic islands near the separatrix and lead to ergodic separatrix [1]. Moreover, recent experiment in DIII-D demonstrated that type I edge localized modes (ELMs) can be effectively suppressed by introducing edge ergodization, without losing the plasma performance [2]. Edge transport barrier (ETB) related to LH transition was observed in high beta regime on LHD [3,4]. The LHD has a magnetic configuration with helical divertor, where nested magnetic surfaces are surrounded by ergodic field layer. It is interesting and important to study how edge magnetic islands and field ergodization affect the formation of ETB and characters of ELMs. The study of ETB plasmas in LHD may provide important information about this issue.

The ETB observed in high beta H-mode plasmas of LHD extends into the ergodic field layer in the vacuum field [4]. Moreover, edge MHD modes of which rational surfaces reside in the ergodic layer are strongly destabilized by the increase in the pressure gradient there. Recently, the LH transition has been achieved also in low beta and low density regime, of which typical shot is shown in Fig.1. The line averaged electron density $\langle n_e \rangle$ and the beta value $\langle \beta_{dia} \rangle$ derived from diamagnetic measurement using the plasma volume in the vacuum field start to increase just after the transition. Note that ELM-like activities in H α emission become significant in about 120 ms after the transition. On H-mode plasmas in high beta regime, the ELM-like activities are immediately excited within ~ 15 ms after the transition [3,4]. The ETB in the shot shown in Fig.1 is also formed inside the ergodic layer, as shown in Fig.2. The profiles of electron temperature and density in the H-phase have a steep and almost constant gradient in the ergodic layer where the ETB extends. The poloidal rotation velocity was measured by charge exchange spectroscopy of doped neon ion. The data indicates that the radial electric field E_r in the H-phase obviously changed to appreciably negative value in fairly wide zone of the plasma edge ($0.8 < \rho$), as shown in Fig.3. However, the information of E_r in the more edge region of $\rho > 0.9$ is still missing. The space potential measurements in the edge region by fast

reciprocating Langmuire probe or heavy ion beam probe are expected in the next experimental campaign.

References

- [1] J. Neuhauser et al., Plasma Phys. Contr. Fusion 31, 1551(1989).
- [2] T.E. Evans et al., Phys. Rev. Lett.92, 235003-1(2004).
- [3] K. Toi *et al.*, Nucl. Fusion **44**, 217(2004).
- [4] K. Toi *et al.*, Phys. Plasma **12**, 020701-1(2005).

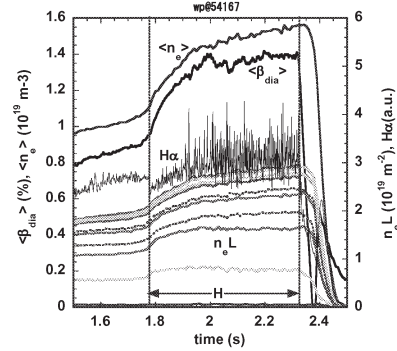


Fig.1 Time evolution of an H-mode shot in low beta regime, where the transition occurs at ~ 1.78 s.

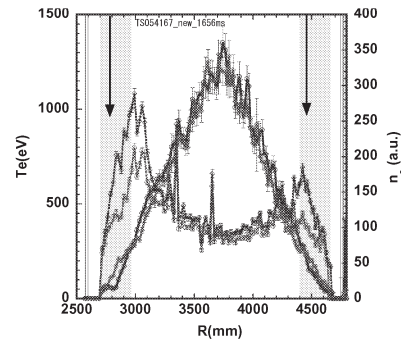


Fig.2 Radial profiles of electron temperature and density measured by YAG Thomson scattering just before and after the transition. The vertical arrows indicate the last closed flux surface.

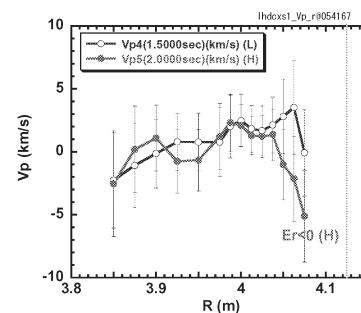


Fig.3 Radial profiles of poloidal rotation velocity measured by charge exchange spectroscopy just before and after the transition. The negative velocity corresponds to the negative E_r . The vertical line indicates the last closed flux surface.

§13. Comparison of Confinement Degradation in High Density and Particle Transport between Tokamak and Helical

Takenaga, H., Oyama, N., Konoshima, S., Takizuka, T., Fujita, T. (JAERI), Muraoka, K. (Chubu University), Tanaka, K., Yamada, H., Miyazawa, J., Peterson, B.J., Nishimura, K., Sakamoto, R.

A comparative study between tokamak and helical plasmas is beneficial for understanding of both common physics in toroidal system and unique physics depending on each magnetic configuration. In the last FY, the confinement degradation at high density in the LHD plasmas with $R_{ax}=3.6$ m was compared with that in the JT-60U ELMy H-mode plasmas. In this FY, the comparison was performed in the LHD plasmas with $R_{ax}=3.75$ m. For the particle transport, the gas-puffing modulation experiments were carried out in the last FY. In this FY, the particle transport was investigated with modulated ECH in the low density region, where it is difficult to use the gas-puffing modulation technique.

In LHD plasmas, an equivalent Greenwald density was estimated as $n_{GW}=(5/\pi)(B/R)\iota$, where ι at the LCFS was used. The dependence of confinement enhancement factor (τ_E/τ_{ISS95}) over the ISS95 scaling on n_e/n_{GW} at $R_{ax}=3.6$ and 3.75 m is shown in Fig. 1 (a). In LHD, n_e of $\sim 1 \times 10^{20} \text{ m}^{-3}$ corresponds to n_e/n_{GW} of ~ 0.6 at $R_{ax}=3.6$ m and ~ 0.8 at $R_{ax}=3.75$ m. The value of τ_E/τ_{ISS95} decreased with increasing n_e/n_{GW} in the region of $n_e/n_{GW} > 0.1$ at $R_{ax}=3.6$ m as reported in the last FY. The confinement improvement factor was smaller at $R_{ax}=3.75$ m than at $R_{ax}=3.6$ m in the region of $n_e/n_{GW}=0.1-0.4$. However, in the region of $n_e/n_{GW} \geq 0.6$, it

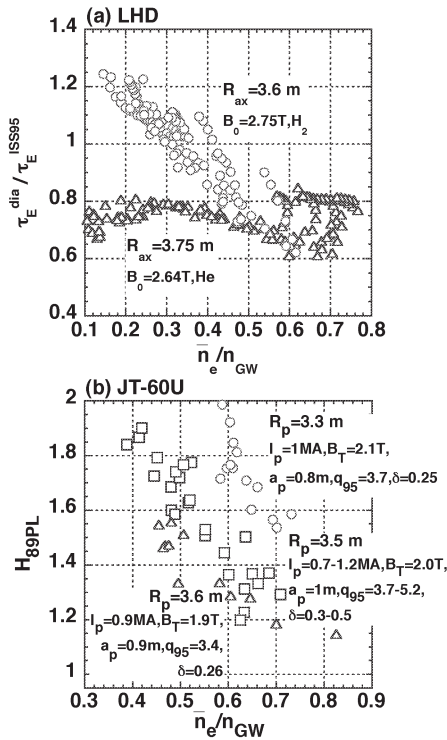


Fig. 1 Dependence of confinement enhancement factor on the density normalized by (equivalent) Greenwald density in (a) LHD and (b) JT-60U for different major radius.

was larger at $R_{ax}=3.75$ m than at $R_{ax}=3.6$ m, because the confinement degradation was small at $R_{ax}=3.75$ m. In JT-60U ELMy H-mode plasmas, the confinement enhancement factor (H_{89P}) over ITER89P scaling decreased in the region of $n_e/n_{GW} \geq 0.4$ as shown in Fig. 1 (b). In the outward shifted plasmas at $R_p=3.6$ m, the confinement degradation was also observed and H_{89P} was smaller than that at $R_p=3.3$ m. The effects of density profile and heating profile should be investigated in future work to understand the dependence of confinement on plasma configuration.

The modulated ECH was applied in the low density plasmas with $R_{ax}=3.5$ m to investigate T_e and/or T_e gradient dependence of particle transport as shown in Fig. 2. The modulation was observed in the line integrated electron density and the central T_e . The modulation was also observed in the $H\alpha$ emission intensity ($I_{H\alpha}$), which might indicate the modulation of the particle source. In fact, the density modulation propagated from the plasma edge to the plasma center, even with the central EC wave deposition as shown in Fig. 3. However, the phase of the modulated $I_{H\alpha}$ and edge density was reversed. The density modulation could be introduced by the T_e modulation rather than the modulation of the particle source. The density modulation was calculated with an assumption that the time scale of the heat transport is sufficiently shorter than that of the particle transport and changing rate of the temperature ($\Delta T_e/T_e$) is larger in the edge region. The calculation results with $D \propto T_e$ and $v \propto \nabla T_e$ indicates that the modulation propagates from the edge region to the central region as observed in experiment under this assumption (Fig. 3). Further study is necessary in future work to find the model, which gives better fitting to the experiment.

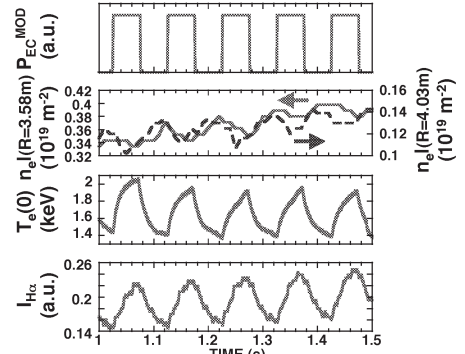


Fig. 2 Wave-forms of modulated ECH power, center and edge line integrated densities, center electron temperature and $H\alpha$ emission intensity.

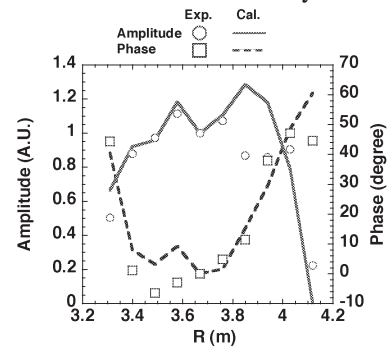


Fig. 3 Amplitude (circles : experiment, solid line : calculation) and phase difference (squares : experiment, dashed line : calculation) for modulated line integrated density.

§14. Experimental Study of Turbulence and Particle Transport in LHD

Tanaka, K., Michael, C.A. (JSPS fellow),
Vyacheslavov, L.N. (Budker Institute of Nuclear Physics), Sanin, A.L. (Budker Institute of Nuclear Physics), Kawahata, K.

The confinements in the most of the operational regime of LHD are dominated by the anomalous transport. Therefore study of the turbulent fluctuation is important. Recently, particle transports at $R_{ax}=3.6m$ are studied from density modulation experiments and parameter dependence of the diffusion coefficient (D) and convection velocity (V) are obtained [1]. The diffusion coefficients are found to be anomaly large compared with neoclassical prediction. The direction of the convection velocities are against neoclassical prediction in several cases. In order to study turbulent fluctuation, recently two dimensional phase contrast interferometer (2D PCI) was developed [2]. The 2D PCI is capable to measured fluctuation with around 0.2 of minor radius spatial resolution within frequency range ($\sim 2MHz$) and wavenumber range ($0.2 \sim 1.5mm^{-1}$).

Figure 1 shows n_e , T_e and fluctuation amplitude under different heating power at $B_t = 1.49T$ and $R_{ax}=3.6m$. As shown in Fig.1 (b), hollow density profiles are observed in all three cases, and the peak density position shifts to outward as heating power increases. This is because V_{edge} increase in the outward direction at higher temperature gradient. As shown in Fig.1 (c), the peaks of fluctuation amplitude exist in plasma edge where density gradients are negative. The fluctuation amplitude becomes larger with higher heating power. Figure 2 shows profile of the particle flux of three cases. These are calculated using estimated D , V from the modulation experiments and measured n_e profiles. The diffusive and convective flux was calculated from $-D \nabla n_e$ and nV respectively. The total flux is sum of two fluxes. The profiles are shown only up to $\rho = 1.05$ because the close to plasma boundary gradients becomes sharp and it becomes difficult to represent the diffusive flux. This sharp gradient around the plasma boundary is due to lack of resolution of the present FIR interferometer. Figure 3 shows relation between fluctuation level and normalized particle flux. Figure 3 consists of 16 shots. Here, the fluctuation level is the ratio of the observed fluctuation amplitude, which is averaged between $\rho = 0.7$ and 1.1 and $k > 0.5 mm^{-1}$ and $5 < f < 500kHz$, to the averaged density at $0.7 < \rho < 1.05$. Because the spatial resolutions of the fluctuation measurements are not very fine, average fluctuation levels are used. The normalized particle flux is calculated also at $0.7 < \rho < 1.05$. As shown in Fig.3, a clear relation between normalized convective flux and fluctuation level are observed. At higher fluctuation level, normalized convective flux becomes larger. Although there is not clear relation is observed between fluctuation level and normalized diffusive flux. Fluctuation induced particle flux is determined not only by density fluctuation amplitude but also by the potential fluctuation amplitude and correlation between density and potential. One of the possible interpretations of lack of the

clear relation between fluctuation level and normalized diffusive flux is due to the role of the potential fluctuation and phase relation between potential and density fluctuation. More detail consideration will be possible with help of the theoretical model about potential fluctuation and phase relation.

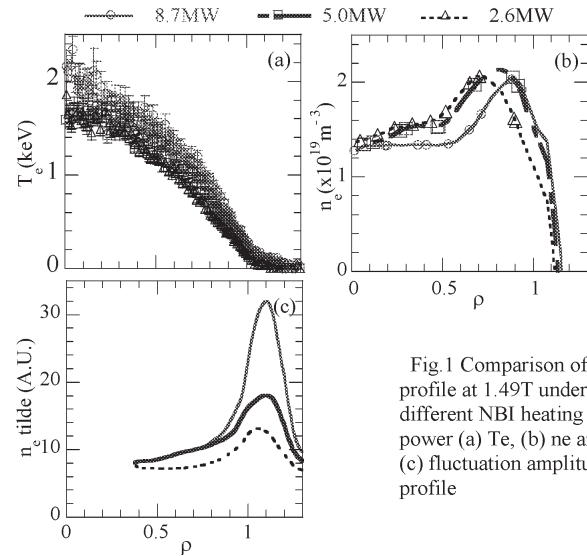


Fig.1 Comparison of the profile at 1.49T under different NBI heating power (a) T_e , (b) n_e and (c) fluctuation amplitude profile

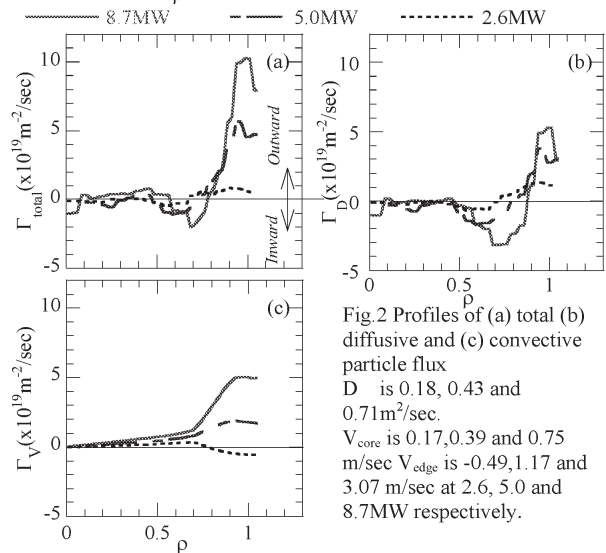


Fig.2 Profiles of (a) total (b) diffusive and (c) convective particle flux
 D is 0.18, 0.43 and 0.71 m^2/sec .
 V_{core} is 0.17, 0.39 and 0.75 m/sec V_{edge} is -0.49, 1.17 and 3.07 m/sec at 2.6, 5.0 and 8.7MW respectively.

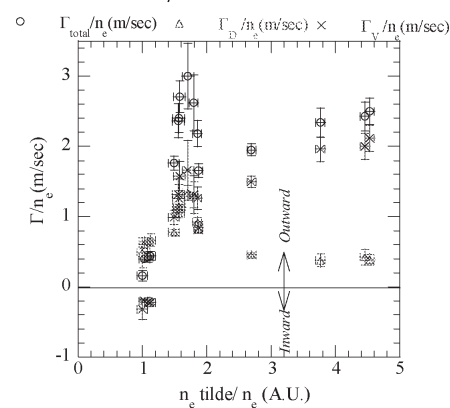


Fig.3 Relation of fluctuation level and normalized particle flu at $B_t = 1.49T$ The error of the normalized flux is due to the fitting error of D and V . The error of the fluctuation level is fluctuation of the signal, which is mainly instability of the laser intensity.

Reference

- 1) Tanaka, K., et al., to be published Nucl. Fusion
- 2) Sanin, A.L., et al., Rev. Sci. Instrum. 75, (2004) 3439

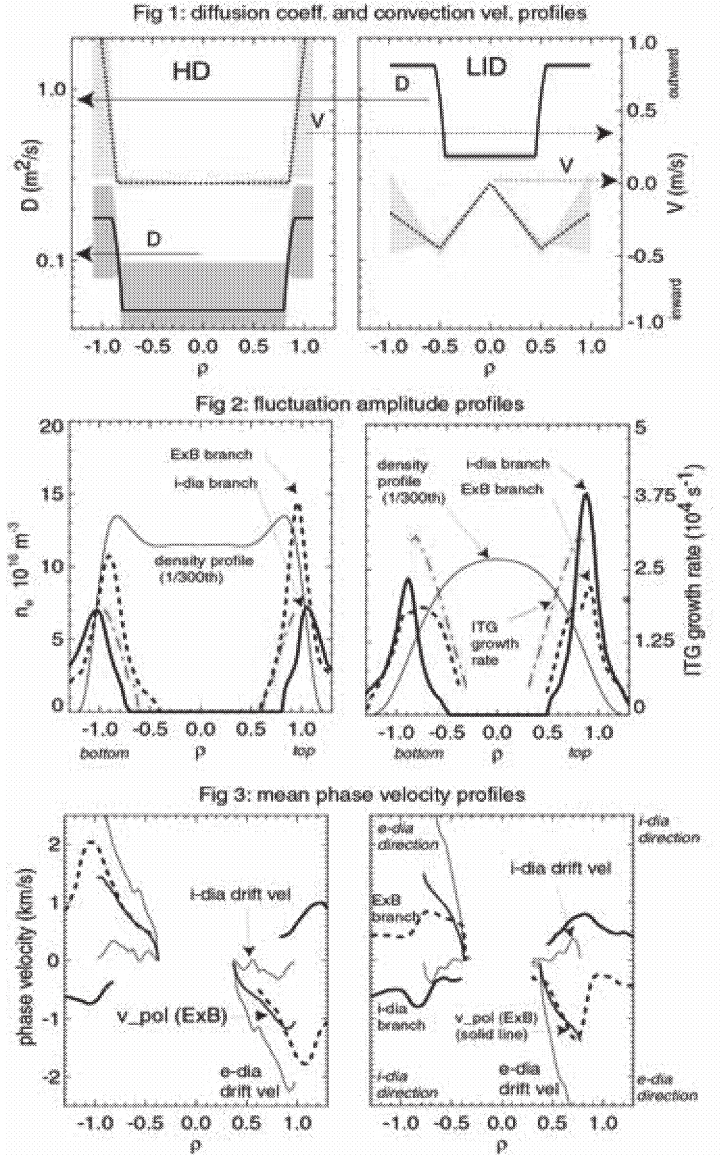
§15. Investigation of Micro-turbulence and Particle Transport in LHD from 2d CO₂ Laser Phase Contrast Imaging

Michael, C.A. (JSPS fellow), Tanaka, K., Vyacheslavov, L.N. (Budker Institute of Nuclear Physics), Sanin, A.L. (Budker Institute of Nuclear Physics), Yamagishi, O., Yokoyama, M., Ida, K., Kawahata, K.

It is well known that particle and energy transport in fusion plasmas is driven strongly by micro-turbulence. Using a recently developed CO₂ 2d laser phase contrast interferometer (PCI), density fluctuations are measured, and their characteristics are compared with the transport coefficients. It is our goal to classify the turbulence and compare it with theoretical predictions in order to understand the driving terms for particle transport.

The principle of the diagnostic technique is to image line-integrated fluctuations in an area of 19x6mm onto a 6x8 CdHgTe detector array using a CO₂ laser beam and phase contrast imaging system [1]. Their position along the line of sight is determined according the propagation direction, assuming fluctuations propagate perpendicular to the field lines. The peak wavelength is comparable or greater than the size of the image. Therefore, to maximize spatial resolution, it is necessary to extrapolate the image beyond the measured region using high resolution non-linear spectral analysis techniques.

A comparison is made between two discharges with different divertor configuration, helical divertor (HD) and local island divertor (LID). The gas-feed was modulated in order to estimate profiles of D and V , shown in Fig. 1 [2]. Shaded areas indicate confidence intervals, and discontinuities are a result of having only 2 fitting variables for the profiles of D and V . Transport is enhanced in this LID discharge, as a result of modification of density and temperature profiles. The fluctuation amplitude profiles are shown in Fig. 2, and their phase velocity is shown in Fig. 3. Different branches are identified, according to phase velocity and propagation direction. In Fig. 3, the plasma poloidal rotation velocity, ion and electron diamagnetic drift velocity profiles, projected perpendicular to the line of sight, are compared with the phase velocities of each branch. The E_r field was obtained from a calculation based on measured n_e, T_e profiles enforcing ambipolarity of the neoclassical particle flux [3]. For the drift velocities, it is assumed that $T_i = T_e$. In both cases, there appear to be two branches, one propagating with the ExB rotation velocity, the other close to the ion diamagnetic drift velocity. The ExB branch is localised slightly closer to the centre than the i-dia branch, though most of the fluctuation power in this branch is not shown since it is at wavelengths larger than the image size,



giving poor spatial resolution.

The amplitude of the i-dia branch is larger in the LID case, consistent with having enhanced particle transport. Determination of the relative density fluctuation level is hampered by the spatial resolution and steep gradients in the edge, however, by comparing with the density profile in Fig. 2, it appears that the relative fluctuation level is considerably larger (>10 times) in the LID case.

Calculations of the growth rate for ion temperature gradient (ITG) turbulence were carried out based on the gyro-kinetic mode equation. The growth rate, indicated by the dash-dot line in Fig. 2, scales approximately with the peak amplitude of the i-dia branch. Based on the propagation direction in the plasma frame, and agreement of the model with the measurements we assert that ITG turbulence plays an important role in determining anomalous transport.

- [1] A. Sanin et al., Rev. Sci. Instrum 75, 3439 (2004)
- [2] K. Tanaka et al., to be published Nucl. Fusion
- [3] C.D.Beidler et al., PPCF 36, 317 (1994)

§16. Observation of Energetic Particle Mode Fluctuation by Using Microwave Reflectometer

Tokuzawa, T., Yamamoto, S. (Osaka Univ.),
Kawahata, K., Sakakibara, S., Toi, K.

The heterodyne reflectometer system is utilized for the fluctuation measurement. The system uses a conventional reflectometer technique and is easy to operate routinely [1]. By using the extraordinary polarized wave, we can measure the corresponding value to the combined fluctuation with the electron density and the magnetic field in the plasma core region even if the radial electron density profile is flat.

Currently the system has three channels of fixed frequencies of 78, 72, 65 GHz. Power combined three microwaves are traveling to/from the LHD by using a corrugated waveguide for avoiding the transmission loss. The simplified super heterodyne detection technique is used for the receiver system. Recently the real-time data acquisition system has been able to be utilized and the sampling rate is up to 10 MSample/sec by using a compact-PCI based digitizer. Reflectometer system has been adapted this data acquisition system from 8th campaign. Then the system is very convenient to observe MHD phenomena such as energetic particle driven Alfvén eigenmodes [2], launching the extraordinary polarized wave. In Fig. 1 the temporal behaviour of the reflectometer signal of 78 GHz and magnetic probe signal and these power spectra are shown. Coherent spectra of around 8 and 16 kHz are caused by low- n mode oscillation. Frequency spectra at $t=1.73$ s is shown in Fig. 2. In the

range of 100~150 kHz there are a lot of coherent mode. These mode are identified the $n=1$ (n :toroidal mode number) mode by the magnetic probe analysis. Also on the reflectometer signal it is observed higher mode around 230 kHz. Just after $t=1.82$ s MHD-burst is occurred and these frequency components are rapidly disappeared and then passing 0.02s these mode are revived. It may be caused that the distribution of high energy particle is changed by such a MHD-burst. Therefore reflectometer is easy to be utilized to study the MHD phenomena.

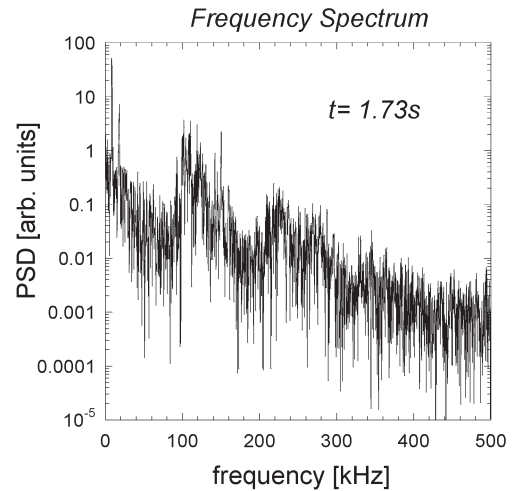


Fig. 2. Frequency spectrum of reflectometer signal at $t=1.73$ s.

References

- [1] T. Tokuzawa *et al.*, 31st EPS Conf. P5-114 (2004)
- [2] S. Yamamoto *et al.*, Nuclear Fusion **45**, 326 (2005)

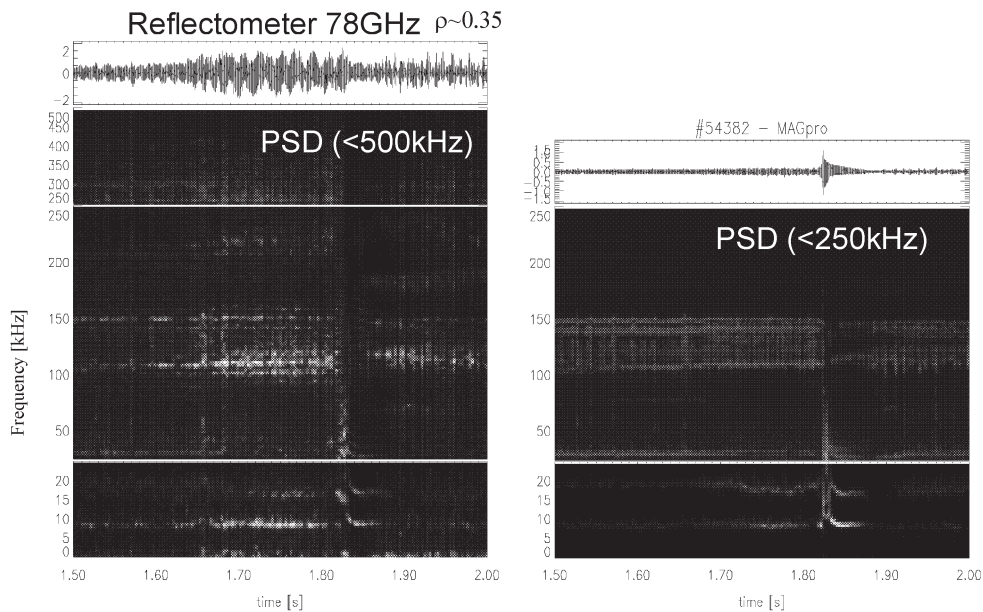


Fig. 1. Time evolutions of reflectometer signal and its frequency spectrum (left) and magnetic probe signal and its spectrum (right)

§17. Scattering Measurement from Gyrotron

Pshenichnikov, A., Kharchev, N. (General Physics Institute, Russian Academy of Sciences)
Kubo, S., Shimozuma, T., Yoshimura, Y., Igami, H.,
Notake, T., Ohkubo, K.

Scattering measurement of the gyrotron power from plasma is continued in the 8th experimental campaign. The correlation analysis between the Sniffer probe signal, power monitor and scattered one are stressed. Signals from horn antenna at (port 9.5-O) mostly from the scattered microwave power from main plasma. Sniffer probes (ports 9.5-L and 2-O) are sensitive to the stray microwave around the plasma. Gyrotron power monitor is set in the transmission line and is not affected by the plasma. The main goals were to prove the reliability of horn antenna signal as a scattering signal and to study the scattering spectra formation mechanism via experiment. Different spectral and correlation techniques were used for analysis.

One possible way of scattering signal distortion could be gyrotron power fluctuations. To study their effect the spectra of gyrotron power monitor signal and the scattering signal can be compared (Fig. 1). The scattering signal has much

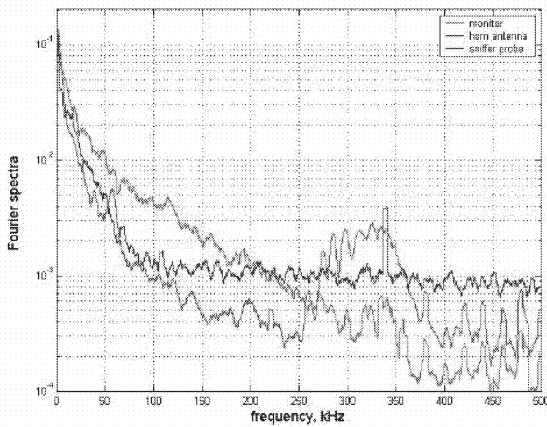


Fig. 1. Smoothed Fourier spectra examples for #11 gyrotron power monitor (blue line) signal, 9.5-L port horn antenna signal (red line) and 9.5-L port sniffer probe (magenta line) at shot 55993. Time window 0.400-0.405 s

broader spectrum than the that of power monitor. This indicates that the high frequency components of the scattering signal is originated from plasma fluctuations but not from the gyrotron power fluctuations. Fig. 2 shows that only low frequency components (mostly below 50 kHz or even lower) are correlated. To study the possibility of multi-scattering the correlations between sniffer probe signal and horn antenna signal were analyzed. Figure 3 shows that the correlation level is rather low. The exceptions are near 350 kHz

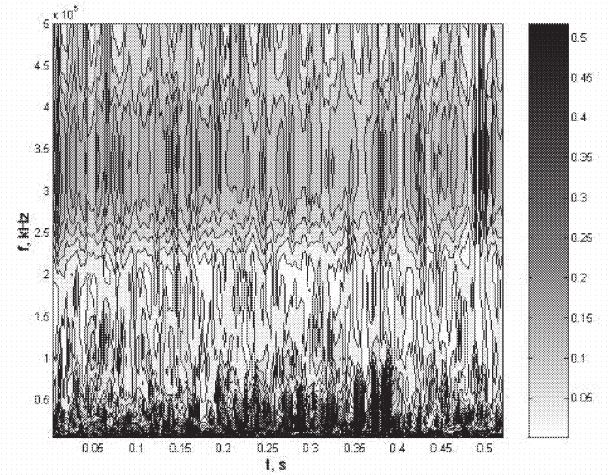


Fig. 2. Wavelet coherency versus time for horn antenna and power monitor signals at shot 55993. The noise component (350 kHz) and a low frequency component have high coherency.

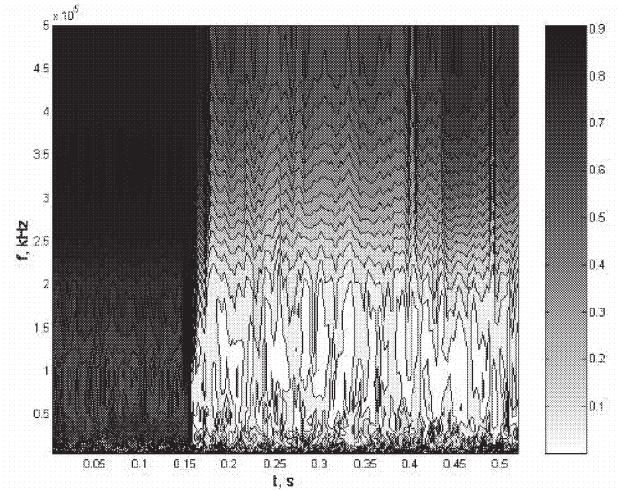


Fig. 3. Wavelet coherency versus time for horn antenna and sniffer probe signals at shot 55993. High coherency level before gyrotron pulse is present due to common noise. The highest noise coherency is in 350 kHz region.

band noise correlation and low frequency components correlations. But sniffer probe receives almost all incident (at probe) radiation of wide polarization angles range and different propagation directions. I.e. it receives almost all stray signals at point of its location (which is close to horn antenna location), while but the horn antenna should receives only scattered radiation from plasma. It may be the reason that sniffer probe spectra are broader than those for scattering (Fig.1). From these differences in spectrum and incoherence between them, it can be concluded that the horn antenna receives radiation scattered on some not very large (in comparison to plasma size) volume which can be estimated theoretically or perhaps found experimentally by some additional measurements.

§18. Control of the Radial Electric Field Shear by Modification of the Magnetic Field Configuration in LHD

Ida, K., Yoshinuma, M., Yokoyama, M., Beidler, C.D. (Max-Planck Institut fuer Plasmaphysik, Greifswald)

Control of the radial electric field, E_r , is considered to be important in helical plasmas, because the radial electric field and its shear are expected to reduce neoclassical and anomalous transport, respectively. In general, the radial electric field can be controlled by changing the collisionality, and positive or negative electric field have been obtained by decreasing or increasing the electron density, respectively. Although the sign of the radial electric field can be controlled by changing the collisionality, modification of the magnetic field is required to achieve further control of the radial electric field, especially producing a strong radial electric field shear. In the Large Helical Device (LHD) the radial electric field profiles are shown to be controlled by the modification of the magnetic field by changing the radial profile of the effective helical ripples, ε_h [1]. Since the radial electric field in LHD is determined by the ambipolar condition of ion flux and electron flux that are trapped in the effective helical ripples, a change in the magnitude and radial profiles of effective helical ripples will be the most straightforward tool to control the radial electric field. In LHD, the radial profiles of effective helical ripples can be modified by a shift of the magnetic axis from 3.5m to 3.9m as seen in Fig.1.

Figure 2 shows the radial profiles of the radial electric field for the ion root (large neoclassical flux with negative E_r in the high collisionality regime), electron root (small neoclassical flux with positive E_r in the low collisionality regime) and the transition regime (between ion root and electron root) for various configurations with different effective helical ripple profiles. When the plasma collisionality decreases by decreasing electron density or increasing the temperature with higher heating power, the radial electric field changes its sign from negative in the ion root to positive in the electron root. Regardless the configuration, the transition from ion root to electron root is observed at the plasma edge if the electron density is decreased below $0.5 \times 10^{19} \text{ m}^{-3}$. When the effective helical ripple increases gradually towards the plasma edge ($R_{ax} = 3.75\text{m}$, 3.9m), the electron root region extends to half of the plasma minor radius and the radial electric field shear produced is relatively weak. However, when the effective helical ripple increases sharply at the plasma edge ($R_{ax} = 3.5\text{m}$), the electron root region is localized at the plasma edge and strong radial electric field shear is produced. When the magnitude of the effective helical ripple is suppressed to a low level ($R_{ax} = 3.6\text{m}$), the transition region of the radial electric field is located at $\rho = 0.9$, not at the plasma edge, because there is no increase in the effective helical ripple at the plasma edge in this configuration. These results show that a strong electric field shear can be obtained at the plasma edge by shifting the magnetic axis inward rather than shifting the magnetic axis outward, where the achievement

of electron root itself is relatively easy (even with higher collisionality).

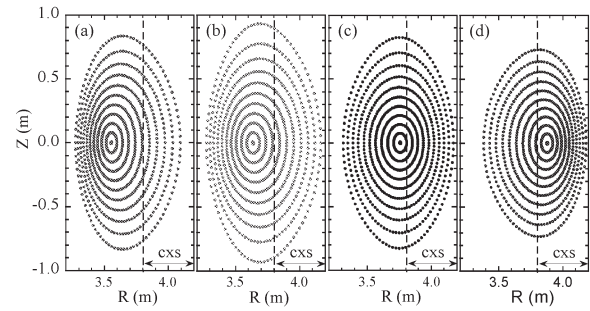


Fig. 1. Poloidal cross section of the magnetic flux surface for plasmas with various magnetic axis, R_{ax} of (a)3.5m, (b)3.6m, (c)3.75m, and (d)3.9m. The region of the radial electric field measurement using the charge exchange spectroscopy (CXS) is indicated with arrows.

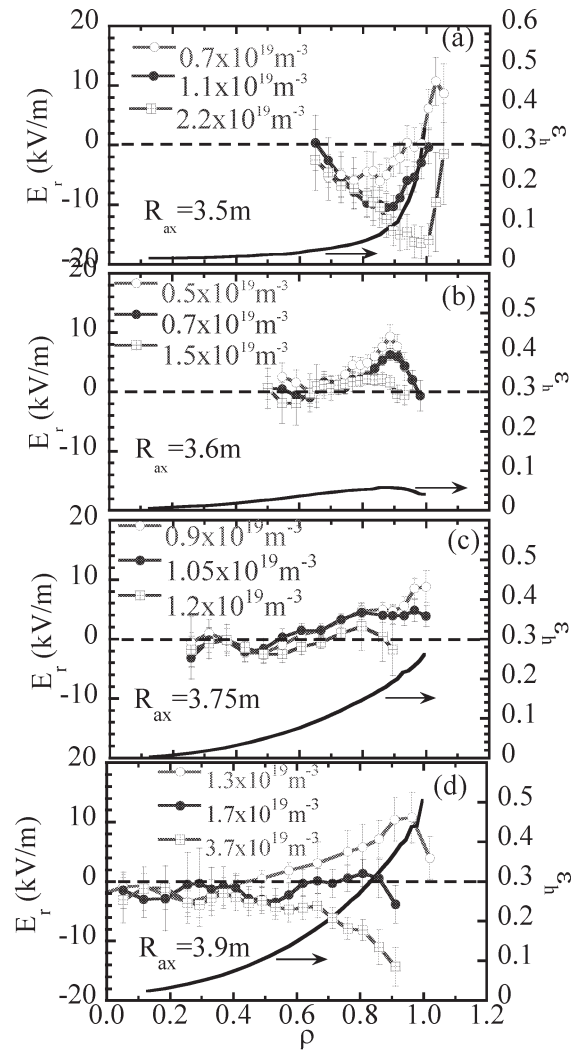


Fig. 2. Radial profiles of radial electric field, E_r and effective helical ripple ε_h for plasmas with various magnetic axis, R_{ax} of (a)3.5m, (b)3.6m, (c)3.75m, and (d)3.9m.

Reference

- 1) Ida, K., et.al., Nucl. Fusion **45**, (2005) 391

§19. Formation of the Radial Electric Field Shear at the Boundary of Magnetic Island with Repetitive Pellet Injection in LHD

Yoshinuma, M., Ida, K., Sakamoto, R.

Since the radial electric field E_r and its shear are expected to reduce neoclassical and anomalous transport, respectively, the control of the radial profile of the radial electric field is considered to be one of the important tools to improve confinement in helical plasmas. In general, the radial electric field can be controlled by changing the collisionality, and positive or negative electric field has been obtained by decreasing or increasing the electron density, respectively. Farther, the radial electric field has been observed to be zero inside the magnetic island in the large helical device (LHD) [1]. When the plasma achieves the ion root (negative E_r) outside the magnetic island by increasing the collisionality, the large radial electric field shear will be formed at the boundary of the magnetic island as shown in Fig.1. We demonstrated that the formation of the radial electric field shear at the boundary of a $n/m = 1/1$ magnetic island induced by external perturbation coils (LID coils) with repetitive pellet injection in the plasma with a magnetic axis of 3.6m and magnetic field strength of 2.75T. The pellet was injected into the NBI sustained plasma with the electron density of $1.0 \times 10^{19} \text{ m}^{-3}$ to fuel the particles inner side of the magnetic island to archive the negative E_r of ion root regime.

Figure 2 shows the radial profiles of the radial electric field with the repetitive pellet injection. The radial electric field is close to zero in the discharge with the LID coil current of 1200A. The radial electric field profile shows that the plasma is in the ion root outside of the magnetic island in the discharge with the LID coil current of 1920A and the radial electric field shear was formed near the boundary of the magnetic island (shaded region in Fig.2). The electron density after the pellet injection is $1.5 \times 10^{19} \text{ m}^{-3}$ and $2.5 \times 10^{19} \text{ m}^{-3}$ in the discharge with the LID coil current of 1200A and 1920A, respectively. Larger increase of the electron density is observed in the plasma with larger magnetic island.

Figure 3 shows the time evolution of the radial electric field at the $R=4.04\text{m}$ measured with the charge exchange spectroscopy with better time-resolution. With the single pellet injection, the formation of the negative electric field and strong E_r shear was transient, and then the E_r shear disappears in the time scale of few 100msec. By injecting a repetitive pellet, the negative electric field and electric field shear can be sustained. Faster change of E_r is observed in the discharge with large pellet injection.

Reference

1) Ida, K., et.al., Phys.Rev.Lett **88**, (2002) 15002.

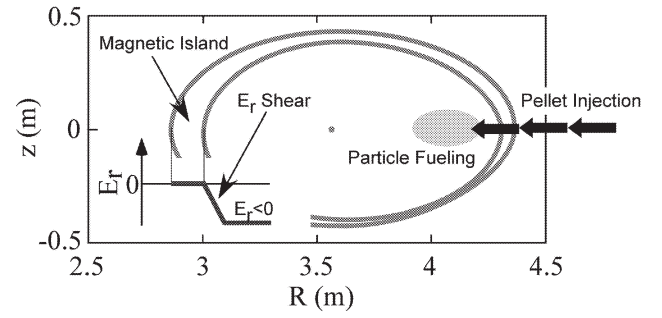


Fig. 1. Schematic view of the E_r shear formation by pellet injection with external induced magnetic island. The red line shows the poloidal cross section of magnetic flux surface near the magnetic island induced by external perturbation coil.

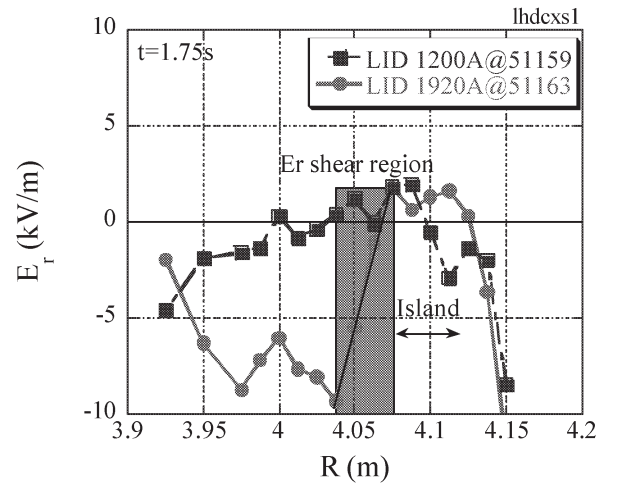


Fig. 2. Radial profiles of radial electric field with the repetitive pellet injection in the case of 1200A (square) and 1920A (circle) of LID coil current.

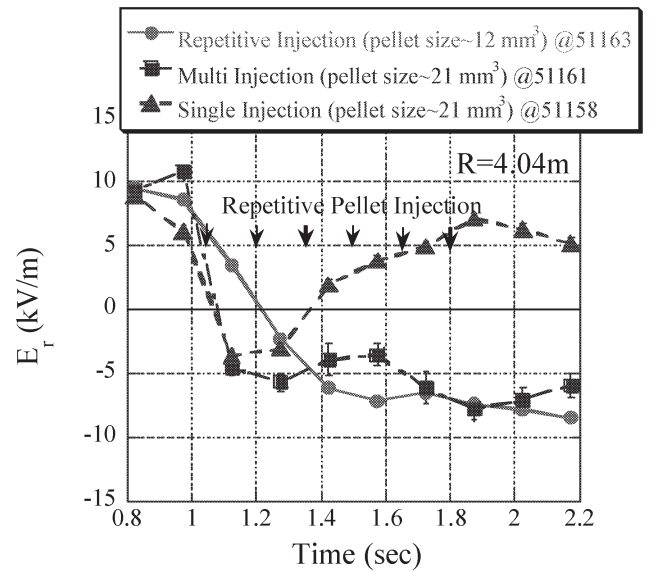


Fig. 3. Time evolution of the radial electric field E_r at the $R=4.04\text{m}$. Pellet which has the size of 12mm^3 is injected repetitively (circle). Pellet which has the size of 21mm^3 is injected three times (square) and singly (triangle).

§20. Characteristics of High -Te Plasmas Related to NBI-Beam-Driven Current

Shimozuma, T., Kubo, S., Inagaki, S., Yoshimura, Y.,
Igami, H., Notake, T., Ohkubo, K.

In the Large Helical Device (LHD), operation at high electron temperature (> 10 keV) and ITB formation have been achieved using high power ECH (> 2 MW) and strongly focused mirror antennas. In the experiments, neutral-beam-driven currents modify the profiles of the rotational transform $\iota/2\pi$, and two different kinds of improved confinement were observed. Using the heat pulse propagation techniques generated by modulated ECH (MECH), we investigated the electron heat transport to elucidate the triggering mechanisms for the improved confinement. and found the difference of heat transport by the direction of the beam-driven current 1).

The ITB formation was only observed in counter injected NBI plasmas with centrally focused ECH. There are two questions: (1) What happens when the magnetic field is reversed? (2) How does the amount of beam-driven current affect the characteristics of ITB formation?

We have three tangential NBI injectors, two counter (BL1,3) and one co (BL2) injection NBI in the normal magnetic configuration. In order to make clear the effect of the plasma current direction on ITB formation (Question (1)), we made the same experiments in the NBI plasmas with reversed magnetic configuration.

The target plasmas were NBI-sustained low density plasmas with $\bar{n}_e = 0.5 \times 10^{19} \text{m}^{-3}$ and $T_{e0} \sim 1.5 - 2.0$ keV. The magnetic axis was placed on $R=3.5$ m, and the field strength was -2.829 T on the axis, where the minus sign means reversed field compared with the normal magnetic configuration.

Figure 1 shows the electron temperature profiles measured by Thomson scattering for a) counter (BL2) and b) co (BL3) injected NBI target plasmas, respectively, at the timings of just before ECH on and ECH off. In this case, BL2 injector drove counter current and BL3 drove co current. There was a narrow peaked T_e profile with steep temperature gradient in the only counter-NBI (BL2) plasma. On the other hand, wide high T_e profile appeared in co-NBI (BL3) sustained plasma. The T_e profile was obviously different from each other before ECH injection. The flattened profile was observed for counter-NBI and the peaked profile for co-NBI plasmas, which is the same feature as in the normal magnetic configuration.

This results assures the fact that the behavior of T_e profiles were affected by the beam driven current, i.e. the profiles of the rotational transform $\iota/2\pi$, not by NBI power deposition profiles.

In order to answer the question (2), we tried ECH

injection into the long pulse counter-NBI (5sec. duration) plasma that had a gradual counter current increase from 0 to 22kA. ECH injection timing was changed shot by shot to investigate the effect of current amount on the ITB formation. However, we could not find big dependence on the total current within this current range. This suggests the current profile is more important than the total amount. Deeper investigation on the current profile is required to make the phenomena clear.

References

- 1) T. Shimozuma, et al., 20th IAEA Fusion Energy Conference, 1-6 November 2004, Vilamoura, Portugal, EX/P3-12.

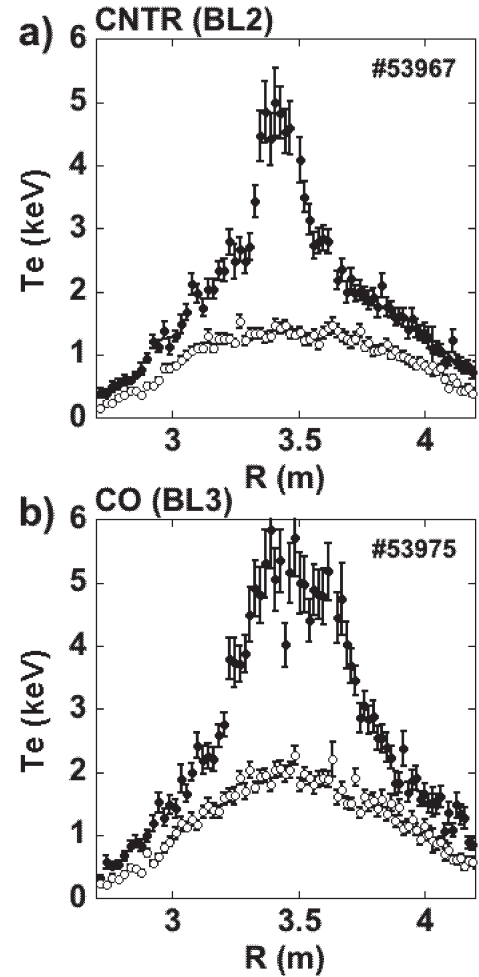


Fig. 1: Electron temperature profiles just before ECH on and off a) for counter-NBI (BL2) and b) for co-NBI (BL3) sustained plasmas.

§21. Recent Progress on High Ion Temperature Experiment with High-Z Discharge in LHD

Ikeda, K., Takeiri, Y., Morita, S., Kaneko, O., Ida, K., Mutoh, T., Nakamura, Y., Tsumori, K., Oka, Y., Nagaoka, K., Ozaki, T., Goncharov, P.

High ion temperature experiment with high-Z discharge progressed year by year. We have achieved the ion temperature 10 keV in the 7th experimental campaign¹⁾. Three negative-ion-based neutral beam injectors are arranged tangentially in LHD. The neutral beam power is mainly deposited on electrons due to the high-energy hydrogen neutral beam of 180 keV. It is important to increase the ion-heating power in order to increasing the ion temperature. High-Z discharges used Ar or Ne are effective to increasing of ion heating power in the low electron density plasma below $0.5 \times 10^{19} \text{ m}^{-3}$. It is also important to reduce contamination of the neutral particle from the wall in order to maintain high beam absorption in the low-density plasma. The Ar- and Ne-glow discharge cleaning have been carried out 41 hours and 22 hours in front of the experiment day, respectively.

Figure 1 shows the time evolution of the density and the temperature of the shot number 54878th on the Ar-puffed plasma with the magnetic field axis of 3.7m. The electron density measured by a far-infrared interferometer, is build up by the short Ar gas puffing. The beam power of 8.7MW of the injected power of 10.5MW is absorbed in the plasma. The central ion temperature rapidly increases as the density decreases, and reaches the new record of 13.5 keV where the ion temperature is measured with the Doppler broadening of ArXVII. The electron temperature measured by the Thomson scattering, is 4.5 keV, it is lower than the ion temperature due to the dominant ion heating. The neutral beam heating at the 8th experimental campaign

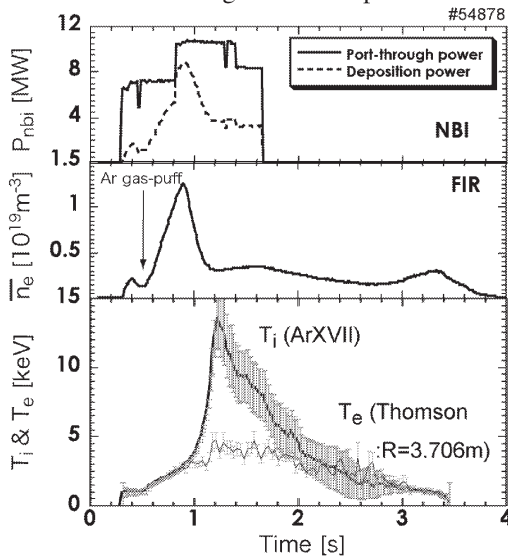


Fig. 1 Time evolution of the density and the temperature in an Ar gas-puffed plasma. The neutral beam power of 10.5 MW is injected totally

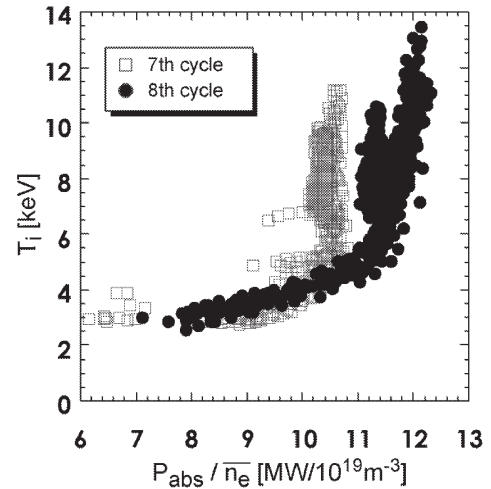


Fig. 2 T_i against absorbed NBI power normalized electron density on the Ar-puffed plasma in the 7th and 8th experimental campaign.

is more effective to the heating at 7th experimental campaign as shown in Fig.2. As the result, the ion temperature increase as the ion heating power per unit density increases. It is indicate that the intensive Ar- or Ne-glow discharge wall conditioning is effective to keep the low density.

Characteristic of the ion temperature with high-Z discharge is researched well in the case of the magnetic field axis below 3.7m. The ion temperature well rises due to the density peaking in case of the magnetic field axis of 3.7m. Figure 3 shows the effect of the neutral beam heating on the Ne-puffed plasma with various magnetic field axes outside of 3.7m. In the case of 4 m, the ion temperature dose not increases as the heating power increases because of the bad confinement. The ion temperature with the case of 3.85m well rises as the case of 3.7m. If it can maintain density low, we expect to produce higher ion temperature by using the Ar-puffed discharge.

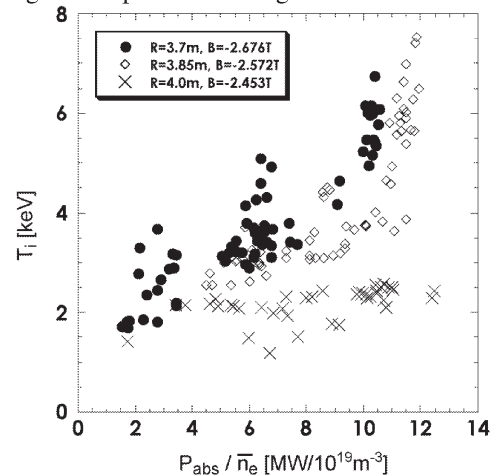


Fig. 3 T_i against absorbed NBI power normalized electron density in various magnetic field axes on Ne-puffed discharge plasma.

1) Y. Takeiri, et al., 20th IAEA Vilamoura, 2004, EX/P4-11

§22. Confinement Improvement in High-Ion Temperature Plasmas in LHD

Takeiri, Y., Morita, S., Ikeda, K., Tsumori, K., Oka, Y., Osakabe, M., Nagaoka, K., Kaneko, O.

High-ion temperature plasmas above 10 keV have been obtained with negative-ion-based NBI heating in LHD. Since the hydrogen injection energy is higher than 150 keV, the electron heating is dominant in hydrogen discharges. In order to enhance the ion heating power effectively, high-Z discharges with Ar or Ne seeding are utilized [1]. Low-density and high-Z plasmas, where the beam absorption power is enhanced and the ion density is reduced, are realized by suppression of the dilution with wall-absorbed hydrogen with intensive Ne and/or Ar glow discharge cleaning. As a result, the central ion temperature (T_i) is increased with an increase in the density-normalized ion heating power, and reaches 13.5 keV.

Considering that the increase in the central T_i is not saturated with the ion heating power, the anomalous transport, which causes the power degradation of the temperature, would be suppressed in the high-ion temperature plasmas obtained in the high-Z discharges. As shown in Fig. 1, the central T_i is increased with an increase in the electron temperature (T_e) gradient in an outer plasma region of around $\rho=0.8$, and no definite correlation is observed between the central T_i and the T_e gradient in a core region of round $\rho=0.6$. The neoclassical ambipolar calculation considering multi-ion species indicates the generation of strong positive radial electric field (E_r) in the outer region for the high-ion temperature plasmas. In the CXRS measurement, positive E_r is observed in the outer region and the positive E_r is increased as the density decreases. Correspondingly, a little rise of the local T_i there is also observed. These results suggest the improvement of the ion transport in the outer plasma region due to the electron root, and that should lead to the central T_i rise.

When the centrally focused ECH is superposed on the high-Z NBI plasma, central T_i rise is observed [1]. Then, the T_e profile shows the electron ITB, in which the T_e gradient is steep in a core region of $\rho=0.4-0.5$. The neoclassical calculation shows the formation of positive E_r in the core region. In the case of the non-high-Z plasmas, positive E_r is observed in the core region with the superposition of the ECH in the CXRS measurement.

As shown in Fig. 2, positive E_r is observed in a core region for an electron ITB plasma in the non-high-Z discharges generated with a combined heating of NBI and ECH, and a little increase in the T_i is recognized. In the electron ITB plasmas the improvement of the electron transport has been confirmed [2], and the core T_e and the T_e gradient are both increased without saturation as the density-normalized electron heating power increases. Considering the above mentioned results, the ion transport should be improved due to the electron root in the high-ion temperature plasmas.

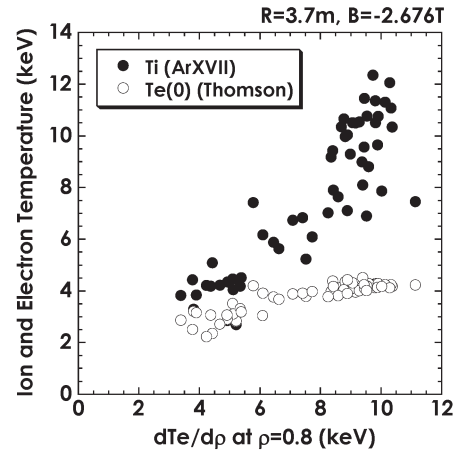


Fig. 1. Central T_i and T_e as a function of the T_e gradient $dT_e/d\rho$ at $\rho=0.8$.

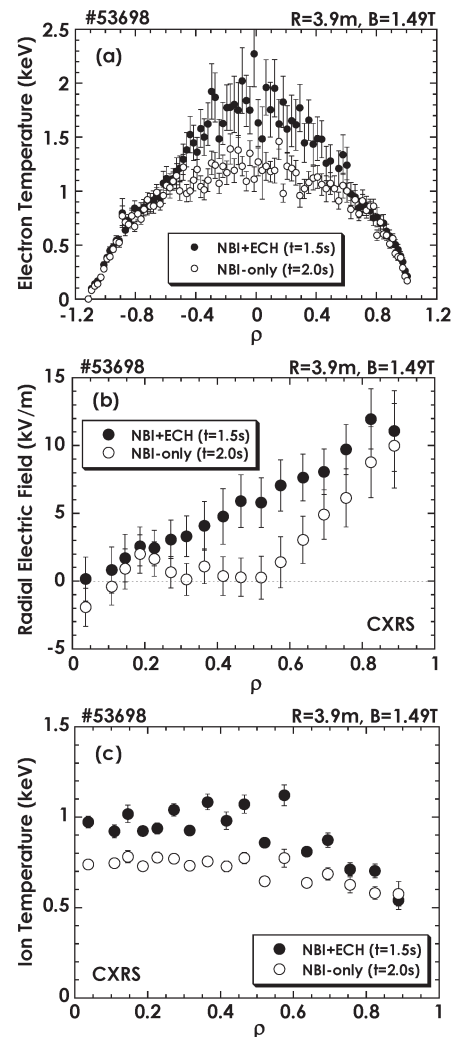


Fig. 2. Radial profiles of (a) T_e , (b) E_r , and (c) T_i for the electron ITB plasma and the non-ITB plasma at $R_{ax}=3.9m$ in the non-high-Z discharges.

References

- [1] Y. Takeiri *et al*, Nucl. Fusion **45** (2005) 565.
- [2] Y. Takeiri *et al*, Fusion Sci. Technol. **46** (2004) 106.

§23. Toroidal Rotation in Ar Discharges

Morita, S., Ikeda, K., Takeiri, Y., Yokoyama, M., Yamazaki, K. (Dept. Energy Eng. Sci., Nagoya Univ.)
Murakami, S. (Kyoto Univ.)

Ne glow discharges were done for 8 hours overnight before daily experiments in order to decrease hydrogen neutrals. The $H\alpha$ intensity further decreased during NBI discharges and roughly became half of that after He-glow discharges. Some amount of hydrogen was replaced by neon. As a result, a further density decrease became possible down to $0.2 \times 10^{13} \text{ cm}^{-3}$.

After the Ne glow discharges the density profile became peaked in Ar discharges, as shown in Fig.1. In Ne discharges after Ne glow discharge, however, an extremely flat density profile was performed by the enhanced edge recycling of neon. It is reported that the inward velocity of impurities in LHD is proportional to their ionization stages, $q_i^{1)}$. This may be a main reason why the Ar discharge has such a peaked density profile in addition to the lower recycling rate.

From these experiments it became clear that the ion temperatures are sensitive to density profiles. The density peaking followed by the reduction of edge density at $\rho=0.8$ is well correlated with high values of ion temperatures, especially in the Ar discharge case.

Central toroidal rotations measured from Doppler shift of ArXVII were analyzed with the ion temperatures and density peaking. The rotations could be also well correlated with the density peaking and ion temperatures. For example, the rotation was smaller than 10km/s in the flat density profile of Ne discharges after Ne-glow cleaning and 30-40km/s in the peaked density profile of Ar discharges (see Fig.2). The $T_i(0)$ was 2-3keV and 7keV for Ne and Ar discharges, respectively (see Fig.3). The heat transport was analyzed between such two discharges. The central ion thermal diffusivity, χ_i , was $25 \text{ m}^2/\text{s}$ and $10 \text{ m}^2/\text{s}$ for Ne and Ar discharges, respectively. Here, it should be noticed that the ion density much decreases in these discharges and then, the analyzed χ_i becomes larger than that in hydrogen discharges ($\chi_i \sim 2\text{-}5 \text{ m}^2/\text{s}$). In the practical discharge the hydrogen ion density becomes still dominant and is estimated to be 2-3 times as much as the Ar ion density. The obtained χ_i are, of course, much larger than the neoclassical values. Then, it is pointed out that the enhanced toroidal rotation followed by the density peaking may improve such an anomalous transport also in LHD. The toroidal rotation velocity of 40km/s corresponds to 30% of the Ar thermal velocity.

The toroidal rotation is mainly reduced by a parallel viscosity due to helical ripple mainly located at plasma outer half region. The density reduction at the plasma outer region leads to the reduction of the parallel viscosity and enhances the toroidal rotation. The recent theoretical analysis predicts the same rotation velocity as the experimentally obtained velocity of 40km/s (see Fig.4).

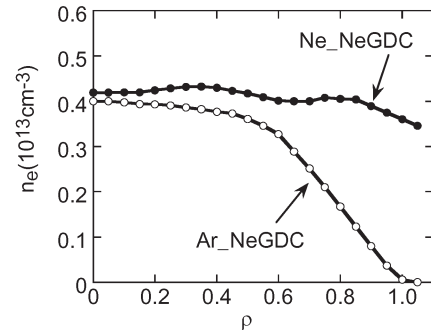


Fig. 1. Density profiles in Ar and Ne discharges.

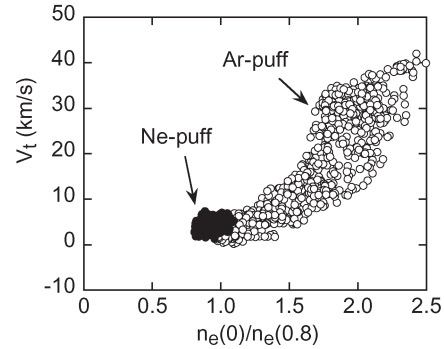


Fig. 2. Toroidal rotation against density peaking.

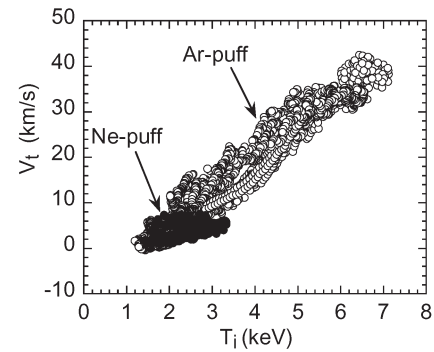


Fig. 3. Toroidal rotation against ion temperature.

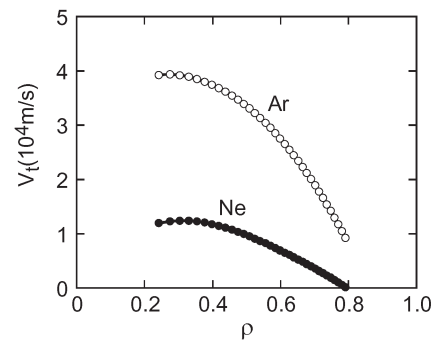


Fig. 4. Theoretical toroidal rotation profiles.

References

- 1) Nozato, H., Morita, S. et al., Phys.Plasmas **11** (2004) 1920.

§24. Estimation of the Particle Confinement Time of the Helium Ash in LHD

Mitarai, O. (Kyushu Tokai University), Goto, M., Morisaki, T., Masuzaki, T, Ashikawa, N. (NIFS)

The ratio of the helium ash confinement time to the energy confinement time (τ_{α}^*/τ_E) should be lower than 7 in the FFHR helical reactor to maintain ignition. However, as such data are not yet available in any helical device, there is the physics uncertainty in a helical reactor design. Although high energy He-beam should be finally injected into the plasma core to simulate the burning plasma, He gas was initially injected to measure such exhaust characteristics as a first step of this type of experiment.

Helium gas was injected by gas puffing at 1.2 sec in the outwardly shifted plasma with $B_0=2.64\text{T}$ and $R_0=3.75\text{m}$. After the plasma density is adjusted to be flat, helium or hydrogen gas were injected. In an actual experiment, it is confirmed that helium gas puff was injected by monitoring the electron density. For comparison, experiment was also conducted without gas puffing.

As shown in Fig. 1, He-II line (4684 Å) has a finite signal before helium gas was puffed. This means that residual helium gas may exists which was absorbed in the first wall. Therefore, it is necessary to check the other discharge with the respect to the wall recycling. Although this small signal starts from the zero at the beginning of discharge, it should be checked without plasmas.

As shown in Fig.1, it is confirmed that He-II line emission is increased by helium gas puffing in the shot of #49346. We have checked experimentally that H-I line is increased by hydrogen gas puffing in the shot of #49351, and that He-II line is not affected by hydrogen gas puffing.

As the waveform of the incremental value of the density Δn and He-II line are both similar, it is found that helium gas is the source of the electron density. However, the density signal is the line average, it cannot be determined whether helium is injected into the core or not. However, as it is certain that at least the helium is injected to the plasma edge and scrape off layer, it may be possible to study the helium exhaust characteristics in the plasma edge.

We have conducted initial rough estimations of the helium particle confinement time using the averaged particle balance equation in the plasma edge.

$$\frac{dn_{\text{HE4}}}{dt} = S_{\text{HE4}} - \frac{dn_{\text{HE4}}}{\tau_{\alpha}^*} \quad (1)$$

Where τ_{α}^* is the effective helium particle confinement time. The helium source term S_{HE4} is determined by the waveform before and during gas puffing pulse. The temporal change in τ_{α}^* provides the helium density n_{HE4} , which was fitted to the observed He-II line emission waveform. The resultant effective helium particle confinement time τ_{α}^* may be roughly 0.25 ~1.5 sec as plotted in Fig. 1, which provides $\tau_{\alpha}^*/\tau_E=7\sim42$ for the energy confinement time of 36 ms (#49346). More accurate determination of the confinement time and analysis on profiles, experiments for various operational conditions and with He-line profile diagnostics are required.

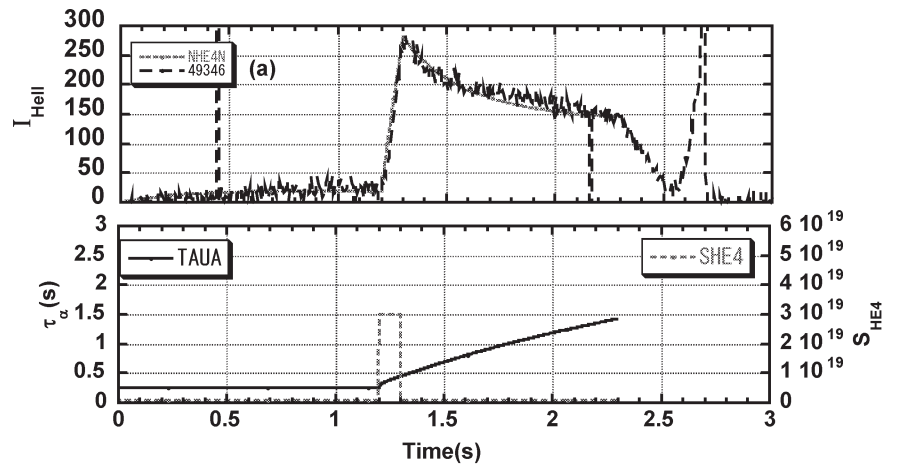


Fig. 1. (a) Observed He-II line (dashed line) in the outwardly shifted LHD plasma (#49346). Dotted curve is the calculated helium density normalized to the He-II line. (b) τ_{α}^* is the effective helium particle confinement time. (solid line) to fit to He-II line. He gas fueling rate (S_{HE4}) is described by dotted line.

§25. Parameter Dependence of Particle Transport in LHD

Tanaka, K., Michael, C.A. (JSPS fellow), Kawahata, K.

The characteristics of the particle confinements are studied from density modulation experiments at standard configuration (Rax=3.6m) [1]. The diffusion coefficient (D) and convection velocity (V) can be estimated without knowledge of absolute value of particle source. The power of NBI and toroidal magnetic field (B_t) were scanned to study electron temperature (T_e), T_e gradient and B_t dependence. Examples of the analysis are shown in Fig.1 ~2. Clear differences of the electron density (n_e) and T_e profiles were observed under different heating power. As shown in Fig.2, two fitting variables of D and V, which represents core and edge value are used. The core and edge value of D are modeled to be constant at $\rho = 0 \sim 0.65$ and $\rho = 0.75 \sim$ plasma boundary respectively and the convection profile increases linearly from $\rho = 0$ till $\rho = 0.7$ and change the gradient. These profiles of D and V can fit not only modulation profile and but also equilibrium profile as shown in Fig.1 (b).

Figure 3 (a) shows T_e dependence of D_{edge} under different B_t. Positive T_e dependence, which is typical character of anomalous dominated L mode plasma, was observed. The observed T_e dependences are $D_{edge} \propto T_e^{1.95 \pm 0.54}$ at 1.49T, $D_{edge} \propto T_e^{1.25 \pm 1.02}$ at 2T and $D_{edge} \propto T_e^{0.89 \pm 0.19}$ at 2.75, 2.8T. Although data number is small (5 shots) and dynamic range of T_e scanning are small at 2T, there is a increase of temperature index as B_t decreases. This suggests turbulence character changes under different B_t. Figure 3(b) shows B_t dependence of D_{edge}. Here, the data, whose edge T_e is from 0.6 keV to 0.7 keV are shown. Ten shots at 1.49T, 4 shots at 2T and 5 shots at 2.75, 2.8T are used for the analysis. Then, observed B_t dependence is $D_{edge} \propto B_t^{-0.73 \pm 0.23}$. The observed T_e and B_t dependences are not simple Bohm like ($\propto T_e/B_t$) nor gyro-Bohm like ($\propto T_e^{1.5}/B_t^2$). Further consideration comparing possible theoretical model is necessary to explain observed dependence.

Figure 4 shows the normalized T_e gradient dependence of V under different B_t. The value of V at $\rho = 0.7$ is considered to be V_{core}, and V_{edge} is considered to be the value at $\rho = 1.0$. The electron temperature gradient is the averaged over the region $\rho = 0.4 \sim 0.7$ for core and $\rho = 0.7 \sim 1.0$ for the edge. At B_t = 2.75, 2.8T, core convection is directed inward at lower $-\text{grad}T_e/T_e$ and reverses the sign at higher $-\text{grad}T_e/T_e$. On the other hands, in the edge region, the dependence is more complicated. There is a minimum value of V_{edge} although clear increase of V_{edge} with increase of $-\text{grad}T_e/T_e$ was observed at B_t=1.49T. In both core and edge, the convection is more outward directed at lower B_t under same $-\text{grad}T_e/T_e$. The toroidal magnetic field and $-\text{grad}T_e/T_e$ influential or maybe determining parameter to determine V and density profile in LHD.

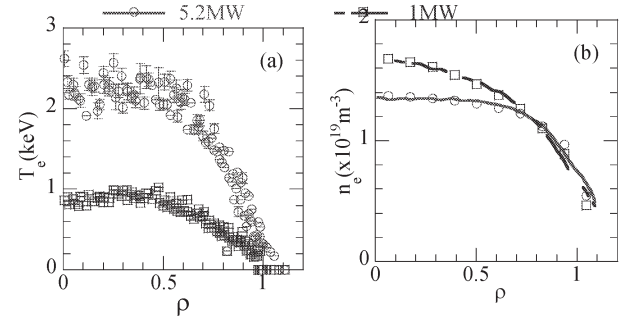


Fig. 1. (a) T_e and (b) n_e profiles. In Fig.1 (b) Lines indicate reconstructed profile, symbols indicate calculated profiles with D_{mod}, V_{mod}, B_t=2.8T

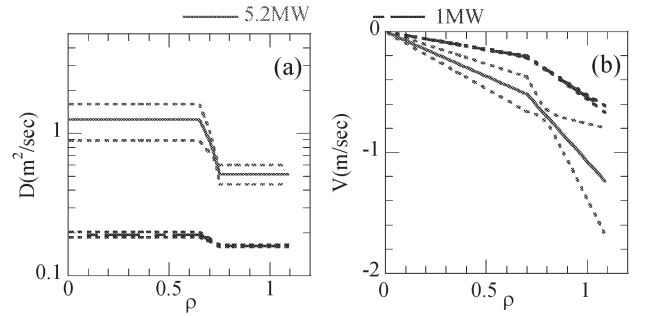


Fig. 2. (a) D and (b) V profiles. Dashed lines indicate upper and lower error limit. Negative V indicates inward directed

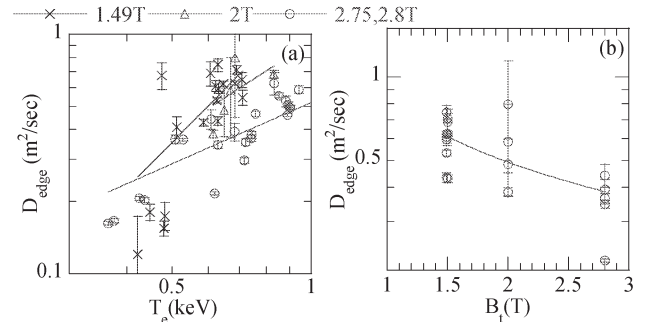


Fig.3 (a) T_e dependence under different B_t and (b) B_t dependence under similar T_e(0.6~0.7keV) of D_{edge}

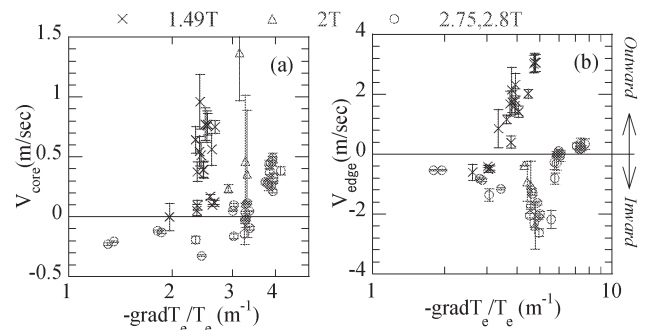


Fig.4 Normalized T_e gradient dependence of (a) V_{core} and (b) V_{edge}

Reference

- 1) Tanaka, K., et al., to be published Nucl. Fusion

§26. Three-dimensional Observation System for Pellet Ablation in LHD Plasmas

Sakamoto, R., Yamada, H.

In order to investigate an ablation of a solid hydrogen pellet, which is injected into high temperature plasmas with high speed (~ 1 km/s) for the plasma refueling, three-dimensional observation system of a fast camera has been developed. A stereo method has been employed to obtain the three-dimensional information of the pellet ablation. A pair of the stereo images, which has been taken from different location, has been focused onto single fast camera by using bifurcated imaging fiber scope, to ensure that the simultaneity of the both images. The projection matrix, which is used for a stereo reconstruction, is calibrated by taking images of a model plane of known coordinates from the actual camera positions.

Accuracy of the stereoscopic measurement is examined by the model plane, which was used at the camera calibration. Fig. 1 shows measuring accuracy of Z axis, namely, depth direction. The horizontal axis and vertical axis indicate the actual Z value of the model plane and the stereo reconstructed Z value, respectively. The stereo reconstructed Z value show good agreement with the actual Z value within the range of the error. The thick error bars indicate maximum and minimum stereo reconstructed Z value for a model plane, which is put at Z . The Z error is about ± 30 mm that is $\pm 2\%$ for the Z coordinate as shown by thin alternate long and short dash lines. The thin error bars indicate the range of scatter in reconstruction, when a stereo matching has ± 3 pixel error. The reconstructed X - Y coordinates have a similar accuracy to the Z coordinate. It is confirmed that the stereo reconstruction provide the good estimation of the spatial coordinates with linearity.

In order to demonstrate the usefulness of this measurement, an ablation behavior of a pellet, which is injected into the LHD plasmas, has been analyzed. Fig. 2 shows temporal change of a pellet ablation light intensity, which is measured by a photo-diode with H_α filter. Assuming that the initial pellet velocity maintains during ablation, the pellet position can be predicted as a broken line in figure. The stereo observation has been carried out with

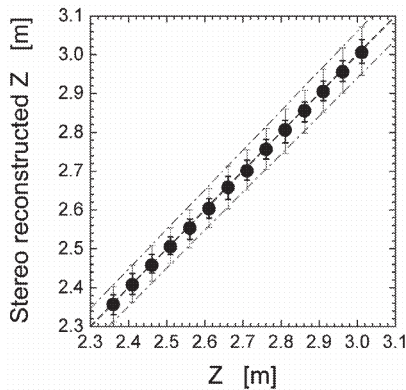


Fig. 1 Stereo reconstructed Z coordinate versus actual position of the model plane. Thin alternate long and short dash lines indicate $\pm 2\%$ error.

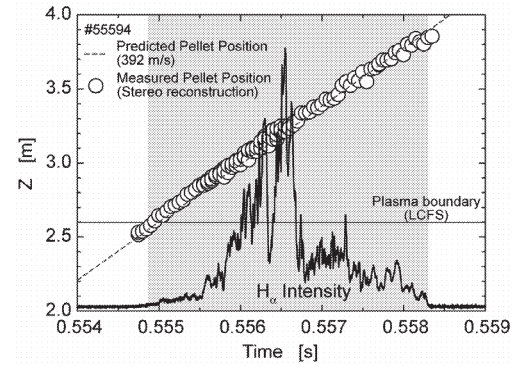


Fig. 2 Temporal change of the predicted and stereo reconstructed pellet position and H_α intensity.

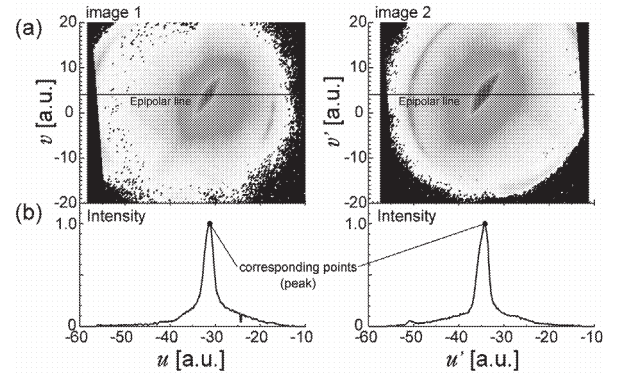


Fig. 3 (a) Typical stereo pair of the ablating pellet and (b) the emission intensity distribution along the epipolar lines.

sampling rate of 20,000 images per second and exposure time of $4\ \mu\text{s}$. In this experiments, a life time of the pellet is relatively long (> 3 ms) because of low temperature target plasma ($T_e(0) = 0.7$ keV) and about 70 pairs of the stereo images are obtained during ablation. Fig. 3(a) shows the stereo pair of the typical pellet ablatant. An epipolar line is parallel to horizontal axis in both images. The emission intensity distribution along the epipolar lines is shown in fig. 3(b). Stereo matching has been carried out by a feature-based stereo matching procedure, i.e. the corresponding points in each images are defined by the brightest points along the epipolar lines. The pellet position, which is measured by the stereo observation, is plotted in the fig. 2 by the open circles. The pellet position, which is reconstructed by the stereo analysis, showed good agreement with the predicted pellet position. In other words, it has been confirmed by this method that the initial velocity of a pellet maintains during ablation in hot plasma. At the same time, we can observe structure of the ablating pellet on X - Y plane by the images.

We acquired ability to obtain three-dimensional information of the obvious corresponding points such as emission peak. In respect of the subject for a further study, full three-dimensional reconstruction using an area-based stereo matching procedure is required to perform more detail observation. In addition, multi-point simultaneous observation is also useful to reduce blind spot and to perform stable stereo analysis

§27. Estimation of the Effect of Fast Ions on Pellet Ablation

Hoshino, M. (Nagoya Univ.), Sakamoto, R., Yamada, H., Kumazawa, R., Watari, T.

To date gas puffing has been successfully used as a fundamental fueling tool. However, for larger devices there is a concern that the fueling efficiency of gas puffing becomes worse because most of fueled gas is ionized by a hot and thick scrape-off layer before it penetrates into the confinement region. Injection of cryogenic solid pellets which is an alternative approach of fueling has been attracting interests because of advantage of deeper and more efficient fueling than gas puffing. In LHD, pellet fueling is performed by two pellet injectors to demonstrate high fueling efficiency and capability to control the electron density. It is necessary for prediction of fueling performance to clarify physical mechanisms in two stages, i.e., ablation process of pellets and subsequent drift motion of ablated plasmoid. We have estimated the pellet ablation with the use of measured and predicted pellet penetration depths.

In LHD, fast ions produced by NBI heating affect the pellet ablation due to their high energy up to 180 keV though the contribution of thermal electrons to the ablation is still predominant. Here the stored energy of fast ions is introduced as the indicator of the effect of fast ions on the ablation, $W_{f0} = P_{\text{dep}} \times \tau_{\text{slowdown}}$, where P_{dep} is the NBI deposition power and τ_{slowdown} is the slowing-down time estimated by plasma parameters at the center. In Fig. 1, the penetration depth becomes shallow as a increase of the energy of fast ions and the curve is saturated at ~ 27 kJ, thus we define it the critical value (i.e. High W_{f0} means the energy is more than this value). Figure 2 shows the comparison of the NGS scaling, which accounts for only the effect of thermal electrons on the ablation with measured pellet penetration depth. In the case of low W_{f0} , the trend agrees well with the NGS scaling even for deep penetration while it shows slightly offset from the NGS scaling. In contrast to this result, the difference between measured and predicted pellet penetration is large for deep penetration in the case of high W_{f0} although there is no difference between measured and predicted penetration depth in two cases for shallow penetration. We conclude that the discrepancy of experimental results from the NGS model is evidence of the effect of fast ions on the pellet ablation since the NGS scaling considers only thermal electrons.

The pellet penetration depth is calculated by means of the ABLATE-code [1] including contributions of not only thermal electrons but also fast ions to the ablation for profiles of measured electron temperature, electron density and calculated density of fast ion [2]. Figure 3 shows the comparison of the penetration depth calculated by the ABLATE with measured pellet penetration depth. The penetration depth of the ABLATE results from the ablation model of consideration of the effect of both electrons and fast ions. Although a systematic discrepancy between

dataset of high and low W_{f0} is mitigated, disagreement between experimental observation and the model calculation still exist.

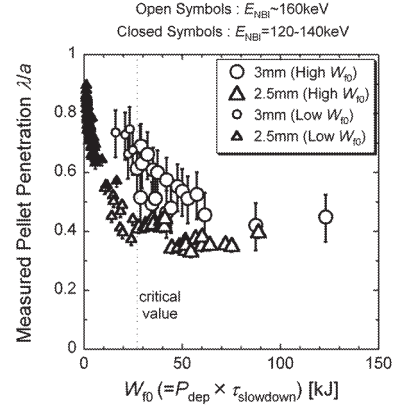


Fig. 1. The relationship between the measured pellet penetration λ/a and the energy of fast ions W_{f0} in LHD pellet fueled discharges.

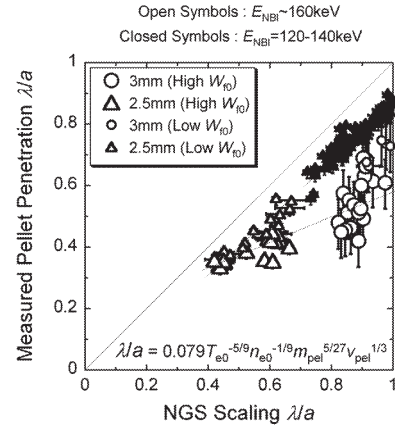


Fig. 2. Comparison of the NGS scaling which accounts for only the effect of thermal electrons on the ablation with measured pellet penetration depth at same magnetic configuration ($R_{ax} = 3.6 - 3.7$ m, $B_t \geq 2$ T).

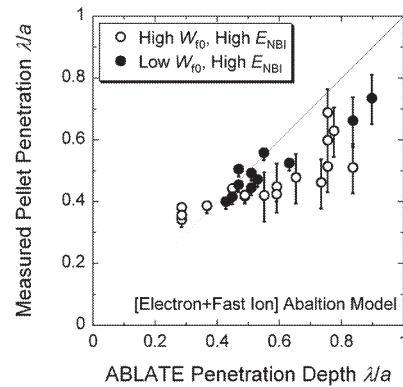


Fig. 3. Comparison of the penetration depth calculated by the ABLATE-code with measured pellet penetration depth.

Reference

- [1] Nakamura, Y. *et al.*, Nucl. Fusion **26**, (1986) 907.
- [2] Murakami, S. *et al.*, Fusion Eng. Des. **26**, (1995) 209.

§28. Injection of Repetitive Ice Pellet during ICRF Heating

Seki, T.

Long pulse plasma discharge more than 30 minutes was achieved by the ion cyclotron range of frequencies (ICRF) heating in LHD. Control of the plasma density is important to accomplish the long pulse operation. Figure 1 shows the example of the long pulse discharge. The line-averaged electron density was kept constant by the feedback control of the helium gas-puffing as shown in the second column. For the ICRF heating, the plasma consists of the helium majority species and the hydrogen minority species. Fueling of the plasma particle was carried out by the gas-puffing of the helium majority species. Low minority ratio is preferable for the ICRF heating. However, the ratio and the density of the hydrogen minority decrease during the long pulse discharge as shown in the bottom column. The temporal fluctuation of the electron temperature and the intensity of the H-alpha and the minority ratio are caused by the swing of the magnetic axis.

The hydrogen ice pellet injection is one candidate of the fueling of the minority ions. However, the ice pellet injection to the ICRF heating plasma was not desirable because the plasma was terminated by the injection of the pellet. The repetitive pellet injector was developed and installed in LHD. The pellet size is smaller than the former. The injection frequency up to 11 Hz and the injection duration more than 1000 seconds are possible.

The repetitive pellet injection was carried out for the ICRF sustained plasma discharge. Figure 2 shows the time history of the plasma parameters during the repetitive pellet injection. The pellet injection started from 67.5 sec. and the injection frequency is 5 Hz. The pellet was injected successfully to the end of the plasma discharge. The line-averaged electron density increased continuously during the pellet injection. The ion and electron temperature rose at beginning and decreased later by the density rise. The intensity of the H-alpha increased and the minority ratio was kept almost constant. The increase of ion and electron temperatures suggests the confinement improvement caused by pellet injection.

The ICRF heating performance was estimated using TASK/WM three-dimensional full wave code¹⁾. The plasma parameters before and during pellet injection were used. The power deposition profile was almost same in the both case. The absorbed power increased double during pellet injection. This is caused by the higher density arose from the pellet injection. The ICRF heating had no harmful effect by pellet injection.

Reference

1) Fukuyama, A., et al., IAEA Conf., Solento, IAEA-CN/THP2/26 (2000).

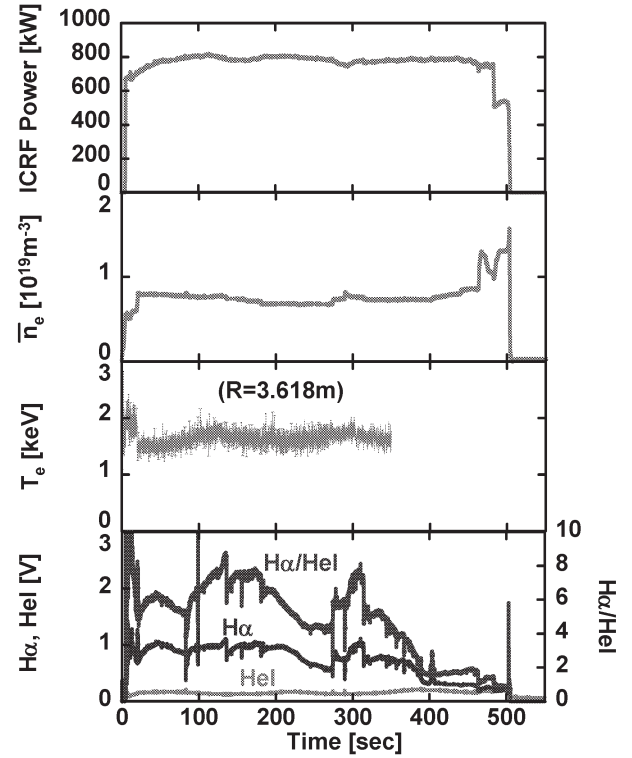


Fig. 1. Time evolution of plasma parameters using helium gas-puffing.

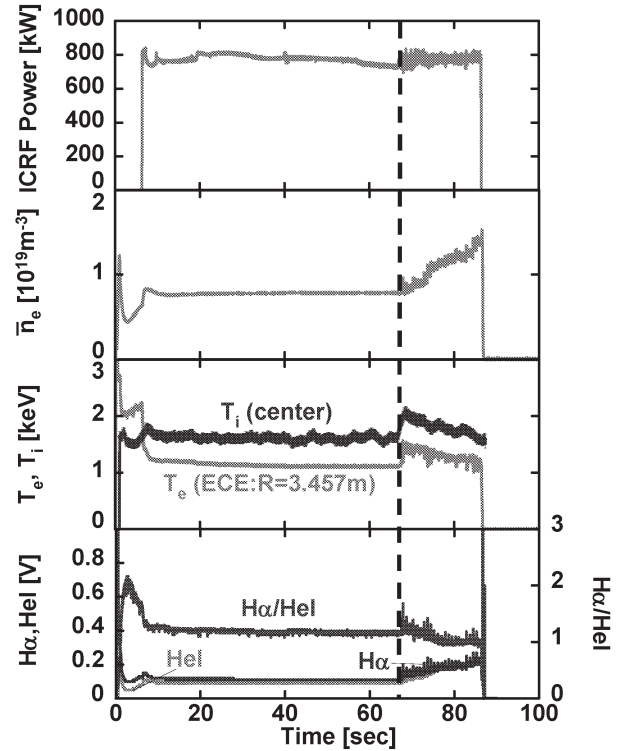


Fig. 2. Time evolution of plasma parameters using the repetitive pellet injection. The pellet injection starts from 67.5 seconds.

§29. Measurement of Inhomogeneous Poloidal Distribution of He Neutral Atom Flux

Goto, M., Sawada, K., Morita, S.

Neutral atom flux in the plasma boundary region has been measured with a spectroscopic method. An emission line in the visible wavelength range shows a clear Zeeman splitting, and the magnetic field strength at location of the line emission is deduced from the splitting width. Since the distribution of the magnetic field strength along the line of sight is well known, the emission location and its intensity can be simultaneously obtained. This kind of measurement is carried out with an array of 40 lines of sight which covers an entire poloidal cross section, and then the poloidal distribution of neutral atom flux is obtained. [1] Because the Zeeman splitting is found more noticeable in helium lines than in hydrogen lines, studies are made with helium discharges. We focus our attention on the measurement of neutral helium line ($\lambda 667.8$ nm) distribution.

In the previous measurement for the poloidal cross section where the plasma is elongated in the horizontal direction, localized atom emissions in the vicinity of inboard-side X-points are observed for the configuration of $R_{ax} = 3.6$ m, where R_{ax} is the radius of the magnetic axis. We have attempted to determine the electron temperature and density at each emission location from the intensity ratios of three emission lines of neutral helium, and have found little variation in the obtained parameters at all the emission locations. This indicates that the observed line emission can be directly interpreted as the inward atom flux and therefore there exists a strong inhomogeneous distribution of atom flux around the plasma. When R_{ax} is shifted outwards to $R_{ax} = 3.75$ m, the localized line emissions at the inboard-side X-points dissipate.

According to the measurement with Langmuir probes embedded on the divertor plates, the divertor flux is dominantly observed in some narrow areas rather than is distributed homogeneously, and these locations change depending on R_{ax} . Specifically, the divertor flux becomes dominant on the inboard-side divertor plates for $R_{ax} = 3.6$ m, and on the upper- and lower-side plates for $R_{ax} = 3.75$ m. This is consistent with a calculation concerning the magnetic field line structure in the plasma boundary region, where we regard the density of open magnetic field lines striking on the divertor plates as a measure of the divertor flux. From these results in addition to our previous measurement, it is most likely that when R_{ax} is shifted outwards to 3.75 m, intensive line emissions take place in the area near the X-points at the vertically elongated plasma cross section.

In order to certify this suggestion, the Zeeman spectroscopy is also applied for the poloidal cross section where

the plasma is vertically elongated. Figure 1 shows the results from the $R_{ax} = 3.6$ m and 3.75 m configurations. In the case of

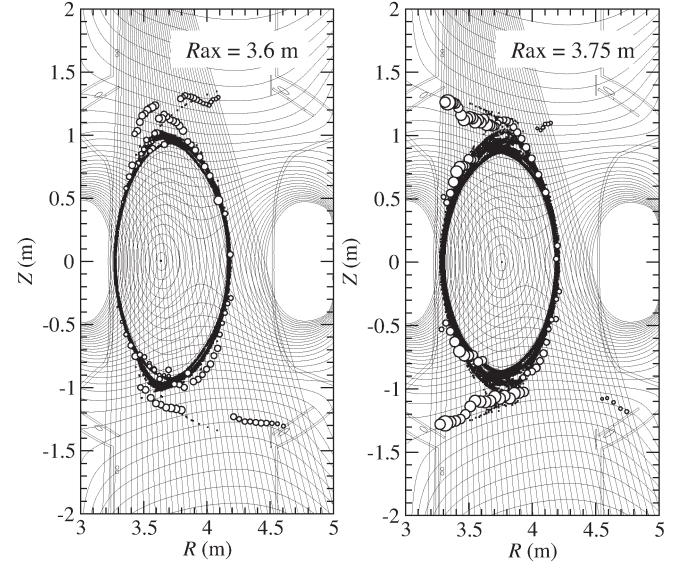


Fig. 1. Derived emission locations of HeI $\lambda 667.8$ nm line for (a) $R_{ax} = 3.6$ m and (b) $R_{ax} = 3.75$ m cases. Open circles stand for the location of line emissions and their sizes show the intensity. Lines of sight of 40 channels are indicated with straight lines.

$R_{ax} = 3.6$ m we find no localized strong atom emissions, but intense line emissions around the X-points and the divertor legs are observed for $R_{ax} = 3.75$ m. This agrees to our expectations, and a close relationship between the divertor flux and the atom flux is confirmed.

It has been pointed out that there might be a strong interaction between the plasma and inboard-side vacuum vessel wall due to a small clearance between them and this can give rise to another strong particle source there. In our measurement, however, the atomic radiation near the inboard-side wall is relatively weak, and the possibility of a strong particle source on the inboard-side wall surface seems to be denied.

For a deeper understanding of the relationship between the divertor recycling and atom flux, a Monte-Carlo simulation code for neutral particle transport has been developed. With this code we have calculated a three-dimensional distribution of neutral line emission intensity under conditions that the particle source is localized on the divertor plates and its strength is proportional to the density of the magnetic field lines striking on the divertor plates. Similar behaviors to the experiments are obtained for both the $R_{ax} = 3.6$ m and 3.75 m cases and therefore it is concluded that the neutral atom flux dominantly originates in the particle recycling at the divertor region.

Reference

- 1) M. Goto and S. Morita, Phys. Rev. E **65**, 026401 (2002).

§30. High-resolution Measurements of $H\alpha$ Line Spectral Profiles in LHD Steady State Plasmas

Kondo, K., Arimoto, H. (Kyoto Univ.),
Oda, T. (Hiroshima Kokusai Gakuin Univ.),
Takiyama, K. (Hiroshima Univ.),
Ohgo, T. (Fukuoka Univ. Educ.),
Masuzaki, S., Miyazawa, J., Shoji, M., Kobayashi, M.,
Morisaki, T., Morita, S., Sudo, S., Ohyabu, N.,
Noda, N., Ida, K., Sato, K.

$H\alpha$ line spectral profiles in LHD hydrogen discharges have been measured with a high wavelength resolution spectroscopic measurement system. The system is designed to distinguish a few eV difference of neutral hydrogen energy along the sight lines.

In this experimental campaign, we investigated \bar{n}_e dependence of the neutral hydrogen behavior in the helical divertor configuration with $R_{ax} = 3.60\text{m}$. With the density feedback gas-puffing and the series injection of NB, steady state hydrogen discharges were performed. The discharge duration was $\sim 6\text{s}$ and \bar{n}_e was varied in the range of $2.0 \sim 6.0 \times 10^{19} \text{ m}^{-3}$ in shot by shot. The spectral profiles can be decomposed into narrow and broad Gaussian components and the asymmetric profiles due to the blue shift of the broad component were obtained. This blue shift can be attributed to the atoms reflected on the inner divertor plates because the particle deposition is intensive at the inboard side of the torus in $R_{ax} = 3.60\text{m}^1$. Figure 1 shows \bar{n}_e dependence of the line intensity and the flow velocity of the hydrogen atoms deduced from the spectral profiles obtained at the sight line viewing an inner divertor plate. In the \bar{n}_e range of $2.0 \sim 6.0 \times 10^{19} \text{ m}^{-3}$, the line intensity of the narrow and broad component increases with $\bar{n}_e^{2.1}$ and $\bar{n}_e^{2.6}$, respectively. The intensity ratio of broad/total increase from 0.3 to 0.5 with the increase of \bar{n}_e from 2.0 up to $6.0 \times 10^{19} \text{ m}^{-3}$. The ion saturation current measured by the 6I divertor probe depends on $\bar{n}_e^{2.3}$. The similarity in \bar{n}_e dependence of the line intensity and the ion saturation current indicates that the interactions with the inner divertor plates such as desorptions and reflections

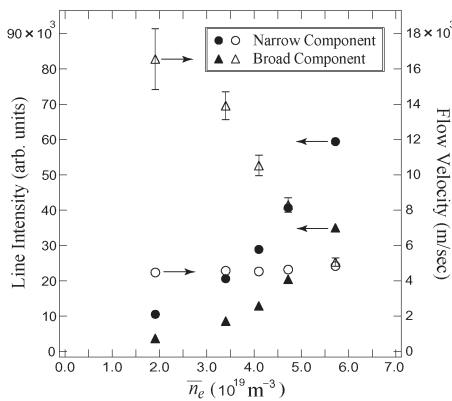


Fig. 1: Line-averaged electron density dependence of $H\alpha$ line intensity and flow velocity of hydrogen atoms.

are progressed caused by the increasing outflux with \bar{n}_e . On the other hand, the flow velocity and the temperature of the hydrogen atoms deduced from the broad component decrease with the increase of \bar{n}_e . Especially in the flow velocity, the rapid decrease is observed as shown in Fig. 1 and the asymmetric feature of the spectral profiles gradually vanishes. This is considered to be due to the falloff of the sheath acceleration, because the edge electron temperature become lower ($\sim 50\%$) with the increase of \bar{n}_e from 2.0 up to $6.0 \times 10^{19} \text{ m}^{-3}$.

In the high density detachment experiment²⁾, line spectral profiles of $H\alpha$ were also investigated. Figure 2 shows the spectral profiles in the attachment(a) and the detachment(b) phase obtained at the sight line viewing an inner divertor plate. In the detachment phase, the contribution of the broad component decreases and the spectral profile of total emission exhibit narrower shape than in the attachment phase. The line-averaged electron density is $\sim 6.0 \times 10^{19} \text{ m}^{-3}$ in the attachment and $\sim 1.4 \times 10^{20} \text{ m}^{-3}$ in the detachment phase. Despite the significant increase in \bar{n}_e , the difference in the total line intensity between the attachment and the detachment phase is not significant ($\sim 7\%$ lower in the detachment phase). This is considered to be due to the suppression of the neutral hydrogen generation by the detachment. In the measurement duration of 0.45sec ($1.35 \sim 1.80\text{sec}$), about 30 ELM-like spikes are observed by $H\alpha$ monitor. These spikes are thought to be deeply concerned with the rotating radiation belt³⁾ which appears during the detachment. Emissions from a rotating radiation belt will be investigated in next campaign.

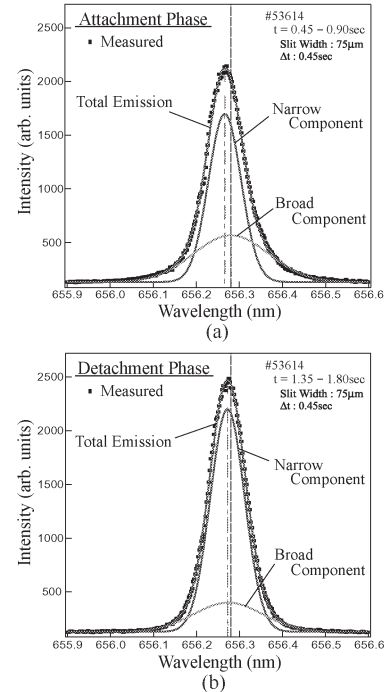


Fig. 2: $H\alpha$ line spectral profiles observed in (a) attachment phase and (b) detachment phase.

References

- 1) Morisaki, T. *et al.* : Contirb. Plasma Phys. **42** (2002) 2–4 321.
- 2) Miyazawa, J. *et al.* : J. Plasma Fusion Res. **81** (2005) 5 331.
- 3) Masuzaki, S. *et al.* : submitted to J. Plasma Fusion Res.

§31. High-beta Experiments in LHD

Sakakibara, S., Watanabe, K.Y., Yamada, H.

To investigate configuration dependence of MHD activities and to optimize the magnetic configuration for production of high-beta plasmas, the control of rotational transform profile by external coils has been done in LHD. The aspect ratio of helical coil current, γ , was changed from 1.22 to 1.13 at the same magnetic axis position, which also changes the central rotational transform $\iota_0/2\pi$ from 0.47 to 0.73. While the increase in $\iota_0/2\pi$ has a disadvantage on MHD stability because it leads to restraint of Shafranov shift restricting spontaneous magnetic well formation in addition to the reduction of magnetic shear, a degradation of particle confinement due to an increment of helical ripples with the plasma outward-shift expects to be avoided.

Figure 1 shows change of achieved average beta as a function of γ . The γ scan experiments had been done in the configuration with $B_t = -0.5$ and -1 T, and achieved beta has a maximum value in the $\gamma = 1.20$ configuration. After these experiments, we tried the high-beta plasma production in $\gamma = 1.20$ configuration, and average beta $\langle\beta_{dia}\rangle$ of 4.3 % was obtained in the configuration with $R_{ax} = 3.6$ m, $B_t = 0.45$ T as shown in fig.2. The previous experiments show that while several MHD modes excited in peripheral region are dominantly observed and enhanced with increasing $\langle\beta_{dia}\rangle$, they saturate and/or intermittently observed when $\langle\beta_{dia}\rangle$ exceeds about 3 %¹⁾. This trend has been shown in fig.2 discharge. In this discharge, an increase in $\langle\beta_{dia}\rangle$ is restricted by an excitation of peripheral MHD modes when electron density increases in spite of constant $\langle\beta_{dia}\rangle$. One of the reasons for electron density dependence of MHD activity may be due to the increment of magnetic Reynolds number, S . The S dependence on the saturation amplitudes of MHD modes have been found out by the database study, and about 10 % of degradation of plasma stored energy due to peripheral MHD modes has been observed in density ramp-up operation with temporal reduction of S . The

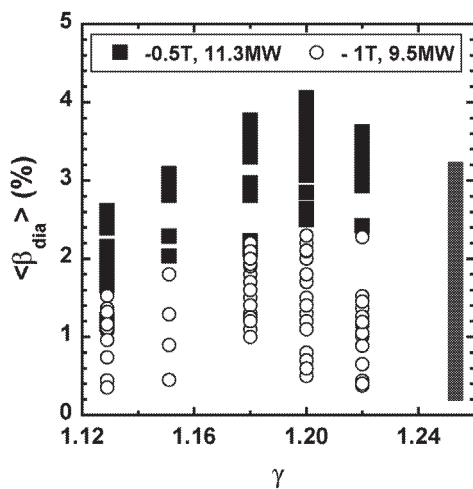


Fig.1 Change of achieved beta in $B_t = -0.5$ and -1 T discharges as a function of γ

linear theory suggests that the growth rate of resistive interchange mode is decreased by an increment of S , and it is qualitatively consistent with characteristics of observed MHD activities.

On the other hand, the achieved beta gradually decreases with the increase in $\iota_0/2\pi$ by external coil control and/or positive plasma current as shown in fig.1. The minor collapse of plasma due to $m/n = 1/1$ mode was observed in the highest $\iota_0/2\pi$ configuration (0.73). Also, even if the vacuum $\iota_0/2\pi$ is relatively small, the large plasma current increasing $\iota_0/2\pi$ causes the similar collapse. The growth of $m/n = 1/1$ island, which was identified as profile flattening of T_e near the resonant surface at $\rho \sim 0.5$, was observed just before the minor collapse in both cases, and it decreases $\langle\beta_{dia}\rangle$ by more than 50 %. Then the peripheral plasma pressure with strong magnetic shear was still maintained before and after the collapse. These phenomena may be caused by the reduction of magnetic shear at the $m/n = 1/1$ resonance in magnetic hill configuration.

Reference

- 1) A.Komori, S.Sakakibara et al., Phys. Plasmas 12 (2005) 0561221.

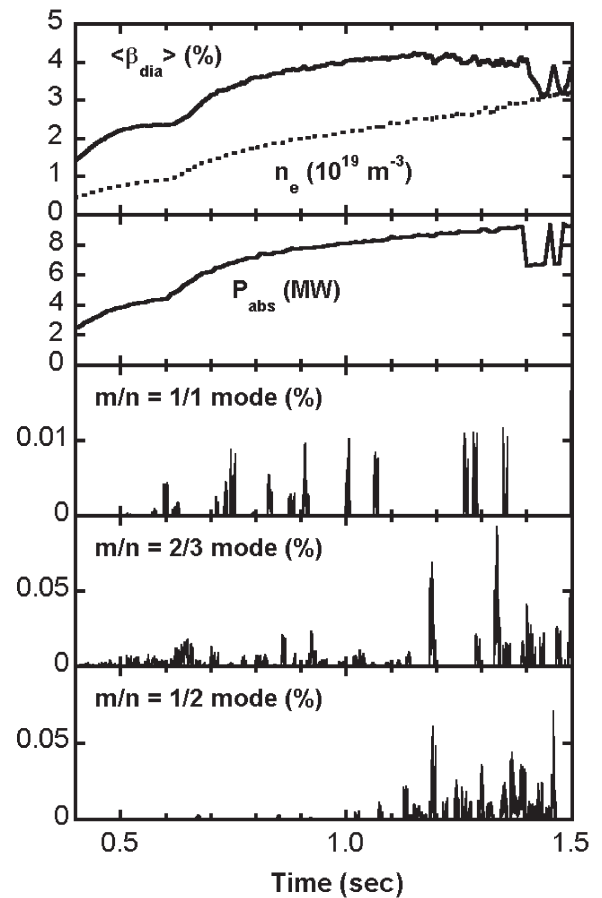


Fig.2 High- β discharge in the configuration with $R_{ax} = 3.6$ m, $B_t = -0.45$ T and $\gamma = 1.20$.

§32. Observed Pressure Gradients at a Peripheral Rational Surface in LHD High Beta Plasma

Watanabe, K.Y., Sakakibara, S., Narushima, Y.

Ideal MHD instabilities have a possibility to strongly limit the operational regime of the plasma parameters such as beta, pressure gradient and/or so on. In tokamaks, it is well known that the operational beta limits are quite consistent with theoretical predictions of ideal linear MHD theory. On the contrary, in helical plasmas, a limited number of systematic studies about the effect of pressure driven ideal MHD instabilities on the operational beta range in experiments have been reported. In order to study the role of low mode number ideal pressure driven MHD modes on the operational beta range in LHD, we compare between the experimentally observed pressure gradients at peripherally located resonant rational surfaces and the theoretically predicted unstable region for ideal pressure driven MHD instabilities in the new high aspect configuration with $R_{ax}=3.6m/A_p=6.3$, where the achieved beta value has been extended to 4%.

Figure 1 shows observed beta gradients and contours of the growth rate of low-n ideal MHD mode with a global mode structure in the $\langle\beta\rangle$ - $d\beta/d\rho$ diagram in a peripheral low order rational surface ($\rho=0.9$, $\iota\sim 1$). Here ρ and ι are a normalized minor radius and a rotational transform, respectively. Solid and dotted lines denote contours of the low-n ($m/n=1/1$) ideal MHD modes (with global mode structure) with $\gamma_{low-n}/\omega_A=10^{-2}$ and 3×10^{-3} for currentless equilibria. The growth rate is calculated with a MHD stability analyzing code (TERPSICHORE). Here $\omega_A=v_{A0}/R_0$, v_{A0} and R_0 are the Alfvén velocity and the major radius at the magnetic axis. The dashed lines are the stability boundary of Mercier modes (with a highly localized mode structure / high-m limit), which corresponds to the $\gamma_{low-n}/\omega_A=0$ contour of the low-n mode. Figures 2 (a) and (b) show the mode structures of the ideal MHD unstable mode at the symbols, “a” and “b” in Fig.1, respectively. Here we are considering a fixed boundary mode. Both eigenfunctions are dominated by an almost single mode. From Figs 1 and 2, the mode width of the MHD unstable modes with $\gamma_{low-n}/\omega_A=10^{-2}$ and 3×10^{-3} are $\sim 5\%$ and $\sim 1\%$ of the plasma minor radius, respectively. The mode width is quite narrower than that of the MHD unstable mode resonant with the core low-n rational surface, for example, $m/n=2/1$ because the magnetic shear is stronger than that in the core region. The circle symbols in Fig.1 correspond to the observed thermal beta gradients, which is estimated based on measured electron temperature profile and density profile. Here $Z_{eff}=1$ and $T_i=T_e$ are assumed. The data were obtained in 0.45T to 1.75T operation. The envelope of the observed beta gradients at $\rho=0.9$ increases with the beta up to $\langle\beta_{dia}\rangle=4\%$. Though a change of the envelope is observed around $\langle\beta_{dia}\rangle=1.5\%$ which corresponds to the Mercier unstable region, clear boundary is not observed up to $\langle\beta_{dia}\rangle=4\%$. The envelope of the observed thermal pressure gradients in the

beta range of $\langle\beta_{dia}\rangle=3-4\%$ corresponds to coincide with a contour of the $m/n=1/1$ ideal MHD mode with $\sim 5\%$ of the plasma minor radius as the mode width.

Figure 3 shows the radial profile of the growth rate of the high-n ideal ballooning modes at the symbols “a” in Fig.1. At $\langle\beta_{dia}\rangle\sim 4\%$, the high-n ballooning mode is as unstable as the low-n interchange mode. The systematic analysis of the relationship between the ballooning modes and experiments is a future subject of exploration.

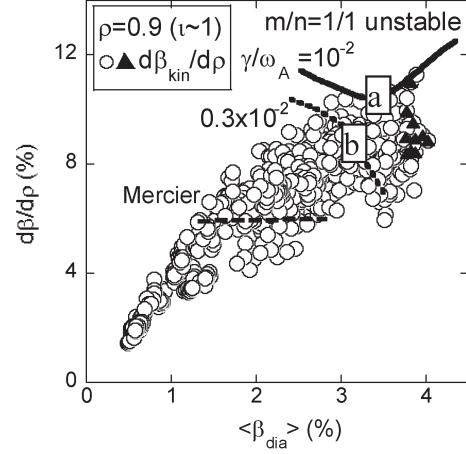


Fig.1

The contours of low-n ideal MHD mode growth rate calculated in $\langle\beta\rangle$ - $d\beta/d\rho$ diagram.

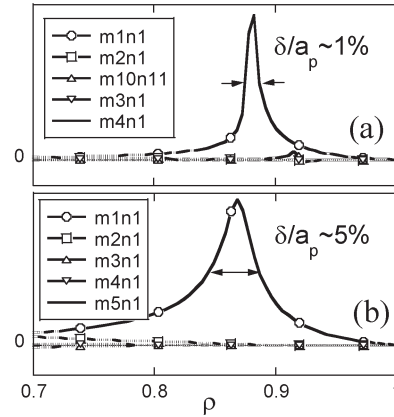


Fig.2

The eigenfunction profiles of the low-n ideal MHD unstable mode for (a) “a” and (b) “b” in Fig.1

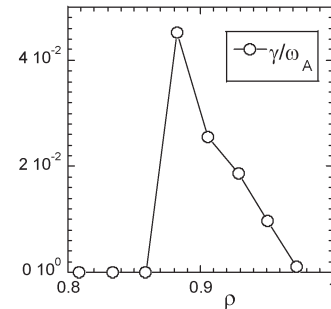


Fig.3 The normalized growth rate profiles of the high-n ballooning mode for the pressure profile corresponding to the point of “a” in Fig.1.

§33. Onset of Pressure Driven Mode

Sakakibara, S., Watanabe, K.Y., Yamada, H.

Relationship between characteristics of magnetohydrodynamic (MHD) modes and the linear stability boundary has been investigated by controlling the edge pressure gradient directly using the movable limiter. A series of experiments have three kinds of advantages on MHD study. One is that they enable us the detail reconstructions of equilibria with clear plasma boundary, which can give the accurate stability calculations. The LHD configuration has an ergodic layer outside last closed flux surface, which makes the accuracy of the calculation of edge stability unclear. Second one is that the movable limiter can directly control the edge pressure and its gradient destabilizing the pressure-driven mode. Also it is useful for confirming them the resonant or non-resonant modes. Third one is that it is possible to identify the onset of MHD instability in steady state plasmas.

Changes of the plasma boundaries defined by different conditions and radial positions of rational surfaces as a function of the limiter position, R_h , are shown in fig.1. The R_h is used here as a matter of convenience, which is the radial position of the limiter tip at $z = 0.33$ m. Clear identification of the plasma boundary in experiments is difficult because of the lack of measurements in the edge, so two kinds of plasma boundary are estimated here. One is defined by the extrapolation of observed T_e profile, and the other are decided by the location where the plasma has the ratio of the specific amount of the electron stored energy to total one. The locations of resonant surfaces, which are calculated by 3-D MHD equilibrium code VMEC, are almost constant at any limiter position. Edge low- n resonant surfaces with $m/n = 2/3, 3/4$ and $4/5$ go outside plasma boundary when $R_h < 4.13$ m, and the $1/2\pi = 1$ surface becomes just the plasma boundary at $R_h = 4.02$ m. Thus, the pressures at $1/2\pi \geq 1$ resonant surfaces could be completely removed in the experiments.

The results of the linear stability analyses on resistive interchange mode and changes of magnetic Reynolds numbers, S , at $1/2\pi = 4/3$ and 1 resonances are shown in Fig.2. The ideal interchange mode is theoretically stable in the edge region by the magnetic shear effect. The D_R is well used as the index of stability boundary of the resistive mode. The positive D_R means the resistive mode is unstable, and edge MHD modes are linearly unstable due to magnetic hill configuration in a series of experiments. When the $1/2\pi = 4/3$ and 1 resonant modes disappear or are sufficiently suppressed, both D_R 's have the same value of $0.08 \sim 0.1$. The S parameter, which concerns the linear growth rate of resistive modes, continues to decrease with the limiter insertion because of reduction of T_e . Both thresholds of the D_R are obtained in the plasmas with S of $5 \times 10^5 \sim 10^6$. According to Ref.1, the low- n resistive modes have the significant growth rate when D_R is $0.15 \sim 0.20$ in the plasmas with $S \geq 10^6$, which is consistent with the experimental results within the factor of two.

Reference

1) M.Wakatani *et al.*, Fusion Eng. Design **15** (1992) 395.

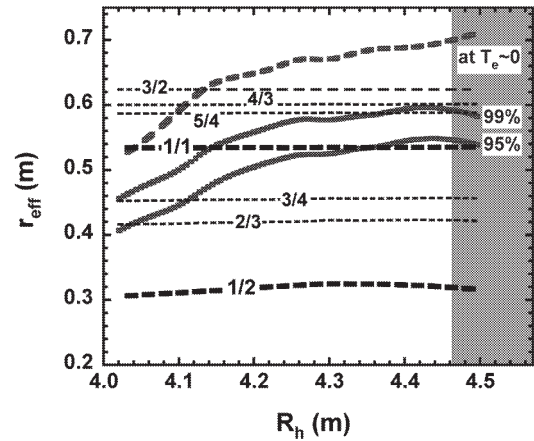


Fig.1 Changes of specific plasma boundaries and radial positions of resonant surfaces as a function of R_h .

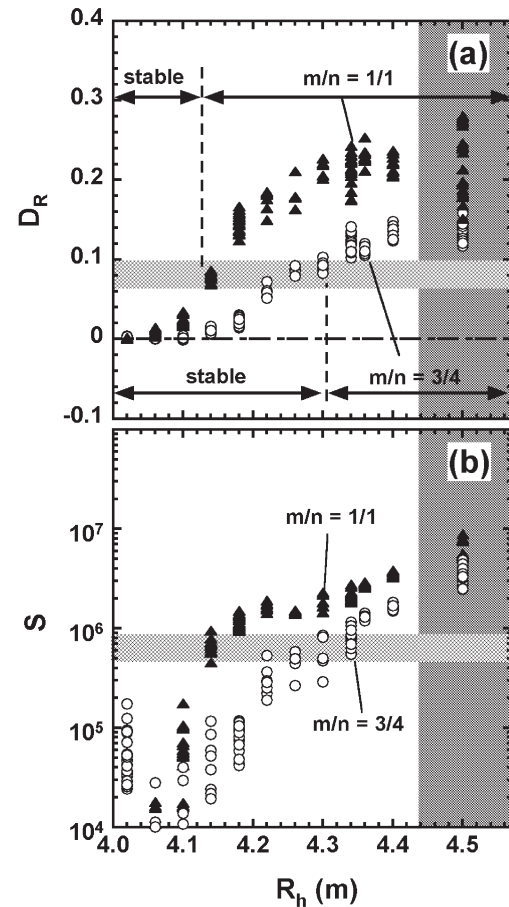


Fig.2 Changes of (a) D_R and (b) S around the $m/n = 1/1$ and $3/4$ resonant surfaces as a function of R_h .

§34. Transport Analysis of High β Plasmas on LHD

Funaba, H., Watanabe, K.Y., Sakakibara, S.,
LHD Experimental Group

High beta plasmas with over 4% of the volume averaged beta, $\langle\beta\rangle$, are obtained in the LHD experiments. According to the results of recent analysis with respect to the global confinement property based on the empirical scaling ISS95, no disruptive degradation was found up to $\langle\beta\rangle \sim 4\%$, while gradual degradation of confinement efficiency was observed. The improvement factor of the energy confinement time compared with ISS95, H_{ISS95} , showed decrement by about 30% when $\langle\beta\rangle$ increased from 2% to 4%¹⁾. Local transport analysis based on the power balance has been made in order to clarify the causes of such degradation. The effective thermal transport coefficients, $\chi^{eff} = (\chi_e^{exp} + \chi_i^{exp})/2$, are derived by using the one-dimensional transport code, PROCTR²⁾. Here, χ_e^{exp} and χ_i^{exp} are experimentally evaluated thermal diffusivities of electrons and ions, respectively. The NBI power deposition profiles are evaluated by a three-dimensional Monte Carlo simulation code in these analyses. The analysis is carried out using the gyro-reduced Bohm (GRB) type model as reference. The dependence of ISS95 on the parameters is almost similar to that of the GRB model. The ratio of χ^{eff} to the transport coefficient by the GRB model, χ_{GRB} , is studied at various radial positions. The plasmas in the density region of $H_{SUDO} < 1.0$, where H_{SUDO} is the ratio of the electron density to a density limit scaling proposed by Sudo *et al.*³⁾ are investigated. It is found that degradation of transport at the peripheral region is large. At the normalized minor radius, $\rho = 0.9$, χ^{eff}/χ_{GRB} becomes large in the high β regime by some factors of 5 ~ 10 (Fig. 1). On the other hand, the degradation of χ^{eff}/χ_{GRB} is weak around $\rho \sim 0.5$ as shown in Fig. 2.

As some possible reasons for this degradation, following causes can be considered. (1) Effects of the pressure-driven MHD modes : In LHD, which is a heliotron type device, it is predicted that the pressure-driven MHD modes become unstable in the high β regime at the peripheral region. (2) Degradation of confinement property at the high density or high collisionality regime : At the high collisionality regime even in low β cases, confinement degradation, which is compared with the GRB type model or the ISS95 model, was also observed⁴⁾ although the reason is not clear. On LHD, high β

was achieved in the density region near the density limit. (3) Increment in ergodicity of magnetic flux surfaces in the peripheral region with the increment in β : From the results of the 3-dimensional MHD equilibrium code which does not assume nested flux surfaces a priori, it is shown that a stochastic region at the edge begins to penetrate to the core region when β increases⁵⁾.

In order to study the effect of the pressure-driven MHD modes which is listed as (1) above, comparison between the experiment and the anomalous transport model by the resistive g-mode will be carried out.

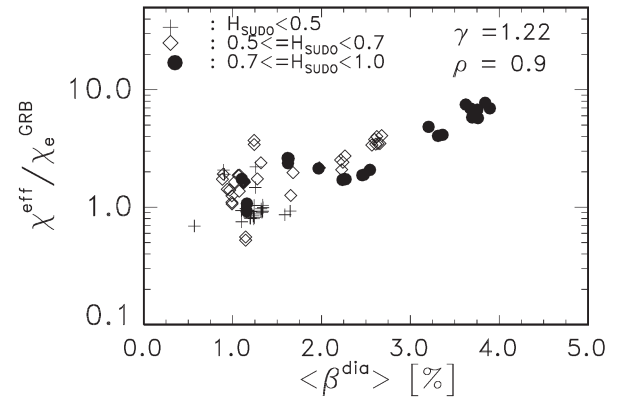


Fig. 1. Dependence of χ^{eff}/χ_{GRB} on $\langle\beta\rangle$ at $\rho \sim 0.9$. Density regions (H_{SUDO}) are distinguished by the symbols.

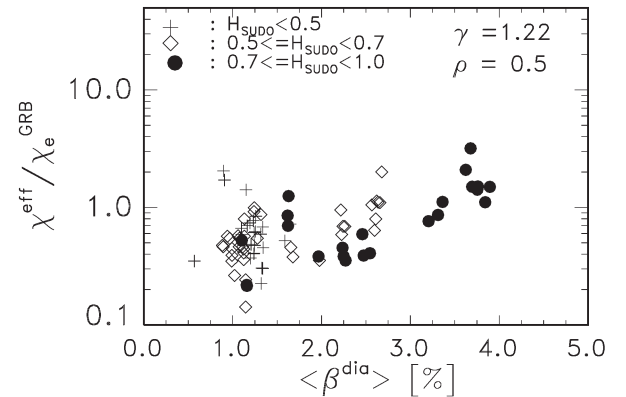


Fig. 2. Dependence of χ^{eff}/χ_{GRB} on $\langle\beta\rangle$ at $\rho \sim 0.5$.

References

- 1) K.Y. Watanabe, *et al.*, Proc. of 20th IAEA Fusion Energy Conf., EX/3-3, (Vilamoura, 2004).
- 2) H.C. Howe, ORNL/TM-11521 (1990).
- 3) S. Sudo, *et al.*, Nucl. Fusion, **43**, (2003) 749.
- 4) J. Miyazawa *et al.*, Plasma Phys. Control. Fusion (to be submitted).
- 5) N. Nakajima, *et al.*, Proc. of 20th IAEA Fusion Energy Conf., TH/5-6, (Vilamoura, 2004).

§35. Observation of Internal Structure of Edge MHD Modes in High Beta Plasmas on LHD

Watanabe, F. (Dep. Energy Eng. Sci., Nagoya Univ.),
Toi, K., Ohdachi, S., Takagi, S., Sakakibara, S.,
Watanabe, K.Y., Morita, S., Narihara, K., Tanaka, K.,
Yamazaki, K.

In LHD, Edge MHD modes such as $m/n = 1/1$, $3/4$, $2/3$ and $1/2$ are excited near the plasma edge region in magnetic hill, with the increase in the plasma beta value [1]. These edge MHD modes sometimes interrupt the increase in the stored energy in high beta regime. In particular, the edge MHD modes are suddenly destabilized just after L-H transition which leads to the formation of edge transport barrier having a steep pressure gradient [1, 2]. To clarify characteristics of edge MHD modes and minimize the effects on plasma confinement, measurements of the internal structure, growth rate and so on are crucially required.

In LHD, we have employed eight sets of 20-channel soft-X-ray (SX) detector array in order to measure the internal structure of the edge MHD modes. An example of these SX detector array systems is shown in Fig. 1. This system is installed inside the vacuum vessel in the vertically elongated section of LHD. The detector array is a silicon PIN photodiode array which consists of 20ch active areas arranged in one dimension. A beryllium foil with $8\mu\text{m}$ or $15\mu\text{m}$ thickness is attached in the front of the system to shut visible and vacuum ultra violet emissions. The viewing sight of the detector system is adjusted through a collimator slit, as shown in Fig.1.

Figures 2(a)-2(d) show the radial profile of SX intensity I_{sx} , the fluctuation amplitude δI_{sx} have high coherence with the observed $m/n = 1/1$ and $2/3$ magnetic fluctuations in a typical high beta hydrogen plasma heated by NBI heating. The rational surfaces of these edge MHD modes locate in the plasma edge region ($\langle r \rangle / \langle a \rangle = \rho > 0.8$). The SX fluctuation δI_{sx} is derived by numerical filtering around the frequency range of high coherence with the magnetic fluctuations, and is averaged over a time window of 20 ms. The relative amplitude $\delta I_{sx}/I_{sx}$ of $m/n = 1/1$ and $m/n = 2/3$ modes increases rapidly toward the plasma edge, as shown in Figs.2(c) and 2(d). The peak of δI_{sx} for respective mode locates slightly inside that of the rational surface, which is caused by the path integral effect in SX signals. Moreover, δI_{sx} of $m/n = 2/3$ mode has a peak in the plasma central region (Fig.2(b)). This is also attributed to the path integral effect. The relative amplitude of $m/n = 2/3$ mode decreases more rapidly toward the plasma center than that of $m/n = 1/1$ mode. This is consistent with the radial dependence of the eigenfunction with different m number, although $\delta I_{sx}/I_{sx}$ or even $\delta I_{sx}/|\nabla I_{sx}|$ does not necessarily correspond to an eigenfunction of the MHD mode because of the path integral effect.

The phase relation among SX fluctuation signals obtained by a SX array will give information of m -number. As shown in Figs. 2(e) and 2(f), the phase difference between SX channels in inboard and outboard plasma edges is roughly $\sim 2\pi$ for $m/n = 2/3$, i.e. the m -number is even, and is $\sim \pi$ for $m/n = 1/1$, i.e. the m -number is odd.

They are consistent with the m -number determined with magnetic probe array.

In conclusion, the edge MHD modes were clearly detected by SX detector arrays as well as magnetic probes. The relative amplitude $\delta I_{sx}/I_{sx}$ of edge MHD modes such as $m/n = 2/3$ and $1/1$ increases rapidly toward the plasma edge, which clearly indicates a character of edge mode. The radial variation of $\delta I_{sx}/I_{sx}$ depends on the m -number. In order to clarify the characteristics of edge MHD modes and their impact on plasma confinement, we need the detailed comparison between experimental data such as SX data and theoretical results on edge MHD modes obtained by MHD stability codes for three-dimensional plasma such as CAS3D3 code [3].

Reference

- 1) Toi, K. *et al.*, Nucl. Fusion **44**, 217 (2004).
- 2) Toi, K. *et al.*, Phys. Plasma **12**, 020701-1 (2005).
- 3) Nakajima, N., 20th IAEA Energy Conf., Villamoura, TH/56(2004).

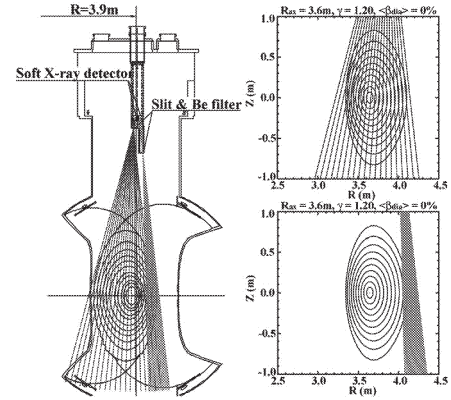


Fig. 1 SX detector array system in LHD. 40 lines of sight by two SX-ray detector arrays are drawn.

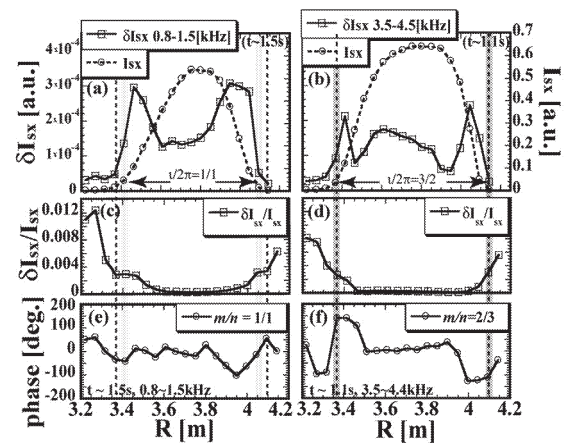


Fig. 2 Radial profiles of SX intensity (I_{sx}), fluctuation amplitude (δI_{sx}) by edge MHD modes ($m/n = 1/1$ and $2/3$) and phase difference between SX channels. The vertical dotted lines indicate the LCFS in the vacuum field. Thin vertical lines stand for the rational surfaces of $1/2\pi = 1$ and $3/2$.

§36. Spatial Structure of the MHD Events Observed in LHD

Ohdachi, S., Toi, K.

Edge magnetic fluctuations are often observed in the high-beta experiments on LHD. From the mode-number analysis, they are localized in the plasma edge region or located even outside the LCFS. It is therefore important to study the spatial structure and to clarify their effect on the plasma confinement. A tangentially viewing soft X-ray camera [1] is suitable to study such kind of edge MHD activities. Since the magnetic islands/perturbed structures extend toroidally along the magnetic field lines, they can be visualized better when they are observed tangentially. In the 8th experimental campaign, the tangentially viewing camera was modified. The quality of the images has been improved significantly; the framing rate and the dynamic range of the fast framing video camera is increased by 15kHz (formerly, 4.5kHz 256x256 pixels) and 12bit(8bit), respectively. With this new system, we tried to study the structure of the MHD modes.

In high beta experiments, the electron temperature is not high enough for the input window of the camera (Be film $40\mu\text{m}$, $E_{\text{cutoff}} \sim 1.5\text{keV}$). In order to increase the SX radiation, neon gas puffing was used. Radiation profiles measured by the SX detector array system are shown in Fig.1. SX radiation from $0.4 < \rho < 10$ are increased significantly.

In Fig. 2, SV decomposed images at a relaxation event in the high-beta experiments are shown. While relaxation of the plasma are shown in the component 1, post-cursor oscillations can be seen in the component 2.

In order to study the structure, we tried to reconstruct a radiation profile at a poloidal plane from the tangential image. From one tangential view, it is not possible to reconstruct a 3-D radiation profile. We assume that radiation along the magnetic field lines is constant and try to reconstruct a 2-D profile on a poloidal plane. We adapt a method based on the least-squares fitting by QR decompositions twice [2]. Reconstructed image are shown in Fig. 3. An $m=1$ island-like structure around $\rho \sim 0.8$ can be seen. So far, we have measured $m = 1, 2$ and 3 pre/post cursors at relaxation events at different rational surfaces. We continue to study the structure of those activities observed in relaxation events.

- [1] S. Ohdachi et al., Rev. Sci. Instrum **74**, 2136 (2003).
- [2] Y. Hosoda, Information Processing Society of Japan Transactions **40** 1051(1999), in Japanese

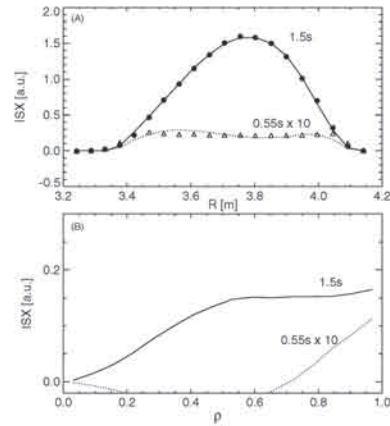


Fig.1: Soft X-ray radiation profiles before (0.55s) and after (1.5s) the neon injection is show. (A):Raw signal profile. (B): Reconstructed profile as a function of ρ .

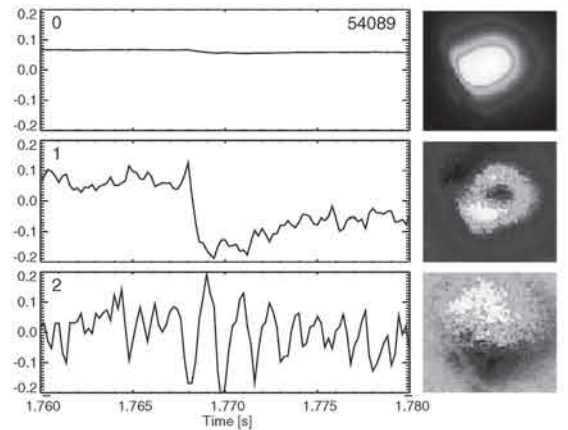


Fig.2: Singular value decomposed components at a relaxation event are shown ($B_t = -0.5\text{T}$, $R_{ax} = 3.6\text{m}$, $\gamma = 1.20$ and $\beta \sim 2.5\%$).

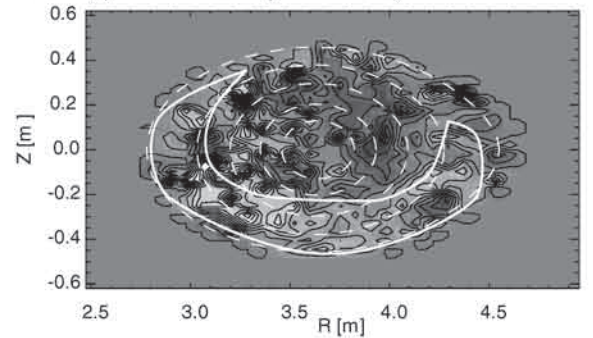


Fig.3: Reconstructed image at a horizontally elongated section (port 6) for the component 2 in Fig. 2. Brighter area having an $m=1$ island-like shape are shown in the figure.

§37. MHD Stability of the Current Carrying Plasma with Finite β in LHD

Narushima, Y., Watanabe, K.Y., Sakakibara, S.,
Cooper, W.A. (CRPP Lausanne, Switzerland)

In Heliotron plasma, it is not concerned with the current driven instabilities because the plasma does not need the plasma current to make its confinement magnetic field. In the actual experiment, there are some kinds of currents like the bootstrap current and Ohkawa current. Therefore, it is worthwhile to study the characteristics of stabilities of the current carrying plasma. The MHD stability analysis with the low-n ideal 3-D MHD stability code TERPSICHORE[1] has been carried out to examine the characteristics of the current carrying plasma with finite β . The equilibrium calculated with VMEC code[2] has the parameters of the magnetic axis ($R_{ax}=3.75\text{m}$) and coil pitch parameter ($\gamma_c=1.15$), in which the configuration has higher rotational transform compared with the standard one. For an equilibrium modeled, the profiles of the plasma current density and the pressure are assumed as $j(\rho)=j_0(1-\rho^2)$ and $\beta(\rho)=\beta_0(1-\rho^2)(1-\rho^8)$, respectively. The fixed boundary condition is adopted for the analysis. Figure 1 shows a result of calculation for $\beta_0=0.5\%$ and $I_p=55[\text{kA/T}]$. The profile of the rotational transform $\iota/2\pi$ goes up by the effects of the finite β and I_p (Fig1(a)). The $m/n=1/1$ mode is destabilized(Fig1(b)) and the current driven term dominates the potential energy((Fig1(c))). The unstable region of $m/n=1/1$ mode is shown in Fig.2 as a β_0 vs. I_p space, which indicates that the plasma is destabilized in the high β and/or high I_p region. In case of the higher I_p region ($I_p>40[\text{kA/T}]$), the current driven term is dominant in the potential energy while the pressure driven term is dominant in the case of lower I_p ($I_p<40[\text{kA/T}]$). In the lower I_p ($I_p<40[\text{kA}]$) and finite beta ($1.0[\%]<\beta_0<3.0[\%]$) plasma, the plasma current contributes to making of the pressure driven mode unstable.

References

- 1) W. A. Cooper, Plasma phys. and Controlled Fusion 34, (1992) 1011
- 2) S. P. Hirshman, W. I. Van Rij, and P. Merkel, Comput. Rhys. Commun. 43, (1986) 143

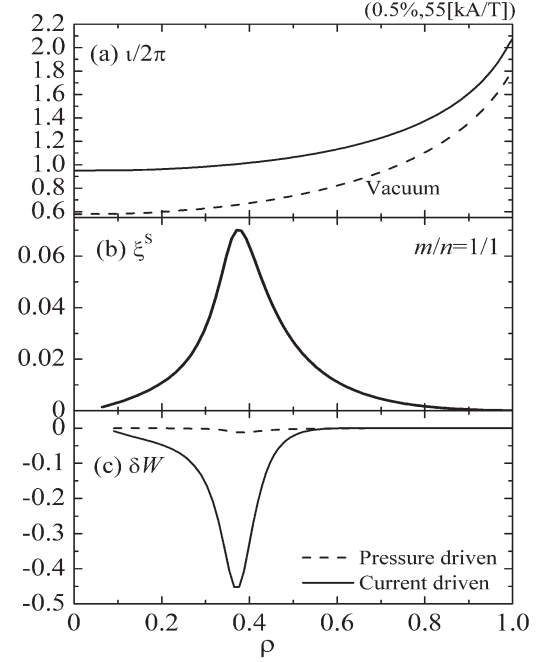


Fig. 1: Profile of (a)rotational transform, (b)Fourier amplitude of $m/n=1/1$ mode and (c)Potential energy.

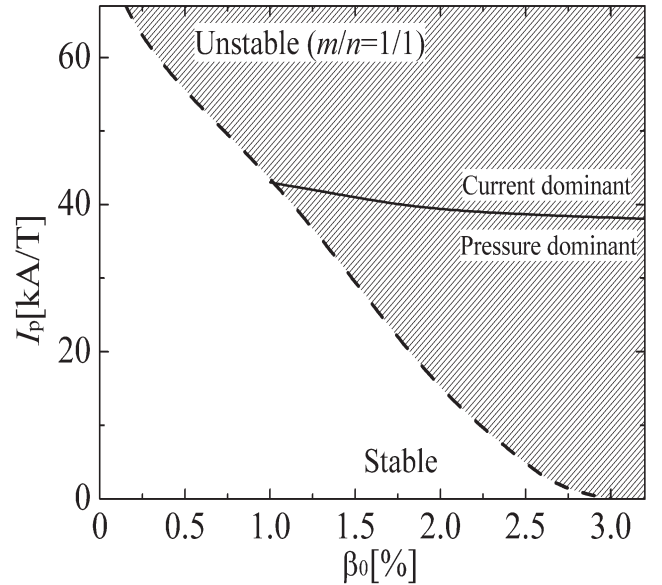


Fig. 2: Unstable region for $m/n=1/1$ mode in β_0 vs. I_p space

§38. Experiment Study of Current Driven MHD Mode in LHD Plasma

Narushima, Y., Sakakibara, S., Watanabe, K.Y.

Heliotrons do not require the plasma current for the magnetic field to confine plasmas. However, net toroidal currents can be generated by the Neutral Beam Injection (NBI) or bootstrap current and so on. These kinds of current play an important role from the viewpoint of Magneto-Hydro Dynamic (MHD) stability because the plasma current modifies the profile of the rotational transform $\iota/2\pi$, which affects the characteristics of the pressure and/or current driven MHD instabilities. Some experiments have reported the influence of the toroidal current on the pressure and/or current driven MHD modes [1-3]. To study the characteristics of the current driven MHD instabilities in Heliotron plasmas, discharged with large net toroidal currents, driven by the two co-NBIs which make the rotational transform $\iota/2\pi$ higher, has been done in the Large Helical Device (LHD). In recent LHD experiments with large net toroidal current and high rotational transform, we observe a plasma collapse. The time evolution of a discharge with a collapse is shown in Fig.1. The co-NBIs continue to drive the plasma current. When the plasma current reaches $I_p=38[\text{kA/T}]$ (kinetic beta is $\beta_0=0.5[\%]$), the electron temperature T_e decreases to half within 0.1[s] (from $t=1.7$ to $1.8[\text{s}]$). The plasma discharge does not terminate in spite of the collapse, in which the collapse is defined by dw_p/dt becoming negative before the termination of the NBI heating. Here, w_p is a stored energy. Here, $\tau_{w_p}^{-1}$ is defined as $\tau_{w_p}^{-1}=(dw_p/dt)/w_p$ (at just before the collapse). Before the collapse ($t<1.7[\text{s}]$), w_p , T_e and \bar{n}_e are constant while the I_p continues rising. The T_e and w_p begin to decrease at $t=1.7$ [s] while the \bar{n}_e does not change. About 0.05[s] later, the electron density starts increasing and the plasma current goes down. The time derivative of magnetic fluctuation (db/dt) does not show any remarkable fluctuation (precursor) before the collapse. Furthermore, precursors are not observed in the soft X-ray diagnostics. The electron temperature profile indicates a wide flat region around the collapse as shown in Fig.2(b). Before the collapse ($t=1.656[\text{s}]$), the profile shows a slight flat region (closed circles). A flat region appears at both sides during the collapse at $t=1.756[\text{s}]$ (triangles). After that ($t=1.856[\text{s}]$), the width (Δ) of the flat region grows up to $\Delta/a_p=0.43$ (Here, a_p is a

minor radius in real coordinate.), which occupies the profile (open circles). As a result, the electron temperature in the core region falls to half while the T_e profile at the peripheral region keeps its gradient. The position of the flat region corresponds to the $\iota/2\pi=1$ resonant surface as shown in Fig.2(a) calculated with VMEC. From the magnetic diagnostics, it is thought that this phenomenon suggests the production of a magnetic island with $m/n=1/1$ mode structure without rotation.

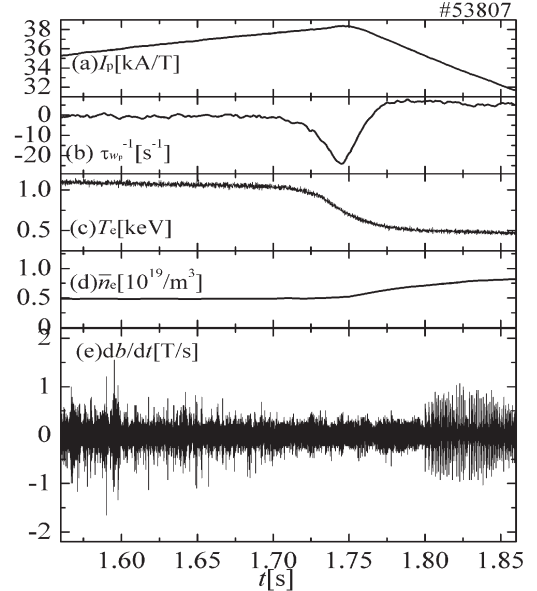


Fig. 1: Time evolution of (a) I_p , (b) inverse of characteristic time of w_p (c) T_e , (d) \bar{n}_e , (e) magnetic fluctuation around the collapse.

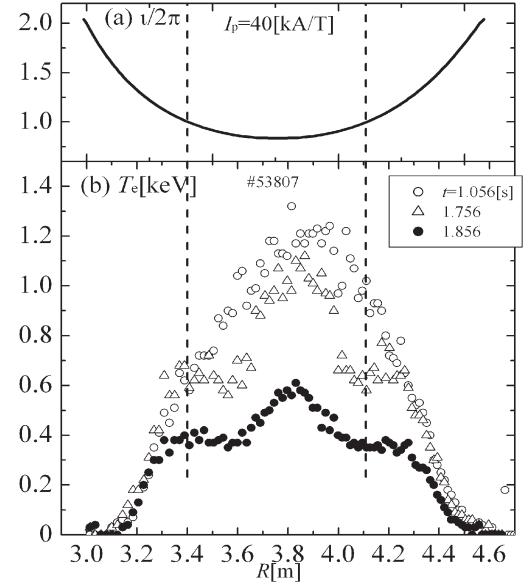


Fig. 2: Electron temperature profile during collapse

- References
- 1) S.Sakakibara, *et al.*, Jpn. J. Appl. Phys. 34, 252 (1995)
 - 2) S.Morimoto, *et al.*, Jpn. J. Appl. Phys. 28, 1470 (1989)
 - 3) M.Wakatani, *et al.*, Nucl. Fusion, 12, 1669 (1983)

§39. Comparative Study of MHD Instability in LHD and JT-60U

Isayama, A. (Japan Atomic Energy Research Institute)
Inagaki, S.

It is generally recognized that in helical systems plasma current in counter direction is favorable to the Mercier stability. However, in LHD experiments, instability localized at $\iota/2\pi \sim 0.5$ was observed during neutral beam injection in counter direction. The objective of this study is to investigate the characteristics of this instability such as onset condition and spatial structure, and to clarify similarities and differences between the instability and that in tokamaks.

Previous analysis clarified that sinusoidal oscillations and sawtooth oscillations localized at $\iota/2\pi \sim 0.5$ are observed under similar discharge conditions. In this study, onset condition of these oscillations, classification of the mode behavior at the onset, and the period of the sawtooth oscillations have been investigated. Typical experimental parameters are as follows: magnetic axis location $R_{ax}=3.60$ m, magnetic field $B_{ax}=2.75$ T, $\gamma=1.254$, $B_0=100\%$.

Figure 1 shows relation between line-averaged electron density and electron temperature at $\rho \sim 0.5$ ($\iota/2\pi \sim 0.5$) at the onset of sawtooth oscillations and sinusoidal oscillations. It can be seen that the sinusoidal oscillations appear at high density and low temperature regime, and that the sawtooth oscillations appear at low density and high temperature regime. Although the onset regime is fairly well separated, the two regimes are laying side-by-side. Actually, in some cases, sinusoidal oscillations appear soon after sawtooth oscillations. It is also found that the magnitude of plasma current does not seem to have a significant effect on the mode onset.

Temporal evolution of sinusoidal oscillations has been investigated in detail by using electron cyclotron emission (ECE) diagnostics. Figure 2 shows electron temperature near $\iota/2\pi \sim 0.5$ at the mode onset. In this series of discharges, three types of onset and evolution have been observed: (a) fast growth (Fig. 2(a)), (b) slow growth (Fig. 2(b)), and (c) onset triggered by a sawtooth crash. The cause for the difference is under investigation.

Investigation on sawtooth period has found that the period changes irregularly in time even under a fixed experimental conditions. This feature is quite different from sawtooth oscillations in tokamak (sawteeth with $m/n=1/1$), where the period is proportional to $T_e^{1.5}$. This suggests that mechanism of the sawtooth oscillations in LHD may be different from those in tokamaks.

Temporal evolution of mode location has been investigated with ECE diagnostics by tracing the inversion radius of the sawtooth oscillations and the location of the maximum amplitude of the sinusoidal oscillations. It has been found that the location can be changed in time when the direction of neutral beam is changed. This suggests that

current profile is actually changed by neutral beam injection as in the case in tokamaks. It is expected that the information can be also used to calibrate the motional Stark effect diagnostic.

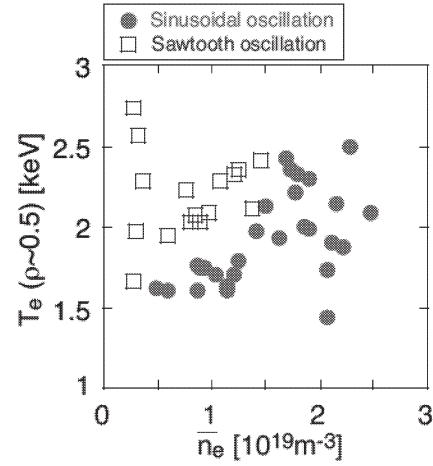


Fig. 1. Relation between line-averaged electron density and electron temperature at the onset of sawtooth oscillations and sinusoidal oscillations. Closed circles and open squares correspond to the sinusoidal oscillations and the sawtooth oscillations, respectively.

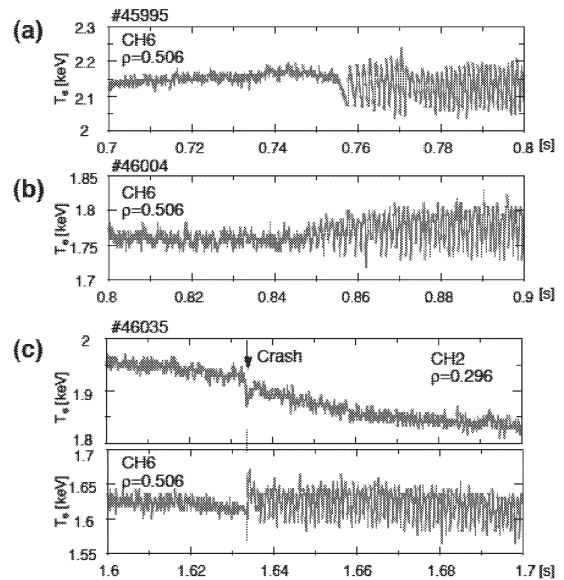


Fig. 2. Temporal evolution of electron temperature near $\iota/2\pi \sim 0.5$ at the onset of sinusoidal oscillations: (a) fast growth, (b) slow growth, (c) sawtooth-triggered oscillations.

§40. Quantitative Evaluation of Pressure Anisotropy by Magnetic Measurements

Yamaguchi, T. (Grad Univ.), Watanabe, K.Y., Sakakibara, S., Narushima, Y.

It has been pointed out that the characteristics of the MHD equilibrium and the instability under the anisotropic pressure are different from those under the isotropic pressure. Therefore a quantitative evaluation of anisotropy is important for the MHD equilibrium and the instability study. Magnetic measurements are useful tools for measuring a pressure anisotropy.

The diamagnetic loop measures the diamagnetic current and the saddle loops measure the Pfirsch-Schlüter(P.S.) current. The P.S. current is induced by $p_{\perp} + p_{\parallel}$, whereas the diamagnetic current is induced by p_{\perp} only. Here p_{\perp} and p_{\parallel} denote the plasma pressure perpendicular and parallel to the magnetic field, respectively. Saddle loops and the diamagnetic loop are adequate to pick up the vertical magnetic field induced by the P.S. current and the toroidal magnetic flux induced by the diamagnetic current, respectively. As another difference, the saddle loops are sensitive to a pressure profile while the diamagnetic loop is not sensitive. In order to evaluate the quantitative anisotropy, the effect of the pressure profile on the magnetic measurements should be avoided.

In Fig.1, the relationship between the line-averaged electron density and $\Phi_{\text{SLeXP}}/\Phi_{\text{SLiso}}$ is shown in many NBI discharges with $R_{\text{ax}}=3.6\text{m}$, $B_t=0.5, 0.75$ and 1.5T . $\langle\beta_{\text{dia}}\rangle$ is in the range between 1% and 2%. Here Φ_{SLeXP} denotes the saddle loop flux which experimentally observed. Φ_{SLiso} is the saddle loop flux evaluated by the VMEC-DIAGNO code for the plasmas with the isotropic pressure. In order to estimate Φ_{SLiso} , the electron pressure profiles measured by Thomson scattering and FIR laser interferometer are used and volume averaged values of those pressures are adjusted to agree with the volume averaged pressure values evaluated by the diamagnetic loop. Therefore, an inconsistency of the isotropic estimation with experimental data can be shown by the difference of $\Phi_{\text{SLeXP}}/\Phi_{\text{SLiso}}$ from unity. Furthermore, we suggest that $\Phi_{\text{SLeXP}}/\Phi_{\text{SLiso}}$ depends on $(W_{\perp} + W_{\parallel})/1.5W_{\perp}$ because Φ_{SLeXP} depends on the flux due to the P.S. current and Φ_{SLiso} is derived based on the measured diamagnetic flux. Here W_{\parallel} and W_{\perp} are the parallel and perpendicular stored plasma energy. Note, $W_{\parallel}=W_{\perp}/2$ in the case of an isotropic pressure. $\Phi_{\text{SLeXP}}/\Phi_{\text{SLiso}}$ approaches unity as the density increases and does not change so much for $\bar{n}_e > 3 \times 10^{19} \text{m}^{-3}$.

In order to study the contribution of the anisotropic beam pressure, the beam pressure is estimated based on the Monte Carlo technique and the steady state Fokker-Planck solution(FIT code). To compare with $\Phi_{\text{SLeXP}}/\Phi_{\text{SLiso}}$, we estimate W_{\parallel}/W_{\perp} which would be more intuitive than $(W_{\perp} + W_{\parallel})/1.5W_{\perp}$ as the anisotropic index. W_{\parallel} and W_{\perp} are expressed as the followings with the thermal energy,

W_{thermal} , and the perpendicular and parallel beam stored energy, $W_{\text{beam}\perp}$ and $W_{\text{beam}\parallel}$,

$$W_{\parallel} = (1/3)W_{\text{thermal}} + W_{\text{beam}\parallel} \quad (1)$$

$$W_{\perp} = (2/3)W_{\text{thermal}} + W_{\text{beam}\perp} \quad (2)$$

Usually, the diamagnetic plasma energy, W_{dia} is estimated under the isotropic pressure, and W_{dia} is expressed as follows:

$$W_{\text{dia}} = (2/3)W_{\text{thermal}} + W_{\text{beam}\perp} \quad (3)$$

From those equations, W_{\parallel}/W_{\perp} can be expressed by W_{dia} , $W_{\text{beam}\perp}$ and $W_{\text{beam}\parallel}$. W_{dia} is estimated based on the diamagnetic measurement. $W_{\text{beam}\perp}$ and $W_{\text{beam}\parallel}$ are estimated based on numerical calculation by the FIT code. Figure 2 shows the relationship between the anisotropic index W_{\parallel}/W_{\perp} and $\Phi_{\text{SLeXP}}/\Phi_{\text{SLiso}}$. The correlation coefficient of them is 0.97, therefore, strong correlation can be shown. Then $\Phi_{\text{SLeXP}}/\Phi_{\text{SLiso}}$ is considered a useful index to evaluate pressure anisotropy. From Fig. 2, in the LHD discharges with $R_{\text{ax}}=3.6\text{m}$ configuration, the anisotropy W_{\parallel}/W_{\perp} is scaled as a function of $\Phi_{\text{SLeXP}}/\Phi_{\text{SLiso}}$ as follows:

$$W_{\parallel}/W_{\perp} = -0.8 + 1.3(\Phi_{\text{SLeXP}} / \Phi_{\text{SLiso}}) \quad (4)$$

The examination of the accuracy of this relationship is a future plan because the scattering of the data is large in Fig. 2.

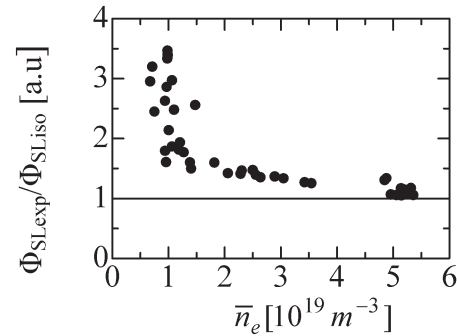


Fig.1 The relationship between \bar{n}_e and $\Phi_{\text{SLeXP}}/\Phi_{\text{SLiso}}$.

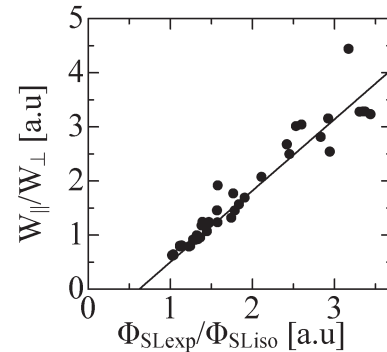


Fig.2 The relationship between $\Phi_{\text{SLeXP}}/\Phi_{\text{SLiso}}$ and W_{\parallel}/W_{\perp} .

§41. The Effect of the Rotational Transform on Shafranov Shift

Kobuchi, T., Ida, K.

The effect of rotational transform on the Shafranov shift in the neutral beam heated plasma has been experimentally investigated in Large Helical Device (LHD). In LHD, the rotational transform is controlled by changing the current distribution in helical coils which consists with three layers of superconductor. When the current center in helical coils is shifted towards the plasma, the effective minor radius becomes small and the central rotational transform increases.

The Shafranov shift of magnetic axis due to the Pfirsch-Scheluter current for the low beta limit can be expressed as

$$\Delta \cong \frac{aA_p^2 \beta_0}{\iota(1)} \int_0^1 \frac{\delta_{1,0}(\rho)}{\iota(\rho) \kappa(\rho)} d\rho, \quad (1)$$

where β_0 is the central beta, A_p is aspect ratio (ratio major to minor radius), ι is the rotational transform, κ is totoidal averaged ellipticity of cross section of magnetic flux surface, and $\delta_{m,n}$ is Fourier component of $1/B^2$ with m (n) is the poloidal (toroidal) mode number.

The magnetic axis is derived from the tangential soft x-ray image measured with the soft x-ray CCD in LHD. The position of the magnetic axis is derived from the best fit of measured x-ray intensity to that calculated soft x-ray intensity based on the magnetic flux surface derived using three-dimensional free boundary equilibrium code (VMEC).

Figure 1 shows the dependence of effective minor radius, central rotational transform and coefficient

$aA_p^2/\iota(1)$, in eq. (1), on the pitch parameter of helical coil γ ($= ma_{\text{coil}}/nR$, where a_{coil} is distance between the plasma center and helical coil current center). The effective minor radius becomes small and the central rotational transform increases as the pitch parameter of helical coil is decreased. The coefficient $aA_p^2/\iota(1)$ increases as the effective minor radius is decreased with constant major radius.

Figure 2 shows the dependence of the Shafranov shift measured with the soft x-ray CCD camera as a function of averaged beta in the plasma with three central rotational transform $\iota(0) = 0.38, 0.46$ and 0.57 at $R_{\text{ax}}^v = 3.60$ m. Lines in Fig. 2 show the theoretical prediction calculated with VMEC code. The results are calculated for plasma with two plasma pressure profiles, $(1-\rho^8)(1-\rho^2)$ and $(1-\rho^8)(1-\rho^8)$. The Shafranov shift become small as γ is decreased because of larger central rotational transform even the coefficient $aA_p^2/\iota(1)$ is increased.

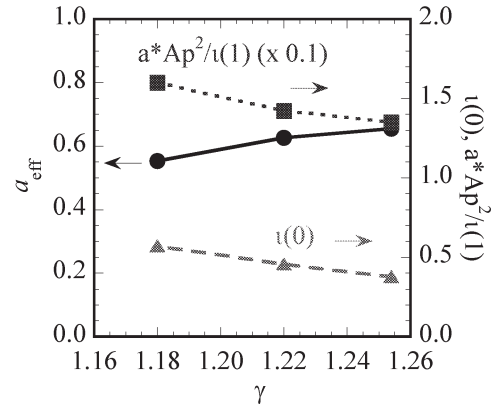


Fig. 1. Dependence of effective minor radius, central rotational transform and coefficient $aA_p^2/\iota(\rho)$ on the pitch parameter of helical coil γ .

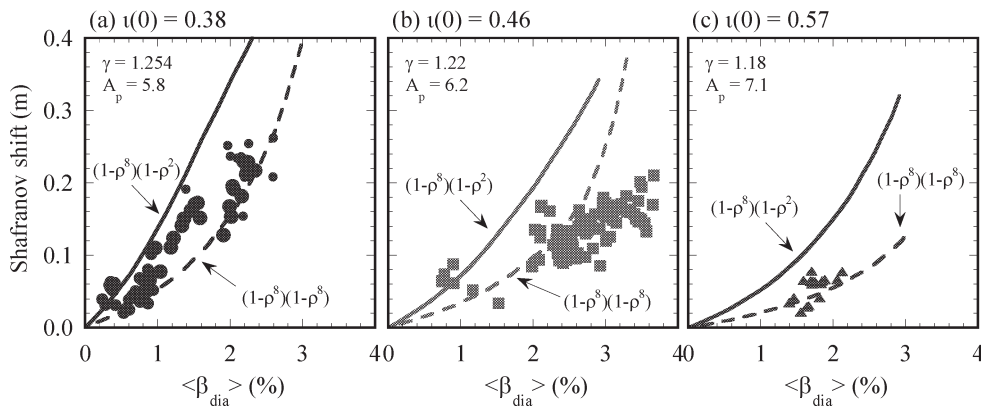


Fig. 2. Dependence of the Shafranov shift on the volume averaged diamagnetic-beta for three central rotational transform $\iota(0) = 0.38, 0.46$ and 0.57 at $R_{\text{ax}}^v = 3.60$ m and $B_Q = 100\%$ configuration. The marks and lines show the experimental results and theoretical predictions calculated with VMEC code, respectively.

§42. Effective Plasma Boundary Behavior in Finite Beta Plasma of LHD

Watanabe, K.Y., Narihara K., Yamaguchi, T. (Grad Univ.) Suzuki, Y.

The identification of MHD equilibrium is very important to study the properties of MHD stability and transport so on. In order to identify MHD equilibrium, information on (1) shape of OMFS (Outermost Magnetic Flux Surface), (2) toroidal current profile and (3) pressure profile is necessary. However the OMFS is not easy to identify in helical plasmas, especially with divertor structure because the “effective magnetic surfaces” exist but the exact ones do not exist in helical systems due to lack of any symmetry. Moreover the “effective magnetic surfaces” become more stochastic especially in the peripheral region as beta increases. Then the identification of the LCFS (Last Closed Magnetic Surface) becomes more difficult as the beta increases.

LHD has powerful profile measurement systems like Thomson scattering, FIR and so on. Here we define “the effective plasma boundary” based on the electron temperature and density profile measurements. They are compared with theoretical prediction by HINT code[1], where the existence of the closed magnetic surfaces is not necessary. In this calculation, the pressure is set zero where the magnetic field line connects with the calculation boundary within 10 toroidal turns. The distance between the calculation boundary and the well-defined OMFS in vacuum is ~70% and ~150% of the plasma minor radius at the torus outside in the horizontally elongated poloidal cross-section and at the torus inside in the vertically elongated poloidal cross-section, respectively. Any artificial radial diffusion is not assumed here. The “effective plasma boundary” is defined as the area which encloses the 99% of the electron thermal energy estimated by the profile measurements.

Figure 1 shows a peripheral magnetic surface shifts as a function of the beta value. Symbols correspond to in $R_{ax}=3.6\text{m}/B_a=100\%/r=1.254$ magnetic configuration (LHD typical configuration) with almost same pressure profiles as the function of ρ (minor plasma radial variable), $p \sim (1-\rho^2)$. Solid line corresponds to the prediction by HINT code. Though the scattering of data is fairly large, the experimental data is consistent with the prediction. Symbols in Fig.2 (a) and (b) show the “effective plasma boundary” at the torus outboard and at the torus inboard in the horizontally elongated poloidal cross section, respectively. Solid lines denote the prediction by HINT code. Dashed lines denote the well-defined OMFS in vacuum. The torus outboard boundary expands to outside of the well-defined OMFS in vacuum by ~10% of the minor radius in the high beta range with more than 2%. The torus outboard boundary becomes torus outer as beta increases up to ~2%, and it keeps almost same position in the beta range of more than 2%. On the contrary, the torus inboard boundary keeps almost same position in the beta range of less than 2%, and it becomes torus outer as beta increases in the beta range of more than 2%. Its qualitative behavior is quite consistent with the prediction by HINT code. However, the observed boundary position expands to outside of the prediction by HINT code by ~10% of the

minor radius. The most probable candidate of the difference between experimental data and the prediction is due to the perpendicular diffusion respect to magnetic field line.

Reference

1) T. Hayashi, Theory of Fusion Plasmas, EUR 12149 EN (1989) 11; K. Harafuji et al, J. Comp. Phys. **81**(1989) 169.

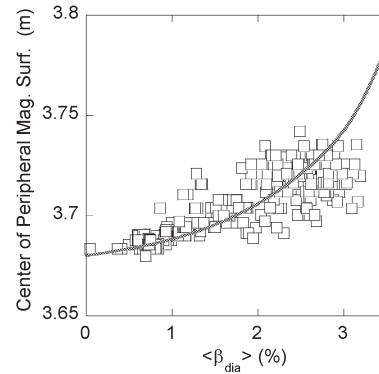


Fig.1 The shift of the center of peripheral magnetic surface as function of beta for almost same pressure profiles as $p \sim (1-\rho^2)$.

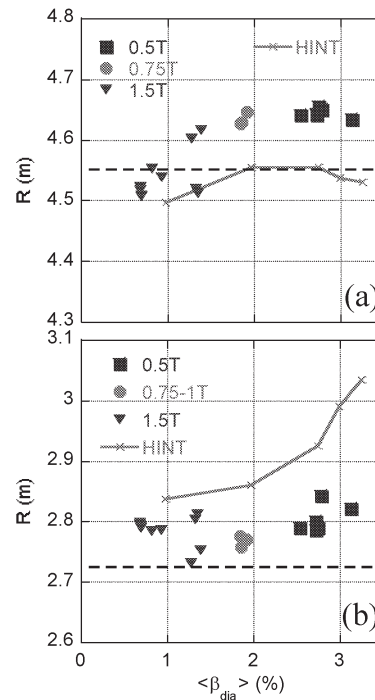


Fig.2 The shift of the torus outboard and torus inboard “effective plasma boundaries” as function of beta for almost same pressure profiles as $p \sim (1-\rho^2)$.

§43. Effects of Magnetic Axis on Formation and Healing of Magnetic Island

Nagayama, Y., Narihara, K., Narushima, Y., Ohya, N., Sakamoto, R.

The neo-classical transport theory tells that the bootstrap current changes the magnetic island width. This theory is useful to explain the neo-classical tearing mode (NTM) in tokamaks. Theoretically, there is a direction of the bootstrap current that enlarges the island width, and the opposite direction reduces the width [1]. In tokamaks, the direction of the bootstrap current is the same as the plasma current. In LHD, however, the direction of the bootstrap current can be changed. The object of this experiment is to investigate the effect of the direction of the bootstrap current. Figure 1 shows the geometric factor of the bootstrap current at the $\iota/2\pi=1$ surface in LHD. This factor indicates the direction of the bootstrap current at the $\iota/2\pi=1$ surface. Since the direction changes at $R_{ax}=3.57$ m, we can expect that the island width is enlarged as the beta is increased when $R_{ax}<3.57$ m, and it is reduced when $R_{ax}>3.57$ m.

In the former experiment [2], we have had a plenty of data in the case of $R_{ax}=3.6$ m, so that the experiment is done in cases of $R_{ax}=3.55$ m and $R_{ax}=3.575$ m in the 8-th LHD experimental campaign. Figure 2(a) show the electron temperature profiles before ($t=1.889$ s) and after ($t=2.056$ s) the hydrogen ice pellet injection in the case of the LID current (I_{LID}) of -400 A. In the case of $I_{LID}=-400$ A, the island width is canceled in vacuum, and the island is not formed before the pellet injection as shown in Fig. 2(a). Due to the pellet injection, an island is generated as shown in Fig. 2(a). In the case of $R_{ax}=3.575$ m, the threshold of the island formation is increased to $I_{LID}=-500$ A. This is consistent with the neo-classical theory.

Figure 2(b) show the electron temperature profiles before ($t=2.189$ s) and after ($t=2.623$ s) the hydrogen ice pellet injection in the case of $I_{LID}=-1800$ A. In the case of $I_{LID}=-1800$ A, a large island is formed in vacuum, but the

island is not formed before the pellet injection as shown in Fig. 2(b). Due to the pellet injection, an island is generated, as shown in Fig. 2(b).

In the high temperature plasma, the bootstrap current is higher because of low collisionality and it enlarges the magnetic island in the case of $R_{ax}=3.55$ m, theoretically. However, the healing of the island is observed in the high temperature plasma, experimentally. It takes further investigation to understand the island dynamics.

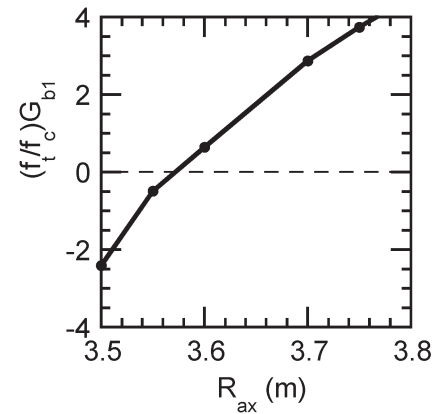


Fig.1. Major radius of the magnetic axis versus geometric factor of the bootstrap current at the $\iota/2\pi=1$ surface.

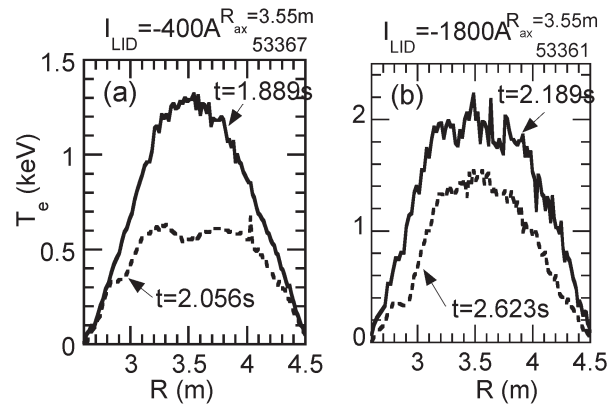


Fig.2. T_e profiles before (solid line) and after (broken line) the pellet injection in the case of $R_{ax}=3.55$ m.

References

- [1] Itoh, K., Itoh, S-I., Yagi, M., Phys. Plasma **12**, 072512 (2005).
- [2] Nagayama, Y., et al., Nucl. Fusion (accepted).

§44. The Local Island Divertor Experiment

Morisaki, T., Masuzaki, S., Kobayashi, M.,
Ohya, N., Komori, A.

The local island divertor (LID) is an advanced closed divertor, utilizing an $m/n = 1/1$ island generated externally by 20 small perturbation coils. In the last two experimental campaigns, fundamental LID functions have been demonstrated experimentally.¹⁾

In the recent LID experiment, relatively good energy confinement was achieved in the high density regime at the outward shifted magnetic axis position, R_{ax} , of 3.75 m.2) Experiments were performed with various \bar{n}_e 's in the LID and helical divertor (HD) configurations. In order to compare with the standard configuration at $R_{ax} = 3.60$ m, the improvement factor of the global energy confinement time, τ_E , over the ISS95 scaling as a function of \bar{n}_e is presented in Fig. 1 (a). It can be seen that the improvement factor in the LID configuration is less than unity in the high density region above $\sim 5 \times 10^{19} \text{ m}^{-3}$ and always inferior to that in the HD. On the other hand, in the outward shifted configuration at $R_{ax} = 3.75$ m, the improvement factor in the LID keeps almost unity in the density range up to $\sim 1.3 \times 10^{20} \text{ m}^{-3}$. This is a remarkable feature of the $R_{ax} = 3.75$ m configuration, which can never be seen at $R_{ax} = 3.60$ m. It can be said that the energy confinement of the LID is better than that of HD in the $R_{ax} = 3.75$ m configuration.

The reason for the different confinement characteristics between $R_{ax} = 3.60$ and 3.75 m configurations is not clear. One candidate of the explanation is the different recycling state between two configurations. In the $R_{ax} = 3.6$ m configuration, the island separatrix is completely isolated from the HD separatrix. Almost all particles diffusing out from the core region are ideally guided to the LID head, and then recycled there. On the other hand, in the $R_{ax} = 3.75$ m configuration, some amount of diffused particles is escaping to the HD target plates without being trapped by the island separatrix because of the edge ergodization. Then, some amount of particle recycling consequently occurs there. In fact, a longer density decay time, τ_p^* , suggesting higher particle recycling, was observed at $R_{ax} = 3.75$ m. Furthermore, the particle recycling at the LID head is also high at $R_{ax} = 3.75$ m, since the outer island separatrix may hit the leading edge of the LID head a little. This problem comes from the design concept of the LID head which was originally designed to fit the magnetic configuration at $R_{ax} = 3.60$ m.

During the high performance discharges, highly peaked ITB-like density profiles, n_e , were obtained in the reheat phase after pellet injections, together with the peaked electron temperature profiles, T_e , as shown in Fig. 2. It seems that those “barriers” exist near the rational surface of $q=2$. The large Shafranov shift of the magnetic axis suggests the high pressure at the plasma center. Although this phenomenon is very transient at present,

such a favorable state may be kept or developed by optimizing the fueling and the magnetic configuration.

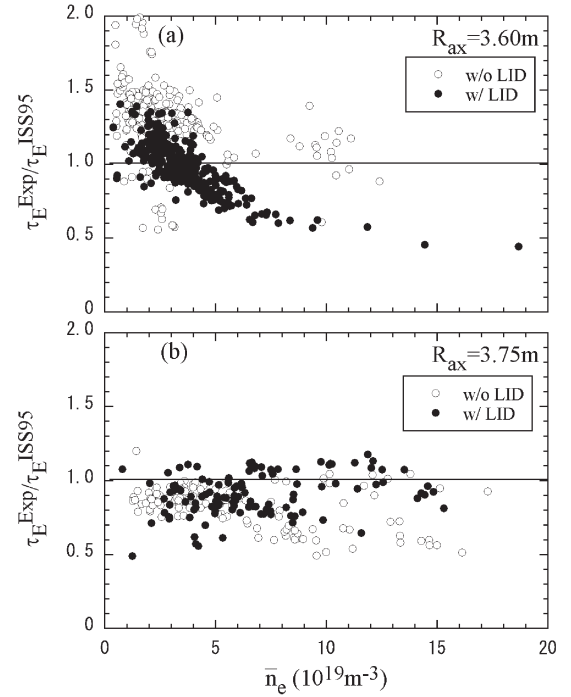


Fig. 1. Improvement factor of the energy confinement time τ_E from the ISS95 scaling law at (a) $R_{ax} = 3.60$ m and (b) $R_{ax} = 3.75$ m as a function of the line averaged density.

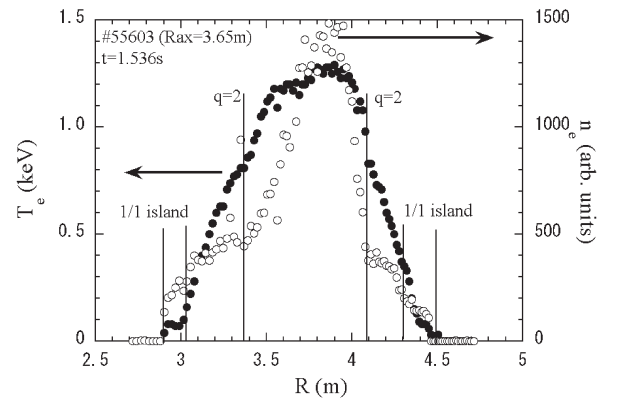


Fig. 2. Highly peaked n_e and T_e profiles in the reheat phase after pellet injections.

References

- 1) Morisaki, T. et al.: J. Nucl. Mater. **337-339**, (2005) 154.
- 2) Komori, A. et al.: Nucl. Fusion (to be published).

§45. Edge Transport Study of LID Configuration in LHD

Kobayashi, M., Feng, Y. (IPP Max-Planck Institute, Germany), Morisaki, T., Masuzaki, S., Sardei, F. (IPP Max-Planck Institute, Germany), Reiter, D. (IPP FZJ, Germany), Ohyaibu, N., Komori, A., Motojima, O., LHD Experimental Group

The Local Island Divertor (LID) configuration has been proposed as one of the schemes controlling edge transport physics of heliotron type devices¹⁾. A separatrix of an $m/n = 1/1$ island induced at the periphery of the plasma is utilized as a scrape-off layer (SOL) for guiding plasma heat/particles to the divertor region (fig. 1). In order to analyze the three dimensional transport physics in this configuration, the 3D edge transport code, EMC3²⁾, has been implemented being coupled with the 3D neutral transport code, EIRENE³⁾. EMC3 solves plasma fluid conservation equations of mass, momentum and energy (electron & ion) with a Monte Carlo scheme, while recycling neutrals from plasma facing components and their ionization profiles are treated by EIRENE.

Figure 1 shows time traces of up/down stream temperature, T_{eu} & T_{ed} , and its ratio, T_{eu}/T_{ed} , where the up/down stream are at the O-point of inner separatrix of the $m/n=1/1$ island and at the surface of the LID head. It is seen that the ratio reaches up to 10 ~ 15. At the typical parameters in LID, a SOL collisionality, $\nu_{SOL}^* = 10^{-16} n_u L_c / T_{eu}^2$, is ~ 10 for $n_u = 2 \times 10^{19} \text{ m}^{-3}$, $T_{eu} = 200 \text{ eV}$ and $L_c = 200 \text{ m}$. According to the two-point model⁴⁾ based on a parallel heat conduction transport and a constant pressure, which is widely used in tokamaks,

$$10^{16} \nu_{SOL}^* = C_2 (T_u/T_d)^{0.5} (1 - (T_u/T_d)^{-3.5}), \quad (1)$$

where $C_2 \sim 10^{17}$, it gives $T_u/T_d \sim 2$ for $\nu_{SOL}^* = 10$. The large deviation from the model is attributed to a cross field energy loss, which in the LID case effectively cool down the temperature along the field lines. Figure 2 shows the parallel temperature profiles predicted by the EMC3-EIRENE code. $L_c = 0$ and 190 m correspond to down and up stream (the LID head and O-point of inner separatrix), respectively. One sees that between X-point ($L_c \sim 90 \text{ m}$) and the LID head there exists significant temperature gradient along the field lines. Because of the short connection length inside the island (private region), the density as well as temperature become low therein. After the flux tubes leave the core plasma at the X-point, therefore, the cross field energy loss takes place at the both sides of the tubes, i.e. towards private region and outside of the island. This geometrical effect gives rise to the effective cooling of the temperature along the field lines, as shown in the Fig. 2.

A power deposition profile onto the LID head was also analyzed with the 3D codes, where we found that the power load is \sim a few tens MW/m^2 at maximum, which greatly exceeds the safety limit imposed by engineering

design. This is due to the small wetted area of the LID head, which is estimated at $\sim 0.1 \text{ m}^2$, while the total input power to the plasma is several MW. In order to save the LID surface from a severe erosion, it is necessary to smear out the heat load, e.g. by divertor detachment. This is currently an ongoing issue for the LID operation.

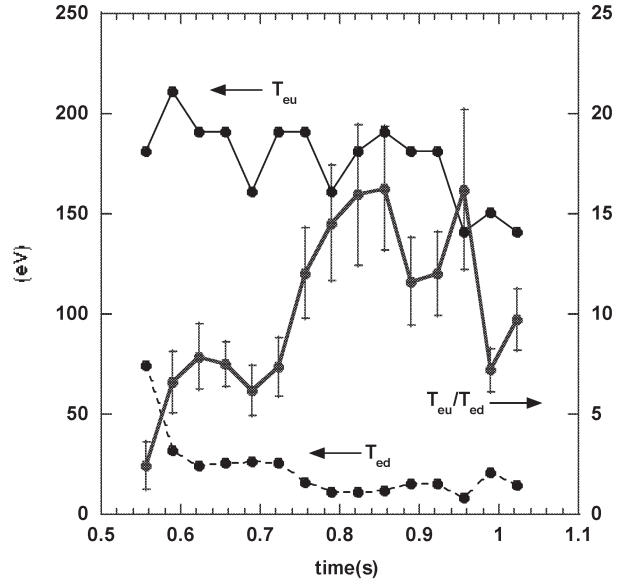


Fig. 1. Time traces of up/down stream temperature (T_{eu} , T_{ed}) and the ratio (T_{eu}/T_{ed}). It is found that the ratio increase up to 10 ~ 15, indicating a significant temperature gradient along the field lines.

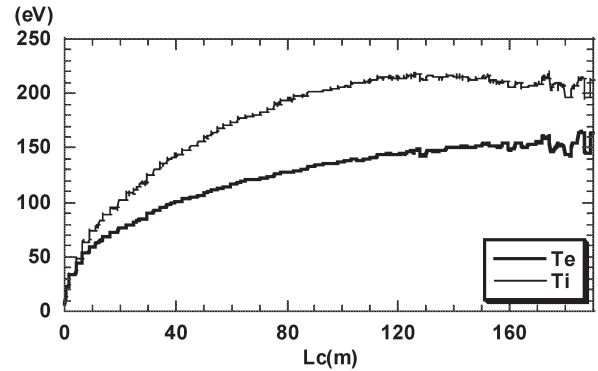


Fig. 2. Parallel temperature profiles calculated by EMC3-EIRENE. $L_c = 0$ and 190 m correspond to the down stream (the LID head) and the up stream (O-point of inner separatrix), respectively. There appears a significant temperature gradient between the LID and the X-point ($L_c = 90 \text{ m}$).

Reference

- 1) T. Morisaki et al., J. Nucl. Mater. **337-339** (2005) 15
- 2) Y. Feng et al., Contrib. Plasma Phys. **44** (2004) 57.
- 3) D. Reiter, Technical Report Jul-1947, KFA Juelich, Germany (1984), and www.eirene.de.
- 4) P.C. Stangeby, "The plasma boundary of magnetic fusion devices", Ch. 4, IOP publishing Ltd 2000, Bristol and Philadelphia.

§46. Titanium Tracer Impurity Behavior in the LHD Plasma with a Plasma Detachment

Tamura, N., Kalinina, D.V., Veshchev, E., Sudo, S., Matsubara, A., Sato, K., LHD Experimental Group

A plasma detachment in LHD plasma has been achieved in the 8th LHD experimental campaign, although it has been done with a different approach from the conventional one. When the plasma detachment occurs, a core plasma confinement is expected to be improved. In order to investigate impurity transport in the core LHD plasma during the plasma detachment, the tracer-encapsulated solid pellet (TESPEL) injection has been performed. The TESPEL can deposit its tracer particles inside the plasma (typically $\rho = 0.7 \sim 0.8$). Thus, the deposition of those is absolutely free from the influence of the plasma detachment. Figure 1 shows typical waveforms of a TESPEL injected discharge with the plasma detachment. The time during the plasma detachment is indicated by the colored area in the figure. In this case, the plasma detachment has been sustained for around 1.8 s from 0.9 s. As has been indicated by the vertical dashed line in the figure, the TESPEL is injected at $t \sim 0.8$ s just before the onset of the plasma detachment. Just after the TESPEL injection, the intensities of emission line for Ti XVI (N-like) and Ti XII (Na-like), measured by a vacuum ultra violet spectrometer (SOXMOS), are increased and decreased rapidly. At about the same time, the intensity of Ti XX (Li-like) is increased. This temporal behavior is attributed to the rapid ionization of the tracer impurity due to the high electron temperature of the LHD plasma. When the plasma detachment occurs, the electron temperature is decreased drastically (Figure 1(b) shows the temporal behavior of the electron temperature around the center ($R = 3.64 \sim 3.67$ m with $R_{ax} = 3.65$ m) of the LHD plasma.) In accordance with the decrease of the electron temperature, the intensity of Ti XX is decreased quickly and those of Ti XVI and Ti XII are increased appreciably. During the plasma detachment, the intensity of Ti XX remains the almost same level. The intensity of Ti XVI is decreased gradually, conversely, that of Ti XII is increased gradually. This experimental result suggests that, during the plasma detachment, Ti tracer impurity seems to be simply re-distributed according to its ionization balance and not to be pumped out from the core plasma. This might indicate that the particle confinement in the LHD plasma is improved during the plasma detachment. The differences of the impurity transport properties in the core plasma between with and without the

detachment are being investigated.

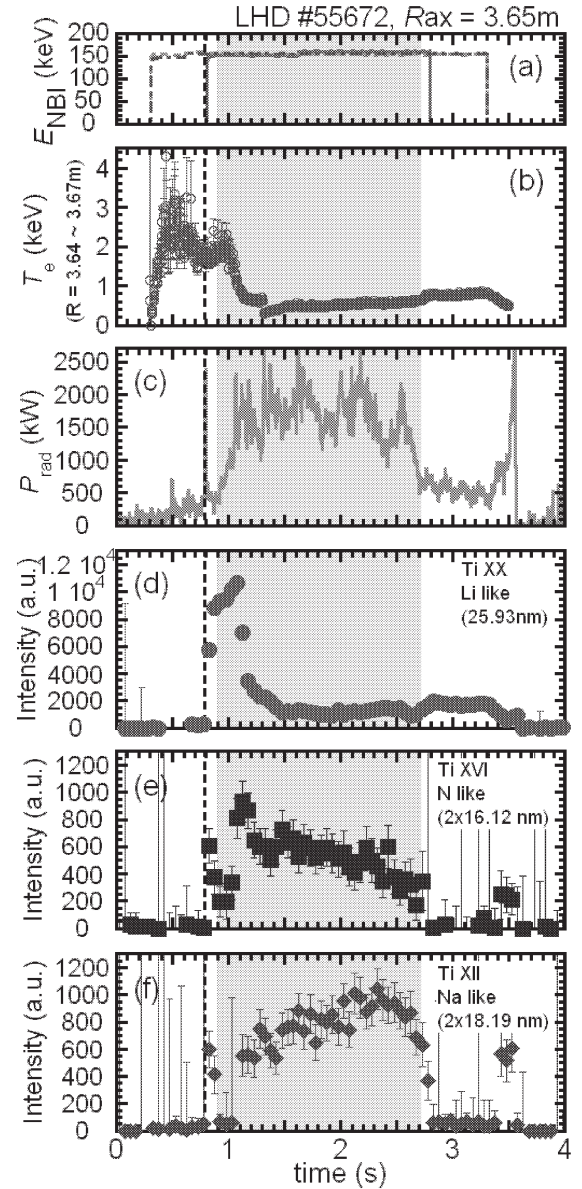


Fig. 1. Typical waveforms of TESPEL injected discharge with the plasma detachment. The TESPEL injection time is at $t \sim 0.8$ s as indicated by the vertical dashed line. The colored area indicates the time during the plasma detachment.

§47. Study of ECRH Effect on Impurity Behavior with Tracer-Encapsulated Solid Pellet Injection on LHD

Kalinina, D. (Graduate Univ. Advanced Studies),
Sudo, S., Tamura, N., Sato, K., Matsubara, A.,
Muto, S., Ida, K., LHD Experimental Group

Studies of impurity behavior in magnetically confined plasmas are highly important, since it could determine the feasibility of controlled fusion. Especially for the realization of the practical fusion reactor, it is important to have an effective tool to suppress an impurity accumulation, which can trigger the degradation of the fusion power efficiency. In order to evaluate whether ECRH can suppress impurity accumulation, the effect of that on the impurity behavior was studied in LHD plasmas.

As a tracer of the Tracer-Encapsulated Solid Pellet (TESPEL), titanium (Ti) was injected into the LHD plasmas, which are sustained by NBI heating. A soft x-ray pulse height analyzer (PHA) and a VUV spectrometer (SOXMOS) are used to observe a temporal behavior of line emissions from the highly ionized Ti tracer impurity. The global (over the whole plasma) properties of Ti impurity confinement are studied with a decay time of Ti K α emissions measured by the PHA. In the experiments, ECR pulse with the total injected power of ~ 0.9 MW and the duration of ~ 0.6 s was applied just after the TESPEL injection. The experimental data shown here are obtained under the condition of $R_{ax} = 3.6$ m, $B_t = 2.75$ T. As shown in Fig. 1, in the moderate density range ($n_e = 1.5 - 3.0 \times 10^{19} \text{ m}^{-3}$), the decay time of Ti K α emissions (it can be considered as the global impurity confinement time) during the ECRH is smaller than that without ECRH. At the lower density, no significant differences of the decay time of Ti K α between with and without ECRH are appreciable. The radial electric field (E_r), which can strongly affect the impurity transport [3]), could be varied when the ECRH enhances a non-ambipolar electron loss. Therefore, the radial electric field is also measured by a Ne CXRS measurement in these experiments. Figure 2 shows radial profiles of the E_r at $t = 1.5$ s (TESPEL is already injected at $t \sim 1.15$ s.) in the NBI-sustained plasma ($n_e = 1.6 \times 10^{19} \text{ m}^{-3}$) with and without ECRH. When the ECRH is applied, the E_r becomes positive, especially around $\rho = 0.45$ and the decay time of the Ti K α emissions become faster than that without the additional ECRH. The impurity transport analysis using a 1D impurity transport code, MIST, is performed with the constant diffusion coefficient (D) and the E_r -dependent convective velocity (V_{conv}), which can be written as $V_{conv} = c_m \times Z_i E_r / T$ (c_m is a factor, which can be determined by the experiment). Figure 3 shows the comparison of the temporal evolution of the Ti K α emissions with that calculated by the time-dependent MIST code. In this analysis, the value of D is fixed at $0.2 \text{ m}^2/\text{s}$. The model with the constant D and E_r -dependent V_{conv} can reproduce the experimental result well. To conclude, the

ECRH would be a useful tool for the control of impurity transport, since the strong ECRH can modify the radial electric field, which has a strong influence over the impurity behavior.

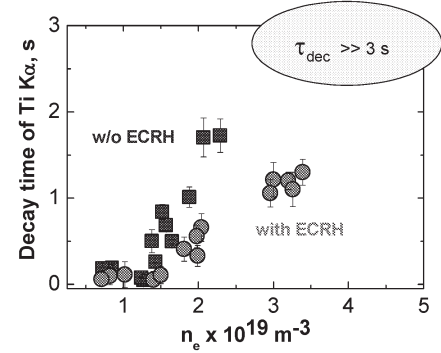


Fig.1. Comparison of the decay time of Ti K α emissions measured by the PHA in the NBI-sustained plasmas with the 0.9 MW ECRH (solid circles) and without that (solid squares) as a function of line-averaged electron density. The data shown here are obtained in the case of $R_{ax} = 3.6$ m and $B_t = 2.75$ T.

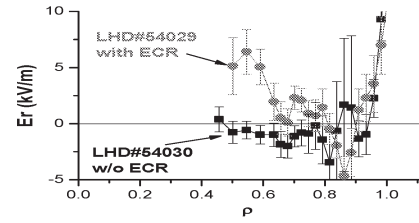


Fig.2. Radial profiles of the radial electric field in the NBI-heated plasma (solid squares) and that overlapped with 0.9 MW ECRH (solid circles). In both cases, the value of line-averaged n_e is $\sim 1.6 \times 10^{19} \text{ m}^{-3}$.

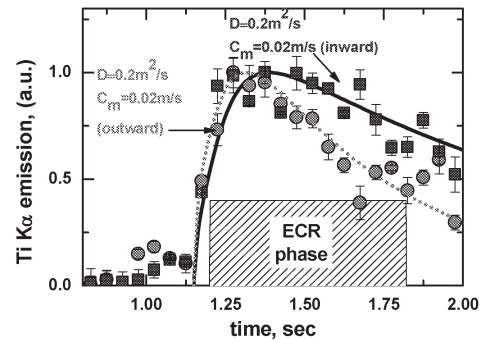


Fig.3. Comparison of the Ti K α emissions measured by the PHA with those calculated by the time-dependent MIST code for NBI plasmas (solid squares) and NBI + 0.9 MW ECRH (solid circles).

References:

- 1) Tamura, N., et al, Plasma Phys. Control. Fusion **45**, p.27, (2003).
- 2) Nakamura, Y. et al, Nuclear Fusion **43**, p.219, (2003).
- 3) Ida, K. et al, Physics of Plasma, **8**, p.1, (2001).

§48. A New Method on Recycling Coefficient Measurement Using Impurity Pellet Injection in LHD

Nozato, H. (AIST, National Metrology Institute of Japan)
Morita, S., Goto, M.

A new method¹⁾ for measuring the impurity recycling coefficient has been applied to hydrogen and helium plasmas using impurity pellets and absolutely calibrated high-spatial resolution bremsstrahlung measurement.²⁾ For the purpose of direct supply of the impurity particles inside the LCFS, an impurity pellet injector was installed on LHD.³⁾ In order to evaluate recycling coefficients of carbon, aluminum and titanium, the pellet were injected into a steady phase of NBI heated plasmas with $R_{ax}=3.6m$ and the recycling coefficient was evaluated from a transient time response of bremsstrahlung intensities using an one-dimensional impurity transport code.

The impurity behavior was analyzed with a diffusive/convective model assuming that the transport of bulk ions is stationary and the functions (diffusion coefficient D , convective velocity V and recycling coefficient R) are constant in time. Then, the impurity particle flux in q^h charge state is given as follows;

$$\Gamma_q = -D_q(r) \frac{\partial n_q}{\partial r} + V_q(r) n_q \quad (1)$$

Here, the recycling coefficient R is defined through Γ_{in}/Γ_{out} where Γ_{in} and Γ_{out} stand for the inward and outward fluxes at $p=1$, respectively. In the simulation, it is assumed that the particles reenter into the plasma in singly ionized state. In typical LHD plasmas with $R_{ax}=3.6m$, the particle transport coefficients D and V are reported as shown in Fig.1.⁴⁾ The D has a spatially constant value, and the inward V exists only at $p>0.6$ with the electron density gradient.

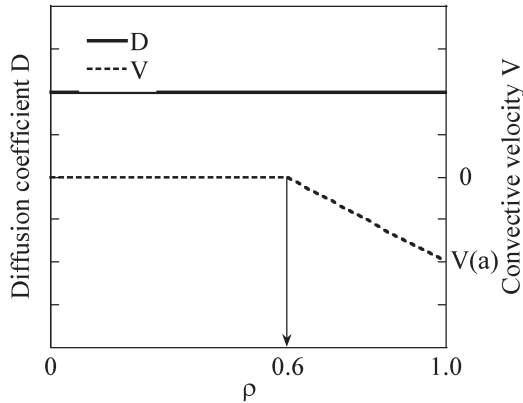


Fig.1 Spatial structure of transport coefficients D and V .

Figure 2 shows a carbon transport analysis in a helium plasma. In the figure, Z denotes the height of viewing sight on the bremsstrahlung diagnostic. In order to fit calculated bremsstrahlung intensities to measured ones, a good combination among D , $V(a)$ and R should be selected. Additionally, the spatial structure of the D and V must be considered. For the evaluation of the R from the time

evolution of absolute intensities, it is necessary to specify an exact particle source. As an initial condition in the simulation, the absolute amount of supplied particles must be given. Figure 3 summarizes the recycling coefficients of carbon in hydrogen and helium plasmas. This result indicates that the recycling process of carbon obviously differs between the two cases.

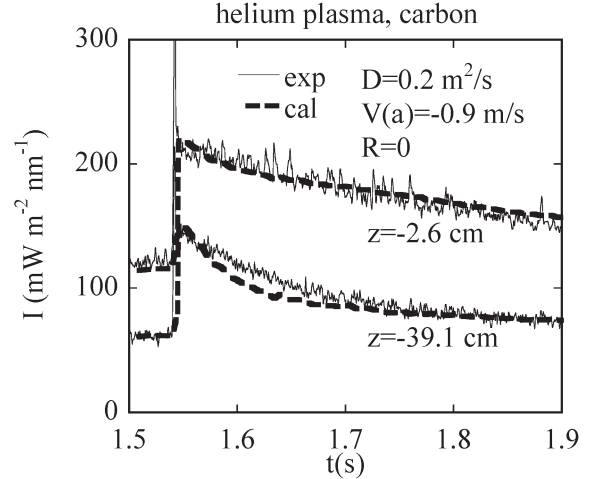


Fig.2 Time evolutions of measured (solid lines) and calculated (dashed lines) bremsstrahlung intensities for carbon pellet injection in a helium plasma.

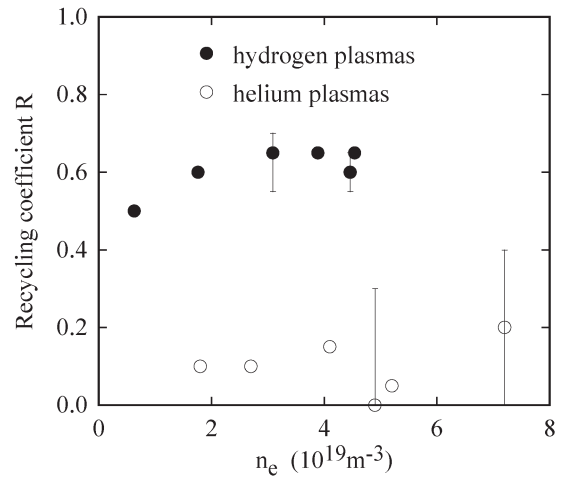


Fig.3 Summary of carbon recycling coefficients in hydrogen (●) and helium (○) plasmas.

In impurity transport studies, metallic impurities such as aluminum and titanium have been traditionally treated as a non-recycling particle. From the analysis on aluminum and titanium pellet injections, it was clearly confirmed that those elements behave as the non-recycling particle.

References

- 1) Nozato, H., Rev. Sci. Instrum. **76**, 073503 (2005).
- 2) Nozato, H., J. Plasma Fusion Res. Series **5**, 442 (2002).
- 3) Nozato, H., Rev. Sci. Instrum. **74**, 2032 (2003).
- 4) Nozato, H., Phys. Plasmas **11**, 1920 (2004).

§49. Forbidden M1 Transitions Emitted from Argon Discharges in LHD

Katai, R. (Grad. Univ. Adv. Stud.)
Morita, S., Goto, M.

Forbidden lines arising from magnetic dipole (M1) transitions of highly charged ions are useful in spectroscopic studies and plasma diagnostic applications. The M1 transitions of highly charged ions have been studied in many laboratory and space plasmas¹⁾. The M1 transitions in $2s^22p^x$ ($x=1$ to 5) ground and $2s2p$ excited configurations of highly charged argon have been also identified using electron beam ion trap (EBIT) in visible spectral region²⁻³⁾. However, the study of those transitions in VUV spectral region has not been done so far⁴⁾.

Observation of the M1 transitions is generally difficult in high-temperature plasmas, because the M1 transitions are much weaker than allowed transitions. In LHD, pure argon discharges have been created for ion heating experiments. Argon discharges were produced by neutral beam heating with injection power up to 12 MW. The density was initiated by argon gas puff at the beginning of the discharge and maintained during 2-3s with electron densities up to $2 \times 10^{19} \text{ m}^{-3}$. The central electron temperature was very high (4 keV) in the argon discharges. Almost pure argon discharges were performed remaining a small amount of hydrogen. In such discharges visible and VUV emissions from argon ions drastically increased and the M1 transitions were observed for the first time in LHD. The M1 transitions of argon are emitted from the edge plasma, because the ionization potentials in such argon ions are smaller than the central electron temperature. On the other hand, x-ray lines from H- and He-like argon ion have been observed for ion temperature measurement in the central column of LHD plasmas⁵⁾.

VUV spectra have been measured using a space-resolved VUV system, consisting of a 3 m normal incidence spectrometer with a 1200 grooves/mm grating, CCD detector and a pair of two focusing mirrors⁶⁾. Visible spectra have been also measured using two 50 cm Czerny-Turner type spectrometers equipped with CCD detectors. Low-resolution 100 and 150 grooves/mm gratings were selected for monitoring a wider spectral band.

Forbidden M1 transitions of Ar ions were successfully detected in such argon discharges. Typical examples of the VUV and visible spectrum are shown in Fig.1 and Fig.2, respectively. Five lines were identified as an M1 transition of ArXII($2s^22p^3$: 649.03Å), ArXIV($2s^22p$: 4412Å), ArX($2s^22p^5$: 5533Å), ArXV($2s2p$: 5944Å) and ArXI ($2s^22p^4$: 6917Å), by analyzing the Doppler broadening and time behaviors. The visible emissions of the Ar M1 transitions were bright. As a result, the relatively strong M1 emissions enabled us to study the physical mechanism of the M1 transitions. Intensities of the M1 transitions are being calculated using a simple model and some of them are compared with the experimental results.

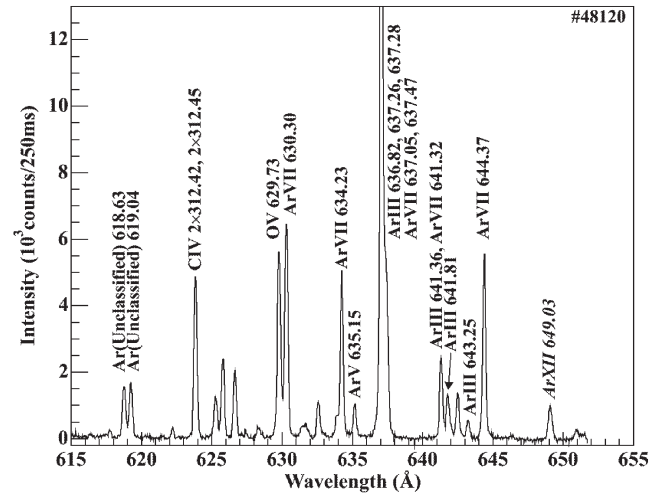


Fig. 1. VUV spectrum obtained from argon plasmas using 3 m normal incidence spectrometer. Italic fonts indicate Ar M1 line.

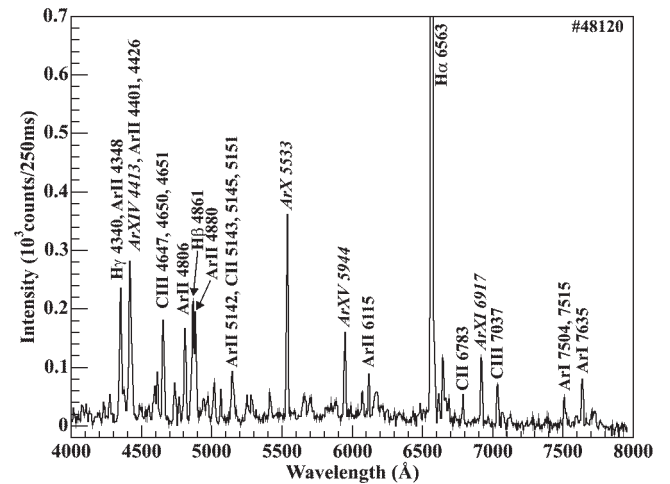


Fig. 2. Visible spectrum obtained from argon plasmas using 50 cm Czerny-Turner type spectrometer. Italic fonts indicate Ar M1 lines.

Reference

- 1) Suckewer, S. and Hinnov, E., Phys. Rev. Lett. **41**, (1978) 756.
- 2) Draganić, I., *et al.*, Phys. Rev. Lett. **91**, (2003) 183001.
- 3) Chen, H., *et al.*, Phys. Scr. **65**, (2002) 252.
- 4) Kaufman, V. and Suger, J., J. Chem. Ref. Data. **15**, (1987) 321.
- 5) Morita, S. and Goto, M., Rev. Sci. Instrum. **74**, (2003) 2375.
- 6) Morita, S. and Goto, M., Rev. Sci. Instrum. **74**, (2003) 2036.

§50. Sustained Detachment - Serpens Mode

Miyazawa J., the High-Density Theme Group

Self-sustained detachment has been obtained since the 8th experimental campaign. In Fig. 1, shown are the waveforms from a neutral beam (NB) heated hydrogen discharge where detachment is self-sustained for 2 s. The NB port-through power, $P_{\text{NB}}^{\text{PT}}$, of ~ 8 MW is applied from 0.8 to 3.3 s (Fig. 1 (a)). The line-averaged electron density, \bar{n}_e , is rapidly increased to $> 1 \times 10^{20} \text{ m}^{-3}$ by short but strong gas puffing of $\Phi_{\text{puff}} \sim 200 \text{ Pa}\cdot\text{m}^3/\text{s}$ at ~ 1.1 s, after the density feedback phase (Fig. 1 (b)). Then, the ion saturation current measured on the divertor plate, I_{sat} (Fig. 1 (b)) decreases significantly (I_{sat} normalized by \bar{n}_e is $\sim 1/10$ of that in the attached phase), indicating that detachment is occurring. Correspondingly, the neutral pressure, p_0 (Fig. 1 (c)) and the H_α intensity (Fig. 1 (d)) also decrease. These suggest that the recycling flux is reduced. Since the high-density is sustained with the reduced recycling, an improved fueling efficiency for the recycling neutrals and/or an improved particle confinement is expected. It should be noted that ELM-like spikes are recognized in I_{sat} , H_α and C_{III} signals. Unlike the usual detachment in other devices, the detachment phase is sustained without gas puffing. No impurity gas puffing is applied in this case and the intrinsic carbon (sputtered from the divertor tiles) is thought to be the main radiator since the C_{III} intensity (Fig. 1 (d)) is well correlated with P_{rad}^* . The electron temperature at the edge region of $\rho = 0.9$ (ρ is the normalized minor radius), $T_{\text{e}09}$, decreases below 100 eV as shown in Fig. 1 (e). Here we define an effective radius of the hot plasma boundary, $\rho_{100\text{eV}}$, by an average of ρ where T_e is in the range of 50 to 150 eV (Fig. 1 (e)). In the attached phase before 1 s, $\rho_{100\text{eV}}$ is slightly larger than 1, indicating that the hot plasma is filled to the last closed flux surface (LCFS). As the detachment proceeds, the hot plasma column shrinks and $\rho_{100\text{eV}}$ decreases to 0.88 ± 0.02 , which corresponds to the radius of $\iota = \iota/(2\pi) = 1/q = 1$ rational surface, and destabilization of $m/n = 1/1$ MHD fluctuation is observed, where m and n denote the poloidal and toroidal mode number, respectively. Also in the other discharges obtained in the same magnetic configuration, $\rho_{100\text{eV}}$ ranges from 0.85 to 0.9 as long as the detachment phase is sustained.

Slight shortage of the strong gas puffing results in the reattachment as shown in Fig. 2. It is apparent from this figure that I_{sat} decreases and stays at low level as long as $\rho_{100\text{eV}}$ is less than 1. In other words, detachment takes place when the hot plasma boundary lies beneath the LCFS. In these cases, however, the detachment phases are not sustained. To achieve the Serpens mode as in Fig. 1, it is necessary to decrease $\rho_{100\text{eV}}$ below 0.88. Excess reduction of

$\rho_{100\text{eV}}$ to less than 0.85 merely leads to the radiative collapse. There is no discharge where the detachment phase is self-sustained with $0.9 < \rho_{100\text{eV}} < 1$, to date. This suggests that the transition to Serpens mode occurs when $\rho_{100\text{eV}}$ becomes close to (or, slightly less than) the radius of the $\iota = 1$ rational surface.

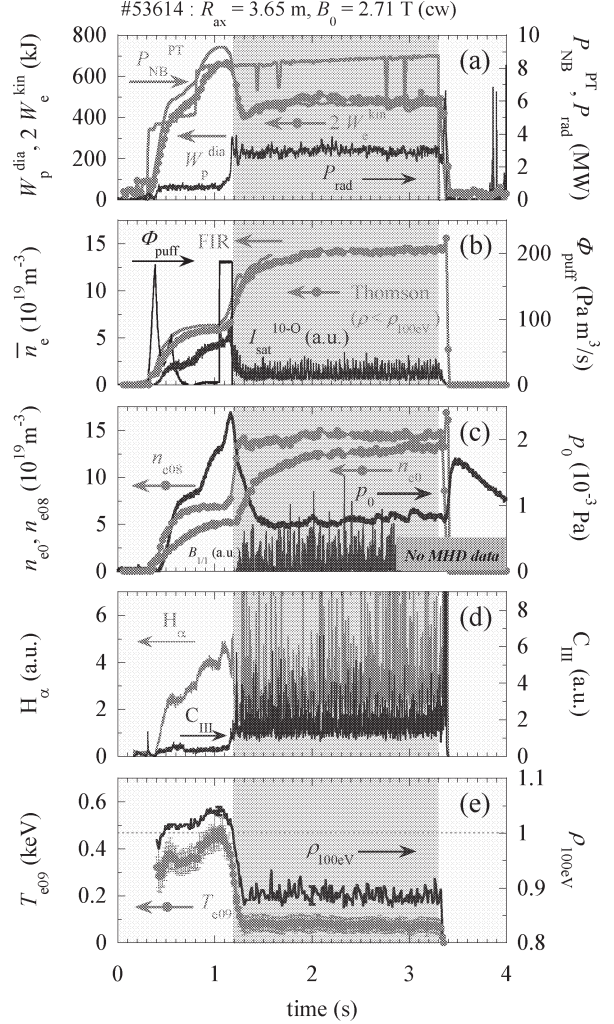


Fig. 1. Typical waveforms in the detachment discharge sustained for 2 seconds (Serpens mode).

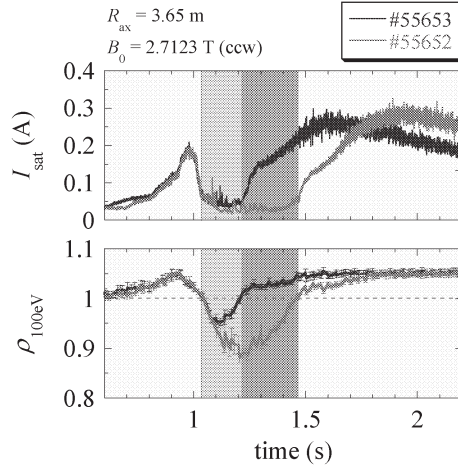


Fig. 2. Examples of reattachment after detachment.

§51. Time Evolution of Divertor Particle Flux during Serpense-mode

Masuzaki, S.

In LHD high-density discharges with a magnetic axis position of $R=3.65\text{m}$, we have observed steady self-sustained fully detached discharges, the so-called Serpens-mode [1]. Figure 1 shows time evolutions of plasma parameters in a Serpens-mode discharge. After the line averaged density, $n_{e\text{bar}}$, rises up to about $6 \times 10^{19} \text{m}^{-3}$ with feedback gas puffing, a strong but short pulse gas puff with about $200 \text{Pam}^3/\text{s}$ of fueling rate is applied. Over $1 \times 10^{20} \text{m}^{-3}$ of $n_{e\text{bar}}$ is achieved, and total radiation loss, P_{rad} , measured by a 2π bolometer increases rapidly to about 40% of the input power. On the other hand, the ion saturation current measured by the Langmuir probe arrays on the divertor plates, I_{sat} , decreases during the strong gas puffing and the discharge moves to a detached plasma. At this stage, T_e is reduced not only in the divertor plasma, but also in the peripheral region, and the hot plasma boundary shrinks up to $\rho \sim 0.88$. After termination of the gas puffing, the detached plasma is sustained without artificial fueling, and intermittent spikes appear in I_{sat} (see Fig.1(c)) and H_α signals. This is the so-called Serpens-mode.

Fig.2 shows I_{sat} waveforms at (a) $t=0.95\text{--}1.2\text{s}$ and (b) $t=2.8\text{--}3.2\text{s}$ in the same discharge with Fig.1. In Fig.2(a), I_{sat} at 6I probe array largely decreased, and that indicates divertor detachment with the strong gas puffing. The strong gas puffing was applied from 6I port, and thus, divertor detachment may be local phenomenon. Indeed, I_{sat} increased with the gas puffing at 10.5U probe array. At the end of the gas puffing, I_{sat} at 10.5U starts to decrease. At the same time, T_e at the LCFS also starts to decrease and it seems to be a sign of the beginning of shrinking of temperature profile leading to full detach. Fig.2(c) shows the intermittent spikes in I_{sat} during Serpense-mode. The frequency of the spikes appearance is close to the rotating frequency of radiation belt, Serpent, and there is phase shifting in the spikes between 6I and 10.5U probe arrays. It suggests that particle source for the spikes rotating. That is very interesting because we have observed similar intermittent spikes in I_{sat} in H-mode like discharges [2], but there are no phase shifting between different positions probe arrays. In helical divertor configuration, stochastic layer surrounds the LCFS, and thus, particle outflux from main plasma lost its origin. One possibility to account the I_{sat} characteristics is blob-like transport.

References

- [1] Miyazawa, J. et al., J. Plasma and Fusion Res. 81(2005)331.
- [2] Morita, S. et al., J. Plasma and Fusion Res. 80(2004)279.

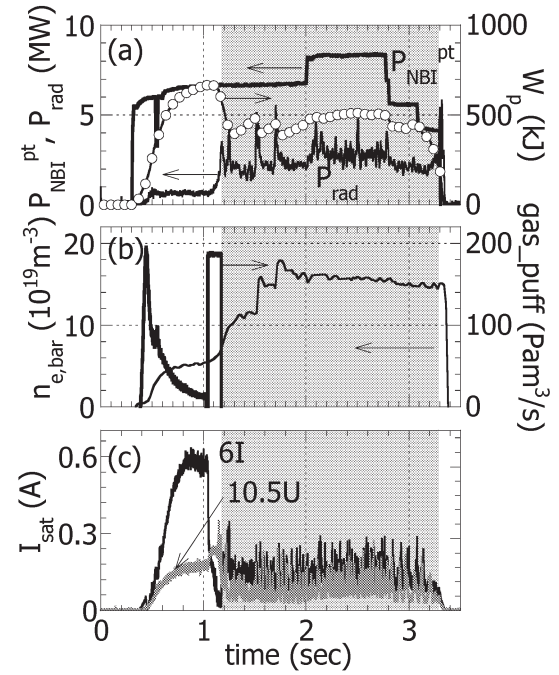


Fig.1 Time evolutions of plasma parameters in self-sustained detached discharge. Hatched area indicates Serpens-mode. Two pellets were injected at $t=1.5$ and 1.7s . I_{sat} is measured by top (10.5-U) and inboard (6-I) divertor probe array, respectively. The former is about 162° toroidally away from the latter. Shot#53630.

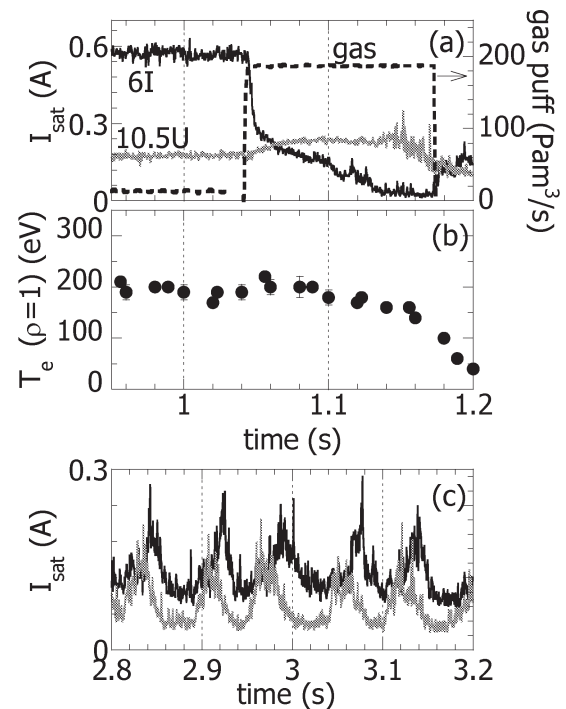


Fig.2. Time evolutions of the ion saturation currents measured top (gray) and inboard (black) divertor probe array at (a) just before the onset of Serpense-mode and (c) at LCFS during Serpense-mode. (b) T_e near the LCFS at same timing with (a).

§52. Observation of Rotating Radiation Belt in LHD

Masuzaki, S., Sakamoto, R., Miyazawa, J.,
Tamura, N., Peterson, B.J.

A poloidally rotating radiation belt with helical structure has been observed in self-sustained detachment discharges by photo diode fan arrays and fast camera in LHD. This phenomenon is similar to the MARFE as far as its poloidal localization, but the crucial difference between them is whether the position of the radiation volume continuously moves or not. The direction and mode number of the poloidal rotation is electron diamagnetic and 1, respectively, and the poloidal rotating frequency is several 10 Hz. After termination of the plasma heating, the rotation continues, but its rotating radius shrinks, and the frequency becomes 10 times higher than that during plasma heating. These observations suggest that the belt location does not relate to rational surfaces unlike Snake-mode, and we have named this radiation belt ‘Serpent’.

A rotating radiation volume was observed during Serpens-mode by absolute extreme ultraviolet photodiodes (AXUVD) fan arrays [1]. Figure 1(b) shows the time evolution of the sight volume integrated radiation power, $\langle P_{\text{rad}} \rangle$, profile during Serpens-mode, measured by an AXUVD fan array in a nearly horizontally elongated poloidal cross-section [1] (see Fig. 1(a)). That looks similar to multi-faceted asymmetric radiation from the edge (MARFE) in tokamaks [2] and in LHD [3] as far as its poloidally localization, but the crucial difference between them is whether the position of radiation volume continuously moves or not. This figure indicates that the poloidal mode number of the rotation is 1, and the rotating frequency is several 10Hz, varying with input power. Turn-rounds of the $\langle P_{\text{rad}} \rangle$ peak in Fig. 1(b) are channel number 4 and 17 (see Fig. 1(a)). That indicates the peak location of the rotating radiation volume to be inside the LCFS. Figure 1(c) shows that the rotation continues after NBI termination ($t=3.3\text{s}$), and its radius and frequency become smaller and about 10 times higher than during Serpens-mode. The shrinking of the rotation radius seems to be related to the shrinking of the T_e profile during the recombination phase, and it suggests that the rotating location is not tied to a rational surface unlike in the Snake-mode [4]. The rotating radiation volume is also observed in other toroidal sections. The fast camera (no filter, 20,000 frames/s, 108° away toroidally from the above mentioned AXUVD fan array, AXUVD#1) viewing the torus inboard and lower helical coil can from an outboard port in a horizontally elongated cross-section found that the poloidal direction of the rotation is electron-diamagnetic. Similar time evolutions of the $\langle P_{\text{rad}} \rangle$ profile to Figs. 1(b) and (c) were observed by another AXUVD fan array (144° toroidally away from AXUVD#1) viewing the torus inboard side in a toroidal section from the outboard port in the adjacent toroidal section obliquely [1]. From this

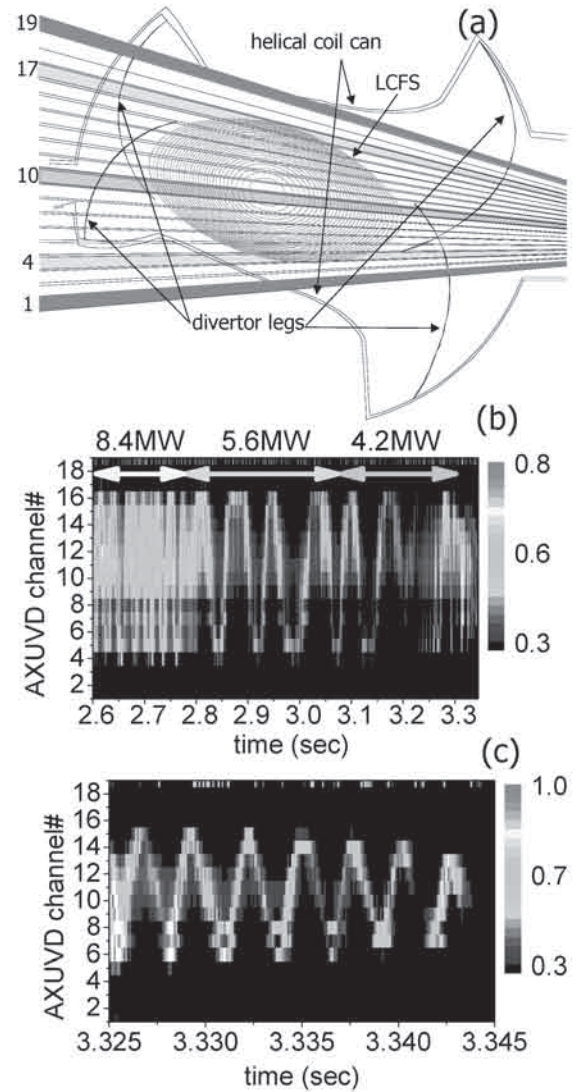


Fig.1. AXUVD sight areas (a). Time evolutions of the $\langle P_{\text{rad}} \rangle$ profile at (b) $t=2.6\text{--}3.345\text{ s}$ (NBI power is shown) and (c) after termination of NBI, at $t=3.325\text{--}3.345\text{ s}$ in Shot#53630. Unit of $\langle P_{\text{rad}} \rangle$ is arbitrary

observation, it is reasonable thinking that the rotating radiation volume forms a helical radiation belt, and it has been named ‘Serpent’. Density condensation is considered to cause such localized radiation belt as in a MARFE, though the mechanism and onset condition of the poloidal rotation are not understood at this time.

References

- [1] B.J. Peterson *et al.*, Plasma Phys. Control. Fusion **45**, 1167 (2003).
- [2] B. Lipshultz, J. Nucl. Mater. **145-147**, 15 (1987).
- [3] B.J. Peterson *et al.*, Phys. Plasmas **8**, 3861 (2001).
- [4] A. Weller *et al.*, Phys. Rev. Letts. **59**, 2303 (1987)

§53. Behavior of Impurity Radiation and Edge Plasma during Radiative Collapse at the LHD Density Limit

Peterson, B.J., Miyazawa, J., Masuzaki, S. (NIFS)

The onset of the radiative thermal instability leading to radiative collapse at the density limit has been empirically defined as the point when the radiated power is increasing with the third power of the density [1]. Since the dominant intrinsic light impurities are oxygen and carbon they should be responsible for the strong increase in the radiation from the edge. First we consider the radiation brightness from the divertor, core and edge plasmas in Fig. 1 as the discharge collapses. One notes that the onset of the thermal instability, as defined by the thick dashed line when $x = 3$ for the total radiation, is followed by the development of the previously observed [2] asymmetry in the radiation as the radiation from the inboard channel starts to diverge from the channel located near the outboard edge of the plasma. At the same time the radiation from the divertor leg region is increasing, but not as dramatically as the radiation from the inboard side. The ion-saturation current from the divertor probe begins to drop with the onset of the thermal instability and the radiation asymmetry as it approaches a detached state. Finally, considering the density exponents of the light impurities signals, CIII and OV, and the radiated power, one notes that the thermal instability begins in the OV, but that the CIII signal most closely matches the total radiated power indicating that the carbon is the dominant impurity. This temporal progression makes sense in that the oxygen should radiate at a higher temperature, and therefore the thermal instability should begin earlier in the oxygen as the edge temperature drops. Also, the above suggestion, that carbon is the dominant impurity, is consistent with observations before and after boronization, that while the reduction of OV radiation is stronger than that seen in the reduction of CIII, the reduction in CIII more closely matches the reduction in the total radiated power [3].

In Fig. 2 the evolution of the radiated power density profile from the bolometer array at the horizontally elongated cross-section [4] is shown. In the steady state portion of the discharge the profile is hollow. After the onset of the thermal instability the strongly radiating zone broadens and moves inward minor radially. Also one notes some indication of growth in the core radiation. At the edge of the plasma one notes the radiation reaches a maximum then decreases, then increases again. This is also seen in the inboard channel of the bolometer in Fig. 1 and may be related to the two peaks observed in the cooling rate of the impurities as a function of electron temperature. One should take care in the quantitative evaluation of the radiation profile during the collapsing phase as the asymmetry in the radiation signal may lead to errors in the tomographic inversion. These errors should be mitigated in this case by the orientation of the array which fans out vertically while the asymmetry has an inboard-outboard nature.

References

- 1) Peterson, B. J., et al., NIFS Annual Report 2003-2004 (2004) 6.
- 2) Peterson, B.J., et al., Phys. Plasmas **8** (2001) 3861.
- 3) Nishimura, K., et al., J. Plasma Fusion Res. **79** (2003) 1216.
- 4) Peterson, B.J., et al., Plasma Phys. Control. Fusion **45** (2003) 1167.

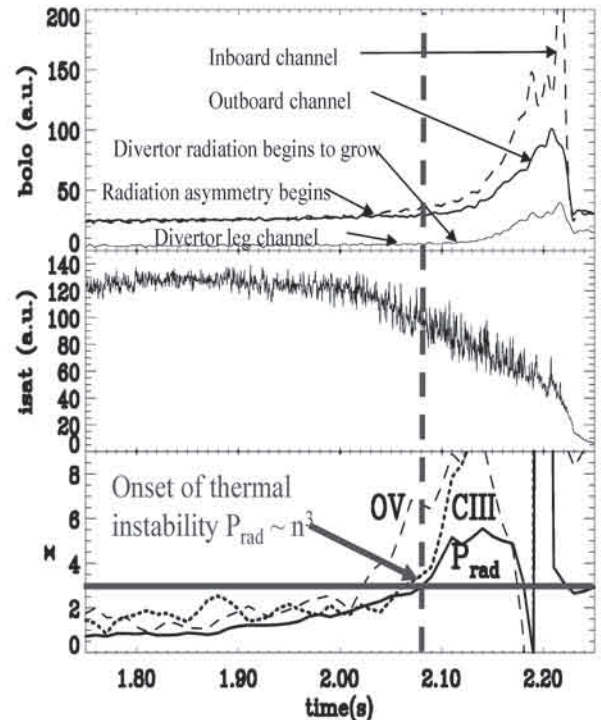


Fig. 1 Time evolution of bolometer brightness, divertor ion saturation current, and the density exponent for the total radiated power, CIII and OV during radiative collapse of shot 43383.

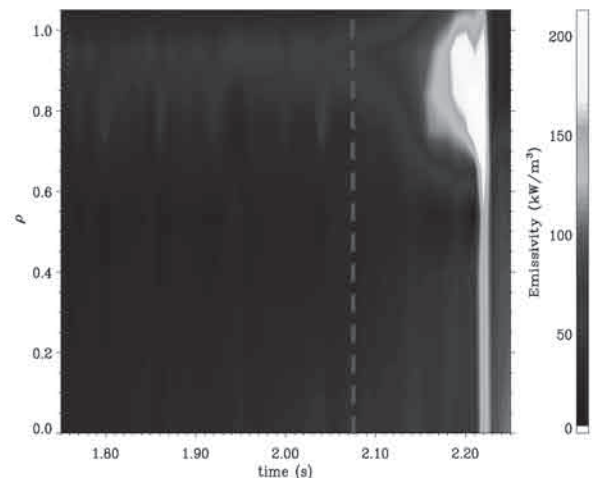


Fig. 2 Evolution of radiated power density profile during radiative collapse of shot 43383.

§54. Temperature Measurement of a Vertically Installed Divertor Plate with an Infrared Radiation Thermometer in Self-sustained Detachment Plasmas

Shoji, M.

In the last experimental campaign (7th cycle), a CCD camera at 3-O port for monitoring divertor plates observed a hot spot (local heating) on the vertically installed divertor plate in 2.5-L port during ICRF heated long pulse discharges. The reduction of the heat load onto divertor plates is a major concern for modern plasma confinement systems. A single channel infrared radiation thermometer (Chino, IR-FBSr) was installed in 7-O port for direct measurement of the surface temperature of the vertically installed divertor plate in 6.5-L port in this campaign (8th cycle). The lowest measurable temperature of the thermometer is 300°C, and the viewing area is about $\phi 35\text{mm}$ on the surface located 3 metres ahead. A CCD camera (Sony, DXC-LS1) with an interference filter for CH band emission measurement ($\lambda_0=429.5\text{nm}$) is fixed to the thermometer to check the viewing area. The viewing area of the radiation thermometer can be changed horizontally and vertically by stepping motors which is controlled from a LHD control room via optical fibers.

In this experimental campaign, we unexpectedly succeeded in production of self-sustained detachment plasmas by strong gas fueling after density feedback control in a magnetic axis configuration ($R_{ax}=3.65\text{m}$). Figure 1 shows the images of the CH band emission profile in the lower divertor region in the case without the self-sustained detachment (a) and with the detachment (b). Divertor leg structures and a bright line appearing on the lower divertor plates are unclear during the detachment. These observations qualitatively indicate the decrease of the particle flux onto the divertor plates, which is consistent with the measurements with electro-static probes embedded in the divertor plates. Gray circles in the middle of the images indicate the viewing area of the infrared radiation thermometer which directly observes the vertically installed divertor plate in 6.5-L port.

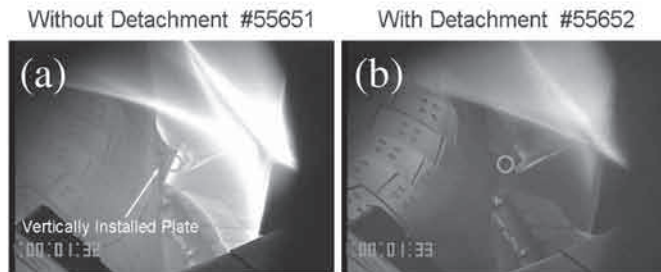


Fig. 1. The images of the CH band emission profile without (a) and with (b) the self-sustained detachment in the lower divertor region in 6.5-L port. The viewing area of the infrared radiation thermometer is also shown as gray circles on a vertically installed divertor plate.

Figure 2 gives the time traces of the temperature of the vertically installed divertor plate measured with the radiation thermometer in the case without (a) and with (b) the detachment. The temperature of the divertor plate kept to be low ($< 300^\circ\text{C}$) during the detachment (between 1.0s and 1.5s in case (b)). The duration time of the detachment is strongly dependent on the quantity of the gas fueling after the density feedback control. When the gas fueling is not sufficient, the detachment was not clearly observed as shown in the case (a). The direct measurements of the temperature with the infrared radiation thermometer successfully show the strong reduction of the heat load onto the vertically installed divertor plate during the self-sustained detachment.

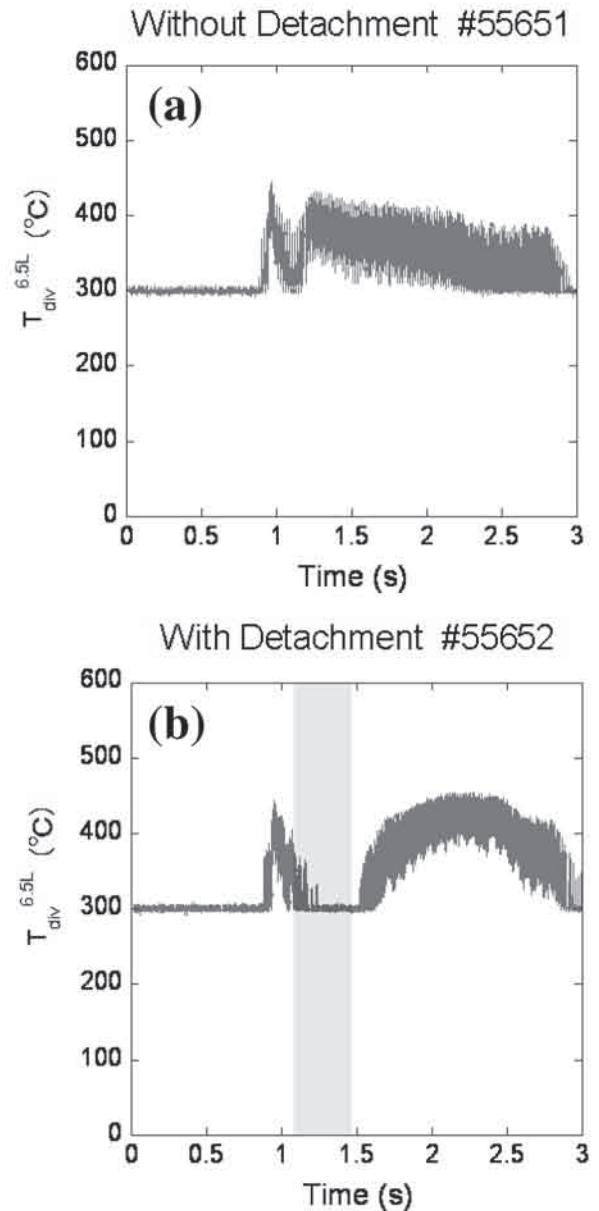


Fig. 2. The time traces of the temperature of the vertically installed divertor plate in 6.5-L port in the case without (a) and with the detachment (b). These experimental data were measured with the infrared radiation thermometer installed in 7-O port.

§55. CH Band Emission Profile Measurement in Self-sustained Detachment Plasmas in LHD

Shoji, M.

The deterioration of the plasma energy confinement due to radiation by hydrocarbons originated from graphite divertor plates is a major concern in LHD plasma discharges. A practical technique to evaluate the hydrocarbon density is the measurement of the intensity of CH band emission¹⁾. A filtered visible CCD camera ($\lambda_0=429.5\text{nm}$) has been installed in 7-O port to measure the emission profile in the divertor region (6.5-L). The viewing angle of the camera can be controlled from a LHD control room, which can directly observe lower divertor plates, divertor legs and X-point.

We unexpectedly succeeded in production of self-sustained detachment plasmas in the last experimental campaign (8th cycle) by strong gas fueling after density feedback control in a magnetic axis configuration ($R_{ax}=3.65\text{m}$). In these discharges, attached plasmas were steadily sustained after the gas fueling without additional gas fueling for plasma density control. During the detachment, a toroidally and poloidally rotating radiation belt was observed with a tangentially viewing CCD camera, bolometer arrays, and a fast-framing CCD camera. Electro-static probes embedded in divertor plates also observed the fluctuation of the ion saturation current which frequency is corresponding to that of the rotating radiation belt.

Figure 1 shows the time evolution of the image of the CH band emission in the lower divertor region in a

self-sustained detachment plasma. In this discharge, the detachment was sustained between 1.1s and 1.4s. The intensity of the CH band near the X-point in the ergodic layer is significantly high just before the detachment (1.09s), and the fluctuation of the intensity was simultaneously observed. Impurities (hydro-carbons) originated from the graphite divertor plates can penetrate into the X-point, which leads to local radiation and cooling in the peripheral plasma. It may trigger the self-sustained detachment and the rotating radiation belt.

As shown in fig. 1, the divertor leg structure and a bright line on the lower divertor plates are unclear during the detachment. These observations qualitatively indicate the decrease of the particle and heat flux onto the divertor plates, which is consistent with the measurements with thermo-couples and the electro-static probes embedded in the divertor plates. An infrared radiation thermometer for monitoring the surface temperature of the vertically installed divertor plate in 6.5-L port also indicated low temperatures ($< 300^\circ$), which clearly shows significant reduction of the heat load onto the plate.

Detailed measurements of impurity radiation profiles and velocities in the X-point, the divertor legs and the divertor plates during the detachment will contribute to elucidation of the relationship between the detachment and the impurity (hydro-carbon) transport in the plasma periphery. Three-dimensional impurity transport simulation which can handle the transport of hydro-carbon molecules, atoms and ions will be useful and powerful tool to clarify the physical mechanism of the self-sustained divertor detachment and the rotating radiation belt.

Reference

1) Pospieszczyk, A.: Nuclear Fusion Research (2005) 135.

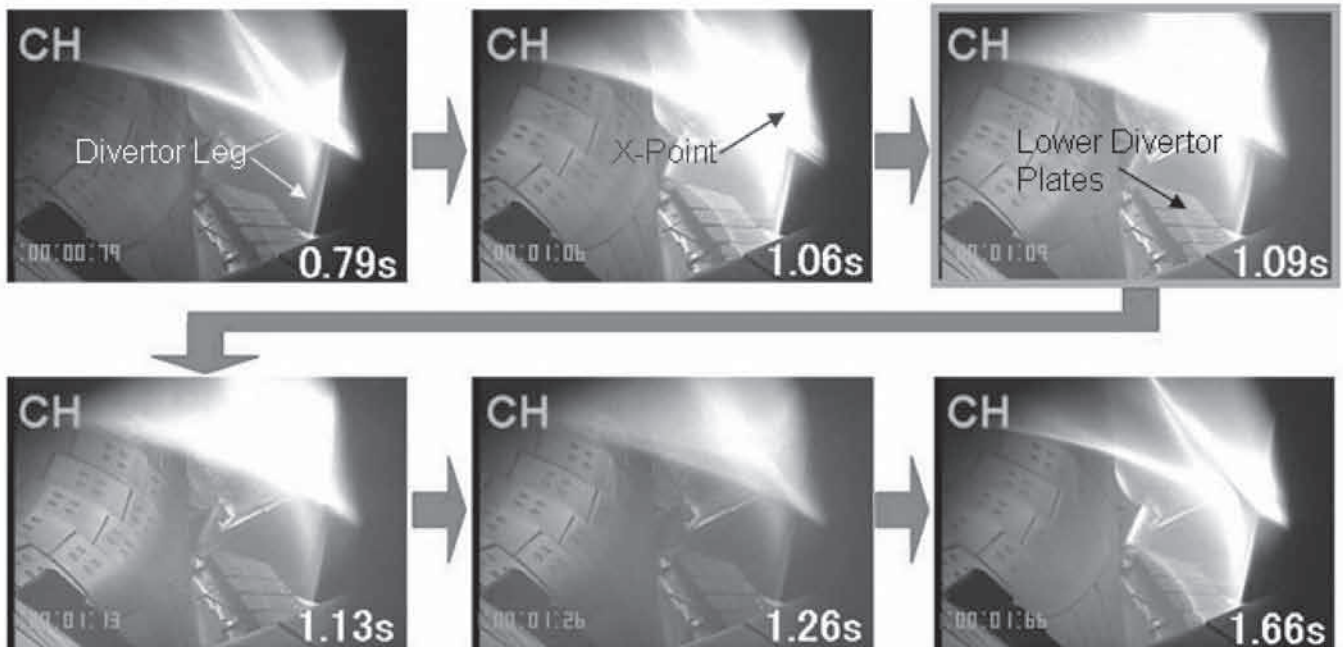


Fig. 1. The time evolution of the image of the CH band emission profile in the lower divertor region in a self-sustained divertor detachment plasma, which is observed with a filtered visible CCD camera ($\lambda_0=429.5\text{nm}$) installed in 7-O port. The detachment was sustained between 1.1s and 1.4s in this discharge.

§56. Heat and Particle Deposition Profiles on the Helical Divertor during Magnetic Axis Swing Operation

Ogawa, H. (Grad. Univ. Advanced Studies),
Masuzaki, S., Ohya, N.

In the helical divertor, heat and particle deposition profiles are not uniform in both toroidal and poloidal directions, and the profile changes with changing magnetic configuration, e.g., major radius of magnetic axis (R_{ax}) [1]. Fig.1 shows temperature rise of torus inboard (Div#1) and bottom (Div#6) divertor plates in 80 seconds ICH discharges with different R_{ax} . In the case of inward shifted R_{ax} , heat deposition is intensive at torus inboard side, and torus top and bottom become the intensive heat deposition area in outward shifted R_{ax} discharges.

In LHD, long pulse discharge experiments have been conducted mainly using ICH. One of the limits of discharge duration is believed to be overheating of divertor plates at intensive heat deposition area [2]. The foregoing characteristic of heat deposition profile in the helical divertor was utilized to avoid the overheating of divertor plates by dispersion of time averaged heat deposition profile with R_{ax} swing operation during discharges, and heat and particle deposition profiles during the operation were investigated.

Fig. 2(a) and (b) show the time evolutions of temperature rise of the divertor plates and rate of temperature rise at torus inboard side and bottom, respectively, and Fig.2(c) shows R_{ax} during a R_{ax} swing ICH discharge. It is very clearly shown that heat deposition to both divertor plates is modulated with R_{ax} swing. As shown in Fig.1, heat load to the torus inboard side divertor plate (Div#1) and bottom plate (Div#6) is almost same at $R_{ax}=3.67\text{-}3.69\text{m}$. This R_{ax} swing operation was conducted in the range of $R_{ax}\sim 3.65\text{-}3.69\text{m}$. It is important that R_{ax} swing range is centered near $R_{ax}=3.67\text{-}3.69\text{m}$ for effective dispersion of the divertor heat load. For example, in the discharge with R_{ax} swing in the range of $R_{ax}=3.62\text{-}3.65$, heat deposition profile is not modulated. Fig.2(d) and (e) shows the ion saturation current, that is, particle flux profiles on the divertor plates at torus inboard side and bottom, respectively, and these profiles were also modified by R_{ax} swing. It means that R_{ax} swing operation can modify heat and particle deposition profiles on the helical divertor, and also on each divertor plate. Therefore, this operation is effective tool to avoid overheating of divertor plates, and to extend the discharge duration. The discharge with duration of over 30 minutes and total input energy of 1.3GJ was achieved with this operation [3].

Reference

- [1] Masuzaki, S. et al., Nucl. Fusion **42** (2002) 750.
- [2] Mutoh, T. et al., Nucl. Fusion **43** (2003) 738.
- [3] Mutoh, T. et al., J. Plasma and Fusion Res. **81** (2005) 229.

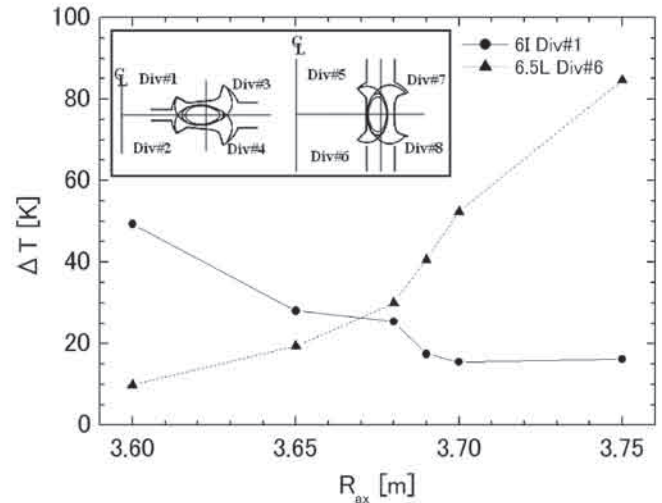


Fig.1. Temperature rises of torus inboard (Div#1) and bottom (Div#6) divertor plates during discharges with different R_{ax} . Insertion shows positions of the divertor plates in which thermocouples are embedded in a toroidal section.

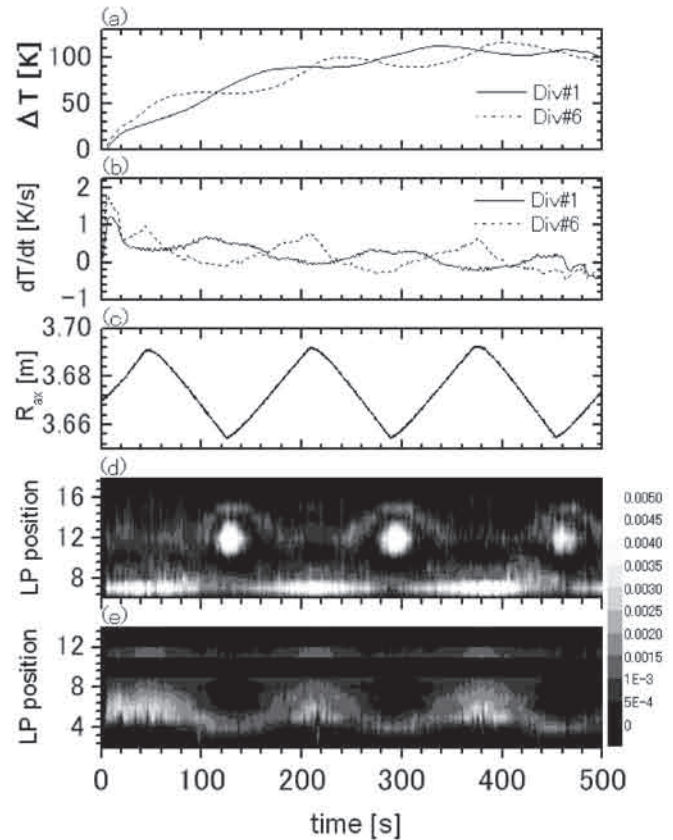


Fig.2. time evolutions of (a) temperature rise of the divertor plates, (b) rate of the temperature rise, (c) R_{ax} position, ion saturation current on the divertor plates at torus inboard-side (d) and bottom (e), respectively.

§57. Transport Analyses of Carbon Atoms in the LHD Divertor Region

Shoji, M.

The deterioration of the plasma energy confinement due to radiation by carbon ions originated from graphite divertor plates is a major concern in LHD plasma discharges. The reduction of carbon ions in the plasma periphery can mitigate radiation collapse which is often observed in high density plasmas in LHD.

Since the 6th experimental campaign, we have observed impurity (carbon ions) radiation profile in the lower divertor region in 2.5-L port with filtered CCD cameras ($\lambda_0=426.7\text{nm}$ for CII, $\lambda_0=465.4\text{nm}$ for CIII). The cameras can directly observe the graphite divertor plates, divertor legs and an X-point. Figure 1 shows the time evolution of the image of the radiation profile of carbon ions (CII and CIII) in the lower divertor region in which the plasma density was slightly increased by controlling the fueling rate from a gas puffer ($R_{ax}=3.75\text{m}$). Significant increase of the radiation of CII in on a lower divertor leg (left side) was observed as the plasma density rise. The plasma discharge was terminated by radiation collapse

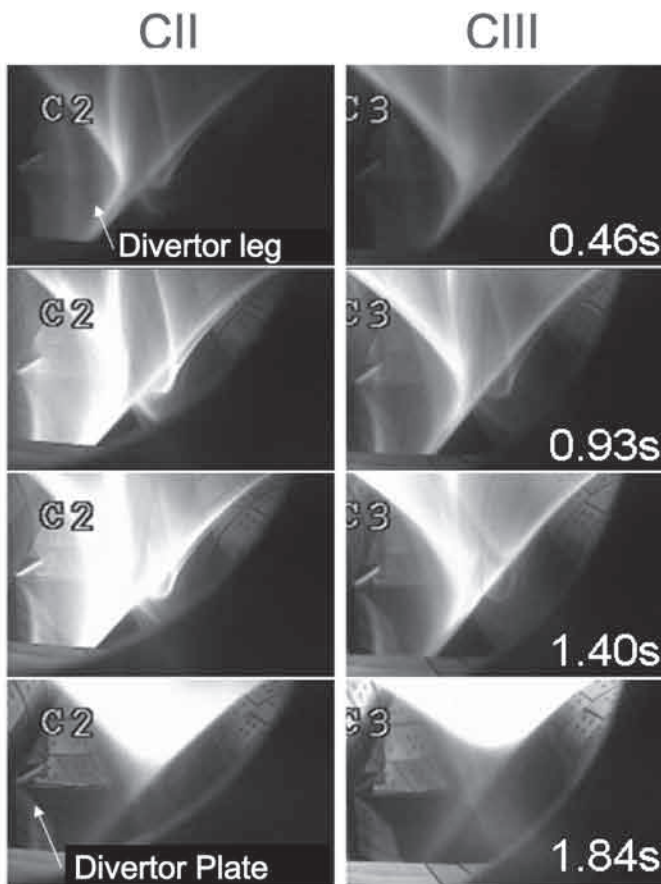


Fig. 1. The time evolution of the image of the emission profile from carbon ions (CII and CIII) in the lower divertor region. In this discharge, the plasma density was slightly increased by controlled gas fueling.

occurred at 1.84s, at which the divertor legs was not clearly observed and the radiation in the main plasma significantly increased.

These observations strongly suggest that the radiation by carbon ions from the graphite divertor plates affects the radiation collapse and limits the plasma density. For detailed analyses of the transport of carbon ions in the divertor region, we calculated the profile of neutral carbon atoms by using three-dimensional neutral particle transport simulation code (EIRENE stellarator version)¹⁾. Figure 2 gives the calculation of the density profile of carbon atoms at a toroidal position where the plasma is vertically elongated. Neutral hydro-carbons (CH_4) are emitted from divertor plates in this calculation, and the three-dimensional profile of the emitted hydro-carbons is based on the calculation of magnetic field line traces from the last closed magnetic surface. The input plasma parameter profiles are determined by the experimental results measured with plasma diagnostic systems just before the radiation collapse. The simulation shows the high density of the carbon atoms on inner divertor legs. In figure 1, the divertor leg (left side) on which high emission from carbon ions appeared corresponds to the inner and lower divertor leg. The calculation using the neutral particle transport simulation code can qualitatively explain the observations of the behavior of carbon atoms just before the radiation collapse.

In the near future, this analysis will contribute to the detailed investigation of plasma wall interactions and impurity transport in the divertor region, and to the achievement of higher density plasmas. It is also useful for the design of optimized closed divertor configurations planned in Phase II in LHD.

Reference

1) Reiter, D. et al.: Plasma Phys. Contr. Fusion 33 (1991) 1579.

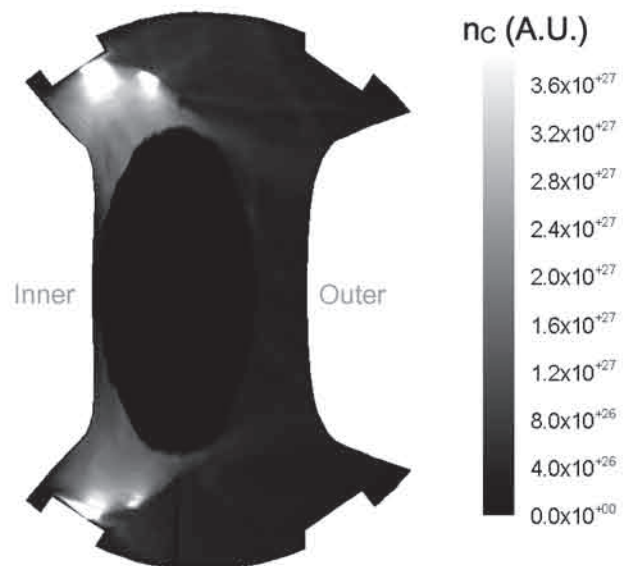


Fig. 2. The calculation of the density profile of carbon atoms just before the radiation collapse. In this calculation, methane is emitted from divertor plates on the basis of the calculation of magnetic field line traces.

§58. Edge Plasma Measurement with Fast Scanning Langmuir Probes

Masuzaki, S.

Unlike the scrape-off layer in poloidal divertor tokamaks, open field lines layer (OFL) outside the last closed flux surface (LCFS) in the helical divertor (HD) configuration has complex field lines structure containing stochastic field line layer, residual islands and whisker layer. To understand the transport, detailed investigation of density and temperature profiles is necessary.

Two fast scanning Langmuir probes (FSPs) driven by pneumatic cylinders have been installed in LHD from 4.5U port as shown in Fig.1. Their stroke is 300mm and 500mm, respectively. Short stroke FSP crosses a divertor leg, and the latter measures near X-point. The probe position is measured by laser distance meter, and the scan speed is about 1 m/s. Two electrodes are equipped in each FSP. They can be a double probe or two single probes. The spatial resolution is determined by frequency of probe voltage swing, and that is about 4 mm.

In Fig.2, connection length profiles for $R_{ax}=3.75m$ and $4.05m$ are shown. Whisker layers appear at $Z > 1.1m$ in $R_{ax}=3.75m$ case and all Z range in $R_{ax}=4.05m$ case as spike like structure. In the 8th experimental campaign, initial FSP data were obtained. Electron density (n_e) and temperature (T_e) are deduced from single probe characteristics. Modulation of profiles of n_e and T_e reflects whisker layer. In $R_{ax}=3.75m$ case, stochastic layer appears at $Z < 1.05m$. In this layer, T_e profile is nearly flat, though n_e profile has gradient. This profile is consistent with early Thomson scattering data [1], and relates with ergodicity in stochastic layer. Systematic data will be collected in the 9th experimental campaign.

After the experimental campaign 2004, FSPs were drawn out, and checked damages. Top part made of boron-nitride partly sublimed. In this campaign, FSP experience up to 6 MW of input power. Therefore, FSP measurement should be limited in low input power discharges.

Reference

[1] Morisaki, T. et al., J. Nucl. Mater. **313-316** (2003) 548.

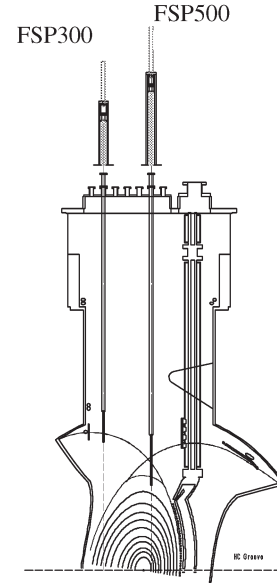


Fig.1 Locations of fast scanning Langmuir probes in 4.5U

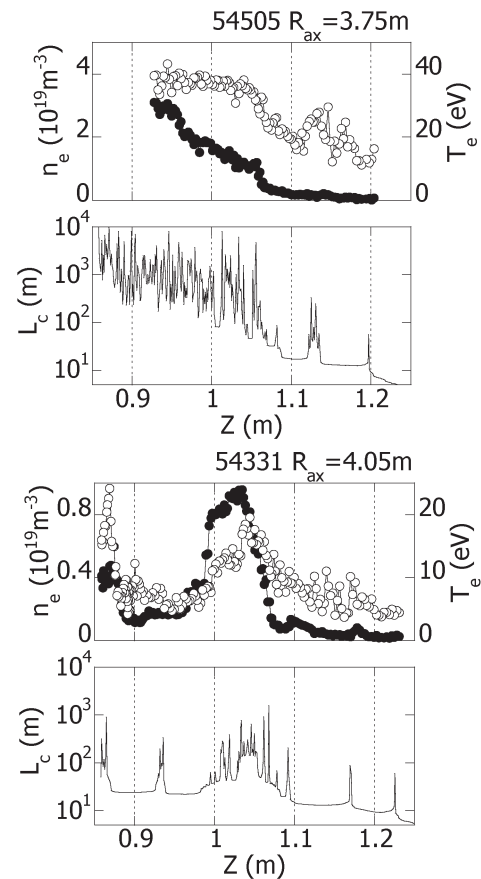


Fig.2. Vertical profiles of electron density, temperature and connection length of field lines along FSP500 trajectory. The origin of Z is the equatorial plane. $R_{ax}=3.75m$ (top). $R_{ax}=4.05m$ (bottom). Open circles: T_e . Closed circles: n_e .

§59. Characterization of the LHD Edge & Divertor Plasma by Ion Sensitive Probe Measurement (II)

Ezumi, N. (Nagano National College of Tech.)
 Ohno, N. (Ecotopia Sci. Inst., Nagoya Univ.)
 Takamura, S. (Dept. Energy Eng. & Sci., Nagoya Univ.)
 Masuzaki, S.

Ion temperature (T_i) is one of the key parameters for characterizing edge and divertor plasmas. A lot of studies have been made on electron temperature (T_e) and electron density (n_e) measurements for the divertor region of the LHD. However, an ion temperature (T_i) profile in this region is not well known. In this study, we investigate the ion's behavior in the LHD edge and divertor region since it is important to reveal the property of edge and divertor plasma for improving the LHD plasma performance. There are some methods for measuring T_i at the boundary plasmas. Conventional optical methods for measuring the T_i , especially a doppler broadening measurement, have a difficulty to obtain the local values and the profile of T_i , because the evaluated values are integrated (averaged over) along the line of sights. In the case of LHD divertor measurement, there are many restrictions for the arrangement of optical devices, because the vacuum chamber of the LHD has the complicated geometric structure. Therefore, in order to measure the profile of T_i in this region, it is necessary to prepare a high spatial resolution diagnostic system. An Ion Sensitive Probe (ISP) [1] is a candidate for such diagnostics because the ISP is electrical probes used for measuring the spatial profile of T_i in the magnetized plasmas and has high spatial resolution. Moreover, T_e and plasma space potential (V_s) can be measured, simultaneously.

T_i measurement using an ISP in the divertor leg in LHD had been done during 4th, 5th and 6th experimental cycles. The prototype-ISP for LHD was installed to the fast scanning probe system and the measurement system was established. In #31256, typical ISP's I - V characteristics were obtained from both electrodes [2]. The estimated T_i and T_e using the I - V characteristics were about 20-35 eV and 5-15 eV at the outside region of the divertor leg, respectively. The spatial distribution of the evaluated T_i is

qualitatively consistent with the results of calculations of particle's orbits in the edge and divertor region of LHD.

In order to measure the hotter T_i region, it is necessary to improve the structure of ISP. During this experimental cycle, we designed a new ISP head as shown in Fig. 1. The outer electrode is placed in slightly inside of BN shield in order to avoid high heat load when positive bias voltage is applied. Coaxial cables are used for wiring the ISP electrodes and the length of both electrodes is to be as short as possible in order to reduce electrical noise, which caused serious problem for analyzing measured data. Moreover, we also reassemble the wiring in the fast scanning probe system. Recent results of the linear plasma generator PSI-2 showed the difficulty of T_i measurement under the condition of the existence of electric field along the axis of the ISP electrodes [3]. Maybe we must consider the influence of the electric field around the ISP when the probe head moves into the edge plasma region. In the next experimental cycle, the probe head connector of the fast scanning probe system will be modified. We plan to redesign the ISP head along the modification of the probe connector.

References

- 1) Katsumata, I., Contrib. Plasma Phys. **36**, (1996) S, 73.
- 2) Ezumi, N. et al., J. Nucl. Mater. **313-316**, (2003) 696.
- 3) Ezumi, N. et al., J. Nucl. Mater. **337-339**, (2005) 1106.

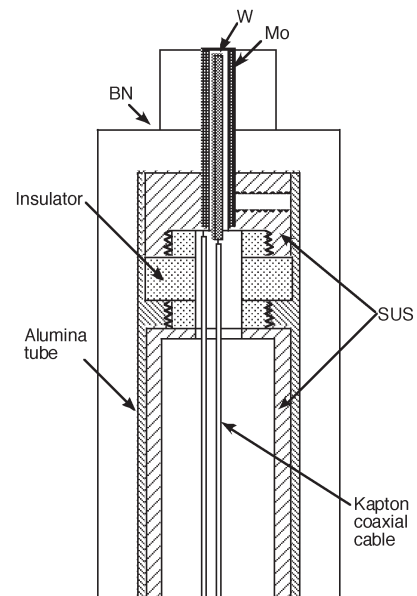


Fig. 1. Schema of redesigned ISP head for measuring the edge and divertor plasma in LHD.

§60. Measurement of Two Dimensional Electron Density Profile in Edge Plasma Region by Thermal Lithium Beam Sheet

Takahashi, Y. (Dep. Energy Eng. Sci., Nagoya Univ.),
Morisaki, T., Toi, K.

Improved understanding and control of edge plasma are very important for tokamaks and helical devices to achieve high confinement mode such as H-mode where edge transport barrier (ETB) is formed, and is partially destroyed by so-called edge localized modes (ELMs). Recently, H-mode is observed also in LHD [1]. The magnetic configuration of LHD is three-dimensional and has helical divertor, where the nested magnetic surfaces are surrounded by complicated ergodic magnetic field layer near the plasma edge [2]. Two dimensional measurement of edge plasma structure is very effective for understanding of edge plasma behavior in this complicated configuration such as LHD. We have developed a new type of lithium beam probing (LiBP) method using thermal beam with a sheet shape, and applied to low density LHD plasmas produced with electron cyclotron waves.

In this newly developed lithium beam probe, metallic lithium in an oven is heated up to about 800 K°, and lithium vapor is conducted to an LHD plasma through three horizontally orifices. This simple technique has successfully produced a thermal sheet beam. The beam is widely spread on the poloidal plane of an LHD plasma but its toroidal divergence is limited to a thin layer, as shown in Fig.1. We could measured two dimensional plasma electron density profile by using this prove system. The energy of the beam is ~0.08 eV, which corresponds to the beam velocity of $1.5 \times 10^3 \text{ ms}^{-1}$. Measurable upper limit of path-integrated electron density is $\sim 3 \times 10^{16} \text{ m}^{-2}$. Two dimensional image of the resonance line Li I (670.8 nm) produced by the sheet beam injection is detected with a CCD camera.

In LHD, the sheet type Li beam was applied to a low density plasma of line averaged density $\langle n_e \rangle \sim 5 \times 10^{17} \text{ m}^{-3}$ produced by low power electron cyclotron waves. For this plasma, the lithium beam is expected to penetrate up to $\sim 200 \text{ mm}$ from the plasma boundary. A typical images of Li I taken by the CCD camera in this plasma is shown in Fig.2. If a beam source is placed far away from a plasma, we can assume that many pencil beams arranged along the major radius of a plasma are injected vertically to the plasma. We can easily derive two dimensional electron density profile from the Li I image as shown in Fig.2.

Figure 3 shows the derived two-dimensional electron density profile from the data in Fig.2, where the profile is overlaid to the magnetic surface. The distortion of the profile near the inner wall may be caused by reflection near the inner wall of the vacuum vessel. This difficulty may be overcome by re-arrangement of the beam optics.

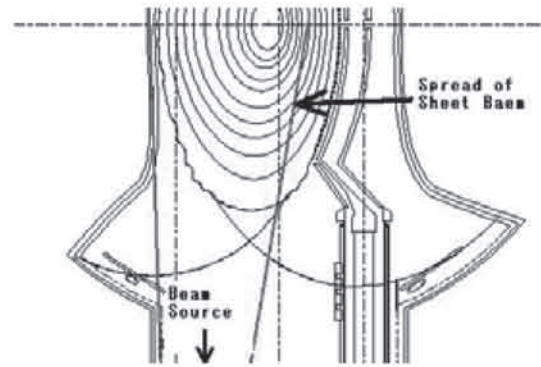


Fig.1 Spread of sheet beam in LHD poloidal plane



Fig.2 Intensity profile of LiI emission.

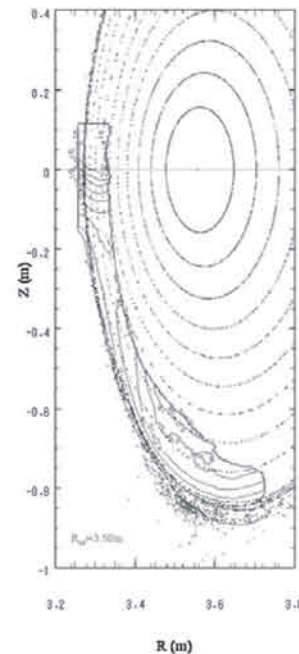


Fig.3 Electron density profile superpose on magnetic surface.

- [1] K. Toi et al., Phys. Plasmas **12**, 020701-1 (2005)
- [2] T. Morisaki et al., J. Nucl. Materials Vol.313-316,548 (2003)

§61. Evaluation of Heating Efficiency of EC Waves for Discharges of LHD 8th Experimental Campaign

Yoshimura, Y., Igami, H., Kubo, S., Shimozuma, T., Kobayashi, S., Ito, S., Mizuno, Y., Takita, Y., Notake, T., Ohkubo, K., Mutoh, T., Sakakibara, S.

Heating efficiency of electron cyclotron (EC) waves on LHD plasmas of 8th experimental campaign is evaluated from a change of time-differentials of plasma stored energy W_p just before and after the termination of EC wave injection as $P_{abs}/P_{inj} = (dW_p/dt_{after} - dW_p/dt_{before})/P_{inj}$. The time-differentials of W_p are obtained by linear fitting of W_p data during 20 ms before and after the termination of EC wave injection. Here, data from discharges in which termination or brief break down of neutral beam power or injection of fueling pellets occur close to the evaluating time are eliminated because those events can cause large error on the evaluation.

In the most of discharges, two 82.7 GHz gyrotrons, two 84 GHz ones and four 168 GHz ones are operated in the same time sequence, respectively. Here, data from discharges in which the gyrotrons of two or three types of frequencies are simultaneously terminated are eliminated so that most of the evaluated efficiency are average of two or four gyrotrons of the same frequencies.

Figure 1 shows the efficiency of 84 GHz gyrotrons, #4 and #5 as functions of magnetic axis position as a representative of parameters of magnetic field configuration. Though the data are widely distributed from 0 to 1, efficiency at R_{ax} larger than 3.8 m show degradation. Averaged value of all the plot points in the figure is 0.46. The same procedure is applied for 82.7 GHz and 168 GHz gyrotrons, and the averaged efficiencies are 0.4 and 0.35, respectively.

Effect of setting of EC wave beam direction is seen in Fig. 2 and Fig. 3. Figure 2 plots the data obtained with a magnetic field setting of $R_{ax}=3.6$ m and $B=2.75$ T, and Fig. 3 of $R_{ax}=3.75$ m and $B=2.64$ T. In those plots, data from “on resonance” heating where the beam aims at the resonant surface closest to the magnetic axis, and “off resonance” heating where the beam aims at other locations are distinguished. In both magnetic configurations, “on resonance” setting shows higher averaged efficiency than “off resonance” case.

Taking averages for data at each magnetic configurations, averaged efficiency is 0.44 for $R_{ax}=3.5$ m and $B=2.83$ T, 0.66 for $R_{ax}=3.55$ m and $B=2.79$ T, 0.52 for $R_{ax}=3.6$ m and $B=2.75$ T, 0.4 for $R_{ax}=3.75$ m and $B=2.64$ T, and 0.63 for $R_{ax}=3.6$ m and $B=1.5$ T, respectively. Except for the data for $R_{ax}=3.5$ m and $B=2.83$ T, it can be said that inward shift of magnetic axis, that is, having resonant surface closer to magnetic axis results in better heating efficiency. Lower electron temperature and density, and prompt helical ripple loss would cause the degradation of heating efficiency in the cases of “off resonance” and outward shift of magnetic axis.

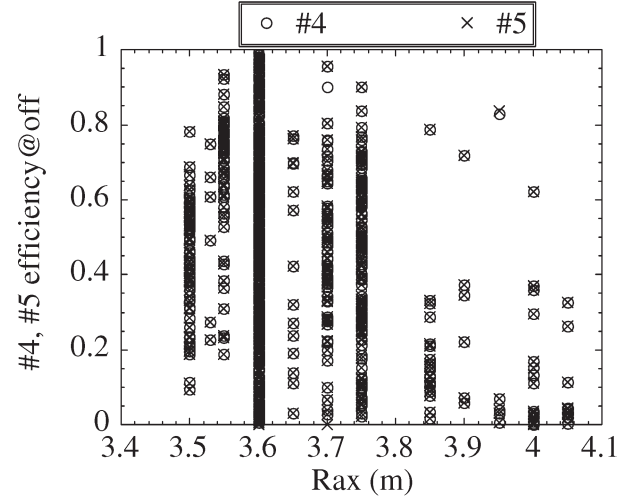


Fig.1 Dependence of heating efficiency of 84 GHz power against magnetic field configuration.

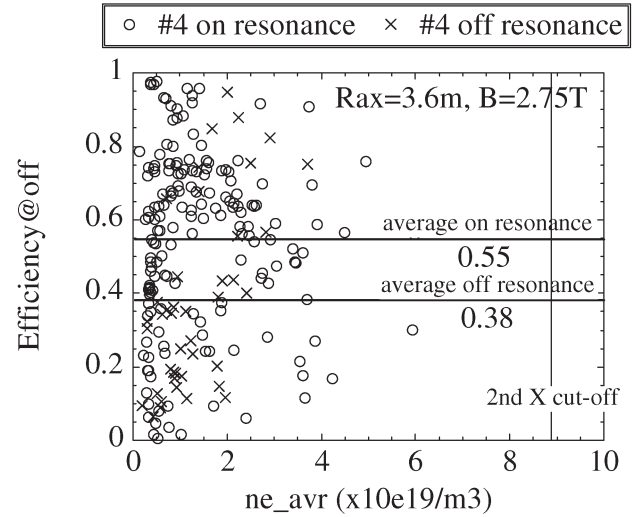


Fig. 2 Dependence of heating efficiency on “on and off resonance” cases for $R_{ax}=3.6$ m and $B=2.75$ T.

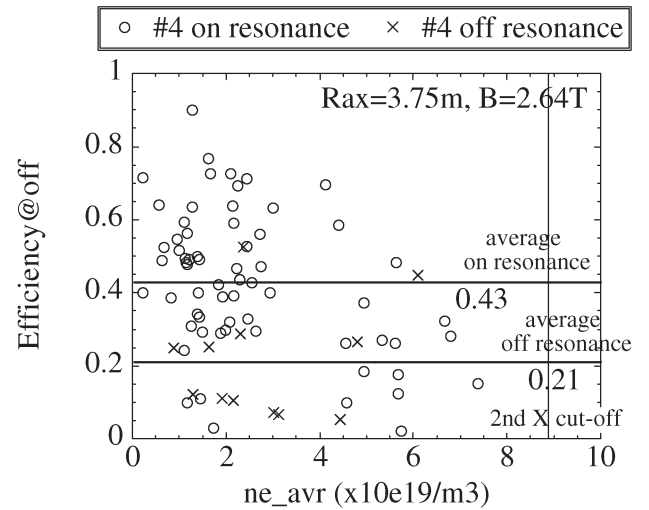


Fig. 2 Dependence of heating efficiency on “on and off resonance” cases for $R_{ax}=3.75$ m and $B=2.64$ m.

§62. Electron Bernstein Heating Experiment in LHD

Igami, H., Notake, T., Inagaki, S., Yoshimura, Y., Shimozuma, T., Kubo, S., Ohkubo, K. (NIFS), Nagasaki, K. (IAE, Kyoto Univ.)

Electron Bernstein wave (EBW) is a kinetic mode propagating in plasmas without the density limit. It is strongly electron cyclotron damped near the Doppler-shifted electron cyclotron resonance (ECR) layer including higher harmonics, even when the electron temperature is low since its group velocity is as low as the electron thermal velocity and the spatial damping rate is large. Therefore electron cyclotron heating (ECH) and current drive (ECCD) by EBW are promising way when the usual way of ECH/ECCD by the normal electromagnetic (EM) waves, such as the ordinary (O) and the extraordinary (X) modes is not available, e.g., when the plasma frequency is higher than the electron cyclotron frequency where EM waves cannot propagate, or when the cyclotron damping is weak due to the low electron temperature. However, since the EBW is an electrostatic wave, which cannot propagate in vacuum, it should be excited at the upper hybrid resonance (UHR) layer via mode conversion process by injection of the EM waves from outside of the plasma. ECH by EBW was tried for the first time in the last 8th experimental campaign of LHD. In a magnetic field configuration of LHD, when a microwave of 84GHz is injected obliquely to the external magnetic field as a quasi-X wave from the mirror antenna installed in the lower port with an appropriate toroidal angle, it can be expected to pass through the “XB access window”, that is, to propagate through the fundamental ECR layer and directly access the UHR layer from the higher field side and excite an EBW as shown in Fig.1 since the fundamental ECR layer is located in the peripheral low temperature region where the absorption of EM waves is weak. Modulated ECE signals were detected when a quasi X wave is injected with 100% power modulation of 34Hz to the target plasma sustained by a neutral beam injection (NBI),

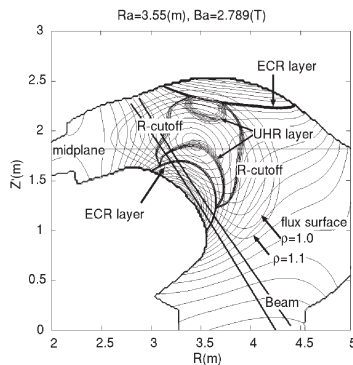


Fig.1. Plasma cross section on the plane created by the incident beam vector and the major radius.

The result of FFT analysis shows a narrow peaked power deposition profile in the lower field side of the ECR layer as shown in Fig. 2-(a) although the incident beam approaches the ECR layer from the high field side at first. On the contrary, when a quasi-O wave is injected in the

same direction the peak of the power deposition profile appears in the higher field side of the ECR layer. When the beam is oriented outward on the same plane in Fig.1, the narrow peak disappears for the case of quasi X wave injection as shown in Fig. 2-(b). When the beam deviates from the “XB access window” and encounters the right-handed cutoff, any distinct peak cannot be seen in both cases of quasi-X and O waves injections as shown in Fig.2-(c).

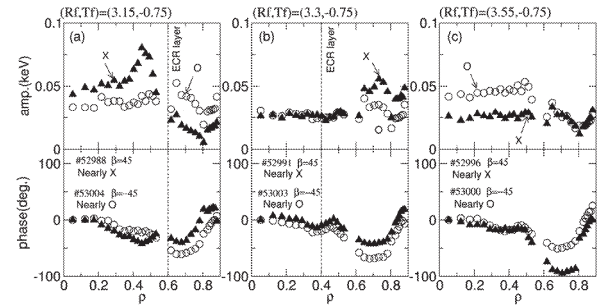


Fig.2. Radial profiles of amplitude and phase, for each case of beam focal point (a): (Rf,Tf)=(3.15m,-0.75m) (b): (Rf,Tf)=(3.3m,-0.75m) (c): (Rf,Tf)=(3.55m,-0.75m)

When the polarization of incident waves is gradually changed from the quasi-X wave to the quasi-O wave in the same incident beam direction as Fig.2-(a). The amplitude of the peak in the lower field side gradually decreases while the amplitude of the peak in the higher field side gradually increases as shown in Fig.3-(a). Different mechanism of heating should exist respectively in each case of the quasi X and the quasi-O wave injections. On the contrary when the polarization of incident wave is gradually changed in the similar way in the same incident beam direction as Fig.2-(b), the height of the peak in the high field side changes but any peak does not appears in the higher field side as shown in Fig.3-(b). These results indicate that ECH by mode converted EBW might take place when a quasi X wave is injected toward the UHR layer from the higher field side.

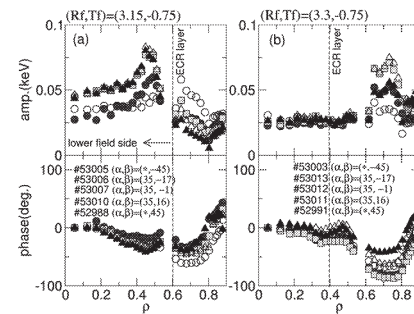


Fig.3 Radial profiles of amplitude and phase for various incident wave polarization from the quasi-X (filled triangle) wave to the quasi-O (open circle) wave, for each case of beam focal point (a): (Rf,Tf)=(3.15m,-0.75m) (b): (Rf,Tf)=(3.3m,-0.75m),

§63. Study on Electron Heating and Current Drive by Electron Bernstein Waves

Nagasaki, K. (IAE, Kyoto Univ.), Igami, H. (NIFS), Murakami, M., Maekawa, T., Tanaka, H., Uchida, M., Shidara, H. (Kyoto Univ.), Isayama, A. (JAERI), Ohkubo, K., Kubo, S., Yanagi, N., Shimozuma, T., Yoshimura, Y., Notake, T. (NIFS), Idei, H. (Kyushu Univ.)

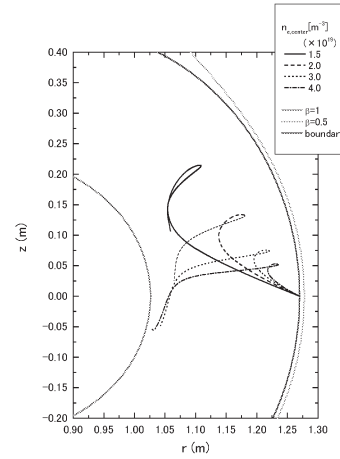
Electron cyclotron heating (ECH) and electron cyclotron current drive (ECCD) provides plasma production, control of electron temperature profile, suppression of MHD instabilities. Electromagnetic waves such as a fundamental O-mode and a second harmonic X-mode are conventionally used for ECH and ECCD because of the high single pass absorption. However, these electromagnetic modes inevitably have upper density limit, so called cut-off, which prevents the waves from accessing the core region at high density plasmas. To overcome this problem and access high density region, use of electrostatic waves is proposed. The electron Bernstein waves (EBW), one of electrostatic waves, can be excited though mode conversion from electromagnetic waves [1][2]. The EBW has advantage of no cut-off density and very high single pass absorption even at low electron temperature. There are three kind of mode conversion method to excite the EBW, that is, O-slow X-B, slow X-B and fast X-B. In this report, we concentrate on the O-slow X-B mode conversion method.

We have developed ray tracing codes for calculating the propagation and power deposition of the EBW in toroidal fusion devices. If we assume that inhomogeneity of plasma parameters is weak and geometrical optics approximation is valid, the ray trajectory of both electromagnetic and electrostatic waves can be obtained by solving the differential ray equations numerically. The dispersion relation of electromagnetic waves is given by using a cold plasma approximation. The numerical method is similar to a ray tracing code for H-1 Helic [3]. The absorption coefficient of electromagnetic waves can be obtained by considering weakly relativistic effect in dielectric tensor. On the other hand, the dispersion relation for the EBW can be given by using a hot plasma approximation.

The EBW is considered to be an important heating and current drive scheme in spherical tori since the conventional electromagnetic waves is not suitable because of low magnetic field strength. Since the toroidal magnetic field is weak and comparable to the poloidal magnetic field compared to conventional tokamaks, the approximation of magnetic field structure using only the toroidal field is not valid as well as helical systems for calculating the power deposition of the EBW heating and current drive. Figure 1 shows the calculation results of the O-X-B mode conversion based on the NSTX model. The injected O-mode is coupled to the slow X-mode at the O-mode cut-off layer, $\omega = \omega_{ce}$, then the slow X-mode is converted into the EBW at the upper hybrid resonance layer, moving toward the core plasma region. The EBW is absorbed at the strongly Doppler-shifted cyclotron resonance. Figure 2 shows the dependence of absorption profile on the electron density. As the core electron density increases, the EBW is

excited earlier, and travels towards to the resonance layer. Although the optimum orientation for O-X mode conversion moves in the outer direction of the plasma with an increase of the electron density, the optimum injection angle changes only slightly, that is, 9 deg and 8 deg in the poloidal and toroidal directions, respectively. The calculation results indicate that the O-X-B heating is realistic in spherical tori, and the absorption profile can be controlled by changing the magnetic field and electron density.

(a)



(b)

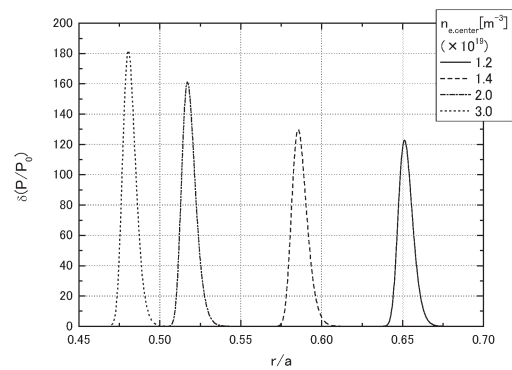


Fig 1 Ray tracing calculation results of O-X-B heating in spherical tori, (a) ray trajectories and (b) power deposition profiles

Reference

- 1) Nagasaki, K., et al., Plasma. Phys. Cont. Fusion 44 (2001) 409
- 2) Mizuuchi, T., et al., J. Plasma Fusion Res. 77 (2001) 484
- 3) Nagasaki, K., et al., J. Phys. Soc. Jpn. 70 (2001) 617-620

§64. Electron Cyclotron Current Drive Experiment in LHD

Notake, T., Shimosuma, T., Kubo, S., Yoshimura, Y., Igami, H., Kobayashi, S., Ito, S., Mizuno, Y., Takita, Y., Mutoh, S., Watanabe, K., Sakakibara, S., Yamaguchi, T.

In recent years, current profile in magnetically confined fusion plasma has been recognized as essential key to improve plasma confinement. Even in helical devices, which don't need plasma current to obtain confinement magnetic field, plasma current control is useful in order to optimize plasma performances through compensation of deleterious currents like bootstrap or modification of iota-profile. Electron cyclotron current drive (ECCD) is an effective tool for current profile shaping because electron cyclotron waves (EC-waves) can penetrate not only plasma periphery region but also core region. In addition, energy absorption region of the EC-waves is highly localized spatially, so we can control plasma current locally in an arbitrary location. The first step to control plasma current profile is to comprehend ECCD physics in large helical device (LHD).

In the 8th experimental campaign of LHD, ECCD was investigated in a magnetic configuration with $R_{ax}=3.55$ m, $B_{ax}=2.789$ Tesla. In order to diagnose change of plasma current due to ECCD, one-turn loop voltage was measured. Figure 1 shows the typical time evolutions of plasma parameters in the experiment. Target plasma was maintained by ICRF heating to suppress the base-current of the target plasma as much as possible, 84GHz EC-waves of 500kW were superposed on it changing incident wave angle with respect to toroidal direction in shot-by-shot basis. In response to incident angle, the polarization was optimized so that incident wave couples to pure O-mode waves in plasma periphery region. In some oblique incident case, one-turn loop voltage was clearly changed and bremsstrahlung emission in the hard X-ray energy range between 10 and 200 keV was detected by using Germanium-semiconductor. Even in the quasi-perpendicular incident case, changes of the one-turn loop voltage were measured but the hard X-ray was hardly detected. These findings may imply that 1) only bootstrap current was enhanced due to the growth of pressure gradient in the quasi-perpendicular incident case, 2) ECCD was accompanied by the creation of suprathermal electrons accelerated asymmetrically in the momentum-space by EC-wave with finite $N_{||}$ in the oblique incident case. (Such suprathermal electrons play an important role in ECCD physics and those kinetic behaviors will be investigated in more detail by using not only the Germanium-detector but ECE radiometer from high field side measurement.) However, the dependences of enhanced current directions shown in Fig.2 and hard X-ray intensities on the incident toroidal angles are not so clear. The bootstrap current and the Ohkawa current induced by trap-detrap mechanism, which never fail to flow in the opposite direction to the EC-current, must influence the experimental results. So the ECCD physics must be carefully considered including these effects.

The crucial quantities in studies of ECCD physics are the wave absorption location, the ECCD efficiency, and the EC-current density profile and so on. At the present stage, we only can estimate the ECCD efficiency. The efficiency, defined as

$$\zeta_{cd} = I_{cd} R \bar{n}_e / P_{ec} [AW^{-1}m^{-2}],$$

is often used for comparison between ECCD efficiency obtained in different machines. Using parameters in the experiment, we obtain $\zeta_{cd} \approx 0.08$ in the maximum under the assumption that L/R time-constant of LHD-plasma is about 30 seconds. The ECCD efficiency is lower than that of many tokamaks yet. Effects of the Ohkawa current due to trapped electrons in helical ripples and radial diffusions of particle and energy might reduce the efficiency in LHD.

More experiments are needed to optimize the efficiency and location of driven current.

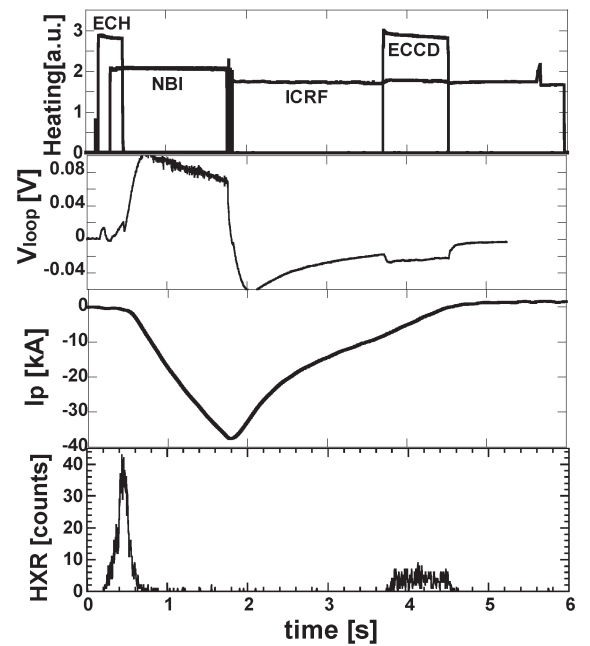


Fig. 1. Typical time evolutions of plasma parameters in the experiment.

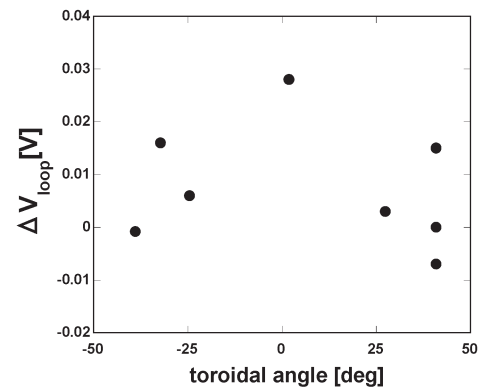


Fig. 2. Dependence of ΔV_{loop} for toroidal angles of incident waves.

§65. Investigation of Polarization and Deposition of EC Wave Beams

Shimozuma, T., Notake, T., Kubo, S., Yoshimura, Y., Igami, H., Itoh, S., Kobayashi, S., Mizuno, Y., Takita, Y., Ohkubo, K.

It is required to adjust an injection polarization for optimizing absorption efficiency of Electron Cyclotron (EC) waves. In the 8th cycle experiments, we investigated the polarization dependences for three lines 168GHz #2, 84GHz #4 and 82.7GHz #11, which were remaining lines in the previous experimental campaign.

The polarization condition of the incident EC wave can be defined by two angles, α and β shown in Fig. 1. The linear polarization corresponds to $\beta = 0$ and α defines the angle between the reference axis of the system, which is the toroidal direction in this case, and the principal axis of the polarization ellipse.

The experiment was performed in the magnetic configuration of $R_{ax}=3.5\text{m}$ and $B=2.829\text{T}$. The target plasmas were produced by the other EC power sources except the line under test. The plasma electron density and temperature were $\bar{n}_e = 0.5 \times 10^{19}\text{m}^{-3}$ and $T_{e0} \sim 1.5 - 2.0 \text{ keV}$. The injection power of 168GHz lines under test was modulated with the frequency of 40Hz. The measured electron temperature by ECE was Fourier analyzed. Figure 2 shows the FFT amplitude dependences on the polarization angle of a) α and b) β . The maximum amplitude was obtained at about $\alpha = -45 \text{ deg.}$, which corresponded to a perpendicularly linear-polarized wave (X-mode) at the plasma boundary. The β angle dependence of the amplitude was shifted to the minus value from the expected one ($\beta = 0$). This is because the angle between the wave vector and the magnetic lines of force a little differed from 90 deg.

The power deposition position was investigated by the same manner. Since the modulation frequency on the EC power was not so high (40Hz, this is a hardware limitation), the profile of the FFT amplitude does not represent a deposition profile, but it includes heat diffusion process. However the minimum of the FFT phase indicates the deposition center. Figure 3 shows the FFT amplitude and phase profiles for 168GHz #2 line for the antenna focal point of $R_{foc}=3.53\text{m}$ and $R_{foc}=3.48\text{m}$. In the figure the calculated deposition profiles by the ray-tracing code were also plotted. The deposition center well agreed with the minimum of the FFT phase profile, though the amplitude profiles considerably differs in both cases. In Fig. 3 a), there is another phase minimum around $\rho = 0.4$. This suggests the existence of a magnetic island around here, which requires more investigation in relation to the heat diffusion process.

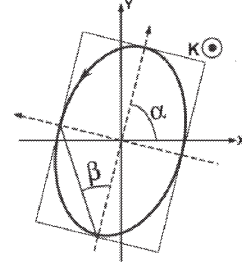


Fig. 1: Polarization ellipse: The polarization state is defined by the angle of α and β . The x-axis corresponds to the toroidal direction in this case

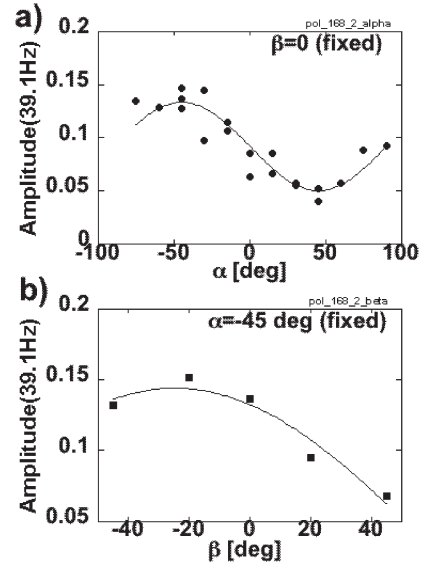


Fig. 2: Fourier amplitude of electron temperature at $\rho = 0.1$ is plotted as a function of a) α and b) β . The line under test was 168GHz #2 line.

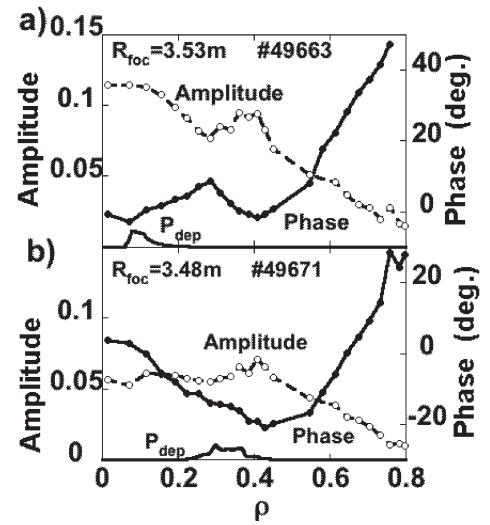


Fig. 3: FFT amplitude and phase profiles are plotted for the antenna focal point settings of a) $R_{foc}=3.53\text{m}$ and b) $R_{foc}=3.48\text{m}$ with calculated absorption power profiles

§66. Development of High Beta Plasma Production by Using Higher Harmonic Fast Wave in ICRF

Takase, Y., Kasahara, H., Taniguchi, T., Kamada, Y., Ishii, N., Oosako, T., Tojo, H. (Frontier Sci. and Sci., U. Tokyo)

Fukuyama, A. (Eng., Kyoto U.)

Watari, T., Mutoh, T., Kumazawa, R., Seki, T., Saito, K., Takeuchi, N.

The purpose of this collaborative research is to develop a radiofrequency heating method that can be used at low magnetic fields for high beta plasma research on LHD. In particular, electron heating by Landau damping and transit time damping of the fast wave at relatively high harmonics of the ion cyclotron frequency can be explored using the existing ICRF transmitters which can provide power in the frequency range of 30 to 80 MHz. The fast wave in this frequency range is called the high-harmonic fast wave (HHFW).

Development of heating scenarios is carried out on both LHD at NIFS and the TST-2 spherical tokamak at the University of Tokyo, which share the same objective of studying high beta plasmas. On LHD, existing ICRF loop antennas are used. On TST-2, two transmitters in the frequency range of 10 to 30 MHz will be used. TST-2 has the advantages of ample experimental time and flexibility with short turn-around time for hardware modifications.

In LHD, HHFW experiments were performed using the 38.4 MHz ICRF system. In order to operate in the HHFW regime, Helium plasmas were used at lower magnetic fields, 1.5 T and 1 T. Plasma was initiated by ECH and NBI. Since the ion cyclotron frequency for helium at 1.5 T is 11.4 MHz, the fast wave frequency is around the third harmonic. The fast wave propagates in the density range exceeding the right-hand (R) cut-off density. At high harmonics of ion cyclotron frequency, ion cyclotron

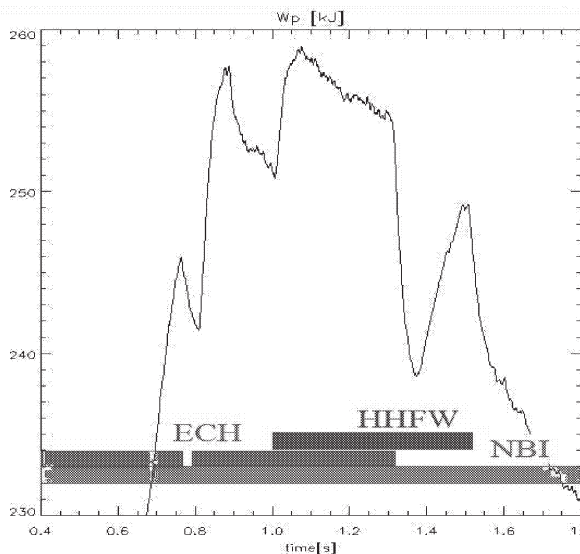


Fig. 1. Evolution of the stored energy (SN50490).

damping becomes weaker, and electron damping by Landau damping and transit time damping is expected to become dominant. The harmonic number is not very high in the present experiment, absorption by energetic ions may not be negligible in neutral beam heated plasmas. The formation of energetic ions is observed experimentally in LHD, but it is not known how much power is absorbed by ions.

The time evolution of the plasma stored energy for shot number 50490 is shown in Fig. 1. In this discharge, plasma was formed by NB (2.5 MW) and EC (1.6 MW). Application of FW (1.2 MW) into this discharge raised the central electron temperature from about 2.5 keV to 3 keV, and the stored energy from about 250 kJ to nearly 260 kJ at an electron density of $3 \times 10^{19} \text{ m}^{-3}$. There was no change in the ion temperature. EC injection was terminated first, then FW injection was terminated 0.2 s later. At this time, the electron density did not change at 2 keV, but the ion temperature decreased from 1.475 keV to 1.45 keV. This result indicates that it is possible to obtain more electron heating than ion heating near the plasma center provided the electron temperature is sufficiently high (greater than 2.5 keV in this case), even in the presence of energetic ions from NB injection.

When ECH works effectively, the central electron density is pumped out by localized electron heating. The rate of decrease of electron density is smaller when HHFW heating was applied. This result suggests that HHFW is absorbed when the central electron temperature and beta are high enough and that parallel heating of electrons by HHFW reduces electron density pump out caused by perpendicular electron heating by ECH.

TST-2 has been moved to the Kashiwa Campus of the University of Tokyo, and is ready to start electron heating experiments using the HHFW in FY2005.

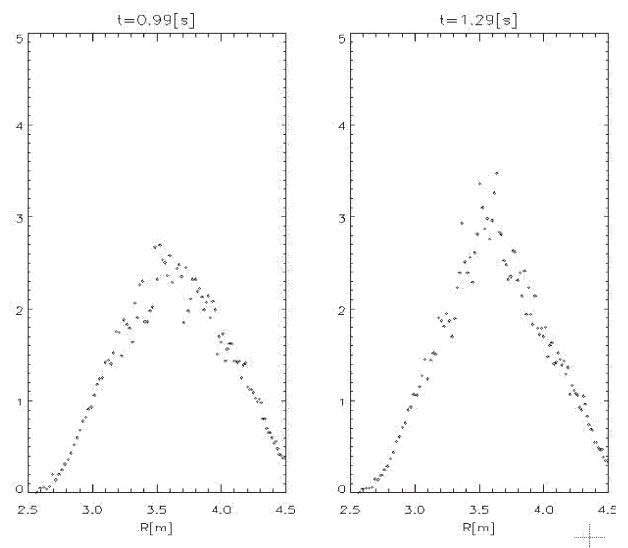


Fig. 2. Electron temperature profiles at 0.99 s (NB 2.5MW + EC 1.6MW) and 1.29s (NB 2.5MW + EC 1.6MW + FW 1.2MW).

§67. Dependence of Magnetic Axis on Neutral Beam Driven Current in LHD

Nagaoka, K., Watanabe, K.Y.

Recently, the control of plasma current and/or iota profile is recognized to be important for confinement improvement not only in tokamaks but also in stellarators. The basic properties of neutral beam driven current have been experimentally investigated in LHD. In this report, the results of neutral beam current drive experiments in 8th campaign of LHD, in particular, the dependence of magnetic axis on the neutral beam driven current are presented.

Three neutral beam injectors has been tangentially installed in LHD, and long pulse beam with the duration of about 5 second has been injected for the neutral beam current drive experiments. The hydrogen gas puffing has been used to keep the plasma density constant during the discharge, and the saturation of plasma current has been evaluated. The plasma current includes two components; one is bootstrap current and the other neutral beam driven current. In order to evaluate the latter, discharges with co- and ctr-injection NBI have been compared. The magnetic axis dependence of neutral beam driven current per NBI deposition power in the same averaged density of $0.4 \times 10^{19} \text{m}^{-3}$ is shown in Fig.1. The neutral beam driven current at $R_{ax}=3.6\text{m}$ is the largest, of which magnetic configuration is almost explained the electron temperature on the magnetic axis, which is also shown in Fig. 1.

In general, neutral beam driven current is given by

$$I_{NB} = \frac{I_b V_b \tau_s}{2\pi R} \left(1 - \frac{1}{Z_{eff}} G \right) = I_{NB0} \left(1 - \frac{1}{Z_{eff}} G \right)$$

where I_b , V_b , τ_s , Z_{eff} and G are neutral beam current injected by NBI, beam velocity, slowing down time of injected ions, effective charged number of bulk plasma ions and geometrical factor, respectively. In LHD case, slowing down time of beam ions is dominated by collisions with electrons, so it depends on electron temperature and density ($T_e^{3/2}/n_e$). For simplicity, electron temperature on the magnetic axis and line averaged density obtained experimentally have been used to evaluate I_{NB0} . The current drive efficiency (I_{NB}/I_{NB0}) is considered to depend on Z_{eff} and G , and is shown in Fig. 2. Here, it is assumed that Z_{eff} does not depend on the magnetic axis. The geometrical factor approximates ratio of toroidally circulating electron ℓ and depends on the magnetic configuration. The larger ratio of circulating electron, the smaller neutral beam driven current, because

circulating electrons produce retarding current against the beam current. The volume averaged ratio of circulating electron $\langle \ell \rangle$ is also shown in Fig.2. The increase of neutral beam current drive efficiency in outward shifted magnetic configuration case ($R_{ax}= 3.9\text{m}, 4.0\text{m}$) can not be understood by ratio of circulating electron, while it in inward shifted magnetic configuration case ($R_{ax}= 3.5\text{m}, 3.6\text{m}$) can be qualitatively understood by the decrease of the ratio of circulating electrons.

In this analysis, the profile of plasma parameters, for example, plasma density, electron temperature, and plasma current, can not be included, which is left for a future study.

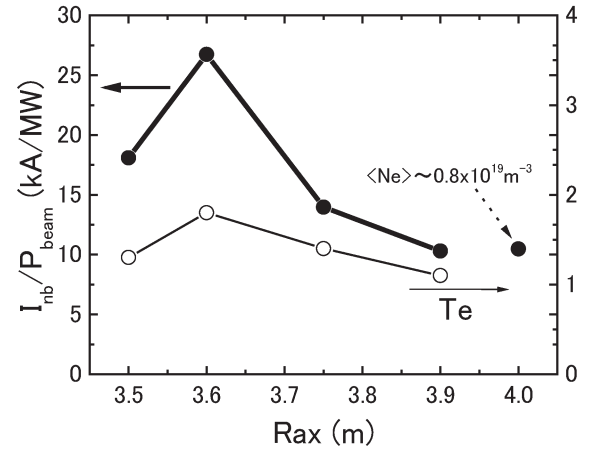


Fig.1 The magnetic axis dependence of experimentally obtained neutral beam driven current. The closed circles represent the neutral beam driven current per beam power in the same plasma density ($0.4 \times 10^{19} \text{m}^{-3}$), and the open circles electron temperature on the magnetic axis.

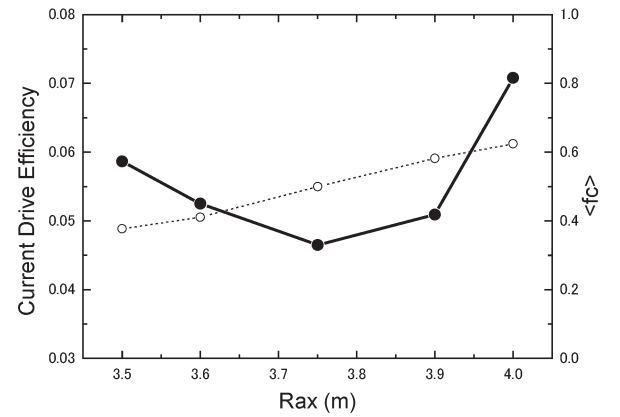


Fig.2 The magnetic axis dependence of current drive efficiency, I_{NB}/I_{NB0} (closed circles), and the ratio of toroidally circulating electrons (open circles).

§68. Neutral Beam Attenuation Measurement in the High Temperature Plasma

Ikeda, K.

It is important to understand the deposition of high-energy neutral beam in order to produce the high temperature plasma with the efficiently heating into the core plasma region. Negative ion based neutral beam injectors (NBI) with a high energy of 180keV have been installed tangentially in Large Helical Device (LHD)¹⁾. We have achieved totally 13 MW hydrogen neutral beam injection²⁾.

To study the beam deposition inside the plasma along the injection beam axis, we applied the beam emission spectroscopy³⁾ for measurement of the neutral beam attenuation. The measurement system consists of twenty optical fibers, a 25cm spectrometer with a grating of 1800 grooves/mm and an intensified charge-coupled device detector. Two observation sight lines with a different beam penetration length are arranged on both the upstream side and the downstream side of the beam injection axis at the 3rd beam line system. We have clearly observed beam emission Ha spectra separated from the background Ha emissions due to the Doppler effect.

High-Z discharges with argon or neon gas puffing are used for high ion temperature experiments in LHD⁴⁾. We have achieved a high ion temperature of 13.5keV±2keV with Ar discharge by totally 10.5MW hydrogen NBI heating at the 8th LHD experimental campaign. The power of 3.4 MW neutral beams with the energy of 167 keV is injected from the 3rd beam line.

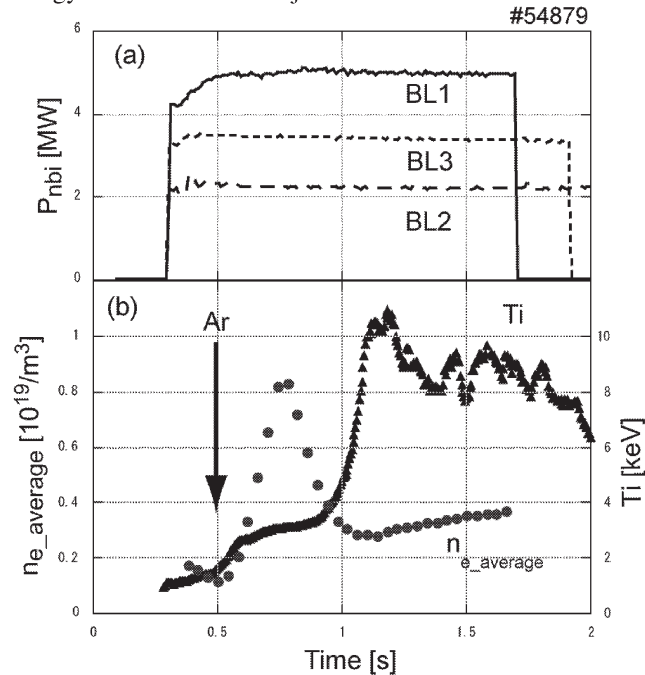


Fig. 1. Neutral beams are injected from the three beam lines (a). The electron density builds up by the argon gas puffing, and the ion temperature increases to over 10keV (b).

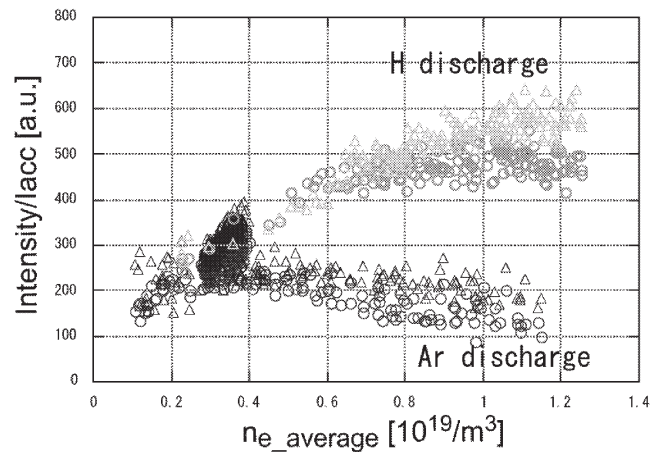


Fig. 2. Normalized beam emission intensity of both the hydrogen and argon discharge.

In this discharge, the electron density rises up by the Ar gas puffing as shown in Fig. 1. The ion temperature rapidly increases as the electron density decreases below $0.5 \times 10^{19} \text{ m}^{-3}$. We observed the decreasing of the beam emission intensity due to the strong beam attenuation by Ar particles as shown Fig. 2. Characteristic of the beam emission of the argon discharge is different from the characteristic of the hydrogen discharge. On the other hand, the beam emission intensity gradually increases as the electron density increases after the maximum ion temperature. The characteristic of the beam emission changes around the electron density of $0.3\text{--}0.4 \times 10^{19} \text{ m}^{-3}$. Figure 3 shows the measured beam emission intensities and the reproduced beam emissions from the density dependence for the argon and the hydrogen discharge. It is indicated that the cross-section of the beam attenuation decreases due to the increase of the hydrogen component with the beam injection. We have observed the change of the hydrogen concentration during the high-Z discharge by the beam emission spectroscopy.

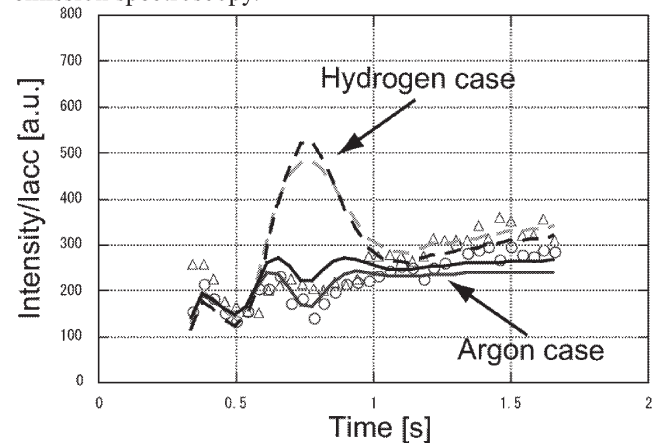


Fig. 3. Solid and dashed lines are the reproduced beam emission intensity of the argon and the hydrogen discharge, respectively.

- 1) O. Kaneko, et al. Nucl. Fusion **43** 692 (2003)
- 2) Y. Takeiri, et al., 20th IAEA Vilamoura, 2004, EX/P4-11
- 3) W. Mandl, et al., Plasma Phys. Cont. Fusion **35** 1373 (1993)
- 4) Y. Takeiri, et al., 30th EPS St. Petersburg, 2003, P-2.171

§69. Doppler Shift Spectra of H α Lines from Negative Ion Based Neutral Beams

Oka, Y., Grisham, L. (PPPL), Umeda, N. (JAERI), Ikeda, K., Takeiri, Y., Tsumori, K., Honda, A. (JAERI), Ikeda, Y. (JAERI), Kaneko, O., Nagaoka, K., Osakabe, M., Yamamoto, T. (JAERI), Asano, E., Kondo, T., Sato, M., Shibuya, M.

The velocity spectra of the negative ion based neutral beams with doppler-shifted H α spectroscopy, as well as the effectiveness of the spectroscopy¹⁾ has been studied / collaborated. In the 8th experimental cycle, the spectra from beam-line-1, BL-1 in addition to BL-2 and BL-3 have been newly measured to study the differences probably reflected by the ion source design and the operation conditions.

An internal mirror (Fig.1) was mounted inside the vacuum vessel of BL-1 to keep the same angle of line of sight as those in BL-2 and BL-3. We conducted systematic observations of the velocity distribution profiles in standard LHD-NBI injection (Fig.2), the spectra over the course of 70 ~ 128s long-pulsed beams with reduced power, and the behavior of negative ion beam stripping in the accelerator. Almost all of the transmitted beam power (Fig.2) was found to be at approximately the full acceleration energy (170keV). A very low energy peak due to beam particles stripped in the extractor gap (at ~8keV) is observed. It was observed that the similar spectrum profiles were repeatedly reproduced throughout the day, while the operating condition for the neutral beam was kept constant with a high power level of ~4.5MW/2.

H- ion uniformity (Fig.3) in an LHD-ion source along the long direction of ~125cm was deduced by the full energy component coming from five vertically arrayed grid sectors¹⁾. It was found that the H- ion current is fairly uniform, and that there is still the prospect of increasing the H- current throughput by about 15% at the optimum perveance, if the uniformity is improved.

For long beam pulses, the magnitude of the full energy peak gradually declined as the beam pulse duration increased. When conductively cooled plasma grid was used, the spectra did not change for a longer time compared to those with a standard (i.e., a thermally isolated-) plasma grid.

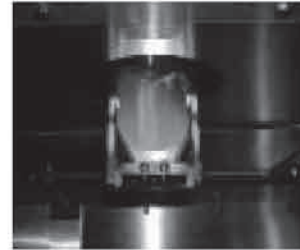


Fig. 1 Mirror system in-side the vaccum vessel.

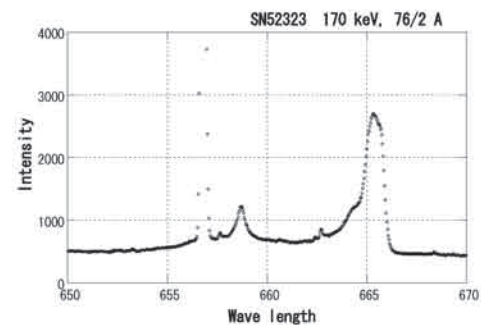


Fig.2 Spectrum in beam line-1 from negative ion based neutral beam.

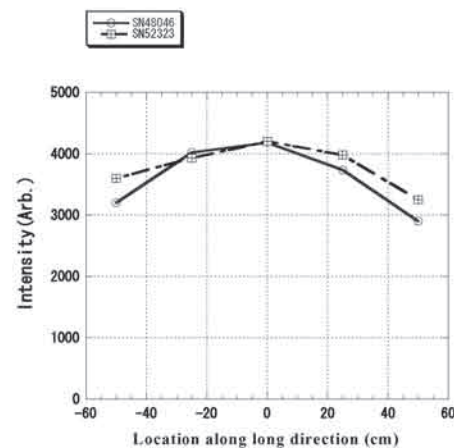


Fig.3 H- ion distribution along long direction in LHD H- ion source.

Reference

- 1) Y. Oka et al., Rev. Sci. Instrum. **75**, (2004)1803.

§70. Study of the Loss Cone Feature Using Neutral Particle Analyzer in Large Helical Device

Ozaki, T.

It is very important to control the trapped particle by the helical ripple to realize the helical type plasma fusion device. High-energy particles generated by the ion cyclotron resonance heating and the neutral beam injection (NBI) heating have a wide pitch angle distribution by the initial heating mechanism and the atomic process in plasma. The particle with large pitch angle has a complicated orbit, sometimes the loss orbit at certain energy and pitch angle, although the particle with large parallel component against magnetic field line is well confined along the magnetic surface. The loss region in the phase space, so call a loss cone, can be clarified by measuring the pitch angle distribution of the high-energy particle. To this purpose, the lost ion has been directly measured near the plasma. Here the charge exchange neutral particle between the high-energy ion and the background neutral is measured to obtain the pitch angle of the high-energy ion in the plasma. In the large helical device (LHD), we have used two different neutral particle analyzers, the time-of-flight (TOF-NPA)¹⁾ and the silicon detector (SD-NPA)²⁾ neutral particle analyzer. NBI heating in long discharge is suitable for this purpose in LHD. Three NBIs are tangentially injected to minimize the particle number toward the loss cone region in LHD. The energy of the high-energy ion supplied from NBI decreases by the plasma electron. The pitch angle scattering is occurred by the plasma ion at the energy of the several times of the electron temperature. Therefore we can easily compare the experimental pitch angle distribution with the simulation result, which is obtained by considering the initial pitch angle distribution and the atomic process. The pitch angle distribution from 40 to 100 degrees can be obtained by horizontal scanning the TOF-NPA during the long discharge over 100 seconds sustained by the NBI#2 (co-injection) at the magnetic axis (R_{ax}) of 3.6 m. The trapped particle by the helical ripple can be clearly observed around the pitch angle of 90 degrees as shown in Fig.1. The loss cone feature is agreed with the result. It is interesting to investigate the dependence of R_{ax} of the loss cone feature. However it is not suitable to use the scanning of TOF-NPA during NBI plasma discharge although it can provide the precise structure of the loss cone because it is very difficult to sustain the long discharge at different magnetic axis. We use SD-NPA, which has ability of 6 different pitch angle measurement at R_{ax} = 3.5, 3.6 and 3.75 m. The much trapped particle can be observed at R_{ax} =3.5 m because the large helical

ripple can be expected at inner magnetic axis as shown in Fig.2.. The electric field is often utilized to minimize the loss cone in the helical system. The electric field can be obtained by the charge exchange recombination spectroscopy in LHD. The effect of the electric field against the loss cone feature will be described.

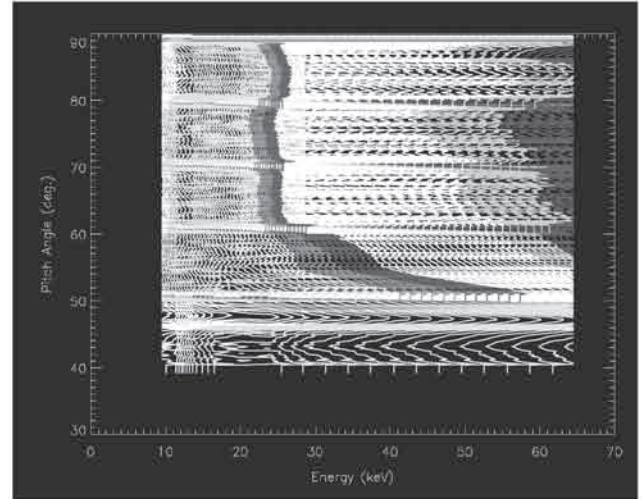


Fig.1 Pitch angle distribution

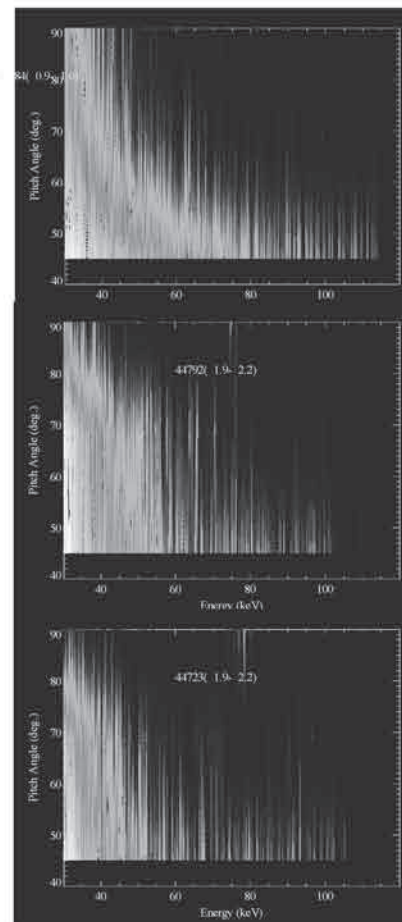


Fig.2 Pitch angle distribution in different magnetic axis

(a) R_{ax} =3.5m,
 B =2.951T

(b) R_{ax} =3.6m,
 B =2.75T

(c) R_{ax} =3.75m,
 B =2.64T

1) T.Ozaki, S.Murakami et al., Rev. of Sci. Instrum., Vol.74, No.3 (2003) 1878-1882.

2) J.F.Lyon, P.R.Goncharov et al., Rev. of Sci. Instrum., Vol. 74, No.3 (2003) 1873-1877.

§71. Local Measurements of Neutral Particle Spectra on LHD by PCX Method

Goncharov, P.R., Ozaki, T.

Production, confinement and thermalization of high-energy particles are the fundamental issues in fusion plasma ion kinetics. The ion distribution function $f_i(E, \mathbf{v}, t)$ and its evolution under the ion cyclotron heating and neutral beam injection are studied by energy resolved charge exchange neutral flux measurements. For helical systems, such as LHD, local diagnostics are required due to the complex 3D magnetic field. To achieve the locality of measurements an active diagnostic method referred to as pellet charge exchange (PCX) [1, 2] has been applied successfully on LHD in the 8th experimental cycle.

To interpret these measurements quantitatively, consider the experiment schematically shown in Fig. 1. The atomic energy analyzer looking along the pellet trajectory observes the toroidally elongated ablation cloud while it crosses the plasma column. Suppose that the distance between the working aperture and the cloud is L , the working aperture area is S_a and the area of the cloud visible to the analyzer is S . The area S depends on the viewing cone opening $d\Omega$, the transverse size and the length of the ablation cloud. The local flux of ions with energies in the range $(E, E+dE)$ equals $n_i v_i f_i(E, \mathbf{r}) dE$ [$s^{-1}cm^{-2}$], where v_i is the ion velocity corresponding to the kinetic energy E . The proportion of the incident ions neutralized by the pellet ablation cloud is determined by the factor $F(E)$. The emission rate of atoms with energies in the same range from the unit area of the cloud is $F(E)n_i v_i f_i(E, \mathbf{r}) dE$. If slowing down and scattering of ions in the cloud are insignificant and the cloud is small compared to the linear scale of $f_i(E, \mathbf{r})$ spatial variation, then the total emission rate of atoms with energy E from the area S is given by

$$\gamma(E, t) dE = S F(E) n_i v_i f_i(E, \mathbf{r}(t)) dE.$$

The experimentally measured quantity that reflects the local ion distribution function at $\mathbf{r}(t)$ is

$$dN/dEdt = \gamma(E, t) S_a / (4\pi L^2) \exp\left(-\int_0^{L(t)} \frac{d\zeta}{\lambda_{mfp}(E, \zeta)}\right).$$

The factor $S_a/(4\pi L^2)$ appears due to the measurement geometry; the exponential factor describes the attenuation of the atomic flux in the plasma between the pellet cloud and the neutral particle analyzer; λ_{mfp} is the mean free path with respect to ionization.

Pneumatically accelerated polystyrene $(-C_8H_8)_n$ balls are injected transversally; typical $D_{pel} = 500-900 \mu m$, $v_{pel} = 300-400$ m/s. The angle between the compact neutral particle analyzer (CNPA) [3] sight line and the pellet injection axis is 2° horizontally and 1° vertically. The values of the local $v_{||}/v$ for the observable particles are in the range -0.25 to $+0.25$ along the average pellet flight.

The neutral fraction $F(E)$ can be calculated from the ionization-recombination balance in the cloud. The cloud

density information is required. The difficulties with polystyrene pellets are the lack of experimental cross-section data and the information about the dominating ion charge states in the cloud during the pellet flight. CNPA can be used in a combination with the upgraded cryogenic pellet injection system. Hydrogen ice pellets are preferable compared to polymer ones because the charge exchange (CX) cross-sections and the pellet ablation cloud composition are well-known. On the other hand, the energy range will be limited in that case due to the CX cross-section drop at high energies. From this viewpoint, Li pellets are preferable since the cross-section data and a more reliable ablation cloud model are available.

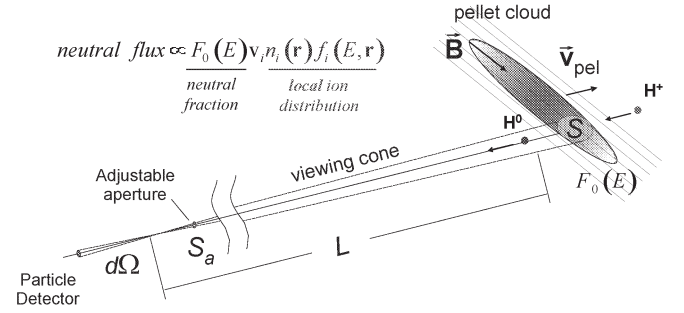


Fig. 1. Local active neutral particle flux measurements by charge exchange on a pellet ablation cloud (PCX)

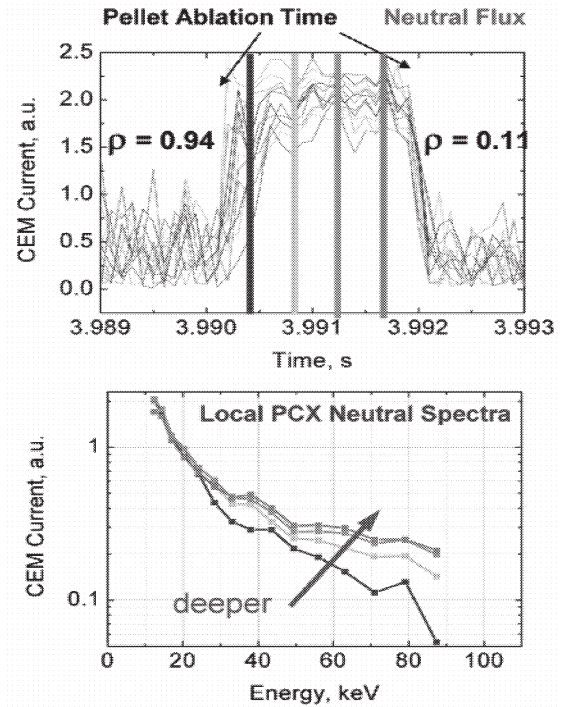


Fig. 2. Time-resolved neutral particle flux in 16 energy channels and resulting radially resolved spectra from ICRF heated plasma $n_e = 0.4 \cdot 10^{13} cm^{-3}$, $R_{ax} = 3.6$ m, $\beta = 0.1\%$.

References

- 1) Goncharov, P.R., et al., Rev. Sci. Instrum. **74** (2003), 1869
- 2) Goncharov, P.R., et al., Rev. Sci. Instrum. **75** (2004), 3613
- 3) Chernyshev F.V., et al., Instr. and Exp. Tech., **47** (2004) 214

§72. Observation of Clump and Hole Pair Creations with TAE-bursts on LHD

Osakabe, M., Yamamoto, S. (Osaka Univ.),
Takeiri, Y., Toi, K.

Observation of clump-formation with toroidal Alfvén Eigen(TAE) mode is recently reported in the energetic particle spectra on LHD[1]. The clumps are observed in tangential energetic neutral spectra and their energy ranges are located between 100keV and 170keV. The energy of the clump decays in time after the TAE-burst disappeared. The clump formation in the spectra is considered as the results of the enhanced radial transport of energetic particles which resonate with TAE-bursts and the decay is the results of the energy slowing-down of these radially transported energetic particles.

In addition to a clump formation, the formation of a hole with the burst is experimentally observed on LHD. Figure 1 shows an typical example of the clump and hole pair creation with a TAE-burst. In Fig.1(c), the tangential NPA-spectra are shown and the flux intensity is expressed by the brightness of the figure. At $t=0.576[s]$, an creation of clump, which correspond to an increase of the NPA flux, is observed with a TAE-burst and the energy of the clump decays in time as is indicated by a solid lines in the figure. Simultaneously, a creation of a hole, which corresponds to a decrease of the flux, is also observed. The energy of the hole also decays in time as is indicated by the dashed lines in the figure. The decay times of the clump and hole are 6[ms] and 8.3[ms], respectively. The location where the hole and the clump are created can be evaluate by comparing the decay time with the energy slowing down time of hydrogen particles. Figure 2 shows the slowing down time distribution on the NPA sight line. From this figure the location of the clump is identified to $\langle r/a \rangle_{\text{orbit}} \lesssim 1$,

while that of hole is to $\langle r/a \rangle_{\text{orbit}} \gtrsim 0.9$. This result clearly shows the radial transport of energetic particles by TAE-activities.

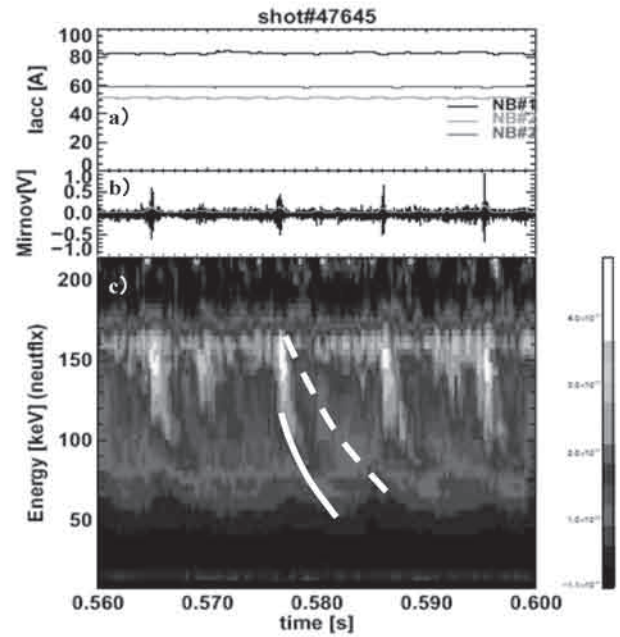


Fig.1 Typical examples of tangential NPA spectra where clump and hole pair creation with TAE-burst were observed. (a)NB signal, (b)Mirnov-coil signal, and (c)tangential NPA spectra are shown.

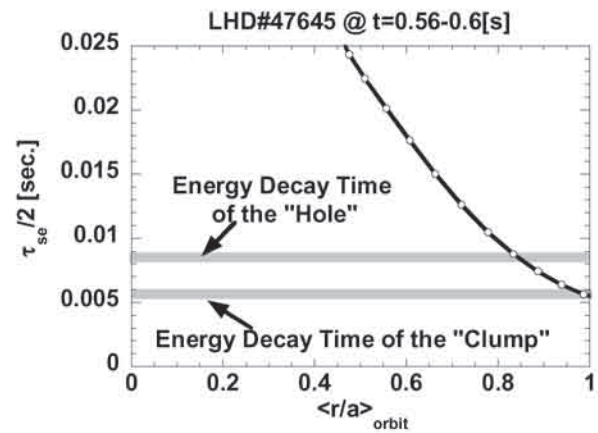


Fig.2 Energy slowing-down time of hydrogen particles which are circulating on the NPA sight line.

Reference

- [1] Osakabe, M., et.al., Proceedings of 20th IAEA Fusion Energy Conference, Vilamoura, Portugal, 1-6 November 2004

§73. Excitation of High Frequency Fluctuations and Their Effects on High Energy Ions in LHD

Higaki, H., Ichimura, M. (Univ. Tsukuba)
Kumazawa, R., Watari, T., Mutoh, T., Seki, T., Saito, K.

When a magnetized plasma has a temperature anisotropy, various fluctuations (or waves) can be excited spontaneously. For examples, Alfvén ion cyclotron (AIC) waves are observed when high energy ions are confined in a mirror plasma and ion cyclotron emissions (ICE) can be observed in Tokamaks associated with the injection of high energy neutral beams (NB). Alfvén eigen modes (AEs) are also observed with NB injection in many fusion oriented devices including LHD¹⁾. The production of high energy ions with ICH can also excite these fluctuations. Investigating these fluctuations is important because they affect the fusion reaction rate and as a result the neutron yield degrades.

Here, magnetic probes (MP) are employed to observe these high frequency fluctuations excited with NB injection or high power ICH injection in LHD. Signals from MPs were recorded by an oscilloscope (250Ms/s) with long memories in a sequence mode. So far, fluctuations were observed in NB sustained plasmas with various magnetic field strength ranging from 1.0 to 2.8 T. An example is shown in Fig.1 when $B = 2.75$ T. Shown in Fig.1 (a) is the plasma density as a function of time. A feature of the observed fluctuations is that they are observed at relatively low density ($< 10^{19} \text{ m}^{-3}$). In Fig.1 (b), the time evolution of FFT power spectrum obtained from a MP signal is plotted. The darker tone has the higher power. An example of FFT power spectrum is plotted in Fig.1 (c) at $t = 0.92$ sec. It is clearly seen that fluctuations are excited much stronger than the noise level.

Accumulating these fluctuation signals at various field strengths B and plasma densities n_e , it was found that the frequencies of observed fluctuations are proportional to B and $n_e^{-1/2}$ as shown in Fig.1 (d). Since the Alfvén velocity V_A is given by

$$V_A = 2\pi f_A / k = B / (\mu n_e m)^{1/2} \quad (1)$$

and the observed fluctuations are discretely excited, it is suggested that these fluctuations are the AEs. Here, k is the unknown wave number, μ is the permeability and m denotes the ion mass. As far as the AEs in LHD are concerned, it was found that the AEs can be excited at much higher frequency and higher magnetic field than reported before.

Since AEs are related with the behavior of high energy ions in plasmas, the details should be investigated more in conjunction with other high frequency fluctuations.

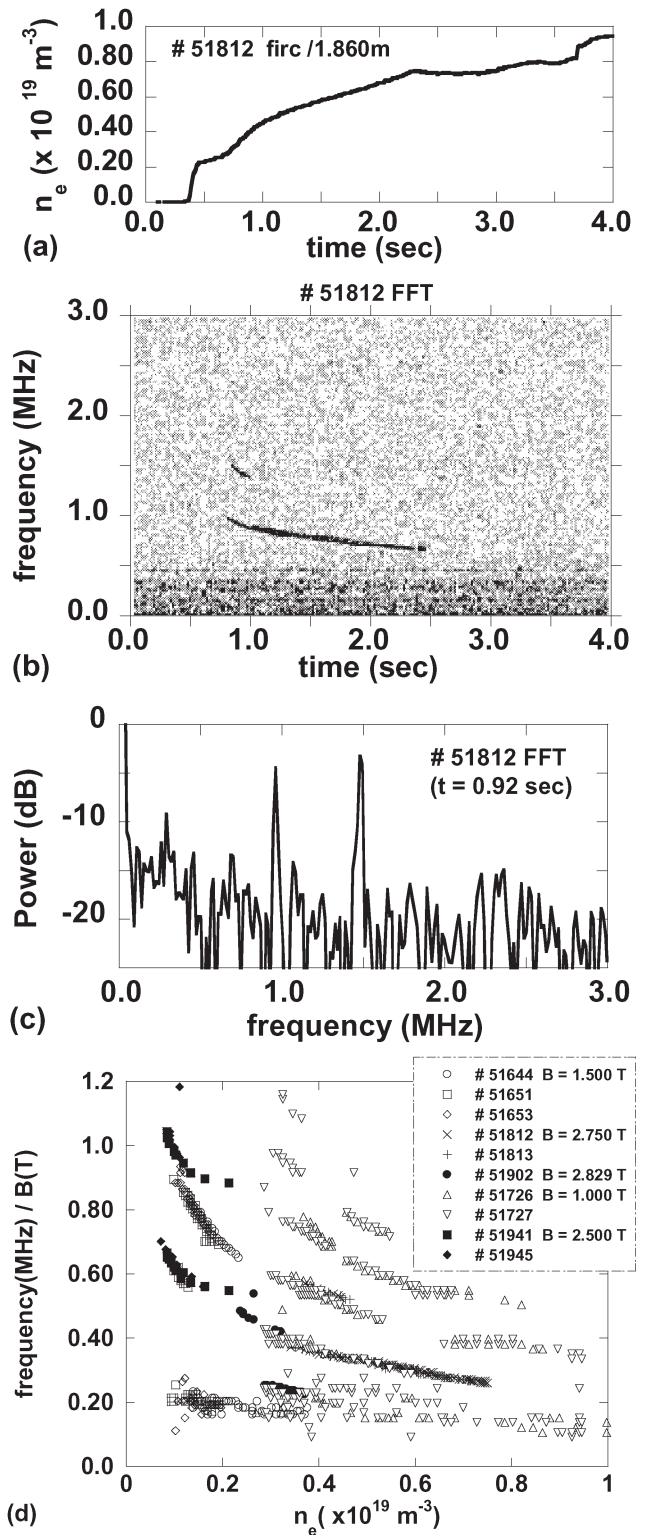


Fig. 1. (a) A plasma density as a function of time. (b) A time evolution of FFT power spectrum. (c) An example of FFT power spectrum at $t = 0.92$ sec. (d) Frequencies of the fluctuations normalized by the field strength are plotted as a function of plasma density.

Reference

- 1) S.Yamamoto, K.Toi, N.Nakajima, et.al., Phys. Rev. Lett. **91** (2003) 245001

\$74. Erosion of Plasma Facing Materials by Charge Exchange Neutrals

Ono, K., Miyamoto, M. (Dept. Mater. Sci., Shimane Univ.)

Tokitani, M., Yoshida, N. (RIAM, Kyushu Univ.)

Masuzaki, S., Ashikawa, N.

PSI (Plasma Surface Interaction) is one of the serious problems related to not only control of plasma but also deterioration of materials. Authors have reported that the surface modifications of PFM (Plasma Facing Material) in plasma confinement devices such as TRIAM-1M and LHD has large impacts on plasma density controlling(). On the other hand, charge exchange (CX) neutrals create radiation damages in the subsurface region of vessel walls and greatly contribute to the surface modification. In the present work, therefore, microscopic damage in metals exposed to hydrogen plasma in LHD was examined and the impact of CX neutrals on surface modification was quantitatively evaluated.

To examine the surface modification caused by CX-neutrals, a materials probe experiment was carried out. Pre-thinned vacuum-annealed disks of 3 mm ϕ made of SUS316L, W and Mo were used as specimens. These specimens mounted on the material probe system were placed at the similar position of the first wall surface through the 4.5 low port (4.5L), and exposed to long discharges for about 50 sec. (Shot No. 50834~50853, hydrogen plasma). Typical plasma parameters were: $T_i \sim 1.5$ keV, $n_e \sim 3 \times 10^{19} \text{ m}^{-3}$. The temperature of the specimen holder during the discharges stayed almost constant at room temperature. After exposing the discharges, the microstructure of specimens was observed by means of transmission electron microscopy (TEM). In addition, irradiation experiments were carried out with hydrogen ions of 2 keV.

Fig. 1 shows dark field images of the microstructure in the W specimen and the SUS316L specimen. The radiation-induced dislocation loops with white contrast were formed in these specimens. In general, radiation induced secondary defects are formed as aggregates of point defects produced by knock-on processes. Since the threshold energies of hydrogen for displacement damage in Mo and SUS316 are about 2.0 keV and 0.36 keV, respectively, these defects indicate the existence of high energy incident particles. By comparison with material damages of the 2 keV hydrogen ion irradiation experiments, the fluence of energetic CX neutrals was roughly estimated to be of order 10^{21} atoms/m². On the other hand, any defect was not observed in the specimens placed in deep holes directing to several directions. This means that the fluence of energetic CX neutrals was less than 10^{22} atoms/m² because the solid angle open to the plasma is rather small. From these results, the mean flux of CX-neutrals with energy high enough to cause radiation damage was estimated to be about 2×10^{19} atoms/m²s.

The depth distribution of the dislocation loops formed in SUS316L is plotted in Fig. 2. As shown in this

figure, damages are distributed to rather a deep range, which also indicates the existence of high energy incident particles. Fig. 3 shows the damage distribution calculated by TRIM91-code for H⁺ of several energy (a) and the energy with Maxwellian distribution at 1.5 keV (b). Since the calculated depth distribution give close agreement with the damage distribution in SUS316L, this widespread depth distribution would be attributed to the high energy components of CX-neutrals with 6-8 keV.

In this materials probe experiment, the incident direction dependence of CX-neutrals was not estimated because any defect was not observed in the specimens placed in deep holes directing to several directions. The detail evaluation of the effects of CX-neutrals on modifications of PFM would be done by increasing the exposure time.

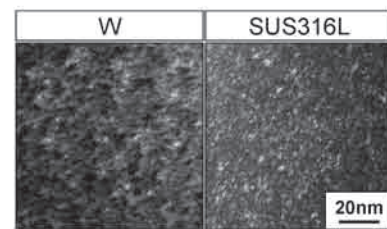


Fig. 1. Dark field images of the microstructures in W and SUS316L.

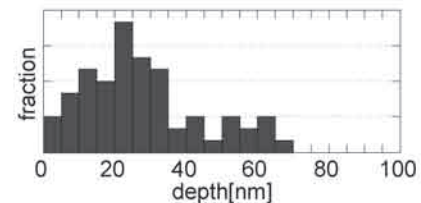


Fig. 2. Depth distribution of dislocation loops in SUS316L.

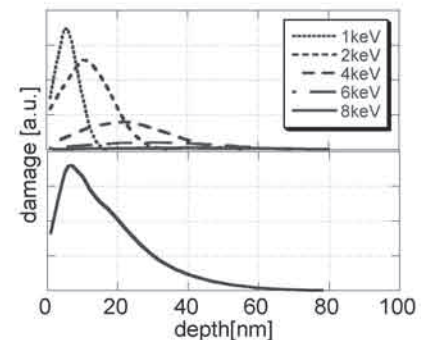


Fig. 3. Calculated depth distribution of damage in SUS316L with TRIM-code. (a) Energy dependence and (b) damage by particles of incident energy with Maxwellian distribution at $T_i = 1.5$ keV.

Reference

- 1) M. Miyamoto et al., J. Nucl. Mater., 313-316 (2003) 82
- 2) M. Miyamoto et al., J. Nucl. Mater., 329-333 (2004) 742
- 3) M. Miyamoto et al., J. Nucl. Mater., 337-339 (2005) 436

\$75. Study on Erosion Mechanism of Materials by High Flux Divertor Leg Plasma

Yoshida, N., Tokunaga, T., Iwakiri, H., Tokitani, M.
(RIAM, Kyushu Univ.)
Masuzaki, S., Ashikawa, N., Komori, A.

i) Background and Objectives

It has been understood that hydrogen atoms injected in metals are not trapped deeply and thus blisters caused by hydrogen bubbles are scarcely formed. However, it was found in the preliminary experiment performed last year that very dense fine cavities and small blisters were formed in W specimens exposed to hydrogen divertor plasma of LHD. This unexpected result indicates that erosion by blistering and resulting plasma contamination is a new concern of the W divertor. This year, therefore, irradiation experiments with divertor plasma have been carried out to understand the mechanism of blistering under the exposure to high flux hydrogen plasma.

ii) Experimental Procedures

A W specimen (35x8x1mm) fixed on the probe head of the material transfer system equipped to the 4.5L port of LHD was moved to the divertor-leg position and was exposed to a long pulse hydrogen plasma (shot No.52730) for 30 seconds. Retention of hydrogen and deposition of impurities were measured by elastic recoil detection (ERD) and Rutherford backscattering spectroscopy (RBS), respectively.

iii) Results and Discussion

Very clear foot-print (local melting) due to high flux heat load at the divertor-leg was formed on the W specimens (See Fig.1). In addition, the probe head made of SS316L was also melted along the foot print and its droplets deposited on the W specimen nearby. Thickness of the deposit (mainly Fe) measured along line A in Fig.1 is plotted in Fig.2. In the areas beside the foot-print (10-30mm and 35-45mm), deposited Fe and substrate (W) are alloyed. It is clear that the surface temperature of this area exceeds 1500°C significantly. Beyond the alloyed areas (<10mm, >45mm), thickness of the deposit decreases drastically. Hydrogen retention in the W specimen is also plotted in Fig.2. It increases with increasing distance from the foot-print and the areal density of hydrogen exceeds $3 \times 10^{20} \text{H/m}^2$ at 70mm. The flux of hydrogen particles is highest at the foot-print (about $1 \times 10^{22} \text{H/m}^2 \text{s}$) but at the same time temperature increase is highest there. Difference of temperature change during the plasma discharge must be the main reason why the hydrogen retention is lower at and near the foot-print but higher at the periphery where the heat flux is lower.

Fig.3 shows an atomic force microscopic (AFM) image showing highly magnified surface morphology at 60mm, where the hydrogen retention is about $2 \times 10^{20} \text{H/m}^2$ and almost no impurity deposition. It is clear that a large number

of fine blisters (200nm in diameter, 20nm in height) are formed homogeneously and many of them have been exfoliated. High retention of hydrogen indicates that the cavities are not voids but highly pressurized hydrogen bubbles which result in blistering. The energy of hydrogen particles is only about 100eV, which is much lower than the threshold energy for the displacement damage in W. Details of the mechanism of bubble formation under such low energy hydrogen irradiation is still an open question.

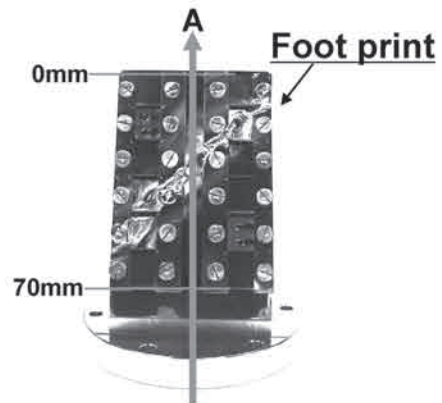


Fig.1 Probe head after exposure to the plasma

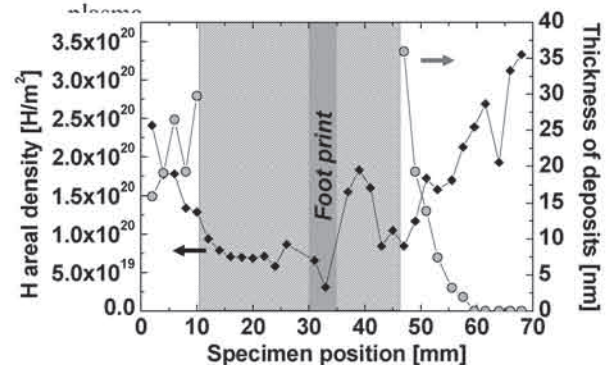


Fig.2 Hydrogen retention and thickness of deposits measured along line A in Fig.1.

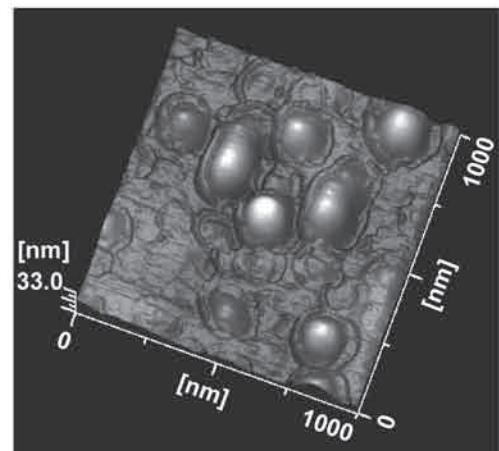


Fig.3 AFM image at around 60mm.

§76. Study on Generation Mechanism of Particles in LHD

Shiratani, M., Watanabe, Y., Koga, K., Kitaura, Y.
(Dept. Electronics, Kyushu Univ.)
Ashikawa, N., Nishimura, K.

Formation of dust particles due to interaction between hydrogen plasma and carbon wall has attracted a great deal of attention in the fusion research field. 1) Carbon dust particles pose two potential problems: those remained in a fusion device are dangerous, as they can contain a large amount of tritium; their existence in the device may also lead to deterioration of plasma confinement.

At present, the following three candidates have been proposed as the erosion mechanism of carbon wall due to the plasma interaction: [1] physical sputtering by incident hydrogen ions, [2] chemical-etching due to H atoms and, [3] embrittlement of the carbon wall surface and/or layer redeposited on it. While these processes have been believed to lead to formation of carbon dust particles, little is known about their formation mechanism.

Kyushu University group of us have already reported on the experimental results of dust particles formation due to the interaction between ECR hydrogen plasma and carbon wall. 2, 3) Here, we will describe the results regarding characterization of dust particles collected from LHD.

Size and shape of dust particles trapped were observed with TEM and SEM. Figures 1 (a) and (b) show the size distributions at the sampling location near the NBI injection port (1-O) and the location between the ports 1-O and 10-O. The particles are classified into two size groups: one is the small particle of size below $1\ \mu\text{m}$, the other is the large particles of size above $1\ \mu\text{m}$. The small particles exist in all locations, whereas the large ones do only in 6 locations out of 16 ones. The shape of small particles is nearly spherical suggesting their formation in gas phase, while that of the large ones is irregular. The size distribution of small ones is quite similar to those of particles formed due to interaction between hydrogen plasma and carbon wall. 2, 3) The large particles have a rather flat size distribution, which is significantly different from the log normal one in ref. 1). Such flat distribution may be explained by that the large particles are mainly flakes originated from peeling off deposits on the reactor wall.

The dust particles collected in LHD have been analyzed with SEM, TEM, and EDX. They have been found to be composed of small and large size groups. The particles in small size group are of spherical shape in the size range of $5\ \text{nm}$ - $1\ \mu\text{m}$, and their major composition is C. Those in large size group are of irregular shape in the size range above $1\ \mu\text{m}$, and their major compositions are Fe, Mo and Cr. The features suggest that the small dust particles are formed in gas phase, whereas the large ones are caused by peeling off from deposits on the reactor wall.

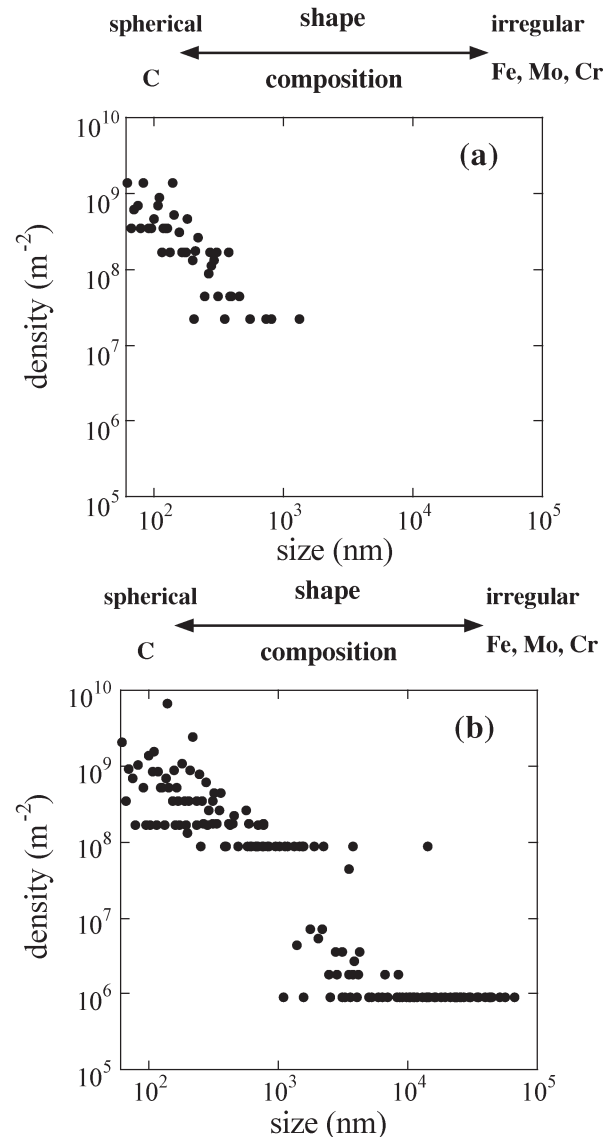


Fig. 1. Size distributions at two locations: (a) near NBI injection port (1-O); (b) between port 1-O and 10-O.

References

- 1) Sharpe, J. P., et al., J. Nucl. Matter., **313-316**, (2003) 455.
- 2) Koga, K., et al., Proc. ESCAMPIG16/ICRP5, (2002) I-173.
- 3) Koga, K., IEEE Trans. Plasma Science, **32**, (2004) 405.

§77. Initial Wall Conditioning in LHD

Nishimura, K., Ashikawa, N., Masuzaki, S.

To reduce impurity release from the chamber wall, wall conditioning is essential. Baking at 95°C, electron cyclotron resonance discharge cleaning, glow discharge cleaning (GDC), titanium gettering and boronization have been attempted for wall conditioning. Using these conditioning techniques, the partial pressures of the oxidized gases, such as H₂O, CO and CO₂, were reduced gradually and the plasma operational regime enlarged. Especially, boronization (boron coating) using diborane (B₂H₆), which was started in FY2001 (5th experimental campaign), is effective to reduce the oxidized gases.^{1,2)} At the beginning of the boronization, one nozzle was used to supply diborane, two more nozzles were added in FY2002 (6th experimental campaign), and flow-control valves were installed to adjust the flow rate of the diborane in FY2004 (8th experimental campaign). The thickness of 30 – 50 nm and the coated area of 60 % of the vacuum vessel were estimated. After boronization, the oxygen concentration was reduced to less than 1 % of the level found in pre-boronization discharges of similar density and input power. The carbon levels were reduced to 50 – 70 % of the pre-boronization levels. As a result, radiation loss decreased about 30 – 50 % and the operational density limit increased.²⁾

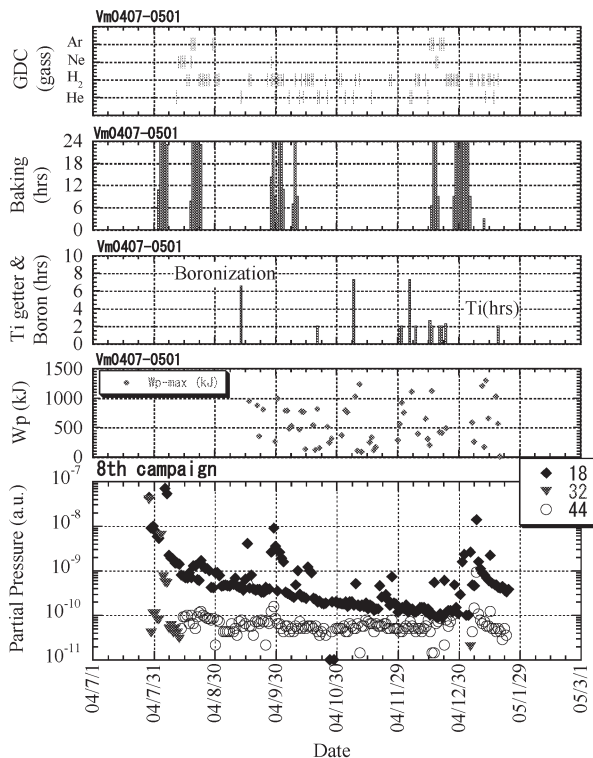


Fig. 1 Evolutions of wall conditioning in the 8th campaign.

Although He-GDC was a popular wall conditioning method, the formation of bubbles on material surfaces by He discharges was reported. To avoid the formation of bubbles and to remove oxidized surface materials quickly, we tried GDC with heavier gases such as neon and argon as an initial wall conditioning at the startup phase of experiments.²⁾ Figure 1 shows the evolutions of wall conditioning in the 8th campaign. Bars in top figure shows operations of GDC with various working gas (ordinate). The second and third figures show operating time of baking, Titanium gettering and boronization. Fourth figure shows the maximum plasma stored energy obtained in a day. Bottom figure shows evolution of impurities related to the oxygen (H₂O, O₂ and CO₂) measure with Q-mass analyzer. These data was obtained at 8:30am, before the start of plasma experiments. O₂ decreased soon to the lower level than the detection level and CO₂ kept low level through the campaign. H₂O decrease gradually through the campaign. Effect of the boronization to the plasmas was well observed in the oxygen light intensity. Figure 2 shows the normalized oxygen light intensity (OV) with the line averaged electron density ($\langle n_e \rangle$) during the plasma experiments in the 7th and 8th campaigns. Intensity of OV in the 8th campaign is lower than 50% of that in the 7th campaign. This effect lasted at the end of the campaign. So boronization at the startup phase as the initial wall conditioning method is effective to reduce impurities related oxygen and its effect lasts during the campaign.

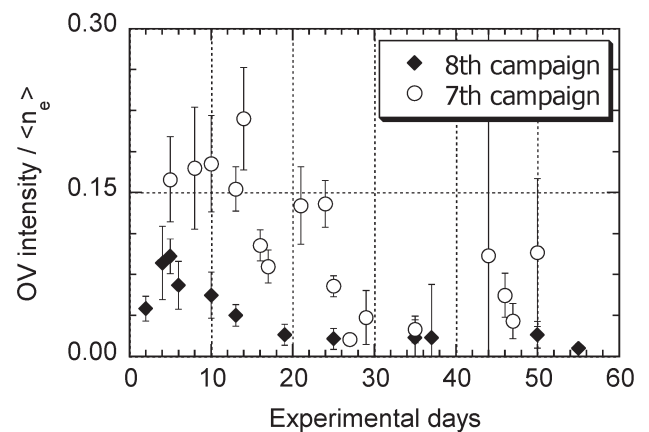


Fig. 2 Comparison of oxygen behavior between 7th and 8th experimental campaigns.

References

- 1) Nishimura, K. et al.: J. Plasma Fus. Res. 79 (2003) 1216.
- 2) Nishimura, K. et al.: J. Nucl. Mater.

§78. The Study of Hydrogen Retention and Existence States in Boron Thin Film Exposed to Hydrogen Glow Discharge

Okuno, K., Yoshikawa, A., Miyauchi, H., Oyaidzu, M. (Fac. of Sci., Shizuoka Univ.)
Oya, Y. (Radioisotope Center, Univ. of Tokyo)
Ashikawa, N., Nishimura, K., Sagara, A.

1) Introduction

Boronization as wall conditioning has been performed on a lot of fusion test devices and remarkable improvement on the plasma performance has been achieved. By gettering oxygen remained in vacuum vessel into boron thin film deposited on plasma facing wall, high plasma performance can be achieved. On the other hand, it is anticipated that energetic tritium, deuterium, helium and neutron are implanted from D-T plasma into the boron coating film. Therefore, hydrogen isotope behavior including tritium in the boron thin film should be elucidated from a viewpoint of fusion safety. To simulate actual hydrogen isotope behavior on the first wall in fusion reactors, the boron thin film boronized in LHD was prepared and compared to that prepared by PCVD at Shizuoka University. The chemical composition and depth profile of hydrogen isotopes were studied by X-ray Photoelectron Spectroscopy (XPS) and Secondary Ion Mass Spectroscopy (SIMS).

2) Experiment

Two kinds of boron thin films were prepared as follows. One was deposited on a Si substrate by a glow discharge using B_2H_6 and thereafter this sample was exposed on hydrogen glow discharge in LHD at NIFS, which named NIFS sample. The other was done in PCVD device using $B_{10}H_{14}$ at Shizuoka University, named Shizuoka Sample. The chemical composition of these samples was analyzed by XPS (ULVAC-PHI ESCA 1600 System) at Shizuoka University and depth profile was evaluated by SIMS (ULVAC-PHI ADEPT 1010 Dynamic SIMS System) at Japan Atomic Energy Research Institute (JAERI). $AlK\alpha$ (1486.6 eV) was used as a X-ray source for XPS analysis. For SIMS measurement, 5 keV Cs^+ ion was used as a primary beam and the sputtered ions were observed by quadrupole mass spectrometer. The beam current was set to be 100 nA. The beam size was about $32\ \mu m$ and the rastering area was set to be $400 \times 400\ \mu m^2$. The sputtered depth was estimated by a Dektak profilometer.

3) Results and Discussion

From XPS analysis, it was found that the boron concentration was reached up to 75% for the NIFS sample and 96% for the Shizuoka sample. Around 9% of carbon and 12% of oxygen and small amount of nitrogen was also contained for the NIFS samples. Figs. 1 and 2 show the depth profiles for the NIFS and Shizuoka samples. It was found that the thickness of boron for NIFS sample was

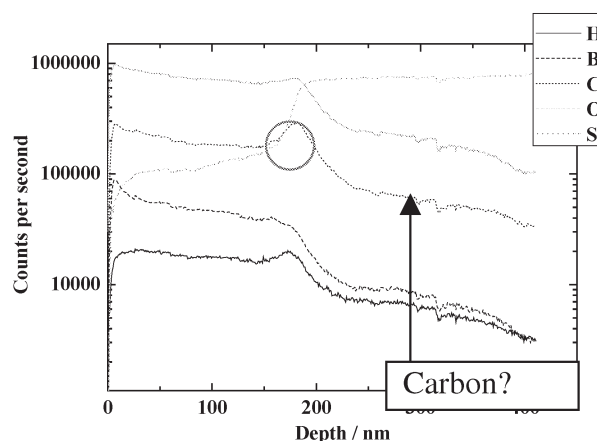


Fig. 1 SIMS results for the NIFS sample

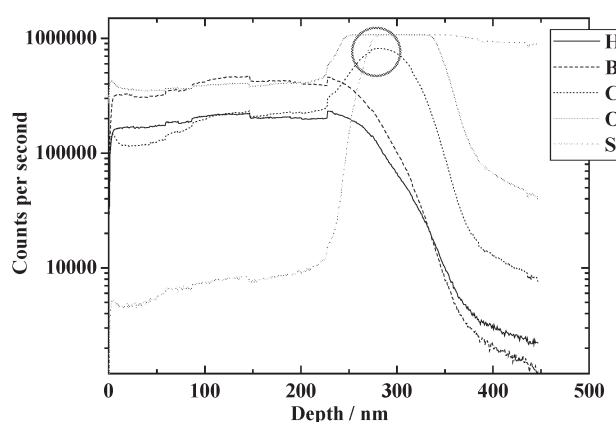


Fig. 2 SIMS results for the Shizuoka sample

about 200 nm and that for the Shizuoka sample, 250 nm. For the NIFS sample, large amount of oxygen was trapped by boron and the profile of oxygen was almost coincident with that of boron. It was also noted that the more impurities were contained for the NIFS sample compared to the Shizuoka sample, indicating that the some impurities, which will come from the first wall materials and residual impurities in vacuum vessel, would be contained into the boron thin film. These facts indicate that the impurities effects will make a large influence on the hydrogen isotope retention in the boron thin film.

4) Conclusion

To evaluate hydrogen isotope behaviors in the boron thin film, two kinds of samples, the NIFS sample and the Shizuoka sample, were prepared and chemical compositions and depth profiles were studied by means of XPS and SIMS. The experimental results show oxygen was trapped by boron for the NIFS sample and the more impurities were contained for the NIFS sample compared to the Shizuoka sample. These facts indicate that these impurities make a large influence on the hydrogen isotope retention in the boron thin film. Further study will be required for understanding detailed mechanism.

\$79. The Effect of Helium Glow Discharge on Boronized Surface in LHD

Kizu, K., Yagyu, J., Ishimoto, Y., Nakano, T.,
Tsuzuki, K., Miya, N. (JAERI)
Ashikawa, N., Nishimura, K., Sagara, A.

The purpose of this study is acquiring basic data for designing effective surface conditioning system for next nuclear fusion experimental devices [1]. It is generally difficult for a nuclear fusion experimental device with superconducting coils to rise wall temperature during coil operation larger than 200 °C indicating that the thermal desorption of hydrogen isotopes after boronization is not expected. Therefore, the glow discharge cleaning using the noble gas like helium (He), neon and argon plays an important role. On the other hand, glow discharge leads surface sputtering which is the source of impurity migration in a vacuum vessel. For these reasons, investigation of an effect of He glow discharge (He-GDC) on the boronized sample was performed in LHD during the 8th campaign.

Two kinds of samples were prepared for this work. One is samples boronized in LHD during the 7th campaign, and the other is samples boronized in Radiochemistry Research Laboratory in Shizuoka University. Sample materials were VPS-W on CFC and F82H which is low activation ferritic steel. These samples were exposed to He-GDC in 8th campaign for three hours or six hours. Then, deposited and sputtered impurities element and change of quantity of accumulated hydrogen by exposed He-GDC duration were investigated.

Chemical composition of samples boronized in Shizuoka University was analyzed by X-ray photoelectron spectroscopy (XPS) and secondary ion mass spectrometry

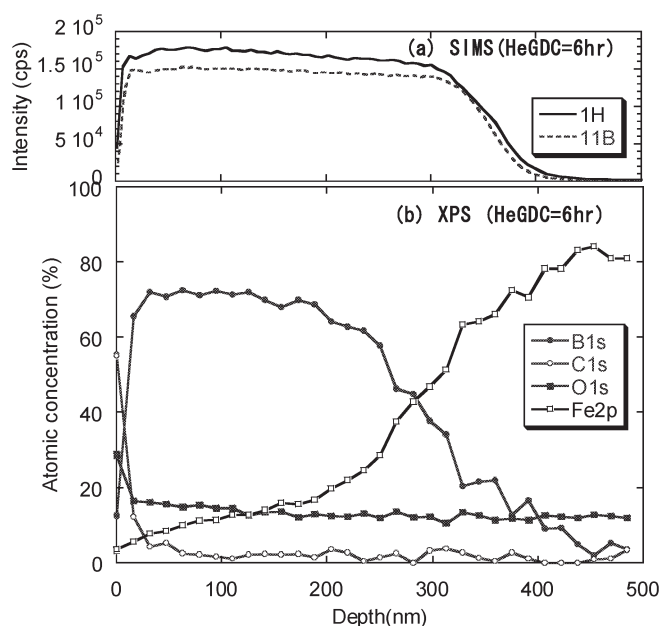


Fig. 1. Depth profile of H, B, C, O and Fe in sample which was boronized in Shizuoka Univ. and was exposed 6hr He-GDC in LHD.

(SIMS). The thickness of boron coating was about 300 nm. Figure 1 shows the analysis result of the F82H sample which was exposed for He-GDC of LHD for six hours. The boron membrane before He-GDC contained oxygen (O) of 12% in constant through the membrane. Carbon (C) was accumulated on the surface. Hydrogen (H) was retained uniformly in a thickness direction of the boron membrane indicating that H deposited on the sample surface with boron (B) during boronization process by decaborane (B₁₀H₁₄). The wear of a boron membrane by He-GDC for six hours was not clear.

In order to clarify the effect of He-GDC, average atomic ratio of C and O against matrix atoms (iron (Fe) and B) near surface (depth 0-40nm) were derived. The relation between the average atomic ratio and He-GDC duration for samples boronized in Shizuoka University is shown in Fig. 2. The decreasing of C and the increasing of O by He-GDC were observed. Increase of O suggests that O atoms sputtered within He-GDC from the wall which was not coated by boron in a LHD vacuum vessel was deposited to the boron coated surface. In addition, decreasing of C indicates that the quantity of C sputtered from sample by He-GDC was larger than that quantity of deposited on the sample that was sputtered at another surface (ex. divertor region). A tendency of increase of oxygen and decrease of carbon was also confirmed by the SIMS analysis of samples boronized during the 7th campaign in LHD. These results indicate that the wall conditioning advances by He-GDC not only during boronization process but also after boronization as long term effect.

The change of retained H was also investigated by SIMS. The H/B signal intensity ratios of SIMS decreased to about 80% of non-irradiation sample with overall B layer after He-GDC of six hours. However, because injection range of He with several hundred eV is around several nm, desorption of H from the depth of several hundred nm cannot be simply explained by sputtering. More examination is necessary as future work.

Reference

- 1) Kizu, K. et al.; Ann. Rep. NIFS (2003-2004) 80.
- 2) Yamaki, T. et al.; J. Nucl. Mater. **217** (1994) 154.

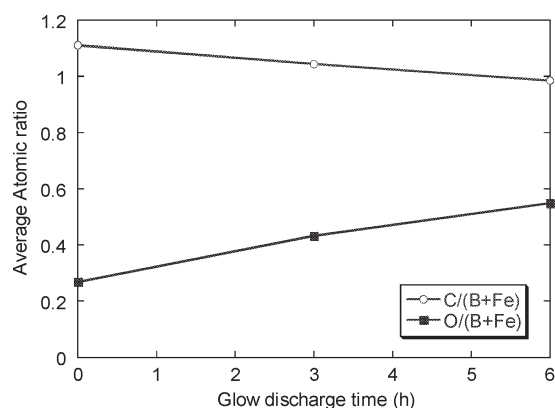


Fig. 2. He-GDC time dependencies of average atomic ratio of C and O in a depth 0 ~ 40 nm.

§80. Surface Analysis for Boronized Wall During 7th Experimental Campaign

Hino, T., Nobuta, Y. (Hokkaido Univ.)
 Ashikawa, N., Sagara, A., Nishimura, K.,
 Masuzaki, S., Noda, N., Ohyabu, N., Komori, A.,
 Motojima, O., LHD Experimental Group

Boronization experiments were conducted from the 5th experimental campaign. Material probes were installed at 10 positions along the toroidal direction from the 6th experimental campaign and the toroidal uniformity of the boron deposition was investigated. In the 7th experimental campaign, the boron deposition was similarly investigated. The boronization during the 7th experimental campaign was three times conducted using glow discharge. Two anodes between toroidal sectors 1 and 10 and between toroidal sectors 4 and 5 were employed for the glow discharge. The diborane gas was driven from the inlets between toroidal sectors 1 and 2, between toroidal sectors 3 and 4 and between toroidal sectors 7 and 8. After the campaign, the material probes were extracted and the depth profile of atomic composition was examined using Auger electron spectroscopy.

The thickness of boron film largely depended on the toroidal position. Figure 1 (a), (b) and (c) show the depth profiles of atomic composition in the probes placed at the toroidal sectors 1, 2 and 3. In the positions close to the anodes (toroidal sectors: 1, 2, 4 and 10), the boron deposition was clearly observed. In opposition, the boron deposition was very small in the positions far from the anode (toroidal sectors 3, 6, 7, 8 and 9). Thickness of the boron film was as high as approximately 300 nm. These results suggest that the diborane gas has to be dissociated and/or ionized for the boron to deposit on the wall.

Figure 2 shows a plot of thickness of boron film against toroidal sector number. The ratio of the boronized wall to the entire wall was approximately 40 %, which was higher than the ratio in the 6th experimental campaign, 20-30 %. The amount of oxygen retained in the boron film was measured based upon the depth profile of atomic composition. This amount is also plotted in Fig. 2. The amount of oxygen was large at the positions with a high boron concentration. The oxygen might have been trapped during the boronization, and main and glow discharges. The oxygen impurity concentration in the LHD plasma was significantly reduced after the boronization. This reduction is clearly owing to the oxygen getter action of the boron film.

In the boron films at the toroidal sectors 1 and 10, the peeling of boron film and the blister formation were partly observed. The energetic particle bombardment and/or increase of heat flux during the NBI heating might have caused these erosions.

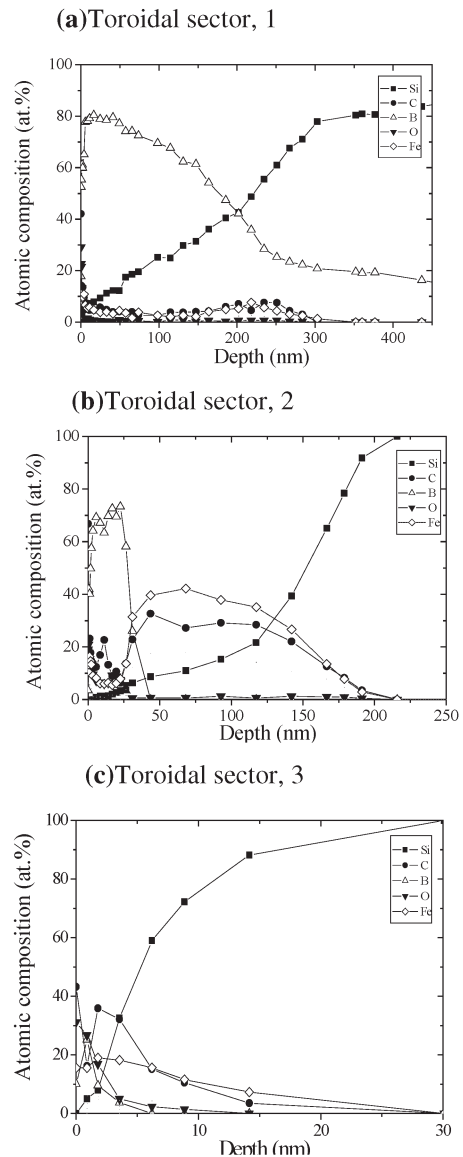


Fig.1 Depth profiles of atomic composition at probes placed at toroidal sectors 1 (a), 2 (b) and 3 (c).

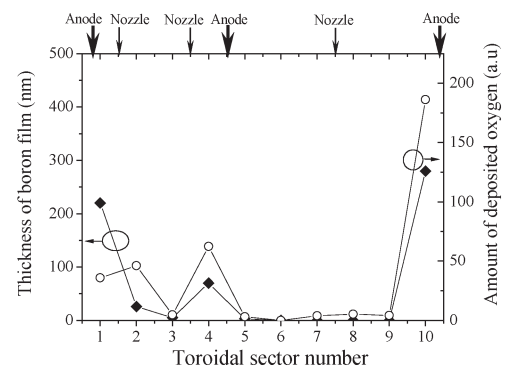


Fig.2 Boron thickness and amount of oxygen retained versus toroidal sector number.

Reference

1) Hino, T., Nobuta, Y. et al, Nucl. Fusion, **44**(2004)496.

§81. ICRF Wall Conditioning

Ashikawa, N., Masuzaki, S., Nishimura, K.,
Sagara, A., Seki, T.

ICRF discharge cleaning is a method to remove retained tritium or re-deposition layer in wall. In ITER, a magnetic field is produced by superconducting coils and typical case this magnetic field keep during experimental term (only sometimes magnetic field will be down to zero). Therefore, a wall conditioning method in the strong magnetic field is importance. In LHD, a deuterium operation can not be used, therefore experiments of hydrogen removal from walls were started in 2004.

Characteristics of ICRF conditioning (ICC) are

- Superconducting coil (maximum 2.9 T), steady state B-fields
- Flexibility of plus phase for input ICRF power.
- Long term operation (31 min, 1.3 MJ in 2004)
- Surface are in vacuum vessel is quite large due to superconducting coil area. (PFM area 210m^2 , PFM + coil area 700m^2)

As an experimental setup of ICRF antenna, a magnetic field is 2.75 T, a magnetic axis is 3.6 m and frequency is 38.47MHz as second harmonics of helium were used. An input power from 8 to 149 kW and a working gas pressure from 10^{-2} to 10^{-1} Pa were scanning during discharge. A total operation time is 115 minutes with a duration time of 3 second (on) and an interval time of 2 second (off) to fix data acquisition system.

Figure 1 shows experimental results of partial pressures, an input power (8-149kW) by ICRF and an electron density. Electron density was depending on the gas pressure and partial pressure did not changed by ICRF input power. At total duration time of operation between before input power and after, hydrogen partial pressure was decreased. To notice after experimental phase with same pumping system, hydrogen partial pressure was increased and this phenomenon was different of helium partial pressure. Therefore, in this experiment, time duration of off phase was not sufficient and an optimization with RF phase is important as future works.

As a reference discharge, helium glow discharge cleaning was operated with ~ 5 Pa and ~ 40 kW as shown in Fig.2 In LHD, hydrogen removal rate by GDC is larger than ICC. From this data, hydrogen removal rate by GDC is larger than ICC.

A sufficient power was observed data of electron density and FNA with accelerated hydrogen as characteristics of ICC.

In other tokamaks of AUG, TEXTOR and JET, a problem by an antenna breakdown has happened in pressure resign from 10^{-2} to 10^{-1} Pa as He pressure and this is one of big subject. But it was not observed during operation region in LHD. Therefore as characteristics of ICC in LHD, no breakdown operation with long working time as important issue is explained.

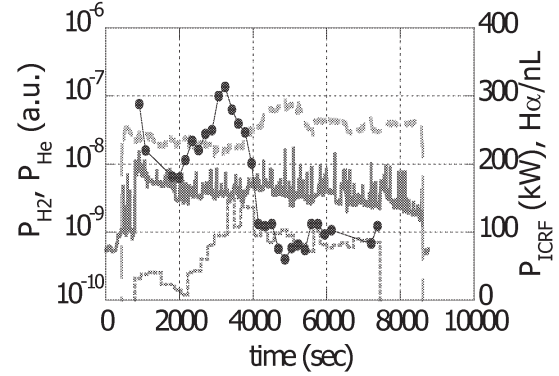


Fig.1 Time evolution of hydrogen partial pressure (solid line), helium partial pressure (broken line) and ICRF input power (dotted line). Normalized $H\alpha$ intensity by line electron density is plotted with circle.

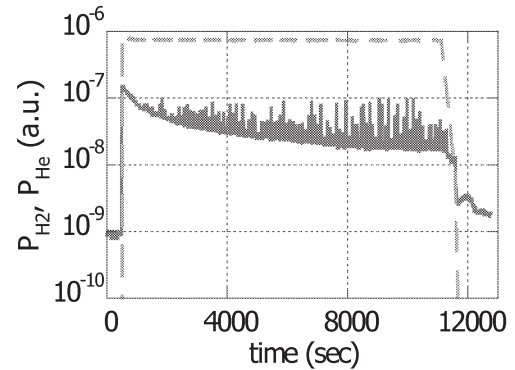


Fig.2 Time evolution of hydrogen partial pressure (solid line), helium partial pressure (broken line) by He glow discharge cleaning.

§82. Development of Integrated Simulation Code for LHD Plasma Experiments

Nakamura, Y., Suzuki, Y. (Grad. School of Energy Sci., Kyoto Univ.)

Fukuyama, A., Murakami, S. (Grad. School of Eng., Kyoto Univ.)

Nakajima, N., Yokoyama, M., Yamada, H., Watanabe, K.Y., Sakakibara, S., Funaba, H.

Recent progress of computers (parallel/vector-parallel computers, PC clusters, for example) and numerical codes for helical plasmas like three-dimensional MHD equilibrium codes, combined with the development of the plasma diagnostics technique, enable us to do the detailed theoretical analyses of the individual experimental observations. There are a lot of experimental data analyses using an individual numerical analysis code and many excellent results have been obtained for the LHD experiments. Now, it is pointed out that the experimental data analysis from the viewpoints of integrated physics, such as transport, heating, MHD equilibrium/stability, is an important issue to understand the confinement physics globally. To do that, the development of the integrated simulation system which has a modular structure and user-friendly interfaces is necessary. The integrated numerical simulation will also be a good help to draw up new experimental plans. In this study, we have started the development of such a system.

The integrated simulation system to be developed has a modular structure which consists of modules for calculating MHD equilibrium/stability, transport and heating. Each module can be selected in accordance with a user's request and can be combined with other modules. In order to maintain the independence of each module, which is an independent and complete program, sequences of the integrated simulation are controlled by a shell or script (perl or ruby, for example). Since some modules are suitable for running on the vector machine and others are on the PC cluster, we are going to develop a module-by-module distributed computing system through the network.

When we want to perform the integrated simulation during the entire plasma duration, a transport module is to be a core module. An integrated tokamak transport code, TASK[1], which is a core code for BPSI (Burning Plasma Simulation Initiative; research collaboration among universities, NIFS and JAERI in Japan) activity, will be extended for the helical configuration and used as a transport module. Figure 1 shows the schematic of a module structure of the integrated simulation system presently considered.

This fiscal year, we have reviewed the modeling and the specifications of interfaces between modules, and developed MHD equilibrium code HINT2 and bootstrap current calculation code BSC. The HINT2 is a revised code of the HINT and coded using Fortran 90. It is used for

calculating accurate MHD equilibrium of LHD including peripheral ergodic region.

Though almost all transport simulations done for LHD plasmas have neglected the net toroidal current, finite net plasma current has been observed in actual LHD experiments. It is considered that the bootstrap current and the beam driven current are included in it, but it is difficult to estimate fraction of these components accurately because plasmas are not stationary in many cases. So, as the first step of the extension of the TASK, time evolution of the plasma net current, which is consistent with the three-dimensional MHD equilibrium (by VMEC), will be solved for LHD plasmas by using time evolution of density and temperature profiles obtained by the experiment and taking into account of the bootstrap current and the beam-driven current. In order to calculate the bootstrap current, we have developed the BSC code, which is suitable for the usage as a module, by improving SPBSC code. The BSC code has been applied to the analysis of the bootstrap current observed in Heliotron J plasmas. It is shown that the neoclassical transport theory can explain the experimental observation that the bumpy field component can change the direction of the bootstrap current.

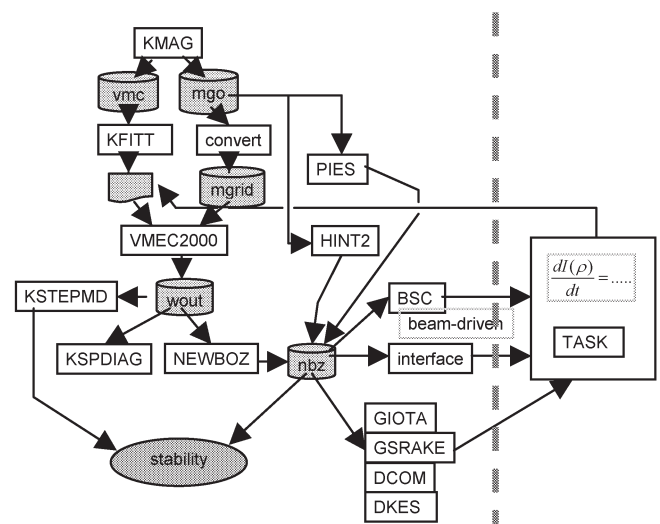


Fig.1 Schematic of the module structure of the integrated simulation system

Reference

- 1) A. Fukuyama, S. Murakami, M. Honda, Y. Izumi, M. Yagi, N. Nakajima, Y. Nakamura, T. Ozeki, Proc. of 20th IAEA Fusion Energy Conf., IAEA-CSP-25/TH/P2-3 (Vilamoura, Portugal, Nov. 1-6, 2004)

(3) LHD Device Engineering Experiments

1. Introduction

The LHD is the world-largest superconducting device that consists of a pair of pool-cooled helical coils (H1 and H2 coil), three pairs of forced-flow-cooled poloidal coils (IV, IS, and OV coils). The coils are connected to six power supplies by nine superconducting bus-lines. These superconducting coils and structures, total weight of which is 822 ton, are cooled by a helium liquefier and refrigerator of 10 KW class. The first cool-down was performed in February to March 1998, and it was the eighth cool-down last time. The results of device engineering experiments and the operations in the eighth cycle are summarized.

2. Eighth Cycle Operation of LHD

The history of the eighth cycle operation of the LHD is summarized in Table 1. The compressor of the cryogenic system started on July 30, 2004 and stopped on February 18, 2005. The total operating time is 4,869 hrs. The main compressors were stopped twice during the cool-down. The first reason was malfunction of the control program of the cryogenic system after the control system had been partial reset to cancel a communication error among the VME memory boards. They had been replaced from the type 5550 to the newest type 5565 several months before. Since the communication error occurred again, we decided to change the VME memory boards to the previous ones. It took three days to restart the cool-down with the previous system setup.

A quench detection was acted by a failure of a quench detector of the helical coils. Since it was occurred at the beginning of excitation, the cryogenic system maintained the stationary state fortunately. The malfunction was caused by the loose connection of solder at the BNC connector. Failure diagnosis and preventive maintenance are necessary to attain the stable operation.

Table 1 The history of the eighth cycle operation.

Operation mode	Date
<Vacuum pumping system>	
Pumping of cryostat	7/26/2004-2/10/2005
Pumping of plasma vacuum vessel	7/28/2004-1/25/2005
<Cryogenic system>	
Purification	7/30/2004-8/10/2004
Cool-down	8/11/2004-9/9/2004
Steady state operation	9/10/2004-1/20/2005
Warm-up	1/21/2005-2/18/2005

3. Device Engineering Experiments

The excitation tests before the plasma experiments were conducted from September 10 to 16. The following values were attained;

- (1) #1-o, $B=2.70$ T @ 3.75 m (H-O/M/I = 11.25 kA)
- (2) #1-d, $B=2.846$ T @ 3.60 m
(H-O/M/I = 11.6/11.55/11.0 kA)

- (3) #1-d-R3.5m, $B=2.901$ T @ 3.5 m
(H-O/M/I = 11.5/11.45/10.9 kA)
- (4) #1-o, $B=1.236$ T @ 3.53 m, $\gamma=1.156$
(H-O/M/I = 0.45/3.0/12.0 kA)
- (5) Mode transition at 11.0 kA of the helical coil.
(radii of the plasma axis were 3.42 to 4.1 m,
quadruple components were 72 to 200%)

The coil currents were same as the previous cycle except for the low γ mode (4) in which the plasma radius was relatively shorter. Any normal zones were not observed in this cycle.

The device engineering experiments were conducted on the following schedule.

November 22, 2004

- (1) Investigation of misalignment of the coils from the imbalance voltage of the coils

- (2) Measurement of the magnetization by excitation of only the IV coils

November 24, 2004

- (1) Slow charge and discharge for strain measurements

- (2) Measurement of the magnetization by excitation of only the IS coils

November 25, 2004

- (1) Measurement of the magnetization by excitation of only the IS coils and #1-d-a mode

November 26, 2004

- (1) Experiments of coil current control by H_∞ scheme

- (2) Measurement of the magnetization by the standard excitation (#1-d mode)

December 28, 2004

- (1) Investigation of temperature instability in 80 parallel paths of cooling pipes for the supporting structure by decreasing its mass flow to the half of the normal value

January 15, 2005

- (1) Reproducibility test of temperature instability in 80 parallel paths of cooling pipes for the supporting structure

4. Summary

New achievement by device engineering experiments and operations are summarized as follows;

- (1) The soundness of the superconducting coils and the supporting structures was confirmed.
- (2) The measurement of mechanical disturbances with AE sensors was advanced. The investigation is progressing by being compared with the balance voltages of the coils.
- (3) Four Hall probes were installed near the OV coils in addition for further estimation of the magnetization of the superconducting coils. Loop currents decaying with a very long time constant were also observed near the OV coils.
- (4) The vertical distribution of residual magnetic field was measured at the inner cryostat. It is in good accordance with the calculation of magnetization of the coils.

(Imagawa, S.)

§1. Observation of Coupling Currents with Very-Long Time Constants in LHD Poloidal Coils Using Hall Sensors

Takahata, K., Imagawa, S.
Hamajima, T., Tsuda, M. (Tohoku University)

Previous studies have reported evidence of magnetic field trapping/shielding with very-long time constants in large-scale superconducting coils which consist of cable-in-conduit conductors¹⁾. The magnetic field trapping/shielding is probably caused by coupling current loops in the conductors. The coupling current will result in an increase in AC losses^{1), 2)} and instability due to non-uniform current distribution. However, it is difficult to estimate the path and amount of the coupling current. In this study, Hall sensors were mounted in LHD poloidal coils and the coupling currents with long time constants have been examined.

Fig. 1 shows the locations of the Hall sensors. The sensors (model BHT921, Bell) are located 78 mm and 52 mm away from the inside surface of the Inner Shaping (IS) and the Outer Vertical (OV) coils, respectively. Two sensors were mounted for each IS coil (IS-U and IS-L) at toroidal angles of 23 and 203 degrees clockwise from the north. The vertical component of the field was then measured. The observations were carried out during the 7th and 8th plasma experimental campaigns. In the device engineering experiments, extended operations in which only IS and OV coils were energized were performed.

Fig. 2 shows the typical results observed in the device engineering experiments of the 8th campaign. The data indicate the residual field near the IS coil. The IS coils were energized up to 14 kA twice. On the day before this experiment, the IS coils were energized up to 14 kA with reversing the polarity. The observations showed the steady residual field of 0.5 mT. The polarity of the steady residual field changed with changing the polarity of the coil current. The steady residual field is probably caused by the magnetization of superconducting filaments. In addition, the changing residual field of 0.2 ~ 0.4 mT was confirmed just after discharging the coils.

Fig. 3 shows the comparison between the residual fields just after the excitations. Although two excitations have the same maximum current, they have different hold times of a flat top. The first excitation has no flat top. The second has the hold time of 2 h. The decay of the residual fields was fitted approximately with an exponential function. The comparison between the residual fields indicates the difference not only in the amount of change but also in a decay time constant. The time constant is 600 s for no hold time and 1200 s for the hold time of 2 h. The steady residual field of 0.5 mT was not affected by the hold time. The change in the decay time constant can be explained by a circuit model for induced coupling currents if the coupling current has a broad distribution of time constants. The results then indicate the existence of the coupling currents

with very-long time constants of more than 1000 s.

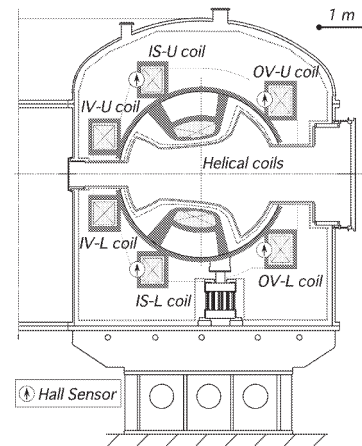


Fig. 1. Cross-sectional drawing of LHD and locations of Hall sensors.

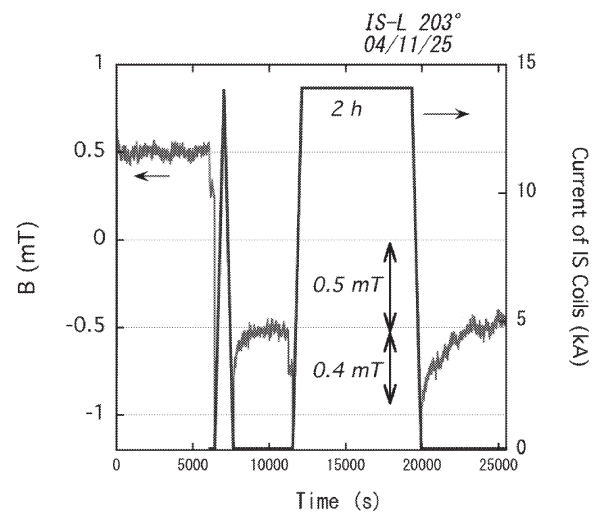


Fig. 2. Observed residual magnetic field after discharging the IS coils from 14 kA.

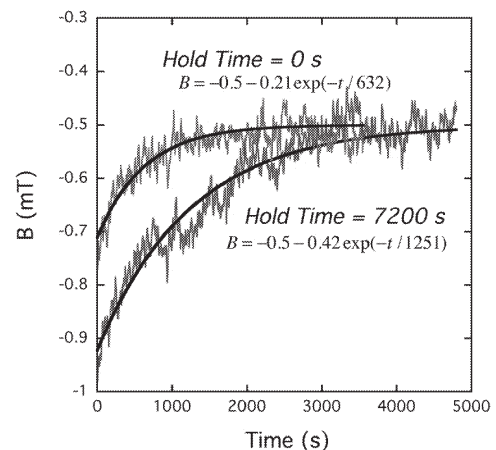


Fig. 3. Effect of the hold time of coil currents on the decay time constant of the residual field.

References

- 1) Hamajima, T., et al.: IEEE Trans. Appl. Supercond. 10 (2000) 812.
- 2) Takahata, K., et al.: Fusion Eng. Des. 65 (2003) 39.

§2. Evaluation of Residual Magnetic Field by Superconducting Coils of the LHD

Imagawa, S., Takahata, K.

After only the poloidal coils had been excited in the Large Helical Device (LHD), the phenomenon of the glow discharge's for the wall conditioning of the plasma vacuum vessel becoming not uniform was observed. The change in the residual magnetic field was measured at five periodic positions on the mid-plane of the inner cylinder of the cryostat in the seventh cooling cycle. As the result, it was clarified that the residual magnetic field was changed by magnetization of the superconducting magnets.¹⁾ For the comparison with the calculation value of the magnetization of NbTi filaments, the measurement positions were changed to five places of a perpendicular direction at the eighth cooling cycle.

In the eighth cooling cycle, the Hall elements were put on the inner cylinder of the cryostat in the height of 0, ± 0.5 , and ± 1.0 m, as shown in Fig. 1. The Hall elements were of high sensitive type of InSb. They were calibrated before installation within ± 3 mT by a coil. The fixed voltage drive was selected to reduce the temperature coefficient, and the voltage was set to DC 1 V. The measurement sensitivity is about 8 V/T in the field less than 60 mT. Outputs from the probes were acquired by a multi-channel data acquisition unit with low pass filter of 3 Hz at a sampling interval of 30 s.

The shift of the residual magnetic field of about 0.1 mT was observed at all the five positions after the first excitation of the superconducting magnet at the seventh cooling cycle. The shift disappeared synchronizing with the transition to the normal state of the inner vertical field coil (IV coil) when warm-up. It shows that the residual field at the inner cryostat after excitation was induced by the magnetization of the superconducting magnets.

Figure 2 shows a typical measurement result in the eighth cooling cycle when the ratio of the coil currents was widely changed. The zero points of the Hall probes are adjusted so that the sum of the residual magnetic field after -14 kA and +14 kA of the IS coils becomes 0. The comparison with the calculated value is shown in Fig. 3. It is assumed that all the superconducting filaments in each conductor are fully magnetized in the direction of the external magnetic field in the last excitation before discharging. The rates of magnetization are proportional to a critical current density, radii of the filaments, and volume densities of the filaments. The critical current density was assumed to be same in all the magnets, and the fitting value is 1.2×10^{10} A/m² that is appropriate as multi-filamentary strands of NbTi. The difference is large after the #1-d (standard mode) and the excitation of only IV coils, in which cases the contribution of the IS coils is large. The cause is not clear. Further research is needed.

The residual field was slightly decreased with a long time-constant of a few hours as shown Fig. 2. It may be induced by loop currents flowing across strands in the cable-in-conduit conductors. In order to clarify the loop, the measurement of the field near the IS coils and OV coils have been carried out.

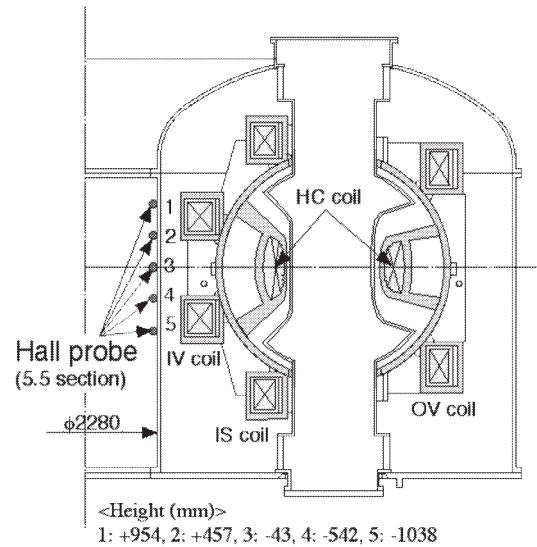


Fig. 1. Position of Hall probes for measurement of residual magnetic field at the Large Helical Device.

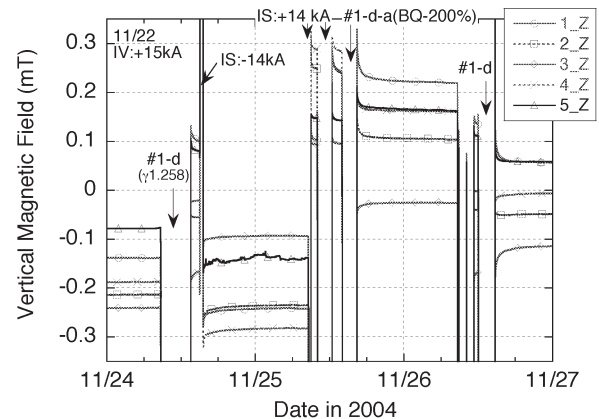


Fig. 2. Change of residual magnetic field after several excitation modes.

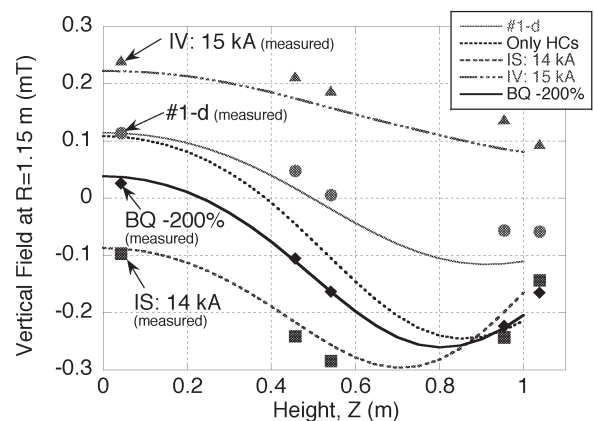


Fig. 3. Calculated field by magnetization of the magnets at the radius of 1.15 m for the critical current density of NbTi filament of 1.2×10^{10} A/m².

Reference

- 1) Imagawa, S. et al., IEEE Trans. Appl. Supercond., **15** (2005) 1419.

§3. Acoustic Emission (AE) Measurement of the LHD Helical Coils

Yanagi, N., Seo, K., Sekiguchi, H., Imagawa, S.
Ishigohka, T., Adachi, Y. (Seikei Univ.)

It has been observed in the helical coils (HC) of the Large Helical Device (LHD) that the balance voltage signals between the corresponding pairs of the coil blocks contain a number of spike signals during excitation. Pulse height analysis (PHA) has been successfully applied to analyze these signals in order to clarify the mechanical properties of the coil windings [1]. In addition, four acoustic emission (AE) sensors are attached to the HC-cans and comparison between the balance voltage and AE signals is conducted, which is useful to investigate the mechanical disturbances in the coil windings and to determine the area where a normal-zone is initiated.

Figure 1 shows a schematic illustration of the toroidal distribution of the AE sensors along the HC-cans. The signal cables of the AE sensors are lead from the LHD cryostat through feed-through connectors and fed into preamplifiers located near the cryostat. Envelopes of the AE signals are output by the AE analyzers and they are digitized with a sampling rate of 10 kHz. The AE data can be observed and stored by computers in the control room via LAN with optical fibers. A number of AE pulses are observed during ramp-up and ramp-down of excitation. It has been confirmed that many of the AE pulses are correlated with the spike signals of the balance voltage of the helical coils as well as those of the poloidal coils. The total intensity of AE signals decreases from the second excitation with the same operation condition.

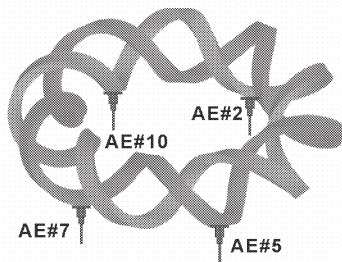


Fig. 1 Distribution of AE sensors along the helical coils.

We have been considering that the normal-transitions in the helical coils are initiated by mechanical disturbances in the windings (conductor motions). In this respect, the AE measurement is supposed to be effective to confirm this scenario. Figure 2 shows the waveforms of the AE signals and balance voltage when the 17th normal-transition was observed. The balance voltage was measured with two

different frequency ranges at 10 Hz and 10 kHz. The 10 Hz signal observes a normal-transition as the resistive component is extracted from the waveform, whereas the 10 kHz one detects a spike signal just before the transition. This indicates that a mechanical disturbance actually initiates a normal-transition.

Expansion of the waveforms (Fig. 3) shows that the AE sensor attached to No.10 sector of the HC-can responds first among the four sensors and its signal amplitude is the largest. This suggests that the mechanical disturbance that caused this normal-transition was generated near this section. Other three sensors also detected signals, and their time delays correspond to the traveling time of the sound waves through stainless-steel plates in the HC-cans and supporting structures. On the other hand, it was confirmed by the measurement with 120 pick-up coils attached along the HC-cans that the normal-zone actually started from No.10 sector in this case, which shows good agreement with the AE measurement.

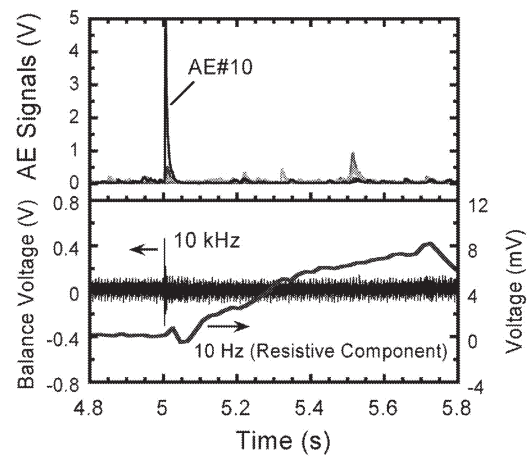


Fig. 2 Waveforms of AE signals and balance voltage signals (at two frequency resolutions).

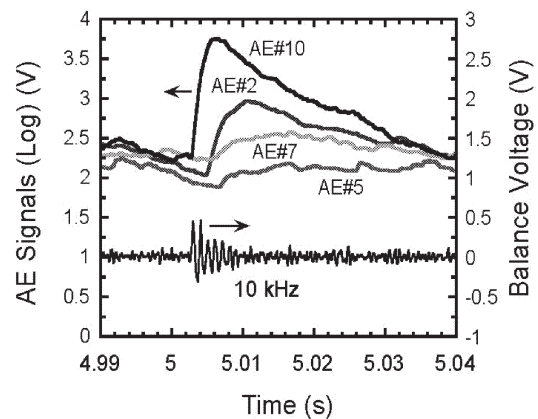


Fig. 3 Expansion of waveforms of Fig. 2 for the AE signals and balance voltage signal (at 10 kHz)

References

- 1) Yanagi, N. et al.: IEEE Trans. Appl. Supercond. 12 (2002) pp.662-665.

§4. Monitoring of the Superconducting Coil System Using Fuzzy Theorem for the Large Helical Device

Ishigohka, T., Uriu, Y., Ninomiya, A. (Seikei Univ.)
Mito, T., Imagawa, S., Yanagi, N., Sekiguchi, H.,
Yamada, S.

We have analyzed the state of the superconducting coil system of LHD at NIFS (National Institute of Fusion Science) using fuzzy theorem to detect a quench at an early stage. In this method, the “warning coefficient” of the coil system is calculated. As for the fuzzy variables, the “effective stored heat” in the coil is introduced in addition to the voltage signal in order to improve the quench detection and the state estimation. Through the experiment on the LHD coils, it was confirmed that quench alarming signals can be issued with enough leading time before a quench. On the other hand, in case of small local disturbances, the system shows only small increase of dangerous level.

The authors introduced a new variable “equivalent stored heat” in order to express the supposed temperature rise in the magnet induced by heat generation of normal conducting point. That is, the equivalent stored heat W_{eff} is given by;

$$W_{eff} = \left| \int_0^T e^{-\frac{T-t}{\tau}} v i dt \right| \quad (1)$$

where v is the balance voltage of the coil, i is the coil current, T is the present time, and τ is the heat dissipation time constant.

The adopted fuzzy variables are (1)the coil current, (2)the balance voltage, (3)the header pressure in the liquid He container, and 4)the equivalent stored heat.

The changes of the balance voltage, the effective stored heat, and the calculated warning coefficient during the normal propagation case are shown in Fig. 1, 2, and 3, respectively.

As shown in Fig. 1, after the balance voltage once increases up to about 0.15 V, it decreases lower than 0.05 V, and after that it increases sharply over 0.6 V. On the other hand, as shown in Fig. 2, the effective stored heat shows steady increase of the internal temperature. By introducing the equivalent stored heat, the calculated warning coefficient shows a clear stepwise increase. From these result, we can consider that the introduction of effective stored heat works considerably for the improvement of the state estimation.

From experimental result, we can conclude that;

- (1) Introduction of fuzzy theorem is effective for the monitoring of the superconducting magnet system of the LHD,
- (2) Introduction of a new fuzzy variable of “equivalent stored heat” is effective to estimate the internal temperature rise in a large superconducting magnet system typically as LHD.

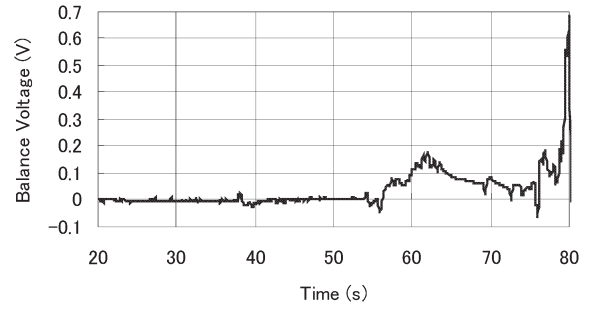


Fig. 1. Balance voltage in normal propagation.

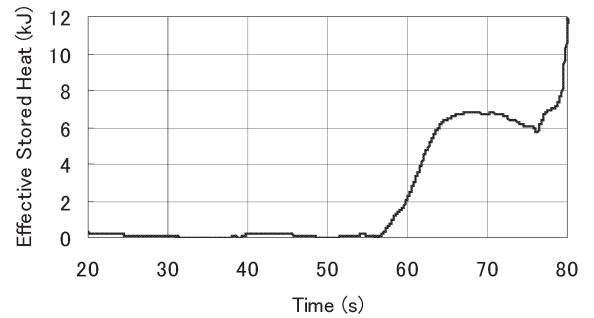


Fig. 2. Effective stored heat in normal propagation.

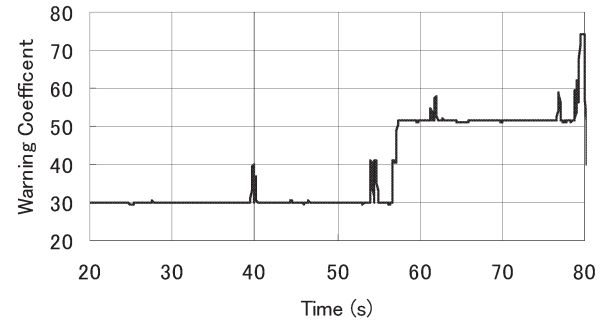


Fig. 3. Warning coefficient in normal propagation

Reference

- 1)Uriu, Y., Ninomiya, A., Kanda, Y., Tanabe, T., Ishigohka, T., Mito, T., and Yamada, S., “Quench Detection of Superconducting Bus-Line of LHD by Fuzzy Theorem”, IEEE Transactions on Applied Superconductivity, Vol. 9, No. 2 pp.248-251, June 1999.
- 2)Imagawa, S., Yanagi, N., Sekiguchi, H., Mito, T., and Motojima, O., "Performance of the helical coils for the Large Helical Device in six year's operation," IEEE Transactions on Applied Superconductivity, Vol. 14, No. 2, pp.1388-1393, 2004.
- 3)Adachi, Y., Ninomiya, A., Uriu, Y., Ishigohka, T., Mito, T., Imagawa, S., Yanagi, N., Sekiguchi, H., Yamada, S., “Introduction of Fuzzy Logic Theorem for Quench Detection in the Superconducting Coil System of the Large Helical Device”, Journal of Cryogenic Society of Japan, Vol. 40, No. 3, pp.93-99, March 2005.

§5. Strain Measurement of Cryogenic Support Structure of LHD

Nishimura, A.

Large Helical Device (LHD) was constructed seven years ago and has been operated during eight campaigns. The LHD consists of one pair of helical coils and three pairs of poloidal field coils. All coils are superconducting ones and supported by a cryogenic support structure. The cryogenic structure sustains large electro-magnetic force generated by the superconducting coils, and it was constructed with ten sectors made of 100 mm thick stainless steel. (SUS316) Each sector is a EB-welded structure and ten sectors were welded to make a shape of half structure. After installation of helical coils and some plasma vacuum structures, the top and bottom halves were welded at inner and outer equators to make one shell structure.

The weld grooves were originally designed taking account of welding deformation and residual stress. The welding process was also discussed to reduce the welding defects and non-destructive inspection was performed severely. Since the welding joint is discontinuous in shape, stress concentration occurs and a crack initiates on occasion. Therefore, the strain monitoring system was installed to evaluate the soundness of the cryogenic support structure and periodic measurement has been conducted as a part of device engineering study in the LHD experiments in the same manner as established in the fourth operation cycle. This report presents the measured results in 2004 and the soundness of the structure is discussed.

The details of the strain gages and the location of the gages are described in Reference 1, 2, 3 and 4.

The strain measurements were carried out on October 4, 2000, January 19 and September 29, 2001, January 11 and November 27, 2002, September 4 and November 18, 2003 and November 24, 2004. The maximum magnetic field at the magnetic axis was 2.85 T under #1-d mode ($R = 3.6$ m). Ramp up and down rate was 0.02 T/min. The temperatures

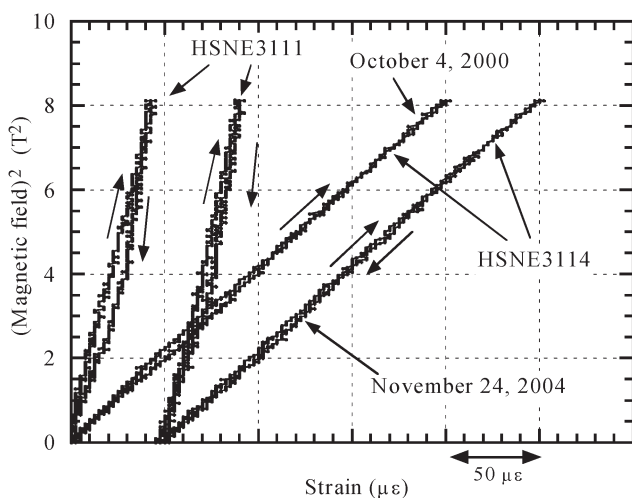


Fig. 1 Comparison of hysteresis curves measured on October 4, 2000 and November 24, 2004.

on the inner and outer equators changes within ± 0.03 K by the eddy current during ramp up and down processes. The results are shown in Fig. 1. HSNE 3111 and 3114 are the strains at inner and outer equators of the first sector, and both are in poloidal direction. It shows hysteresis curves as the same manner as before. The strain was plotted against another set of data at the same magnetic field as shown in Fig. 2. The dotted lines in the figure show ± 3 digits (1 digit is 2.5×10^{-6} strain). It is clear that all data are plotted in the scatter. The measured strains at 10 sectors are summarized in Fig. 3. The measured values are different depending on the location of the gage. However, the measured strain at each point changes within ± 3 digits and does not show significant difference.

From the above discussion, it would be concluded that the cryogenic support structure in the LHD is working well.

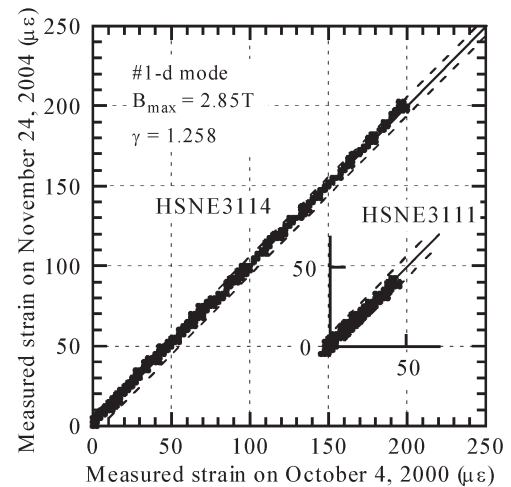


Fig. 2 Comparison of strains measured on different days.

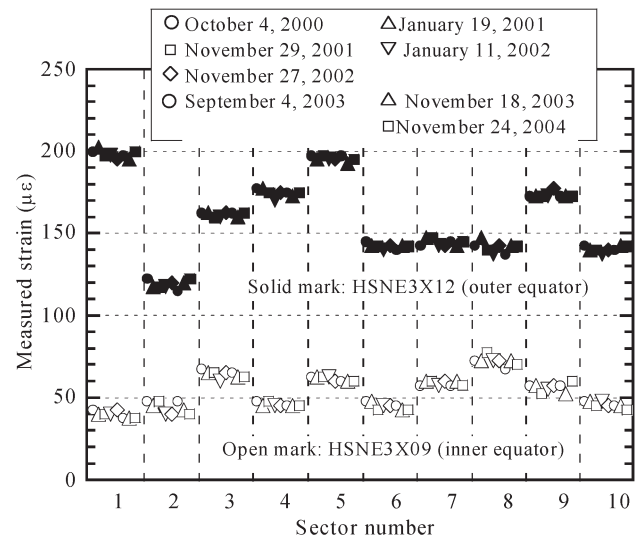


Fig. 3 Change in poloidal direction strain measured.

Reference

- 1) A. Nishimura et al., Adv. in Cryo. Eng., 45 (2000) 745.
- 2) A. Nishimura et al., Fusion Eng. & Design, 58-59 (2001) 253.
- 3) A. Nishimura et al., J. Plasma Fusion Res. SERIES, 5 (2002) 250.
- 4) A. Nishimura et al., Fusion Eng. & Design, 66-68 (2003) 1087.

§6. Advanced Current Control Scheme Using H-infinity Design for LHD Superconducting Coils

Ise, T. (Osaka Univ.), Chikaraishi, H.

In these years, some basic control schemes for the LHD power supplies have been designed and operated. For some plasma operations, the experimental group requires more precise control and robust schemes, and some advanced control schemes were designed, installed and tested. In the controller design, the information of plasma current I_p was used directly but the signal of plasma current becomes too large when the plasma current shut down suddenly. This over scaled signal disturbs the control system. Therefore the non-linear LPF (Low Pass Filter) to clip the signal has been installed and tested.

Figure 1 and Figure 2 show the control diagram of $H_\infty(1)$ and (2) controllers with the non-linear LPF, which keep coil current or magnetic flux constant while the plasma experiment, respectively.

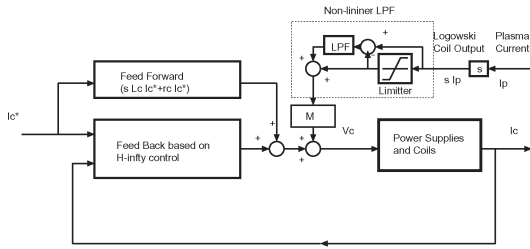


Figure 1: Block diagram of $H_\infty(1)$ controller, which keeps coil current constant while plasma experiment.

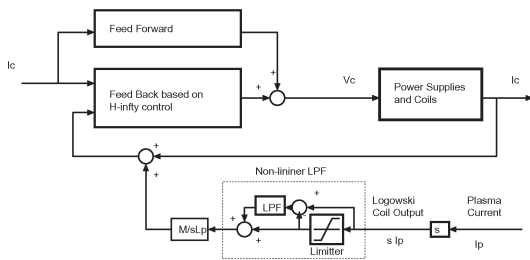


Figure 2: Block diagram of $H_\infty(2)$ controller, which keeps interlinked magnetic flux constant while plasma experiment.

Figure 3 shows the reaction caused by a plasma current with the $H_\infty(1)$ which uses non-linear LPF. The non-linear LPF clips the peak of $s I_p$, which means $\frac{dI_p}{dt}$ signal and limits the signal in the operation range. Therefore the coil currents and terminal voltages are not disturbed so largely when plasma discharge is finished. In Figure 4, the HI coil current drifts while plasma discharges because

the $H_\infty(2)$ control scheme has an integrator to observe the plasma current. The offset voltage of the non-linear LPF causes a drift. Therefore, the long-term operation using this control scheme is difficult with above reason. However, as the control system has ability to swap the current control scheme and usual plasma experiments are shorter than 30 s, this scheme can be applied to plasma experiments.

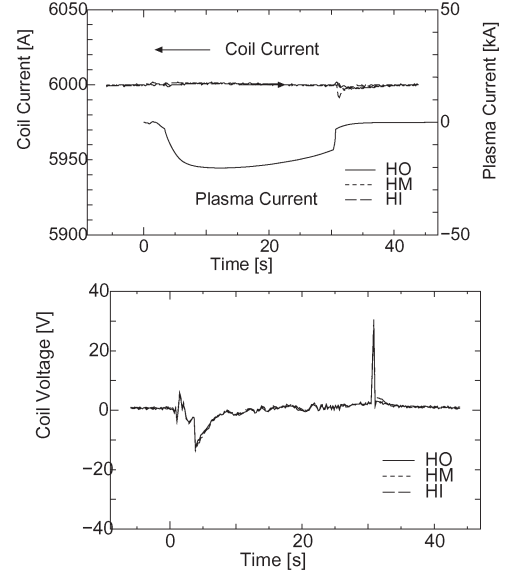


Figure 3: Reaction caused by plasma current, when $H_\infty(1)$ control is applied.

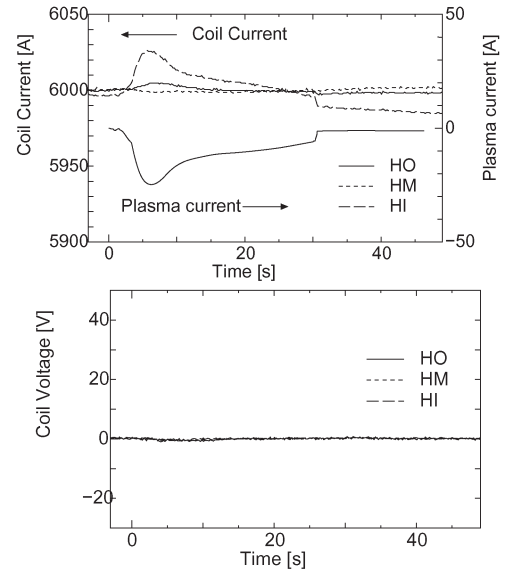


Figure 4: Reaction caused by plasma current, when $H_\infty(2)$ control is applied.

1-2. Device Engineering and Cooperative Development Research

(1) Physics and Engineering of LHD Torus System

High density tungsten is coated by vacuum plasma spraying technique on a rhenium interface of tiles. The tiles are carbon / carbon composite (CX-2002U), isotropic fine grained graphite (IG-430U). Thickness of the tungsten coating layer is 0.5 mm. The tungsten coated tiles are jointed on OFHC surface with a cooling tube. Thermal response and thermal fatigue lifetime tests using an electron beam facility have been carried out on the mock-ups under the actively cooling condition. The heat flux experiments have been carried out under the condition that the water flow velocity, pressure and temperature are 15.0 m/s, 0.5 MPa and 293 K, respectively. Use of the high density VPS-W improves the performance of mock-ups under steady state heat flux condition. In the case of W-coated CX-2002U on OFHC, it is demonstrated that the mock-up successfully withstood 100 cycles of heat loads at 10 MW/m² and the rhenium interface has good thermal and adhesion properties at steady state.

When the pellet is traveling in the curved drift tube, the pellet undergoes mass attrition due to melting /evaporation caused by radiation from the tube wall and friction heat with the wall and the erosion by collision with the wall. We estimate numerically the effects of behavior when the pellet attacks/leaves on the wall, especially contact angles of the pellet, on the mass attrition by means of Material Point Method incorporated with Smoothed Particle Hydrodynamics method..

A pumping panel made of a Group Va metal (V, Nb or Ta) is one of promising means for particle flux control in the divertor region. For Nb panels, it was found that the absorption rate remarkably decreased in the low temperature range (80 ~ 200 C). Therefore, The temperature dependence of H atom absorption by V panel was investigated in the range of 30 ~ 500 C. Three panel temperature (T_p) ranges can be distinguished: $T_p=(30-200)$ C, $T_p=(200-400)$ C and $T_p>400$ C. the absorption rate (S_{ab}) increases with T_p very gently in the range (30-200) C; the most probable cause of such a behavior appears to be saturation of panel surface by adsorbed H atoms. The increase of S_{ab} with T_p becomes stronger in the range of (200-400) C. The causes of S_{ab} change in this temperature interval remain unclear at the moment. S_{ab} reaches its maximum at $T_p\sim 400$ C and remains

constant at $T_p>400$ C where V is covered by an O monolayer segregated from the metal bulk. Besides, one can find that there is a significant hysteresis for the absorption rate in the cycle of increasing and decreasing of panel temperature. The cause of this hysteresis remains unclear and further investigation would be required.

We developed a novel technique for high energy secondary electron measurements. This technique enables one to obtain ion-induced secondary electron current even under a plasma-existing condition. We investigated the secondary electron emission coefficient (SEEC) derived from a comparison between overall target current and the measured secondary electron current. Furthermore, time variations of the SEEC during the plasma-exposed period were examined. Measuring the overall target current and the secondary electron current, the SEEC of the target exposed to the plasma was obtained successfully. Repetition of the measurements revealed time variations of the SEEC; the SEEC gradually increases and reaches a steady state, and this will be caused by impurities contained in the plasma such as oxygen.

(Ohyabu, N.)

§1. Studies on Behavior of Solid Hydrogen Pellets in a Drift Tube

Yokomine, T. (Kyushu Univ.)

When the pellet is traveling in the curved drift tube, it is expected that the pellet undergoes mass attrition due to melting/evaporation caused by radiation from the tube wall and friction heat with the wall and the erosion by collision with the wall. Present study aims to estimate the effects of behavior when the pellet attacks/leaves on the wall, especially contact angles of the pellet, on the mass attrition numerically.

Material Point Method is applied for calculation of pellet's motion. For prediction of temperature inside the pellet and the impingement wall, Smoothed Particle Hydrodynamics (SPH) method is used. That is, in present scheme, both pellet and tube wall are regarded as assembly of material particles. For SPH method, the resultant reproduction of heat conduction at the interface of contact between pellet and tube wall strongly depends on the distance between each material particle. Therefore, contact heat transfer is approximated by the analytical solution of contact heat transfer rate of two semi-infinite bodies. Sliding friction is described by means of Amonton and Coulomb's law and frictional heat is assumed that the decrease in total energy of pellet is converted to the heat. After calculation of input energy of pellet as frictional heat, the temperature of material particles of pellet located in vicinity of contact surface is calculated. If above obtained temperature exceeds the melting point of hydrogen, the exceeded energy is assumed to be spent for sublimation of pellet. Then mass attrition for the sublimation is calculated from the latent heat of sublimation.

The pellet is assumed to be a cube moving at 100m/s as initial velocity. The initial temperatures of pellet and tube wall are 4K and 300K, respectively. Before impingement, the flight attitude of pellet is inclined: 0, 10, 20, 30 and 40 degrees. When the pellet impinges the wall, the impact angle is varied from 4 to 8 degree as a calculation parameter. The friction coefficient is assumed to be constant value of 0.15.

Fig.1 shows the snapshots of pellet's behavior in the case that flight attitude angle is 10 degree. The pellet impinges on the wall twice. When first contact is occurred, the edge of pellet is deformed and additional rotational force is added to the pellet. Then the pellet leaves from the wall after second contact is succeeded. Fig.2 shows the effect of flight attitude angle of pellet on the mass attrition rate. For all impact angles, the mass attrition rate becomes minimum when the flight attitude angle of pellet is 30 degree. When the flight attitude angle of pellet is below 30 degree, the pellet is rotated by the additional force due to first contact and the contact period is elongated. In the case of 30 degree, the second contact is not occurred. So that, the mass attrition rate is decreased in the case of 30 degree compared to cases of the shallow angles. Though the pellet also impinges the wall once in the case of 40 degree, the

amount of eroded mass at the contact is larger than that of 30 degree case. That makes the contact area of pellet broad, so that the mass attrition rate is increased.

As next step, actual pellet configuration, the effect of gasified hydrogen near the heat transfer interface, plastic deformation of pellet and meso-scale modeling of friction should be taken into account.

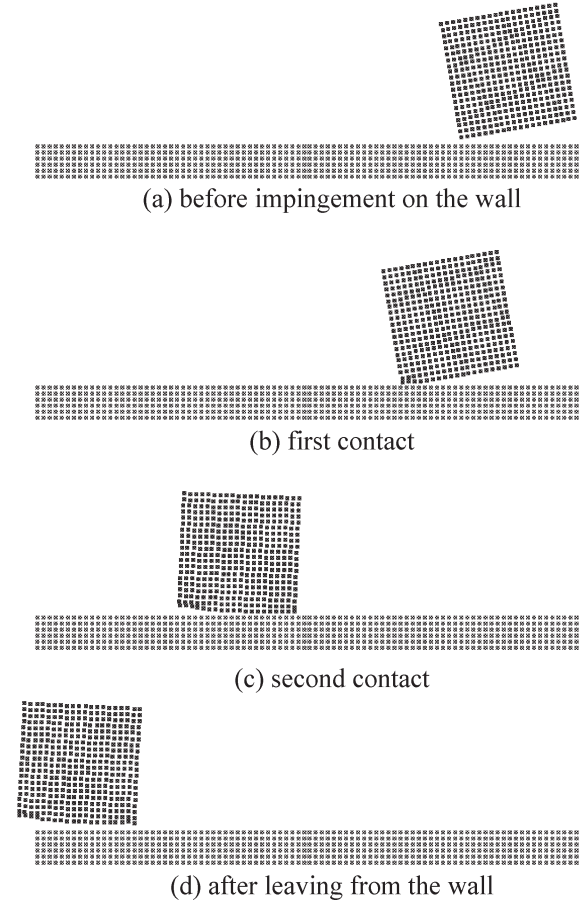


Fig. 1. Snapshot of behavior of pellet impingement

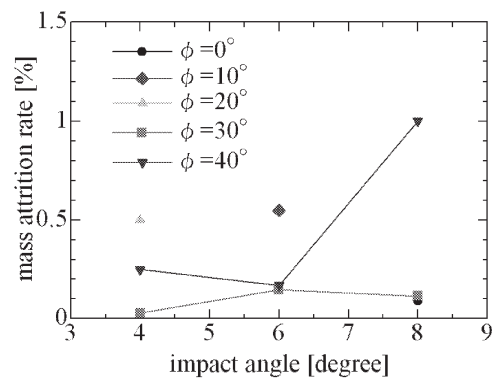


Fig. 2. The effect of flight attitude of pellet on the mass attrition rate.

§2. Characteristics of Hydrogen Absorption in Vanadium Pumping Panel

Nakamura, Y., Livshits, A.I. (Bonch-Bruyevich Uni.), Hatano, Y. (Toyama Uni.), Ohyaabu, N.

A pumping panel made of a Group Va metal (V, Nb or Ta) is one of promising means for particle flux control in the divertor region. In the case of steady-state regime, a superpermeable membrane should be used for particle control, while a periodically regenerated absorption panel (simpler and cheaper) can be acceptable for an intermittent operation in non-tritium devices.

The capability of a niobium panel to absorb atomic hydrogen so far has been investigated for particle control application in divertors [1]. For Nb panels, we found that the absorption rate remarkably decreased in the low temperature range (80 ~ 200 °C). In order to investigate the absorption rate in the vicinity of room temperature (< 80 °C), the experimental setup was rearranged so as to control the panel temperature independently of atomizer heating. At first, H absorption properties of V panel were investigated. The panel was degassed at 600 °C and then kept in vacuum for cooling to room temperature during a night. The basic vacuum was $\sim 5 \times 10^{-7}$ Pa. Then hydrogen was admitted to required pressure and the atomizer was switched on (Fig. 1) for relatively short time (typically a few tens of seconds). The pressure drops due to absorption in the panel but this decrease is not very large due to high pumping speed of Turbo Molecular Pump during the experiment. Thus the absorption rate is measured by the change of H partial pressure of QMS at any panel temperatures. The panel temperature increases during the atomizer operation and the procedure is repeated at next higher temperature. At reaching a definite panel temperature due to heating by atomizer radiation (~ 200 °C) the temperature is increased further by electric current through the panel. At a definite temperature (~ 450 °C) a noticeable desorption of H_2 begins. Then the hydrogen influx is stopped and the panel is degassed at 600 °C. Then the same influx of gas is admitted again and the absorption is observed by the same way but at step-by-step decrease of panel temperature.

Figure 2 shows the results of experiments at two initial hydrogen pressures: 0.01 and 0.21 Pa. In this case, the maximum (at $T_p \sim 400$ °C) densities of H atom absorption flux corresponding to 0.01 Pa and 0.21 Pa are 1.1×10^{15} and 1.1×10^{16} H/cm²/s, respectively. In order to simplify the comparison of temperature effects at different pressures, the absorption rate for each pressure are normalized to the absorption rate being maximum for the given pressure (i.e. to 650 l/s and 340 l/s for 0.001 and 0.21 Pa, respectively). The temperature dependence of H atom absorption by V panel, $S_{ab}(T_p)$, was investigated in the range of T_p of (30-500) °C at different flux densities of H atoms. S_{ab} was

found to change with T_p but not very much: the ratio $S_{abmax}/S_{abmin} < 3$ over the whole temperature interval investigated. Three temperature ranges can be distinguished: $T_p = (30-200)$ °C, $T_p = (200-400)$ °C and $T_p > 400$ °C. S_{ab} increases with T_p very gently in the range (30-200) °C; the most probable cause of such a behavior appears to be saturation of panel surface by adsorbed H atoms. The increase of S_{ab} with T_p becomes stronger in the range of (200-400) °C. The causes of S_{ab} change in this temperature interval remain unclear at the moment. S_{ab} reaches its maximum at $T_p \sim 400$ °C and remains constant at $T_p > 400$ °C where V is covered by an O monolayer segregated from the metal bulk. Besides, one can see that there is a significant hysteresis for the absorption rate in the cycle of increasing and decreasing of panel temperature. The cause of this hysteresis remains unclear and further investigation would be required.

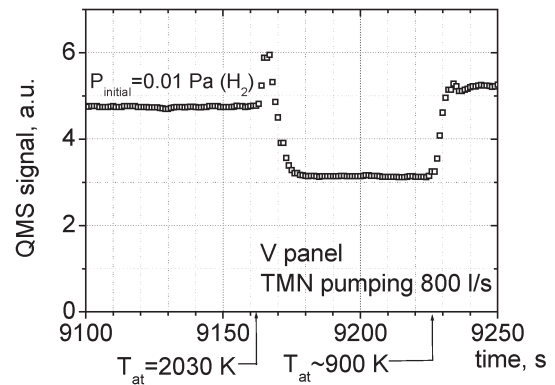


Fig. 1. Typical picture of H atom absorption observed by a Quadra Mass Spectroscopy

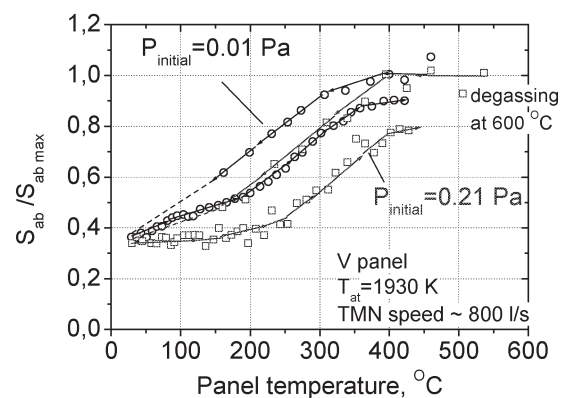


Fig. 2. Temperature dependence of normalized hydrogen absorption rate for different gas pressures

References

[1] Nakamura, Y., et al., J. Nucl. Mater., 337-339(2005)461.

§3. In-situ Measurements of Secondary Electron Emission Coefficient in Plasma-Surface Interaction

Nakamura, K., Moriguchi, M. (Chubu University)
Kubota, Y.

High energy particles such as neutrals, ions and photons produced in a fusion reactor are exhausted through diverter area, then a large heat load is applied to the diverter plate. In this meaning, there are strong plasma-surface interaction on a surface of the diverter. As one of the interactions, there is secondary electron emission, and its secondary electron emission coefficient (SEEC) has been measured for various target materials and incident ions. However, in most cases, such a measurement has been carried out with beam experiments in a ultra high vacuum environment for a pressure lower than 10^{-6} Torr which is much different from actual plasma environment. Therefore, new measurement technique is necessary to obtain the actual secondary electron emission coefficient in the plasma environment. Recently, a scintillation-based novel technique for high energy secondary electron measurements in PIII has been developed [1]. In the previous study, we extend the technique by replacing the scintillation detector with a semiconductor diode detector for more precise measurements, enabling one to obtain ion-induced secondary electron current. In this report, we investigate the secondary electron emission coefficient (SEEC) derived from the measured secondary electron current, and time variations of the SEEC during the process.

In the present experiment, one turn loop antenna is set in a 35-cm-diam. and 50-cm-long cylindrical stainless steel chamber, and a 13.56 MHz inductively-coupled plasma is generated at argon pressures of 1.3 Pa by supplying the antenna with RF powers up to 600 W. Under typical conditions, the electron density is $1.1 \times 10^{17} \text{ m}^{-3}$ and the electron temperature is 2.3 eV. 10 μs -long high voltage pulses up to 6 kV are applied to a spherical copper target inserted into the plasma with a repetition rate of 10 pps. In order to measure the high-energy secondary electrons, a thermoelectrically-cooled Si-PIN diode are used. As shown in Fig. 2, when the high-energy electrons are incident on the diode detector, hole-electron pairs are created. Since an inverse bias is applied to the detector, the resultant charges are extracted to a charge amplifier whose output voltage is proportional to the total amount of the created charges. The secondary electron current I_{se} obtained by differentiating the integrated output voltage enables one to discriminate high

energy electrons ($>2 \text{ keV}$) from background low-energy electrons in the plasma. The absolute calibration revealed that the detector has a sensitivity of $\sim 0.2 \text{ mA/mm}^2$ with a fast response time shorter than $\sim 0.1 \mu\text{s}$.

As shown in Fig. 1, immediately after applying the target pulse voltage V_t of -6 kV at $t=0$, the target current I_t flows with a peak component for $0 < t < 2 \mu\text{s}$ followed by a constant component ($t > 3 \mu\text{s}$). The secondary electron current I_{se} measured by the diode detector also has a waveform similar to I_t . However the peak of I_{se} is significantly lower than that of I_t because I_{se} obtained by the high energy electron measurement essentially does not include displacement current. Therefore the present technique is available for the selective measurement of the secondary electron current. Taking account of the detector sensitivity, the solid angle of the detector, and the spatial profile of the plasma density around the target, a current ratio of I_t/I_{se} gives the SEEC γ during the ion implantation as ~ 5 by $I_t/I_{se} = 1 + \gamma^{-1}$. Repeating such a measurement, time variation of the SEEC are examined during the PIII process. The SEEC is approximately ~ 2 just after starting the process. However the SEEC gradually increases and reaches a steady state of ~ 5 . This will be caused by impurities contained in the plasma such as oxygen.

References

- [1] K. Nakamura et al: Plasma Sources Sci. & Tech. 6, 86 (1997).

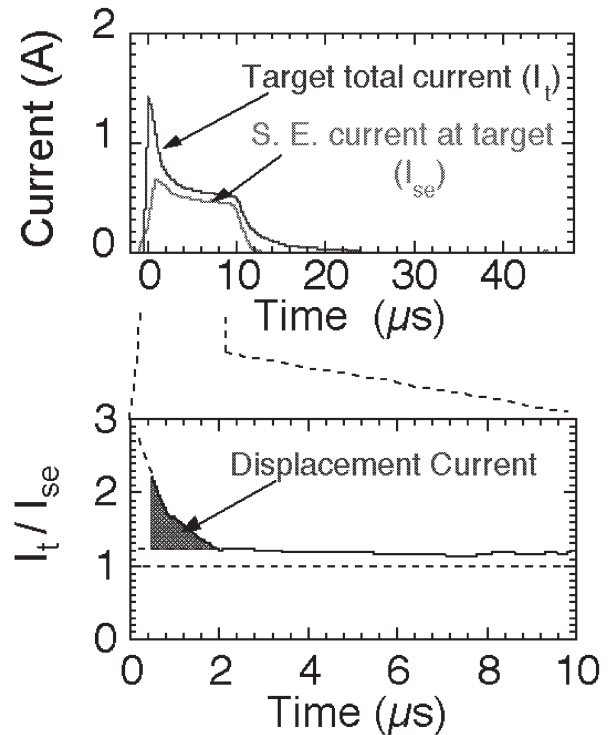


Fig. 1 Time variations of target total current I_t and secondary electron current I_{se}

§4. Behavior of Rhenium Interface on Tungsten Coated Carbon by Heat Load

Tokunaga, K., Miyamoto, Y., Fujiwara, T., Yoshida, N. (Res. Inst. Appl. Mech. Kyushu Univ.)
Sogabe, T. (Toyo Tanso Co., Ltd.)
Kato, T. (Nippon Plansee K.K.)
Schedler, B. (Plansee Aktiengesellschaft)
Kubota, Y., Noda, N.

Thick tungsten coatings on CFC and isotropic fine grain graphite have been successfully produced by vacuum plasma spray (VPS) technique and their good thermal and adhesion properties have been confirmed by high heat flux tests. For the near term application for LHD, tungsten coated tiles could be convenient because the tiles could be easily replaced without big change in heat transfer properties to cooling channels.

In recent, higher density VPS-W(Vacuum plasma spraying tungsten) coated CFC and isotropic fine grained graphite comparing with the previous ones have been developed. In the present work, to investigate behavior of rhenium interface under steady state heat flux condition, thermal response and thermal fatigue lifetime tests using an electron beam facility have been carried out on the VPS-W coated CFC and isotropic fine grained graphite brazed on the OFHC with a cooling tube under the actively cooling condition. In addition, FEM analyses have been performed to evaluate the thermo-mechanical behavior.

Tiles (20mm x 20mm x 10mm) of carbon/carbon composite CX-2002U and isotropic fine grained graphite IG-430U made by Toyo Tanso Co. were coated with tungsten by the vacuum plasma spraying technique(VPS). The thickness of the VPS-W layer was 0.5 mm and its density was 98% of the theoretical value. Mock-ups were made by brazing the VPS-W/CX-2002U, VPS-W/IG-430U on OFHC block with a cooling tube by inserting a Ti foil of 0.05mm-thick in between.

Heat load tests were performed on the Active Cooling Teststand (ACT) of National Institute for Fusion Science (NIFS). Uniform electron beam at 30keV was irradiated on the tungsten surface through a beam limiter with an aperture of 20mm x 20mm. Beam duration during ramp-up, plateau and ramp-down were 20s, 22s and 0s, respectively. Heat flux was changed from 1 to 10 MW/m². Thermal fatigue tests were also carried out for up to 100 cycles at a heat flux of 10 MW/m². Surface

temperature of the tile was measured with an optical pyrometer. Temperatures of upper side(T1) and down side(T2) of interface of brazed area were also measured with thermocouples. The heat flux tests have been carried out under the condition that the water flow velocity, pressure and temperature were 15.0 m/s, 0.5 MPa and 293 K, respectively. After the heat flux experiments, the mock-ups were observed with a scanning electron microscope to investigate modification such as crack and exfoliation formation.

Figure 1 shows typical time evolutions of the electric current(a) through W/CX-2002U/OFHC mock-up and temperatures(b) at its surface, upper (T1) and lower (T2) parts of the brazing interface under heat loading of 7 - 10 MW/m². The temperatures closely follow the changing electric current. The thermal fatigue tests indicate that temperature change is not observed. In addition, no failure occurred at the braze interface or in the W coating during cyclic heat load. Therefore, it is demonstrated that the mock-up successfully withstood of heat load 10 MW/m² and the rhenium interface shows good thermal and adhesion properties at steady state condition.

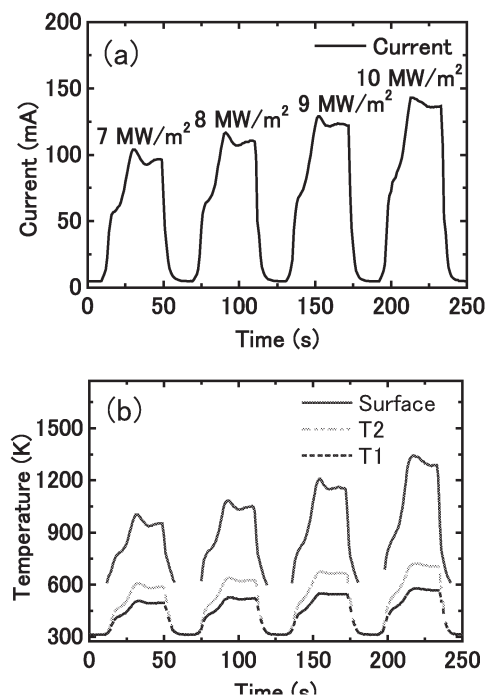


Fig.1 Time evolutions of the electric current(a) through W/CX-2002U/OFHC mock-up and temperatures(b) at its surface, upper (T1) and lower (T2) parts of the brazing interface under heat loading of 7, 8, 9 and 10 MW/m².

(2) Applied Superconductivity and Cryogenics

1. Introduction

Research activities concerning with applied superconductivity and cryogenics are summarized in this section. The research items concerning on the superconducting system for LHD are summarized in 1-1-(3) LHD Device Engineering Experiments. The related activities for applied superconductivity are also included in 1-4 LHD joint researches, 7 Bidirectional joint researches and 13 Interactive Coordinated Researches.

2. Research activities of collaboration

A variety of collaboration has been carried out such as fundamental researches about cryogenic characteristics, electromagnetic phenomena and mechanical properties, a development study of an advanced superconductor, superconducting coil and cryogenic system, applied researches of systems development, etc. The titles of researches are list in the following.

- (1) Study on Long Loops with Long time constants in cable-in-conduit superconductors. (Hamajima, T., Tohoku Univ.)
- (2) Optimization of Stress Distribution in Helical Coils. (Shimada, R., Tokyo Inst. of Tech.)
- (3) Study on Electrical Insulation Characteristics of Superfluid Helium. (Hara, M., Kyushu Univ.)
- (4) Database Development for He II-cooled Superconducting Magnet System Design. (Haruyama, T., KEK)
- (5) Study on the Strength and Fracture Mechanisms of Rare Earth HTC Bulk Single Crystal. (Katagiri, K., Iwate Univ.)
- (6) Development of a Current-Feed System with Low Heat Load using a Pulse Tube Cooler. (Maehata, K., Kyushu Univ.)
- (7) Fundamental Study on Application of Magnetic Levitation using YBCO Bulk Superconductor to Fusion Research. (Tsuda, S., Yamaguchi Univ.)
- (8) Fundamental Study on Cryogenic Characteristics of SiC Power Device and Its Application to AC/DC Converter. (Matsukawa, T., Mie Univ.)
- (9) A Development of a General-Purpose Pressure Sensor for In-Situ Measurement under Cryogenic Environment (Kimura, N., KEK)
- (10) Development of Observation and Diagnosis Systems for Superconducting-Coil Operations using the Poynting Vector Method (Sumiyoshi, F., Kagoshima Univ.)
- (11) Basic Research on the Oxide Superconductors for a Nuclear Fusion Reactor. (Iwakuma, M., Kyushu Univ.)
- (12) Effect of the Phase Transition on Heat Transfer in He II. (Kobayashi, H., Nihon Univ.)
- (13) Ensuring Composite Electrical Insulation Reliability for LHD. (Nagao, M., Toyohashi Univ. of Tech.)
- (14) Design and Optimization of High Tc Superconductor for Current Lead. (Yamada, Y., Tokai Univ.)

3. Research activities of the Applied Superconductivity & Cryogenic Group of NIFS

The Applied Superconductivity & Cryogenic Group, belonged to the Device Engineering Division of the Department of Large Helical Device, had been demonstrated their abilities for the intensive research & development of Large Helical Device (LHD) since the establishment of NIFS 1989. In 2003, as Natural Institutes for Natural Science has been established, the restructuring of NIFS was taken place and the Group is now belonging to the Fusion & Advanced Technology Systems Division. We are pursuing not only the safe operation of LHD superconducting system but also the rigorous research to improve the performance of LHD. Furthermore, our focus is on the design work of a helical type fusion reactor (which can be realized as a power plant) and the development of its key technologies.

To accomplish these tasks, the Group is being highly motivated to collaborate with universities, national laboratories and industries to encourage their research activities to fulfill their goal. Recent activities of the Device Engineering Division including the industrial application by downsizing of Fusion Technology are listed below.

- (15) Development of Conduction-Cooled LTS Pulse Coil. (Mito, T., NIFS)
- (16) Cryogenic Stability of the Model Coil of the LHD Helical Coil in Saturated Helium. (Imagawa, S., NIFS)
- (17) Elimination of Variable Harmonics on Motor Generator Circuit. (Yamada, S., NIFS)
- (18) Thermal Contact Conductance between the Bundle and the Conduit in Cable-in-Conduit Conductors. (Takahata, K., NIFS)
- (19) Effective Resistivity of HTS Tapes with Shielding Currents. (Yanagi, N., NIFS)
- (20) SMES System Designed to Protect from Momentary Voltage Drop. (Chikaraishi, H., NIFS)
- (21) Development of a Pulse Tube Current Lead. (Maekawa, R., NIFS)
- (22) HTS Conical Bulk for Current Lead Use. (Tamura, H., NIFS)
- (23) Cooldown Performance of the Cryogenic System Applied for the Cryogenic Target of the FIREX Project. (Iwamoto, A., NIFS)
- (24) Performance of Cold Compressors in the Cooling System for the R&D Coil Cooled by Subcooled He I. (Hamaguchi, S., NIFS)
- (25) Simulation of Electromagnetic Behaviors of Lap Joints for Fusion Magnet Systems (Seo, K., NIFS)
- (26) Interaction between the Transport Current and Shielding Currents in Bi-2223/Ag HTS Tapes. (Henmi, T., Graduate Univ. of Advanced Studies)

(Mito, T.)

§1. Study on Long Loops with Long Time Constants in Cable-in-Conduit Superconductor

Hamajima, T., Yagai, T. (Tohoku University),
Tsuda, M., Nakamura, S. (Yamaguchi Univ.),
Takahata, K.

In recent years there has been a growing interest in irregular AC losses that cannot be measured from short conductor sample tests. The irregular AC losses with long time constants were typically observed in a Japanese SMES model coil, and the similar long time constants were estimated in poloidal superconducting coil conductors of Large Helical Device in National Institute for Fusion Science in Japan. Current loops, which must be irregularly formed in the cable, decay with the long time constants, and hence enhance the AC losses. The loops can induce an imbalanced current distribution in a conductor, and lead to RRL (ramp rate limitation), which was observed in DPC coils at Japan Atomic Energy Research Institute.

In this research, we propose a mechanism forming the long loops. The CIC conductor is composed of several staged sub-cables. If one strand on the surface of a sub-cable contacts with the other strand on the surface of the adjacent sub-cable, the two strands should encounter each other again at LCM (Least Common Multiplier) distance of all staged cable pitches, and thereby result in forming a pair of a long loop. There are a number of such long loops in the CIC conductor. The time constants of these loops are fundamentally described as ratios of their inductances to their contact resistances.

In order to estimate the time constants $\tau = L/R$ of the long LCM loops, we measured the cross contact resistance between the two strands of the SMES and LHD in LHe. The test results showed that the cross contacting resistances were about $50 \mu\Omega$ for both conductors. The results suggest that the time constants are around 0.1 s for SMES and 0.3 s for LHD, which are shorter than the measured time constants of 5 to 100 s. This stems from the fact that the cross contact area, which is estimated about $10 \mu\text{m}$ in the elastic limit, is very small compared with the line contact area, which is the order of cm.¹⁾

It is important to investigate the contact conditions in more detail. We used pressure-sensitive papers, which are comprised of two types of papers; the one paper has dye capsules and the other has color developer. The paper color changes according to experienced pressure due to a

chemical reaction between the two papers. We wound the pressure-sensitive papers on the strand surfaces of all sub-cable stages, as shown in Fig.1, and fabricated a third-order cable ($3 \times 3 \times 3$) with 2 m in length, then squeezed the cable through a die to form 38 % void fraction in the cable.²⁾

It is found that the averaged contact lengths between strands in 1-st, 2-nd and 3-rd sub-cable stages before the squeezing process are 13.0, 28.2 and 3.9 mm, respectively. This result comes from that the tension acting on the strand is not enough large in fabrication of the cable.

It is also found the averaged contact lengths between strands in 1-st, 2-nd and 3-rd sub-cable stages after the squeezing process are 79.0, 58.9 and 16.4 mm, respectively. The squeeze process elongates the contact lengths between strands 2 to 5 times larger than those before the squeeze.

This allows us to conclude the squeeze process plays an important role to form the long contact length between strands and suggests a mechanism of generating the long time constants of more than 100s.

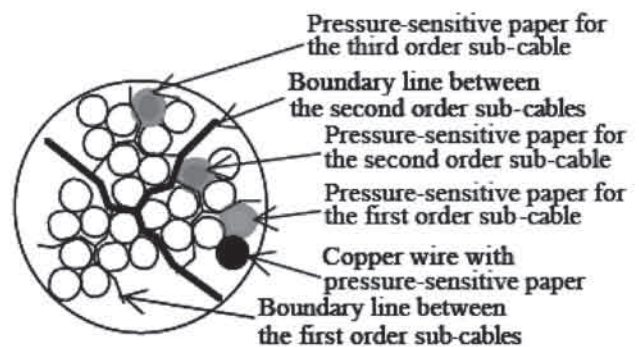


Fig. 1. Locations of pressure-sensitive papers on strand surfaces of all sub-cable stages.

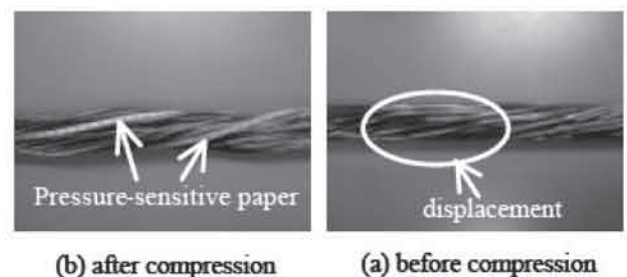


Fig. 2. Relative position between strands before and after compression.

References

- 1) Hamajima, T., et al., IEEE Trans. on Appl. Supercond. **13**, (2003) 2384
- 2) Tsuda, M., et al., IEEE Trans. on Appl. Supercond. **15**, (2005) 1533

§2. Experimental Plan of a 7-T Force-Balanced Helical Coil

Nomura, S., Ohta, Y., Hagita, T., Tsutsui, H., Tsuji-Iio, S., Shimada, R.

Force-Balanced Coil (FBC) is a helically wound toroidal coil that can minimize the required mass of its structure by selecting an optimal number of poloidal turns per toroidal turn. A 7-T Force-Balanced Coil (7-T FBC) was designed in order to demonstrate the feasibility of the FBC concept for high field superconducting magnets. Fig. 1 shows a schematic illustration of the 7-T Force-Balanced Coil (7-T FBC) using NbTi superconductor. The 7-T FBC with an outer diameter of 0.53 m will have 270-kJ stored magnetic energy at maximum magnetic field of 7.0 T. Based on the virial theorem, the maximum working stress of the 7-T FBC is estimated to be 52 MPa[1]. This stress is lower than the elastic limit of the Cu matrix so that the 7-T FBC can be excited up to the rated magnetic field of 7.0 T without reinforcing materials for the NbTi strand. Then the winding of the 7-T FBC will be carried out without reinforcing materials for the NbTi strand.

The winding form made of aluminum alloy is constructed by using a numerically controlled (NC) lathe as shown in Fig. 2. The NC lathe has 5 driving axes: a horizontal movement of the table (X axis), up and down movements of the spindle head (Y axis), forward and backward movements of the column (Z axis), tilting the table (A axis), and rotating the table (B axis). These axes are controlled by the NC data of the helical winding pitch.

The experiments will be conducted with pool boiling liquid helium cooling in order to measure the quench properties of the 7-T FBC and evaluate the working stresses in the helical windings. Fig. 3 illustrates a schematic diagram of the cryostat for the 7-T FBC. The 7-T FBC is set on the board made of fiberglass reinforced plastic (FRP). The liquid helium level is monitored with a level meter. If the 270-kJ stored energy of the 7-T FBC is discharged into the coil windings due to a quench, the evaporation of liquid helium is estimated to be 104 liters from the latent heat of helium (2.59 kJ/liter). In this case, the liquid helium level of the Dewar vessel is lowered by 280 mm because of 690-mm inner diameter of the vessel. Then, since the coil height of the 7-T FBC is 130 mm, the liquid helium level should be higher than 410 mm from the FRP board during quench tests in order to keep the pool boiling liquid helium cooling.

References

- [1] S. Nomura et al.: Construction of a 7-T Force-Balanced Helical Coil, IEEE Trans. Appl. Superconduct. **15**(2) (2005) 1911-1914.

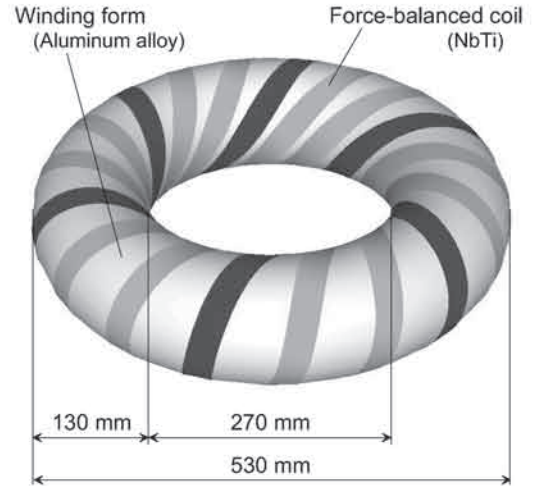


Figure 1: Schematic illustration of the 7-T force-balanced coil (7-T FBC).

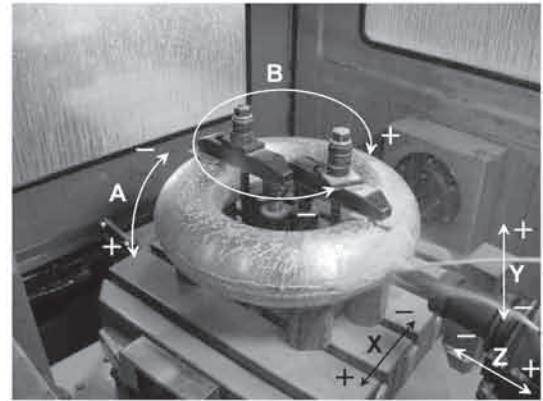


Figure 2: Construction of the winding form for the 7-T FBC by using a numerically controlled (NC) lathe.

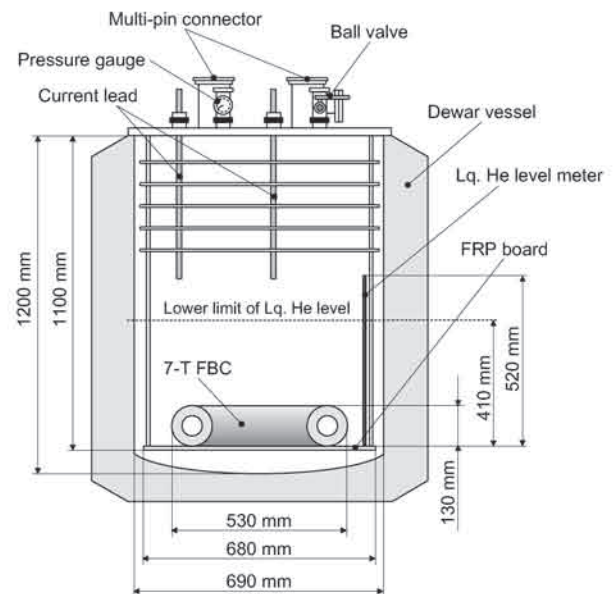


Figure 3: Schematic elevation view of the cryostat for the 7-T FBC.

§3. Study on Electrical Insulation Characteristics of Superfluid Helium

Hara, M., Suehiro, J. (Kyushu Univ.)
Yamada, S.

A superconducting coil of LHD is exposed to various stresses, such as a thermal, electrical or mechanical one. The LHD coil should be stably operated even under these stresses. In this project, the authors studied electrical insulation under practical coil operation conditions. One of the most severe causes of insulation degradation in the pool cooling SC devices is a foreign particle intruding into its insulation space during fabrication and operation. This year, special efforts were made to clarify behavior of contaminant metallic particle under high electric field in superfluid liquid helium as well as normal liquid helium. Effects of the particle shape were investigated in detail using spherical and cylindrical particles as model contaminants. Data obtained in this project would be useful for electrical insulation design of LHD coils. Main results are summarized as follows.

- 1) The metallic particle repeatedly moved between the upper and the lower electrodes before the electrical breakdown took place under high electric field. This suggested that the electrical breakdown could be considerably influenced by the particle.
- 2) The particle generated gaseous bubbles and micro discharge when it collided with the electrodes. Detail observation revealed that the bubble formation was due to kinetic energy of moving particle rather than electrical discharge energy.
- 3) The breakdown voltage of liquid helium contaminated with cylindrical particles was lower than that with spherical ones over the whole pressure range (Fig. 1). This seemed to be attributed to higher field enhancement effect of cylindrical particles with sharp edges.
- 4) The breakdown voltage of normal liquid helium was mainly determined by the discharge onset electric field strength E_o when the particle diameter was large and by the discharge propagation electric field strength E_p when the particle diameter was small (Fig. 2). On the other hand, the breakdown voltage of superfluid liquid helium did not show clear dependency on E_p and E_o , and seemed to be influenced by the other factor such as preceding corona discharge.

Reference

- 1) Hara, M., Maeda, Y., Nakagawa, N., Suehiro, J., Yamada S.: "DC Breakdown Voltage Characteristics in the Presence of Metallic Particles in Saturated Liquid Helium", Proc. of 2005 IEEE ICDL, pp.373-376 (2005)
- 2) Nakagawa, N. Maeda Y., Suehiro, J., Hara, M., Yamada, S.: "Breakdown Voltage Characteristics in the

Presence of Metallic Needle-Particles in Saturated Liquid Helium", Annual meeting record of IEEJ (2005)

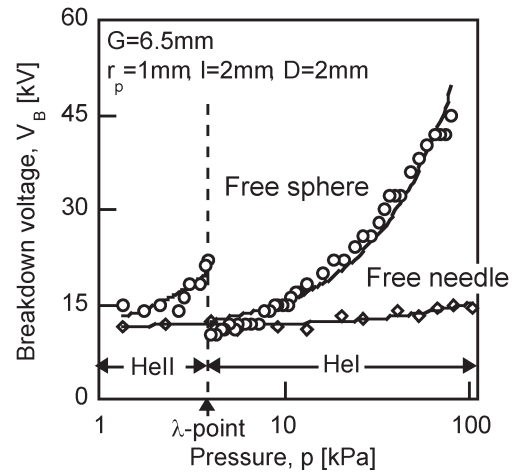


Fig. 1. Pressure dependency of the breakdown voltage of the liquid helium contaminated with a free spherical metallic particle or needle.

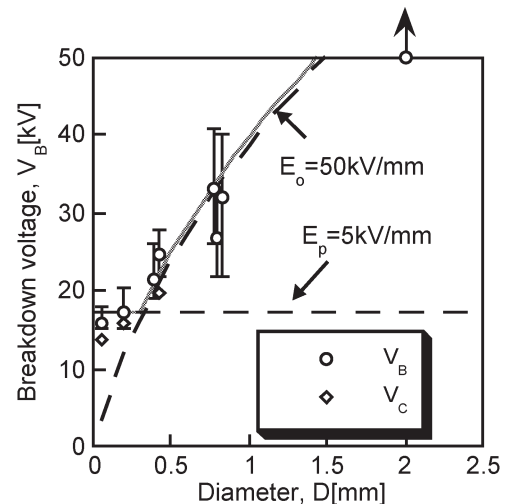


Fig. 2. Effects of needle tip diameter on the breakdown voltage (V_B) or corona onset voltage (V_C) of the normal liquid helium. E_o : Discharge onset electric field, E_p : Discharge propagation electric field.

§4. Database Development for He II-cooled Superconducting Magnet System Design

Haruyama, T., Kimura, N., Nakai, H. (KEK)
 Shintomi, T. (Nihon Univ.)
 Shiotsu, M., Shirai, Y., Hata, K. (Kyoto Univ.)
 Sato, A., Yuyama, M., Maeda, M. (NIMS)
 Mito, T., Yanagi, N., Maekawa, R., Iwamoto, A.,
 Hamaguchi, S.

i) Introduction

Recently, R&D and constructions of large superconducting magnet systems cooled with superfluid helium (He II) have been conducted. However, the database for the design of He II system has not been arranged systematically and is insufficient to be utilized. Therefore, it is important to integrate the required information to design large superconducting systems with the He II cooling.

We have arranged the database for He II, which researchers can use and apply for system design, from a large number of papers and from our complimentary experiments of He II. These works were performed with a Grant-in-Aid for scientific research of the MEXT for three years from year 2000 to 2003. Its continuous maintenance have been followed by the collaborative program of NIFS from 2003.

This group consists of four institutions of various fields: high-energy physics, applications of high magnetic field, power application, fusion science, and so on. Therefore, data from various field can have been integrated for the database.

ii) Arrangement of the database

In FY 2004, we integrated the database by searching and collecting data from literatures published after year 2000. New data of the number of 155 have been collected from accessible papers. Those data have been checked in the effectiveness and reliability, and the graphs, figures and required information have been selected for the database. The collected data are categorized as shown in Table I.

The utility of the database was also upgraded. User can search and access requiring data by key words. Moreover, the content of literature is completed for easy understanding of users requiring the data.

iii) Experimental studies for the He II database

We have performed the following supplementary experiments:

1. experimental and analytical studies on heat transfer in He II to apply to large super-conducting magnet systems,
2. pressure dependence of heat transfer function of He II,
3. heat transfer and boiling-off properties in He II.

By studies 1 and 2, we could make it clear that some phenomena are peculiar to large superconducting magnet systems cooled by He II. The pressure dependence of the heat transfer function could be revised to the more precise data by our experiments. Moreover, we could confirm reliability of some data in the database.

iv) Published papers

The following abstract was published.

1. T. Haruyama, et al., "Database development for He II-cooled superconducting magnet system design (2) – research results and DB publication-", Abstracts of CSJ Conference, Vol.70(2004), p. 35.

Table I Technical items for document

Head items	Items	Sub items
Heat transfer	He II pressurized	plate
		channel
	He II saturated	plate
		channel
System	Cryostat	
	Heat exchanger	JT HeIIp-HeIIs
	Pumping	vacuum pump cold compressor
	Materials	
Cooling technology	Measurement	temperature
		pressure
		flow rate
		level
		miscellaneous
	Special technique	seal miscellaneous
Operated cases	Refrigeration Magnet Magnet stability Conductor	

§5. Studies on the Mechanical Properties and Fracture Mechanisms of Single Crystal RE High T_c Bulk Superconductors

Katagiri, K., Kasaba, K., Shoji, Y. (Fac. Eng., Iwate Univ.)
Iwamoto, A., Mito, T.

Mechanical properties of high T_c RE123 (RE: rare earth elements) single-grain bulk superconductors, which have low thermal conductivity as well as high transport current and trapped field are important for their practical applications such as current leads for large scale devices. We have been studying the tensile and 3-point bending characteristics of RE123 bulks at room and cryogenic temperatures¹⁾. In this study, compressive mechanical properties and the fracture mechanisms of the bulk were investigated so as to obtain the directions of development of the bulk.

Specimens with the dimensions of $3 \times 3 \times 8 \text{ mm}^3$ were cut from a $\text{SmBa}_2\text{Cu}_3\text{O}_x$ (Sm211 mol. fraction 16.7%, 10wt% Ag addition), Sm123, with the dimensions of 45 mm in diameter and 15 mm in thickness samples such that the longitudinal (loading) directions of them corresponded to the direction of c-axis or perpendicular to the c-axis of the bulk samples. The compressive tests were carried out under the stroke control mode with the crosshead speed of 0.15 mm/min by using the 5 kN Shimadzu Autograph testing machine. By measurements through the wire strain gages adhered in the longitudinal and transverse directions adhered on the specimens, the elastic constants were also evaluated.

Elastic constants: As shown in Fig. 1, the initial part of stress-strain curves obtained from the compressive tests at room and 77 K were basically straight, and then some of them clearly deviated into concave to upward or jumped toward the strain axis beyond certain stress levels. They are thought to be resulted from the propagation of pre-existing cracks induced during the processing of the bulk. Due to the closure of the pre-existing cracks perpendicular to the c-axis in the specimens, the Young's modulus at 77K in the c axis direction, 93 GPa, was significantly lower as compared with that perpendicular to it, 150 GPa. Although the former was higher than that at room temperature, 75 GPa, the latter was lower than that at room temperature, 165 GPa. The Poisson's ratio obtained using the measurements on the strains transverse to the specimen are shown in Fig. 2. The anisotropy originated from the closure/opening behaviors of latent micro-crack perpendicular to the c-axis superposed on that intrinsic to crystal structural was clearly observed. This has to be taken into account in the thermal stress analysis.

Compressive strength: The fracture strength at 77K in the c-axis direction, 466 MPa, was higher than that, 368 MPa, in the direction perpendicular to it. This anisotropy

can also be comprehended by the existence of the micro-cracks; the reduction of the strength is associated with buckling to be described in the following. These are higher than those at room temperature, 350 and 335 MPa, respectively. These values are utilized as a database for designing current lead made of the bulk. Many of the test pieces loaded in the direction perpendicular to the c-axis fractured into 2 or 3 pieces separating along the cleavage plane. This means the buckling load controls the compressive strength. On the other hand, in the case of loading in the c-axis, they fractured into many small fragments.

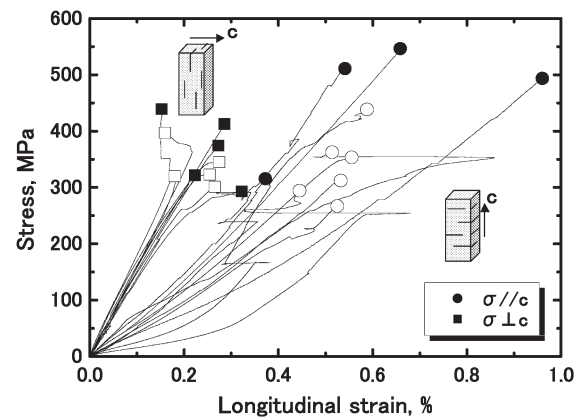


Fig.1 Compressive stress-strain curves of Sm123 bulk. (Open symbols and solid ones denote the fracture points at RT¹⁾ and 77K, respectively)

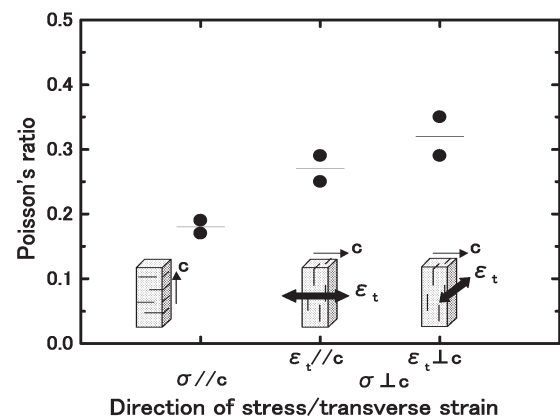


Fig.2 Anisotropy of Poisson's ratio of Sm123 bulk in compression tests (77K)

Reference

- 1) Katagiri, K., et al. Physica C **412-414**, (2004) 633.

§6. Development of a Current-Feed System with Low Heat Load Using a Pulse Tube Cooler

Maehata, K., Ishibashi, K. (Kyushu Univ. Eng.)
Matsubara, Y., Maekawa, R., Hamasaki, S., Mito, T.

In operating usual large superconducting magnets such as LHD coils, the high current of 10 kA class is supplied through current leads into the cryogenic region from a power supply located at room temperature. The heat leak from the current leads causes a large load of the refrigeration system. Therefore it is necessary to reduce the heat leak from the current leads with a minimum refrigeration load for a low cost and stable operation of the superconducting magnet system. Optimization methods have been studied for designing gas cooled current leads with copper conductor, and the heat leak into the liquid helium region is evaluated to be 1 W/kA for the optimum gas cooled current leads. Several types of high temperature superconducting (HTS) current leads were developed for further reduction of the heat leak. The HTS conductor is employed in the HTS current leads in the temperature region below ~ 50 K, while the copper conductor feeds the current from a room temperature to the HTS conductor. Although a large reduction in the heat leak has been demonstrated in the operation of the HTS current leads, large heat load to the refrigeration system is still generated in the conventional copper conductor part.

In this work, we apply advantageous characteristics of a pulse tube refrigerator to the copper conductor region of the 3kA HTS lead system for a reduction of the refrigeration load caused by with a compact structure.

Since the thermoacoustic effect is utilized for operation, the pulse tube refrigerator consists of a pulse tube, a regenerator and warm-and cold heat exchangers without moving element in the cryogenic region. Fig. 1 shows a schematic drawing of a pulse tube current lead. The copper-rod conductor is concentrically inserted into the pulse tube. In Fig. 1, geometrical dimension of the copper conductor was optimized for supplying current of 3 kA to a temperature of 80 K in the adiabatic condition. The heat leak through the copper rod is estimated to be 200 W at the cold end of 80 K. The heat leak of 200 W from the copper rod is removed by the cold heat exchanger in the pulse tube fridge. An advancing pressure wave is induced in the pulse tube by open-close operation of 4-valves. The refrigeration power is generated by the expansion-work in the cold region caused by the pressure wave. The high performance of the pulse tube refrigerator is obtained by modulating the phase of the pressure wave in the optimum inner volume of the tube. In this work, the inner volume of the pulse tube is optimized to be 650 cm^3 by employing numerical analysis of the dynamics of a virtual gas piston in the pulse tube. The cooling power is estimated to be 196 W at 80 K.

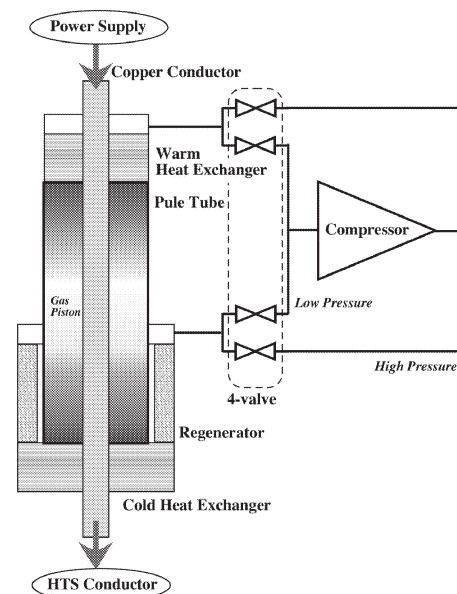


Fig. 1 Concept of the pulse tube current lead.

§7. Fundamental Study on Application of Magnetic Levitation Using YBCO Bulk Superconductor to Fusion Research

Tsuda, M. (Yamaguchi Univ.)
Hamajima, T. (Tohoku Univ.)
Ishiyama, A. (Waseda Univ.)
Noguchi, S. (Hokkaido Univ.)
Mito, T., Yanagi, N., Iwamoto, A.

For the application of HTS bulk to a spherical cryogenic target in a laser fusion system, stable levitation and large levitation force should be realized by a concentric spherical thin layer of HTS bulk. The stability of levitation has been already investigated in many kinds of HTS bulks both experimentally and theoretically. The most of investigations, however, are about disk-shaped bulks and the characteristics of levitation in a concentric spherical thin-shaped HTS bulk have not been investigated yet. The thickness of HTS layer in a spherical cryogenic target should be less than 100 μm and levitation force, larger than the weight of cryogenic target, should be produced in such the thin HTS layer. Since levitation force is closely related to supercurrent distribution, we prepared four types of cylindrical HTS bulk samples with the same outer diameter and height but different inner diameter to investigate influence of HTS layer thickness on levitation force. A spherical HTS bulk sample was also prepared to compare supercurrent distribution in the spherical bulk with that of disk-shaped one.

For high efficiency levitation of a cryogenic target with a thin HTS layer, supercurrent should be flowed in the whole HTS layer. When the supercurrent flows in the whole HTS layer, levitation force depends on the thickness and critical current density of the HTS layer. The critical current density can be estimated by both measurements and numerical simulations of levitation force and trapped flux density. Therefore, we measured the levitation force and trapped flux density as a function of coil current in field-cooling process in four types of cylindrical DyBCO bulks. The trapped flux density on a top surface of the bulk was measured by a hall probe at the coil current of 0 A. Then the levitation force was measured by a load cell as a function of the coil current. The height and outer diameter are 10 mm in the four DyBCO bulks, while the inner diameters are 5 mm, 6 mm, 7 mm and 8 mm. The inner and outer diameters and height of electromagnets were 200 mm, 500 mm and 55 mm, respectively.

An experimental result of trapped flux density as a function of coil current in field-cooling process is shown in Fig.1. The trapped flux density was almost proportional to the coil current in field-cooling process less than 6 A. The difference between applied magnetic flux density and trapped flux density gradually increased with the coil current in field-cooling process. Finally, the trapped flux density became almost constant as seen in Fig.1. The magnitude of the constant trapped flux density decreased with the inner diameter of DyBCO bulk. Independent of the magnitude of coil current in field-cooling process, the

levitation force was increased with the coil current after the field-cooling process. As observed in Fig.1, however, the increase of levitation force became smaller with the coil current, and finally the levitation force became constant. The magnitude of the constant levitation force decreased with the inner diameter of DyBCO bulk. The constant trapped flux density and levitation force mean that the DyBCO bulk was finally saturated by supercurrent; the maximum supercurrent flowed within the bulk when the trapped flux density and levitation force became constant. The maximum supercurrent depends on the thickness and critical current density of DyBCO bulk.

We also investigated stability, levitation force and trapped flux density in a spherical DyBCO bulk sample, 10mm in diameter. Anisotropy of critical current density may affect the stability, levitation force and trapped flux density. Therefore, trapped flux density and levitation force were measured in the following two cases: 1) the magnetic field was parallel to the c-axis of the bulk; and 2) the magnetic field was perpendicular to the c-axis. An experimental result of trapped flux density as a function of coil current in field-cooling process is shown in Fig.2. The trapped flux density as well as levitation force in the parallel magnetic field to the c-axis was much larger than that of perpendicular magnetic field. Stable levitation, however, was achieved in both cases; this means a spherical HTS bulk could be levitated stably independent of the directions of c-axis.

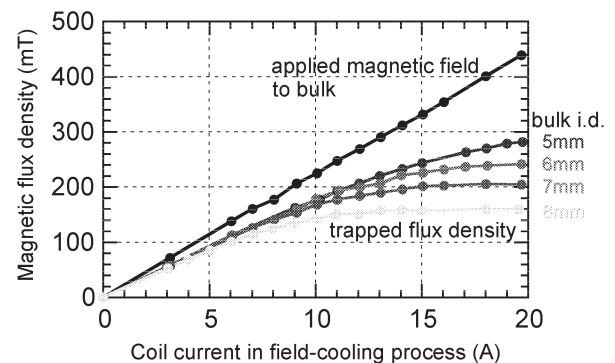


Fig. 1. Dependence of trapped flux density on coil current in field-cooling process in four types of cylindrical bulk samples.

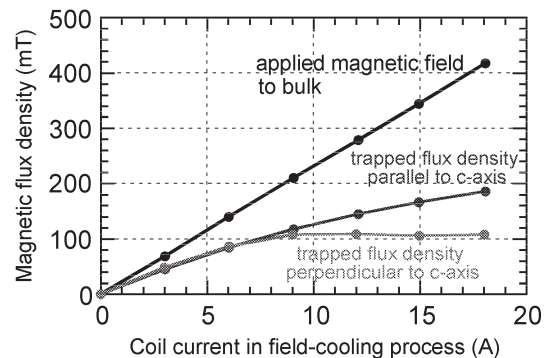


Fig. 2. Dependence of applied magnetic field direction against the c-axis of a spherical bulk sample on trapped flux density.

§8. Fundamental Study on Cryogenic Characteristics of SiC Power Device and Its Application to AC/DC Converter

Matsukawa, T., Ishida, M. (Dept. of Electrical and Electronic Eng., Mie Univ.)
Sato, Y. (Dept. of Electrical and Electronic Eng., Daido Inst. of Tech.)
Chikaraishi, H.

Fundamental Study on Improvement and Stabilization of Electric Power Quality by Flywheel Energy Storage System

Ishida, M., Matsukawa, T. (Dept. of Electrical and Electronic Eng., Mie Univ.)
Chikaraishi, H.

For application to flywheel energy storage system or magnetic field coil system of nuclear fusion experimental machine, its power supply has been constructed with the power electronics device as switching element of AC/DC converter, for example IGBT, GTO etc. As the large capacity power supply is required for such application in future, high efficiency and low operational loss of power supply are important issues. Especially, for high current operation of large capacity power supply, more efficient power electronics device than conventional one should be used. Recently, some advanced power electronics devices have been developed, which are based on crystallized SiC material or super junction type modified one based on crystallized Si material.

In our previous study, the Schottky Barrier Diode (SBD) based on crystallized SiC material was investigated in comparison with conventional Si-based SBD. In this study, the super junction type power-MOSFET is investigated, which is one of unipolar power electronics devices and an advanced device based on crystallized Si material. Power-MOSFET is well known device to be applied to high efficient power supply, not so large capacity one. To use power-MOSFET for large capacity power supply, it is required that its on-state resistance is lowered with high withstand voltage specification.

The super junction type power-MOSFET is one of advanced power electronics devices to achieve lower on-state resistance value in higher voltage region. The static voltage-current characteristics and the on-resistance value are investigated with SPA20N60C3 (650V, 20.7A) and the temperature dependence of the voltage-current characteristics is clarified. Considering to cool down the power electronics device for high current operation, the static voltage-current characteristics are measured in room and liquid nitrogen temperature. Main results are summarized as follows.

- (i) The on-state resistance value in room temperature is about 0.16 ohm. (See Fig. 1)
- (ii) The on-state resistance value in liquid nitrogen temperature is about 0.035 ohm, which is 20 % of that in room temperature approximately. (See Fig. 2)
- (iii) The built-in voltage of body diode of power-MOSFET is about 0.7 (V) in room temperature and about 1.0 (V) in liquid nitrogen temperature respectively.

As the measured result of voltage-current characteristics of super junction type power-MOSFET, the reduced on-state resistance in liquid nitrogen temperature can promise to conduct high current without increasing the operational loss of AC/DC converter. Furthermore, SiC-based power-MOSFET would be expected to show the same trend of static voltage-current characteristics as that of Si-based power-MOSFET and to contribute to high efficiency operation of large capacity power supply.

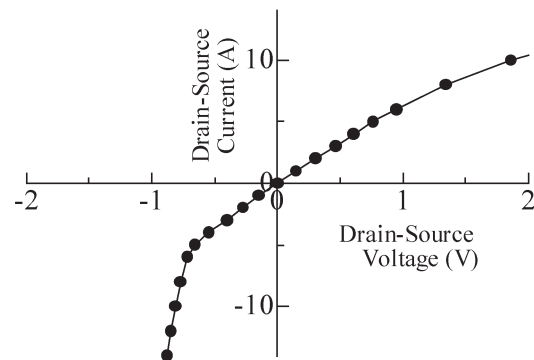


Fig. 1. The static voltage-current characteristics of super junction type power-MOSFET(SPA20N60C3) in room temperature

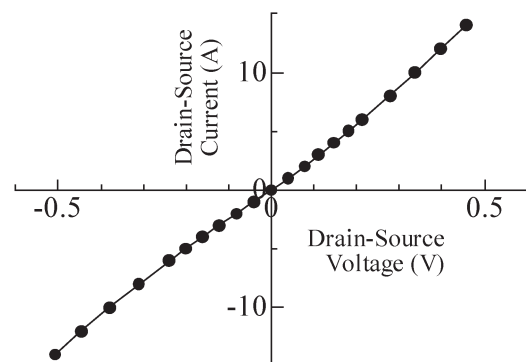


Fig. 2. The static voltage-current characteristics of super junction type power-MOSFET(SPA20N60C3) in liquid nitrogen temperature

§9. Research and Development of Small General-purpose Pressure Sensor in Cryogenic Environment

Kimura, N. (High Energy Acc. Research Org.)

1. Introduction

In the LHD secondary project, it is planned that subcooled helium below 4K is utilized for cooling the helical coil that should generate the stable high magnetic field. If the small pressure sensor, that can use *in-situ*, is located at the cooling channel of the helical coil and the pressure variation can be measured directly, it is thought that the characteristic of the coolant can be evaluated from the aspect of the pressure. And the behavior of the coolant in case of pre-cooling or warming up of the helical coil can be measured in more detail. Furthermore, in the case of quench, it is expected to detect the detailed appearance of the local pressure variation of the coolant and the generation of quench.

Recently, however, the manufacturing of the small general-purpose pressure sensor usable in cryogenic¹⁾ was discontinued. Now, such a pressure sensor can not be obtained. The purpose of the present study is the research and development of the new pressure sensor that is small, high sensitive and usable *in-situ* and cryogenic environment. This study is developed based on the result of the characteristic test on the current pressure sensor.

2. Pressure sensor

The picture of the pressure sensors is shown in Fig. 1. In this picture, shown in the right is a pressure sensor (KH18) manufactured by NAGANO KEIKI and used in the present study, and shown in the left is a pressure sensor (KPY18) manufactured by SIEMENS for reference. The pressure sensor was selected on the following condition.

- (a) It must be an absolute pressure type sensor.
- (b) It must be an all-metal chassis.

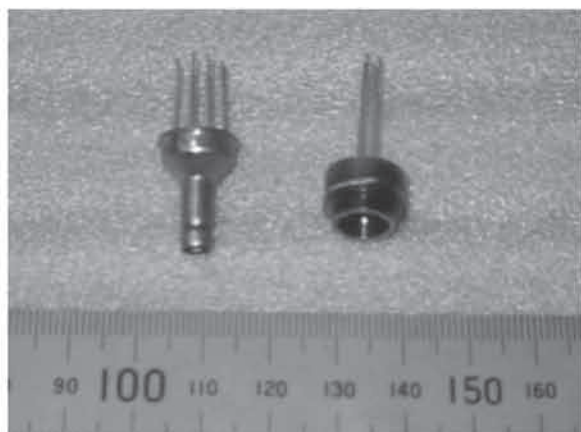


Fig. 1 Picture of the pressure sensors. Left: SIEMENS KPY18, Right: NAGANO KEIKI KH18.

Table 1 Specification of the pressure sensor.

Items	Specification
Sensor type	absolute pressure
Diaphragm	Stainless steel 630
Pressure Range	0~0.5 MPa
Output	60mV±25mVDC
Power Source	5 VDC
Weight	5 g

(c) Taking out the lead line must be a hermetic seal structure.

(d) It must be small size and lightweight.

The specification of the pressure sensor is shown in Table 1.

3. Experimental procedure and results

First, the resistance-temperature characteristic of the semiconductor strain gauge that is the pressure-sensitive device of the sensor was examined. The measurements were conducted at the room temperature (300 K), liquid nitrogen (77 K) and liquid helium (4.2 K). From this result, the characteristic in cryogenic can be estimated.¹⁾

Next, in the cryogenic temperature region, the variation of the sensor output with the pressure was measured. The measurement was conducted in saturated liquid helium. The result is shown in Fig. 2. It is seen that the variation of the pressure sensor output is proportional to the variation of the liquid helium pressure.

4. Summary

The product that could be used under the low temperature was selected about a pressure sensor on the market. And the characteristic test under the cryogenic temperature including the superfluid helium temperature field was conducted. It was confirmed that the variation of the sensor output was proportional to variation of the pressure even in the cryogenic temperature region from 4.2 K down to 2.17 K. In future, the characteristic of the pressure sensor will be measured in more detail, and small size and high sensitive pressure sensor will be developed.

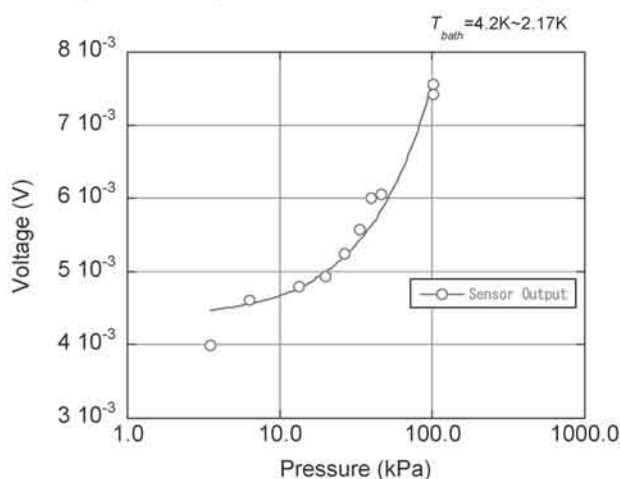


Fig. 2 Relation between pressure in cryostat and the voltage output of the pressure sensor.

Reference

- 1) Haruyama, T. et al. Adv. in Cryog. Eng. **43A** (1996) 781

\$10. Development of Observation and Diagnosis Systems for Superconducting-coil Operations Using the Poynting Vector Method

Sumiyoshi, F., Kawabata, S., Kawagoe, A.
(Kagoshima Univ.)
Kawashima, T. (Fukuoka Jo Gakuin Univ.)
Mito, T.

For the operation of devices composed of several superconducting coils, a system which can detect the abnormal conditions produced at one part of the coils and diagnose the conditions of the coils after maintenance is of considerable importance. The purpose of this study is to develop a system which can observe and diagnose coils in devices composed of several coils and electrically measure the losses in the coil by measuring the Poynting vectors around the coil. We have already clarified that our proposed system can measure the losses in both a normal conducting coil and in the individual coils of a device where two coils are combined. In order to investigate whether the system can measure ac losses in superconducting coils, measurement of the distributions of Poynting vectors and ac losses in the Bi-2223 sample, which were wound loosely into a single layer solenoidal coil shape with a Bi-2223 multifilamentary tape, were carried out.

As shown in Fig. 1, the sample was wound into a solenoidal coil shape with long length necessary for measurements. We measured Poynting vectors on the inner and the outer surfaces near the center of the sample coil for a few turns. The measurements were carried out by using the pairs of pick up coils and potential leads which were set as shown in the figure. And the Poynting vectors were locally measured along the coil axis by moving these pairs between 1 pitch length of the sample coil, and then losses were calculated from the summation of all Poynting vectors. The Bi-2223 multifilamentary tape of 1m in length, 3.8mm in width, 0.21mm in thickness, was wound on a bobbin of 80mm in outer diameter into a solenoidal coil, with 10mm pitch, and 4 turns. Furthermore, the current leads of the Cu wires were wound in series at both ends of Bi-2223 tape into a solenoidal coil shape with the same pitch as Bi-2223 tape. In order to discuss the measured distributions of the Poynting vectors, we also measured two dummy samples wound with Cu tape of 4mm width, 1.5mm thickness, and stainless steel tape of 4mm width, 0.2mm in thickness.

Figure 2-a shows the measured results of Bi-2223 tape in the external magnetic fields of 20mT in amplitude, 20Hz in frequency. The measured Poynting vectors around the Bi-2223 sample are shown by circle symbols. From 4mm to 8mm, the range of width of the Bi-2223 tape, the observed Poynting vectors are large. This indicates the possibility of identifying the points at which large energy flows exist. Calculated ac losses from these

Poynting vectors agreed with theoretical values.

The profile of Poynting vectors is sloped. In order to discuss the slope, measurements were carried out on dummy samples. The square symbols in Fig. 2-a represent the measured data on the Cu sample. As the resulting slope of the profiles of Poynting vectors is the same as the Bi-2223 sample, it is found that the slope is not a characteristic of the Bi-2223 tape. Fig. 2-b shows the results on the stainless-steel sample. The measured data is considered not to be the signals of the sample itself, because the losses in the stainless steel sample are smaller by five orders of magnitude than that of the Bi-2223 sample and Cu sample. We found that a slope similar to the Bi-2223 sample and the Cu sample exists on the stainless-steel sample. In addition, for the results at room temperature, which are shown by circle symbols in the figure, the slope of Poynting vectors become small compared with the results at 77K. From the above mentioned it is clear that the slopes of the profiles of Poynting vectors are signals which are produced by the measuring system, in particular the Cu magnet to apply the external magnetic fields to the sample. Accordingly, measurements of Poynting vectors can give us not only ac losses but also some information on the location of existing energy flow. It was found that our system has the potential to be applied to an observation and diagnostic system for large-scale coils.

References

- H. Kasahara, et al., IEEE Trans. Appl. Supercond., Vol. 14, No. 2, pp. 1078-1081.
- Y. Kawabata, et al., Abstracts of CSJ Conference, Vol. 71, p. 126 (2004).

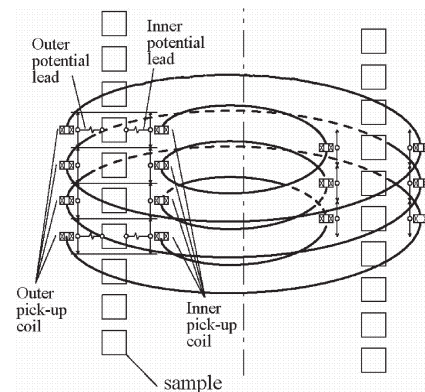


Fig.1 Apparatus of the Poynting vector method

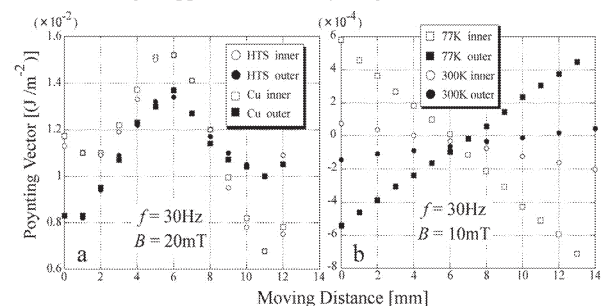


Fig. 2 Profiles of Poynting vector around a sample in external ac magnetic fields, a - HTS and Cu tapes, b - SUS tape

§11. Basic Research on the Oxide Superconductors for Fusion Reactors

Iwakuma, M. (Kyushu University)
Mito, T.

1. Introduction

To develop oxide superconducting magnets for fusion reactors, it is necessary to grasp the basic electromagnetic properties of oxide superconducting wires in detail. Oxide superconducting wires are usually deformed into thin tapes and have the anisotropy in ac loss property. This year we investigated the field angular dependence of the ac loss in YBCO superconducting thin tapes theoretically and experimentally. We report the results.

2. Theoretical expression of the field angular dependence of the ac loss

We studied the field angular dependence of the ac loss in YBCO superconducting tapes on the basis of their electromagnetic properties and derived the following theoretical expression by which we can estimate the ac loss for any field angle θ by using the observed ac loss in a perpendicular magnetic field to the wide surface,

$$W(B_m, \theta, n) = \begin{cases} W(B_m \sin \theta, 90^\circ, n) & \text{for } B_m < B_{pe}' \\ W(B_m, 90^\circ, n) \sin \theta & \text{for } B_m \geq B_{pe}' \end{cases}$$

where B_m is the field amplitude and B_{pe}' is the effective penetration field and n is the number of stacked tapes.

3. Ac loss measurement

We measured the ac loss by using a saddle-shaped pickup coil as shown in Fig.1. We prepared a 6-tape stack. Sample YBCO tapes with a length of 60mm were inserted into the center of a pickup coil. Kapton sheets with a thickness of 50 μ m were inserted between the tapes for insulation. Magnetic field angle was changed by rotating the sample around its axis. The characteristics of sample YBCO tapes are listed in Table 1. They were fabricated by a IBAD-PLD technique. Ac loss measurement was carried out at 77K in LN₂.

Observed field amplitude dependencies of the ac losses are shown in Fig. 2 with a parameter of field angle θ . We can see that the ac loss decreases with decreasing field angle monotonically for any amplitude. The lines represent the theoretically estimated ac losses by using the observed ac losses in a perpendicular field, that is $\theta=90$ deg.. You can see that the estimated ac losses agree with the experimental ones for the whole-range of field amplitude. The validity of the derived theoretical expression was verified.

Table 1 Characteristics of a YBCO sample wire

Width	10mm
Substrate	Hastelloy
Thickness of	
Silver layer	10 μ m
YBCO layer	0.5 μ m
Buffer layer	1 μ m
Substrate	100 μ m
$I_c(77K, 0T)$	48A

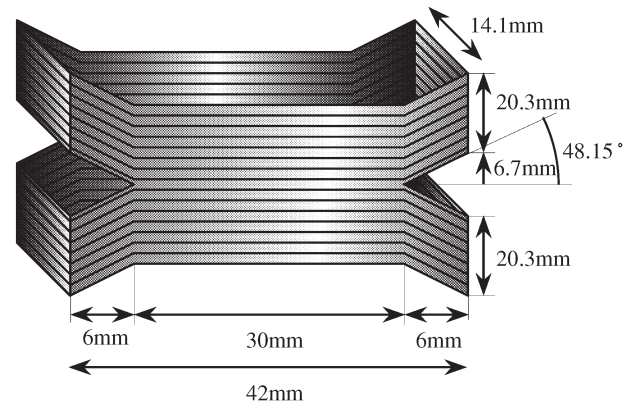


Fig.1 Dimensions of a saddle-shaped pickup coil.

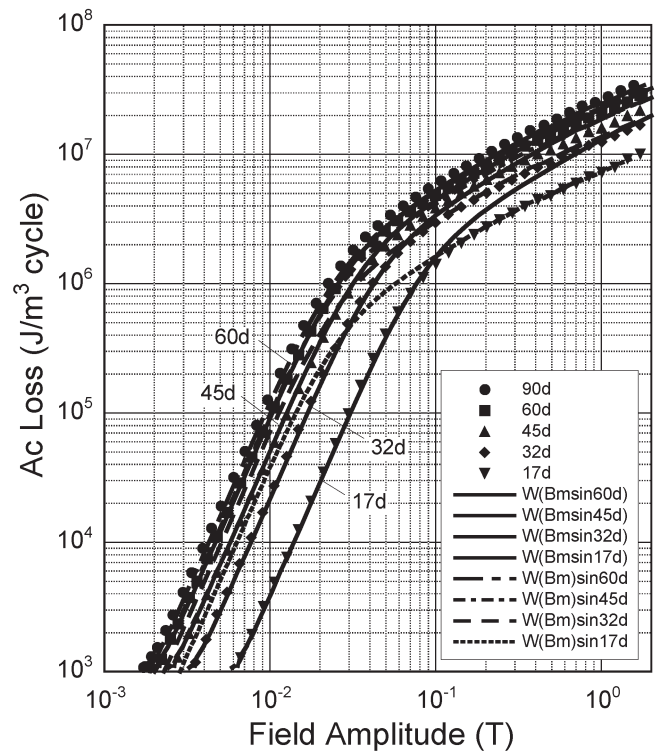


Fig.3 Amplitude dependencies of the ac losses in a YBCO 6-tape stack.

§12. Effect of the Phase Transition on Heat Transfer in He II

Kobayashi, H. (Inst. Quantum Sci., Nihon Univ.)

If a good conductor such as stabilizer for a superconductor is cooled in a narrow two-dimensional channel filled with the pressurized He II (He II_p) the hottest place on the heated surface is covered with He I above the critical heat Q_λ at which He II changes into He I locally¹⁾. By the localized insulation of He I induces the intermediate state in which the gradual transition appears in steady heat transfer characteristics. During the area of He I grows with the increase in heat Q , He II keeps on cooling the rest of the surface, since some heat in the good conductor would bypass the thermally insulated area behind the He I layer.

The intermediate state comes out similarly in He II (He II_s) below the λ -point pressure P_λ where no subcooled He I exists in the phase diagram in equilibrium. The superheated He I followed by the superheating in He II²⁾ covers the hottest spot. Thus the superheating brings about an equivalent critical heat Q_λ obtained in He II_p. The narrow two-dimensional channel used in this experiment is schematically shown in Fig.1. The copper disk of 17 mm in diameter and 13 mm long is heated from the bottom. The channel gap is changed from 0.15 mm to 0.1 mm. Figure 2 shows an example of heat transfer characteristics indicating the temperatures T_{c1} of the copper near the center and ΔT_1 ($=T_{c1}-T_b$) of He at the centers. Since the superheating reaches the extended λ -temperature (T_λ) below the λ -point pressure, thus Q_λ is also equivalent to that obtained in He II_p as seen in the bath temperature T_b dependence of Q_λ (Fig.3).

The bypass effect due to the large heat conduction of the copper as well as that of He II seems to stabilize apparently the metastable superheating so that the non-boiling Kapitza state is sustained up to Q_λ . Not the saturation temperature but T_λ determines Q_λ also in He IIs. In addition to the enlargement of Q_λ , the localized pseudo periodic film boiling⁴⁾ ignited at another critical heat flux Q_n restricts the temperature rise of the copper disk after onset of vaporization. The vapors destructs the superheating distributed over the heated surface in the channel. Above Q_λ to Q_{max} the temperature of the copper disk is restricted below 3 K level without the transition to the entire film boiling. This is different from the fact that the transition to the film boiling at Q_n in He II_p is unavoidable.

References

- 1) Kobayashi, H. et al.: Cryogenics **37** (1997) 851
- 2) Nishigaki, K. et al.: Phys. Rev. **B33** (1986) 1657
- 3) Rybaryk, L.J. et al.: J. Low Temp. Phys. **43** (1981) 197
- 4) Gentile, et al.: Cryogenics, 234 (1981)

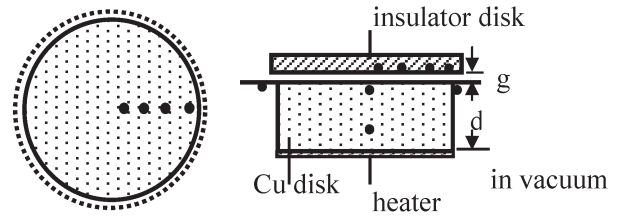


Fig.1. Schematics of the circular parallel channel. The top view of the channel, D : 17 mm, 13 mm thick. The side view, d : 0.15~0.3 mm channel gap. The points indicate the positions of the thermometers along the diameter of the circular parallel channel.

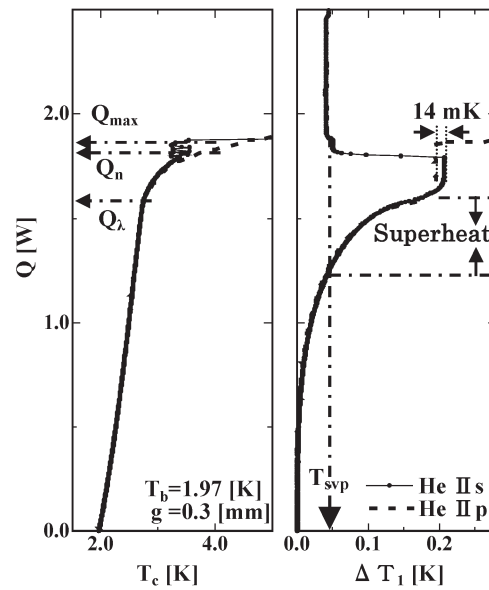


Fig.2. Temperature rises in T_{c1} and ΔT_1 as a function of heat Q .

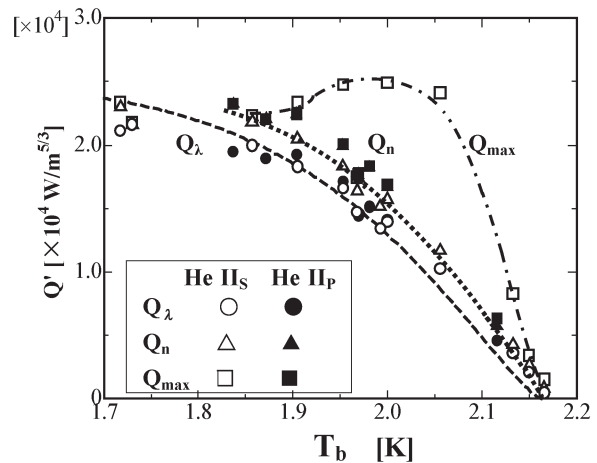


Fig.3. Bath temperature dependence of critical heat flux Q_λ ($= G \cdot Q'_\lambda$), G : Factor of the channel geometry

§13. Composite Electrical Insulation and its Reliability at Cryogenic Temperature for LHD

Nagao, M., Hozumi, N., Murakami, Y.
(Toyohashi University of Technology)
Hara, M., Suehiro, J. (Kyushu University)
Kosaki, M. (Gifu College of Technology)
Shimizu, Y., Muramoto, Y. (Meijo University)
Mizuno, Y. (Nagoya Inst. of Technology)
Minoda, A. (Matsue College of Technology)
Yamada, S. (National Institute of Fusion Science)

The world's largest class superconducting coil is used for the "Large-scale Helical Device". Its electrical insulation system might be exposed to considerably severe multiple stresses including cryogenic temperature, large mechanical stresses and strong magnetic fields. It is therefore very important to study its electrical insulation performance under these severe conditions in order to establish the reliability of the coil. If a superconductor quenches from superconducting state to normal state, the liquid coolant vaporizes very easily and turns into high-density gas at cryogenic temperature, which may reduce its withstanding voltage. Furthermore, it is very difficult to completely remove minute gaps from the insulated space. So it is required to clarify the influence of minute gaps and electrification on the insulation performances.

1. Influence of Micro-bubble on Breakdown Voltage of Electrode System Imitated Minute Gap in LN₂

This research was conducted using electrode system that simulated the insulation system included minute gaps to investigate the behavior of micro-bubble with the breakdown characteristics of insulation in LN₂. Fig.1 shows electrode system arrangement.

The breakdown voltage of insulation system that has a minute gap is shown in Fig.2. The breakdown voltage was measured by changing the angle of electrode to buoyant force with minute gaps and without minute gaps. The breakdown voltage increased with increase of the cooling time in all cases. When an angle is 0-degree that buoyant force direction and electric field direction are the horizontal, the breakdown voltage with minute gaps is smaller than it without minute gaps. The tendency is also same with an angle of 90-degree that buoyant force direction and electric field direction are the perpendicular. It is considered that micro-bubble agglomerates in minute gap and the agglomeration of the micro-bubble encourage the electric breakdown.

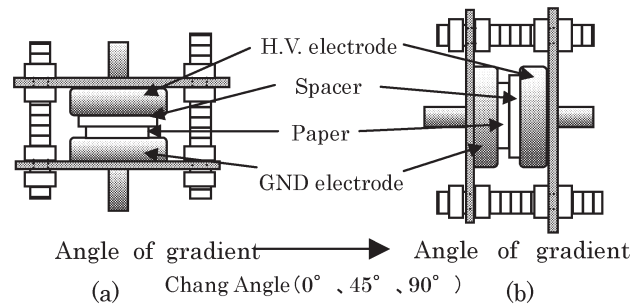


Fig.1 Electrode system arrangement

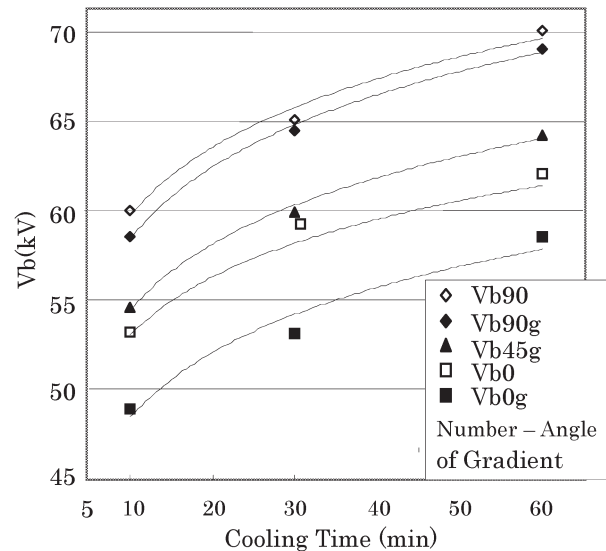


Fig.2 Influence on breakdown voltage by difference between gap position and angle of gradient

2. Effect of surface electrification on flashover voltage of polymeric rod immersed in liquid nitrogen

Flashover voltage of acrylic rod (20mm in diameter and 5mm in length) between disk electrodes of 30mm in diameter was measured in liquid nitrogen by increasing applied ac voltage till flashover occurred.

Two kinds of pre-treatments were made for the rod. One is cleaning of a rod surface with alcohol in order to remove surface charge, which was confirmed with surface potential meter. The other is rubbing a rod with a cloth in order to produce surface charge artificially.

Flashover voltages of alcohol-cleaned samples were higher than those of rubbed ones. The result may be attributed to enhancement of local electric field caused by surface charge of the sample.

Reference

- 1) Shimomura, M., Murakami, Y., Hozumi, N., Nagao, M., Minoda, A., Muramoto, Y., Kosaki, M. & Yamada, S., 2005 National Convention Record I.E.E. Japan, No. 2-071 (2005)
- 2) Okada, H., Noda, T., Mizuno, Y. and Minoda, A., 2005 Annual meeting record IEE JAPAN, Vol.2, p.86, 2005.

§14. Design and Optimization of High T_c Superconductors for Current Lead Application

Yamada, Y., Watanabe, M., Ohkubo, J., Tachikawa, K. (Tokai University)
Tamura, H., Mito, T.

High temperature superconductors HTS can be synthesized through the two components diffusion process in an appreciably shorter reaction time than that of the HTS prepared by the conventional sintering process. In the Bi-Sr-Ca-Cu-O system, a thick and homogeneous HTS layer of Bi₂Sr₂CaCu₂O_{8+x} (Bi2212) is easily synthesized by the diffusion reaction between Bi-free Sr-Ca-Cu oxide substrate and Bi-Cu oxide coating¹⁾. In the present study, scaling-up of the specimen dimension and the transport current performance of Bi2212 HTS conical tubular bulk specimen will be reported. Referring to the transport performance and heat load due to the Joule heating at the joint and heat leakage through the bulk specimen, the Bi2212 HTS cylinders synthesized by the diffusion process seem to be promising for a current lead in both cryocooler-cooled superconducting magnets²⁾ with small allowable heat load and conventional superconducting magnets with large transport current³⁾⁴⁾.

Fig. 1 schematically shows the preparation procedure of Bi2212 HTS conical tubular specimen through the diffusion process. The substrate is composed of Bi-free Sr-Ca-Cu oxide with the composition ratio of Sr:Ca:Cu = 2:1:2. The calcined Sr-Ca-Cu oxide powder was formed into conical tubes 37/29 mm in outside/inside diameter at the larger end, 27/19 mm in outside/inside diameter at the smaller end, and 200 mm in length by cold isostatic pressing. It was then sintered at 1020°C in open air. The coating is composed of Bi-Cu oxide with the composition ratio of Bi:Cu=2:1. The calcined Bi-Cu oxide powder with 30wt%Ag₂O addition was mixed with wax to form slurry, and was coated around the conical substrate. The diffusion reaction was performed at 850°C for 20h in open air to produce the Bi2212 HTS layer about 150 μm in thickness around both outside and inside of the conical tubes. Ag added to the coating accumulates on the surface of the specimen after the reaction. Then, the Ag paste was coated around both ends of the diffusion specimen, and was heat-treated at 800°C in air to form the Ag contacts.

The transport performance for the Bi2212 HTS specimen at 4.2K and self-field is shown in Fig. 2. No voltage on the HTS part (between V2 and V4) was generated at a transport current of 6,500A. The HTS voltage appeared at near 6,800A, and a voltage of 40 μV on HTS part was generated at 7,000A which corresponds to the current density of 32,000A/cm². The voltages of both joints increased with increasing transport current, and were 450 μV at lower joint (V4-5) and 90 μV at upper joint (V1-2)

after reaching 7,000A.

The temperature dependence of transport current of the conical specimen at upper end warmed up by the attached resistive heaters was measured. The transport current decreases with increasing temperature, and is about 6,300A at 20K or 3,200A at 40K.

The total heat loads composed of heat leakage conducted through the tube and joule heating at the joint are estimated to be about 320 mW at 3,000 A between the warm end of 42 K and the cold end of 4.2 K, and is 400 mW at 2,000 A between 50 K and 4.2 K, respectively. Present Pb-free Bi2212 conical tubes seem to be promising as large transport current leads with small heat loads for superconducting magnets.

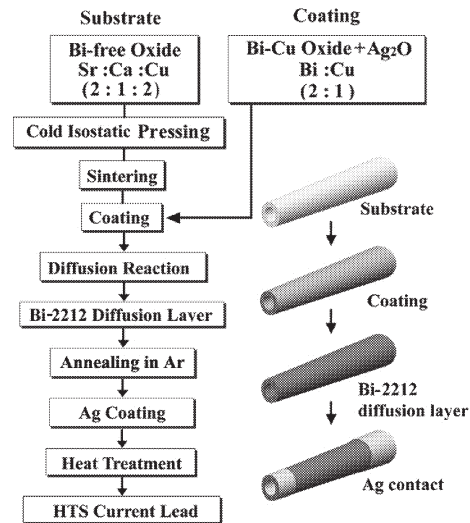


Fig. 1. Preparation procedure of the Bi2212 HTS conical specimen by the diffusion process.

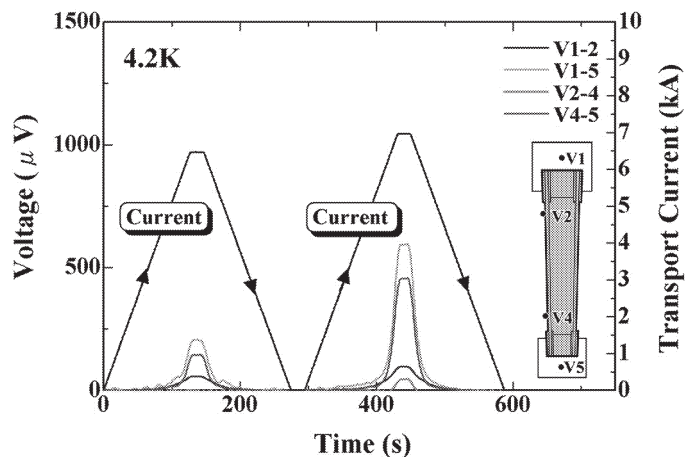


Fig. 2. Transport current performance of the Bi2212 HTS conical conductor at 4.2 K.

References

- 1) Yamada, Y. et al. : Adv. Cryo. Engr., 44 (1998) 547.
- 2) Watanabe, K. et al. : Cryogenics., 34 (1994) 639.
- 3) Yamada, Y. et al. : IEEE Trans. Appl. Supercond., 14 (2004) 638..
- 4) Tamura, H. et al. : IEEE Trans. Appl. Supercond., 14 (2004) 686.

\$15. Development of Conduction-Cooled LTS Pulse Coil

Mito, T., Chikaraishi, H., Maekawa, R., Baba, T., Yokota, M., Morita, Y., Ogawa, H., Yamauchi, K., Kawagoe, A., Sumiyoshi, F. (Kagoshima Univ.), Iwakuma, M. (Kyusyu Univ.), Henmi, T. (Graduate Univ. for Advanced Study), Okumura, K. (Technova), Abe, R. (Shibuya Kogyo Co.)

We have been developing a 1 MW, 1 sec UPS-SMES for a protection from a momentary voltage drop and an instant power failure. A conduction-cooled low temperature superconducting (LTS) pulse coil has excellent characteristics, which is adequate for a short-time uninterruptible power supply (UPS). The LTS coil has better cost performance over the HTS coil and the conduction cooling has higher reliability and easier operation than the conventional cooling schemes. To demonstrate the high performances of the LTS pulse coil is a key technology of the UPS-SMES, we have fabricated a prototype LTS pulse coil with stored energy of 100 kJ and have conducted cooling and excitation tests.

The coil was wound with a circular cross sectional high specific heat conductor, consisting of an NbTi compacted strand cable extruded with low purity aluminum. The conductor was wound while twisted along with the direction of the coil's magnetic field, reducing the AC loss. The prototype 100 kJ class conduction-cooled LTS pulse coil retained the structure of a GFRP frame and used a coiling wire of NbTi/Cu formed strands. They had an outer diameter of 5.9 mm, coated in a circular cross sectional aluminum through Kapton tape acting as electrical insulation. The coil has a total of 67 turns x 14 layers while twisting the conductor, thus forming a coil section 303 mm in the inner diameter, 516 mm in the outer diameter, and 409 mm in length. Figure 1 shows the inner structure of the coil. Once the initial winding layer is complete, a spacer made of Dyneema FRP (DFRP) and a Litz wire are alternately inserted between layers in the circumferential direction. The heat flow through the longitudinal direction of the coil is secured by Litz wires. Figure 2 shows the structure of the cooling and excitation test apparatus. Two GM cryocoolers are applied to generate 3 W of cooling capacity at 4K and 120 W at 50K, respectively. Through the Litz wire withdrawn from the coil edge, the coil is conductively cooled to 4K, while the low and high temperature ends of the high temperature superconducting current lead, accepting a rated current of 1000 A, are also cooled by conduction.

The coil was cooled from 300 K to 4 K within 3 days, which indicated the excellent thermal characteristics of this coil. Steady-state operation at the rated current of 1000 A was verified and over current test of 1230 A was also confirmed. Current shut-off test from 1230 A with a time constant of 1.37 s was successfully performed without normal transition. The temperature rise in the coil was limited to 0.8 K, which indicated a sufficient safety margin

for the rated pulse discharge from 1000 A to 707 A in 1 sec. Repeated excitation of a triangular waveform with the peak current of 1000 A and ramp rate of 50 A/s was also tested. The temperature rise in the coil was limited to 1.1 K, which shows availability of continuous pulse operation because of the outstanding heat removal characteristics of this coil.

The developed conduction cooling LTS pulse coil is applicable not only to the SMES for compensating for instantaneous voltage drops but also to various uses of the superconducting coil which require pulse excitation. Accordingly, the extended applications are likely to open up for the previously limited usage of the superconducting coil.

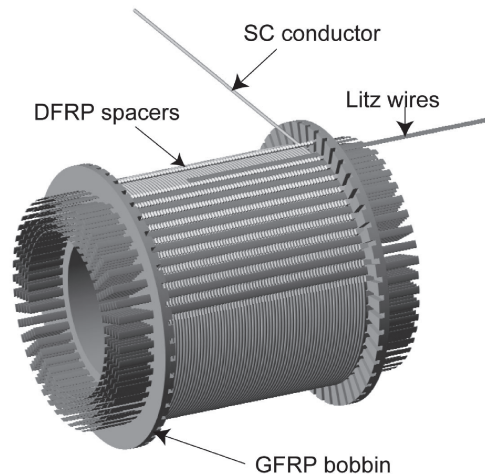


Fig. 1. Structure of conduction-cooled LTS pulse coil.

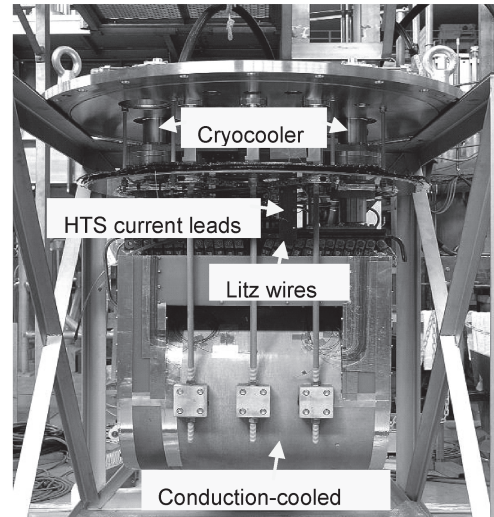


Fig. 2. Cooling and excitation test apparatus for conduction-cooled LTS pulse coil.

References

- 1) T. Mito, et al., "Development of UPS-SMES as a Protection from Momentary Voltage Drop", IEEE Trans. Appl. Supercond, Vol. 14, No. 2, (2004), pp. 721-726.
- 2) T. Mito, et al., "Prototype Development of a Conduction-Cooled LTS Pulse Coil for UPS-SMES", IEEE Trans. Appl. Supercond, Vol. 15, No. 2, (2005), pp. 1935 -1938.

\$16. Cryogenic Stability of the Model Coil of the LHD Helical Coil in Saturated Helium

Imagawa, S., Yanagi, N., Hamaguchi, S., Mito, T.

The LHD helical coils have been operated below 90% of the design current because normal-zones have seldom propagated at almost the same current. It is planned to improve the cryogenic stability by lowering the inlet temperature. In order to estimate the effect, a model coil was made of the same conductor as the helical coil.¹⁾ The first cool-down and stability tests were carried out without a thermal shield on the coil. In the second cool-down, a thermal shield with multi-layer insulators was added to reduce the heat load to a coil. Furthermore, the third cool-down and stability tests were carried out to examine uncertainty of stability in saturated helium and to confirm the reproducibility in subcooled helium.

The magnetic field becomes the highest at the middle turn of the first layer, which is the testing region for the cryogenic stability. The value is 6.9 T at 13 kA, same as the LHD helical coil. The wetting surface fraction of the first layer is 67%, same as the highest field turns of the LHD helical coil. Liquid helium is supplied from the bottom of the coil and exhausted through the coil-leads pipe to a current-leads tank, the pressure in which is 0.12 MPa. The inlet helium is subcooled by a pre-cooler. Tape heaters are inserted between the conductor and the layer-to-layer spacer for initiating a normal zone. The heater at the bottom of the middle turn of the first layer was used. The propagation was detected by voltage taps.

At first in the third cool-down, the stability test in saturated helium was executed after the model coil had been immersed with liquid helium and 24 hours or more passed. The next day, the stability test in saturated helium was executed again after the stability in subcooled helium of 3.5 K had been examined. The result is shown in Fig. 1(a). It is understood that the stability of the model coil in saturated helium was greatly improved after once being cooled down to the lower temperature. The result in the second cool-down is shown in Fig. 1(b) for the comparison. In that case, the stability test in subcooled helium of 3.5 K was executed at first. The temperature was raised up gradually, and the stability in saturated helium was examined at the end. In saturated helium, the propagation of a normal-zone started at 10.8 kA. A normal zone initiated at the bottom propagated in only downstream side and stopped within a half turn. The minimum current to propagate over a half turn was 11.2 kA. This means that the quality of helium had become worse at the bottom where helium bubbles gather in the first layer by the natural convection. In the case of just after the third cool-down, the quality of saturated helium must be not good at the whole area by the heat input from the thick coil case.

In subcooled helium, in which the quality is zero, the increment of the minimum currents to begin propagation is almost proportional to the degree of subcooling with good reproducibility, as shown in Fig. 2. In saturated helium it

decreases with the larger value of quality. Thus, the value and uniformity of the quality must be considered in a large-scale pool-cooled coil. The evaluation of the quality is indispensable to compare the LHD helical coil with the model coil. The propagation velocity will be useful for evaluating the quality.

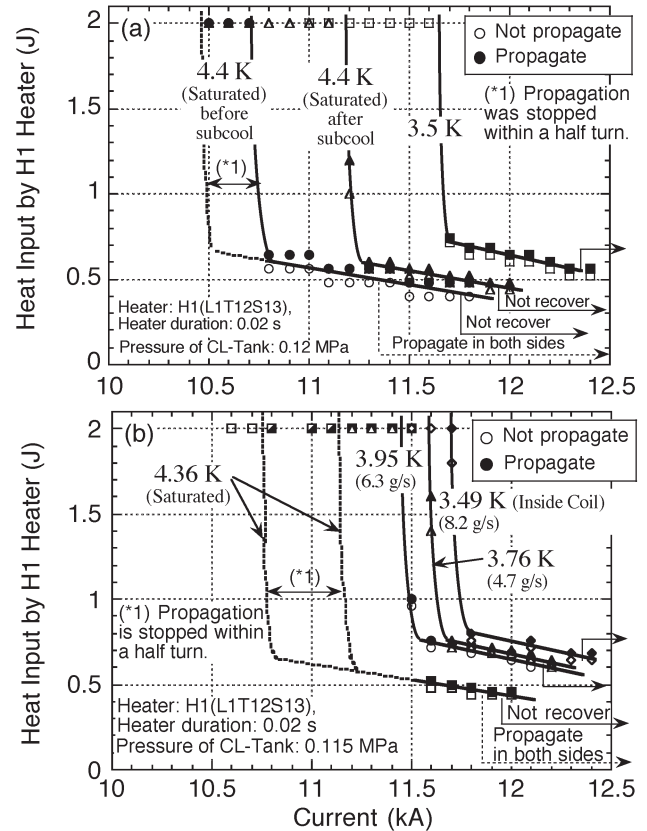


Fig. 1. Minimum heat input for the dynamic propagation of a normal-zone in the HC model coil in the 3rd (a) and 2nd (b) cool-down. The open or closed symbol means without or with propagation, respectively.

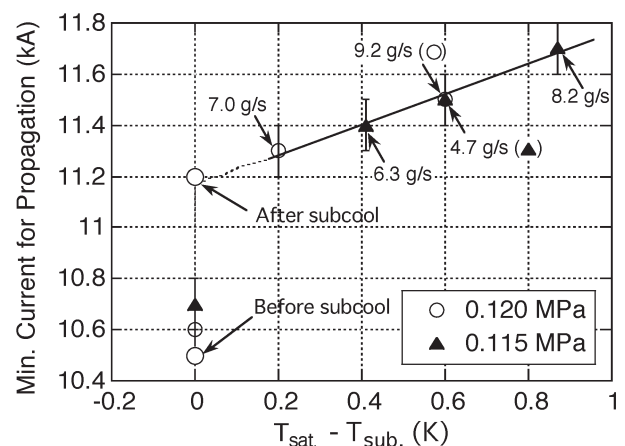


Fig. 2. Temperature dependence of minimum currents for dynamic propagation of a normal-zone in the R&D coil.

Reference

1) Imagawa, S. et al.: IEEE Trans. Appl. Supercond., **14** (2004) 1511.

§17. Elimination of Variable Harmonics on Motor Generator Circuit

Yamada, S.

The LHD experiment will require more than 20 MW heating power to achieve high temperature plasmas in a high-density regime. The pulsed power for heating experiments requested by the NBI must be drawn from a 250 MVA FW-MG. It should be considered that higher order harmonic currents with variable frequency are observed in the output line of the FW-MG. Frequency spectrum of the harmonics is estimated to be $f_0(6n \pm 1)$, when the power supply of the heating device is composed of the full-wave SCR rectification. In the case of the LHD frequency f_0 changes from 93.5 Hz to 58 Hz.

A block diagram of an active filter is shown in Fig. 1. It has the following major functions: 1) detection of the variable frequency of the power line, 2) elimination of current component of fundamental frequency, 3) extraction of current components of higher harmonics, and 4) compensation of harmonic current by generating the counter-flow current. The frequency of the active filter varies and is synchronized with that of the FW-MG. We have considered an active filter with variable frequency. The transfer function of the band pass filter is given by:

$$H(S) = G \frac{[S / \omega_0]}{[S^2 / \omega_0^2 + 2ZS / \omega_0 + 1]}$$

Where, G and Z are the gain and the selectivity of the filter. The ω_0 is the resonant angular frequency of the band pass filter. Bode diagrams of this band-pass filter are shown in Fig. 2. If a parameter Z is made small, the selectivity is sharper, but the phase margin for higher harmonic will go down. Here, Z and G were determined as 0.5 and 1, taking into consideration the following analysis result.

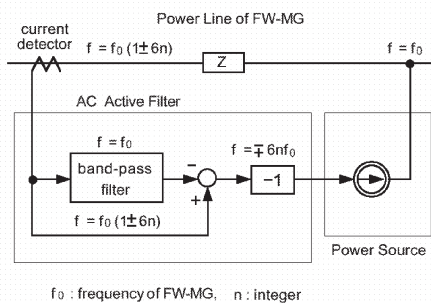


Fig.1 Block diagram of ac active filter.

Dynamic simulations of the active filter, FW-MG and power supplies of heating devices for the experimental fusion device of LHD have been carried out. The frequency of the FW-MG was changed from 95 Hz to 55 Hz in 10 seconds. The power supply component is modeled as a constant current power supply model including the 5th and 7th harmonic currents with optional amplitude.

Figure 3 gives a typical example of the simulation results: (a) $f = 95$ Hz at initial top speed phase, (b) $f = 75$ Hz at intermediate phase, and (c) 55 Hz at running-down phase. Upper waveforms show input current of the power supply component including seventh harmonic current of 20% and fifth harmonic current of 10 %. Middle waveforms indicate the compensation current generated by the active filter. The lower waveforms show the line current from the FW-MG after elimination of the harmonics. It was confirmed that the harmonic currents were suppressed one tenth in the whole frequency range of the FW-MG from 95 Hz to 55 Hz.

Reference:

S. Yamada et al, presented at 23rd SOFT, 20-24 Sept. 2004, Venice, Italy.

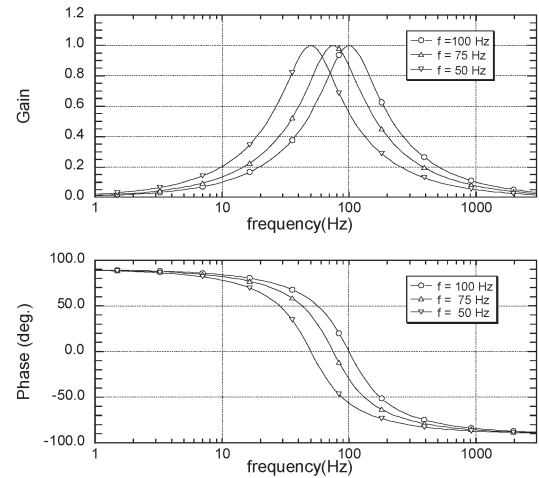


Fig.2 Bode diagram of the band pass filter.

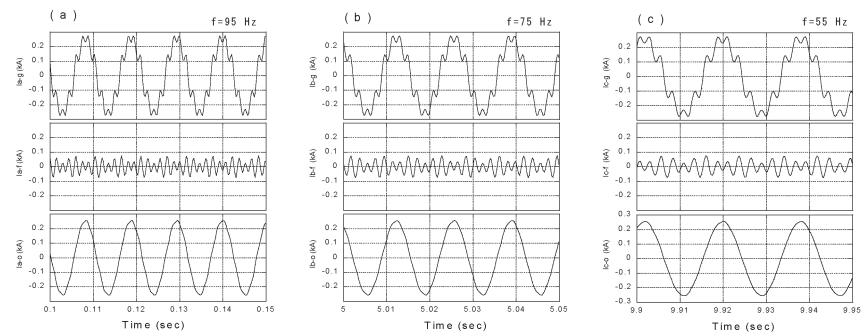


Fig.3 Results of the dynamic simulation.

§18. Thermal Contact Conductance between the Bundle and the Conduit in Cable-in-Conduit Conductors

Takahata, K., Tamura, H.

Temperature rise in a quenching cable-in-conduit conductor is strongly affected by thermal contact conductance between the bundle and conduit. To evaluate this temperature rise, the conductance has been measured under surface pressure at room temperature by using a simple technique¹⁾.

The cable-in-conduit conductor used in the measurement of thermal contact conductance is the same conductor used for the inner vertical coil of the LHD. The experimental arrangement is schematically presented in Fig. 1. The lower half of the conduit was cut from the conductor, and the lower surface of the bundle, wrapped with tape, was attached to a copper block equipped with two heaters. The copper block and lower half of the bundle were then covered with a fiber-reinforced plastic (FRP) block on a load cell. A compressive load of up to 3 kN was applied vertically by using a mechanical testing instrument. The resulting maximum surface pressure at the upper surface of the block was 3.4 MPa.

To measure conductance, a transient technique was applied. First, the copper block was heated to 340 K. After shutting off the heat, we observed the decay of temperatures in the copper block and the strands touching the block using thermocouples (TC #1 and #2 in Fig. 1). The conductance was evaluated with the following equations:

$$C_{block} (dT_{block} / dt) = -hS(T_{block} - T_{strand}) - Q_{leak} \quad (1)$$

where C_{block} is the heat capacity, h is the conductance, and S is the area of the upper surface of the block. Symbols T_{block} and T_{strand} represent the temperatures of the block and strands, respectively. Heat leakage to the surroundings, Q_{leak} , was measured by replacing the conductor with cotton as a thermal insulating material.

All measured data are presented as a function of surface pressure in Fig. 2. The first and second loading was made in the atmosphere of air. The results confirm that the contact conductance is strongly affected by the surface pressure. Therefore, to evaluate temperature rise in a quenching conductor, it is necessary to measure conductance under a surface pressure equivalent to an electromagnetic force. To examine the effect of ambient gas, conductance in an atmosphere of helium was also measured. Helium has higher thermal conductivity than air by a factor of six. The results are also shown in Fig. 2. The conductance increases by about 500 W/(m²·K) over the entire range of loaded surface pressure.

The subject of contact conductance is generally discussed in the field of electronics. In the calculation of conductance for solid-to-solid contacts, the following relationship has

been proposed:

$$h = h_c + h_g \quad (2)$$

Contact conductance, h_c , is related to conduction across the true contact points. It depends on the properties of the materials in contact and the surface pressure. On the other hand, gap conductance, h_g , expresses conduction across an interstitial gas. The experimental results evidently show the effects of both h_c and h_g .

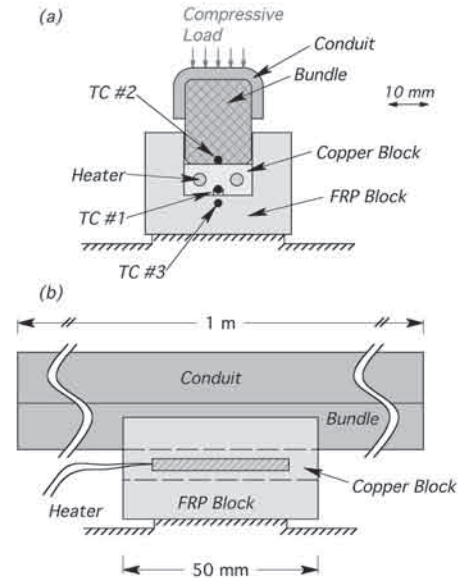


Fig. 1 Experimental arrangement for measuring thermal contact conductance under surface pressure; (a) cross-sectional and (b) side view.

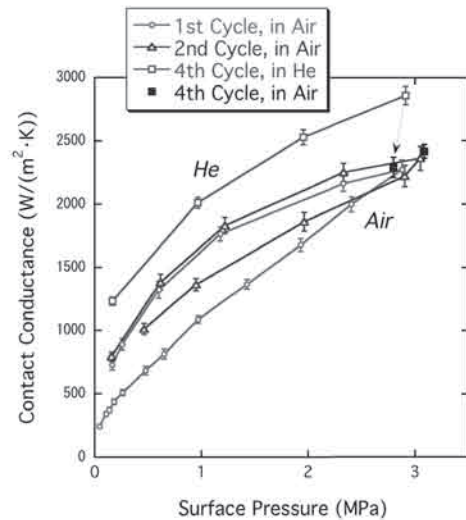


Fig. 2. Thermal contact conductance as a function of surface pressure.

Reference

- 1) Takahata, K., et al.: IEEE Trans. Applied Superconductivity 14 (2004) 1477-1480.

§19. Effective Resistivity of HTS Tapes with Shielding Currents

Yanagi, N., Mito, T., Takahata, K., Seo, K.
Hemmi, T. (Graduate Univ. of Advanced Studies)

In some high-temperature superconducting (HTS) coils operated in persistent current mode, the current decay rate is found to be shorter than the expected value. Figure 1 shows the electric field along the coil cable observed in a persistent current operation of the magnetically levitated floating coil of the Mini-RT device[1]. The electric field increases by triple power of the coil current, which is far from the expected curve based on the n -value model. Mechanical damage during the winding process should be accountable for this degradation, however, we consider that there might also be some electromagnetic effects, since large shielding current is supposed to be induced among non-twisted filaments in the present silver-sheathed Bi-2223 tape. Thus, interaction between the transport current and shielding current is being examined by experiments and numerical calculations.

A sample coil was wound with an Ag-sheathed Bi-2223 tape (width/thickness: 4.1/0.305 mm, critical current at 77 K, self-field: 126 A). The outer diameter of the single pancake coil is 150 mm and the tape length is 14.7 m. A photograph and a cross-sectional view are shown in Fig. 2. A uniform magnetic field was applied in the perpendicular direction of the tape surface and the magnetic field was measured with two Hall probes[2]. Figure 3 (a) shows the waveforms of the measured magnetic field when the coil temperature was kept at 40 K. It is seen that the magnetic field just above the cable continues to increase even after the external magnetic field reaches to a flat-top. This might be due to the decay of the shielding currents which are supposed to be induced by the application of the external magnetic field. The amplitude of the shielding current can be evaluated by the magnetic field and it is confirmed to be as large as the critical current. The field change can be well simulated by a simple calculation using the n -value of the cable, critical current and inductance of the shielding current path.

It has also been found that the temporal change of the magnetization is mitigated by reducing the coil temperature (Fig. 3 (b)) or by externally reducing the magnetic field. This suggests that the amount of shielding currents can be controlled by choosing an appropriate excitation procedure. On the other hand, the field change was found to become more rapid by applying a transport current. We consider that loss generation is also increased by adding transport current to shielding currents.

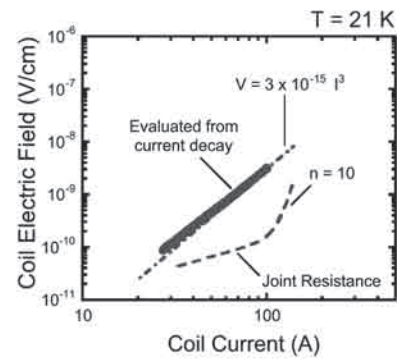


Fig. 1 Dependence of the electric field on the coil current measured in the floating coil of Mini-RT.

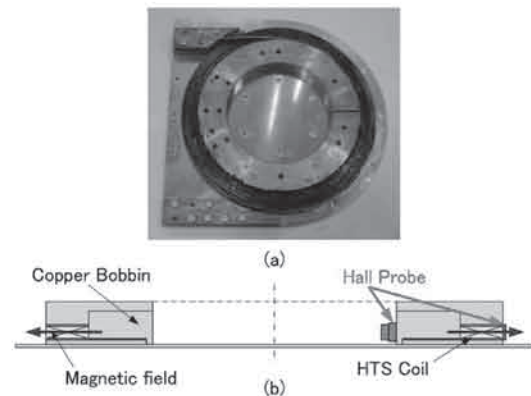


Fig. 2 Photograph and illustration of an HTS sample coil.

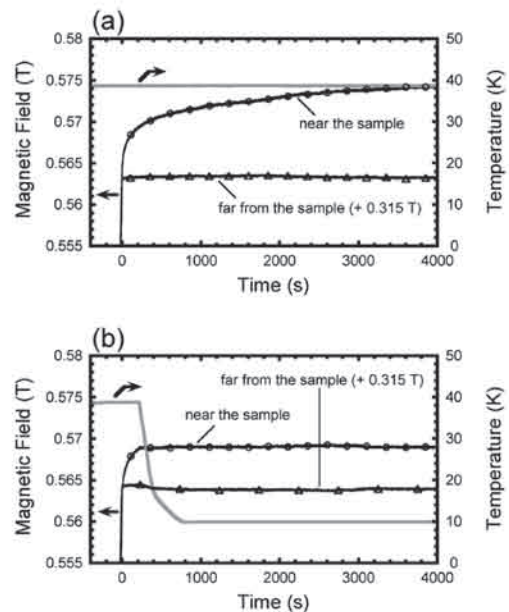


Fig. 2 Magnetic field measured by Hall probes with (a) temperature fixed at 40 K and (b) reduced to 10 K.

References

- 1) Yanagi, N., Hemmi, T., et al., IEEE Trans. Appl. Supercond. 15 (2005) pp.1399-1402.
- 2) Hemmi, T., Yanagi, N., et al., IEEE Trans. Appl. Supercond. 15 (2005) pp.1711-1714.

§20. SMES System Designed to Protect from Momentary Voltage Drop

Chikaraishi, H., Mito, T., Abe, R. (Shibuya), Hayashi, K. (IDX), Okumura, K. (Technova)

For short time SMES, the cost of the power converters becomes important. To reduce the cost of converters, some special designed are done. In this SMES system, the inverter and dc-dc chopper works only 1 seconds. Therefore the cooling device can be simplified compared with the usual inverters. We estimate the IGBT losses and the junction temperature when any additional heat sink is not used. As a result, the generated heat flows to the copper plate of the IGBT modules and the maximum temperate of junction stays around 80 degree. With this estimation, the additional heat sink is not necessary for this inverter and the cont and size of it can be reduced.

While the SMES is in standby state, the power converter requires only small output voltage to keeps coil current constant. For this purpose, we use another dc power supply of small capacity to reduce the switching loss of main converter with stopping its switching. Fig shows the diagram of the main circuit of the converter. The current charger and main chopper are connected via diode shown as in Figure 1 and the current pass changes automatic when charger stopped. To confirm the SMES concept, we built a demo coil and converters. The specifications of the demo system is shown in Table 1. After the excitation test was complited sucessfully, the experiment using demo coil and power converter was carried. In the experiment, the inverter is stopped and a dummy load is connected to dc lin in the converter to discharge the stored energy.

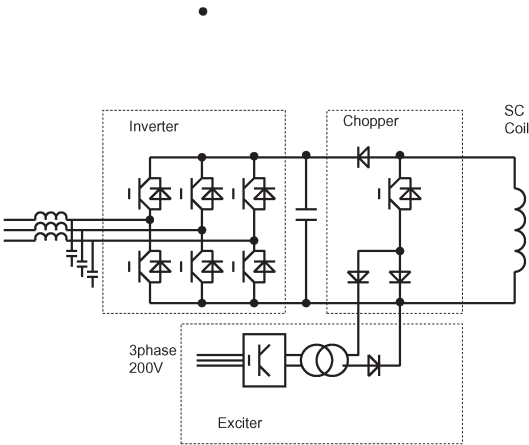


Figure 1: Main Circuit of Power Converter for the SMES.

Figure 2 shows the test result with load. In the

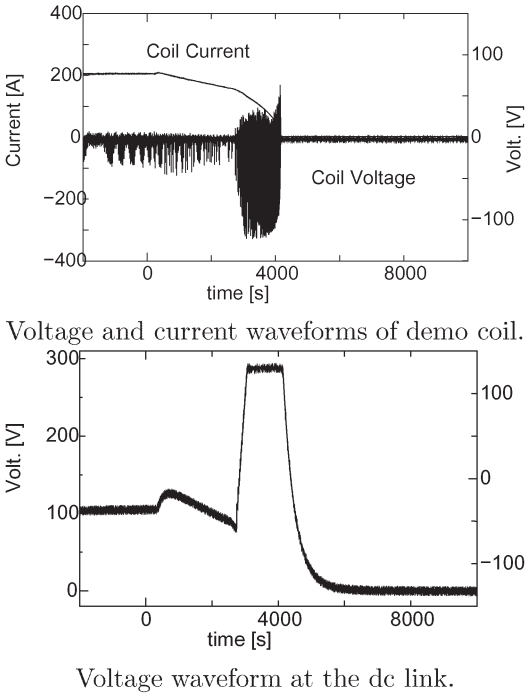


Figure 2: Experimental result for demo SEMS.

Table 1: Specifications of demo SMES	
Specification of the system	Line voltage: 400V, Rated power: 100 kW, Compensation time: 1 second.
Specification of the coil	Current: 1 kA, Voltage: 140 V, Inductance 0.2H, Stored energy: 100kJ
Inverter and DC chopper	Ac side volt. : 400 V, Dc link volt : 300V Dc link curr. 330A Capacity: 100 kVA 10 s

experiments, we limit the coil current to 250 A because of the line capacity. At beginning, the coil current is set to 200A. After that, the charge power supply stopped and the chopper start operation. The dc voltage reached to 300V and the energy dumps in the regisyer quickly. In this experiment, the pulsated voltage of 300 V is induced to the coil terminal but it doesn't affect to coil operation.

§21. Development of a Pulse Tube Current Lead

Maekawa, R., Matsubara, Y.

1. Introduction

Development of a prototype pulse-tube current lead has been conducted as a part of the Power-Stabilization Superconducting Magnetic Energy Storage (SMES) project. The hybrid-type current lead consists of a co-axial pulse tube cryocooler with a current lead, a copper rod, penetrating its axis. The configuration was chosen to assure the compactness and a high voltage tolerance (1). The design work has been performed, using a numerical program. The program had been written based upon an Equivalent Pressure-Volume (EPV) method, developed by Matsubara et al (2). Since the target for the current carrying capacity is approximately a few kA with a high voltage tolerance of 5kV, the refrigeration power required for the hybrid-current lead is estimated to be about 150 W at 65K.

2. Pulse-Tube Current-Lead Design

The EPV is a powerful tool to design a pulse-tube refrigerator, according to the design parameters such as, volumes of a pulse-tube and a regenerator, operation schemes and flow coefficients through valves. A fundamental idea of the program is to determine the position of a gas-piston within the pulse tube as a function of time. Fig. 1 shows one of examples with a 4-valve operation mode. The model consists of a pulse-tube connected with a regenerator via a heat exchanger. The gas piston, which can be compressed and/or be expanded as a function of pressure, is presented by a sky-blue rectangle. The refrigerator is divided by red-dot lines, which indicate the control volumes for mass-balance calculations. Four-valve connected at the ends of refrigerator is adjusted to produce optimized phase-shift within the pulse-tube. As a result, the cold-end volume V_e would be changed as a function of time and pressure, this result in the refrigeration power obtained by the numerical calculation. Fig. 2 shows the calculated P-V diagram as a function of the lowest temperature.

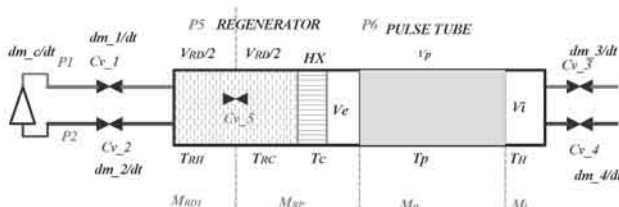


Fig. 1 A schematic of pulse-tube model to calculate the refrigeration capacity of 4-Valve Pulse tube, using the equivalent PV method. dm/dt : massflow rate, M : mass of gas, P : pressure, Cv : valve coefficient, V : volume and T : temperature.

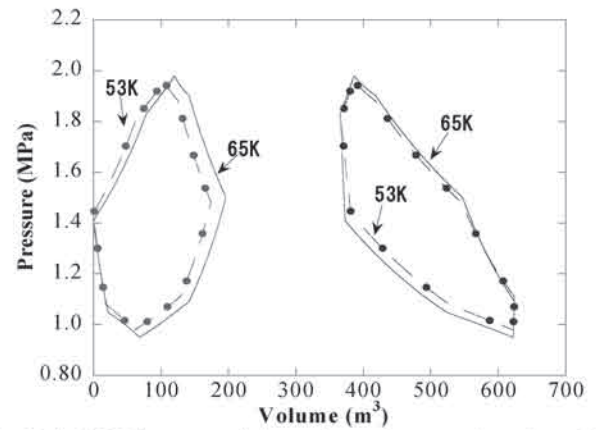


Fig. 2 A P-V diagram of the pulse tube as a function of refrigeration capacities.

3. Fabrication of a Prototype

Prototype of a pulse-tube current-lead has been fabricated reflecting the numerical calculation as well as operating experience of the first prototype (1). Two major modifications were taken place for the prototype; one is having an isolation vacuum between the regenerator and the pulse tube, the other is shortening the length of the regenerator. These modifications improve the operation stability and reduction of pressure drop through the regenerator. Fig. 3 shows the schematic of the prototype, while Fig. 4 shows its picture.

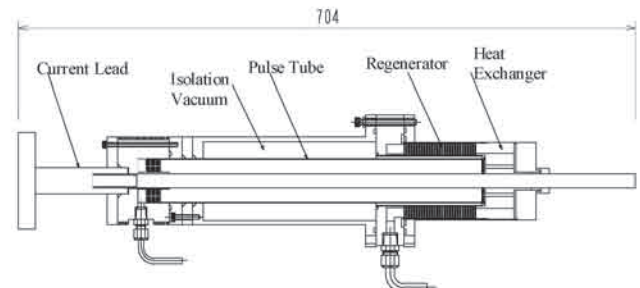


Fig. 3 A schematic of prototype co-axial type pulse-tube current lead.

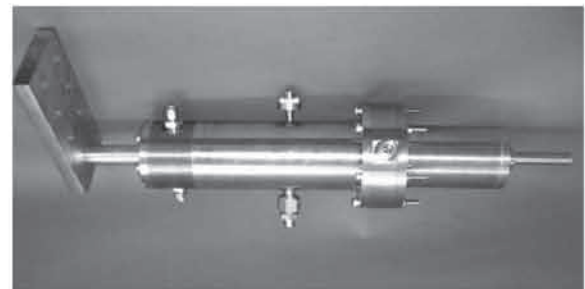


Fig. 4 A picture of a prototype pulse-tube current-lead.

References

1. "A couple of pulse tube cryocoolers as current leads for the superconducting magnet", Y. Matsubara, H. Kasahara and S. Akita, Proc. ICEC 19, pp625-628 (2003).
2. "An experimental and analytical investigation of 4K pulse tube refrigerator", Y. Matsubara, J.L. Gao, K. Tanida, Y. Hiresaki and M. Kaneko, Proc. ICC pp166-196 (1993).

§22. HTS Conical Bulk for Current Lead Use

Tamura, H., Mito, T.
Yamada, Y., Tachikawa, K. (Tokai Univ.)
Heller, R. (FZK)

Bi-Sr-Ca-Cu-O HTS system has been expected as a current lead for a superconducting apparatus. We have developed Bi-2212 bulk prepared by using a diffusion reaction. The substrate of the Bi-2212 HTS could be made in any shape because it is made by using a cold isothermal pressing method. In this point, the Bi-2212 bulk has a potential for flexible design.

We have made some cylindrical bulk to investigate properties of this kind of HTS bulk and the maximum transport current of 8 kA was achieved at 4.2K. A current lead usually has a temperature distribution for a warm end to a cold end. From the result of the transfer current against temperature rise, the maximum transfer current was 2 kA under the condition of warm end temperature was 50 K. Under this condition, the cross section of the cold end can be smaller since the temperature of cold end is almost 4.2K. From this point of view, if a conical shaped HTS bulk was made, it could be an advantage for heat leakage. To confirm this effect, we calculated heat leakage of the prototype current lead. Fig. 1 shows a design example of a current lead using HTS superconductor and a heat leakage was estimated by this example. The heat leakage of the conical shaped HTS was estimated almost half of that of the cylindrical one.

We made the first prototype conical HTS bulk with the size of 37/29 mm in outer/inner diameter at the warm end, 27/19 mm in outer/inner diameter at the cold end, and 200 mm in length. Fig. 2 shows a photograph of the samples we have made. The bottom one was reinforced by using Alumina fiber and epoxy resin. The current transport test was done without any reinforcement on the surface of the sample at first. The sample was immersed into liquid helium up to the warm end section to know the maximum transport performance. When the whole HTS section was immersed in the liquid helium, the maximum transport current of 7 kA was achieved. After the flow level of the liquid helium was decreased under the cold end of the sample, the warm end was warmed up by using electrical resistive heater. As the temperature of the warm end section increased, the quench current decreased. The quench current of 2 kA was observed at 50 K. Fig. 3 shows the transport current against the warm end temperature. The reinforced sample and a steeper conical sample have been made and performance tests are being planned.

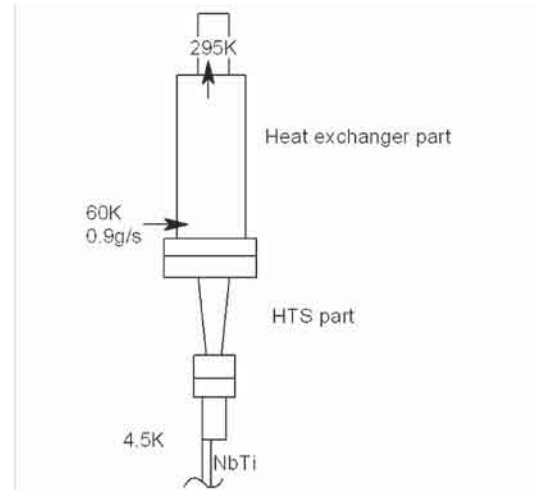


Fig. 1. Current lead model using conical shaped Bi-2212 HTS.

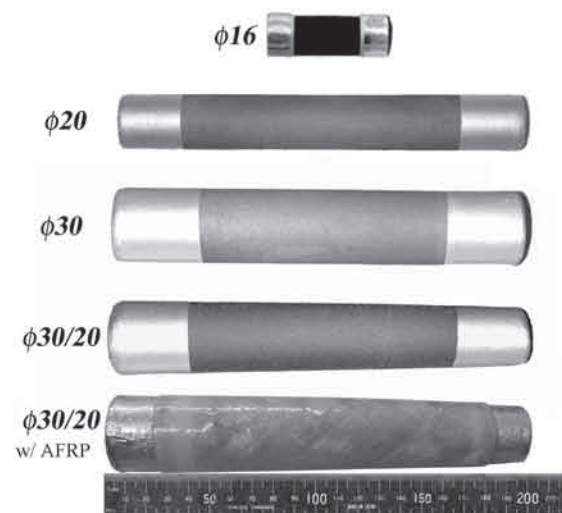


Fig. 2. Bi2212 cylindrical and conical specimens.

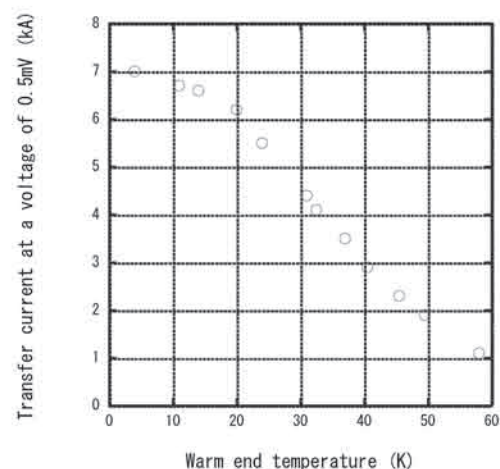


Fig. 3. Transport current performance of the conical Bi-2212 HTS against the temperature of the cold end.

§23. Cooldown Performance of the Cryogenic System Applied for the Cryogenic Target of the FIREX Project

Iwamoto, A., Maekawa, R., Mito, T.
Nakai, M., Norimatsu, T., Nagai, K. (ILE, Osaka Univ.)

Introduction

The program of the fast ignition realization experiment (FIREX) project is underway at Institute of Laser Engineering (ILE), Osaka University. The project is divided into two phases: FIREX-I and FIREX-II corresponded with powers of the compression and the heating lasers. To accomplish the project, two important technologies must be developed. One is higher power lasers than the present lasers. For FIREX-I, the PW laser is being upgraded up to the maximum power of 10 kJ/10 ps until the end of 2007. In FIREX-II, both the compression and the heating lasers will be upgraded. Another is a solid fuel target, what is called a cryogenic target. D₂ or DT is used as the fuel for the project. The target appearance has been modified for the fast ignition experiment.

The foam shell method has been proposed to realize the target design for the fast ignition experiment. To develop the method, the collaboration research between ILE and National Institute for Fusion Science (NIFS) was started in 2003. The experimental apparatus has been fabricated at NIFS, and the foam shell method will be demonstrated. In this report, the development at NIFS is focused on, and the detail of the apparatus and the result of first cooldown test are described.

Specification of the target

Fig. 1 shows the schematic illustration of the target applied for FIREX-I. The target consists of three parts: a foam shell, a conical laser guide made of a gold thin plate and a gas or liquid feeder made of a glass tube. The foam is low density and porous plastic. The foam shell is expected to be impregnated with solid fuel and results in being an ideal target. The shell is a sphere shape with uniform and thin foam layer and has a diameter of 500 μm with a thin layer of $\sim 20 \mu\text{m}$ for FIREX-I, whereas has a diameter of 2 mm with a thin layer of $\sim 100 \mu\text{m}$ for FIREX-II.

Cryogenic system to demonstrate the fuel layering process

A schematic of cryogenic system is shown in Fig. 2. For the facility of cooling operation, a cryocooler was utilized. Gaseous H₂ (GH₂) and He (GHe) were prepared as fuel and coolant, respectively. For the FIREX project, the fuel is not H₂ but D₂ or DT which cannot use on self-imposed control of NIFS. However, we assumed H₂ to be a surrogate for the demonstration of the layering process. A GH₂ cylinder was connected to the target via a pressure controller. The target was encased in double vacuum cans made of stainless steel. The outer can was connected to a turbo molecular pump for vacuum insulation. The coolant of GHe can be supplied

in the inner can which was thermally linked with the second stage of the cryocooler.

Countermeasures for the throb of the cryocooler were prepared. The cryocooler was structurally isolated from other components, mounted on an individual support. Flexible thermal conductive links (FTCLs) were utilized to thermally connect the cryocooler with either the inner can or the 50 K shield.

First cooldown of the cryogenic system

Fig. 3 shows the trend graph of the first cooldown. It took approximately 30 hours to reach the steady state operation. The achieved temperature at the target can was $10.9 \pm 0.5 \text{ K}$. At this point, the heat leaks to the 50 K shield and to the inner can were estimated to be 27.3 W and 2.2 W, respectively. The throb of the target was investigated utilizing visual images of a digital camera, preliminarily. It can be estimated less than 10 μm .

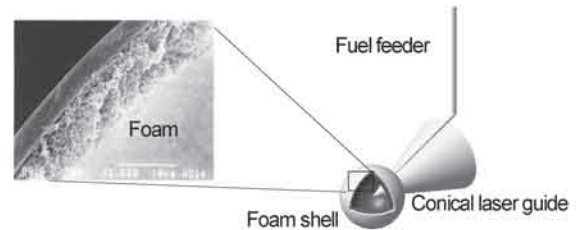


Fig.1 Cryogenic target for FIREX project

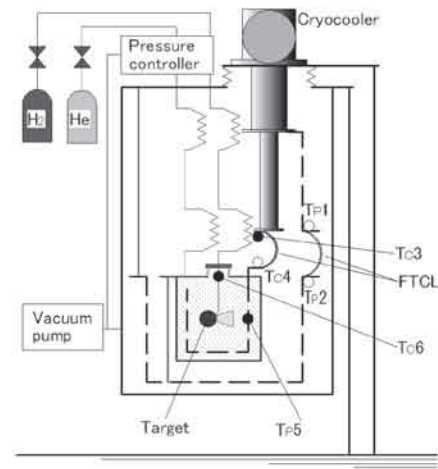


Fig.2 R&D System

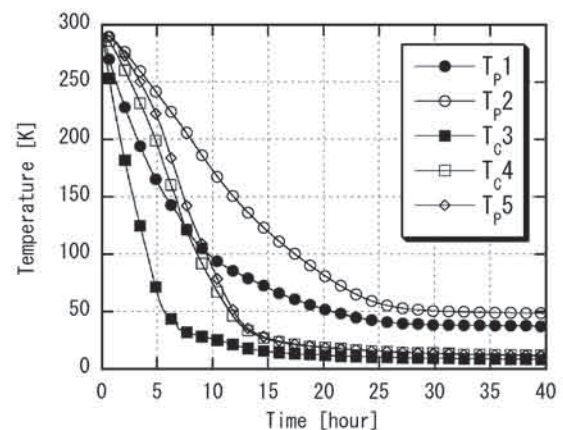


Fig.3 Cooldown curve

§24. Performance of Cold Compressors in the Cooling System for the R&D Coil Cooled by Subcooled He I

Hamaguchi, S., Imagawa, S., Yanagi, N., Mito, T.

Superconducting magnets of the helical coils for the Large Helical Device (LHD) have been operated by saturated helium at the temperature of 4.4 K and the pressure of 120 kPa. So far, plasma experiments have been carried out at the magnetic field lower than 3 T successfully. However, the operating field has not reached the nominal field of 3 T. So, it is considered that the superconducting magnets of the helical coils will be cooled with subcooled He I to achieve the field of 3 T. To use subcooled He I as the coolant for the superconducting magnets of the helical coils, an R&D superconducting coil, wound with superconductors of the helical coils, was tested in subcooled He I.¹⁻³⁾ Two cold compressors were used to generate subcooled He I in the cooling system of the R&D coil. In the present study, the performance of cold compressors has been studied in order to apply the cooling system of the R&D coil to the cooling system of the helical coils.

Fig. 1 shows the flow diagram of the cooling system of the R&D coil. The saturated He I bath was pumped by the cold compressors up to 3.0 K. Subcooled He I was generated at the heat exchanger in the saturated He I bath. Subcooled He I was supplied from the bottom of the R&D coil. The mass flow rate of subcooled He I was 5-10 g/s throughout the present experiments.

First, the area which the cold compressors could be operated stably and safely was examined. The area is called the stable operation area in the following sentence. Fig. 2 shows the performance curve of the cold compressors under the various conditions. Open marks express the performance of the cold compressors. The solid line is the surge line from the present experiments, while the dashed line is the surge line estimated by the air test at the room temperature. It was found that the surge line from the present experiments was larger than the estimated surge line. Therefore, the stable operation area was expanded.

Second, the automatic operations were performed to operate the cooling system within the stable operation area. In the present automatic operations, the pressure of the saturated He I bath, which was decided by the number of rotation of the cold compressors, was controlled by the bypass valve. Fig. 3 shows the history of the performance of the cold compressors in an automatic operation. The automatic operation could be completed within the stable operation area. The stable operation of the cooling system for the helical coils will be expected in this way.

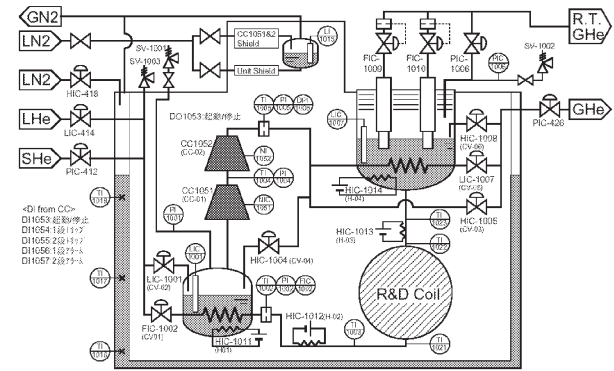


Fig. 1. Flow diagram of the cooling system for the R&D coil.

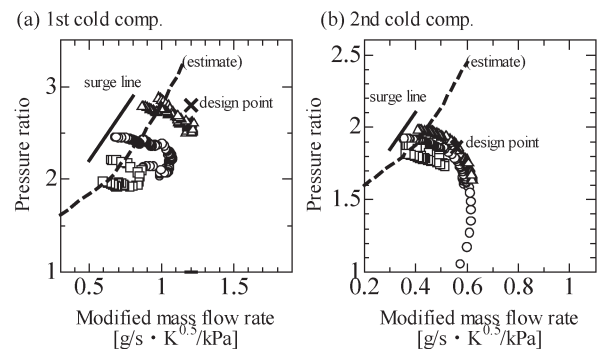


Fig. 2. Performance of the cold compressors under the various conditions.

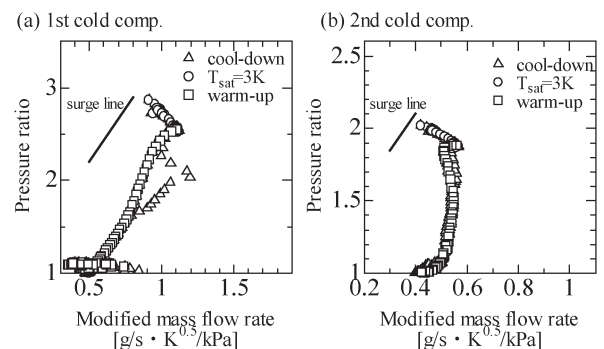


Fig. 3. History of performance of the cold compressors in an automatic operation.

Reference

- 1) Hamaguchi, S. et al. : IEEE Trans. on Appl. Supercond. Vol. 14, No. 2 (2004) 1439-1442.
- 2) Imagawa, S. et al. : IEEE Trans. on Appl. Supercond. Vol. 14, No. 2 (2004) 1511-1514.
- 3) Hishinuma, Y. et al. : IEEE Trans. on Appl. Supercond. Vol. 14, No. 2 (2004) 1435-1438.

\$25. Simulation of Electromagnetic Behaviors of Lap Joints for Fusion Magnet Systems

Seo, K., Mito, T.,
Kawabata, S. (Dept. Elec. Eng. Kagoshima Univ.)

The joint between superconducting cable-in-conduit-conductors (CICC) is the key technology in magnetic confinement fusion apparatus and several hundreds of joints are involved in generally. In the Large Helical Device (LHD), there are 104 joints (44 joints in the helical coils and 60 in the poloidal coils). For the International Thermonuclear fusion Experimental Reactor (ITER), the number of joints are assumed be more than two hundred. DC resistance of the lap joint is typically designed less than several n-ohms and allowable joule loss is several watts. AC loss due to external field is also limited less than several watts. Reduction of AC loss and lower joint resistance are required simultaneously and those are conflicting trade-off. The lap joint had been examined under both self-field and external transverse field experimentally at Kagoshima Univ.^{1), 2)}. In this study, we established the numerical model for the joint and analyzed numerically. In the simulation, modeling of contact resistances between parallel strands is important. Circuit constants were determined to reproduce the experimental results; those are the magnetic diffusion time constants and the DC joint resistance. The relation between the joint resistance and the AC loss were discussed. Constitution of the joint doesn't only influence on the joint resistance and the AC loss but also current distribution in the cable. Non-uniform current distribution (NUCD) among the strands is reported to result in the degradation of the stability. We also discussed about the current distribution with our numerical code and models and showed representative numerical results for NUCD in this report.

Figure 1 represents the numerical model of lap-joint. Experimental joint sample is made with two legs of Nb₃Sn CICC. The cable is multiply twisted by (2+1Cu) x 3 x 3 x 3 x 4, however we reduced it into the cable with 3 x 3 x 4 superstrands (SSTs) as the numerical model. Here, the final twist pitch is 190 mm and copper sleeve and/or joint length is 250 mm in the experiment. We selected joint length as a parameter and three models are prepared; model-a) L_j=250 mm, b) 125 mm and c) 62.5 mm. Figure 2 illustrates the XY plane projections of SST-tracks. In this figure, encounters of SSTs and the lap-joint-interface are not fair and joint resistances between individual SSTs in different leg must not be equal. Figure 3 shows the simulated results of the DC current distributions among 36 SSTs. Currents thorough individual SSTs are not even and remarkable NUCD occurs in the shorter joint case c).

Our conclusions are as follows. DC joint resistance is merely determined by the size, e.g. length of the lap-joint-interface. NUCD in the steady state depends on the distribution of contact points to the lap-joint-interface among the superstrands. NUCD is found enhanced for short joints, as at given twist pitch, the probability for single superstrands to reach the lap joint

interface is lower. In contrast, The AC-losses from self-field and external magnetic field increases with the joint length. Both effects compete with each other and magnet operating condition will be decisive for optimizations. The model presented above may be found useful in joint design to find a good compromise.

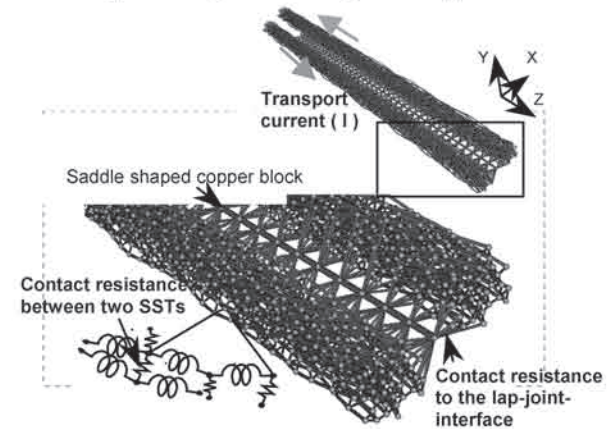


Fig. 1 Numerical model of lap-joint. The saddle-shaped copper block is modeled into a single line. Identical voltages are applied to parallel SSTs. Tracks of SSTs have close relations to both mutual inductances and contact resistances. Contact resistances are described as transverse connections between SSTs.

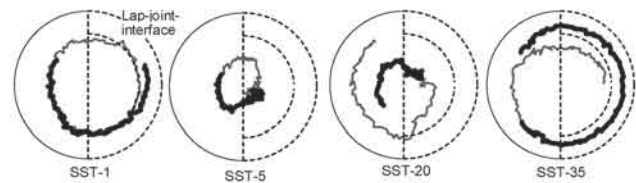


Fig. 2 XY plane projections of SST-tracks. The SST in the area surrounded by two dashed arcs is expected to encounter the lap-joint-interface. The thick lines are extracted from Model-b. Both thick and thin lines are from Model-a. The tracks are determined by the twist-pattern.

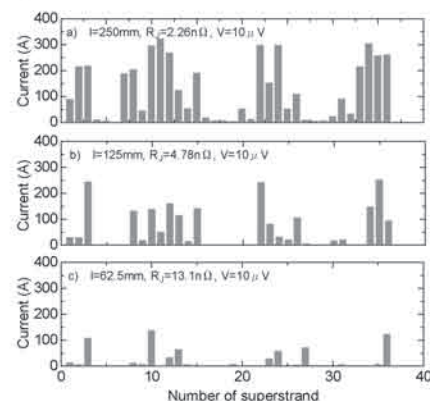


Fig. 3. DC current distributions among 36 SSTs.

Reference

- 1) Kawabata, S. et al., Presented at MT-18 (2003)
- 2) Seo, K., IEEE Trans. on Appl. Supercond. **15**, (2005) 1595

§26. Interaction between the Transport Current and Shielding Currents in Bi-2223/Ag HTS Tapes

Hemmi, T. (Graduate Univ. of Advanced Studies)
Yanagi, N., Mito, T., Takahata, K., Seo, K.

Electromagnetic properties and loss generation in high temperature superconducting (HTS) cable is an important issue to be clarified so that HTS cables and coils can be applied for many applications including fusion research[1]. As there is no twist among filaments in the present Ag-sheathed Bi-2223 cable, a relatively large amount of shielding current is supposed to be generated by applying external magnetic field especially in the perpendicular direction to the tape surface. In this respect, we investigate the magnetization characteristics and loss generation of a single pancake HTS coil using a special apparatus with which a uniform perpendicular magnetic field can be applied to a coil sample also with a temperature control[2]. Figure 1 shows an example of the measured waveforms of the electric field and magnetic field when the transport current is applied under the external magnetic field. As is shown in Fig. 1, the magnetic field just above the cable surface keeps increasing after the external magnetic field becomes constant (at ~ 770 s), which is due to the decay of the shielding currents. When the transport current is applied, the field increases even more rapidly, and at the same time, the terminal voltage of the sample coil shows a relatively high value than that expected from the n-value model. Thus, we observe that there is an increase of loss generation due to the interaction between the transport current and shielding currents.

Numerical calculations have also been performed in order to examine the experimentally observed results. A new finite element analysis (FEM) code has been developed by assuming the cross-section of the HTS filaments as a single oval-shaped core (Fig. 2). A pancake coil structure is dealt with a three-dimensional axisymmetrical configuration and fundamental equations are derived from Maxwell's equations and Kirchhoff's law. The magnetic vector potential and electrical potential are solved using the nonlinear properties of the HTS cable, such as the E-J characteristics given by the n-value model. The magnetic field change observed with a sample coil can be well simulated by the present calculation and the interaction between the transport current and shielding currents has been confirmed as the current distribution in Fig. 3 indicates. The current decay rate in the case of persistent current operation is also being examined.

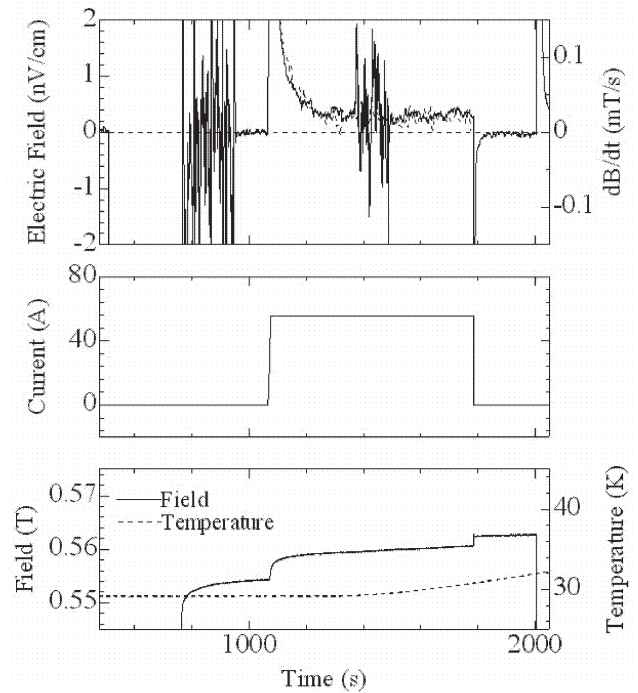


Fig. 1 Electric field and magnetic field measured with a sample coil.

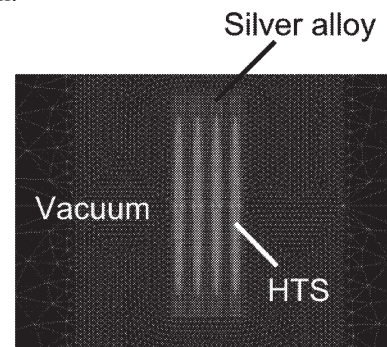


Fig. 2 Model for FEM calculation.

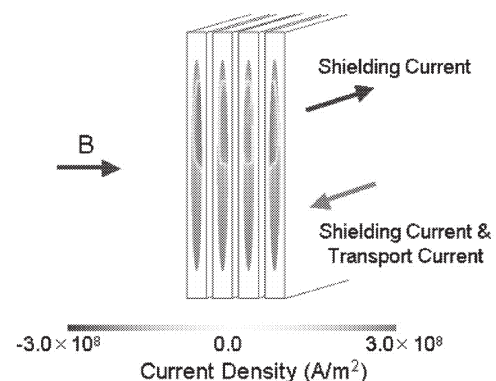


Fig. 3 Example of current distribution obtained by FEM.

References

- 1) Yanagi, N., Hemmi, T., et al., IEEE Trans. Appl. Supercond. 15 (2005) pp.1399-1402.
- 2) Hemmi, T., Yanagi, N., et al., IEEE Trans. Appl. Supercond. 15 (2005) pp.1711-1714.

(3) RF Heating Technologies

In the experimental campaign of 2004FY, ECH and ICRF heating teams successfully achieved long duration plasma operation in LHD. Steady state operation is one of the most important subjects in LHD project. For these trials, whole hardware systems have been developed and improved through several previous experimental campaigns. As described on LHD experiment section of this report, 30 minutes plasma sustainment was achieved by using the ICRF, ECH and NBI heating methods. The total plasma input energy reached up to 1.3 GJ which is the highest record including the tokamaks in the world. There are several reasons of this successful result. One is the finding of new operation technique which could mitigate the local heat load on the carbon plates along the divertor traces near the ICRF antenna by small swing of magnetic axis radius. This operation scenario was described at LHD experiment pages. Other reason is the innovative improvements on ECH and ICRF heating technologies especially for long pulse operation. During the 30 minutes operation, ICRF power of 580 kW and ECH power of 100 kW were stably injected into the LHD plasma.

The ECH heats the electrons, therefore it has a large advantage to sustain the plasma easily in helical confinement system as LHD. At the last experimental campaign, ECH sustained long duration plasma of 65 minutes at the injection power of 110 kW. These steady state operations with RF heating in LHD had gave us a lot of valuable information for the future high power long pulse operations in fusion devices.

ECH In LHD, ECH system has nine equipped gyrotrons and could deliver over 2 MW microwave power in LHD. This high power system allowed us to achieve many LHD physics subjects including high electron temperature operation, achieving internal transport barrier, current drive, EBW heating and high ion temperature trails during the 2004FY experimental campaign. Among the system, one gyrotron/transmission line could deliver CW power for long pulse experiment. In 2004FY, we improved gyrotron system and evacuated transmission line to operate stably. In 2003FY operation, waveguide pressure rise limited the pulse length less than 13 minutes. To suppress the pressure rise, pump-out-tees were newly designed and installed at 9 sections to evacuate efficiently. The enforced cooling systems for transmission line and MOU were also effective to suppress the temperature and pressure rise within safely level. During the 65 minutes operation, gyrotron worked very stably with the output power of 160 kW and the temperatures of all parts were saturated. The plasma operation was switched-off manually due to data

acquisition limit. This shows the high potential of ECH for the maintain tool of long duration plasma.

ICRF During the 2003FY, ICRF experiment was stopped to prepare the stable and reliable operation for the experiment in 2004FY. Antenna, transmission line, tuners and transmitters were improved totally. Antennas were modified to avoid severe arcing problem in vacuum section, which caused vacuum leak at previous experiment. The coronal rings were installed at the bellows section of the inner conductors of coaxial vacuum section. And Faraday shield pipes in which the cooling water circulated were modified to the rod type to prevent vacuum leak problem.

The impedance matching tuners were also improved to keep the matched condition automatically by controlling the liquid levels. The transmission line were thermally expanded during the long operation time, therefore manual frequency change could partially suppress the reflection power in 2002FY experiment. The feedback control of impedance matching by liquid levels during the long operation time helped us to inject the ICRF power stably.

The cooling capability of transmission lines and ceramic feedthrough section was also upgraded. The co-axial transmission line of 240 mm ϕ and feedthrough are water cooled at both inner and outer conductors by circulated water which have been developed in LHD.

The transmitters were newly reassembled to reliable operations for long operation time. The interlock system for safety operation was newly designed and installed. Four transmitters have a capability of over 2 MW CW operations.

For the optimization of LHD experimental condition, the monitoring IR camera for ICRF antenna was newly installed at the horizontal port in LHD. This allowed us to control the plasma and the antenna positions at proper relations. In the 2002FY experiment, the antenna temperature rise was one candidate of the uncontrollable plasma density rise which caused plasma termination within several minutes. The antenna temperature and the antenna coupling resistance are competing parameters for the optimizing the long operation conditions. The antenna position is usually around 6-7 cm from the last closed flux surface (LCFS) of plasma. However in case of long operation experiment, we set the antenna position at 10-11 cm from the LCFS.

(Mutoh, T.)

§1. CW Gyrotron Operation

Kubo, S., Shimosuma, T., Yoshimura, Y., Igami, H., Notake, T., Kobayashi, S., Ito, S., Mizuno, Y., Takita, Y., Ohkubo, K.

The stable and higher power operation regime of the CW gyrotron was explored after 7th LHD experimental campaign. This gyrotron had achieved 140 kW, 1000 s for test injection or 120 kW, 756 s for plasma experiment during the last experimental campaign. The phenomena that the output power measured at the dummy load set just after MOU decreased during CW operation were found. This decrease in power attributed to the small part of the reflected power from dummy load or transmission line back to the gyrotron. Even with small power, this reflected power can affect the oscillation mode in the gyrotron cavity and can cause decrease in the efficiency. After the last experimental campaign, a mode filter which absorbs 95 % of the higher mode power, but transmits HE₁₁ mode with negligible loss is introduced. By insertion of this mode filter, the gyrotron operation regime

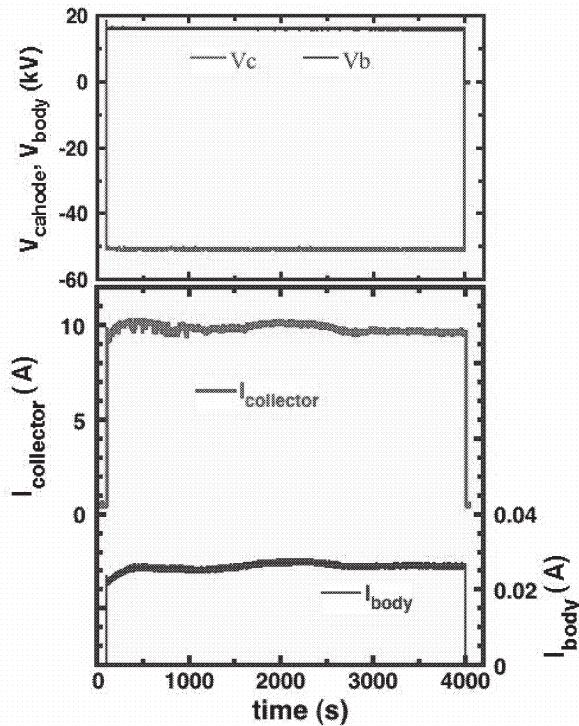


Fig. 1. CW Gyrotron attains full steady state conditions at the output power of 160 kW at MOU. The heater power is manually controlled so as to keep the beam current at near 9 A. Time traces of body and cathode voltage (top), beam current and body current (bottom).

is extended and 160 kW more 1 hour operation became possible. Gyrotron is stably operated for 3900 sec. As shown in Fig. 1, power supply for the beam, body voltages is well regulated and the beam current is maintained at 9 to 10 A by manually controlling the heater power. Almost all parameters of the gyrotron attained at saturation level as shown in Fig. 2, here, are shown the temperature differences in each cooling channel of the CW gyrotron components, saturation power level for each is also shown. The calibrated power at the output of MOU was 163 kW. The saturated temperature differences of the cooling water indicated that the power lost at the body, MOU, filter, and window is 8, 16, 8 and 0.6 kW for this operation. These are close to the designed level for the normal operation. The change in the temperature difference in the filter cooling water might indicate some change in the reflection power from load (transmission line or plasma). The waveform of the power monitor set at second and last second miter bend is shown in Fig. 3. Similar tendency of the two monitor indicates that the transmission mode did not drastically change during such long pulse operation and gyrotron oscillation is stabilized after 1500 sec.

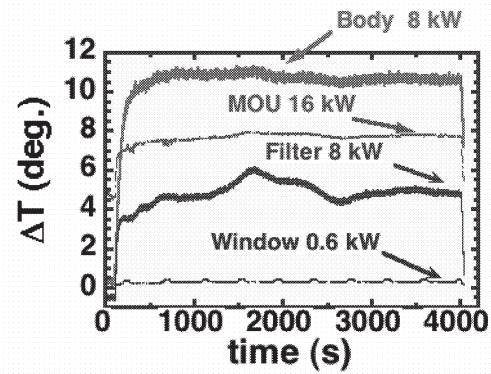


Fig. 2. Temperature differences and estimated power loss at each component of gyrotrons during 3900 s operation.

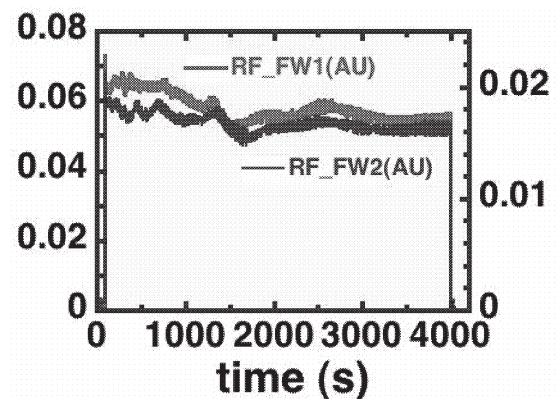


Fig. 3. Waveform of the power monitor set at gyrotron side (FW1) and LHD side (FW2)

§2. Improvement of ECH Transmission Line for CW Experiments

Kubo, S., Shimosuma, T., Yoshimura, Y., Igami, H., Notake, T., Kobayashi, S., Ito, S., Mizuno, Y., Takita, Y., Ohkubo, K.

In the 7th experimental campaign, 84GHz power at the MOU output of 120 kW was injected up to 756 s. Several transmission components had been overheated and damaged during this operation. The temperature rise of the transmission components also made the excess out gassing from the waveguide wall that had limited the pulse duration of the injection.

In order to reduce the temperature rise in the waveguide system, almost all the straight waveguides are covered with copper plates with a water cooling pipe. The comparison of the temperature rise in several parts of the waveguide transmission line before and after the enforcement of the cooling are shown in Fig. 1. Temperature rises of several components in the transmission line before enforcement the cooling at the MOU output power of 120 kW, 756 s are shown by dotted lines and those after the enforcement at higher power of 160 kW, 1910 s are shown by solid lines. After the enforcement of the cooling, temperature rise rates become small even though the increased power and furthermore, these rise shows saturation.

In the last 756 s operation, out gassing from the waveguide wall due to the temperature rise caused the pressure increase over the critical pressure level that is set to prevent arcing inside waveguide. To control the out gassing from waveguide wall, enforcement of the cooling system should be the main solution, but due to the huge surface area of the waveguide wall, it is also necessary to increase the pumping rate through the waveguide. Up to the last experimental campaign, the pumping section of the waveguide had been set near the both end of the transmission line. Since the gas conductance of the 1.25 inch waveguide is very low, the evacuation from both end of the transmission line is not enough even if one set high performance evacuation port. It is essential to set many but not so much high performance pumping ports along the transmission line in such circumstance. We have developed new evacuation port for the 1.25 inch waveguide. The principle of the evacuation section utilizes a small gap in the corrugated waveguide. In order to minimize the loss and leakage power at the gap but to keep enough evacuation efficiency, the gap length is designed to be 1 mm which causes microwave leakage less than 0.1 %. Estimated molecular flow conductivity at this gap is $0.0022 \text{ m}^3/\text{s}$ while that of smooth 1.25 inch waveguide of 1 meter is $0.00387 \text{ m}^3/\text{s}$. Nine of this type of new pumping section are distributed along the 62 m waveguide system. The comparison of the pressure rise in several parts of the transmission line before and after these improvements are shown in Fig. 2. Although

the power level increased by 30 %, the equilibrium pressure reduced to $1.0 \times 10^{-2} \text{ Pa}$ and this pressure level attained after 1000 s. These are result of both enforcements of cooling and evacuation. It is also noted that equilibrium pressure level after long pulse operation decreased shot by shot. This indicates that the waveguide wall conditioning proceeded by the long pulse operation and the out gassing rate decreased shot by shot.

Another component damaged in the last experimental campaign is the DC break. This DC break with a small gap in the waveguide and vacuum sealed by a ceramic disk had been used. The leakage microwave have heated this disk locally and finally made a crack which lead the break in the vacuum. This ceramic is replaced by an aluminum disk with the same size but alumite coated for electric insulation.

These improvements had been the key to succeed more than one hour injection of the ECH power into LHD at the power level of 110 kW.

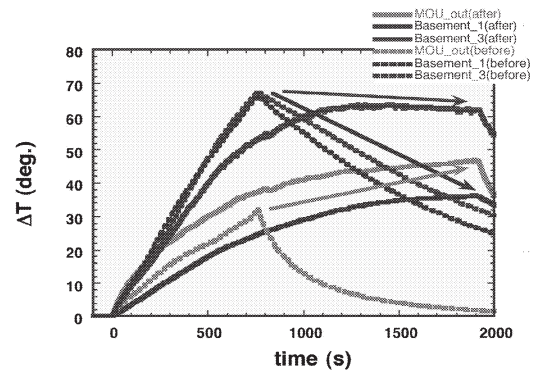


Fig. 1. Time evolution of temperature rise in the transmission components during long pulse operation before enforcing the cooling (dotted lines) and after (solid lines).

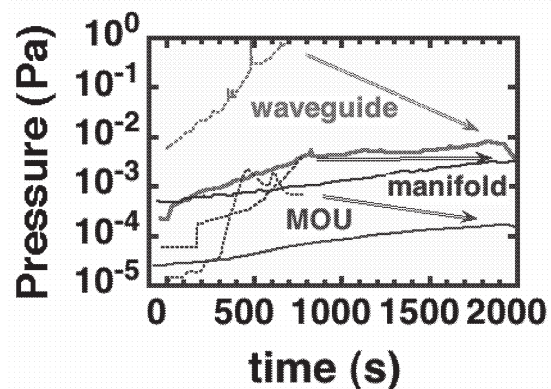


Fig. 2. b) Time evolution of the pressure in the transmission line at MOU, mid-way on the waveguide line, and evacuation manifold before (dotting lines) and after (solid lines) improvements.

§3. Workshop on Generation, Application and Measurement of High Power Millimeter Waves

Maekawa, T. (Graduate School of Energy Science, Kyoto Univ), Shimozuma, T.

1. Objectives

In National Institute for Fusion Science, there are a lot of high power millimeter wave sources such as gyrotrons for plasma production and heating. The millimeter wave power is transmitted over long distance by using corrugated waveguides for transmission. On the other hand, the electron cyclotron emission from the LHD plasmas is utilized as a diagnostic method of plasma temperature. Since the millimeter wave technology, which includes power sources, detectors and components, is still developing, it is important to catch up with the leading edge of such technology for the improvement of ECH and ECE system. The objectives of this workshop are the information change between the researcher of millimeter wave and microwave technologies, the improvement of each millimeter wave systems through the workshop and development of combined research fields.

2. Activities

The activities of this fiscal year consist of three lecture talks and discussions. These lectures are related to high resolution millimeter and sub-millimeter wave diagnostics, millimeter wave scattering diagnostics and development of millimeter wave components for ECH.

Program and contents of the lectures are as follows.

(1) "Atacama Large Millimeter/Sub-millimeter Array: Challenge to THz Region" by Ryohei Kawabe (National Astronomical Observatory of Japan)

Dr. Kawabe belongs to the group of millimeter wave interferometer in Nobeyama and LMSA (Large Millimeter/Sub-millimeter Array). He presented the details of the ALMA (Atacama Large Millimeter Array) project, which is proceeded in Chilean Andes and also explained required high resolution millimeter and sub-millimeter wave diagnostics. The ALMA project consists of the construction of 64 radio telescopes with 12m diameter. As for the millimeter wave technology, superconducting detectors upto THz and submillimeter wave photonic local oscillators are being developed.

(2) "History of application of scattering diagnostics in gyrotron heating group of GPI" by N. K. Kharchev (General Physics Institute).

Dr. Kharchev was a guest professor in NIFS from General Physics Institute in Moscow. He made a review

of millimeter wave scattering experiments by using gyrotrons. He introduced the experimental method and results made in L2-M in Moscow, TJ-I, TJ-II in Spain and LHD in NIFS. The methods of signal analysis are FFT spectrum, wavelet spectrum and coherency.

(3) "My odyssey of RF plasma heating technology" by Dr. K. Ohkubo (NIFS).

He surveyed his research history of the interaction between microwaves and plasma waves in Kyoto university, Institute of Plasma Physics in Nagoya University and NIFS. For example, transverse propagation of whistler waves (KU), lower hybrid wave heating / current drive and electron cyclotron heating (IPP) and electron cyclotron heating and remote steering antenna for ITER (NIFS). He placed emphasis upon the R&D, technical know-how and experimental results during the construction of the systems, RF components and so on.

The attendances distributed over wide area related to the millimeter wave technology. About 30 members joined the workshop.

- Millimeter diagnostics: Dr. R. Kawabe (NAOJ)
- High power millimeter wave application to plasma heating: NIFS, Tsukuba Univ. Kyushu Univ. Kyoto Univ.
- Generators of high power micro and millimeter waves: Fukui Univ. Niigata Univ. Kanazawa Univ. Tohoku Univ.
- Millimeter wave technology: JAERI, Ibaragi Univ.

This work shop is useful and should be continued to keep in close touch between researchers in this area. The future plan of this work shop is to promote technological information exchange through lectures, presentations and discussions.

§4. Temperature Measurement of ICRF Antennas in LHD

Saito, K.

Hot spots were observed by CCD cameras during long pulse operation on two ICRF antennas (3.5U antenna and 7.5U antenna) in the same positions at the top of the left side protectors attached to the upper antennas. For the 7.5U antenna, an infrared (IR) camera was installed to measure the temperature of the antenna. Figure 1 shows the temperature distribution on the antenna measured by the IR camera. Without plasma (vacuum), this position was not heated. Additionally, in the case of discharge by NNBI only, this position was also not heated. The position of the hot spot was not shifted by changing magnetic field strengths of $B_{ax}=1.375$ T, 1.5 T, 2.5 T and 2.75 T. Therefore the position was independent of the position of the ion cyclotron resonance layer. The temperature increment of the hot spot was proportional to the RF input power from the antenna, as shown in Fig. 2a. In this experiment, the distance between the antenna and the LCFS Δ was 8 cm and the pulse width was 5 seconds. The line-averaged electron density was $0.7\text{--}1.0 \times 10^{19} \text{ m}^{-3}$. The major radius and magnetic field strength on the axis were set at $R_{ax}=3.55$ m and $B_{ax}=2.789$ T, respectively. The input power from the other antennas was kept almost constant at approximately 500 kW. Therefore, the hot spot was heated by the antenna itself. Loading resistance indicates the strength of power coupling between antenna and plasma. The definition of the loading resistance R is

$$P = \frac{1}{2} R \left(\frac{V}{Z_0} \right)^2$$

where P is the net injected ICRF power, V is the maximum voltage in the coaxial transmission line, and Z_0 is the characteristic impedance of the line. The temperature of the hot spot and the loading resistance decreased with increasing distance Δ , as shown in Fig. 2b. In the long pulse discharges, a long distance was selected to decrease the temperature, though the loading resistance decreased. Figure 3 shows the time evolution of the temperature of the hot spot. The conditions of the two discharges were identical except for distance Δ . The line-averaged electron density was $0.7 \times 10^{19} \text{ m}^{-3}$, and the major radius and magnetic field strength on the axis were set at $R_{ax}=3.55$ m

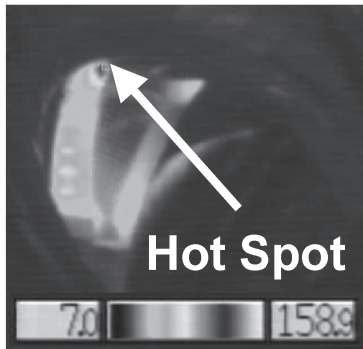


Fig. 1. Hot spot on 7.5U ICRF antenna

and $B_{ax}=2.789$ T, respectively. The input power of the 7.5U antenna was 250 kW. By changing the distance from 8 cm to 10 cm, the temperature rise was drastically mitigated. The longest plasma duration time with ICRF heating of 31 minutes and 45 seconds was achieved by employing maximum Δs (13 cm for 3.5U, L antennas and 14 cm for 7.5U antenna).

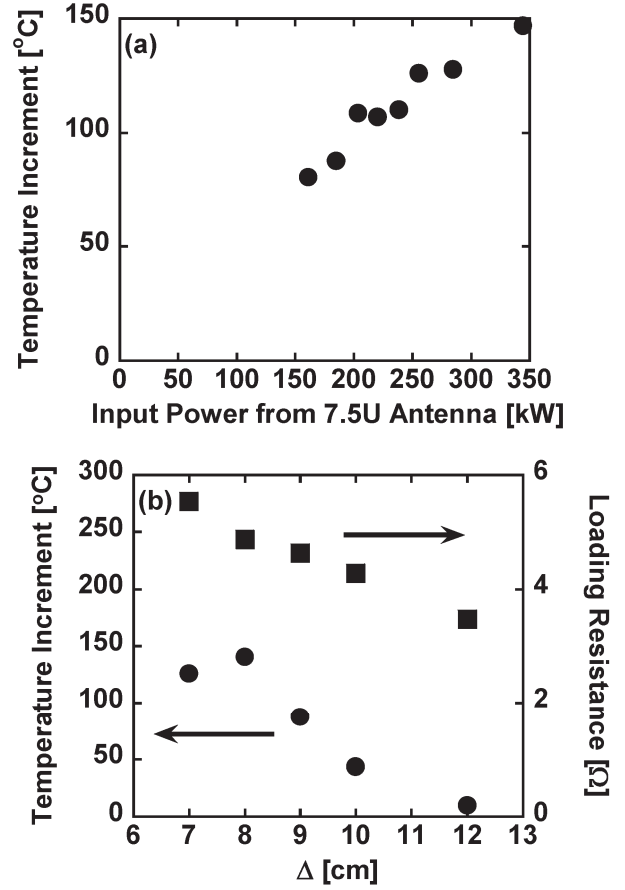


Fig. 2. Temperature increment depending on (a) input power and (b) distance between the antenna and the LCFS.

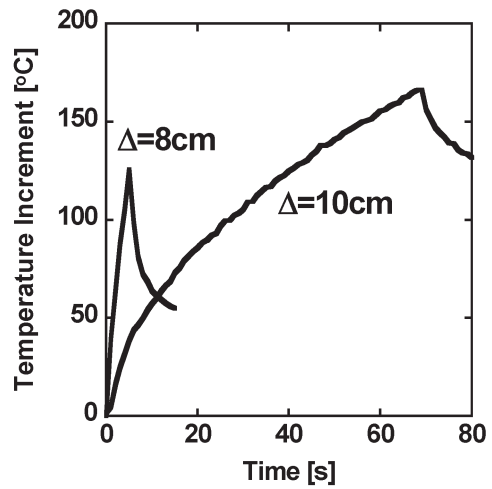


Fig. 3. Mitigation of hot spot temperature by the large distance between the antenna and the LCFS.

§5. Impedance Matching during Long Pulse Discharge in LHD

Saito, K.

Impedance of an ICRF antenna changes depending on the frequency, plasma density, and distance between the loop antennas and the plasma, etc. Therefore a tunable impedance matching system is necessary to reduce the reflected power from antenna to oscillator for high-power injection and protection of the tetrode tube. For high-power and steady-state operation in LHD, we used a liquid impedance matching system [1,2] consisting of two or three liquid stub tuners and a U-shaped link. Impedance matching was conducted by shifting the liquid heights, making use of the difference in RF wavelength between gas and liquid due to the difference of the relative dielectric constants.

For a long pulse discharge, two methods of impedance matching were employed. One was the manual-frequency control method, which can adjust the electric length between the antenna and the tuning system without changing the liquid heights of the stub tuners. The frequency control method is useful for rapid changes of plasma condition. Figure 1a shows temporal increases in a reflected RF power fraction. Without frequency control, the reflected power fraction increased to 20%, and RF operation was stopped by the interlock system. The frequency was initially 38.47 MHz, and then was decreased manually to 38.44 MHz by increments of 0.01 MHz. The final power amplifier could not function at frequencies under 38.44 MHz with the same output tuning conditions, therefore frequency control was stopped at 55 seconds and the reflected power fraction gradually increased. The frequency decrement of 0.03 MHz provides effective expansion of the transmission line from the tuning system to the antenna by 3 cm, because the distance from the stub tuners to the antenna was approximately 40 m. The effective expansion of 3 cm could not be explained by the real expansion since the maximum temperature rise in the coaxial line was only several °C. The other was an automatic feedback control method using the liquid stub tuners (trial and error method). The procedure of this control method was as follows. Two of three stub tuners were used. First, the liquid height in one stub tuner was shifted up or down. After an interval, usually 7 seconds for settlement of the liquid, the liquid height in the other stub tuner was shifted up or down. These two shifts of liquid heights may be incorrect. After the interval, the liquid height of the first stub tuner was shifted toward the first direction if the reflected power fraction decreased in the first trial and shifted toward the other direction if the reflected power fraction increased. The second stub tuner was then controlled in the same manner. This operation was repeated until the reflected power fraction was smaller than 4%. Figure 1b shows the temporal evolution of the reflected power fraction with this method. The liquid height of one stub tuner was shifted at 70 seconds because

the reflected power fraction became larger than 4%. This direction was unfortunately not correct and the reflected power fraction increased, then the liquid height of the other stub tuner was shifted 7 seconds later and this direction was also incorrect. The reflected power fraction reached 10%, at which point the correct directions were determined and the reflection fraction decreased gradually to under 4%. This method is useful only for very slow variation of loading resistance or effective length between stub tuners and the antenna because the direction is determined based on changes in the reflected power fractions with an interval. If a change in loading resistance or effective length is too large during the interval, the chosen direction may be incorrect. Furthermore, it takes a long time to reduce the reflection ratio to under 4% because stub tuners must be controlled one by one and many steps are needed to obtain impedance matching. However, an automatic impedance matching with liquid stub tuners was conducted first, and the reflected power fraction was sufficiently reduced until the end of the discharge.

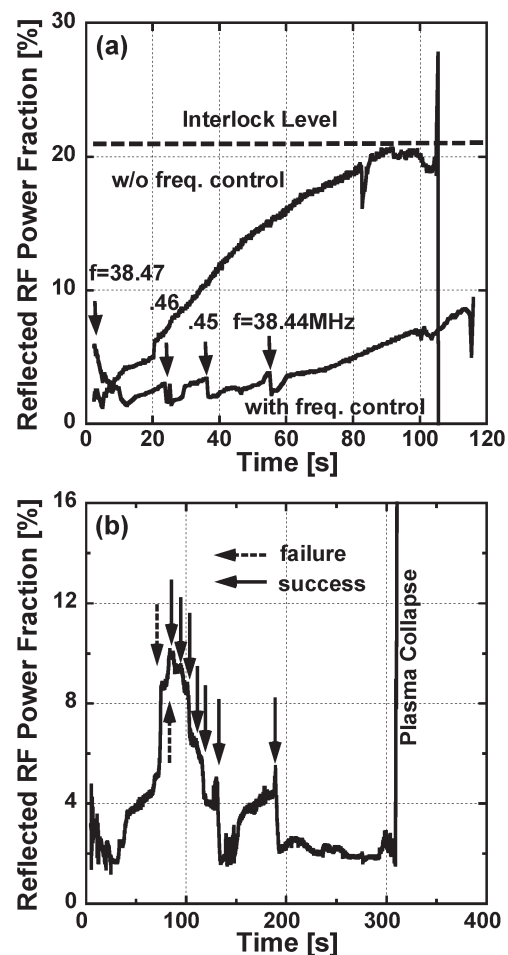


Fig. 1. Impedance matching (a) with frequency control and (b) with control of liquid heights.

Reference

- 1) Kumazawa, R. et al., Rev. Sci. Instrum. 70 (1999) 2665.
- 2) Saito, K. et al., Rev. Sci. Instrum. 72 (2001) 2015.

§6. Liquid Stub Multi-computer Control System for ICH on LHD

Takahashi, C., Yokota, M., Saito, K.

We developed a many-variable number feedback control system which could control 10 liquid stub tuners at the same time for the long-pulse plasma discharge on LHD. This control system is the multi-computer feedback system to maintain the reflected RF power fraction at the allowable level. There are many causes to increase the reflected RF power, such as plasma condition and expansion of the coaxial transmission line due to the temperature increase during the long-pulse plasma discharge. It is very important to reduce the reflected RF power because of effective ICRF heating and protecting a tetrode vacuum tube for an excess heat load on the anode plate. It is possible by employing the frequency control to keep the RF reflected power in the allowable level during the long-pulse plasma discharge. However a large shifted value of the frequency usually affects the high RF power output from the final amplifier. Therefore the method to control the liquid surface level was employed in the fixed frequency. This control system is composed by multi-computer, local LAN and UNIX server and does the compensation of liquid of the position of ten stub tuners using CW/CCW and Stop/Start of the pulse motor. Usually the liquid surface position control has a dead time and the measurement of the liquid surface level contains a noise, which results from the bubble on the liquid surface. The LAN system is usually employed at the fundamental control, but it can be used in the system, in which a waste time is abundant. If the LAN is available, the powerful control system is constructed by connecting the computer with LAN. This control system is the CINOS of the signal-processing unit, which has the multiple functions of multi-computer/multi-OS/no OS, and it is done with the computer group connected with LAN. The CINOS utilizes the Linear Time-Invariant Method (LTIM), which is the feature. Then, the CINOS can maintain LTIM when multiple interrupt from the I/O machine happens. Fundamental composition is shown in Fig.1. Two of Loder_1_3.5U/L and Loder_1_7.5U/L are used to control the 10 liquid stub tuners in two ICRF heating antenna systems (3.5U Antenna /7.5U Antenna): These two Loaders are connected as a control device of the actuator of liquid stub tuners. That is, Loader reads the liquid surface position and drives the liquid cylinder using a pulse motor, and has the duty that makes a liquid surface keep a proper position. This Loader_1 and Loader_2 are connected in the LAN that

is a special network. This LAN is connected to Loader_3. Loader_3 analyzes pre-process value of the feedback and acquires the data of the forward and the reflect RF power from the antennas. The UNIX servers of Unix_3.5U/L and Unix_7.5U/L are the main control devices, which are connected with special LAN. LAN uses the electric standard of IEEE802.3 and TCP/IP socket communication. LAN receives or sends the control information data from the computer and liquid stub tuners. The pre-process value, which has been sent by Loader_3, is changed into the speed value of liquid cylinder and the liquid cylinder shifted value to do PI control by the quadratic transformation with the Unix_3.5U/L and Unix_7.5U/L. The quadratic transformation value is sent back to Loder_1_3.5U/L and Loder_1_7.5U/L, which control an actuator to keep RF, reflected fraction less than 4%.

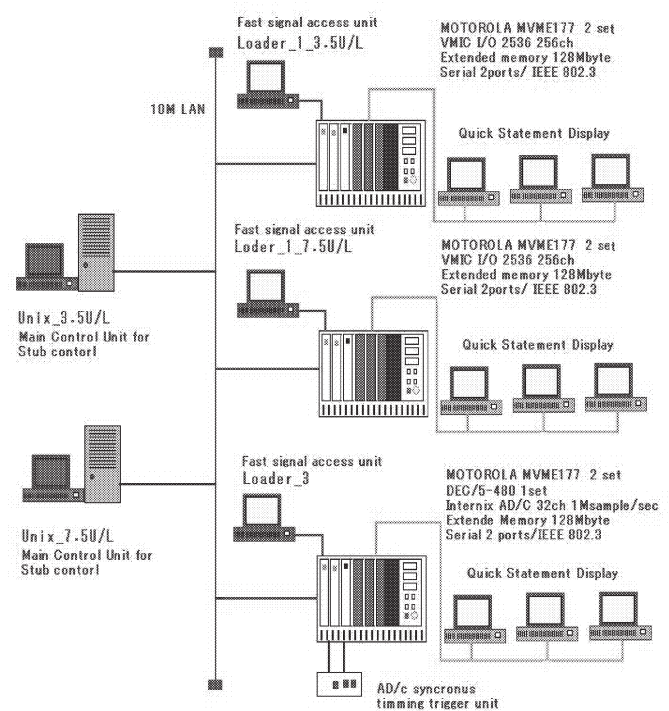


Figure.1. Liquid stub tuner control system by multi-computer control system with LAN.

Reference:

- [1] Takahashi, C. et al., Annual report of NIFS, April 2002-March 2003 285(2003)
- [2] G.Nomura, et al., 14th Topical Conference on Radio Frequency Power in Plasmas, AIP Conference Proceedings 595(2001), pp.502-505.

§7. Power Circulation System on LHD Comblne Antenna

Takeuchi, N. (Nagoya Univ.), Seki, T., Takase, Y. (Univ. of Tokyo), Watari, T.

A power circulator should be used in order to draw full performance from the LHD comblne antenna. A “ring power coupler” is employed as illustrated in Fig. 1 [1].

Let α^2 ($=1-\beta^2$) be the power transmission coefficient defined as the power transmitted to the other end of the antenna normalized to the input power. Since the comblne antenna has a wide area, it is expected that α^2 is smaller than that of a conventional antenna. Yet, it is not expected to be too small, being in the range between 0.5 and 0.9. In the present analysis, $\alpha^2 = 0.7$ is assumed [2]. A small value of α^2 is desirable in principle from the point of view of power handling capability. It is noted that a well-defined wave spectrum will not be obtained with a too small value of α^2 .

The antenna system will have a phase shifter and two impedance matching circuits. The No-3 port of the ring power coupler is terminated with 50-ohm dummy load. The RF power out of the No-2 port is circulated to the No-4 port. The RF generator is connected to the No-1 port. Z_a and Z_b are characteristic impedance of the coaxial lines composing the ring power coupler. For $\alpha^2 = 0.7$, $Z_a = 27.6$ ohm and $Z_b = 33.1$ ohm are chosen so that power is re-circulated appropriately. The characteristic impedance of other coaxial lines Z_0 is 50 ohm.

Electrical properties of the whole system were studied [2]. In Fig. 2(a), P_{ref}/P_{in} , P_{dummy}/P_{in} and P_{abs}/P_{in} are plotted versus frequency. We find an improvement of factor 3 in P_{abs} at the central frequency of 65MHz over the case without the circulator. The optimal frequency band 5MHz is not enough to cover the entire frequency range of the comblne antenna. Therefore, it

will be needed to develop a frequency tunable circulator. The parameter β^2 depends on plasma parameters. Therefore, it is important to examine the sensitivity of the circuit to β^2 . In Fig. 2 (b), P_{ref}/P_{in} , P_{dummy}/P_{in} and P_{abs}/P_{in} are plotted versus β^2 . It is find that the power circulation circuit works well over wide range of $0.1 < \beta^2 < 0.5$, i.e., $0.5 < \alpha^2 < 0.9$.

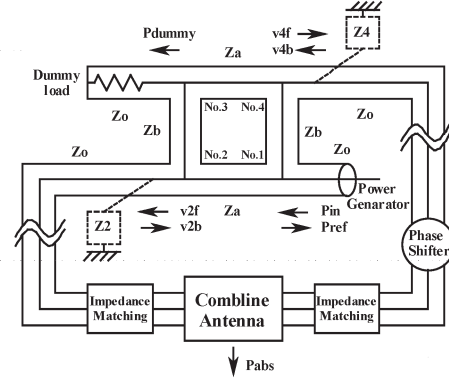


Fig.1: Power circulation system

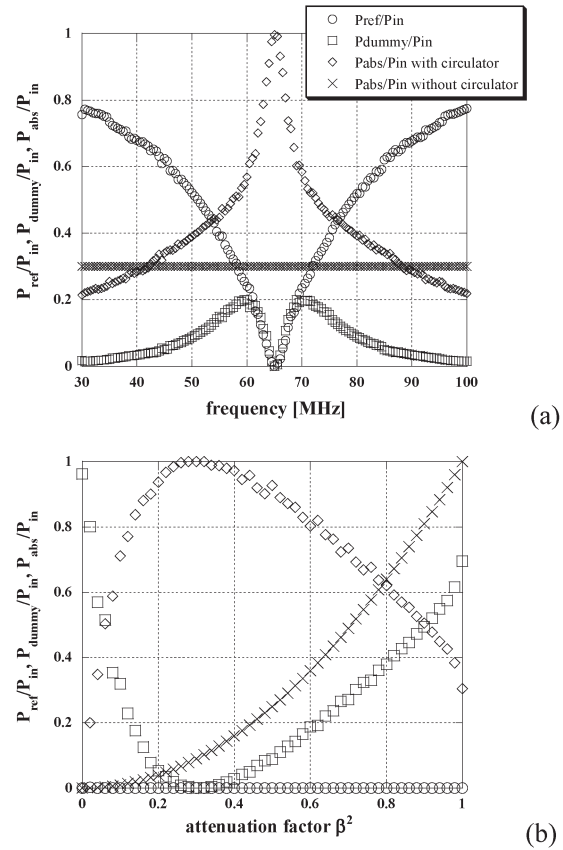


Fig.2: Calculated performance with a power circulator

Reference

- [1] H. Ikezi, GA-C23396 (2000).
- [2] Takeuchi, N., *et al.*, to be published in Fusion Science and Technology (2005) .

§8. Study on High Energy Particles Escaped from LHD Using Lost Ion Probe

Nishiura, M., Isobe, M.
Kubo, N., Sasao, M. (Tohoku Univ.)
Murakami, S. (Kyoto Univ.)
Darrow, D.S. (PPPL)

For lost ion measurements, a scintillator type lost ion probe is installed into the 5-O port of the LHD. The lost ion probe has measured the loss signals of fast ions outside the last closed flux surface (LCFS) throughout the 8 campaign.

The lost ion probe measures the pitch angles and the gyro radii of fast ions directly and simultaneously by observing the ion strike points on the scintillator plate passing through the entrance slit and the collimator slit. The emitted light from the scintillator plate is detected by a CCD camera for relatively slow signals of 33 msec/frame and by a 3x3 photomultiplier array for fast signals from dc to 20 kHz. Figure 1 shows that the gyro radius estimated from the peaks of striking points on the scintillator plate becomes small as the toroidal magnetic field increases. As a reference, both energies for negative ion based neutral particles (N-NB) and thermal ions are plotted in the same figure. The observed signals do not exceed the gyro radius estimated from the energies of N-NB, and thus the signals consider to be valid. The small difference would come from the slowing down of fast ions and the error of the probe position.

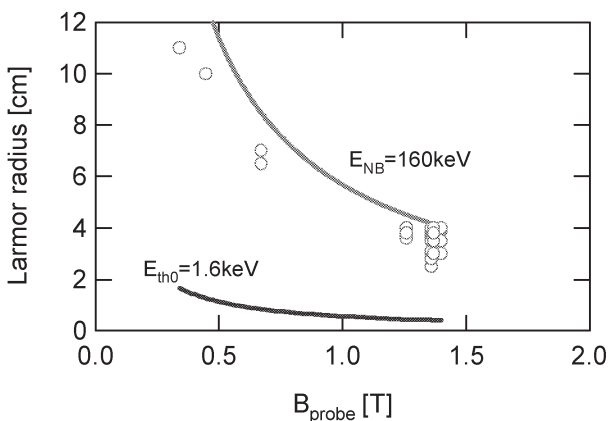


Fig. 1. Gyro radii are plotted with the magnetic field at the probe position. Gyro radii are calculated from the N-NB energy and thermal ion temperature.

The spatial distribution of lost fast ions is measured in the vicinity of the LHD plasmas, shown in Fig. 2. The intensities of the lost fast ions are plotted in Fig. 3. At 5100 mm, the decrease of the intensities of lost fast ions is observed. These data are important, and

can use the estimation of deposition profile of NB with the combination of HFREYA code.

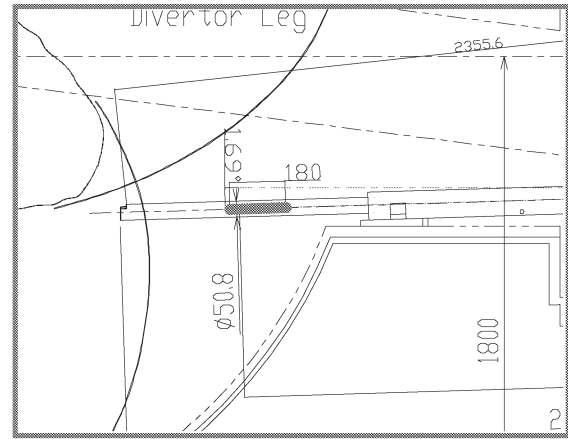


Fig. 2. Spatial distribution of lost fast ions is measured in the region of bold line on the probe shaft axis in the figure.

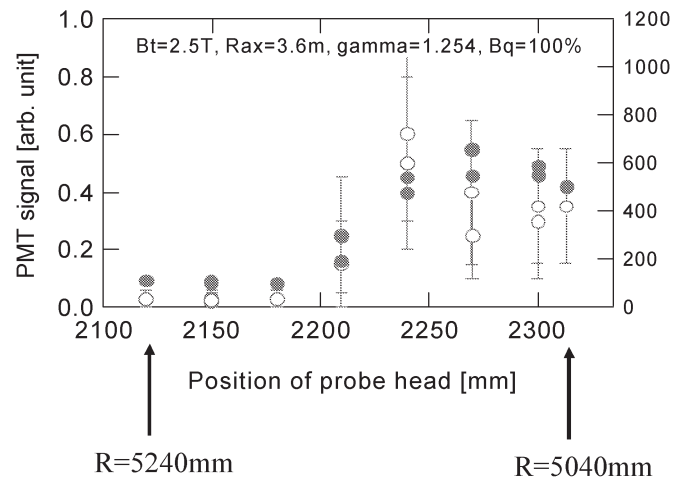


Fig. 3. The intensities of spatial distribution of lost fast ions. The electron density and temperature are $n_e(\text{FIR})=0.6\text{--}0.8 \times 10^{19} \text{ m}^{-3}$, and $T_e=2\text{keV}$, respectively.

In the high density plasma experiments, the fluctuation signals are detected with the frequency of 5 kHz before the detached plasmas phase. Under the detached plasmas, the fluctuation and intensity of lost fast ions are disappeared immediately. This phenomena would mean the changes of the deposition of NBs.

The degradation of emission light is not appeared clearly throughout this cycle, although the scintillator plate increased the temperature of up to about 190°C. Further endurance test of scintillator would be performed for severe conditions.

References

- 1) Nishiura, M., Isobe, M., Saida, T., Sasao, M., and Darrow, D. S., Rev. Sci. Instrum. **75**(2004)3646.

(4) High Energy Beam Technology

High energy beams are used in various fields of magnetic field confining nuclear fusion research. Neutral hydrogen/deuterium beam is commonly used for plasma heating, current drive, and diagnostics such as charge exchange recombination spectroscopy (CXRS) and beam emission spectroscopy (BES). Heavy Ion Beam Probe (HIBP) is another diagnostic tool using high energy beam. These tools are also used in LHD, and the successive development on the beam formation system or improvement of the measuring system is undertaken through the collaborations. Among them, the activities on the development of NBI system are reported here. Those of diagnostics (BES and HIBP) are reported in other category of this annual report.

In LHD, neutral beam injection (NBI) is a main plasma heating source as in other helical devices and tokamaks. NBI is also utilized as plasma production, which is a unique feature of LHD assisted by the fact that the confining magnetic field exists in steady state. The neutral beam is also used for measurement of ion temperature and velocity profiles via CXRS and the induced current can be used to change magnetic field configuration for MHD studies under the weak magnetic field strength.

The very specific feature of LHD NBI systems is that all of them are negative-ion based injection systems. Using negative ion is an advanced technology for making a high energy neutral beam that can be applicable for future reactors ($>1\text{MeV}$). In LHD, the maximum injection energy of hydrogen beam is 180 keV, which is even too high to construct an injector using a conventional positive ion because the neutralization efficiency is so small.

Although the negative-ion-based NBI has been in operation in LHD and JT-60U for several years, the negative ion technology is still in the course of development. Therefore, the R&D activity continues in NIFS as well as other institutes such as JAERI and CADARACHE. The most important component is a high current ($\sim 30\text{A}$) and high power ($\sim 2\text{MW}$) negative ion source, which is big for uniform plasma production, and is small for dealing with high power.

The report-1 by Takeiri et al. is a summary of all the injected beam power of three NBI beamlines in LHD through the 8th experimental campaign in FY 2004. Although total input power had increased year by year by successive improvement of negative ion sources, the results of the last campaign could not exceed that of 2003 (13MW). This is because the water leak occurred in the ion source due to the thermal fatigue of cooling channel bellows. In BL-2, the cooling of plasma grid was strengthened for long pulse operation. However, it was hard to optimize its condition for short pulse high power operation at the same

time.

The report-2 by Tsumori et al. is on the improvement of negative ion source of BL-1. The ground grid of this ion source was converted from multi-aperture type to multi-slot type, which was a big success to reduce conditioning time. However there is a problem that the optimum conditions of beam convergence are different between vertical and horizontal directions. It is demonstrated that the problem can be solved by changing the shape of holes of screen grid from circle to race track. Modified grid will be available after 2006.

The report-3 by Oka et al. is on the measurement of energy spectra of injected negative ion beam. It was confirmed that almost all the beam has fully accelerated energy as expected. A spatial uniformity of the beam is also discussed.

The report-4 by Wada et al. is on a study of transport of negative hydrogen ions in the ion source. They propose the probability for H⁻ to be extracted from the aperture of the grid as a function of size of hole, distance, ion energy and electrostatic potential.

The report-5 by Oka et al. is on development of alternative cathode other than direct-heated tungsten wire, which is a small cesiated hollow cathode (CHC). Followed from the test of single CHS in the previous year, arc discharge using four CHCs was tested. The cathode can be operated without cesium but assisted by Ar or Xe.

The report-6 by Shoji et al. is on the development of multi-antenna RF ion source which has advantage as a cathode-less log-life ion source and is easily scaled up. In this year, new parallel arrangement was tested, and the result was much better than the old loop arrangement.

The report-7 by Shinohara et al. is on the study of dense plasma source produced by helicon wave, which can also be used as a unit source for constructing a large ion source. Using Ar gas, high density plasma of 10^{19} m^{-3} can be obtained with input RF power of 1kW in the quartz tube of 10 cm in diameter, 90 cm in length, and magnetic field strength of 640 G.

(Kaneko, O.)

\$1. Operational Status of Negative-Ion-Based Neutral Beam Injection System in LHD

Takeiri, Y., Kaneko, O., Oka, Y., Tsumori, K., Osakabe, M., Ikeda, K., Nagaoka, K., Asano, E., Kondo, T., Sato, M., Shibuya, M., Komada, S.

The negative-ion-based neutral beam injection (NBI) system in LHD has progressed in its performance year by year. In the present LHD plasma experiments, the NBI is the most reliable and the most powerful heating method. The NBI system consists of three tangential injectors, BL1, BL2 and BL3, and various modifications and their tests of ion sources are carried out every year to improve the performance. These modifications and tests in the 8th LHD experimental campaign are reported, including the injection summary in the plasma experiments. Figures 1 and 2 show an injection history in the 8th LHD experimental campaign for the total port-through injection power and the individual injection powers of three injectors, respectively.

BL1 achieved a high power injection of 5.7MW in the previous campaign. The modified ion sources equipped with multi-slotted grounded grid enabled this high-power injection. However, there is a problem of large vertical beam divergence and different operational conditions for the vertical and horizontal beam steering, which cause excess heat load on the injection port. To solve this problem, a round aperture shape of the steering grid, which is used for the beamlet steering by the aperture displacement technique, was modified to a race-track shape, and the operational test was carried out. The results show mitigation of anisotropical properties of the vertical and the horizontal steering conditions. This modification will be applied to the BL1 ion sources in the next campaign.

In BL3, the outputs of the arc and filament power supplies are divided into twelve circuits, and the individual arc and filament voltages were simultaneously controlled so as the arc power distribution was made uniform. As a result, the beam uniformity was improved, leading to enhancement of the injection efficiency. The injection power was also increased to 4MW, as shown in Fig. 2.

The injection duration has been extended over several tens seconds in the long-pulse experiments. However, the further extension is restricted by an excessive rise of the plasma grid (PG) temperature, which should be maintained at 200-300°C for efficient negative ion production in the cesium operation. To suppress the PG temperature rise in the long-pulse injection, stainless-steel cooling tubes have been mechanically attached on the PG in BL2. As a result, the injection duration was extended to above 120sec with an injection power of 0.2-0.3MW using one ion source. On the other hand, the pre-arc duration must be extended to above 15sec to maintain the appropriate PG temperature in the short pulse injection. This nearly doubled arc discharge duration led to reduction of the filament lifetime and enhancement of the Cs consumption. Since the operational conditions were not optimized in the short pulse injection, the injection efficiency was lowered and the injection power was no more than 3MW in BL2.

The total injection power was 11.3MW at maximum in the 8th campaign, which was a little less than that of 13.1MW in the previous campaign. In BL1, there happened water leak at the flexible tube for cooling the grounded grid due to mechanical fatigue. The injection power of BL2 was reduced with the cooled PG in the short pulse operation. These caused the reduction of the total injection power.

The new grid system in BL1 is expected to increase the injection power, and by using the uncooled PG for the short pulse injection the injection power will be recovered in BL2. Therefore, the total injection power is expected to be increased in the next campaign.

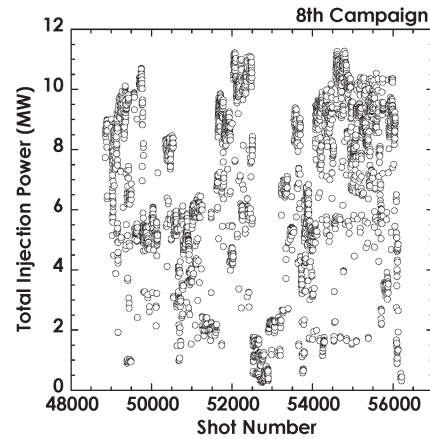


Fig. 1. History of the total injection power in the 8th experimental campaign.

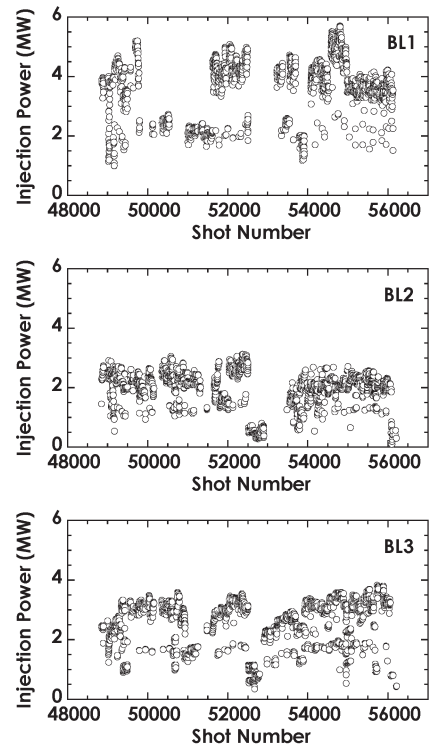


Fig. 2. History of the injection power of the individual injectors of BL1, BL2, and BL3.

§2. Correction of Beam Profile by Modifying Aperture Shape of Steering Grid II

Tsumori, K., Nagaoka, K., Osakabe, M., Ikeda, K., Takeiri, Y., Kaneko, O., Oka, Y., Shibuya, M., Asano, E., Sato, M., Kondo, T. (NIFS)
Asano, S., Watanabe, J., Suzuki, Y., Ichihashi, K., Okuyama, T. (TOSHIBA Co.)

Heat load carried by accelerated beams onto grounded grids (GG) is one of the essential points to increase the beam power and the pulse duration in large scaled hydrogen negative ion (H^-) sources for the neutral beam injection (NBI). In the acceleration of the H^- ions, some part of H^- beam separates to hydrogen atoms and electrons via the collision of H^- ion and H_2 gas diffused from the ion source. The electrons are accelerated after the collision and their trajectories are bent by the magnetic field leaked from the ion source. The electron beams collide onto the GG, and the spatial concentrations of the electron beams are high enough to melt the GG surface. It is, therefore, effective to reduce the H_2 gas load inside accelerator and to design the GG with smaller beam accepting area. To realize those two conditions, the beam accelerator consisting of steering grid (SG) and multi-slot grounded grid (MSGG) has been applied to one of the beam line for LHD-NBI since 2002 [1]. A cut view of the accelerator is indicated in Fig. 1. As shown in the figure the MSGG has a high transparency, which is twice higher than the conventional multi-circular aperture grid, and gas conductance between SG and MSGG is expected to be lower. In 2003, the maximum injection energy and power of 189 keV and 5.7 MW have been achieved using the ion sources with the accelerator [2].

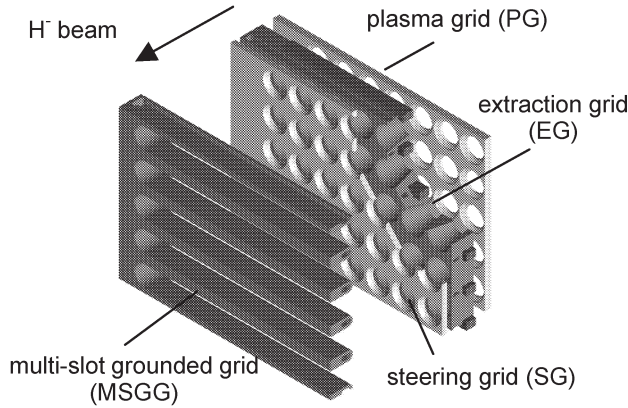


Fig. 1. A cut view of beam accelerators with the steering grid, SG, and multi-slot grounded grid, MSGG.

Although the accelerator with the MSGG has an advantage to increase the injection power, the system involves a large demerit caused by the different symmetry of electric field near the SG and MSGG [3]. The influence is observed as the separation of focal condition in the direction of the slot long and short sides; the feature is not observed in accelerators consisting of multi-circular aperture grids. Figure 2 shows the beam widths in the both directions as the functions of voltage ratio (R_v) of acceleration voltage (V_{acc}) to extraction voltage (V_{ext}). In the practical operation of the ion source, R_v is chosen in the gray area in Fig. 2, and the beam profile elongates in the one direction. The profile distortion induces the irregular

concentration of the beam inside the beam line, and the beam injection port and beam dump had been melted.

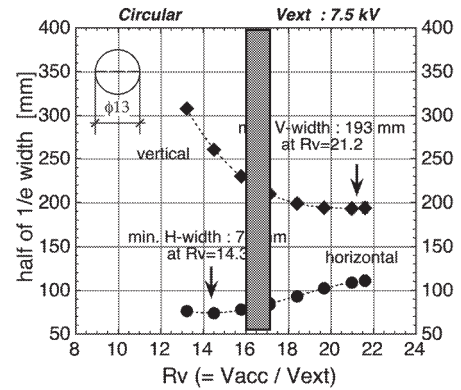


Fig. 2. e-folding half width of beam profile as a function of voltage ratio (R_v) of acceleration voltage (V_{acc}) to extraction voltage (V_{ext}). The solid circles and solid diamonds indicate the widths parallel and perpendicular to the slot-long-side of the MSGG, respectively. The shape of the SG aperture is circular on with the diameter of 13 mm.

The investigation has been done to decrease the separating focal condition using a small-scaled ion source consisting of the SG with multi-racetrack apertures [3]. There are some differences in small-scaled source and LHD ion source, for instance the grid gaps, applied voltages and so on. The SG with racetrack apertures is investigated to confirm the validity for the reduction to focal separating characteristics in LHD-NBI.

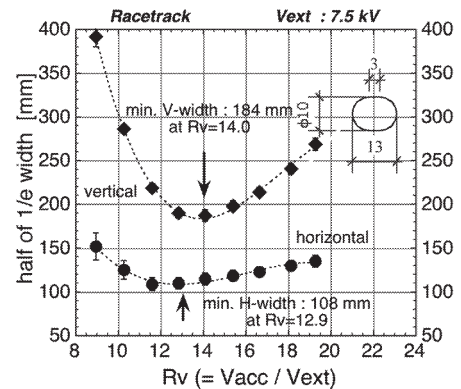


Fig. 3. e-folding half width of beam profile as a function of voltage ratio (R_v). The data was obtained with use of the accelerator with MSGG and racetrack SG apertures ($\phi 10 \times 13$ mm).

The focal characteristic on a combination of the SG racetrack apertures and MSGG is indicated in Fig. 3. The long and short sides of the racetrack are 13 and 10 mm, and the long side corresponds to the slot long side of the MSGG. The voltage ratios obtaining the minimum widths in the long and short direction of MSGG slot become closer in the system with racetrack-SG apertures comparing to that with circular apertures. By modifying the shape of SG aperture, the damages inside the beam line is considered to decrease, but also the beam port-through efficiency is expected to increase.

[1] K. Tsumori et al, Rev. Sci. Instrum, 75 5 pp.1726-1728 (2004)

[2] K. Tsumori et al, proceedings of 20th IAEA conf, FT/1-2b, Vilamoura (2004).

[3] K. Tsumori et al, proceedings of 10th International Symposium on the Production and Neutralization of Negative Ions and Beams, Kiev, (2004).

§3. Doppler Shift Spectra of H α Lines from Negative Ion Based Neutral Beams

Oka, Y., Grisham, L. (PPPL), Umeda, N. (JAERI), Ikeda, K., Takeiri, Y., Tsumori, K., Honda, A. (JAERI), Ikeda, Y. (JAERI), Kaneko, O., Nagaoka, K., Osakabe, M., Yamamoto, T. (JAERI), Asano, E., Kondo, T., Sato, M., Shibuya, M.

The velocity spectra of the negative ion based neutral beams with doppler-shifted H α spectroscopy, as well as the effectiveness of the spectroscopy¹⁾ has been studied / collaborated. In the 8th experimental cycle, the spectra from beam-line-1, BL-1 in addition to BL-2 and BL-3 have been newly measured to study the differences probably reflected by the ion source design and the operation conditions.

An internal mirror (Fig.1) was mounted inside the vacuum vessel of BL-1 to keep the same angle of line of sight as those in BL-2 and BL-3. We conducted systematic observations of the velocity distribution profiles in standard LHD-NBI injection (Fig.2), the spectra over the course of 70 ~ 128s long-pulsed beams with reduced power, and the behavior of negative ion beam stripping in the accelerator. Almost all of the transmitted beam power (Fig.2) was found to be at approximately the full acceleration energy (170keV). A very low energy peak due to beam particles stripped in the extractor gap (at ~8keV) is observed. It was observed that the similar spectrum profiles were repeatedly reproduced throughout the day, while the operating condition for the neutral beam was kept constant with a high power level of ~4.5MW/2.

H- ion uniformity (Fig.3) in an LHD-ion source along the long direction of ~125cm was deduced by the full energy component coming from five vertically arrayed grid sectors¹⁾. It was found that the H- ion current is fairly uniform, and that there is still the prospect of increasing the H- current throughput by about 15% at the optimum perveance, if the uniformity is improved.

For long beam pulses, the magnitude of the full energy peak gradually declined as the beam pulse duration increased. When conductively cooled plasma grid was used, the spectra did not change for a longer time compared to those with a standard (i.e., a thermally isolated-) plasma grid.

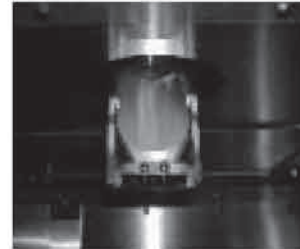


Fig. 1 Mirror system in-side the vaccum vessel.

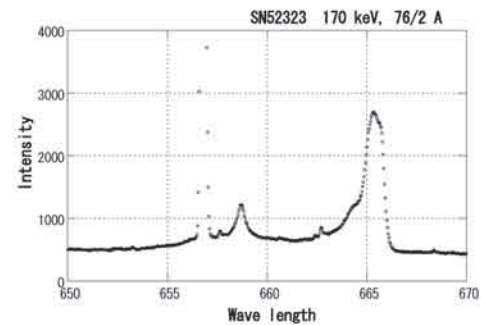


Fig.2 Spectrum in beam line-1 from negative ion based neutral beam.

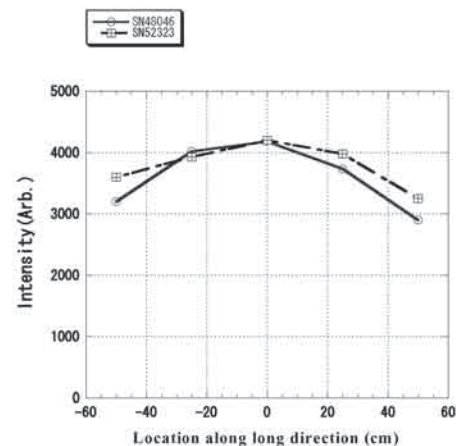


Fig.3 H- ion distribution along long direction in LHD H- ion source.

Reference

- 1) Y. Oka et al., Rev. Sci. Instrum. **75**, (2004)1803.

§4. Fundamental Processes in H⁻ Ion Source Plasma

Wada, M. (Doshisha Univ.)
 Matsumoto, Y. (Grad. School Adv. Studies)
 Yamaoka, H. (RIKEN)
 Sasao, M. (Tohoku Univ.)
 Tsumori, K.
 Nishiura, M.

Neutral beam heating based on electrostatic acceleration of negative hydrogen ions (H⁻) is one of the most promising candidates to heat magnetically confined plasmas up to temperatures necessary to realize thermonuclear fusion conditions. The optimization study of the H⁻ ion source and that of the acceleration system are being carried out at the National Institute for Fusion Science, and a reliable plasma heating system for Large Helical Device has already been achieved. However, a further development to improve reliability of the heating system is desirable for extending the operation time of a plasma confinement device. Fundamental processes influential upon the H⁻ ion extraction is being studied by measuring the perturbation in the extracted H⁻ beam caused by destroying local H⁻ by pulse laser photodetachment.¹⁾

The experimental setup is schematically illustrated in Fig. 1. The spacing between the plasma electrode and the laser beam, z , is changed to investigate the relative importance of the local H⁻ density on the laser path to the extracted laser beam. A 9-cm diameter, 11-cm long magnetic multicusp ion source is equipped with a magnetic filter to realize an efficient extraction of H⁻ ions. Local plasma parameters and an H⁻ density are measured with a movable Langmuir probe. A beam of H⁻ is formed with a single gap extraction system. The beam current is measured by a Faraday cup after separating electrons with a permanent magnet electron suppressor unit.

Typical oscilloscope traces of the H⁻ current signals at the time of photodetachment of H⁻ in the near plasma electrode region of the ion source are shown in Fig. 2. As shown in the figure, the signal amplitude is smaller and the delay time for the signal to reach its maximum is larger for larger z . Through conducting a series of precise experiments, the probability for an H⁻ ion to be extracted from an aperture of radius R is found to be expressed by the following equation.

$$P(z) = \frac{1}{2} \left(1 - \frac{z}{\sqrt{z^2 + R^2}} \right) \exp \left(\frac{3}{2} \frac{\Delta\Phi(z)}{K(z)} \right) \quad (1)$$

Where $\Delta\Phi(z)$ and $K(z)$ are the local potential and the H⁻ kinetic energy, respectively.

Necessary conditions for equation (1) to be valid are negligible effects of collisions and a weak intensity of the magnetic filter field. These effects upon the H⁻ transport toward the extraction aperture have been investigated with the present device. The filter field effect is qualitatively

understandable, while the effect due to collision is not straight forward to interpret. A particle trajectory based numerical simulation model was developed to clarify the effects of ion-neutral collisions near the plasma electrode. Results of the model reasonably agree with ones obtained from experiments for near collision free conditions. Modification of the model is being made to properly simulate plasmas of high collision frequencies.

Other factors affecting the extractable H⁻ current are studied with various methods. These include VUV spectroscopy,²⁾ and the dc laser photodetachment diagnostics, which has revealed the transport velocity of negative ion containing plasma is substantially slower than the ion acoustic speed of H⁻.³⁾ The enhanced H⁻ cooling effect due to neutral collisions will be further studied so as to realize better extraction geometry for H⁻ ion sources.

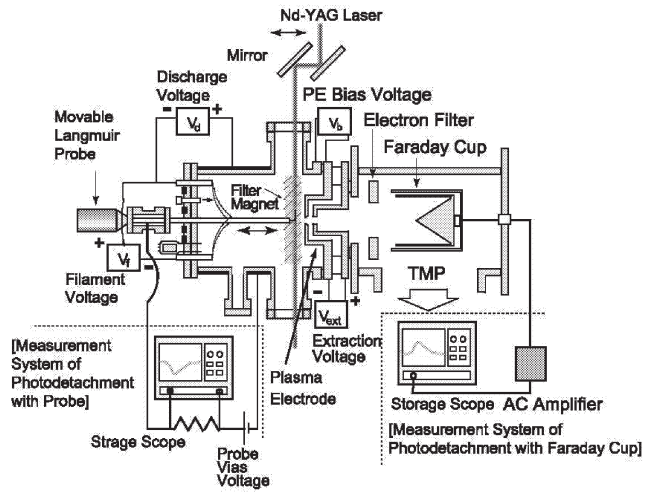


Fig. 1. Experimental setup.

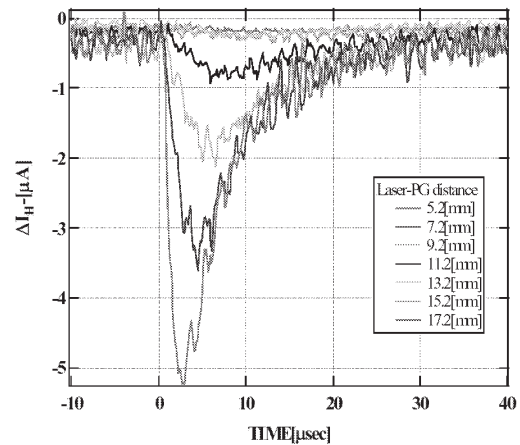


Fig. 2. Typical oscilloscope traces showing the change of H⁻ beam current induced by laser irradiation into the extraction region of a H⁻ ion source.

References

- 1) Matsumoto, A., Nishiura, M. *et al.* Rev. Sci. Instrum. **75**, 1757 (2004).
- 2) Bacal, M. *et al.* Rev. Sci. Instrum. **75**, 1699 (2004).
- 3) Takahashi, H. *et al.* Rev. Sci. Instrum. **75**, 1780 (2004).

§5. Plasma Injection from Several Cesiumated-Hollow Cathodes into the Large H⁻ Ion Source¹⁾

Oka, Y., Belchenko, Yu. (BINP, Russia), Davydenko, V. (BINP, Russia), Ikeda, K., Kaneko, O., Nagaoka, K., Osakabe, M., Takeiri, Y., Tsumori, K., Asano, E., Kawamoto, T., Kondo, T., Sato, M.

To develop the long lifetime plasma source, we started to establish the system of compact cesiated-hollow cathode which will be available for the multi-cusp plasma source of LHD-NBI²⁾. Hollow cathode is considered to be a reliable cathode and can produce plasma injection for long time. Seeded cesium for CHC in H⁻ ion source would potentialize H⁻ ion production efficiently. In contrast to previous experiments with a single high current hollow cathode, we have suggested to use the set of compact Cesiumated Hollow Cathode (CHC) for production of uniform plasma in the large area multi-cusp source. CHCs which was investigated and fabricated in BINP³⁾ was newly fitted to large multi-cusp H⁻ ion sources on the LHD-NBI test stand. Advanced hollow cathode operation without Cs was tested in the discharge voltage-current characteristics.

Four CHCs were attached on side wall in large 1/3rd scale H⁻ ion source with external magnetic filter. Dimension of plasma source was 38 x 62 x ~20cm³. Plasma-, extraction-, and acceleration grids had multi-holes over the area of 25 x 25cm². Specially designed power supply system for CHC operation was prepared on the test stand.

We ignited the CHC numbers in due order and succeeded to operate simultaneously three CHCs (Fig.1). Waveforms of discharge voltage and the current had quiet waveforms for ~5sec pulse. Discharge voltage in range 20~50V, and discharge current in range 50~70A were independently controlled for each cathode. Gas pressure in multi-cusp plasma chamber, measured with baratron gauge ranged 0.5~4mT.

Cold-hollow cathode was operated without Cs introduction in 1/3rd scale source (Fig.2)¹⁾. There was no wiring to CHC heater and Cs-pellet oven heater, although the pellet oven was filled with new pellets (without activation for Cs). 100% Ar, 100% Xe, or mixture of 30% Xe + 70% H₂ gases, instead of H₂ gas were introduced into cold-HC. Xe pressure was 0.6 – 1.1 mT and Ar 0.6 – 0.9 mT. Stably, discharge current up to ~70A were obtained for 5s every 120sec. Discharge ignition strongly depended on kind of gases, and the discharge impedance with Xe is lower than that with Ar.

We established the new system of simultaneous operation of

several hot CHCs in LHD-NBI 1/3rd scale plasma source. Technical issue of the system and operation were studied and in part solved via the R&D on the test stand.

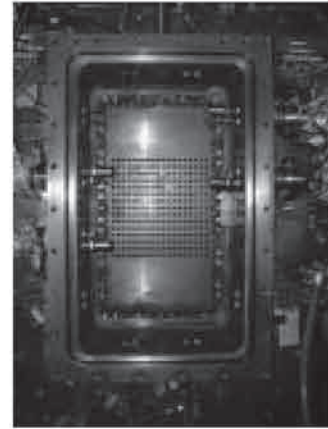


Fig.1 Photo of four CHCs on filament feedthrough port in 1/3rd scale H⁻ ion source

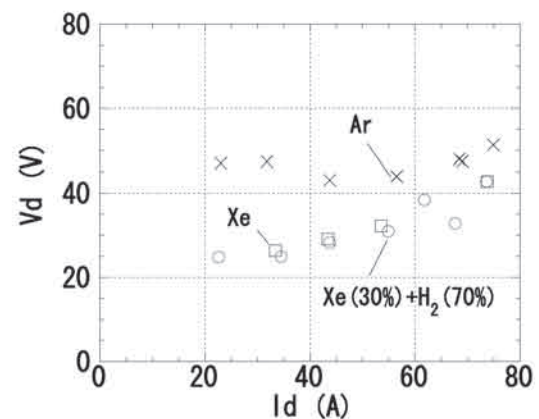


Fig.2 Discharge voltage vs discharge current with one cathode in cold-HC. This is the case without Cs and without heating the hollow cathode.

The authors would like to acknowledge NIFS and BINP for supporting continuously the collaboration.

References,

- 1) Y. Oka et al, in 10th International Symp. on the PNNIB, Kiev, Ukraine, Sept. 2004
- 2) Yu. I. Belchenko et al., Rev.Sci.Instrum., vol.73, 940(2002)
- 3) Yu. I. Belchenko and A. S. Kupriyanov, Rev. Sci. Instrum., vol.69, 929(1998)

§6. Rf Power Performances for Ring Shaped and New Parallel Rod Multi-antenna Systems of Rf Ion Source

Shoji, T. (Dept. Energy Eng. And Sci., Nagoya Univ.)
Oka, Y.

As a filament less system, rf ion sources have several advantages, such as easy maintenance, long operation time, less contamination from the filament metals etc. However, high beam current and large diameter beam are necessary to be developed for the practical NBI source for the fusion research. We have been developing the multi-antenna rf ion source for these purposes¹⁻³⁾. The ring shaped rf antennas were exchanged to the new rod shaped one designed for the higher power operation.

The old ring shaped antenna elements (Fig.1 (b)) are made of copper rods and placed in ceramic pipes to avoid taking the net electron current from the plasma, which raise the plasma potential. The new antenna (Fig.1 (c)) is designed to reduce the antenna inductance, increase a breakdown voltage and improve density uniformity. The antenna consists of four parallel copper pipes (6φ, 200mm long) inserted into 20φ quartz tubes. The antennas are installed in 35 cm x 35 cm x 18 cm rectangular multicusp plasma chamber and are connected electrically outside the chamber as shown in Fig.1(a).

The maximum rf power is 50kW and frequency is 9MHz. The ion saturation current I_{ion} is measured by Langmuir probe. Preliminary result of rf power dependence on I_{ion} for old and new parallel antenna system is shown in Fig. 2. The number of parallel antenna segments is four in both cases. I_{ion} for the old antenna jumps around 10kW and rf breakdown occurs at ~15kW. The new antenna does not show any break down below 40kW and creates high ion current. Further investigation of the plasma characteristics produced by the new antenna is now underway.

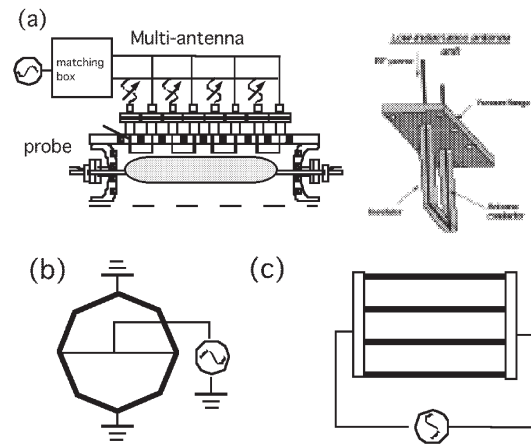


Fig. 1 (a) Multi-antenna RF ion source and segmented antennas, (b) old segmented loop antenna system and (c) new 4 parallel antennas.

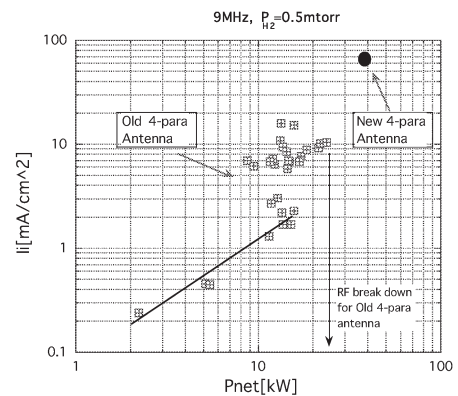


Fig. 2 Ion saturation current at the center of bucket chamber as a function of rf input power for old ring shaped and new parallel antenna systems. rf frequency is 9MHz. Hydrogen pressure is 0.5mtorr.

Reference

- 1) Shoji, T, Sakawa, Y, Hamabe, M and Oka, Y., Ann. Rev, NIFS, (2001) 141
- 2) Y. Oka, T. Shoji, in 5th JA-EU Workshop on NBIs (Super JDC), Sept. 18, 2000, CIEMAT Madrid.
- 3) Y. Oka, T. Shoji, et al, 10th ICIS2003, Sep.2003, Dubna, Russia

§7. Development of RF Plasma Source for Negative Ion NBI

Shinohara, S., Mizokoshi, H. (Interdis. Grad. Sch. Eng. Sci., Kyushu Univ.)
Kaneko, O., Tsumori, K.

The high power neutral beam injection (NBI) heating utilizing negative ions have been actively executing in NIFS. Concerning the future plasma source in NBI, key issues to be studied are easier plasma production with a good stability, higher plasma density and higher ionization, and developments of large or compact sources. In addition, developing a neutral beam source with the high particle flux is important in the charge-exchange recombination spectroscopy. The present objective is, first, characterizing a high-density, compact plasma source, using a helicon wave scheme [1] in the range of radio frequency. Then, developing a negative ion source with, e.g., hydrogen gas, will be carried out to apply to the advanced NBI in NIFS.

The construction of the compact helicon plasma source with the strong magnetic field has been completed. The main device parameters are as follows: the discharge chamber uses a quartz tube, which has an outer (inner) diameter of 10 (9.5) cm and 90 cm axial length. The magnetic field B can be applied up to 10 kG, whose main strong field region extends to ~ 30 cm in the axial direction. Here, iron yokes are added to increase the field.

Two parallel plates with 3 cm in the axial direction each used as the rf antenna, are wound around the quartz tube at the midplane. Here, the spacing between two copper plates is 6 cm. By changing the electrical connection between two plates (parallel and anti-parallel current directions), the excitation of the axial wavenumber spectrum can be changed [2,3]. The rf frequency can be varied in the range of 3 - 15 MHz, 145 MHz and 435 MHz (with pulsed as well as continuous operation modes). In order to estimate the antenna loading, a directional coupler monitoring the incident and reflected power is used in addition to measure the antenna voltage and current. A Langmuir probe is scanned radially at the midplane, and two probes inserted from the top and the bottom flanges move axially. For the electron density calibration, 70 GHz microwave interferometer system has also been installed.

We will present the results on the plasma performance using an argon gas [4]. Figure 2 shows an example of the plasma density n_e , changing input rf power P_{rf} (rf frequency is 7 MHz) with argon pressure P_{Ar} of 10 mTorr. A so-called density jump to the range of 10^{13} cm $^{-3}$ was observed with less than 1 kW of P_{rf} . Here, due to the better radial confinement with the

increase of the magnetic field, n_e was higher in the high field region before the density jump. This jump became weaker with the increase of this field (see, e.g., $B = 3,040$ G case). Figure 2 shows the relationship between the electron density and the magnetic field with $P_{rf} = 1.6$ kW. In both cases of $P_{Ar} = 4$ and 10 mTorr, n_e was higher near $B = 640$ G, which corresponds to the condition that the excitation frequency is close to the lower hybrid frequency.

In conclusion, the experiments on the plasma production in the electron density range of 10^{13} cm $^{-3}$ were successfully carried out using a compact, high magnetic field device. The more detailed characterization in a wide range of operating parameters will be done. The optimized condition obtained will be expected to contribute to the advanced NBI system in NIFS.

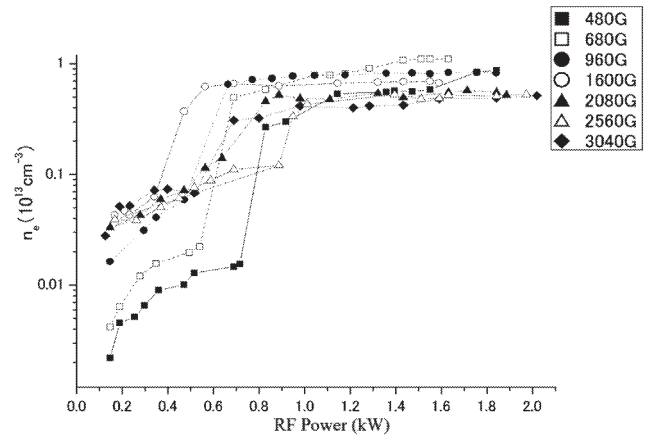


Fig. 1. Electron density as a function of rf power.

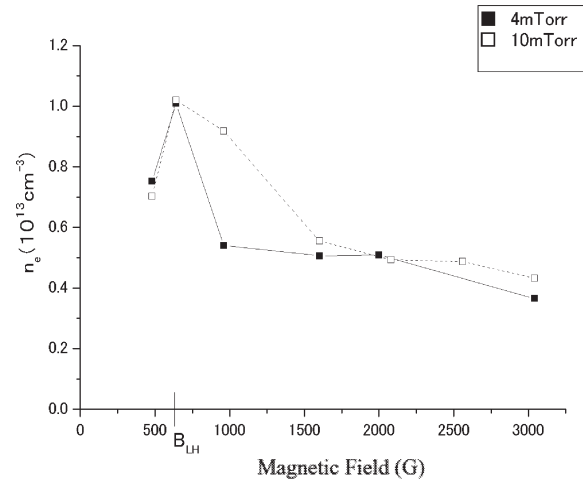


Fig. 2. Electron density vs. magnetic field.

Reference

- 1) S. Shinohara, J. Plasma Fusion Res. **78** (2002) 5.
- 2) S. Shinohara *et al.*, Plasma Phys. Control. Fusion **42** (2000) 41 and **42** (2000) 865.
- 3) S. Shinohara *et al.*, Phys. Plasma **8** (2001) 3018.
- 4) H. Mizokoshi and S. Shinohara, 21st JSPF Annual Meeting (2004) 25pA30P.

(5) Diagnostic Systems

For the precise measurement of plasma parameters in the three dimensional helical plasma, an extensive set of diagnostics have been routinely operated. The present status is that the total number of diagnostics is over 45 owing to the continuous efforts for the development of new diagnostic instruments by researchers.

The YAG laser Thomson scattering system and the ECE system have proven as reliable diagnostics for the temporal evolution of the electron temperature profile. The YAG laser TS system works routinely to provide the electron temperature profile with a flexible repetition rate (from μs to hundreds of ms). On the other hand, the data quality of the electron density is far from satisfactory due to incomplete absolute calibration of each polychromator. So far, we have tried absolute calibration using hydrogen Raman scattering and nitrogen Raman scattering several times, but the results were not reproducible. For the sake of more efficient calibration work a conventional method using a diffusive light reflected from a BaSO₄-coated plate has been developed.

A 13-channel far infrared laser interferometer has been routinely operated for the precise measurement of the electron density profile in the Large Helical Device. The spatial and time resolutions are 90 mm and 1 μs , respectively. A CO₂ laser imaging interferometer has been developed for detailed profile measurements of density and density fluctuations. The imaging system is employed by using three slab-like beams and multi-channel detector arrays to measure the fine structure of the density profile with a spatial resolution of 15 mm. In addition to these density diagnostics, a new type of reflectometer using an ultra-short sub-cycle pulse has been developed in order to get a fine structure of a density profile. An ultra-short pulse has broad band frequency components in a Fourier space. This means one ultra-short pulse can take the place of a broad band microwave source. A new two color FIR laser interferometer system using short wavelength laser sources ($\lambda = 57.2 \mu\text{m}$ and $47.6 \mu\text{m}$) is under development for future high-performance LHD plasmas. By introducing Ge:Ga photoconductive detectors two color beat signals were successfully detected.

The plasma potential profile is an important quantity in a helical system since the radial electric field plays an important role in particle orbits and their losses. A heavy ion beam probe (HIBP) is being developed to measure potential and density fluctuation in high temperature plasmas. The LHD-HIBP system is composed of a negative ion source, a tandem accelerator of 6 MeV, beam lines, and an energy analyzer. In the last experimental campaign, the secondary

beam was successfully detected, but the signal beam is extremely low so that the signal to noise ratio corresponds to the change in plasma potential of 400 eV. In order to improve the S/N, further improvement of the ion source and the beam line is necessary.

A tracer-encapsulated solid pellet (TESPEL) has been developed for impurity particle and heat transport studies. A TESPEL ball consists of polystyrene polymer as an outer shell in diameter of 300 – 900 μm and tracer particles as an inner core. The TESPEL injection has been implemented for various important studies as well as for impurity transport studies. In order to reduce extra impurities due to capsule evaporation and ionization a new injector for making solid hydrogen pellets around cores has been developed. When such a pellet enters the plasma, the outer solid hydrogen layer is ablated first, keeping the impurity core from ablation up to the plasma axis. This results in an intensive ablation of the core providing the small localization of the deposited tracer ions.

For multi-dimensional measurements of the non-axisymmetric LHD plasma 2-D or 3-D imaging diagnostics are under intensive development with national and international collaborators: tangential cameras (Fast SX, photon counting CCD, H α CCD), tomography (tangential SX CCD, AXUV) and mm wave imaging (ECE, reflectometer). A 3-D ECE imaging system has been developed in collaboration with Kyushu University. The imaging system is composed of a detector array, quasi-optical system, and IF system. By using microwave integrated circuit (MIC) technology, the IF system including broadband amplifiers, power dividers and band-pass filters has been realized on a dielectric substrate.

A data acquisition system with parallel processing technology has been developed for diagnostics with a 3 minute cycle during LHD operation. Data of most diagnostics are taken by the CAMAC system. The total number of CAMAC modules and channels are about 300 and 2000, respectively. The raw data size is up to 2GB/shot with 150 shots/day. In the 8th campaign wide-band real-time data acquisitions using Yokogawa WE7000 digitizer and NI PXI/CmpactPCI are introduced in addition to conventional CAMAC systems. The longest discharge duration of LHD was over than one hour. The LHD data acquisition system had established a new world record for the acquisition data amount ~ 84 GB in a single plasma discharge. For effective remote participation with domestic universities, LHD has a powerful network realizing 1 Gbps streaming by introducing the super science information network.

(Kawahata, K.)

§1. A Convenient Method of Calibrating Relative Sensitivity of Multi-Channel Thomson Scattering Diagnostic System

Narihara, K., Yamada, I., Hayashi, H.

The Large Helical Device (LHD) is equipped with a 200-channel Thomson scattering diagnostic (TS) [1], which can yield space-resolved electron temperature (T_e) and density (ne) profiles along the major radius passing the magnetic axis at a horizontally elongated poloidal section. Through repeated spectrum calibrations of the polychromators, the data quality of the electron temperature profile has reached a satisfactory level, though not yet perfect. On the contrary, the data quality of ne is far from satisfactory due to incomplete absolute sensitivity calibration of each polychromator. Initially we planned to do absolute-calibration using hydrogen-Raman scattering, but abandoned this for the safety reason. Instead, we tried several times nitrogen-Raman scattering calibration, but, to date, the results are not reproducible and far from satisfactory. The deduced ne profile with the calibration has much larger channel-to-channel variations than the un-calibrated ne profile. The reason for this was speculated that the nitrogen-Raman spectra lie at the very steep wing of the first filter in the polychromator, which makes the measurement to be very sensitive to change of the filter-characteristics caused, for example, by changes in room temperature or in the light-collection-geometry. We must repeat many trials further. In order to pursue this tedious calibration work efficiently, we developed a convenient method to measure relative sensitivities among the polychromators as described below.

To simulate light coming from the scattering volumes in a plasma and passing the view window, we used light diffusively reflected from a BaSO₄-coated plate (33 cm x 60 cm) set on the surface of the viewing window in the airside. The thickly coated BaSO₄ was checked to reflect with little spectrum distortion. The BaSO₄-plate was illuminated by 10 ns pulse light guided by an optical fiber from an optical parametric oscillator (OPO). A light-expander with a rectangular aperture similar to the window shape was attached at the exit of the optical fiber. The wavelength of the OPO was swept between 1020-1060 nm to measure the sensitivity of the first filter-detector combination. Trial and errors and careful checks were necessary to eliminate stray optical paths linking the OPO to the input of the polychromators. The OPO output, which fluctuates appreciably, was monitored by an ultra-fast thermopile detector to normalize the spectrum-responsivity. With this experimental setup, we measured the sensitivities of the first spectral-channel of the polychromators. The wavelength-responsivity relations (filter functions) of the color channel proximate to the laser wavelength (1064.3 nm) are over-plotted for 114 polychromators in Fig.1. We can see that the height and width of the filter-function varies appreciably polychromator-to-polychromator. The repeated measurements over weeks showed a good

reproducibility. Combining the calculated data on the scattering length and the solid angle for each spatial-channel with the filter-function thus measured, we can obtain the coefficients necessary for deducing ne profile. The ne profile thus obtained (OPO channel#4 data) are shown in Fig.2 together with the uncalibrated profile (DC all channel data). There still remains large channel-to-channel variations, though much larger one are removed. In addition to these channel-to-channel variations, the right-left asymmetry in the profile is a problem yet to be solved. We must make continued great efforts.

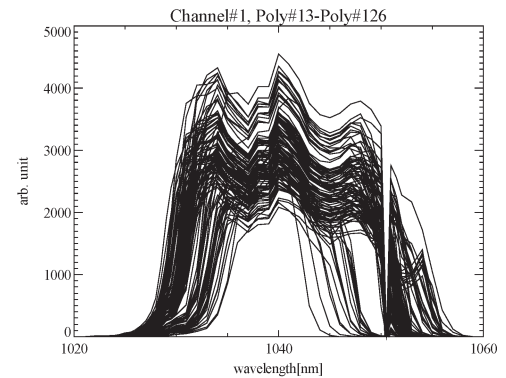


Fig. 1. Wavelength-dependent-responsivities of the color channel proximate to the laser wavelength.

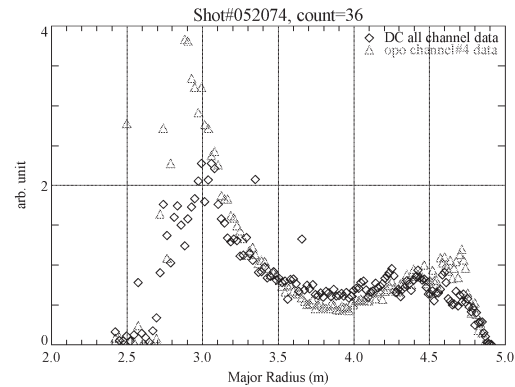


Fig. 2. ne profiles with (triangle-mark) and without (diamond-mark) the calibration.

[1] Narihara, K., Yamada, I., Hayashi, H., Yamauchi, K. Rev. Sci. Instrum. 72, (2001), 1122.

§2. An Estimation of Uncertainties in Electron Density Measurements due to the Beam Spatial Variations in the LHD YAG Thomson Scattering

Yamada, I., Narihara, K., Hayashi, H., Funaba, H.,
LHD Experimental Group

The LHD YAG Thomson scattering [1][2] has been applied successfully to the measurements of electron temperature profiles of LHD plasmas, however it gives not always satisfactory, reliable electron density profiles [3]. Laser beam pointing instability and misalignment are candidates for ones of the major sources of experimental errors in the absolute density measurements. As shown in Fig.1(b), when the laser beam image slips off the center of optical fibers on which Thomson scattered photons are collected, photon collection efficiency decreases. In addition, the image is unfocused, and then the image becomes wider, the collection efficiency decreases also as shown in Fig.1(c). In order to estimate the influence of such laser beam path variations and/or misalignment on the electron densities measured, we carried out laser beam modulation experiments by moving two beam steering mirrors actively in LHD steady-state discharges.

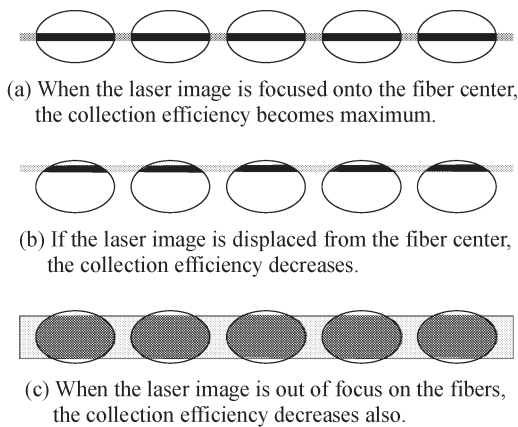


Fig.1, Decrease in collection efficiency due to misalignment and unfocused image.

An example of raw data detected with a five-channel polychromator is shown in Fig. 2. The signal intensities are proportional to plasma density. In this laser modulation experiment, modulated and fixed laser beams were used. As expected, the signal intensity from the modulated beam is modulated (upper curve) and that from the other fixed laser is free from modulation. We estimated experimental errors due to laser path variations from the amplitude of the modulated component in the signal intensity.

Fig. 3 shows the estimated errors due to laser beam variation and misalignment. In the figure, results for ten polychrometers are plotted. We believe that realistic beam pointing variation is smaller than 125 μrad . Then, possible errors originated from beam spatial variation have been estimated to be less than 10-15 %. It is noted that beam

pointing stabilities in the laser systems themselves have been measured actually to be less than 25-30 μrad .

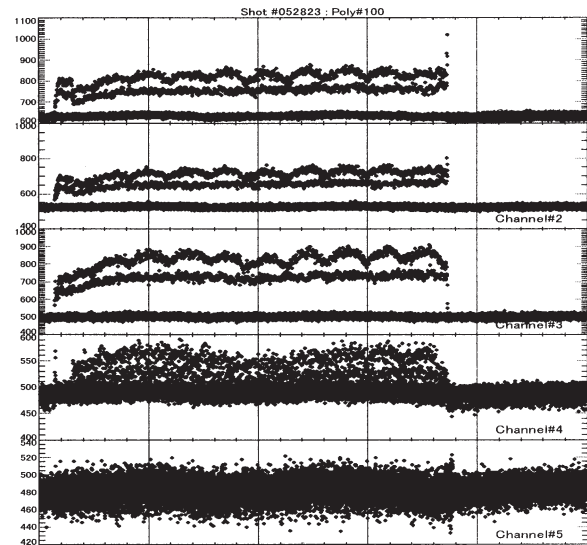


Fig.2, Raw signals from a five-channel polychromator. Upper modulated signals from the modulated laser and lower one from the fixed laser.

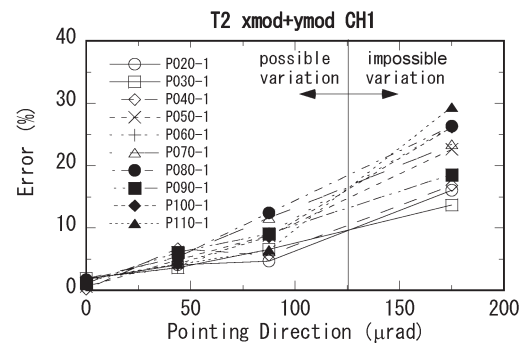


Fig.3, Estimated experimental error due to laser beam path variation and misalignment.

The beam modulation experiments have provided useful information on the reliability of electron density profiles measured with the LHD YAG Thomson scattering. However, complete understandings have not yet obtained. We are planning further experimental checks, careful calibrations and sophisticated simulations.

References

- [1] Narihara, K., *et al.*, Fusion Eng. Design, Vol.34-35, 67-72 (1997).
- [2] I. Yamada *et al.*, J. Plasma Fusion Res., Vol.76, 863-867 (2000).
- [3] I. Yamada *et al.*, Rev. Sci. Instrum., Vol.74, No.3, 1675-1678 (2003).

§3. Development of *Ka*-band Ultrashort Pulsed Radar Reflectometer for Electron Density Profile Measurement

Tokuzawa, T., Kawahata, K.

Recently we have been developing a new type of reflectometer which is used an ultrashort sub cycle pulse. It is called as an ultrashort pulsed radar reflectometer. An ultrashort pulse has broad band frequency components in a Fourier space. It means one ultrashort pulse can take the place of a broad band microwave source.

The ultrashort pulsed radar reflectometer system was shown in the previous annual report. An impulse of -2.2 V, 23 ps full-width half-maximum is used as a source. To extract the desired probing range of the frequency, we utilize a *Ka*-band rectangular waveguide. When the impulse is launched into the waveguide, it is transformed to the chirped wave including broad frequency components. It is caused by the dispersion effect of the electromagnetic wave in the waveguide. The output chirped wave from the waveguide is amplified by a power amplifier and then is launched into the plasma. The incident wave reflects back from the cut-off layers corresponding to each frequency component. The reflected wave is mixed with 42 GHz continuous wave of the local oscillator. The output from the mixer is amplified by the intermediate frequency (IF) amplifier (2 – 18 GHz) and then divided to ten. Each IF signal is filtered by band pass filters which the centre frequencies are 3, 5, 6, 7, 9, 10, 11, 12, 13, 14 GHz and they correspond to 39, 37, 36, 35, 33, 32, 31, 30, 29, 28 GHz, respectively, in the incident frequency components. The ten signals are detected by the Schottky barrier diode detectors to obtain the reflected signal pulses. The reflected pulses are amplified by pulse amplifiers and leaded to constant fraction discriminators (CFD). A part of the incident wave is extracted with a directional coupler and is detected to obtain the reference pulse. Both the reference pulse as the start signal and the reflected pulse as the stop signal are leaded to the time-to-amplitude converter (TAC). The output voltage of TAC is proportional to the time difference between the start and the stop signal. The spatial ambiguity estimated from the TAC output has been tested and defined lower than 6 mm.

By using the ordinary wave the measured flight time of each frequency pulse reflected from the plasma has been described by

$$\tau_p(\omega_0) = \left(\frac{\delta\phi(\omega)}{\delta\omega} \right)_{\omega=\omega_0} = \frac{2}{c} \int_{r_a}^{r_c(\omega_0)} \left(1 - \frac{\omega_{pe}^2(x)}{\omega_0^2} \right)^{-1/2} dx, \quad (1)$$

with r_a the edge of the plasma, c the velocity of the light, ω_0 the probing frequency, ω_{pe} the plasma frequency, and $r_c(\omega_0)$ the position where the plasma frequency equals the probing frequency, respectively. The result of the time evolution of TOF measurement is shown in Fig. 2. The delay time is defined by the travelling time from the assumed plasma edge to each cut off layer. When the

corresponding cut-off layer is generated in the plasma, each reflected wave is observed in order. By using Abel inversion the position of the reflecting layer is given by

$$r_c(\omega_0) = \frac{c}{\pi} \int_0^{\omega_0} \tau(\omega) / \sqrt{\omega_0^2 - \omega^2} d\omega. \quad (2)$$

Figure 3 shows the time evolution of the reconstructed density profile. In this inversion the cubic spline interpolation is used for connecting the data points between the lowest frequency cut-off layer and the assumed plasma edge.

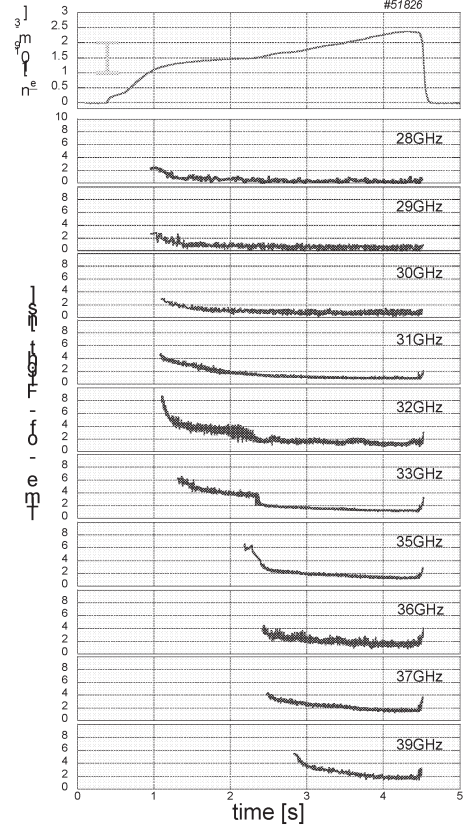


Fig. 1. Time evolution of the averaged density (top) and the delay time of the reflectometer each channel.

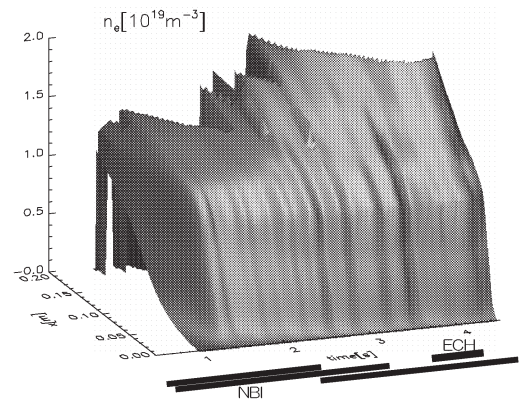


Fig. 2. Time evolution of the reconstructed density profile

§4. The First Detection of the Secondary Beam of the 6 MeV Heavy Ion Beam Probe on LHD

Ido, T., Shimizu, A., Nishiura, M., Katoh, S., Nishizawa, A., Tsukada, K., Yokota, M., Ogawa, H., Inoue, T., Hamada, Y.

A heavy ion beam probe (HIBP) is being developed to measure potential and density fluctuation in high temperature plasmas. We achieved to inject the primary beam in the LHD vacuum vessel and to detect it in the previous experimental campaign in 2003 - 2004. So, we tried to detect the secondary beam produced in the plasma in this campaign.

The secondary beam current is predicted to be attenuated to 10^{-3} or less of the injected beam when the line averaged density of the LHD plasma is $1.0 \times 10^{19} \text{ (m}^{-3}\text{)}$, and to decrease corresponding to the increase of the plasma density¹⁾. At present, the injected beam current is $1 \text{ }\mu\text{A}$ at the maximum, thus the secondary beam current $10^{-3} \text{ }\mu\text{A}$ or less. On the other hand, $10^{-1} \text{ }\mu\text{A}$ of the secondary beam was necessary for the potential measurement with the sufficient accuracy in the previous HIBPs. Therefore, the secondary beam current must be increased. We are developing the ion source to increase the source beam²⁾, the beam line to improve the beam transport efficiency, and the detector with high detection efficiency to detect the lower beam current.

One of the noteworthy improvements is the installation of the new detector with micro channel plates (MCPs). MCPs are available to detect charged particles through the multiplication of the secondary electron current, and actually they are used as the detectors of the HIBP on GAMMA-10 in Tsukuba university. However, they have not been used for heavy ions with MeV range of the energy, yet. Moreover, the MCPs also respond to the light emitted by the plasma and it causes a noise possibly. So, it is necessary to check the performance of the MCPs in the real experimental situation. The MCPs were tested by use of doubly charged gold ions (Au^{2+}) with the energy of a few MeV³⁾⁴⁾, and we confirmed the MCP could detect the high energy heavy ions.

As the results of the improvement, the secondary beam produced in the plasma was detected successfully for the first time. The experimental conditions are the magnetic field strength of 2.75 T, the major radius of the magnetic axis of 3.6 m, and the plasma is produced with electron cyclotron heating (ECH). The energy of the probe beam of the HIBP is 5.04 MeV and the primary beam current is about $0.1 \text{ }\mu\text{A}$. Figure 1(a) shows the temporal behavior of the line averaged electron density. Figure 1(b) shows the voltage of the injection sweeper which is used to control the injection direction of the primary beam, and the beam is injected toward the center of the plasma during the voltage of 0 kV and it is not injected into the plasma during the voltage of 14 kV. The secondary beam signal is shown in Fig. 1(c), where the nominal current gain of the MCP is 10^5

and the signal is averaged for 10 ms. The signal appears only while the primary beam is injected into the plasma, and that means the signal is not noise, such as the emission from the plasma, but the secondary beam. The secondary beam is detected before the start of the discharge, and it is produced through the collisional ionization by the neutral gas in the vacuum vessel. The secondary beam current increase at the start of the discharge, and it changes corresponding to the change in the plasma density. Unfortunately, the potential of the plasma can not be calculated with the data because the beam alignment was not complete, yet. However, the signal to noise ratio corresponds to the change in the plasma potential of 400 V, therefore the change in the potential profile will be measured during the formation of the internal transport barrier.

In this campaign, the secondary beam could be detected successfully, but the signal is extremely low so that it must be integrated for several ms. The high temporal resolution, that is one of the advantages of HIBPs, is lost consequently. Although the ratio of the secondary beam current to the primary beam current is predicted to be 10^{-3} or more, the ratio is 10^{-6} in this experiment and it is rather low. The detection efficiency to the high energy heavy ions of the MCP may be lower than the nominal value. The calibration of the MCP is necessary. The ion source and the beam line must be also improved further in order to increase the injected beam current on the other hand.

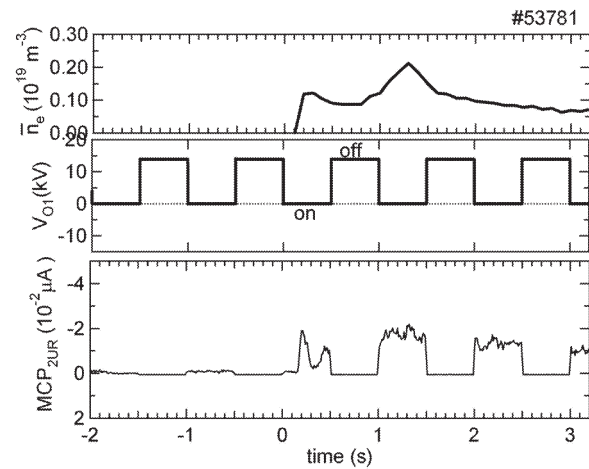


Figure 1: (a) Line averaged electron density. (b) Sweep voltage of the HIBP. (c) Secondary beam current signal measured with MCPs.

Reference

- 1) A. Fujisawa, et al.: IEEE Trans. Plasma Science, 22 (1994) 395
- 2) M. Nishiura, et al.: in this Annual report
- 3) A. Katoh, et al.: in this Annual report
- 4) A. Shimizu, et al.: in this Annual report

§5. Confirmation of Beam Orbit of the Heavy Ion Beam Probe on LHD

Shimizu, A., Ido, T., Nishiura, M., Katoh, S., Nishizawa, A., Tsukada, K., Yokota, M., Ogawa, H., Inoue, T., Hamada, Y.

The installation of 6 MeV heavy ion beam probe (HIBP) system to LHD was completed in previous year, and the secondary beam was tried to be detected for checking beam orbit and calibrating energy analyzer in this year. The secondary beam was successively detected by using micro channel plates (MCP) that are high gain current detector and that provide us with the capability to measure a very small amount of current. In this report, an experimental result to check the beam orbit by using the signal from MCP is shown.

The beam orbit of HIBP in LHD is deflected by sweepers, which are 8-pole type electric deflector. Sweepers are installed at the beam injection point to plasma and at the front of the energy analyzer. In the experiment shown in this report, only the first sweeper was used. The electric field produced by this sweeper is characterized by two parameters, V1 and V2, which are the voltage supplied to plates in two perpendicular directions. Both V1 and V2 were swept as sine wave, and the signal from MCP located at the front of the entrance slit of analyzer was investigated.

In Fig.1, the time traces of sweeper voltage, V1, V2, and the detected signal with MCP are shown. The condition of magnetic field was, $B_t=2.75T$, $R_{ax}=3.6m$. The secondary beam arose from collision with neutral gas in this experiment. Since the MCP detects electron, the signal appears as minus value. The detected signal is The gain of this MCP is about 10^3 , therefore the total current of secondary beam was about 0.1 nA. In Fig.2, the shading map of signal intensity in V1-V2 space is shown. Shading level of map means the intensity of detected signal. In V1-V2 space, the region where signal intensity is large is localized. The secondary beam is the sheet beam, because the secondary beam ions arise from the primary beam path anywhere. This secondary sheet beam orbit was numerically calculated, and the minimum distance between this sheet beam and the position of MCP detector was estimated. In this calculation, V1, V2 were swept and the map of the

minimum distance in V1-V2 space was produced. The contour lines shown in Fig.2 are drawn by using this calculation result. As shown in Fig.2, the detected current intensity by MCP coincides with these counter lines, therefore the beam was controlled well by sweeper as we intend to do.

The calibration of energy analyzer is not complete yet, since the ratio of signal to noise is small at the detector in the energy analyzer. By optimizing beam line and improving ion source, the current intensity will be increased in the next experiments and the calibration will be done.

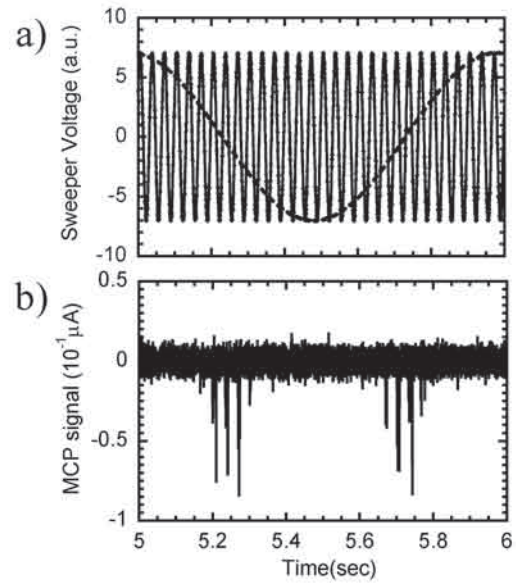


Fig.1 a) Voltages supplied to plates of sweeper. Solid line and dotted line correspond to V1 and V2 respectively. b) Detected signal with MCP located at the front of energy analyzer.

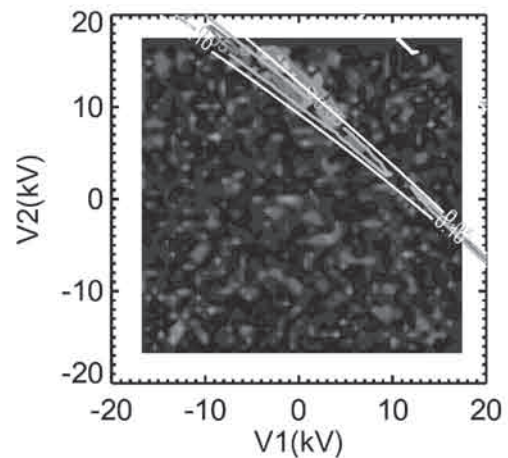


Fig.2 Shading map of detected signal intensity in V1-V2 space. Counter lines are made from calculation result, and which mean the minimum distance between secondary beam and MCP detector.

§6. Performance and Development of Au⁻ Beam Source for a Heavy Ion Beam Probe of the LHD

Nishiura, M., Matsumoto, Y., Shimizu, A., Ido, T., Tsukada, K., Kato, S., Nishizawa, A., Hamada, Y., Mendenilla, A. (Doshisha Univ.), Wada, M. (Doshisha Univ.)

Heavy-ion-beam-probe (HIBP) system is being developed for understanding of plasma behavior, especially the potential profile and density fluctuation in the Large Helical Device (LHD). A sputter type negative ion source is adopted for the HIBP system of the LHD. During the fiscal year 2002, the gold negative ion (Au⁻) beam with the current of a few micro amperes has been achieved at the exit of the ion source. However in the HIBP system of the LHD, we need to inject stable gold negative ion beams of at least a hundred micro amperes at the entrance of the 6 MV tandem accelerator. For higher Au⁻ beam current operation, we have investigated the basic characteristics of the ion source and have started to optimize the ion source at a test stand facility.

Ion sources were operated at the test stand facility in the diagnostic building and the actual facility in the LHD main building. Figure 1 shows the former Au⁻ ion source and the first extraction system. The size of the cylindrical ion source is 8 cm in diameter and 9 cm in length. The gold target for sputtering is inserted into the ion source. The electrostatic extraction system consists of an electrode with the 5-mm-diam. hole. By adding cesium vapor into the ion source, ion beams are extracted from the ion source.

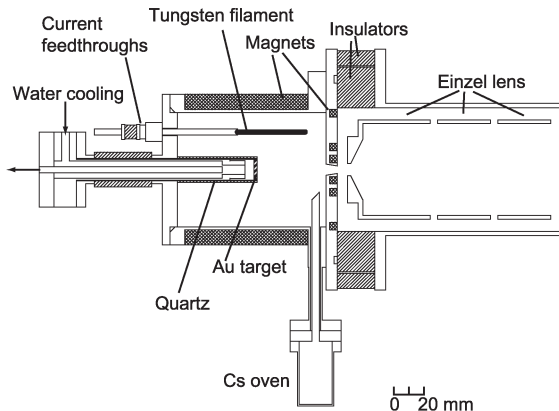
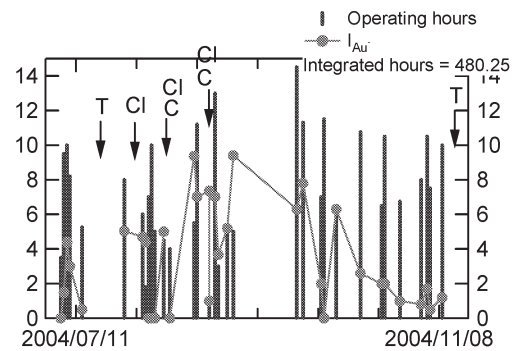


Fig. 1. Sputter type negative ion source and extraction system.

At the test stand facility, the Au⁻ ion source yielded the Au⁻ beam current of 39 μ A at the target voltage $V_t = -500$ V and the beam energy of 10.5 keV. However we could not keep the discharge stable under the operation of the beam current larger than 10 μ A. Performance of the beam output at the LHD-HIBP beam line is shown in Fig.

2. The Au⁻ beam current of about 5 ~ 10 μ A was extracted stably, and thus doubly charge stripped Au⁺ beam current of around 0.1 μ A was injected into the LHD vacuum vessel successfully. The conversion efficiency from Au⁻ to Au⁺ was more than 0.1. For high current and stable dc-operation, a new ion source, shown in Fig. 3, has been built. The characteristics are compared between the two ion sources of Figs. 1 and 3. Further optimizations will be made to achieve higher beam current.



Operating dates

Fig. 2. Au⁻ beam current(μ A) and operating hours corresponding to the operating dates using the LHD-HIBP system. The characters in the figure denote T: change of gold target, Cl: cleaning of ion source, and C: change of cathode, respectively.

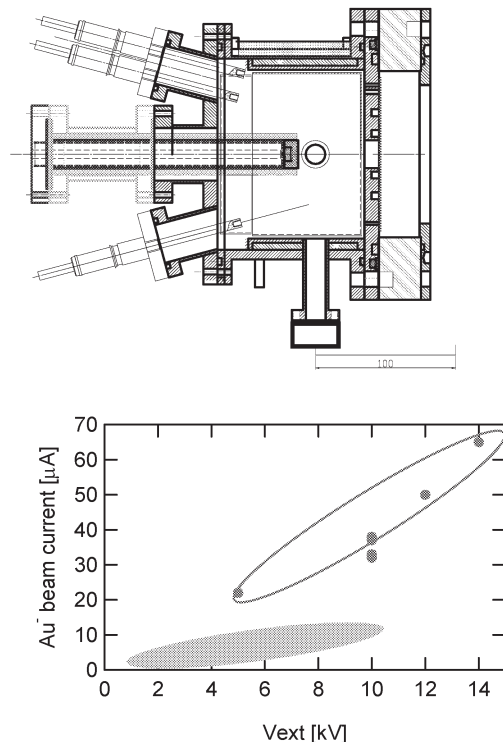


Fig. 3. Schematic of new ion source and the graph of regions of Au⁻ beam current.(open ellipse: new ion source, closed one: present ion source)

§7. Measurements of Rotational Transform Due to Non-inductive Toroidal Current Using Motional Stark Effect Spectroscopy in Large Helical Device

Ida, K., Yoshinuma, M., Watanabe, K.Y., Kobuchi, T., Nagaoka, K.

The change of rotational transform due to the non-inductive plasma current driven by negative neutral beam, which is typically less than 10 % of rotational transform determined by the external current in the helical coils, are measured in the Large Helical Device with Motional Stark Effect (MSE) spectroscopy. Radial profiles of rotational transform are derived from the radial profiles of the polarization angle of the σ component in the H_α line emitted from the high energy hydrogen atom of the beam with four sets of linear polarizers, spectrometers and CCD detectors. The radial profile of the change in rotational transform due to the non-inductive toroidal current driven by the neutral beam is measured[1].

Figure 1 shows the CCD image for the H_α emission emitted from the neutral beam measured with different polarization angle. Each group has four spectra with 0, 45, 90 and 135 degree linear polarizers starting from the top. Clear peaks corresponding to the σ components (which is parallel to the magnetic field) are observed for the spectra with a 0 degree linear polarizer at the top of each group. Two peaks with a separation of 40–50 pixel are observed for the spectra with the 90 degree linear polarizer at the second line from the top of each group, which correspond to the π component (perpendicular to the magnetic field). The third line and forth line correspond to the spectra with 45 and 135 degree, respectively. These spectra are contributed by both σ components and π component and the contribution depends on the direction of the magnetic field. The spectra with a 45 degree linear polarizer (third line) has a larger contribution from σ components for groups 7–13, which indicates that the magnetic field is tilted upward. On the other hand, the spectra with a 135 degree ($= -45$ degree) linear polarizer (fourth line) has a larger contribution from σ components for groups 17–20, which indicates that the magnetic field is tilted to downward.

In order to derive the rotational transform, the equilibrium code VMEC is used. The radial profile of the polarization angle measured is compared with that calculated with a VMEC database with various pressure profile and current profiles. The VMEC data consists of a few hundred equilibria with various total pressure, total toroidal current, and current density profile. Figure 2(a)(b) show the radial profile of the rotational transform in the equilibrium magnetic field which gives the best fit to the polarization angle measured. The total toroidal current measured with a coil is used in this best fit process. Then the central rotational transform depends on the current profile for a given total toroidal current. When the current profile is peaked at the plasma center, the central rotational

transform becomes large (small) for the positive (negative) toroidal current.

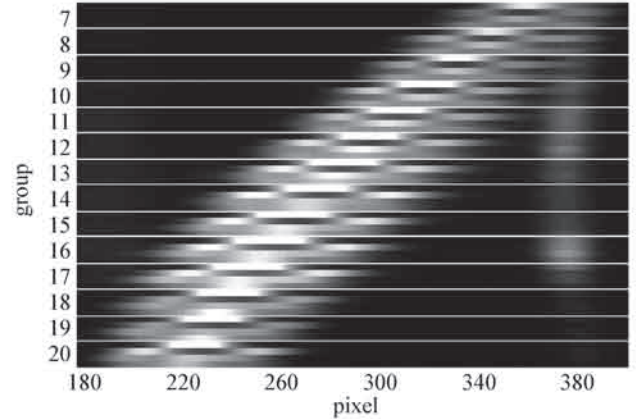


Fig. 1. CCD image for the spectra of Doppler shifted H_α emission from beam hydrogen atom.

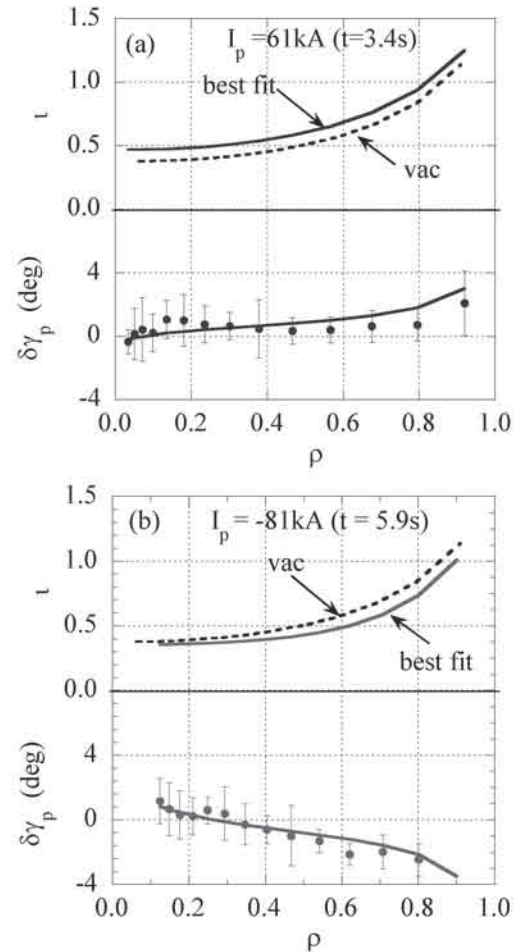


Fig. 2. The radial profile of the shift of polarization angle due to plasma and rotational transform for the best fit to the measured polarization angle and vacuum rotational transform in the plasma with (a) a positive toroidal current of 61kA (co-injection) and (b) a negative toroidal current of -81kA (counter-injection).

Reference

- 1) Ida, K., et.al., Rev. Sci. Instrum. **76**, (2005) 053505

§8. Argon Transport Obtained with an Assembly of Pulse Height Analyzer in LHD

Muto, S., Morita, S.

Spatial- and time-resolved spectroscopy in the x-ray region is required to obtain significant information about impurity transport as well as the time evolution of electron temperature-profile. In the present article the experimental result of argon transport in Large Helical Device (LHD) is preliminary reported.

An assembly of Pulse Height Analyzers (PHA) has been designed and constructed to investigate the profiles of the x-ray spectra in LHD.[1] The assembly is equipped with a spatially scanning system which makes it possible to measure the radial profile of x-ray spectrum. With the system, the sight line of the PHA can be scanned in the radial direction of LHD. The most specific feature of the assembly is that the inversion of a line integrated spectrum is available. The range of x-rays measured with the assembly is regularly from 1 to 13 keV. In this region, both continuous radiation and the K_{α} lines emitted from argon have been observed.

In the present research a diffusion coefficient and a convective velocity of argon particles in LHD plasma have been successfully estimated. The continuity equation for an impurity ion is described by

$$-\frac{\partial}{\partial t} n(\vec{r}, t) = \nabla \bullet \vec{\Gamma}(\vec{r}), \quad (1)$$

where $n(r, t)$ and $\Gamma(r)$ are an impurity density and an impurity flux, respectively. It is assumed that the impurity flux is expressed by the summation of a diffusion term and a convective term as follows;

$$\vec{\Gamma}(\vec{r}) \equiv -D(\vec{r}) \nabla n(\vec{r}) + \vec{V}(\vec{r}) n(\vec{r}), \quad (2)$$

where $D(r)$ and $V(r)$ are the diffusion coefficient and the convective velocity, respectively. In an assumption of following equation

$$n(\rho, t) = A(\rho) f(t - \phi(\rho)), \quad (3)$$

it is possible to solve Eq.(1) approximately as follows;

$$D(\rho) \cong -a^2 \left(\rho A(\rho) \frac{\partial \phi(\rho)}{\partial \rho} \right)^{-1} \int_0^{\rho} d\xi \xi A(\xi), \quad (4)$$

where a , ρ , $A(\rho)$, $f(t)$, and $\phi(\rho)$ denote an averaged plasma radius, a normalized plasma radius which is a non-dimensional parameter, the amplitude of the impurity profile, the time evolution of the impurity, and the profile of a phase shift which is a time necessary for the impurity particles to penetrate to a position of ρ in the plasma. In addition the convective velocity is approximately solved as follows;

$$V(\rho) \cong \frac{1}{a} D(\rho) \frac{\partial}{\partial \rho} \ln A(\rho). \quad (5)$$

Fig.1 shows a measured phase shift-profile of the argon particles in LHD. In the present experiment several identical discharges have been performed, while the position of the sight line has been changed shot by shot. In Eq.(4) and (5) it is qualitatively demonstrated that the profile of the diffusion coefficient and the convective velocity are depending on the derivative of the phase shift-profile.

The diffusion coefficient and the convective velocity of the argon particles have been estimated from the experimental result as shown in Fig.2. As is shown in the figure, it is especially suggested in Eq.(4) and (5) that the local structures of the diffusion coefficient- and the convective velocity-profiles can be evaluated in LHD.

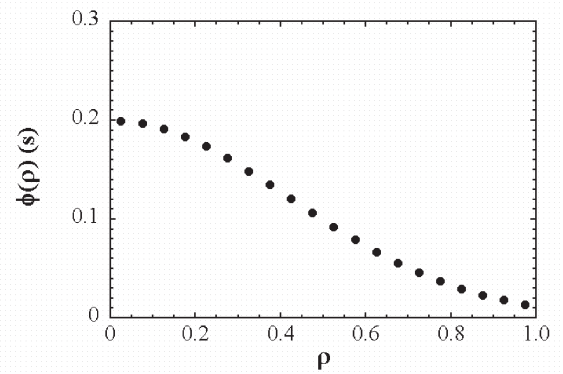


Fig.1. The measured phase shift-profile $\phi(\rho)$ of the argon particles in LHD. The time when argon was puffed is corresponding to 0 sec in the vertical axes. The time necessary to penetrate into the plasma center is estimated to be approximately 0.2 sec.

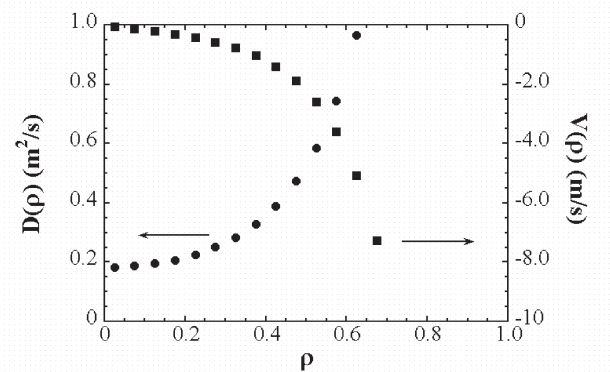


Fig.2. The diffusion coefficient (filled circles) and the convective velocity (filled squares) of the argon particles estimated from the experimental result obtained with the assembly of PHA.

Reference

[1] Muto S., and Morita S., Rev.Sci.Instrum. **72**,1(2001)1206.

§9. Microwave Imaging Reflectometry for the LHD Edge Plasma

Pavlichenko, R., Nagayama, Y., Kawahata, K., Mase, A., Ignatenko, M., Kogi, Y. (Adv. Sci. & Tech. C. Coop. Res., Kyushu Univ.)

A reflectometer part of a new diagnostic tool for simultaneous measurements of the temperature and density fluctuations was installed at LHD during last campaign. The main aim of this diagnostic is to extend the range and detail of turbulence measurement capability in fusion plasmas. Both the Microwave Imaging Reflectometry (MIR) and ECE Imaging techniques take advantage of large aperture optics to form an image of the reflecting layer onto an array of detectors located at the image plane, enabling localized sampling of small plasma areas.

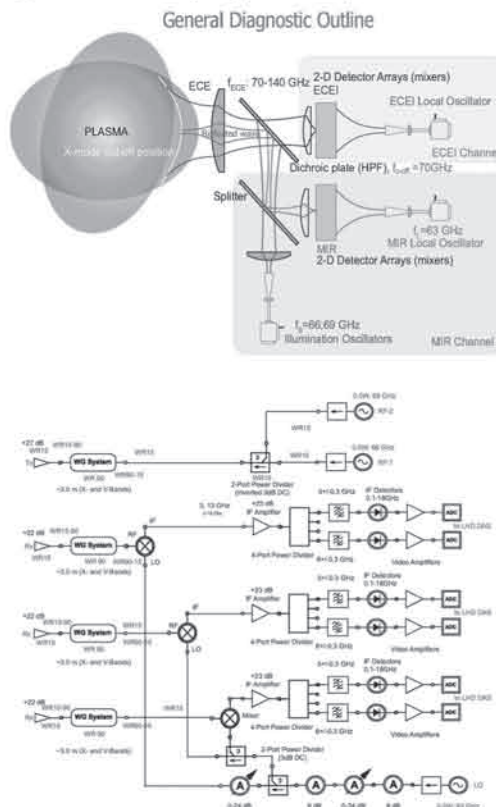


Fig.1. Schematic layout of the combined MIR and ECEI systems (top); microwave layout of the 3-channel reflectometer (bottom).

Based on LHD edge plasma densities the reflectometer utilized frequencies of 66, 69 GHz (V-band) for the probing the plasma with X-mode polarized radiation. The basic schematic of system is depicted in the Fig.1. The focusing elements of the microwave imaging system are consisting of main focusing elliptical mirror and one plane reflector. Both mirrors are located inside the LHD vacuum chamber. For the test run the MIR system was exclusively occupied the LHD 4O-CC01 diagnostic port. In spite of not optimal plasma conditions (low electron plasma density)

the system shows the strong reflected signal from the LHD plasmas. Because of using the heterodyne receiving technique (Fig.1) for signal detection with combination of high powered launching oscillators the test run shows the capability of the receiving system to acquire the plasma reflected signals in the range of -45 to -50 dB. For 2004-2005 LHD campaign MIR was operated as 3-channel system. The channels were focusing at three different plasma locations, which are separated in radial, azimuthal and toroidal directions. This allows performing the auto- and crossing correlation analysis of the obtained data.

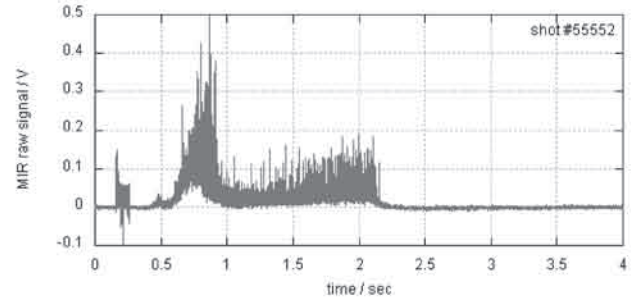


Fig.2. Time evolutions of the reflected RF signal; shot #55552

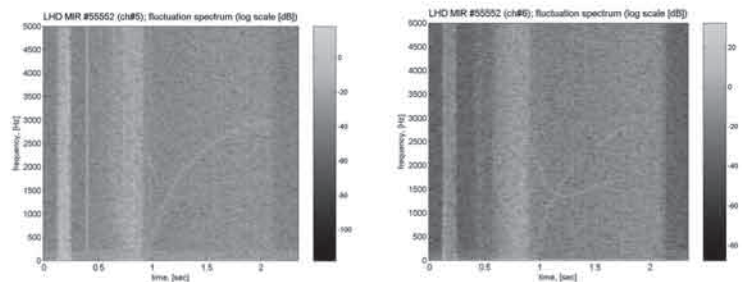


Fig.3. Spectrograms of the reflected signals at 66 GHz for the central (left) and radial for 69 GHz (right) of the MIR for the LHD plasma; shot #55552

The Fourier spectra for the data windows of 100 μ s are plotted in the Fig.3. Based on current data the cross-correlation for the *center* and *poloidal* channel was calculated. From the Fourier analysis the time of $\tau_{corr} = 1.5$ sec the partial correlation of 2.5 ms is obtained.

We can estimate the poloidal rotation velocity from the values of poloidal correlation length and poloidal correlation time $V_\theta \propto L_\theta / \tau_{corr} = 0.11 / 2.5 \times 10^{-3} = 44 \text{ m/s}$.

Those low frequencies and rotation velocities could not be considered as the evidence of the any drift waves. One of the possible origins is General Acoustic Modes (GAM), but it must be confirmed by future measurements.

It is become clear that a new elliptical focusing mirror has to be installed. This mirror has to be able to change the focusing point in both toroidal and poloidal directions. Thus, it will expand the ability of present system operate under a wider range of plasma parameters.

\$10. Application of Ultrashort-Pulse Reflectometer to LHD

Mase, A., Kogi, Y., Uchida, K. (KASTEC, Kyushu Univ.)
 Ejiri, A. (Frontier Sci., Univ. Tokyo)
 Kawahata, K., Tokuzawa, T.

Ultrashort-pulse reflectometry (USRM) is one of the methods to measure density profiles of plasmas. The frequency source of the reflectometer is replaced by an ultrashort pulse which pulse width is less than 100ps. The density profiles can be reconstructed by collecting time-of-flight (TOF) signal of each frequency component of an impulse reflected from each cutoff layer.

The detail of the USRM system was shown in elsewhere.¹⁾ Remote control system using super science information network (super-SINET) has been introduced to the USRM system since 2003. Bandwidth of the main backbone and branch line is 10 Gbps and 1 Gbps, respectively. The control client can operate the control server by using this network. The general purpose interface bus (GPIB) card is installed in the control server. The remote console, which has graphical user interface (GUI) is prepared to control the instruments of USRM via GPIB. The operations such as the adjustment of supply voltage fed to amplifiers and the frequency doubler, timing control of the impulse, data acquisition and monitoring can be performed from the remote site. The monitor can display the current view of a sampling scope for various times and their analyzed data as well as the machine parameters. In FY2004, the position of the transmitter and receiver antennas can be controlled remotely as shown in Fig. 1. The two antennas can be rotated in order to observe the cut-off layer depending on the various plasma conditions even between the plasma shots. In Fig. 1 the solid line from the antenna corresponds to the radiation angle, and the dotted line correspond to the maximum radiation angle when the antenna is rotated.

The directly recorded signal by the sampling scope is analyzed and reconstructed by means of the signal record analysis (SRA) method.²⁾ In Fig. 2 are shown the examples of reconstructed density profiles for the high density and low density plasma experiments of LHD. We assumed here the initial position where the electron density equals to 0 corresponds to the one of the separatrix. It is noted that for the high density operation the incident wave is reflected at the position close to the vacuum wall comparing with the low density operation, which means that the plasma is filled in wide region of the vacuum chamber for the high density operation..

In the LHD experiment, a multi-channel far-infrared (FIR) laser interferometer is utilized for measurement of density profiles. However, in the edge plasma region ($n_e < 2.0 \times 10^{19} \text{ m}^{-3}$), the FIR laser interferometer can measure only two chords or less. The behavior of the edge plasma and the plasma position is quite important for the control of the plasma. This USRM system seems to be useful for this purpose

In summary, we have completed a remote operation

system of an USRM, and succeeded to reconstruct electron density profiles using SRA method. As an upgrade of the present system, it is planned to widen the frequency regime of an incident pulse from 26-40 GHz to 12-40 GHz.

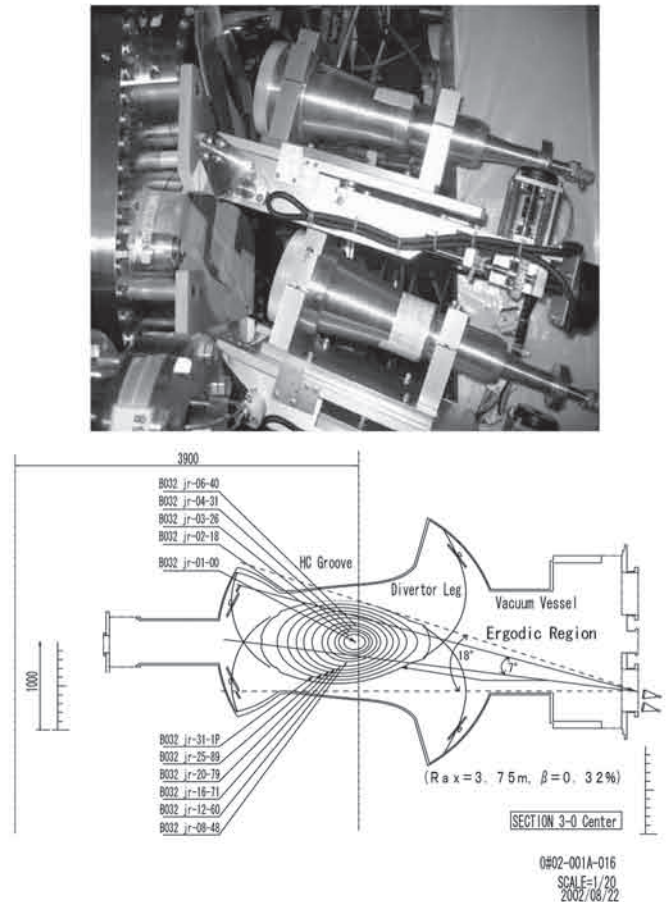


Fig. 1 USRM antennas installed in LHD (top), Distribution of antenna patterns (bottom).

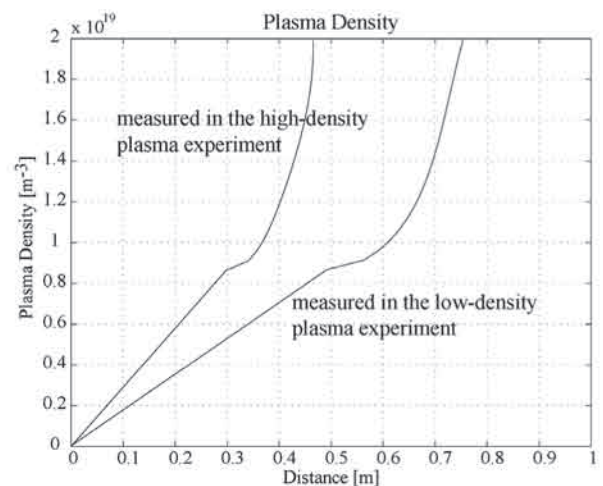


Fig. 2 Profile reconstruction by signal record analysis.

References

- 1) Kogi, Y. et al., Rev. Sci. Instrum. **75**, 3837 (2004).
- 2) Bruskin, L. Mase, A., Yamamoto, A., and Kogi, Y. et al., Plasma Phys. Control. Fusion **43**, 1333 (2001).

§11. Study of High-performance Array Antennas for Millimeter-wave Imaging Array

Kogi, Y., Kudo, K., Mase, A., Ignatenko, M. (ASTEC Kyushu Univ.)
Nagayama, Y., Kawahata, K.

It is considered to be one of the major issues to clarify the behavior of various instabilities and relations between instabilities and plasma confinement. ECE imaging (ECEI) is a promising method to measure electron-temperature profile and its fluctuations precisely. An ECEI system is composed of a detector array, quasi-optical system, and IF system. Each subsystem plays following roles. The optical system is composed of optical mirrors and dielectric lens. These optics are utilized to focus ECE from plasma on the detector array within the specific bandwidth. In the present plan of the beginning experiment, we will collect the 2nd harmonic of ECE with frequency range from 70 to 80 GHz. The ECE is then received by the detector array, and is frequency-converted to IF signal by means of LO. In the IF system, signal is then fed to power dividers and bandpass filters to resolve radial temperature distribution, since the frequency of ECE is proportional to magnetic field strength. While poloidal and toroidal temperature distribution is obtained by 2D array of the detector. We have studied and improved design of the detector to be suitable for ECEI measurement. In this report, we will describe prototype design of newly developed detector for ECEI.

In the last year, we have developed the detector called DBMA¹ which works in X-band range, and confirmed that properties such as conversion loss, antenna directivity and antenna pattern show good performances. We have proceeded to develop this detector which works in E-band range in this year. Figure 1 shows a sample of the detector fabricated on a Teflon substrate by Electro Fine Forming (EF2) technology.

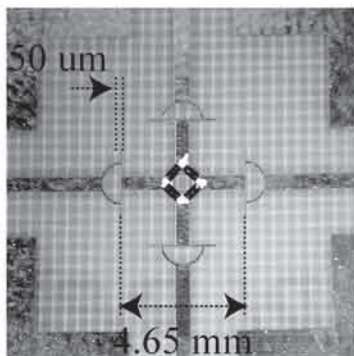


Fig. 1 Picture of E-band DBMA

This detector consists of two dipole antennas, four diodes, and four low-pass filters connected to end of the antenna legs. One dipole antenna is arranged perpendicular to another dipole antenna. One is used for detecting RF (LO), and another is used for detecting LO (RF).

We have performed this detector sensitivity measurement by injecting LO and RF power from the back and forth of the substrate, and we have confirmed IF output by a spectrum analyzer as shown in Fig. 2.

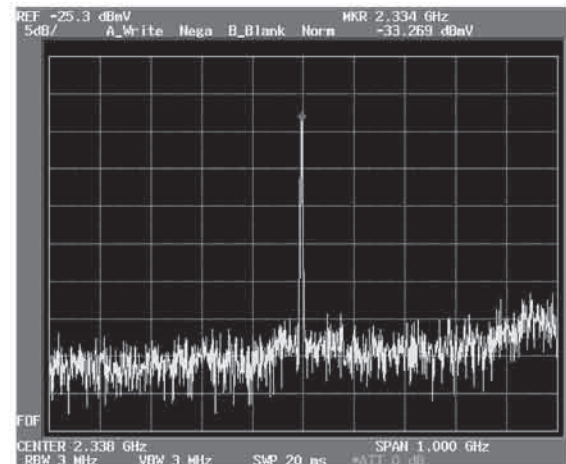


Fig. 2 Confirmation of IF output and detector sensitivity

In addition to development of the ECE detector, we have proceeded to develop the microwave components utilized in the IF system. Components indicated inside the broken line box in figure 3 show a block diagram of the IF system. Each component such as broadband amplifiers, power dividers, and band-pass filters have been realized on a dielectric substrate by microwave integrated circuit (MIC) technology.

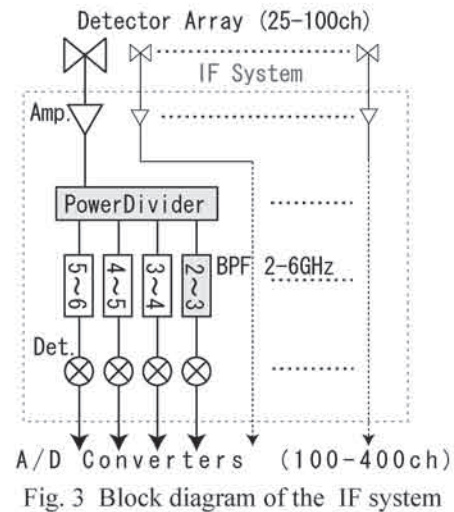


Fig. 3 Block diagram of the IF system

When we apply ECEI measurement, number of microwave component in the IF system attains over several hundreds. If we employed the microwave components on the market, huge cost and installation space become a important problem. By using MIC technology, we have succeeded to develop the microwave components of low-cost and small space installation.

[1] S. Maas, "The RF and Microwave Circuit Design Cookbook", Artech House, 1998.

§12. A New Tracer-encapsulated Pellet Injector for Plasma Diagnostics

Sudo, S., Viniar, I. (St. Petersburg Univ.), Tamura, N.

A new injector for making solid hydrogen pellets around impurity cores has been developed for plasma transport study in Large Helical Device. A new technique has been employed for automatic loading carbon or polystyrene cores of 0.2 mm diameter from a gun magazine to a light-gas gun barrel. The injector is equipped with a cryorefrigerator and is able to form a 3.2 mm long and 3 mm diameter cylindrical solid hydrogen pellet at 7-8 K with an impurity core in its center within 6 minutes and to inject it in the light-gas gun up to 1 km/s.

The sequence of tracer-encapsulated pellet formation is represented in Fig. 1. In a gun magazine, every impurity core is placed in a separate cell. A small amount of hydrogen gas is slowly admitted into the barrel and condensed on the walls of a pellet former creating a solid hydrogen shell, which is cooled to 8-9 K. The needle comes down and is preset under the cell with the next core to be loaded. The gas flow blows through the magazine cell and pushes the core out of it. Because the whole gas flow is sucked off through the needle and the formed shell closed a channel through which the needle can enter the barrel, the core fallen out of the magazine cell hits the top of the needle, trying to get inside of it together with the gas flow Fig.1(b). However, the needle diameter is so chosen, that the core could not get through it, but close the hole in the needle like a gag. The temperature of the pellet former is increased to 30 K and the hydrogen shell is evaporated being opened the channel into the barrel. A weak gas flow leaks through untight sealing of the needle hole to hold the core on the needle top during its upward movement Fig.1(c). The pellet former is cooled to 9K once more; at the time of hydrogen inflow, it condenses on the pellet former walls, gradually filling up the whole of its cross-section Fig.1(d) and even getting inside the needle. The needle is pulled out of the pellet back to the relatively warm magazine, leaving the core and an empty channel inside Fig.1(e), and hydrogen, condensed in the top of the needle, sublimates from the needle and recondenses again in the channel formed by the extracted needle, filling it and completing the pellet formation as shown in Fig.1(f). Thus, the needle is used as a vacuum tweezers to capture and hold up a core and as a source of hydrogen to complete the pellet formation. The pellet, formed around the impurity core, is located exactly in the injector barrel. It can be

observed through the barrel duct subject to suitable illumination and availability of an optical system with long-focus lens. Photos of the needle positioning and its movement according the above process are shown in Fig.2.

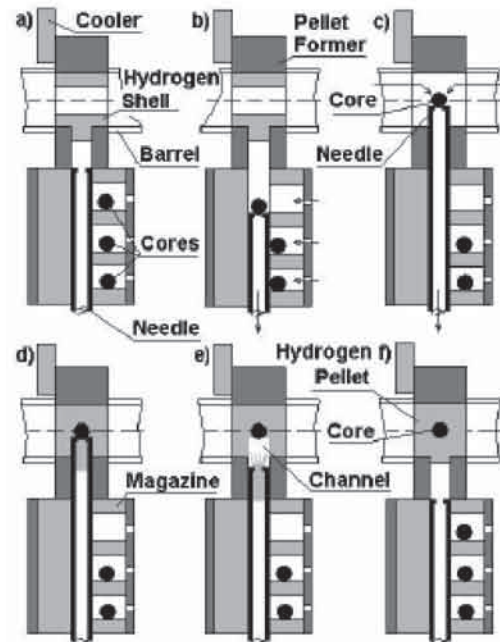


Fig. 1. The sequence of operations for pellet formation around an impurity core.

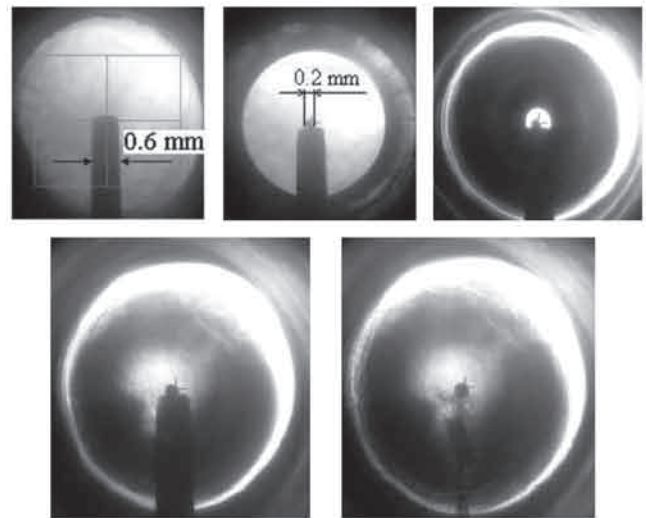


Fig. 2. Photos of the needle positioning and its movement control into the solid hydrogen watched through the quartz window.

References

- 1) S. Sudo. J. Plasma and Fusion Research, **69** (11) 1349 (1993).
- 2) S. Sudo, H. Itoh, K. Khlopenkov. Rev. Sci. Instrum. **68**, 2717 (1997).

§13. Ultra-Wideband Data Acquisition and Real-Time Data Streaming in LHD Steady-State Experiments

Nakanishi, H., Ohsuna, M., Kojima, M., Nonomura, M., Imazu, S. (Pretech Corp.)
LABCOM Group

In the 8th campaign of LHD experiment in 2004-2005, the steady-state plasma discharges had been practically held, and their longest duration went over one hour. The LHD data acquisition system, namely LABCOM system, had established a new world record of the acquisition data amount 84.0 GB in a single plasma discharge, which broke by far the previous record of 3.16 GB/shot in LHD's 7th c.

Drastic Growth of LHD Plasma Diagnostics

Most of this data amount has been produced by the new real-time digitizers, therefore, the world record has also proved their practical usefulness very well. In recent few years, we have been preparing for the brand-new digitizer systems that can continuously run in steady-state operations. (See Fig. 1).

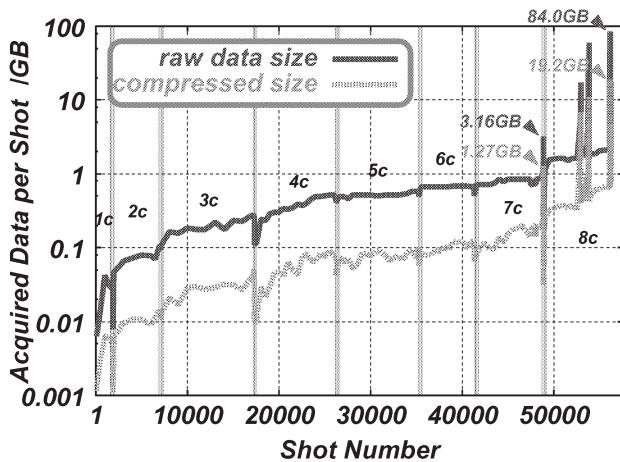


Fig. 1 Growth of shot-by-shot acquisition data amount in LABCOM system: At the end of 8th campaign, normal, i.e. short-pulse discharges produced about 2.5 GB/shot constantly.

Simultaneously with the growth of total data amount, we also have to deal with the increasing number of plasma waveforms with longer time duration. In LHD case, the real steady-state plasma experiments have much accelerated the technological shift from conventional batch processing digitizers to real-time capable ones. At the end of 8th campaign, LHD has 15 real-time diagnostics in addition with the present 30 CAMAC ones. In normal, short-pulse experiments, therefore, total 45 diagnostics were operated even though we had 30 in 7c.

Wide-band real-time data acquisitions using Yokogawa WE7000 and NI PXI/CompactPCI are now 15, compared to 30 conventional CAMAC. In the last two

campaigns, drastic increase of total number of diagnostics and made by those real-time DAQ (See Fig. 2). They also gave some prominent peaks of acquired data amount during the steady-state plasma challenges of LHD.

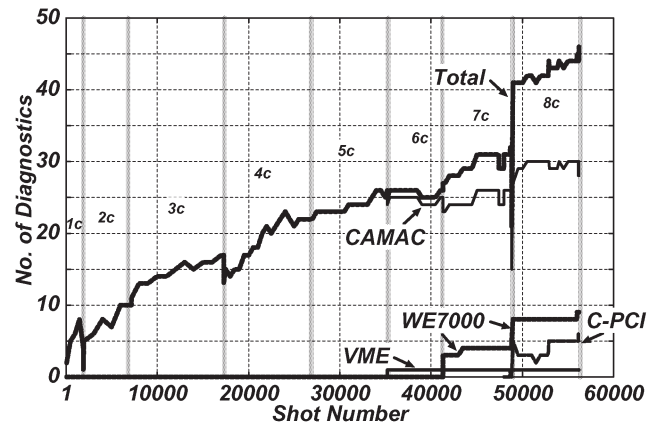


Fig. 2. Growth of number of LHD diagnostics by digitizer kind: In the last 7th and 8th campaigns, a drastic increase occurred by WE7000 and C-PCI digitizers.

Real-Time Data Streaming System

For the ultra-wideband data acquisition, such as high-resolution cameras and multi-channel fluctuation measurements, we have continued R&D for so-called "fast data streaming" systems in recent few years¹⁾. In the 8th campaign, some parts of their functions, such as real-time acquisition and saving, have started their operations. For example, laser imaging interferometer¹⁾ successfully acquired continuous 80 MB/s raw data from PXI digitizer front-end and stored them into host PC.

The remaining function to be implemented was the data streaming server programs with the real-time data monitoring (displaying) clients. Before the beginning of the 9th campaign, we have finished the implementation of this function, as shown in left-hand part of Fig. 3.

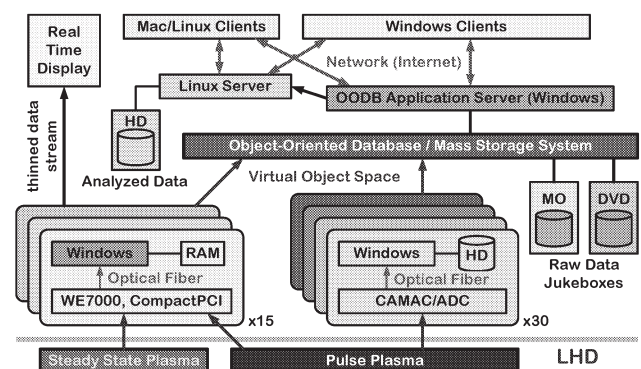


Fig. 3 Schematic view of real-time data acquisition systems (left) and conventional batch ones (right): All the data are equivalently retrieved from data storage.

Reference

- 1)Nakanishi, H. et al., Fusion Eng. Des. **56-57** (2001) 1011
- 2)Tanaka, K. et al., Rev. Sci. Instrum. **72** (2001) 1089

§14. Enhancement of the Experimental Database

Emoto, M., Yoshida, M., Komada, S., Nagayama, Y.

The Kaiseki Server System serves the researchers the unified retrieving methods for various kinds of the experimental data, and it have helped the researchers get data easier than before. Since the system began to work, more than 1,000,000 physical data (Kaiseki Data) have been registered. However, because more than 50,000 discharge experiments have been done since the LHD experiment began, it is difficult for the look for the interest experiment. In order to look for the experiment easier, the authors have developed the experimental database.

The database provides two kinds of information for each discharge experiment. One of them is basic information of the experimental condition, such as, magnetic axis, coil current, injected gas, etc. Another one is summarized physical quantity of each discharge experiment, such as, stored energy, pulse width, electron density, and the like.

The experimental condition is maintained mainly by the LMS database that stores the status of devices attached to the LHD. A daemon¹ program checks the LMS database every one minutes, and if it is updated, the program copies updated records into the Kaiseki Database. There are other information that aren't maintained by the LMS database, for example, gas puff timing, LID current, pellet timing, and so on. These data are managed by different groups. The information is recorded into text files, and another daemon program copies the contents into the database in every three minutes.

The summarized physical quantities are calculated from the Kaiseki Data. When a new Kaiseki Data is registered into the database, its information is added to a queue. At every night, a batch program sees the queue, and checks if the summarized quantities should be updated. If it is necessary to update the quantities, it recalculates the values.

The users can use the database directly from their programs. However, in order to use the database, they have to use SQL language. To make it easier, the authors developed the GUI interface to use the database. Fig.2 shows the WEB interface of the system. The program itself is written by PHP, but from the client side, it looks just like a normal web page, and the standard web browser can use the program. The user can enter the search condition on the upper part of the page, for example, pulse width ≥ 1.0 sec, magnetic axis = 3.6, etc. Therefore, they can look for the information without using SQL. The results are shown on the down part of the page. From this region, the user can get the PDF files. These PDF files are shot summary graph of each discharge experiment. As this figure, the default result output is shown as a webpage, but the results can be obtained as a CSV file. This format is convenient to use from other programs.

¹ The daemon is a program that runs at background and usually doesn't have an interface to users. A typical daemon is a WEB server.

This service is available from the public server. This public server can be used basically by any person, but it needs registrations. The public server is located on DMS (De Military Zone). This is the subnet where the user cannot access to the computers in other LANs except for connecting to the Kaiseki Database.

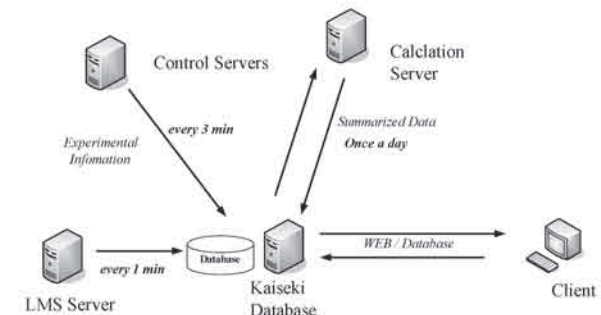


Fig. 1 System Overview

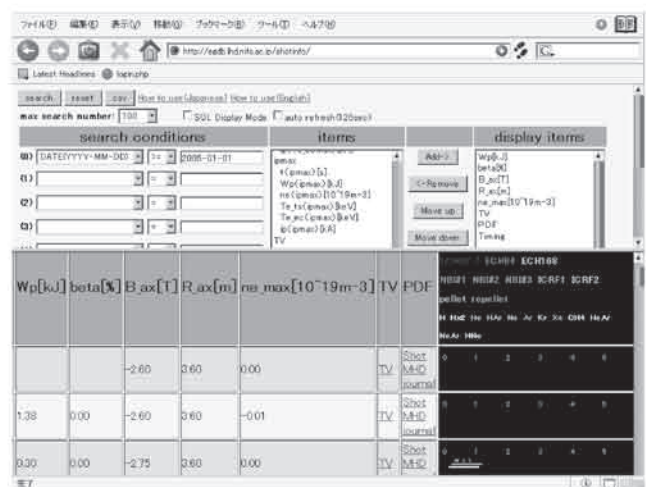


Fig.2 WEB Interface for the Experiment Database

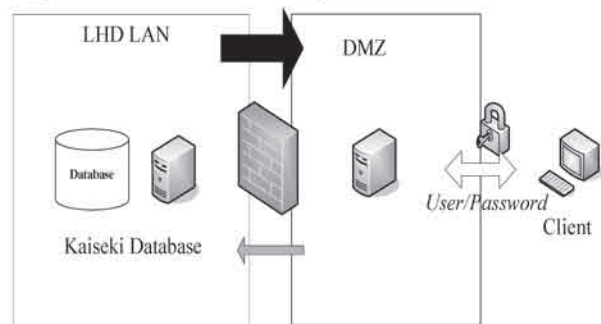


Fig.3 Public Server

Reference

- 1) Emoto, M., et. al., IAEA TCM on Control, Data Acquisition, and Remote Participation for Fusion Research Budapest, 2005

§15. Development of a New Two Color FIR Laser Interferometer (II)

Kawahata, K., Akiyama, T., Tanaka, K., Tokuzawa, T., Okajima, S., Nakayama, K. (Chubu Univ.)

Measurements of the refractive index of the plasma by using electromagnetic waves are a well-established tool for measuring electron density profiles in high temperature plasmas. In the Large Helical Device, a 13-channel far infrared laser interferometer has been routinely operated for the precise measurements of the electron density profile[1]. The optical configuration of the interferometer is of the Michelson interferometer type with a heterodyne detection system. The light source is a highly stable twin 118.8- μm CH_3OH laser pumped by a cw CO_2 laser. The overall accuracy of the system is about 1/100 of a fringe, corresponding to a line averaged density of $5.6 \times 10^{16} \text{ m}^{-3}$ at the central chord. The interferometer routinely provide density profiles almost every shot except in the case of a high-density plasma produced by an ice pellet injection. When a large sized pellet is injected into the plasma steep density gradient is formed in the peripheral region of the plasma, which sometimes causes the fringe jumps on the density traces measured by fringe counters. In order to overcome this difficulty we have been developing new laser sources in the wave length region of 40 to 70 μm , which is optimum value from view points of the plasma refraction and mechanical vibration effects, since the beam bending effect can be reduced by a factor of ~ 4 compared with that of 119 μm . On the way to search short wavelength laser oscillation lines, the most powerful line was found to be a 57.2- μm CH_3OD laser line [2] and be able to oscillate simultaneously at a 47.6 μm every 5 x 57.2 μm ($\sim 6 \times 47.6 \mu\text{m}$) by tuning the FIR laser cavity length. These new laser oscillation lines enables us to develop a new two color FIR laser interferometer [3].

One of the key issues to construct the two color interferometer system is to develop a high quality detector operating at the wavelength of $\sim 50 \mu\text{m}$. This fiscal year we have newly introduced Ge:Ga photoconductive detectors operating at liq. He temperature, which have a signal bandwidth of 1200 GHz centered at 3000 GHz. The responsivity of the detector is 0.4 amps/watt around 50 μm , which is about 30 % of the peak value. Figure 1 shows the experimental set-up for the detection of two color beat signals. Figure 2 shows the two color beat signals detected, 1.5 MHz for 57.2 μm and 900 kHz for 47.6 μm . The beat frequency of each oscillation line can be adjusted at a suitable value for phase measurement by tuning the length

of the FIR laser cavity and changing the operating pressure of the lasing molecule. The achieved signal to noise ratio is about 30 dB when the input power to the detector is reduced by 30 dB. These beat signals will be fed to a phase comparator for phase measurement after passing through a band-pass filter.

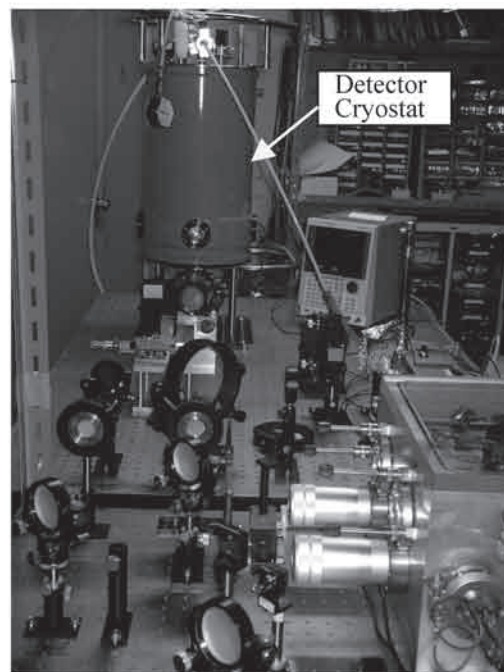


Fig.1. Experimental set-up for the detection of two color beat signals.

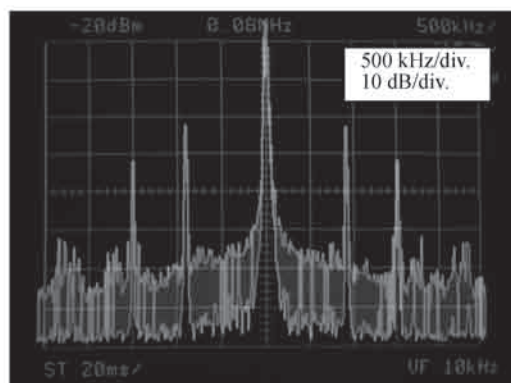


Fig.2. Two color beat signals at 1.5 MHz for 57.2 μm and 900 kHz for 47.6 μm .

3. References

- [1] K. Kawahata, K. Tanaka, Y. Ito et al., Rev. Sci. Instrum. **70**, 1 (1999) 707.
- [2] S. Okajima, K. Nakayama, H. Tazawa et al., Rev. Sci. Instrum. **72**, 1 (2002) 1094.
- [3] K. Kawahata, K. Tanaka, T. Tokuzawa et al., Rev. Sci. Instrum. **75**, 10 (2004) 3508.

§16. Two Dimensional Ion Temperature and Velocity Measurements by Use of Visible Light Tomography Technique

Ono, Y., Balandin, A.L., Imazawa, R., Kawamori, E., Murata, Y., Itagaki, T., Yamanoue, T., Sato, K., Arimoto, K., Timura, T., Tawara, T. (Univ. Tokyo, High Temperature Plasma Cent./Dept. Electr. Eng.), Narushima, Y., Nagayama, Y., Yamazaki, K.

For the past four years, we have been developing a new visible-light tomography system for two dimensional (2-D) measurements of ion temperature and velocity. It is now installed in TS-4 device, and will be in LHD together with a well-controlled compact toroid (CT) injection system. The coaxial plasma gun will deposit impurity plasma at an arbitrary spatial position of the Large Helical Device (LHD) plasma at an arbitrary time. Its injection time is much shorter than the conventional pellet injection, leading us to a new fast particle diffusion measurement in MHD time scale. The 2-D visible light tomography system was designed to measure directly 2-D profiles of its ion diffusion, temperature and velocity.

In 2004, the visible tomography system was installed for LHD and TS-4 devices, using 120 channel optical fibers and three polychromators with three ICCD cameras. Its major problem is that the measured Doppler shift and width for ion velocity and temperature measurements are integrated along the viewing line. The conventional reconstruction for the local data is to solve the inverse problem at each wave length and to fit a Gaussian profile to the obtained local spectrum.. However, the reconstructed local data have no relation with each other, though their spectra are close to the Gaussian profile, so that we observed a significant increase in S/N ratio especially around the tail (short and long wavelength) regime of line spectrum.

We demonstrated for the first time, a new spectrum reconstruction method based on assumptions of Gaussian profile of line spectrum. Unlike the conventional MEM (Maximum Entropy Method) tomography only for the spatial profile, the MEM was applied not only to the spatial profile but also to wavelength profiles. This double assumption, causes a significant reduction of reconstruction error, especially around the edge regions whose S/N are low.

The measured spectrums are obtained by integrating the local line spectrum with the Gaussian profiles over the viewing lines, as shown in the following equations:

$$\tilde{f}(y, k) = 2 \sum_{r_i=y}^{r_i=R} a_{0i} \exp\left\{-\frac{k^2}{a_{2i}}\right\} \frac{r_i \delta r}{\sqrt{r_i^2 - y^2}},$$

$$L = \sum_{i=1}^M \sum_k g_{ik} \log g_{ik} + \gamma \sum_{i=1}^M \sum_k (f_{ik} - \tilde{f}_{ik})^2,$$

$$(g_{ik} = a_{0i} \exp\left\{-\frac{k^2}{a_{2i}}\right\})$$

where M and N are number of radial positions for reconstruction, an number of measurement channels, respectively. We determined the parameters λ , a_0 , a_0 , a_2 ($i=1 \dots M$) by minimizing the L parameter mentioned above. The Akaike parameter was used for optimization of those parameters that strongly depend on γ parameter. Figures 1 (a) and (b) show the radial profiles of light emmissivity and ion temperature: the assumed profiles, profiles reconstructed by the conventional Abel inversion and profiles reconstructed by the new method mentioned above. The 10% and 20% noise components were added to the signals in cases (a) and (b), respectively. These data indicates that the new method is more robust against the noise component, especially in case (b).

References

- [1] A. Balandin and Y. Ono, J. Comp. Phys., **202**, (2005), 52.
- [2] Y. Ono et al., Fusion Energy 2004, IC/P6-44, (2005).

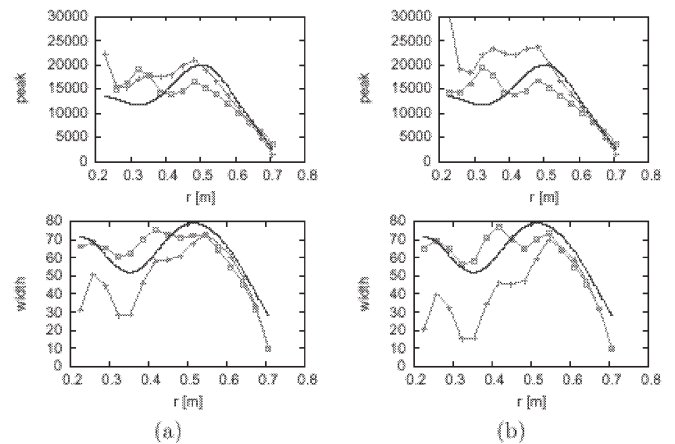


Fig. 1 Radial profiles of light emmissivity and ion temperature : assumed profiles, reconstructed profiles by the conventional Abel inversion (+) and the new inversion method (□). The 10% and 20% noise components were added to the signals in cases (a), and (b), respectively.

§17. Image Reconstruction by Hopfield Neural Network for Bolometer Tomography of LHD Plasma

Iwama, N. (School of Informatics, Daido Institute of Tech.)

Hosoda, Y. (Dept. of Information Science, Fukui Univ.)

Peterson, B.J.

Hopfield neural network is a tool of regularizing the ill-behaved least-squares solutions of linear equations. With mutually interconnected neurons, the Hopfield system has such a dynamical behavior as an energy function tends to decrease with time when the system has a monotone increasing input-output function of neuron with symmetry of the interconnection weights. This dynamics can be used for the tomographic image reconstruction from projections when the Lagrangian function of Tikhonov-Phillips type [1] to be minimized is analogously regarded as the energy function.

In the formulation of image reconstruction $Hf=g$, where an unknown K -dimensional image vector f is operated by a projection matrix H to produce the M -dimensional data vector g , the analogy leads to the following design of a Hopfield model having neurons as many as the number of pixels K :

the weight matrix $W = -2(H^T H + M\gamma C^T C)$;

the bias vector $\theta = (2/M)H^T g$.

Here, C is the K -dimensional Laplacian operator. By this design, the matrix W is symmetric as required with the (i, j) element w_{ij} (interconnection weight from the j -th neuron to the i -th neuron) such that $w_{ij} = w_{ji}$. To fit the neuron outputs to the projection data, the term $H^T H$ leads to negative weights interconnecting the neurons that are located on each line of sight. The term $M\gamma C^T C$ gives to each neuron a negative self-connection weight w_{ii} and positive weights w_{ij} from 4 neighboring neurons; these weights increase in magnitude with the regularization parameter γ and assume a role of statistical stabilization and spatial smoothing of the neuron outputs f_i , that is, the reconstructed image. On the other hand, the bias θ is the back-projection, which is well-known in computerized tomography, and involves the projection data g , which is time-variant as the M -channel detector signals. When the sigmoid function is used as the input-output function of neuron, the Tikhonov-Phillips solution will be nonlinearly modified so that the pixel values f_i are guaranteed to be positive.

This Hopfield model design has been made on the system of two 20-channel fan-beam cameras ($M=40$) with AXUVD silicon photodiodes that has been installed in a semi-tangential cross section using 3.5-U and 4-O ports of LHD [1,2]. The temporal change of the neural net was simulated by computer simply in Euler approximation of the differential equation system of Hopfield. The square region of imaging that covers the triangular region of magnetic surface was divided into $K=32 \times 32$ pixels. Both the time interval Δt in Euler approximation and a parameter u_0 relating to the slope of the sigmoid function were

appropriately chosen. The amplitude scaling of detector signal data was made to avoid the stagnation and saturation of the neuron outputs due to the lower and upper limits of sigmoid function. On an observation of the asymmetric radiative collapse of NBI heated plasma (Shot 28961, 2.162 sec), a result is shown in Figs. 1 and 2. With an initial uniform image nearly zero over the square region of imaging, the energy function was monotonically decreased with an evolution of plasma image. The image obtained in convergence is similar to that of the maximum entropy method (MEM) [1]. Instead of the preblur technique in MEM, the nonlinear method of Hopfield has a feature of simple adoption of the smoothing operator C . Also, using the Euclid norm in place of the Kullback-Leibler information, the model image can be easily adopted by modifying only the bias vector.

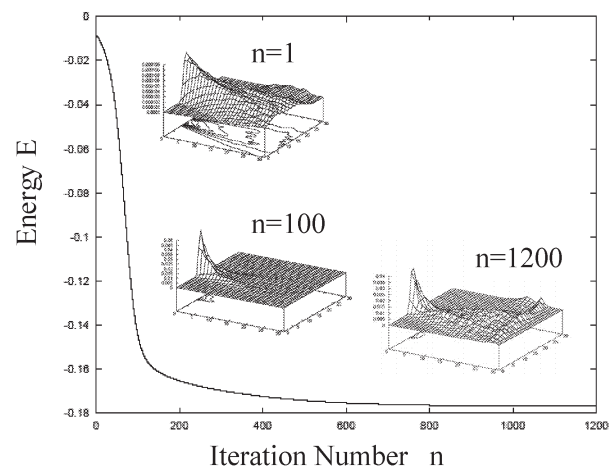


Fig. 1. Changes of the energy function E and the plasma image; $\gamma = 1.0 \times 10^{-4}$, $\Delta t = 0.01$, $u_0 = 1.0$.

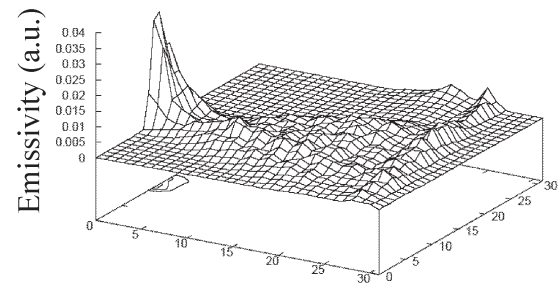


Fig. 2. Reconstructed plasma image at the iteration number $n=1200$ of changing the whole image.

References

- 1) Liu, Y., Kostrioukov, A.Yu., Peterson, B.J. et al., Rev. Sci. Instrum. **74**, (2003) 2312.
- 2) Peterson, B.J. et al., Plasma Phys. Contr. Fusion **45**, (2003) 1167.
- 3) Iwama, N., Hosoda, Y. and Peterson, B.J., Ann. Rep. NIFS (2002-2003) 162; ibid. (2003-2004) 167.

\$18. Bench Testing of New Polarimeter with Use of Photo Elastic Modulator for 57 & 48 Micron Laser

Akiyama, T., Kawahata, K. (NIFS)
 Tsuji-Iio, S. (TITech)
 Okajima, S. (Chubu Uni.)

As the electron density in LHD is getting higher, reliable electron density measurement is indispensable. The 57 and 48 micron CH₃OD laser has been developed [1, 2] because the beam bending effect ($\propto \lambda^2$) in a plasma, which causes fringe jump errors, is small due to the short wavelength and is suitable for a laser source of an interferometer in LHD. On the other hand t profile can be evaluated from polarimetry and the importance is becoming larger since the position of a rational surface considered to be correlated to the confinement improvement mode. Therefore we are designing an interferometer combined with polarimeter with the CH₃OD laser conceptually now. This system will be adapted to poloidal polarimeter plane in ITER.

On the view point of the maintenance and compatibility with the present interferometer system, method with use of photo elastic modulators (PEMs) are appropriate. The optical system is basically interferometer and the probe beam is divided just in front of detector for polarimeter. The feasibility was demonstrated in JT-60U [3]. The stability for a long time and the time resolution less than milliseconds are demonstrated. Although the range of wavelength of commercial PEM is limited shorter than IR region, we found that PEM can be fabricated with silicon for the photo elastic material through a discussion with PEM maker HINDS. One of the disadvantages of this method is the expense of a couple of PEMs necessary for each channel and the total cost becomes significant in the case of a multi-channel system. The new configuration shown in Fig. 1 needs only a couple of PEMs even in a multi-channel system. This system is also based on interferometry configuration and PEMs are inserted before a plasma.

We performed the bench testing of the new configuration at Iio laboratory of TITech with a near IR laser and PEMs. Figure 2 shows the relationship

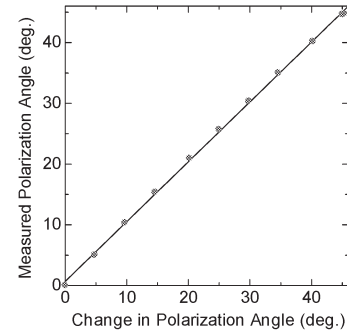


Fig.2: The relationship between actual and measured rotation angle

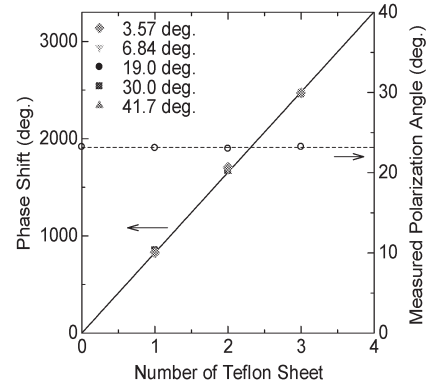


Fig.3: Test of phase shift with sheets of Teflon in the case that polarization angle is changed.

between real and measured polarization angle. Here a rotation half wave plate is used instead of a plasma. Good linearity is obtained and this demonstrates this configuration works as polarimeter. Figure 3 shows results of phase shift measurement for interferometer. It shows also good linearity against the number of Teflon sheets and independent on polarization angle. The problem is slight harmonic components of modulation frequencies of PEMs appear on beat signals and the amplitude depends on polarization angle. The estimation of signal to noise ratio in the case of LHD and ITER is under study.

Reference

- 1) K. Kawahata et. al., Rev. Sci. Instrum **70** (1999) 707.
- 2) S. Okajima et. al., Rev. Sci. Instrum **72** (2001) 1094.
- 3) Y. Kawano et. al., Rev. Sci. Instrum **72** (2001) 1068.

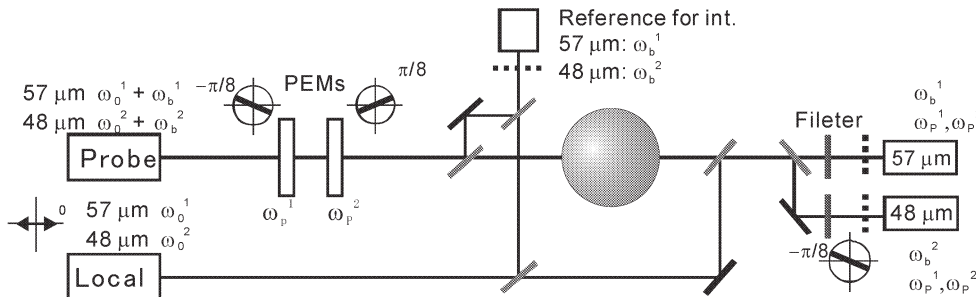


Fig.1: New configuration of a interferometer combined with a polarimeter with use of PEMs.

\$19. Research and Development of an Extremely Compact Fusion Neutron Source by Spherically Converging Ion Beams

Yoshikawa, K., Masuda, K., Yamamoto, Y., Toku, H.
(Inst. Advanced Energy, Kyoto Univ.)
Sudo, S., Tomita, Y.

An inertial electrostatic confinement fusion (IECF) neutron source is a device injecting ions towards the spherical center through a transparent hollow cathode (see Fig. 1), trapping them in the electrostatic self-field and making fusion reactions in the dense core. An IECF device can be promising for a portable neutron source. At present, D-D fusion neutrons of more than 10^7 sec^{-1} are successfully produced continuously by an IECF device of 340 mm in diameter shown in Fig. 1 at our research group, and at several institutions, as well.

Among current major requirements of compact neutron sources, anti-personnel landmine detection is one of the most urgent issues. For this application in the very near future, further smaller device is required. An extremely compact IECF device of 200 mm in diameter has been thus newly developed. A neutron yield of 10^7 sec^{-1} in DC operation is required for landmine detection through back-scattered neutrons and neutron-captured gamma rays. $4 \times 10^6 \text{ sec}^{-1}$ has been achieved so far.

In order to enhance the neutron yield by an IECF source, it is effective to produce sufficient ions, particularly, in the vicinity of the vacuum chamber to provide full energy under a relatively low pressure to prevent accelerating ions from unnecessary charge-exchange with background gases. For this objective we have been developing a magnetron discharge system^{1, 2)} which shows in general an ample ion current supply with a compact and simple configuration even under a low gas pressure of several mTorr. Negatively biased inner electrode in the coaxial configuration²⁾ as shown Fig. 2 is essential, otherwise the produced ions would be lost onto the facing wall of the grounded spherical chamber without bouncing motions.

Recently we have refined the magnetron discharge system with an outer Nd-Fe-B permanent magnet additional to the original inner one. With an optimal configuration, i.e. axial lengths and positions of the two magnets, a more than five times higher magnetron discharge current has been



Fig. 1. The hollow cathode at the center of the spherical vacuum chamber as the anode, and an IECF plasma within the hollow cathode.

achieved (see Fig. 3). The refined magnetron ion source was then set up on the IECF spherical chamber. Ions supplied by the magnetron ion source were experimentally found essential and effective for maintaining a glow-magnetron hybrid discharge under an envisaged low gas pressure condition. We expected that a higher negative voltage applied to the central gridded cathode would result in a higher extraction ion current from the magnetron source, and accordingly a higher IECF cathode current. It is found however that, as shown in Fig. 4, there is an optimum voltage in terms of a high gridded cathode current. Numerical and experimental studies are being carried out for understanding these phenomena.

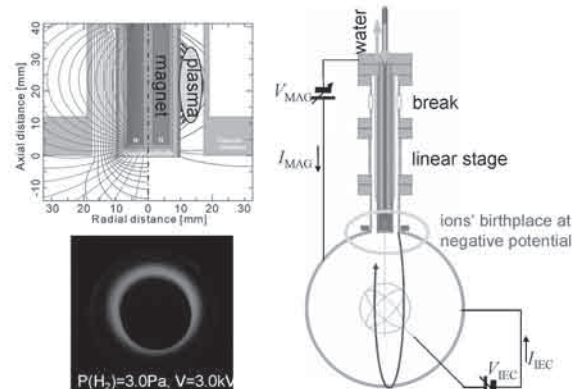


Fig. 2. Schematic configuration of electrodes for magnetron ion source and discharge plasma.

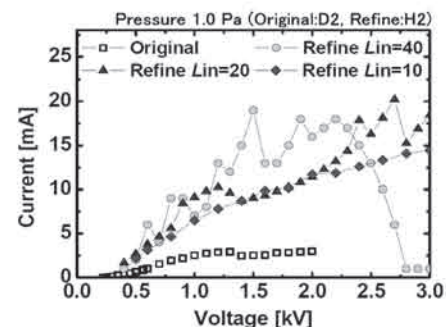


Fig. 3. Magnetron discharge current as the function of magnetron cathode current.

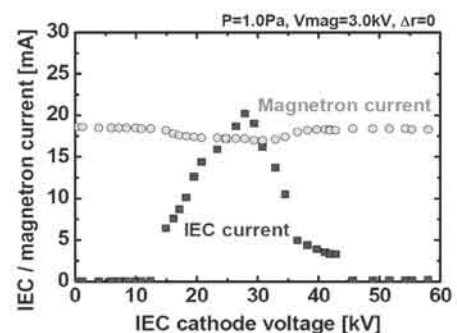


Fig. 4. Glow-magnetron hybrid discharge characteristics under low gas pressure condition of 1.0 Pa.

References

- 1) Yoshikawa, K. et al.: Ann. Rep. NIFS (2002-2003).
- 2) Yoshikawa, K. et al.: Ann. Rep. NIFS (2003-2004).

§20. On the Construction of Databases of Experiment Data

Hochin, T. (Osaka Prefecture Univ.)
Nakanishi, H., Kojima, M.

Experiments of the fusion phenomena produce a lot of sequences of time-varying values. A sequence of the values forms a waveform. If the waveforms similar to a desired one can be obtained by using computer system, the burden of researchers in searching similar waveforms will be extremely decreased. Finding the similar waveforms may bring us new breakthrough. We have addressed to the issue on this kind of retrieval [1]. The proposed method is based on the Fourier Transformation [1]. The first several Fourier coefficients are used to narrow the search space. The candidates obtained are again evaluated by using high dimensions' and distinctive coefficients. This method is called the *two-step method*. This method is designed for the whole matching of waveforms.

Another type of matching of waveforms is the subsequence matching. In the subsequence matching, the query sequence is smaller than the evaluated sequences. A sequence is searched in the large sequence that best matches the query sequence. The subsequence matching of waveforms is also strongly required. This paper addresses to the method of the subsequence matching.

The simplest way of the subsequence matching of waveforms is that every point of a waveform is compared with that of a query waveform with shifting the retrieval start position to the next point. This method is simple, but retrieval performance will not be tolerable. The method with good retrieval performance is required.

One of the way of improvement is that a waveform is divided into segments, and the similarity of a waveform is evaluated by using those of the component segments. There may be several methods of evaluating the similarity. We use the two-step method in evaluating the similarity of each segment. This method is called the *simple two-step method*. From here on, the first segment is first evaluated, and the following segments are evaluated according to their order in a waveform for the simplicity.

Following the simple two-step method, the more the number of segments composing a query waveform is, the less the number of the candidates obtained is. No candidates can be obtained when a query waveform is long. The method is improved to keep the number of the candidates. That is, when the number of candidates is smaller than the pre-defined lower bound, the method asks the multi-dimensional index to return more candidates and set the lower bound to the smaller one in evaluating each segment. This method is called the *candidate-keep two-step method*.

The methods described above use multi-dimensional index in evaluating every segment. When one segment that may be the component of a required waveform can be

obtained, similarity of the waveform can be evaluated by consulting the segment next and/or prior to that segment. There are two approaches to this evaluation. One approach modifies the structure of the multi-dimensional index to be able to reach directly to the next or prior segment. The other keeps the information on the neighbor segments outside of the multi-dimensional index. The next or prior element is evaluated by using the information outside of the multi-dimensional index. We adopt the latter approach because we do not have to change the multi-dimensional index. Fourier coefficients of the segments that are the same ones as those used in the two-step method are stored into a file, which is called a binary file, outside of the multi-dimensional index. The first segment is evaluated by using the multi-dimensional index. The following segments are evaluated by using the binary file. This method is called the *binary file method*.

The retrieval performance of three methods (the simple two-step, the candidate-keep two-step, and the binary file methods) is evaluated. SX flux waveforms are used for the evaluation. The number of waveforms is 10000. A waveform is divided into 450 segments. Each segment has 256 points. The simple two-step method asks the index to return 1000 segments. The candidate-keep two-step method uses 1000 as the initial candidate number, and 100 as the initial lower bound. For the binary file method, performance is measured under both of the hot and the cold states of the index. The hot state means that the whole of the index is on memory. The index is not on memory in the cold state. The retrieval time is measured by varying the number of segments of a query waveform. The result is shown in Fig. 1. This figure clarifies that the binary file method is the best. This may be caused by the number of consulting the multi-dimensional index. The binary file method consults the index only once.

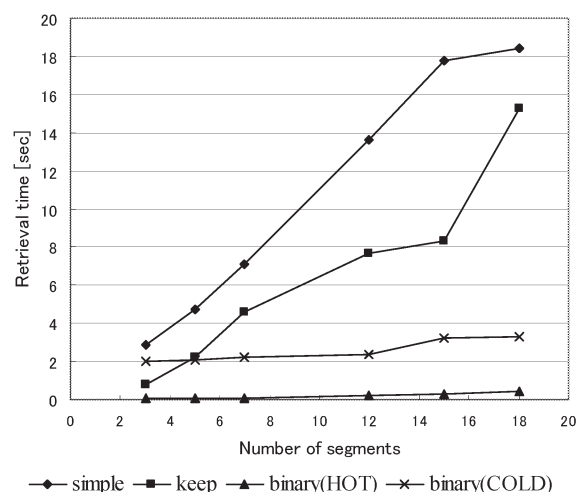


Fig. 1. Result of performance evaluation.

Reference

1) Hochin, T., Nakanishi H. and Kojima M.: On the Construction of Databases of Experiment Data, Ann. Rep. NIFS (2002) 167.

1-3. Theoretical Study

Various theoretical investigations on helical systems and other magnetically confined plasmas have been carried out during the period from April 2004 to March 2005. With the aim of contributing to the comprehension of plasma confinement in a toroidal magnetic field, theoretical research on LHD and other fusion plasmas, and pioneering theories of nonequilibrium plasmas are promoted. Theories of complex and complicated phenomena in confined plasmas have stages in which reliable models are applied and stages in which the construction of a model is itself at issue. The researches executed during the year described in the following includes both stages.

[MHD]

Nonlinear evolution of interchange modes in the LHD plasma are studied with computer simulation based on the reduced MHD equations, focusing on the poloidal uniform flow. Effect of the resistive wall on the growth rate of weakly unstable external kink mode in general 3D configuration is investigated by developing a simplified theoretical model. Stabilization property of the compressibility on pressure-driven perturbations in helical plasmas is studied. Formation of filamentary structure in edge-localized mode of spherical tokamak is revealed by computer simulation. New theoretical approach to 3D equilibrium of LHD is developed.

[Neoclassical transport and Er]

Property of the ripple transport depending on the configuration of LHD is studied for wide parameter range by using the GIOTA code. A systematic theoretical study is executed to clarify the impact of ion species on ambipolar radial electric field for LHD. Transport analysis of radial electric field in helical plasmas is investigated to find formation of transport barrier and transport reduction. Non-local neoclassical transport simulation in LHD is executed by using the FORTEC-3D. Geodesic acoustic mode (GAM) oscillation is observed, and its damping rate is analyzed. Particle drift in static magnetic fields is analyzed to find analytical expressions for particle trajectory. Test particle simulation is carried out for neoclassical effects on strike point patterns on the Local Island Divertor (LID) head of LHD. A Monte-Carlo simulation code is developed to study radial profile of ion temperature and the plasma flow in magnetic island.

[Turbulence transport]

Self-consistent model for two-dimensional structures at transport barrier in tokamak H modes are analyzed to investigate a large poloidal flow and steep profile of the electrostatic potential and density. Two-dimensional structures at the edge of a tokamak are investigated to find the poloidal

asymmetry of the structure generates inward particle pinch, and gives explanation for the rapid establishment of the edge density pedestal. The growth of the zonal flow in the presence of the drift-wave turbulence is discussed on the basis of space and time scale separation. Coherent structure of zonal flow and nonlinear saturation are obtained. Excitation of the geodesic acoustic mode (GAM) in tokamak turbulence is analyzed. The GAMs are more unstable for high safety factors. The periodic oscillation of the inhomogeneous rotation of the sun is studied by use of the MHD dynamo theory. There exists a turbulent electromotive force which is driven by the vorticity of the flow, which corresponds to the gamma dynamo. The nonlinear evolution of neoclassical tearing mode (NTM) in the presence of drift wave turbulences investigated using the four-field neoclassical MHD equations. Importance of the turbulent pump on the rapid growth of the tearing mode is demonstrated. Collisionless time evolutions of zonal flows in tokamaks are investigated by the gyrokinetic theory and simulation. How the collisionless damping of the geodesic acoustic mode (GAM) oscillations is enhanced is shown when the ratio of the typical drift orbit width of passing ions to the radial wave length of the zonal flow increases. Collisionless zonal flow dynamics in helical systems is investigated. After oscillations of the geodesic acoustic mode are damped, the zonal flow amplitude is shown to approach the predicted value. The magnitude of axial-flow retardation near the center of a turbulent swirling flow is estimated from the results of the variational analysis with the aid of the helicity concept. The axial flow reversal in a swirl is shown to occur if the bulk helicity exceeds a critical value. Effects of flow shear on the temperature gradient driven short wavelength ion (SWITG) modes and electron temperature gradient (ETG) modes are investigated in a sheared slab. A set of integral eigenvalue equation is employed to study toroidal short wavelength ion temperature gradient modes. The electron temperature gradient driven mode in the very short wavelength region is identified with a gyrokinetic integral equation code in toroidal plasmas. The laser wakefield excitation is studied when a plane laser pulse propagates at an angle to the density gradient of an inhomogeneous plasma slab. Powerful coherent emission around the plasma oscillation frequency can be produced. An equilibrium equation of a magnetized rotating plasma is obtained. Dust plasma experiments and collisional oscillations are studied to obtain the parameters on the dust plasma. Dust grains and inter-particle collision in boundary plasmas are investigated.

(Hayashi, T.)

§1. Effects of Self-Consistent Flow on Island Generation in Interchange Mode

Ichiguchi, K., Carreras, B.A. (ORNL)

We investigate the time evolution of the magnetic islands generated by the resistive interchange mode in the straight LHD configuration¹⁾. The effect of the self-consistent poloidal uniform flow is focused. The NORM code²⁾ based on the reduced MHD equations is utilized for the study. We examine the nonlinear evolution of the single helicity perturbations with $n/m = 1/2$, where m and n are the poloidal and the toroidal mode numbers, respectively. Fairly large resistivity ($S \sim 10^4$) is used, and the viscosity and the heat conductivity are chosen so that the mode with $(m,n)=(2,1)$ should be dominant. In this case, the magnetic islands are generated spontaneously in the linear phase because of the cylindrical effect as shown in Fig.1 (a). The number of the island in the poloidal cross section is the same as the poloidal mode number of the dominant mode.

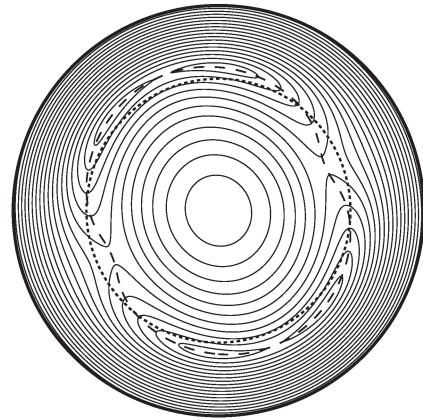
In the nonlinear phase, the dominant mode saturates firstly. The radial flow, which is part of the vortex induced by the interchange mode, pushes the plasma outward at the positions of the O-point of the linear magnetic island. Hence, around these points, the radial curvature of the perturbed flux contour increases and the direction of the radial magnetic field is reversed. Then, the O-points of the linear island changes to the X-points. The number of the newly generated island becomes twice of the poloidal mode number of the dominant mode as shown in Fig.1 (b).

After the saturation of the dominant mode, the $(m,n)=(0,0)$ mode grows self-consistently and saturates, which corresponds to the poloidal uniform flow. The radial flow of the interchange vortex is twisted by the poloidal uniform flow. Then, the curvature of the perturbed flux contour becomes weak and asymmetric with respect to the position of the nonlinearly generated X-point. As a result, the direction of the radial magnetic field is reversed again and the X-points are annihilated. Hence, the number of the resultant island returns to the poloidal mode number of the dominant mode. However, the shape is asymmetric with respect to each O-point, as shown in Fig.1 (c). Thus, the X-points are generated or annihilated depending on the growth of the poloidal uniform flow.

(a)



(b)



(c)

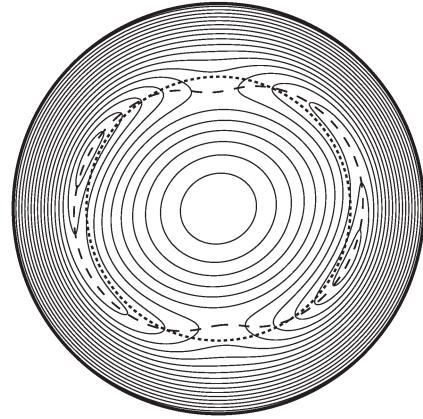


Fig.1 Contour of helical magnetic flux for $r \leq 0.8$ in (a) linear phase, (b) nonlinear phase just after dominant mode saturation and (c) nonlinear phase after uniform flow saturation.

References

- 1) Ichiguchi, K., Carreras, B.A. J. Plasma Fusion Res. Vol.6 (2004) 589.
- 2) Ichiguchi, K., et al., Nuclear Fusion **43** (2003) 1101.

§2. Effects of the Resistive Wall on the Growth Rate of Weakly Unstable External Kink Mode in General 3D Configuration

Chu, M.S. (GA), Ichiguchi, K.

Formulation of a method for the systematic computation of the growth rate of the weakly unstable resistive wall mode (RWM) in 3D configurations by using results from ideal stability codes was investigated¹⁾. We obtained that the growth rate of the RWM is approximately given by

$$\gamma_r \tau_w \simeq -\frac{\delta W_p(\alpha) + \delta W_v(\alpha)}{D_w(\alpha)}, \quad (1)$$

where α symbolizes the equilibrium quantities. Here, $\delta W_p(\alpha)$ and $\delta W_v(\alpha)$ denote the potential energy in the plasma region and the vacuum region of the ideal kink mode for the equilibrium parameter α and the wall located at infinity, respectively. The term $D_w(\alpha)$ means the energy dissipation due to the resistivity in the thin wall located at a given position. This formulation means that the growth rate of the RWM is approximately given by the rate at which the available free energy for the ideal external kink mode can be dissipated by the resistive wall. The eigenfunction is also approximated by that of the external kink mode.

We evaluated the growth rate of RWM in low beta LHD plasma carrying net toroidal current by utilizing eq.(1) and the KSTEP code²⁾. Figure 1 shows the profiles of the rotational transform. The $\tau = 1$ surface exists in the plasma column for $I < 150\text{kA}$. First we examined the ideal kink mode with $m=1$ and $n=1$. Figure 2 shows the dependence of the growth rates on the net toroidal current. for several positions of the conducting wall shown by b/a . This figure shows that the RWM is non-trivial in the range of $130\text{kA} \leq I \leq 135\text{kA}$, because the ideal kink mode is stable even in the case of $b/a = \infty$ for $I < 130\text{kA}$ and the internal kind mode is unstable even in the case of $b/a = 1$ for $I > 135\text{kA}$. Thus, we calculated the RWM for the cases of $I = 130, 133$ and 135kA . Figure 3 shows the growth rate. The growth rates are much less than those of the ideal kink modes. There is a tendency that the growth rate increases as b/a and I increases. By using a fully 3D ideal code instead of the KSTEP, we can calculate the growth rate in any 3D configuration.

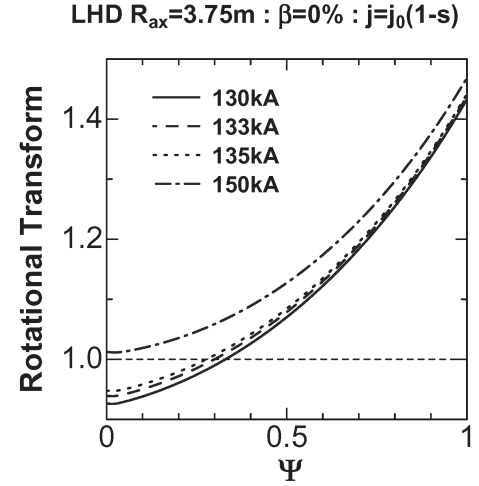


Fig.1 Profiles of rotational transform.

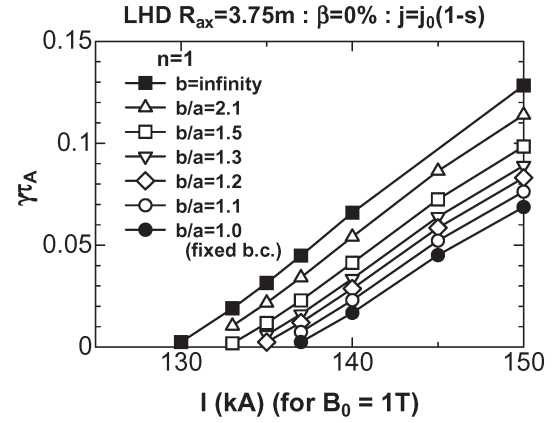


Fig.2 Growth rate of $n=1$ ideal kink mode.

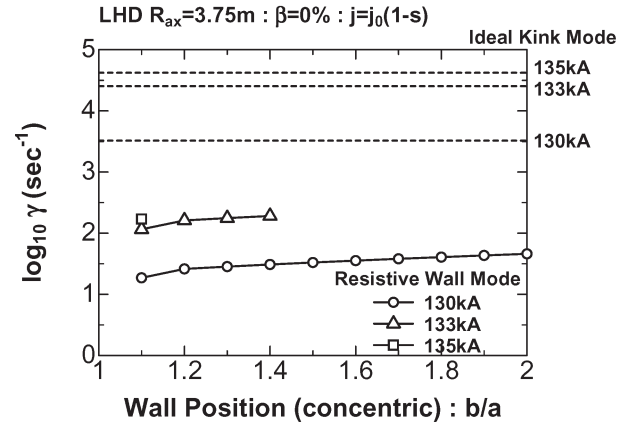


Fig.3 Growth rate of $n=1$ RWM.

References

- 1) Chu, M.S., Ichiguchi, K., Nuclear Fusion (to be published).
- 2) Nakamura, Y., et al., J. Comp. Phys. **128** (1996) 43.

§3. Properties of the Compressible Pressure-driven Perturbations

Nakajima, N.

The ideal MHD stability analyses for compressible perturbations are performed by the cas3d3 code [1], where 300 radial meshes, 20 poloidal and 20 toroidal Fourier modes in the Boozer coordinates are used for the mapping of equilibrium. As a perturbation, 60 Fourier modes are used to express each component in $\vec{\xi}_\perp$, the component perpendicular to the equilibrium magnetic field, and 490 Fourier modes are used for ξ^\parallel . Note that quite large Fourier space is needed to correctly express the incompressible properties of the perturbations in the compressible calculations [1].

The radial distributions of the potential energy W_P and kinetic energy W_K are shown in Fig. 1 and Fig. 2, respectively, for the ballooning mode under free boundary condition. The potential energy is divided into the shear Alfvén term noted by 1, the fast magnetosonic term by 2 (quite small), the slow magnetosonic term by 3 (magnified 5 times), the pressure-driven term by 4, the current-driven term by 5. W_P itself is indicated by 6. The kinetic energy is divided into two parts: one is due to ξ^\parallel ($W_k(\xi^\parallel)$) indicated by 1, and the other is due to $\vec{\xi}_\perp$ ($W_K(\vec{\xi}_\perp)$) by 2. W_K itself is indicated by 3. The kinetic energy W_K of the unstable modes mainly comes from the component of the displacement vector parallel to the equilibrium magnetic field ξ^\parallel , namely $W_k(\xi^\parallel) \gtrsim W_K(\vec{\xi}_\perp)$. This is due to the fact that the incompressibility condition is almost satisfied except for the mode rational surfaces as shown in Fig. 1, so that a strong ξ^\parallel is created around the mode rational surfaces as shown in Fig. 2. This tendency becomes stronger for interchange modes with an almost uniform amplitude of the perturbed pressure along the equilibrium magnetic field line, compared with ballooning modes where the amplitude of the perturbed pressure is non-uniform along the equilibrium magnetic field line.

In the present analyses, $W_k(\xi^\parallel)/W_K(\vec{\xi}_\perp) \sim 4$ for interchange modes, and $W_k(\xi^\parallel)/W_K(\vec{\xi}_\perp) \gtrsim 1$ for ballooning modes. As β increases or modes become more unstable, the contribution by ξ^\parallel becomes same as that by $\vec{\xi}_\perp$. Note that, in usual incompressible treatments, ξ^\parallel component is eliminated in both linear and nonlinear calculations. In the incompressible perturbations, the counter parts of the unstable modes are shear Alfvén modes, since the slow magnetosonic waves are excluded. In contrast with it, the counter parts of the unstable modes become slow magnetosonic waves for the compressible perturbations, since the shear Alfvén continuum spectrum moves up from the marginal point. These properties in the stable side of the ideal MHD spectrum will influence on the point spectra like Toroidicity-induced Alfvén Eigenmodes, and Helicity-induced Alfvén Eigenmodes in LHD configuration.

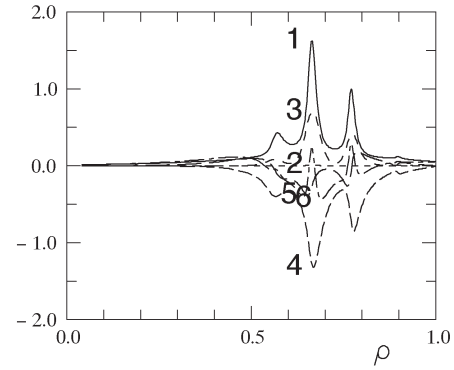


FIG. 1: Radial profile of potential energy. Slow magnetosonic term denoted by 3 is magnified 5 times.

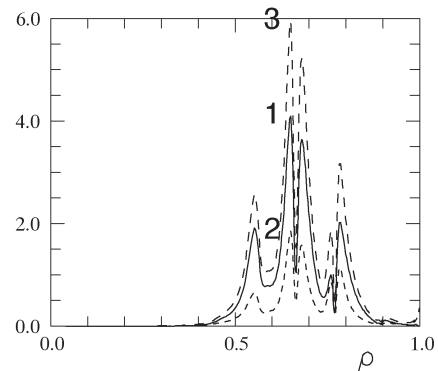


FIG. 2: Radial profile of kinetic energy corresponding to Fig. 1.

[1] C. Nührenberg, Phys. Plasmas **6**, 137 (1999).

§4. Nonlinear Simulation of Edge-Localized Mode in Spherical Tokamak

Mizuguchi, N., Hayashi, T.
Khan, R. (Sokendai)

The edge-localized mode(ELM) is an instability which is observed near the edge of the torus plasma. Experimentally, ELMs are often observed in some H-mode operations and are thought to have an important role for advanced confinement regime. However, detailed mechanisms of ELM remain to be solved. In spherical tokamak, such as the Mega-Amp Spherical Tokamak (MAST) device, the overall structure of the ELM activity has been observed in detail by using cameras. The camera image clearly shows a belt-like structures along the magnetic field. These structures are called "filaments" or "blobs". Detailed analysis shows that a plasmoid is separated radially from the main part of the torus. Such filament structures are also observed in the National Spherical Torus Experiment(NSTX). We have executed a numerical simulation which is based on the nonlinear resistive magnetohydrodynamic(MHD) model to reveal such mechanisms on an ELM.

The initial condition of the simulation is given by the reconstructed equilibrium of the NSTX plasma, where the $\beta_0=28\%$, $q_0=0.89$, and $A=1.4$. The initial equilibrium is unstable for some ballooning modes under the resistive MHD regime. The three-dimensional structure of this instability is shown in Fig.1. The shape of the plasma surface is drawn by the light gray iso-pressure contour. One can see that the plasma surface is wrinkled, and that several numbers of the ridges which are equivalent to the most dominant toroidal mode number emerge along the surrounding magnetic field. Since the "balloon" of the plasma pressure rapidly distorts the cross-field component of the magnetic field, current filaments are partly induced along the magnetic field, as shown together in Fig.1 by the dark gray iso-pressure contour. These structures well agree with the experimental observations of MAST. It should be also noted that the number of the filaments is reduced compared to the ballooning mode number. This can be explained by the coexistence of the multiple modes.

In Fig.2, the temporal changes in the pressure profile in a poloidal cross-section are shown. At the beginning of the nonlinear stage(Fig.2(b)), the plasma surface is wrinkled compared to the initial state(Fig.2(a)) due to the growth of the ballooning mode. Then the balloons grow rapidly. In particular, one of the balloons, the outermost one in the figure, changes largely in the shape. The leg of the balloon gets thin gradually(Fig.2(c)). Finally, the head of the balloon is separated from the bulk(Fig.2(d)) plasma, as indicated by the arrow in Fig.2(d). This separation process is clearly observed experimentally in MAST. By this simulation, it is revealed that such a formation of the filament structures and the separation phenomenon on ELMs can occur as a result of only the nonlinear MHD process.

The simulation results described above show some good agreement with the experimental observations. If we list the agreements, (1)the blobs are formed along the magnetic field lines, (2)the amplitude of the blobs appears non-uniformly in toroidal directions, and (3)a plasmoid is ejected radially from the ridge of the blobs. Though these comparisons with our present simple model may be still rough, they provide us with valuable information to better understanding of such a complicated phenomenon.



Fig.1. Three-dimensional structure of the filaments.

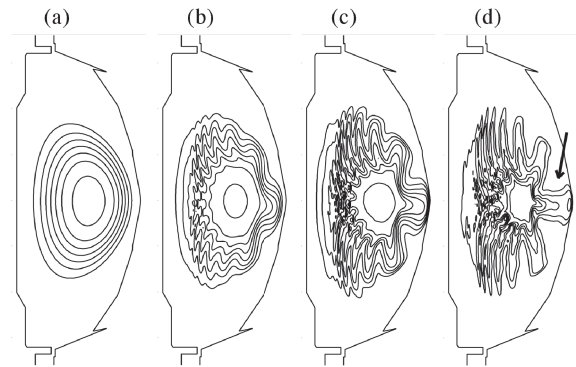


Fig.2. Time development of the poloidal pressure profile.

Reference

- 1) Mizuguchi, N., Khan, R., Hayashi, T., IEEJ Trans. A **125**(11), (2005) in press.

§5. New Theoretical Approach to 3D Equilibrium of the LHD

Watanabe, T., Hojo, H. (Plasma Research Center, Univ. Tsukuba)

LHD has potentiality of the high beta plasma confinement.

The chaotic field line-layer, which surrounds the outside of the outermost magnetic surface, plays a key role for an efficient plasma confinement in LHD. High magnetic shear of the LHD lengthens the connection length of the chaotic field lines. The connection length of the diverter field line which approaches close to the outermost magnetic surface exceeds 10 km. The cold plasma on surface of diverter plates does not cool down the core plasma directly therefore. Besides, the chaotic field lines neutralize the charge separation that cause the plasma collapse by an interchange mode. The lines of force that break away the chaotic field line region reach the vacuum vessel wall soon. Then, it is, also, expected in chaotic field line region that the plasma pressure can be sustained stably by the line-tying effect of the field lines fastened to the vacuum vessel wall.

The bootstrap current driven by the plasma pressure play another important role for the high beta plasma confinement. The bootstrap current reduce the magnetic field in the outside region of helical coils. Then, the bootstrap current contributes to the high beta stability of LHD plasma through the reduction of the total magnetic field energy.

The new approach to 3D equilibrium of the LHD does not depend on the assumption of the nested flux functions. The new approach is composed of the new expression scheme for the magnetic field and the introduction of a rotating helical coordinate system (X, Y, ϕ) .

The magnetic field \mathbf{B} satisfies always the relation $\nabla \cdot \mathbf{B} = 0$. Consequently, the essential freedom of \mathbf{B} is two, and \mathbf{B} can be expressed as follows by the 2 component of a vector potential \mathbf{A} without loss of generality.

$$\mathbf{B} = \nabla \times \mathbf{A}, \mathbf{A} = \begin{pmatrix} 0 \\ \Phi \\ p\{\Psi - X\Phi\}/r \end{pmatrix}. \quad (1)$$

LHD equilibrium, $\{P(X, Y, \phi), \Phi(X, Y, \phi), \Psi(X, Y, \phi)\}$,

composed of magnetic surface region and chaotic field line region can be obtained numerically by the force balance equation

$$\nabla P = \mathbf{J} \times \mathbf{B}, \quad \mathbf{J} = \frac{1}{\mu_0} \nabla \times \mathbf{B}. \quad (2)$$

A numerical example of $\{\Phi(X, Y, \phi), \Psi(X, Y, \phi)\}$ for the vacuum magnetic field of the LHD is shown in Fig.1.

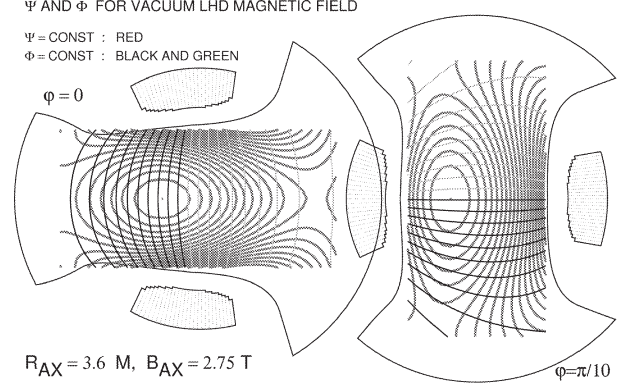


Fig.1 Numerical example of $\Phi(X, Y, \phi), \Psi(X, Y, \phi)$.

The MHD equilibrium (2) can be reduced to a compact differential equation for the Ψ , if analysis is constrained to the flux function region and introduced smallness parameters of $1/p$ (p is pitch parameter of helical coils ($= 5$)) and aspect ratio.

$$0 = \frac{r^2 + p^2 Y^2}{S} \frac{\partial^2 \Psi}{\partial X^2} + \frac{r^2 + p^2 X^2}{S} \frac{\partial^2 \Psi}{\partial Y^2} - \frac{2XY}{S} p^2 \frac{\partial^2 \Psi}{\partial X \partial Y} - \frac{3r^2 + p^2(X^2 + Y^2)}{S^2} p^2 \left(Y \frac{\partial \Psi}{\partial Y} + X \frac{\partial \Psi}{\partial X} \right) + \frac{r^2}{S} F(\Psi) F'(\Psi) - 2p \frac{r^3}{S^2} F(\Psi) + \mu_0 \frac{r^2}{p^2} P'(\Psi) \quad (3)$$

where $S \equiv r^2 + p^2(X^2 + Y^2)$ and $F(\Psi) = \frac{r}{p} B_\phi + X B_Y - Y B_X$ is an arbitrary function of Ψ . A numerical example of eq.(3) is shown in Fig.2.

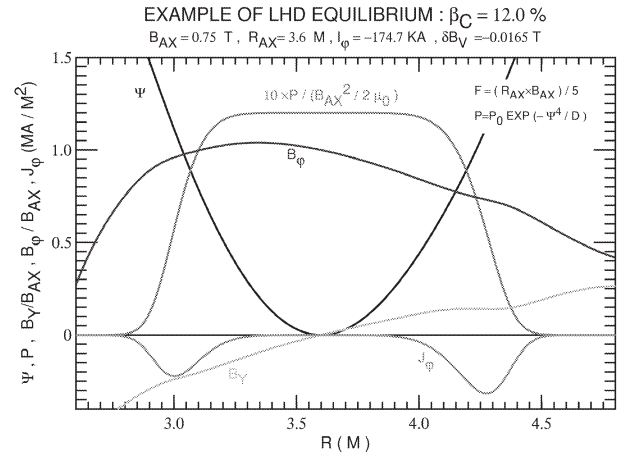


Fig.2 Numerical example of eq.(3) for the LHD

§6. The Configuration Dependence of Ripple Transport in LHD

Yokoyama, M., Watanabe, K.Y., Nakajima, N.

As introduced in Ref.1), GIOTA code is an appropriate code for evaluating ripple transport properties in helical systems. The magnetic topography can be rigorously treated through the magnetic field spectrum and also the finite rotational transform. To clarify the configuration dependence of ripple transport in LHD by utilizing this capability of the GIOTA code, the effective ripple (ε_{eff}) has been evaluated in a wide range of equilibria. The ε_{eff} has been frequently considered to estimate the level of ripple transport in helical systems as the comparative parameter among different configurations 2). It reflects the effect of the multiple helicity of the magnetic configuration on ripple transport. The definition of ε_{eff} 2) is

$$\varepsilon_{\text{eff}} = \left[\frac{9\sqrt{2}\pi}{16} \frac{v}{v_d^2} D \right]^{2/3},$$

where v , v_d and D are the collision frequency, drift velocity and particle diffusion coefficient, respectively.

Figure 1 shows the contour of $\log(\varepsilon_{\text{eff}}^{3/2})$ on the (R_{ax}, β) plane for the radial positions of $\rho=0.5$. Here, R_{ax} denotes the magnetic axis position at vacuum configuration, and β the volume averaged beta value. The MHD equilibria for these calculations are based on the fixed-boundary VMEC calculations 3). This condition corresponds to an operation with a feedback control of the vertical field to keep the plasma position identical to that used in the vacuum configuration. The pressure profile employed for these VMEC calculations is $P(\rho) = P(0)(1-\rho^2)(1-\rho^8)$. This kind of parameter scan calculations in a wide range of configuration space can be relatively easily done with the GIOTA code. This is a significant advantage of this code. The designated numbers denote the value of $\log(\varepsilon_{\text{eff}}^{3/2})$ for each contour. The minimum of $\varepsilon_{\text{eff}}^{3/2}$ appears around R_{ax} of approximately 3.53-3.55 m, which has been shown to be regardless of radial position under the vacuum conditions. This feature accurately reproduces previous finding of the

“neoclassical-optimized configuration in LHD” with the DCOM code 4). The $\varepsilon_{\text{eff}}^{3/2}$ increases as β is increased for configurations with $R_{\text{ax}} \geq 3.53$ m. This is not the case, however, for configurations with a smaller R_{ax} value; in such configurations, $\varepsilon_{\text{eff}}^{3/2}$ decreases as β is increased in this β range. It is also recognized that this property appears regardless of ρ from plasma core to edge region. This interesting feature indicates the possibility of improving ripple transport in finite- β situations by carefully tailoring the magnetic field structure. The GIOTA code is appropriate for this extensive study, since the contribution of each Fourier component of the magnetic field to ripple transport can be systematically specified to clarify the dominant contributor.

References

- 1) M.Yokoyama, L.Hedrick, K.Y.Watanabe, N.Nakajima, submitted to NIFS Report (2005).
- 2) C.D.Beidler and W.N.G.Hitchon, Plasma Phys. Control. Fusion, **36**, 317(1994).
- 3) S.P.Hirshman and D.K.Lee, Comput. Phys. Commun. **39**, 161(1986).
- 4) S. Murakami, A. Wakasa et al., Nucl. Fusion **42**, L19(2002).

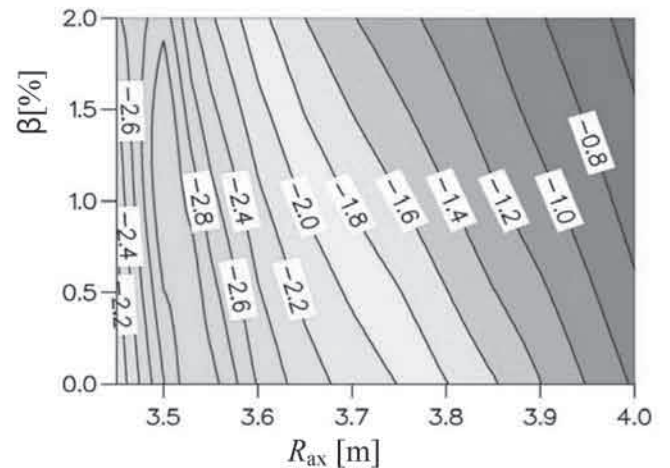


Fig. 1. Contour of $\log(\varepsilon_{\text{eff}}^{3/2})$ on the (R_{ax}, β) plane for the radial position of $\rho=0.5$ in a wide range of LHD fixed-boundary equilibria.

§7. Impact of Ion Species on Ambipolar Radial Electric Field in LHD

Yokoyama, M., Beidler, C.D. (Max-Planck, Greifswald)

High ion temperatures have been achieved in LHD experiments in high Z plasmas (such as Ne and Ar) 1,2). The radial electric field, E_r , deduced from CXRS measurements 3) and the corresponding neoclassical calculations for such high- Z experiments have been reported 2,4). The systematic theoretical study is presented to clarify the impact of ion species on E_r in such discharges.

The GSRAKE 5) code has been employed to calculate the neoclassical radial particle flux, Γ_j (j is the particle species index), to determine E_r based on the ambipolarity condition $\sum_j Z_j \Gamma_j = 0$ where $Z_e = -1$ is taken for electrons. The results presented below are for the $\rho = 0.8$ flux surface of the LHD with $R_{ax} = 3.75\text{m}$ and $B_0 = 1.5\text{T}$, for which GSRAKE calculations have been thoroughly benchmarked with other numerical approaches 6). Density and temperature profiles of $n_j(0)(1 - \rho^8)$ and $T_j(0)(1 - \rho^2)$ are assumed with fixed $n_e(0) = 0.5 \times 10^{19} \text{m}^{-3}$. The central temperatures, $T_i(0)$ and $T_e(0)$, are taken to be free parameters.

Figure 1 shows E_r diagrams in the T_i, T_e plane for pure H ($Z_H = 1$), He ($Z_{He} = 2$) and Ne ($Z_{Ne} = 10$, $T_i > 1.36\text{keV}$ for full ionization) plasmas. For H and He cases, two curves are indicated which separate the diagram into three regions. Above the upper curve, only one solution for E_r , the so-called “electron” root, is found. A single solution also exists below the lower curve, referred to as the “ion” root. In the region bounded by the two curves multiple solutions exist 7). It will be noted that for a given T_i , the upper curve is shifted to lower T_e in the He case. For Ne plasma, only a single solution of the ambipolarity condition for E_r exists. The dotted curve in Fig. 1 indicates the temperatures for which the ambipolarity condition is satisfied by $E_r = 0$; above (below) the curve $E_r > 0$ ($E_r < 0$) holds. This contrast to H, He results is due to the increase in charge; large Z magnifies the importance of the so-called mobility term in Γ (the term in which E_r appears as a thermodynamic force) for ions, while at the same time shifting them to higher collisionality where ripple transport plays a reduced role in determining the transport coefficients.

The effect of a gas mixture is examined below. The case of $n_H = 0.5n_e$ and $n_{Ne} = 0.05n_e$, (assuming $T_H = T_{Ne}$) is considered. The boundary separating the regions with only the ion root and with multiple solutions is shifted towards higher T_e for a case of a gas-mixture. This can be explained by plotting the neoclassical particle fluxes as a function of E_r for the two cases, as in Fig. 2. The temperatures are $(T_i,$

$T_e) = (1.48, 0.76)\text{keV}$, corresponding on the boundary curve for pure H but below the boundary curve for the H+Ne mixture. In Fig. 2 it will be noted that the monotonic increase of the Ne flux with increasing E_r enhances the total ion flux at large positive E_r . As a further hindrance to the appearance of the electron root, the higher Z_{eff} of the H+Ne plasma increases electron collisionality and thereby reduces electron ripple transport at moderate E_r values.

Acknowledgements

CDB wishes to thank his Japanese colleagues for their hospitality during his stay at NIFS in February 2005.

References

- 1) S.Morita et al., Nucl. Fusion **43**,899(2003).
- 2) Y.Takeiri et al., 20th IAEA Fusion Energy Conf., EX/P4-11, submitted to Nucl. Fusion (2004).
- 3) K.Ida et al., Rev. Sci. Instrum. **71**(2000)2360.
- 4) H.Sasao and K.Y.Watanabe, J.Plasma Fus. Res. SERIES **3**,431 (2003).
- 5) C.D.Beidler and W.D. D’haeseleer, Plasma Phys. Control. Fusion **37**, 463(1995).
- 6) C.D.Beidler et al., Proc. 13th Int. Stellarator Workshop(2003), see paper *Beidler_007_SWsSa.pdf* at URL www.ipp.mpg.de/eng/for/veranstaltungen/workshops/stellarator_2003/SWS-CDROM/papers/papers_alphabetic.html.
- 7) K.Ida et al., Phys. Rev. Lett. **86**,5297(2001).

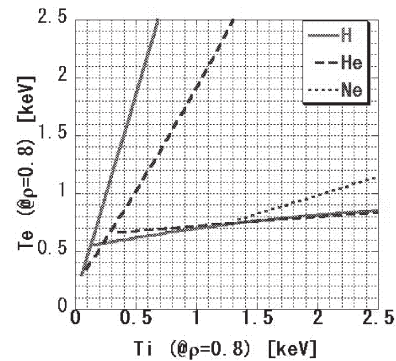


Fig. 1. E_r diagrams in the T_i, T_e plane for pure H, He and Ne cases at $\rho = 0.8$ of the LHD ($R_{ax} = 3.75\text{m}$, $B_0 = 1.5\text{T}$).

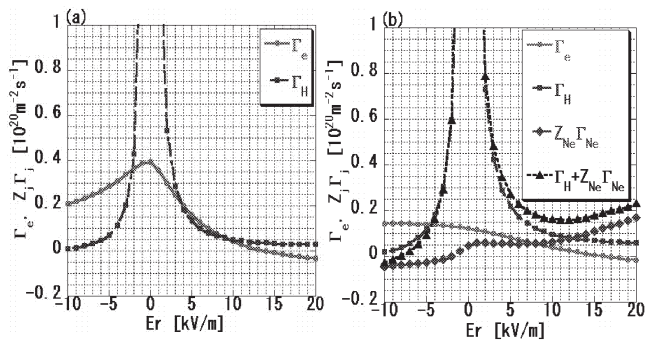


Fig. 2. Charge-weighted particle fluxes for (a) pure H and (b) H+Ne mixture cases are shown as a function of E_r for the temperatures $(T_i, T_e) = (1.48, 0.76)\text{keV}$.

§8. Transport Analysis of Radial Electric Field in Helical Plasmas

Toda, S., Itoh, K.
Itoh, S.-I., Yagi, M. (RIAM, Kyushu Univ.)

The steep gradient in the radial electric field is obtained in the inner plasma region and the transport barrier was confirmed in the Electron Cyclotron Resonance Heating (ECRH) plasma in the compact helical system (CHS) as well as in the Large Helical Device (LHD). A pulsating behavior of electrostatic potential (or the radial electric field) is also observed in the core region in CHS, illustrating a new dynamical state in magnetically-steady-state plasmas. In Wendelstein7-AS (W7-AS), a change in the anomalous transport in the core region was reported. We have examined the one-dimensional transport equations which describe the temporal evolutions of the density, the electron and ion temperatures, and the radial electric field in a cylindrical configuration. The radial electric field E_r is assumed to be determined by the ambipolar condition for the neoclassical particle flux. We have used the transport model for anomalous diffusivities to describe the turbulent plasma. This model has been confirmed by the present observations in CHS experiments so long as the static profile is concerned. In this study, the stationary structure of the radial electric field is examined and the hysteresis characteristic is found to form the shear layer of the radial electric field. Next, we study the dynamics of the radial electric field in the core plasmas.

In the simulations, the absorbed power of electrons is chosen as 100kW, where there is no absorbed power of ions. The stationary solutions of the radial electric field are obtained for the line-averaged density: $\bar{n} = 3.4 \times 10^{19} \text{m}^{-3}$, the line-averaged electron temperature: $\bar{T}_e = 310 \text{eV}$ and the line-averaged ion temperature: $\bar{T}_i = 170 \text{eV}$ as the results of the calculation. The temperature profiles of the electrons and the ions are obtained in Fig. 1. In Fig. 1, the dashed curve represents the case of the ion temperature and the full curve shows the profile of the electron temperature, respectively. At the point $\rho = \rho_T (0.38)$, the transition of the radial electric field is found, where $\rho = r/a$. We can find multiple solutions of the electric field which satisfy the local ambipolar condition from the calculated profiles of the density and the temperatures. The hard transition occurs when the transition takes place between the multiple solutions for the local ambipolar condition. The electron root for $\rho < \rho_T$ is sharply connected to the ion root for $\rho > \rho_T$ between them. It is found that there is a clear transport barrier in the electron temperature profile in Fig. 1. At the transition layer, the reduction of the anomalous transport diffusivities of electrons is obtained due to the strong gradient of the electric field. The value of the anomalous transport diffusivities of ions is set to be a third of that of electrons. The total suppression of electron transport can be clearly seen, because the explicit reduction of the anomalous transport of electrons is obtained.

Next, we study the dependence on initial conditions of the obtained steady calculation results. At first, we obtain two stationary solutions for different external parameters and use them as two different initial conditions. They have the positive E_r (electron root) and the negative E_r (ion root) in the entire radial region, respectively. Secondly, we analyze the coupled equations using these steady states as two initial conditions. The absorbed power of electrons is 100kW and the absorbed power of ions is 10kW, respectively. In the first case, the particle source term S_0 increases from $5 \times 10^{22} \text{m}^{-3} \text{s}^{-1}$ to $7 \times 10^{22} \text{m}^{-3} \text{s}^{-1}$ at $t=0$. In the second case, S_0 is reduced from $10^{23} \text{m}^{-3} \text{s}^{-1}$ to $7 \times 10^{22} \text{m}^{-3} \text{s}^{-1}$ at $t=0$. A difference between two kinds of the calculations is only the initial conditions. In the case that the steady state is obtained from the initial condition of the electron root, the positive E_r in the core ($\rho < 0.5$) region is retained and the solution in the outer region becomes negative. In contrast, if the steady state is obtained from the initial condition of ion root in the entire radial region, the radial electric field takes the negative value in the entire radial region. This difference only comes from two different kinds of the initial conditions. In the case when the positive value of E_r is shown in the core region, the change of the gradient for T_e and T_i can be seen. Therefore, the formation of the transport barrier depends on the history of the control parameters. Furthermore, the influence of the history of the control parameters on the achieved stationary solutions appears dominantly in the core ($\rho < 0.5$), not in the outer region ($\rho > 0.5$). Temporal oscillation of E_r was already obtained in the plasma edge region. In the present work, the dependence on different kinds of initial conditions is shown specially in the core region. That is, a hysteresis effect is shown to exist in the core electric field. However, the state of the temporal oscillation of E_r is not yet obtained in the core region.

In summary, the steady state of the radial electric field is shown and a hard transition between the multiple ambipolar E_r , which induces a steep gradient of E_r , is obtained. The clear transport barrier and the transport reduction are demonstrated. Next, the sensitivity to the initial conditions was found. Therefore, the initial condition can determine the final plasma state and crucial physical quantities such as the confinement time.

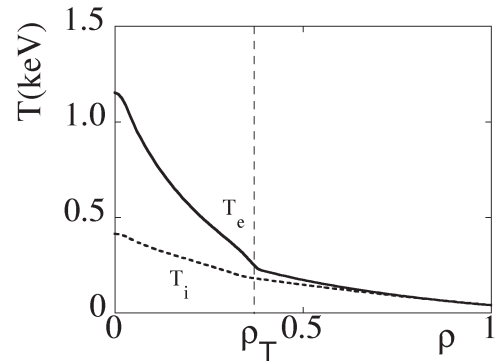


Fig. 1 Radial profiles of electron and ion temperatures

1) Toda S. and Itoh K., 12th International Congress of Plasma Physics Nice Acropolis, 25-29 Oct.2004 P1-064

§9. Non-local Neoclassical Transport Simulation in LHD

Satake, S., Okamoto, M., Nakajima, N., Sugama, H., Yokoyama, M.

Because of the recent progress in super computers, direct simulation study of neoclassical transport including the non-local nature appearing from the finite-orbit-width (FOW) effect is becoming possible. The non-local treatment of neoclassical transport is important to evaluate accurately the transport level and the self-consistent radial electric field profile in a plasma.

As concerns neoclassical transport in LHD, analytical approaches that is based on the ripple-averaged (or bounce-averaged) drift kinetic equation has been the most popular one. However, these analytical studies lack in the preciseness as follows: 1) approximation in the collision operator 2) simplified model used in order to describe magnetic field configuration and particle motion 3) the FOW effect 4) short time-scale behavior of electric field evolution such as geodesic acoustic mode (GAM) oscillation.

In order to simulate the transport phenomena with considering the points as mentioned above, we have develop a numerical simulation code FORTEC-3D, which is applicable to 3-dimensional configurations like LHD plasma. FORTEC-3D is based on the δf Monte Carlo method, which directly solves the time evolution of plasma distribution function according to the drift-kinetic equation. In FORTEC-3D, the collision operator is implemented by the random scatterings in the velocity space. It also retains the basic properties of the Fokker-Planck collision operator. The FOW effect is essentially included in the δf method, in which the exact guiding center motion is traced.

In adopting the δf method to 3D transport simulation, the most difficult problem is the large amount of consumption of both calculation time and resources. Therefore, FORTEC-3D has been developed with High Performance Fortran so that the code can be executed on the vector-parallel supercomputer SX-7 in NIFS with the good calculation efficiency.

As concerns the FOW effect, it is effective only for ions. Calculating both ion and electron transport by the δf method is heavy for the computers available now, therefore we have invented a hybrid simulation model. In FORTEC-3D, only the ion transport is solved with the δf method, while electron transport is obtained from a numerical solver for a ripple-averaged kinetic equation (GSRAKE[1]), which is used to make a table of electron particle flux in a form $\Gamma_e(r, E_r)$. Then the time evolution of radial electric field $dE_r/dt \propto -(\Gamma_i - \Gamma_e)$ is solved in FORTEC-3D, which is finally converges into an ambipolar state. If both Γ_i and Γ_e from are used, the result corresponds to the conventional SOW limit. Then one can easily compare the transport between with and without the FOW effect.

As far as we know, FORTEC-3D is the first application in the world of the δf neoclassical simulation which can calculate the time evolution of plasma in the whole plasma region at once, including the FOW effect. Its primal results were reported in IAEA conference[2]. Some examples of the results of simulations in LHD are shown below. In Fig.1, the ambipolar- E_r profile is compared between the result from FORTEC-3D and the SOW limit. We found that the difference of the ambipolar field becomes smaller as the magnetic axis is shifted inward. Therefore, the difference is considered to be the result of the FOW effect on ion transport, since the contribution of transit particles, which has a large orbit width, is suppressed in inwardly shifted configuration. In Fig. 2, the time evolution of E_r on 3 radial points are shown. The rapid oscillation is GAM, and the oscillation frequency in the simulation agrees with the analytical value. On the other hand, the damping rate of GAM seems much faster than that expected from previous analysis[3] in the SOW limit. By comparing the recent simulations of gyrokinetic GAM oscillation[4], we expect that the rapid damping of GAM found in our simulation is also because of the FOW effect. We continue to investigate the details of the GAM damping both by analytical way and by simulations.

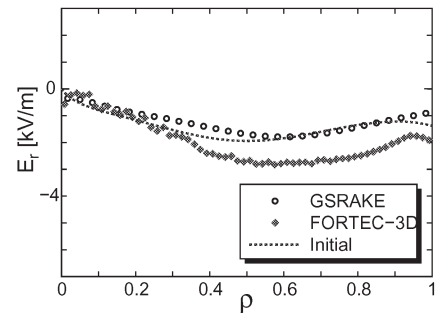


Fig.1 : The ambipolar E_r profile from FORTEC-3D and an expectation in the SOW limit (open circles).

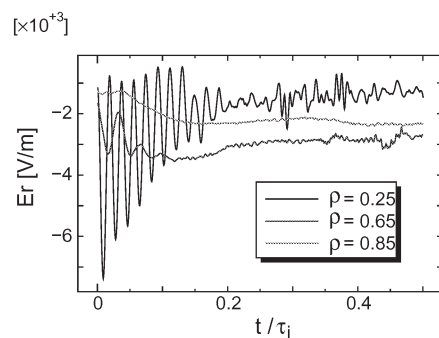


Fig. 2: Time evolution of E_r on each flux surface.

Reference

- 1) Beidler C. D. and Maassberg H., Plasma Phys. Control. Fusion **43**, 1131 (2001).
- 2) Satake S. *et al*, Proc. of 20th IAEA Fusion Energy Conf., TH/P2-18 (2004)
- 3) Novakovskii S. V. *et al*, Phys. Plasmas **4**, 4272 (1997)
- 4) Sugama H. And Watanabe T.-H., to appear in Proc. of ICNSP&APPTC 2005, A6-2.

§10. Particle Drift in Static Magnetic Fields

Oikawa, S. (Hokkaido Univ.)

1. Introduction

Analytical expressions for particle trajectory, and hence the drift velocity, in static magnetic fields are presented. The magnetic field configurations include: a slab configuration with a magnetic field gradient length L_B , and a toroidal configuration. These expressions for the particle drift velocity is valid irrespective of the ratio, $0 < \rho/L_B < \infty$, where ρ stands for the gyro-radius. Also derived are analytical expressions for the guiding center motion on the drift surface in a toroidal plasma with a plasma current. In the case of the banana particles, the average excursion, Δr , from the magnetic surface is found to be positive. As a result, a banana particle makes the above radial displacement in a collision time τ .

2. Slab Configuration

Let us assume that the magnetic field has only z -component which varies along x : $B(x) = (1 - x/L_B)B(0)$, where L_B denotes the length scale of magnetic field. Defining parameters

$$\varepsilon \equiv \frac{\rho_0}{L_B} = \frac{v_0}{\omega_0 L_B}, \text{ and } m \equiv \frac{4\varepsilon}{1 + 4\varepsilon \sin^2(\alpha/2)},$$

we have derived the exact drift velocity V_D normalized by the initial speed v_0 as follows:

$$\frac{V_D(m)}{v_0} = 1 - \frac{2}{m} \frac{K(m) - E(m)}{K(m)}, \quad (1)$$

where K and E are the complete elliptic functions of the first and the second kinds, respectively. The average x -position over the initial velocity direction, α , is

$$\langle x \rangle = x_0 + \frac{\rho_0^2}{L_B} \quad (2)$$

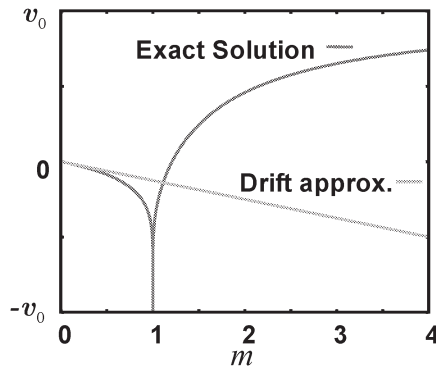


Fig. 1: Comparison of the exact ∇B drift velocity with drift approximation.

3. Toroidal Configuration

A banana particle moves around on a drift surface

slightly deviated from the corresponding magnetic surface. Let us now assume that the circular magnetic surface on the poloidal plane (r, θ) , and that two particles of the same species collide at a point $(r^+, \theta) = (r^-, \theta) = (r_0, 0)$ at a time $t = 0$. Other initial conditions are identical except for the pitch angle $\gamma_0^\pm = \gamma^\pm(0)$. Let the initial pitch angles are $\gamma_0^+ + \gamma_0^- = \pi$, i.e., the same parallel kinetic energy. Their radial positions of guiding centers are $r_G^\pm(t)$. The conventional neoclassical theory, in which ρ^2 terms are ignored, gives the time average of $\bar{r} = r_i$ at the turning point, since $r(\theta) = r_i \pm \Delta r(\theta)$. If the plasma current profile $J(r)$ is either parabolic or filamentary, the average deviation $\overline{\Delta r}$ over the banana orbit can be shown to be

$$\overline{\Delta r} = \frac{4r_0}{\varepsilon_i} \left(\frac{q\rho}{a} \right)^2 \left\{ m - 1 + \frac{E(m)}{K(m)} \right\}, \quad (3)$$

where $m \equiv \cos^2 \gamma_0 / 2\varepsilon_i$, and $\varepsilon_i \equiv r_i/R_0$ is the inverse aspect ratio with the major radius of R_0 . The average of $\{\cdot\}$ (of the above equation) over the initial pitch angle γ_0 can only be obtained numerically, and is nearly $0.2 \times \sqrt{\varepsilon_i}$. Thus, we have the average radial position and deviation:

$$\langle \overline{\Delta r} \rangle \approx 0.80 \frac{r_i}{\sqrt{\varepsilon_i}} \left(\frac{q\rho}{a} \right)^2 \quad (4)$$

In the case of $\gamma_0^\pm = 90 \pm 25$ deg considered here, equation (3) gives $\overline{\Delta r} = 4.0$ cm, while $\overline{\Delta r} = 8.0$ cm numerically by using the Runge-Kutta method as shown in Fig. 2. The major radius is $R_0 = 3$ m. The particle energy is 1 MeV. A simple magnetic field configuration is adopted: the plasma current is concentrated on the magnetic axis at $r = 0$. The toroidal field at the axis is 5 T and the plasma current is 2 MA. It should again be noted that the neoclassical theory gives $\overline{\Delta r} = 0$ even though the collision is between unlike particles, whereas equations (3) and (4) in the present study deal with like particle interactions.

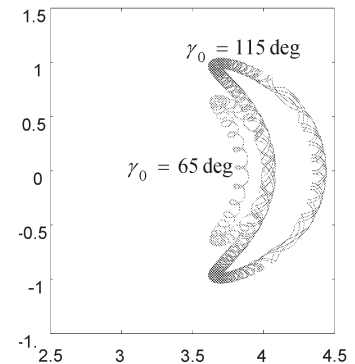


Fig. 2: Particle trajectories of the same species with the initial pitch angles of 65 deg and 115 deg at the starting point $(r_0, \theta_0) = (1, 0)$ on the projected poloidal plane.

§11. Strike Point Patterns on the LID Head in Various LHD Configurations

Kanno, R., Jimbo, S., Satake, S.,
Takamaru, H. (Chubu Univ.),
Nunami, M., Hayashi, T., Okamoto, M.

The test particle simulation is carried out in order to investigate the neoclassical effect on strike point patterns of ions on the Local Island Divertor (LID) head in various Large Helical Device (LHD) configurations. Control of the edge plasma by means of the LID is aimed to realize high temperature divertor operation (HT-operation). It is important to investigate whether or not the particle flux, in particular the ion flux crossing the island separatrix, is successfully guided to the rear side of the island where the target plates are placed to receive the particle load.

According to the collisionality and the magnetic field line structure, the particle orbits mainly contributing the particle flux from the core region to the LID head vary; in the present paper we call it the neoclassical effect on the edge transport phenomena. The pattern on the LID head is numerically observed by tracing the guiding center orbits of the test particles under the effects of the Coulomb collision.

In the vacuum field for the case with $R_0 = 3.6$ m, almost all particles are expected to drift into the island and to be guided to the rear part of the LID head, because the island separatrix is not seriously perturbed by the currents in the island control coils, where R_0 is the major radius of the magnetic axis. On the other hand, the island in the case with $R_0 = 3.75$ m is surrounded with ergodic field lines, and the performance of the island divertor is expected to be deteriorated because a fraction of the particles can escape to the wall, being guided along field lines in the ergodic zone.

We find in the test particle simulations that the strike point patterns on the LID head are varied according to the collisionality and the field line structure. The pattern for the case of $R_0 = 3.6$ m sensitively depends on the collisionality. For the case of $\lambda_{\text{mfp}}/L_c \approx 0.3$, the particles strike the edge of the LID head and the pattern is given by the trapped particle orbits, see Fig.1(a), where λ_{mfp} is the mean free path and $L_c \approx 100$ m is the connection length given as a length along a field line connecting the core region to the LID head. Of course, for the case of $\lambda_{\text{mfp}}/L_c > 1$, almost all particles are guided to the rear

part of the LID head and the pattern is characterized by the passing particle orbits along to the field lines of the island separatrix. On the other hand, for the case of the configuration with $R_0 = 3.75$ m the pattern is characterized generally by the passing particle orbits along the field lines of the island separatrix. In particular, for the case of $\lambda_{\text{mfp}}/L_c \approx 0.3$, almost all particles are guided to the rear part of the LID head, against our forecast, see Fig.1(b). When the case of $\lambda_{\text{mfp}}/L_c \ll 1$ is considered, the particles strike the edge of the LID head.

We have seen that the neoclassical effect plays the important role in determining the strike point patterns on the LID head. Since the mean free path under HT-operation is very large ($\lambda_{\text{mfp}}/L_c \gg 1$), the passing particles mainly contribute the particle transport. The passing particles move along the island separatrix, and the improvement of the performance of the LID in both the configurations is expected.

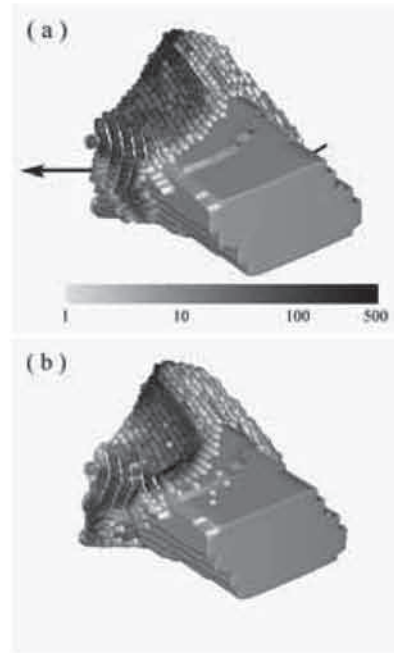


Figure 1: The strike point patterns, indicated by colored dots, on the LID head for the case of $E = 300$ eV and $\lambda_{\text{mfp}}/L_c \approx 0.3$, where (a) $R_0 = 3.6$ m and (b) $R_0 = 3.75$ m.

References

- [1] Komori, A. et al. : Plasma Physics and Controlled Fusion Research, 1994 (IAEA, 1995).
- [2] Ohyabu, N. et al. : J. Nucl. Mater. **220-222** (1995) 298.

§12. Development of a Monte-Carlo Simulation Code for Radial Profiles in Magnetic Island

Nunami, M., Kanno, R., Jimbo, S., Satake, S., Takamaru, H. (Chubu Univ.), Hayashi, T., Okamoto, M.

Almost magnetized plasmas are confined by magnetic surface, however, sometimes shape of external perturbation coil, and electric current in plasmas form magnetic island which is one of magnetic structure. The structure of magnetic island is observed by various plasma experiments, and the thermal distribution is flat at the interior of magnetic island. Recently, however, the Large Helical Device (LHD) experiments found that if the field which is made by external perturbation magnetic field is sufficiently large, and if the the vacuum magnetic island width exceeds the critical value (15% – 20% of minor radius), the flow along the magnetic flux surface inside the magnetic island in the direction to reduce the flow shear at the boundary of the magnetic island is observed. And radial profiles of temperature of ion and the plasma flow are measured in $m/n = 1/1$ island^{1),2)}. These results says that the potential is not flat in magnetic island, then this is very interesting for us.

We attacked for this results in terms of neoclassical particle transport. At first, we must specify magnetic surfaces, so we developed a code to label magnetic surface in island by calculating arbitrarily toroidal flux with high accuracy. (See Fig.1)

Next, to calculate radial electric field without magnetic island, we use δf Monte-Carlo method in terms of neoclassical transport. In this method, the distribution function of plasma is separated into

$$f = f_M + \delta f,$$

where f_M is a local Maxwellian and δf is considered as a small perturbation from f_M . And then, using two weight scheme, we solve the linearized kinetic equation for δf ,

$$\left(\frac{\partial}{\partial t} + (\mathbf{v}_{\parallel} + \mathbf{v}_{\perp}) \cdot \nabla + k \frac{\partial}{\partial k} - C_T \right) \delta f = C_F - k \frac{\partial}{\partial k} f_M - \mathbf{v}_{\perp} \cdot \nabla f_M \quad (1)$$

where k is kinetic energy ($k = mv^2/2$), and C_T is the test particle collision operator implemented by random kicks in the velocity space, and C_F is the field particle collision term.

Then we compare the results of our calculation and the results in 3).

At next step, we calculate radial electric field in magnetic island where MHD equilibrium is generated by three-dimensional MHD equilibrium code “HINT”. After this, we have to compare our results and the data of the LHD experiments.

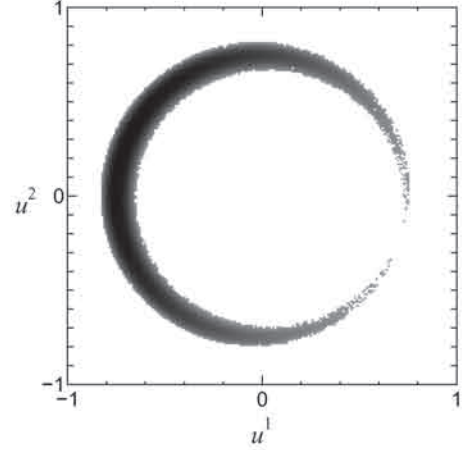


Figure 1: Toroidal flux in $m/n = 1/1$ magnetic island at a poloidal section. As color darker, the flux becomes smaller.

References

- 1) K. Ida, *et al*
Phys. Rev. Lett., Vol. **88**, No. 1 (2002), 015002.
- 2) K. Ida, *et al.* ,
Nucl. Fusion, Vol. **44** (2004), 290.
- 3) R. Kanno, *et al.* ,
Nucl. Fusion, Vol. **37** (1997), 1463.

§13. Self-consistent Model for Two-dimensional Structures in Tokamak H Modes

Kasuya, N., Itoh, K.

The formation of transport barriers in toroidal plasmas has been the focus of numerous researches, and significant attention has been devoted to studying the steep radial electric field structure in the L/H transition physics¹⁾. On the other hand, poloidal shock has been predicted theoretically when a large poloidal flow exists²⁾. In a tokamak H-mode, a large poloidal flow exists in an edge transport barrier, and the electrostatic potential and density profile can be steep both in the radial and poloidal direction. Therefore, it is necessary to study the formation mechanism of the two-dimensional structure at the barrier.

We construct a model describing a two-dimensional structure of the electrostatic potential, density and flow velocity near the edge of a tokamak plasma. A set of equations, which describes the transition to the steep radial electric field structure as well as poloidal inhomogeneity, is derived by considering the nonlinearity in bulk-ion viscosity and (turbulence-driven) shear viscosity. The shear viscosity couples the radial and poloidal structure, so self-sustained structures can be obtained by solving the equations.

We consider a large aspect ratio tokamak with a circular cross-section and the coordinates (r, θ, ζ) are used (r : radius, θ : poloidal angle, ζ : toroidal angle). Poloidal variations of the density and the electrostatic potential are considered. Electrons are isothermal, ions are adiabatic, and $n_i = n_e \equiv n$ is assumed, where n_i and n_e are the ion and electron density, respectively. Derivation of the model equation follows Ref. 2, but the radial flow and shear viscosity are taken into account here³⁾. By these terms, radial and poloidal structures are coupled with each other. The structures are governed by the momentum balance equation

$$m_i n \frac{d}{dt} \vec{V}_i = \vec{J} \times \vec{B} - \vec{\nabla}(p_i + p_e) - (\vec{\nabla} \cdot \vec{\pi}_i)_{\text{bulk}} - (\vec{\nabla} \cdot \vec{\pi}_i)_{\text{shear}}, \quad (1)$$

where \vec{V}_i is the flow velocity, \vec{J} is the plasma current, p_i and p_e are the ion and electron pressure, $\vec{\pi}_i$ is the viscosity tensor of ions, and m_i is the ion mass. Pressure $p = nT$, and constant temperature T is assumed. The viscosity is divided into two terms: bulk viscosity given by neoclassical process⁴⁾, and shear viscosity given by anomalous process¹⁾. The viscosity of electrons is neglected because it is smaller by a factor of the order of $\sqrt{m_e/m_i}$. The flow velocity is written

$$\vec{V} = \vec{V}_\parallel + \frac{\vec{E} \times \vec{B}}{B^2} = \left(-\frac{I}{rRB^2} \frac{\partial \Phi}{\partial \theta}, \frac{KB_p}{n}, \frac{KB_\zeta}{n} - \frac{1}{B_p} \frac{\partial \Phi}{\partial r} \right), \quad \text{where}$$

Φ is the electrostatic potential, $K = nV_p/B_p$ corresponding to the poloidal flow, and $I = R^2 \vec{B} \cdot \nabla \zeta$. The toroidal symmetry is utilized in this description. The parallel component and averaged poloidal component of the

momentum balance Eq. (1) are given to be

$$\begin{aligned} & -\frac{nI}{KB^2 r R} \frac{\partial \Phi}{\partial \theta} \frac{\partial}{\partial r} \left[\frac{1}{2} \left(\frac{KB}{n} \right)^2 \right] + \frac{B_p}{r} \frac{\partial}{\partial \theta} \left[\frac{1}{2} \left(\frac{KB}{n} \right)^2 \right] \\ & + \frac{IB_\zeta}{B^2 r R} \frac{\partial \Phi}{\partial \theta} \frac{\partial}{\partial r} \left[\frac{I}{RB_p B_\zeta} \frac{\partial \Phi}{\partial r} \right] - \frac{KB_p B_\zeta}{nr} \frac{\partial}{\partial \theta} \left[\frac{I}{RB_p B_\zeta} \frac{\partial \Phi}{\partial r} \right] \\ & = -\frac{B_p}{m_i r} \frac{\partial}{\partial \theta} \left(\frac{\langle p_e \rangle}{\langle n \rangle} \ln n + \frac{5}{2} \frac{\langle p_i \rangle}{\langle n^{5/3} \rangle} n^{2/3} \right) \\ & - \frac{1}{m_i n} (\vec{B} \cdot \vec{\nabla} \cdot \vec{\pi}_i)_{\text{bulk}} - \frac{1}{m_i n} (\vec{B} \cdot \vec{\nabla} \cdot \vec{\pi}_i)_{\text{shear}}, \quad (2) \end{aligned}$$

$$\begin{aligned} & \left\langle -\frac{nI}{KB^2 r R} \frac{\partial \Phi}{\partial \theta} \frac{\partial}{\partial r} \left[\frac{1}{2} \left(\frac{KB_p}{n} \right)^2 \right] + \frac{B_p}{r} \frac{\partial}{\partial \theta} \left[\frac{1}{2} \left(\frac{KB_p}{n} \right)^2 \right] \right\rangle \\ & = \frac{1}{m_i} \left\langle \frac{JB_p B_\zeta}{n} \right\rangle - \frac{1}{m_i} \left\langle \frac{\vec{B}_p \cdot \vec{\nabla} \cdot \vec{\pi}_i}{n} \right\rangle_{\text{bulk}} - \frac{1}{m_i} \left\langle \frac{\vec{B}_p \cdot \vec{\nabla} \cdot \vec{\pi}_i}{n} \right\rangle_{\text{shear}}, \quad (3) \end{aligned}$$

where $\langle \rangle$ denotes the flux surface average. The radial flow is taken into account, so $\partial \Phi / \partial \theta$ terms are involved in the left side of Eqs. (2) and (3). Using the viscosity tensor $\vec{\pi}_i = (p_\parallel - p_\perp) (\hat{b} \hat{b} - \vec{I}/3)$, where $(p_\parallel - p_\perp)$ is the pressure anisotropy, \hat{b} is the unit vector parallel to the magnetic field and \vec{I} is the unit tensor, the bulk viscosity term can be written as

$$(\vec{B} \cdot \vec{\nabla} \cdot \vec{\pi}_i)_{\text{bulk}} = \frac{2}{3} \frac{B_p}{r} \frac{\partial}{\partial \theta} (p_\parallel - p_\perp) - (p_\parallel - p_\perp) \frac{B_p}{B} \frac{1}{r} \frac{\partial B}{\partial \theta}. \quad (4)$$

The first term of Eq. (4) is dominant, so only this term is kept in Eq. (2) hereafter. In contrast, the surface average is taken in Eq. (3), in which the second of Eq. (4) remains. The pressure anisotropy is rewritten in terms of B and n in Ref. 5. The shear viscosity is given by the second derivative of the flow velocity, and here simply given to be

$$(\vec{B} \cdot \vec{\nabla} \cdot \vec{\pi}_i)_{\text{shear}} = -m_i n \mu \vec{B} \cdot \nabla_\perp^2 \vec{V}, \quad (5)$$

where μ is a shear viscosity coefficient. The coefficient μ depends on the radial electric field and has spatial variation. The Boltzmann relation

$$n = \bar{n} \exp \frac{e \Delta \Phi}{T_i} \quad (6)$$

is adopted here to determine variables, where \bar{f} and Δf represent the spatial average and perturbed parts of quantity f , respectively. The variable that must be determined from Eqs. (2), (3) and (6) are K , Φ and n , which have radial and poloidal variations.

References

- 1) K. Itoh, S.-I. Itoh and A. Fukuyama: *Transport and Structural Formation in Plasmas* (IOP, Bristol, 1999).
- 2) K. C. Shaing, R. D. Hazeltine and H. Sanuki, Phys. Fluids B **4** (1992) 404.
- 3) N. Kasuya, K. Itoh and Y. Takase, J. Plasma Fusion Res. SERIES **6** (2004) 283.
- 4) K. C. Shaing, E. C. Crume and W. A. Houlberg: Phys. Fluids B **2** (1990) 1492.
- 5) S. P. Hirshman and D. J. Sigmar: Nucl. Fusion **21** (1981) 1079.

§14. Two-dimensional Structure and Particle Pinch in Tokamak H Mode

Kasuya, N., Itoh, K.

In tokamak H modes, a large poloidal flow exists in an edge transport barrier, and the electrostatic potential and density profiles can be steep both in the radial and poloidal direction. Two-dimensional structures of the potential, density and flow velocity near the edge of a tokamak plasma are investigated. The poloidal asymmetry of the structure generates inward particle pinch, and gives explanation for the rapid establishment of the edge density pedestal on the onset of L/H transition, the small time constant of which has not been clarified yet.

The analysis is carried out with the momentum conservation law with the shock ordering ¹⁾, which is $\ln(n/\bar{n}) = O(\varepsilon^{1/2})$, where n and ε are the density and the inverse aspect ratio, respectively. The model includes the nonlinearity in bulk-ion viscosity and turbulence-driven shear viscosity ²⁾. The radial and poloidal structures are coupled with each other by the shear viscosity term, and the magnitude of the shear viscosity determines steepness and position of the shock structure. In shock ordering, a structure of the flux-surface-averaged part is solved first, and using this poloidal flow profile, a two-dimensional structure can be obtained iteratively.

For the case with a strong radial electric field (H mode), a two-dimensional structure in an edge transport barrier is obtained, giving a poloidal shock with a solitary radial electric field profile. Figure 1 shows a profile of the poloidal electric field in the electrode basing H-mode ³⁾. The region where the poloidal Mach number has large value is localized in the middle of the electrode-biased region, so a localized large poloidal electric field exists at the points of the shock in those with large poloidal Mach number. In addition, the magnitude of the poloidal Mach number varies in the radial direction, and the poloidal position of the shock varies in the radial direction accordingly.

The poloidal electric field induces convective transport in the radial direction, and poloidal asymmetry makes the flux-surface-averaged particle flux direct inward with a pinch velocity on the order of 1 [m/s]. Figure 2 represents the radial profiles of the flux-surface-averaged radial flux in the strong and weak E_r cases. In the strong E_r case, which is relevant to the H-mode or biased electrode experiments, a larger convective particle flux is induced in the radial direction. The radial flux has negative value, so it points inward to the plasma center. A large poloidal flow with radial shear enhances the inward pinch velocity. Figure 2 shows that the radial flux has maximum in the radial position where the poloidal flow shear is large. That is coming from the form of the shear viscosity.

The increase of the inward convective particle flux has a large impact on the density pedestal formation on the onset of L/H transition. The H-mode pedestal can be formed in

shorter time $\tau \ll 10[\text{ms}]$. Suppression of turbulence and reduction of diffusive transport occurs in transport barriers. The reduction of diffusion coefficient explains steepening of the H-mode pedestal, but the time constant of the pedestal formation is difficult to explain. That is, it takes longer time to form the pedestal with a reduced transport coefficient in the H mode. In L/H transition, the magnitude of a poloidal flow changes abruptly, so that the convective transport changes abruptly in the transport barrier region in the same time. If the convective velocity increases abruptly, the time constant of the pedestal formation is represented to be $\tau = \delta / V_r$ ($\tau = 5$ [ms] when barrier width $\delta = 5$ [cm] and radial convective velocity $V_r = 10$ [m/s]), so sudden increase of the inward pinch flux induced by the two-dimensional structure is candidate for the cause of the rapid establishment of the density pedestal at the onset of L/H transition.

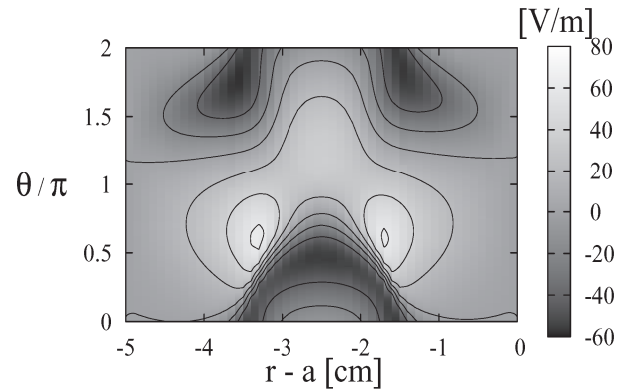


Fig.1: Two-dimensional structure of the poloidal electric field with strong and inhomogeneous E_r (electrode basing H-mode case).

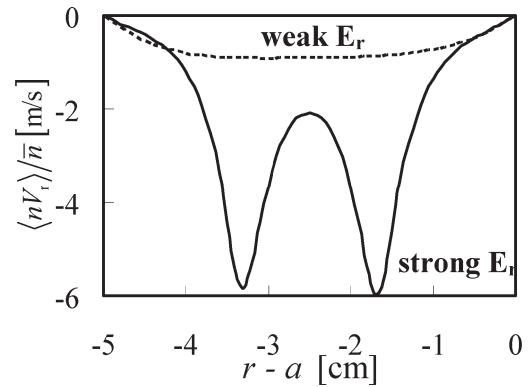


Fig. 2: Radial profiles of flux-surface-averaged particle flux in the case of weak homogeneous and strong inhomogeneous E_r (L-mode and electrode basing H-mode case, respectively).

References

- 1) K. C. Shaing, R. D. Hazeltine and H. Sanuki, Phys. Fluids B **4** (1992) 404.
- 2) N. Kasuya and K. Itoh, Phys. Rev. Lett. **94** (2005) 195002.
- 3) N. Kasuya, K. Itoh and Y. Takase, Nucl. Fusion **43** (2003) 244.

§15. Coherent Structure of Zonal Flow and Nonlinear Saturation

Itoh, K., Toda, S., Sanuki, H.
Hallatschek, K. (IPP, Germany)
Itoh, S.-I., Yagi, M. (RIAM, Kyushu Univ.)

The growth of the zonal flow in the presence of the drift-wave turbulence has been discussed on the basis of space and time scale separation. We also consider the space and time scale separation between zonal flow and ambient turbulence, and the evolution of the zonal flow and ambient turbulence are governed by

$$\frac{\partial}{\partial t} \left(\frac{\partial}{\partial r} V_Z \right) = \frac{\partial^2}{\partial r^2} \frac{c^2}{B^2} \int d^2 k \frac{k_\theta k_r}{(1 + k_\perp^2 \rho_s^2)^2} \bar{N}_k - \gamma_{damp} \frac{\partial}{\partial r} V_Z$$

and

$$\frac{\partial}{\partial t} N_k + \frac{\partial \omega_k}{\partial \mathbf{k}} \cdot \frac{\partial N_k}{\partial \mathbf{x}} - \frac{\partial \omega_k}{\partial \mathbf{x}} \cdot \frac{\partial N_k}{\partial \mathbf{k}} = 0 ,$$

where V_Z is the zonal flow velocity, \bar{N}_k is the slow modulation of drift-wave action N_k , which is induced by V_Z , and γ_{damp} denotes the damping rate of zonal flow by other processes. The zonal flow has a slow dependence as expressed by $\exp(iKr - i\Omega t)$.

Calculating up to the third order nonlinear terms, we have the equation for the zonal flow vorticity as

$$\begin{aligned} \frac{\partial}{\partial t} U + D_{rr} \left(\frac{\partial^2}{\partial r^2} U + K_0^{-2} \frac{\partial^4}{\partial r^4} U \right) - D_3 \frac{\partial^2}{\partial r^2} U^3 \\ - \mu_{||} (1 + 2q^2) \frac{\partial^2}{\partial r^2} U = 0 \end{aligned}$$

where

$$D_{rr} = -\frac{c^2}{B^2} \int d^2 k \frac{R(K, \Omega) k_\theta^2 k_r}{(1 + k_\perp^2 \rho_s^2)^2} \frac{\partial N_k}{\partial k_r} ,$$

$$R(K, \Omega) = (\Delta \omega_k)^{-1} D_3 / D_{rr} \simeq R(K, \Omega)^2 k_\theta^2 \left(\partial^2 / \partial k_r^2 \right) ,$$

$\gamma_{damp} = \mu_{||} (1 + 2q^2) K^2$, where $\mu_{||}$ is the turbulent shear viscosity for the flow along the field line and q is the safety factor. With an appropriate normalization, $x = r/L$, $\tau = t/t_Z$ and $u = U/U_0$, where $L^{-2} = K_0^2 (1 - \mu)$, $t_Z = D_{rr}^{-1} K_0^{-2} (1 - \mu)^{-2}$ and $U_0^2 = D_{rr} D_3^{-1} (1 - \mu)$, one has

$$\frac{\partial}{\partial \tau} u + \frac{\partial^2}{\partial x^2} u - \frac{\partial^2}{\partial x^2} u^3 + \frac{\partial^4}{\partial x^4} u = 0 \quad (1)$$

We investigate the case in which the flow is generated from the state with a small noise level where no net flow exists, $\int dx u = 0$. Conservation of the total momentum holds for the periodic boundary condition and the flow evolves to satisfy the condition $\int dx u = 0$. The stationary solution of eq. (1) in the domain $0 < x < d$, for the periodic boundary condition, is given by an elliptic integral as

$$\int \left(1 - 2u^2 + u^4 - \kappa^2 \right)^{-1/2} du = \pm \frac{x}{\sqrt{2}} , \quad (2)$$

where κ is an integral constant satisfying $0 \leq \kappa < 1$.

The integral constant κ is given by the periodicity

$$\int_{-u_c}^{u_c} \left(1 - 2u^2 + u^4 - \kappa^2 \right)^{-1/2} du = d/2\sqrt{2}n \quad (u_c = \sqrt{1 - \kappa^2} ,$$

and $n = 1, 2, 3, \dots$).

The temporal evolution of eq. (1) is solved numerically. It is shown that the growth is dominated by the component which has the largest linear growth rate. That is, the integer n is given by the integer which is closest to $d/n = 4\sqrt{2}\pi$. Figure 1 illustrates the stable stationary state. The peak value of $u(x)$ is given as $u_c \simeq 0.95$. Compared to a simple sinusoidal function (eigenfunction of the linear operator), the result in Fig. 1 is closer to a piecewise constant function.

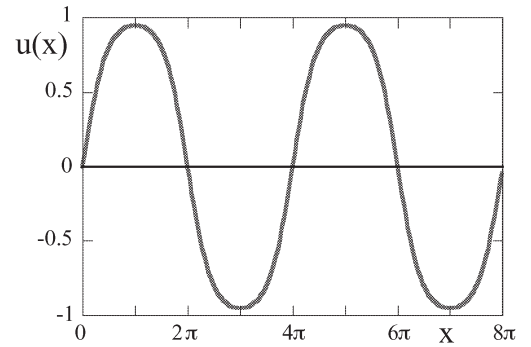


Fig.1 Stationary state of the normalized solution $u(x)$ for the case of $d = 8\pi$. Radial length x and vorticity u are normalized values.

Reference

- [1] A. Yoshizawa, S.-I. Itoh and K. Itoh: *Plasma and Fluid Turbulence* (IOP, England, 2002).
- [2] K. Itoh, K. Hallatschek, S. Toda, H. Sanuki, and S.-I. Itoh: J. Phys. Soc. Jpn. **73** (2004) 2921

§16. Excitation of Geodesic Acoustic Mode in Toroidal Plasmas

Itoh, K.

Hallatschek, K. (IPP, Germany)

Itoh, S.-I. (RIAM, Kyushu Univ.)

The instability of the geodesic acoustic mode (GAM) in tokamak turbulence is analyzed. It can be caused by dynamic shearing of the ambient turbulence by GAMs combined with the poloidal inhomogeneity of the turbulent flux. The GAMs are more unstable for high safety factors.

The new mechanism of GAM excitation results from the modulation of the flux by the dynamic shearing of the turbulent waves. This dynamic shearing mechanism has been found by numerical simulations in [1]. The analytic theory is derived as follows.

We are interested in the case that the background drift wave fluctuations are in the strong turbulence regime. In such a case, the modification of the drift wave turbulence by the superposed $\tilde{V}_{E \times B}$ can be evaluated by use of the conservation of wave action. In order to apply this method, we calculate the change of k_r of the drift waves. In toroidal plasmas at the outboard midplane, the phase of the dominant modes varies slowly in the direction of the major radius but rapidly in vertical direction, which is a consequence of the ballooning effect. A superposed sheared poloidal rotation shifts the radial wavenumber k_r of the drift wave fluctuations with time. (See Fig.1) Let θ_1 denote the angle between the mid plane and the wave front. In the absence of GAM, one has $\theta_1 \simeq 0$ and the phase front starts to rotate, after the zonal flow has been superposed, with the angular frequency $d\theta_1/dt = \partial \tilde{V}_{E \times B} / \partial r$. That is, the quantity k_r^2 evolves as $dk_r^2/dt = 2 k_r dk_r/dt = - (2k_\theta^2 s \theta) d\theta_1/dt$ up to the first order in θ_1 . The perturbation of k_r^2 , $\delta(k_r^2)$, ensues as $\delta(k_r^2) = -2k_\theta^2 s \theta \int^t dt \frac{\partial}{\partial r} \tilde{V}_{E \times B}$. The drift wave action $(1 + k_\perp^2 \rho_s^2)^2 |\phi_{\text{micro}}^2|$ is adiabatically conserved during a change of perpendicular wavenumber. The change of the turbulence amplitude, $\delta |\phi_{\text{micro}}^2|$, can be computed to be

$$\delta |\phi_{\text{micro}}^2| \simeq -2 \frac{\rho_s^2 \delta(k_r^2)}{(1 + k_\perp^2 \rho_s^2)} |\phi_{\text{micro}}^2|,$$

The modulation of the source $F \equiv (S - \nabla \cdot \Gamma) / n_0$ is calculated and the amplitude of the $\sin \theta$ component is calculated by the $\sin \theta$ -weighted flux surface average as

$$\tilde{F}_1(r, t) = u_{\text{WH}} \left(\int^t dt \frac{\partial^2}{\partial r^2} \tilde{V}_{E \times B} \right)$$

with $u_{\text{WH}} = \frac{3 s k_\theta^2 \rho_s^2}{(1 + k_\perp^2 \rho_s^2)} F_0 L$. The growth rate of the GAMs oscillation is given as

$$\text{Im}(\omega) = \frac{q^2}{1 + 2q^2} \frac{R u_{\text{WH}} K_r^2}{2} - \frac{\mu_\parallel K_r^2}{2(1 + 2q^2)}.$$

If the condition

$$q^2 R u_{\text{WH}} > \mu_\parallel$$

holds, the drive by dynamic shearing exceeds the stabilization by turbulence viscosity, and the GAM is expected to be excited. An order estimate of the divergence of the particle flux results in $F_0 \simeq D L^{-2}$, where D is the anomalous particle diffusion coefficient. One has $u_{\text{WH}} \simeq s k_\perp^2 \rho_s^2 D L^{-1}$ for $k_\perp^2 \rho_s^2 < 1$. One has the condition for GAM instability by this mechanism as

$$\frac{s q^2 R}{L} k_\perp^2 \rho_s^2 > \frac{\mu_\parallel}{D}.$$

Noting that μ_\parallel / D is close to unity, the GAM is induced by turbulence for the higher q cases that satisfy $q^2 > q_c^2 \sim L R^{-1} k_\perp^{-2} \rho_s^{-2} s^{-1}$. If one considers the application to ion-temperature-gradient (ITG) driven turbulence, the microfluctuations are excited in the range of $k_\perp^2 \rho_s^2 \sim 0.1$ for $s \sim 1$. The GAM excitation is expected to occur when $q^2 > q_c^2 \sim 10 \frac{L}{R}$ holds.

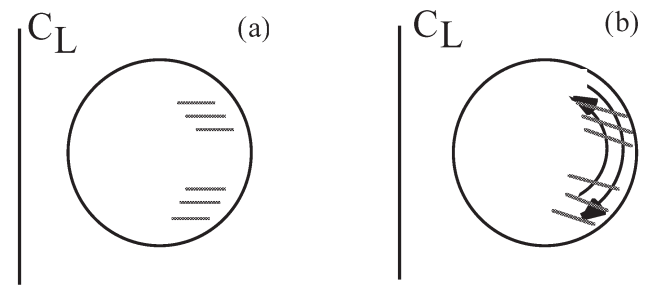


Fig.1 Schematic illustration of dynamic shearing of ambient fluctuations by GAM. Contours of phases of toroidal fluctuations are shown by thick lines in (a). In the presence of poloidally-symmetric shearing motion, the phase contours are modified with up-down asymmetry.

Reference

- [1] K. Hallatschek and D. Biskamp: Phys. Rev. Lett. **86** (2001) 1223
- [2] K. Itoh, K. Hallatschek, S.-I. Itoh: Plasma Phys. Control. Fusion, **47** (2005) 451

§17. Periodic Change of Solar Differential Rotation

Itoh, S.-I. (RIAM, Kyushu Univ.)
 Itoh, K., Yoshizawa, A.
 Yokoi, N. (Univ. Tokyo)

The periodic oscillation of the inhomogeneous rotation of the sun is studied by use of the MHD dynamo theory [1]. There exists a turbulent electromotive force which is driven by the vorticity of the flow (i.e., the γ -dynamo).

In addition, its counterpart exists in the vorticity equation, that is, the rotation is induced by inhomogeneous magnetic field in turbulent plasma. Based on this dynamo theory, a periodic change of solar differential rotation with the period of 11 years is theoretically explained. The predicted amplitude is compared with observations.

The dynamo theory of turbulent plasma has provided the mean field equation as

$$\frac{\partial \boldsymbol{\omega}}{\partial t} = \nabla \times \left(2 \left(\boldsymbol{u} - \frac{\gamma}{\beta} \boldsymbol{B} \right) \times \boldsymbol{\omega}_F + \nu_T \nabla^2 \left(\boldsymbol{u} - \frac{\gamma}{\beta} \boldsymbol{B} \right) \right). \quad (1)$$

Equation (1) describes an interesting effect of the magnetic field on the *generation* of global vorticity. The terms which have the coefficient ν_T in the RHS of Eq. (1) are induced by the microscopic turbulence. The term $\nabla \times \nu_T \nabla^2 \boldsymbol{u}$ is the well-known turbulent viscosity term, i.e., the localized vorticity decays in time. It tends to eliminate the inhomogeneity of the vorticity. (For instance, the tachocline is weakened by this term.) On the contrary, the term $\nabla \times \nu_T \nabla^2 (\gamma \boldsymbol{B} / \beta)$ generates the velocity so that the velocity \boldsymbol{u} becomes parallel to \boldsymbol{B} . If the localized magnetic field exists, then this dynamo term *generates* the localized flow profile.

From Eq. (1), we study that the response of the toroidal velocity appears against the change of the magnetic field \boldsymbol{B} . When the change is slow in comparison with the diffusion time, the response of the relative velocity \boldsymbol{u} in the presence of the temporal variation of \boldsymbol{B} , $\delta \boldsymbol{u}$, is given as

$$\delta \boldsymbol{u} = \gamma \beta^{-1} \boldsymbol{B}. \quad (2)$$

When we apply this result (2) to the case of sun, the modulation of the toroidal velocity by the dynamo magnetic field is deduced. Here we use polar coordinates (r, ζ, θ) . The dynamo magnetic field is known to have a strong toroidal magnetic field. This magnetic field is localized in the mid- and low-latitude regions. Equation (2) shows that the azimuthal velocity in the rotation frame is stronger in the mid- and low-latitude regions. This localized azimuthal flow has an up-down symmetry. The polarity rule of solar dynamo is well known: the sign of dynamo magnetic field is opposite between northern and southern hemispheres. It should be also noticed that the

dynamo coefficient γ is a pseudoscalar while β is a scalar. That is, the ratio γ/β changes the sign in the northern and southern hemispheres. From these facts, the induced modification of the velocity $\delta \boldsymbol{u}$ has an up-down symmetry. This symmetry property of the induced velocity $\delta \boldsymbol{u}$, together with the localization in the latitude, is common to the profile of the solar rotation velocity.

We next estimate the magnitude of the induced velocity $\delta \boldsymbol{u}$. The strength of the magnetic field is evaluated as about 1T or less in the convective zone of the sun. The location $r/r_{\text{SUN}} \sim 0.8 - 0.9$ may be relevant as the representative value in the study of the inhomogeneous rotation velocity. As the mass density in this region [2], we adopt the number density of hydrogen as $O(10^{28}) \text{ m}^{-3}$ or $\rho \sim 10 \text{ kg m}^{-3}$, which gives that $B \sim 300 \text{ m/s}$ for $B = 1 \text{ T}$ in the Alfvén unit. An estimate of the ratio of $|\gamma/\beta| = O(10^{-2}) \sim O(10^{-1})$ has been given for the study of the γ -dynamo mechanism for the generation of solar magnetic field [2]. If one employs the mean value of the range this estimate, $|\gamma/\beta| \simeq 10^{-1.5}$, we have an evaluation of $\delta \boldsymbol{u}$ as

$$|\delta \boldsymbol{u}| \sim 10 \text{ m/s}. \quad (3)$$

This is a few per cent of the differential rotation velocity in the solar convective zone.

The solar magnetic field shows a quasi-periodic change with the period of about 22 years. As a result of this periodic change of \boldsymbol{B} , the induced velocity $\delta \boldsymbol{u}$ is also subject to the (quasi-)periodic change. Two cases can be considered depending on the changeability of the sign of γ/β . If the sign of γ/β is not altered by the change of the polarity of the magnetic field, then $\delta \boldsymbol{u}$ changes its direction and magnitude with the period of 22 years. In the opposite case, i.e., γ/β changes the sign together with \boldsymbol{B} , then $\delta \boldsymbol{u}$ changes its magnitude with the period of 11 years. It is therefore plausible that the periodic oscillation of differential rotation is composed of the component with the 11-year period and the one with 22-year period.

These theoretical predictions are compared with observational results. First of all, the resemblance of the spatio-temporal patterns of the periodic change of rotation and of the magnetic activity is understood naturally. Second, the amplitude of the periodic oscillation is in a range of observation: the amplitude of oscillation of $1 - 5 \mu\text{Hz}$ has been observed in the upper convective zone. The radial profile of the amplitude of oscillation is reported, and $\delta \boldsymbol{u}$ is shown to have larger amplitude near the surface. The main elements of the observation on the periodic change can be explained by the γ -dynamo theory.

Reference

- [1] Itoh S-I, et al. 2005 *Astrophys. J.* **618** 1044
- [2] Yoshizawa A, et al. 2000 *Astrophys. J.* **537** 1039

§18. Life Time of Plasma States Near Transition Boundary

Itoh, S.-I., Yagi, M. (RIAM, Kyushu Univ.)
Itoh, K.

A stochastic equation for the amplitude of the neoclassical tearing mode (NTM) has been derived, and the life time of a state free of the onset of NTM is obtained. The model and basis are explained in refs.1 and 2. One has an explicit form of the life time as [3]

$$t_{\text{life}} = \frac{2\pi}{\eta \sqrt{\Lambda_0 \Lambda_m}} \exp(S(A_m)), \quad (1)$$

where the time rates $\Lambda_{m,0}$ are given as

$\Lambda_m = 2A \left| \partial \Lambda / \partial A \right|$ at $A = A_m$ and $\Lambda_0 = \Lambda(\langle A_0 \rangle)$, and the nonlinear dissipation function was given as

$$\begin{aligned} S(A) = & \Gamma_0 \frac{r_s^2}{\rho_b^2} \left(-\frac{4}{3} \Delta'_0 A^{3/2} + h A^2 \right) \\ & + \Gamma_0 \frac{r_s^2}{\rho_b^2} \frac{\rho_b^2}{2r_s^2} \frac{L_q}{L_p} \frac{\beta_p}{\beta_{pn}} \ln \left(1 + \frac{r_s^4 A^2}{\rho_b^4} \right) \\ & - \Gamma_0 \frac{r_s^2}{\rho_b^2} \frac{\beta_p}{\beta_{pn}} \left(A - \frac{w_{\text{cut}}^2}{r_s^2} \ln \left(1 + \frac{r_s^2}{w_{\text{cut}}^2} A \right) \right) \end{aligned} \quad (2)$$

with $\beta_{pn} = L_p / 2a_{bs} \varepsilon^{1/2} L_q$ and

$$\Gamma_0 = \frac{2\ell}{R_M k^3 k_h^4 C^2 A_h^4 \tau_{ac}} \frac{\rho_b^2}{r_s^2}. \quad (3)$$

An explicit value of the transition rate was examined by specifying a micro mode for typical experimental parameters. For the L-mode plasmas, when one employs the current-diffusive ballooning mode (CDBM) as the micro mode, one has Γ_0 as

$$\begin{aligned} \Gamma_0 = & \frac{2 \times 10^{-4} \ell}{k^3 \left(-\alpha^{-1/2} (1 + \alpha) + s \sqrt{\beta m_i / m_e} \right)^2 s^4 R_M} \\ & \times \frac{r_s^6 \rho_b^2}{\delta^8} \alpha^{-11/2} \end{aligned} \quad (7)$$

where δ is the collisionless skin depth and $\alpha = \varepsilon r_s \beta_p / L_p$ is the normalized pressure gradient.

For a set of typical parameters, $r_s / \rho_b \simeq 10$, $r_s / \delta \simeq 10^2$, $R_M \simeq 10^8$, $\beta m_i / m_e \sim 10$, $kr_s = 3$, $s = 1$, $\alpha \sim \beta_p / \beta_{pn}$, one has $\Gamma_0 \sim 3 \left(\beta_p / \beta_{pn} \right)^{-11/2}$. The life time of the state $A = 0$ (i.e., free from the NTM) is

shown in Fig.1. The unit of the life time is $2\pi / \eta \sqrt{\Lambda_0 \Lambda_m}$, which is of the order of Rutherford growth time. The dependence on plasma beta is shown. (Other parameters are fixed, $\Delta'_0 = 0$ and $h \rho_b^2 r_s^{-2} = 1/40$.) The life time strongly decreases as the plasma beta increases. And if it exceeds the effective phase limit β_p^* , the life time becomes of the order of the magnetic diffusion time. The contour of the life time is shown in Fig.2.

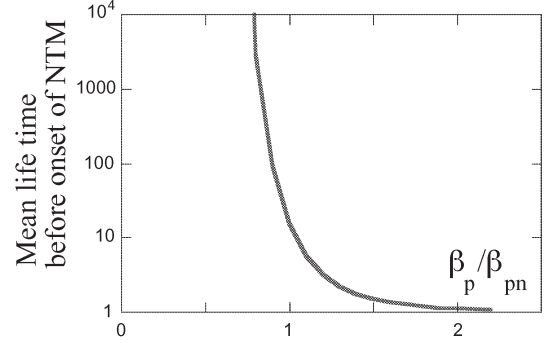


Fig.1 Mean life time before the onset of the NTM as a function of the plasma beta value. ($\Delta'_0 = 0$) Other parameters are $h \rho_b^2 r_s^{-2} = 1/40$, $w_{\text{cut}} = \rho_b$ and $L_q / L_p = 2$.

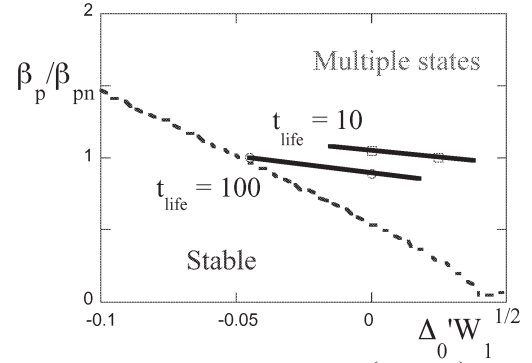


Fig.2 Contour of life time on the (Δ'_0, β_p) plane.

Cusp for the multiple solution is also shown by the dotted line. Above the dotted line, multiple solutions are allowed and stochastic transition takes place. (Other parameters are $h \rho_b^2 r_s^{-2} = 1/40$, $w_{\text{cut}} = \rho_b$ and $L_q / L_p = 2$.)

Reference

- [1] S.-I. Itoh and K. Itoh: J. Phys. Soc. Jpn. **69** (2000) 427
- [2] S.-I. Itoh, K. Itoh, M. Yagi: Phys. Rev. Lett. **91** (2003) 045003.
- [3] S.-I. Itoh, K. Itoh, M. Yagi: J. Phys. Soc. Jpn. **74** (2005) 947

§19. A Novel Turbulence Trigger for Neoclassical Tearing Modes in Tokamaks

Yagi, M., Yoshida, S., Itoh, S.-I. (RIAM, Kyushu Univ.)
 Naitou, H., Nagahara, H. (Yamaguchi Univ.)
 Leboeuf, J.-N. (UCLA),
 Matsumoto, T., Tokuda, S., Azumi, M. (JAERI)
 Itoh, K.

The nonlinear evolution of neoclassical tearing mode (NTM) in the presence of drift wave turbulence is investigated using the four-field neoclassical MHD equations, where the fluctuating ion parallel flow and ion neoclassical viscosity are taken into account[1,2]. The model equations are written as

$$\frac{d}{dt} \nabla_{\perp}^2 F = -\nabla_{\parallel} \nabla_{\perp}^2 A + \mu_i \nabla_{\perp}^4 F - \frac{q_s \mu_i^{nc}}{\varepsilon_s} \frac{\partial U}{\partial r} \frac{p_i}{r} - \frac{q_s m_e}{\varepsilon_s} \mu_i^{nc} \frac{\partial U}{\partial r} \frac{p_e}{r}$$

$$\frac{\partial}{\partial t} \left(A - \alpha^2 \frac{m_e}{m_i} \nabla_{\perp}^2 A \right) = -\nabla_{\parallel} (\phi - \alpha_e p) + \alpha^2 \frac{m_e}{m_i} [\phi, \nabla_{\perp}^2 A] + \eta_{\parallel} \nabla_{\perp}^2 A - 4\mu_e \alpha^2 \frac{m_e}{m_i} \nabla_{\perp}^4 A + \alpha \frac{m_e}{m_i} \mu_e^{nc} U_{pe}$$

$$\frac{dv}{dt} = -\nabla_{\parallel} p + 4\mu_i \nabla v - \mu_i^{nc} U_{pi} - \frac{m_e}{m_i} \mu_e^{nc} U_{pe}$$

$$\frac{dp}{dt} = -\hat{\beta} \nabla_{\parallel} (v + \alpha \nabla_{\perp}^2 A) + \eta \hat{\beta} \nabla_{\perp}^2 p - \alpha \hat{\beta} \frac{m_e q_s}{m_i \varepsilon_s} \mu_e^{nc} \frac{\partial U}{\partial r} \frac{p_e}{r}$$

where $d/dt = \partial/\partial t + [\phi,]$, $\nabla_{\parallel} = \partial/\partial z - [A,]$ and $[,]$ is the Poisson bracket. The normalization: $v_A t/R \rightarrow t$, $r/a \rightarrow r$ is adapted. Other parameters are explained in [1,2]. The subscript 's' indicates the value evaluated at the resonance surface. The energy balance in the system is given by

$$H = \frac{1}{2} \int dV (|\nabla_{\perp} F|^2 + |\nabla_{\perp} A|^2 + |v|^2 + \hat{\beta}^{-1} |p|^2 + \alpha^2 \frac{m_i}{m_e} |\nabla_{\perp}^2 A|^2)$$

$$\frac{dH}{dt} = - \int dV (\mu_i |\nabla_{\perp}^2 F|^2 + \eta |\nabla_{\perp}^2 F|^2 + 4\mu_i |\nabla_{\perp} v|^2 + \eta |\nabla_{\perp} p|^2)$$

The nonlinear simulation with single helicity modes is performed using spectral code. The boundary condition is given by $f_{m,n}(0) = f_{m,n}(1) = 0$ and $f_{0,0}(0) = 0$, $f_{0,0}(1) = 0$ [3]. Figure 1 shows the time evolution of electromagnetic energy in the cases with different Fourier mode in the spectral space. For 2 Fourier modes case, the linear growth and quasi-linear saturation are obtained. It is newly found that the nonlinear acceleration occurs in the early growing phase as the number of Fourier modes increase; However, saturation amplitude is weakly affected by high n modes. Figure 2 shows the time evolution of power spectrum of electromagnetic energy. The case with 64 Fourier modes is plotted. It is seen that high- n modes saturate at lower level and (2,1) mode dominates the electromagnetic energy in the final phase. The acceleration of the growth of the tearing mode by the

background microscopic turbulence is clearly demonstrated.

The effects of fluctuating bootstrap current and of the collisional drift wave turbulence on the development of magnetic island for linearly unstable TM were investigated. The changes in radial structure and temporal growth rate, which are caused by turbulence, were demonstrated. The saturation was attained by the quasi-linear effect. We found that the structure of fluctuating bootstrap current inside the island, which is not taken into account in the conventional theory of NTM. This study demonstrated the importance of the turbulent pump on the rapid growth of the tearing mode.

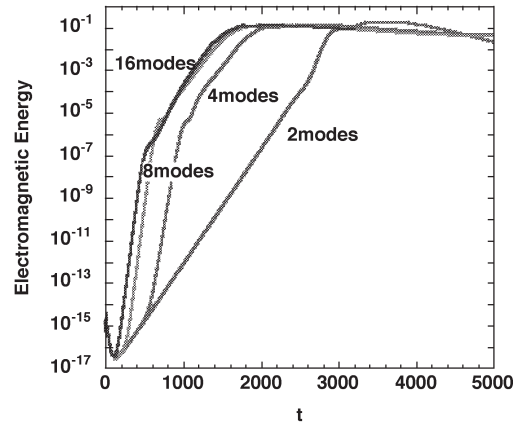


Fig.1 Time evolution of electromagnetic energy with various Fourier modes.

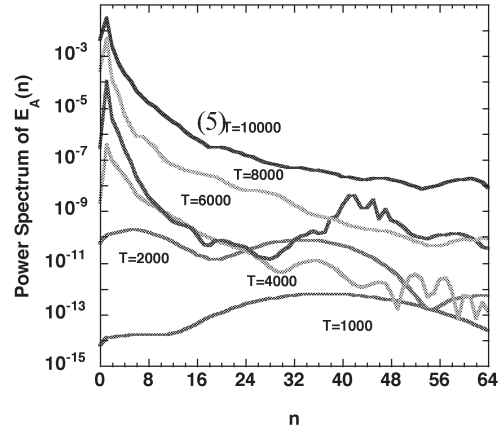


Fig.2 Time evolution of power spectrum of electromagnetic energy.

Reference

- [1] M. Yagi et al., Proc. of 19th Fusion Energy Conf. 2002, TH-1-4.
- [2] A. Furuya, M. Yagi and S.-I. Itoh, J. Phys. Soc. Jpn. **72** (2003) 313.
- [3] M. Yagi et al., Proc. of 20th Fusion Energy Conf. 2004, TH/P5-17.

§20. Collisionless Damping of Geodesic Acoustic Modes

Sugama, H., Watanabe, T.-H.

The geodesic acoustic mode (GAM) was first predicted by Winsor *et al.*[1] based on the fluid model and it has also been studied by several authors using the drift kinetic theory. Conventional drift kinetic calculations of frequencies and damping rates of the GAM assume the radial widths of ion drift orbits to be negligibly smaller than the radial wave length of the fluctuation and their local drift kinetic models do not include the magnetic drift term of the perturbed distribution function that the gyrokinetic equation does. In the present work [2], collisionless time evolutions of zonal flows in tokamaks are investigated by the gyrokinetic theory and simulation. It is shown from the analytical theory how the collisionless damping of the GAM oscillations is enhanced when the ratio of the typical drift orbit width of passing ions to the radial wave length of the zonal flow increases.

Time evolutions of the zonal-flow potential obtained by the gyrokinetic Vlasov simulations [6] for $\epsilon \equiv r/R_0 = 0.1$ and $T_e/T_i = 1$ are plotted by open circles in Figs. 1 (a)–(c). The normalized radial wave number and the safety factor are given by $(k_r a_i, q) = (0.0654, 1.5)$, $(0.131, 1.5)$, and $(0.0654, 3)$ in (a), (b), and (c), respectively, where $a_i \equiv (T_i/m_i)^{1/2}/\Omega_i$. The analytical results are also plotted in Figs. 1 (a)–(c), where thin solid curves is plotted by using the complex GAM eigenfrequencies $\omega = \omega_G + i\gamma$ obtained from numerical solutions of the GAM dispersion relation while the approximate expressions for (ω_G, γ) are used to plot thick solid curves. A good agreement between our analytical predictions and the simulation results on the GAM frequencies and damping rates is verified. Especially, the analytical theory well describes how the collisionless damping of the GAM is enhanced due to the finite-orbit-width effect when $k_r a_i$ is increased. Dotted curves plotted in Figs. 1 (a) and (c) represent conventional analytical results which do not include the finite-orbit-width effect. We see that, without the finite-orbit-width effect taken into account, the GAM damping is estimated to be significantly slower even for $k_r a_i = 0.0654$.

The reason of the damping-rate enhancement by the finite orbit width is explained as follows. When the ratio of the typical orbit width of passing ions to the radial wave length of the zonal flow increases, the radial magnetic drift of the perturbed ion gyrocenter distribution strengthens the poloidal mode number coupling and grows the oscillation component with the poloidal wave number doubled. Since the parallel velocity required to resonate with the GAM is lowered, this higher poloidal wave number component yields a significant population of resonant ions and increases the resonance damping of the GAM.

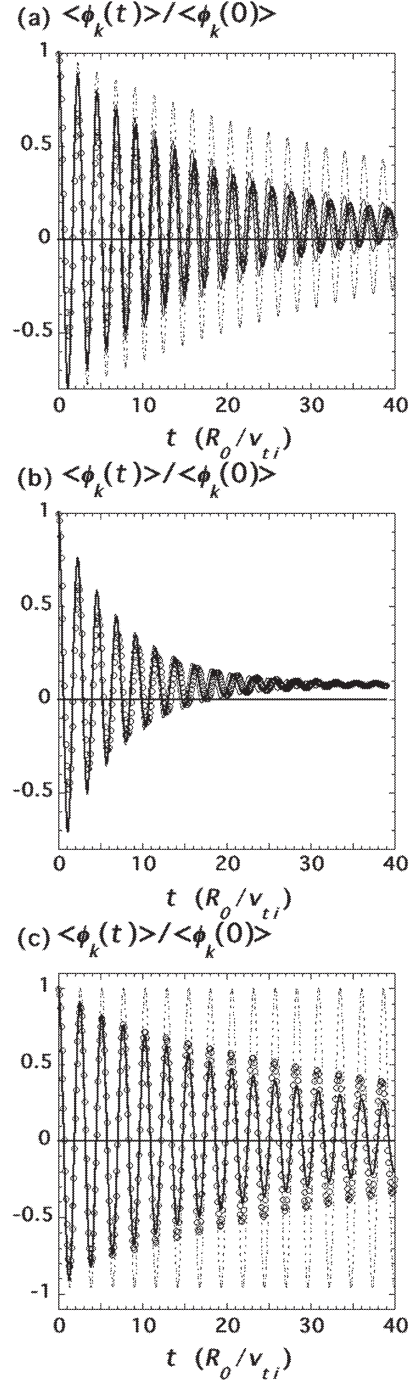


Fig.1. Time evolutions of the zonal-flow potential for $\epsilon \equiv r/R_0 = 0.1$ and $T_e/T_i = 1$. The unit of time is give by R_0/v_{ti} where $v_{ti} \equiv (T_i/m_i)^{1/2}$. The normalized radial wave number and the safety factor are given by $(k_r a_i, q) = (0.0654, 1.5)$, $(0.131, 1.5)$, and $(0.0654, 3)$ in (a), (b), and (c), respectively. Open circles represent the simulation results while thin and solid curves are plotted by using the analytical results. Dotted curves plotted in (a) and (c) represent conventional analytical results which do not include the finite-orbit-width effect.

References

- 1) N. Winsor, J. L. Johnson, and J. J. Dawson, Phys. Fluids **11**, 2248 (1968).
- 2) H. Sugama and T.-H. Watanabe, in 19th ICNSP and 7th APPTC, 2005, A6-2.

§21. Dynamics of Zonal Flows in Helical Systems

Sugama, H., Watanabe, T.-H.

Zonal flows are observed in numerous natural systems such as atmospheric currents while in fusion science they are intensively investigated as an attractive mechanism for realizing a good plasma confinement. Rosenbluth and Hinton [1] showed that initial $\mathbf{E} \times \mathbf{B}$ rotation in tokamaks is not fully damped by collisionless processes but it approaches a finite value. Collisional decay of zonal flows occurs in the long course of time although the residual zonal flows in a collisionless time scale still influence the turbulent transport. Since zonal flows are a key issue for improved confinement in helical systems as well, it is necessary to examine how helical geometries affect zonal-flow damping. In the present work [2], collisionless zonal-flow dynamics in helical systems is investigated. In the same manner as in Rosenbluth and Hinton [1], we here treat the ITG turbulence as a known source and analytically derive the response kernel which relates the zonal-flow potential to the source and also represents dependence on an initially given zonal flow. We also verify the validity of the derived response kernel by a recently-developed gyrokinetic-Vlasov-simulation code.

In helical configurations, the radial drift motion of particles trapped in helical ripples yields neoclassical ripple transport in the weak collisionality regime. This radial drift also causes a significant difference between long-time zonal-flow behavior in helical systems and that in tokamaks. We define a characteristic transition time τ_c by $\tau_c \sim 1/|k_r \bar{v}_{dr}|$ where \bar{v}_{dr} is the bounce-averaged radial drift velocity evaluated by considering helical-ripple-trapped thermal particles. When $t \ll \tau_c$, effects of the radial drift is weak and the long-time behavior of the zonal-flow potential is written as

$$\frac{e\phi_{\mathbf{k}_\perp}(t)}{T_i} = \mathcal{K}_< \left[\frac{e\phi_{\mathbf{k}_\perp}(0)}{T_i} + \frac{\int_0^t dt' \langle \int d^3v F_{i0} S_{i\mathbf{k}_\perp}(t') \rangle}{n_0 \langle k_\perp^2 a_i^2 \rangle} \right], \quad (1)$$

where $S_{\mathbf{k}_\perp}$ represents the $\mathbf{E} \times \mathbf{B}$ nonlinearity source term. Here, the response kernel $\mathcal{K}_<$ for $t \ll \tau_c$ is given by

$$\mathcal{K}_< = 1/(1 + G) \quad (2)$$

where the geometrical factor G measures the ratio of the neoclassical polarization due to toroidally trapped particles to the classical polarization.

Next, when $t \gg \tau_c$, the density of nonadiabatic helical-ripple-trapped particles is strongly damped because of phase mixing caused by the bounce-averaged radial drift motion. Then, the long-time behavior of the zonal-flow potential for $t \gg \tau_c$ is given by

$$\frac{e\phi_{\mathbf{k}_\perp}(t)}{T_i} = \mathcal{K}_> \left[\frac{e\phi_{\mathbf{k}_\perp}(0)}{T_i} + \frac{\int_0^t dt' \langle \int_{\kappa^2 > 1} d^3v F_{i0} S_{i\mathbf{k}_\perp}(t') \rangle}{n_0 \langle k_\perp^2 a_i^2 \rangle \{1 - (2/\pi) \langle (2\epsilon_H)^{1/2} \rangle\}} \right], \quad (3)$$

where the response kernel $\mathcal{K}_>$ for $t \gg \tau_c$ is given by

$$\begin{aligned} \mathcal{K}_> &= \langle k_\perp^2 a_i^2 \rangle \left[1 - (2/\pi) \langle (2\epsilon_H)^{1/2} \rangle \right] \\ &\times \left\{ \langle k_\perp^2 a_i^2 \rangle [1 - (3/\pi) \langle (2\epsilon_H)^{1/2} \rangle + G] \right. \\ &\left. + (2/\pi)(1 + T_i/T_e) \langle (2\epsilon_H)^{1/2} \rangle \right\}^{-1}. \quad (4) \end{aligned}$$

Here, ϵ_H represents the helical-ripple parameter. A term with T_i/T_e appears in the response kernel $\mathcal{K}_>$ for $t \gg \tau_c$ because not only ions but also electrons influence the quasineutrality condition through their helical-ripple-bounce-averaged radial drift motion. The dependence on electrons and on the radial wave number shown in Eq. (4) is not seen in the tokamak case. In the axisymmetric limit $\epsilon_H \rightarrow +0$ with $\epsilon_T = \epsilon_t \cos \theta$, we obtain $G \rightarrow 1.6 q^2 / \epsilon_t^{1/2}$, which reduces both Eqs. (2) and (4) to the Rosenbluth-Hinton formula $\mathcal{K}_{R-H} = 1/(1 + 1.6 q^2 / \epsilon_t^{1/2})$ [1].

Time evolution of the zonal-flow potential obtained by the simulation is plotted by a solid curve in Fig. 1, where $\epsilon_t = 0.1$, $\epsilon_h = 0.1$, $q = 1.5$, and $k_r a_i = 0.131$ are used. Here, a dashed horizontal line represents the response kernel $\mathcal{K}_>$ given by Eq. (4) for $t > \tau_c (= 7.6 R_0 v_{ti})$. It is seen that, after oscillations of the geodesic acoustic mode (GAM) are damped, the zonal-flow amplitude approaches the predicted value $\mathcal{K}_> = 0.038$, which is smaller than $\mathcal{K}_< = 0.39$ and $\mathcal{K}_{R-H} = 0.081$ for the used parameters. Under the conditions used in our simulation, the GAM oscillations dominate the zonal-flow evolution for $t < \tau_c$ so that we cannot identify $\mathcal{K}_<$ given by Eq. (1) which describes the long-time behavior for $t \ll \tau_c$ with rapid phenomena such as the GAM neglected.

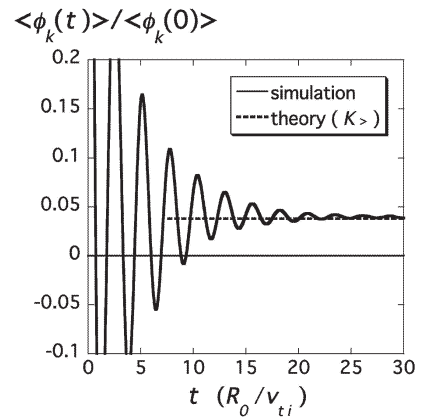


Fig.1. Time evolution of the zonal flow potential obtained by the gyrokinetic-Vlasov simulation for a helical system with $L = 2$, $M = 10$, $q = 1.5$, $\epsilon_t = \epsilon_h = 0.1$, and $k_r a_i = 0.131$. A dashed horizontal line corresponds to $\mathcal{K}_>$ given by Eq. (4) for $t > \tau_c$.

References

- 1) M. N. Rosenbluth and F. L. Hinton, Phys. Rev. Lett. **80**, 724 (1998).
- 2) H. Sugama and T.-H. Watanabe, Phys. Rev. Lett. **94**, 115001 (2005).

§22. A Variational Analysis of Flow-reversal Condition in a Turbulent Swirling Pipe Flow Using the Bulk-helicity Concept

Yokoi, N. (Univ. Tokyo)
Yoshizawa, A., Itoh, K.
Itoh, S.-I. (RIAM, Kyushu Univ.)

The magnitude of axial-flow retardation near the center of a turbulent swirling flow is estimated from the results of the variational analysis with the aid of the helicity concept. It is analytically shown that the axial-flow reversal in a swirl occurs if the bulk helicity imparted to the mean flow exceeds the critical value, which is proportional to the square of the flux. It is suggested that the bulk helicity in the center region plays an important role in determining the flow-reversal condition. Through the comparison with the experimental observations in a turbulent swirling pipe flow, the reliability of the theoretically-derived reversal condition is confirmed [1].

One of the prominent features of the mean-velocity distributions in a turbulent swirling pipe flow, as compared with the counterparts in a usual turbulent (non-swirling) pipe flow, is a dip or dent of the axial velocity near the center of pipe. This is a persistent flow structure accompanied by a finite mean axial-velocity gradient. In order to investigate this feature of the swirling flow, we introduce two functionals that characterize the mean-flow structure in a turbulent swirling flow. Namely, the total amount of the mean-flow enstrophy Φ defined by

$$\Phi = \int_V W^2 dV = \int_V (\nabla \times U)^2 dV$$

and the total amount of the mean-flow helicity Ψ defined by

$$\Psi = \int_V U \cdot W dV = \int_V U \cdot (\nabla \times U) dV,$$

where U is the mean velocity, $W (= \nabla \times U)$ is the mean vorticity, and V is the volume of the whole fluid region.

The mean-flow helicity Ψ characterizes a swirling flow which is constituted by both the circumferential or azimuthal velocity and the axial or longitudinal velocity. This functional serves as a measure for the intensity of swirl.

We examine what velocity profiles are realized under a given intensity of swirl in the aggregate. To put it in terms of an extremalization problem, we seek a function U that extremalizes the functional Φ subject to a constraint that the total amount of the mean-flow helicity is constant: Following the usual procedure for a variation problem with a constraint, our conditioned variation problem is transformed into a free variation problem $\Phi + \lambda \Psi = \text{extremum}$, where λ is the Lagrange undetermined multiplier. We seek a flow distribution that satisfies a condition

$$\delta(\Phi + \lambda \Psi) = 0 \quad (1)$$

with respect to the velocity variation δU . This treatment is directly related to our considering the strong turbulence limit, where the transport coefficients such as λ are to be uniform in the whole region of the flow considered.

Equation (1) is solved, and the critical condition for the flow reversal is plotted on the plane of the flow helicity H per unit volume and total flux F is shown in Fig.1. Figures 2 shows the observation in experiments (by crossed-circle or by crossed-square) that all the swirling flows with reversal lie at the right of the corresponding H_c curve and that all those without reversal are at the left of the corresponding H_c curve. This comparison shows that this model explains essential element for the reversal in the swirling flow.

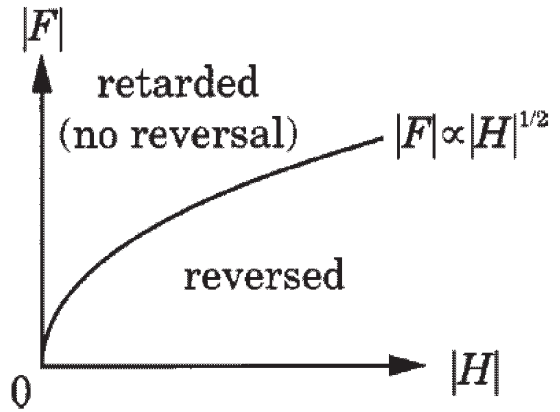


Fig.1 Critical condition for the reversal.

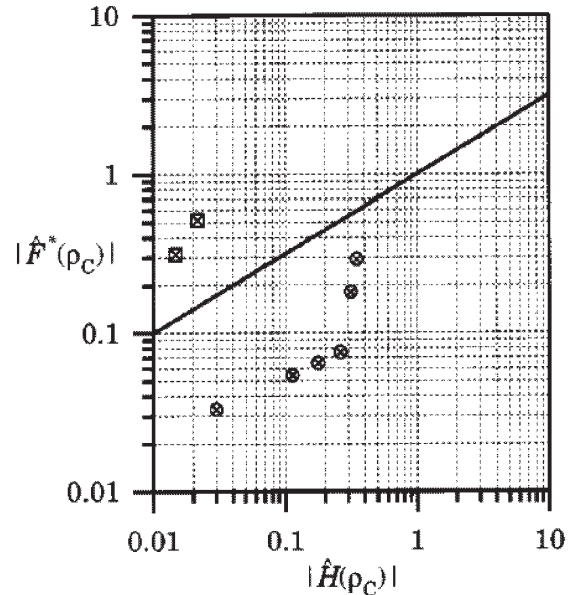


Fig.2 Experimentally observed data in swirling flows with an axial-flow reversal (circle) and that without (cross). The curves denote the critical bulk helicity.

Reference

[1] Yokoi N, Yoshizawa A, Itoh K, Itoh S-I, Phys. Fluids 16 (2004) 1186

§23. Effect of Flow Shear on Temperature Gradient Driven Short Wavelength Modes

Gao, Zhe (Tsinghua Univ., China),
Dong, J.Q. (SWIP, China),
Sanuki, H.

Progress in understanding the anomalous transport in magnetically confined plasmas has been continuing for decades. It is now widely accepted that the anomalous transport is induced by turbulent plasma fluctuations with small scales, the so-called microinstabilities. In particular, the temperature gradient (TG) driven instabilities are proposed as the plausible candidates responsible for anomalous thermal transport and have been studied extensively.

Effects of flow shear on the temperature gradient driven short wavelength ion (SWITG) modes and electron temperature gradient (ETG) modes are investigated in a sheared slab. The SWITG mode can be stabilized at arbitrary beta when the $E \times B$ velocity shear, V_E' reaches above a critical value. Since the SWITG modes has a lower frequency, a lower V_E' is needed to stabilize the SWITG mode than to stabilize the conventional ITG mode. However, the critical values of V_E' for stabilization of both SWITG and conventional ITG modes are much less than v_{ti}/L_n , where $v_{ti}(L_n)$ are ion thermal speed and the scale length of density gradient,

respectively. Contrastively, the ETG mode can not be stabilized until the V_E' is larger than v_{ti}/L_n . Similarly, a parallel shear with order v_{ti}/L_n has significant effects on the SWITG mode but is too small to influence the ETG mode. The different behavior of flow shear effects on the SWITG and ETG modes may indicate that the ETG mode is more reasonable than the SWITG as the candidate responsible for anomalous electron thermal transport.

In this study, the integral equations for the study of the ITG mode in the presence of sheared flows in arbitrary beta plasmas are upgraded and then employed for the study of SWITG mode in a sheared slab.

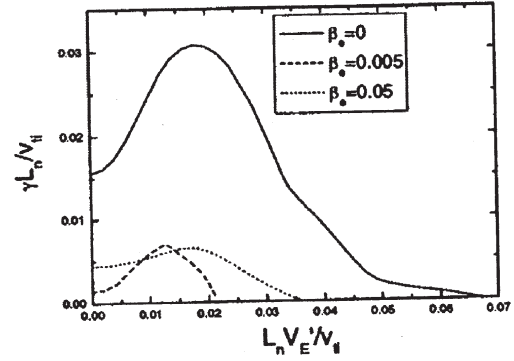


Fig.1 Mode growth rate of the SWITG mode as the functions of V_E' .

The initial rise in V_E' causes an increase of growth rate and it reaches its maximum value. Further increase of V_E' causes a decrease of growth rate. Then, the mode is fully stabilized by a large enough velocity shear.

Ref.: Zhe Gao, J. Q. Dong and H. Sanuki, Physics Plasmas, Vol.11, No.6(2004) 3053.

§24. Short Wavelength Ion Temperature Gradient Instability in Toroidal Plasmas

Gao Zhe (Tsinghua Univ., China),
Sanuki, H., Itoh, K.
Dong J.Q. (SWIP, China)

Recently, intensive research attention is paid on understanding the anomalous electron transport in magnetically confined plasmas. Experimental evidence shows that this anomalous electron transport is governed by short wavelength turbulence, after the stabilization of the long wavelength turbulence.

Observation of electron temperature profile stiffness in most experiments indicates that the short wavelength instability responsible for electron transport should have a threshold in electron temperature gradient.

In this study we employ a set of integral eigenvalue equation for the further study of toroidal short wavelength ion temperature gradient (SWITG) modes. The magnetic curvature and gradient drift, the transit effect, and the finite Larmor radius effect are retained in the model for both electrons and ions. Also, the electron response is easily switched to be adiabatic. Using this model, we investigate the SWITG modes in detail. The physical driving mechanism in the toroidal geometry will be discussed with comparison with that in the sheared slab configuration. Higher order modes

will be introduced and parameter dependence of the toroidal SWITG modes will be investigated in wide parameter regions. From that point, this study is an essential preparation for estimating the critical temperature gradient and possible transport driven by the SWITG instability.

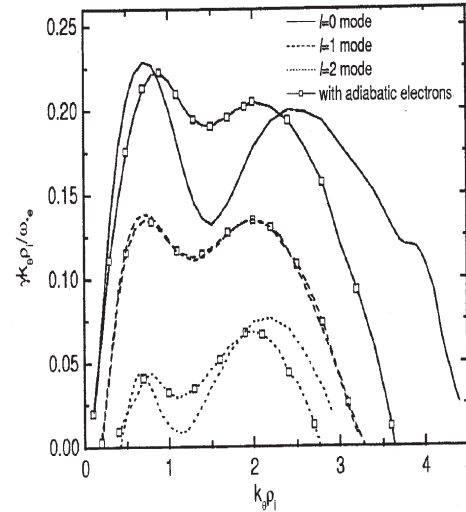


Fig.1 Normalized growth rate vs. $k_y \rho_i$. The solid, dashed, dotted lines denote the different harmonic modes with $l=0, 1$, and 2 , respectively. The lines with squares are the corresponding results when electron is assumed adiabatic.

In Fig.1, three unstable branches are presented with and without nonadiabatic electron effects consideration, respectively. As $k_y \rho_i$ increases, the growth rate behaves double humps: the first peak is the conventional ITG mode and the second peak is the SWITG.

Zhe Gao, H.Sanuki, K. Itoh and J.Q.Dong, Physics plasmas, Vol.12 (2005) 02252.

§25. Short Wavelength Electron Temperature Gradient Instability in Toroidal Plasmas

Gao Zhe (Tsinghua Univ., China),
Sanuki, H., Itoh, K.
Dong J.Q. (SWIP, China)

Short wavelength microinstabilities with a characteristic perpendicular wavelength of the order of electron Larmor radius are much less studied than its ion counterpart since it was believed that turbulence driven by such small size microinstabilities would not be able to drive a large transport. However, nonlinear gyrokinetic simulation has shown that the turbulence driven by electron temperature gradient (ETG) instabilities can yield a large electron heat flux through radially highly elongated vortices, so called “streamers”. Experimental evidence also shows that the anomalous electron transport is governed by short wavelength turbulence with $k_{\perp}\rho_i > 1$ after the suppression of long wavelength turbulence.

The electron temperature gradient (ETG) driven mode in the very short wavelength region with $k_{\perp}\rho_i > 1$ is identified with a gyrokinetic integral equation code in toroidal plasmas. The curvature and magnetic gradient drifts, the transit effect, and finite Larmor radius effect are retained in the model for both

electrons and ions. The ballooning representation for an axisymmetric toroidal geometry with circular flux surface is employed.

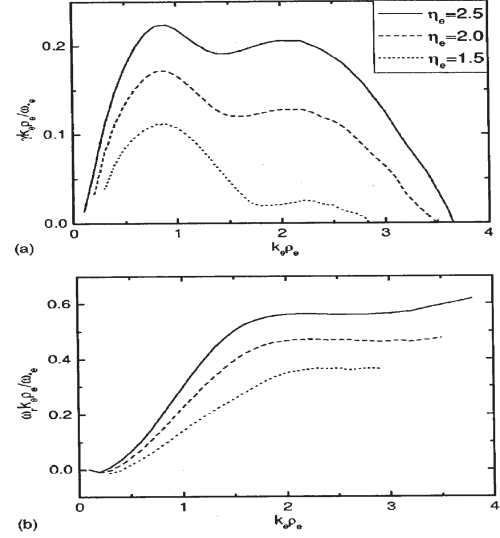


Fig.1 Normalized growth rate (a) and frequency (b) vs. $k_{\perp}\rho_e$ for $\eta_e = 2.5, 2.0$ and 1.5 , respectively.

In Fig.1, this double humped growth rate of the conventional ETG and short wavelength ETG modes is attributed to the toroidal drift resonance mechanism and the nonmonotonic behavior of normalized frequency as the poloidal wavelength varies. This instability provides a possibility existence of a kind of turbulence source with very small size of cells. The wavelength of SWETG mode is too short and induced transport may be small unless the inverse cascade effect.

Zhe Gao, H. Sanuki, K. Itoh and J. Q. Dong, Physics Plasmas, Vol12 (2005) 022503.

§26. Emission of Electromagnetic Pulses from Laser Wakefields through Linear Mode Conversion

Sheng Zheng-Ming (Lab. of Optical Physics, IoP, CAS, China and ILE Osaka Univ.),
Mima, K. (ILE, Osaka Univ.)
Zhang, Jie (Lab. of Optical Physics, IoP, CAS, China)
Sanuki, H.

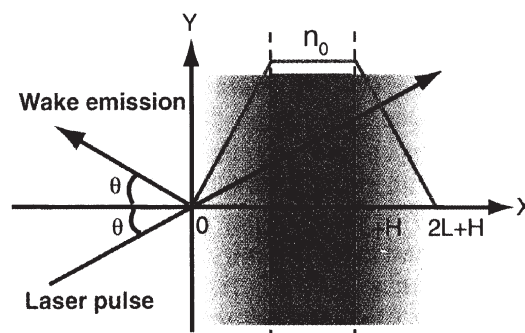


Fig.1 Schematics of electromagnetic emission from a wakefield generated by a laser pulse incident obliquely to the plasma density gradient.

A large wakefield is an electron plasma wave driven by the ponderomotive force of a laser pulse. It has been studied intensively for the purpose of particle acceleration or frequency up-conversion of a laser pulse, laser pulse compression, and more recently light intensification. Since the typical plasma oscillation frequency for these applications is in the terahertz (THz) range, the wakefield can potentially serve as a powerful THz emitter. Currently, it is still challenging to obtain intense THz emission for various applications.

In this study, we consider the laser wakefield excitation when a plane laser pulse propagates at an angle to the density gradient of an inhomogeneous plasma slab, as shown in Fig.1. The plasma slab is underdense with a trapezoid density profile along the x-direction.

Powerful coherent emission around the plasma oscillation frequency can be produced from a laser wakefield through linear mode conversion.

The emission spectrum and conversion efficiency are obtained analytically, which are in agreement with particle-in-cell simulations. The emission can be tuned to be a radiation source in the terahertz region and with field strengths as large as a few GV/m, suitable for high-field applications. The emission also provides a simple way to measure the wakefield produced for particle acceleration. In other word, it provides a new diagnostics of laser wakefield amplitudes and even wave breaking in the context of wakefield accelerators.

This work was supported in part by the JSPS-CAS Core –University Program on Plasma and Nuclear Fusion.

Zheng-Ming Sheng, K. Mima, Jie Zhang and H. Sanuki, PRL, Vol.94 (2005) 095003.

§27. An Equilibrium Equation of a Magnetized Rotating Plasma

Saeki, K. (Dept. of Physics, Shizuoka Univ.),
Tsushima, A. (Dept. of Physics, Yokohama
National Univ.)
Sanuki, H.

The existence of equilibrium solution is one of the most important keys to construct the nuclear fusion devices. The equilibrium of tokamak plasma is sustained by a toroidal current and described by the Grad- Shafranov equation [1]. On the other hand, Stix proposed the plasma confinement by a magnetoelectric torus where the potoidal plasma rotation reduces the charge accumulation.

To get the equilibrium equation, we here start the MHD equations. Then, we employ the momentum balance equation of steady state plasma, the Ohm's law in case of zero resistivity, Poisson equation and the continuity equations for the magnetic field, the electric current density and the plasma flow. Also we treat axisymmetric plasma by using the cylindrical coordinates r, ϑ, z . After the lengthy calculations, we get the Grad- Shafranov equation including the electric field in case of neglecting the convective derivative term, in the form

$$\frac{1}{(2\pi r)^2} \left[\frac{1}{\mu_0} L\psi + \mu_0 I \frac{\partial I}{\partial \psi} \right] + m C_s^2 \frac{\partial n}{\partial \psi} - \epsilon_0 \Delta \phi \frac{\partial \phi}{\partial \psi} = 0, \quad (1)$$

where $\psi(r, z)$ is the magnetic flux function ϕ is the electric charge density and n is the plasma density. In Eq. (1), we used the following notation

$$L\psi = r \partial / \partial r (\partial \psi / r \partial r) + \partial^2 \psi / \partial z^2.$$

If we neglect the plasma potential, E1. (1) reduces to the conventional Grad-Shafranov equation describing the tokamak equilibrium. It should be noted that Eq. (1) describes both the tokamak and the magnetoelectric torus at the same time.

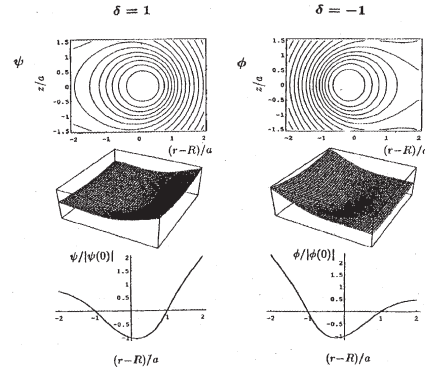


Fig.1 Equilibrium magnetic surface $\psi(r, z)$ of a Tokamak ($\delta=1$) and equilibrium potential surface ϕ of a magnetoelectric torus ($\delta=-1$).

We note that $\delta=1$ and $\delta=-1$ means the pure tokamak and the pure magnetoelectric torus, respectively. The change of δ leads the plasma from the tokamak to the magnetoelectric torus continuously.

§28. Dust Plasma Experiments and Collisional Oscillations

Taniguchi, S., Nejoh, Y.N. (Dept. of Electrical and Electric Eng., Hachinohe Inst. Of Tech.), Nakamura, Y. (ISAS)
Sanuki, H.

In Plasmas, the diverter is bearing an important role in the study, which aims at combustion plasmas. However, the impurities are incorporated into plasmas in many cases, which cause the problems of decreasing the temperature of the plasma and of damaging the wall of devices. It is because impurities are charged negatively and evolve the collective motion. Positive ions and negatively charged particles easily collide the neutral particles because the neutrals are independent on the external fields. Large amplitude oscillation may occur due to the collision between ions (dust grain) and neutral. The oscillation propagates and causes the damage of the wall.

The present purposes of the study are to obtain the parameters on the dust plasma and to analyze these problems numerically by proposed model, to compare experimental observations with the results based on the present model and to simulate oscillation

phenomena due to interparticle collisions.

We propose a model of the system as follows:

$$n_e = n_{e0} \exp(e\Phi/T_e),$$

$$n_i = n_{i0} / (1 - (2e\Phi/m_i v_i^2)^{0.5}),$$

$$n_d = (n_{i0}/n_{e0} - 1) / (Z(1 - 2Ze\Phi/m_d v_d^2)^{0.5})$$

together with the Poisson equation,

$$\epsilon_0 \frac{d^2\Phi}{dx^2} = e(n_e - n_i + Zn_d).$$

We investigated the properties of dust grains and oscillating phenomena in plasmas. The potential profile obtained in the experiment coincides with our results based on the present model. Also, an electric double layer is obtained. It turns out that the variation of the dust density and it depends on the input voltage. Oscillations near the wall due to ion-neutral and dust –neutral collisions. Although these oscillating phenomena have not been found, they may be observed in experiments in the near future.

References:

- (1) S. Taniguchi, Y. N. Nejoh, Bulletin 19th JSPF Annual Meeting, (2002) p161.
- (2) N. Nejoh, Phys. Plasmas, Vol.8, (2001) 3545 ibid, Vol.9 (2002) 3811.
- (3) S. Taniguchi, Y.N.Nejoh, Y. Nakamura and H. Sanuki, Proc. Of the 21st Symposium on Plasma Processing, Hokkaido Univ., Jan28-30 (2004), p72-73.

1-4. LHD Project Research Collaboration

The Large Helical Device (LHD) project has two purposes: to perform plasma confinement research in a steady-state machine and to elucidate physical and engineering issues for a helical fusion reactor. In order to realize such purposes, both fusion technology and the scientific foundations must be developed in a long-term program. Success with this program will require collaboration with scientists and researchers from universities and institutes in Japan and also from all over the world.

The aim of the LHD Project Research Collaboration, being reported here, is to research and develop both technology and the scientific foundations that are useful for both the LHD group and the universities, and then, to apply these results to LHD experiments for the improvement of LHD. The characteristic of this collaboration program is that some R&D's are performed in each domestic university or institute, instead of in NIFS as conventional research collaborations. The advantage of this type collaboration over conventional one is that co-workers can devote themselves to R&D's more efficiently and enthusiastically by spending much more time.

From last year, the LHD Project Research Collaboration started to invited public participation from universities and institutes in Japan. Three committees and one advisory council participate in selection process of collaboration subjects. At the beginning, the committees of the Fusion Network in Japan select and recommend some proposed plans to the committee of the LHD Project Research Collaboration in NIFS. NIFS has partnerships with Fusion Network linking three major research fields in Japan: fusion engineering, fusion science and plasma science. Although these fields have been developed independently, intimate collaboration between them is essential for further progress of fusion research. NIFS, as a Center of Excellence (COE) should develop a network of fusion research activities of universities and government institutions, including information exchange, planning, collaboration with foreign institutions and education of graduate course students. The Fusion Network has two committees related to this collaboration: one deals with the fields of fusion and plasma science and another with fusion engineering. Then, the committee of the LHD Project Research Collaboration in NIFS determines the collaboration subjects, together with their budgets. They finally require the approval of the Advisory Council for Research and Management of NIFS. An important point to choose a subject of collaboration is to know whether it was already carried out or will be done firstly in NIFS. A new attempt, which is useful for the LHD project and is not planned in NIFS, is, of course, always welcome to the collaboration program for LHD project. Another important point is whether that program can contribute to stimulate university researches and LHD programs.

As the fusion-plasma science program, following subjects were approved last year and reported in this book.

1. Direct energy conversion for advanced fueling fusion.
2. Development of high beta plasma formation using ICRF high harmonic fast wave.
3. Experimental study of compatibility of a transport barrier and energetic ion confinement.
4. Study of repetitive fueling pellet transportation in the guiding tube.
5. ECH and ECCD using new remote steering antenna.
6. Production mechanism of D⁻ ions and evaluation of D⁻ ion current extraction.
7. Analysis of a graphite plate interacting with high-density hydrogen plasma.
8. Development of 2 color multi channel interferometer using 48- and 57- μ m FIR lasers.
9. Anisotropy of proton velocity distribution function in argon plasma analyzed by means of plasma polarization spectroscopy.
10. Spectroscopy and atomic modeling of EUV light from LHD plasmas.
11. Development of wide band and compact X-ray spectrometer.
12. Development of divertor plasma diagnostics using laser scattering and photodetachment method.

As the fusion-engineering program, following subjects were also approved last year and reported here.

1. Study on effects of bending strain to critical current characteristics of Nb₃Al CIC conductors.
2. Change in properties of superconducting magnet materials by 14 MeV neutron irradiation under cryogenic temperature.
3. Development of new high field and high current density superconductors for fusion devices.
4. Stability of superconducting coil with various surface conditions in pressurized He II.
5. Suitability of boron-titanium as first wall material.
6. Measurement of the negative ion and control of recombination plasma in the LHD divertor.
7. Kinetics of hydrogen isotopes at surfaces and bulks of plasma facing materials based on Group 5 materials.
8. Heat removal enhancement of plasma-facing components by using nano-particle porous layer method.
9. Investigation of tritium behavior and tracability in in-vessel systems of LHD during D-D burning.
10. Assessment study on biological effects of radiation in LHD.
11. Study on environmental behavior of tritium.

These subjects are planned basically as the three years program. Therefore, the reports presented here represent one portion of the total subjects.

(Mutoh, T., Sagara, A.)

§1. Experiment on Charge Separation in a Small-Scale CUSPDEC Device

Yasaka, Y., Yamamoto, T., Takeno, H. (Kobe Univ.)
Tomita, Y.
Ishikawa, M., Nakashima, Y., Cho, T. (Univ. Tsukuba)
Ohnishi, M. (Kansai Univ.)
Sato, K. (Hyogo Univ.)

It is necessary to separate, discriminate and guide electrons, thermal ions with hundreds of keV, and fusion protons with 14.7 MeV, which are created from D-³He fusion reactor, in order to produce electric power by using a Venetian-blind direct energy converter (DEC) for the thermal ions and a traveling wave DEC for the protons. For this purpose, a use of cusp magnetic field is proposed. The electrons are deflected and guided along the field line to the line cusp, while the ions pass through the point cusp, because each Larmor radius is quite different.

We use a CUSPDEC experimental device, which consists of a low-energy plasma source, a guide field section, and a cusp magnetic field section. The device is capable of changing the curvature of the magnetic field from normal cusp to slanted cusp fields. We inject a plasma beam with ions accelerated up to a few hundreds of eV into the slanted cusp fields to simulate the separation of electrons and ions.

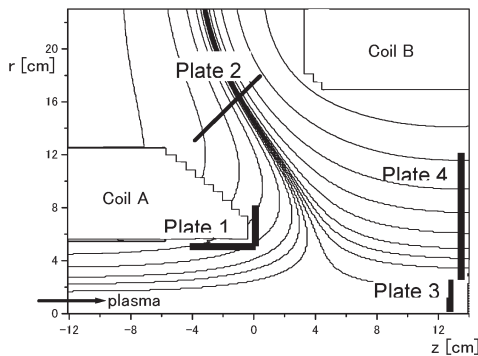


Fig. 1. CUSPDEC experimental device and typical field lines.

The CUSPDEC experimental device has two magnetic coils, A and B, as shown in Fig. 1 to form a slanted cusp field. By adjusting the current in the two coils, I_A and I_B , the field line curvature can be varied. In Fig. 1, the field lines are plotted for $I_A = 30$ A and $I_B = 20$ A as an example. The magnetic field strength at $z = -12$ cm is ~ 350 G, with $z = 0$ being 0.8-cm right from the right edge of the coil A. A plasma beam of densities $1\text{--}10 \times 10^7 \text{ cm}^{-3}$, electron temperatures 5–15 eV, and a diameter of about 2.5 cm is injected from the left side into the slanted cusp field. The ions can be accelerated by the voltage applied at the exit of the plasma source up to 300 V in this experiment. If the density of the incident plasma is sufficiently low, electrons flow along the field line to the line cusp exit, whereas, ions can traverse wide regions and preferentially enter into the point cusp end. Plane

electrodes shown in Fig. 1 are located at the entrance-line cusp (Plate 1), the line cusp exit (Plate 2), the inner point cusp (Plate 3), and the outer point cusp (Plate 4) to detect the particle flux..

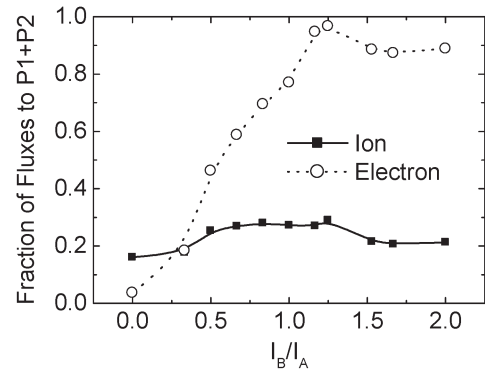


Fig. 2. Fraction of ion and electron flux as a function of I_B/I_A .

Saturation currents of ions and electrons at Plates 1~4 are measured in Ar plasma with changing I_B for a fixed $I_A = 15$ A. The fraction of flux to Plates 1 and 2 is the ratio of sum of currents at Plates 1 and 2 to sum of currents at Plates 1 to 4. It is shown in Fig. 2 that 95% of electrons are deflected by the magnetic field, while $\sim 30\%$ of ions flow into the line cusp region if an appropriate I_B/I_A is chosen.

We measure the ratio of the saturation current into Plate3 in Ar and He plasma at $z = 11.45$ cm to that at -6.55 cm for several ion energies with $I_B/I_A = 1.33$. The ratio, i.e., the transmission ratio is plotted as a function of the ion energy in Fig. 3. It is confirmed that electrons and ions can be separated by the slanted cusp field even for higher ion energies than in the previous experiments.¹⁾ It is seen that He^+ with lower energy is influenced more sensitively by the magnetic field. Increased electrons arriving at the point cusp exit for higher ion energies may be due to the generation of secondary electrons.

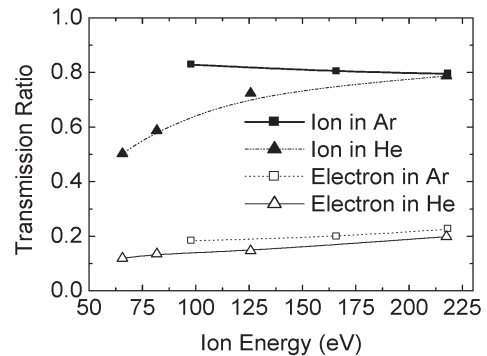


Fig. 3. Transmission ratio of ions and electrons in Ar and He plasmas as a function of the ion energy.

Reference

- 1) Tomita, Y., Yasaka, Y., Takeno, H., et al.: Proc. 5th Int'l. Conf. on Open Magnetic Systems, 2004.

§2. Experiment on Direct Energy Conversion in a Small-Scale CUSPDEC Device

Yasaka, Y., Takeno, H. (Kobe Univ.)

Tomita, Y.

Ishikawa, M., Nakashima, Y., Cho, T. (Univ. Tsukuba)

Ohnishi, M. (Kansai Univ.)

A small-scale experimental device is used to study the basic characteristics of discrimination of electrons and ions in the cusp magnetic field. Ions separated from electrons are guided to an ion collector, which is operated as a one-stage direct energy converter.

Once the ions and electrons are discriminated by the slanted cusp magnetic field, it is necessary to decelerate and collect ions to recover their kinetic energy and generate electricity. A plane-electrode-type ion collector¹⁾ is located at a point cusp region of exit side of the cusp magnetic field. In Fig. 1, the current to the ion collector normalized to its value at $V = 0$ is plotted versus V for various acceleration voltages V_{acc} of the plasma source, where V is the collector voltage. When the value of V is high enough for each V_{acc} , the collector current reduces to zero (even negative for $V_{acc} = 290$ V due to generation of secondary electrons or insufficient separation of electrons). This means that when the value of V is set at an appropriate value, a large fraction of ions is decelerated almost to zero velocity and flows into the ion collector plate at a high positive potential. A load resistor connected to the ion collector would obtain electric power, which is directly converted from the kinetic energy of incoming ions.

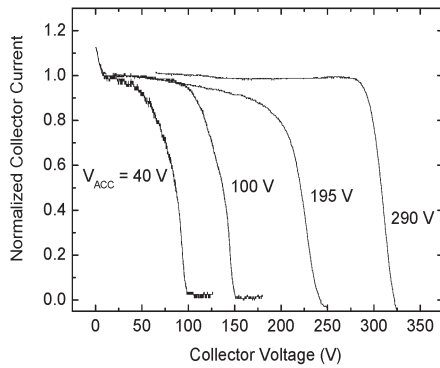


Fig. 1. Normalized ion collector current versus the collector voltage for several V_{acc} .

We plot the output power P , i.e., the ion collector current times V , as a function of V in Fig. 2 for the case of $V_{acc} = 290$ V in Fig. 1. The curve has a maximum at a certain voltage, which we call the optimum operating voltage V_{opt} . If the incoming ions have an energy distribution function represented by the delta function and secondary and/or ionization electrons are negligible, the V-I characteristics would be such that the collector current is constant at I_0 until the collector voltage exceeds the value

V_{max} corresponding to the ion energy, then goes to zero abruptly. In this case, the conversion efficiency defined by $\eta = P(V = V_{opt}) / (I_0 \cdot V_{max})$ is 1.

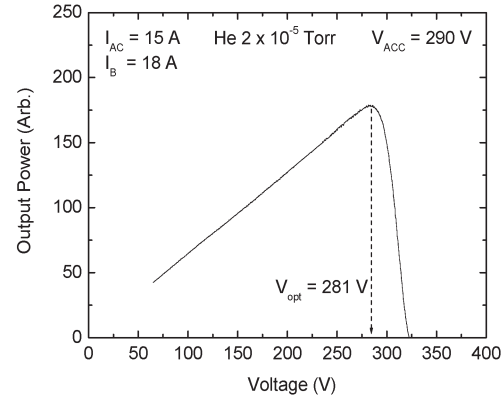


Fig. 2. The output power as a function of the ion collector voltage for $V_{acc} = 290$ V.

In the case shown in Fig. 2, using $V_{max} = 325$ V from Fig. 1, the value of η is calculated to be 0.84. The energy distribution function is measured to find that $\Delta E/E$ is 0.1, where ΔE is the full width half maximum of the energy distribution function with E being the average energy.

Open circles plotted in Fig. 3 represent the values of η as a function of $\Delta E/E$. In our experiments, since the energy of the primary ions is low, the charge exchange with and the ionization of the residual gas are negligible. Therefore, the loss of I_0 would be produced by the secondary electrons from the electrodes or the wall. The loss of I_0 is estimated from the electron current at large V in the V-I curve of the ion collector to be 5–10 %. The dotted curve in Fig. 3 is a fit to the experimental points with the assumption that $\eta = 0.95$ for $\Delta E/E = 0$.

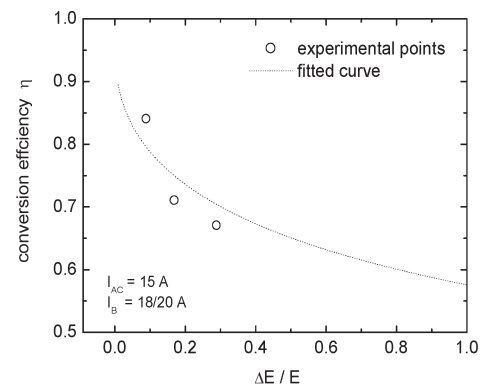


Fig. 3. The values of η as a function of $\Delta E/E$ with the dotted curve fitted to the experimental points.

Reference

- 1) Barr, W. and Moir, R.: Nucl. Technol. /Fusion, **3**, 98 (1983).

§3. Characteristics of Single Slanted Cusp-DEC

Tomita, Y.,
Yasaka, Y., Takeno, H. (Kobe Univ.),
Ishikawa, M., Nemoto, T. (Univ. Tsukuba)

In order to study the performance of a cusp DEC, we investigate characteristics of a single slanted cusp, which might be better than a conventional vertical cusp from the view point of separation of electrons from ions. One of the indices for the separation is a Störmer region [1], Fig.1, where the radii of the inlet and outlet circular cusp coils are R_0 and $1.5 R_0$ and axial positions are $-R_0$ and R_0 , respectively, where R_0 is the normalized radius. The numbers in Fig.1 indicate the Störmer potential ($V_{st}(r, z) = [P\theta - q_j\psi(r, z)]^2 / 2m_j r^2$, where P = canonical angular momentum and ψ = flux function) normalized by $m_p v_n^2 / 2$, where $v_n = I_{in} e / m_p$, I_{in} = current of an inlet coil, and m_p = proton mass. The stagnation point ($\partial V_{st}(r, z) / \partial r = \partial V_{st}(r, z) / \partial z = 0$) of the Störmer potential gives classification between trapped charged particles in a line cusp region and those which are passed through a single cusp field to a point cusp region. The effects of slant of cusp magnetic field lines is shown in Fig.2, where the Störmer potential at the stagnation is presented as a function of the current ratio of the outlet magnetic coil to the inlet, where the normalized P by $m_e R_0 v_n$ equals to 10.0 as an example and the coil arrangement is the same as Fig.1. As the increase of the outlet coil current, which corresponds to the strong slant of the magnetic field lines, the Störmer potential at the stagnation point increased almost proportionally to the current ratio.

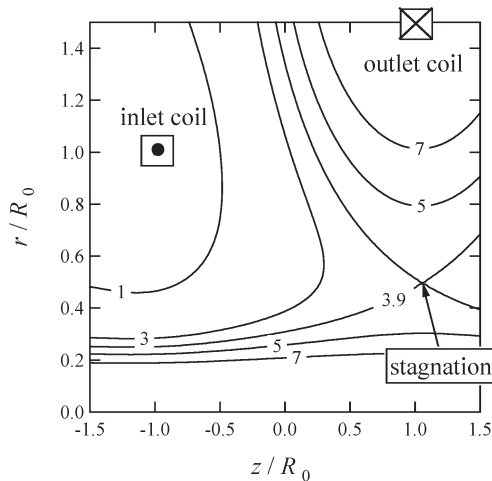


Fig.1 Contour lines of the Störmer potential in the slanted cusp magnetic configuration. The numbers indicate the normalized Störmer potential.

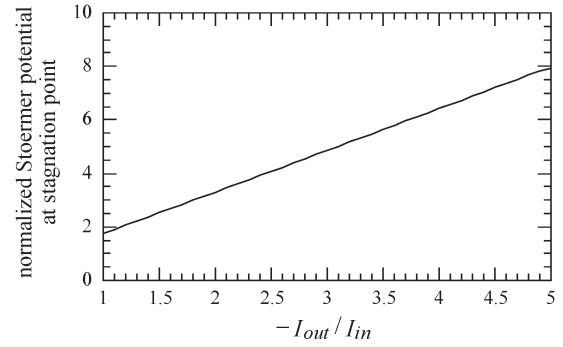


Fig.2 Störmer potential at the stagnation as a function of the current ratio of the outlet cusp magnetic coil to the inlet, where the normalized P is 10.0 and the coil arrangement is the same as Fig.1.

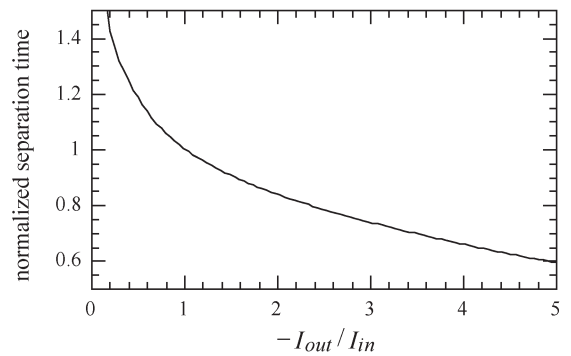


Fig.3 Separation time normalized by that of $I_{in} = -I_{out}$ as a function of current ratio. Here the separation time is defined by the time when distance between an electron and an ion is $R_0/2$. The coil arrangement is the same as Fig.1.

The stronger slant of magnetic field lines separates effectively charged particles with lower energy like electrons from those with high energy like ions, where the electrons are guided to the line cusp region and ions are led to the point cusp region. In order to confirm this effect, the separation time between an electron and an ion is calculated by tracing their orbits. Initially these particles are injected from the inlet coil region (r, z) = $(0.5R_0, -1.5R_0)$ with the same axial velocity. Here the separation time is defined by the time when distance between an electron and an ion is $R_0/2$. The separation time normalized by that of $I_{in} = -I_{out}$ is shown in Fig.3. One can see the stronger slant makes the short separation time, which might be better for effective separation. As the electrons are mirror-trapped in the line cusp region, the early removal of electrons might be one of the ways to get good separation. These results mean the stronger slanted cusp configuration has a possibility of effective separation of electrons and ions.

Reference

- 1) W. Schuurman and H. de Kluiver, Plasma Phys., 7, (1965) 245.

§4. Numerical Simulation of Large-Scale TWDEC and HelmholtzDEC Devices

Ishikawa, M. (Univ. Tsukuba)
Yasaka, Y., Takeno, H. (Kobe Univ.),
Tomita, Y.

The self-excitation processes of commercial-scale traveling wave direct energy converter (TWDEC) are analyzed, where the real size is treated, although the previous studies could treat only reduced sizes because of limitation of capability of available computers. Then separation capability of charged particles in the Helmholtz type direct energy converter device (HelmholtzDEC) is analyzed.

(1) Self-excitation Processes of Commercial-scale TWDEC

An optimization has resulted in the cross-section of $25 \pi \text{ m}^2$ with 5 m radius and the period of the traveling wave of $0.12 \mu\text{s}$ when the energy input from a fusion reactor is 272.5 MW. The modulator has five electrodes, whereas the decelerator has 25 electrodes with four cycles of the traveling wave. A few million numerical time steps are required for the self-excitation process and therefore one-dimensional analyses has been used, although we have developed two-dimensional codes.

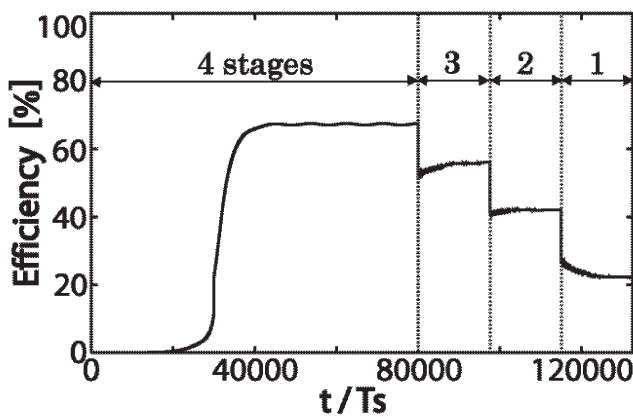


Fig. 1. Capability of Fast Control of Large-Scale TWDEC.
(switching time of about 0.23 ms)

Figure 1 shows the time variation of the efficiency of the TWDEC, which corresponding to the ratio of the electric power of the full design power. The operation of TWDEC is changed from four to three, two, one with about 0.23 ms, where the electric power becomes 84 %, 63 % and 33 % by decreasing the number of active stages.

It has been shown that the electrode voltage (operation voltage) is self-excited and becomes about 1.0 MV at about 7 milliseconds by switching the load resistances. About 65 % energy conversion efficiency is obtained, and that the TWDEC has the capability of fast control of the electric power when required by the commercial grid.

(2) Separation Capability of Charged Particles in HelmholtzDEC

The separation capability of charged particles is one of the most important requirements for direct energy converters. Time-dependent axisymmetric two-dimensional analyses have been carried out for a commercial-scale HelmholtzDEC with the energy input of 250 MW. A series of optimization of the design of the HelmholtzDEC results in a shape shown in Fig.2, where trajectories of the fusion protons and the fast electrons are depicted. It has been demonstrated that the fusion protons can pass the HelmholtzDEC and reach the TWDEC as designed, whereas the fast electrons can reach the cathode. The separation of the fusion proton and the fast electrons is almost perfect.

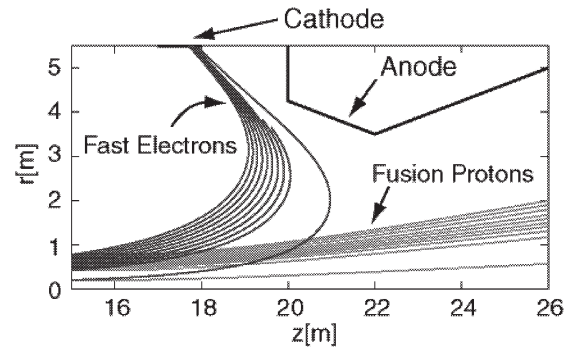


Fig. 2. Separation of fusion protons and fast electrons in Helmholtz type DEC (anode and cathode earthed).

Figure 3 shows the trajectories of the thermal ions and the slow electrons, indicating that the separation is relatively good with 61 % of ions to cathode.

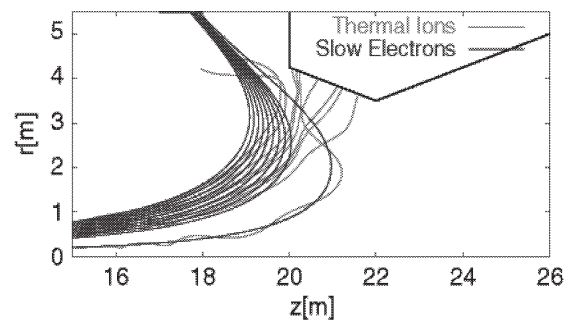


Fig. 3. Separation of thermal ions and slow electrons in Helmholtz type DEC
(anode with 10kV and cathode with 100 kV).

Reference

- 1) Kobayashi, T., Nemoto, T. and Ishikawa, M.: AIAA 2004-2168, pp.1-10, 35th AIAA Plasmadynamics and Lasers Conf., 2004.
- 2) Kawana, R. and Ishikawa, M.: Proc. 15th Int. Conf. On MHD Energy Conversion, Vol.2, pp.302-130, 2005.

§5. Suppression of Harmonic Frequencies of Induced Voltages in a Decelerator of a TWDEC Simulator

Takeno, H., Yasaka, Y. (Kobe Univ.),
Ishikawa, M. (Univ. Tsukuba), Tomita, Y.

Efficient energy recovery of fast protons of 14.7 MeV is one of the key issues to realize a D-³He fusion power plant. As the energy of the fast protons is too high, use of a traveling wave direct energy converter(TWDEC) is necessary. In a TWDEC, a fast proton beam is velocity-modulated by RF, which becomes a density modulated beam in the downstream. The beam induces traveling wave in a transmission circuit, and fields created by the wave decelerate the beam.

We are studying desirable structure of TWDEC experimentally. We had performed proof of principle experiments of TWDEC, and investigated beam deceleration characteristics. We also try to enhance deceleration fields induced by an ion beam by improvement of a transmission circuit. We introduced a loop type transmission circuit, and succeeded in enhancement of deceleration field¹⁾. However, because of the problem of inductive elements in the circuit, the third harmonic frequency with large amplitude is observed. This is not desirable for operation of TWDEC, and we present improved experiments in this paper.

Schematic diagram of our experimental equipments is shown in Fig. 1(a). Helium plasma is created by helicon wave plasma production in the ion source. Helium ion beam, velocity-modulated by 7 MHz, is introduced in the decelerator. The electrodes in the decelerator are connected to a transmission circuit, the detail of which is shown in Fig. 1(b). In the last experiments, inductors L in the circuit were made of coaxial cables with a shorted end¹⁾. This method is simulating with coaxial tubes used in a practical TWDEC. The impedance of this element has a non-linear characteristic to frequency. Not only the existence of harmonic

components in a modulated beam, but also this non-linear characteristic might be the cause of an appearance of the third harmonic frequency. In this study, those elements are modified to usual loop-wire type ones with employing ferrite cores although it is difficult to apply them to a practical TWDEC.

After the modification of inductor elements and test operations by using oscillators as in the last time¹⁾, we apply the new circuit to the TWDEC simulator. Fig. 2 shows an example of spectra of induced voltage in the transmission circuit. Solid and dashed curves indicate voltages on the terminals connected to D₁ and D₃(Fig. 1(a)), respectively. As shown in the figure, the third harmonic frequency is well suppressed in this time. However, it is found that 56 and 63 MHz components have large intensities, which correspond to eighth and ninth harmonic frequencies, respectively. These components are considered to be induced by inductive components of electrode-circuit lines and their stray capacities to the ground. We are planning some measures to reduce those effects.

Reference

- 1) Takeno, H., *et al.*: Ann. Rep. NIFS(2002-2003) 361.

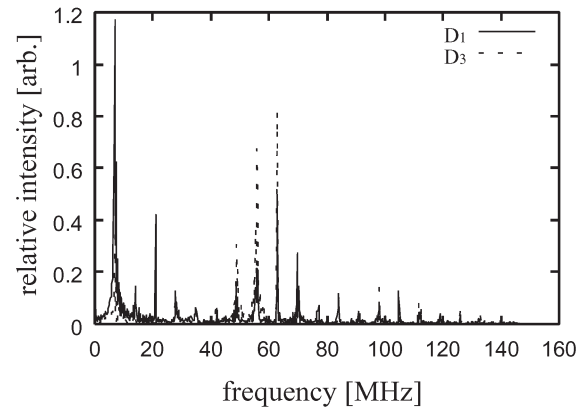


Fig. 2 An example of spectra of induced voltage in the transmission circuit.

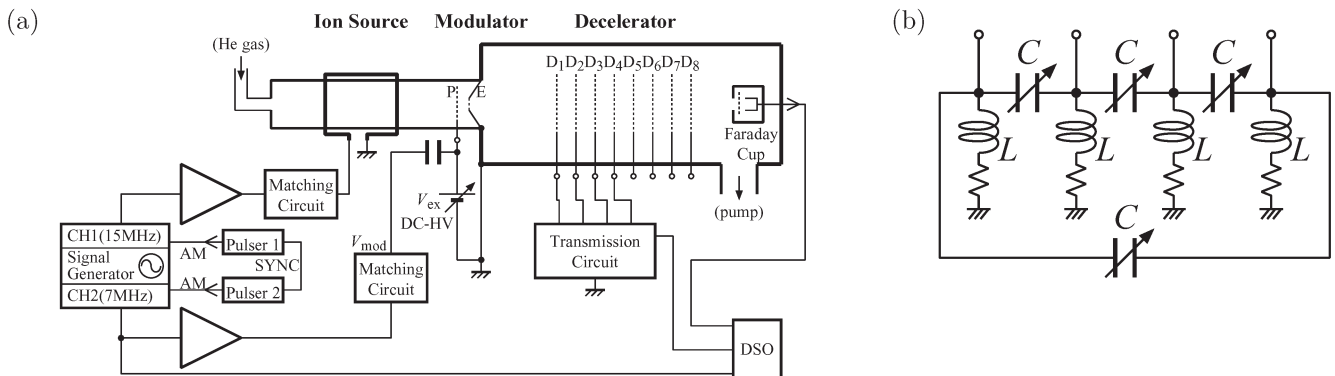


Fig. 1 (a) Schematic diagram of the TWDEC simulator, and (b) the transmission circuit.

§6. Active Deceleration Experiments in TWDEC Simulators

**Takeno, H., Yasaka, Y. (Kobe Univ.),
Ishikawa, M. (Univ. Tsukuba), Tomita, Y.**

For D-³He fusion, energy recovery of fast protons of 14.7 MeV is one of the most important issues. Traveling wave direct energy converter(TWDEC) was proposed as an efficient device. In a TWDEC, a fast proton beam is velocity-modulated, and the bunched proton beam excites traveling wave in a transmission circuit. Energy of proton beam is recovered via deceleration by the traveling wave field.

We are continuing fundamental experiments in a TWDEC simulator¹⁾ and a separate new simulator which is in preparation. The experiments are divided into two modes: one is for voltage induction process on decelerator electrodes and we call this mode as ‘passive decelerator’. The other is for beam deceleration process and we call this mode as ‘active decelerator’. In this report, we show an empirical scaling of energy recovery for various experiments in the active decelerator mode.

Active decelerator experiments are performed by using a setting shown in Fig. 1. Helium plasma is produced in the ion source region, and by applying DC high voltage(V_{ex}) to an extraction electrode, a helium ion beam flows into the deceleration region. A beam modulation RF voltage V_{mod} is also applied to the extraction electrode. Another RF voltage V_{dec} synchronized with V_{mod} is supplied to a transmission circuit. The circuit consists of coaxial cables, the length of which is designed to supply appropriate time delays between electrodes. In a real TWDEC, V_{dec} is induced by the proton beam itself. In the simulator, however, fundamental researches are performed by controlling V_{dec} externally to examine the interaction between the beam and the deceleration field.

The scaling of energy recovery is summarized in Fig. 2. For unified treatment of various results, we

introduce modified beam energy E^* and modified efficiency for unit wave length η_1^* . Using V_{dec} , $E^* = E_{ex}(V_{dec}/V_{dec0})$ is defined, where $E_{ex} \simeq eV_{ex}$ is an initial beam energy and V_{dec0} is 200 V_{0p}. Efficiency for unit wave length η_1 is also modified by $\eta_1^* = \eta_1(J_1(1.84)/J_1(X))$ where J_1 is a Bessel's function of the first kind and X is a bunching parameter. The variation of V_{mod} is taken into account with the variation of X .

Open circles are for experimental data, and filled circles are for numerical calculations²⁾. The gray elliptical region indicates numerical calculation for real TWDECs. The dashed ellipse indicates an expected region in the new simulator. In the numerical calculations, the structure of decelerator is optimized according to an equation:

$$\frac{\lambda(z)}{\lambda_0} = \left\{ 1 + \frac{3}{2} \frac{E_{M0}}{V_{ex}} z \right\}^{1/3},$$

where z is an axial coordinate in which the origin is at the entrance of the decelerator, and E_{M0} is wave field strength at $z = 0$. $\lambda(z)$ and λ_0 are wavelength of traveling wave at z and the one at $z = 0$, respectively. In the present simulator, this optimization is not necessarily applied. In the new simulator, however, the decelerator is designed by taking account of the above equation.

According to the definition of E^* , η_1^* increases as E^* in the same simulator because beam divergence is smaller for larger E_{ex} , and larger deceleration is obtained with a shorter length for larger V_{dec} . In the present simulator, $E^* = 10^3 \sim 10^4$ eV, and the experimental data are consistent with this expectation.

The best value of η_1^* is expected to be $20 \pm 4\%$ which is obtained by interpolation of numerical results. In the new simulator, around those values of η_1^* are expected in $E^* = 10^4 \sim 10^5$ eV.

Reference

- 1) H. Takeno, *et al.*: Jpn. J. Appl. Phys. **39**(9A), 5287 (2000).
- 2) Ishikawa, M., *et al.*: Ann. Rep. NIFS(2002-2003) 358.

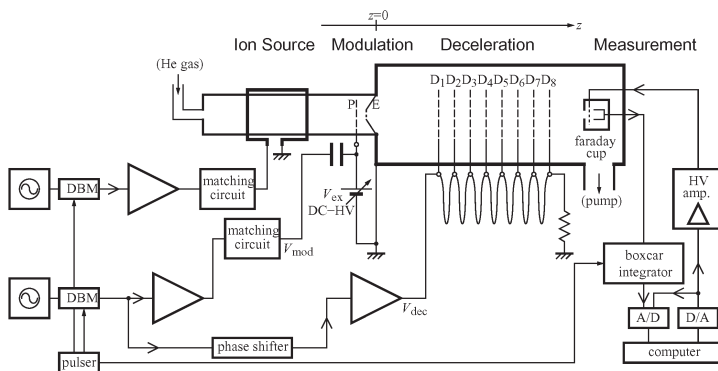


Fig. 1 A setting of active decelerator mode of the TWDEC simulator.

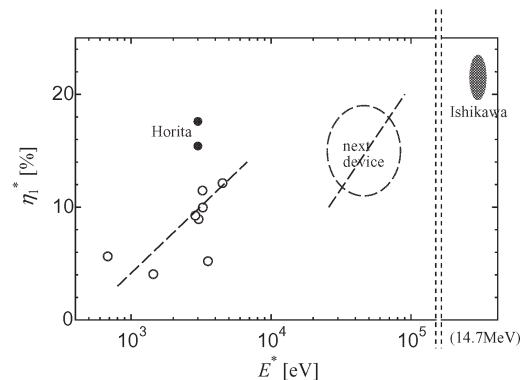


Fig. 2 Scaling of energy recovery.

\$7. Development of High Beta Plasma Formation Using ICRF High Harmonic Fast Wave

Takase, Y., Kasahara, H., Taniguchi, T., Kamada, Y., Ishii, N., Oosako, T., Tojo, H. (Frontier Sci. and Sci., U. Tokyo)

Fukuyama, A. (Eng., Kyoto U.)

Watari, T., Mutoh, T., Kumazawa, R., Seki, T., Saito, K., Takeuchi, N.

The purpose of this collaborative research is to develop a radiofrequency (RF) heating method to produce high beta plasmas, which is a common issue in spherical tokamaks (ST) and helical systems. In particular, electron heating and current drive by Landau damping and transit time damping of the fast wave at relatively high harmonics of the ion cyclotron frequency are explored. The fast wave in this frequency range is called the high-harmonic fast wave (HHFW).

Development of heating scenarios is carried out on both LHD at NIFS and the TST-2 spherical tokamak at the University of Tokyo. On LHD, existing ICRF transmitters and ICRF loop antennas can be used. The transmitters can provide power in the frequency range of 30 to 80 MHz. TST-2 is presently the largest ST device in Japan, with $R = 0.38$ m and $a = 0.25$ m (aspect ratio $/ = 1.5$). It has already achieved toroidal magnetic fields of up to 0.3 T and plasma currents of up to 0.14 MA. RF power of up to 400 kW in the frequency range 10–30 MHz is available for this experiment. In addition, transmitters at 200 MHz, previously used on the JFT-2M tokamak, have been transferred from JAERI during this fiscal year. TST-2 has the advantages of ample experimental time and flexibility with short turn-around time for hardware modifications. For example, different wave excitation schemes using different antennas can be studied.

During Fiscal Year 2004, experiments were not performed on TST-2 because of power supply and RF system upgrades and modifications following relocation of the device to the Kashiwa Campus of the University of Tokyo. While TST-2 was located in the Hongo Campus, only one transmitter was used for a short pulse (1 ms) because of space limitation. After relocation to the Kashiwa Campus, two transmitters were installed and the full power supply capability was restored. This upgrade enables higher power (400 kW) operation for a longer pulse (> 10 ms) duration. Power supplies for the coil systems were also upgraded, in order to enable operation at higher toroidal fields and plasma currents for longer durations (several tens of ms). A power crowbar circuit has been implemented to produce a more constant toroidal field waveform. In order to provide more flux swing (Volt seconds), the ohmic heating (OH) coil circuit was modified to enable a double-swing operation. This improvement has enabled the loop voltage to stay positive for several tens of milliseconds.

While TST-2 was at the Hongo Campus, an antenna consisting of two current straps was used to excite the

HHFW. This antenna had a fixed spacing between the two current straps (18° center to center), and the Faraday shield orientation was horizontal. The antenna was modified to enable excitation of different toroidal mode numbers (and therefore, the wavenumber parallel to the magnetic field) by varying the distance between the two current straps. Since the excitation of the slow wave at the plasma periphery can lead to increased edge electric fields, and therefore generation of impurities, the Faraday shield was modified to follow the average inclination of the magnetic field for typical operation (about 30°) in order to short out the electric field parallel to the magnetic field lines. The modified antenna is shown in Fig. 1. The RF current flows on the current strap (width 10 cm, height 60 cm). The separation between the two current straps can be adjusted in the range 25 – 35° by changing the feeder connectors. This range corresponds to toroidal mode numbers 10.3–14.4, which should be absorbed strongly by electrons with temperature around 200 eV.

The TASK/WM full wave code was used to identify promising heating scenarios and to design a proper antenna for such scenarios. A typical example for a central density of $3 \times 10^{19} \text{ m}^{-3}$, central electron density of 300 eV, toroidal magnetic field of 0.3 T, and toroidal mode number of 9 is shown in Fig. 2. It can be seen that there are two wavelengths across the plasma minor radius, and that the absorption profile is peaked off-axis under this condition.

TST-2 is currently back in operation, and RF heating experiments are scheduled to resume in FY2005.

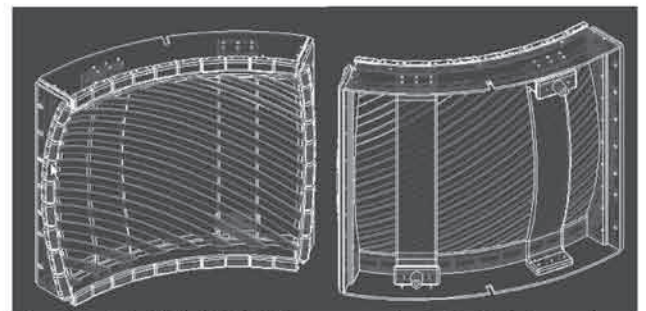


Fig. 1. Modified HHFW antenna for TST-2. Front view (left) and rear view (right).

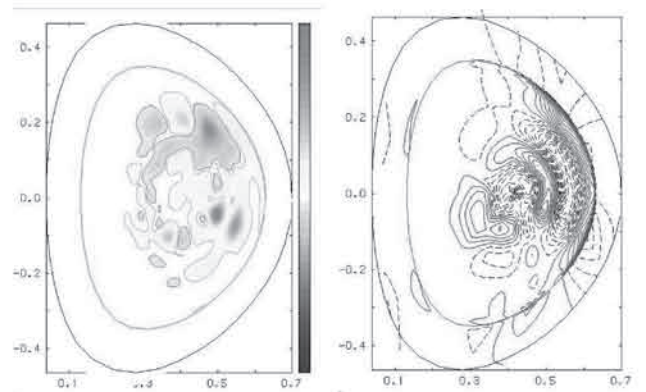


Fig. 2. HHFW absorbed power profile (left) and electric field profile (right) for TST-2, calculated by TASK/WM.

§8. Experimental Study of Compatibility of a Transport Barrier and Energetic Ion Confinement

Sasao, M., Kitajima, S., Shinto, K., Takahashi, H., Tanaka, Y., Utoh, H., Nishimura, H., Kubo, N. (Tohoku Univ.)

Ogawa, H. (JAERI)

Takayama, M. (Akita Pref. Univ.)

Nishimura, K., Nagayama, Y., Isobe, M., Nishiura, M., Inagaki, S., Yokoyama, M.

The confinement of energetic ions is one of key issues for the prospect to a steady state reactor plasma using a helical system[1]. Complex motions of trapped particles in helical systems tend to enhance the radial transport. It has been known that a radial electric field might effect on the confinement of trapped particles, while it play an important role to form transport barriers and to realize improved modes. In this Joint Research, we study the compatibility of a transport barrier and energetic ion confinement in helical systems.

In the Tohoku University Heliac (TU-Heliac), the influence of a radial electric field on the improved modes has been investigated by electrode-biasing experiments. In both positive and negative biasing experiments with a stainless steel (SUS) electrode (cold-electron or ion collection), the improvement of plasma confinement was clearly observed when the radial electric field was formed [6]. Furthermore, by negative biasing with a hot cathode (electron-emission), the radial electric fields can be actively controlled as a consequence of control of the electrode current, I_E .

In this academic year, two diagnostic systems, a 1m high a new Titanium (Ti) electrode was fabricated, installed on TU-Heliac, and first experimental results were obtained. Using an electrode made of a hydrogen storage metal, such as Titanium (Ti) or Vanadium (V), the following can be expected: (1) ions accelerated from the positive-biased electrode allow simulation of the orbit loss of high-energy particles, and (2) the electrons or neutral particles injected from the negative-biased electrode provide production of high density plasma if hydrogen is successfully stored in the electrode.

Positively biased experiments were carried out after treatment for hydrogen storage ($p_{H_2} = 2.7 \times 10^5$ Pa, 12 hours). The biasing resulted in increases in the plasma potential, and the line intensity of H_α and the electron density increased by about 2-fold as compared with those before biasing. Figure 1 shows the differences in the profiles of (a, e) the electron density, n_e , (b, f) the electron temperature, T_e , (c, g) the plasma potential, V_s , and (d, h) the radial electric field, E_r , measured with the triple probe, between the SUS electrode (left side) and the Ti electrode (right side) biasing experiments, both before biasing (solid circles) and during biasing (open triangles). In the case of Ti electrode biasing, the radial distribution of the electron density sloped steeply at $r = 60 \sim 90$ mm (e) and a strong positive radial electric field was formed at $r = 100 \sim 120$ mm (h), indicating improvement of plasma confinement. In positive biasing, an electrode is collecting electrons. In

biasing of both the SUS electrode and the Ti electrode, the electrode currents were almost the same. This current level was too high to induce the improved mode for SUS electrode biasing. On the other hand, in the plasma biased by the Ti electrode, the electron density increased inside the electrode position. This suggested that the hydrogen storage electrode made of Titanium injected hydrogen ions.

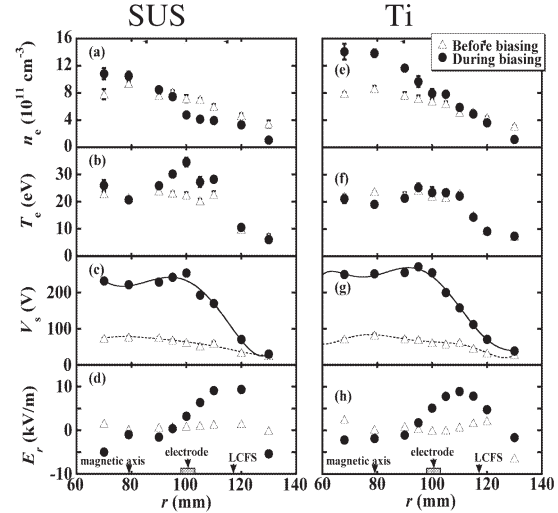


Fig. 1 Comparison of the SUS electrode (left side) biasing experiment with the Ti electrode (right side) biasing experiment profiles of (a) the electron density, n_e , (b) the electron temperature, T_e , (c) the plasma potential, V_s , and (d) the radial

In order to study the energetic particle confinement in an Heliac configuration, the classification of orbits were investigated using a full-gyro-orbit calculation. In fig. 2 is shown the confinement region of a proton of 75 eV in a ρ - χ plane. If the electrode biased at 75V emits protons in TU-Heliac, particles of initial pitch angles over 60 degrees might be promptly loss.

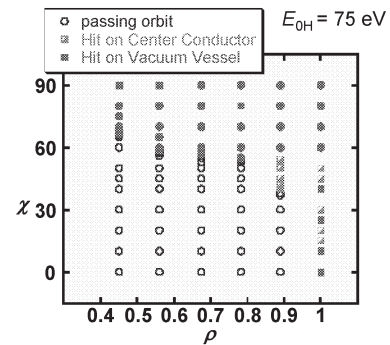


Fig. 2 The energetic particle loss region of TU-Heliac in a ρ - χ plane.

References

- [1] Sasao, M. et al., Proceedings of 18 IAEA Fusion Energy Conference, IAEA-CN-77/EX9/1(Sorento, October 2000).
- [2] Kitajima, S. et al. Proceedings of 20 IAEA Fusion Energy Conference, IAEA-CN-116/EX/9-3(October 2004).
- [3] Utoh, H. et al. Proceedings of EPS2005 (P2.006).

§9. Study of the Repetitive Fueling Pellet Transportation in the Guiding Tube

Yoshikawa, M., Kubota, Y., Kobayashi, T., Saito, M., Nakashima, Y. (Univ. Tsukuba, PRC)
Yamada, H., Sakamoto, R.

In recent fusion devices, a hydrogen ice pellet injection is an indispensable method for fueling to plasmas. The measurement of pellet parameters (velocity, mass and shape) just before the injection to the plasma is important for the evaluation of the fueling efficiency and the transport efficiency (the loss of the pellet velocity and mass) through the guide tubes in the repetitive pellet injection. Considering the difference of pellets used in various fusion devices and the pellet transportation in the guide tube, the diagnostic system must be able to measure the various pellet velocities and sizes. We have developed a new diagnostic system of the hydrogen ice pellets.^{1,2)} The system is designed to be detectable for the pellet size from sub-millimeter to several millimeters. Especially, by using multiple mirror systems, the light gate system can achieve high detective probability with high signal to noise ratio for the sub-millimeter pellet. The microwave mass detection system in the diagnostic system had low signal to noise ratio. Then, we use a new microwave cavity for microwave mass detection system and an amplifier. In this report, we describe the results of the bench tests of the pellet diagnostic system using a repetitive pellet injection system in the Large Helical

Device (LHD) at the National Institute for Fusion Science.³⁾

The bench test of the new diagnostic system was carried out using the repetitive pellet injector in LHD. The pellet used in this experiment is cylindrical (2.5 mm in diameter and 2-4 mm in length). The example of total signals of the diagnostic system is shown in Fig. 1. The solid line, the broken line and the dotted line show the signals of the microwave mass detector system, the first stage and the second stage of the light gate system, respectively. The photographs of the shadowgraph system show the pellet size. The position of the pellet in the photograph moves according to the speed of the pellet. In this experiment, the detective probability of the light gate system is 100%. The pellet velocity is measured by a time of flight between the two light gate systems. The microwave cavity detected the pellet signal with large signal to noise ratio, after installation of an amplifier, change of the cavity size and optimization of microwave frequency.

It is found that the newly developed pellet diagnostic system is capable of simultaneous measurement of the pellet parameters required for the LHD experiments.

Reference

- 1) Yoshikawa, M., et al.; Annual Report of NIFS, April 2003-March 2004 (2004) 98.
- 2) Kubota, Y., et al.; Rev. Sci. Inst., 75 (2004) 4228.
- 3) Sakamoto, R., et al.; Annual Report of NIFS, April 2002-March 2003 (2003) 77.

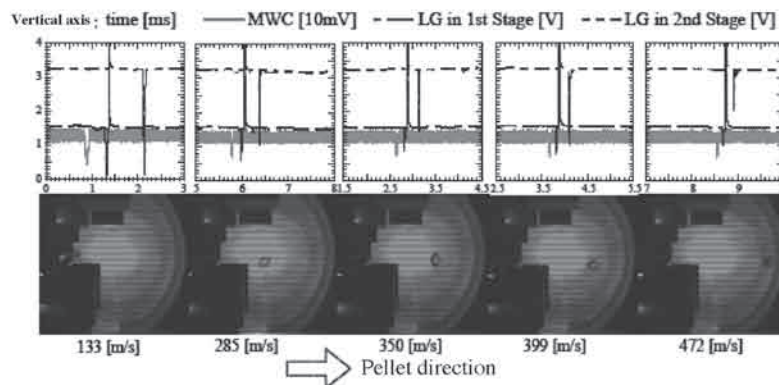


Fig. 1. Total output signals of the pellet diagnostic system.

§10. Quasi-Optical Analysis of Output Beam from Remote Steering Antenna

Idei, H. (Kyushu Univ.), Shimozuma, T., Notake, T.
Kubo, S., Zushi, H. (Kyushu Univ.)

A remote steering antenna system is considered as the upper port launcher at International Thermonuclear Experimental Reactor (ITER) for Electron Cyclotron Heating / Current Drive (ECH/ECCD), in order to avoid an installation of plasma-facing movable mirrors. The well-defined Gaussian output beam is required in a steering capability of ± 10.5 degrees. Asymmetric direction antennas in the steering angles of ± 12 degrees have been tested at low and high power levels in relation to the ITER application. A full-scale mock-up of the upper-port launcher is being designed and constructed for the low and high power tests.

A symmetric direction antenna with extended steering capability was prepared to the ECH/ECCD experiments on the TRIAM-1M tokamak in Kyushu University. The TRIAM-1M tokamak has super-conducting magnet coils to generate the high field up to 8T. In the tokamak, there is a long distance between the plasma and the device port, and is not enough space for a mirror array to be installed in the vessel, due to the large bell jar for the magnets. Fundamental ECH and ECCD at the ITER frequency from the low field can be experimentally tested using the developed antenna system in the tokamak. A remote-steering antenna system for a large experimental device is newly being developed under the collaboration between National Institute for Fusion Science (NIFS) and Kyushu University. The output beam of the antenna prepared for the TRIAM-1M experiments is analyzed, based on moment and matching coefficient methods [1]. This work is partly done under the collaboration between NIFS and Kyushu University, to evaluate output beams from remote steering antennas in detail.

Figure 1 shows intensity and phase profiles in the x direction of the E_y component in the output beam at propagation position $z = 65\text{mm}$ in the 15 degree steering case, which are measured at a low power level. The detector stage or the measuring z axis is rotated in the steering $x - z$ plane corresponding to the incident steering angle. The intensity profile is Gaussian-like beam of $w_x = 11\text{mm}$, however, there is a side lobe. The phase profile is parabolic with a phase curvature of $R_x = 218\text{mm}$ in the main lobe. The phase rapidly changes near the side lobe, therefore, the side lobe part is spread out from the main lobe along the propagation. First this output beam from the antenna is analyzed by the moment theory of quasi-optical beams. Here, the

n -th moment is defined with the amplitude distribution $A(x, y)$ as,

$$\langle x^n \rangle = \int x^n A^2 dx dy / \int A^2 dx dy. \quad (1)$$

The first moment $\langle x \rangle$ expresses the beam center position in the x direction. The first moment $\langle x \rangle$ of the beam in shown Fig.1 is evaluated as 8mm from the intensity profile. The evolution of the beam center position along the propagating can be written in terms of the moment theory by using the phase distribution $\Phi(x, y)$ as the following,

$$\langle x(z) \rangle = \langle x(0) \rangle - z \frac{\int A^2 (\partial \Phi / \partial x) dx dy}{k \int A^2 dx dy}, \quad (2)$$

where k is the wave number of the propagating beam. The integrated coefficient of z in Eq.2 expresses a slope of the propagating axis. The tilt angle of the slope is evaluated as -0.2 degrees in this case. The phase profile is flat near the beam center. The beam propagates along the measuring z -axis. The propagating angle of the beam corresponds to the steering angle as designed. Secondly, the Gaussian content of the beam is evaluated from a matching coefficient defined as,

$$\left| \int f g^* dx dy \right|^2 \left(\int |f|^2 dx dy \cdot \int |g|^2 dx dy \right)^{-1}, \quad (3)$$

where f and g are the complex amplitudes. Here, the complex amplitudes, f and g , are evaluated from the intensity and phase distributions of the fitted Gaussian beam and of the measured profiles, respectively. The Gaussian content is evaluated as 0.85 for the output beam. The well-defined Gaussian beam with a correct steering angle is obtained, although there is the beam center offset of 8mm. This antenna is successfully used to the ECH/ECCD experiments on the TRIAM-1M tokamak.

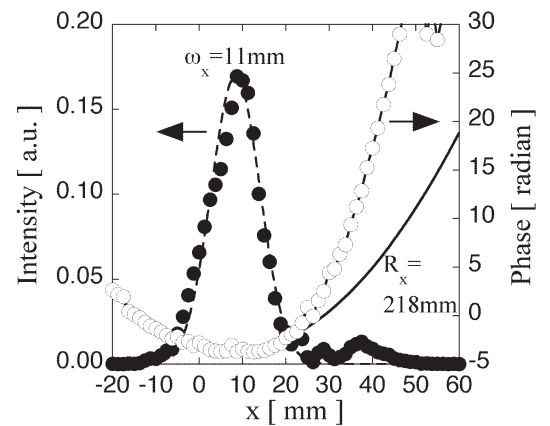


Fig. 1: Intensity and phase profiles in x -direction of the E_y component in the 15 degree steering case.

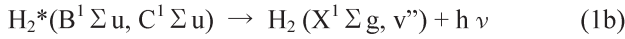
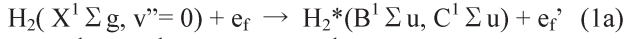
References

- [1] H. Idei, *et al.*, Journal of Plasma and Fusion Research 81 No.3, 186 (2005).

§11. Production Mechanism of D⁻ Ions and Evaluation of D⁻ Ion Current Extraction

Fukumasa, O., Naitou, H., Tauchi, Y., Mori, S. (Dept. Elect. Electronic Eng., Yamaguchi Univ.)
Sawada, K. (Shinsyu Univ.), Hamabe, M. (Chubu Univ.)
Takeiri, Y., Tsumori, K.

In a tandem volume source, H⁻ ions are generated by the dissociative attachment of slow plasma electrons e_s ($T_e \sim 1$ eV) to highly vibrationally excited hydrogen molecules $H_2(v'')$ (effective vibrational level $v'' \geq 5 \sim 6$). These $H_2(v'')$ are mainly produced by collisional excitation of fast electrons e_f with optimum energy of about 40 eV. Namely, H⁻ ions are produced by the following two step process, i.e. $H_2(v'')$ production and H⁻ formation:



Production process of D⁻ ions is believed to be the same as that of H⁻ ions described above. We have studied relationship between negative ions (i.e. H⁻ and D⁻ ions) production^{1, 2, 3)} and plasma parameters across the magnetic filter (MF).

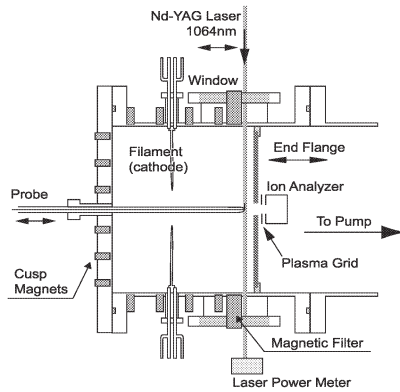


Fig. 1. Schematic diagram of the ion source.

Figure 1 shows a schematic diagram of a rectangular ion source. The arc chamber (plasma generator) is 25×25 cm in cross-section and 19 cm in height. Details of experimental procedures are reported elsewhere³⁾. By varying the intensity of the MF, axial distributions of T_e and n_e in both H_2 and D_2 plasmas are changed strongly in the downstream region^{2, 3)}.

Variations of H⁻ and D⁻ productions due to changes in plasma parameter distributions across the MF are discussed by taking into account main collision processes for production and destruction^{4, 5)}, i.e. dissociative attachment (DA: $H_2(v'') + e \rightarrow H^- + H$) process and collisional electron detachment (ED: $H^- + e \rightarrow H + 2e$) process. Influence of D⁻ destruction by ED process on D⁻ density is higher than that of H⁻ distribution although n_e in D_2 plasma is higher

than n_e in H_2 plasmas. Extracted D⁻ current is also lower than H⁻ current, and the ratio of H⁻ to D⁻ current is almost the same as the ratio of H⁻ to D⁻ density in front of the extraction hole. Therefore, extracted D⁻ current is mainly determined by D⁻ density in front of the extraction hole.

Figure 2 shows pressure dependence of (a) D⁻ ion densities in the source and (b) extracted D⁻ currents, where the intensity of the MF is a parameter. As a whole, the patterns of pressure dependence in D⁻ ion densities are nearly the same as those in extracted D⁻ currents. Namely, the extracted D⁻ currents are proportional to the D⁻ densities in the source. According to the results shown here and related other results^{4, 5)}, the values of extracted negative ion currents are mainly determined by the negative ion densities in front of the extraction hole.

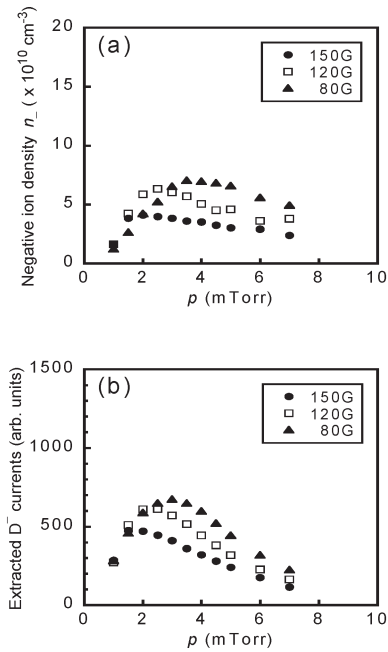


Fig. 2. Pressure dependences of (a) D⁻ ion densities in the source and (b) extracted D⁻ currents. Experimental conditions are as follows: $V_d = 70$ V, $I_d = 5$ A and $V_{ex} = 1.5$ kV. D⁻ ion densities are measured at $z = -0.5$ cm. Extraction hole is set at $z = -1.5$ cm. Parameter is the magnetic field intensity of the MF.

It is reconfirmed^{4, 5)} that T_e in the extraction region should be reduced below 1 eV with keeping n_e higher by using the MF, including good combination of filament position and the MF with a certain intensity. Control of not only T_e but also n_e in the extraction region is very important for enhancement of D⁻ production.

References

- 1) Mori, S. et al., 30th IEEE Conf. Plasma Science (2003).
- 2) Mori, S. and Fukumasa, O., 7th APCPST (2004).
- 3) Fukumasa, O. et al., Contrib. Plasma Phys. **44** (2004) 516.
- 4) Fukumasa, O. and Mori, S., 10th Int. Symp. PNNIB (2004).
- 5) Fukumasa, O. and Mori, S., 4th IAEA TCM on Negative Ions (2005).

§12. Analysis of a Graphite Plate Interacting with a High-density Hydrogen Plasma

Sasaki, K. (Nagoya Univ.)
Shibagaki, K. (Suzuka National College of Tech.)
Aramaki, M., Kono, A. (Nagoya Univ.)
Goto, M., Muto, S., Morita, S.

We are investigating the interaction between high-density hydrogen plasma and a graphite plate by using a compact divertor simulator excited by helicon-wave discharge.^{1,2)} In this year, we carried out the analysis of the graphite plate using a scanning electron microscope (SEM) and a laser-desorption time-of-flight mass spectrometer.

A graphite plate was installed on the end plate that terminated the high-density plasma column with a diameter of 16 mm. The temperature of the graphite plate was controlled at 400 °C using a heater. The rf power and the H₂ gas pressure were 2.5 kW and 40 mTorr, respectively. The plasma density in this discharge condition was roughly $8 \times 10^{12} \text{ cm}^{-3}$. To avoid over heating of the plasma source, the plasma was produced in a pulsed mode with a duration of 4 ms and a repetition rate of 10 Hz.

A remarkable change was seen with the naked eyes on the graphite plate after the irradiation of the high-density hydrogen plasma. The changed region corresponded to the diameter of the plasma column. The change at the center was most significant. Figure 1 shows a SEM image at the center of the graphite plate after the irradiation of 8 hours (the net irradiation duration was 19.2 min). It was observed that many particulates with a diameter of several micrometers were produced on the graphite plate. The production efficiency of particulates was significantly dependent on the radial position.

The laser-desorption time-of-flight mass spectrometer employed the forth harmonics (266 nm) of a Nd:YAG laser. The fluence, the duration, and the repetition frequency of the YAG laser pulse were 50 mJ/cm², 10 ns, and 10 Hz, respectively. Positive ions were produced by the irradiation of the laser pulse, and the ions were accelerated by electric field. After flying a free space, the ions were detected using a microchannel plate. To enhance the mass resolution, the trajectories of the ions were turned using a reflectron. The masses of the ions were determined from their flight times. Figure 2(a) shows the mass spectrum obtained from the graphite plate that was irradiated by the hydrogen plasma for 8 hours. For the sake of comparison, Fig. 2(b) shows the mass spectrum obtained from an original graphite plate. It was found that bigger-size cluster ions were produced from the graphite plate with the irradiation of the hydrogen plasma. In addition, it is not seen from the figure clearly,

mass peaks corresponding to CH⁺, C₂H₃⁺, and C₂H₄⁺ are included in the spectrum shown in Fig. 2(a). This result confirms the existence of hydrogen in the particulates and/or the bulk graphite plate after the irradiation of the hydrogen plasma, and suggests a critical problem from the view point of safety hazards such as tritium inventory in D-T nuclear fusion reactors.

- 1) M. Aramaki, K. Kato, M. Goto, S. Muto, S. Morita, and K. Sasaki: Jpn. J. Appl. Phys. 43 (2004) 1164.
- 2) K. Sasaki, T. Maeda, N. Takada, M. Aramaki, M. Goto, S. Muto, and S. Morita: submitted to Jpn. J. Appl. Phys.

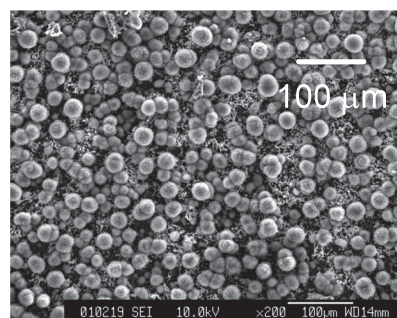


Fig. 1 SEM image of a graphite plate irradiated by the high-density hydrogen plasma for 8 hours.

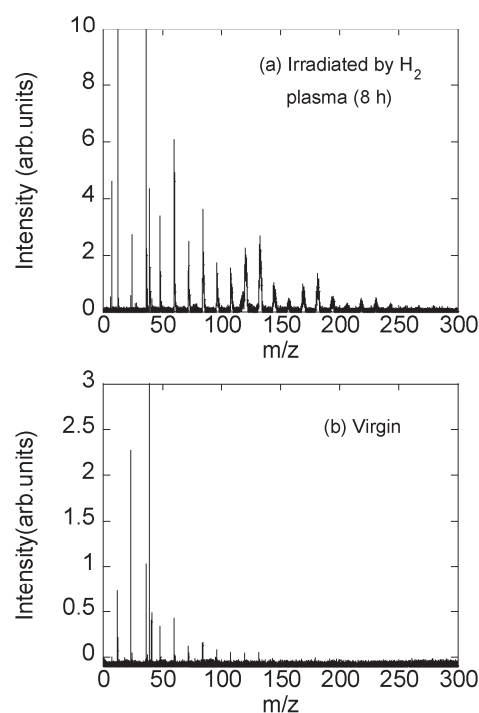


Fig. 2 Mass spectra obtained using a laser-desorption time-of-flight mass spectrometer (a) from a graphite plate with the irradiation of the hydrogen plasma for 8 hours and (b) from a virgin graphite plate

§13. Development of Continuously Size-Controllable Pellet Injector and Detailed Study of Passage Properties in Drift Tube

Sato, K.N., Kawasaki, S., TRIAM Exp. G.
(RIAM, Kyushu Univ.)
Ichizono, K., Aoki, A. (IGSES, Kyushu Univ.)
Sakakita, H. (AIST)
Fujita, H., Misawa, T. (Saga Univ.)
Kogoshi, S. (Fac. Sci. Tech., Tokyo Univ. of Sci.)
Yamazaki, K., Yamada, H., Sakamoto, R.

From the viewpoint of performance of nuclear fusion plasmas, pellet injection experiments have been actively carried out in many toroidal devices in the sense of controlling density profile, obtaining high density or improved confinement, and diagnostic purposes. In order to have a common measure of pellet ablation, the regression study has been performed as an international cooperation activity, obtaining "IPAD" (International Pellet Ablation Database) [1]. However, these are an empirical scaling, and the mechanism of pellet ablation still remains to be studied.

According to the code calculations based

on a typical pellet ablation model (e. g., so-called the neutral gas shielding model), it is understood that the penetration depth into plasma is always quite sensitive to the pellet size. If the pellet size is too large, the pellet passes through the plasma, and if it is too small, it is trapped at the plasma surface. Also, an effective or suitable range of the pellet size for a certain plasma is generally very narrow, and this range largely varies depending on each plasma size and plasma parameters. Thus, the precise controllability of the pellet size, especially the size controllability with continuously variable system will be quite effective in order to carry out the detailed studies on pellet ablation and associated phenomena.

A pellet injector of new type with precisely and continuously controllable system of pellet size is being developed. This has a unique mechanics and structure of producing a frozen pellet in extremely low temperature region. The central part of the pellet injector with continuously size-variable system is given in Fig.1. In the device presently developed in this research, we will precisely adjust the length of the cylindrical pellet (Φ 1.0mm) from 0.5 to 3 mm by using the special "length restriction rod".

[1] L.R.Baylor et al. : An International Pellet Ablation Database, Nucl. Fusion 37 (1997) 445.

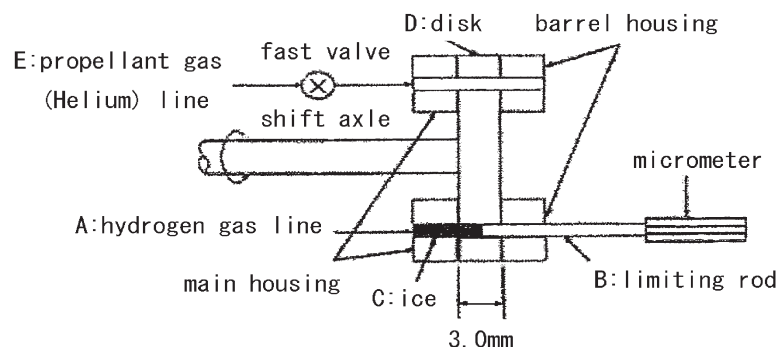


Fig.1 The central part of the pellet injector with continuously size-controllable system

§14. Temperature Dependence of Optical Constants of Silicon for 48- and 57- μ m FIR Lasers

Nakayama, K., Okajima, S. (Chubu Univ.)
Ohkuma, H. (JASRI)
Kawahata, K., Tanaka, K., Tokuzawa, T., Akiyama, T., Ito, Y.

We have developed a new two color multi channel interferometer using 48- and 57- μ m FIR lasers for plasma diagnostics [1]. A choice of optical materials of a window and a beam splitter is important especially for the multi channel measurement system. A crystal quartz etalon is often used in a FIR region. However, crystal quartz has a large absorption for both wavelengths. We have already confirmed that a CVD-diamond etalon is an excellent material for the short wavelength FIR region [2]. A silicon etalon with high resistive is also a useful material in this region. In order to design the window and the beam splitter, it is necessary to know precise optical constants such as a refractive index and an absorption coefficient. Although the optical constants of silicon measured by Fourier spectroscopy have been reported [3], the reliable optical constants for short-wavelength FIR laser lines are unknown. Therefore, we have measured the optical constants (refractive index and absorption coefficient) of silicon by using 48- and 57- μ m lasers. Because the optical constants of silicon depend on temperature, the optical constants at 10, 19, and 29 $^{\circ}$ C have been measured. The beam splitter at several temperatures has been designed.

The optical constants have been obtained from the transmission measurement of a rotating etalon. The temperature is measured by two thermometers. The temperature of the silicon etalon is also checked by a thermistor. In this measurement method, the accuracy of the refractive index is strongly dependent on that of the etalon's thickness and the laser wavelength. We have used three samples of different thickness (2.1704 mm, 2.1718 mm, and 1.5452 mm). The thickness has been measured by two linear gages with 0.0001 mm resolution. The uncertainty of the thickness is ± 0.0003 mm. A change in the thickness of 2 mm thick by the thermal expansion ($\sim 2.6 \times 10^{-6}$ /K at 293 K) for this measurement is about 0.0001 mm. The flatness is under $\lambda/2$ for visible light. The resistivity is about ~ 2.8 k Ω ·cm.

Table 1. Optical constants of silicon at 10, 19, and 29 $^{\circ}$ C for 48- and 57- μ m laser lines.

Wavelength (μ m)	Refractive index		
	29 $^{\circ}$ C	20 $^{\circ}$ C	10 $^{\circ}$ C
47.65	3.417	3.416	3.414
57.1511	3.4179	3.4164	3.4147

Wavelength (μ m)	Absorption coefficient (cm^{-1})		
	29 $^{\circ}$ C	20 $^{\circ}$ C	10 $^{\circ}$ C
47.65	0.35	0.33	0.30
57.1511	0.40	0.36	0.35

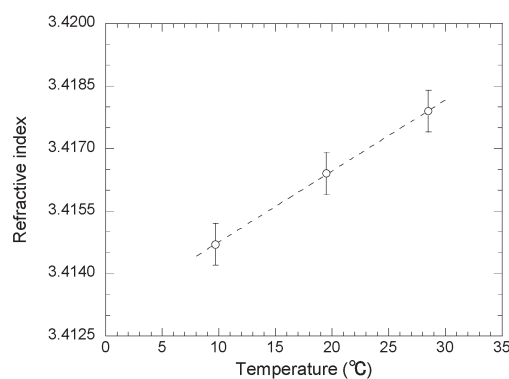


Fig. 1: Temperature dependence of the refractive index of silicon for 57- μ m laser.

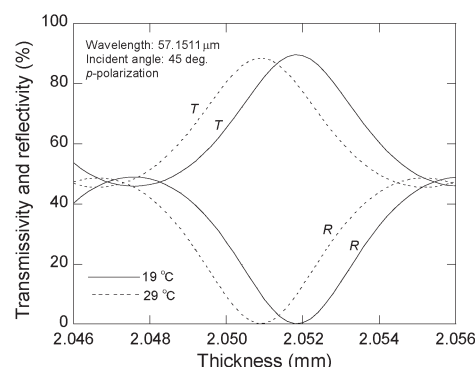


Fig. 2: Example of the design of a beam splitter.

Table 1 shows the optical constants of silicon at 10, 19, and 29 $^{\circ}$ C. The accuracy of the refractive index of 57- μ m laser light is obtained at five figures. The estimated uncertainty of the refractive index is ± 0.0005 on account of that of the thickness (± 0.0003 mm). The uncertainty of the absorption coefficient is ± 0.05 cm^{-1} . The uncertainty of the refractive index and the absorption coefficient of 48- μ m laser light are ± 0.001 and ± 0.10 cm^{-1} , respectively, because the precise wavelength is unknown. The optimum transmissivity at 20 $^{\circ}$ C for 2.1718 mm thick is ~ 88 % for both lasers. Figure 1 shows the refractive index as a function of the temperature for 57- μ m laser. The refractive index depends strongly on the temperature, and that is directly proportional to the temperature. The temperature dependence of the absorption coefficient is small, as shown in Table 1. Fig 2 shows an example of the design of the beam splitter at 19 and 29 $^{\circ}$ C for 57- μ m laser. The beam splitter can be designed by choosing the etalon's thickness. The silicon etalon becomes a beam splitter with the different ratio of transmission and reflection by the difference between temperatures. When designing the window and the beam splitter using the silicon etalon, the temperature of an experiment environment must be considered.

Reference

- 1) Kawahata, K., et al., Rev. Sci. Instrum. **75**, (2004) 3508
- 2) Nakayama, K., et al., Int. J. Infrared Millim. Waves **24**, (2003) 1421
- 3) M. N. Afsar et al., Infrared Phys. **18** (1978) 835

§15. Anisotropy of Proton Velocity Distribution Function in Argon Plasma Analyzed by Means of Plasma Polarization Spectroscopy

Iwamae, A., Atake, M., Sakaue, A., Fujimoto, T.*
(Dept. Mech. Eng. Sci., Kyoto Univ.) Katai, R. (The
Grad. Univ. for Advanced Studies) Goto, M., Morita, S.

The proton (or deuteron) velocity distribution function (PVDF) in a magnetically confined fusion plasma can be anisotropic in the velocity space on a certain condition. The PVDF in low density plasma heated with neutral beam injection (NBI) is expected to be anisotropic. The magnetic dipole (M1) transitions between the levels of ground state configuration of multiply ionized ions are observed in a visible spectral region and the population of the upper level of M1 transitions are created due to the collisional excitation by protons[1]. Anisotropic collisional excitation produces population imbalance or alignment on the upper level. The emission from the aligned level is polarized.

Argon gas was puffed into the LHD vacuum vessel then the NBI started plasmas. The emission from the plasmas was resolved into orthogonally polarized components with the polarization separation optics (PSO). Two types of the PSO were used. One consisted of a polarization separation Glan-Thompson prism and a pair of lens couplers. The other consisted of two Glan-Taylor prisms and a pair of lens couplers. The each image of the optical fiber cores of 400 μm diameter for the orthogonal polarization components was coaxially overlapped. The image was 50 mm-diameter circle at $R=3.75$ m. Ten lines of sight were equipped to cover the poloidal cross section at #1-O port for the poloidal observation as shown in Fig. 1.

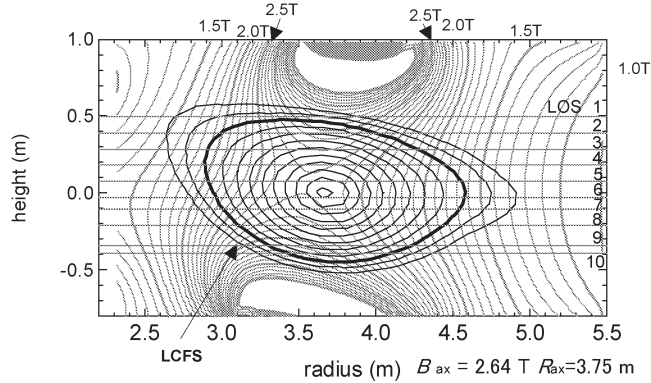
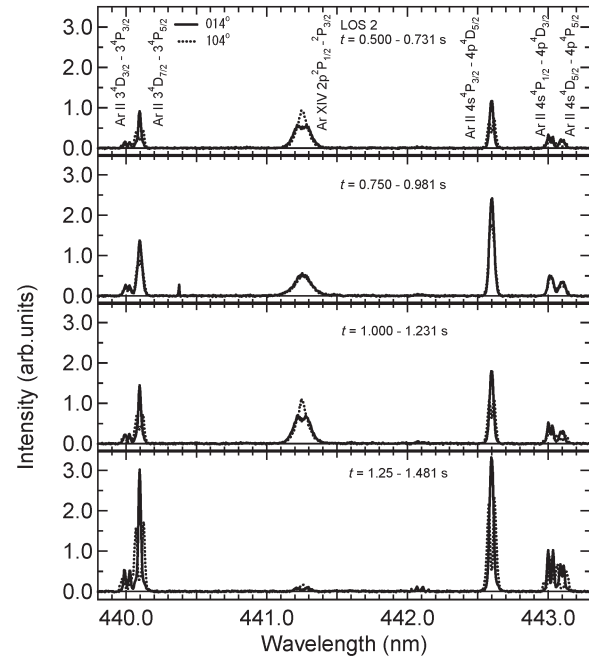


Fig. 0. Ten lines of sight cover the poloidal cross section at #1-O port.

An example of the time evolution of the polarization separation spectra is shown Fig. 2. The observed spectra are M1 transitions in Ar XIV ions and E1 transitions in Ar II ions. The σ components of anomalous Zeeman spectra at $\lambda 441.2$ nm are dominant in the 104° polarized, close to horizontal direction and the π components are dominant in the 14° polarized, close to vertical direction., while the σ and π components of the E1 transitions are contra-

directionally polarized. The anomalous Zeeman components of the M1 transitions calculated at the magnetic field strength of 2.5 T describe the observed line positions.



The relative intensities for 14° and 104° polarized components are calibrated with a standard spectral irradiance lamp and a white diffuse reflectance target. The polarization degree $P = (I_{14^\circ} - I_{104^\circ}) / (I_{14^\circ} + I_{104^\circ})$ of the M1 transitions varies -0.026 , 0.034 and -0.016 on three sequential exposures started at $t = 0.500$, 0.750 , 1.000 s shown in Fig. 2. The negative polarization degree represents qualitatively that the intensity of the σ components is higher than the π components. The longitudinal alignment A_L of the M1 transition between $^2P_{1/2} - ^2P_{3/2}$ terms is expressed as

$$A_L^{M1} = \frac{I_\sigma - I_\pi}{I_\sigma + 2I_\pi} = -\frac{a(p)}{n(p)},$$

where I_σ and I_π are the intensity of σ and π polarized components. The alignment $a(p)$ and the population $n(p)$ are expressed as

$$a(p) = \frac{1}{2}(\rho_{\frac{3}{2}, \frac{3}{2}} - \rho_{\frac{1}{2}, \frac{1}{2}} - \rho_{-\frac{1}{2}, -\frac{1}{2}} + \rho_{-\frac{3}{2}, -\frac{3}{2}})$$

and

$$n(p) = \rho_{\frac{3}{2}, \frac{3}{2}} + \rho_{\frac{1}{2}, \frac{1}{2}} + \rho_{-\frac{1}{2}, -\frac{1}{2}} + \rho_{-\frac{3}{2}, -\frac{3}{2}}$$

where ρ_{M_J, M_J} is the population of the magnetic sublevel M_J . The negative polarization degree is explained by the negative alignment, or positive A_L , created via the collisional excitation by directional protons. When the PVDF is prolate spheroid or axially dominant in velocity space, the negative alignment is excited by the proton collision. The qualitative analysis is underway with population-alignment collisional-radiative (PACR) model.

[1] S. Suckewer and E. Hinnoy, Phys. Rev. Lett. **41**, 756, (1978). K. Sato, et al., Phys. Rev. Lett. **56**, 151, (1986).

* Professor emeritus

\$16. Spectroscopy and Atomic Modeling of EUV Light from LHD Plasmas

Nishimura, H. (Institute of Laser Engineering, Osaka U.)

i) Introduction

Radiations emanated from high-Z elements are of great importance to understand energy balance in fusion plasmas. Such radiations are also interesting as a highly bright source for various applications including next-generation lithography of semi-conductor devices. Although researches and developments of 13-14 nm extreme ultraviolet (EUV) are very actively undertaken, a lot of issues must be addressed to generate a clean and efficient EUV source. In general, laser-produced plasmas inevitably have a sharp gradient in temperature and density distributions so that spectra obtained from the plasma are not suitable as a database for the development of detailed atomic modeling. Magnetically confined plasmas such as LHD are one of the best suited, because the temperature and density profiles are well known in addition to its uniformity in time and space.

ii) Injection of Sn-coated pellets

In order to study the transport of impurity in LHD plasmas, low-Z pellets coated with various materials are injected using a pressurized gas gun. The size of core pellets is typically 0.8 mm in diameter and 0.8 mm in length. Most of the core was made of graphite through fabrication using a precise lathe. The pellets, however, had a large tolerance in size. Then, the pellet disk and the acceleration pipe of the gun were sometimes choked with such pellets. To solve this problem, a commercially available graphite rod has been used. The rod was cut using a laser scribe machine after coating the high-Z metals such as Sn. These processes were done at the Institute of Laser Engineering in Osaka University. A picture of the newly produced pellets is shown in Fig.1. By adjusting the Sn overcoat thickness to an adequate range, discharges could be maintained without radiation collapse.

iii) Improvement of spectrograph

As a first step of this study an EUV spectrograph, consisted of a generally used curved grating, an MCP, and a CCD camera, was used to observe spectra in a range of 5-20 nm at the line-of-sight perpendicular to the magnetic field in the equator plane of LHD. Although the EUV emission spectra were obtained, the spectral resolution of 0.1-0.2nm was not high enough to benchmark the detailed atomic model. In order to improve the poor resolution, a new spectrograph with a varied-line-space grating, so called flat-field spectrograph, has been developed. After fine adjustment of the spectrograph components, we implemented it to LHD to check the spectral image and

resolution power using line emissions from intrinsic high-Z impurities in LHD plasmas. The experimental examination was made by changing the distance between the spectrograph and the CCD camera. Figure 2 shows the result. The horizontal axis represents the relative distance between the spectrograph and the CCD camera, and the vertical axis the spectral width measured at line foot (i.e., twice of FWHM) in units of CCD pixel (26 $\mu\text{m}/\text{pixel}$). The figure clearly denotes that the best resolution is obtained at 4-5 mm longer than the design-best position. Furthermore, it is observed that the best focal position becomes different to each wavelength. Comparing with a theoretical calculation, we understood the defocus is due to a slight difference in the incident angle to the grating, which is roughly estimated to be 0.3 degrees. Further improvement will be made by introducing a better alignment method, which can accomplish accuracy better than 0.1 degree.

iv) Collaborators

The author would like to express his sincere appreciation to all contributors for their invaluable collaborations by listing their names below:

Morita, S., Goto, M., and Katai, R., (NIFS), Nozato, H., (AIST), Amano, T. (Prof. Emeritus of NIFS), Nishihara, K., Noritatsu, T., Fujioka, S., Nagai, K. (ILE, Osaka U.).

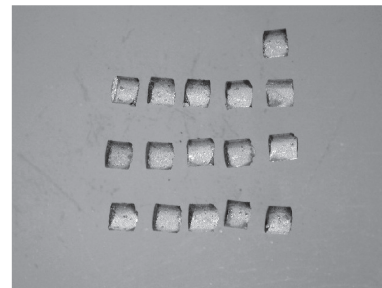


Fig. 1 New Sn-coated pellets produced with laser processing.

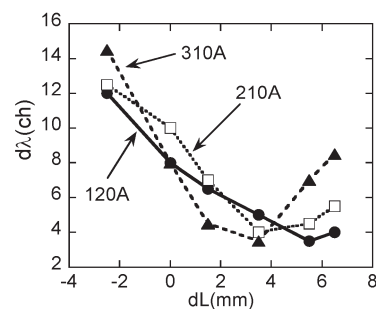


Fig. 2 Spectral line widths represented in a unit of detector pixel size (26 μm) as a function of distance between spectrograph and CCD detector.

\$17. Development of Wide Band and Compact X-ray Spectrometer

Tawara, Y., Sakurai, I., Matsumoto, C., Furuzawa, A.
(EcoTopia Sci. Inst. Nagoya Univ.)
Morita, S., Goto, M. (NIFS)

X-ray spectrometer so far developed for LHD plasma diagnostics using various impurities covers narrow energy band of 8-20 eV around He-like resonance lines of Ar, Ti, Cr, or Fe to measure an ion temperature. Though this system (ref. 1) has been working well, it is also important to measure wide band spectra, since it can determine charge state distribution as a measure of electron temperature. On the observation of astrophysical plasma, we will be able to use X-ray micro-calorimeter (XRS, ref. 2), which has an excellent energy resolution and good detection efficiency for X-rays above several keV in comparison with spectroscopic instruments so far in orbit. Such instrument will give us important data on the high temperature plasma, having similar temperature of fusion plasma in laboratory.

Thus we started to develop wide band and compact X-ray spectrometer. Since there is a small space around the available observing port of LHD, we need to make a compact system. Basic design of this system is shown in Figure 1. As the first step of this development, we chose iron as a target impurity and adopted LiF (2d=0.2848 nm) curved-crystal spectrometer in the

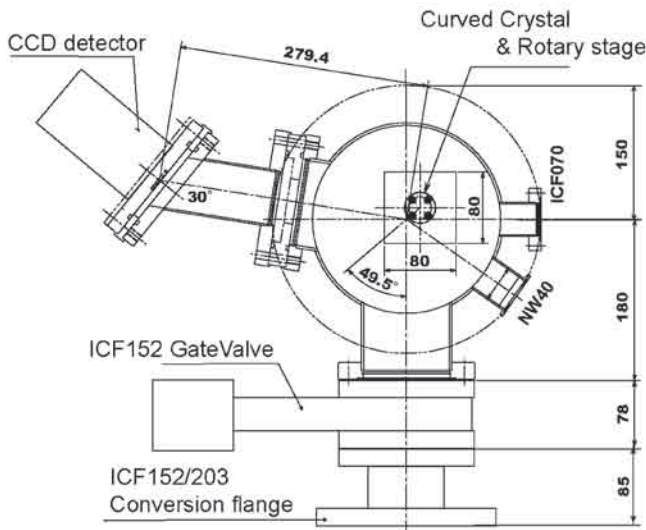


Fig. 1. Wide band and compact X-ray spectrometer system

Johann configuration to cover K-lines of all charge states of iron for 6.4-7.0 keV.

The curvature of the crystal is 215 mm and the size of the crystal is 15 x 15 mm², which is provided by Saint Gobain. This curved crystal is set in a crystal holder, which is directly connected to an electric pulse motor and rotated by an external controller to adjust a Bragg angle.

The back-illuminated CCD (ANDOR model DO420-BN) is selected as a X-ray detector and is mounted on a vacuum flange (see Fig. 2a) and connected to the spectrometer. The CCD surface normal direction is tilted with an angle of 30 deg. to the line of sight of the spectrometer, in order to put the CCD on the Rowland circle. The X-ray detection efficiency is 45-35 % at 6.4-7.0 keV (see Fig. 2b). The total size of the CCD is 26.6 mm (1024 ch; direction of dispersion) horizontally and 6.7 mm (256 ch) vertically. The pixel size is 26 x 26 μ m.

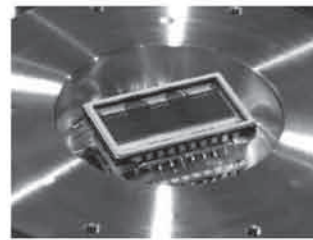


Fig. 2a. Photograph of the CCD (Andor model DO420-BN)

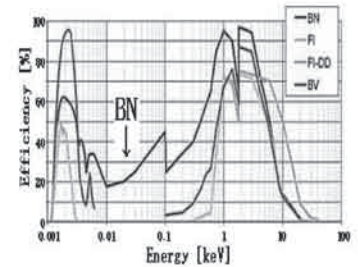


Fig. 2b. X-ray detection efficiency

The distance between the crystal and the detector is 279.4 mm at the CCD center and energy dispersion is 0.6 eV/ch. Energy resolution of the spectrometer is estimated and is shown in Fig. 3. Due to the geometrical deviation in Johann geometry, results show anti-symmetric wide line profiles except for 6.7 keV X-ray, where the configuration is adjusted to get best performance. But these are still better than XRS, which are shown as Gaussian profile.

This X-ray spectrometer will be set at #1-0 port of LHD. The line of sight of the crystal spectrometer is tilted tangentially with an angle of 22 deg.

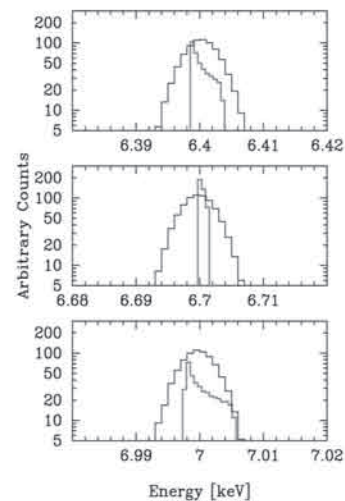


Fig. 3. Expected profiles of the spectrometer (narrow ones) Wide Gaussian profiles are those of XRS for comparison.

Reference

- 1) Morita, S. and Goto, M., Rev. Sci. Instrum., **74**, 2375 (2003)
- 2) Mitsuda, K. et al., Proc. SPIE, **5488**, 177-186 (2004).

§18. Development of Laser Thomson Scattering System Applicable to Low Temperature Recombining Plasmas in Divertor Simulator MAP-II in the Univ. Tokyo (NIFS04KOAB009)

Kado, S., Okamoto, A. (Univ. of Tokyo)

Investigation of the recombining plasmas requires efficient methods of electron temperature measurement which are applicable to the recombining conditions, where the Langmuir probe measurement encounters the anomalous current-voltage characteristics. 1) In addition, it is also challenging to obtain Doppler-broadened Thomson scattering spectra of free electron in low-temperature recombining plasmas, since the narrow Doppler spectra is interfered by stray light attributable to scattering from chamber walls and Rayleigh scattering caused by residual neutral gas. Therefore, interference filter system is not applicable. Then, we have applied a double-monochromator equipped with commercial camera lenses.

Laser Thomson scattering system is installed in the steady-state linear divertor / edge plasma simulator, MAP (Material and Plasma)-II.2,3) Configuration of a laser Thomson scattering system is schematically shown in Fig. 1. A frequency doubled Nd:YAG laser beam (10 Hz, 500 mJ, 532 nm) is directed to a plasma with an mirror located beneath the chamber. A lens with a focal length of 1 m focuses the beam in the center of the plasma through a Brewster window and three baffle plates. An F/4.1 collection lens images the 12 mm vertical scattering region onto a 64-channel fiber array, which transfers the light to a double monochromator. The scattered light is finally detected with an image-intensified charge-coupled device (ICCD).

The double-monochromator disperses Thomson spectra, and suppresses stray light and Rayleigh spectra. The monochromator consists of four camera lenses ($f=135$ mm, $F/2.8$), two gratings (50 mm \times 50 mm, 1800 lines/mm) as shown in Fig. 2. The first grating produces dispersed Thomson spectra in the image plane, where a spatial filter, called Rayleigh-block, is located and filtered out the stray light and Rayleigh scattering spectra. Reciprocal linear dispersion of the monochromator for 532 nm is determined to be 1.57 nm/mm at the photocathode, corresponding to 0.020 nm per pixel of the CCD. Wavelength resolution, which is evaluated in full width at half maximum (FWHM) of the line spectra, is 0.13 nm for the slit width of 0.085 mm.

Then width of the Rayleigh block, 0.35 mm, consequently determines lower limit of measurable Doppler broadening of Thomson spectra as 1.34 nm, which corresponds to the electron temperature of 0.29 eV.

In order to check the system performance, the present laser Thomson scattering measurement is being performed in relatively higher density plasma, near plasma source region of the MAP-II device. Thomson scattering spectrum observed in a helium plasma gives the electron temperature of 7.8 ± 0.8 eV and electron density of $5.7 \pm 0.6 \times 10^{12}$ cm⁻³, respectively. When hydrogen gas is puffed into the helium plasma, on the other hand, phenomenon called “density roll over” associate with the plasma recombination is observed. Relationship between the phenomenon and hydrogen molecular assisted/activated recombination (MAR) will be investigated in our future work.

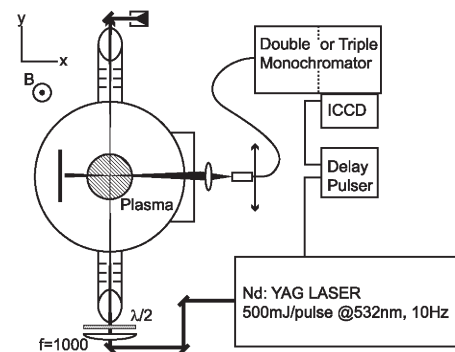


Fig. 1. Schematic drawing of experimental setup perpendicular to plasma column.

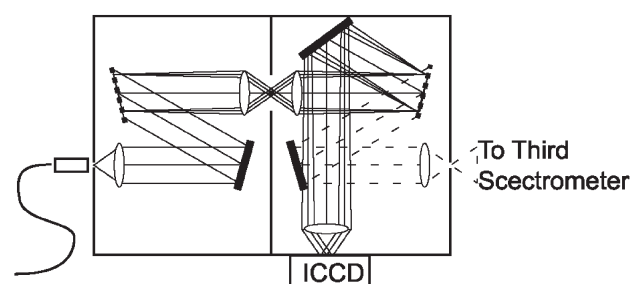


Fig. 2. Optical arrangement of a double-monochromator.

Reference

- 1) Ohno, N. et al. : Contrib. Plasma Phys. 41 (2001) 473
- 2) Kobayashi, H. et al. : Jpn. J. Appl. Phys. 42 (2003) 1776
- 3) Kado, S. et al. : J. Nuclear Mat. 313-316 (2003) 754

§19. Diagnostics of Plasma with Negative Ions Using the Eclipse Laser Photodetachment Method in Divertor Simulator MAP-II in the Univ. Tokyo (NIFS04KOAB009)

Kado, S., Kajita, S. (Univ. of Tokyo)

A probe-assisted Laser photodetachment (LPD) method has been applied for the measurement of negative ions in linear divertor plasma simulator MAP-II in the University of Tokyo.¹⁾ We have revealed that the probe surface adsorbates released by the irradiation of a laser pulse can disturb the measurements.²⁾

For the purpose of avoiding this probe surface ablation, we have proposed a method, "eclipse" laser photodetachment method (Eclipse-LPD) (Fig. 1).³⁾ The name comes from the lunar eclipse in which shadow of the earth (wire) protects the moon (probe) from direct irradiation of the sunlight (laser beam).

Moreover, the method yields direct measurement of sheath thickness around the probe tip and the minimum laser diameter to supply photo-detached electrons, which is often referred to as "collection region of photo-detached electrons", which are important in validating the applicability to magnetized plasmas.

The MAP-II consists of a dc arc source, a source chambers for differential evacuation and a target chamber.

The electron density n_e and the temperature T_e at the center of the plasma column in the target chamber are about 10^{12} cm^{-3} and 5 eV, respectively, while those at the peripheral region ($r \sim 5 \text{ cm}$) are about 10^{11} cm^{-3} and 1 eV, respectively.

Temporal evolutions of the excess electron current for conventional LPD and Eclipse-LPD are compared in Fig. 1(b). Shift of the peak position corresponds to the travel time of the photo-detached electron swarm to the sheath edge across the shadow region. Therefore, the sheath width can be estimated from the waveform.

By making use of the waveform of the Eclipse-LPD signals, we can evaluate the sheath thickness around the probe in three independent ways. Details of this method are described in ref. 4. The electron sheath thicknesses deduced from the three processes are plotted in Fig. 2. These values show good agreement with each other. The theoretical sheath thicknesses using Child-Langmuir (CL) law for plane-parallel and cylindrical geometry are also plotted in Fig. 2. The experimental values are much thicker than that calculated based on the cylindrical CL theory, and close to

that base on the plane-parallel CL theory, especially at the probe-bias voltage higher than about 50 V.

This result suggests that the shape of the sheath is distorted by the magnetic field and that it behaves more as plane probe rather than cylindrical one, although the field is not so high.

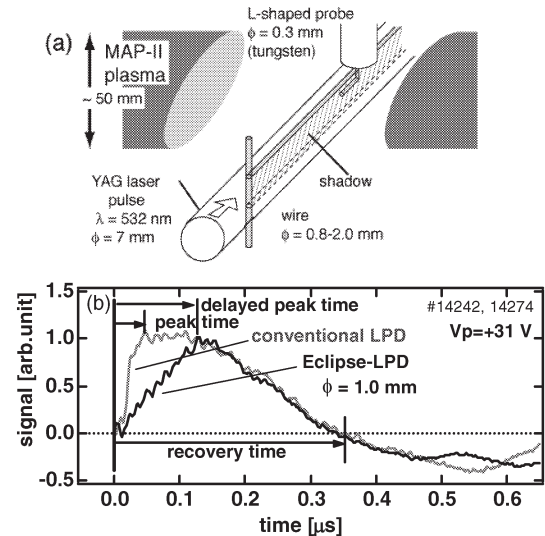


Fig. 1 (a) Schematic view of experimental setup for Eclipse-LPD. (b) Waveforms of the signal from conventional and Eclipse-LPDs.

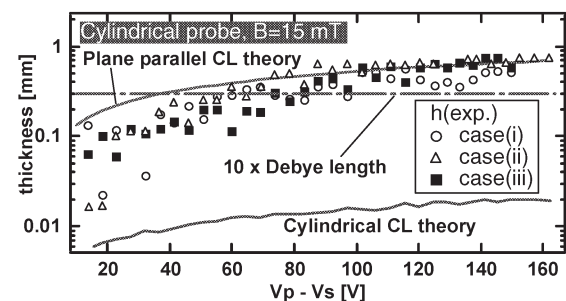


Fig. 2. Thickness of the electron sheath around a cylindrical probe at 15 mT, deduced from independent ways, (i), (ii) and (iii). Theoretical thicknesses of plane-parallel C-L sheath and cylindrical C-L sheath (solid lines) and Ten times the Debye length (dashed line) are plotted for comparison. Diameter of the wire used is 2 mm.

Reference

- 1) Kado, S. et al. : J. Nuclear Mat. 337–339 (2005) 166
- 2) Kajita, S. et al. : Contrib. Plasma Phys. 44 (2004) 607
- 3) Kajita S, et al. : Phys. Rev. E 70 (2004) 066403
- 4) Kajita S, et al.,: Plasma Sources Sci. Technol. 14 (2005) 566

\$20. Study on Effects of Bending Strain to Critical Current Characteristics of Nb₃Al CIC Conductors

Tamai, H., Kizu, K., Tsuchiya, K., Shimada, K., Matsukawa, M., Koizumi, N., Okuno, K., Ando, T. (JAERI) Miura, Y.M. (Osaka Univ.) Nishimura, A., Hishinuma, Y., Yamada, S., Takahata, K., Seo, K.

Nb₃Al is one of attractive materials for the strand of superconducting coil. The critical current (I_c) of Nb₃Al strand is decreased by strain. In cable-in-conduit conductor (CICC), strands suffer thermal and bending strain. However, no decrease of I_c by bending strain of 0.4% was observed for a Nb₃Al D-shaped coil made by react-and-wind (R&W) method in the R&D campaign for the National Centralized Tokamak. The same tendency was also observed in the Nb₃Al-insert coil manufactured for ITER. Those observations indicate that some relaxation of bending strain in strands can be expected due to cabling effect. In order to evaluate such an effect in CICC, the effect of tensile and compressive strains on a strand and the relaxation effect of strain on strands in the CICC were investigated. It is of also great importance to clarify the maximum attainable bending strain in R&W method for the manufacturing of advanced large helical coils.

Nb₃Al strand manufactured by jerryroll process was 0.74 mm in diameter with a Cu/non-Cu ratio of 4.05. In order to investigate the behaviour of I_c by the tensile/compressive strain and the bending strain, three types of the test sample are planned. For the dependence on tensile/compressive strain, two samples are produced this year. One is Nb₃Al strand wound around the spring-shape holder (strand sample). The other is two Nb₃Al strands and one Cu wire inserted into a stainless steel conduit wound around the spring-shape holder (triplex CIC sample). For the dependence on bending stress, 54 Nb₃Al strands and 27 Cu wires contained in a stainless-steel conduit and formed in a spring-shape (CIC conductor sample) will be prepared next year.

Figure 1 illustrates the schematic setup of the test apparatus produced this year, for the measurement of I_c -characteristics against the various range of stress at 4.2 K in the presence of the external magnetic field. Stress is loaded through the shaft, by which an external twist force is converted to tensile/compressive stress in the strand sample and the triplex CIC sample, and to bending stress in the CIC conductor sample. The spring-shape holder with a diameter of 82 mm consists of 4.5 turns spiral winding, made of

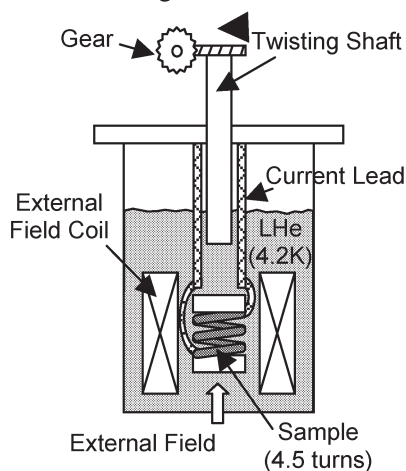


Fig.1 Schematic setup of the test apparatus.

beryllium-copper alloy not to yield against the strain of about 1%. FEM structural analysis is performed to estimate the stress loaded on the holder and the samples. In the holder the strain at the inner surface of the spiral is 20% larger than that at the outer surface. The longitudinal stress profile is almost the same between turns although there appears the difference within 5% in each turn. The torsion strength of the holder is experimentally investigated by the tension test on the test sample after the heat treatment. Based on the test results, summarised in Table 1, the maximum available tensile strain estimated by $\sigma_{0.2}/E$ is 0.92% at the inner surface and 0.76% at the outer surface.

Table 1 Mechanical characteristics of the test sample

	RT	4.2K
Young's modulus E (GPa)	134	144
0.2% proof stress $\sigma_{0.2}$ (MPa)	1120	1320
Tensile strength σ_u (MPa)	1269	1534

The I_c of the strand sample against the strain is measured at 4.2 K in the range of magnetic field from 6 to 11 T. The I_c is defined as the current measured when the voltage of 0.1 μ V/cm is detected between each divided segment of central one turn (4 segments here). Figure 2 shows the dependence of I_c on the strain for each segment. The I_c shows almost the same tendency against the strain, and the maximum I_c is observed at 0.12% strain, at which the net strain would be cancelled out. It is considered that the Nb₃Al filament suffers the compressive strain due to the difference in thermal contraction between the holder or stabilising Cu and the Nb₃Al filament. Therefore, it corresponds to the real strain range from -0.86% to +0.18%. Based on the measured I_c of strand sample, relation of the I_c and the strain in the CIC conductor sample will be precisely analysed next year.

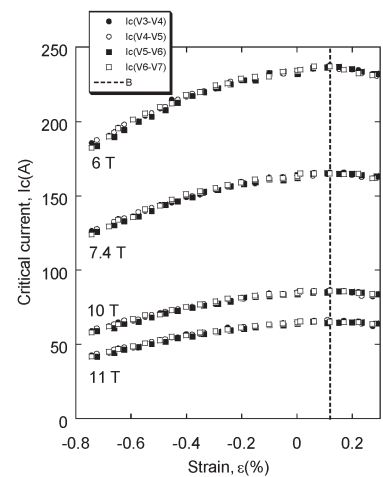


Fig.2 Dependence of I_c on the strain in each segment of the turn.

Reference

- 1) Kizu, K., 20th IAEA Fusion Energy Conference (Nov. 2004, Vilamoura, Portugal) IAEA-CN-116/FT/P1-6.
- 2) Kizu, K., to be presented at 19th International Conference on Magnet Technology (Sep. 2005, Genova, Italy).

§21. Change in Properties of Superconducting Magnet Materials by 14 MeV Neutron Irradiation under Cryogenic Temperature

Nishijima, S. (Osaka University)

Neutron streaming from NBI ports is expected on the design of ITER and DEMO reactor. To investigate the neutron irradiation effect on the superconducting magnet, a new cryogenic target system was installed at FNS in JAERI. In September of 2004, the first irradiation test was carried out at FNS for three weeks and additional test was performed in March, 2005, for one week.

In this report, the outline of the cryogenic target system is described and some test results are presented.

The fusion neutron source (FNS) in JAERI has a capability to produce 14 MeV neutron at the rate of 3×10^{12} n/s. A new facility to carry out irradiation test at cryogenic temperature was installed in FNS, which consists of a GM refrigerator and a thermo-control system. Temperature of the second stage was controlled at 4.5 K during 14 MeV neutron irradiation. On the cold stage, the following five samples were attached.

1. Tough pitch copper wire (0.28 mm ϕ)
2. Oxygen free copper wire (0.299 mm ϕ)
3. Nb₃Al wire (As-RHQ. 0.79 mm ϕ)
4. Nb₃Al wire (RHQ + annealed. 0.79 mm ϕ)
5. Nb₃Sn wire (0.70 mm ϕ)

Copper wires were irradiated and change in resistivity was measured. Two Nb₃Al wires were prepared. One was rapid heated and quenched (RHQ). The other was annealed at 1073 K for 10 hours after RHQ. Critical temperature of these wires was 13.8 K for the RHQ sample and 18.3 K for the RHQ + annealed sample. The temperature of the cold stage was measured with Cernox sensor and temperature was kept at 4.5 K. Two Cernox sensors were attached at location of 57 mm far to compare the irradiation damage.

On the top of cryostat, the following samples were attached as shown in Fig. 1.

1. Glass Fiber Reinforced Plastic (GFRP, G10-CR)
2. Polystyrene powder. (Molecular size was selected)
3. TEM samples of Nb₃Sn and NbTi wires.

GFRP samples are three-point tested after irradiation and interlaminar shear strength is evaluated. Polystyrene powder, of which molecular size was selected, was irradiated and effect of 14 MeV irradiation was investigated.

The irradiation test was carried out twice in 2004 fiscal year. The first irradiation test was carried out from August 31 to September 17, 2004. Total neutron production was 5.35×10^{17} n/12 days and neutron fluence at the center of the cold stage was 1.47×10^{20} n/m². And the second irradiation test was carried out from March 7 to March 11, 2004. Total neutron production was 2.54×10^{17} n/5 days and neutron fluence at the center of the cold stage was 0.70×10^{20} n/m². Therefore, the total neutron fluence at the center of the cold stage in 2004 was 2.17×10^{20} n/m².

Results of critical temperature (T_c) measurement of Nb₃Al wires are shown in Fig.2. T_c was measured by rising up the temperature of cold head with heater at the rate of 0.1 K/min to 25 K. T_c of RHQ and annealed Nb₃Al wire did not change. (Difference of 0.1 K is considered to be within scatter range.) However, RHQ Nb₃Al wire showed clear degradation of T_c. It is recognized that T_c has strong relation with long range of ordering of A15 structure. Therefore, it is thought that the RHQ and annealed Nb₃Al wire has long range ordering and there may be many bypass lines to detour damaged area. On the other hand, in case of RHQ Nb₃Al wire, the ordering would not expand so widely and damaged area might disturb the superconducting current running, and it results in the decrease of T_c.

Other remarkable results would be as follows: (1) T_c of Nb₃Sn wire did not change after irradiation. (2) Resistivity of copper wires increased, and there is good relation between increment of resistivity and displacement per atom converted from neutron fluence. (3) Cernox sensors could endure the irradiation of at least 9.29×10^{19} n/m². (4) When polystyrene powder was irradiated, decomposition and polymerization happened. The molecular size distribution became broader and another peak appeared at the larger molecular region.

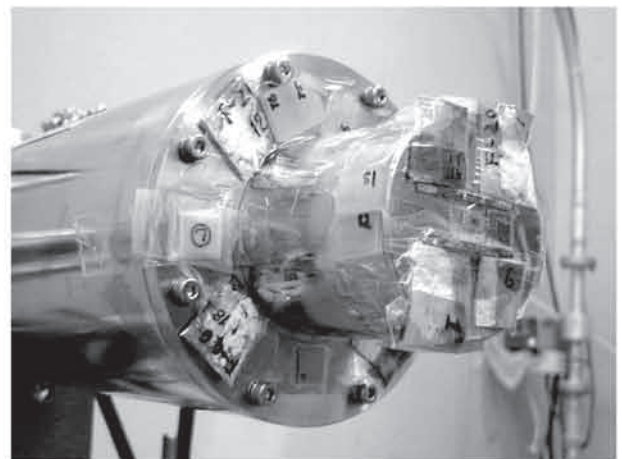


Fig. 1 Set up of samples on cryostat of GM refrigerator. (August 31, 2004)

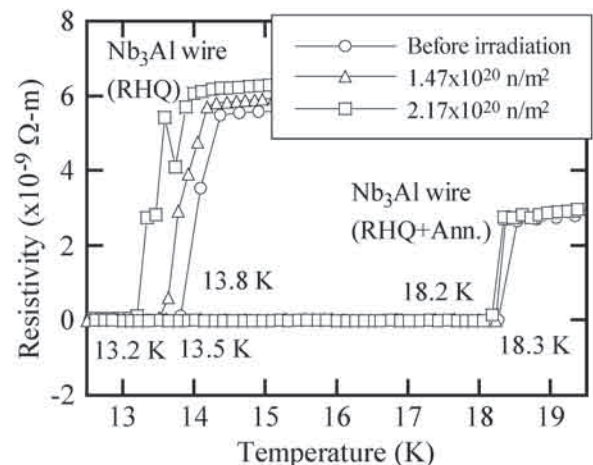


Fig. 2 Change in T_c of Nb₃Al wires before and after neutron irradiation.

§22. Development of New High Field and High Current Density Superconductors for Fusion Devices

Tachikawa, K., Koyata, Y., Nakaze, T. (Faculty of Engr., Tokai Univ.), Mito, T.

Excellent high-field performance capable of generating $\sim 20\text{T}$ at 4.2K has been reported for $(\text{Nb,Ti})_3\text{Sn}$ conductors fabricated by bronze process and internal tin process. However, in these processes residual bronze reduces the overall critical current density J_c of the conductors. Improved overall J_c might be expected when a Nb_3Sn conductor could be fabricated from a Sn-based alloy/Nb composite. Present authors recently revealed that a Sn-Ta alloy with ductility can be synthesized by reacting a mixture of Sn+Ta powder containing $\sim 30\text{at}\%\text{Ta}$. Then $(\text{Nb,Ta})_3\text{Sn}$ wires with attractive performance at 22T and 4.2K were fabricated through a Jelly Roll(JR) process using Sn-Ta-(Cu) and Nb sheets¹⁾. Ta in the Sn-Ta sheet is incorporated into the Nb_3Sn layer improving the high-field performance, while a small amount of Cu addition to the sheet reduces the reaction temperature of the wire. In the present study, the relation between J_c in high fields and structure of the $(\text{Nb,Ta})_3\text{Sn}$ wires has been studied. Subsequently a preliminary study for the fabrication of long-length $(\text{Nb,Ta})_3\text{Sn}$ wires through the JR process has been performed.

Sn-Ta alloys with Sn/Ta ratio of 7/3 and 3/1 with 2.5wt% and 5wt%Cu addition were melted at 800°C for 10h in vacuum. The melted Sn-Ta-Cu button, typically 30gr. in weight, was pressed into a plate and flat rolled into a sheet $100\mu\text{m}$ in thickness. For the fabrication of longer length wire bar-shaped alloys, 180gr. in weight, have been prepared. Fig.1 illustrates Sn-Ta-Cu specimens of different form prepared in the present study. The Sn-Ta-Cu sheet was laminated with a Nb sheet of the same thickness, and wound around a Nb-3.3at%Ta rod. The resulting JR composite was encased in a Nb-3.3at%Ta tube and then fabricated into a wire 1.40mm in diameter. The resulting wires were heat treated at $700\text{--}800^\circ\text{C}$ for 80h in vacuum.

Fig.2 shows the critical current I_c and non-Cu J_c versus heat treatment temperature of the 7/3+2.5Cu sheet wire at different magnetic fields. At 22T the maximum I_c is obtained after the reaction at 775°C . A non-Cu J_c of $\sim 100\text{A}/\text{mm}^2$ is achieved at 22T and 4.2K . The reaction temperature where the maximum I_c is obtained is lowered with decreasing applied field reaching 725°C at 16T . Then, average grain size of $(\text{Nb,Ta})_3\text{Sn}$ was evaluated in parallel (parallel to the diffusion direction, i.e. perpendicular to the sheath) and perpendicular direction by scanning electron microscope study. These are $0.66\mu\text{m}$ and $0.53\mu\text{m}$ at 725°C , and $0.99\mu\text{m}$ and $0.61\mu\text{m}$ at 775°C , respectively. The grain boundaries are considered to be major flux pinning centers at lower fields in

A15 phase. The shift of the optimum reaction temperature with decreasing field shown in Fig.2 may be related to the change of $(\text{Nb,Ta})_3\text{Sn}$ grain size.

For practical application, superconducting wires should be embedded in a Cu stabilizing matrix. Then a preliminary study was performed for fabricating the JR composite where a Cu tube was used instead of a Nb-3.3at%Ta tube described before. The reaction between the Cu stabilizer and the Sn-Ta-(Cu) sheet during the heat treatment may be avoided when an extra Nb sheet is wound in the outer-most layer of the JR composite. The resulting JR composite with outer Cu stabilizer has been successfully fabricated providing a positive prospect for producing long-length practical $(\text{Nb,Ta})_3\text{Sn}$ wires.

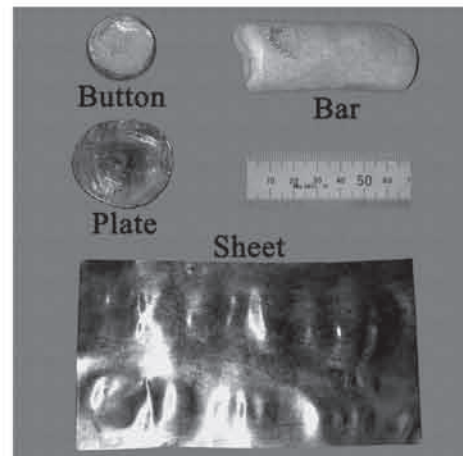


Fig.1 Sn-Ta-Cu specimens in different forms.

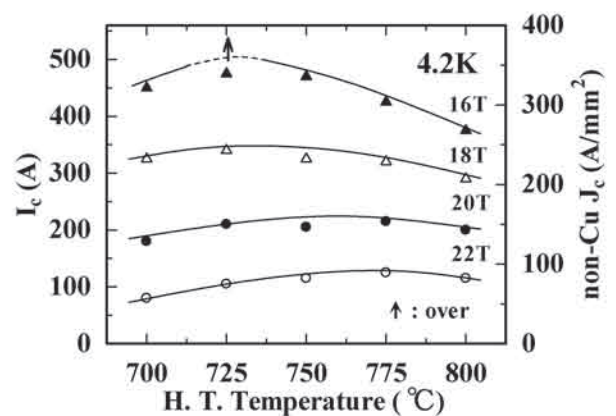


Fig.2 I_c and non-Cu J_c versus heat treatment temperature of the 7/3+2.5Cu sheet wire at quoted magnetic fields.

Reference

1) Tachikawa, K. et al: Fabrication of High-Field $(\text{Nb,Ta})_3\text{Sn}$ Conductors through Jelly Roll Process, Adv. Cryogenic Engineering, Vol.50(2004) pp387-394.

§23. Stability of Superconducting Coil with Various Surface Conditions in Pressurized He II

Shiotsu, M., Shirai, Y., Ohya, M. (Kyoto Univ. Ene. Sci.)
Imagawa, S.

Stability tests were carried out with two superconducting coils wound with a bare wire on a G-FRP bobbin (Coil-I), and with a surface oxidized wire on a G-FRP bobbin (Coil-II). The first wire is a 0.50 mm-diameter NbTi/Cu composite bare wire with the copper ratio of 1.3. The second is the same wire with a chemically oxidized copper surface. The schematic illustration of the test coil is shown in Fig. 1. Each superconducting wire is wound about 30 turns around the bobbin respectively. The wire is fixed in the groove on the bobbin only with tension. A manganin insulated heater is buried inside the bobbin. Experiments were performed according to the following procedure. 1) Set up a fixed external magnetic field and the constant current to the test coil. 2) Give the pulsed heat input by use of the heater to cause a bud of normal transition in the wire. 3) Measure the tap voltages and the temperature signals along the wire to know the behavior of the normal zone propagation. The tests were performed for the magnetic flux densities, B , from 1.1 T to 7.6 T and the bulk liquid helium temperatures, T_b , from 1.6 K to 4.2 K.

Characteristics of the normal zone propagation are classified into the following three groups depending on the magnetic flux density and the test coil current, I . (Group I) The normal zone is generated only around the heater as soon as the heat input was applied to the wire. After shutting off the heat input, the wire recovers to the superconducting state. (Group II) As shown in Fig. 2(a), the generated normal zone does not shrink even after shutting off the heat input. The normal zone neither spreads nor shrinks, that is, a stationary normal zone is observed. (Group III) As shown in Fig. 2(b), the tap voltages arise one after another. The normal zone continues to spread through each of the taps until a quench protection circuit shuts off the test coil current. Additionally, the wire temperature continues to rise up sharply. It means that the heat transfer on the wire surface shifts to the film boiling.

We define the recovery current I_R as the largest current for which a normal zone will automatically disappear, and the film-boiling current I_F as the smallest current with which the heat transfer on the wire surface in normal state will shift to film boiling regime. Fig. 3 shows the stability test results at $T_b = 4.2$ K and 2.0 K. I_F for both coils at a certain magnetic field increase greatly by shifting to He II cooling from He I cooling. The difference between I_F of Coil-I and that of Coil-II at 2.0 K is small since the critical heat flux (CHF) on a wire surface in He II hardly depends on the wire surface condition. However, the difference between I_R of Coil-I and that of Coil-II becomes very large. Even if a stationary normal zone occurs, the coil will not quench. However, the wire cannot recover to the

superconducting state unless the transport current is lowered to less than I_R . The stationary normal zone will deeply affect the stability of a superconducting coil immersed in He II. The stationary normal zone originates from lower T_c of NbTi at higher magnetic field, and it is observed for larger current area with decreasing the Kapitza Conductance on the wire surface^{1,2)}. Making the Kapitza conductance as large as possible is important in order to make the effective use of the high CHF of He II and improve the stability of a superconducting coil immersed in He II.

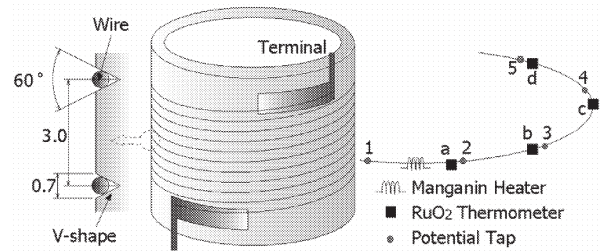


Fig. 1 Schematic illustration of test coil and test part

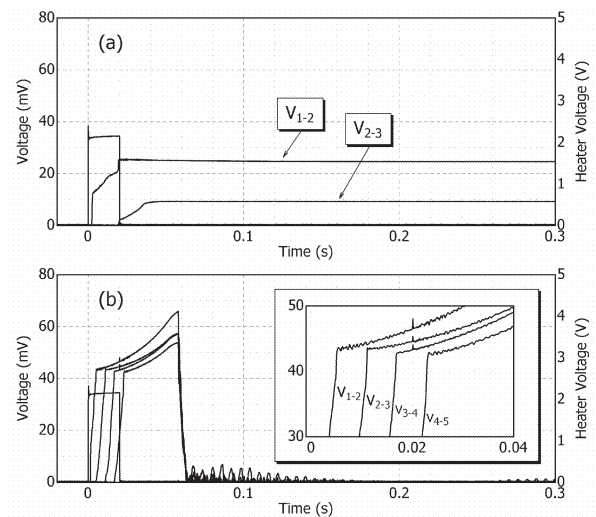


Fig. 2 Typical waveforms of the voltages for Coil-II at $T_b = 4.2$ K and $B = 7.2$ T. (a) $I = 130$ A, (b) $I = 152$ A

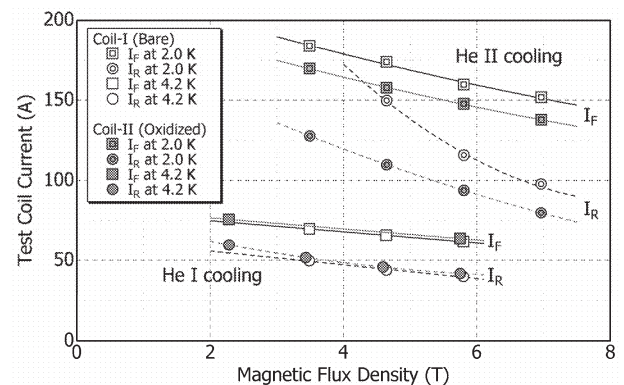


Fig. 3 Stability test results at $T_b = 4.2$ K and 2.0 K

Reference

- 1) Ohya, M. et al.: IEEE transactions on Applied Superconductivity **15** (2005) p.1703-1706.
- 2) Shigemasu, S. et al.: IEEE transactions on Applied Superconductivity **15** (2005) p.1707-1710.

§24. Suitability of Boron-titanium as First Wall Material

Hino, T., Hashiba, Y. (Hokkaido Univ.)
Nishimura, K., Ashikawa, N., Masuzaki, S., Sagara, A., Noda, N., Ohyabu, N., Komori, A.

Boron and titanium have been employed to control fuel hydrogen recycling and oxygen impurity level in plasma. If both boronization and titanium flash are used, the boron-titanium is produced on the first wall. The fuel hydrogen retention of this material has not been studied so far. In the present experiment, the boron-titanium was prepared using electron beam evaporation, and irradiated by deuterium ions. After the deuterium ions irradiation, the deuterium retention and desorption behavior was investigated.

The boron-titanium was prepared by the titanium deposition followed by the boron deposition on stainless steel substrate. The annealing at 1000 K was conducted to mix the boron and the titanium. Figure 1 (a) shows the depth profile of atomic composition. The boron concentration was approximately twice of the titanium concentration at the surface. The boron-titanium was irradiated by deuterium ions with energy of 1.7 keV and fluence of $1 \times 10^{18} \text{ D/cm}^2$ at RT. Figure 1 (b) shows the depth profile of atomic composition after the deuterium ion irradiation. The boron rich layer with a thickness of 20 nm was sputtered.

The boron-titanium irradiated was transferred to the chamber of thermal desorption spectroscopy. Here, the sample temperature was increased to 1100 K, and the deuterium desorbed during the heating was measured. In order to compare the retention and desorption behavior with cases of titanium and boron, the similar experiments were conducted for both titanium and boron films prepared by electron beam evaporation.

Figure 2 shows the desorption spectra of deuterium for boron, titanium and boron-titanium films. The scale for titanium in this figure is 1/20 of the actual value. The desorption peaks of the boron-titanium were 500 K and 600 K. The former peak corresponds to the de-trapping of deuterium from B-D-B bond, and the later one from Ti-D bond. It is seen that the desorption temperature was lower than those of the boron and the titanium. The deuterium amount retained in the boron-titanium was 1/2 in the boron and 1/3 in the titanium.

The present results indicate that the use of boron-titanium reduces the fuel hydrogen retention and the baking temperature for reduction of hydrogen retention becomes low.

Further study on the relation of fuel hydrogen retention in the boron-titanium with the structure will be conducted.

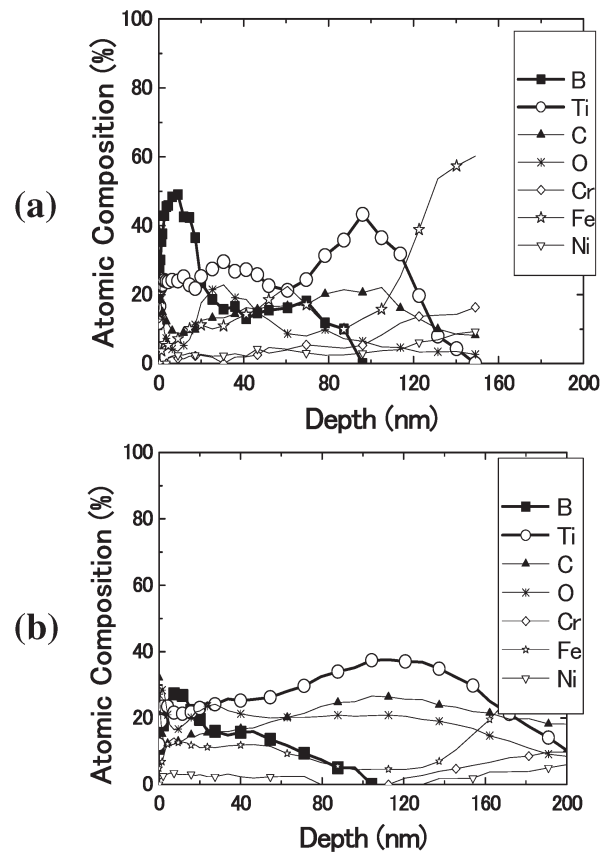


Fig. 1 Depth profiles of atomic composition after annealing (a) and after deuterium ion irradiation (b).

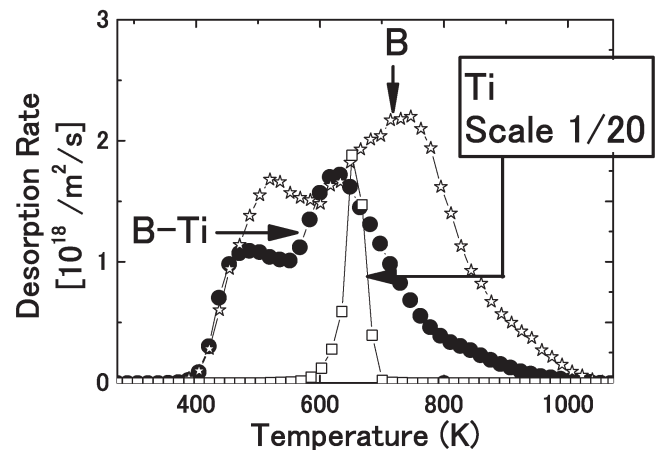


Fig. 2 Thermal desorption spectra of deuterium after deuterium ion irradiation for boron-titanium (B-Ti), boron (B) and titanium (Ti).

Reference

- 1) Hino, T., Hashiba, Y. et al, To appear in Fusion Eng. and Design, (2005)

§25. Measurement of the Negative Ion and Control of Recombination Plasma in the LHD Divertor

Tonegawa, A., Shibuya, T., Kawamura, K. (Dept. Phys. Tokai Univ.)
Masuzaki, T., Sagara, A., Ohya, N.

The detached plasma is a very complex phenomenon with atomic and molecular collision processes. Recently, we have presented the experimental observation of the spatial structure of MAR in the detached hydrogen plasma at the periphery of the plasma on the linear divertor plasma simulator, TPD-SheetIV[1]. It is shown from the results of mass-analysis (H^+ , H_2^+ , H_3^+) that dissociative recombination is dominant in the center of the plasma over a range of low gas pressures [2]. At the same time, it is observed that the mutual neutralization in MAR via H^- ion formation, which is produced by dissociative electron attachment to $H_2(v)$, occurs in the periphery of the plasma where cold electrons (~ 1 eV) are found. In other words, H^- ions play an important role in the mutual neutralization of MAR, providing a new method of controlling detached plasmas. In this report, we have developed a new method to control a detached plasma based on utilizing H^- ions which are formed as part of the MAR mutual neutralization process occurring in the periphery of the plasma [3].

The experiment was performed in the linear divertor plasma simulator TPD-SheetIV. Ten rectangular magnetic coils formed a uniform magnetic field of 0.08 T in the experimental region. The neutral pressure P_{Div} in the divertor test region was controlled between 0.1 and 20 mtorr with a secondary gas feed. The heat load on the target plate Q was measured by a calorimeter. At a discharge current of 100 A, the value of Q reaches about 1 MW/m². A cylindrical probe made of tungsten was used to measure the spatial profiles of the negative hydrogen ion density by a probe-assisted laser photodetachment method. At a repetition rate of 50 Hz, the Nd-YAG laser had an energy per pulse of 100 mJ.

The concept of control of a detached plasma using negative ions can be illustrated through the following steps; (1) measure the experimental data related to the minimum and maximum basic parameters (gas pressure P_{Div} , heat load Q) in order to determine for controlled region, (2) control the secondary gas-flow rate G_{Div} rapidly so as to maximize the value of the negative ion density n_{H^-} , (3) carry out a real time feedback control in order to maintain a steadily

detached plasma in the neighborhood of the target plate.

By defining Q_{att} as the heat load in attached plasma and Q_{pm} as the heat load at the maximum negative ion density for a particular pressure n_{H^-max} , we can express the reduction of the heat load as the ratio of Q_{att} to Q_{pm} , that is, $\Delta Q = Q_{pm}/Q_{att}$. The variations of n_{H^-max} , heat load Q_{att} , Q_{pm} , and the heat load ratio ΔQ with the discharge current I_d is shown in Fig. 1. As I_d changes from 50 to 100 A, Q_{att} increases from 0.32 to 1.1 MW/m². At the same time, n_{H^-max} increases linearly from 1.8 to 5.1 $\times 10^{16}$ m⁻³ and Q_{pm} increases from 0.1 to 0.4 MW/m². Therefore, ΔQ remains nearly constant at around 30-40 % with increasing the heat load to the target. These results indicate that this new way of controlling a detached plasma, based on the feedback control of the negative hydrogen ion density in the high density part of the plasma, is promising. The new system has achieved the goal of reducing the target heat flux while simultaneously minimizing the amount of gas puffed in a detached plasma without radiative and three-body recombination processes.

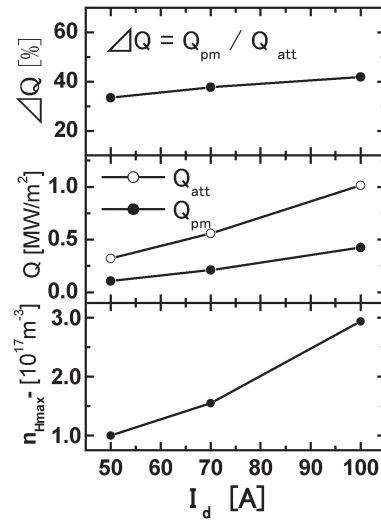


Fig.1 The variations of n_{H^-max} , heat load Q_{att} , Q_{pm} , and the heat load ratio ΔQ with the discharge current I_d .

Reference

- 1) H.Ogawa, K.Kumita, M.Ono, A.Tonegawa, T.Shibuya and K.Kawamura, J. Plasma Fusion Res.SERIES, **6** (2004) 453.
- 2) M.Ono, K.Kumita, A.Tonegawa, T.Shibuya and K.Kawamura, J. Plasma Fusion Res. SERIES, **6** (2004) 457.
- 3) M.Ono, A.Tonegawa, K.Kumita, T.Shibuya, and K.Kawamura, J. Nucl. Mater. **337-339** (2005) 264.

§26. Kinetics of Hydrogen Isotopes at Surfaces and Bulks of Plasma Facing Materials Based on Group 5 Metals

Hatano, Y., Hara, M. (Toyama Univ.), Hashizume, K. (Kyushu Univ.), Saito, H., Homma, H. (Muroran Inst. Tech.), Suzuki A. (U. Tokyo), Hirohata, Y. (Hokkaido Univ.), Nita, N. (Tohoku U.), Ashikawa, N., Nagasaka, T., Sagara, A., Muroga, T., Nakamura, Y.

Group 5 metals including V are candidate materials for superpermeable membranes used to pump the fuel particles in edge plasma. In addition, V alloys have attractive mechanical and nuclear properties as structural materials of fusion blankets. From these viewpoints, the interactions of hydrogen plasma and gas with pure V and V alloy were investigated by several different experimental techniques.

The regime of *superpermeation* is achieved by the strong suppression of reemission of incident hydrogen particles by non-metallic surface impurities such as oxygen and sulfur. In other words, removal of surface impurities by sputtering leads to the reduction in permeability. Therefore, the durability of V superpermeable membrane under sputtering was examined by the permeation device described elsewhere¹⁾. Namely, the plasma-driven permeation rate of hydrogen was measured for a membrane of pure V (0.1 mm in thickness) at the bias voltage of 0 - 260 V and the incident ion flux of $0.6 - 1.2 \times 10^{19} \text{ m}^{-2}\text{s}^{-1}$. The temperature of the membrane varied with bias voltage owing to the change in energy deposition from plasma in the range from 430 to 560 °C. A typical result is shown in Fig. 1. It should be emphasized that no significant reduction in the permeation rate was observed even in the range of bias voltage above 100 V where the degradation of Nb membrane took place²⁾. This result indicates that non-metallic impurities removed from the surface by sputtering were compensated instantly by those segregated from the bulk in the temperature range examined.

Surface analysis by means of X-ray photoelectron spectroscopy (XPS) was carried out for a pure V specimen heat-treated in an ultra-high vacuum. It was shown that oxygen was the major surface impurity below 800 °C, while sulfur became dominant at 1000 °C. It appears that the sustained superpermeation under sputtering was due to the continuous surface segregation of oxygen from the bulk. Surface analysis after hydrogen ion bombardment, however, is necessary to derive a conclusion.

Interaction of hydrogen gas with the surfaces of V and V-4Cr-4Ti alloy (NIFS-Heat-2) was examined by absorption experiments. The details of experimental procedure are described elsewhere³⁾. In the case of V-4Cr-4Ti alloy, the sticking coefficients of H₂ and D₂ were markedly reduced by heat treatments at 700 °C for 1 h, whereas no significant change was observed for pure V at this temperature. Surface analysis by XPS showed that Ti in V-4Cr-4Ti alloy was segregated to the surface above 700 °C. In addition, the surface coverage of oxygen increased by

the surface segregation of Ti through preferential interaction between oxygen and Ti. The reduction in the sticking coefficients was ascribed to this increase in oxygen coverage. It was concluded that the interaction between V alloy and gaseous hydrogen is sensitively dependent on the heat treatment condition through the redistribution of Ti.

Trapping effects for hydrogen isotopes (tritium) absorbed in V-4Cr-4Ti alloy were shown by diffusion experiments below 250 °C. Observation of concentration distribution of tritium by imaging plate technique indicated that the distribution of trapping sites is also influenced by the fabrication process including heat treatment conditions.

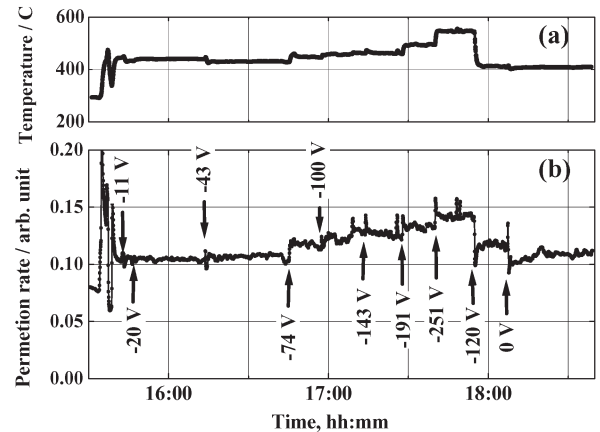


Fig. 1 Influence of bias voltage on membrane temperature (a) and plasma-driven permeation rate of hydrogen (b).

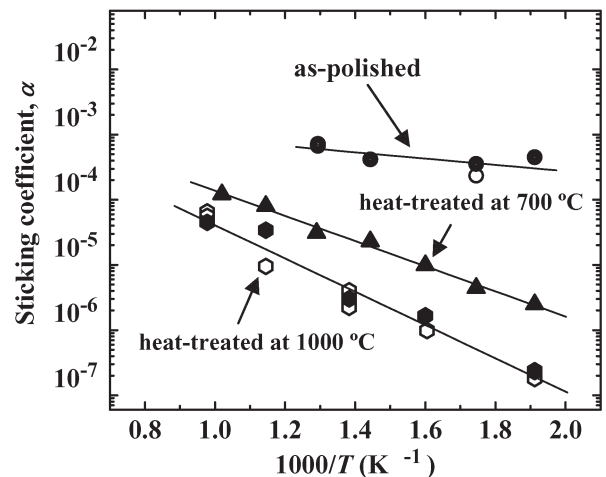


Fig. 2 Sticking coefficients of H₂ (filled symbols) and D₂ (open symbols) on surface of V-4Cr-4Ti alloy under different heat treatment conditions.

References

- 1) Hatano, Y. et al., Annual Report of Hydrogen Isotope Research Center, Toyama Univ. 21(2001)13.
- 2) Nakamura, Y. et al., J. Appl. Phys., 89(2001)760.
- 3) Hatano, Y. et al., Mater. Trans. 46(2005)511.

§27. Heat Removal Enhancement of Plasma-Facing Components by Using Nano-Particle Porous Layer Method

Kunugi, T., Kawara, Z., Okamoto, Y. (Dept. Nuclear Eng., Kyoto Univ.)
Shibahara, M. (Dept. Mech. Eng., Osaka Univ.)
Satake, S. (Tokyo Univ. of Sci.)
Hashizume, H., Yuki, K. (Tohoku Univ.),
Sagara, A.

i) Nano- and Microscale Porous Layer Experiment

Heat transfer enhancement is one of key issues of saving energies and compact designs for mechanical and chemical devices and plants. Until today people have made effort to enhance convective heat transfer by means of the surface enlargement using obstacles such as ribs and fins and the increase of flow turbulence. However, additional pressure losses increase with increases of introducing obstacles and turbulence.

An ultrahigh convective heat transfer performance compared to the well-known conventional heat transfer correlations caused by a nano-particle porous layer formed on the heat transfer surface was discovered: the maximum increase of heat transfer performance was around 160~180%. A nano-porous layer formed on the heat transfer surface by a chemical etching with some acids or alkalis including nano-particles can provide an ultrahigh convective heat transfer performance. This method was named as a “Nano-Particle Layered (NPL)” method. This nano-porous layer formed on the substrate was confirmed by a scanning electron microscope (SEM). Moreover, we developed a new porous layer fabrication technique, named a “Fine Precipitate (FP)” method. This porous layer also showed a good heat transfer performance, but this layer has a little weak feature because of the adhesion of the stains contained in the fluid flows. In order to examine the applicability of these methods to the real size heat exchanger, some experiments for a parallel flowing heat exchanger consisted of hot and cold water-channels making from an acrylic double open-ended box and a thin copper partition plate were conducted and got a very high performance: over 200% increase compared to the bare heat transfer surface. Combining two methods: NPL and FP, we develop a new “nano- and micro-scale porous layer surface (NMPLS)” method and confirm the heat transfer enhancement feature as same as that of NPL and FP methods.

In the present study, in order to investigate the temperature profile near the wall, we have made a small test channel: 500 mm in length, 50mm in width and 5mm in height as shown in Fig. 1 and have been conducting a fundamental heat transfer test for two cases: case-1) a bare copper plate was installed as the top wall with heating and the bottom wall is adiabatic, case-2) the top wall covered by the NMPLS or FP with heating. We used three types of thermometer: Platinum resistance thermometer, 25 and 250 μm thermo-couples, and measured the temperature profiles near the wall. Figure 2 shows the comparison of the temperature profiles between both cases. However, it is difficult to evaluate whether the effect of nano- and micro layer on the heat transfer is obvious or not. This is because

the thermal boundary layer could be too thin to realize the nano- and micro-scale porous layer effect. We are planning to make a larger test section at Kyoto University in 2005.

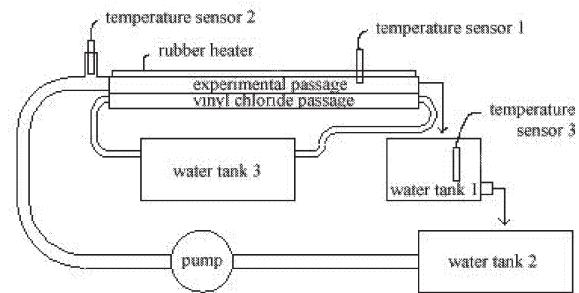


Fig.1 Preliminary heat transfer test section for nano- and micro-scale porous layer 1000.

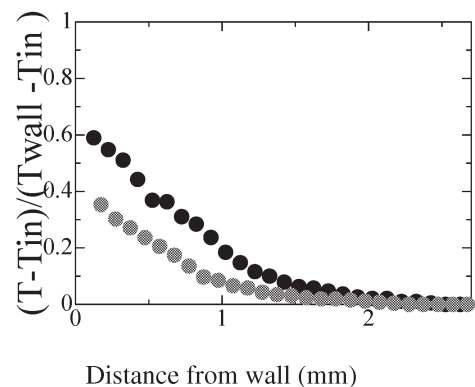


Fig.2 Normalized temperature distribution from the wall
Reynolds number is around 1000.

ii) Approach to the Mechanism of these phenomena

In order to investigate the mechanism of this ultra-high heat transfer process, we have been conducting the molecular dynamic (MD) simulation. Until today, the MD results show that the surface to be the maximum was not to be the maximum energy transfer because the fluid molecule could not flow in/out through such a very narrow clearance between the nano-scale obstacles. The results suggest us the effect of the nano-structure on the thermal properties of the fluid could be large.

As for the macro-scale simulation via a direct numerical simulation, we have examined several types of wall conditions such as low friction wall. However, it is not clear to clarify the effect of the low friction on the heat transfer. It would be necessary to develop a new type wall boundary condition to match the experimental results.

iii) Experiment of Molten Salt Flow and Heat Transfer

In order to investigate the enhancement of the molten salt for the FFHR application, we have reconstructed the TNT-loop at Tohoku University to keep the experimental area and make a test section. The basic experiment has been conducting to check the loop performance such as ordinary heat transfer test and pressure drop measurement.

\$28. Investigation of Tritium Behavior and Tracability in In-vessel Systems of LHD during D-D Burning

Tanabe, T. (Nagoya University), representative of cooperation program with 24 participants

Tritium produced by D-D reactions is a safety concern in deuterium discharges planned in LHD. In this work, behavior of hydrogen isotopes in large tokamaks have been studied from literature and also examined experimentally. Recent studies clearly show that tritium produced by DD-reaction behaves quite different way from hydrogen isotopes (hydrogen (H), and deuterium (D)) and even tritium (T) fueled into the tokamaks.

Fig. 1 is an example to see how differently T was retained in carbon tiles of ASDEX-Upgrade divertor compared to the retention of D used for discharges.¹⁾ As well know, most of D was retained in carbon deposited layers on the baffle plate and divertor target tiles of the inner divertor, while D retention in the outer divertor area was quite small. On the other hand higher T retention was observed on the dome top tile and the outer baffle tiles. This is because T produced by D-D reaction did not fully lose its initial energy of 1MeV and implanted into a depth of more than 1 μ m.

Recent simulation shows around 40% of produced tritium could be implanted without fully losing its initial energy through ripple-loss mechanism even in a DT reactor.²⁾ Actually, toroidal tritium distribution in JT-60U clearly shows the ripple loss due to toroidal field inhomogeneity.³⁾ Although the cross section for D-D reaction is below 1/10 of that for D-T reaction, tritium produced by the D-D reaction (around 1/200-1/500 of the produced neutron amount in a D-T reactor) might be a serious concern because it can reach deeper regions in the plasma facing materials and is difficult to remove compared to the tritium absorbed or codeposited on the surface or near surface layers. In fact, tritium retention in deeper regions than hydrogen and deuterium was confirmed in graphite tiles used in TEXTOR³⁾ and JT-60U.⁴⁾ Remaining 60% must be thermalized to plasma temperature and also injected to plasma facing surface. However, T retained very near surface must be always replaced by D coming from the succeeding plasma discharges. Accordingly T is not likely retained in very near surface.

Thus, nearly a half of tritium produced by D-D reaction in LHD is always pumped out as a quite diluted gas with D and hydrocarbons during discharges, and the latter half is likely implanted directly to the plasma facing materials and only small amount of tritium would be released after the discharges.

Therefore, we have to think about two points.

- 1) How to recover or remove diluted T in exhausted D gas during discharge, if it is necessary.
- 2) How to remove tritium implanted rather deep (more than 1 μ m) in the plasma facing wall.

This is very important for the ventilation of the LHD torus to keep people going into the vacuum vessel safe.

The amounts of the retained tritium in the vessel will be strongly modified by temperature and plasma facing materials. The high energy tritium is implanted deeply with quite low concentration compared to the highly concentrated hydrogen co-depositions; the former is likely trapped strongly and hard to remove. If we could keep the temperature of the deposited area above 800 K, tritium inventory may be reduced significantly. However, LHD can not be baked at such a high temperature.

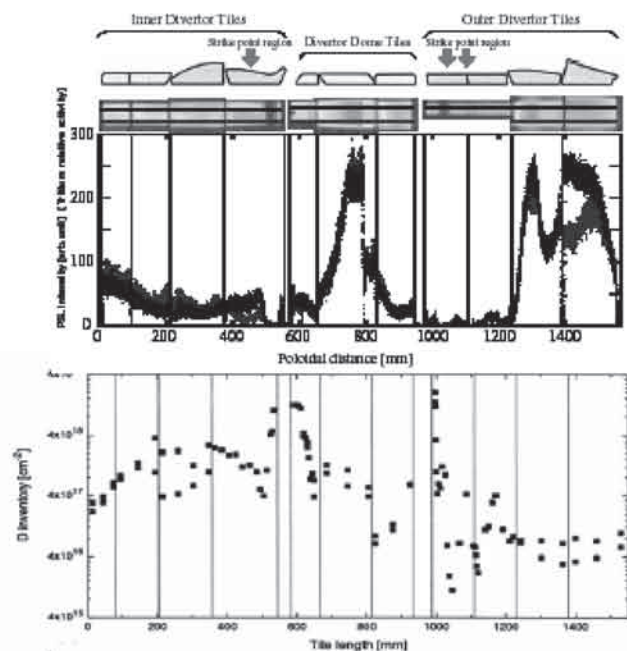
All above results are for tokamaks using carbon as a plasma facing material. In LHD, large part of PFM is composed of stainless steel, in which hydrogen solubility is less and hydrogen diffusivity is larger than those in carbon. Nevertheless, most of tritium having its initial energy of 1MeV is not thermalized in LHD plasma but implanted into plasma facing surfaces. Hence behavior of hydrogen implanted in stainless steels with rather high energy, up to 1MeV becomes important and should be investigated.

In LHD, divertor tiles are made of graphite and, accordingly, carbon could be widely distributed on plasma facing wall. Hence hydrogen behavior in not only bare stainless steels but also carbon deposition on them are our research targets for the next year.

Reference

- 1) Sugiyama, K., Tanabe, T. et al.: J. Nucl. Mater. **337-339**(2005) 634
- 2) Tobita, K. Nishio, S. et al.: Fusion Eng. Design **65** (2003)561
- 3) Tanabe, T., Miyasaka, K., Rubel, M. et al.: Fusion Science & Technol. **41**(2002)924
- 4) Masaki, K., Sugiyama, K., Hayashi, T. et al.: J. Nucl. Mater. **337-339**(2005)553

Fig. 1 Poloidal distributions of tritium (upper) and deuterium (bottom) in divertor region of ASDEX-Upgrade



§29. Assessment Study on Biological Effects of Radiation in LHD

Ichimasa, Y. (Fac. Sci., Ibaraki Univ.), Komatsu, K. (Fac. Sci. Rad. Biol. Center, Kyoto Univ.), Kamiya, K. (Res. Inst. for Radiat. Biol. and Med., Hiroshima Univ.), Norimura, T. (Univ. Occupational and Environ. Health, Japan), Tauchi, H. (Fac. Sci., Ibaraki Univ.) Takeda, H. (NIRS), Ono, T. (Tohoku Univ., Graduate School Med. & School Med.), Uda, T.

The main results of this program were as follows.

- (1) Effect of exposure to tritiated water and gamma rays during gestation on androgen receptor mRNA expression in the offspring mice epididymis (Ichimasa, Y.)

The fetus is known to be radiosensitive. Vergouwen et al (1995) reported that the radiosensitivity of the gonocytes was increased with fetal age when pregnant mice were exposed to single doses of X rays. Fetuses are also very sensitive to environmental endocrine disruptors. In the present study, we examined whether low dose radiation exposure at fetal period caused similar antiandrogenic effects such as feminized males and change of androgen receptor (AR) mRNA expression in epididymis etc. in offspring male mice or not. Pregnant mice were orally administered HTO (10.9kBq/g body weight) or exposed to ¹³⁷Cs gamma rays (0.3Gy/h) at gestational day 14, and then body weight, ano-genital distance, survival rate, ability of reproduction and organ weight of its offspring were determined, and quantitative AR mRNA expression in caudal epididymis at day 82 of male offspring by using competitive RT-PCR. As for each measurement items and AR mRNA expression in caudal epididymis, no significant effects of HTO or gamma ray exposure were observed.

- (2) Uptake of tritium from tritiated water exposure in the medaka and zebra fish and estimation of DNA damage due to tritium (Ichimasa, Y.)

In the present work, the biological effect of tritium on tissue and erythrocyte DNA of fresh water fishes was estimated by the comet assay during long term exposure of tritiated water (HTO). Medaka or zebra fishes were exposed to HTO (146 – 1042Bq/ml) added to an aquarium for 10-26 days and the uptake, retention and release of tritium in fish body were investigated. Total tritium per g fresh weight of medaka equilibrated rapidly, around 40min after the start of exposure, to about 50% of the aquarium water concentration while organically bound tritium reached only 1% of the aquarium water concentration after 10 days exposure. The biological half time of tritium in the fishes transferred to fresh water after 26days exposure was 14 min. The effect of long term exposure to low dose tritium on fresh water fish was examined using medaka fed in HTO (2Bq/ml) containing aquarium for 232 days. No significant effect was observed in the liver cell.

- (3) Mutation induction by low dose rate tritium radiation: An analysis using hyper sensitive detection system (Tauchi, H.)

An exposure condition of tritium radiation from nuclear fusion reactor could be a long-term exposure with low dose rate. The biological effects of low dose (rate) radiation are not clear because any suitable detection system has not been established. Regarding to mutation induction by high LET radiation such as neutrons, the reversed dose rate effect has been reported when the dose rate is lower than a certain value. This might be caused by hypersensitivity of G2/M cells for mutation induction by high LET radiation. However, it is not clear whether this phenomenon could be seen in the case of tritium radiation. To examine the low dose rate effect of tritium, we established a hypersensitive mutation detection system using hamster cells carrying a human X-chromosome. We have tested mutation induction by tritiated water at dose rate between 0.15 and 4.4 cGy/h. Our results suggest that mutation frequency seems to be slightly increased at lower dose rate tritium radiation but the increase level was much less than that by neutrons.

- (4) Subcellular distribution of organically bound tritium in the rat liver after ingestion of tritiated water and some tritiated organic compounds (Takeda, H.)

Tritiated water and some tritiated organic compounds (leucine, glucose and thymidine) were administered to rats by oral ingestion and the content of organically bound tritium (OBT) in subcellular fractions (cold PCA soluble, ethanol-ether soluble, hot PCA soluble and alkali soluble) of the liver were determined at various time points after ingestion. In the case of tritiated water, the initial OBT content was high in the cold PCA soluble fraction, which contains low molecular weight components, but as the time proceed the OBT was distributed to other fractions, which contains relatively high molecular weight components. Significant time variation in the OBT content was observed in the hot PCA soluble fraction containing nucleic acids, in which the OBT content, expressed as percentage of OBT content in all fractions, changed from 1 % at 12 hours to 15 % at 50 days. In the cases of tritiated organic compounds, the subcellular distribution of OBT was widely changed owing to their biochemical and metabolic characteristics. Thus, the OBT distribution among subcellular fractions was changed depending on the chemical form at ingestion and on the time after ingestion. The OBT distribution among four subcellular fractions after 22 day' continuous ingestion was also dependent on the chemical form of ingested tritium. Present results should be taken into account for internal dose estimation of tritium in different chemical forms.

- (5) Nbs1 and its functional role in the DNA damage response. (Komatsu, K.)

- (6) Interaction of ligand-receptor system between stromal-cell-derived factor-1 and CXCR4 chemokine receptor 4 in human prostate cancer: a possible predictor of metastasis. (Kamiya, K.)

Reference

- 1) Kobayashi, J. and Komatsu, K.: DNA Repair, 3(2004)855
- 2) Iijima, K. and Tauchi, H. :Chromosoma, 113(2004)53
- 3) Kamiya, K.: Biochem. Biophys. Res. Commun., 320(2004)656

§30. Study on Environmental Behavior of Tritium

Momoshima, N. (Fac. Sci. Kumamoto Univ.)

Okai, T. (Fac. Eng. Kyushu Univ.)

Amano, H., Atarashi, M. (JAERI)

Miyamoto, K. (NIRS)

Takahashi, T. (Kyoto Univ.)

Uda, T., Sakuma, Y., Yamanishi, H., Sugiyama, T.

i) Tritium measurement

Atmospheric concentrations of three different chemical forms of tritium were measured at Kumamoto (Kumamoto Univ.) and Toki (NIFS) to elucidate a dependence of concentration upon sampling locations and a seasonal variation. In the atmosphere, water vapor (HTO), hydrogen gas (HT) and hydrocarbon, mostly methane (CH_3T) is the major species related to tritium. Sampling apparatus developed for successive collection of three species was applied in which at first HTO was collected by adsorption on molecular sieve (MS), followed by HT by oxidation to water and adsorption on MS, finally CH_3T by oxidation to water and adsorption on MS. During oxidation of HT and CH_3T tritium free hydrogen evolved by electric decomposition of tritium free water and bomb CH_4 were added to increase water to be adsorbed on MS. Waters adsorbed on MS were recovered by heating the MS and flowing N_2 gas and tritium activity in the recovered water was measured by liquid scintillation counting.

The concentrations of HTO, HT and CH_3T between Kumamoto and Toki were not so different, indicating no difference with sampling location. Considering the geographical situation of Kumamoto in south of Japan and Toki in central Japan, sources of three chemical forms were not a local origin. The concentrations (Bq/m^3) was in the order $\text{HT} > \text{CH}_3\text{T} > \text{HTO}$, indicating a large difference of specific activity, tritium atom to hydrogen atom, due to large difference of water vapor, hydrogen and CH_4 concentrations in the atmosphere. Significantly high specific activity in hydrogen and methane speculate their origin from nuclear industry.

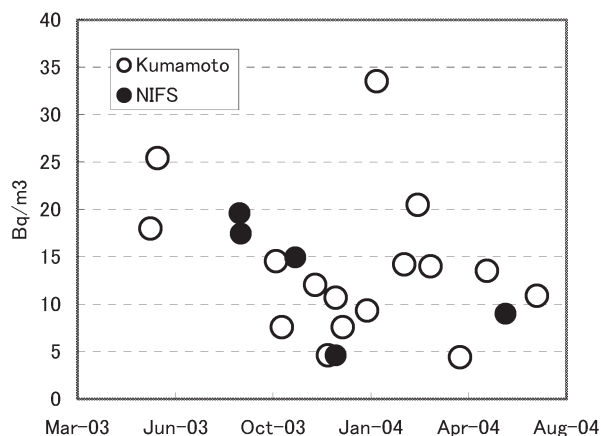


Fig. 1. Atmospheric HT concentrations collected at Kumamoto and NIFS.

Measurement of atmospheric tritium species at Fukuoka, Japan from 1984 suggests that overall continuous decrease in their concentrations. The HT revealed temporal increases in 1985 and 1988; however from 1989 a concentration seems to have decreased. The apparent half time of decline was 11.8 year in the period from 1984 to 2002. While CH_3T showed a half time of 26.6 year in the period from 1984 to 2002, and highest concentration was recorded in 1988 as HT. A latitude dependency was reported on HTO concentrations in rain and atmospheric vapor and increased HTO concentration was observed at north area of Japan. It would be necessary to carry out measurement of atmospheric tritium species at northern area of Japan.

ii) Model calculation

In evaluation of radiation dose of tritium that is released from nuclear installations to the environment, model calculation would be an only possible powerful tool. At NIFS site 1g of tritium release was assessed using a guideline for commercial nuclear power plant, in which reemission from surface ground was not considered, though reemission is a characteristic phenomenon in tritium dynamics in the environment. The reported maximum atmospheric concentration was 20 Bq/m^3 for 1 g annual release of tritium. We evaluated an effect of reemitted tritium on atmospheric concentration; reemission should elevate tritium concentration by release from the ground surface. The evaluation code of ETDose, which was developed for modeling of tritium behavior in the environment, was used and atmospheric concentrations were calculated using the meteorological data taken at Toki. The ground was divided into equal size meshes and influence of tritium reemitted from each mesh on interested point was accumulated with assuming that all of the tritium was reemitted when the interested point was located downward of wind for some period. A height of a stack was 40m and 50% of the released tritium was HTO were used as described in the guideline. Deposition velocities of HTO and HT were assumed to be $3 \times 10^{-3} \text{ m/s}$ and $3 \times 10^{-4} \text{ m/s}$, respectively.

The evaluation was carried out for northwest wind direction, which gave the maximum atmospheric tritium concentration of 20 Bq/m^3 for the calculation based on the guideline. For the case of HTO release tritium concentration in the atmosphere was not increased clearly within 1km from the release point of NIFS compared to the calculation based on the guideline and maximum concentration of about 20 Bq/m^3 was evaluated, suggesting validity of evaluation based on the guideline. However, a clear increase in atmospheric tritium concentration was observed beyond 1 km due to reemission of tritium. For the case of HT release, elevation of atmospheric tritium concentration with HTO released from ground surface was insignificant. The HTO was derived by oxidation of HT and deposition to ground and reemission to atmosphere. The evaluation based on the guideline was confirmed to be valid for HTO and HT release because the maximum tritium concentration were appeared at the same distance from the NIFS and the same level for both evaluations.

2. Collaboration on Fusion Engineering

(1) Fusion Engineering Studies

In the fusion engineering research field, 24 collaboration programs in total have been carried out. Subjects are relating to low activation structure materials, insulating materials, plasma-facing materials, blanket technology and neutronics, superconducting materials and technology *etc.* A short summary is given here for results in this fiscal year. Details can be seen in each subsection.

Characterization of a vanadium alloy, NIFS-HEAT2 and its further optimization is in progress.

Creep tubes have been successfully fabricated filled with pressurized helium gas and thermal creep tests have started. Dimensional changes of the tubes were measured with a precision laser profilometer. Results are discussed and preparation for creep tests in neutron irradiated conditions has completed.

It is important to understand mechanisms of oxygen pick-up in V alloys with a neutron irradiation environment. Microstructural evolution of laser welded samples at several distances from the bead center, which were irradiated at 873K, is studied.

Effects of impurities on the helium clustering process have been studied using THDS (Thermal Helium Desorption Spectrometry). It has been found that effects of oxygen and nitrogen on the stabilization behavior of vacancy type complex were comparative.

An impact of adding chemically reactive elements such as yttrium was investigated. It has been shown that the alloys have fairly good ductility and tensile strength even in liquid nitrogen temperature.

Another approach is addition of Ti aiming at finding a way for suppressing grain boundary sliding at high temperatures. Impacts on microstructures and behavior of fine-grained, particle dispersed V-1.7mass%Y alloy have been examined.

Fracture toughness and fatigue crack growth (FCG) have been studied. Variation of FCG rate with stress intensity factor range (ΔK) for full-size and half-size CT specimen was investigated. Results suggest that the FCG behavior of JLF-1 steels can be evaluated by using small sized specimens at RT.

Fracture toughness tests of the JETT (J evaluation on tensile test) specimens with various notch lengths and radiuses and those of standardized CT specimens for comparison were conducted. the specimen with $a/R=0.75$, $R=8\text{mm}$ showed fracture surface of general toughness tests, fractured from notch root.

Development of joint technique for SiC and SiC/SiC composites is in progress. Mechanical properties of the joint

were evaluated using the bars by tensile test. The joint has been found to be approximately 40 % of porosity including the large pore, which might induced the stress concentration during the loading.

Studies in the dislocation dynamics simulations for material deformations have progressed. The mechanisms of interaction between SFT (stacking-fault tetrahedral) and line dislocations have been studied by MD simulations, and results indicate that the strength as the obstacles for the dislocation motion appears to be strongly dependent on the cross section between SFT and the line dislocation.

Two-dimensional analysis is performed to evaluate effect of inner metal wall thickness on the MHD pressure drop in Li loops of a vanadium blanket system. Results of numerical and theoretical calculations indicate both these two approaches are valuable for evaluating impacts of insulator layers.

Er_2O_3 coatings fabricated by arc source plasma-assisted deposition were exposed to liquid Li and stability of the coating layers was investigated. Specimens exposed at 973 K for 1000 h were found to be stable, but unstable at lower temperatures. Further study is in progress.

Ion beam irradiation to Er_2O_3 was performed in Institute for Materials Research of Tohoku University. Significant change in the electrical conductivity was observed for the order of $1.0 \times 10^{16} \text{H/cm}^2$.

Gamma ray irradiation to insulating materials was performed at the ^{60}Co irradiation facility in Osaka University. The results indicate that the radiation induced conductivity in the candidate materials is correlated with the dose rate under neutron and gamma ray irradiations.

Tungsten (W) and its alloys are very promising for a use as a plasma facing material. Significant progress was achieved concerning ductile W alloy development, W surface modification, plastic working, joining technology and fundamental properties of several commercially available W alloys.

Divertor-plate model specimens of tungsten materials are manufactured and joined with copper block to study removing high heat flux to plasma facing components. Formation of cracks parallel to the joining line has been observed in high heat flux cases. The joining technique needs to be improved further.

Critical Heat Flux (CHF) $q_{cr,sub}$ on rough, smooth, and mirror finished inner surfaces for the lowest dissolved oxygen concentration was studied. The $q_{cr,sub}$ for each flow velocity was found to be almost constant independent of the surface roughness.

Development of V_3Ga compounds, one of the V-based superconducting materials, has started because of its compatibility in "low activation" and "high magnetic field", which is required in future fusion reactors. Multifilamentary wire was fabricated and relationship between heating energy density and T_c value was investigated.

Sintered bulk Bi-2223 has a critical temperature of over 77 K and low thermal conductivity, which is attractive for a current lead. Bi-2223 and Ag-plated nickel (Ni) wires composite bulk with high superconducting and mechanical property have been developed. Its mechanical and superconducting properties are investigated and reported.

Fatigue crack growth rate tests were performed with CT specimens at room temperature (RT), liquid nitrogen temperature (77 K), and liquid helium temperature (4 K). Fiber/matrix debonding and fiber pull-out are the main fracture mechanisms of the CT specimen at high J -integral range levels, while matrix cracking is the dominant fatigue crack growth mechanism at low J -integral levels.

Scatter of the crack length measurement with the unloading elastic compliance method was investigated, which was necessary for evaluating mechanical properties, such as fracture toughness of structural materials at cryogenic temperature. At initial crack length, all results agree well, which indicates line immediately after the unloading starts is very important.

Utilization of a spherical-tokamak reactor is proposed for transmutation of high level waste. Neutronics analysis is carried out for ARIES-ST blanket. Results indicate that the neutron flux would transmute minor actinides and fission products produced from the pressurized water reactor of 1 $GW_{(e)}$. However, tritium breeding ratio is insufficient for self-supplying the fuels.

Thermoelectric generator has an advantage that it exchanges the heat energy directly to the electric energy. Measurement of the longitudinal magnetoresistance (LMR) was carried out for the bulk Bi. The characteristics of the LMR of bulk Bi at 90 K is similar to that of nanowire Bi, which suggests that the negative LMR of Bi is supposed to be dependent on the strong magnetic field, not on the nano-wire geometry.

For the qualification of materials up to the full lifetime of DEMO and Power Plant Reactors, irradiation testing with IFMIF is recognized to be essential. Activities in universities for development of key elements of the IFMIF was organized under Fusion Engineering Center since 1999 and completed in FY2004. Details can be seen in Chapter 10, Fusion Engineering Research Center

(Noda, N.)

§1. Influence of Inner Surface Roughness on Subcooled Flow Boiling Critical Heat Flux in a Short Vertical Tube

Hata, K. (Inst. of Advanced Energy, Kyoto Univ.)
Shiotsu, M. (Dept. of Eng. Sci. and Tech., Kyoto Univ.)
Noda, N.

The subcooled flow boiling CHF and the heat transfer characteristics for the flow velocities ($u=4.0$ to 13.3 m/s), the inlet subcoolings ($\Delta T_{sub,in}=137.49$ to 153.87 K), the inlet pressure ($P_{in}=740.67$ to 975.78 kPa) and the dissolved oxygen concentration ($O=8.63$ to 0.0288 ppm) are systematically measured by the experimental water loop installed the pressurizer. The SUS304 tubes of $d=3$ mm and $L=66.5$ mm ($L/d=22.17$) with the inner surfaces of rough, smooth and mirror finished (RF, SF and MF) are used [1]. The inner surface roughness (Ra) measured for each test tube was 3.18 , 0.26 and 0.14 μm respectively.

Heat Transfer

The heat transfer curves on RF, SF and MF surfaces for flow velocities of 4 and 13.3 m/s are shown in Fig. 1 to see the effect of surface roughness clearly. At a fixed flow velocity, the heat flux gradually becomes higher with an increase in $\Delta T_{sat}=T_s-T_{sat}$ on the non-boiling forced convection curve derived from Nusselt correlation up to the point where the slope begins to increase with heat flux following the onset of nucleate boiling, and increases up to a value called CHF where the heater surface temperature rapidly jumps from the nucleate boiling heat transfer regime to the film boiling one. The CHF and its superheat become higher with an increase in flow velocity. The nucleate boiling curves in higher heat flux range for the

flow velocity agree with each other forming a single straight line on the log-log graph. The equation of incipient boiling superheat given by Sato and Matsumura [2] is shown in the figure for comparison. The incipient boiling superheat for each

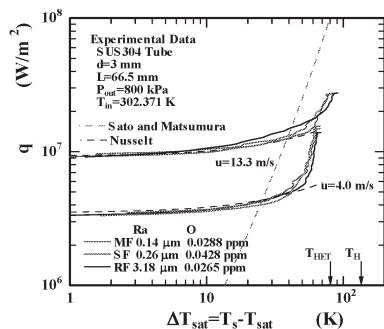


Fig. 1 Heat transfer characteristics for $d=3$ mm with $Ra=0.14$ to 3.18 μm .

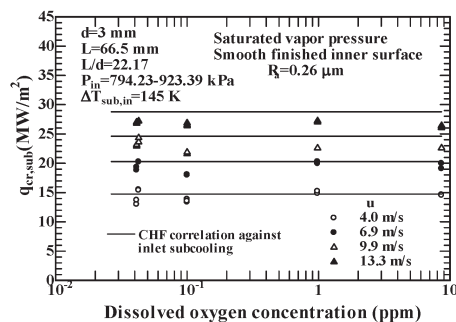


Fig. 2 The $q_{cr,sub}$ for $d=3$ mm with $Ra=0.26$ μm for $O=0.0413$ to 8.63 ppm.

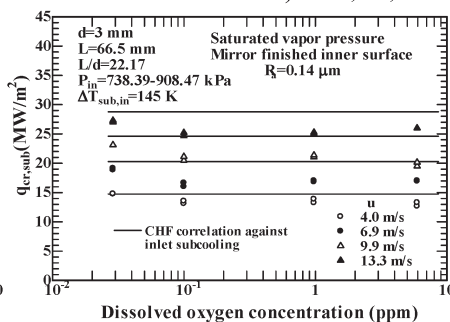


Fig. 3 The $q_{cr,sub}$ for $d=3$ mm with $Ra=0.14$ μm for $O=0.0288$ to 5.94 ppm.

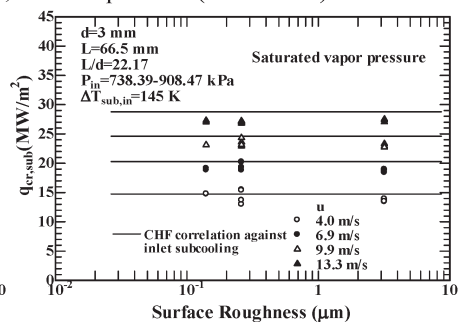


Fig. 4 The $q_{cr,sub}$ for $d=3$ mm with $Ra=0.14$ to 3.18 μm .

flow velocity is slightly higher but almost in agreement with that predicted by the equation. The nucleate boiling curves in the higher heat flux range are almost parallel to the curve by Sato and Matsumura. Little effect of surface roughness can be seen for low and high heat flux ranges, although the measured average roughness, Ra , varied from 0.14 to 3.18 μm .

Critical Heat Flux

The CHF for the test tube with smooth finished inner surface were measured at dissolved oxygen concentrations, O , of 8.63 , 0.983 , 0.1004 , 0.428 and 0.0413 ppm. Typical CHF data for inlet subcooling of about 145 K at the outlet pressure of around 800 kPa with the inlet flow velocities of 4 to 13.3 m/s are shown in Fig. 2. The corresponding curves obtained from the CHF correlation against inlet subcooling [3] are also shown in the figure. The CHF for smooth inner surface for higher flow velocities seem to be lower than those for the rough. Reproducibility of the data was very good as shown in the figure.

The CHF for the test tube with mirror finished inner surface at dissolved oxygen concentrations, O , of 5.94 , 0.974 , 0.0997 and 0.0288 ppm are shown in Fig. 3. The curves given by the CHF correlation against inlet subcooling are shown in figure for comparison. The CHF for mirror finished inner surface for higher flow velocities seem to be lower than those for the smooth surface shown in Fig. 3 (further lower than those for the rough finished surface). However, the $q_{cr,sub}$ data for higher flow velocities at the lowest dissolved oxygen content are higher than those for others and seem to be slightly lower than the predicted values.

The CHF on rough, smooth, and mirror finished inner surfaces for the lowest dissolved oxygen concentration are shown versus the surface roughness, Ra , with the flow velocity as a parameter in Fig. 4. The $q_{cr,sub}$ for each flow velocity are almost constant independently of the surface roughness. The corresponding curves for each flow velocity obtained from the CHF correlation against inlet subcooling are also shown in the figure. The $q_{cr,sub}$ are well expressed by the equation. It seems that the influence of surface roughness disappeared at the lowest dissolved oxygen concentration. The mechanism is not clear at present. Reproducibility of the data at the lowest dissolved oxygen concentration need to be further studied.

Reference

- 1) Hata, K., et al., Paper No. IMECE 2004-61453, (2004) 1
- 2) Sato, T., Matsumura, H., Bulletin of JSME 7, (1963) 392
- 3) Hata, K., et al., Ann. Rep. NIFS (2003-2004) 216

§2. Development of Low Activation Compound Superconducting Wires for Fusion Reactor

Kikuchi, A., Iijima, Y., Takeuchi, T. (NIMS)
Hishinuma, Y., Nishimura, A.

The burning plasma experiments between Deuterium and Tritium were planned in the ITER project. There will be fear that degradations of superconducting properties in coil conductors are caused by radiations such as streaming neutrons in the advanced fusion reactor. In the case of advanced fusion reactor such as DEMO or commercial fusion plants, there is problem that the streaming of radiation dose over the ITER level seems to become larger with increasing fusion power. We considered that it is necessary to develop the superconducting conductor which is "low activation" compatible with "high magnetic field". V-based compound superconductors are suitable for applying as a high field conductor for advanced fusion reactors, because they show neutron irradiation resistance and low activation in the fusion reactor compared with those of Nb-based A15 wires. Therefore, we started to develop the V_3Ga compound which was one of the V-based superconducting materials.

Though the rapidly heating and quenching (RHQ) processing has been applied until now to various A15 compounds such as Nb_3Sn , Nb_3Ga , Nb_3Ge and $Nb_3(Al,Ge)$ wires, supersaturated solid solution filament like the Nb_3Al wire can not have been formed in each case. In this study, the RHQ process was applied at the V_3Ga compound which existed by stabilizing the V-25at%Ga solid solution in the high-temperature region above 1300°C. We focused and observed that the stacking fault was formed in the V_3Ga phase transformed from supersaturated solid solution as well as Nb_3Al compound.

V_3Ga compound powder was produced to grinding by hands using Arc-melted V_3Ga compound button. We confirmed composition of V_3Ga compound powder using XRD and ICP analysis. Prepared V_3Ga compound powder was packed into Nb tube having 20 mm outer diameter and 10 mm inner diameter, and then this composite was cold rolled with a grooved and the wire drawn a diameter of about 2.00 mm through Powder-In-Tube method. This mono-cored wire was cut into short piece, and they were stacked into Nb tube. The number of stacked mono-cored wire was 55 pieces. The stacked composite was cold-rolled with a grooved roller and drawing machine to wire of about 0.74 mm diameter. This multifilamentary wire was set into RHQ apparatus, and it was applied to the RHQ treatment in a dynamic vacuum chamber with moving at 0.4 m/sec of velocity. Then some of as-RHQ wires were additionally post-annealed at 800°C for 12 hours in vacuum.

Fig.1 shows that typical SEM image on the cross-section of the V_3Ga/Nb multifilamentary wire. This composite has good workability without breaking of wire

during wire deformation, and average diameter of V_3Ga filament is about 20 μm . Fig.2 shows that the relationship between heating energy density and T_c value of as-RHQ samples. The heating energy density J (J/mm^3) indicate normalized heating condition regardless of diameter and moving velocity of wires, and J value is given by

$$J = V \times I \times (L \times A)^{-1}$$

where V is applied voltage (V), I is current (A), L is length of heating area (mm) and A is the cross-sectional area of wire (mm^2), respectively. The heating temperature during RHQ treatment was increased with increasing of J value, and this tendency agreed well the change of maximum heating temperature measured by radiation thermometer shown in Fig.2. In the case of V_3Ga wires, T_c values of pure Nb within 9 K appeared remarkable lower heating energy region compared with that of Nb_3Al wire, and V-Ga supersaturated solid solution was formed at lower heating temperature (above 1300 °C) compared with Nb-Al supersaturated solid solution (above 2200 °C). This result is agreed well with V-Ga equilibrium diagram.

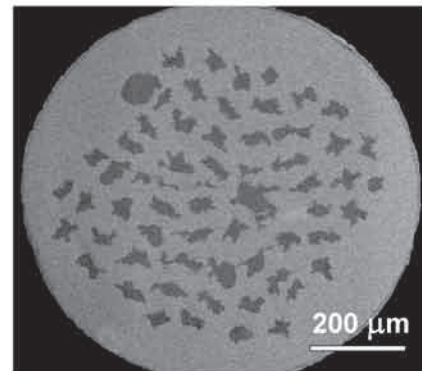


Fig. 1 Typical SEM image on the cross-section of the V_3Ga/Nb multifilamentary PIT wire.

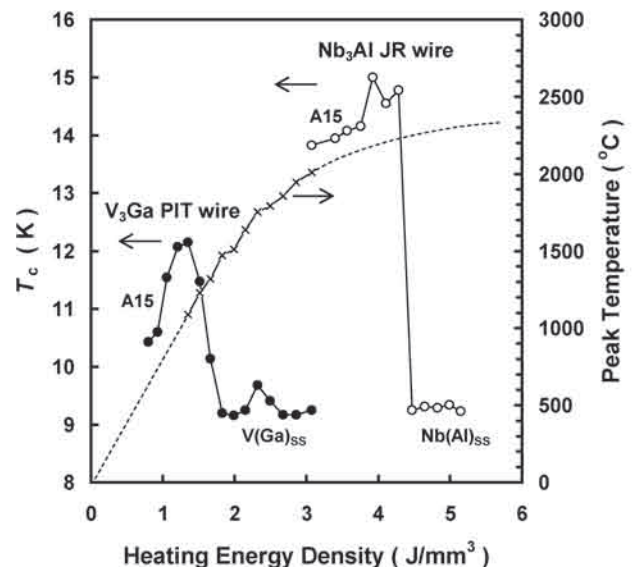


Fig. 2 Relationship between T_c and heating energy density on rapid-heating/quenching treatment for V_3Ga PIT wire and Nb_3Al JR wire.

§3. Development of Strength Evaluation Methods of Cryogenic Material Systems

Shindo, Y., Horiguchi, K., Narita, F., Takeda, T., Inamoto, A., Komatsu, T., Takano, S. (Dept. of Mater. Processing, Graduate School of Engineering, Tohoku Univ.)

Sanada, K. (Dept. of Mechanical Systems Engineering, Faculty of Engineering, Toyama Prefectural Univ.)

Kumagai, S. (Dept. of Materials Science and Engineering, Miyagi National College of Technology)
Nishimura, A., Tamura, H.

1. Purpose

Superconducting magnets for use in fusion reactors may use large quantities of nonmetallic composite materials. There are a variety of applications where GFRP (glass fiber reinforced polymer) woven laminates can provide thermal insulation, electrical insulation and structural support. The reliability and safety of the fusion reactor are entirely dependent on good design which in turn rely heavily on predictable materials performance. However, a great deal of confusion has arisen in recent years surrounding the general topics of fracture and fatigue of the composites. Due to heterogeneity in fiber reinforced composites, fracture and fatigue processes emanating from crack tip are far more complicated than those occurred in metals. The composite materials made from woven-fabric glass/epoxy laminates have poor through-thickness properties, poor impact damage tolerance, and low interlaminar fracture toughness. Depending on the microstructural details of the composite and the magnitude of the cyclic stress concentration, fatigue crack growth and subsequent fracture of the composite materials can be very complicated in nature. The purpose of the present study is to characterize the fatigue crack growth behavior of woven fiber reinforced epoxy composites at low temperatures. The study was undertaken using both experimental and simulation work in an effort to contribute to the understanding of the basic mechanisms governing cyclic fatigue crack growth in these composites¹⁾. This combined numerical-experimental study used CT (compact tension) specimens.

2. Procedure

Fatigue crack growth rate tests were performed with CT specimens at room temperature (RT), liquid nitrogen temperature (77 K), and liquid helium temperature (4 K) in accordance with ASTM (American Society for Testing and Materials) E 647-00²⁾. The fracture surfaces were also examined by SEM (scanning electron microscopy) to correlate with the fatigue properties. A finite element method coupled with fatigue damage was adopted for the extensional analysis. The effects of

temperature and loading condition on the fatigue crack growth rates are examined.

3. Results

(1) Fatigue crack growth rates for the CT specimens of GFRP woven laminates decrease with decreasing temperature from RT down to 77 K but the values at 4 K are higher than those at 77 K. Cyclic fatigue crack growth rate da/dN in G-11 woven laminates for the CT specimens is plotted in Fig. 1 as a function of the J -integral range ΔJ at 77 K and 4 K. (2) The fiber/matrix adhesion of fracture surfaces for the CT specimens is increased with decreasing temperatures. (3) Fiber/matrix debonding and fiber pull-out are the main fracture mechanisms of the CT specimen at high J -integral range levels, while matrix cracking is the dominant fatigue crack growth mechanism at low J -integral levels. (4) The finite element analysis with damage is an efficient way to predict the J -integral range and damage zone for the CT specimens at low temperatures.

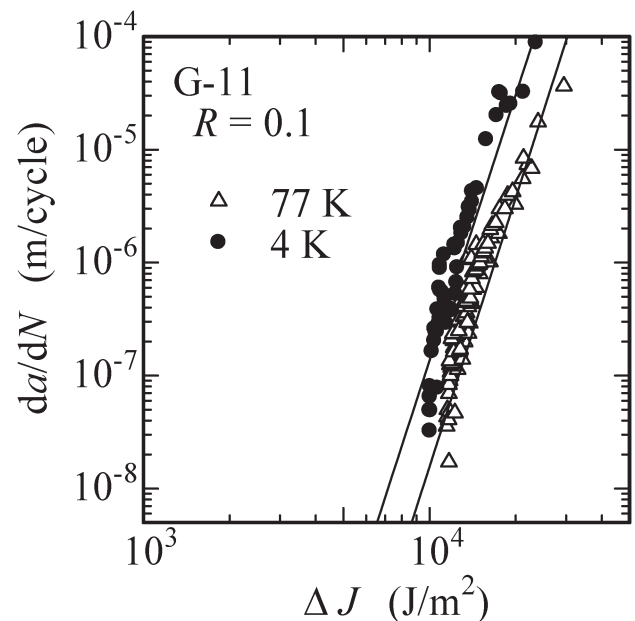


Fig. 1. Fatigue crack growth rate in G-11 woven laminates at 77 K and 4 K (load ratio $R = 0.1$, frequency 3 Hz)

References

- 1) Y. Shindo, A. Inamoto and F. Narita, Acta Materialia, **53**, (2005) 1389
- 2) ASTM E 647-00, Standard test method for measurement of fatigue crack growth rates, ASTM (2000)

§4. Development of the Fracture Toughness Test Method by Round Bar with Circumferential Notch

Kasaba, K., Katagiri, K., Shoji, Y. (Iwate Univ.)

1. Introduction

Fracture toughness is one of the most important mechanical properties among various properties of structural materials for machinery. Test methods of plain strain fracture toughness K_{Ic} and elastic-plastic fracture toughness J_{Ic} are standardized in ASTM¹⁾. However the methods are time-consuming and expensive. And furthermore, laboratories being capable of conducting the experiments are limited due to the required experimental equipments. On the other hand, a convenient new test method, named J evaluation on tensile test (JETT), has been proposed to evaluate the fracture toughness of the tough materials²⁻³⁾. A JETT specimen, round bars with circumferential notch, is easier to be machined than a standardized specimen. Smaller specimen size is another advantage of JETT.

In this research, fracture toughness tests of the JETT specimens with various notch lengths and radiuses and those of standardized CT specimens for comparison were conducted. The purpose of the research is to get the knowledge about the development of that new fracture toughness test method from the experiments.

2. Experimental Procedure

For the development of the convenient test method by avoiding the many efforts of introducing axisymmetric fatigue crack, the possibility of the test using EDM (electro-discharge machining) notch has been tried²⁻³⁾. Fig.1 shows the dimensions of the specimen. All the specimens were machined from a Manganese steel plate quenched from 840 °C in a oil. Its yield stress, ultimate tensile stress and reduction of area are 313 MPa, 546 MPa and 66 % respectively.

3. Results and Discussion

$J=225 \text{ KJ/m}^2$ was obtained by the standardized J test method. On the other hand, various J values were obtained by JETT depending on the notch length a and radius R like shown in Fig.2. The J values of the specimen with $a/R=0.75$, $R=4\text{mm}$ were the nearest value to that of standardized specimen. However the specimens with both $R=2\text{mm}$ and $R=4\text{mm}$ showed the fracture surface of the cup and corn type. Therefore the test results were not effective for the fracture toughness tests. On the other hand, the specimen with $a/R=0.75$, $R=8\text{mm}$ showed fracture surface of general toughness tests, fractured from notch root. Q-factor,

one of the strain constraint parameters⁴⁾, of the specimen with $a/R=0.75$, $R=8\text{mm}$ (not shown here) was also the same value with the standardized test. The best estimation for J value of the round bar with circumferential notch has been thought to be the Rice's approximate equation⁵⁾. However the effectiveness of Rice's equation is limited in specific range of a/R and that after large amount of the plastic deformation and especially after necking was not known yet. J value of the specimen with $a/R=0.75$, $R=8\text{mm}$ estimated by numerical line integral in FEM was $J=190\text{KJ/m}^2$, 15% less than the value obtained by the standardized CT specimen 225 KJ/m^2 . Although there are some problems to be solved about new test method yet, the method has a possibility to be used to obtain fracture toughness of the structural material conveniently and at low cost.

References

- 1) ASTM E1820-99a.: Annual book of ASTM standards (1999) 1000
- 2) Nishimura A. et al. : Adv. Cryogenic Engng 44 (1998) 145
- 3) Nishimura A. et al. : Adv. Cryogenic Engng 46 (2000) 33
- 4) Shih C F. et al. : ASTM STP 1171 (1993) 2
- 5) Rice JR, Paris PC: ASTM Special Technical Publications 536(1973) 231

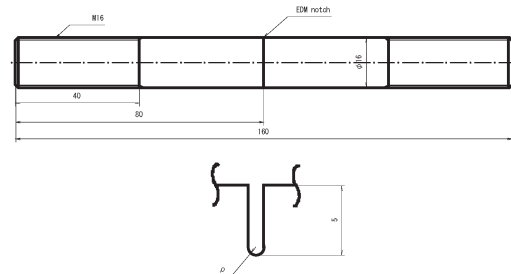


Fig.1 JETT Specimen.

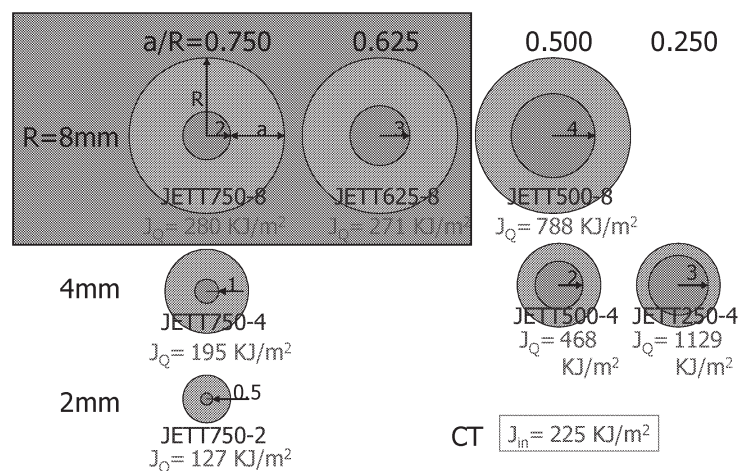


Fig.2 Experimental results

§5. Examination of Materials Irradiation Test Program Using Intense Neutron Source (IFMIF)

Matsui, H., Kurishita, H. (Tohoku U), Kimura, A. (Kyoto U.), Jitsukawa, S. (JAERI)
Muroga, T.

The major mission of IFMIF is described in the Comprehensive Design Report published in January, 2004, as follows: "The primary mission of a fusion irradiation facility will be to generate a materials irradiation database for the design, construction, licensing, and safe operation of a Fusion Demonstration Reactor (DEMO)." The focus is obviously on materials while it is also emphasized that "Tests of blanket elements will be an important use of the facility, and will complement the tests of blanket test modules in the International Thermonuclear Experimental Reactor (ITER)." Thus, the mission of IFMIF is not limited to materials but is to cover a wider range in the fusion technology area. For the construction of IFMIF itself, there are a number of technical issues to be addressed. These issues are related to technical areas such as: accelerator system, RF power system, liquid metal handling, heat management system, neutronics, remote handling, etc. These technical areas are also quite relevant to the construction of fusion power systems.

In the IFMIF activities so far, in the Key Element Technology Phase (KEP) in particular, a number of technical issues in those areas as listed above have been addressed. The outcomes of these activities have been already presented in some of the international conferences related to fusion development. They are sufficiently convincing for the project to move on to the next phase of Engineering Validation/ Engineering Design Activity, i.e. EVEDA phase. The current projected IFMIF schedule is shown in Fig. 1.

The objective of the present activity is to examine the materials irradiation test program using IFMIF based on the results on small-specimen test technology and advanced design of irradiation test cell obtained through the KEP activity.

In the KEP activity, database has been obtained on the size effects of pre-cracked bend bar specimens and compact-tension specimens for Reduced Activation Ferritic/Martensitic Steels (RAFM). These results will be used for standardization of the test specimen geometry for application to IFMIF.

The materials irradiation program needs to be consistent with other fusion programs such as breeding blanket development and DEMO licensing and construction. In Japanese fusion materials development strategy, the candidate structural materials are categorized into reference and advanced materials. As the reference materials, RAFMs were selected because they have the most matured industrial infrastructure. Development of the reference materials is crucial for realization of DEMO in timely manner. On the other hand, vanadium alloys and

SiC/SiC were nominated as the advanced materials, which will contribute to increasing attractiveness of the fusion system in terms of cost of electricity and environmental benignity. It is recognized that the development of the advanced materials must also be enhanced now, due to the long lead time necessary for their development.

For the qualification of materials up to the full lifetime of DEMO and Power Plant Reactors, irradiation testing with IFMIF is recognized to be essential. The Test Blanket Module (TBM) to be installed in ITER is also considered to be an important milestone for technological integration. A roadmap of materials development is under construction. The materials development is planned to proceed with IFMIF and ITER in a coordinated way. Early period of IFMIF testing will be dominated by testing of RAFM for obtaining irradiation data to be applied for designing DEMO. For advanced materials, small scale testing will be carried out in initial operation period of IFMIF and ITER-TBM followed by full size testing.

The materials irradiation test program for IFMIF will be made based on the materials development strategy and technical database on small-specimen test technologies.

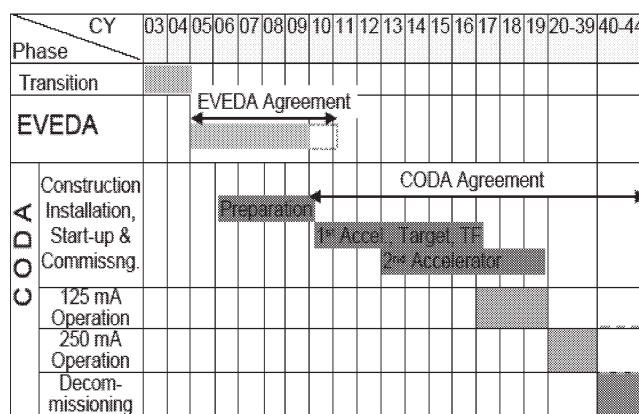


Figure 1. Projected IFMIF schedule.

§6. Thermal and Mechanical Properties of Composite Materials for Superconducting Coils

Takao, T., Nakamura, K., Watanabe, A. (Sophia University)

Low weight of a large-scale superconducting coil such as the coils for nuclear fusion reactor is one of important issues. One solution is that high strength and high-thermal-conduction non-metallic composites are used in the coils. In the study, we proposed those materials and experimentally studied to apply the composites to a structural material in the coil.

We used a Dyneema fiber reinforced plastic (DFRP), a glass fiber reinforced plastic (GFRP), and aluminum nitride (AlN) as the sample materials. An experimental setup is that a short Bi-2223 tape is clamped from both sides of the tape faces by the material. That experimental arrangement is cooled down using a GM refrigerator. In the experiments, liquid nitrogen as a coolant has not been used. At a cryogenic temperature, a constant DC current was applied to the Bi tape, and the voltage and temperature rise of the tape were measured.

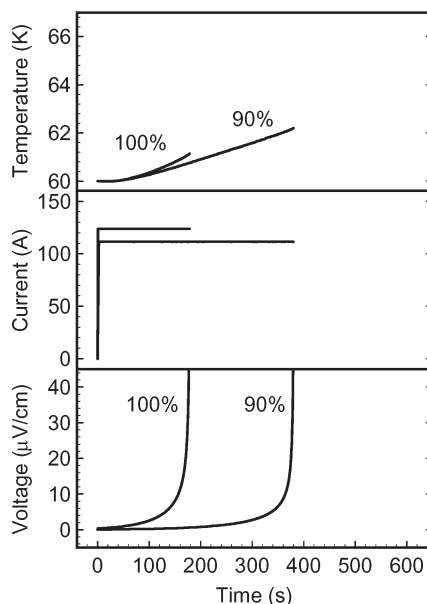


Fig. 1. Example of observed waveform.

A typically observed waveform of the voltage and the temperature rise are shown in Fig. 1. The

sample material is DFRP, and currents are 90 and 100 % of I_c . We compared the voltage rise and generated heating between the three materials at the time of 280 seconds after starting of the experiment. The result is summarized in Fig. 2.

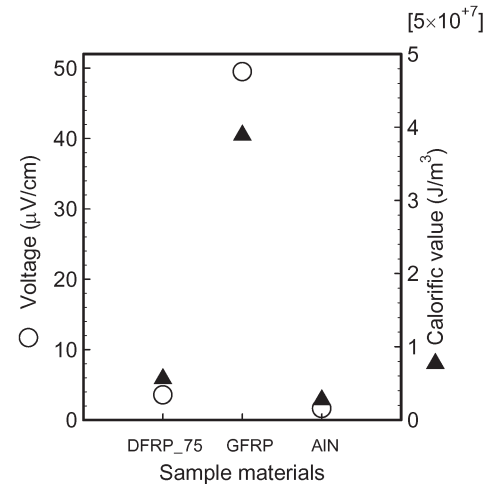


Fig. 2. Voltages and heating in three materials.

From the figure, both of the voltage and the heating were of the material of GFRP were largest in the three materials. Those in DFRP and AlN were relatively small. The cooling performance of the AlN is as same as that of DFRP, or a little better as shown in the figure.

List of publications and presentations:

- (1) K. Nakamura, H. Suko, T. Takao and A. Nishimura, "Relation between contact resistance and twist pitches in superconducting doublets," IEEE Trans. on Applied Superconductivity (in press).
- (2) T. Takao, M. Yamaguchi, H. Yamamoto, H. Watanabe, A. Yamanaka, "Stability of conduction cooled Bi2223 tapes using high thermal conduction plastics," presented at ASC2004, USA, October 2004.
- (3) K. Nakamura, M. Yamanouchi, K. Hashimoto and T. Takao, "Effects of contact resistance between strands with Cr/non-Cr coating in cable-in-conduit conductors," IEEE Transactions on Applied Superconductivity, vol. 14, no. 2, pp. 1306-1309, June 2004.
- (4) A. Watanabe, A., M. Yamaguchi, H. Yamamoto, Y. Iso, T. Takao, A. Yamanaka, Estimation of cooling performance of structural materials for conduction cooled superconducting magnets, Cryogenics and superconductivity, 1C-a02, Hachinohe, Autumn, 2004.

§7. Development of Fine-Grained, Particle-Dispersed Vanadium Alloys with Improved Resistances to High-Temperature Deformation and Embrittlement by Neutron and Helium Irradiations

Kurishita, H., Matsui, H. (IMR, Tohoku Univ.)
Oda, S., Kobayashi, S., Nakai, K. (Ehime Univ.)
Nagasaka, T., Muroga, T., Noda, N.

A V-4Cr-4Ti alloy with reduced contents of solute oxygen and nitrogen processed by electron-beam melting is a primary candidate material for fusion reactor structural applications^{1,2)}. In order to make the alloy more attractive, it is necessary to improve both the resistance to embrittlement by neutron and helium irradiations and strength at high temperatures. So far, the authors showed that the microstructure of fine grains and fine dispersoids of Y₂O₃ and YN, which are produced by powder metallurgical methods including mechanical alloying (MA)³⁻⁶⁾ is very effective in improving the resistance to radiation embrittlement in vanadium. They also studied the high temperature deformation of V-(1.7-2.4) mass% Y alloys and showed that grain boundary sliding occurs significantly above 1100K and the resultant strength loss cannot be compensated by dispersion hardening by Y₂O₃ and YN particles⁷⁾. This indicates that suppression of grain boundary sliding is required to improve the high temperature strength of V-(1.7-2.4) mass% Y alloys above 1100K.

Addition of Ti to vanadium causes solution hardening and is expected to suppress grain boundary sliding by changing grain boundary chemistry and/or structures. In this paper, the effect of Ti addition on microstructures and high temperature behavior of fine-grained, particle dispersed V-1.7mass%Y alloy is examined, aiming at finding a way for suppressing grain boundary sliding above 1100K.

Powders of pure vanadium (particle size: <150μm, oxygen: 0.08%, nitrogen: 0.07%, in mass%), pure yttrium (<750μm, 1.56%, 0.05%) and Ti (78μm, 0.35%, 0.02%) were used as the starting materials. They were mixed to provide the nominal compositions of V-1.7%Y-2.1%Ti and V-1.7%Y in a glove box filled with purified Ar gas (purity 99.99999%). Each of the mixed powders and WC/Co balls was charged into two WC/Co milling vessels having an inside volume of 250cc. The vessels sealed with oxygen-free copper gasket were taken out of the glove box and set to a planetary ball milling apparatus for MA.

Each of TIG sealed mild steel capsules containing MA processed powder was subjected to HIP at 1273K and 200MPa for 3h. The as-HIPed compacts had the density of 6.08 g/cm³, approximately 99.7 % of theoretical. From the as-HIPed compacts, specimens for microstructural observations, X-ray diffraction analysis and tensile tests were prepared. The dimensions of the tensile specimens are 16mm x 4mm x 0.5mm with the gauge section of 5mm x 1.2mm x 0.5mm. All of the specimens were wrapped with Ta foil and then Zr foil and annealed for 3.6ks at 1273 K for

V-1.7%Y-2.1%Ti and 1373K for V-1.7%Y in a vacuum better than 5 x 10⁻⁵Pa. Tensile tests were performed at temperatures from 873 to 1273K at an initial strain rate of 1 x 10⁻³ s⁻¹ in a vacuum better than 3 x 10⁻⁴ Pa. Ta and Zr foils having the dimensions identical to the tensile specimens and being separable into two parts were placed in contact with the specimens to suppress pick-up of gaseous interstitial impurities from the surrounding during the test. Microstructural examinations were made by transmission electron microscopy (TEM) with JEM-2000FX operating at 200kV. The main results are as follows.

1) Comparison of microstructural parameters between V-1.7Y-2.1Ti and V-1.7Y alloys (table 1) shows that V-1.7Y-2.1Ti has larger grain size and lower particle density than V-1.7Y in spite of lower annealing temperature.

2) The amount of 1% Ti is in solution in V-1.7Y-2.1Ti and the remainder exists as the constituent of large dispersoid of Y₂Ti₂O₇.

Table 1 Microstructural parameters in two alloys developed.

	Grain diameter (nm)	Particle density (10 ²⁰ /m ³)	Particle diameter (nm)
V-1.7Y-2.1Ti	518	6.0	14.7
V-1.7Y	339	31.3	12.9

3) The yield stress for V-1.7Y-2.1Ti is considerably higher than that estimated from the grain size dependence of yield stress for V-(1.7-2.4)Y alloys⁷⁾. In particular, at 1273K where V-(1.7-2.4)Y alloys exhibit no grain size dependence of yield stress due to significant grain boundary sliding, V-1.7Y-2.1Ti shows that appreciable grain size dependence of yield stress, indicating the occurrence of suppression of grain boundary sliding even at 1273K.

4) In view of both less contribution of dispersion hardening to high temperature strength in V-1.7Y-2.1Ti due to less particle density and the presence of 1% solute Ti, the observed high strength at 1273K is most likely due to solution hardening by Ti. This indicates that solution hardening is very effective in suppressing grain boundary sliding in fine-grained, particle dispersed V-1.7Y alloy. It is thus expected that larger amounts of Ti addition may lead to further improvement in high temperature strength.

Reference

- 1) Muroga, T., Nagasaka, T., Iiyoshi, A., Kawabata, S., Sakurai, M., Sakata, M., J. Nucl. Mater. **283-287**, (2000) 711.
- 2) Nagasaka, T., Muroga, T., Imamura, M., Tomiyama, S., Sakata, M., Fusion Technol. **39**, (2001) 659.
- 3) Kuwabara, T., Kurishita, H., Hasegawa, M., J. Nucl. Mater. **283**, (2000) 611.
- 4) Kobayashi, S., Tsuruoka, S., Nakai, K., Kurishita, H., Mater. Trans. **45**, (2004) 29.
- 5) Kobayashi, S., Tsuruoka, S., Nakai, K., Kurishita, H., J. Nucl. Mater. **329-333**, (2004) 447.
- 6) Kuwabara, T., Kurishita, H., Hasegawa, M., Mater. Sci. and Eng. A, (2005) in press.
- 7) Oda, S., Kurishita, H., Kobayashi, S., Nakai, K., Matsui, H., J. Nucl. Mater. **329-333**, (2004)462.

§8. Development of Simulation Models for Irradiation Performance of Fusion Materials

Sekimura, N., Abe, H., Okita, T. (Dept. Qua. Eng. and Syst. Sci., Univ. Tokyo)

Morishita, K. (IAE, Kyoto Univ.)

Muroga, T.

(i) Introduction

The development of fusion materials must be performed without any experimental evidence derived from truly prototypic neutron flux-spectra, because, at the present time, there exists no fusion reactors or test reactors operating at fusion relevant flux-spectra. Therefore, it is very important to develop the multi-scale models for material behavior under 14 MeV neutron irradiation, and to make predictions of irradiation performance of fusion materials.

Toward these objectives and challenges, we have three approaches in this project; (1) Simulations for fundamental processes of defect production and agglomeration under irradiation, (2) Simulations and comparisons of material behavior under irradiation between pure materials and their alloys, and (3) Simulations for plastic deformation of irradiated materials.

(ii) The outline in this fiscal year

In this fiscal year, we had mainly three accomplishments, corresponding to the approaches shown in the previous section.

(1) We have evaluated the factors which control the one-dimensional motion of interstitial clusters directly generated by collision cascade.

(2) We have improved the methods to simulate the effects of transmutant helium and/or other impurities on defect agglomeration and cluster formation. We have also made a more quantitative evaluation for the circumstances of fusion reactor.

(3) We have evaluated the current issues to improve the dislocation dynamics simulations for material deformations, and to clarify the roles for defect clusters in the initial stage of the plastic deformation.

Among these three, we will mainly discuss the defect behavior under the plastic deformation, because we consider that it is one of the most difficult problems to complete the multi-scale modeling.

(iii) The accomplishments

In the previous enormous studies for plastic deformations by dislocation dynamics, the behaviors of the stacking-fault tetrahedral (SFT) had not been well clarified, and they had been treated the similar way just as other defects or

impurities comprised in the matrix. This used to be the local rule of SFT for the dislocation dynamics, and this too much simplified model had been input into the simulations and the effects of SFT on plastic deformation had been evaluated.

However, since the SFT is one of the major defects observed in the irradiated materials for fcc metals, especially for materials with low stacking-fault energy such as Cu, it is essential to fully and precisely evaluate the mechanisms of interaction between SFT and line dislocations by MD simulations, and compare the results with the linear elastic theory.

We have used the Mishin potential, the advantage of which is that it can reproduce the phase stability for both FCC and HCP, and that it is suitable for the deformation simulations. SFT can be obstacles for dislocation motion, because there are interactions between line dislocations and stair-rod dislocations in the SFT. Figure 1 shows one snapshot describing the interaction between the line dislocation and SFT. The strength as the obstacles for the dislocation motion appears to strongly depend on the cross section between SFT and the line dislocation, because the cross section determines the length of the stair-rod dislocation physically intersecting the line dislocation, and the bowing angles of the line dislocations.

Therefore, the cross section is an essentially good indicator to describe the strength of the obstacles for dislocation motion. And, the angle between the SFT and the glide plane appears to also affect the interaction and to be an important parameter.

In the previous local rule for the dislocation dynamics, only the size of the clusters and the bowing angles of the line dislocations were taken as the local rules. We have improved and modified them with the physical base model and developed the new local rule by incorporating the cross section and the angle between SFT and the glide plane.

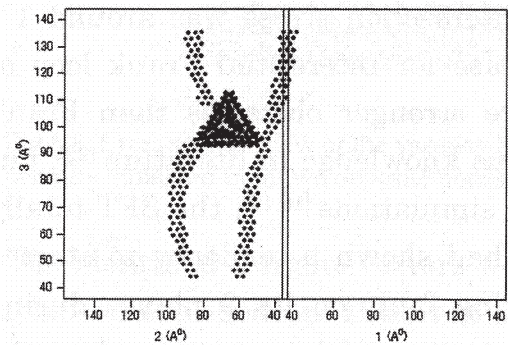


Figure 1. Interaction between line dislocation and an overlapping 28-vacancies SFT. The inserted edge dislocation was $a_0/2[101]$, but it dissociated into two partial dislocations.

§9. Evaluation of MHD Pressure Drop in Multi Layer Wall Channel

Hashizume, H., Yuki, K., Satake, M. (Tohoku Univ.)
Muroga, T., Sagara, A. (NIFS)

When liquid lithium is employed as coolant material in blanket system, it becomes critical to reduce MHD pressure drop. For this purpose, some concepts are proposed where insulating material is coated on the inside wall of metal channel. In these concepts, however, cracking in the insulator layer might become fatal to increase the MHD pressure drop drastically. In order to avoid this fatal failure, three layer wall is proposed where inner thin metal layer protect permeation of lithium into the crack of coated layer. In this study, therefore, two-dimensional analysis is performed to evaluate effect of inner metal wall thickness on the MHD pressure drop. Also the theoretical model is proposed to evaluate the MHD pressure drop in three layer wall channel.

In the numerical analysis, the following equations for the fully-developed MHD flow are solved, based on the finite element method with 8-noded isoparametric elements;

$$0 = -\frac{1}{\rho} \frac{\partial p}{\partial z} + \nu \left(\frac{\partial^2 v_z}{\partial x^2} + \frac{\partial^2 v_z}{\partial y^2} \right) - \frac{1}{\rho} \sigma \left\{ B_y \frac{\partial \phi}{\partial x} - B_x \frac{\partial \phi}{\partial y} + (B_x^2 + B_y^2) z \right\}$$

$$\frac{\partial^2 \phi}{\partial x^2} + \frac{\partial^2 \phi}{\partial y^2} = -B_y \frac{\partial v_z}{\partial x} + B_x \frac{\partial v_z}{\partial y}$$

Here p , v_z and ϕ are pressure, velocity component in z direction and electric potential, respectively. Figure 1 shows the model used in this analysis, where hatched regions correspond to insulator. Parameters used in the analysis are listed in table 1.

In the theoretical analysis, the wall thickness is explicitly treated in the circuit theory and then for the single layer wall, the following equation is derived;

$$\frac{dp}{dz} = \frac{b}{a} \frac{1}{\left(\frac{b}{\sigma_{Li} a} + \frac{t_w}{\sigma_w a} + \frac{a}{3\sigma_w t_w} + \frac{t_w}{\sigma_w t_w} + \frac{2}{\sigma_w t_w} + \frac{b}{\sigma_w t_w} \right)} \bar{u} B^2$$

R_{Li} R_{wy} R_{px} R_c R_{py} R_p

For the three layer wall, the above equation is modified as follows;

$$\frac{dp}{dz} = \frac{b}{a} \frac{1}{R} \bar{u} B^2, \quad R = R_{Li} + R_{wy} + R_{123}$$

$$R_{p1} = R_{px1} + R_{c1} + R_{py1}, \quad R_{p2} = R_{px2} + R_{c2} + R_{py2}$$

$$R_{p3} = R_{px3} + R_{c3} + R_{py3}$$

$$\frac{1}{R_{23}} = \frac{1}{R_{wy3} + R_{p3}}, \quad \frac{1}{R_{123}} = \frac{1}{R_{wy2} + R_{23}} + \frac{1}{R_{p1}}$$

Further the Hartmann and M-shape layers are also treated as conducting walls and then the following modification for the resistance of inner layer wall is necessary;

For inner layer

$$\frac{a}{3\sigma_w t_w} \Rightarrow \frac{1}{\frac{3\sigma_{Li} b}{a} + \frac{3\sigma_w t_w}{a}}$$

$$\frac{b}{\sigma_w t_w} \Rightarrow \frac{1}{\frac{\sigma_w t_w}{b} + \frac{\sigma_{Li} a}{b}}$$

Figure 2 shows the results of both numerical and theoretical calculations. We can see extremely good agreement between the results. The performance required to the insulator is evaluated to be

$$\frac{\sigma_{insulator}}{\sigma_V} \approx 10^{-8} - 10^{-9} \quad \frac{t_{insulator}}{\sigma_{insulator}} \approx 10^{-3} - 10^{-2}$$

The dp/dz is given by

$$\frac{dp}{dz} \propto t_{inner\ wall} \times velocity \times B^\alpha \quad (\alpha = 1.75 - 1.88 < 2)$$

The reason that $\alpha < 2$ is that the thickness of Hartmann and M-shape layers depends on the magnetic field intensity.

Table 1 Parameters used in analysis

conductivity	Li	$\sigma_{Li} = 3.0 \times 10^6 [S/m]$
	wall	$\sigma_V = 1.35 \times 10^6 [S/m]$
Inner wall thickness	10, 15, 20, 25 μm	
Li velocity	0.5	[m/sec]
Bx	5	[T]

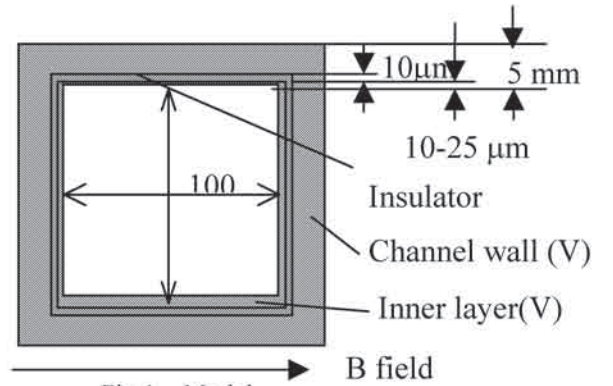


Fig.1 Model

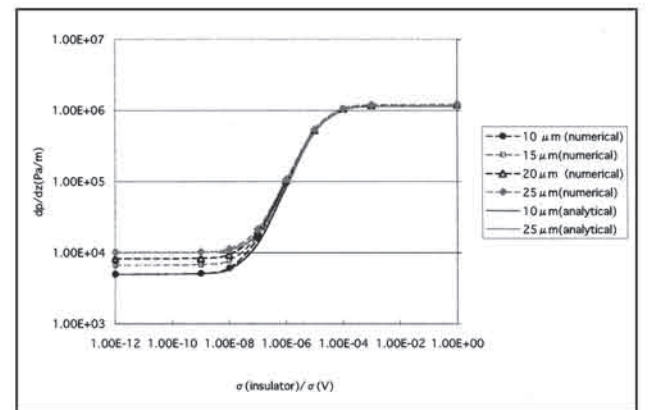


Fig.2 MHD pressure drop

\$10. Preparation of Cylindrical Superconductor Composed with Ni Mesh for Current Lead

Yoshizawa, S. (Meisei Univ.)

1. Introduction

Sintered bulk Bi-2223 has a critical temperature of over 77 K and low thermal conductivity. It has been used as a current lead for the liquid He-free cryocooler-cooled magnet. However, Bi-2223 bulk has some problems that limit the application field. One of the typical problems is that the critical current density (J_c) of the bulk materials is much smaller than that of the wire and tape materials. And another is that the sintered bulk is fragile because Bi-2223 bulk is ceramic material. The author developed recently Bi-2223 and Ag-plated nickel (Ni) wires composite bulk, which has high superconducting and mechanical property.

In this study, we prepared two types of Bi-2223 sintered bulk composed with Ag-plated Ni wire meshes, rectangular and cylindrical sample. By adding meshes into the sintered bulk, it can be expected that the mechanical property of the composite is strengthened for the bending stress from various directions. In preparing a cylindrical sample, it is mentioned that the sample is easy to produce compared with the sample composed with many wires.

2. Experimental Procedure

2-1 Composite with Ni mesh sample

2-1-1 Rectangular sample

We prepared Bi-2223 bulk composed with meshes of Ni wire 0.25 mm in diameters. Ni wire is plated with Ag by 0.03 mm in thickness. The constant mass of 1 g calcined powder was picked up. Ni mesh composite bulk was made by stacking alternately the calcined powder and Ni mesh. The number of composite Ni meshes was from 0 to 4. The composite sample were molded by metal dies, 5 mm in width, 22 mm in length and 2 mm in thickness, using coaxial pressing equipment. The samples were sintered at 840°C for 50 hours, intermediate pressed by a cold isostatic pressing (CIP) method and then, re-sintered at 840°C for 50 hours.

2-1-2 Cylindrical sample

Included mesh in cylindrical sample was same as the mesh used in the rectangular sample. Calcined powder of the constant mass of 27 g was picked up. Sample size was 27 mm in diameter and 50 mm in length was prepared by CIP method. The prepared samples were sintered at 845°C for 50 hours in air.

2-2 Measurement

The mechanical property of the rectangular sample was estimated by a three point bending test. Superconducting properties was estimated by the J_c at 77 K under self-field. Crystal characteristics and microstructures of the interface region between the oxide and Ni meshes were observed in Scanning Electron Microscope (SEM).

3. Results and Discussion

3-1 Rectangular sample

The bending stress of ca. 90 MPa was obtained in the bulk without Ni meshes, which was ruptured separately. The composite did not rupture but fine cracks were induced after the maximum bending stress, which were 100 MPa in the composite with one layer of the meshes and 50 MPa in the composite with two or more layer of the meshes. When one layer of the meshes was composed, the J_c was increased to 600 A/cm² from 200 A/cm² of the sample without the meshes. The results of SEM observation on the microstructure of the composite sample showed that highly c-axis oriented and densely structured Bi-2223 plate-like grains could be formed along the Ni mesh. A micro crack was observed between Bi-2223 and the Ni wire. Deterioration in the mechanical characteristic of the composite Ni mesh two layers over expects that the micro crack was a cause.

3-2 Cylindrical sample

Fig. 1 shows photograph of cylindrical sample. The J_c of sample 5 mm in width, 22mm in length and 2 mm cut out from the cylinder was increased to 145 A/cm² from 66 A/cm² of the sample without the meshes. The result of cross sectional SEM observation was saw Bi-2223 plate-like grains could be formed along the plated with Ag around. It is expected that J_c increased by formed plate-like grains.

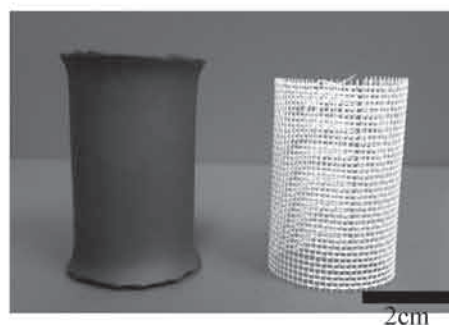


Fig. 1 Composite sample with Ni mesh and Ag-plated Ni mesh.

4. Rerences

- 1) Hirano, S. Yoshizawa, S. Hishinuma, Y. Nishimura, A.: Superconductivity and Mechanical Property of Bi-2223/Ni-wire Mesh Composite Bulk, *Pysica C* 412-414 (2004) 734-738.
- 2) Hirano, S. Yoshizawa, S. Hishinuma, Y. Nishimura, A.: Current Remaining after Fracture by Three Point Bending Test of Bi-2223 bulk Composed of Ag-Plated Ni wires, *Applied Superconductivity* 2003, Institute of Physics Publishing, 2004, pp. 2465-2470.

§11. Dynamic Behavior of He-vacancy Complex in Highly-purified Vanadium Alloys

Nita, N., Miyawaki, K., Matsui, H. (IMR, Tohoku Univ.) Nagasaka, T.

Introduction

Vanadium alloys are considered to be one of the leading candidates for the fusion reactor blanket material. Although vanadium has many attractive features, its use at high temperature may be limited by helium embrittlement. Another problem concerning helium, in a technical point of view, is the enhancement of nucleation and growth of cavity. It is well known that helium atoms stabilize the cavity, which affects the microstructural evolution such as swelling. Effects of the helium on the macroscopic mechanical properties have been studied rather extensively, while the evolution processes of the helium-defect complex, especially during the earlier stage of their clustering process is not clearly understood. This is mainly because of the complexity of helium clustering process in vanadium caused by a large amount of interstitial impurities (C, N, O) in the matrix. The objective of present paper is to investigate effects of impurities on the helium clustering process in the early stage, using THDS (Thermal Helium Desorption Spectrometry)[1], one of the most effective techniques to study He-V-X(X=C,N,O) type complexes.

Experimental procedures

Specimens used were pure vanadium. Oxygen contents in samples were systematically controlled by regulating the atmosphere during annealing and by using Zr-treatment technique [2]. Specimens whose nitrogen contents were controlled by regulating the atmosphere during arc-melting were provided by NIFS. Table 1 shows the concentration of the impurities in vanadium detected by the chemical analysis.

THDS were performed in the following manner to examine the nature and behavior of the helium-defect complexes. First, the helium implantation at the accelerating voltage of 1keV were conducted up to 3.2×10^{17} ions/m², then the specimen was heated to 1700K at a constant rate of 40K/s while monitoring the release rate of helium gas with a quadropole mass spectrometer. Note that the 1keV helium bombardments produce frenkel pairs in vanadium.

	O	N	C	Total
VO140	140	30	50	220
VO850	850	30	50	930
VO1600	1600	30	50	1680
VN430	130	430	300	860
VN620	160	620	340	1120
VN1700	130	1700	300	2130
VN2600	150	2600	320	3070

Concentration: appm

Table.1 Impurity concentration in vanadium

Results and discussions

In the THDS spectra, several desorption peaks have been observed and these peaks may be concerned with vacancy type defects which are one of the effective trap sites of helium in metals. Prominent peaks appeared at 530-570K, 730K as the function of the fluence in the VO140, while the peak at 700K grew as well as 550K peak in the sample with higher oxygen concentration (VO850, VO1600) and

Defect type	T _{Peak}	E _{diss}
He _n XV	530	1.3
	550	1.4
	570	1.5
He _n XV ₂	690	1.7
	740	1.9
He _n V _m	790	2.0
	940	2.4
He _{n>1} V _{m>1}	1010	2.6

Table. 2 Identification of the desorption peaks

550K peak was split into double peaks with increasing the fluence.

THDS spectra were fitted with the theoretical equations based on the one order desorption mechanism. Deconvolution of the peaks was carried out and the peaks that were depended with the impurity level were successfully separated to the peaks independent of the impurity. Population and temperature of the peaks in VO specimen were similar to VN specimen.

The peaks observed in present work were assigned as He_nOV, He_nOV₂ and He_nOV_m, respectively. Table 2 shows the summary of identification of the desorption peaks.

Conclusions

1 HeV clusters which is impurity-free-defect-complex were detected when the concentration of oxygen was extremely low (110appm)

2 THDS peaks were assigned as independent peaks or dependent peaks with the impurity.

3 Effects of oxygen and nitrogen on the stabilization behavior of vacancy type complex was comparative in the present work.

4 Effective levels of impurity on the formation of He-V-X(X=C,N,O) type complexes were saturated around 2000appm.

References

- [1] E.V.Kornelsen et al, Rad. Eff 42(1979)113
- [2] K. Takahashi, Master thesis, Tohoku university, 2001

§12. Joining and Heat Load Test of Tungsten Divertor

Tomota, Y., Kurumada, A., Imamura, Y. (Ibaraki Univ.), Oku, T. (The Univ. of the Air), Kurishita, H. (Tohoku Univ.), Kubota, Y., Noda, N.

Tungsten materials have a high heat resistance, a high thermal shock resistance and an excellent erosion resistance. From the viewpoints of thermal characteristics and a plasma particle control, the tungsten materials are expected to be used as an armor tile material of the next divertor plate for the LHD during the steady state and the long pulse operations. In this study, the divertor plate model specimens made of tungsten materials are manufactured to contribute to the development of the plasma facing components having high performances. And the integrity of the divertor plate model is tested by a deflection-type electron beam heating apparatus.

Tested materials are the stress removal and the re-crystalline processing specimens of the pure tungsten material made by Allied Materials Corp. The re-crystalline processing tungsten material is treated further to the stress removal one for obtaining the grain size from 10 to 20 micron.

Fig.1 shows the joining method of tungsten materials. Tungsten materials of 4 pieces ($20 \times 5 \times 5$ mm) are joined with an oxygen-free copper block ($20 \times 20 \times 20$ mm) having a cooling pipe (7 mm in inner diameter, 10 mm in outer diameter and 70 mm in length) after polishing and acetone washing. Titanium (0.05 mm in thickness) and copper (0.05 mm in thickness) foils are inserted for the joining. The joining specimens are held for 40 minutes at 1000 degrees C in a vacuum of 1×10^{-4} Torr. [1]

In heat load tests, heat fluxes from 0.5 to 15 MW/m^2 are irradiated to the tungsten divertor plate model specimens by a deflection-type electron beam heating apparatus. The one cycle is 10-sec irradiation and 15-sec interval. The speed and the temperature of the water coolant are 15 l/min and 15 degrees C, respectively. And the temperatures of the surface and the joining part are measured by a radiation thermometer and CA thermocouples, respectively. The microstructures are observed by SEM before and after the heat load tests.

Fig.2 shows a crack in the re-crystalline processing tungsten material near the joining part. The crack parallel to the joining line is considered to occur by the thermal stress due to the difference of the thermal expansion between tungsten and copper materials. The crack is also

observed in the stress removal one. The joining technique needs to be improved further.

Fig.3 shows the relationship between temperatures of the tungsten divertor plate model specimen and the heat flux. In this figure, the data of the C/C composite divertor model specimen are also indicated. So the surface temperatures of the tungsten materials are lower at the high heat flux region, the tungsten divertor is considered to be effective in the case of receiving the severe plasma attack. On the other hand, the temperatures of the joining parts are nearly the same because of the good heat transfer.

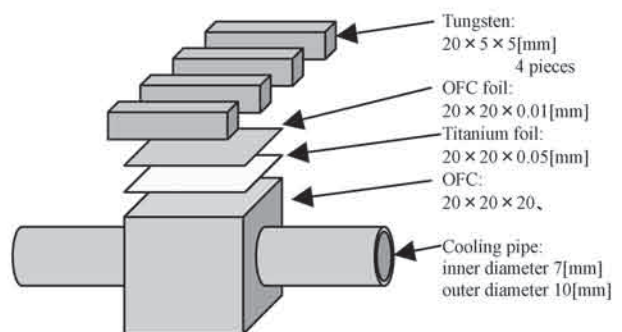


Fig.1 Joining method of tungsten materials.

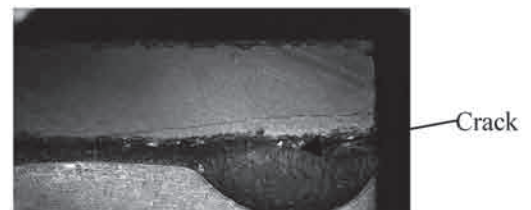


Fig.2 Crack in the re-crystalline processing tungsten material near the joining part.

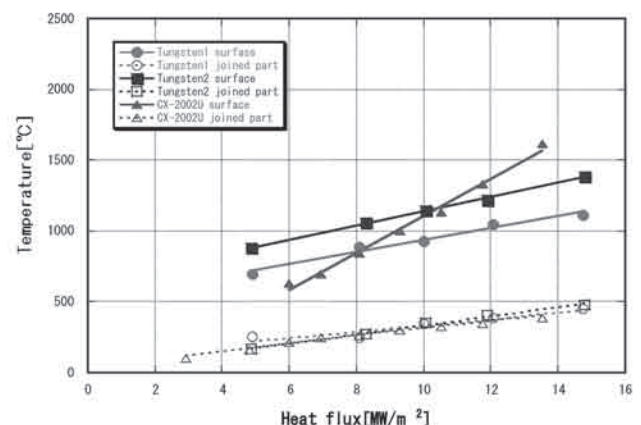


Fig.3 Relationship between temperatures of the tungsten divertor plate model specimen and the heat flux.

Ref. [1] Suzuki, A., Imamura, Y., Kurumada, A., et al., Extended Abst. of Ibaraki District Conf. (2003.9.19) 55-56.

§13. Overall Characterization of High Purity Reference Vanadium Alloys NIFS-HEATs

Satou, M., Abe, K., Hino, T. (Tohoku Univ.)
Nagasaka, T., Muroga, T.

Vanadium alloy is metallic and nonmagnetic material among the prime candidates for fusion reactor first wall application, yet lack of industrial background that include large-heat productivity and fabricability was weakness from viewpoints of material developments. Successful production of high purity reference vanadium alloys known as NIFS-HEATs alloy demonstrates its capability for large production and provides an opportunity to carry out round-robin tests and full size industrial standard tests. Research activities in each organization were also utilized for overall characterization of the vanadium alloy for fusion applications. Basic physical properties, workability, weldability, interaction with gaseous elements, defects production after irradiation, mechanical properties, compatibility, joining or coating with ceramics materials, etc. were studied. Guideline for the alloy development was discussed in this collaboration study based on individual research results.

Since mechanical properties of the V-Cr-Ti type alloy depend on interstitial impurity levels, controlling the interstitial elements is a key for the alloy development. Initial impurity levels can be reduced by modification of melting process as NIFS-HEATs. Further modification of the high purity Vanadium alloy is possible by means of a small addition of chemically reactive elements such as yttrium. In this report, tensile and Charpy impact properties of a series of V-4Cr-4Ti-xY alloys are briefly described.

The alloys used in this work were V-4Cr-4Ti-0.1Y, V-4Cr-4Ti-0.2Y, V-4Cr-4Ti-0.3Y and V-4Cr-4Ti-0.5Y (nominal weight percentage) fabricated by levitation melting method. Miniaturized specimens annealed at 950 °C for 3.6ks were used. Tensile tests were carried out using an INSTRON-type machine with an external cooling bath at strain rates of 6.7×10^{-4} to 10^{-2} s^{-1} . Charpy impact tests were carried out using an instrumented machine at the Oarai Branch, Institute for Materials Research, Tohoku University. Test temperatures were from ambient and to liquid nitrogen temperature. After these testing, specimens were examined by scanning electron microscopy in order to characterize the fracture surface.

The alloys showed fairly good ductility and tensile strength even in liquid nitrogen temperature. Little dependence of the levels of yttrium contents on the tensile properties was shown. The only difference was reduction in area became the smallest and the size of dimples observed in the fracture surface became the largest in the V-4Cr-4Ti-0.5Y alloy tested with strain rate of $6.7 \times 10^{-2} \text{ s}^{-1}$ at

liquid nitrogen temperature. From these results with higher strain rate deformation at low temperature, yttrium oxide that perhaps exists as inclusions might be starting point of the fracture.

Figure 1 shows the test temperature dependence of absorbed energy for the V-4Cr-4Ti-Y alloys measured by instrumented Charpy impact test. Absorbed energy, E , was normalized by size parameter of the specimen using a following equation:

$$E = E_{\text{obs.}} / Bb^2$$

, where $E_{\text{obs.}}$ is the observed value of absorbed energy, B is the width and b is the ligament size (= thickness - notch depth) of the specimen, respectively. The DBTTs of the alloys are as low as -150 °C. The alloys of V-4Cr-4Ti-0.1Y and V-4Cr-4Ti-0.2Y show higher upper shelf energy (USE) compared to the alloys V-4Cr-4Ti-0.3Y and V-4Cr-4Ti-0.5Y. NIFS-HEATs showed a little higher USE than the V-4Cr-4Ti-0.1Y alloy as 0.5 J/mm³ at -196 °C. The dependence of the levels of yttrium contents on the USE may indicate heterogeneous distribution of yttrium as precipitates. To clarify and to control the distribution of yttrium is a key issue to understand the properties of the alloys even though the most of them considered to be distributed as nano-size precipitates.

The amount of yttrium contents has the optimum between 0.1 and 0.2 weight percents so far from the Charpy impact properties. The characterization of the alloys from other viewpoints such as irradiation behavior and weldability of the V-Cr-Ti type alloy with small addition of Si, Al and Y are under way compared to the NIFS-HEATs.

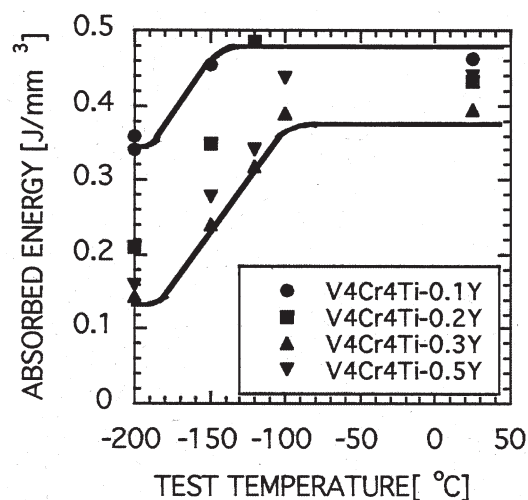


Fig. 1 Comparison of impact properties for the V-4Cr-4Ti-Y alloys, containing various levels of Y.

\$14. Environmental Effects on Radiation Effects in V-4Cr-4Ti Alloys

Watanabe, H., Yamasaki, K., Yoshida, N. (RIAM, Kyushu Univ.)
Nagasaka, T., Muroga, T. (NIFS)

1. Introduction

In the V-4Cr-4Ti alloy, it is well established that interstitial impurities such as oxygen and nitrogen play an important role in radiation effects such as microstructure change, irradiation hardening and embrittlement. Among them, oxygen is regarded as the most effective atom in the alloy. Furthermore, the alloy is considered to be used as a fusion blanket structural material that face to a vacuum and helium gas, which may contain a low partial pressure of oxygen. Recently, our ion irradiation experiments on V-4Cr-4Ti alloys at 473-973K revealed that oxygen pick-up from irradiation environment (namely, vacuum) is very minor up to the levels of 1 dpa [1,2]. But at higher dose levels, the effects might cause degradation of mechanical properties due to enhanced formation of titanium oxide precipitates during irradiation. To understand the radiation induced phenomena related with oxygen, such as oxide formation in the matrix, not only oxygen level in the alloy but also oxygen pick-up from radiation environment must be considered. The objective of the present study is, therefore, to understand the detailed mechanisms of oxygen pick-up from irradiation environment which related with titanium oxide.

2. Experimental Procedure

For ion irradiation, welded joint samples by YAG laser were used in this study. These samples were prepared from a high purity V-4Cr-4Ti alloy, which was designated as NIFS HEAT2. Before the welding (bead-on-plate welding) in a high purity argon atmosphere, the samples were annealed in a vacuum at 1273K for 2hr. The detailed welding procedure was described elsewhere. Oxygen concentrations of the sample before welding, and weld metal are 139 and 158 wt ppm, respectively. The samples were irradiated with 2.4MeV copper ion irradiation with a tandem accelerator at Kyushu University. The TEM specimens were sliced from welded materials and irradiated at 573 and 873K up to the dose of 12 dpa. After irradiation, the specimen was electro-polished by a back thinning method, and the area near the peak damage region (at about 700 nm) was observed by TEM.

3. Results

Microstructural evolution of laser welded samples at several distances from the bead center, which were irradiated at 873K, is shown in Fig.1. At 873K, fine titanium oxides were observed even at the dose of 0.75 dpa. These precipitates were identified to be Ti(C,O,N) with {100} habit planes. Dose dependence of the measured number density and size of Ti(C,O,N) in several specimens sliced from different positions are shown in Fig.2. The number density of these Ti(C,O,N) precipitates formed in

weld metal is about one order higher than that of base metal. The number density of Ti(C,O,N) decreased with increasing dose (region ① in Fig.2) and well grown Ti(C,O,N) precipitates were observed at higher dose levels above 7 dpa (region ② in Fig.2). On the other hand, almost same size and density of Ti(C,O,N) precipitates were observed at 12 dpa. Estimated oxygen levels from the measured density and size of Ti(C,O,N) precipitates were also shown in Fig. 1. In this estimation, Ti(C,O,N) precipitates are assumed to be TiO (NaCl type crystal structure). The estimated oxygen levels from the microstructure increased with dose and about 20 times higher than that of before irradiation at 12 dpa. The same oxygen pick-up from vacuum environment using different levels of nitrogen and oxygen samples is also reported in ref [3]. Therefore, in higher dose levels, effects of oxygen from irradiation environment are essential, and thus further studies are needed to avoid oxygen pick-up during ion irradiation.

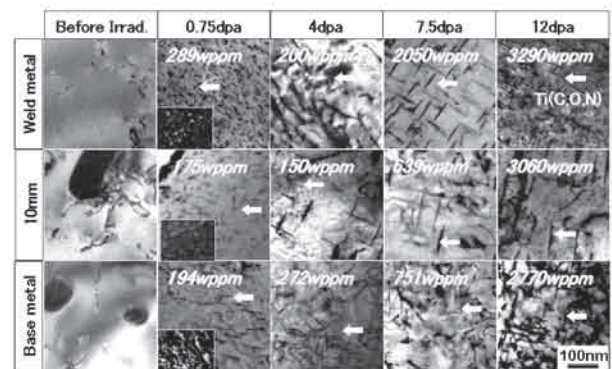


Fig.1 Dislocation loop formation at 873K

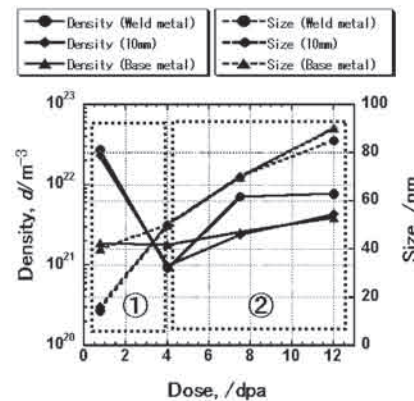


Fig. 2 Dose dependence of measured density and size of Ti(C,O,N) precipitates at 873K.

References

- [1] H. Watanabe, T. Arinaga, K. Ochiai, T. Muroga and N. Yoshida, J. Nucl. Mater. 283-287 (2000)286-290
- [2] H. Watanabe, M. Suda, T. Muroga and N. Yoshida, J. Nucl. Mater. 307-311 (2002)408-411
- [3] H. Hatakeyama, H. Watanabe, T. Muroga and N. Yoshida, J. Nucl. Mater. 329-333(2004)420-424

\$15. Measurements of Radiation Induced Conductivity of Ceramic Insulators for Fusion Blanket

Iida, T., Sato, F. (Osaka Univ. Eng.)

Ikeda, T. (Osaka Univ. ISIR)

Tanaka, T., Muroga, T.

Radiation effect data on electrical properties of ceramic insulators in the liquid Li/V blanket system¹⁾ are very important for a design of the fusion blanket system. In the blanket system, degrading of insulation performance becomes a serious problem in the condition of high temperature and high radiation dose rate. Thus, measurements of the radiation induced conductivity (RIC) on candidate ceramic materials (Y_2O_3 , Er_2O_3 , CaZrO_3 , AlN etc.) have been performed with a fusion neutron generator and a fission reactor. In this report, moreover, detailed irradiation experiments on newly developed ceramic samples were performed with a ^{60}Co gamma-ray source. Comparison of irradiation effects induced by different types of radiations and understanding of the difference in the irradiation effects are useful for the evaluation of the candidate materials.

The candidate materials with good chemical stability against high temperature liquid lithium were prepared for the irradiation experiments. Three disc specimens of Y_2O_3 (supplied from TEP Corp.), CaZrO_3 and Er_2O_3 (from TYK Corp.) were made with a sintering method, and their dimensions were 10 mm ϕ x 1 mm. For the electrical conductivity measurements of the specimens, appropriate electrodes were made with vapor deposition of silver. The thickness of the electrodes was ~ 30 nm. The electrical conductivity of the Y_2O_3 , CaZrO_3 and Er_2O_3 specimens was order of 10^{-13} - 10^{-14} S/m before irradiation.

The gamma ray irradiation was performed at the ^{60}Co irradiation facility of Institute of Scientific and Industrial Research of Osaka University. The experimental setup was described in previous papers. The maximum dose rate at the sample position was estimated to be ~ 2.1 Gy/s by calculation with the photon-electron transport code. In addition, the same specimens were irradiated with 100 keV H^+ beams for the comparison between the gamma-ray and ion irradiation effects. The beam intensity was 0.6 – 2.2 $\mu\text{A}/\text{cm}^2$. The arrangement for the current measurement was similar to that in the gamma ray irradiation experiment.

Measured results of the current-voltage (I-V) curve under the gamma ray irradiation are shown in Figs 1 (a) and (b). The I-V curves of the three specimens were symmetric to the polarity of the bias voltage. The RIC values evaluated from the induced currents for bias voltage of +250 V were 1.3×10^{-10} S/m for Y_2O_3 (1.8 Gy/s), 1.7×10^{-11} S/m for CaZrO_3 (1.8 Gy/s) and 9.4×10^{-12} S/m for Er_2O_3 (2.1 Gy/s), respectively. In the ion beam experiments, the ion-induced conductivity was 2.9×10^{-11} S/m for Y_2O_3 , 3.7×10^{-11} S/m for CaZrO_3 , 3.9×10^{-11} S/m for Er_2O_3 , respectively.

The RIC data evaluated from the present gamma ray irradiation experiment were compared with our

previous data obtained by fusion neutron and fission reactor irradiation experiments. The dose rate for the fission reactor irradiation was reevaluated by detailed calculation of the neutron and gamma ray spectra with MCNP transport code. As shown in Fig. 2, the present data were plotted almost within one order of magnitude as compared with data from the previous irradiations. The results indicate that the RIC effect in the candidate materials is correlated with the dose rate under neutron and gamma ray irradiations, which deposit the energy uniformly in the materials. However, the magnitude of ion induced current was 1 or 2 orders lower than that predicted from the gamma ray and neutron irradiations as plotted in Fig. 2. The response under the ion beam irradiations was complicated and included various factors to be considered. Since the thin layer below the high-voltage-side electrode had high ion induced conductivity under irradiation, the specimen was considered to be a series of two regions with low and high conductivities. The density of electron-hole pair production under ion beam irradiation was estimated to be 10^5 times higher compared with the gamma ray irradiation. Therefore electrons and holes might recombine effectively and it is imagined that the electrical field near the high-voltage-side electrode was weakened due to the existence of the space charge (charge up).

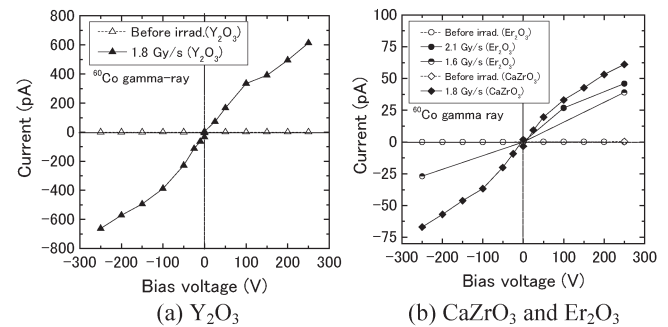


Fig. 1. Results of current-voltage (I-V) curve measurement under gamma ray irradiation.

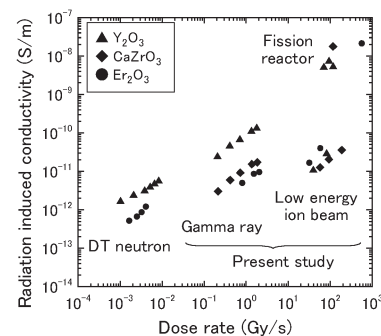


Fig.2. Comparison of radiation induced conductivity evaluated in present experiment with that in previous DT neutron and fission reactor irradiation.

References

- 1) S. Malang, et al., Fus. Eng. Des. 16 (1991) 95-109.
- 2) T. Tanaka, et al., J. Nucl. Mater. 329-333 (2004) 1434-1437.
- 3) T. Tanaka, et al., Fusion Engineering and Design, to be published.

\$16. Examination of Electrical Degradation of Ceramic Coating Materials Using Ion Beam Irradiation

Shikama, T., Nagata, S., Tsuchiya, B., Toh, K. (IMR, Tohoku Univ.)

Tanaka, T., Muroga, T.

Suzuki, A., Sawada, A. (Univ. of Tokyo)

In the development of the electrical insulating coating for the liquid Li cooled blanket system, radiation damage is one of the concerned factors degrading the performance. Previous studies on Al_2O_3 insulators have reported the possibility of RIED (Radiation Induced Electrical Degradation), which is permanent electrical degradation due to irradiation damage, under the condition of high neutron fluence, high temperature and high electric field. However, almost no data is available for the irradiation effects on the candidate coating materials such as Er_2O_3 , Y_2O_3 , CaZrO_3 , AlN etc. The objective of the present study is to examine the effect of irradiation damage on the ceramic materials using a high-energy ion beam. Result of preliminary irradiation experiment on Er_2O_3 coating is described in this report.

Schematic arrangement of the ion beam irradiation is shown in Fig.1. A sample of Er_2O_3 coating was made on a stainless steel plate of $15 \times 15 \times 2 \text{ mm}^3$ by the RF sputtering method at University of Tokyo. Thickness of the coating was $1 \mu\text{m}$. Electrical performance of the coating sample was examined at NIFS. On the surface of the coating, three Pt electrodes of $2 \times 2 \text{ mm}^2$ were made by sputter deposition with thickness of $\sim 100 \text{ nm}$. Bias voltage was applied to the stainless steel plate. Electrical insulating performance of the coating was evaluated by measurement of currents flowing into the electrodes. The electrical conductivities under the three electrodes were 1.7×10^{-10} , 5.4×10^{-11} and $6.9 \times 10^{-10} \text{ S/m}$.

Ion beam irradiation was performed in Institute for Materials Research of Tohoku University. A beam of 1 MeV H^+ was collimated to 1 mm in diameter and injected into the Pt electrodes. During the irradiation, the electrodes were grounded to prevent electrical breakdown due to charge up in the coating layer. The irradiation flux of the H^+ beam was $7.9 \times 10^{11} \text{ H/cm}^2/\text{s}$. The total fluences at the three electrodes were 1.0×10^{15} , 1.0×10^{16} and $2.6 \times 10^{16} \text{ H/cm}^2$, respectively.

Figure 2 shows examples of current-voltage (I-V) characteristics measured before and after the ion beam irradiation. Both of the curves indicate ohmic characteristics. Electrical conductivities after the irradiation were $2.6 \times 10^{-10} \text{ S/m}$ (fluence: $1.0 \times 10^{15} \text{ H/cm}^2$, conductivity before irradiation: $1.7 \times 10^{-10} \text{ S/m}$), $9.6 \times 10^{-10} \text{ S/m}$ (1.0×10^{16}

H/cm^2 , $5.4 \times 10^{-11} \text{ S/m}$) and $1.3 \times 10^{-7} \text{ S/m}$ ($2.6 \times 10^{16} \text{ H/cm}^2$, $6.9 \times 10^{-10} \text{ S/m}$), respectively. Significant change was observed for the order of $1.0 \times 10^{16} \text{ H/cm}^2$ in the present experiment. By calculation using the charged particle transportation code TRIM, it is estimated coarsely that the range of hydrogen ions was $5\text{--}10 \mu\text{m}$ in the Er_2O_3 layer and displacement after the irradiation of $2.6 \times 10^{16} \text{ H/cm}^2$ corresponded to $\sim 0.005 \text{ dpa}$.

Further irradiation is planned to examine the relation between the insulating performance and various factors of fluence, temperature, applied electric field etc. Examination of luminescence emission spectrum under ion beam irradiation is also planned to obtain information on the defect formation.

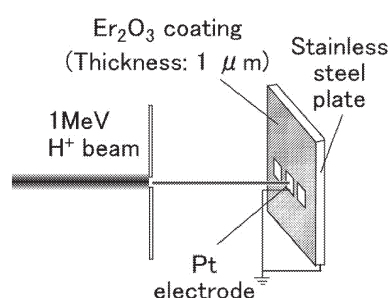


Fig. 1 Schematic arrangement of ion beam irradiation on Er_2O_3 coating.

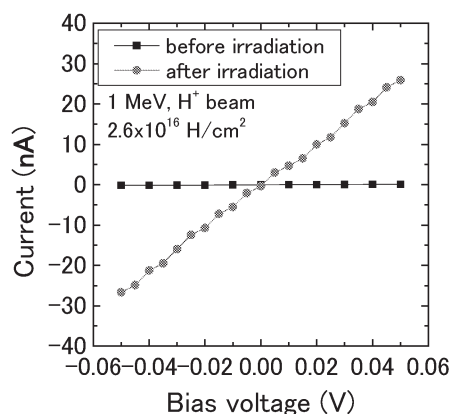


Fig. 2 Example of current-voltage (I-V) characteristics before and after irradiation (Electrode: $2 \times 2 \text{ mm}^2$, Thickness of coating: $1 \mu\text{m}$)

§17. Development of Joint Technique of SiC/SiC Composites

Hinoki, T., Eiza, N. (Institute of Advanced Energy, Kyoto University)
Muroga, T.

SiC/SiC composites are considered for use in extremely harsh environments at high temperature primarily due to their excellent thermal, mechanical and chemical stability, and the exceptionally low radioactivity following neutron irradiation. In particular, recent improvement in the crystallinity and purity of SiC fibers and improved composite processing have improved physical and mechanical performance under harsh environments¹⁾. The novel processing called Nano-powder Infiltration and Transient Eutectic-phase (NITE) Processing has been developed based on the liquid phase sintering (LPS) process modification²⁾. The NITE processing can achieve both the excellent material quality and the low processing cost. The important issues to use the NITE SiC/SiC composites for industry are development of joining technique. Several kinds of joining techniques have been developed for SiC and SiC/SiC composites using polymer, glass-ceramics and reaction bonding. One of the key for the development is the stability of the joining at application temperature. Using the SiC for joint of SiC or SiC/SiC composites has the advantage at the high temperature due to the no coefficient of thermal expansion (CTE) mismatch. The objective of this work is to develop joint technique for SiC and SiC/SiC composites modifying NITE processing.

The substrate material for joining was Hexoloy® SA SiC (sintered α -SiC) and SiC/SiC composites fabricated by NITE processing. The substrates with dimension 23 mm (long) \times 2.7 mm (wide) \times 3 mm (thick) were machined from plate. The substrate SiC bars were joined with the slurry including SiC nano-powder (<20nm) and the sintering additive of Al_2O_3 , Y_2O_3 , SiO_2 . They were hot-pressed at 1800 °C with the pressure of 15-30 MPa in Ar environment. Butt joint was applied to the SiC bars and 46 mm (long) \times 2.7 mm (wide) \times 3 mm (thick) bars were formed. Mechanical properties of the joint were evaluated using the bars by tensile test according to ASTM C1275 and asymmetric four points bend according to ASTM C1469. For the tensile test, the gauge section was 20 mm-long in the middle of the specimen. The specimens were gripped using a pair of wedge-type grips. The grips were connected to the load train using universal joints to promote self-alignment of the load train during the movement of crosshead and to reduce unwanted bending strains in the specimen. All tests were conducted at a cross-head speed of 0.3 mm/min at ambient temperature. Asymmetric four point flexural test was conducted using the same specimen for the tensile test. Inner span and outer span of the asymmetric four points test were 8 mm and 44 mm, respectively. The microstructure and fracture surfaces following mechanical test of the joint, coating and their interfaces were observed by optical microscopy (OM) and

field emission scanning electro microscopy (FE-SEM), and analyzed by energy dispersive X-ray spectroscopy (EDS).

Silicon carbide substrates were successfully joined with forming thin NITE-SiC of approximately 10 μm -thick at interface. Figure 1 shows the backscattering image of the joint. No concentration of sintering additive was seen, while small white dots including the sintering additive were observed. In tensile test, specimens failed at the joint. The tensile strength was approximately 40 MPa on average, while relatively large scatter of data was seen. Apparent shear strength was approximately 50 MPa on average with relatively small scatter of data. Indeed the specimens did not fail at the joint. Actual shear strength was more than 50 MPa. The other test method or the notched specimen at the joint for the asymmetric four point flexural test is required to evaluate actual shear strength.

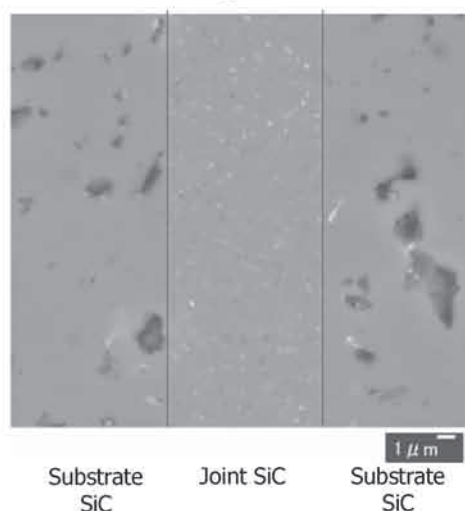


Figure 1: SEM Image of interface of joint of monolithic SiC

Fracture surfaces following the tensile test were observed. It was found the joint had approximately 40 % of porosity including the large pore, which might induced the stress concentration during the loading. The reason of the relatively small tensile strength of 40 MPa for SiC was due to the large non-bonded region, although even with the large porosity and the stress concentration the joint showed large strength compared with the other joint for SiC or SiC/SiC composites³⁾.

SiC/SiC composites were also joined using the same technique. The processing conditions were not optimized, and it showed similar tensile strength with the strength for monolithic including 40 % porosity at interface. Major difference of SiC/SiC composites from monolithic SiC for joint is the surface roughness. Pores were likely to appear compared with the joint for monolithic SiC.

References

- 1) Hinoki, T. et al.: J. Nucl. Mater., 307-311 (2002) 1157-1162.
- 2) Kohyama, A. et al.: Ceramic Transactions, 144 (2002) 3-18.
- 3) Katoh, Y. et al.: J. Nucl. Mater., 283-287 (2000) 1262-1266.

§18. Development of Reduced Activation Ferritic Steels with Improved Heat Resistance and Elemental Property Characterization for High Cycle Efficiency Steel-based Blankets

Kohyama, A., Kim, S.W., Ogiwara, H. (Institute of Advanced Energy, Kyoto University)
Muroga, T.

It is critical for the blanket structural material of fusion reactor to understand fatigue behavior in order to estimate the safety margin, life-time and reliability in terms of the crack initiation and critical crack length before and after irradiation^{1,2)}. The existing database of the reduced activation ferritic steels (RAFTs) (JLF-1 steels and F82H steels) including neutron irradiation effect are relatively rich compared with the other candidate materials. However experimental data such as fatigue life, fracture toughness and fatigue crack growth (FCG) are still insufficient for the blanket design. Fatigue testing of RAFTs after neutron irradiation is supposed to be carried out in hot cells with remote control system. Considering limited ability of specimen manipulation in the cells, the specimen and the test method must be arranged for simple operation. The objective of this study is to examine and understand the microstructural mechanism on the FCG behavior of JLF-1 steels. The effects of test specimen size were discussed within the Paris region. Especially, the correlations between crack growth behavior and microstructure were focused on.

The materials used were reduced activation ferritic/martensitic steels, JLF-1 IEA heat (Fe-9Cr-2W,V,Ta). Heat treatments were normalized at 1323 K for 1 h followed by air cooling (AC), followed by tempering at 1053 K for 1 h followed by AC, and post-welding heat treatment (PWHT) at 740°C for 3h furnace-cooled (FC) was applied. FCG tests were carried out according to ASTM E647 standard using a full-sized compact tension (CT) specimen and half-size CT specimen at room temperature. The crack growth test results were summarized in terms of FCG rate (da/dN) versus stress intensity factor range (ΔK) curves using an incremental polynomial method. These curves are divided into regions I, II and III. The FCG rate in the sub-critical region II is related to the stress intensity factor range as follows 3);

$$da/dN = C(\Delta K)^m, \quad (1)$$

where m is the Paris exponent and C is the Paris constants. Fracture surfaces of tested specimen were observed using a scanning electron microscope (SEM) in order to determine the fracture mode.

The variation of FCG rate (da/dN) with stress intensity factor range (ΔK) for full-size and half-size CT specimen at room temperature is shown in Fig. 1. Stable fatigue crack growth (Paris region) started from approximately 17 $\text{MPa}\cdot\text{m}^{1/2}$ of ΔK , although the initial stage of the fatigue crack growth showed unstable crack growth. The FCG rate

of half-size specimen was almost the same as those of full size specimens as shown in Fig. 1. Therefore, it is considered that the specimen size slightly affected the FCG rate for JLF-1 steels at RT. Although it is still necessary to evaluate of crack closure and fracture mechanics, it is suggested that the FCG behavior of JLF-1 steels can be evaluated by using small sized specimens at RT.

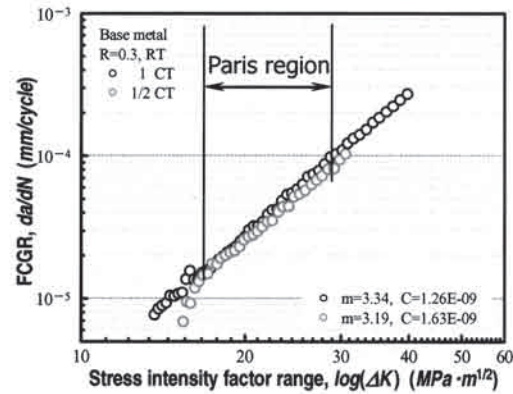


Fig. 1. Fatigue crack growth rate as a function of stress intensity factor range in full-size and half-size CT specimen at room temperature

Fig. 2 shows the SEM images of the fracture surface of Paris region in the FCG tested specimen. In this figure, trans-granular fracture surface accompanied by the striation pattern, which is a particular striped pattern of model I fracture, and the local ductility tearing were observed. The clear difference between each fracture surface accompanying the increase (Fig.2 A→B→C) in ΔK was not confirmed.

Paris region ($\Delta K=17\sim29 \text{ MPa}\cdot\text{m}^{1/2}$)

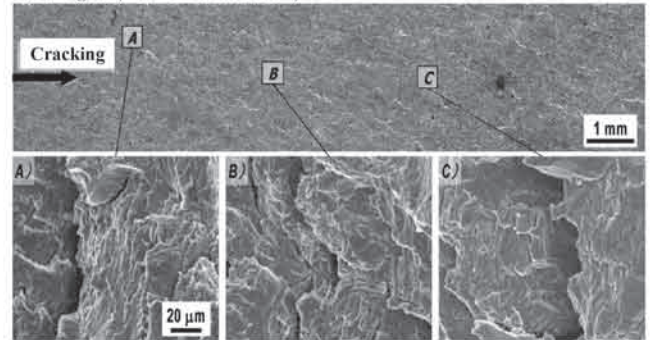


Fig. 2. SEM micrographs showing fatigue fracture surfaces after FCG test at room temperature

These results showed the possibility of evaluation using miniaturized CT specimen in evaluation of the FCG in JLF-1 steels.

References

- 1) Kohno, Y. et al. : J. Nucl. Mater. 271-272 (1999) 145.
- 2) Nishimura A et al. : J. Nucl. Mater. 258-263 (1998) 1242.
- 3) Paris, P.C. et al. : Trend. Engng. 13 (1961) 9.

\$19. Crack Length Measurement in Cryogenic Environment Using Unloading Elastic Compliance

Nishimura, A.

To investigate mechanical properties, such as fracture toughness, of structural materials at cryogenic temperature, a crack length must be evaluated precisely. Generally, a mechanical test is carried out in the double wall cryostat and it is not easy to measure the crack length directly using an optical system. Therefore, unloading elastic compliance method is traditionally adopted and the evaluated crack length has been used when fracture toughness is obtained in experiments. However, when the smaller size specimen, such as 1/4 inch compact tension specimen (1/4 CT), is employed, the absolute crack length must have a certain precision, like less than 1/100 mm, to keep a significant figure.

In this study, the scatter of the crack length measurement with the unloading elastic compliance method was investigated. The specimen targeted was a 1/2 CT specimen. To perform the fatigue test off small size specimen precisely, a small capacity fatigue testing machine was installed. The maximum load for fatigue is ± 5 kN and it has a servo-control system. The apparatus of the testing machine is shown in Fig.1. It is compact one and has an actuator at upper position of the cross head.

The specimen was a 1/2 CT specimen and prepared from a SUS304 stainless steel plate. An initial notch with 0.1 mm width was induced by electro-discharge machining. The both surfaces of the specimen were polished and the crack length was measure by a microscope of which magnification was 25 times, i.e. minimum scale was 0.05 mm. The specimen was fatigued under the load condition of 5 kN of maximum load and 0.2 kN of minimum load. The frequency was 5-6 Hz and down to 0.2 Hz when the measurement was done. Digital data sampling was carried out at 20 Hz with Digital Scope, DL708.

The compliance was measured by four ways. The first was determined by full hysteresis curve between 0.2 kN and 5 kN. The second was obtained from full hysteresis curve between 3 kN and 5 kN. In these cases, the compliance was measured making a linear regression line using full hysteresis curves. The third one was done making a regression line from 5 kN to 3 kN unloading process and the fourth was evaluated from the line from 5 kN to 4 kN as shown in Fig.2.

The evaluated results from these four methods are shown in Fig.3. At initial crack length, all results agreed well. However, as crack growing, the difference becomes larger and there is no tendency to saturate to a certain value. As far as the data obtained, the fourth method gives a stable results and smallest scatter.

From these results, it would be concluded that the line immediately after the unloading starts is very important and it makes a small scatter, high precision data.



Fig. 1 Test apparatus for servo-controlled fatigue testing machine (maximum for fatigue; ± 5 kN).

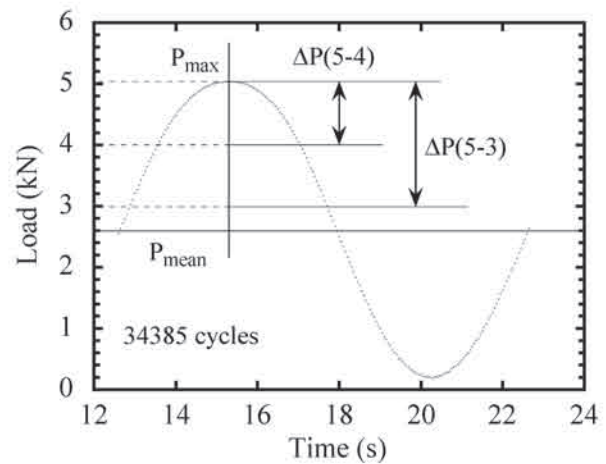


Fig.2 Determination of unloading elastic compliance.

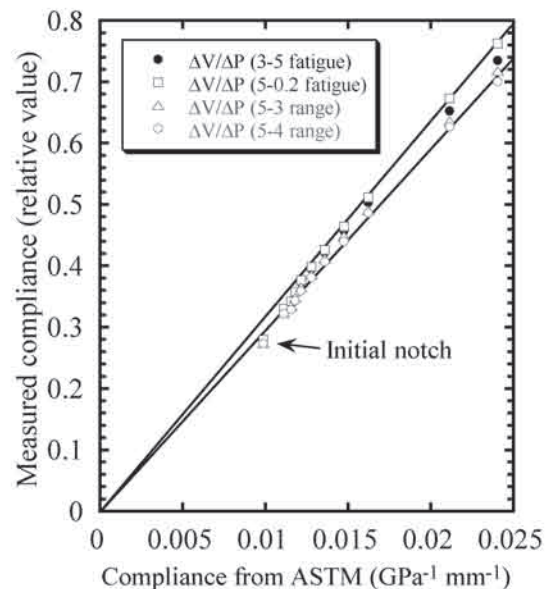


Fig. 3 Change in poloidal direction strain measured.

\$20. Lithium Compatibility of MHD Coatings Fabricated by Arc Source Plasma Deposition Method

Terai, T., Suzuki, A. (Nuclear Engineering Research Laboratory, Univ. of Tokyo), Sawada, A. (Quantum Eng. and Systems Sci., Univ. of Tokyo), Muroga, T.

For a D-T fusion reactor system, a blanket is a necessary component, where tritium is produced from lithium, heat is generated, and radiation is shielded. In fusion reactor designs, the liquid blanket concepts are the promising ones in order to realize a DEMO (demonstration) fusion reactor system of high power density, because it has advantages such as continuous replacement of breeders for reprocessing, no radiation damage for breeders, larger TBR (tritium breeding ratio) and better thermal transfer than solid blankets. Liquid lithium is considered to be one of the most attractive candidates as a liquid breeding material. In the self-cooled liquid lithium blanket system, the liquid lithium can be used not only as the tritium breeding material, but also a coolant for the blanket system. Moreover, sufficient TBR could be obtained without neutron multipliers, such as Be, due to high lithium density in the blanket. Thus, the liquid lithium blanket concept has a possibility to propose a blanket with the simplest structure.

A crucial issue for the self-cooled liquid lithium blanket concept, so-called magnetohydrodynamics (MHD) pressure drop, however, had been pointed-out that a large pumping power may be required due to the pressure drop in the conductive coolant induced by MHD effect with the magnet field. In order to solve this issue, insulating ceramic coatings on the inner surface of the tubing for the liquid lithium had been proposed. The coating should have high electrical resistivity, high corrosion resistance, and high thermomechanical integrity. Aluminum nitride (AlN), yttrium oxide (Y_2O_3), erbium oxide (Er_2O_3) have been chosen for the coating candidate materials by the investigations on compatibility with liquid metals. Some studies on the application of these candidate materials to the MHD coating shows fabrication of the coating with sufficient abilities is an important investigation point. In this study, erbium oxide coatings were fabricated and exposed in liquid lithium to observe compatibility with liquid lithium.

Arc source plasma assisted deposition method was used to fabricate erbium oxide coatings. In this method, 99.9% purity of erbium metal target was used as cathode. Vanadium metal or V-4Cr-4Ti alloy of $25 \times 25 \times 1 \text{ mm}^3$ plates were used as substrates, current of 80 A was introduced to generating arc on the cathode. Erbium ions were accelerated with the bias of 15 V and turned by magnetic field and went through the oxygen plasma, which oxygen gas was introduced at $5 \times 10^{-2} \text{ Pa}$. Erbium ions and oxygen ions formed erbium oxide on the substrates, where DC bias of $\sim 690 \text{ V}$ voltage were applied with 100 V radio frequency voltage to accelerate ions. The substrate was heated up to \sim

700 K, and deposition time was 0.25-1.5 h. The coated specimens were exposed to liquid lithium to observe compatibility. In the experiment, lithium was heated up to $\sim 973 \text{ K}$. After the exposure, residual lithium on the specimens were heated and distilled in the vacuum chamber.

The coatings fabricated by arc source plasma assisted deposition were transparent and had uniform thicknesses. The coatings fabricated at room temperature and 576 K were observed by XRD. The coating fabricated at low temperature had a few sharp peaks, some of the JCPDS peaks were not observed. On the other hand, the pattern of the coating fabricated at 576 K has many sharp peaks, and they were close to JCPDS peaks angle. It is considered that the coatings fabricated at low temperature had orientation, and the orientation was lost and the crystal grains grow at random as the temperature of fabrication became higher. Some of the coatings fabricated at low temperature had many peaks and the peaks shifted to JCPDS peaks by annealing. It is considered that the crystal grains became random as higher the fabricating temperature of the coating by annealing process after fabrication of the coatings.

After the exposure, the specimens were removed the residual lithium on the surface and observed. The specimen exposed at 973 K for 1000 h were stable as shown in Fig. 1. In the figure, upper area is coated area, and lower metallic area is uncoated area and the substrate of NIFS-HEAT-2 is revealed. On the other hand, the coatings exposed at lower temperatures (773 K or 873 K) were peeled off from the substrates as shown in the Fig. 2. In the figure, upper dark area is coated area, and lower metallic area is where the coatings were peeled off and the substrate of NIFS-HEAT-2 is revealed. It is considered as follows; there were vanadium oxides interlayer between the coatings and the substrates, which were unstable in liquid lithium. In the exposure of lower temperature, liquid lithium went through the cracks of the coatings and dissolved the interlayer, and caused peeling off of the coatings. In the exposure of higher temperature, the interlayer disappeared by the movement of oxygen to vanadium layer of the substrates, and the coatings became more adhesive.



Fig. 1. Specimen after 973K 1000h exposure



Fig. 2. Specimen after 873K 1000h exposure

§21. Creep Mechanism of NIFS-Heat2 Alloys by Using Pressurized Creep Tubes

Fukumoto, K. (Univ. Fukui)
Matsui, H., Narui, M. (IMR/Tohoku Univ.)
Nagasaka, T., Muroga, T.

Vanadium alloys are candidate materials for fusion reactor blanket structural materials because of their potentially high operation temperatures. However the knowledge about mechanical properties of vanadium alloys at high temperatures is limited and there are uncertainties that may have influenced the results such as the interstitial impurity content of specimens. The National Institute for Fusion Science (NIFS), in collaboration with Japanese industry has initiated a program to fabricate a large ingot of highly purified V-4Cr-4Ti alloys [1]. A medium size (~160kg) ingot of V-4Cr-4Ti was fabricated by EB and VAR methods, which was designated as NIFS-Heat2. The impurity level for fabricating large V-Cr-Ti ingots was achieved as ~80wppm C, ~100ppm O, ~120wppm N and 1wppm or less of metallic elements. The objective of this study is to investigate the creep properties and microstructural changes of the high-purified V-4Cr-4Ti alloys, NIFS-HEAT2 by using pressurized creep tubes (PCTs), in order to prepare for in-pile creep tests.

The V-4Cr-4Ti alloy used in this study was produced by NIFS and Taiyo Koko Co. and designated as the NIFS-HEAT2 [1]. Tube processing of NIFS-Heat2 alloys was successfully done by NIFS and Daido Co. The tubes were cut into pieces of pipes with one-inch (25.4mm) length. The end plugs were fabricated from a rod by using a lathe, and a 0.6mm ϕ / 0.25mm ϕ hole was bored in the top end plug with electro-discharge machining. The circumferential plug-to-tube welds were made with an electron-beam (EB) welder in vacuum in a machine shop in Japan Atomic Energy Research Institute (JAERI), Tokai. The final heat treatment of PCTs was done at 1000°C for 2 hrs in vacuum of $<1 \times 10^{-4}$ Pa. A helium gas sealing was done in a helium gas enclosure at the Oarai branch of Japan Nuclear Cycle Development Institute (JNC), Oarai. The detailed tubing process and fabrication process of pressurized creep tubes have been reported in the ref [2]. The PCTs wrapped with Ta and Zr foils were enclosed in a quartz tube in vacuum. Thermal creep tests were done using the sealed quartz tubes in Muffle furnace at 600, 700, 750, 800 and 850°C. Dimensional changes of PCTs were measured with a precision laser profilometer at five axial and 18 azimuthal locations to an accuracy of 1 μ m for the outer diameter measurement. After a creep strain exceeded 20% in a measurement, the creep test was finished and the TEM observation was performed for the specimen pieces cut out from PCTs.

A macroscopic examination of the welds indicated relatively smooth weld zones without any cracks, porosity, or other significant weld flaws. The incursion of impurities at the time of manufacturing PCTs was not

accepted by a result of analysis of chemical composition before and after creep tests. The result of chemical analysis is shown in table 1.

Table1. Chemical analysis before and after creep test.

Condition	Oxygen conc. (wppm)	Nitrogen conc. (wppm)
Pre-creep test	370	80
850°C, 150MPa 120hrs (Ex.2times)	520	140
850°C, 200MPa 50hrs	330	110

From the results of dimensional changes, the activation energy of creep deformation in the NIFS-Heat2 alloys was about 180kJ/mol. This amount of creep activation energy of PCTs is very similar to that of uniaxial creep specimens of NIFS-Heat1 alloys in the previous study [3]. The creep strain rate of PCTs is several times larger than that of uniaxial specimens.

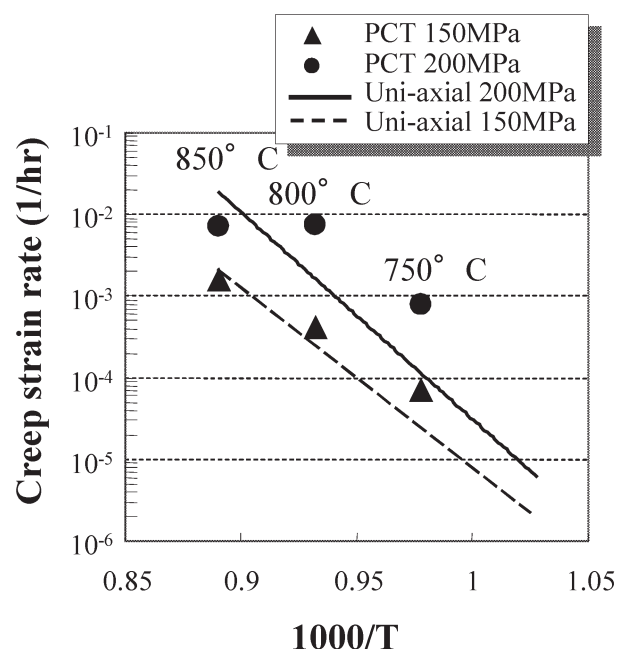


Fig. 1. An Arrhenius plot of creep strain rate examined by using PCTs and uniaxial tensile specimens.

The creep tests at 750 and 700°C are being continued. TEM microstructural analyses for fully deformed PCTs are also undergoing. The creep mechanism for NIFS-Heat2 alloys will be apparent by combining the information between the deformed microstructure after creep test, activation energy of apparent creep deformation and creep exponent for each creep temperature for NIFS-Heat2 in the future.

Reference

- 1) Muroga, T., et al., J. Nucl. Mater. 283-287 (2000) 711
- 2) Fukumoto, K., et al., J. Nucl. Mater. 335 (2004) 103
- 3) Fukumoto, K., et al., J. Nucl. Mater. 283-287 (2000) 535

§22. Negative Longitudinal Magnetoresistance of Bulk Bismuth in Low Temperature

Hamabe, M., Yamaguchi, S. (Dept. Elec. Eng., Chubu Univ. Eng.)

Yonenaga, I. (Inst. Mater. Res., Tohoku Univ.)

Sato, M.

Thermoelectric (TE) generator has the advantage that it exchanges the heat energy directly to the electric energy. The magnetic field effect on the TE properties can improve the conversion efficiency of the TE generator. The following magnetic field effects on TE properties have been observed for the polycrystalline bismuth (Bi): [1] increase of the electric resistivity (positive magnetoresistance), [2] increase of the Seebeck coefficient, [3] decrease of the thermal conductivity, and [4] occurrence of the high Nernst coefficient. These magnetic field effects are remarkable for the lower temperature. Effects [2]~[4] improve the performance of the TE exchange, whereas effect [1] decreases. Supposing that the electric resistivity reduced for the applied magnetic field (negative magnetoresistance), this also can contribute to the improvement of the performance of the TE exchange.

Recently, Heremans et al. measured the longitudinal magnetoresistance (LMR), where the magnetic field \mathbf{B} is applied parallel to the current density \mathbf{J} , of the *nanowire array* of single crystal Bi within 5 T at low temperatures less than 70 K. They showed that the LMR turned positive to negative at some magnetic field and the LMR for the lower temperatures decreased less than the resistance at 0 T¹⁾. Heremans et al. explained that the negative LMR of the nanowire Bi depends on the one-dimensional moving of the carrier in Bi owing to the nanowire geometry. The size of electrons are, however, sufficiently smaller than nanowire radius. Therefore, it is considered that the strong magnetic field, rather than the nanowire geometry, limits the carrier moving to the one-dimension, since the strong magnetic field inhibit the perpendicular component of the motion of carrier. Yamaguchi analytically calculated the Boltzman equation in one-dimension, assuming the parabolic band, and the conventional expression of magnetoresistance. Consequently, the electric resistivity η without thermal motion of carriers is expressed as,

$$\eta = \eta_0 \frac{1 + \mu_H^2 B^2}{1 + (\omega_c \cdot B)^2} \quad (1)$$

where η_0 is the resistivity at 0 T, μ_H is the Hall mobility of a carrier, \mathbf{B} is the magnetic field, ω_c the cyclotron frequency of a carrier. Figure 1 show the results of the numerical calculation of eq. (1) including suitable values of μ_H and ω_c for Bi. Negative LMR can occur at $\omega_c = 0.6$ from Fig. 1.

We carried out the LMR measurement for the bulk Bi to confirm this consideration. Figure 2 shows the LMR of the polycrystalline bulk Bi. The dimension of the bulk

Bi is 10.12 mm in longitudinal length, 10.30 mm in width, and 2.00 mm in thickness. The size of grain, which composed the polycrystal, was a several μm ; then the dimension of the grains were larger by far than the radii of nanowires. The LMR at 290 K was positive within 8 T as similar to the normal magnetoresistance. On the other hand, the LMR at 90 K increased up to 3 T and then turned to decrease for the increase of the applied magnetic field. The characteristics of the LMR of bulk Bi at 90 K is similar to that of nanowire Bi in Ref. 1. Therefore, the negative LMR of Bi is supposed to depend on the strong magnetic field, not on the nanowire geometry. The LMR of the bulk Bi in Fig. 2 shows that carriers in Bi move three-dimensionally at high temperature by the thermal motion of carriers and that they move one-dimensionally at sufficient low temperature trapped by the longitudinal magnetic field.

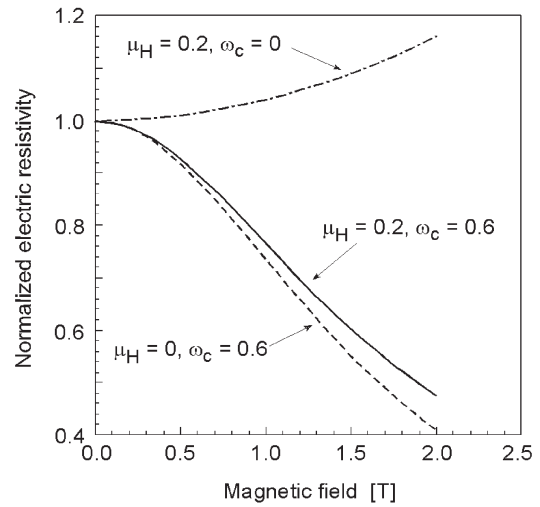


Fig. 1 Longitudinal magnetoresistances calculated from the one-dimensional Boltzman equation. Electric resistivity for each parameter is normalized by that at $B = 0$ T.

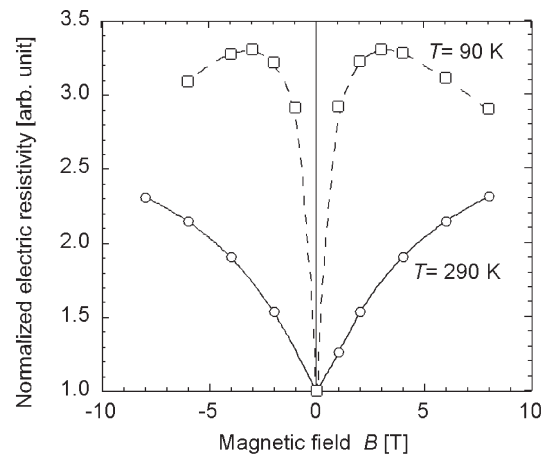


Fig. 2. Measured longitudinal magnetoresistances ($\mathbf{B} // \mathbf{J}$) of bulk Bi. Electric resistivity for each temperature is normalized by that at $B = 0$ T.

Reference

- 1) Heremans, J. et al, Phys. Rev. **B61**, (2000) 2921

§23. Development and Synthetic Evaluation of High-Z Plasma Facing Materials

Kurishita, H. (IMR, Tohoku Univ.)
 Yoshida, N. (RIAM, Kyushu Univ.)
 Tanabe, T. (Nagoya Univ.)
 Noda, N.

Tungsten (W) and its alloys, are very promising for use as PFM and PFC. However, they exhibit significant embrittlement, in several regimes; i.e., low temperature embrittlement, recrystallization embrittlement, radiation embrittlement and helium embrittlement. In addition, data on the physical and mechanical properties required for the use of W and its alloys as PMC/PFC are very limited. Therefore, a LHD research project entitled "Development and synthetic evaluation of high-Z plasma facing materials" was performed for three years from 2001, by an organized research group consisting of PSI and materials researchers from universities, NIFS, JAERI and private corporations. After that research activities related to the project are still being continued by each member of the group.

The following meeting was held on February 7, 2005 at NIFS in order to report the main results obtained through the three-year LHD project and discuss the future task. Approximately 20 members got together. After the meeting, a LHD tour was also offered. The program of the meeting was as follows:

9:00-9:05	Opening	H. Kurishita (Tohoku Univ.)
9:05-9:45	Features and issues of W for fusion reactor applications	N. Yoshida (Kyushu Univ.)
9:45-10:10	Development of ductile W alloys with ultra-fine grains and nano-sized dispersoids	H. Kurishita
10:10-10:35	Surface modification of refractory metals by multi-step nitriding	M. Nagae (Okayama Univ.)
10:35-10:55	Fundamental study on plastic working of tungsten based on its superplastic deformation	T. Kurumada (Ibaraki Univ.)

10:55-11:20	Study on irradiation by mixed beams of hydrogen and carbon to W	Y. Ueda (Osaka Univ.)
11:20-11:45	High heat and particle loading on W materials	K. Tokunaga (Kyushu Univ.)
11:45-12:10	Deuteron irradiation effects for tungsten and its alloys	H. Iwakiri (Kyushu Univ.)
12:10-13:00	Lunch	
13:00-13:25	Effects of microstructures in tungsten on solid-state reaction rate of amorphous carbon films with bulk tungsten	Y. Hatano (Toyama Univ.)
13:25-13:50	Joining of bulk tungsten with oxygen free copper and high heat loading of joined specimens	Y. Imamura (Ibaraki Univ.)
13:50-14:15	Mechanical property changes and surface damage in tungsten irradiated with light ions	A. Hasegawa (Tohoku Univ.)
14:15-14:40	Effects of neutron irradiation on microstructures and hardness of pure W and W-0.3wt%TiC	S. Kobayashi (Ehime Univ.)
14:40-15:05	Deformation and fracture of pure tungsten	Y. Hiraoka (Okayama Sci. Univ.)
15:05-15:25	Mechanical properties of W materials at very high temperatures	K. Tanoue
15:25-15:45	Fracture toughness of Mo alloys with elongated grain structures	T. Igarashi ((Ion Eng. Co.)
15:45-16:15	Discussion	
16:15-16:25	Summary and closing	N. Noda (NIFS)

These presentations showed that significant progress was achieved concerning ductile W alloy development, W surface modification, plastic working, joining technology and fundamental properties of several commercially available W alloys; the scope of the project included radiation effects, heat/particle loading, solid-state reaction, low and high temperature mechanical properties. The discussion made was also very useful.

This project will be continued in 2005 as a new NIFS subject "Synthetic evaluation of ultra-fine grained W alloys as PFC materials"

§24. Transmutation of High-level Waste in a Spherical-tokamak Reactor

Tanaka, Y. (Nagoya Inst. of Tech.), Arita, K. (Nagoya Inst. of Tech.), Nagayama, Y., Sagara, A.

We have studied transmutation of high-level waste (HLW) in a spherical-torus tokamak reactor(ST). Among the fusion reactors, ST has various advantages when used for transmutation of HLW; (1) ST could offer a compact volumetric neutron source. (2) Owing to the nearly cylindrical shape of a blanket, HLW inventory could be made simple and compact. (3) Requiring relatively low external fields, ST could be economically and technically attractive, etc.

A fusion neutron needs breeding so that the tritium fuel is self-sustained. In a hybrid system, the (n,f) reaction is the main neutron breeding source. We here employed light water as the cooling material. In the water environment, fusion neutrons are readily slowed down to thermal ones. Thermal neutrons have (n,f) and ${}^6\text{Li}(n,t)$ cross sections several hundred times larger than the fast ones, the fact that could make the hybrid blanket compact.

Neutronic analysis was performed on a model of the ARIES-ST blanket shown in Fig. 1. A fuel zone [4], which is composed of the nuclear fuel + zircalloy + water, is placed between the first and the second walls. Volume fractions of the structural materials are taken from a large pressurized water reactor.

A tritium breeding zone [5], composed of the LiH + zircalloy + water, is placed between the second and the third walls. Lithium hydride (LiH) in a zircalloy cladding is employed as a suitable tritium breeder material to the water coolant. Graphite reflector [6] is put between the third wall and the shield. The walls and the shield [7] are composed of the Ferritic steel (Fe9Cr2W).

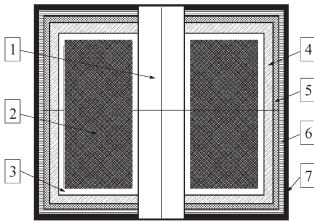


FIG. 1: The model for a spherical-torus tokamak.

In the fuel zone, we considered the spent PWR fuel with burn up= 39,560MWd/MTHM, enrichment= 3.69 percent and decay time= 25.9 years. The recovered fuel is composed of the uranium and plutonium isotopes of the spent fuel. The reprocessed waste is composed of 0.1% of the uranium and plutonium isotopes and 100% of the minor actinides and fission products of the spent fuel. We have also studied natural UO_2 fuel, though it is not a high-level waste.

It is noted that the atoms of all structural materials in the same zone were uniformly distributed in the

present calculation. No structure was imposed on the structural materials

Fusion neutrons were created uniformly in the plasma region [2] and were emitted isotropically in all directions. We performed neutron transport calculation using the computer code MCNP and obtained neutron flux, energy deposition, fission cross sections and neutron absorption cross sections averaged over a zone as well as (n,f), (n, γ), (n,t) and (n,n't) reaction cross sections for individual nuclides. The results are shown in Table I, where the criticality factor k_{eff} , number of fissions, multiplication factor of fusion energy (MFE), conversion ratio of ${}^{239}\text{Pu}$ (CR) and the amount of ${}^{239}\text{Pu}$ added to the fuel are displayed as a function of the tritium breeding ratio (TBR).

In the table, we see that 2.4 fissions are needed in order to make TBR unity. Since the energy of 200 MeV is produced per fission, we expect the fusion neutron energy is amplified by a factor of 30. Carefully designed structure and disposition of structural materials could reduce the number of fissions. With these efforts though, we could not reduce the number of fission less than 1, implying that the fusion energy is amplified by a factor of 14. Large amplification of fusion energy seems typical to a hybrid reactor. The conversion ratio of ${}^{239}\text{Pu}$, i.e., ${}^{238}\text{U}(n,\gamma)/\{{}^{239}\text{Pu}(n,f)+{}^{239}\text{Pu}(n,\gamma)\}$, is 1.0 for the spent and recovered fuels, while 1.8 for the natural UO_2 fuel. It should be noticed that the CR of greater than unity could be achieved in a water-cooled subcritical reactor.

TABLE I: The criticality factor k_{eff} , number of fissions, multiplication of fusion energy (MFE), conversion ratio (CR) of ${}^{239}\text{Pu}$ and the amount of ${}^{239}\text{Pu}$ added to the fuel are shown as a function of tritium breeding ratio (TBR).

fuel(tons)	TBR	k_{eff}	Fissions	MFE	CR	${}^{239}\text{Pu}(\text{tons})$
spent fuel(82)	1.0	0.85	2.4	32	0.98	0.23
recovered fuel(82)		0.83	2.4	31	1.06	0.04
natUO_2 fuel(90)		0.81	2.4	31	1.80	0.28
spent fuel(82)	2.0	0.91	5.1	66	0.66	0.84
recovered fuel(82)		0.92	5.3	69	0.70	0.56
natUO_2 fuel(90)		0.91	5.3	68	0.98	0.53
spent fuel(82)	3.0	0.96	8.4	109	0.57	1.29
recovered fuel(82)		0.95	8.1	105	0.63	0.81
natUO_2 fuel(90)		0.95	8.1	104	1.02	0.65

The reprocessed waste is composed dominantly of minor actinides and fission products. By the (n, γ) reaction, long-lived fission products, ${}^{93}\text{Zr}$ and ${}^{99}\text{Tc}$, are transmuted by 0.068 and 0.198 per fusion neutron and they become stable. Similarly, by the (n,f) reaction, ${}^{237}\text{Np}$ and ${}^{241}\text{Am}$ are transmuted by 0.024 and 0.047 per fusion neutron. If we assume the fusion energy of 100 MW, the neutron flux would transmute 15 kg/year (${}^{93}\text{Zr}$), 46 kg/year (${}^{99}\text{Tc}$), 13 kg/year (${}^{237}\text{Np}$), and 27 kg/year (${}^{241}\text{Am}$), respectively. They amount to those produced from the generation of $1\text{GW}_{(\text{e})}$ year in a large pressurized water reactor. However, TBR is calculated as 0.22. Tritium fuel may not be self-produced in a reprocessed-waste hybrid reactor.

(2) Helical Reactor Design

§1. Modification of Design Parameters on LHD-type Reactor FFHR2

Sagara, A., Imagawa, S.
Mitarai, O. (Kyushu Tokai University)

In order to make clear the key R&D issues for D-T fusion power plants on the basis of major advantages such as current-less plasma and intrinsic diverter configuration in helical system, with including common engineering issues in other plasma confinement concepts, the conceptual design studies on LHD-type helical reactors have been carried out by introducing physics and engineering results obtained in the LHD project, with collaboration works in wide research areas on fusion science and engineering in the universities of Japan.

In the LHD-type reactor design the coil pitch parameter γ of continuous helical winding has been adjusted beneficially to reduce the magnetic hoop force (Force Free Helical Reactor: FFHR) while expanding the blanket space, and a self-cooled liquid blanket using molten salt FLiBe (BeF₂-LiF) has been proposed, due to its advantages of low MHD pressure loss, low reactivity with air, low pressure operation, and low tritium solubility. Standing on these advanced concepts, the design study on FFHR has been carried out from 1991 under construction and operation of LHD.

In the direction of decreasing reactor size, many issues still remain, such as insufficient tritium breeding ratio (TBR) and nuclear shielding for superconducting (SC) magnets, and replacement of blanket due to high neutron wall loading and narrowed maintenance ports due to the support structure for high field coils.

Therefore, the design parameters of FFHR2 are modified to those of FFHR2m, as shown in Table 1. The coil pitch parameter γ is 1.15 in FFHR2m1 to expand the blanket space and to reduce electromagnetic force, while γ is 1.25 in FFHR2m2 with inner shift of the plasma center as same as the standard condition in the present LHD. In both cases the major radius R is increased and the toroidal field B_0 is decreased within B_{\max} of 13T. Then the blanket space is as wide as 1.2m, resulting in sufficient TBR and nuclear shielding for SC magnets. At the same time the wide maintenance ports are possible due to simplification of coil-supporting structures(Fig.2).

The self-ignition analyses have revealed the enhancement factor can be reduced below 2 of ISS95 confinement scaling with introducing the recent LHD results on the density of 1.5 higher than the Sudo limit (Fig. 1). The next design issues are on start-up heating, fueling, diverter pumping, and so on.

Reference:

A. Sagara et al., Nuclear Fusion 45 (2005) 258-263.

Table 1. Design parameters of helical reactor FFHR

Design parameters		LHD	FFHR2	FFHR2m1	FFHR2m2
Polarity	l	2	2	2	2
Field periods	m	10	10	10	10
Coil pitch parameter	γ	1.25	1.15	1.15	1.25
Coil major Radius	Rc m	3.9	10	14.0	17.3
Coil minor radius	ac m	0.98	2.3	3.22	4.33
Plasma major radius	Rp m	3.75	10	14.0	16.0
Plasma radius	ap m	0.61	1.2	1.73	2.80
Blanket space	Δ m	0.12	0.7	1.2	1.1
Magnetic field	B0 T	4	10	6.18	4.43
Max. field on coils	Bmax T	9.2	15	13.3	13.0
Coil current density	j MA/m2	53	25	26.6	32.8
Weight of support	ton	400	2880	3020	3210
Magnetic energy	GJ	1.64	147	120	142
Fusion power	P _f GW		1	1.9	3
Neutron wall load	MW/m2		1.5	1.5	1.3
External heating power	P _{ext} MW		70	80	100
α heating efficiency	$\eta\alpha$		0.7	0.9	0.9
Density lim.improvement			1	1.5	1.5
H factor of ISS95			2.40	1.92	1.76
Effective ion charge	Z _{eff}		1.40	1.34	1.35
Electron density	n _e (0) 10 ²⁰ m ⁻³		27.4	26.7	19.0
Temperature	Ti(0) keV		21	15.8	16.1
Plasma beta	< β > %		1.6	3.0	4.1

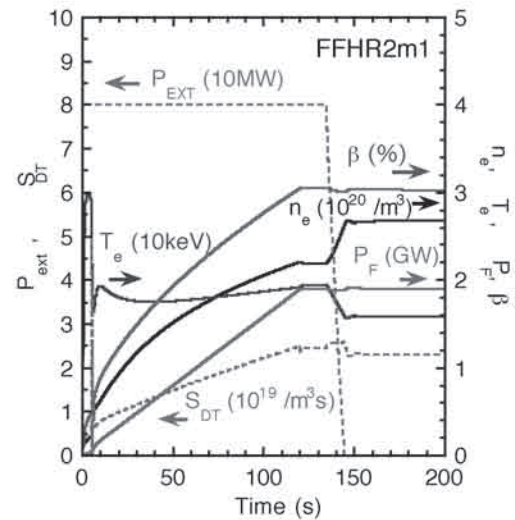


Fig.1. Self-ignition access calculation in FFHR2m1.

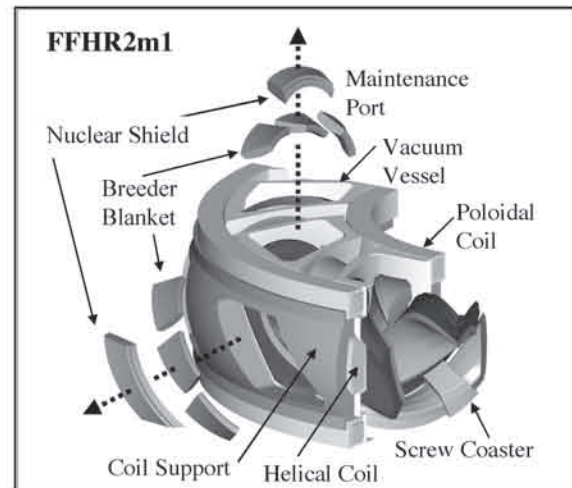


Fig.2 3D illustration of wide maintenance ports

§2. Design Studies on Long-life Breeder Blanket for LHD-type Reactors

Sagara, A., Tanaka, T.

In case of a liquid blanket, since the breeder liquid can be continuously circulated and refreshed during the reactor operation, the blanket lifetime is essentially limited by the total displacement damage and He production in structural materials under irradiation by fusion neutrons. There are many candidates for structural materials such as reduced activation ferritic steel (RAFS), vanadium alloy, and SiC/SiC composite. In case of RAFS, which has a very mature material database and is chemically compatible with Flibe even at the outlet temperature of about 830K, the design limit is about 15MWa/m² of 14MeV D-T fusion neutron irradiations, which is equivalent to about 120 dpa of neutron damage. This means that the lifetime is 10 years under 1.5MW/m² as adopted so far in FFHR designs, and replacement of blanket units is needed three times in the reactor life of 30 years. Therefore, if the effective wall loading could be reduced by a factor of 3, then no replacement would be required.

This concept was proposed about 30 years ago as ISSEC (Internal Spectral Shifter and Energy Converter) by employing thick carbon shields as armor tiles on the blanket wall. In this concept, therefore, the breeder

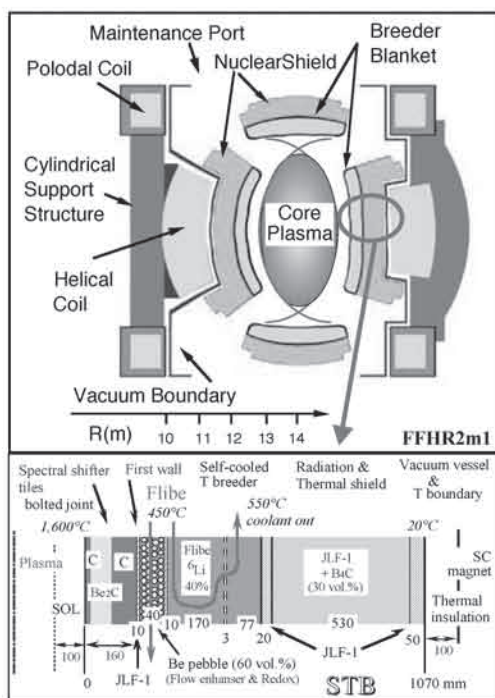


Fig.1. Spectral-shifter and Tritium breeder Blanket (STB) in FFHR2m1.

blanket radioactive waste is largely reduced, while the carbon armors, low-level waste with no g-ray, have to be replaced due to neutron damage. In that ISSEC study,

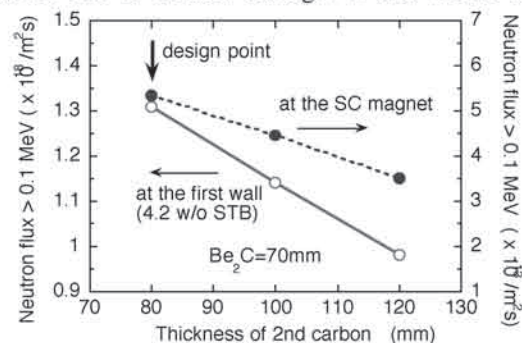


Fig.2. Fast neutron flux at the first wall and the SC magnet.

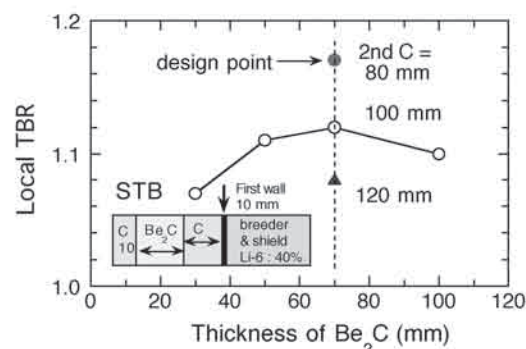


Fig.3. Local TBR vs. the thickness of Be₇C zone.

however, the TBR was below 1.05 even with the Be neutron multiplier in C and 90% enriched liquid Li, and there was no practical means for actively cooling the carbon tiles below about 2000°C to avoid high carbon vapor pressure.

Figure 1 shows the new proposal of STB (Spectral-shifter and Tritium breeder Blanket), where the thickness of Be₂C layer in C and the flibe zone are optimized by MCNP-4C calculations using JENDL3.2 nuclear data. The fast neutron flux (> 0.1MeV) at the first wall of JLF-1 (RAF) is reduced to 1/3 of the original flux (Fig.2). The local TBR over 1.2 is obtained, and the fast neutron fluence to SC magnets is one order reduced to $5 \times 10^{22} \text{ n/m}^2$, which is sufficient to keep $T_c/T_{c0} > 0.9$ for Nb₃Sn, for instance.

Thermal analyses using ANSYS shows the surface temperature of the carbon armor is about 1600°C under conditions of nuclear heating. Replacement of carbon tiles are needed every few due to neutron irradiations.

References:

- A. Sagara et al., Fusion Science and Technology, Vol.47 (2005) pp.524-529.
A. Sagara et al., Nuclear Fusion 45 (2005) 258-263.

§3. Study of the Burning Plasma Physics Issues in Helical Reactors

Mitarai, O. (Kyushu Tokai University),
Oda, A. (Yatsushiro National College of Technology),
Matsumoto, Y. (Hokkaido University),
Sagara, A., Imagawa, S., Watanabe, T., Watanabe, K.
Yamazaki, K., Shimizu, A., Tomita, Y.

Based on the inwardly shifted plasma of $R=3.6$ m in LHD ($a=0.6$ m, $B_0=3$ T), where the best confinement has been achieved so far, we have determined the FFHR reactor size using the LHD size scaling including the blanket thickness and machine weight. So far the Sudo density limit has been used without any improvement. If the density limit is higher than that as observed in LHD, the operational regime can be expanded significantly. In this report, the density limit is set to 1.5 times larger than the Sudo limit.

FFHR reactor with $R=14$ m and the pitch parameter $\gamma=1.25$ can have a blanket thickness of 0.9 m, which is less than the required value of 1.2 m for D-T blanket characteristics. However, adoption of $\gamma=1.15$ provides a blanket thickness of 1.2 m and enough minor radius. On the other hand, although an $R=16$ m reactor with $\gamma=1.25$ can have a blanket thickness of 1.2 m, the machine weight is too heavy. Therefore, we consider 14m reactor in this report.

When the density limit is determined by the Sudo scaling without any improvement ($\gamma_{\text{SUDO}}=1$), the confinement factor of $\gamma_{\text{ISS}}=2.16$ over ISS95 scaling ($\gamma_{\text{LHD}}=1.35$ over present LHD scaling) provides ignition. On the other hand, if the density limit is improved by 50 % ($\gamma_{\text{SUDO}}=1.5$), the confinement factor of $\gamma_{\text{ISS}}=1.92$ ($\gamma_{\text{LHD}}=1.2$) is enough for ignition.

In Fig. 1 is shown the temporal evolution of plasma parameters of FFHR with $R=14$ m, $a=1.73$ m, $B_0=6$ T, $P_F=1.9$ GW, $\gamma_{\text{SUDO}}=1.5$, $\gamma_{\text{ISS}}=1.92$ ($\gamma_{\text{LHD}}=1.2$) and $\eta_\alpha=90$ %. When the external heating power of 80 MW is switched off at 150 s, ignition is reached. The peak density at the steady state is $2.67 \times 10^{20} \text{ m}^{-3}$, the density limit is 10% over the operation density, temperature is 15.8 keV, average neutron wall loading is 1.5 MW/m^2 . Beta is 3 % which is already achieved in LHD. As high energy alphas are assumed to be lost promptly by 10%, it should be confirmed in numerical simulation. As the density limit is 1.8 times larger than the Sudo scaling in the present LHD experiments, assumption of $\gamma_{\text{SUDO}}=1.5$ is reasonable.

In Fig.2 we have shown POPCON for ignition in this

case. When the density limit is increased, the operating point can go down to the bottom of the ignition boundary with stable-unstable boundary. Therefore, the confinement factor can be reduced. When the density limit is decreased, the operating point goes up to the higher temperature side on the ignition boundary, requiring the larger confinement enhancement factor.

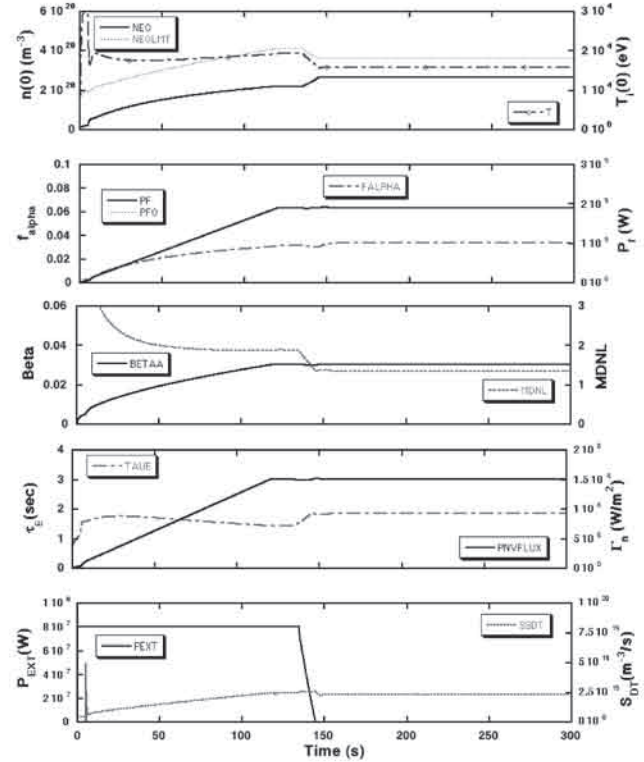


Fig. 1. The temporal evolution of the plasma parameters in FFHR ($R=14$ m).

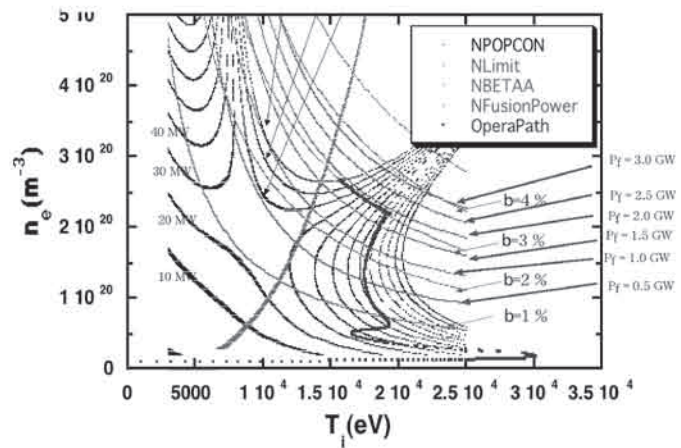


Fig. 2. POPCON diagram for FFHR ($R=14$ m) with the density limit of 1.5 over the Sudo scaling.

§4. Design Study of Magnets for Heliotron Type Fusion Reactor FFHR

Imagawa, S., Sagara, A.

In the design of the helical type fusion reactor, the maximum magnetic field and the electromagnetic force of a helical coil are important factors. The miniaturization is preferable from the viewpoint of the construction cost. The larger device scale, however, has advantages that a necessary central toroidal field becomes lower to achieve the same Q value, and that it becomes easy to secure the installation space for blankets. Scale effects on superconducting magnet systems have been estimated under the conditions of a constant energy confinement time and the same aspect ratio. After that, a typical helical reactor is selected and the optimization of the coil support structure has been in progress.

In order to estimate scale effects on magnet systems, the energy confinement time τ_E is appropriate for the index of comparable reactors. The scaling law of ISS95 is adopted in this study. In the case that plasma heating power P per unit volume and an electron density n_e are constant, τ_E becomes

$$\tau_E^{ISS95} \propto a^{1.03} R^{0.06} B_0^{0.83} \quad (1)$$

where a , R , and B_0 are a plasma minor radius, plasma major radius, and central toroidal field, respectively. Consequently, the necessary central toroidal field is in inverse proportion to the 1.31 power of the major radius under the conditions of the constant τ_E and a same aspect ratio.

The improvement factor for τ_E is set almost 2 in this study under the conditions of the center electron density of $30.4 \times 10^{19} \text{ m}^{-3}$ and center temperature of 15 keV. The estimated results are shown in Fig. 2 for the pitch number m of 8 and 10. The minimum space for blankets is derived by being subtracted by 0.1 m from the minimum gap between the helical coil and the last closed surface of the plasma for installing thermal shields. The current density j of the helical coil is set 25 MA/m^2 . Since the required thickness of the blankets is considered to be more than 1 m for breeding tritium and shielding neutron, the smallest major radius is determined mainly by the space for blankets. The major radius around 15 m is necessary for a reactor similar to LHD. In order to realize more compact reactors, the lower aspect reactor with the equivalent confinement is promised.

Since the electromagnetic force on the helical coil is mainly in the minor radius direction, the necessary cross-section of coil support can be estimated from the integration of minor radius hoop force. As the results of estimation under the constant τ_E and the constant average stress, weight of the coil support is proportional to only the 0.37 power of the major radius. The influence of the radius on the construction cost of the magnet system will not be strong.

The optimization of the coil support structure has been carried out for the FFHR2m1, the major radius of which is enlarged to 14.0 m to improve the maintainability of

blankets and to reduce the neutron wall load. A typical structural analysis example is shown in Fig.3. When the big port for maintenance is secured, the maximum stress is within 1,000 MPa.

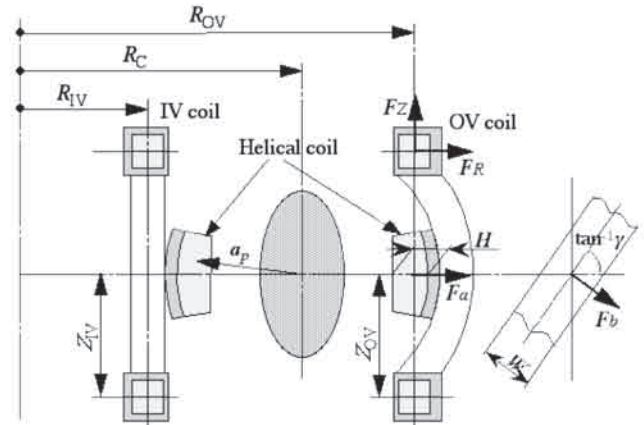


Fig. 1. A coordinate of helical coils and plasma

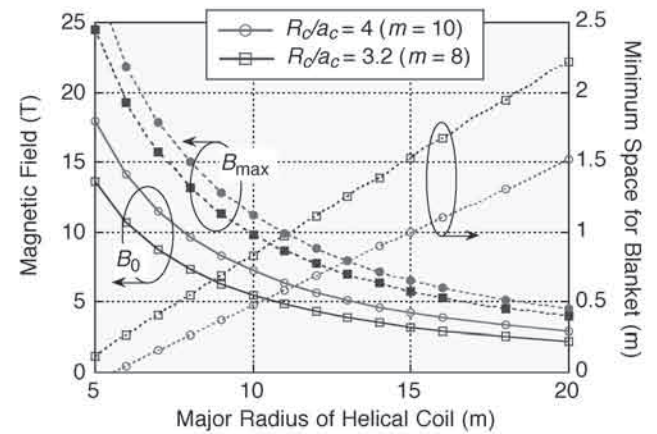


Fig. 2. Scale dependence of the central magnetic field B_0 , the maximum magnetic field B_{\max} and space for blankets under the conditions of $\tau_E = \text{const.}$, $\gamma = 1.25$, $j = 25 \text{ MA/m}^2$, $W/H = 2$, and $S_m = 200 \text{ MPa}$.

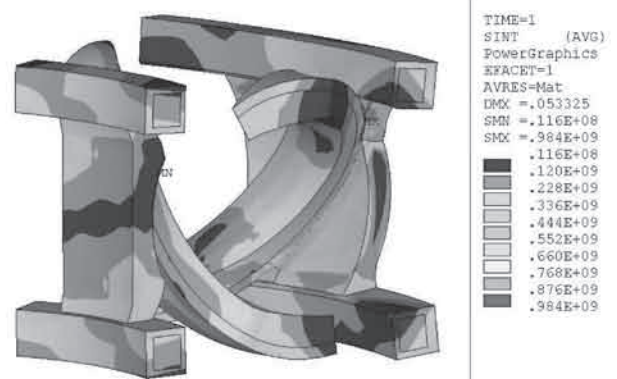


Fig. 3. Stress intensity of a FE model for FFHR2m1, where $R_0 = 14.0 \text{ m}$, $B_0 = 6.18 \text{ T}$, and $\gamma = 1.15$

Reference

- 1) S. Imagawa and A. Sagara, Plasma Science & Technology, Vol. 7, No.1 (February 2005) 2626-2628.

§5. Effect of Surface Angle on Mechanical Jointing of HTS

Hashizume, H., Ito, S., Yamamoto, Y. (Tohoku Univ.)
Sagara, A. (NIFS)

For realization of commercial fusion power plant, remountable HTS (high-temperature superconductor) magnet is proposed to reduce both construction and maintenance costs [1]. The remountable HTS magnet can make it possible to simplify fabrication of reactor and facilitate access into inner structural components. In addition, when electromagnetic force produced by self magnetic field of HTS magnet can be used as joint force, there is possibility to mount and demount parts of the remountable HTS magnet easily.

In this study, the joint resistance in the butt joint of the BSCCO 2223 cable which has variable angle of the joint surface is evaluated experimentally to investigate the influence of shear stress on the resistance and clarify optimum joint condition.

10 ply BSCCO 2223 cable is used as a test cable in this experiment. Specifications of the BSCCO 2223 tape used for the cable are as follows. Critical current is 90A under liquid nitrogen temperature 77K with self magnetic field. The tape sizes are 4.2 mm wide and 0.21 mm thick. The joint surface of cable is cut down by angle of 30, 40, 45, 50 and 60 degrees inclined from length direction of the cable. Figure 2 shows the experimental system with the samples. Normal and shear stresses on the joint surface is loaded by compressing the cable with a rod in perpendicular direction of the cable as shown in Figure 1. The joint resistance of each sample is evaluated with changing the stress acting on the joint surface.

Results obtained through this experiment are shown in Figure 2. Figure 2(a) shows relationship between the normal stress and normalized joint resistance. The joint resistance decreases with increase of the normal stress in each case. Values of the normalized resistance are almost the same when the joint surface angles are 30, 40 and 45 degrees. In case of 50 and 60 degrees, however, the normalized resistance increases with increase of the angles. This result implies that the joint resistance is not inversely proportional to joint area when the angle of the joint surface becomes larger than 50 degrees. Figure 3(b) shows relationship between the shear stress and normalized joint resistance when the normal stress is 62MPa and 101MPa. When the shear stress is smaller than the normal stress, the values of normalized resistance are almost constant, while the shear stress becomes larger than the normal stress, the joint resistance shows larger value with increasing the shear stress. It is considered that the shear stress larger than the normal stress degrades the joint performance due to displacement of the joint surface. Consequently the joint performance is improved by forming the large joint area with surface configuration to give the most suitable stress distribution where the normal stress itself is large and the shear stress is smaller than the normal stress.

In this study, the joint resistance is evaluated in the butt joint of the BSCCO 2223 cable with changing angle of the joint surface. From experimental results, the joint performance varies with changing the joint area and stress distribution on the joint surface. Therefore, in designing phase of the remountable HTS magnet, it becomes important to form the joint surface in order to obtain the optimum stress distribution with the large normal and small shear stresses to achieve better butt joint performance

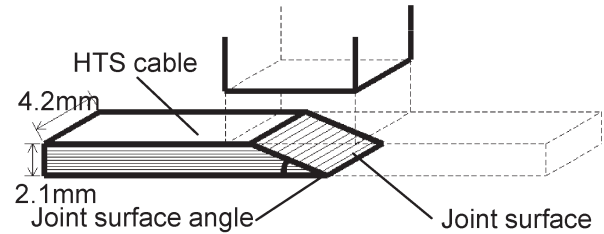
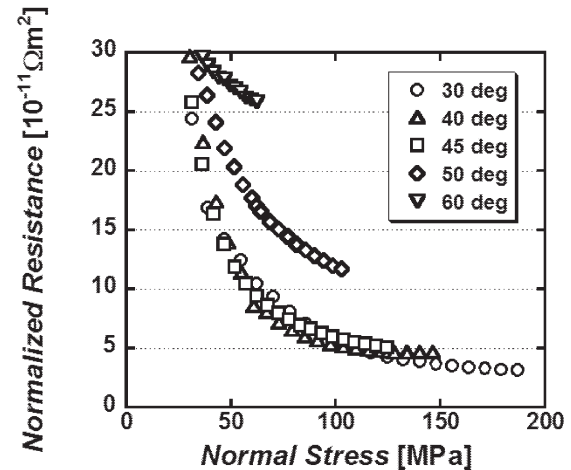
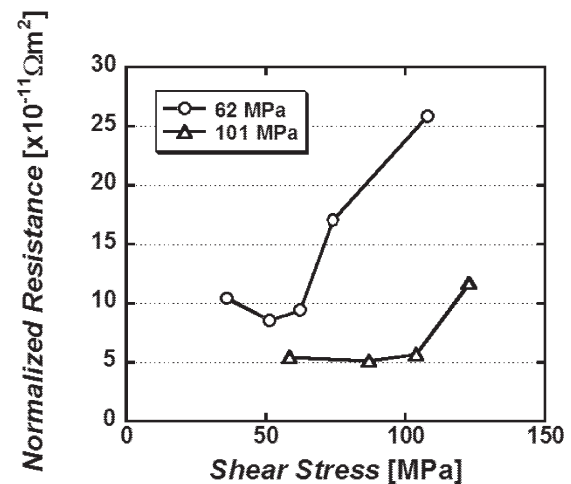


Figure 1: Experimental system.



(a) Normal stress and resistance characteristic



(b) Shear stress and resistance characteristic

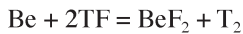
Figure 2: Experimental results

§6. System Design Study of Hydrogen Isotope Recovery from Molten-Salt Blanket of Fusion Reactor

Fukada, S. (Kyushu University)
Sagara, A.

Molten salt Flibe ($2\text{LiF}+\text{BeF}_2$) as an advanced blanket has several attractive advantages of simple self-cooled blanket system, easy maintenance, a stable salt, low MHD effect and so on. The largest disadvantage is chemical control of TF to be generated in the blanket. Relating with tritium behavior in the molten salt Flibe blanket of FFHR-2 including physical or chemical properties on tritium recovery and tritium leak, to control chemical form of tritium in Flibe becomes a critical issue. Therefore, it has been intensively investigated in the JUPITER-II program [1,2]. When the chemical state of tritium in Flibe is successfully controlled by the use of Be, the tritium chemical form is considered T_2 or HT in Flibe. In this NIFS collaboration study, a design of a tritium recovery apparatus and an effective way to control of tritium leak were investigated closely relating with the FFHR-2 design. In this report we focused on the expected TF concentration in the Flibe blanket and impurity effects because of the limit of paper length.

The generation of tritium fluoride (TF) can cause corrosive action to Flibe-facing materials. In the Flibe blanket, Be is used for the neutron multiplier and is also expected as a redox-control agent as follows:



Based on the experimental study of JUPITER-II, we obtained the Be dissolution rate and the saturated Be concentration in Flibe. Their values were as follows:

Be dissolution rate: $1.8 \times 10^{-3} \text{ mol/m}^2\text{s}$ at 530°C

Saturated Be concentration: $4 \times 10^{-3} \text{ Be/Li}_2\text{BeF}_4$

The dynamic behavior of redox control by Be in the Flibe blanket was analyzed using two material balance equations on tritium and Be and a tritium generation rate. As the first approximation, it was assumed that the tritium chemical form immediately after the nuclear reaction is TF. As the second assumption, the bulk tritium concentration is constant throughout the self-cooled blanket under the complete mixing condition. In this analysis, we focused on the overall material balance of TF and T_2 in the self-cooled Flibe blanket. Variations of the TF and T_2 concentrations in the Flibe blanket with time were determined using two material balance equations in terms of the reaction rate constant, k_{BeF_2} . The reaction rate may decrease with the decrease of the TF concentration in the blanket. The reaction order was assumed of the second-order. From fitting the numerical simulation to the experimental data, the reaction rate constant was determined. The value was $1 \times 10^9 \text{ mol/m}^3\text{s}$ at the HF partial pressure of 10^2 Pa .

Under steady-state operation, the concentration of TF in Flibe was calculated using the three parameters, the Be dissolution rate, the saturated concentration and the

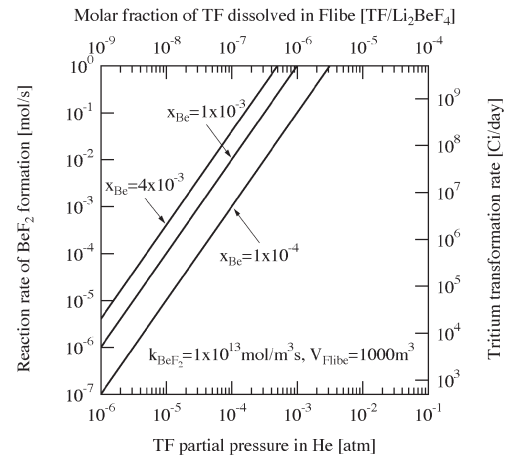


Fig. 1 TF-to- T_2 conversion rate as a function of HF

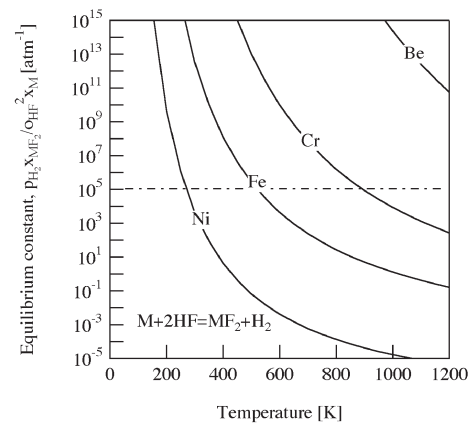


Fig. 2 Concentration ratio of metallic impurities in Flibe as a function of temperature

reaction rate constant. **Fig. 1** shows the TF concentration expected in the Flibe blanket of FFHR-2. If k_{BeF_2} is independent of the TF concentration, the calculated TF concentration was estimated 10^{-2} in molar fraction. The concentration is sufficiently low, and, therefore, we can expect that Be can act as a redox agent as well as neutron multiplier.

Fig. 2 shows the concentration ratio of metallic impurities in Flibe as a function of temperature. Ferritic steel or Ni alloy such as Hastelloy is expected for the structural material of Flibe blanket. In this case, Ni, Fe and Cr are impurity metals expected in Flibe. Thermodynamic calculation and the reaction rate equations showed us that iron is the most influential one for the redox control by Be. Therefore we need to remove Fe in the Flibe blanket loop.

References

- (1) S. Fukada, A. Sagara, et al., Proc. Tritium 2004, Fus. Sci. Technol., 48 (2005) 666-669.
- (2) S. Fukada, N. Nakamura, J. Radioanal. Nucl. Chem., 261 (2004) 291-294.
- (3) R. A. Anderl, S. Fukada, et al., J. Nucl. Mater., 329-333 (2004) 1327-1331.
- (4) A. Sagara, et al., Proc. of TOFE 2004, Fus. Sci. Technol., 47 (2005) 524-529.

§7. Study on Heat Transfer Region for Fluid System in a Liquid Blanket

Satake, S. (Tokyo University of Science), Kunugi, T. (Kyoto University), Yokomine, T. (Kyushu University), Kawahara, Z. (Kyoto University), Yuki, K. (Tohoku University), Sagara, A.

1. Objectives

In the region of transition Reynolds numbers, the increase or decrease of friction coefficients of the coolant like a Molten Salt having a low magnetic conductivity is obtained: a transition Hartmann number behavior. This behavior also leads the deterioration of heat transfer. Therefore, the thermo-fluid design of blanket under the magnetic field fluctuation is very important. Since the magnetic field is strongly influenced by mean velocity when the magnetic field applies perpendicular to the flow direction, it is necessary to investigate the turbulent MHD flow behaviors for each direction of the applied magnetic field normal to the main flow one. Furthermore, in case of considering the wall with various electrical conductivities, the flow characteristics of the coolant could be different from the usual turbulent non-MHD flows. In this sense, the numerical simulation is very convenient to evaluate the flow changes due to the change of physical properties of the wall materials or the direction of applied magnetic field.

In the present study, to evaluate the effect of interaction of wall and fluid in 3D field, fully developed turbulent channel flow is carried out with high conducting wall. The difference for turbulent statistics of conduction wall is clearly observed compared with that of insulated wall.

2. Numerical method and boundary condition for turbulent channel flow with conducting walls

Our DNS code is hybrid spectral finite difference method. The periodic boundary conditions are applied to the streamwise (x) and the spanwise (z) directions. As for the wall normal direction (y), non-uniform mesh spacing specified by a hyperbolic tangent function is employed. The mesh number of $128 \times (64) + 128 + (64) \times 128$ are used for the computational domain of $5\pi\delta \times (\delta) + 2\delta + (\delta) \times 2\pi\delta$ in the streamwise, the wall-normal, and spanwise directions. The all velocity components imposed the non-slip condition at the wall. The non-slip condition is used at the wall. A uniform magnetic field B_0 defines that the magnetic orientation is parallel to the axis of the streamwise direction in Fig.6. The Neumann condition for the electrical potential is adopted at outside the wall: Conducting wall assumption. The Hartmann numbers ($Ha = B_0\delta(\sigma/\rho\nu)^{1/2}$) based on the magnetic field B_0 , the kinematic viscosity ν , the electrical conductivity σ and the channel width δ are set to 15.0. The σ at fluid is 1.0. The σ at solid wall is 62.27. If these parameters are assumed as actual material, fluid and solid wall are mercury and copper, respectively. The Reynolds number is 4590 based on the bulk velocity. The fluid flows with constant mass flux condition.

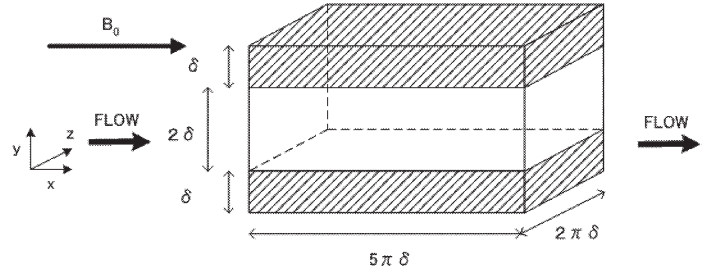


Figure 1 Computational domain.

Table 1

	Cf	Cf/Cf,0
Non MHD	8.5523×10^{-3}	1
Insulated wall, Ha=15	8.2894×10^{-3}	0.969
Conducting wall, Ha=15	8.1848×10^{-3}	0.957

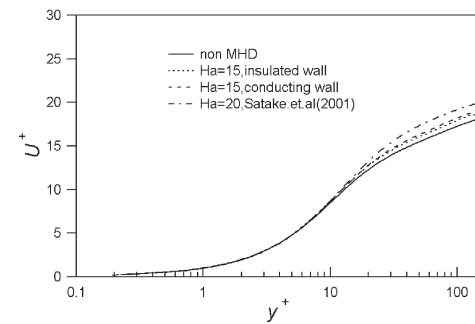


Figure 2 Mean velocity profiles.

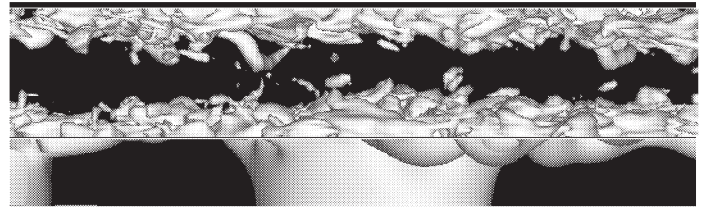


Figure 3 3D contour surfaces for second invariant and potential.

In Fig.2, the mean velocity profile near the wall is normalized by friction velocity u_τ . The velocity profile in conducting wall is slightly increased at the logarithmic region compared with that of insulated wall. Thus, the drag at the conducting wall is reduced compared with that of insulated wall. To confirm the phenomena, the friction coefficients for the both cases and Non MHD one is examined in Table 1. Although the difference is very small, the coefficient value of conducting wall is smaller than that of insulated wall. When the coefficient is normalized by that of Non MHD, the difference is more clearly observed. The difference is 1.2 %. Figure 3 shows 3D contour surface for second invariant tensor and potential value inside wall at the conducting wall. The large potential region is located at near the vortical structures. The region around the vertical structures exist high shear of the velocity gradient, especially it is remarkable for the region which has many vortex adjacent to the wall.

§8. Development of Heat Transfer Enhancement Technique in High Pr Number Fluid Blanket

Yuki, K., Chiba, S., Hashizume, H. (Tohoku Univ.)
Sagara, A.

To enable design of Flibe liquid blanket system in a helical type of nuclear fusion reactor FFHR, it is indispensable to enhance Flibe's heat transfer performance that is unique to high Prandtl (Pr) number fluid. In this study, Sphere Packed Pipes (SPPs) are chosen as the heat transfer promoter, and the fundamental flow structure and heat transfer characteristics are evaluated in order to develop innovative SPP.

In order to elucidate the heat transfer mechanism of the SPPs flow, the flow field was visualized with a PIV in isothermal experiments. Generally, the observation of flow field in SPPs is quite difficult due to existence of many obstructions, so that sodium iodide solution (NaI, 61.6wt%) was employed as the working fluid to match the refractive indexes of the fluid, acrylic pipe, and the spheres [1]. As a result, the strong bypass flow was observed in the SPP (Fig. 1). The heat transfer experiments were performed so as to clarify the correlation between the flow field and the heat transfer characteristics. The pipe was electrically heated, and lots of thin thermocouples and a thermography were used to measure the wall temperature distribution. The results showed that the heat transfer was deteriorated at stagnant points where the spheres contact with the pipe. Moreover, it was confirmed that the Nusselt number in this study showed almost the same data as the reference [2] (Fig. 2). Additionally, the bypass flow as presented above is so effective for the reduction of the high-temperature area behind the spheres. In order to apply the SPPs in the fusion reactor blanket, it is necessary to optimize the SPPs from the viewpoint of the thermofluid mechanics in the future. This work should be performed in consideration of the effects of the bypass flow. Moreover, improvement of thermal conduction between the heated wall and the spheres would be critically important to remove the heat flux of $1\sim 2\text{MW/m}^2$ at the 1st wall.

The experiments mentioned above employ the NaI solution as the working fluid. However, it is not high Pr number fluid comparing with Flibe. The heat transfer experiments by use of high Pr number fluid were also performed in a molten salt forced-circulation loop (TNT: Tohoku-NIFS Thermofluid Loop). The heat transfer experiments using high-temperature molten salt HTS (Heat Transfer Salt), which has the equivalent thermofluid characteristics to Flibe, were performed. Although the heat transfer enhancement of SPPs was confirmed before in the ref [3], the Nusselt numbers without the spheres were slightly lower than the empirical equation. The main reason conceivably results from short length of test section. Due to this, the TNT loop was modified in order to expand the inlet and heated length at the test section (T.S.). Furthermore, the direct electrical heating was employed at the modified test section instead of sheath heaters. These

improvements make the heat transfer data more reliable. Figure 3 shows the heat transfer results in a smooth pipe without the spheres at the new T.S. The results at the old T.S. are also plotted in the figure. Obviously, the results obtained by the new T.S. agreed well with the empirical equation rather than that by the old T.S. The accuracy of the new results has the 6 % error compared with the empirical equation. Accordingly, the heat transfer data using the SPPs should be higher than that at the old T.S. [3]. The experiments using the SPPs will be performed at the new T.S. in the next fiscal year (2005).

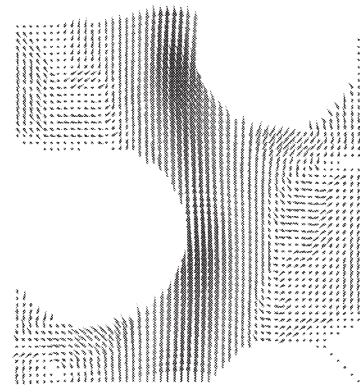


Fig. 1 Bypass flow through SPPs.

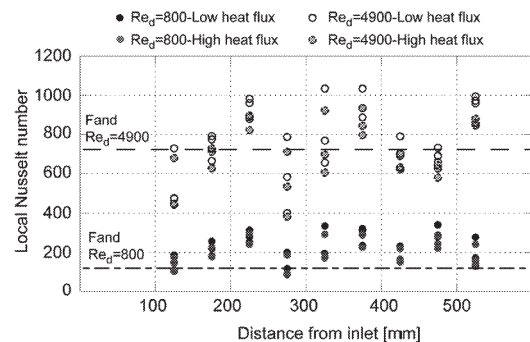


Fig. 2 Local Nusselt number.

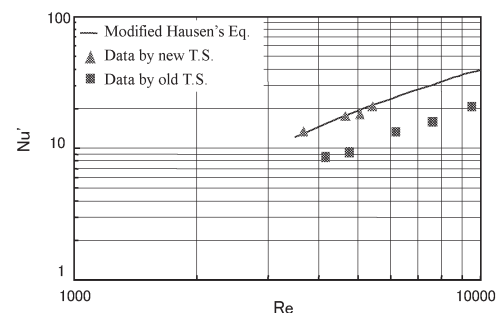


Fig. 3 Re vs Nu in a smooth pipe

REFERENCES

- [1] M.Okumura et al., Fusion Science and Technology., 47-4 (2005), 1089-1093.
- [2] M.Varahasamy and R.M.Fand, Int. J. Heat and Mass Transfer, 39-18 (1996), 3931-3947.
- [3] S.Chiba et al., Fusion Science and Technology, 47-3 (2005), 569-573.

§9. Feasibility of Helium Gas Turbine System for Molten Salt Blanket

Shimizu, A., Yokomine, T., Ebara, S. (Interdisciplinary Grad. Sch. Eng. Sci., Kyushu Univ.),
Imagawa, S., Sagara, A.

1. Introduction

Gas turbines for nuclear energy use must be closed cycle and its maximum inlet temperature is restricted. Therefore, an improvement of thermal efficiency cannot be realized by any extension of conventional Brayton cycle and adoption of multi-stage compression/expansion process is a quite natural choice for cycle improvement.

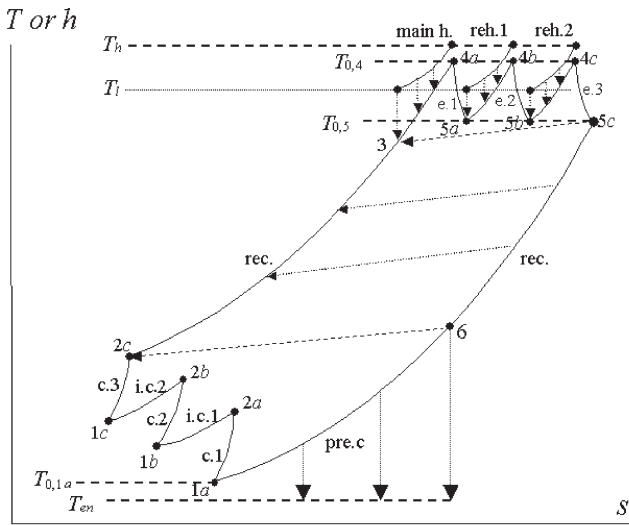


Fig. 1 Ts diagram for 3 stage-compression/expansion

3. Calculation of thermal efficiency

Following this, numerical estimation was performed on the thermal efficiency of multi-stage closed gas turbine cycle, the typical example of which is illustrated in Figs. 1. In the calculation, compression/expansion ratio was assumed to be common over all stages and optimized to give the maximum efficiency. Relative pressure loss was assumed to be,

$$\sum \left(\frac{\Delta p_0}{p_0} \right) = (\text{Number of heat exchanger path}) \times 0.02,$$

while cycle maximum temp. $T_{0,4}$ was varied as 823~1273 [K] (550~1000 [°C]), every 50[K]. Environmental temp. was fixed at $T_{0,1}=300$ [K]. Inter cooler heat exchange efficiency,

$$\varepsilon_{ic} = \frac{T_{0,2a} - T_{0,1b}}{T_{0,2a} - T_{0,1a}} = \frac{T_{0,2b} - T_{0,1c}}{T_{0,2b} - T_{0,1a}} = \dots = \frac{T_{0,2(x-1)} - T_{0,1x}}{T_{0,2(x-1)} - T_{0,1a}},$$

was assumed to be 0.9.

As Fig. 2 suggests, the perfect inter cooling with infinite numbers of infinitesimal cooling/compression stages is equivalent to approaching to isothermal heat rejection process of the Carnot cycle, while removal of the inter

cooling corresponds to the adiabatic compression process of the Carnot cycle.

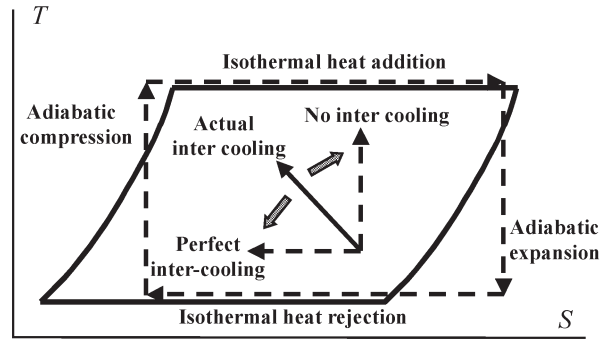


Fig.2 Carnot and Ericsson: meaning of inter cooling level

Regenerative heat exchanger efficiency, $\varepsilon_{hx} = (T_{0,3} - T_{0,2c}) / (T_{0,5} - T_{0,2c})$, was assumed to be 0.9 and polytropic efficiency was fixed at 0.9.

Table 1 Numerical results

	m	n	H.Ex. path	Pres. loss	$T_{0,4}$	ε_{hx}	ε_{ic}	$r_{c,best}$	$r_{e,best}$	η_{th}
①	1	1	2	0.04	823	0	-	3.78	0.276	0.227
②	1	1	4	0.08	823	0.9	-	2.00	0.541	0.288
③	2	1	5	0.10	823	0.9	0.9	1.55	0.463	0.308
④	1	2	5	0.10	823	0.9	-	2.29	0.696	0.295
⑤	2	1	5	0.10	823	0.9	1.0	1.57	0.451	0.313
⑥	3	1	6	0.12	823	0.9	0.9	1.39	0.423	0.310
⑦	3	1	6	0.12	823	0.9	1.0	1.41	0.405	0.316
⑧	1	3	6	0.12	823	0.9	-	2.49	0.769	0.289
⑨	2	2	6	0.12	823	0.9	0.9	1.72	0.619	0.328
⑩	2	3	7	0.14	823	0.9	0.9	1.84	0.699	0.331
⑪	3	2	7	0.14	823	0.9	0.9	1.53	0.568	0.339
⑫	3	3	8	0.16	823	0.9	0.9	1.62	0.652	0.347
⑬	3	4	9	0.18	823	0.9	0.9	1.70	0.703	0.348
⑭	4	3	9	0.18	823	0.9	0.9	1.51	0.614	0.355
⑮	4	4	10	0.20	823	0.9	0.9	1.57	0.674	0.358
⑯	4	5	11	0.22	823	0.9	0.9	1.62	0.711	0.358
⑰	5	5	12	0.24	823	0.9	0.9	1.53	0.687	0.366
⑱	5	5	12	0.24	823	0.9	1.0	1.57	0.669	0.376
⑲	5	5	10	0.20	823	0	1.0	2.13	0.489	0.291
⑳	3	3	6	0.12	823	0	1.0	2.42	0.430	0.263

4. Numerical results and summary

Table 1 summarizes the numerical results of thermal efficiency in which heat receiving temperature was fixed at corresponding liquid blanket allowable maximum temperature 823K (550°C). Indices (m,n) indicate the number of compression and expansion stages. Beginning with the simple Brayton cycle case ①, the thermal efficiency of various conditions were calculated.

As the table indicates, adoption of regenerative heat exchanger and perfect inter-cooling as well as increasing the number of compression/expansion stages means the departure from the Brayton cycle and entering the Ericsson cycle which is ideally equivalent to the Carnot cycle. The only way of decreasing the pressure loss, the perfect inter cooling being retained, is to adopt the heating/cooling of the operating gas from the casing walls or within the flow paths between stator blades in both compressors and expanders, namely to adopt the isothermal expansion/heating and isothermal compression/cooling, which approaches the cycle shape from Brayton to Ericsson.

§10. Design on New Type First Wall under High Temperature and Particles for Nuclear Fusion Reactor

Furukawa, H. (ILT, Osaka), Norimatsu, T., Kozaki, Y., Jozaki, T., Mima, K. (ILE, Osaka University) Sagara, A.

Critical issue in designing an advanced fusion reactor with high output energy density is the ablation of the hot first wall exposed by energetic particles from plasma. In a case of a dry wall reactor for laser fusion operated with a 150 MJ yield target, the total thermal load on the surface is estimated to be 4.5×10^{18} W/cm², which heats the initially 500°C tungsten surface to 3000°C at the chamber radius of 6 m [1].

Before November 2001, we investigated ablation of tungsten and liquid lead under irradiation of x-rays, ions and α particles through computer simulation. The stopping power of plasma was calculated using dielectric response function of plasma and Bethe equations. We found that the stopping process in the ablated plasma is very important to discuss the ablation rate of the first wall.[2]

This year, we formulated the stopping power including influence of bound electrons to evaluate the vapor shielding effect. In this model, the ionization rate, the ionization energy of atoms and ions were involved to accurately evaluate the stopping process. A new model for hydrogen-like ions developed by Nishikawa of Okayama University[3] was used to calculate the number density of neutral particles, the ionization energy and the ionization rate.

The stopping power W of partially ionized gas was given by [4]

$$W = -\nabla \cdot E_k(x, t) = \frac{4\pi m_i Z_0^2 e^4}{m_e v^2} L \quad (1)$$

$$L = Z^* L_f + (Z - Z^*) L_b \quad (2)$$

$$L_b = \ln \left(1 + \frac{2m_e v^2}{I} \right) \quad (3)$$

where

L , the stopping number;

I , the ionization energy;

Z^* , average charge of partially ionized gas.

Here, $Z^*=0$ means it is neutral gas (vapor shielding). These equations indicate that accurate evaluation for the ionization rate and the ionization energy over a wide temperature range is very important to evaluate the vapor shielding effect.

Figure 1 shows the ionization rate of lead at temperature of 0.01 eV to 10 eV calculated over a wide density range from 10^8 to 10^{24} cm⁻³. These results are

very important for designing the first wall under a high thermal load such as the first wall of the laser fusion reactor and a diverter of the magnetic confinement system.

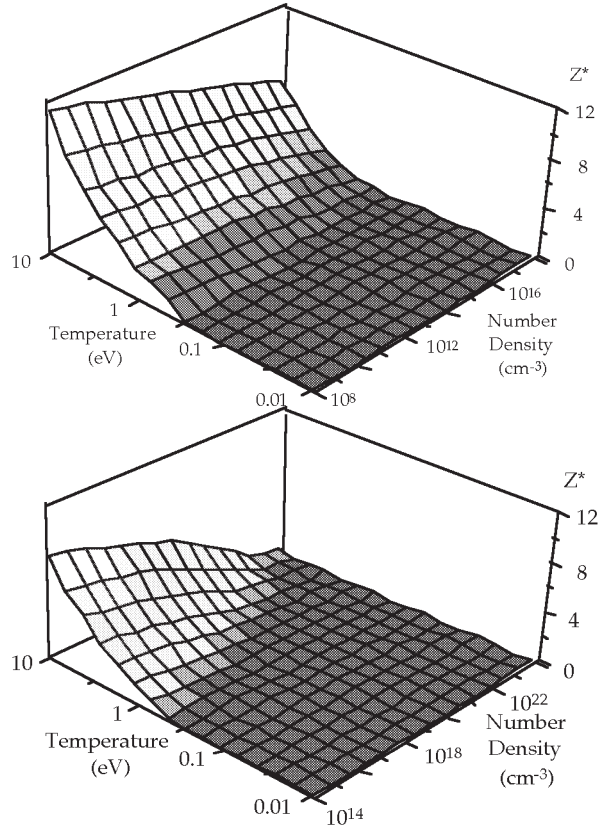


Fig. 1 Ionization rate of lead calculated over a wide density range from 10^8 to 10^{24} cm⁻³.

References

- 1) A. R. Raffray et al., Presented at ISFNT-7, May 22-27 (2005) Yokohama, Japan.
- 2) Simulation on Interactions of X-Ray and Charged Particles with First Wall for IFE Reactor; H. Furukawa, Y. Kozaki, K. Yamamoto, T. Jozaki, and K. Mima; Fusion Engineering and Design, to be published (2005).
- 3) T. Nishikawa, Private Communications.
- 4) T. Peter and Meyer-ter-Vehn, Phys. Rev. A **43** (1991) 2015-2030

(3) Fusion Reactor System and Safety

Safety and environmental research and development are important to design and construction of a future nuclear fusion reactor and to secure sufficient safety. Major issues are as follows.

- (1) Fundamental concept to secure safety in fusion reactor.
It includes studies of radiation protection considering radiation generating devices and radioactive materials in a nuclear fusion reactor.
Safety analysis presuming a helical type power reactor had been made considering engineering safety systems, functions, and sequential schemes presuming abnormal events.
- (2) Safety consideration of tritium fuel cycle.
The fusion reactor system includes large amount of tritium in the vacuum vessel and fuel cycle. So safety handling technology and robust confinement system are required. Major safety issues are to prevent tritium release accident and to recovery of the tritium released to a radiation control room. Also research of tritium behavior in the environment and its biological effect is important considering radiation protection for occupational health hazard.
- (3) Biological shields and radiation monitoring.
Much induced radioactive materials are produced in a nuclear fusion reactor. Shielding analysis of neutron and radiation from the radioactive materials are required. Also radiation measurements and monitoring are important for radiation protection.
- (4) Radioactive waste management.
Waste management of tritium containing gas, liquid and contaminated solid are important problems. Major issues are recovery of tritium, decontamination or volume reduction of the wastes.
- (5) Safety and public consent.
Comprehensive safety analysis and risk analysis should be made and the accountability is required.

Major safety issue specific for a future fusion reactor is to avoid the release accident of large amount of tritium. Fundamental safety of tritium processing would be secured by low tritium inventory, tritium dispersion to various partitioned components, and multiple protection systems.

Results of some collaborating studies are shown as follows. They will be useful not only for the DD experiment of LHD, but also for a future fusion reactor.

- (a) Investigation of tritium behavior and traceability in vessel system of LHD during DD burning.
This was made as collaboration with Nagoya University and many universities and research institutes. Tritium retention in TFTR, JET, and JT-60U were compared. It has been elucidated that hydrogen is mostly retained in carbon redeposited layers and high energy triton produced by D-D burning has directly impinged into the

vessel wall more than 1 μ m in depth. These basic findings will be useful for the tritium safety consideration of the LHD as well as for a future fusion reactor.

- (b) Tritium behavior in cooling pipe of stainless steel
This basic study has been carried out as collaborations with University of Tokyo and Shizuoka University. D₂ or D₂O was sorbed on/in the stainless steel samples by water adsorption, ion injection or electrolysis. Chemical states of metal elements and oxygen on the steel were evaluated by XPS (X-ray photoelectron spectroscopy). To evaluate desorption effect TDS (thermal desorption spectroscopy) was applied. It has been elucidated that the oxyhydroxide layer would have a large influence on hydrogen isotope retention, and the surface finishing would be an effective method for decreasing tritium retention on/in 316-SS.
- (c) Hydrogen isotope separation system
Two collaborating developments have been carried out. One is the study with Nagoya University on higher performance tritiated water volume reduction system by chemical exchange reactions between hydrogen gas and liquid water. The other is the study with Kyushu University on gaseous hydrogen isotope separation and purification system by pressure swing adsorption (PSA). Progresses in these basic studies will be expected to realize advanced tritium recovery systems in a future D-T burning reactor.
- (d) Atmospheric tritium recovery system
Recovery of released tritium gas in working area is a major safety system. The conventional tritium recovery process is to oxidize the tritium to water with catalyst and to dehumidify with dry absorber. To develop more compact and cost-effective system two collaborating developments have been carried out. One is the study with Shizuoka University on polymer membrane type dehumidifier. The other is the study with Kyushu University on honeycomb catalyst. Promising experimental results will be expected to realize advanced tritium recovery systems in the DD experiment of LHD.

As for a candidate blanket system, molten salt Flibe liquid blanket, that is using compound of LiF and BeF₂ is selected. It has inherent safety features like low tritium inventory, self cooling effect and low chemical activity. But the Flibe contains Beryllium, which is known as poisonous material and it causes occupational health hazard. To prevent the acute and chronic health hazard, safety handling technology must be accomplished. The Flibe safety handling study has been performed and reported as the collaboration project with US-Japan.

(Asakura, Y.)

§1. Investigation of Tritium Behavior and Tracability in Invessel Systems of LHD during D-D Burning

Tanabe, T. (Nagoya University), representative of cooperation program with 59 participants

Retention of hydrogen isotopes in plasma facing carbon materials in tokamaks has extensively studied, and it is found that most of hydrogen is retained in carbon redeposited layers on the inner divertor tiles and plasma shadowed area. However, hydrogen concentration in the carbon redeposited layers is quite machine dependent and mixing of hydrogen (H) and deuterium (D) makes analysis very difficult. Moreover tritium (T) produced by D-D reaction during D discharges behaves quite differently from H and D, because T produced by the reaction has initially 1 MeV and most of them are directly implanted into plasma facing surface more than 1 μ m in depth.

In order to discuss detailed tritium behavior in tokamaks, discussion meeting was held at September 4-5, 2004 in NIFS with more than 40 participants. And in particular, profiles of T retentions in TFTR bumper limiters and in the Mark IIA divertor of JET, and H/D and T retention in the W-shaped divertor of JT-60U were compared. The results are summarized in table 1¹⁾.

Hydrogen (H, D and T) is mostly retained in carbon redeposited layers with nearly constant concentration throughout the layers, except high energy triton directly impinging into more than 1 μ m in depth. However, carbon deposition profiles and hydrogen retention are strongly influenced by geometrical structure of the divertor and tile alignment as well as by magnetic field lines.

In JET and TFTR²⁾, profiles of tritium retention and carbon redeposition on deposition dominated area agree

quite well with hydrogen concentration in the redeposited carbon layers of $Q(H+D+T)/C \sim 0.1-1.0$. In TFTR, significant amount of tritium retention was observed on all sides of surface eroded tiles, indicating most of carbon originates from the eroded surface and the eroded carbon does not travel long, though the mechanism of tritium incorporation in the redeposited carbon layers is not clear. In JET, carbon deposition and tritium retention on toroidal gap facing sides were very small. Plasma shadowed area, particularly facing to the pumping duct, was heavily deposited with very high level of tritium. This carbon transport mechanism to plasma shadowed area is not clear, too.

In JT-60U^{3,4)}, toroidal carbon deposition profile were quite uniform with hydrogen concentration less than ~ 0.04 in $(H+D)/C$ ratio, which is far less than that for JET and TFTR and carbon deposition at toroidal sides were very small. Contribution of high energy deuterium coming from NBI was appreciable on the outer divertor area, particularly the outer dome area. Collected dust in JT-60U was also very small compared to that of JET.

The differences between JT-60U and JET could be attributed to those of divertor structure, including geometry of pumping duct, tile alignment, and temperature of the divertor tiles but need further studies. It seems possible to reduce tritium inventory significantly by increasing the surface temperature of the plasma facing components.

References

- 1) Tanabe, T.: Fusion Eng. & Design, to be published
- 2) Tanabe, T., Bekris, N., Coad, P. et al. J. Nucl. Mater. **313-316** (2003) 478
- 3) Masaki, K., Sugiyama, K., Hayashi, T. et al.: J. Nucl. Mater. **337-339**(2005) 553
- 4) Hirohata, Y., Shibahara, T. Tanabe, T. et al.: J. Nucl. Mater. **337-339** (2005) 609

Table. I Comparison of JET with Mark-IIA divertor and JT-60U with W-shaped divertor

	JET	JT-60U
Deposition rate at inner divertor	5g /h 6.5x10 ²⁰ atoms/s	6 nm/s 3 x 10 ²⁰ atoms/s
Erosion rate at outer divertor	2.3nm/s	0.7nm/s
D/C in deposits	0.4-0.1	< 0.05
Deposition at remote area	Louvers at inner pumping slot	Beneath outer divertor
Collected dust	1kg	7g
Pumping slot	Inner side	Bottom
Tile alignment in toroidal direction	A few mm step between tiles	No step between tiles
Divertor temperature	Below 500K with base structure water cooled	Above 600K Only inertially cooled

\$2. Studies of Interaction between Cooling Pipe Materials and Tritium, and Their Chemical Behavior

Oya, Y. (Radioisotope Center, Univ. of Tokyo)
Onishi, Y., Yoshikawa, A., Okuno, K. (Fac. of Sci., Shizuoka Univ.)
Tanaka, S. (Dept. Quantum Eng. & Systems Sci., Univ. of Tokyo)
Kawano, T., Asakura, Y., Uda, T.

1) Introduction

Stainless steels (SS) are expected to be used in fusion reactors as various component materials like cooling pipe, vacuum vessel and so on, because of its good mechanical properties and corrosion resistance. The behavior of tritium in SS is one of the most important issues for the assessment of fusion safety. However, the chemical behaviors of hydrogen isotopes with various adsorption/absorption have not been well studied. These backgrounds motivate us to study the detailed analysis of hydrogen isotopes behavior in SS. In the present study, the typical material for components, 316-SS, was chosen as specimen and deuterium was charged with various absorption/adsorption methods like water adsorption or electrolysis. The chemical states of iron, chromium, nickel and oxygen on SS-316 were observed by the XPS. Depth profiles of chemical states of elements were also evaluated by using Ar^+ sputtering technique. The TDS was also applied to the analyses of the thermal desorption behaviors of D_2 and D_2O from 316-SS for comparison.

2) Experimental

The 316-SS sample with size of $10 \times 10 \times 1 \text{ mm}^3$ was used. Two kinds of sample with different surface finish, namely the non-pretreated sample and pretreated sample by mechanical polish and annealing at 1273 K in vacuum for 30 minutes to remove surface oxide layers, have prepared. For these samples, D_2 or/and D_2O was sorbed on/in the sample by various methods, such as water adsorption and electrolysis. In the water adsorption, the sample was immersed in heavy water for 30 min. In the electrolysis experiment, the sample was used as a cathode for 60 min

with the current of 0.1A. The chemical states of iron, chromium, nickel, molybdenum, carbon and oxygen on the 316-SS sample were evaluated by X-ray photoelectron spectroscopy (XPS). The thermal desorption spectroscopy (TDS) was also applied to the evaluation of the desorption behavior of hydrogen isotopes from the stainless steel. The heating rate was set to 30 K/min from room temperature to 1273K.

3) Results and discussion

In our previous studies [1,2], it was found that the oxyhydroxide was mainly formed on the surface of SS after electrolysis. For the sample after water adsorption, hydroxide was the major chemical form of the surface. To elucidate the chemical behavior of 316-SS as a function of depth, XPS analysis and the depth profiling by Ar^+ sputtering was conducted for the non-pretreated 316-SS sample. Fig.1 shows the chemical compositions of 316-SS as a function of depth. It was found that the thickness of the oxide layer for the non-pretreated sample after electrolysis was the largest compared to the as received sample and the sample with water adsorption. This fact indicates that the oxyhydroxide layer made the oxide layer thicker and a large amount of hydrogen isotopes would be trapped in this thin layer.

It can be concluded that the oxyhydroxide layer would have a large influence on hydrogen isotope retention including tritium, and the surface finish would be an effective method for decreasing its retention on/in 316-SS.

4) Conclusions

The chemical states of 316-SS after various hydrogen adsorption/absorption treatments were evaluated by XPS. These results were compared to the hydrogen isotope desorption behavior by TDS. A large amount of hydrogen isotope was trapped in the oxyhydroxide layer for the non-pretreated sample after electrolysis. The hydrogen isotope trapping by this layer would be a major influence on hydrogen retention. The surface finish would be one of the effective improvements for decreasing tritium retention in 316-SS.

References

- 1) Oya, Y., et al., Fusion Sci & Tech. **44** (2003) 359.
- 2) Oya, Y., et al., Fusion Sci & Tech., in press

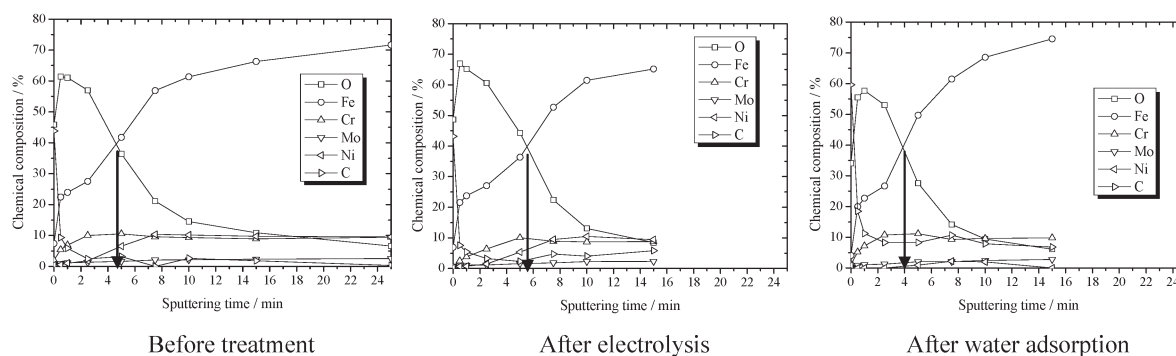


Fig.1 Depth profiles of the sample with various treatment estimated by XPS with Ar^+ sputtering.

§3. Advancement of Water-Hydrogen Chemical Exchange Apparatus by Introducing Trickle Bed Reactor

Yamamoto, I., Enokida, Y., Tsushima, S., Sawada, K., Shiozaki, T. (Nagoya Univ.), Uda, T., Asakura, Y., Sugiyama, T.

Experimental studies on hydrogen isotope separation by a Combined Electrolysis Catalytic Exchange (CECE) have been carried out in order to apply it to the system of water detritiation for fusion reactors.

In the present study we try to improve the separative performance of the CECE process by developing effective trickle beds.

i) Experiments

The reactor column is a Pyrex glass tube with 25 mm internal diameter and 60 cm length. The column is filled with Kogel catalysts (0.8 wt% Pt deposited) and Dixon gauze rings in two ways. One is the layered bed where layers of Kogel catalysts and that of Dixon gauze rings are filled in the column alternately. The other is the homogeneous bed where Kogel catalysts and Dixon gauze rings are mixed and filled in the column homogeneously. These packed beds are shown in Fig. 1.

Hydrogen-deuterium isotope separation with the CECE equipment was performed at 101 kPa, 343 K. Flow rate of hydrogen gas was selected to 4, 8 and 12 L/min. Feed rate of distilled water was adjusted respectively as the molar flow ratio of hydrogen gas to feed water became the same value in all tests. The concentrations of HD or HDO in gas and liquid samples were measured using a stable isotope ratio mass spectrometer (MAT252, Thermo Finnigan) with a relative accuracy to 1 %.

ii) Separation factors of the packed beds

Separation factor of the water phase α and that of the hydrogen gas phase β are defined as follows with the molar concentration of deuterated molecule C and the molar flow ratio F :

$$\alpha = C_{(\text{Feed})} / C_{(\text{Extracted water})} \quad \beta = C_{(\text{Extracted hydrogen gas})} / C_{(\text{Feed})}$$

$$C_{(\text{Feed})} = \frac{F_{(\text{Feed water})} C_{(\text{Feed water})} + F_{(\text{Feed hydrogen gas})} C_{(\text{Feed hydrogen gas})}}{F_{(\text{Feed water})} + F_{(\text{Feed hydrogen gas})}}$$

Calculated separation factors are summarized in Table I. The α values of the both packed beds keep almost constant values of about two in the present range of hydrogen flow rate. The values of the homogeneous bed are slightly larger

than that of the layered bed. On the other hand the β values of the homogeneous bed are about twice as large as that of layered bed. In either case the results indicate that the homogeneous bed is more efficient than the layered bed.

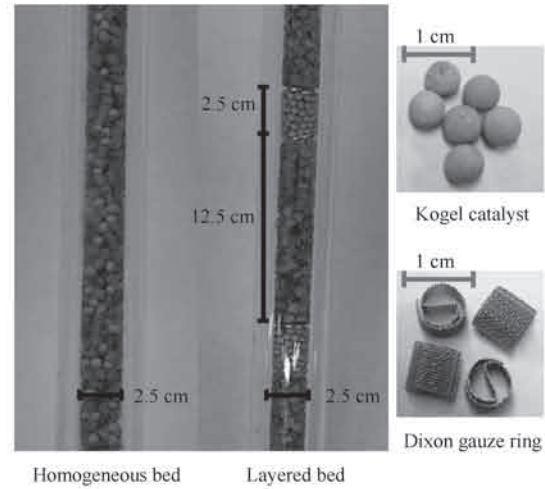


Fig. 1: Two types of packed beds

Table I: Separation factors of the packed beds

	α			β		
F [L/min]	4	8	12	4	8	12
Homogeneous	2.27	2.22	2.12	6.00	5.51	4.80
Layered	2.01	1.88	1.91	3.14	2.63	2.45

iii) Mass transfer coefficients of the homogeneous bed

In the case of homogeneous packed bed deuterium mass transfer coefficient between hydrogen gas and water vapor k_g and that between water vapor and liquid water k_l can be obtained from a simultaneous solution of material balances represented the mass transfer process. Calculated values are summarized in Table II.

The values previously reported were in the range 100-350 kmol/m³/h for k_g and 40-280 kmol/m³/h for k_l . The value of k_l is much improved in our experiments. This fact indicates that the homogeneous packed bed of Kogel catalyst and Dixon gauze ring is promising for one of the candidate column.

Table II: Mass transfer coefficients of the homogeneous bed

F [L/min]	4	8	12
k_g [kmol/m ³ /h]	89	147	181
k_l [kmol/m ³ /h]	300	639	926

Reference

- 1) Sugiyama, T., Asakura, Y., *et al.*: *Fusion Sci. Technol.*, 48 [1], pp. 132-135 (2005).
- 2) Sugiyama, T., Asakura, Y., *et al.*: *ISFNT-7*, P1-33, Tokyo, May (2005).

§4. Development of High-power Adsorbents for Hydrogen Isotope Separation by Pressure Swing Adsorption Method

Kotoh, K., Kudo, K. (Kyushu Univ. Eng.)
Nishida, T. (Kinki Univ. Ind. Eng.)
Sugiyama, T., Asakura, Y., Uda, T., Kawano, T.

A process of hydrogen isotope separation is necessary in the environmental safety treatment of exhaust gases from LHD deuterium experiments. We attempt to develop a practical system of pressure swing adsorption (PSA) process for hydrogen isotope separation, applicable to the processing of the LHD exhaust gases. From the result of break-through experiments using adsorption columns with synthetic zeolite adsorbents at 77.4 K, we already confirmed that the PSA process is available for hydrogen isotope separation²⁾. At the aim of developing the practical system, however, the PSA process must be improved to operate the separation at a more increased efficiency. The efficiency of separation depends on the characteristics of adsorption equilibrium and mass transfer of hydrogen isotopes on an adsorbent in use. Therefore, we reached the conclusion that the next step of this work should be to investigate or/and develop adsorbents more suitable for the PSA process.

An adsorbent useful to the PSA process should satisfy the following conditions: (1) A stepwise profiling isotherm for hydrogen is exhibited, and its sharp turn appears in a range of practical pressure swing operation. (2) Large numbers of separation factors are obtained in adsorption of a hydrogen isotope mixture. (3) The mass transfer onto/from adsorbent is sufficiently speedy. (4) Its body is tough, mechanically and chemically, and so on.

i) Investigation of Functional Adsorbents

We made a survey of materials having the adsorptive functions advantageous to the PSA operation. The result shows the following complexes promising as a functional adsorbent, which have angstrom-order-diameter channels in their crystal lattice frameworks.

◦ Cobalt Tris-ethylenediamine

has one-dimensional regular channels of ϕ 0.6 nm in effective diameter, and shows stepwise isotherms for adsorption of water vapor.

◦ Terephthalic Acid

has two-dimensional regular channels of ϕ 0.6 nm in effective diameter.

◦ Copper Terephthalate Tris-ethylenediamine

has three-dimensional regular channels of ϕ 0.74 nm in effective diameter, and exhibits stepwise isotherms for adsorption of argon, nitrogen and carbon dioxide.

On cobalt tris-ethylenediamine, adsorption isotherms for H₂O and D₂O were already examined experimentally and analytically in our work. We have developed techniques of finer crystal-powder preparation and its pellet-fabrication.

The next work is to develop the techniques for one of the best candidates: copper terephthalate tris-ethylenediamine.

ii) Development of Volumetric Adsorption Apparatus

As shown in Figure 1 an improved volumetric adsorption apparatus was developed for the purpose of observing the isotherms for hydrogen isotopes and these multi-component adsorption behaviors in detail with accuracy. This apparatus can perform the ultimate vacuum in a range of 10^{-7} Pa, and can measure the adsorption equilibrated at a pressure in the order of 10^{-3} Pa within an error of 10 %.

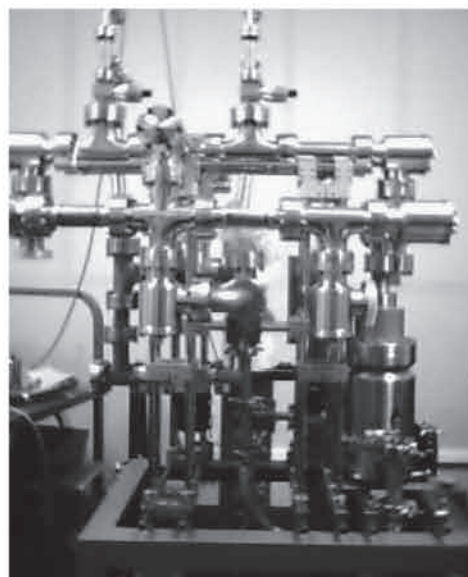


Fig. 1 Volumetric Adsorption Apparatus

iii) Development of Crystalline Adsorption Theory

The adsorption potential theory is most appropriate for describing the adsorption into micro-pores such as zeolite crystalline pores. In this theory, however, there are some problems should be resolved or improved. In this study, we developed a theoretical expression in order to describe the adsorption behavior of hydrogen isotope mixtures in zeolites. This expression assumes that the crystalline void space is identical with the adsorbed-phase volume corresponding to the adsorption potential field, where are molecules trapped on adsorptive inner-surface sites and the others not trapped but attracted over the other active sites^{1,3)}.

Experimental behaviors of H₂, HD and D₂ adsorbed on several types of zeolite at 77.4 and 87.3 K are interpreted consecutively by this expression. From relationships of its parameters between hydrogen and deuterium, the behaviors of all hydrogen isotopes can be predicted in simple but coherent description³⁾. The dependence of parameters on temperatures also is becoming clear in theoretical analysis.

References

- 1) Kotoh, K., Kudo, K., *Fusion Sci. Technol.*, 48 [1], pp. 148-151 (2005)
- 2) Sugiyama, T., *et al.*, *Fusion Sci. Technol.*, 48 [1], pp. 163-166 (2005)
- 3) Kotoh, K., Kudo, K., *Meeting on Isotope Sci.*, Nagoya Univ. COE, Nagoya, March, (2005)

§5. Studies of Tritiated Water Vapor Removal with a Hollow-filament Type Polyimide Membrane Dehumidifier

Okuno, K., Oyaidzu, M., Yoshikawa, A. (Fac. of Sci., Shizuoka Univ.)

Oya, Y. (Radioisotope Center, Univ. of Tokyo)
Asakura, Y.

1) Introduction

In future DD experiments for LHD devices, it is important to establish the removal technique of tritium produced in vacuum vessel by DD reaction. In this collaborative study, the acquirement of dehumidify characteristics for a membrane type dehumidifier and theoretical study was done for achievement of high performance dehumidify compared to molecular sieve method. In this fiscal year, simulation study using perfect mixture model was performed. These results were compared to the achieved data at NIFS and discussed.

2) Model

There are lots of simulation model proposed for analyzing gas separation behavior using a membrane type dehumidifier. In particular, it is well known that the combination of counter-flow and cross-flow model is the most ideal model. However, some specific parameters related to membrane are required and it is difficult to find out these specific parameters. To avoid these problems, we adopted the model of two component mixture gases. Fig. 1 shows schematic drawing of gas stream inside of a membrane module. In this figure, F_f [mol/s] is supply mixture gas flow rate, and x_f , x_o and x_p are, respectively, mole fraction of inlet, high pressure outlet and low pressure outlet gas stream of each component. The gas component

$$y_p = \frac{(\alpha - 1)(\phi + x_f) + 1 - \sqrt{\{(\alpha - 1)(\phi + x_f) + 1\}^2 - 4\phi(\alpha - 1)\alpha x_f}}{2\phi(\alpha - 1)}$$

for outlet side was expressed by the following equation,

In this equation, ϕ is an operation factor, and explained in the following equation.

$$\phi = \gamma + \theta - \gamma\theta$$

where, θ is a cut rate and γ is a pressure ratio.

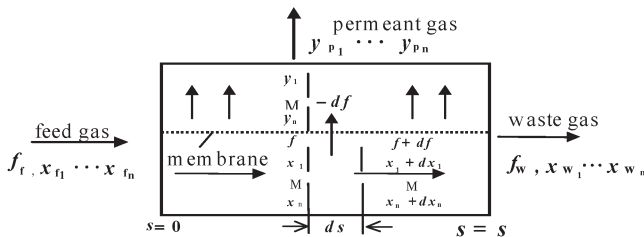


Fig.1 Schematic drawing of membrane module

3) Results and discussion

Fig.2 shows the experimental results of recovery rate as a function of cut rate, which was achieved using polyimide type dehumidifier produced by Ube Industries, Ltd. [1]. The calculation result using the complete mixing model was also shown in this figure.

It was found that the recovery rate of the experimental result was exceeded over 99 % under the cut rate of 0.2. However, only 30 % was achieved by the calculation result. It is also known that the good agreement was found between experimental results and calculation ones for the hydrogen isotope separation. These facts indicate that the permeation rate in membrane would give a large influence for water vapor separation, although it was assumed to be constant in this model.

Further study on the evaluation of permeation rate in membrane will be done and optimized model for water vapor separation will be established.

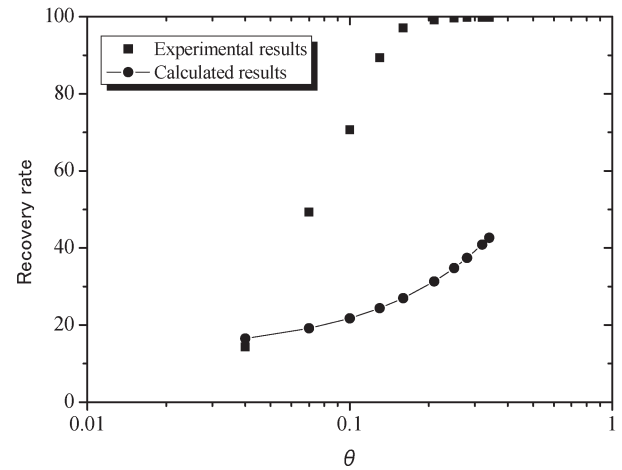


Fig.2 Correlation between recovery rate and cut rate

4) Conclusions

To establish suitable water vapor separation system for DD experiment in LHD device, the experimental data was achieved at NIFS and these data were compared to the calculation one using perfect mixture model. It was found that the inconsistency was found between the experimental result and calculation one and these facts indicated that the permeation rate in membrane would give a large influence for water vapor separation.

References

- 1) Asakura, Y., et al.: *Fusion Sci. Technol.*, 48 [1], pp. 401-404 (2005).

§6. Development of Advanced Catalyst for Oxidation of Tritium and Quantification of Mass Transfer Coefficient

Munakata, K., Okabe, Y. (Interdisciplinary Graduate School of Engineering Sciences Kyushu University), Kawano, T., Asakura, Y., Uda, T.
Tanaka, M. (Nippon Kucho Service Co., Ltd.)

For the establishment of the safety of the fusion technology, recovery of tritium released into the working area of fusion power plants or tritium-handling facilities is quite important. It is also necessary to develop a technique that enables accurate monitoring of environmental tritium around the facility where tritium is handled. The catalytic oxidation and adsorption is the most conventional and reliable method for removing tritium that is accidentally released into the working area of these facilities. The catalytic oxidation and adsorption is also a key process for monitoring of environmental tritium, which is used to capture tritium in the atmosphere. The catalysts used for these purposes need to possess high catalytic performance for low temperature combustion of tritium and tritiated methane as well as selectivity in catalytic reactions. Up to now, the authors have worked on the development of such catalysts. However, if the actual process is considered, there are further demands for catalyst and catalytic process. For example, if accidental tritium releases take place, large amounts of air should be processed by the air cleanup system. Therefore, the air cleanup system needs to be designed to be able to deal with the air with high volumetric velocity. Other than this, compactness and simplicity, efficient heating and endurance in long term use and repeated use are also required. With this background, the purpose of this study is to reexamine required catalytic performance from wider perspective and to develop advanced catalysts in a scientific way. This time, the authors intensively investigated the oxidation performance of honeycomb catalysts, which is considered to be effective for the treatment of high throughput process gas and efficient heating, for catalytic oxidation of tritium and tritiated methane. Furthermore, the sorption of hydrogen into carbon nano-tube was investigated.

In the experiments, a reactor made of quartz was used. The temperature of the reactor was changed in the range of ambient to 673 K. The argon gas containing hydrogen and methane of 0.1 % was introduced to the reactor. The concentration of hydrogen and methane at inlet and outlet stream of the reactor was measured with a gas chromatograph. The flow rates were controlled with conventional mass flow controller. The catalytic activity of honeycomb catalysts deposited with platinum and palladium was investigated using the experimental apparatus described above.

The honeycomb catalysts possess favorable characteristics in comparison with conventional pellet type of catalysts used in the packed bed reactor. If the honeycomb is made of metals, the honeycomb catalysts possess higher heat conductivity. Furthermore, there is a possibility that the catalyst itself can be directly heated by applying currents. The pressure drop along the honeycomb catalysts is smaller than packed bed catalysts, as well. For this reason, the catalysts used to deal with the exhaust gas of automotive are of honeycomb type. In practice, the pressure drop along the honeycomb catalyst was calculated by assuming actual cell sizes. The pressure drop along the axial direction in the packed bed catalyst reactor was also estimated using empirical equations. The results of these estimations indicate that the pressure drop can be substantially decreased when the packed bed catalyst is replaced with the honeycomb catalysts in the air cleanup system.

The effect of the cell density of the honeycomb and the amounts of deposited noble metals on the catalytic activity was examined, and it was found that the increase of content of catalyst metal and the increase of cell density raise the performance of the catalysts. Therefore, the honeycomb catalysts with the cell density of 400 CPSI were intensively examined. The experimental results obtained using the experimental apparatus were analyzed and reaction constants for oxidation of hydrogen and methane were quantified. The results of the analysis indicate that cordierite honeycomb catalysts deposited with platinum has the best performance for the oxidation of hydrogen. It is also suggested that the metal honeycomb catalyst deposited with platinum has the oxidation performance comparable to a conventional packed bed catalyst deposited with platinum for the oxidation of hydrogen. With regard to the oxidation of methane, it was found that the metal honeycomb catalyst deposited with palladium has the best oxidation performance. It is also found that the cordierite honeycomb catalyst deposited with palladium has the oxidation performance comparable to a conventional packed bed catalyst deposited with palladium for oxidation of methane. The quantification of reaction constants for oxidation of hydrogen and methane over the honeycomb catalysts enables the quantitative design of catalyst bed of larger scale for recovery of tritium and tritiated methane.

Furthermore, the sorption of hydrogen in carbon nano-tube was investigated. The packed bed reactor charged with particles of carbon nano-tube was used for this study. An argon gas containing hydrogen was introduced to the reactor at ambient temperature, and the concentration of hydrogen in the outlet stream of the reactor was measured. However, the experimental result indicates no appreciable sorption of hydrogen. Several researchers have reported the sorption of hydrogen into carbon nano-tubes. Thus, it is necessary to investigate the effect of temperature and carrier gas. Additionally, the effect of catalyst on the sorption of hydrogen needs to be investigated.

3. CHS Experiments

Various topics of the edge transport barrier (ETB) formation physics have been studied in CHS. It was confirmed that the heating power threshold for the ETB formation exists and its dependencies on the plasma density and the magnetic field were investigated. These are similar to tokamak H-mode scaling. There is also the lower density limit for the ETB formation. Finding of the dependence of the power threshold on the magnetic configuration is unique in CHS experiment. The ETB formation is observed for a wide range of the rotational transform at plasma boundary (0.91 to 1.17) and characteristics of the transition (power threshold and the delay time of the spontaneous transition) varies continuously. Measurements of ion temperature and the plasma flow during the ETB formation showed negligible change of the ion temperature profile and small plasma rotation speed compared to the H-mode in tokamaks.

Progresses have been made in studying more specific topics in the ETB formation. The change of radiation profile was measured at the transition using AXUV photodiode array. The radiation starts to increase at the transition making more flat profile than before. The beam emission spectroscopy (BES) using the heating NBI showed low frequency coherent oscillations with harmonics of about 4 kHz during the H-mode phase. This oscillations starts with the increase of density gradient and the gradient itself is saturated with the development of this type of oscillations. The dynamics is very similar to the edge harmonic oscillation (EHO) observed in tokamak H-mode. The understanding of the dynamics of ETB formation at the plasma edge was improved with the probe measurements. The probability density function was discussed and the clear difference was obtained at the transition. Local electron density and temperature profiles were measured as well as the plasma potential and the gradient changes of those parameters were observed at the normalized radius of 0.96.

Highest plasma energy was obtained in CHS with two co-injection NBIs of 1.6 MW port-through power. When the line-averaged density reached $1 \times 10^{20} \text{m}^{-3}$ with strong gas puffing at 1.9 T magnetic field, the gas puffing was stopped to raise a reheat mode for a further increase of plasma energy resulting the record of 8.0 kJ (0.6% beta). The density profile was very flat at the time of peak energy. High density plasma production was also successful with 106 GHz ECH up to its theoretical cut-off limit. The confinement of high energy ions in CHS was directly studied using the diagnostic neutral beam (DNB) as a probe beam source and the neutral particle energy analyzer. The dependence of the confinement on the magnetic configuration was studied with different magnetic axis positions.

Fluctuation measurement with two heavy ion beam probe system (dual HIBP) is a pioneering work in CHS for

the transport study of plasma turbulence. A wavelet analysis was made for the density and potential fluctuations measured at the internal transport barrier formation. Time behaviour of spectra of both signals was obtained and it was found that the fluctuation levels increased at the back transition (when the transport barrier is lost). A new challenge of measuring the magnetic fluctuation with HIBP was made and the signal from the MHD mode (burst mode in CHS) was successfully measured as well as the radial mode structure information. Careful analysis of the density fluctuation signal was made including the path integral effects along the beam trajectory. New technique of obtaining the spatial mode structure of a coherent mode which has a very small amplitude in the spectrum. Combining with the magnetic probe signal, the analysis of the coherence of the potential signal to the magnetic one gave the spatial profile information of the potential measurement.

For more fluctuation diagnostics, YAG laser imaging method and the HCN laser scattering have been developed. The maximum entropy spectral analysis was applied to the YAG laser data and the distribution of the propagation direction was obtained with a better resolution. The HCN laser scattering measurement produced the first signal at the wavenumber of about 5.5 cm^{-1} .

Development of diagnostics have been made also for the ECE measurements, the hybrid probe with the rotating mechanism, MHz range fluctuation probe, lithium beam probe (LiBP) for the plasma edge density measurements. New system of LiBP was developed for the purpose of two dimensional measurement using a CCD camera. For understanding the neutral particle dynamics near the plasma boundary, the simulation study has been continued using DEGAS code. The model was improved to directly include a three dimensional structure of CHS device.

The plasma confinement study using low density plasma with low magnetic field was also made in CHS based on the dimensional similarity concept. The experiment using 2.45 GHz microwave produced the internal transport barrier and the probe measurement gave the information of the internal structure of the barrier formation. Low field experiment with a microwave also showed an evidence of the plasma production well above the cut-off density limit. The experiment of the radial electric field control for the confinement improvement was also made with the low magnetic field. The combination of the microwave and the Whistler wave was studied for the possibility of higher density production. The pure electron plasma was produced in CHS for the basic physics study of the non-neutral plasma. CHS also provide a good plasma for the EUV spectroscopy research for the basic research of the lithography development.

(Okamura, S.)

§1. Study on Parameter Dependences of Power Threshold for Edge Transport Barrier Formation

Akiyama, T., Okamura, S., Minami, T., Fujisawa, A., Isobe, M., Suzuki, C., Nishimura, S., Matsuoka, K., Yoshimura, Y., Nagaoka, K., Takahashi, C., Kawahata, K., CHS Experimental Group (NIFS)
Tsuji-Iio, S. (TITech)
Okajima, S. (Chubu Univ.)

The confinement improvement by the formation of edge transport barrier (ETB) is observed in the Compact Helical System (CHS) by inducing large net plasma current [1] and increasing co-injected neutral beam power [2, 3]. Similarly to H-mode in tokamaks, the power threshold for ETB formation exists and depends on various plasma parameters.

From NB power-scan experiments the power threshold for transition was found. In the case of enough power H α emission signal drops abruptly. It drops in two steps. The first drop takes more than several milliseconds, which is comparable to or longer than the energy confinement time. The second takes less than 1 ms. We presume that changes during the first drop induce the transition. The power approaching to the threshold, the delay time and the first H α drop phase become longer. Spiky H α signals, whose time width is 1-2 ms, are observed when the power is close to the threshold. Finally the second sharp drop in H α signal disappears ("Obscure Transition" shown in Fig. 1) and then the first slow drop does not occur ("No Transition" in Fig. 1).

Dependences of threshold power on plasma and configuration parameters have been studied well and reported in tokamak devices. Figure 1(a) shows the

dependence on electron density in CHS. In these parameter scan experiments the position of magnetic axis is 92.1 cm. In this figure the line averaged electron density at 15 ms after NB injection, that is almost the same as the time of a transition, is plotted. The threshold increases with increasing electron density. In addition the drop in H α signal was not observed for the electron density of less than about $1 \times 10^{19} \text{ m}^{-3}$. Since increase in threshold power near the density threshold is reported in some tokamaks, the detailed investigation in a low density range is planned.

The threshold also increases with increasing magnetic field strength as shown in Fig. 1(b). In this magnetic-field-scan experiment electron density at the transition is constant to be $2.5 \times 10^{19} \text{ m}^{-3}$ and the position of magnetic axis is 92.1 cm.

Although these dependences are similar to those in tokamaks, it is under study whether these similarities are attributed to the same mechanism of ETB formation or not. In H-mode in tokamaks $E \times B$ velocity shear plays important role. However, change in radial electric field after transitions near plasma edge region has not been observed with both CRX and a Langmuir probes in CHS at a moment. Investigation of the mechanism is a future work.

Reference

- 1) K. Toi et. al., Plasma Phys. Control. Fusion **38** (1996) 1289.
- 2) S. Okamura et. al., J. Plasma Fusion Res. Vol.79, No.10 (2003) 977.
- 3) S. Okamura et. al., Plasma Phys. Control. Fusion **46** (2004) A113.

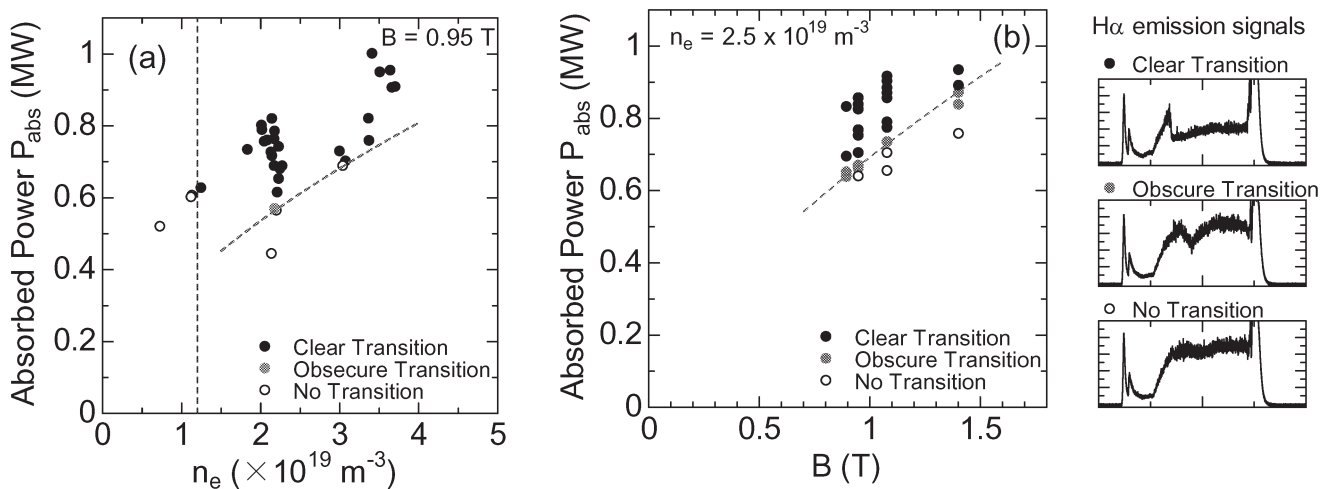


Fig.1 Dependence of power threshold on (a) line averaged electron density and (b) magnetic field. Black, gray solid circles and open circles denote clear, obscure, no transition, respectively, as shown in right side figures.

§2. Power Threshold for ETB Transition Based on NBI Power Deposition Calculation

Minami, T., Akiyama, T., Okamura, S., Nagaoka, K., Isobe, M.

The NBI power threshold for the ETB formation evaluated by the port-through value was reported in the last fiscal year. The threshold power is evaluated using the deposited NBI power. The deposited power is defined as follows,

$$P_{deposit} = P_{port} - P_{shine} - P_{orbit} - P_{cx} \quad (1)$$

,where the $P_{deposit}$, the P_{port} and P_{shine} are the deposited, port-through and shine-through power, respectively. The P_{orbit} and P_{cx} is the orbit loss and the charge exchange loss during the slowing-down of injected beams, respectively. We use the following formula empirically obtained in the CHS experiments for estimating the deposited power.

$$P_{deposit} = P_{port} \times (1.0 - 2.35 \times 10^{-2} \exp(-B_T)^{0.363} \times \exp(-n_e)^{2.60} E_{nbi}^{1.35} (R_{ax} - 0.8)^{0.509} a^{-0.061}) \quad (2)$$

,where $B_T(T)$ is the magnetic field strength at the magnetic axis, $n_e(\times 10^{14} cm^{-3})$ is the electron density, $E_{nbi}(kV)$ is the acceleration voltage of the NBI, $R_{ax}(m)$ is the major radius, and the $a(m)$ is the minor radius.

Figure 1 shows the delay time of the L-H transition from the second NBI injection for three experiments of the different days. The data are plotted as the function of deposited power normalized by the line-averaged electron density. All experiments are performed under the condition of $B_T=0.95$ T, $R_{ax}=92.1$ cm. In the case of the 2003/6/19, the timing of the second NBI injection is delayed approximately 20ms after the first NBI injection, while the two NBIs are simultaneously injected in the other cases. Because the wall conditions of the three experiments and the NBI injection methods are various, the delay times for the three experiments are different. However, the delay times get longer when the normalized NBI power is close to the specific value of $200 \times 10^{-13} kW/cm^{-3}$ for all the experiments, and the ETB is not formed below this specific threshold value. The value of the threshold power for the barrier formation is approximately two times as large as that expected from the tokamak H-mode scaling. When the delay times are plotted as a function of the NBI deposited power without being normalized, the data points are more scattered. The threshold for the formation of the ETB is determined by the averaged deposited power density, and accordingly the required NBI power for the transition increases as the density increases.

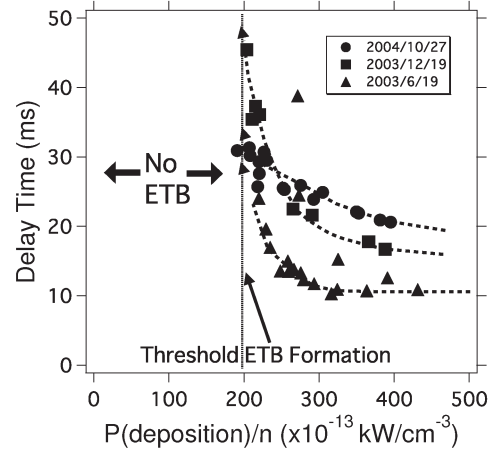


Fig. 1: Delay time of L-H transition after NBI injection are plotted as a function of deposited NBI power normalized by electron density. Circles, triangles, and squares denote data in different experiments that have different wall conditions.

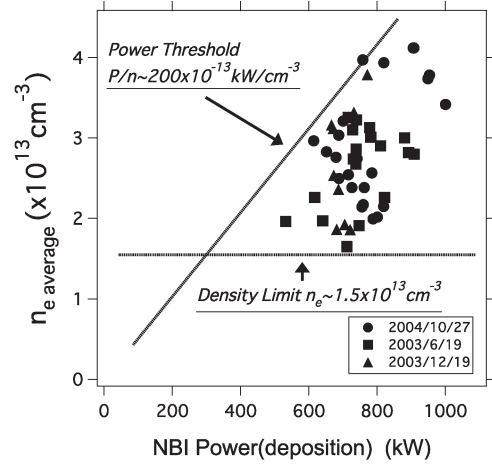


Fig. 2: Averaged electron densities for plasmas with ETB are plotted as a function of deposited NBI power.

We plot the average densities at the first drop of the H_α emission as the function of the injected powers. The figure 2 shows the ETB is formed when the deposited power exceed the ~ 500 kW at $n_e \sim 2 \times 10^{13} cm^{-3}$. The required power increases as the density increases as described above. In addition, the ETB formation has been observed when the plasma density exceeds $\sim 1.5 \times 10^{13} cm^{-3}$ with the gas-puffing, and the ETB has not been observed when the density is below the limit. The lower density limit increases as the deposited NBI power increases. These observations for the density limit are similar to the results in the WS-7AS experiments or the Heliotron J experiments.

§3. Dependence of Power Threshold on Magnetic Field Configuration

Minami, T., Akiyama, T., Okamura, S., Nagaoka, K., Isobe, M.

The magnetic field configuration can be changed by the shift of the magnetic axis location through the control of the poloidal field coil currents in CHS. The magnetic well, the orbit of trapped particles, the plasma viscosity and the distance of the last closed flux surface from the wall can be controlled by the magnetic axis shift. The inward shifted configuration is favorable for drift orbit optimization, and provided stable plasma discharge in spite of the expected instabilities from the Mercier criterion. The CHS plasma contacts the inner wall, when the magnetic axis location is smaller than ~ 98 cm, and the contact area increases by the inward shift. The low viscosity of the inward shift is favorable for the plasma rotation.

Clear dependence of the normalized threshold power on the magnetic configuration has been found, as shown in figure 1. The magnetic axis location of 92.1cm is the standard configuration to realize good plasma performance in CHS. The formation of the ETB has been observed for the magnetic axis locations between 89.9 cm and 94.9 cm, as shown in figure 1 (a). When the magnetic axis is inside 89.9 cm or outside 94.9 cm, the ETB formation has not been observed. The experiments are performed for different port-through NBI powers and densities controlled by the gas-puffing. We have not found the formation of the ETB below the lowest threshold value denoted by the dotted line. The threshold power shows the minimum around $R_{ax} = 93.5$ cm. The lowest power decreases as the R_{ax} increases, however, the formation of the ETB has not been observed outside 94.9 cm.

The same characteristics as the power threshold have been observed for the delay time of the ETB formation from the NBI injection. Figure 1 (b) shows the delay time as a function of the magnetic axis location. The delay time gets longer by the inward shift. The minimum delay time is found in the same location of 93.5 cm as the power threshold.

The increase of the power threshold and the delay time for the inward shifted configuration suggests that the contact area to the inner wall is important for the barrier formation. The contact area affects the neutral particles and the amount of the impurity in the edge region. The relation of the ETB formation to the effect of the drift orbit optimization and the decrease of the viscosity by the inward shift is not clear. However, the ETB has not been observed for the outward shifted configuration with > 96.9 cm, and , moreover, has not been observed under the divertor configuration when $R_{ax} > 98$ cm.

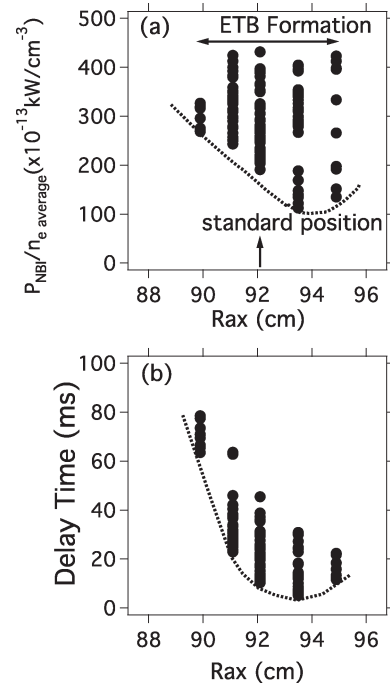


Fig. 1: (a) NBI power values normalized by densities at L-H transition on various magnetic configurations (magnetic axis locations). (b) Delay times from the beam injection. Dotted curves denote the power threshold.

These results might be contradictory to the results of inward shifted configurations.

It is noted that in these experiments whether the ETB is formed or not is judged by the observation of the transition phenomena: the observation of the spontaneous drop of the H_α emission. If the ETB is formed from the start of the discharge, the confirmation of the ETB formation is difficult because of no existence of the transition phenomena during the discharge. When the magnetic axis is shifted to the outer direction, the threshold power becomes decrease, on the other hand, it becomes difficult to sustain the NBI plasma because the injection NB power becomes lower. The threshold power for the ETB formation is close to the minimum power for maintaining the plasma discharge at R_{ax} of 94.9 cm. Accordingly, it is possible to form the ETB just after the start of the discharge when the plasma axis shift to the outer direction from 96.9 cm, however, the judgment whether the ETB is formed or not is difficult.

Consequently, these results suggest that the ETB formation relate to the neutral particles profile around the edge region. The further investigations such as the neutral particle measurement for the edge region are required to clear physical mechanism.

§4. Time Evolutions of the Ion Temperature in the Edge Transport Barrier (ETB) Operations in CHS

Nishimura, S., Okamura, S., Minami, T., Akiyama, T., Nagaoka, K., Yoshimura, Y., Ida, K., Isobe, M., Suzuki, C.

As previously reported [1], the main feature of the edge transport barrier (ETB) in CHS is the change of the density profile after the L→H transition, and the electron temperature profile does not change clearly at the transition. Here we show time evolutions of ion temperature profiles in the ETB operations. Fig.1 shows the ion temperature. The magnetic configuration is that with the magnetic axis position of $R_{ax}=92.1\text{cm}$ and a quadrupole magnetic field of $B_q=0\%$. Although this configuration is not the standard one ($B_q=-50\%$), it is often used to investigate the transition phase. Two neutral beams (30-40kV, 800kW×2) heated the plasma, and a strong gas puffing increases the line averaged electron density ($n_e \sim (2-4) \times 10^{13} \text{cm}^{-3}$). The L→H transition occurred at $t \approx 75\text{ms}$ in these example shots. It seems that the ion temperature was already increased to be $T_i(0) \approx 400\text{eV}$ in the starting phase of $t \sim 50\text{ms}$ before the transition and retained this value after $t > 70\text{ms}$. This time evolution is typical one in previous NBI heated plasmas without the L→H transition. Since the central electron temperature is also $T_e(0) \approx 400\text{eV}$ before and after the transition, the both of the central electron and ion temperatures retain the relation $T_e(0) \approx T_i(0)$ during the transition. However, the time resolution of ion temperature is not as good as the electron temperature measured by YAG Thomson scattering, since the charge exchange spectroscopy (CXS) system used here to measure the ion temperature utilizes the integration of 20ms. Therefore, we are investigating various plasma shots having different transition time to confirm this tendency in that ion temperature is increased only in the starting phase and retain the same value after the transition. Fig.2 shows results in the other shots in which the transition occurred at $t \approx 85\text{ms}$. The magnetic configuration and heating scheme are almost identical to those in Fig.1. It seems that the time evolution measured by the CXS is not sensitive to this shift of $\pm 5\text{ms}$, and therefore the temperatures can be considered to be almost steady at the transition. The impurity poloidal rotation approximately indicating the radial electric field also is almost steady in the core region of $r/a \leq 0.9$ [2].

Another feature of the ion temperature profile in the steady state is a relatively flat profile having a high edge temperature of $T_i \approx 100\text{eV}$ at the edge of measured region ($R \approx 1.06\text{cm}$). In contrast to this $T_i(r)$ profile, the $T_e(r)$ profile is a relatively peaking one with a low edge temperature of $T_e(r/a \approx 0.8) \approx 50\text{eV}$ [1]. This ion temperature suggests that a “pedestal” or a “barrier” structure exist near the edge and their structure may change at the transition. Since we have already found such a “barrier” structure of $\Delta T_i \approx 100\text{eV}$ and $\Delta R \approx 1\text{cm}$ in the N-ITB operations [3] with this measurement, the detail structure of the edge profile is a future theme. Since these CXS results in FY2004 were

obtained by a vertical viewing at a vertically elongated section, the diameter of the chord 7mm was the dominant factor limiting spatial resolution and corresponded to $\Delta r/a \approx 0.07$. To investigate the structure at the edge region of $0.9 \leq r/a \leq 1$ also by spectroscopic methods, a vertical viewing at a horizontally elongated section is planned in FY2005. A possibility for a toroidal non-uniformity of the edge plasma flows [2] in non-symmetric toroidal plasmas is another theme in FY2005 using this method.

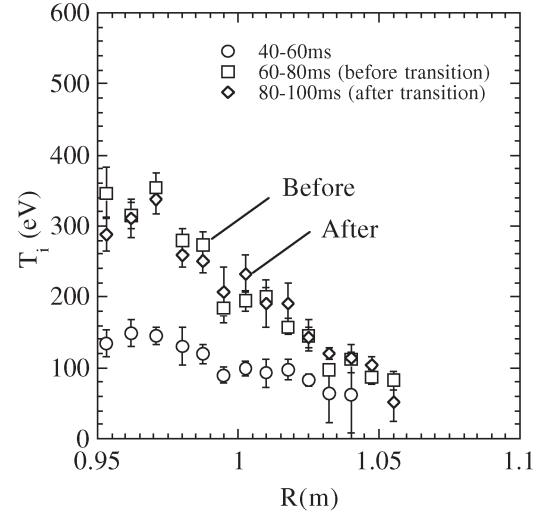


Fig.1 The ion temperature in ETB shots #114115-114121.

In these shots, the transition occurred at $t \approx 75\text{ms}$.

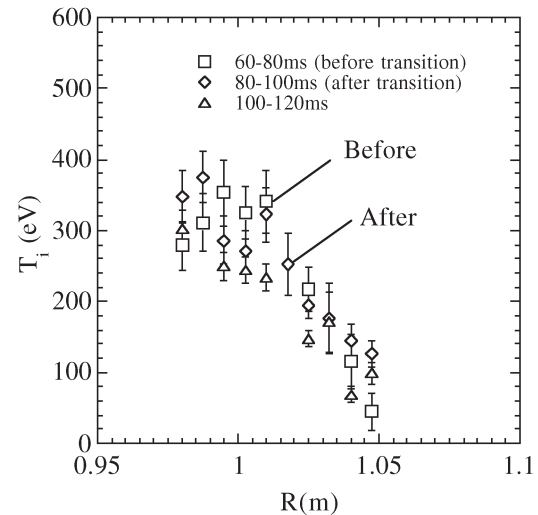


Fig.2 The results in ETB shots #117612-117614 in which the transition occurred at $t \approx 85\text{ms}$.

References

- [1] Okamura, S., et al., in 20th IAEA EX8-5Ra (2004)
- [2] Nishimura, S., et al., in this report
- [3] Minami, T., et al., Nucl. Fusion **44**, 342 (2004)

§5. Comparison of Impurity Poloidal Rotations in Recent Improved Modes in CHS

Nishimura, S., Okamura, S., Nagaoka, K., Yoshimura, Y., Minami, T., Akiyama, T., Ida, K., Isobe, M., Suzuki, C., Toi, K.

Rotations and electrostatic potentials in plasmas with the neoclassical internal transport barrier (N-ITB)[1] were previously investigated in Higashiyama-site experiments [2]. In these operations in a low density ($n_e \sim 10^{12} \text{ cm}^{-3}$) and high temperature ($T_e(0) \sim 2\text{-}3\text{keV}$) region achieved by applying the 53GHz 2nd harmonic electron cyclotron heating ($B=0.9\text{T}$), the strong positive radial electric fields of $E_r \sim 20\text{kV/m}$ were observed. This value is comparable to that of the negative radial electric fields in tokamak H-mode [3] and therefore their shear of $\sim 100\text{kV/m}^2$ was the most plausible candidate for mechanisms of the improved confinement. A quantitative theoretical calculation using a recently developed method was also done and the possibility of the strong positive radial electric fields is confirmed [4]. Fig.1 shows recent results of the charge exchange spectroscopy using fully ionized carbon ions (C^{6+}) in the N-ITB operations investigating the configuration dependence of this phenomenon. Since the poloidal rotation term is nearly equal to the radial electric field term in the impurity radial force balance equation in heliotron configurations [5], these poloidal rotation velocities of up to 20km/s in the direction of ion diamagnetic drifts indicate the radial electric field of $E_r \sim 20\text{kV/m}$. These strength and direction are universally observed in various magnetic configurations with the vacuum magnetic axis positions of $R_{ax}=92.1\sim 97.4\text{cm}$.

The edge transport barrier (ETB) [6] was found in a relatively high density ($n_e \sim (2\text{-}4) \times 10^{13} \text{ cm}^{-3}$) and low temperature ($T_e \sim 300\text{-}400\text{eV}$) regime with the high power neutral beam injection (NBI) ($30\text{-}40\text{kV}$, $800\text{kW} \times 2$). This operating condition corresponds to the plateau collisionality regime defined in the neoclassical theory, and therefore a weak negative radial electric field is expected as observed in previous NBI heating experiments. Fig.2 shows the measured results in an ETB operation in the configuration with the magnetic axis position of $R_{ax}=92.1\text{cm}$. The magnetic field strength is $B=0.9\text{T}$. The poloidal rotation in the electron diamagnetic direction with the velocity of $< 10\text{km/s}$ indicates weak negative radial fields of $|E_r| < 10\text{kV/m}$. These values and the profile are typical ones in previous NBI heated plasmas [5]. In spite of the L \rightarrow H transition that occurred at $t \approx 60\text{ms}$ in these example shots, the poloidal rotation remains to be $< 10\text{km/s}$ before and after the transition.

This dependence of the radial electric fields on the collisionality observed in these recent contrastive two operational conditions also support the theoretically predicted tendency that has been confirmed in various types of helical devices. The next remaining theme may be the transition of the radial field in an intermediate collisionality

regime. However, this conclusion by the measurement using fully ionized carbon relates to characteristics of the plasmas in the core regions of $r/a \leq 0.9$. At the edge region of $0.9 \leq r/a \leq 1$, the large density gradient in ETB may cause changes of E_r or some other parameters, therefore the Langmuir probe measurement is in progress [7].

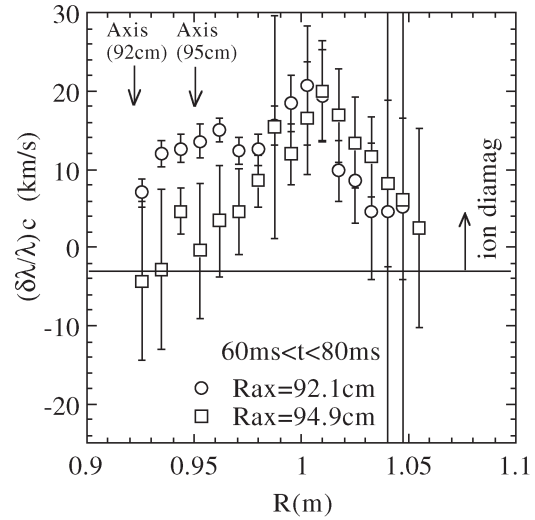


Fig.1 Doppler shift of CVI spectral line ($\lambda=529\text{nm}$) observed in the N-ITB plasmas by a vertical viewing at a vertical elongated section.

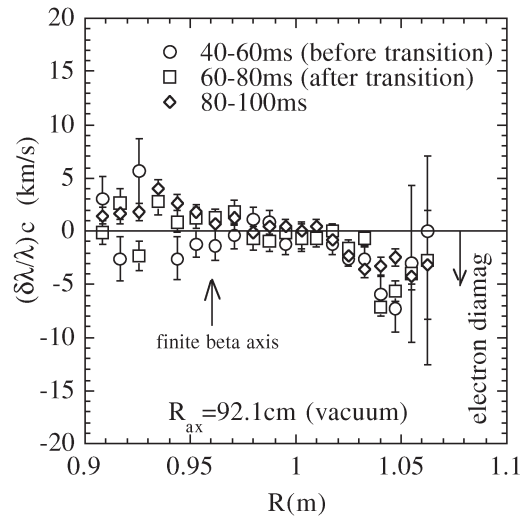


Fig.2 Poloidal rotation in an ETB plasma. The diagnostic method is identical to that in the cases of Fig.1

References

- [1] Minami, T., et al., Nucl. Fusion **44**, 342 (2004)
- [2] Fujisawa, A., et al., PRL **82**, 2669 (1999),
Ida, K., et al., Phys. Rev. Lett. **86**, 3040 (2001)
- [3] Ida, K., et al., Phys. Rev. Lett. **65**, 1364 (1990)
- [4] Nishimura, S., et al., FS&T **46**, 77 (2004).
- [5] Nishimura, S., et al., Phys. Plasmas **7**, 437 (2000),
Fujisawa, A., et al., Phys. Plasmas **7**, 4152 (2000)
- [6] Okamura, S., et al., in 20th IAEA EX8-5Ra (2004)
- [7] Takeuchi, M., Toi, K., et al., in this report

§6. Radiation Profile Measurements for Edge Transport Barrier Discharges in the Compact Helical System Using AXUV Photodiode Arrays

Suzuki, C., Okamura, S., Minami, T., Akiyama, T., Fujisawa, A., Ida, K., Isobe, M., Matsuoka, K., Nagaoka, K., Nishimura, S., Peterson, B.J., Shimizu, A., Takahashi, C., Toi, K., Yoshimura, Y.

The formation of the edge transport barrier (ETB) has recently been found in the Compact Helical System (CHS) plasmas heated by co-injected neutral beam injection (NBI) with strong gas puffing.¹⁾ The ETB mode is characterized by the rapid increase in the electron density near the edge following the abrupt drop of hydrogen Balmer alpha (H_α) line intensity. Recently the absolute extreme ultraviolet (AXUV) photodiode which has near theoretical quantum efficiency for a wide range of photon energies are used for bolometric measurements in fusion plasma experiments. In addition to single channel pyroelectric detector as a conventional bolometer, we have employed the AXUV photodiode arrays as a simple and low-cost diagnostic to investigate spatial and temporal variations of radiation emissivity in the CHS plasmas with ETB. A compact mounting module for a 20 channel AXUV photodiode array including an in-vacuum preamplifier has successfully been designed and fabricated.²⁾ Two identical modules were installed in the upper and lower viewports within the horizontally elongated cross section of the CHS plasma. Lines of sight of the detector arrays and magnetic flux surfaces ($R_{ax}=92.1$ cm, 0% quadrupole com-

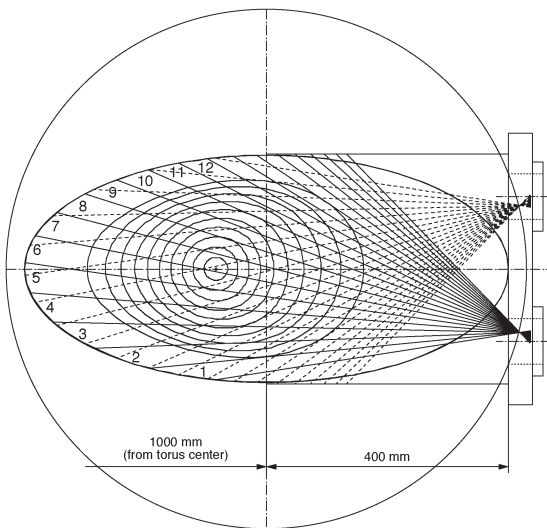


Fig. 1. Lines of sight of 20 ch AXUV photodiode arrays and magnetic flux surfaces ($R_{ax}=92.1$ cm, 0% quadrupole component). The 12 channels can be simultaneously measured at present.

ponent) are illustrated in Fig. 1. The 12 channels out of 40 are available for simultaneous measurements at present due to the limitation of the data acquisition system.

Figure 2 displays the result of the measurement in a typical ETB discharge for the configuration shown in Fig. 1. The transition to the ETB mode occurred at $t=76$ ms. The AXUV photodiode signals for channel numbers 2 (near the edge) and 6 (through the center) are shown in the lower figure together with the H_α signal. It has been confirmed that the signals of AXUV photodiode and pyroelectric detector in the ETB discharges show roughly the same behavior except for the very beginning and end of the discharges. The signals of all the channels of the AXUV photodiode arrays begin to increase more rapidly at the moment of the transition than before. The rate of the increase is larger for the edge viewing chord (ch2) than for the center viewing one (ch6), which indicates the flattening of the radiation profile following the change in the electron density and impurity profiles after the formation of the ETB. However, the signals for the edge chords tend to saturate after several tens of milliseconds, while they still continue to increase for the central chords until the back transition, which results in the peaking of the radiation profile near the plasma center. Although an accumulation of impurity ions near the plasma center is assumed, the details should be investigated based on the electron density and temperature profiles measured by Thomson scattering diagnostic.

References

- 1) Okamura, S. et al.: Plasma Phys. Control. Fusion **46** (2004) A113.
- 2) Suzuki, C., Peterson, B. J., Ida, K: Rev. Sci. Instrum. **75** (2004) 4142.

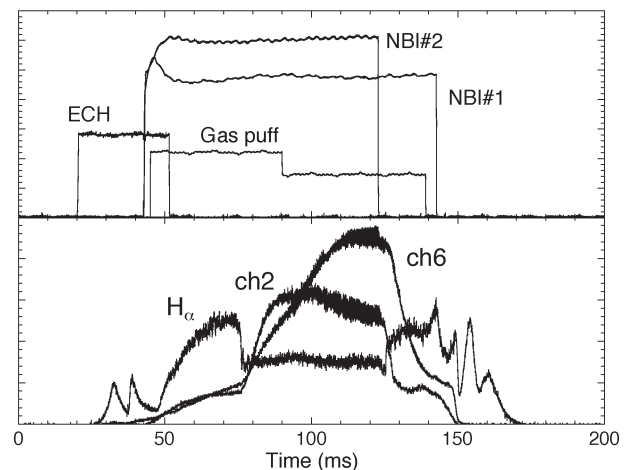


Fig. 2. The temporal variations of heating, gas puff, H_α signal and AXUV photodiode signals for channel numbers 2 (near the edge) and 6 (through the center) in a typical ETB discharge.

§7. EHO-like Density Fluctuations Measured Using Beam Emission Spectroscopy in ETB Discharge on CHS (NIFS02KZPD003)

Kado, S., Oishi, T. (Univ. of Tokyo)
Yoshinuma, M., Ida, K., Okamura, S.

The behaviors of the density fluctuations and the density gradients accompanied by the edge particle transport barrier (ETB) formation in compact helical system (CHS)^{1,2)} have been investigated by using the beam emission spectroscopy (BES).^{3,4)} The BES system in the present study detects Doppler-shifted H_α emissions from the collisionally excited neutral beam atoms injected for the additional heating. 16 sightlines are located so that the radial correlation along the minor radius of CHS is obtained.⁵⁾ BES can also provide the density gradient ∇n from the difference between the intensity of signals measured in adjacent sightlines.

A typical heating condition for the ETB discharge is shown in Fig. 1(a). Plasma was initiated by electron cyclotron heating (ECH) and further heated by two neutral beam injection (NBI) systems. In the case that the heating power exceeds a certain threshold, a transition phenomenon characterized by sudden drop in the temporal evolution of the H_α intensity signal as shown in Fig. 1(b) can be observed. Figure 1(c) and (d) show the BES signals for $\rho = 0.95$ and $\rho = 1.03$, respectively, which indicates that the density inside the last closed flux surface (LCFS) increases while that outside the LCFS decreases at the transition. We categorize the waveform into three phases as indicated in Fig. 1: (1) L-phase representing that before transition, (2) density building-up phase, in which the density continues to increase, and (3) the ETB-formation phase, which is after a saturation of density building up.

Figure 2 shows the fluctuation power spectra in the BES signals at $\rho = 0.95$ averaged over L-phase (52-62 msec), density building-up phase (64-74 msec), and the ETB-formation phase (110-120 msec). Coherent fluctuations having the fundamental frequency of around 4 kHz and the 2nd harmonic frequency of around 8 kHz appear at only this location in the ETB formation phase. The mode which is similar to the edge harmonic oscillations (EHO) in Tokamaks⁶⁾ is observed only in the case that the heating power is much higher than the threshold of the ETB transition. The threshold port-through heating power of the ETB transition in the standard magnetic configuration is about 1.0 MW for the density range of the discharge shown in Fig. 1, while the EHO-like mode was observed for that higher than 1.2 MW.

Figure 3 shows the amplitude of the fundamental mode as a function of ∇n . The EHO-like mode is enhanced when ∇n achieves a certain threshold. ∇n keeps almost constant after the enhancement of the mode.⁶⁾ For the discharges with EHO-like mode, ∇n in the ETB-formation phase did not vary significantly even if the heating power was increased. There is a possibility

that the onset of the EHO-like mode saturates the density gradient. It seems analogous to the fact that the EHO enhances the particle transport in Tokamaks.⁷⁾ This should be investigated more detailed in the future.

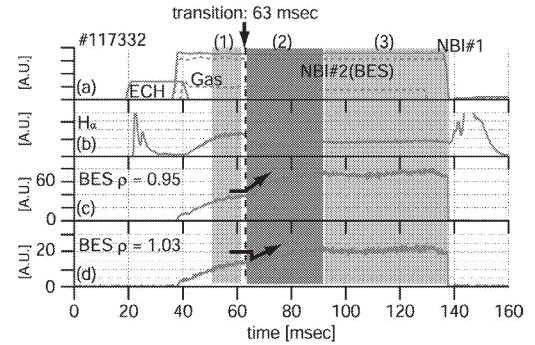


Fig. 1. Typical waveforms of the discharge with the ETB transition. (a) heating and fueling, (b) H_α intensity, (c) and (d) BES signals for $\rho = 0.95$ and $\rho = 1.03$, respectively.

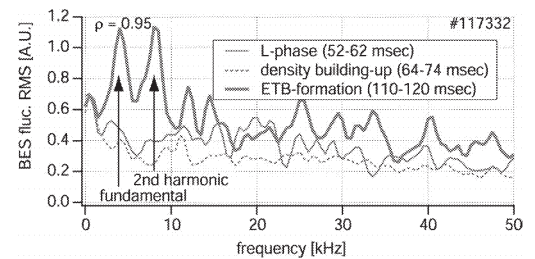


Fig. 2. The density fluctuation power spectra at $\rho = 0.95$ averaged over L-phase, density building-up phase, and the ETB-formation phase.

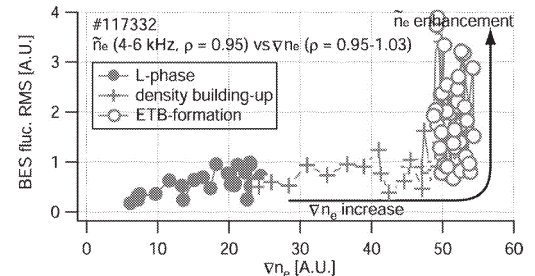


Fig. 3. The amplitude of the fundamental frequency of the EHO-like mode as a function of the density gradient measured using BES.

Reference

- 1) Okamura, S. et al., J. Plas. Fus. Res. **79**, (2003) 977
- 2) Okamura, S. et al., Plasma Phys. Control. Fusion **46**, (2004) A113
- 3) Oishi, T. et al., Rev. Sci. Instrum. **75**, (2004) 4118
- 4) Oishi, T. et al., J. Plasma Fusion Res. SERIES **6**, (2004) 449
- 5) Fonck, R. et al., Rev. Sci. Instrum. **61**, (1990) 3487
- 6) Oishi, T. et al., *proc. 32nd EPS conference on plasma physics* (Tarragona, Spain) (2005)P4.094.
- 7) Greenfield, C. M. et al., Phys. Rev. Lett. **86**, (2001) 4544

§8. Statistical Analysis of Peripheral Plasma with Edge Transport Barrier in CHS

Nagaoka, K.

Recently, zonal flow generation due to nonlinear coupling of microscopic drift waves is considered to be an essential mechanism of transport barrier formation in magnetically confinement devices [1], and the zonal flow has been observed in the plasma with the internal transport barrier (ITB) in CHS [2]. So, nonlinearity of fluctuation in plasmas is one of the key issues to understand the mechanism of transport barrier formations. In this report, statistical analysis of the probe measurement in NBI sustained plasmas with an edge transport barrier (ETB) in CHS is presented.

The formation of the ETB, which is indicated by spontaneous drop of $H\alpha$ intensity, has been also observed in plasmas sustained by NBI on CHS [3]. The increase of edge plasma density has been observed by Thomson scattering, Li-beam probe, beam emission spectroscopy and Langmuir probe measurements [3]. The fluctuations of edge plasma with and without ETB have been measured by a Langmuir probe, which is shown in Fig. 1. The ion saturation current significantly increases inside the last closed flux surface (LCFS), when the ETB formation with $H\alpha$ drop is occurred. The increase of ion current is attributable to the density increase of the edge plasma and the expansion of LCFS due to increase of the plasma beta. The probability density functions (PDF) with and without ETB are shown in Fig. 2. The PDF without ETB has asymmetric tail structure, while it with ETB agrees well a Gaussian profile. The asymmetric tail structure of the PDF implies the existence of burst-like fluctuations, which is strongly suppressed after the ETB formation.

The first, second, third, and fourth moments show average (μ), variance (σ), skewness (S), and kurtosis (K), respectively, which are shown in Table 1.

The average and variance increase after the ETB formation, which indicate the increase of the plasma density and the fluctuation level inside and outside of the LCFS. The skewness showing anti-symmetry is almost 0 and the kurtosis showing sharpness is almost 3 inside LCFS with ETB, which indicate Gaussian profile.

In concluding, the strong suppression of burst-like fluctuation (nonlinear phenomenon) has been observed inside of the LCFS after the ETB formation in CHS, which is confirmed by PDF and moment analysis of Langmuir probe measurement. However further examination is needed for understanding of the transport mechanism of ETB formation.

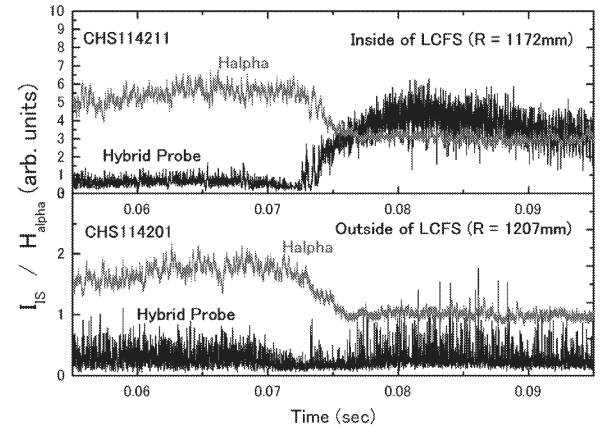


Fig.1 The time variation of ion saturation currents inside (upper) and outside (lower) of the LCFS, when the ETB formation is occurred, which is indicated by $H\alpha$ drops.

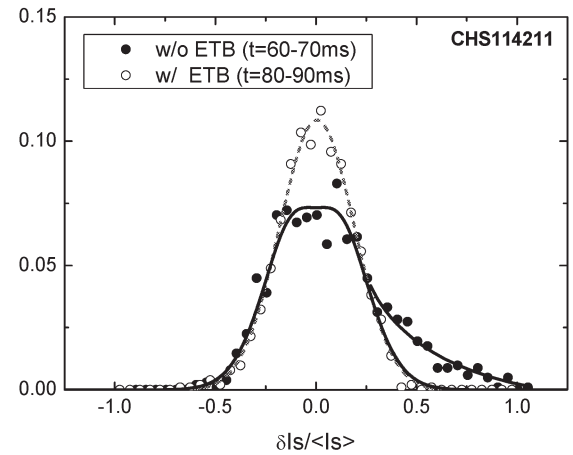


Fig.2 The probability density function of ion saturation current measured inside the LCFS of with (open circles) and without ETB (closed circles).

LCFS	ETB	μ	σ	S	K
inside	w/o	0.70	0.06	0.69	3.51
inside	w/	2.67	0.34	<u>0.01</u>	<u>3.02</u>
outside	w/o	0.51	0.06	0.78	3.40
outside	w/	1.23	0.21	0.90	3.62

Table 1. The moments from first to fourth inside and outside of LCFS with and without ETB.

References

- [1] P. H. Diamond *et al.*, Plasma Phys. Control Fusion **47** (2005) R35.
- [2] A. Fujisawa *et al.*, Phys. Rev. Lett. **93** (2004) 165002.
- [3] S. Okamura *et al.*, J. Plasma Fusion Res. **79** (2003) 977.

§9. Measurement of Edge Transport Barrier Structure by Langmuir Probe in the Compact Helical System

Takeuchi, M. (Dep. of Energy Eng. and Sci., Nagoya Univ.),
Toi, K., Nagaoka, K., Suzuki, C., Minami, T., Akiyama, T.,
Yoshimura, Y., Nishimura, S., Isobe, M., Shimizu, A.,
Takahashi, C., Matsuoka, K., Okamura, S., CHS Group

Edge Transport Barrier (ETB) formed by L-H transition was observed in CHS by control of the rotational transform ($t/2\pi$) with ohmic plasma current [1] and by about doubled NBI power [2]. Detailed measurements of plasma parameters and their fluctuations in ETB region are crucial for clarifying transition mechanisms. However, they are still insufficient for ETB plasmas in CHS. Recently, we have succeeded in the measurements of electron temperature (T_e), electron density (n_e), space potential (V_s) and their fluctuations simultaneously with high time (1 μ s) and high spatial resolutions (1 mm) by a triple-type Langmuir Probe (LP). The LP was moved radially shot by shot from $\rho \sim 0.92$ to $\rho \sim 1.1$ for reproducible ETB shots.

The experiments for ETB study were carried out in hydrogen plasmas, where absorbed NBI power by co-injection was about 800 kW at the toroidal field $B_t = 0.88$ T and a magnetic axis position of the vacuum field $R_{ax} = 0.92$ m. Figure 1 shows a typical discharge waveform of a plasma with ETB. The L-H transition occurs spontaneously at $t_{\text{tran}} \sim 64$ ms. At the transition, H_α emission suddenly drops, and line average electron density (\bar{n}_e) rapidly rises in the edge chord rather than the center chord. Plasma current (I_p) gradually increases up to $I_p \sim 6$ kA by co-injected NBI. We show typical time evolutions of T_e , n_e , floating potential (V_f) and V_s measured by LP for four shots in this experimental campaign in Fig.2. At the transition, n_e and T_e inside $\rho \sim 0.96$ clearly increase. V_f clearly decreases down to negative inside $\rho \sim 0.96$, as similar to that measured in the past experiment in CHS [1]. The present experiment has clarified that the change in V_s is less visible in contrast to that in V_f .

We compare radial profiles of n_e , T_e , V_f and V_s at just before (-4 ~ -3 ms) and after (+3 ~ +4 ms) the transition in Fig.3. Just after the transition, the radial profiles of n_e and T_e have a steep gradient inside $\rho \sim 0.96$, having a dip of n_e at $\rho \sim 0.96$ and a plateau of T_e in the region of $0.96 < \rho < 1.0$. This peculiar edge structure seen in n_e and T_e profiles may link to the presence of the magnetic island at $t/2\pi = 1$, of which position of the rational surface is calculated to be $\rho \sim 0.96$ in the phase with $I_p \sim 5$ kA. Note that n_e at $\rho \sim 0.98$ also increases appreciably as seen in Fig.3. It is concluded that ETB was formed inside $\rho \sim 1$, but the growth of ETB in n_e may be locally blocked by the presence of the magnetic island.

It is generally thought that radial electric field E_r and its shear E_r' play an important role in the formation of the ETB. V_f is sometimes employed to get information about E_r and E_r' [3]. V_f inside $\rho \sim 0.96$ changed obviously from small positive to negative, as seen in Fig.2. On the other hand, V_f slightly increased outside $\rho \sim 0.96$. Similar result

was observed in the past experiment in CHS [1] where only V_f was measured by a single LP. Note that V_s is evaluated as $V_s = V_f + \alpha T_e$ having $\alpha \sim 3$ for hydrogen plasma and should be used to derive E_r . In contrast to the time evolution of V_f , V_s does not exhibit a significant change across the transition, as seen in Figs. 2 and 3. This is caused by the simultaneous rise in T_e and drop in V_f across the transition inside $\rho \sim 0.96$.

Reference

- [1] K. Toi *et al.*, Plasma Phys. and Control. Fusion 38, 1289 (1996).
- [2] S. Okamura *et al.*, Plasma Phys. and Control. Fusion 46, A113 (2004)
- [3] F. Wagner *et al.*, 15th IAEA Conf. on Plasma Phys. and Control. Fusion Res. 1, 559 (1994), Seville

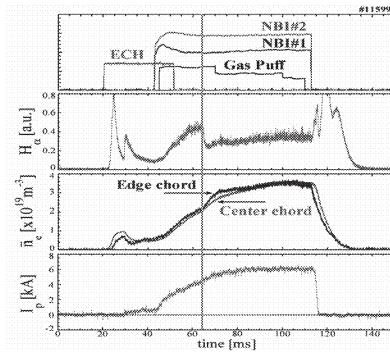


Fig.1 Typical waveform of an NBI heated plasma with L-H transition.

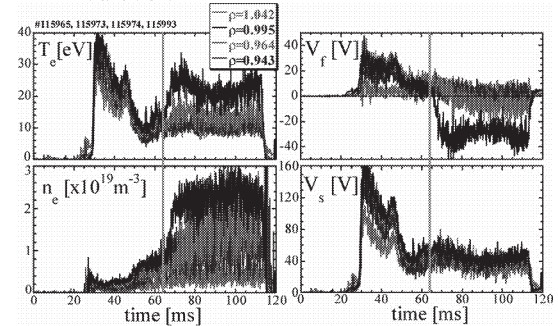


Fig.2 Time evolutions of T_e , n_e , V_f and V_s measured by LP for four reproducible plasmas with ETB.

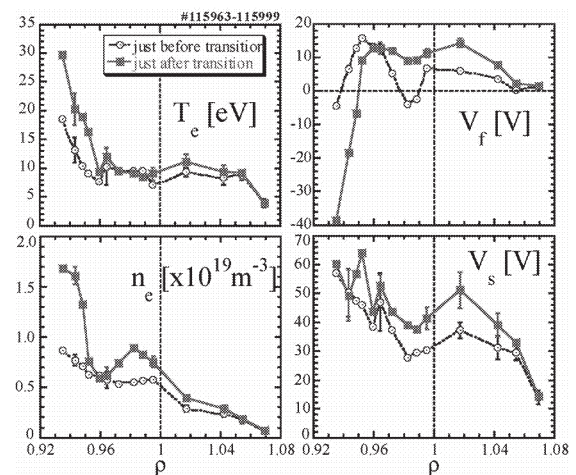


Fig.3 Comparison of T_e , n_e , V_f and V_s profiles just before and after the L-H transition.

\$10. Discharge Aiming at High Stored Energy in Compact Helical System (CHS)

Isobe, M., Yoshimura, Y., Nagaoka, K., Suzuki, C., Akiyama, T., Minami, T., Shimizu, A., Nishimura, S., Matsuoka, K., Okamura, S., CHS Group (NIFS)

The large increment of plasma stored energy has been observed in the neutral beam(NB)-heated high density plasmas of Compact Helical System (CHS) after the intense gas puffing is terminated[1,2]. This is called 'reheat mode'. Similar phenomena are also seen in Wendelstein7-AS for both NB-heated and electron cyclotron resonance-heated (ECRH) plasmas[3] and LHD. Currently, the reheat mode experiment is being conducted under the maximum NB heating power and the highest magnetic field strength to bring out the maximum performance of CHS while exploring improved confinement regime in high density helical plasma.

Figure 1 shows temporal behavior of a reheat mode discharge, giving the record value of the stored energy W_p in CHS. This discharge was obtained in an inward shifted configuration having the magnetic axis position R_{ax} of 0.949 m and toroidal magnetic field strength B_t of 1.9 T. The plasma volume was 0.75 m^3 in this case. Two NB injectors are equipped in CHS. Both beams were tangentially cojected to heat target plasmas as efficient as possible. The total port-through heating power $P_{nb-port}$ of two NBs was 1.6 MW. It is seen that the evolution of W_p tends to saturate as the line-averaged electron density n_e increases in the gas puffing phase and begins to drop when n_e exceeds $8.0 \times 10^{19} \text{ m}^{-3}$. This suggests degradation of confinement with increase of n_e . The total radiation loss power P_{rad} measured with a pyroelectric detector increases as n_e increases. After the gas puffing is turned off at $t=105 \text{ ms}$, P_{rad} is significantly suppressed and W_p begins to increase, going up to 8.0 kJ which is the current highest value of W_p in CHS. The volume-averaged β value was 0.60 % at the timing of W_p peak. Titanium gettering was indispensable to reach this parameter range. One of the remarkable differences between the gas puffing and the reheat phases is in the n_e profile. The n_e profiles at 90 ms and 130 ms are shown in Figure 2(a) and 2(b), respectively. The line-averaged n_e is very similar between the two cases as seen in Figure 1(d). The Thomson scattering diagnostic indicates excessively hollowed n_e profile in the gas puffing phase due to intense gas fueling from the outside while n_e is relatively flat in the reheat phase. Also the reheat mode is characterized by enhanced electron temperature T_e at the peripheral region. Figure 2(c) and 2(d) show the T_e profile at 90 ms and the ratio of T_e at 130 ms to T_e at 90 ms, respectively. It is clearly seen that in the reheat phase, T_e in the outer region ($R < 0.85 \text{ m}$ and $R > 1.1 \text{ m}$, corresponding to $r/a > 0.55$) increases compared with that in the gas puffing phase. The fan-arrayed compact absolute extreme ultraviolet (AXUVD) photodiodes suggest that impurities have an

inward velocity and are continuously accumulated in the core domain during the reheat phase. Currently, the reheat mode spontaneously terminates. The impurity accumulation is supposed to be a candidate to explain the spontaneous termination of the mode.

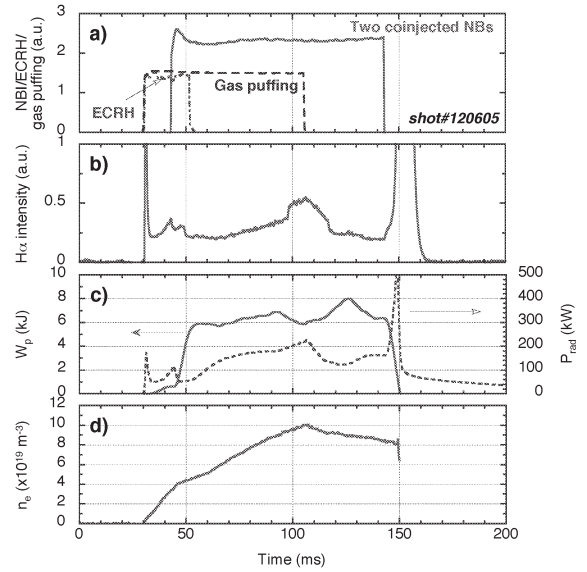


Fig. 1. Time evolution of the reheat discharge heated by cojected two NBs with P_{nb} of 1.6 MW. R_{ax} and B_t were 0.949 m and 1.9 T, respectively.

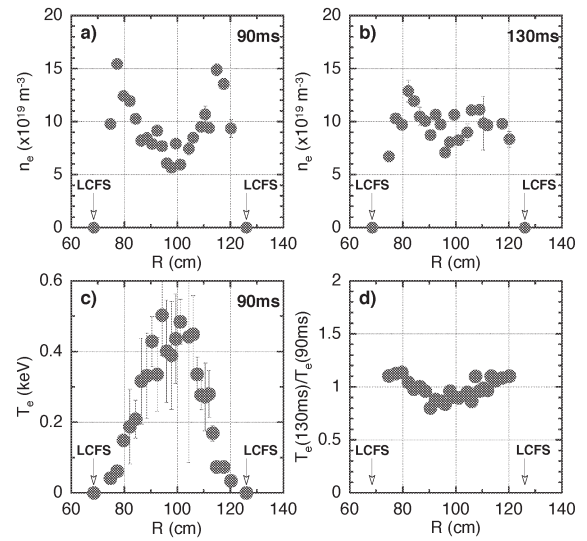


Fig. 2. (a) n_e profile at $t=90 \text{ ms}$ in Figure 1, (b) n_e profile at $t=130 \text{ ms}$. (c) T_e profile at $t=90 \text{ ms}$. (d) Ratio of T_e at $t=130 \text{ ms}$ to T_e at $t=90 \text{ ms}$.

References

- 1) Morita, S. *et al.*, in Plasma Physics and Controlled Nuclear Fusion Research 1992 (Proc. 14th Int. Conf. Würzburg, 1992), Vol.2, IAEA, Vienna (1993) 515.
- 2) Okamura, S. *et al.*, Nuclear Fusion **35**, 283(1995).
- 3) Morita, S. and Baldzuhn, J., Max-Planck-Institut für Plasma Physik, IPP III/199 (1994).

§11. Efficient Heating of High Density Plasmas Up to Cut-off Density of 106.4 GHz ECH Power on CHS

Yoshimura, Y., Akiyama, T., Isobe, M., Shimizu, A., Suzuki, C., Takahashi, C., Nagaoka, K., Nishimura, S., Minami, T., Matsuoka, K., Okamura, S., CHS Group Kubo, S., Shimosuma, T., Igami, H., Notake, T., Ohkubo, K.

Extending the CHS plasma parameter to high density and high temperature regime is the most important objective of application of 106.4 GHz power. In this report probability of electron heating at higher density up to the limit of cut-off is described. For the waves with frequency of 53.2 GHz, theoretical cut-off density for $B=0.95$ T by 2nd harmonic X-mode and for $B=1.9$ T by fundamental O-mode are 1.8 and $3.5 \times 10^{19} / \text{m}^3$, respectively. Applying the frequency of 106.4 GHz, the cut-off density for $B=1.9$ T by 2nd harmonic X-mode increases up to $7 \times 10^{19} / \text{m}^3$.

Plasma heating at higher density than cut-off density of 53.2 GHz is experimentally demonstrated. In the experiment, 106.4 GHz power in X-mode aiming at the magnetic axis is injected to $B_{ax}=1.9$ T magnetic field to generate plasma and the initial plasma is heated and sustained by NB power of about 700 kW. To the high density NB-sustained plasmas, second ECH pulses are injected from 60 ms to 91 ms. 53.2 GHz power of 120 kW in O-mode is also applied with the same time sequence.

The density of target plasma is scanned by adjusting gas puffing during the discharges. Representative time traces of line averaged electron density measured with HCN laser interferometer are plotted in Fig. 1. Injection timings of ECH pulses are denoted by hatched regions. When the density is kept low, effect of density clumping by ECH is clear while with higher density the density keeps increasing. The discharge #120554 is terminated immediately at the end of 2nd ECH pulses though the NB power is applied until 93 ms.

Figure 2 shows the increment of stored energy by 2nd ECH pulses, and the increment divided by the density and stored energy at the starting time of the 2nd pulses as functions of the density at that time. With the averaged density higher than $5.6 \times 10^{19} / \text{m}^3$, the effect of the 2nd ECH pulses degrades and it vanishes at over $6.8 \times 10^{19} / \text{m}^3$.

The evolution of stored energy is plotted as a function of averaged density in the discharge #120540 in Fig. 3. The data during the 2nd ECH pulses are stated in the figure. The gradient of the plot is slightly increased at first by the application of ECH pulses, that is, electron temperature is increased. However when the density reaches at $6.8 \times 10^{19} / \text{m}^3$, the stored energy starts decreasing though the ECH and NB powers are still applied.

Those experimental results clearly demonstrate that the 106.4 GHz power applied to CHS works very well for high density plasma heating up to its theoretical limitation by 2nd harmonic X-mode cut-off.

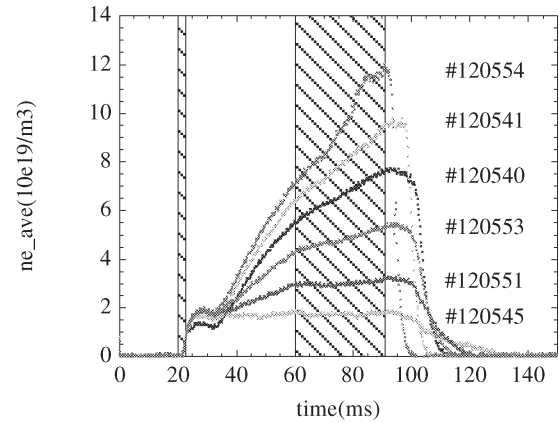


Fig. 1. Time traces of line averaged electron density measured with HCN laser interferometer.

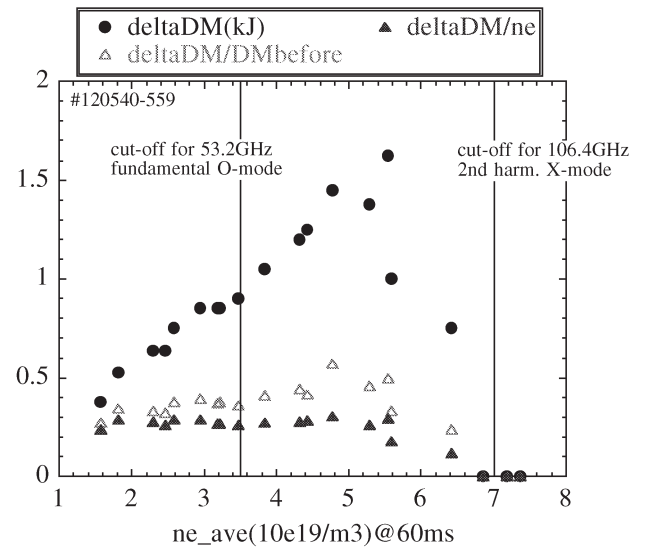


Fig. 2. Increment of stored energy by 2nd ECH pulses and that divided by density and stored energy.

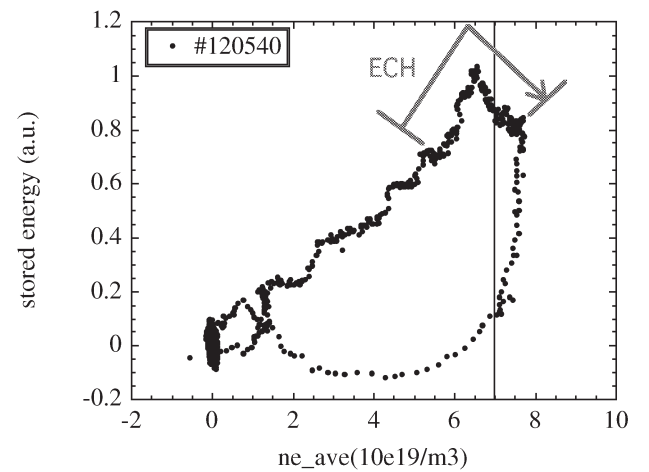


Fig. 3. The evolution of stored energy plotted as a function of averaged density in the discharge #120540.

§12. Confinement of Perpendicularly Injected Energetic Ions on Different Magnetic Configurations in CHS

Matsushita, H., Ida, K., Okamura, S., Isobe, M., Akiyama, R., CHS Group

Confinement of helically trapped ions is one of the key issues in the slowing down process of energetic ions injected by neutral beam on helical devices. In CHS, confinement of collisionless trapped ion confinement depends on the magnetic field configuration. In the configuration with the strong inward shift, the distortion of $|B_{min}|$ contours from the magnetic flux surfaces is minimized. In this configuration, the drift motion of the helically trapped particles does not deviate significantly from the magnetic flux surfaces and good confinement of fast ions are expected. In contrast, in outward shifted magnetic field configuration, the distortion of $|B_{min}|$ contours from the magnetic flux surfaces is large and helically trapped ions crossing the magnetic flux surfaces will be lost.

In order to investigate magnetic axis dependence of trapped particle confinement in CHS, diagnostic neutral beam (DNB) was perpendicularly injected into electron cyclotron resonance heating (ECRH) sustained plasma with magnetic axis position, R_{ax} of 88.8 cm (inward shifted configuration) and 99.5 cm (outward shifted configuration). Line averaged n_e and central electron temperature is $1 \times 10^{19} \text{ m}^{-3}$, 0.43 keV for R_{ax} 88.8 cm and $0.46 \times 10^{19} \text{ m}^{-3}$, 1.1 keV for R_{ax} 99.5 cm in this experiment. The beam energy (E_b) of DNB is set to be 27 keV and there are three components of beam energy: full energy (27 keV), half energy (13.5 keV) and one-third energy (9 keV). Injected energetic ions are observed with the horizontally scannable neutral particle analyzer (NPA).

Figure 1 shows the energy spectrum when the DNB is injected at tangential radius (R_T^{DNB}) of 31 cm in co-direction in the magnetic configuration of R_{ax} 88.8 cm (a) and R_{ax} 99.5 cm (b). The NPA was scanned horizontally shot by shot from tangential radius (R_T^{NPA}) of 18 cm to 74 cm and the neutral flux is integrated over 40 msec during the discharge. Each energy component of the DNB, E_b (27 keV), $E_b/2$ (13.5 keV), $E_b/3$ (9 keV) was clearly observed. E_b component shows slowing down process while $E_b/2$ and $E_b/3$ components show pitch-angle scattering. When the energy of injected ions is high enough not to be affected by pitch-angle scattering, the slope of the energy spectrum is determined from the ratio of energetic ion slowing down time (τ_{se}) to the confinement time (τ_{conf}) as:

$$f(E) \cong \left(\frac{S_0 \tau_{se}}{2E_b} \right) \left(\frac{E_b}{E} \right)^{-(\tau_{se}/2\tau_{conf}+1)} \quad (1)$$

where S_0 is the energetic ion source term. Applying the eq.(1) as a fitting curve, τ_{conf} is derived from energy spectrum (Fig.2). In this experiment, estimated τ_{conf} is 6.2 msec for R_{ax} 88.8 cm and 5 msec for R_{ax} 99.5 cm respectively. This result indicates that inward shifted

configuration has better confinement of perpendicularly injected energetic ions compared with that of outward shifted configuration.

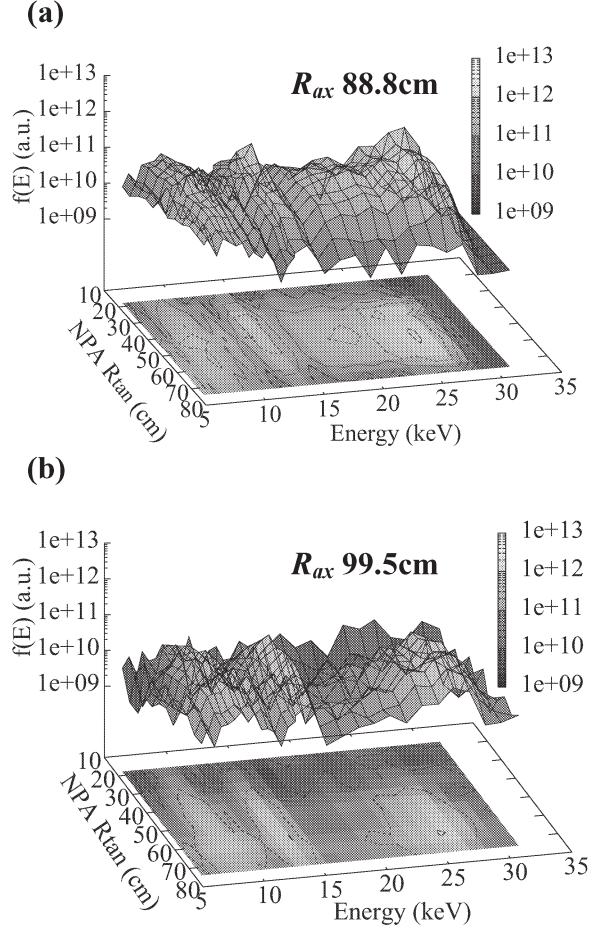


Fig.1 Energy spectrum of energetic ions measured at each tangency radius of NPA for DNB injection with R_T^{DNB} of 31 cm in (a) Inward sifted configuration (R_{ax} 88.8cm) and (b) Outward shifted configuration (R_{ax} 99.5cm)

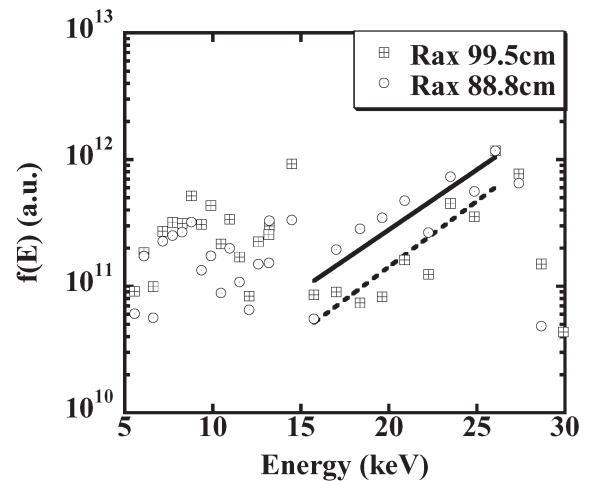


Fig.2 Energy spectrum of energetic ions measured at R_T^{NPA} 49cm (64cm) for the plasma with R_{ax} 88.8cm (99.5cm), and solid (dashed) line shows eq.(1) fitted to experimental result.

§13. Wavelet Analysis on Density and Potential Fluctuation on Internal Transport Barrier

Fujisawa, A., Shimizu, A., Nakano, H., Ohshima, S., Okamura, S., Matsuoka, K., Itoh, K., CHS Group

An internal transport barrier, now common in toroidal helical plasmas, was found in CHS. In a recent experiment in CHS, the dual HIBPs succeeded to catch an exact moment of a transition. The report describes the observation of turbulence properties on the barrier position, before and after the transition using a wavelet analysis.

The target plasma for the experiments was sustained with electron cyclotron resonance heating of ~ 200 kW. The magnetic field strength of the discharges was $B=0.88$ T, and the density was constantly maintained at $n_e \sim 5 \times 10^{12} \text{ cm}^{-3}$. The dual HIBP measurements were performed in the core region of the plasma.

Figure 1 shows the discharge to exhibit transition from the state with a barrier to the state without a transport barrier. The solid lines represent the potential waveforms of the center channels of two HIBPs. The observation point of an HIBP is located ~ 1.5 cm inside the barrier, and the potential signal clearly shows transition at $t=71.3$ ms. The transition occurs in a time scale of less than a hundred micro seconds due to neoclassical characteristics. On the other hand, the observation point of the other, showing no significant change in potential, is located on the exact barrier foot-point ($r=6.4$ cm, $\rho=0.34$).

An analysis using the Morlet's (or Milligen's) wavelet is performed on the signals of the barrier in order to estimate turbulence-driven particle flux. The wavelet is a natural extension of the traditional Fourier transformation. Figure 2 shows the image plots for time evolution of power spectra of density and potential fluctuations. The plots clearly show both fluctuations increase after the barrier is broken down. Particularly increases in the frequency range from ~ 50 to ~ 100 kHz is obvious.

Furthermore, the analysis can provide cross-correlation between density and potential fluctuations in a time-dependent way. In addition the information of

wavenumber is available from the phase difference of adjacent spatial channels of HIBPs. The full knowledge of these quantities, e.g., density and potential fluctuations, their coherence, phase difference, and wavenumbers, allows us to estimate the particle flux crossing the barrier position. The relation between estimated particle flux and zonal flow [1] is now being investigated to find a significant effect of zonal flow on transport [2].

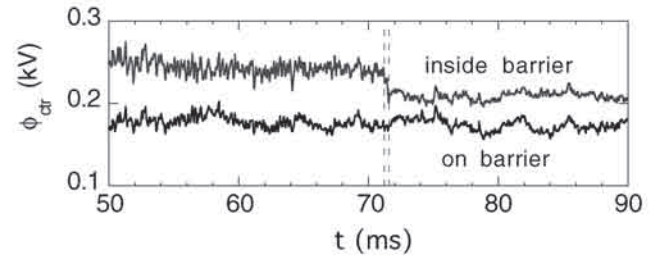


Figure1. Time evolution of potential waveforms. The signal inside the barrier indicates the exact moment of transition.

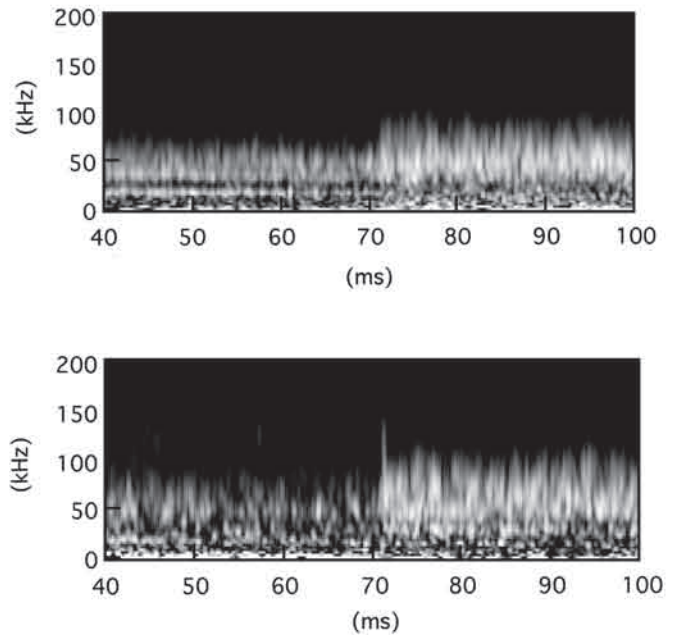


Figure 2. Evolutions of power spectra of density (above) and potential (below) fluctuations using a wavelet analysis. The analysis shows that both fluctuations increase after the barrier is decayed (at $t=71.3$ ms).

References

- 1) A. Fujisawa et al., Phys. Rev. Lett. **93** 165002 (2004).
- 2) Submitted to Phys. Rev. Lett.

§14. Magnetic Field Fluctuation Measurement with Heavy Ion Beam Probe in CHS

Shimizu, A., Fujisawa, A., Nakano, H. (Univ. Adv. Study), Ohshima, S. (Nagoya Univ.), Iguchi, H., Okamura, S., Matsuoka, K., CHS Group

Magnetic field fluctuation is important to study MHD instability, anomalous transport, etc. In many experimental devices, Mirnov coils are used to measure magnetic fluctuation and to study MHD instability mode. Mirnov coils are economical and simple tools to measure magnetic fluctuation, however, they cannot allow us to know the profile of fluctuation amplitude in core plasma. Heavy Ion Beam Probe (HIBP), which is ordinarily used to measure plasma potential, can give us the information of magnetic field fluctuation in the core. In CHS experimental device, we have tried to obtain the magnetic field fluctuation with HIBP. The report describes the preliminary results.

With the detector in the energy analyzer of HIBP system, we can obtain the deflection of beam in the toroidal direction. This deflection reflects the change in magnetic field in the plasma. In the axisymmetric approximation, the deflection of beam observed with HIBP is as follows,

$$\phi_D = \frac{qR_s \tilde{A}_{\phi s}}{mv} \int_{\ell_s}^{\ell_d} \frac{1}{R} d\ell - \frac{q}{mv} \int_0^{\ell_s} \frac{\tilde{A}_{\phi}}{R} d\ell - \frac{2q}{mv} \int_{\ell_s}^{\ell_d} \frac{\tilde{A}_{\phi}}{R} d\ell. \quad (1)$$

Here, ϕ_D is the deflection of beam in toroidal angle, ℓ is the beam path, A_{ϕ} is the toroidal component of vector potential, R is the major radius, q is charge, v is the beam velocity, m is mass of beam. Subscript s and d mean the positions of sample volume and detector, respectively, and tilde means the fluctuated component. The first term on the right-hand side is local fluctuation in plasma. The second and third terms are the path integrals of fluctuation on primary and secondary beam paths, respectively. An analysis shows that the local fluctuation of vector potential could be the dominant cause for the fluctuation of beam deflection [1].

In CHS experiment, a sort of MHD instability mode, "burst mode" is observed in low-density NBI plasmas. This is characterized by fishbone like signals in magnetic probes. An example of magnetic probe signal in burst mode is shown in Fig.1 (the upper signal). In this case, the axis of major radius was 92.1 cm, the strength of magnetic field was 0.88 T, and line averaged density was typically $1.5 \times 10^{13} \text{ cm}^{-3}$. The lower signal in Fig. 1 shows the time trace of normalized beam deflection (or magnetic field fluctuation) in the toroidal direction. The position of sample volume of HIBP was at $\rho = 0.5$. This signal is strongly correlated with the magnetic probe ones. The power spectra of HIBP signal and of magnetic probe signal (integrated by time) are shown in Fig.2 (upper). The power spectra of both signals have sharp peaks at 5 kHz. The magnetic probe signal has a broadband peak between 10 and 40 kHz. The coherence between these signals is shown in

Fig. 2(lower). The coherence is very large (~ 1) at 5 kHz. In the frequency regime from 20 to 40 kHz, high coherence (~ 0.8) is also seen, though the HIBP signal shows no clear peak in the power spectrum.

The radial profile of fluctuation obtained from HIBP signal is shown in Fig.3. The solid and dotted lines are the integrated powers in the range of from 2 to 8 kHz and that from 20 to 40 kHz, respectively. A clear peak is seen close to $\rho = 0.5$, demonstrating that fluctuation should be localized on the rational surface where the rotational transform is 0.5.

This is the first measurement of magnetic field fluctuation in core plasma of helical device. The investigation of mode structure for several MHD instabilities is a future subject.

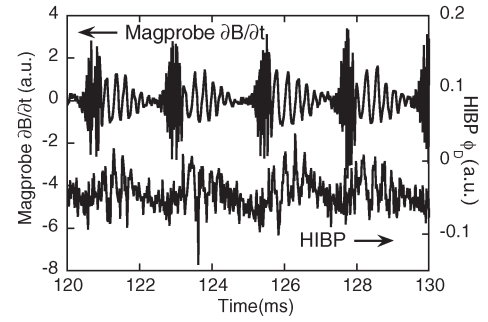


Fig.1 Time trace of magnetic probe signal (upper) and toroidal beam deflection of HIBP (lower)

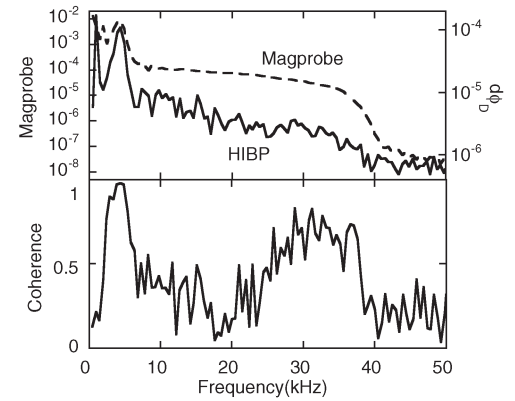


Fig.2 Upper: power spectra of magnetic probe signal integrated by time and HIBP signal. Lower: Coherence between magnetic probe and HIBP signals.

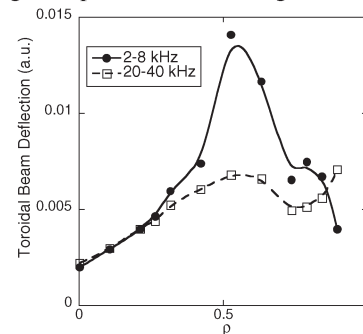


Fig.3 Radial profile of toroidal beam deflection obtained from HIBP.

[1] A. Shimizu, A. Fujisawa, S. Ohshima, H. Nakano *et al.*, Review of Scientific Instruments, **76** (2005) 043504-1

§15. Consideration of a Necessary Condition for Local Density Fluctuation Measurements with Heavy Ion Beam Probe

Nakano, H., Fujisawa, A., Shimizu, A., Ohshima, S., Minami, T., Yoshimura, Y., Okamura, S., Matsuoka, K.

Local fluctuation measurements are important to investigate plasma turbulence and transport. Heavy ion beam probe (HIBP) is able to measure *density fluctuation* inside a magnetically confined plasma of high temperature. The detected beam fluctuates according to the local density fluctuation at the ionization point. However, the beam fluctuation is also contaminated with the fluctuations along the beam orbit. This report describes a consideration of the path-integrated fluctuation and a necessary condition for the local density fluctuation measurement.

The relation between the local density and path-integrated fluctuations is written as

$$\begin{aligned} \tilde{\eta}^2(\rho_*) &= \tilde{\xi}^2(\rho_*) \\ &- 2 \int \langle \tilde{\xi}(\rho_*) \tilde{\xi}(\rho_1) \rangle S_1(\rho_1) d\bar{l}_1 \\ &- 2 \int \langle \tilde{\xi}(\rho_*) \tilde{\xi}(\rho_2) \rangle S_2(\rho_2) d\bar{l}_2 \\ &+ \iint \langle \tilde{\xi}(\rho_1) \tilde{\xi}(\rho_1') \rangle S_1(\rho_1) S_1(\rho_1') d\bar{l}_1 d\bar{l}_1' \\ &+ \iint \langle \tilde{\xi}(\rho_2) \tilde{\xi}(\rho_2') \rangle S_2(\rho_2) S_2(\rho_2') d\bar{l}_2 d\bar{l}_2' \\ &+ 2 \iint \langle \tilde{\xi}(\rho_1) \tilde{\xi}(\rho_2') \rangle S_1(\rho_1) S_2(\rho_2') d\bar{l}_1 d\bar{l}_2' \end{aligned} \quad (1)$$

where $\tilde{\eta}(\rho_i)$, $\tilde{\xi}(\rho_i)$, $S_i(\rho_i)$ indicate detected beam fluctuation, local density fluctuation, ionization cross-section of primary and secondary ion, respectively. And subscript *, 1 and 2 indicate ionization point, primary and secondary, respectively. The first term and the other terms on the right-hand side represent the local density fluctuation and the path-integrated fluctuations, respectively.

The above expression can be simplified if the correlation length of the fluctuation is sufficiently short, and if the correlation is assumed to be written in the following form

$$\langle \tilde{\xi}_1(\rho_1) \tilde{\xi}_2(\rho_2) \rangle = \tilde{\xi}_1^2(\rho_1) \bar{l}_c(\rho_1) \delta(\rho_1 - \rho_2) \delta(\bar{l}_1, \bar{l}_2)$$

where the $\delta(\bar{l}_1, \bar{l}_2)$ and \bar{l}_c are the Dirac's delta function, and correlation length, respectively. Then, Eq.(1) can be reduced into

$$\begin{aligned} \tilde{\eta}^2(\rho_*) &= (1 - 2S_c(\rho_*)) \tilde{\xi}^2(\rho_*) \\ &+ \int \bar{l}_c(\rho_1) \tilde{\xi}^2(\rho_1) S_1^2(\rho_1) d\bar{l}_1, \\ &+ \int \bar{l}_c(\rho_2) \tilde{\xi}^2(\rho_2) S_2^2(\rho_2) d\bar{l}_2 \end{aligned} \quad (2)$$

where $S_c(\rho_*) \equiv \bar{l}_c(S_1(\rho_*) + S_2(\rho_*))$. From this simplified expression, it is known that the second and third term of Eq. (1) should represent an effect to

screen the local fluctuation by a factor of $1 - 2S_c$ (a screening effect), while the 4-th to 6-th terms are exactly the *path-integral effect* that increases the measured fluctuation. The simplified expression indicates that the local fluctuation can be rather easily deduced by solving the integral equation numerically if the correlation length of the fluctuation is sufficiently short.

In addition, the further approximation of Eq. (2) gives an idea of a necessary condition for local density fluctuation measurement. The approximated form is expressed as

$$\tilde{\xi}^2(\rho_*) = \frac{\tilde{\eta}^2(\rho_*)}{1 - 2S_c(\rho_*) + A_{\pi}}, \quad (3)$$

where $A_{\pi} \equiv \bar{l}_c(\langle S_1^2 \rangle L_1 + \langle S_2^2 \rangle L_2)$, with $\langle L_i \rangle$ and $\langle S_i^2 \rangle$ being the lengths and the averaged ionization

rate on the orbit. Equation (3) shows that a degree of path-integral effect can be evaluated from the ratio of $A_{\pi}/(1 - 2S_c)$.

Figure 1 shows the ratios for the cases of Cesium and Rubidium beams as a function of electron density for CHS geometrical parameters. Here, both L_1 and L_2 are 0.2 m from the HIBP trajectory calculation. These figures show that Rubidium beam is more suitable to detect local density fluctuation in wider plasma parameter regime of CHS, compared to Cesium beam.

However, Rubidium beam is less sensitive to potential fluctuation than Cesium. The Cesium beam should have an advantage in simultaneous measurements of density and potential fluctuation to deduce turbulence-driven transport. Consequently, it is still necessary to establish a method to extract local density fluctuation for this purpose.

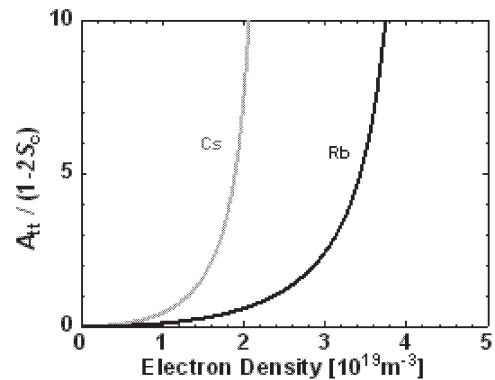


Fig. 1. Ratios of path-integral to screening effect for Cesium and Rubidium beam. Electron temperature, plasma radius and beam energy are 1keV, 0.2m and 70keV, respectively. Rubidium beam can measure higher density plasma.

§16. A Method to Infer Internal Mode Structure with HIBP and Magnetic Probes

Ohshima, S. (Dep. Energy Eng. Sci., Nagoya Univ.),
Fujisawa, A., Shimizu, A., Nakano, H., CHS Group

Heavy ion beam probe (HIBP) can measure potential fluctuations directly with no disturbance to high temperature plasma, and has possibility to estimate mode structure from the profile of potential fluctuation amplitude if the corresponding fluctuation is identical from the background turbulence. This report describes a method to infer the internal mode structure using the HIBP by a help of magnetic probes in the case that detectable potential fluctuation is weak and buried in the background.

The measurement was carried out on ECR-heated plasmas in CHS with the following operational conditions; toroidal magnetic field $B_t=0.88\text{T}$, magnetic axis $R_{\text{Axis}}=0.92\text{m}$, and the line-averaged density $n_e \sim 4 \times 10^{18} \text{m}^{-3}$. In the plasmas, the fluctuation power spectrum of magnetic probes, as is shown in Fig. 1(a), indicates a peak exists around 130kHz. On the other hand, potential signals of HIBP has no appreciable peak in the power spectrum of Fig. 1(b), therefore, estimation of the mode structure from the potential fluctuation amplitude is difficult. Then, coherence is examined between magnetic field and potential fluctuations, as shown in Fig. 2. Obviously, a significant peak exists around 130kHz, corresponding to the spectrum of the magnetic field fluctuation. This result suggests that the mode localization should be estimated from the coherence. Radial profile of the coherence is shown in Fig. 3. The plotted coherence values are the peak values obtained by Gaussian fitting to coherence curves around 130kHz. The mode should be localized around $\rho=0.5$ where the profile has a high value, since higher coherence implies that the mode amplitude should be higher as is discussed below.

The definition of the coherence is described as $\text{coh} = |E[X^*(f) \cdot Y(f)]| / (E[|X(f)|^2] \cdot E[|Y(f)|^2])^{1/2}$, X and Y are the complex Fourier coefficients of potential and magnetic signals, respectively, and E denotes ensemble average. The signals are assumed to be composed of two parts, as $X(f) = X_{\text{mode}}(f) + X_{\text{noise}}(f)$ and $Y(f) = Y_{\text{mode}}(f) + Y_{\text{noise}}(f)$. The subscripts, *mode* and *noise*, mean the electromagnetic fluctuation part of the mode and noise part, respectively, (which containing electrostatic fluctuation part). Assuming $Y_{\text{mode}}(f) \gg Y_{\text{noise}}(f)$ and using ensemble average, we deforms above definition and obtains a next simple description, $\text{coh} = 1 / (1 + E[|X_{\text{noise}}(f)|^2] / E[|X_{\text{mode}}(f)|^2])^{1/2}$. As a result, the coherence is a function for fraction of amplitudes for $X_{\text{noise}}(f)$ and $X_{\text{mode}}(f)$. Even if signal-to-noise ratio is ~ 1 (or $X_{\text{noise}}(f) \sim X_{\text{mode}}(f)$), the formula shows that the coherence gives a high

value, i.e., $\text{coh} \approx 0.703$. Hence, in case that signal-to-noise ratio is very low (or in case that a mode amplitude is comparable to amplitude for background level of the fluctuation), the radial location of the mode is possible to be inferred using coherence between HIBP and magnetic probes.

In summary, we present a simple method to deduce inner mode structure using HIBP and magnetic probes. The method will be widely applicable to other diagnostics to sense the internal fluctuations.

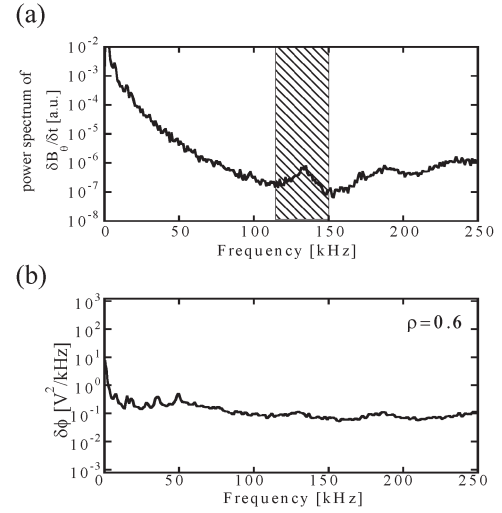


Fig. 1. Typical power spectra of (a) magnetic probe signal and (b) potential signal detected by HIBP at $\rho=0.6$.

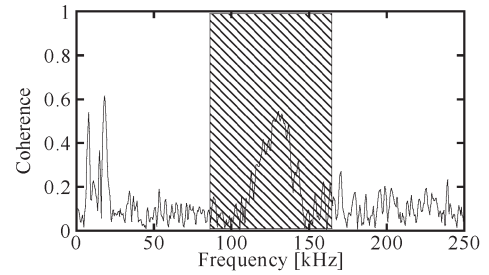


Fig. 2. Coherence between magnetic probe signal and potential signal ($\rho=0.6$). A clear peak exists around 130kHz

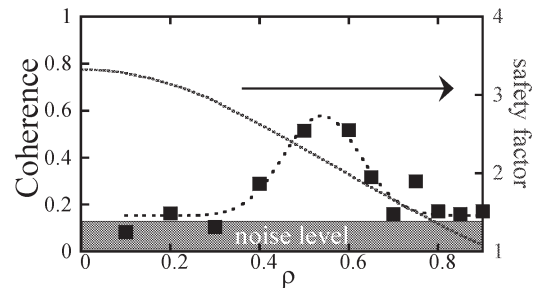


Fig. 3. Radial profile of the peak value for the coherence around 130kHz between magnetic and potential signals. The mode is localized at $\rho=0.5$.

§17. Measurements of Electron Density Fluctuations in CHS Plasmas by Using YAG Laser Imaging Method

Matsuo, K. (Fukuoka Institute of Technology), Hata, S. (Fukuoka Institute of Technology), Iguchi, H., Okamura, S., Matsuoka, K.

We have applied a novel technique of a YAG laser imaging method for obtaining information on electron density fluctuations, including the spatial distribution in CHS plasmas.¹⁾ In this fiscal year, i) a development of a dual beam optical system was advanced for increasing further the signal intensity, ii) a sound isolation cylinder was installed to prevent contamination of noise by acoustic wave in the air, iii) a application of the maximum entropy spectral analysis (MEM) was being tried with the aim of the improvement on the spectral resolution.

Figure 1 shows the optical system for CHS. The YAG laser ($\lambda = 1.064 \mu\text{m}$, 1.2 W) beam is transported by a SM optical fiber near the CHS plasma. A radiation beam from the SM fiber is expanded and collimated by a beam-expander and passes through the plasma. The probe beam is then transmitted through focusing and imaging lenses along with a phase mirror, and then received by a one-dimensional 16-fiber array connected to low noise detectors. In addition to the one-dimensional spatial measurements, two-dimensional spatial measurements at the detecting plane were performed by making the detector array to rotate shot by shot under the condition of fixed operation to observe 2D image equivalently. The measurable frequency range determined by the frequency response of the detector is 20 kHz to 1 MHz. The measurable wavelength determined by the beam width and number of detector channels ranges 2 mm to 47 mm. (This optical system will be improved into the dual beam optical system in the middle of next fiscal year.)

Plasma is initially produced and heated by ECH and further heated by NBI. The spectrum of the density fluctuation distributes broadly between 20 kHz - 300 kHz, and decreases as the frequency increases. Figure 2 shows an example of a distribution of propagational direction of the fluctuations as a function of the frequency by the contour lines, which is analyzed by the MEM. 0 and 90 degrees show the components which propagate in major radius and toroidal directions respectively. In this method spatial positions of the density fluctuations are required by the correspondence of observed propagational direction with direction of magnetic line of force, because the observed micro-turbulence generally propagates toward perpendicular direction to a magnetic field. In Fig. 2, “+” means upper half region and “-” means lower half region along the probe beam path in the plasma cross section. The fluctuations are strong near +40 and -30

degrees. These angles are corresponding to normalized radius $\rho \sim 0.9$ when they are correspondent to the direction of magnetic lines of force of CHS. The improvement of the resolution can be expected from the analyzed result by the MEM, because the spectral band width narrows in comparison with the analysis by the conventional FFT.

By such original method, the data is going to be obtained on the spatial positions of the fluctuations in CHS.

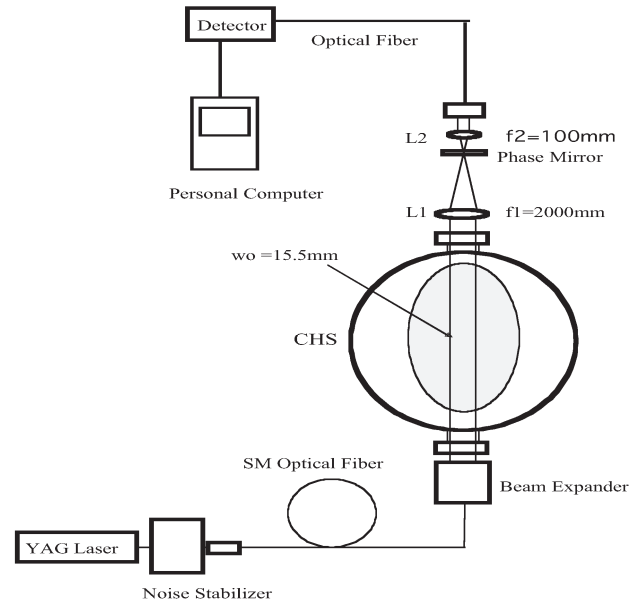


Fig. 1 Laser Imaging System for CHS.

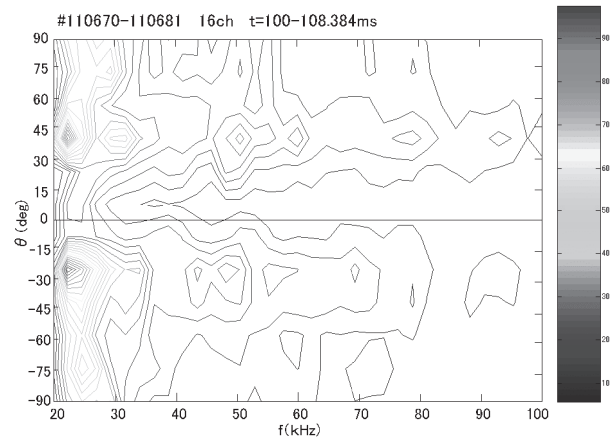


Fig. 2 An example of the distribution of the propagational direction analyzed by MEM as a function of the frequency.

1)JJAP Vol.43, No.5A, 2004, pp2721-2725 “Applicability of Laser Imaging System Using a Near Infrared Laser to Measure Density Fluctuations in High-Temperature Plasmas”

§18. HCN Laser Scattering Measurement on CHS

Iio-Tsuji, S., Shimada, R., Tsutsui, H. (Tokyo Tech.)
 Akiyama, T., Okamura, S., Kawahata, K., Tanaka, K. (NIFS)
 Okajima, S. (Chubu Univ.)

Anomalous transport plays a dominant role in the confinement in magnetic confinement fusion devices. Hence it is indispensable to understand fluctuations to improve confinement since they are supposed to cause the anomalous transport. The edge transport barrier (ETB), which can improve particle transport in the edge region, has been observed in CHS [1,2]. The relationship between transport and fluctuations can be made clear in these plasmas with transitions to H-mode. In this research we develop an HCN laser scattering measurement system to examine the correlations between electron density fluctuations and confinement. In order to reveal the relation of transport barriers to fluctuations we plan to investigate changes in features of turbulences before and after a transition to an improved mode.

An HCN laser interferometer on CHS works routinely. The HCN laser scattering measurement system utilizes optics of the interferometer with slight modification for heterodyne detection of the scattered beam. Scattered angle θ_s and frequencies of scattered beam ω_s are given as follows;

$$\theta_s = 2 \sin^{-1} \{k/(2k_0)\}$$

$$\omega_s = \omega_0 \pm \omega$$

where k , k_0 , ω and ω_0 are wavenumbers and frequencies of fluctuations and incident beam, respectively. Accordingly the wavenumber and spectrum of fluctuations can be evaluated from the scattered angle and spectrum of scattered beam. A collective heterodyne scattering measurement was adopted because it can distinguish the directions in which electron density fluctuations propagate.

By changing the incident beam path, we can select the measured wavenumber k component k_r or k_θ as shown in Fig. 1. The measurable range of k is limited by the aperture width of window and possible area of arrangement of optics. Since CHS has a strong magnetic shear near the plasma edge region, the scattered beam has displacement in the toroidal direction. Hence a scattered beam by density fluctuations with large wavenumber cannot come out of the vacuum vessel. Considering these effects, measurable ranges of wavenumber are;

$$1.4 \text{ cm}^{-1} < k_\theta^{\text{upper}} < 13 \text{ cm}^{-1}$$

$$1.4 \text{ cm}^{-1} < k_\theta^{\text{lower}} < 34 \text{ cm}^{-1}$$

$$1.4 \text{ cm}^{-1} < k_r < 20 \text{ cm}^{-1}.$$

The upper limit of k_θ^{upper} is smaller than that of k_θ^{lower} because the distance between the scattered position and an output window is longer and the displacement in the poloidal direction becomes larger. The lower limit of measurable wavenumber is set from the beam separation of incident and scattered beams.

Figure 2 shows initial measurement results of k_r component. The spatial resolution along the radial direction is 30 mm, which is determined by the width of the incident beam, and that along the beam axis is 360 mm. Because of integration effect along the beam axis the range of measured k_r is;

$$5.1 \text{ cm}^{-1} < k_r < 5.7 \text{ cm}^{-1}.$$

Study of dependences of spectrum on electron temperature and magnetic field strength are future works. A present problem is that signal to noise ratio is small because there are significant switching noises of thyristors from a power supply for coil discharge.

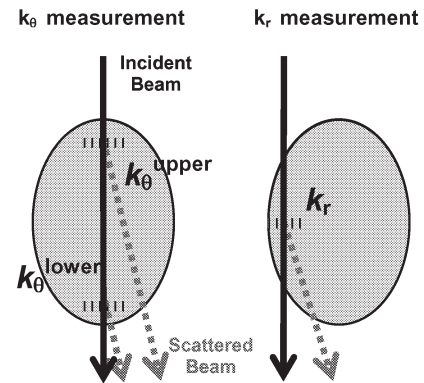


Fig. 1. Measured wavenumber components depend on the path of incident beam.

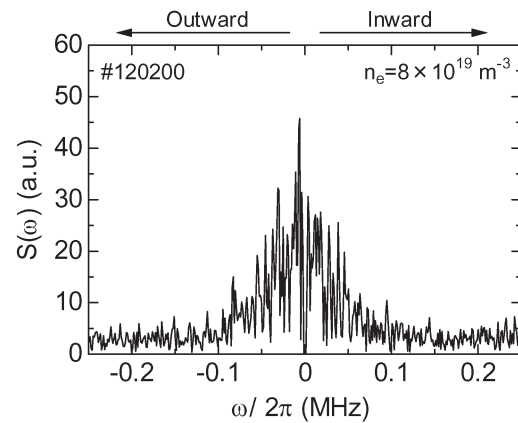


Fig. 2. Initial measurement result of frequency spectrum of density fluctuations.

References

- 1) S. Okamura *et al.*, J. Plasma Fusion Res. Vol.79, No.10 (2003) 977.
- 2) S. Okamura *et al.*, Plasma Phys. Control. Fusion **46** (2004) A113.

§19. 2nd and 3rd Harmonic ECE Measurement on CHS

Yoshimura, Y., Takahashi, C., Fujisawa, A., Shimizu, A., Minami, T., Nakano, H., Ohshima, S., Akiyama, T., Isobe, M., Suzuki, C., Nagaoka, K., Nishimura, S., Matsuoka, K., Okamura, S., CHS Group
Inagaki, S., Nagayama, Y., Kubo, S., Shimozuma, T., Igami, H., Notake, T., Ohkubo, K.

Electron cyclotron emission (ECE) measurement system on CHS has been improved by applying amplifier and filter on it this fiscal year. The ECE system has 16 detecting frequencies: 72, 74.5, 76.5, 78.5, 79.8, 81.5, 84.5, 88, 92, 95, 98, 100.5, 103, 105, 106.4, 108 GHz.

By magnetic field scanning experiment, the ECE measurement system was checked about its frequency sensitivity as seen on Fig. 1. Magnetic field setting so called B_t on CHS was scanned from 1.76 T to 1.3 T. Here magnetic field at plasma axis in the horizontally elongated poloidal cross section with axis position setting R_{ax} of 92.1 cm is 1.92 T with $B_t=1.76$ T. Distribution of magnetic field strength along the major radius direction in the cross section has a peak a little inside of the plasma axis. 2nd harmonic ECE frequency is proportional to the magnetic field strength and the peak value is 111 GHz for $B_t=1.76$ T case. Reducing the value of B_t decreases the peak frequency as plotted by closed circles in Fig. 1. The detecting frequencies of the ECE system are also indicated by horizontal lines. The open circles denote the highest ECE signal frequency detected in the experiment. The highest frequencies should be equal to or lower than the peak frequencies at each B_t setting. These two values show good agreement within differences corresponding to two neighboring detecting frequencies. In 2nd harmonic ECE measurement, it is confirmed that the ECE system correctly measures the ECE signals from inside of plasmas.

Figure 2 shows an example of cut-off effect on ECE signals with high density plasmas. The waveforms are of frequencies of 76.5, 78.5, 79.8, 81.5, 84.5, 88, 92, 95, 98, 100.5, 103, 105, 108 GHz from the bottom one to the top one. The plasma is generated by 53.2 GHz EC power and sustained by NB power until 142 ms. The magnetic field setting and the magnetic axis position are 1.76 T and 92.1 cm, respectively. As the electron density increases with time, ECE signals from peripheral region, or, lower field side are shielded by cut-off effect and the cut-off layer go inside the plasma. Finally when the density reaches at about $7 \times 10^{19}/\text{m}^3$, no 2nd harmonic ECE signal is free from the cut-off effect and the detected signals vanish though the plasma is still sustained. The cut-off effect should be carefully considered for correct ECE measurement.

Potential pulsation in low density ECH plasmas with lower magnetic field around $B_t=0.9$ T has been observed by HIBP on CHS. The 3rd harmonic ECE signals are measured simultaneously with potential measurement by HIBP for the first time. In Fig. 3, potential data and ECE signal are plotted as functions of time. At 88 ms, the potential jumps to high state and then pulsation between the high and low states occurs. It is confirmed that the rapid drop of potential accompanies drop of 3rd harmonic ECE signal which is attributed to decrease of electron temperature.

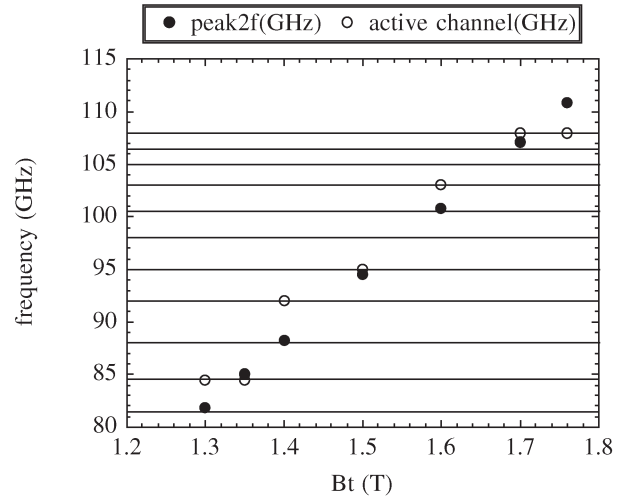


Fig. 1 Dependence of detected highest ECE frequency on magnetic field strength.

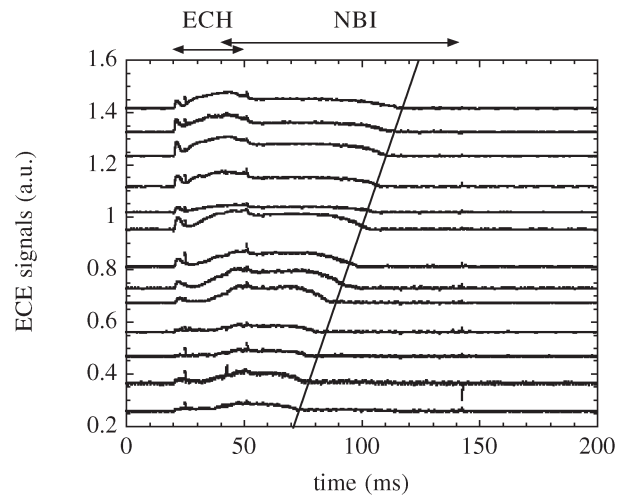


Fig. 2 Example of cut-off effect on ECE signals.

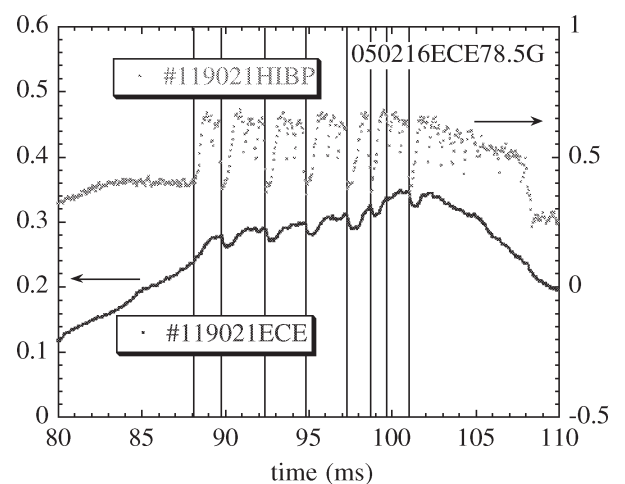


Fig. 3 The first simultaneous measurement of plasma potential by HIBP and 3rd harmonic ECE signal.

§20. Fast Ion Measurement Using the Hybrid Probe in CHS

Nagaoka, K., Isobe, M.

Fast ion confinement and transport properties are very important issue for burning plasmas in magnetically confinement fusion devices. So far, many diagnostic tools have been developed and observed some significant properties of fast ion transport. In this report, it is shown two results of fast ion observation by a kind of Langmuir probe, which is called “hybrid probe”.

The hybrid probe consists of ten Langmuir probe tips including thermocouple to measure heat flux and is installed by two-dimensional probe drive system on CHS. The hybrid probe is also able to be rotated along the probe axis and to turn the probe tip into co and counter-direction, that is, this probe can measure the co flux and counter flux in the same magnetic surface. The probe collects ion flux flowing in the co and counter-direction, when the probe turns on the counter and co direction, respectively.

In general, the difference of ion saturation currents between two anti-parallel fluxes is mainly produced by plasma flow, so it is used to evaluate plasma flow velocity [1]. For plasmas sustained by NBI heating, it is, however, dominated by fast ion flux tangentially injected from NBI. In order to confirm this assumption, the comparison of results of hybrid probe measurement and a neutral particle analyzer (NPA) has been performed in NBI modulation discharges and in plasmas with MHD bursts.

The ion saturation currents in the probe facing counter- and co-direction are shown in Fig.1 (b), the ion saturation current in case of collecting co-flowing ions is significantly larger than that in case of collecting counter-flowing ions. The difference of the two currents, which is shown in Fig.1 (c), is strongly synchronized with the modulation of co-NBI shown in Fig.1 (a), and is agree well with the results of the NPA, which is shown in Fig.1 (d).

MHD Bursts and the fast ion loss synchronized with the MHD bursts have been observed in CHS [2]. The ion saturation current measured near the last closed flux surface in case of collecting co-flowing ions responds to the MHD bursts, while it does not do in case of collecting counter-flowing ions, which are shown in Fig.2. This result is also consistent to the observation of NPA [2].

In concluding, it is shown that the hybrid probe can measure toroidally rotating fast ions by two experimental confirmations; one is beam modulation experiment and the other is the measurement of fast ion loss synchronized with the MHD bursts. It should be noted that it is possible to apply this method to fast ion measurement in core plasmas, which is next step of this research.

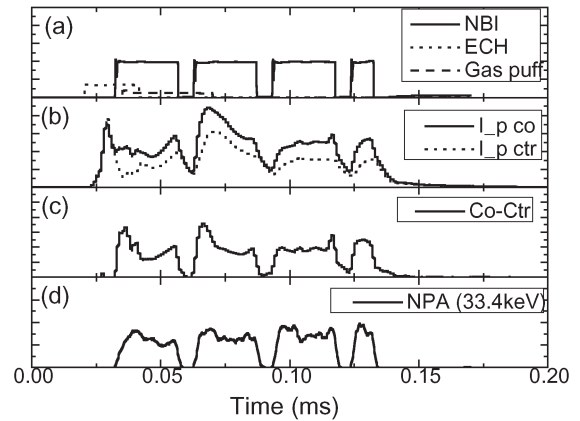


Fig.1 The time traces of a neutral beam modulation discharge; (a): heating power and gas puffing, (b): ion saturation currents in case of collecting co-flowing ions and counter-flowing ions, (c): the difference of the two ion saturation currents, (d): high energy neutral particle flux with energy of 33.4keV observed by NPA.

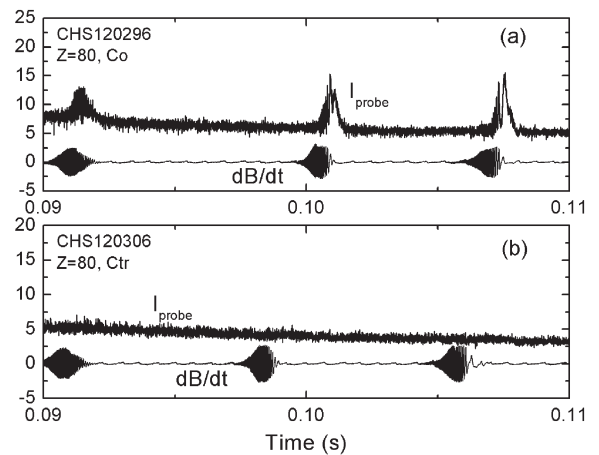


Fig.2 The ion saturation current and the signal of magnetic probe in case of collecting co-flowing ion (a), and counter-flowing ion (b).

References

- [1] K. Nagaoka *et al.*, J. Phys. Soc. Jpn. **70** (2001) 131.
- [2] T. Kondo *et al.*, Nucl. Fusion, **40** (2000) 1575.

§21. MHz Range Fluctuation Measurements in Electron Cyclotron Resonance Heating Plasmas on Compact Helical System

Nagashima, Y. (Research Institute for Applied Mechanics, Kyushu Univ.)

Isobe, M., Yoshimura, Y., Ida, K., Matsushita, H., Okamura, S. (National Institute for Fusion Science)

High energy tail formation in ion distribution function has been observed in low-density electron cyclotron heating/current-drive (ECH/ECCD) plasmas using Fast Neutral Analyzer (FNA) on Compact Helical Systems. Time scale of the tail formation is much faster than electron-ion collision rate. A picture describing the tail formation is ion heating by wave-particle interaction. In order to investigate the ion heating mechanism, direct measurements of the wave fluctuations which resonate ions have been performed using a Langmuir probe for potential fluctuations and a 1-turn loop probe for magnetic fluctuations.

Estimation of the target waves is indispensable. A candidate wave which can resonate ions is the lower-hybrid wave. However, the frequency of launcher wave in the ECH system is the 2nd electron cyclotron harmonics, therefore, the lower-hybrid wave can not be excited by a parametric decay of launched EC wave. B. Coppi presented a theory of excited waves which can resonate ions¹⁾. Positive slope formation in electron distribution function parallel to confined magnetic field generates the longitudinal waves through Landau amplification. Positive slopes of distribution functions could be generated by parallel current drive like ECCD. When parallel momentum of the longitudinal wave is scattered in the perpendicular direction and is coupled to ions, the resonance condition between the wave and ions can be written as, $k_{\parallel}v_{e\parallel} = \mathbf{k} \cdot \mathbf{v}_i$, where k_{\parallel} is parallel wavenumber, $v_{e\parallel}$ is parallel electron velocity, \mathbf{k} is wave vector, and \mathbf{v}_i is ion velocity vector, respectively. Simulation results of Vlasov equations suggest that $f_{\text{target}} < f_{\text{pi}}$ or $f_{\text{pi}} < f_{\text{target}} \ll f_{\text{ce}}$, and k_{\perp} is much larger than k_{\parallel} , where f_{target} is the target wave frequency, f_{pi} is ion plasma frequency, f_{ce} is electron cyclotron frequency, and k_{\perp} is perpendicular wavenumber, respectively. f_{target} is in the range a few hundreds MHz to a few GHz in typical discharge conditions where the ion tail formation is observed ($B_0=0.88\text{T}$, line averaged density $<5.0 \times 10^{18}\text{m}^{-3}$, magnetic axis position is 94.9 cm, and electron temperature is 1-3keV).

Measurement systems are described. Potential fluctuations can be observed by a cylindrical electrode with a diameter of 1mm and a height of 1mm. The electrode is made of Molybdenum, and is mounted on the probe head made of boron-nitride. The electrode is directly connected with center conductor of a semi-rigid coaxial cable, leading to a SMA vacuum feedthrough connector. The feedthrough in the air-side is jointed to DC block. Signals are amplified by 40dB and are transmitted to an analog spectrum analyzer. Magnetic fluctuation measurements are available by a 1-turn loop, and signals are obtained in the same way, but without DC block because the signal current should be transmitted. The loop is mounted inside the probe head,

and it is noted that the loop can not detect magnetic fluctuations as it is in plasmas, but may detect magnetic fluctuations mode-converted at the boundary between the plasma and the vacuum (inside the probe head).

The experiments have been performed under the discharge conditions described above. The various conditions of plasma current magnitude and direction were tested. The probe head is located 5cm outside the last closed magnetic flux surface, and magnetic fluctuation measurements were mainly performed.

Figure (a) shows the maximum current dependence of the ion temperature calculated from the tail region of ion distribution function obtained by FNA. The increase of ion temperature is corresponding to the decrease of plasma current and to the decrease of density. The bulk ion temperature is around 80eV. The ion temperature strongly depends upon density. Figure (b) shows the current dependence of magnetic fluctuation power at 700 MHz. The increase of the fluctuation power is corresponding to the decrease of plasma current. This relationship was also observed in the broad frequency range higher than f_{pi} . It is noticeable that increase of fluctuation power is also corresponding to the decrease of density. Therefore, the fluctuation power depends upon both density and plasma current, consistent with the ion tail energy.

For investigating the ion tail formation by wave-particle interaction, further studies are necessary. It is indispensable to obtain parallel electron distribution function and k_{\parallel} of potential fluctuations of the waves resonating ion. Using above information, wave dispersion relation can be estimated. The propagation of the wave inside and outside the last close flux surface should be calculated for checking the consistency with experimental results.

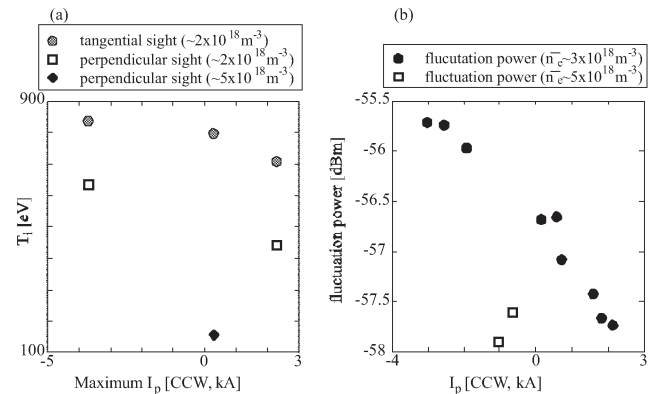


Figure (a) Maximum current dependence of ion temperature calculated using high energy region of ion distribution, (b) current dependence of magnetic fluctuation at 700 MHz.

Reference

- 1) Coppi, B., et al., Nucl. Fusion **16**, 2 (196) 309

§22. Lithium Beam Probe for Edge Plasma Diagnostic in CHS

Nakamura, K., Iguchi, H.

Plasma structures near and out side of the last closed flux surfaces (LCFS) have been measured by the use of the lithium beam probe (LiBP) in CHS. There are two typical magnetic configurations, namely, the inboard limiter configuration and the magnetic limiter configuration. Each configuration is realized by inward-shifted or outward-shifted magnetic axis, respectively. In the inboard limiter configuration, the inboard wall plays a role of material limiter, making the connection length outside of the LCFS very short. The ergodic layer disappears, which is in contrast to the magnetic limiter configuration.

A lithium neutral beam with the energy up to 15 keV and with the equivalent beam current of a hundred microamperes is injected from the M-port (located upside of the torus). Light emission from the beam due to plasma particles impact excitation (670.8 nm) is collected through a window mounted on the O-port (located outside of the torus).

Experiments have been carried out for the inboard limiter configuration for magnetic axis of $R_{ax} = 0.921$ m and the magnetic limiter configuration for magnetic axis of $R_{ax} = 1.016$ m. At the inboard limiter configuration, hydrogen plasmas are produced by electron cyclotron resonance (ECR) heating with a gyrotron of 53 GHz. Neutral beam injection (NBI) heating is additionally applied using the two beam lines (both in co-direction) with 40 keV. Plasma density is controlled by preprogrammed gas puff system. In the present experiments, the average electron density in the ECH phase is about $1 \times 10^{19} \text{ m}^{-3}$. The average electron density in the NBI phase depends on the heating schemes and is $4 \times 10^{19} \text{ m}^{-3}$ in the present experiment.

On the other hand, the average electron density in the ECH phase is about $0.8 \times 10^{19} \text{ m}^{-3}$ and in the NBI phase is $2 \times 10^{19} \text{ m}^{-3}$.

The electron density profiles at the inboard limiter configuration are shown in Fig. 1. The LCFS is in the vicinity of position 35 mm. Triangle dots show the profile of ECH phase and cross dots show NBI phase. It is shown that the NBI plasma density is always higher than the ECH plasma density. The core electron density profile is measured with YAG laser Thomson scattering, showing flat and parabolic profiles in ECH and NBI plasmas, respectively.

As for the magnetic limiter configuration, the electron density profiles are shown in Fig. 2. The LCFS is in the vicinity of position 30 mm. It is shown that the ECH plasma density is higher than the NBI plasma density in the edge region. The ECH plasma is showing hollow profile.

The difference of such distributions is considered to be due to the presence of the ergodic layer. By comparing the electron density profiles of the inboard limiter

configuration and the magnetic limiter configuration in detail, it is expected to be clarified how ergodic layer contributes to the plasma confinement in helical device.

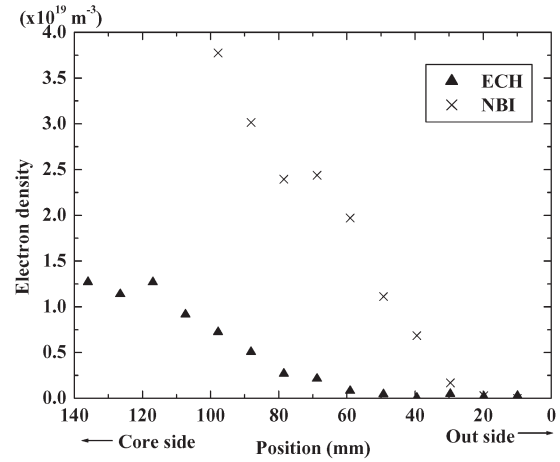


Fig. 1 ECH and NBI plasma density profiles at the inboard limiter configuration. The LCFS is in the vicinity of position 35 mm.

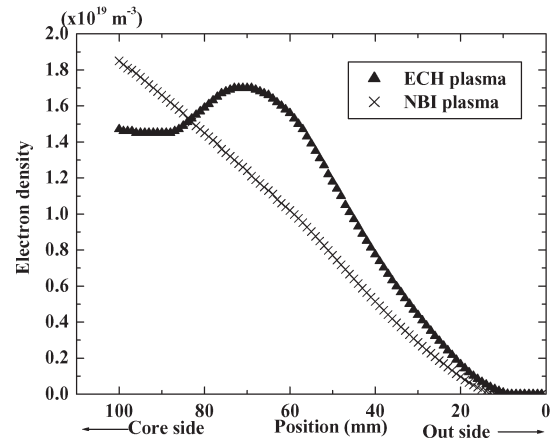


Fig. 2 ECH and NBI plasma density profiles at the magnetic limiter configuration. The LCFS is in the vicinity of position 30 mm.

§23. Lithium Beam Probe (LiBP) Imaging Using CCD Camera

Narihiro, Z. (Dep. Energy Eng. Sci., Nagoya Univ.)
Nakamura, K., Iguchi, H.

In the present LiBP diagnostic system in CHS, eight channel APD detectors have been used to measure light emission from the neutral lithium beam. The emission intensity profiles can only be obtained along the beam line. Two-dimensional measurements are performed by changing the beam injection angle shot by shot.

A new detector system using a CCD camera (656x494 pixels) has been installed on CHS to observe light emission as a two-dimensional picture. The time resolution can be increased up to 2 ms by the use of the binning function of the camera. The view of the CCD camera is set to be 150 mm x 200 mm at the position of $R = 1200$ mm, where R is the major radius, which covers the plasma area from inside the last closed flux surface and the outer separatrix region of the helical magnetic field configuration. The full emission profile can be taken densely along the beam in a single shot. Although a real two-dimensional observation is impossible with the present beam, the detector can straightly be extended to two-dimensional measurements or imaging measurements in future.

An example of beam emission measured by the CCD camera system in an NBI plasma is shown in Fig. 1. The picture is taken by binning pixels over 4x4 with the exposure time of 29 ms. The bright straight line shown in the right half of the picture is the emission from the injected lithium beam. The beam energy is 15 keV and equivalent beam current is one hundred microamperes. The average electron density is about $1 \times 10^{19} \text{ m}^{-3}$ in the present experiment.

Figure 2 shows the emission intensity profiles along the beam for different exposure time. The gradual decrease of the emission intensity is due to beam attenuation. The emission intensity decreases as the exposure time does. The exposure time of 9 ms is too short to resolve the emission profile clearly. Electron density profiles reconstructed by the use of beam attenuation method are shown in Fig. 3. The emission profiles obtained with longer exposure time than 19 ms gives consistent and reasonable electron density profile along the beam. However, the electron density calculated from the emission data with the exposure time of 9 ms deviates from other results. Higher beam intensity is required to improve time resolution.

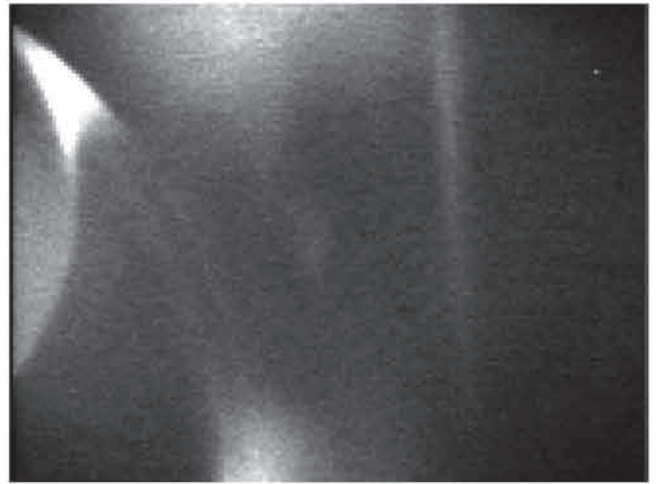


Fig. 1 Beam emission measured by CCD camera.

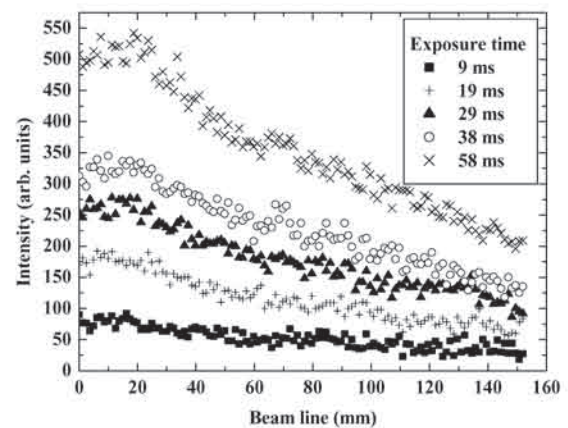


Fig. 2 Beam emission profiles for different exposure time of the CCD camera.

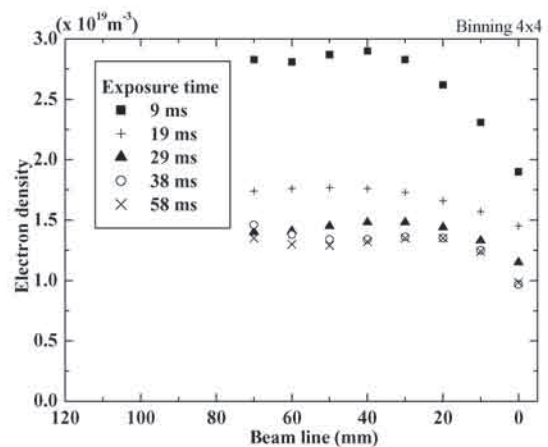


Fig.3 Electron density profiles reconstructed from the emission profiles in Fig. 2.

§24. Neutral Particle Transport in CHS Edge Region

Matsuura, H., Iguchi, S. (Osaka Pref. Univ.)
Okamura, S.

Improvement of plasma confinement such as H-mode is one of urgent issues in the fusion research. Edge transport barrier(ETB) discovered recently in the compact helical system(CHS)¹⁾ is characterized by clear drop of $H\alpha$ emissions. As $H\alpha$ emission intensity is often used as the measure of recycling particle flux, particle confinement is thought to be improved. Quantitatively, however, this conclusion must be checked carefully, since $H\alpha$ emission has deep relationship with the profile of atomic/molecular hydrogen, which is very complicated in helical systems like CHS.

In order to study the neutral particle behavior in CHS, we have used Monte Carlo simulation code DEGAS. In Fig. 1, calculation geometry at $\phi = 0$ cross section is shown²⁾, where the CHS plasma in the standard magnetic configuration has contact with the inside wall like as the material limiter and the neutral recycling becomes dominant. When we move along toroidal direction, the gap between plasma and wall becomes large and partial magnetic limiter configuration is established at $\phi = \pi/8$. In this report, we expand the simulation model to three-dimension to include the toroidal behavior of neutral particle³⁾. We made two model geometry and compare their results more clearly. One is referred as “CHS”, which include toroidal periodicity of $m = 8$. Another is “torus”, which is axial symmetric around the major axis and has cross sections like Fig. 1 for all toroidal angle ϕ .

In the Fig. 2, poloidal profile of atomic hydrogen is shown. Neutral density is localized to torus inside (poloidal angle is 0 or 360[deg.]) and poloidal transport is almost prohibited. Hydrogen molecules are produced at the recycling area on the wall(indicated with arrows in the Fig. 1 and 2) Hydrogen atoms are also produce near the recycling area by interactions between molecules and plasma particles. As the mean free path of these neutral particles is a few cm or less, they have little chance to reach the right-side vacuum region in Fig. 1 along the poloidal (also radial) direction. If the poloidal extension of effective recycling region is large, however, this chance becomes large and neutral density in the vacuum region increases. So the precise modeling of the recycling region is important.²⁾

As for toroidal transport, there exist a gap between Last Closed Flux Surface (LCFS) and chamber wall. So neutral particle can easily move several cm in toroidal direction. Fig. 3 shows toroidal profile of atomic hydrogen for two model geometry. In “CHS” model, the gap between LCFS and wall becomes wider and then narrower periodically. But the gap is kept to be narrow in “torus” model. So the atomic density in “torus” (thin lines in Fig. 2 and 3) becomes smaller far away from recycling areas. The difference of two models is clearer for molecular density profile.

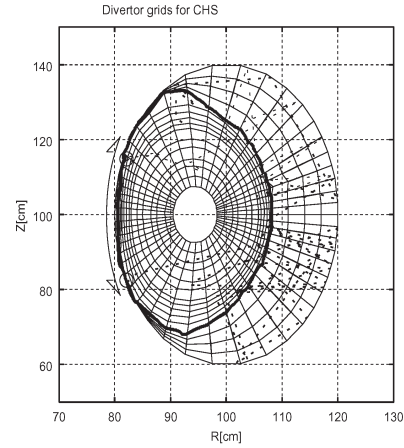


Fig. 1: Calculation geometry for the DEGAS simulation. trajectories of some test particles are also indicated with dashed lines.

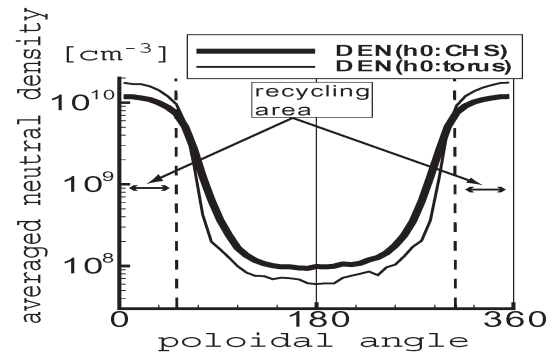


Fig. 2: Poloidal profile of atomic hydrogen radially-averaged density at $\phi = 0$ cross section.

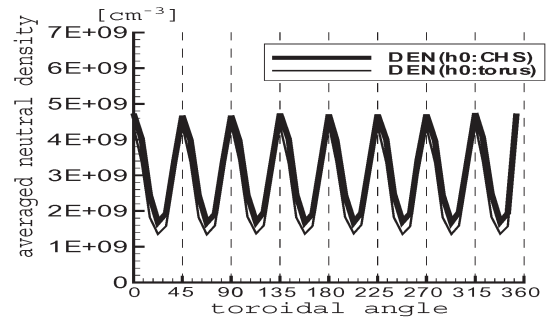


Fig. 3: Toroidal profile of atomic hydrogen surface-averaged density.

References

- 1) S. Okamura et al., J. Plasma Fusion Res., **79**,(2003)977.
- 2) H.Matsuura et al.: to be publish in J.Plasma Fusion Res. SERIES, **7**.
- 3) S.Iguchi et al., Joint Conf. PSS-2005/SPP-22 P2-093, (Nagoya, 2005).

\$25. Detailed Dynamics of Internal Transport Barrier Formation in Low Temperature CHS Plasmas

Toi, K., Takeuchi, M. (Dep. Energy Eng. Sci., Nagoya Univ.), Ikeda, R. (Dep. Energy Eng. Sci., Nagoya Univ.), Suzuki, C., CHS Experimental Group

Energy and particle transport in a toroidal plasma is a very important and challenging issue in magnetic confinement fusion research. There is general consensus that transport of high temperature toroidal plasmas is governed by plasma turbulence. Therefore, correlation measurement among plasma fluctuations is crucial to clarify underlying physics mechanisms in turbulent particle and heat transport of a toroidal plasma. However, the correlation measurement is extremely difficult in high temperature plasma. The Langmuir probes (LPs) are the most promising tool for the correlation measurement, but are only applicable to low temperature and low density plasma. In CHS, we are attempting to study a possibility to simulate plasma transport in high temperature plasma with low temperature one, by adjusting various dimensionless plasma parameters [1]. We have found that this new approach is very promising [2]. Recently, detailed dynamics of internal transport barrier formation of which similar event is often observed in high temperature plasma have been investigated in low temperature and low density plasmas produced at very low toroidal field B_t (<0.1 T).

In a low density hydrogen plasma produced by launching about 15 kW microwaves at $B_t=0.0613$ T, line averaged electron density $\langle n_e \rangle$ rapidly increases up to $\sim 1.1 \times 10^{17} \text{ m}^{-3}$ and gradually decreases down to $\sim 5 \times 10^{16} \text{ m}^{-3}$. During the decay of $\langle n_e \rangle$, electron temperature T_e linearly increases till the transition. Plasma collisionality decreases continuously toward the transition and reaches the boundary between $1/\nu$ and plateau regimes. When $\langle n_e \rangle$ decreases to $\sim 7\text{--}8 \times 10^{16} \text{ m}^{-3}$, electron density n_e in the core region ($\rho < 0.45$) suddenly increases and that in the outer region suddenly decreases, as shown in Fig.1, where these data were taken shot by shot basis for many reproducible shots using LP. This transition in electron density n_e clearly indicates the formation of internal transport barrier (ITB). The formation of ITB is also observed in electron temperature T_e , but is not significant. The ITB observed in T_e is inside $\rho \leq 0.3$ and the size is smaller than that of ITB in n_e . Note that after the ITB formation the decay of $\langle n_e \rangle$ becomes slow, and $H\alpha$ emission slightly decreases. These results suggest the reduction of particle transport. It is interesting how the radial electric field E_r behaves across the transition. Figure 2 shows the space potential V_s derived from measured floating potential V_f and electron temperature T_e as $V_s = V_f + \zeta T_e$, here $\zeta \approx 3$ for hydrogen plasma. Before the transition, V_s profile in the core region of $\rho < 0.5$ is flat,

which means $E_r \sim 0$ there. Across the transition, V_s profile changes to a centrally peaked one, which means that large positive E_r of $\sim 600 \text{ V/m}$ is generated in the region of $\rho < 0.5$. This positive E_r corresponds to large poloidal rotation velocity of $\sim 10 \text{ km/s}$ because of very low B_t . However, the velocity shearing rate in these plasmas is less than 10^5 s^{-1} and is not significant. Relationship between the ITB transition and most relevant quantities such as E_r , E_r -shear and fluctuation characteristics should be clarified in future studies. This result again suggests that this new approach using low temperature plasma based on the *non-dimensional similarity hypothesis* is very promising.

- [1] K. Toi, S. Kawada, G. Matsunaga et al., in Proc. 29th EPS on Plasma Phys. Control. Fusion (Montreux, 2002), Paper No. P-4.061.
- [2] K. Toi et al., J. Plasma Fusion Res. SERIES Vol.6, 516.

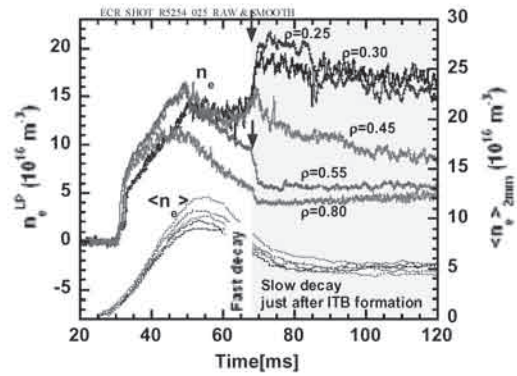


Fig.1 Time evolutions of local and line-averaged electron densities, where the transition occurs at $t \sim 69$ ms. The vertical arrows indicate the transition. The decay in $\langle n_e \rangle$ after the transition slows down.

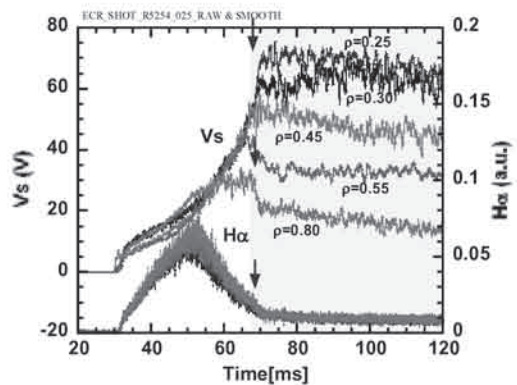


Fig.2 Time evolutions of space potential V_s and $H\alpha$ emission.

§26. Electron Heating of an Over-Dense Plasma by 2.45 GHz Microwaves in CHS

Ikeda, R. (Dep. Energy Eng. Sci., Nagoya Univ.),
Takeuchi, M. (Dep. Energy Eng. Sci., Nagoya Univ.),
Toi, K., Suzuki, C., Matsunaga, G. (JAERI)

A new transport simulation based on the concept “dimensional similarity” using a low temperature and density helical plasma is currently underway in the CHS [1]. Previous experiment showed that an over-dense plasma was generated by 2.45 GHz microwaves of which power was absorbed in the inaccessible region for the waves [2]. This result suggests a possibility of the mode conversion to electron Bernstein wave (EBW).

In order to clarify and enhance the mode conversion of launched electron cyclotron wave to EBW, we tried to superimpose a power of the #1 microwave source (#1 in Fig.1) to a plasma produced by the #2 microwave source (#2 in Fig.1). At $B_t=613\text{G}$ in the configuration of $R_{ax}=97.4\text{cm}$, the target plasma for the #1 source has already reached an over dense plasma having a steep density gradient at the upper hybrid resonance layer which locates in the plasma edge, as shown in Figs.2 and 3. In Fig.3 (a), time evolutions of line averaged electron density (n_e^{2mm}) and the electron kinetic energy (E) are compared for both cases with and without a superimposed power of the #1 source, where E is evaluated as

$$E = \int_V \frac{3}{2} n_e T_e(\rho) dV$$

The superposition of the ECH power increases E by about 50 % compared with that in the case without the power superposition, while the increase in n_e^{2mm} is suppressed less than 15%. This result indicates obvious electron heating of an over-dense plasma by the superimposed ECH power. The radial profiles of n_e and T_e just before and immediately after superimposing the #1 source power are shown in Fig.3 (b). The absorbed power P_{abs} derived by power step-up technique is also shown in Fig.3 (b). The electron temperature is increased over the whole radial region by injection of the #1 source power, while the n_e profile remains unchanged by the injection. The additional ECH power injection contributes to clear electron heating. Although the O-mode, right-hand and left-hand cutoff layers are condensed near LCFS ($\rho=1$), the observed absorption of the additional injection power widely takes place beyond these cutoff layers. The values of the Budden parameter (η) and the maximum mode conversion efficiency (C_{max}) [3] in the target plasma are respectively about 0.19 and 0.99 at the moment of the injection of the #1 source power. The total deposited power is evaluated to be about 5kW across the power step-up ($P_1 \sim 14\text{kW}$), and corresponds to be fairly high experimentally evaluated absorption rate has reached about 35%.

- [1] K. Toi *et al.*, 29th EPS on Plasma Physics and Controlled Fusion, Montreux, 2002, paper No.P4-06.
- [2] R. Ikeda *et al.*, to be published in J. Plasma Fusion Res. 2005.
- [3] A.K. Ram *et al.*, Phys. Plasmas 7, 4084 (2000).

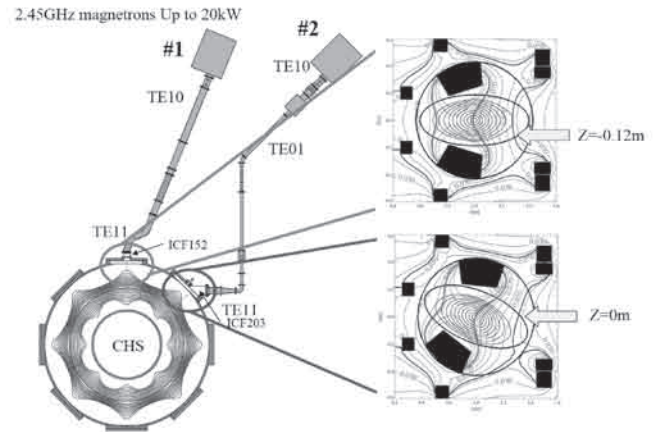


Fig.1 Arrangement of microwave systems in CHS and the contour of the magnetic field strength in the poloidal cross section at the launching ports of microwaves.

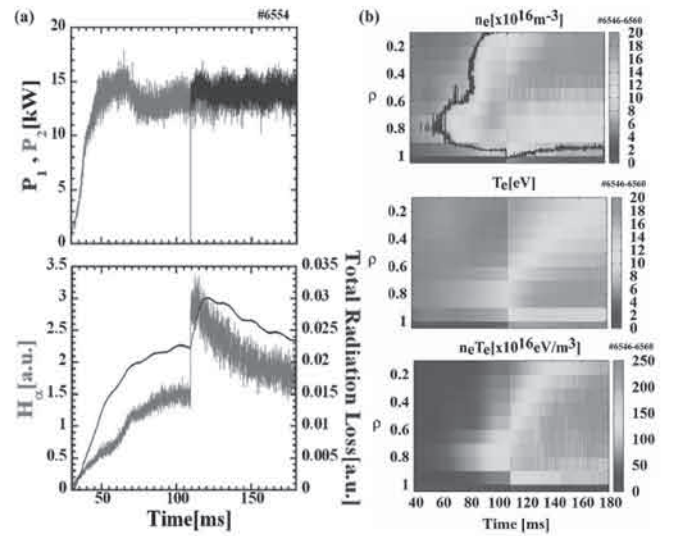


Fig.2 (a) Time evolutions of ECH power of #1 source (P_1), that of #2 source (P_2), H_α and total radiation loss. (b) Contour plots of n_e , T_e and $n_e T_e$ in the time and normalized radius plane.

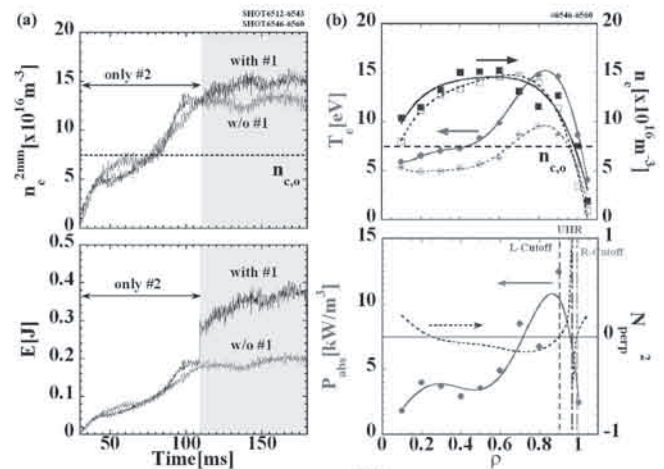


Fig.3 (a) Time evolutions of n_e^{2mm} and E with and without the ECH power superposition. (b) Radial profiles of T_e , n_e and n_e just before and immediately after superimposing the #1 source power. The deposition profile of the additional ECH power is shown as P_{abs} .

§27. Hot Cathode Biasing Experiment in CHS

Takahashi, H., Kitajima, S., Sasao, M. (Tohoku Univ.)
Isobe, M., Okamura, S.

The electrode biasing experiment in Compact Helical System was carried out in order to investigate the role of a radial electric field for an improvement of plasma confinement. The hot cathode made of LaB₆, used as an electrode to form a radial electric field, is inserted horizontally from the low magnetic field side. The filament is cylindrical (diameter is 10 mm, length is 17 mm) and double spiral structure to cancel the induced magnetic field. It is heated to ~ 1800 °C using a power supply. The electrode was biased against the vacuum vessel by a current control power supply. In this study, we attempted to control the poloidal driving force to clarify the bifurcation originated from the ion viscosity. The poloidal driving force is the Lorentz force of $\mathbf{J} \times \mathbf{B}$. Thus, it can be changed continuously by the electrode current control. The position of the electrode for the plasma is shown in Fig. 1.

The neoclassical theory points out the criterion of LH transition from the viewpoint of the ion viscosity. In this theory, the ion viscosity has local maxima against the rotation velocity [1, 2]. When the driving force in poloidal direction exceeds a critical value, the poloidal rotation velocity increases rapidly and the plasma makes transition to the H mode. It means that LH transition mechanism is the bifurcation phenomena originated from the existence of the local maxima in the ion viscosity. Figure 3 shows the dependence of calculated ion viscosity $\Pi_{p,n}$ for CHS based on the Shaing [1] or Rozhansky model [2] on the poloidal Mach number M_p . M_p is the poloidal flow velocity normalized by the ion thermal velocity. As can be seen in Fig.3, ion viscosity has local maximum near $M_p \sim 2$ in both model of Shaing and Rozhansky. If enough radial electric field corresponding to $M_p > 2$ is attained, the plasma make transition to enhanced mode. In the experiment, which the target plasma was produced by an electron cyclotron heating of 2.45 GHz, the estimated M_p was 1.2; therefore it is thought that the plasma remained low confinement state in that condition. Moreover, the friction force which is one of the poloidal momentum damping force caused by charge exchange between ion and neutral particle was not negligible in such high collisional plasma. It means that larger poloidal driving force was required for transition.

The experiment will be extended to a low collisional and/or high temperature plasma at high toroidal field in order to clarify the role of the ion viscosity for the transition to the enhanced confinement mode.

Reference

- [12] K. C. Shaing and E. C. Crume, Jr.: Phys Rev. Lett. **63**, 2369 (1989).
- [25] V. Rozhansky and M. Tendler: Phys. Fluids B **4**, 1877 (1992).

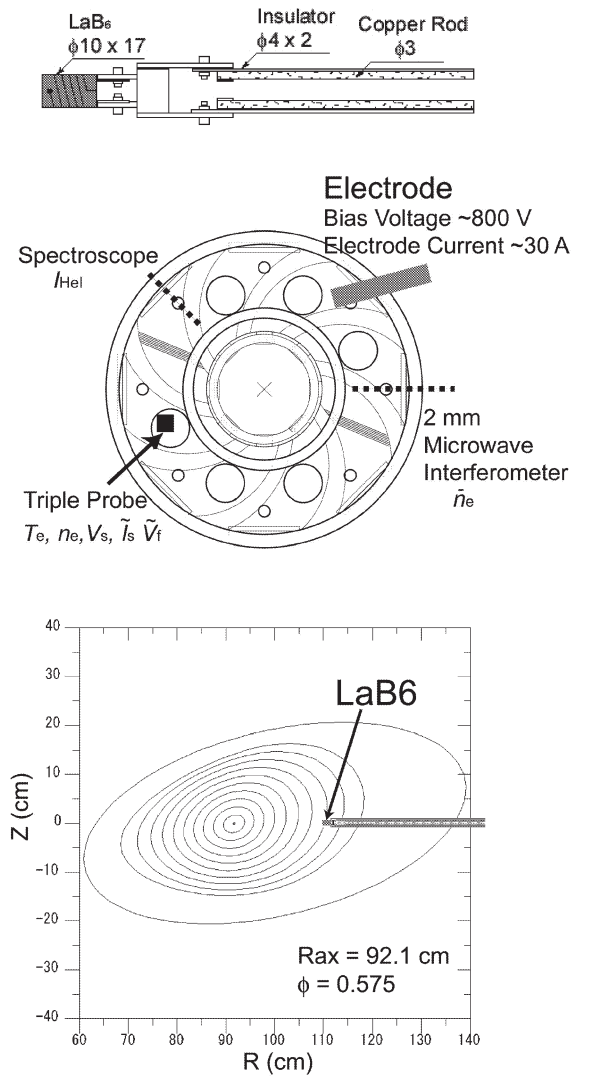


Fig. 1. The location of hot cathode for CHS plasma.

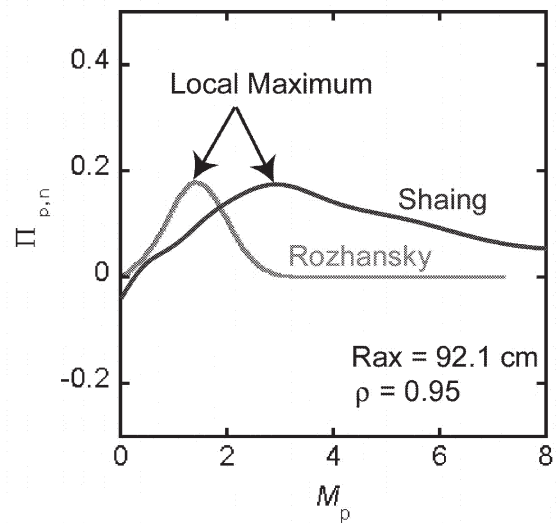


Fig. 2. Relation between ion viscosity and poloidal Mach number.

§28. Radial Electric Field Control by Electron Injection in CHS

Kitajima, S., Sasao, M., Shinto, K., Takahashi, H., Tanaka, Y., Utoh, H., Takenaga, M., Shinde, J., Ogawa, M., Aoyama, H., Iwazaki, K. (Dept. Eng., Tohoku Univ.)

Takayama, M. (Akita Prefectural Univ.)

Takeuchi, M., Ikeda, R. (Dept. of Energy Engineering and Science, Nagoya Univ.)

Okamura, S., Toi, K., Iguchi, H., Fujisawa, A., Isobe, M., Suzuki, C., Yokoyama, M.

The effects of the viscosity maxima on the L-H transition have been experimentally investigated in the Tohoku University Heliac (TU-Heliac), a small helical axis stellarator. The poloidal viscosity was estimated from the $\mathbf{J} \times \mathbf{B}$ driving force for a plasma poloidal rotation, where \mathbf{J} was a radial current controlled externally by the LaB₆ hot cathode biasing. It was experimentally confirmed that the local maxima in the viscosity play the key role in the L-H transition¹⁻²⁾. However, in the operation condition on TU-Heliac the collisionality is comparatively high (plateau regime) and the friction of neutral particles affects the poloidal damping force. Therefore it is important to perform this biasing experiments mentioned above in the confinement system that has sophisticated diagnostic systems, abilities to produce low collisional plasmas and changeability of the location of a magnetic axis. The purposes of our electrode biasing experiments in Compact Helical System (CHS) were, (1) to estimate the ion viscous damping force from the driving force for the poloidal rotation, and (2) to study the dependence of the ion viscosity on helical ripples.

Preliminary biasing experiments at low magnetic field were carried out in CHS. The target plasma was produced by 2.45 GHz electron cyclotron heating for a He gas (input power ~ 15 kW $\times 2$, electron density $\sim 10^{11}$ cm⁻³, electron temperature ~ 12 eV). The hot cathode of LaB₆ (diameter is 10 mm, length is 17 mm) was inserted from low magnetic field side. The tip of the hot cathode was located at plasma edge ($\rho \sim 0.8$) and biased negatively against the vacuum vessel of CHS by using current control power supply (electrode current ~ 5.4 A) as shown Fig. 1. We observed following results; (1) the improvement of electron density by the factor of 2 \sim 3, (2) the increase of electron stored energy, (3) the formation of steep gradient in electron density and electron pressure profiles, (4) the transition of plasma space potential from positive to negative, (5) the formation of negative radial electric field (~ -250 V/m) as shown in Fig. 2. These results implied that the plasma confinement was improved.

The experiment will be extended to a low collisional and/or high temperature plasma at high toroidal field in order to clarify the role of the ion

viscosity for the transition to the enhanced confinement mode.

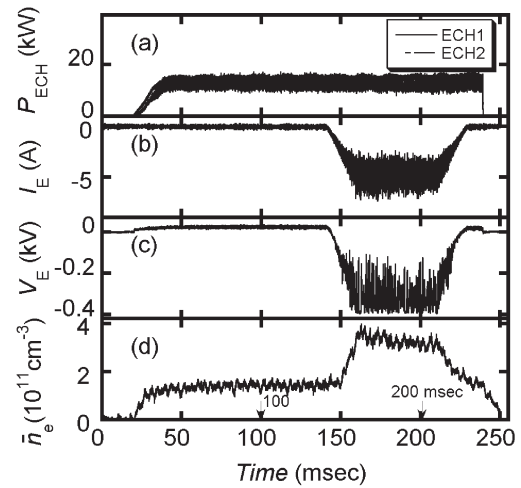


Fig. 1. Typical time evolutions of (a) input power of ECH, (b) electrode current, (c) electrode voltage and (d) electron line density.

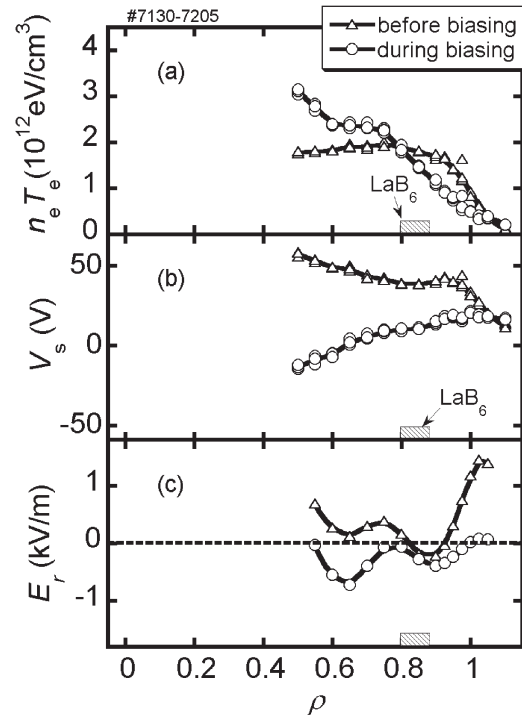


Fig. 2. Radial distributions of (a) kinetic pressure, (b) space potential and (c) radial electric fields before and during biasing. The normalized radius is indicated by ρ .

Reference

- 1) Takahashi, H. *et al.*: Comparison of Bifurcation Phenomena During LH/HL Transition Observed in Biasing Experiment in Tohoku University Heliac, presented at ICPP2004 [Nice, Oct., 2004] D1-5.
- 2) S. Kitajima, *et al.*: LH Transition by a Biased Hot Cathode in the Tohoku University Heliac, presented at 20th IAEA FEC [Vilamoura, November 2004] IAEA-CN-116/EX/9-3.

§29. Radial Density Profiles of Microwave and Whistler Wave Discharges

Shoji, T., Sakawa, Y. (Dept. Energy Eng. and Sci., Nagoya Univ.)

Suzuki, C., Takeuchi, M., Ikeda, R., Toi, K.

Whistler wave discharges in MHz range of frequency studied in CHS[1-2] have the notable feature of producing plasmas in a low magnetic field strengths of kG range, which is important in the high beta and some Alfvén wave related studies of helical systems. We compare the density profiles of the plasma production by the Whistler wave discharge and 2.45GHz microwave discharges.

The perpendicular propagation region of Whistler waves (fast wave) for 13MHz in density n and toroidal field B_t space is shown in Fig.1. Above 400G where the lower hybrid resonance takes place, there exists the evanescent region (hatched area) of the waves but there is no density limit for the fast wave propagation. An example of the radial propagation in this region is shown in Fig.1 for the parabolic density and CHS B_t profiles. The evanescent region (R cut off) appears at the plasma periphery, so if the fast waves are excited through this region, high density plasmas can be produced by the fast waves.

The maximum power of 500kW, pulse width of 10msec and the frequency of 9MHz is used for Whistler wave discharge. The 2.45GHz power of 50kW (200msec) is used for microwave plasma production and heating of the rf plasmas. The antenna for the wave exciter is Nagoya type III. The plasma density is measured by Langmuir probe near the antenna. In Fig. 2, the radial profiles of the electron density n_e (He plasma) where the radius ρ is normalized by the outmost flux surface are shown.

The microwave plasma can make an over dense plasma (cutoff plasma density is $7.4 \times 10^{10} \text{cm}^{-3}$) by some mode conversion process but tends to make hollow density profile. When rf power is superimposed on the microwave plasma, the central density increases and the profile changes to be more flat. This is due to the fact that there is no density limit for the Whistler wave propagation as is shown in Fig.1 and the wave can penetrate deep in the core plasma. The electron temperature for both rf and microwave plasmas is $\sim 8\text{eV}$.

Reference

- 1)Shoji, T., Nishimura, K, et al., Nagoya Univ. Ann.Report 6(1989)1
- 2)Nishimura, K., Shoji, T., et al., Fusion Tech. 17(1990)86

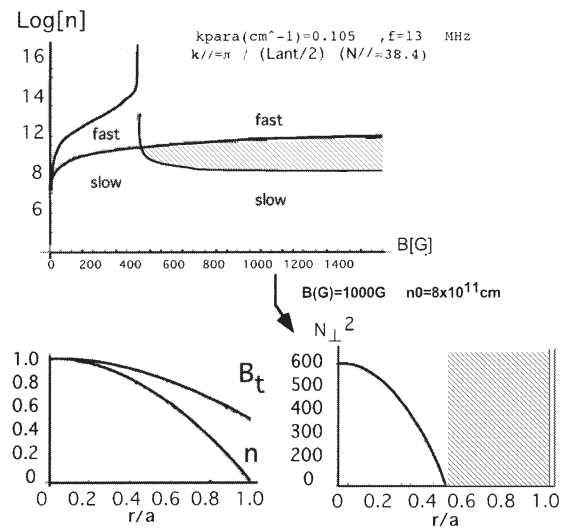


Fig. 1 Perpendicular wave propagation of Whistler (fast) and slow waves in plasma density n and toroidal field B space. The rf frequency $f=13\text{MHz}$ and parallel wave number $k_{\parallel}=0.105 \text{ cm}^{-1}$. Example of radial profile of perpendicular refractive index N_{\perp} for the Whistler wave.

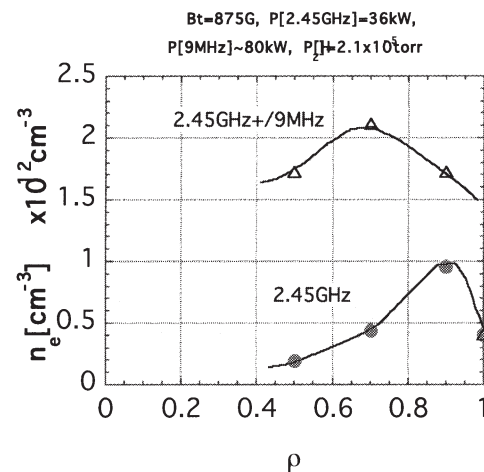


Fig. 2 Radial profile of the density profiles for microwave and rf+microwave plasmas (He). $B=875\text{G}$, $f=9\text{MHz}$, $P_{\text{rf}}=80\text{kW}$ and $P_{\text{microwave}}=36\text{kW}$.

§30. Observation of Space Potential Variation on Magnetic Surfaces on CHS

Wakabayashi, H. (Grad. Sch. Adv. Sci.), Himura, H. (Kyoto Institute of Technology), Isobe, M., Okamura, S., CHS Group

Magnetic surface is one of the most important and fundamental concepts in toroidal plasma confinement devices such as tokamaks and stellarators. In quasi-neutral fusion plasmas, physical parameters such as density and potential are thought to be constant on a magnetic surface.

However, in low density electron plasmas with finite temperature and irregular density, that is not the case. The parallel component of equilibrium force balance is written as

$$en_e \nabla_{\parallel} \phi_s = \nabla_{\parallel} p,$$

where ∇_{\parallel} and ϕ_s stands for derivative along a magnetic field line of force and the space potential, respectively. Assuming that T_e is constant on the magnetic surfaces, this equation can be written as

$$en_e \nabla_{\parallel} \phi_s = T_e \nabla_{\parallel} n_e,$$

which leads to the Maxwell-Boltzmann distribution. As we can see in the equation above, if T_e is finite and there is steep gradient of n_e , the pressure gradient should be balanced with the parallel component of the electric force by the potential gradient. So ϕ_s can vary along the magnetic field lines of force, as well as on the magnetic surfaces.

In our experimental studies on electron plasmas, we have investigated the ϕ_s profile of the electron plasma on helical magnetic surface configuration. And we have observed that there are cases on which ϕ_s is not uniform on each magnetic surface. The experiments were performed in CHS. An electron gun (e-gun) is inserted horizontally in 2-O port of the CHS along the r axis. Electrons are launched out into the vacuum magnetic field $B \sim 0.09T$ from the e-gun with acceleration voltage V_{acc} up to

1kV and emission beam current I_b up to 100mA. The electron plasma is generated by continuous injection of electrons for 40ms. For diagnostics, a Langmuir emissive probe is inserted vertically on 6-U port along the z axis. The probe is terminated with 100M Ω impedance to measure the space potential ϕ_s of the electron plasma.

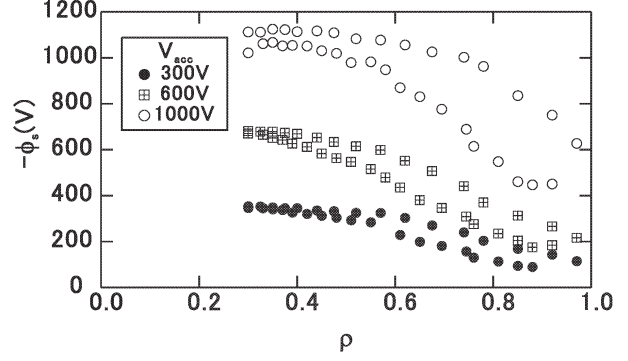


Fig. 1 Profiles of ϕ_s measured on the 6-U port of CHS. Two series of ϕ_s are recognized for each V_{acc} , insisting that ϕ_s is not constant on each magnetic surface. The e-gun is placed at $\rho=0.9$.

Figure 1 shows profiles of ϕ_s plotted against the normalized minor radius ρ . Three data sets are shown for $V_{acc}=300V$, 600V and 1kV. The position of the e-gun is 0.9 in this measurement.

Substantial differences of ϕ_s are clearly recognized on each magnetic surface, especially at the boundary region of the electron plasma. Two profiles of ϕ_s for each V_{acc} are measured in the $z>0$ and $z<0$ regions each other, and values at $z>0$ are negatively larger than $z<0$. The difference between the two series is almost proportional to V_{acc} , which implies that the variation is closely related to the electron energy.

By a dimensional analysis of the force balance equation, one can find that the value of potential variation along a magnetic field line of force can be on the same order of T_e . On our experimental situation T_e is not known properly so far, but it is estimated to be some hundreds of eV, which seems to be approximately consistent with the observed potential variations. Further investigations quantitatively verifying the potential variations will be shown later.

§31. Extreme Ultraviolet Spectroscopy of CHS Plasma for Use in Detailed Atomic Modeling

Nishimura, H. (Institute of Laser Engineering, Osaka U.)

1. Introduction

Radiations emanated from High-Z elements are of great importance to understand physics of energy transport in fusion plasmas. Such radiations are also useful as a bright source for various applications such as lithography of next-generation semi-conductor devices. Although developments of 13-14 nm extreme ultraviolet (EUV) are extensively undertaken, a lot of issues including atomic modeling must be clarified to generate an efficient EUV source for practical applications. Laser produced plasma inherently has sharp gradients in temperature and density so that spectra obtained from the plasma are generally not suitable as benchmark data for detailed spectroscopic modeling. Magnetically confined plasma is one of suitable candidates as a temporally and spatially uniform plasma source of well characterization with advanced plasma diagnostics.

2. Experiments

Last year, we have started the spectroscopic observation using Xe as an objective material. Overall EUV emission spectra were obtained with a grazing-incidence spectrograph covering the range from 0 to 100 nm with a 0.5 nm spectral resolution. But, it was not high enough to benchmark the detailed atomic model.

This fiscal year, temporal behavior of EUV emission from CHS plasmas consisting of a pure Xe gas was observed by implementing a flat-field grazing incidence spectrograph of the Institute of Laser Engineering, Osaka University. This covered the spectral range of 5-30 nm with a resolution of 0.06 nm. First, a preliminary experiment was made with HYPER-I facility [1] then, the spectrograph was moved to CHS. Wavelength calibration was made using He plasma and the observed lines were fitted to a theoretical response of the spectrograph. Overall wavelength identification better than 0.01 nm was attained.

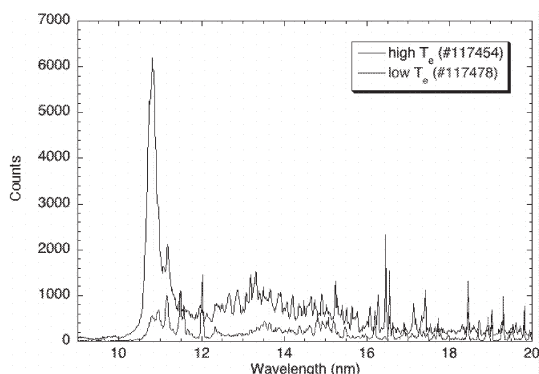


Fig. 1 Xe spectra from CHS plasma

Electron density and temperature distributions were measured using a probe in HYPER-I and the laser Thomson scattering in CHS. Temporal resolution of 10 ms was attained with a mechanical shutter set between the object plasma and the spectrograph.

Figure 1 is a typical spectrum for a pure Xe gas in the CHS for two different electron temperatures. Figure 2 shows electron density and temperature profiles for the case of higher temperature shown in Fig. 1. Observation was made from the direction perpendicular to the CHS torus. As a consequence obtained spectra were the accumulation along the plasma center to the edge. In comparison with the result of last year, an order of magnitude better resolution was attained so that very fine spectroscopic structures are obtained. The spectrum for the lower temperature compares well with that obtained by Sandia National Lab.. It is expected to obtain the data for the electron temperature of 20-60 eV and spatially resolved spectra.

3. Reports

- C. Suzuki, et al., Joint Meeting of 14th International Toki conf. and ICAMDATA4 (Oct. 2004, Toki, Japan)
- C. Suzuki, et al., 21st Annual Meeting of JSPF.
- H. Nishimura, et al., Plasma Science Symposium 2005 (January 2005, Nagoya).
- C. Suzuki, *ibid.*

4. Collaborators

The author would like to express his sincere appreciation to all contributors for their invaluable collaborations by listing their names: Okamura, S., Suzuki, C., Kato, T. and More, R., Tanaka, M. and Yoshimura, S. (NIFS), Ogawa, H. (JAERI Kansai), Nishihara, K. Fujioka, S. and Ochiai, M. (ILE, Osaka U.).

Reference

- [1] M. Y. Tanaka, M. Bacal, M. Sasao, and T. Kuroda, "High-Density Plasma Production for Neutralizing Negative Ion Beam", *Rev. Sci. Instrum.* 69 (1998) 980-982

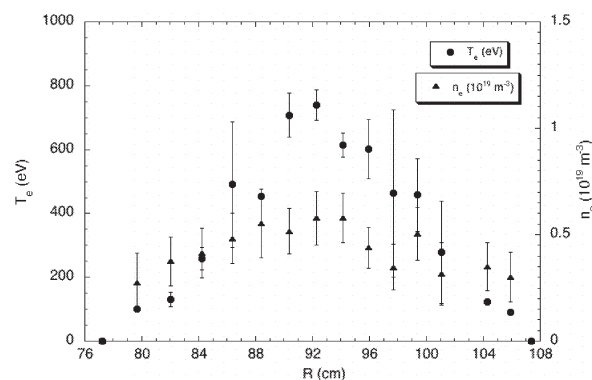


Fig. 2 Spatial profiles of electron density and temperature

§32. Trial Production of a Simple Neutral Particle Analyzer

Ishii, K., Kojima, A., Miyata, Y., Yamaguchi, T.
(Tsukuba Univ.)
Iguchi, H.

We investigated a simple type of neutral particle analyzer in order to measure both pitch angle and energy of the charge exchanged neutral particle caused by the ion trapped in the open and closed systems.

Ionization efficiency was estimated in the following two cases, that is, a carbon thin film with the thickness of 25 Å was used to ionize the charge exchanged neutral particle, and the other method was a gas stripping type. As an example, in case of the hydrogen atom with the energy of 5 keV, the ionization efficiency is about ten times as compared with using the gas stripping type, however the full width at half maximum of the scattering angle profile is about ten degrees in case of perpendicular injection. We calculated the detection efficiency of the charge exchanged neutral particle in conjunction with the toroidal type of energy analyzer having 5 channel detectors as shown in Fig.1.

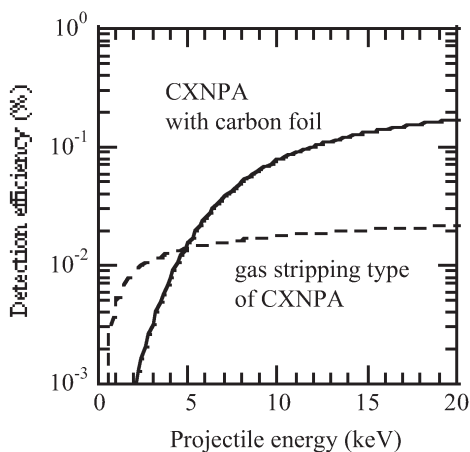


Fig.1. Detection efficiency of the charge exchanged neutral particle. The toroidal type of energy analyzer is used in the calculation.

The carbon thin film is better than the gas stripping type for the neutral particle with higher energy more than about 5 keV. The radius of the main path is 90 mm in the toroidal analyzer, the deflection angle is 155 degrees and

the azimuthal angle is spread to 35 degrees.

As the other method, we applied the gas stripping type of energy analyzer to the neutral particle detection with lower energy than about 5 keV. The cylindrical type of electrostatic energy analyzer was adopted, which had the deflection angle of 63.6 degrees and a wide entrance aperture. The analyzer has the useful characteristics of energy resolution for the parallel incident ions passing through the wide entrance aperture. The micro-channel plate is used as the ion detector and three channels are inserted behind the exit slit as shown in Fig.2.

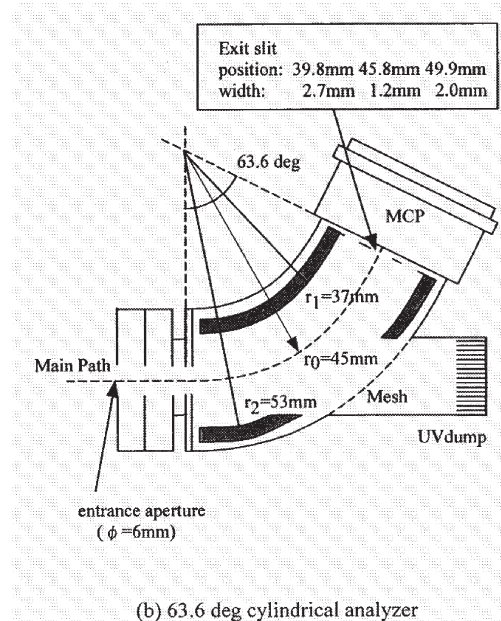


Fig.2. Cylindrical type of neutral particle analyzer with the deflection angle of 63.6 degrees.

The radius of the main path is 45 mm, the maximum of the analyzing energy is about 10 keV. We set the analyzer near the inner mirror throat of the plug/barrier cell in the tandem mirror with a pitch angle adjuster, and measured both pitch angle and energy of the charge exchanged neutral particles due to the bounced ions by the plug potential and the mirror throat of the plug/barrier cell.1) This type of analyzer is available to other magnetic confinement devices.

Reference

- 1) Ishii, K., et al.: Rev. Sci. Instrum. **75**, No.10 (2004) 3619.

§33. CHS Data Acquisition and Analysis System

Takahashi, C., Okamura, S., Ida, K., Fujisawa, A., Iguchi, H., Yoshimura, Y., Minami, T., Isobe, M., Nishimura, S., Suzuki, C., Nagaoka, K., Matsuoka, K.

CHS data acquisition and analysis systems, the Cinos and the VAX systems have been operated steadily without serious problem in this fiscal year. Total experimental data of 160 Gbytes have been acquired, which is 20 Mbytes/shot and 2.0 Gbytes/day in average. This number is smaller than that of the last year by 12 %. This is because CHS had stopped for three months due to trouble of the coil power supply. The 80 % of the total data has been acquired by the Cinos system. The rest 20% is by the VAX system. However, as the VAX system is getting old troubles are increasing, which are on the magnetic disk, the power supply unit and the terminal device. And we prepared for the Digital Linear Tape (DLT 600Gbyte on compression) drive unit when the old troubles happened.

Major improvements in this fiscal year are as follows. Two types of AD/c modules have been newly installed. One is a 4-channel CAMC high speed, single-end AD/c modules (12bit, 25MHz, 1Mbyte memory/channel) as shown in Fig. 1, which is used for plasma fluctuation analysis by HIBP and HCN laser scattering. The other is a 12-channel CAMAC high speed AD/c (12bit, 100KHz, 128K memory/channel) for the plasma fluctuation diagnostic. The Cinos system consists of eleven units, which is the same as that in last year. Six of new AD/c modules are installed on one of the local Cinos units for plasma fluctuation diagnostic.

Fundamental structure of the Cinos system in each unit is the same as in last year. Cinos is the multi computer system and each unit has three computers at present. One of three computers is running by UNIX. Since the load on UNIX computer becomes large, an additional computer module was installed and tested. This new computer has simple Linux operating system with better efficiency than the UNIX one. This Linux is the version of an early stage and has no GUI.

Many mechanical troubles occurred in the VAX system as mentioned above. But such troubles could be coped with by replacing peripheral devices. However, it is anticipated that such troubles will increase from now on. Therefore, the replacement of VAX with Cinos is being requested urgently.

Improvement and solving problems in the Cinos system

have been continued. The most serious problem is that the Cinos computer halts when irregular interruption occurs. This problem has lasted for a year. It is found to occur when two or more interruption appear within 10 μ second interval. This is because the Linear Time-Invariant Method (LTIM) of Cinos system cannot resolve two events with such short interval. We have analyzed details of the LTIM, CPU and VME bus timings, then found that it is necessary to have more than 10 μ seconds to complete one set of calculation with LTIM. In order to solve this problem, it is necessary to improve the microcomputer architecture and the speed of the VME bus.

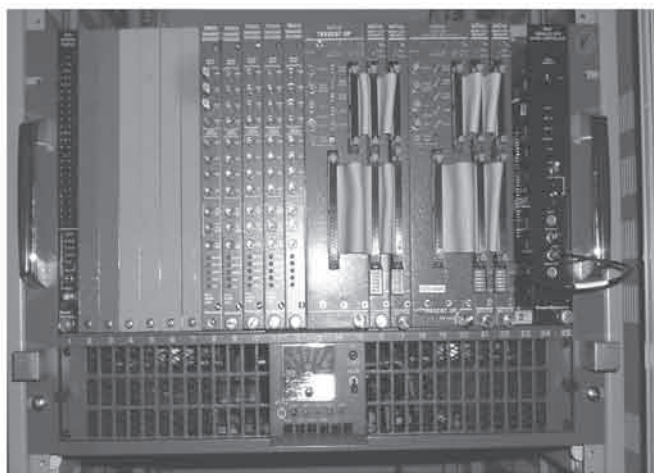


Figure.1. CAMAC fast AD/c modules are newly installed on the Cinos signal processing system.

Reference:

- [1] Takahashi, C. et al., Annual report of NIFS, April 1999-March 2000 277(2000)
- [2] Takahashi, C. et al., Annual report of NIFS, April 2000-March 2001 298(2001)
- [3] Takahashi, C. et al., Annual report of NIFS, April 2001-March 2002 302(2002)
- [4] Takahashi, C. et al., Annual report of NIFS, April 2002-March 2003 285(2003)
- [5] Takahashi, C. et al., Annual report of NIFS, April 2003-March 2004 297(2003)

4. Basic Research and Development

A variety of research activities are under progress with collaborations of many universities and institutions. These activities are categorized into basic plasma physics, atomic/molecular physics, application oriented plasma physics, and fusion oriented basic physics including design studies of advanced stellarator configurations.

The study on vortex formation has been continued in a series of experiments using the HYPER-I device. Since the plasma hole, which was found in a HYPER-I plasma for the first time, is identified as a viscous vortex, an experimental activity of HYPER-I group is focused on the measurement of anomalous viscosity. Other physics issue related to vortex formation is the occurrence of anti- \mathbf{ExB} vortex. To understand the mechanism of anti- \mathbf{ExB} rotation, flow velocity measurement of the background neutrals is under development. MHD phenomena in a HYPER-I plasma are also examined. Spontaneous magnetic fluctuations have been observed.

Experiments on atomic/molecular processes have been done in the NICE device. Charge exchange cross-section between highly charged ions and neutral species has been measured. Excitation processes in electron-ion collisions have been also examined in the ACE-IT II device. This research aims at getting the detailed information of excitation processes from an ejected-electron spectroscopy.

The experiments using the TPD-II device are focused on basic studies of divertor plasma, spectroscopy, and EUV source development. Reduction of reversed gas flow toward main plasma and impurity transport of divertor materials are important issues in divertor physics. A Thomson scattering system using a 532nm Nd:YAG laser was installed this year to examine a divertor-simulated TPD-II plasma. A macroscopic oscillation of detachment plasma is also examined with emphasis on plasma pumping effect. Basic studies on EUV source and negative ion source developments are in progress.

A variety of basic and novel experiments on plasma physics have been carrying out at Tohoku

Univ., Kyoto Univ., Kyushu Univ., Saga Univ., Kanazawa Univ. and Tokyo Univ..

Physics and engineering studies for the advanced stellarator configurations have been continued in the group of basic research and development. As well as studying specific topics of our basic design of a quasi-axisymmetric stellarator CHS-qa, a new method of optimization was dopted to study different types of configurations. Two topics were studied for the CHS-qa. Simulation of particle orbits was made to evaluate the eating efficiency of NBI. Orbits of high energy ions injected tangentially to the torus were followed with collision effect down to the thermal energy level. The spectrum and the distribution of the lost particles are calculated. The engineering problems are investigated in the design of scaled-up device of CHS-qa for the fusion reactor size. It is pointed out that the spacing problem between the plasma boundary and the inner surface of magnetic coils would be less critical for the larger scale device. A new principle of the configuration optimization was applied to the CHS-qa design to improve the alpha particle confinement. The distribution of the second adiabatic invariant is calculated on the magnetic surface and the optimization was made to minimize its variation on the surface. The technique of modular coil design used for the CHS-qa modular coils was applied to the new configuration of N=2 stellarator which was designed by the quasi-isodynamic (qi) principle. This qi-optimized configuration has a larger winding of the magnetic axis in three-dimensional space. This structure makes modular coil design more difficult than CHS-qa. Two theoretical works were made for refining a calculation procedure for the bootstrap current. New formula is proposed for the geometric factor, which is useful in numerical evaluations. A method of avoiding a logarithmic singularity is given in the Fourier series of parallel viscosity calculation.

(Tanaka, M.Y.)

§1. High Density Plasma Experiment HYPER-I

Tanaka, M.Y., Yoshimura, S., Tomida, A. (Nagoya Univ.), Yamaguchi, H. (Nagoya Univ.), Aramaki, M. (Nagoya Univ.), Okamoto, A. (Tohoku Univ.), Tsushima, A. (Yokohama National Univ.), Saitou, Y. (Utsunomiya Univ.)

High Density Plasma Experiment-I (HYPER-I) is a linear device with magnetic fields designed for various basic plasma experiments. Plasmas are produced and sustained by electron cyclotron resonance heating with an electron cyclotron wave (ECW), which is excited by a 2.45GHz microwave launched along the magnetic field line from an open end of the cylindrical chamber. Two microwave sources are available; one is a magnetron oscillator with 15 kW output, and is used for low power experiments. A klystron amplifier with 80 kW output (CW) is also available for high power and high density experiments.

The maximum plasma density is two orders of magnitude higher than the cutoff density of ordinary mode with a same frequency. The characteristic features of HYPER-I plasma are large diameter (30 cm) and high density ($< 10^{13} \text{ cm}^{-3}$). In 2001, a set of probe driving systems was installed to measure the flow vector field on a plane perpendicular to the magnetic field. Velocity vector measurements are possible over 80% of the whole cross-sectional area of the plasma. A tunable dye laser system was introduced in 2003 to develop a laser-induced fluorescence (LIF) Doppler spectroscopy. The dye laser is excited by a pulsed Nd:YAG laser, and produces 30 pulses per second (max. 100 mJ /pulse) in a range of wavelength 600-630nm. A tunable diode laser system for measuring the flow velocity of

background neutrals is under development in collaboration with Nagoya University.

The research activities are mainly focused on vortex formation, viscosity anomaly, and flow velocity measurement using an asymmetric probe.

(i) vortex formation and anomalous viscosity

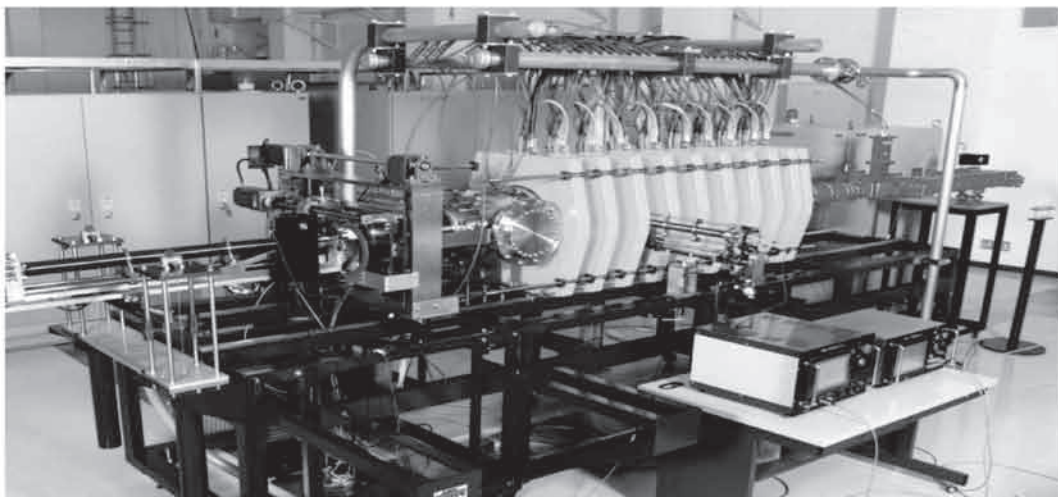
A vortex with a cylindrical density cavity (referred to as plasma hole) has been observed, and identified as a viscous vortex such as Burgers vortex. The characteristic feature of viscous vortex is the existence of radial flow, which is driven by the azimuthal velocity shear and finite viscosity. We proposed that effective viscosity can be determined by measuring the radial flow velocity and azimuthal velocity shear. The preliminary experiment was carried out and revealed that the effective viscosity is at least 2 orders of magnitude higher than the classical estimation.

(ii) anti- $E \times B$ vortex

Usually, vortical motion in a plasma is driven by the $E \times B$ drift. We have observed a peculiar vortex, which rotates to the opposite direction to the $E \times B$ drift. It is found that this vortex always accompanies with a deep density hole in the background neutrals. If the charge exchange process is dominant, a net momentum exchange between the neutral flow and plasma may drive the anti- $E \times B$ rotation. We are now developing a LIF system using a tunable diode laser to detect the flow of neutrals.

(iii) velocity measurement using an asymmetric probe

For the simultaneous measurement of flow velocity, we are developing a new method using an asymmetric probe. This probe detects an unbalanced ion current between two electrodes and provides an easy-to-use method for flow velocity measurement. The dye-laser LIF Doppler spectroscopy will be used for the calibration of this probe.



§2. Observation of Plasma Hole Transition Induced by Microwave Power Modulation

Yoshimura, S., Tanaka, M.Y.,
Tomida, A., Yamaguchi, H. (Nagoya Univ.)

Spontaneous formation of a stationary vortex structure with density depletion, or *plasma hole*, has been observed in a magnetized plasma. We have so far reported many characteristic properties of the plasma hole as follows. (i) The flow-velocity field is analogous to that of typhoon. (ii) The vorticity distribution is identified as Burgers vortex. (iii) Strong electric field that drives $E \times B$ rotation is attributed to anomalous quasi-neutrality breaking.

However the transitional behavior of plasma hole formation is not entirely revealed yet. In previous experiments, we have observed that the hole structure has been formed and sustained in a definite microwave power range. Thus we conducted a microwave power modulation experiment so as to investigate the detailed change in density and plasma potential. The experiment was carried out in the HYPER-I device at NIFS. A cylindrical plasma (30 cm in diameter and 200 cm in length) was produced by electron cyclotron heating. Helium gas was used at a pressure of 5.0×10^{-4} Torr. The frequency of the power modulation and the range of power variation are 0.1 Hz and 5.1 ± 3.3 kW, respectively. The temporal evolution of ion saturation current, which approximately corresponds to that of plasma density, was measured by a Langmuir probe, and that of plasma potential by an emissive probe.

Figure 1 shows the change in density and potential profile due to microwave power variation. When the microwave power is 1.8 kW, the density profile is almost flat and the potential forms a convex distribution with a gentle slope. By increasing the microwave power to a certain threshold value, which lies between 3.5 kW and 4.7 kW, an abrupt density drop in the central region takes place and the density depletion characterizing the plasma hole is established. Note that once the density hole is developed, the size of that remains unchanged. In other word, it is independent of the microwave power. In conjunction with the hole formation, the plasma potential starts building up around the central axis to establish a bell-shaped distribution. It is noteworthy that a steep gradient in potential, or strong electric field, is localized inside the hole, which gives rise to the vortex

motion due to $E \times B$ drift. Moreover the potential attains its maximum value of +100 V, which is five times higher than the electron temperature.

The measurement of the evolution of flow-velocity field is planning to understand the dynamic behavior of vortex formation in detail. It should be emphasized that a definite inward-directed radial flow has been observed under the existence of hole structure in our preliminary experiments. In general, it is derived from the fluid equation that a viscous fluid with shear flow inevitably has radial flow. This fact implies that we should take a nonnegligible viscosity of the plasma into account to comprehend the property of the plasma hole integrally. In addition, a general relation between radial flow and viscosity has a possibility to provide a novel means for viscosity measurement.

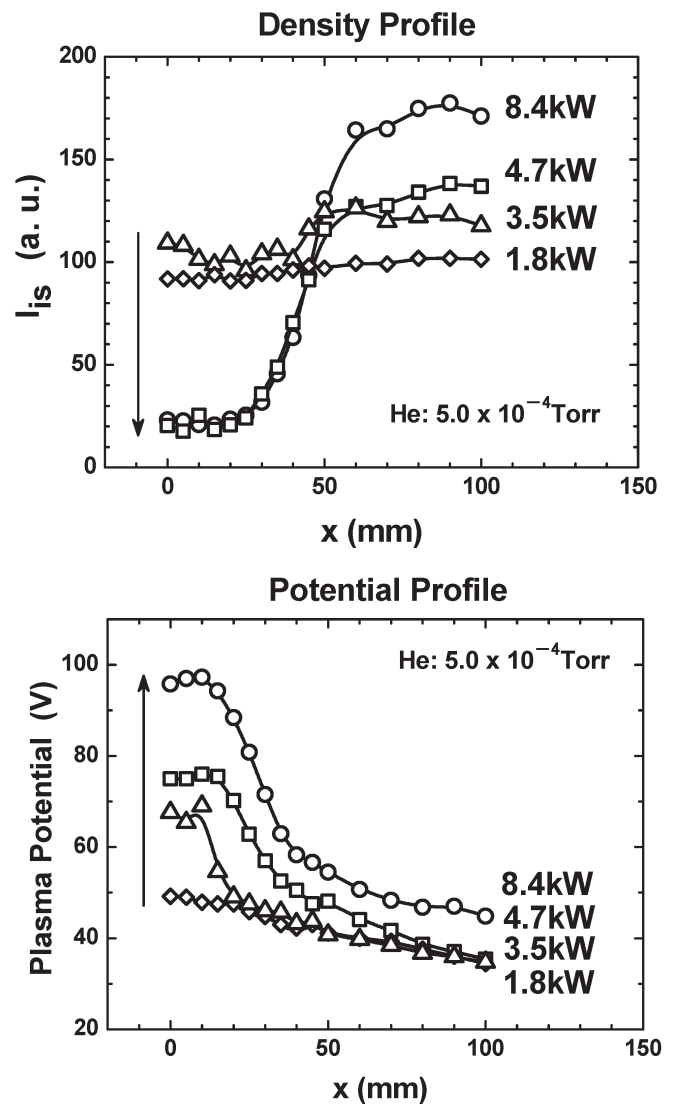


Figure 1 Change in density and potential profile due to microwave power variation.

§3. Measurements of Neutral-gas Flow in High-density Plasma Using a Tunable Laser Diode

Aramaki, M., Kono, A. (Nagoya Univ.)
Okamoto, A. (Tokyo Univ.)
Yoshimura, S., Tanaka, M.Y.

Various types of selforganized vortex were found in HYPER-I. In order to clarify the dynamics of the selforganization of the plasma, it is important to get to know both of ion flow and neutral-gas flow in the plasma. In this collaboration, we will perform a Doppler laser induced fluoresce (LIF) measurements of argon atoms. The neutral-gas flow will be estimated from the frequency shift of Doppler spectrum. In this fiscal year, we made a external-cavity diode laser (ECDL) which excites the metastable argon atoms. We performed Doppler LIF measurements of a test plasma using the laboratory-made ECDL.

Figure 1 shows our laboratory-made ECDL. We used a single mode AlGaInP laser diode HL-6738MG which was manufactured by HITACHI Corporation. The output power of the laser diode was 35 mW at 690 nm. The setup of the ECDL was assembled on an aluminum plate which was kept at 28.7 ± 0.1 °C in temperature by using a Peltier device. The wave length of the ECDL was adjusted to 696.543nm which excites the $4s'[3/2]_2^o - 4p'[1/2]_1$ transition of argon atom by horizontally tilting the grating with the fine adjustment screw. Because the wave length is near the edge of gain curve of the laser diode, the output power of the ECDL was decreased to 17mW. Continuous wavelength scan of 10 pm was achieved by means of the grating PZT. The maximum scan width of wavelength can be extended by changing synchronously the grating PZT and the current of LD.

We construct a test chamber and applied the ECDL to LIF measurements of the metastable argon atom in test plasma. Figure 2 shows our experimental setup for LIF measurement. Both of the diameter and the axial length of the vacuum chamber were 100 mm. A Pyrex glass discharge tube with a length of 300 mm and a diameter of 30 mm was attached to one end of the chamber. Argon gas was introduced from the other side of the glass tube. The vacuum chamber was evacuated using a turbo molecular pump. A three-turn helical rf antenna was wound around the discharge tube. The rf antenna was placed at 250 mm from the chamber. The rf power supply at 14 MHz was connected to the antenna via a matching network. We measured the LIF signal at the position of 300 mm from the rf antenna. LIF signal was focused on the entrance slit of a spectrometer. The observation wavelength was 727.293 nm. The resolution of the spectrometer was significantly lower than the Doppler width of argon atoms, therefore the spectrometer did not affect the shape of the Doppler spectrum. LIF signal was detected by a photomultiplier and recorded by an oscilloscope which was controlled by a personal computer. Figure 2 shows a Doppler LIF spectrum

of metastable argon atoms. The horizontal axis indicates the detuned wavelength from the resonant center. The wave length was measured by using a wavelength meter. The argon gas temperature was estimated as 220 K from the Doppler broadening. The unusual low temperature was caused by the inaccurate horizontal axis. In the next step, we will calibrate the wavelength by using a Fabry-Perot interferometer in order to perform precise measurements of a gas flow inside the HYPER-I.

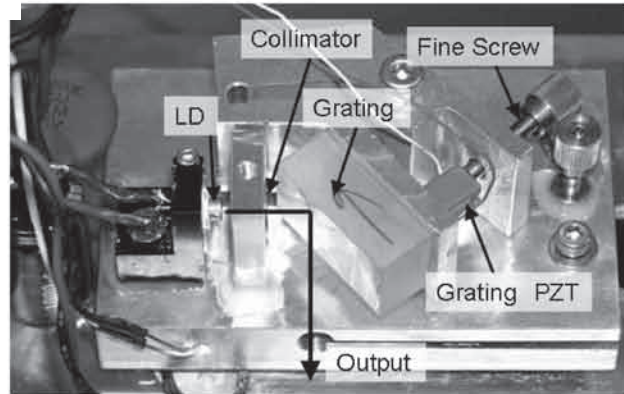


Fig. 1 Laboratory-made 696nm-ECDL. Continuous wavelength scan of 10 pm was achieved by means of the grating PZT.

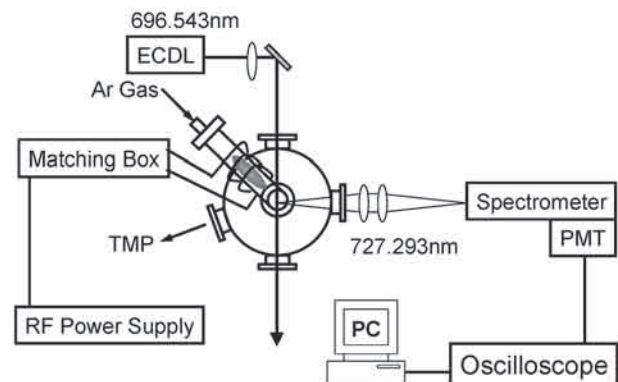


Fig. 2 Experimental setup for LIF measurement using ECDL

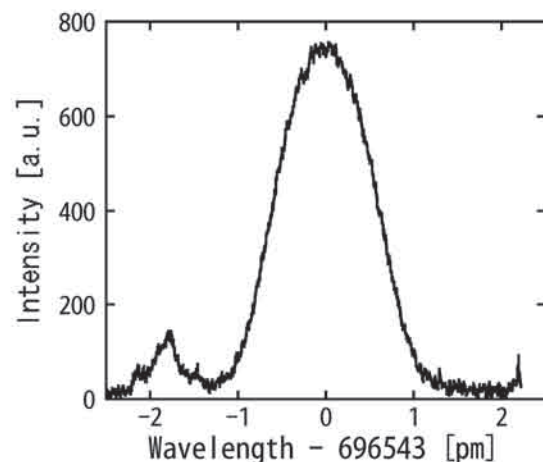


Fig. 3 Doppler LIF spectrum of argon atoms. The horizontal axis should be calibrated by using a Fabry-Perot interferometer.

§4. Measurement of Rotational Flow Velocity Using Laser-Induced Fluorescence Spectroscopy

Okamoto, A., Kado, S. (Univ. of Tokyo)
Yoshimura, S., Tanaka, M.Y.

Recently, a variety of vortical flow structures have been observed in an electron cyclotron resonance plasma,^{1,2)} and are attracting much attention with respect to self-organization and transport. To study vortices in a plasma, which are identified by a vorticity distribution, we have to have velocity field data to construct the vorticity distribution on a plane under consideration. Thus, a direct method of absolute velocity measurement, which also has spatial resolution, is needed. Doppler-shifted fluorescence induced by a tunable laser (LIF) has the advantages of both spatial resolution and absolute velocity measurement.³⁾

In the present experiment, the laser wavelength is tuned to 611.5 nm, which excites an ArII metastable state ($3d^2G_{9/2} - 4p^2F_{7/2}$). We observe de-excited spontaneous emission of wavelength, 461.0 nm ($4s^2D_{5/2} - 4p^2F_{7/2}$). The experiments were performed in the HYPER-I device at the National Institute for Fusion Science.⁴⁾ A schematic drawing of the experimental setup is shown in Fig. 1. A tunable dye laser excited by a Nd:YAG laser produces 30 laser pulses per second, which are transferred with mirror optics and injected into the plasma from a side viewing port. The chord of the laser beam is changed by the position of the side mirror, and its movable range is vertically ± 75 mm.

The laser-induced fluorescence from argon ions is observed from counter-directed fiber optics with collimator lenses, and is detected using a monochromator equipped with a photomultiplier tube. The output signal of the photomultiplier tube is integrated with a boxcar integrator synchronized with the laser pulse. By changing the vertical position of the laser beam, we measured the rotation (azimuthal) velocity of an argon plasma. The output of the boxcar integrator is shown in Fig. 2 as a function of dye laser wavelength. We note that the horizontal scale in Fig. 2, which is the value indicated in the dye laser controller, is shifted about 0.06 nm from the wavelength in the air. Although the line profiles include Zeeman effect due to the external magnetic field (~ 0.09 T), the effect is too small to be distinguished in the present experiment. The solid lines are the Gaussian fitting curves for each case ($y=\pm 30$ mm).

The peak positions of the two profiles relatively shift by 0.008 nm, which corresponds to a velocity difference of 4 km/s. The LIF spectrum, which blue-shifts for the $y=30$ mm case and red-shifts for the $y=-30$ mm case, means that the ions rotate counterclockwise (see Fig. 1).

These results show that LIF spectroscopy is a promising tool for local and absolute measurement of flow velocity. They may also suggest that a combined system of directional Langmuir probe (DLP)⁵⁾ and LIF spectroscopy as a calibration standard resolves the ambiguity of absolute value in the DLP method and improves reliability, particularly in the supersonic region.⁶⁾

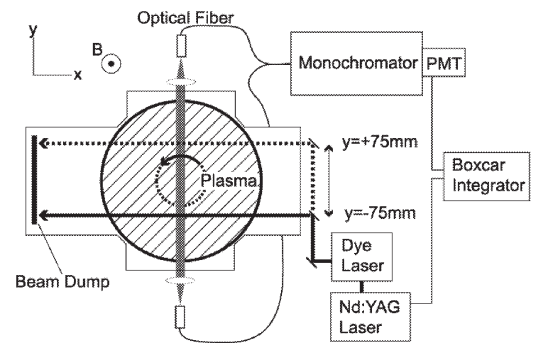


Fig. 1 Schematic drawing of experimental setup

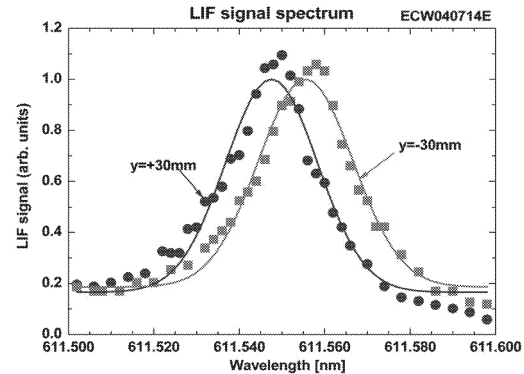


Fig. 2 Output of boxcar integrator as a function of dye laser wavelength. The solid lines indicate Gaussian fitting curves for each case.

Reference

- 1) Nagaoka, K. et al. : Phys. Rev. Lett. **89** (2002) 075001
- 2) Okamoto, A. et al. : Phys. Plasmas, **10** (2003) 2211
- 3) Anderegg, F. et al. : Phys. Rev. Lett. **57** (1986) 329
- 4) Tanaka, M. et al. : J. Phys. Soc. Jpn. **60** (1991) 1600
- 5) Nagaoka, K. et al. : J. Phys. Soc. Jpn. **70** (2001) 131
- 2) Okamoto, A. et al. : J. Plasma Fusion Res. SERIES, **6** (2005) 606

§5. Observation of Neutral Particle Distributions in a Plasma Vortex Using a Few Lines of Sight of Visual Light

Saitou, Y. (Utsunomiya Univ.)
Tsushima, A. (Yokohama National Univ.)
Yoshimura, S., Tanaka, M.Y.

In plasmas, various vortical structures are formed depending on experimental conditions. Mechanisms on their formation are physically interesting and attracting. It is reported that such vortical structures are formed in the HYPER-I device of National Institute for Fusion Science. The vortex shows several variations when strength of magnetic fields of the device, gas pressure, and injecting power of microwaves are tuned properly. A lot of investigations on the structures have been reported.^{1,2)} A purpose of the present work is to observe the density distributions of ions and neutral particles in the vortical structures using a few lines of sight of visual light, a non-contact observation, without disturbing plasma.

Experiments were carried out using the HYPER-I device. Argon gas was used at a pressure of 1.8×10^{-2} Torr, and a flow rate of 0.39 sccm. An electric current applied to each magnetic coil to induce a magnetic field was 115.8 A. A microwave was injected at a power of 9 kW. Under these experimental conditions, a vortex with a “single-eye”, where there is a bright part of relatively strong emission of the visible light, is formed at a center of a cross section of the device along the chamber axis. To observe the neutral particle distribution at a cross section of the device, two lines of sight, horizontal (x) and vertical (y) directions, are adopted. These lines of sight detect the strength of visible light from the vortex with wavelengths 425.9 nm from neutral particles (ArI) and 488.0 nm from monovalent argon ions (ArII). From the detected strength of the visible light at each position of the detector, spatial profiles of the strength of the emission are obtained. The neutral particle distribution is reconstructed using the spatial profiles with Abelian transformation method.

On the basis of these obtained profiles, spatial density profiles of the ion and neutral densities are estimated using equations, $n_i \propto \sqrt{I_i}$ and $n_n \propto I_n / \sqrt{I_i}$, where n_j and I_j denote the density and intensity of the emission of j ($= i$ for ion and n for neutral particle) species, respectively. The spatial density profile of the ions and neutral particles are shown in Fig. 1 and 2. It is hard to find a huge difference in the horizontal and vertical distributions on both cases of the ions and neutral particles. It is also found that the ion

density approximately distributes uniformly or shows a small convex in space. On the other hand, the neutral density shows a concave distribution. This means that the ion density is slightly high and the neutral density is low at the bright part around the center of the vortex.

In summary, the density distributions of ions and neutral particles in the vortical structures using a few lines of sight of visual light are obtained. This method is a non-contact observation. Plasma and the vortex structure are never disturbed by the observation. It will be clarified that a role of neutral particles for the vortical structure formation in near future.

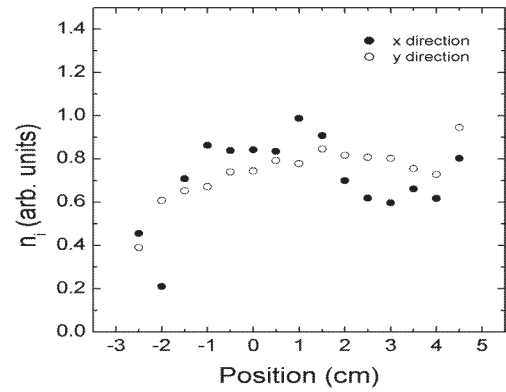


Fig. 1. The spatial density profile of ions.

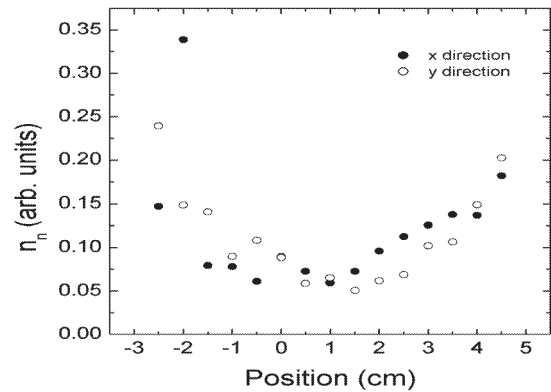


Fig. 2. The spatial density profile of neutral particles.

References

- 1) A. Okamoto, K. Nagaoka, S. Yoshimura, J. Vranješ, S. Kado, M. Kono, and M. Y. Tanaka, IEEE Trans. Plasma Sci. **33** (2005) 452
- 2) M. Y. Tanaka, K. Nagaoka, A. Okamoto, S. Yoshimura, and M. Kono, IEEE Trans. Plasma Sci. **33** (2005) 454

§6. Spontaneous Magnetic Fluctuation in HYPER-I Plasma

Tsushima, A. (Yokohama Nat. Univ.),
Yoshimura, S., Tanaka, M.Y.

MHD phenomena commonly play an important role in astrophysical plasmas and confined plasmas in toroidal devices. There are increasing demands in laboratories to realize an MHD plasma in a linear device since the basic understanding on MHD phenomena can be easily obtained in a plasma with simple geometry. However, MHD plasmas are only produced in a few specially-designed linear devices except toroidal confinement devices because of difficulty of producing a high density plasma.

The characteristic features of HYPER-I plasma are high density and low magnetic field intensity, which may provide an MHD plasma condition in an open linear device, and thus an experimental environment for studying MHD phenomena.

Spontaneously excited magnetic fluctuation has been observed in a high density operation of the HYPER-I device, where an argon plasma is produced by high power (10 kW) microwave with a frequency of 2.45 GHz. The typical plasma parameters are as follows: $n \sim 1 \times 10^{13} \text{ cm}^{-3}$ and $T_e \sim 10 \text{ eV}$. Since the ambient magnetic field is 900 G, the beta value of the plasma is as high as 0.4%, which is exceptionally high among existing open-ended linear devices.

Figure 1 shows the magnetic fluctuation measured with a magnetic probe located at 3 cm from the center axis of plasma. In the magnetic probe, a 100-turn coil with a diameter of 2 mm was installed in a ceramic tube of 8 mm in diameter for thermal insulation. The detected fluctuation is the perpendicular component with respect to the magnetic field, and the parallel component is much smaller than the perpendicular one. The frequency of the largest component of the measured magnetic fluctuation is about 100 kHz, which is about three times higher than the ion cyclotron frequency (36 kHz) and much lower than the lower hybrid frequency. Since the magnetic fluctuation was synchronously observed along the magnetic field, we measured the radial profile of the time averaged square of the fluctuation field. The result is depicted in Fig.2, which

indicates that the intensity of the magnetic fluctuation peaks at $r \sim 3 \text{ cm}$. When the spontaneous magnetic fluctuation occurs, high energy electron bursts ($\sim 100 \text{ eV}$) are observed in the core region of the plasma. Furthermore it is quite interesting to note that these high energy electrons are axially emitted both sides from a fixed position corresponding $\omega/\omega_{ce}=0.9$. It is also interesting that there exists a burst in magnetic fluctuations synchronous with the high energy electron emission. Although the detailed understanding on this phenomenon has not been obtained, the experimental results shows that there may be a close relation between the MHD activities and particle acceleration. We may conclude that the HYPER-I device provides a new environment for studying MHD phenomena in a simple geometry and in a steady state plasma condition.

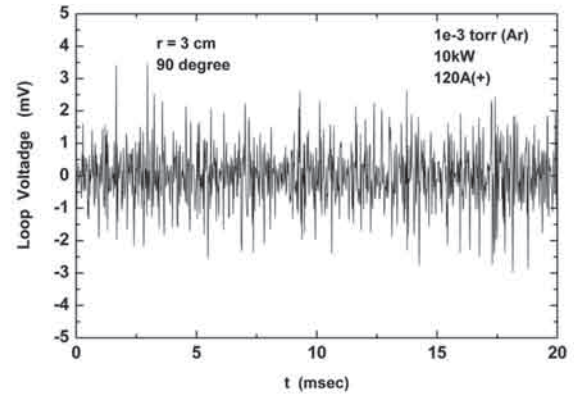


Fig.1 Perpendicular magnetic fluctuation measured with a magnetic probe. Radial position $r = 3 \text{ cm}$.

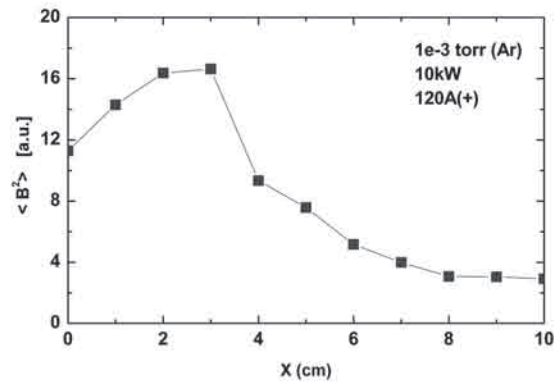


Fig. 2 Radial profile of intensity of magnetic fluctuation. High-energy electron bursts are observed $r \sim 3 \text{ cm}$.

§7. A Study of Charge Exchange Processes by Collision with Excited Atoms

Matsuda, W., Sakai, Y., Miyauchi, N., Jin, W.G.
(Dept. of Phys., Toho Univ.)
Sakaue, H.A., Yamada, I.

In collision between highly charged ions(HCIs) and neutral species, charge exchange processes are the dominant ones. In the charge exchange spectroscopy(CXS), using these processes the plasma diagnosis is carried out for thermonuclear plasma. When HCIs collide with excited neutral species, a large growth in charge exchange cross section is possible under the classical overbarrier model as a resonance. The present study is a elementary experiment to discuss the probability of the resonant charge exchange spectroscopy(RCXS) that is proposed substitution for the CXS. On the other hand, since the charge exchange processes work as a cooling mechanism in plasma of the nuclear fusion reactor and most of the particles in plasma are expected to be in excited states, this study is fundamental one for the quantitative analysis of the edge plasma behaviors. In this study, we used alkali atom as the target, because it is easy to produce excited species. The goal for this study is the measurement of the total absolute electron capture cross sections for HCI-excited atom collisions.

We had already reported about the total absolute electron capture cross sections in the HCI collisions with rare gas atom targets (Ne, Ar, Kr and Xe) and simple molecular targets(H_2 , N_2 , CO, CO_2 and CH_4), and a scaling law had been proposed, which is described by the ratio of the charge to the squared first ionization energy of target¹⁾. In the previous work, it is found that the coefficient of that scaling law as a scaling factor for alkali atom targets, Na, Rb and Cs, is different from that of rare gas ones²⁾. In this work, we tried to do the experiment on HCI collision with the excited Rb target.

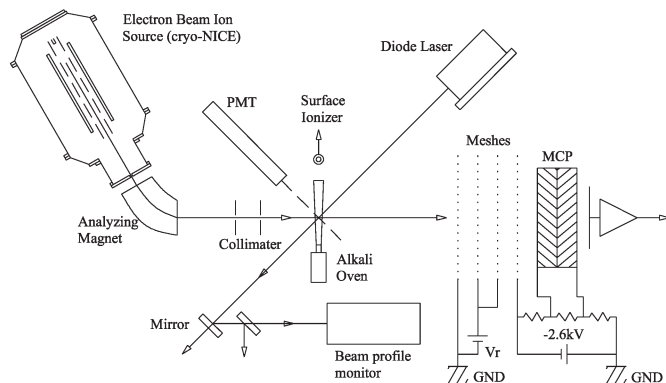


Figure 1: The experimental apparatus for excited alkali metal atom targets.

Figure1 shows the simplified schematic of experimental setup. The HCI was produced by the electron beam ion source(NICE) and led to the collision region after the charge

selection. In this work, I^{q+} ions were used as the HCI, where I^{q+} is the q-fold charged iodine ion($q=6\sim30$).

The Rb atom beam was generated through a thermal oven and excited from the ground state to np resonance state with a diode laser. The light from laser at center wavelength 780 nm was delivered to the collision chamber, and operated on the $5s \rightarrow 5p$ transition. The photomultiplier tube(PMT) with a band-pass filter was used to ascertain the ratio of excited Rb atoms to no-excited ones. When the fluorescence signal observed from $5p$ resonance state was saturated, it is indicated that the 50% Rb atoms were excited in the Rb beam. The power and wavelength of laser were measured after passing through the Rb beam. We modulated the laser wavelength by using an externally generated analog signal to modulate the voltage of the piezoelectric actuator.

Both the I^{q+} ions and $I^{(q-j)+}$ ions changed the charge were led toward the four meshed electrodes situated at the front of microchannel plate(MCP) after interacting between HCI beam I^{q+} and Rb beam in the collision chamber. The retarded voltage V_r was applied to the second and third meshes which were connected together. The ions, retarded between the first and second meshes yet passed through the third mesh, were accelerated to the fourth mesh, and the ions were finally detected with MCP. The HCIs collided with both excited and no-excited Rb atoms when the laser system was operated, while they collided with only no-excited Rb ones when the light from laser was not delivered. Since the absolute electron capture cross sections in I^{q+} -no-excited Rb collision had been already measured, we can determine the cross sections for excited Rb by comparing two results, as follows.

$$\sigma_{ex} = \sigma_n \times (2I_{ex} - I_n)/I_n. \quad (1)$$

Where σ_{ex} and σ_n mean the total electron capture cross sections, and I_{ex} and I_n are the signal intensities, the subscript ex is for the excited target and n for the no-excited one, respectively.

In order to determine the correct cross sections for excited Rb, we have to keep the Rb beam intensity, laser power and wavelength. The Rb beam intensity was monitored by a surface ionizer. We can change the target density from the current and temperature of the atomic oven. The current is about 20 nA on average at that beam monitor under the condition of the temperature at 50°C in the Rb oven. Besides, it was confirm that the fluorescence signal was saturated and the stray light of laser is less than 1% for any laser power conditions. Thus the quantity of excited Rb target was good enough for this experiment. Although any electron capture signals have not been detected yet, the experimental setup have been constructed.

References

- 1) M.Kimura et.al., J.Phys.B **28**, L643(1995).
- 2) H.A.Sakaue et.al., Abstracts of Contributed Papers of 21st. ICPEAC **2**, 552(1999).

§8. Ejected Electron Spectroscopy in Electron-Ion Collisions

Sakaue, H.A., Yamada, I.,
Hirayama, T. (Rikkyo Univ.),
Ohtani, S. (Univ. Electro-Communications),
Sakurai, M. (Kobe Univ.)
Takayanagi, T. (Sophia Univ.)

The understanding of the interaction of electron-ion collision process is important not only for the control and diagnostic of plasma but also for the atomic physics at many atomic processes in high temperature plasma. The research of ionization process in the electron-ion collision had been done for a long time, and the data were offered to the plasma control, the diagnostics of plasma and so on. At present, however, there are few atomic data for the excitation processes of electron-ion collisions, because of its experimental difficulties such as a low signal-to-noise ratio due to a low target ion density and very small cross sections, etc.

So, we have started the systematic research of ionization and excitation processes in electron-ion collisions. This research aims at getting the detailed information of excitation processes from high resolution ejected electron spectroscopy and measuring the ionization cross section within errors of 1%. Presently, we reconstructed the high density ion source for the exclusive use of the electron-ion collision experiments and we developed the ejected electron energy analyzer which is electrostatic tandem type uniquely.

We show the experimental parameters which were achieved in the following.

Ion Beam:

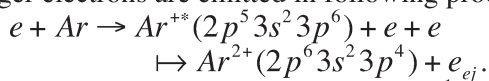
Ar^+ $I=340\mu A$ at 33keV, Kr^+ $I=160\mu A$ at 33keV, Xe^+ $I=40\mu A$ at 16keV, beam configuration 3mm ϕ .

Electron Beam:

$I=200\mu A$ at 500eV, beam configuration 15 \times 3mm.

We fine-tuned the ejected electron analyzer by using the Auger spectrum at the electron atom collisions.

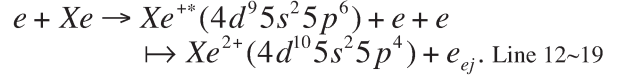
The spectra of LMM Auger at electron-Ar collisions are shown in figure 1-(a). The collision energy is 800eV and observation angle is 90 degree. These Auger electrons are emitted in following processes,



Then, Auger electrons of $L_3M_{2,3}M_{2,3}(^1D_2), (^3P_{0,1,2})$ are dominant. In figure 1-(b), we show the Auger spectrum of T.Kondow et al. [1] ($E_c=860eV$, $\theta=15^\circ$).

In figure 2-(a), we show the NOO Auger spectrum

of electron-Xe collisions. The collision energy is 500eV and observation angle is 90 degree. These Auger electrons are emitted in following processes,



Then, Auger electrons of $N_{4,5}O_{2,3}O_{2,3}$ are dominant. The line 7~11 are peaks of $N_{4,5}O_1O_{2,3}$ Auger processes. In figure 2-(b), the Auger spectrum of B.S.Min et al. [2] ($E_c=500eV$, $\theta=70^\circ$) is shown.

The resolution of our spectrum is not good rather than other one. From now on, we will have to improve the resolution of our spectrum. Then we will proceed with the research of the electron-ion collision processes

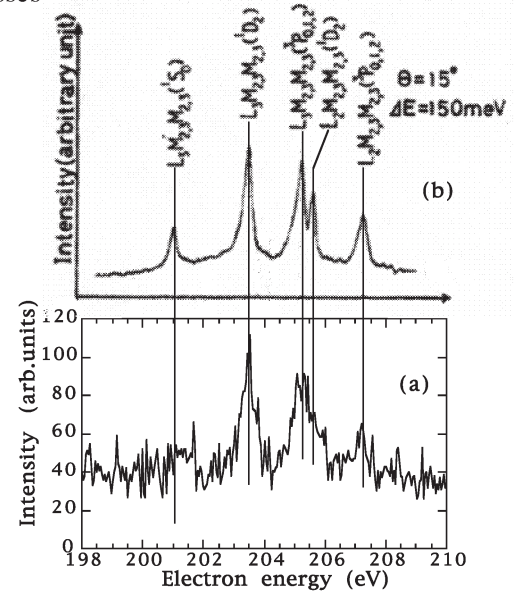


Fig. 1 Ar LMM Auger spectrum.

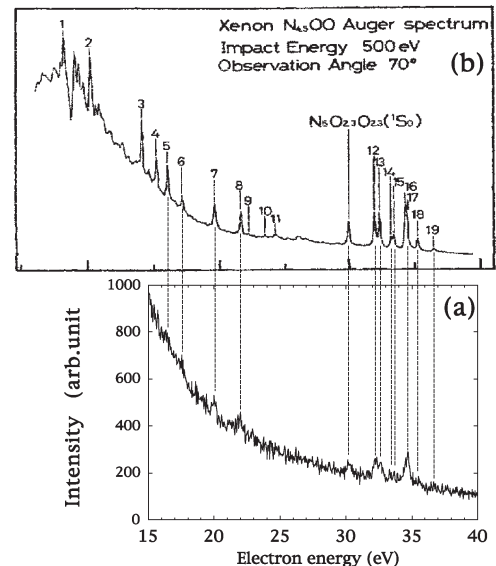


Fig. 2 Xe NOO Auger spectrum.

Reference

- 1) T. Kondow et al., J. Phys. B6 L156(1973)
- 2) B.S.Min et al., J.P.S.J.64 1183(1993)

§9. Isotope Effect on Charge Transfer by Slow Hydrogen Ions from Hydrogen Molecules

Kusakabe, T. (Dept. Phys., Kinki Univ.)
Kimura, M. (Kyushu Univ.)
Pichl, L. (Div. Natural Sci., ICU)
Sakaue, H.A.

Among many dynamical processes, charge transfer process of slow H^+ ions in collisions with H_2 molecules is the most fundamental “ion-molecule” collision. Therefore a number of measurements for the $H^+ + H_2$ collision had been reported over a wide range of the collision energy in past decades. It has long been believed that there is no, or very little, difference in the charge transfer cross sections between $H^+ + H_2$ and $H^+ + D_2$ collisions in the collision energy above a few tens of eV, because the difference of the binding (ionization) energy, one of the most critical parameters in charge transfer, of an electron between H_2 and D_2 is merely 41 meV. Only one data set of earlier experimental attempts suggested a possible difference at the energy range between 0.05 to 0.4 keV/u.^{1,2)} We have recently revisited this problem and indeed clearly observed, for the first time, the significant difference in charge transfer cross sections between H_2 and D_2 for H^+ ions at energies below 2.0 keV.^{3,4)}

The above charge-transfer processes at low collision energies are known to be important in a number of applications, especially in the controlled thermonuclear fusion research. In order to obtain more comprehensive understanding about the isotope effect on charge transfer in ion-molecule collisions of the hydrogen family, therefore we have measured the charge transfer cross sections, which have been determined by the initial growth rate method, of H^+ ions colliding with the HD molecules in the energy range of 0.18 to 1.5 keV and D^+ ions colliding with HD and D_2 molecules in the energy range of 0.3 to 2 keV. And theoretical analyses based on the molecular-orbital expansion method have been applied to these collisions taking into account the Frank-Condon principle.

Figure 1 shows the present cross section ratio of the charge transfer by H^+ ions with HD and H_2 , i.e., $\sigma(H^+ + HD)/\sigma(H^+ + H_2)$, together with the previous $\sigma(H^+ + D_2)/\sigma(H^+ + H_2)$ ratio. As apparent, the ratio of $\sigma(H^+ + D_2)/\sigma(H^+ + H_2)$ decreases to smaller value than unity below 1 keV/u, and reaches a value of 0.57 at the collision energy of 0.18 keV/u. Our theoretical results are in excellent accord with the experimental results in the entire energy region. Contrary to the case of $H^+ + H_2$ and D_2 , the experimental $\sigma(H^+ + HD)/\sigma(H^+ + H_2)$ ratios are found to be almost unity in the entire energy region from 0.18 keV/u to 1.5 keV/u investigated. The present theoretical calculations, however, begin to show the decreasing trend below 1 keV/u, and reach a ratio of 0.65 at 0.05 keV/u.

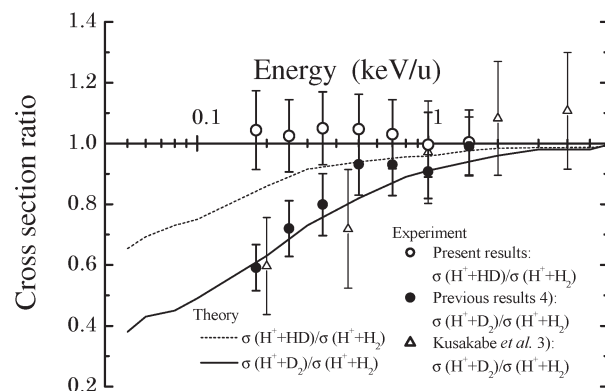


Fig. 1. Cross section ratios of charge transfer for $H^+ + HD$ and D_2 to $H^+ + H_2$ collisions as a function of the collision energy per nucleon.

Figure 2 shows the present results of the $\sigma(D^+ + HD)/\sigma(H^+ + H_2)$, and $\sigma(D^+ + D_2)/\sigma(H^+ + H_2)$, together with the previous and present theoretical results. It is also clear that the present experimental ratio of $\sigma(D^+ + D_2)/\sigma(H^+ + H_2)$ becomes smaller than unity below 1 keV/u, and reaches a value of 0.665 at the collision energy of 0.18 keV/u. Our previous theoretical results for $\sigma(H^+ + D_2)/\sigma(H^+ + H_2)$ are again in excellent accord with the present experimental results in the entire energy region. The present experimental $\sigma(D^+ + HD)/\sigma(H^+ + H_2)$ ratios are again almost unity.

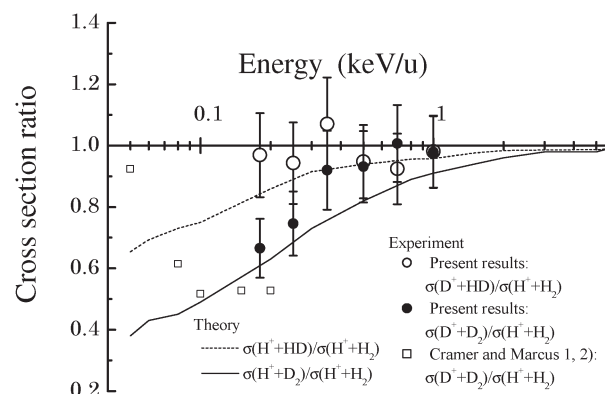


Fig. 2. Cross section ratios of charge transfer for $D^+ + HD$ and D_2 to $H^+ + H_2$ collisions as a function of the collision energy per nucleon.

The present results are described in detail.⁵⁾ The joint experimental and theoretical studies are now in progress for Li^+ ions in collisions with H_2 , HD, and D_2 molecules.

Reference

- 1) Cramer, W. and Marcus, A.: J. Chem. Phys. **32** (1960) 186.
- 2) Cramer, W.: J. Chem. Phys. **35** (1961) 836.
- 3) Kusakabe, T. *et al.*: Phys. Rev. A **62** (2000) 062714.
- 4) Kusakabe, T. *et al.*: Phys. Rev. A **68** (2003) 050701(R).
- 5) Kusakabe, T. *et al.*: Phys. Rev. A **70** (2004) 052710.

\$10. Laser Thompson Scattering Measurement of High Density Plasma Produced by TPD-II

Shibuya, T., Wakaki, M., Tada, S., Sumi, T., Kimura, T., Furuya, Y., Ono, M. (Dep. Appl. Sci., Tokai Univ.), Kawamura, K. (Res. Inst. Sci. Tech., Tokai Univ.), Tonegawa, A. (Dep. Phys., Tokai Univ.), Matsubara, A., Sugimoto, T., Sato, K.

i) Introduction

Reduction of reversed gas flow toward main plasma in a gas divertor is required to achieve both a low thermal load on a divertor plate and high magnetic confinement in the main plasma. In the divertor system proposed by us, a high vacuum region is placed between the divertor region and the edge plasma region[1]. In this paper, a plasma diagnostics method using laser Thompson scattering is investigated by using high density plasma produced by TPD-II and TPD-Sheet-II.

ii) Experimental apparatus

The helium plasma generated in a plasma source traveled through a measurement chamber, contacted with a divertor plate, and finally relaxed to neutral gasses. Electron density of the plasma was around 10^{19}m^{-3} depending on the discharge current. The SHG beam of Nd:YAG laser with the pulse energy of 400mJ, the wavelength of 532nm, and repetition frequency of 10Hz was used as a light source for exciting a plasma. Observation windows were located at the position 0.8m downstream of plasma flow direction from the anode electrode. Cross sectional view of the experimental region is shown in Fig.1.

A laser beam was incident from a side window along with the horizontal axis of a sheet plasma. Scattered light of the plasma was observed at the vertical axis. Scattered light was guided into a spectrophotometer through the

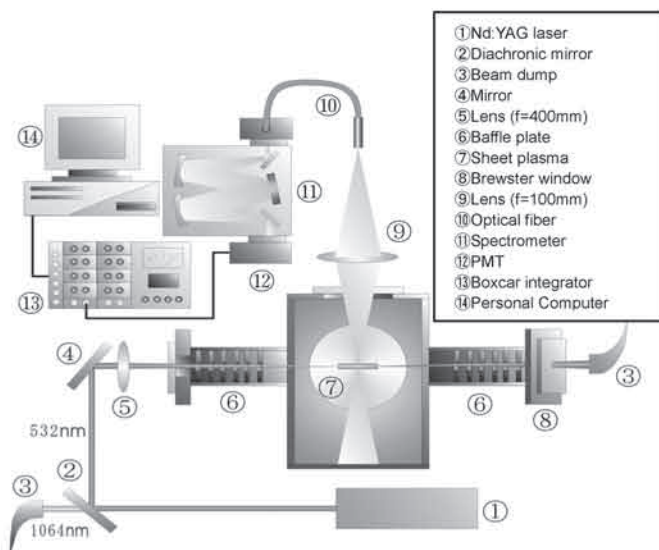


Fig. 1. Schematic diagram of the experimental region.

optical window, lens, and optical fiber. A photo multiplier tube of Hamamatsu Photonics (R3896) was attached to the spectrophotometer of ISA with 1200 l/mm grating.

Baffle plates were used to reduce stray light. The baffle plate consists of five pieces of anodized aluminum plates with small size of hole for transmission of the laser light beam. The baffle plates were located near the optical vacuum windows inside vacuum chamber. Signals of Thomson scattering light of the plasma were averaged over 1000 times using a Boxcar Integrator. Electron temperature was estimated from the full width at half maximum of the observed Thomson scattering spectra.

iii) Results and discussions

The intensity of stray and scattering lights at the experimental region without plasma was measured to estimate the performance of handmade baffle plates. As a result, it was found that the intensity of stray and scattering light can be reduced to one sixth compared with one without baffle plates.

The signal of Thomson scattering is calculated using the results from three different measurements for i.e. a laser light only, emission light of plasma, and the emission light of plasma with laser light. Experimental results were shown in Fig. 2. The similar value of the electron temperature calculated from the measurement of Thomson scattering were obtained corresponding to the values of a conventional single probe method. The electron temperature using the Thomson scattering will be measured for spatial distributions of sheet plasma as a function of the discharge current.

Reference

- 1) A. Matsubara et. al. J. Nuclear Material **337-339** (2005) 181.

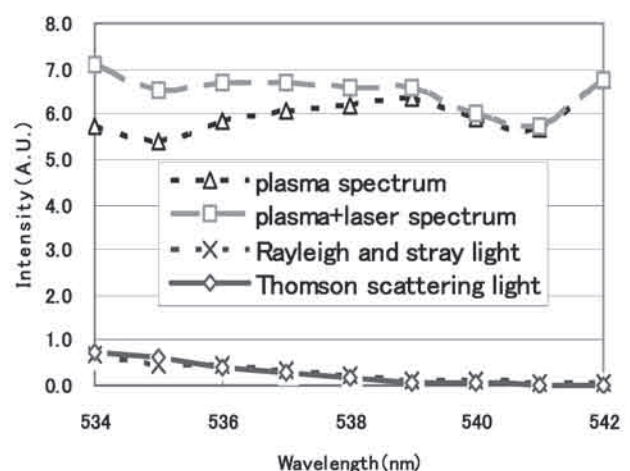


Fig. 2. Thomson scattering spectra of sheet plasma.

§11. Period of the Macroscopic Oscillation of Detached Plasma in the TPD-II

Matsubara, A., Sato, K.

Sugimoto, T. (Dept. of Fusion Sci., Grad. Univ.),
Kawamura, K. (Res. Inst. Sci. Tech., Tokai Univ.),
Shibuya, T. (Dept. Elect. Photo. Opt., Tokai Univ.),
Tonegawa, A. (Dept. Phys. Sci., Tokai Univ.)

The baffled/closed divertor configuration, the neutral leakage through the opening of the baffle expected to be reduced by friction due to ion-neutral collisions. The friction effectively decreases the gas conductance of the opening, which is the so-called “plasma plugging” effect. This effect depends on the position of the detachment front, z_f , since if z_f is outside the divertor region, the plasma pressure at the inlet of divertor region is lost and along with the friction holding the neutrals backs.

The stability of the detached plasma was experimentally investigated in a linear machine, TPD-II (Test Plasma by Direct current) with a baffle. As shown in Fig. 1, the baffle plate partitioned the experimental space into two regions: a low-neutral-pressure region and a high-neutral-pressure region, labeled the edge plasma (E) and divertor (D) regions, respectively. It was observed that when helium gas was injected into the D region, z_f oscillated between the D and E regions.[1] The back-and-forth motion of z_f was accompanied by a significant oscillation of neutral gas pressures in the E and D regions. Here, we report that the period of the oscillation is closely related to the plasma plugging effect. [2]

As schematically shown in Fig. 1, the helium plasma enters the E region first and then the D region. The orifice (15 mm in length and 15 mm in diameter somewhat larger than the plasma diameter) is the equivalent of divertor opening in magnetic confinement devices. The axial magnetic field was 0.2 T and the discharge current was 95 A. The electron plasma density was 10^{19} m^{-3} and the electron temperature was 6 eV, which was obtained by a Langmuir probe located in the E region at 0.2 m from the orifice under the condition without gas injection into the D region. Neutral gas was injected to cause plasma detachment into the D region, and is pumped at the E region. The neutral gas pressures at the D and E regions, P_D and P_E , were measured using baratron gauges.

Figure 2(a) shows the typical P_D -oscillation accompanied by the back-and-forth motion of z_f . There are two parts in the cycle: the slow rise and the rapid fall. The first part begins after z_f suddenly changes to the D region. The increase in P_D is a transient; we postulate that P_D increases toward the saturation value, P_{DS} , given by $P_{DS} = P_E + Q_D/C_{\text{eff}}$, where C_{eff} is the effective orifice-conductance decreased by

the plasma flow coming into the D region at the beginning of the first part of the oscillation, and Q_D is the flow rate of the injection gas. If the transient waveform is described simply as $P_D = P_{DS} - (P_{DS} - P_{D0}) \exp\{-(t-t_0)/\tau\}$ (where P_{D0} is the initial pressure for $t = t_0$), the mean time-constant τ is given by $\tau = V_D/C_{\text{eff}}$, where V_D is the volume of the D region.

The second part of the oscillation begins after z_f enters the E region. In this part, P_E experiences a sudden increase and decrease, and P_D decreases rapidly. This clearly shows that the neutral gas accumulated in the D region flows into the E region, which is due to the enhancement of C_{eff} , i.e., the disappearance of plasma plugging when z_f changes to the E region.

Figure 2(b) shows comparison between the duration of the first part, t_1 , and mean time-constant τ (described before) for various discharge currents I_d and gas species. In order to estimate the value of τ , we derive the value of C_{eff} from the mean slope, $\langle \partial \Delta P / \partial Q_D \rangle$ [where $\Delta P = P_D - P_E$] corresponding each experimental condition. From Fig. 2(b), we can see that t_1 and τ behave in a similar way, suggesting that the period of the oscillation depends on the plasma plugging effect.

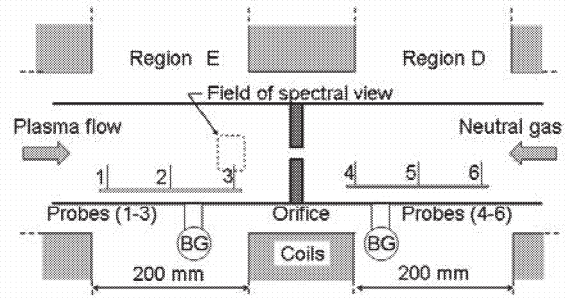


Fig. 1. Schematic of experimental region of the TPD-II.

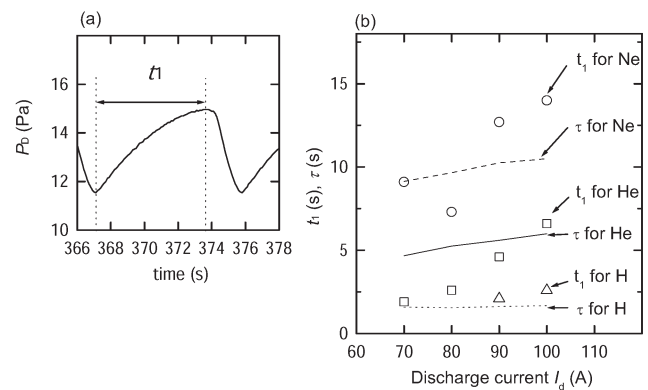


Fig. 2. Typical P_D -oscillation (a), and comparison between t_1 and τ .

[1] Matsubara, A., et al., J. Plasma Fusion Res. 78, 196 (2002).

[2] Matsubara, A., et al., J. Nucl. Mater. 337-339, 181 (2005).

§12. The Role of H⁻ Energy and Electric Field in the Extraction Region for H⁻ Extraction Probability of a Negative Ion Source

Matsumoto, Y., Nishiura, M.
Wada, M. (Doshisha Univ.)
Sasao, M. (Tohoku Univ.)
Yamaoka, H. (RIKEN)

Hydrogen negative ion sources are important devices for NBI(neutral beam injectors) systems. To develop higher efficient ion sources, many H⁻ studies have been reported. However, H⁻ transport, which is also essential knowledge to improve efficiency of ion sources, was not experimentally measured, because we had no experimental method for this purpose. Therefore, we developed the new measurement method of H⁻ transport, PD-FC (Photodetachment with Faraday Cup). This method gives us the spatial distribution of the number of H⁻ ions that are extracted from an ion source. We can estimate the H⁻ extraction probability from the combination of PD-FC results and H⁻ density profiles, which can be measured by PD-LP(Photodetachment with Langmuir probe)¹⁾. The experimental apparatus is showed in Fig.1. These experimental data are analyzed to study the physical mechanism of H⁻ extraction by the numerical approach which calculates H⁻ orbits in an ion source plasma with Monte Carlo method.

Fig.2(a) shows the experimental results of the spatial distributions of the H⁻ extraction probability under several gas pressure conditions. From this figure, the extraction probability is affected by gas pressure conditions and the maximum value is observed around 1Pa. It is considered that this gas pressure dependence is caused by the change of H⁻ energy and the electric field in the extraction region; The electric field exists near the plasma electrode (PE) and prevents H⁻ ions from reaching the extraction hole. Besides, H⁻ transport is strongly affected by the electric field near the extraction hole, because H⁻ energy in ion sources are almost room temperature and much lower than plasma potential in this region. To confirm the change of H⁻ energy and the electric field by gas pressure change, they are measured by movable Langmuir probe in these gas pressure conditions. As the result of the measurement, lower H⁻ energy and lower electric field are observed in higher gas pressure condition. The lower H⁻ energy makes it difficult that H⁻ ions arrive to the extraction hole, while, the decrease of the electric field makes it easy. From only this experimental data, we cannot determine whether these parameters are key factors of H⁻ extraction mechanism or not. We should quantitatively analyze in order that the influence of them for the extraction probability is clarified. Therefore, we carry out more detail analysis utilizing the numerical approach with Monte Carlo calculation. Extraction probabilities are calculated with many H⁻ energy and electric field situations. As the result of the calculation, we find the dependence of the extraction probability, $P(Z)$, on H⁻ energy, $K(Z)$, and the electric field, E , as follow equation.

$$P(Z) \propto \exp\left(-\alpha \cdot eE \cdot Z / K(Z)\right) \quad (1)$$

Z is the distance from PE, α is the coefficient whose value is about 1.5.

Fig.2(b) shows gas pressure dependence of the spatial distribution of the extraction probability estimated by eq.(1) using the experimental data of the H⁻ energy and electric field. We can see the same tendency between Fig.2(a) and (b) below 1.2Pa. Though discrepancy between experiment and theory is observed above 2Pa, we conclude that H⁻ energy and electric field near the PE are key factors for the H⁻ extraction mechanism, especially in low gas pressure conditions.

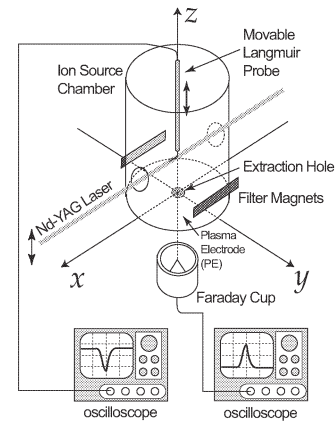


Fig. 1. Experimental apparatus

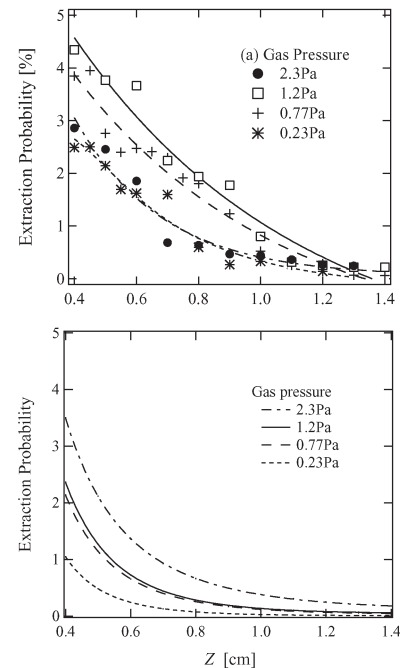


Fig. 2. The spatial distributions of the extraction probability. (a) experiment (b) calculation

Reference

- 1) Matsumoto, Y., Nishiura, M., Matsuoka, K., Sasao, M., Wada, M., Yamaoka, H., Thin Solid Films (To be published)

§13. Determination of Plasma Temperature and Density in Laser Produced Tin Plasmas

Namba, S., Takiyama, K. (Grad. School Eng., Hiroshima Univ.)

Oda, T. (Fac. Eng., Hiroshima Kokusai Gakuin Univ.)
Sato, K.

High-density and high-temperature plasmas have attracted a great deal of interest for potential applications to high brilliance x-ray sources, which are expected to provide the useful tools in the fields of biology, medicine, and solid-state and atomic physics. Especially, in order to realize the next generation semiconductors with a node < 45 nm, the development of extreme ultra-violet (EUV) light source suitable for the lithography has been considered to be one of the urgent issues. For the purpose of this, xenon and tin plasmas produced by a high-intensity laser and z-pinch have been used so far. However, since the properties of these plasmas drastically change during plasma expansion as well as energy deposition into plasmas, the studies of elementally processes, which are strongly dependent upon the plasma parameters such as electron density and temperature, are not feasible. Therefore, we investigate the stationary high-density Sn and Xe plasma from the view point of the atomic physics. Indeed, the TPD (Test plasma by Direct current) device that can readily generate high-density ($\sim 10^{14} \text{ cm}^{-3}$) and low-temperature (<10 eV) plasmas was extensively studied for the application to a VUV laser by Sato *et al* [1] and Otsuka *et al.*[2].

In this report, we show the results of preliminary researches concerning the derivation methods of plasma density from the Stark broadening spectrum in a laser produced Sn plasma, instead of TPD-plasma, to study the validity of this method.

The experiments were carried out by using a YAG laser (wavelength:355 nm, pulse width: $\sim 5 \text{ ns}$, energy: $\sim 100 \text{ mJ}$). The plasma emissions were measured by a visible

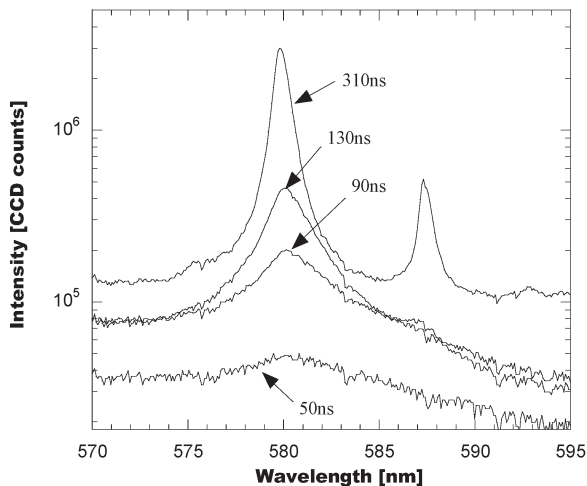


Fig. 1. Time evolution of Sn II 579nm spectrum.

spectrometer whose detector was a charged-coupled device (CCD) camera with a gated image intensifier (gate width: 20 ns). The target was high-purity tin disk (20mm ϕ , $t=5 \text{ mm}$).

Figure 1 shows the temporal evolution of Sn II 579nm. In the early stage, the broadened spectrum due to Stark effect was observed, and gradually its width became narrower. Considering that instrumental width was 0.36nm, the broadening indicates the production of high-density plasmas in the initial stage. From the width of this transition, the electron densities can be deduced, and its relationship (FWHM of the spectral profile) is expressed by [3],

$$w_{eG} = 8 \left(\frac{\pi}{3} \right)^{3/2} \frac{\hbar}{m a_0} n_e \left(\frac{E_H}{kT} \right)^{1/2} \left[\langle i | \vec{r}^2 | i \rangle \bar{g}_{se} + \langle f | \vec{r}^2 | f \rangle \bar{g}_{sf} \right], \quad (1)$$

where a_0 is the Bohr radius, E_H is the ionization potential of hydrogen atom, i and f are the levels corresponding to the transition, \bar{g}_{se} the Gaunt factor and the others are the usual meanings. In order to determine the Stark width w_{sG} accurately, the observed spectra were deconvoluted by Lorentzian profile. The electron temperature that is involved in this equation was estimated from the Boltzmann relationship in terms of the population densities between the excited levels. By substituting the parameters into Eq. (1), we successfully obtained the plasma density and temperature as a function of time after the laser irradiation (see Fig. 2).

In the next fiscal year, we will measure the plasma densities of Xe and Sn plasma produced by TPD-II, and also investigate the possibility as an EUV light source as well as the atomic structure of these elements.

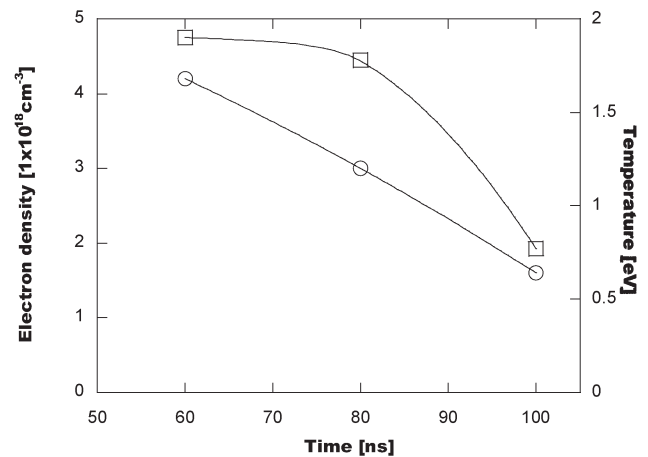


Fig. 2. Electron density and temperature as a function of time after the laser pulse.

References

- [1] Sato, K, et al., Phys. Rev. Lett. **39**, 1074 (1977).
- [2] Otsuka, M., et al., J. Quant. Spectrosc. Radiat. Transf. **21**, 41 (1979).
- [3] Griem, H.R., Phys. Rev. **165**, 258 (1968).

§14. Ion Heating in a Supersonic Plasma Flowing through a Magnetic Nozzle

Inutake, M., Ando, A., Hattori, K., Tobari, H., Hatanaka, M.
Shibata, M. (Dept. Electrical Eng., Tohoku Univ.)

Recently a plasma flow has been recognized to play an important role in space and fusion plasmas. Intensive researches to develop a fast flowing plasma with high particle and heat fluxes are required for the purpose of basic plasma researches as well as various wall material researches and space applications.

A magnetic nozzle acceleration and ion heating in a fast flowing plasma attracts much attention in an advanced electric propulsion system. In the Variable Specific Impulse Magnetoplasma Rocket (VASIMR) project, it is proposed to control a ratio of specific impulse to thrust at constant power.[1] This is a combined system of an ion cyclotron heating and a magnetic nozzle, where a flowing plasma is heated by ICRF (ion cyclotron range of frequency) power and the plasma thermal energy is converted to flow energy via a magnetic nozzle.

The purpose of this research is to investigate effective methods of wave excitation and to establish an ion heating technology in a fast flowing plasma for the advanced plasma thruster and other applications.

We have performed an ion heating experiment in a supersonic plasma flow produced in the HITOP device.[2,3] RF waves are launched by a right-handed helically-wound antenna in a helium plasma. This antenna is set at $Z=0.6\text{m}$ downstream of the Magneto-Plasma-dynamic Arcjet (MPDA) and excite RF waves with an azimuthal mode number of $m=-1$. The RF frequency can be changed from 100kHz to 500kHz with an input power up to 15kW.

When RF waves excited in a flowing plasma with a density around $1 \times 10^{13} \text{cm}^{-3}$, we observed an increase of plasma stored energy W_{\perp} measured by a diamagnetic coil located at $Z=2.23\text{m}$ downstream from the MPDA. Ion temperature T_i also increased during the RF pulse. However, no clear indication of the cyclotron resonance is observed, because the ion-ion collision frequency ν_{ii} is larger than the ion cyclotron frequency f_{ci} in the high density region and the waves are damped not by cyclotron resonance but by collisional damping. We decreased a plasma density from $1 \times 10^{13} \text{cm}^{-3}$ to $5 \times 10^{11} \text{cm}^{-3}$ so that the cyclotron heating phenomena appeared and a diamagnetic coil signal W_{\perp} increases drastically as shown in Fig.1. It is also observed that the peak position is shifted to lower magnetic field than that corresponding to $\omega/\omega_{ci}=1$, i.e. ω/ω_{ci} higher than 1. This is due to the Doppler effect caused by the fast plasma flow.[4]

Figure 2 shows a dependence of W_{\perp} on the RF input power P_{RF} . It linearly increases with P_{RF} . We have also measured ion temperature by an electrostatic energy analyzer, of which collection surface faces to perpendicular direction to the plasma flow. The perpendicular component of ion temperature $T_{i\perp}$ can be obtained. When P_{RF} increases, $T_{i\perp}$ increases almost linearly as shown in Fig.3.

Experimental researches on the energy conversion from thermal energy to flow energy by a magnetic nozzle should be pursued further.

Reference

- 1) F.R.ChangDiaz, et al.: Proc. of 36th Joint Propulsion Conf., (Huntsville,2000), AIAA-2000-3756.
- 2) M.Inutake, et al.: Proc. of 26th ICPIG, Vol.1, (2003), p.127.
- 3) A.Ando, et al.: Advances in Applied Plasma Science, 4 (2003) 193.
- 4) A.Ando, et al.: Proc. the 7th APCPST, (Fukuoka, 2004), A2 (2004) 45.

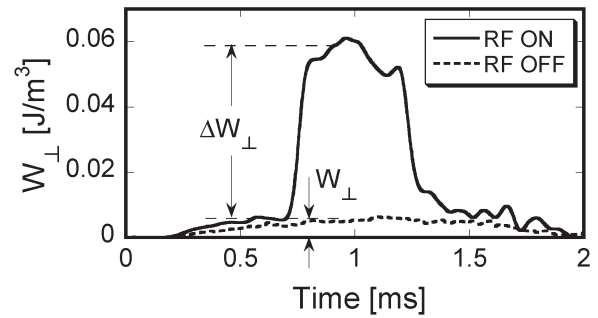


Fig.1 Time evolutions of diamagnetic coil signal W_{\perp} . $f_{\text{RF}}=236\text{kHz}$, $P_{\text{RF}}=15\text{kW}$.

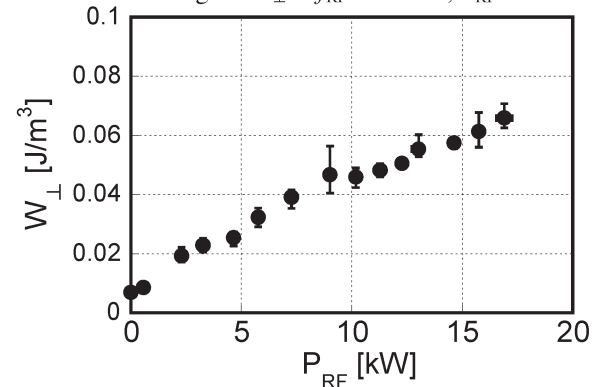


Fig.2 Dependence of diamagnetic coil signal W_{\perp} on input RF power P_{RF} . $f_{\text{RF}}=236\text{kHz}$.

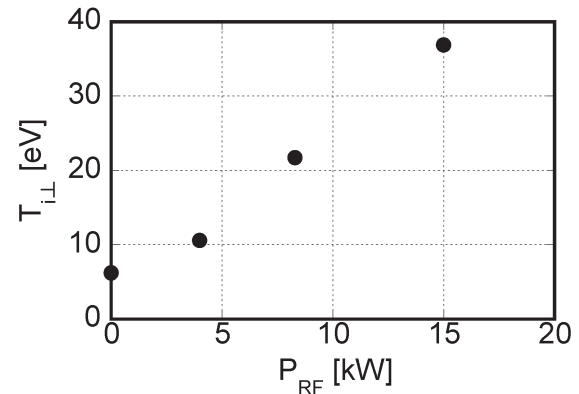


Fig.3 Dependence of perpendicular component of ion temperature $T_{i\perp}$ on input RF power P_{RF} . $f_{\text{RF}}=236\text{kHz}$.

§15. Physical Mechanism of Self-organization of Novel Density Distribution in a Pure Electron Plasma Driven by Rotating Wave Field

Kiwamoto, Y., Soga, Y., Aoki, J. (Kyoto Univ.),
Tanaka, M.Y., Yoshimura, S. (NIFS)

Observations have been accumulated that demonstrate substantial contribution of azimuthally-rotating radio-frequency (RF) electric fields to the reduction of radial particle losses and sometimes to the compression of the radial distribution of non-neutral plasmas. Physical mechanism of this “rotating-wall technique”¹⁾ has not been well clarified in spite of its implications in fundamental plasma physics as well as in understanding processes involved in improved confinement in fusion-oriented plasmas.

The purpose of this collaboration program is to precisely examine details involved in the RF-driven transport phenomena toward the integration of the whole processes into a unified model. The experimental advantage of high controllability, high confinement properties and high resolution diagnostics inherent to pure electron plasmas has led us to the construction of a clear model as proposed in this report.

Technical achievements in FY2004 are,

- (1) Improvement of mode-selectivity of rotating electric field and widening of the ramp-up width of the RF frequency from 0.1 -2MHz to the new range of 0.1-40MHz.
- (2) Extension of the magnetic field strength from $B < 0.05T$ to $B < 2.2T$.
- (3) Improvement in the capability of correlation analyses of experimental data.

Relevant observations include the following,²⁾

- (1) It is found that, as the frequency of the rotating electric field is ramped-up linearly in time, the on-axis density increases in such a way that the wave frequency normalized by the on-axis plasma frequency goes down to eventually be locked at a small number that corresponds to an eigen frequency of Trivelpiece-Gould mode that has a global radial structure satisfying the boundary condition.
- (2) The wave signals in the downstream are heavily attenuated while the on-axis density goes up. This observation suggests that the radial transport process includes Landau-damping, resonant interaction parallel to the magnetic field.
- (3) The electric field rotating in the direction of the equilibrium $E \times B$ drift drives inward flux. The direction of the radial flux is reversed when the sign of the azimuthal mode number changes. The outward flux forms a flattened density distribution that drops abruptly to zero at the expanding boundary.

A theoretical model³⁾ is constructed on the basis of the experimental studies. The key points are summarized as follows:

- (1) The essential features are described by the drift-kinetic equation that include resonant wave-particle interactions in the axial direction (i.e. Landau-damping on warm plasma), equilibrium azimuthal rotation $\omega_r(r)$ with radial shear associated with observed density profile, and guiding-center drifts of the particles in the transverse plane.
- (2) The RF voltages applied to the azimuthally-segmented wall generate a Trivelpiece-Gould mode wave that satisfies the wave equation constructed on the basis of the drift-kinetic equation and the Poisson equation under the condition of the observed density profile that is surrounded by the conducting wall. The wave function as a solution has a unique spatial structure that maintains its global shape under the axial dissipation due to Landau damping.
- (3) Particles axially running resonantly with the wave suffer resonant $E \times B$ drift in the radial direction due to the azimuthal wave field. The average of the microscopic drift leads to the expression of radial flux.

$$\Gamma = \frac{\pi e n_0 |\phi|^2}{2mBr} \left\{ \frac{\partial \hat{f}_0}{\partial v} - \frac{1}{k r \omega_c} \frac{1}{n_0} \frac{\partial n_0}{\partial r} \hat{f}_0 \right\}_{v=(\omega - l \omega_r)/k}$$

where ℓ is the azimuthal mode number.

- (4) The increment of the potential energy dU due to the radial flux is found to be equal to the work exerted by the torque of the azimuthal electric field to the macroscopic body of the plasma.
- (5) Within a radial shell between r and $r + dr$ the wave energy dW is converted to the axial kinetic energy dK and to the potential energy dU at the ratio of $dK/dU = (\omega - l \omega_r)/l \omega_r$. We also obtain a relation $d(K + U + W)/dt = 0$, indicating that the damped energy of the wave is totally converted to the axial heating of the particles and to the radial compression that leads to the increase in the potential energy.

The theoretical model successfully provides a closed scenario of the wave-driven compression process.

References

- 1) X. -P. Huang, F. A. Anderegg, C. F. Driscoll and T. M. O’Neil, Phys. Rev. Lett. 78 (1997) 875.
- 2) Soga, Y., et al. Contributed paper in *12th International Congress on Plasma Physics*, Nice 2004/10/25-29.
- 3) Kiwamoto, Y., Soga, Y. and Aoki, J., submitted for publication in Phys. Plasmas (May, 2005).

§16. Dynamic Control of Bifurcated Transition in Magnetized Plasma

Shinohara, S., Horii, S. (Interdis. Grad. Sch. Eng. Sci., Kyushu Univ.)
Fujisawa, A., Ida, K., Iguchi, H.

In NIFS, transport barrier and its formation mechanism have been actively investigated, and understanding of them are crucial in the future nuclear fusion studies. Plasma rotation driven by so-called $E \times B$ drift has been also studied in relation to improvement of the magnetic confinement. Therefore, investigations of the dynamic process of the electric field and its effect on transition phenomena are very important.

We have been trying to control the density transition phenomena along with plasma rotation and density profile modification, using ten concentric circular rings as biased electrodes [1-3]. Here, dynamic changes of plasma performance were studied by applying the steady or pulsed bias voltages. Argon plasma at a pressure P of 0.1 - 10 mTorr in the cylindrical chamber, 45 cm in diameter and 170 cm in axial length, was produced by a RF wave of 7 MHz using a spiral antenna. Plasma parameters were measured by a developed 24 ch. Langmuir probe and a 3D scanning probe [3]. Data were stored with a data logger. Using this system, detailed spatio-temporal behavior was investigated. Typical plasma density n_e and electron temperature were $4 \times 10^9 - 4 \times 10^{10} \text{ cm}^{-3}$, 3 - 6 eV, respectively.

Applying a pulsed bias voltage from the low to the high voltages to satisfy the change from state I only (high density) and state II only (low density), different time responses were observed, as shown in Fig. 1. Here, the spatio-temporal behaviors from state I to state II of the ion saturation current I_{is} and the floating potential V_f are shown. Although the change of bias voltage is less than μs , I_{is} in the bulk plasma region changed slowly with less than ms. On the other hand, the bias current I_b , which is the electrode current, changed very fast with less than 10 μs . Here, V_f in the bulk region changed much slower on the order of ms. Note that, near the electrode region, I_{is} and V_f changed fast with less than a few tens of μs [4]. In addition, we have observed the hysteresis characteristics [4] in a statistical sense, which is different from the dc hysteresis, as is shown in Fig. 2. Here, PDFs (probability distribution functions) were different between the increasing and decreasing phases of the bias voltage: probability having state II in the increasing phase is lower than that of state II in the decreasing phase.

In conclusion, we have investigated the detailed spatio-temporal characteristics of density transitions by voltage biasing, and found the stochastic hysteresis. Obtained results suggest that the plasma parameters near the electrode play an important role causing the transition, which may be interpreted from the particle. These understandings will be expected to contribute to the plasma confinement and stability control.

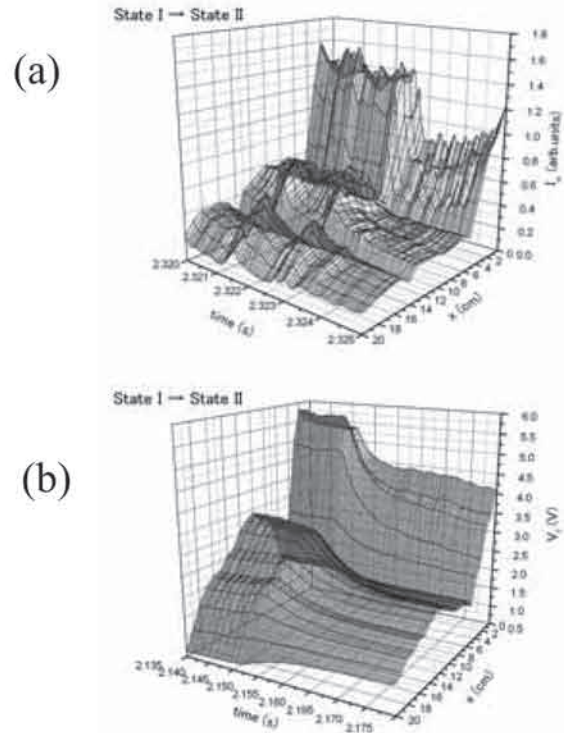


Fig. 1. Spatio-temporal behaviors of (a) I_{is} and (b) V_f

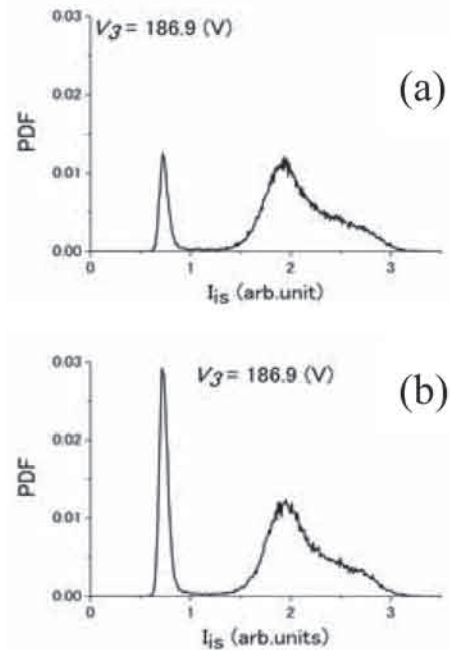


Fig. 2. PDFs in the (a) increasing and (b) decreasing phases of bias voltage.

References

- 1) S. Shinohara *et al.*, Trans. Fusion Technol. **39** (2001) 358; Phys. Plasma **8** (2001) 1154, **9** (2002) 1834.
- 2) S. Matsuyama and S. Shinohara, J. Nucl. Fusion Res. **4** (2002) 528.
- 3) S. Shinohara, Phys. Plasma **9** (2002) 4540; Rev. Sci. Instrum. **74** (2003) 2357.
- 4) S. Shinohara *et al.*, Thin Solid Films (2005) in press.

§17. Basic Process of Solid Hydrogen Ablation by Plasma

Fujita, H., Ohtsu, Y., Misawa, T. (Saga Univ.)
Sato, K.N. (Kyushu Univ.)
Yoshimura, S.

Interaction between plasma and solid is one of the important themes, which should be studied in the sense of plasma science. On the other hand, from the viewpoint of performance of nuclear fusion plasmas, pellet injection experiments have been actively carried out in many toroidal studies in the sense of the control of density profile, obtaining high density or improved confinement, and diagnostic purposes. However, it is, so far, an empirical scaling and the essential part of solid hydrogen ablation by plasmas, such as the interaction between pellet and plasma, have not been clarified. For instance, observation of so-called “Tail Mode”, which may be the result of charge exchange equilibrium state and the plasma rotation by the potential, might be affected by the density profile of the edge plasma. Thus, the study on pellet plasma interaction is one of the most interesting issues to be investigated as the fundamental plasma science.

In this research, an accumulation of data on the interaction between plasma and solid hydrogen is planned by measuring the fundamental process of pellet injection into an inductively coupled plasma (ICP). ICP is possible to get high-density of 10^{12}cm^{-3} and uniform density profile at low pressure of a few mTorr. This plasma is considered to be utilized as target plasmas to simulate edge plasmas. In this report, we present fundamental characteristics on spatial structure in ICP.

As shown in Fig.1, the experiments were done in a cylindrical stainless steel vessel of 16 cm in diameter and 116 cm in length connected by a glass tube of 36 mm inner diameter and 200 mm in length in argon pressure of 3 mTorr. A schematic diagram of an experimental apparatus and an axial profile of magnetic flux density \mathbf{B} with three different divergent configurations in the glass tube are predicted in Fig. 1. These profiles are called “focus”, “flat” and “diverge” types, respectively. Here, the focus type provides profile that \mathbf{B} tends to increase gradually and then saturates, the flat type is a roughly uniform one and the diverge type \mathbf{B} is decreasing in the tube. A radio frequency (RF 13.56 MHz) power generator is connected to a helical external antenna mounted on the glass vessel. The location of $z = 0$ cm is the end of the glass vessel attached to the side of the grounded stainless steel vessel.

As shown in Fig.2, when the magnetic field is switched off, n_e is almost uniform with keeping a high value ($n_e \approx 5 \times 10^{10} \text{ cm}^{-3}$) for $-13 < z < -1$ cm corresponding to the antenna location. In the cases of both focus and flat types, axial profiles of n_e are quite similar to each other. It is seen in these profiles that n_e gradually increases from 2×10^7 to $4 \times 10^{10} \text{ cm}^{-3}$ from $z = -15$ to 25 cm. Here, electrons in the glass tube are strongly magnetized because of a big value of electron hole parameters (product between

electron cyclotron frequency and collision time) of about 270 ~ 340 around the closed end of glass tube. Precisely speaking, the magnetic fields of these types decreases near the closed end of glass tube ($z = -20$ cm) causing $-\nabla_{\parallel} \mathbf{B}$ drift as approaching the tube end.

In the case of the diverge type, it is seen in Fig.2 that n_e around $z = -14$ cm is higher by about two order magnitude in comparison to that in the cases of other types. For the diverge type, a spatial profile of the plasma potential V_S estimated by the probe predicted that V_S decreased from about 8 to -11 V for $-16 < z < -3$ cm, increased from -11 to 5 V for $-3 < z < 4$ cm and then remained roughly constant of 5-7 V for $z > 4$ cm. Due to the potential difference ($=V_S(z=-3\text{cm}) - V_S(z=-16\text{cm}) \approx -11\text{V} - 8\text{V} = -19\text{V}$) between $z = -16$ and -3 cm, electrons in this region would be accelerated towards the closed end of the glass tube to realize a bigger ionization around this region. Since the magnetic field strength amounted to the highest value (around $z = -17$ cm), the ionized electrons tend to move towards the $-\nabla_{\parallel} \mathbf{B}$ drift against the potential barrier as mentioned above. In addition to this fact, the magnetic field of the diverge type is stronger than that of other types in the region of $z \leq -10$ cm. This would cause a higher density in comparison to other type's ones. For $z > -3$ cm, the n_e profile in the case of the diverge type is similar to ones corresponding to the focus and flat types.

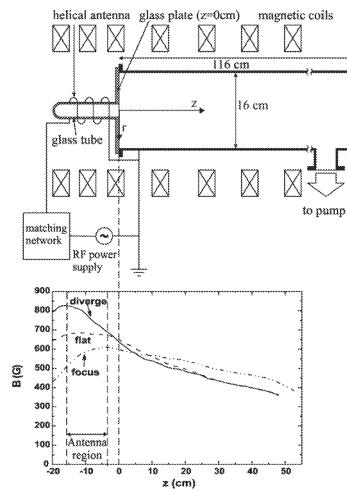


Fig.1 Experimental apparatus

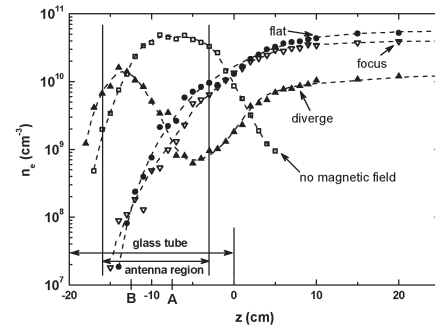


Fig.2 Axial profiles of n_e at various magnetic field configurations

§18. Plasma-quenching Efficiency of CO₂ by Estimation of C₂ Rotational and Vibrational Temperatures in High-pressure High-power Ar-CO₂ Induction Plasmas

Tanaka, Y., Uchida, T., Uesugi, Y. (Kanazawa Univ.)
Ohno, N. (Nagoya Univ.)

High-power and high-pressure inductively coupled plasmas are widely used in various fields such as material processings, the destruction of waste, etc.. Such high power induction plasmas have some advantages such as no contamination, good repeatability and high heat flux. On the other hand, the investigation of plasma-quenching efficiency of gases is nowadays very important in various fields. For example, in a high-voltage circuit breaker field, a circuit breaker must extinguish an arc plasma formed between the electrodes during a large electric-current interruption process. The recent gas circuit breaker extinguishes the arc plasma by blowing SF₆ gas. However, SF₆ has been specified as one of greenhouse effect gases whose emission to the atmosphere should be reduced. Thus, alternative gases of SF₆ for arc plasma quenching are greatly required in a circuit breaker field. Another field in which plasma-quenching gases are needed is the divertor fusion plasmas. The divertor is exposed to high heat flux that has to be quenched.

In our previous work, we used the inductively coupled plasma technique to investigate the plasma-quenching efficiency of various molecular gases, and found that CO₂ has a high plasma-quenching efficiency compared with other natural environmental-friendly gases such as N₂, O₂, Air, Ar and He [1]. In this experiment, the CO₂ injection was found to decrease Ar excitation temperature and the diameter of the high-power plasma region. However, we only estimated Ar excitation temperature on the assumption of local thermal equilibrium.

In the present work, we focus C₂ vibrational and rotational temperatures in high-power Ar-CO₂ induction plasmas to study plasma-quenching efficiency of CO₂ in detail from the observed C₂ Swan spectra. Rotational temperature is considered to be close to heavy particle temperature, while vibrational temperature to electron temperature because of rate of rotational and vibrational excitation and de-excitation processes by electrons or heavy particles.

The plasma torch used in the experiment is composed of two coaxial quartz tubes. The length of the inside tube is 161 mm, and its diameter is 82 mm. Argon and CO₂ gas mixture is supplied as a sheath gas along the inside wall of the inside tube. The total gas flow rate was fixed at 100 slpm(=liters/min). The gas flow rate of CO₂ gas was set to 0, 2, 5 and 10 slpm. The pressure of the torch is fixed at atmospheric pressure. The input power at the plate terminal in the vacuum tube oscillator was set to 50 kW. Spectroscopic observation was carried out for wavelength range of 400-800 nm to measure C₂ Swan molecular spectra and Ar I line spectra in Ar-CO₂ induction plasmas. Such C₂ spectra were found to have an increased radiation intensity with increasing CO₂ gas flow rate. On the contrary, the radiation intensities of Ar I spectra was seen to decrease with increasing CO₂ gas flow rate.

The emission coefficient of C₂ Swan spectra can be calculated theoretically using molecular structure data. We assumed that the population of excited C₂ particles follows the Boltzmann law, but with different temperatures T_{ex} , T_{vib} , T_{rot} for electronic, vibrational and rotational excitations, respectively. Vibrational and rotational temperatures T_{vib} and T_{rot} were estimated by fitting the theoretically calculated emission coefficient to the experimentally observed radiation intensity. Fig.1 shows comparison of the theoretically calculated radiation intensity of C₂ Swan spectra to the experimentally observed one at 10 mm below the coil end in 90%Ar-10%CO₂ plasmas. From this figure, we estimated T_{vib} to be 9000 K, while T_{rot} to be 5000 K. The similar estimation was carried out for different CO₂ gas flow rate and different spectroscopic observation positions. Fig.2 indicates the estimated radial distribution of T_{vib} and T_{rot} at 40 mm below the coil end. It is noted that T_{vib} is always higher than T_{rot} , which may mean thermal non-equilibrium state even in such high-power atmospheric pressure induction plasmas. Another important point is that increasing CO₂ decreases T_{vib} , which indicates that CO₂ decreases T_{vib} , then electron temperature by the CO₂ high plasma-quenching efficiency. This high plasma quenching efficiency is considered mainly to arise from energy consumption by dissociation of CO₂ to CO and O by another numerical simulation.

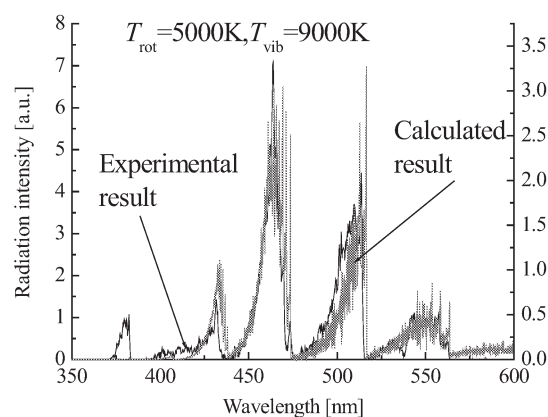


Fig.1 Comparison of C₂ Swan Spectra calculated and observed at 10 mm below the coil end in 90%Ar-10%CO₂ induction plasma.

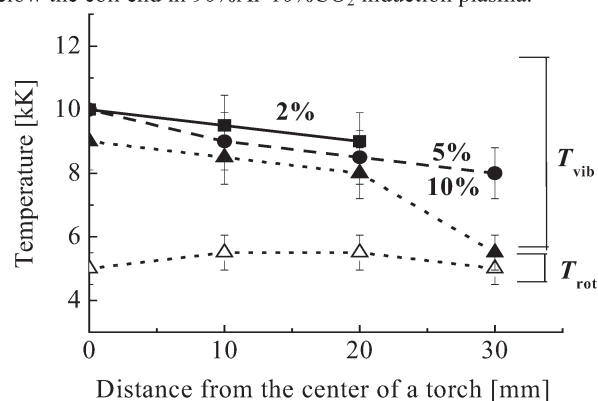


Fig.2 Radial distribution of vibrational and rotational temperatures at 40 mm below the coil end in Ar-CO₂ induction plasmas.

Reference

[1]Tanaka, Y.,Sakuta T., J.Phys.D:Appl.Phys. **35**, (2002) 2149

§19. Transient Response of the Induction Coil Loading in the Initial Startup Phase of rf Induction Thermal Plasmas

Uesugi, Y., Tanaka, Y. (Kanazawa Univ.)
Razzak, M.A., Ohno, N., Takamura, S. (Nagoya Univ.)

Generation and sustainment of rf induction thermal plasmas in atmospheric pressure range requires high voltage in the initial startup phase and high rf power during the steady state sustainment phase. The high rf electrostatic field induced between induction coil conductor wound around a glass discharge tube generates surface electrostatic discharges in which the discharge current flows through the dielectric glass tube. After several hundreds microseconds the electrostatic discharges grow sufficiently to change to a volumetric electromagnetic discharge which is maintained by the inductive electric field as shown in Figs. 1. During this discharge mode transition the loading impedance of the induction coil changes significantly, which shows coupling characteristics between induction coil and generated plasmas. This loading impedance change of the induction coil leads a deviation from a series resonance condition of the LCR output circuit including the induction coil, which strongly affects the output characteristics of a semiconductor rf inverter power supply.

In this study transient response of the induction coil loading impedance in the initial startup phase of the rf thermal plasma generation is studied experimentally[1~3]. Dynamic interactions of the rf inverter power supply with generated rf plasmas are also investigated and strong deterioration of the inverter output efficiency is found experimentally. It is shown by the loading impedance measurement and the fast camera observation that characteristic features of the induction plasmas dynamically developing from the initial streamer-like electrostatic discharges to the volumetric electromagnetic thermal plasmas are clearly found. Preliminary frequency tracking experiments show a successful improvement of the inverter output efficiency and ab-

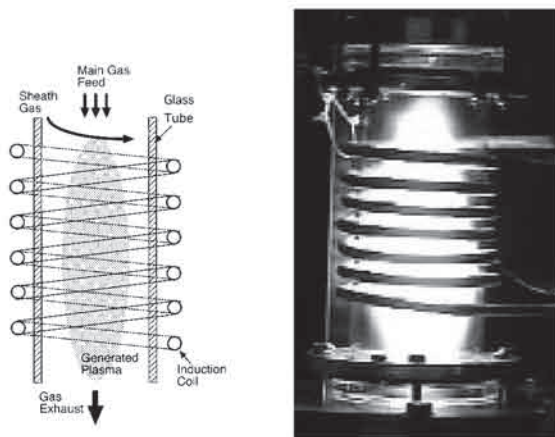


Fig. 1 Schematic structure and typical picture of the rf induction plasma torch

sorbed rf power in the generated plasma[4]. Figures 2 show time traces of the rf inverter dc and rf power(top), and the LCR series resonance frequency of the induction coil circuit and gate driving frequency of the inverter(bottom). With the ignition of the thermal plasma the LCR series resonance frequency deviates from the driving frequency, which reduces the power coupling efficiency strongly as shown in the figure. When the driving frequency of the induction coil is changed close to the resonance frequency, the coupling efficiency is greatly improved. It is found that the frequency feedback using Phase Locked Loop(PLL) may work well to keep a good power coupling between the inverter power supply and generated thermal plasmas.

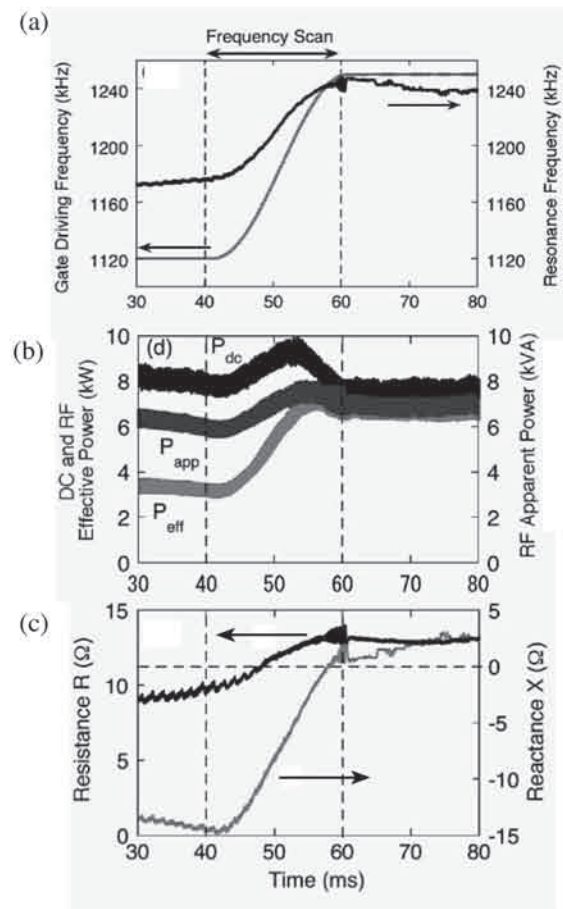


Fig. 2 Time traces of the output and resonance frequencies(a), inverter output power(b) and loading resistance and reactance(c) when the driving frequency is changed.

References

- [1] M. A. Razzak, et al., J. Appl. Phys. **95**(2004)427.
- [2] M. A. Razzak, et al., J. Appl. Phys. **96**(2004)4771.
- [3] M. A. Razzak, et al., J. Plasma and Fusion Research **81**, (2005)204.
- [4] Uesugi, Y., et al., to be published in IEEJ Trans. FM.

§20. Experimental Study of Current Drive Using Nernst Effect

Kawamori, E. (High Temperature Plasma Center, The Univ. of Tokyo),
Tokuzawa, T.

A method of plasma current drive in a low- q plasma using the Nernst effect is proposed by Hassam.¹⁾ If a plasma has a steep temperature gradient in radial profile,

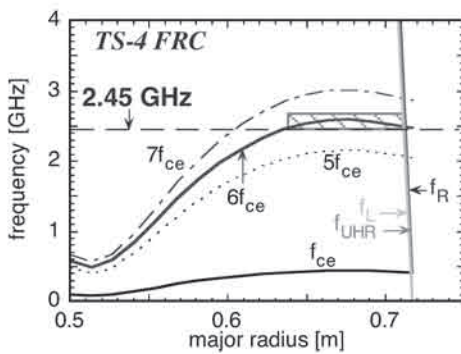


Fig. 1 Characteristic frequencies in the electron cyclotron range of frequencies on the TS-4 Field Reversed Configuration at the University of Tokyo. f_L , f_R are the right and left hand cutoff frequencies, f_{UHR} is the upper hybrid frequency.

the cross-field thermoelectric force is in the opposite direction to the usual resistive friction, thus maintaining the plasma current. In low- q plasmas such as an Field Reversed Configuration (FRC), however, maintaining the electron temperature profile by electromagnetic wave is difficult because of its high beta property. Electron Cyclotron resonance heating (ECRH) is a very powerful method to heat magnetically confined plasmas. However, the accessible plasma density is limited by a critical density. Electron Bernstein wave is considered as a possibility for overcoming the density limit. In the W7-AS, it was clearly demonstrated that the mode conversion heating from an O-wave to an X-wave and, finally, to an EBW.²⁾ Therefore, we plan to employ an EBW in order to increase and maintain the electron temperature of a low- q plasma in the TS-4 device. A 2.45 GHz magnetron with microwave power of 20kW for up to 200 μ s was installed to TS-4 at the University of Tokyo. A launched X-mode electromagnetic radiation will efficiently couple power to EBWs through a mode conversion process at the upper hybrid resonance UHR. Figure 1 shows characteristic frequencies in the electron cyclotron range of frequencies on the TS-4 Field Reversed Configuration (FRC).

In order to investigate the heating effect by EBW and a principle of the current drive by the Nernst effect, multipoint Thomson scattering system for electron

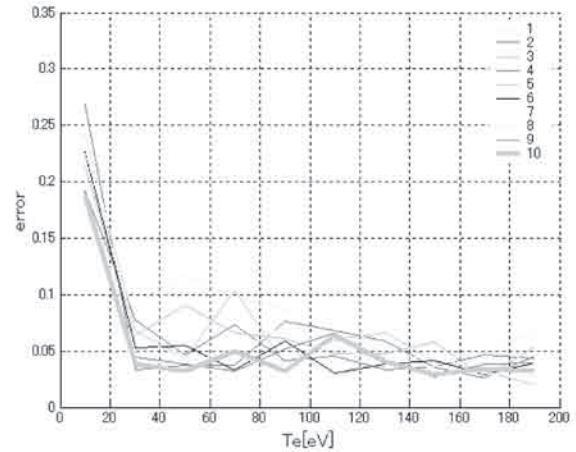


Fig. 2 Error estimation of the deduced electron temperature for various electron temperatures. The curve numbered 10 is the error in the case of the designed spectral responsibilities of the optical filters

temperature measurement has been designed and constructing. Error estimation of the deduced electron temperature for various electron temperatures is calculated as shown in Fig. 2. We adopted the combination of optical filters numbered 10 in Fig. 2. The error of the deduced electron temperature for $30 < T_e < 190$ eV is within 5 %.

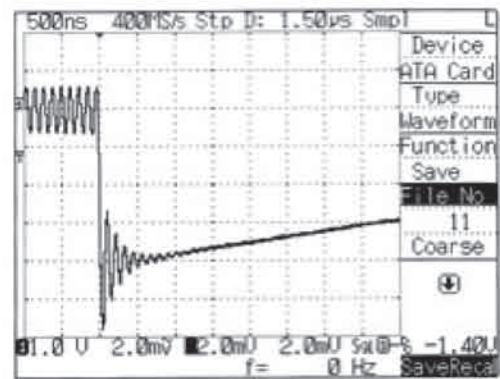


Fig. 3 Signal of Rayleigh scattering.

After the optical lens and the detection systems for scattering light collection were set up, measurement of Rayleigh scattering light was carried out. Figure 3 shows the signal of Rayleigh scattering from the injected YAG laser beam. In the next step, the heating effect by EBW and the correlation between electron temperature gradient and the plasma current are investigated in the experiment.

Reference

- 1) Hassam, et al., Phys. Rev. Lett, 83, (1999) 2969.
- 2) H. P.Laqua, V. Erckmann, and H. J.Hartfu, Phys. Rev. Lett. 78,(1997) 3467.

§21. A Solar Wind Simulator Using An Intensive Arc-Jet System

Hirano, K., Fujisawa, A.

If an artificial energetic plasma flow similar to the solar wind were available, there must appear many applications. Among others, a cleaner and a safer D-D based advanced fusion reactor system may well have a chance to fall into the scope for the more important target rather than the present day D-T burning system. The solar wind tells us that its upper limiting speed takes the order of the electron thermal velocity of the plasma itself [1], and thereby the energy of the plasma beam achieves quite a high value of the range \sim keV. In the old experiment [2], it had been shown that such acceleration is really possible and the Deuterium plasma of the energy \sim 5 keV or more was achieved and trapped successfully in the cusp magnetic field. A detailed inspection of the data reveals the fact that all the plasma components including impurities have the same velocity in approximate sense. This suggests that the energy from the external power source is firstly given mainly to the electron component, and the ions are simply following up the electrons so as overall charge neutrality is maintained.

The core part of the present experimental system is shown schematically shown in Fig.1. The H_2 working gas is injected into the system from the left hand side end using a fast acting gas valve with the valve opening time of about 150 μ sec. It was found that the super shots similar to the old experiment, were also confirmed. For achieving such a state, the timing control between the fast gas injection and the arc ignition are the most important factor as was so in the old case. We noted that the energetic plasma appears only when the case that the plasma expands freely into vacuum without passing through the cold gas precursor in the down stream. It may be said, therefore, that both the plasma expansion into vacuum and high power heat input into the plasma are concluded to be the most important items for producing the energetic beam, as was so in the old case. In the present super shot case, for example, such a high power input into the final main heating up stage in Fig.1 is estimated to be \sim 400 kW and lasts for more than \sim 600 μ sec. We are interested to fact that such high power input is stably maintained in a small tube of the volume with the diameter of 3.5 mm and the length of 9 mm. These observations show that, for an energetic quasi-steady plasma beam production, a rapid

pinching action as in the old experiments is not always necessary, but the most essential item must be in keeping up of quite intensive Ohmic heating.

For a fusion reactor, however, further acceleration of the beam up to the energy by an order of magnitude is necessary. The only solution for that may be found in the appropriate use of the JxB motor force [3,4]. The main topics, therefore, of the present study are said in figuring out the possibility of quite a powerful plasma acceleration system in a laboratory circumstance. A simple estimate predicts that such an energetic beam must have power density of $\sim 10^4$ times as large as the usual beam injector of the present day electrostatic system.

This is quite an important and definite property for an actual fusion reactor, since the cross-section of the beam injection aperture can be 10^4 times as small as the one for the present day system. In one sense, this is quite a natural consequence since no electro-static force drives the actual daily system.

Reference

- 1) Hirano, K., Phys. of Plasmas **8**, (2000) 1734
- 2) Hirano, K. and Ito, H., J. Phys. Soc. JP. (1966) 1787
- 3) Hirano, K., Nuclear Fusion **28**, (1988) 207
- 4) Hirano, K., Nuclear Fusion **29**, (1989) 955

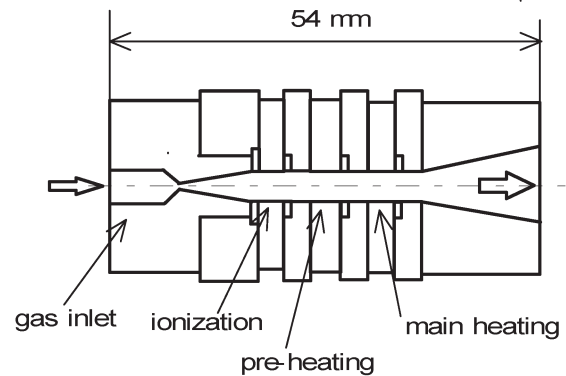


Fig.1 The main part of the arcjet gun: H_2 gas is injected into the Laval nozzle in the left by the fast acting gas valve having the opening time of $\sim 150 \mu$ s attached in the upper stream of the system. The gas through the Laval nozzle is guided into the channel of the three series of stages with the diameter 3.5 mm for production of the energetic plasma beam: the gas ionization, the plasma pre-heating and the final main intensive heating up for intensive acceleration. In the last heating up stage, the power of about 400 kW is injected to produce energetic plasma beam.

§22. Spatial Distribution of Losses of Neutral Beam-injected Fast Ions in Quasi-axisymmetric System

Isobe, M., Shimizu, A., Okamura, S., Suzuki, C., Nishimura, S., Akiyama, T., Matsuoka, K. (NIFS)
Spong, D.A. (ORNL)

The quasi-axisymmetric system (QAS) provides good neoclassical confinement as well as magneto-hydrodynamic stability while realizing tokamak-like, toroidally-symmetric magnetic field structure on the Boozer coordinates[1]. However, it is required to verify whether energetic ions can be well confined in QAS because even if neoclassical confinement is much better than that in conventional helical system like CHS, it does not guarantee good confinement property for energetic ions. In a tokamak, it is well known that ripple loss of energetic ions makes localized heat spot on the first wall due to finite number of toroidal coils[2]. Such a local heat load has to be avoided because it may give serious damage to the device. QAS is analogous to a rippled tokamak in magnetic field structure because residual non-axisymmetric magnetic field ripples still exists in QAS's peripheral domain. Therefore, the similar situation may appear in the viewpoint of energetic ion loss. In this work, we investigate spatial loss distribution of energetic ions originating from neutral beam injection and check how much localized it is. The orbit analysis is performed by use of the DELTA5D code[3,4]. The DELTA5D follows guiding center orbits in the presence of slowing-down and pitch angle scattering processes on the Boozer coordinates. The equilibrium magnetic field is obtained from the VMEC code. The target QAS configuration has toroidal periods of 2, aspect ratio of 3.2, major radius of 1.5m and toroidal magnetic field of 1.5T[5].

Figure 1 shows energy distribution of escaping beam ions from the QAS plasma. The neutral beam is tangentially co-injected and its injection energy is set to be 38 keV. The detailed plasma parameter used in this analysis is well described in Ref.6. The beam ion losses begin after they slow down to 30 keV. The primary losses of partially thermalized beam ions is supposed to be due to ripple trapping in a ripple well existing in the peripheral region. This is because the DELTA5D shows that pitch angle v_{\parallel}/v of escaping ions is very localized and ranges from 0 to 0.03. Next, we show the spatial distribution of losses of escaping beam ions in Figure 2. Dots represent the location where beam ions intersect the last closed flux surface of QAS. It can be seen that beam ion losses take place in the lower half of the plasma because ion grad- B drift is directed to be downwards in this case. The losses are not uniform and are somewhat localized in the particular toroidal angle. This loss pattern is quite different from that in CHS. The ripple loss in CHS mainly appears in the small major radius side due to helically trapped ions.

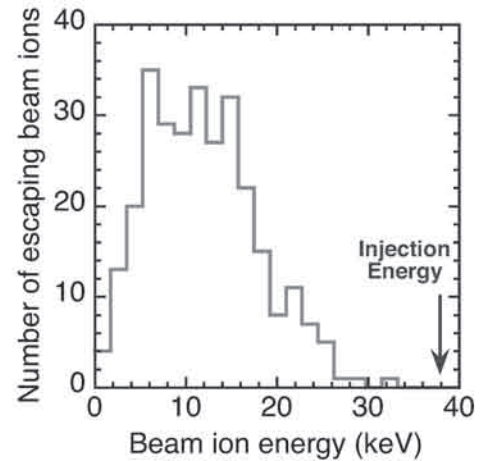


Fig. 1. Energy distribution of escaping beam ions in QAS. Beam ions are tangentially co-injected with E_b of 38keV



Fig. 2. Spatial distribution of losses of escaping beam ions in the Cartesian coordinates.

References

- 1) Nemov, V.V. *et al.* Plasma Phys. Control. Fusion **45** (2003)1829
- 2) Tobita, K. *et al.*, Nuclear Fusion **35**(1995)1585.
- 3) Spong, D.A. *et al.*, Bull Am Phys Soc. **44**(1999)215.
- 4) Kugel, H. *et al.*, to be published in Fusion Science and Technology.
- 5) Okamura, S. *et al.*, Nuclear Fusion **41**(2001)1865.
- 6) Isobe, M. *et al.*, J. Plasma Fusion Res. SERIES, **6**(2004)622.

§23. Consideration on Scale-up of Quasi-axisymmetric Stellarator with Low Aspect Ratio

Matsuoka, K., Okamura, S., Nishimura, S., Isobe, M., Suzuki, C., Shimizu, A., Tanaka, N., Hasegawa, M., Naito, H. (Mitsubishi Fusion Center),
Urata, K., Suzuki, Y. (Mitsubishi Heavy Industries, Ltd)

Scale-up of quasi-axisymmetric stellarators with low aspect-ratio is discussed to make a survey of the future prospect, which is based on the engineering design of CHS-qa with the major radius of 1.5m.

The stress analysis on modular coils and coil frames was done in the most severe case where the power supply (PS) did not work because of its failure. Here, modular coils are energized with multiple PS. The result under the failure of one PS showed that the maximum stress in the coil frame was within the allowable level of SUS. The stress was larger than 140MPa in supporting legs of modular coil assembly (quadrant). However, the remedy could be easily found by inserting additional supporting bars between 4 quadrants [1].

Next, engineering design of the vacuum vessel of CHS-qa is discussed. To make the control of wall recycling easy the vacuum vessel made of SUS is to be contained inside the modular coils, which inevitably results in a highly deformed shape. In the process of designing the coils the current-carrying surface is located between the inner and outer limiting surfaces that are separated by 19 cm in the radial direction. At the vertically elongated cross-section the modular coil touches the inner limiting surface on the inboard side to make the indentation large for obtaining high beta plasma. The radial distance between the outermost magnetic surface (OMC) and the inner limiting surface is 26 cm as is shown by “d” in Figure 1, and this space is mainly for the vacuum vessel including in-vessel components and for assembling the whole system. The vacuum vessel with the thickness of 10mm is separated from OMC by 8 cm that is utilized for in-vessel components and divertor structure. The process of assembly is as follows; 5 modular coils of the quadrant (total 20 coils as a whole) are to be inserted separately into the quadrant of vacuum vessel. Most difficult coil to insert is, of course, the middle one. Because of non-axisymmetry the movement of the coil must be composed of radial and vertical shifts and rotations in the toroidal and poloidal directions. The middle coil can be set up in the right position within a reasonable number of shifts and rotations. After this process four quadrants of vacuum vessel with 5 modular coils are welded together to make the whole

assembly and ports are welded thereafter. The vacuum vessel has one-turn resistance of 1 m Ω in the toroidal direction by using two welded bellows as is in CHS vacuum vessel. The buckling analysis of the vacuum vessel shows that the deformation takes the maximum value of 1.37 mm in the horizontally elongated position and the von Mises's stresses are 47.5 MPa and 42.4 MPa at inner and outer surfaces, respectively. The vessel is robust having the eigen-value of 15.9 for the primary mode although there are a lot of ports.

Scale-up to reactor-grade size is necessary to be discussed for the future prospect. To compare plasma performance in a variety of magnetic configurations helical reactors are designed, as a reference, with the plasma volume of 1000 m³ (1 GW fusion power output) and the magnetic field strength Bt of 5 Tesla. Here, simple consideration on the size and the magnetic field strength is given. Extrapolation from the plasma volume of CHS-qa of 6.5 m³ to 1000 m³ leads to the major radius of 8 m (larger by 5.36 times). The distance between OMC and the inner limiting surface of modular coil, “d” in Figure 1 can be larger than 1 m. Although the details of blanket and maintenance process are out of the scope of this report, the compact reactor design might be possible. The maximum field strength is about two times of that at the magnetic axis, which means the maximum of 10 Tesla when Bt is 5 Tesla. When the coil current density is kept constant, the cross-section is larger by about 18 times ($=3.33 \times 5.36$). This is less than the square of linear scale ratio (5.36×5.36), which means that design of structures supporting electromagnetic forces gets easier.

References

- 1) Matsuoka, K., et al., Annual Review (Apr.2004 - March 2005), p.323.

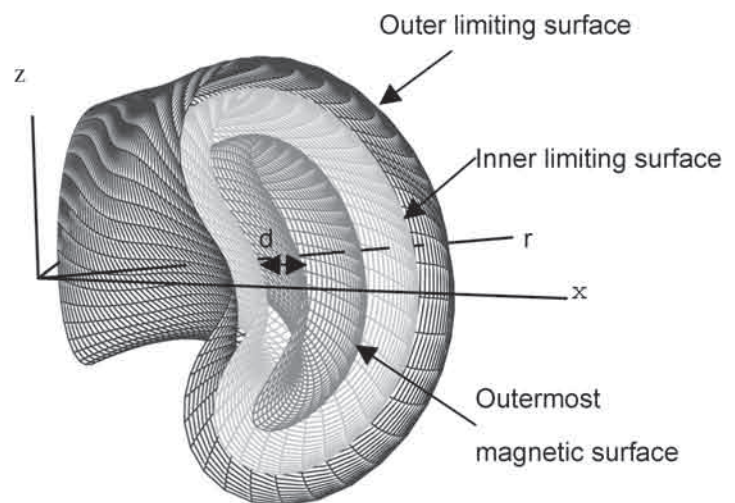


Fig.1. Radial build. “d” in the figure is 26cm in CHS-qa.

§24. Preliminary Investigation of a Quasi-Axisymmetric Configuration Optimized for Contours of the Second Adiabatic Invariant

Suzuki, C., Okamura, S., Akiyama, T., Isobe, M., Matsuoka, K., Nishimura, S., Shimizu, A., Isaev, M. Yu (Kurchatov Inst.)

Improvement of collisionless alpha particle confinement is one of the essential issues in the optimization of the stellarator configuration. Theoretically, this can be achieved by closure of contours of the second adiabatic invariant J within flux surfaces. J is defined by a line integration of parallel velocity of a trapped particle along the particle orbit,

$$J(s, \theta, \phi) = \int v_{\parallel} dl, \quad (1)$$

where s is a flux surface label and θ and ϕ are poloidal and toroidal angles in Boozer coordinates, respectively. Recently this concept has been employed in the configuration optimization of the Wendelstein 7-X, in which J contours are made closed poloidally, $J(s, \theta) = J(s)$.¹⁾ It has also been applied to LHD-like configuration.²⁾ In this fiscal year we began to explore the possibility of the further optimization of a quasi-axisymmetric (QA) configuration by applying this concept. In the QA case, $J(s, \phi) = J(s)$ must be satisfied as far as possible. We have successfully installed the necessary code package into the NIFS supercomputer. The package consists of the equilibrium code VMEC2000, the configuration optimizer, and the guiding center orbit code for the evaluation of the actual alpha particle confinement.

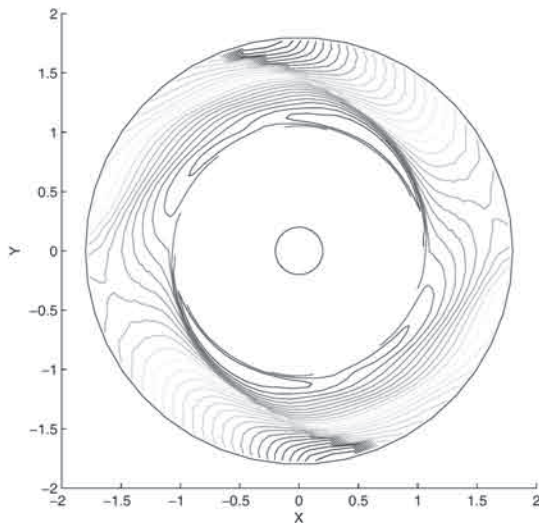


Fig. 1. J contours drawn in the topview of the torus equatorial plane for a reference configuration (called 2b32m3) of a QA stellarator. Major radius is normalized to unity and minor radius is enlarged to 0.8 for all toroidal positions.

Figure 1 shows the topview of the J contours drawn in the torus equatorial plane for a QA configuration called 2b32m3, one of the reference configuration for a compact QA stellarator. Major radius is normalized to unity and minor radius is enlarged to 0.8 for all toroidal positions in Fig. 1. The contours are not drawn in the inboard side of the torus, where there is no trapped particles. As shown, the contours are largely deviated from concentric ones, which indicates that the alpha particle confinement is not so good. Radial profiles of the maximum and minimum values of J in each flux surface are shown in Fig. 2. The large difference between J_{\max} and J_{\min} means that trapped particles can escape easily towards the edge region due to the J invariance. In contrast, $J_{\max} = J_{\min}$ everywhere in the equivalent tokamak case, due to real axisymmetry.

The optimizer runs so as to minimize “penalty function” which can be customized in the code. First we used a penalty function to close J contours in the (s, ϕ) plane as far as possible. As a result, the penalty function itself was reduced less than one-fifth of the initial value. However, actual alpha particle confinement calculated by the orbit code was not improved in spite of the reduced penalty function. We are now trying a new function so as to satisfy $J_{\max}(i) < J_{\min}(i-1)$ as far as possible in order to prevent trapped particles from escaping toward the edge, where i is the number of flux surface. According to a preliminary calculation, we could obtain a further improved configuration with better actual alpha particle confinement.

References

- 1) Mikhailov, M. I. et al.: Nucl. Fusion **42** (2002) L23.
- 2) Isaev, M. Yu et al.: Nucl. Fusion **43** (2003) 1066.

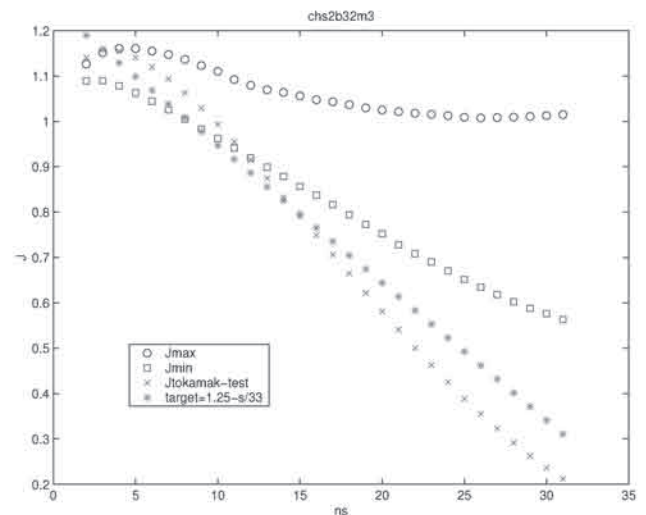


Fig. 2. Radial profiles of the maximum and minimum values of J in each flux surface for the same configuration as Fig. 1. Times symbols show the radial profile for the equivalent tokamak.

§25. The Trial Modular Coil Design for a N=2 Quasi-isodynamic Stellarator

Shimizu, A., Okamura, S., Akiyama, T., Isobe, M., Suzuki, C., Nishimura, S., Matsuoka, K., Yamazaki, K.

In stellarator configurations, helical trapped particles have the second adiabatic invariant, $J_{||} = \int v_{||} d\ell$. If we make contours of $J_{||}$ closed inside the plasma column and make $J_{||}$ constant on magnetic surfaces, the centers of helical trapped particles will drift along magnetic surfaces and good confinement property of helical trapped particles is achieved. These configurations based on $J_{||}$ conservation are called "quasi-isodynamic", which has an advantage of alpha particle confinement because non collisional diffusion of trapped particles is very low.

The configurations that have constant $J_{||}$ on magnetic surfaces was found as ref. [1] with systematic optimization, however the modular coil systems for these configurations are not considered yet. Here, we report the result of trial modular coil design for a quasi-isodynamic (qi) configuration of toroidal periodic number 2 ($N = 2$) that is one of $J_{||}$ optimized configurations.

The outermost magnetic surface of $N = 2$ qi configuration used in this report is shown in Fig.1. It has a relatively low aspect ration, 4, and has the large mirror ratio in the toroidal direction. The magnetic axis is deviated largely from the equator plane. For the optimization of modular coil system, NESCOIL code is used, in which the coil geometry is parameterized with the coefficients of Fourie series. And the coefficients are numerically optimized, so that normal components of magnetic field produced by coils at the torus surface, which we will intend to produce here (usually boundary surface for VMEC), should be zero. In this optimization, conditions from the engineering aspect are imposed on modular coils, which are the minimum distance between coils and the minimum radius of curvature of coils. From the previous engineering investigation of qa modular coil system of which major radius was 1.5 m, we knew that the minimum distance between coils and the minimum radius of curvature should be larger than 21 cm and 25 cm respectively [2]. In our trial coil design of qi, the major radius was assumed to be same to this qa coil design (namely $R = 1.5$ m), therefore same conditions were imposed. As the total number of coils, 20 was selected, which was also the same to qa coil design.

The modular coil system obtained from the optimization is shown in Fig.2. The shapes of modular coils are very complicated. The minimum distance between coils and the minimum radius of curvature are 16 cm and 21 cm respectively in this design, and which was smaller than objective levels. In spite of this complicated shape, the objective boundary surface was not able to produce with good accuracy: the error field estimated from the average of $|\mathbf{B} \cdot \mathbf{n}| / |\mathbf{B}|$ is 6 %. Here, \mathbf{B} is the magnetic field produced by modular coils at the torus surface that we intend to produce here

(namely same torus to Fig.1), and \mathbf{n} is the normal vector to this surface. In our previous coil design for the qa configuration, this value was 1.4 % [2], and this level was needed to realize good magnetic surface and features of magnetic field configuration characterized by VMEC. The reason of bad accuracy of produced magnetic field for $N=2$ qi configuration is considered for the large deviation of magnetic axis from the equator plane. Compared with our qa configuration, the deviation of magnetic axis to vertical direction in qi case is three times larger: In qa case, the deviation is 0.25m, however, 0.7m in qi case. The deviation to radial direction is same level: In both cases, it is below 0.3m. In order to realize the good accuracy in $N = 2$ qi case, the major radius must be larger, otherwise we must reduce the deviation of magnetic axis in the vertical direction. The selection of $N=1$ may also lead to good result because the deviation of magnetic axis per one toroidal period is small, therefore we will continue the coil design for that case.

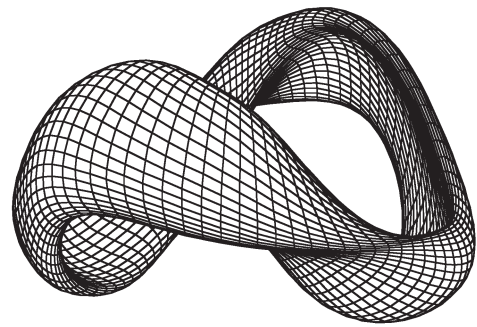


Fig.1 Outermost magnetic surface of $N=2$ qi configuration.

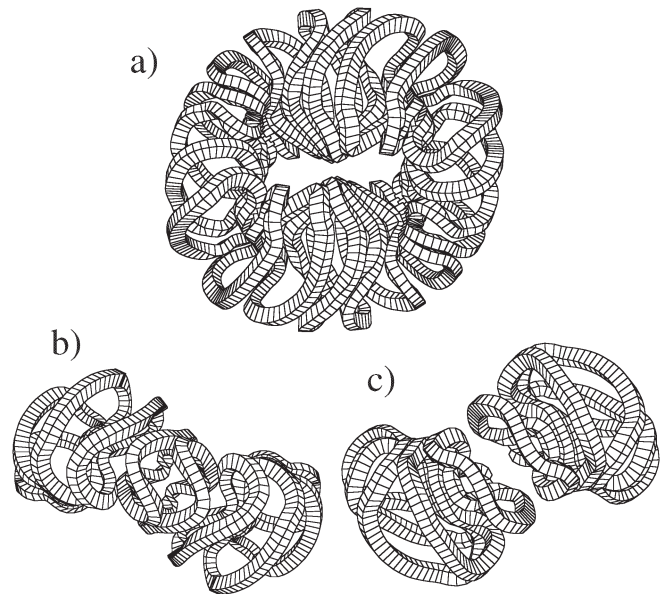


Fig.2 Modular coils optimized for $N=2$ qi configuration shown in Fig.1. a) top view b), c) are side views at the toroidal angle of 0 and 90 degrees (only half coils are shown).

- [1] M. I. Mikhailov, K. Yamazaki, NIFS Research Report, NIFS-797 (2004).
- [2] A. Shimizu, S. Okamura, M. Isobe, C. Suzuki, S. Nishimura, *et. al.*, Fusion Engineering Design, **65** (2003) 109

§26. A Numerically Robust Formula for Bootstrap Current Coefficients in the Banana Regime in Boozer Coordinates

Nishimura, S., Sugama, H., Nakamura, Y. (Kyoto Univ.)

In many applications of the theory of neoclassical bootstrap currents, an analytical expression derived by Shaing, Carreras, et al.[1] in the Boozer coordinates is often used. This representation was an extension of the previous theory developed in the Hamada coordinates [2-3]. To derive parallel viscosity forces driving the parallel flows, we have to solve the lowest order drift kinetic equation in the banana regime expansion. In general non-symmetric toroidal plasmas, this equation does not satisfy the solubility condition $\oint (\mathbf{v}_{da} \cdot \nabla s / v_{||}) dl = 0$ for the trapped particle part in the phase space. On the other hand, the incompressible particle and energy conservation laws enable us to derive the parallel viscosity forces without solving full part of the equation [2-3]. The results of this method, however, depend on the poloidal and toroidal coordinates giving the maximum value of the magnetic field strength B_M on the flux surface as shown later. Such coordinates cannot be determined uniquely in symmetric plasmas. The ingenious technique developed in Ref.[2-3] for this problem was the following separation of the lowest order perturbation.

$$f_{a1}^{(0)} = -\frac{m_a c}{e_a} \frac{\partial f_{aM}}{\partial s} v_{||} \left(\frac{H_1}{B} + \frac{V'}{4\pi^2} \frac{B H_2}{2\chi' \psi'} \right) + \frac{m_a c}{e_a \chi' \psi'} \frac{V'}{4\pi^2} \frac{\partial f_{aM}}{\partial s} v B_M h \quad (1)$$

Here, H_1 expresses a part of the incompressible particle and energy flows, and H_2 is a constant indicating the magnetic flux surface averaged effects of the local structure (i.e., high frequency modulation) of the magnetic field on the trapped particle flow pattern. This constant is defined in Ref.[2-3]. The first term, which is proportional to $v_{||}$, satisfies the solubility condition. The treatment of this part is substantially identical with that in symmetric plasmas. For the remaining part of the perturbation h , the parallel viscosity was derived directly not by calculating the trapped particle distribution but by only calculating circulating particle distribution. The constant H_2 is therefore chosen to satisfy the condition in that the h vanishes in symmetric configurations. The explicit expression for H_1 and the equation for h in the Hamada coordinates were simple as shown in Ref.[2-3].

In contrast to the Hamada coordinates, the equations in the Boozer coordinates are generally complicated. It depends on the explicit expression for H_1 . Shaing, Carreras, et al.[1] used the expression, which is mathematically equivalent to that in Ref.[2-3],

$$H_1 = \frac{\psi' B_\xi - \chi' B_\theta}{2\chi' \psi'} + \frac{B^2}{2\chi' \psi'} \frac{V'}{4\pi^2} \sum_{\substack{(m,n) \\ \neq (0,0)}} \frac{\chi' m + \psi' n}{\chi' m - \psi' n} \varepsilon_{mn}^{(\text{Boozer})} \cos(m\theta_B - n\zeta_B) \quad (2)$$

Another expression of H_1 equivalent to Eq.(2) is given by

$$H_1 = \frac{B^2}{\langle B^2 \rangle} \frac{\psi' B_\xi - \chi' B_\theta}{2\chi' \psi'} + \frac{B^2}{\langle B^2 \rangle} \sum_{\substack{(m,n) \\ \neq (0,0)}} \frac{B_\xi m + B_\theta n}{\chi' m - \psi' n} \varepsilon_{mn}^{(\text{Boozer})} \cos(m\theta_B - n\zeta_B) \quad (3)$$

Here, ε_{mn} in Eqs.(2-3) is Fourier coefficients of $(\langle B^2 \rangle / B^2 - 1)$ [1,4]. The second term in Eq.(3) is obtained as the solution of the equation for the incompressible flow pattern associated with the Pfirsch-Schlüter transport $\mathbf{B} \cdot \nabla (U/B) = (\mathbf{B} \times \nabla s) \cdot \nabla (1/B^2)$ [4]. By the procedure in Ref.[2-3] starting from Eq.(3), we obtained an expression for the geometrical factor $G^{(\text{BS})}$ [1-4], which expresses the driving force for the flows,

$$G^{(\text{BS})} = \langle H_1 \rangle + \frac{\langle B^2 \rangle H_2}{2\chi' \psi'} \frac{V'}{4\pi^2} - \frac{3\langle B^2 \rangle}{4\chi' \psi' f_t} \frac{V'}{4\pi^2} \int_0^1 d\lambda \frac{\lambda W(\lambda)}{\langle (1 - \lambda B/B_M)^{1/2} \rangle}$$

$$W(\lambda) = \sum_{\substack{(m,n) \\ \neq (0,0)}} \frac{Rm + Sn}{\chi' m - \psi' n} \left[f_c \frac{-1\langle B^2 \rangle}{B_M^2} \cos(m\theta_M^{(\text{Boozer})} - n\zeta_M^{(\text{Boozer})}) \left\{ \frac{3}{2} \alpha_{mn}^{(\text{Boozer})} (\lambda=1) + d_{mn}^{(\text{Boozer})} \right\} \right. \\ \left. - 2 \frac{\partial \alpha_{mn}^{(\text{Boozer})}}{\partial \lambda} \left\langle \frac{v_{||}}{v} \right\rangle \cos(m\theta_B - n\zeta_B) \right] + \\ + \frac{\chi' \psi'}{\langle B^2 \rangle} \frac{4\pi^2}{V'} \sum_{\substack{(m,n) \\ \neq (0,0)}} \frac{B_\xi m + B_\theta n}{\chi' m - \psi' n} \left[f_c \frac{-1\langle B^2 \rangle}{B_M^2} \cos(m\theta_M^{(\text{Boozer})} - n\zeta_M^{(\text{Boozer})}) \left\{ \frac{3}{2} \beta_{mn} (\lambda=1) + e_{mn} \right\} \right. \\ \left. - 2 \frac{\partial \beta_{mn}}{\partial \lambda} \left\langle \frac{v_{||}}{v} \right\rangle \cos(m\theta_B - n\zeta_B) \right] \quad (4)$$

Here, $R = \chi'(1 - H_2)/2$ and $S = \psi'(1 + H_2)/2$, respectively, and (θ_M, ζ_M) are the poloidal and toroidal coordinates giving the maximum value of the magnetic field strength on the flux surface as $B(\theta_M, \zeta_M) = B_M$. Fourier coefficients $\alpha_{mn}(\lambda)$, $\beta_{mn}(\lambda)$, d_{mn} , e_{mn} are defined in Ref.[1]. When we replace $\chi' \psi' (B_\xi m + B_\theta n) / (\langle B^2 \rangle V / 4\pi^2)$ by $(\chi' m + \psi' n)/2$, Eq.(4) coincides with the result obtained by Shaing, Carreras, et al.[1] who started from Eq.(2). The mathematical equivalence of Eq.(2) and Eq.(3), and that of Eq.(4) and result in Ref.[1] can be easily confirmed by using a relation $B_\xi \psi' + B_\theta \chi' = \langle B^2 \rangle V / 4\pi^2$ and the definition of β_{mn} , e_{mn} . In actual applications, however, these Fourier series must be truncated to be series with finite modes. By the relations $|\chi' m| \ll |\psi' n|$ and $|B_\xi m| \gg |B_\theta n|$ in many practical cases, it can be understood that the expressions in Ref.[1] contain many non-axisymmetric Fourier components $n \neq 0$ that are canceled by each others in Σ , while those in Eqs.(3), (4) are removed from the part using the series expression Σ in advance of the final expression Eq.(4). Therefore Eq.(4) is more useful in many practical applications. This technique was already used in studies in Ref.[5], and the validity is confirmed there by comparing with a direct numerical calculation of the drift kinetic equation.

References

- [1] Shaing, K.C., Carreras, B.A., et al., Phys.Fluids B1, 1663 (1989)
- [2] Shaing, K.C., et al., Phys.Fluids 29, 2548 (1986)
- [3] Shaing, K.C., et al., Phys.Fluids B1, 148 (1989)
- [4] Sugama, H., Nishimura, S., Phys.Plasmas 9, 4637 (2002)
- [5] Nishimura, S., Sugama, H., et al., FS&T 46, 77 (2004); J.Plasma Fusion Res.SERIES 6, 437(2004)

§27. A Method to Eliminate the Logarithmic Singularity in Fourier Series, Which Appear in Parallel Viscosity Calculations in the Banana Regime

Nishimura, S., Sugama, H., Nakamura, Y. (Kyoto Univ.)

One of troublesome problems in analytical calculations of the neoclassical transport is a singularity of the drift kinetic equation in the banana regime expansion [1]. Although the singularity corresponding to the characteristics of the collisionless orbits conserving magnetic moments μ is usually integrable, the singularity due to the collision operator finally appears explicitly. However, in most of applications, final expressions of diffusions and viscosities result in integrable problems. In the analytical theories for non-symmetric toroidal plasmas, this problem apparently appears in the bootstrap current calculations [2]. The functions $\partial h / \partial \lambda$, $d\alpha_{mn}(\lambda)/d\lambda$ and $d\beta_{mn}(\lambda)/d\lambda$ appearing in Ref.[2-4] have a logarithmic singularity at the poloidal and toroidal coordinates of $(\theta, \zeta) = (\theta_M, \zeta_M)$, and at the pitch angle of the circulating/trapped boundary $\lambda=1$, which originates in the singularity of the equation at $v_{||}=0$. Since the final expressions of the parallel viscosity forces are given by the $\langle B/d^3 \mathbf{v} \cdot \mathbf{v}_{||} L_j^{(3/2)} \rangle$ moments of the collision operator, this singularity does not severely affect the final results also in this case. However, we should note that, in the method in Ref.[2-4] where this logarithmically singular function is expressed by a Fourier series, infinite number of Fourier modes of $|m| \leq \infty$, $|n| \leq \infty$ are required to retain some mathematically guaranteed characteristic of the formulas. One of the most important characteristics of these formulas is that the part expressed by this series must vanish in symmetric configurations [2]. For practical applications in which the mode number must be truncated to be finite, a technique to eliminate the singularity before the Fourier expansion to retain the mathematically guaranteed characteristics even in the case of truncated series.

We show here the numerical scheme for the formula in Ref.[4] as an example. The formulas in Ref.[2-3] also can be calculated in analogous manners. By changing the order of $/d\lambda$, Σ , $\langle \rangle$, and $/d\theta_B/d\zeta_B$, we can obtain another expression for the integral of the function $W(\lambda)$ defined in Ref.[2-4] as

$$\begin{aligned} \int_0^1 d\lambda \frac{\lambda W(\lambda)}{\langle (1-\lambda B/B_M)^{1/2} \rangle} &= \frac{1}{2\pi^2} \int_{-\pi}^{\pi} d\theta_B \int_{-\pi}^{\pi} d\zeta_B Q(\theta_B, \zeta_B) \\ &+ \frac{4}{3} \frac{1}{2\pi^2} \sum_{\substack{(m,n) \\ \neq (0,0)}} \frac{\cos(m\theta_M^{(\text{Boozer})} - n\zeta_M^{(\text{Boozer})})}{\chi' m - \psi' n} \times \\ &\int_{-\pi}^{\pi} d\theta_B \int_{-\pi}^{\pi} d\zeta_B \cos(m\theta_B - n\zeta_B) \left(\frac{1}{2} \frac{B(\theta_B, \zeta_B)}{B_M} + 1 \right) (1 - B(\theta_B, \zeta_B)/B_M)^{1/2} \\ &\times \left\{ Rm + Sn + \frac{\chi' \psi'}{\langle B^2 \rangle} \frac{4\pi^2}{V'} \left(\frac{\langle B^2 \rangle}{\{B(\theta_B, \zeta_B)\}^2} - 1 \right) (B_{\zeta} m + B_{\theta} n) \right\} \end{aligned} \quad (1)$$

$$\begin{aligned} Q(\theta_B, \zeta_B) &\equiv \frac{1}{4\pi^2} \frac{\langle B^2 \rangle}{\{B(\theta_B, \zeta_B)\}^2} \sum_{\substack{(m,n) \\ \neq (0,0)}} \frac{\cos(m\theta_B - n\zeta_B)}{\chi' m - \psi' n} \times \\ &\int_{-\pi}^{\pi} d\theta_B' \int_{-\pi}^{\pi} d\zeta_B' \cos(m\theta_B' - n\zeta_B') F\left(B(\theta_B, \zeta_B), B(\theta_B', \zeta_B')\right) \left(\frac{B(\theta_B', \zeta_B')}{B_M} \right)^2 \\ &\times \left\{ Rm + Sn + \frac{\chi' \psi'}{\langle B^2 \rangle} \frac{4\pi^2}{V'} \left(\frac{\langle B^2 \rangle}{\{B(\theta_B', \zeta_B')\}^2} - 1 \right) (B_{\zeta} m + B_{\theta} n) \right\} \end{aligned} \quad (2)$$

using the function $F(B_1, B_2)$ defined by

$$F(B_1, B_2) \equiv \int_0^1 d\lambda \frac{\lambda (1 - \lambda B_1/B_M)^{1/2}}{\langle (1 - \lambda B/B_M)^{1/2} \rangle (1 - \lambda B_2/B_M)^{1/2}} \quad (3)$$

We made the spline function of $F(B_1, B_2)$ using the spline of $\langle (1 - \lambda B/B_M)^{1/2} \rangle$ as the function of λ and then calculated Eqs.(2) and (1).

It is obvious that the truncation of the Fourier modes in Eqs.(1-2) shown here is better approximation than that in $d\alpha_{mn}(\lambda)/d\lambda$ and $d\beta_{mn}(\lambda)/d\lambda$ having the singularity. The λ, θ, ζ dependence of $\partial h / \partial \lambda$ in Ref.[2-3] has a singularity at $(\theta, \zeta) = (\theta_M, \zeta_M)$, $\lambda=1$ although, $\langle (1 - \lambda B/B_M)^{1/2} \rangle^2$ and $F(B_1, B_2)$ (as the function of $(B_M - B_1)^{1/2}$ and $(B_M - B_2)^{1/2}$) calculated here are moderate functions without singularity and with monotonic dependences on the variables. Therefore we made, in numerical examples described in the previous studies[5], the tabulation of $\langle (1 - \lambda B/B_M)^{1/2} \rangle^2$ in λ space with 10 grid points for the range of $0 \leq \lambda \leq 1$, and $F(B_1, B_2)$ in $((B_M - B_1)^{1/2}, (B_M - B_2)^{1/2})$ space with 10×10 points for $0 \leq (B_M - B_1)^{1/2}, (B_M - B_2)^{1/2} \leq (B_M - B_{\min})^{1/2}$. The $F(B_1, B_2)$ can be commonly used for both of the Boozer and the Hamada coordinates. Spline functions are used also to calculate $/d\theta'/d\zeta'$ integrals in Eq.(2) as the function of $(B_M - B(\theta, \zeta))^{1/2}$ for each (m, n) modes.

In the axisymmetric and helically symmetric cases [5], the good agreements were obtained by using only 5~6 "symmetric" (i.e., $m/n = \text{const}$) Fourier modes (m, n) to expand the circulating particle distribution. The reduction of the high frequency modulation components in the Fourier expanded part of the perturbation [4], combined with this technique removing the logarithmic singularity in the Fourier series, improves the approximations and extends the application areas of the theories in Ref.[2-3]. It will be useful also for transport calculations in recently designed advanced helical devices [6].

References

- [1] Hazeltine, R.D. and Meiss, J.D., *Plasma Confinement* (Addison-Wesley, Redwood, CA, 1992), p.348
- [2] Shaing, K.C., et al., Phys.Fluids **B1**, 148 (1989)
- [3] Shaing, K.C., et al., Phys.Fluids **B1**, 1663 (1989)
- [4] Nishimura, S., et al., in this report
- [5] Nishimura, S., Sugama, H., et al., FS&T **46**, 77 (2004); J.Plasma Fusion Res.SERIES **6**, 437(2004)
- [6] Spong, D.A., Phys.Plasmas **12**, 056114 (2005)

5. Theory and Computer Simulation Project

Quite wide range of computer simulation researches has been pursued in the framework of the simulation science, which includes simulations related to magnetic fusion plasma physics, laser fusion plasma physics, space plasma physics, basic plasma physics, physics of molecular dynamics and so on, and the area supporting computer simulations, like numerical technique, visualization technique, and virtual reality technique. Some of them are originally initiated by NIFS, and the others are initiated through the NIFS collaboration program. The NIFS collaboration program is important in deepening the physics understanding and extending the range of the simulation science.

In this fiscal year, computer simulations of the fusion plasmas have been done extensively using Fluid, Vlasov, PIC, Monte Carlo, and other simulation codes according to the physics targets.

To resolve the discrepancy of the MHD stability between the LHD experiment and theoretical and computational result, the effect of the boundary modulation induced by the free boundary MHD equilibrium motion on ideal MHD stability has been examined in the inward-shifted LHD vacuum configuration. The boundary modulation are interpreted as a large Shafranov shift of not only the magnetic axis, but also the plasma boundary. The large Shafranov shift produces the significant stabilization of the low- n modes and the second stability of the ballooning modes, as β increases.

However, such a stabilizing effect by the boundary modulation are not enough to suppress the instability in the low- β plasma. For such a plasma, the nonlinear MHD simulations using Eulerian grid have been performed by using MINOS code to see how much low- n MHD instabilities affect the plasma confinement. To obtain the precise information of the linear and nonlinear evolution, the Fourier decomposition of the perturbations have been done firstly by using the HINT equilibrium and mapping to the Boozer magnetic coordinates. It is found out that the toroidal flow and the compressibility act to relax the violent nonlinear evolution.

The instabilities driven by energetic particles become important when NBI is introduced into thermal plasmas or α -particles are produced by the thermonuclear fusion. The linear properties of the instability driven by energetic-ions in JT-60U and TAE modes in LHD have been investigated by us-

ing MEGA code. The former is considered to be a nonlocal Energetic Particle Mode (non-local EPM), and the latter shows the important role of the low magnetic shear in driving TAE modes. Simulations of the nonlinear evolution of fishbone instability observed in PDX has been carried out by using MEGA code. The result shows that the saturation mechanism is not wave-particle trapping but energy transfer balance.

Related to the anomalous transport by toroidal ITG mode, the gyrokinetic-simulations with high velocity-space resolution have been done in the toroidal flux tube geometry by using GKV code. It is confirmed that the steady state of the turbulence, where the transport balances with the collisional dissipation, is obtained in the same way as found in the slab ITG.

Resistive Wall Modes (RWM) are one of the key issues in ITER MHD physics. The linear and nonlinear simulations have been done under the equilibrium poloidal rotation in the cylindrical geometry by using reduced-equations. Good agreement of the linear growth rates is confirmed between theory and numerical results, and the dependence of the nonlinear saturation level on the poloidal rotation and energy transport have been precisely investigated.

Related to the LHD experiments with pellet injection, a new type of pellet ablation code, CAP, has been developed, which handles solid, liquid, and air phases of neutral particles and the ablation. As a first step, model calculations have been done in order to explain the difference between the experimental results and simple theoretical consideration. This CAP is now under development so as to include the MHD phenomena.

Peripheral (edge) plasma near the separatrix or the last close flux surface, and SOL plasma including divertor function are being investigated. edge plasma A 3D electrostatic PIC code has been developed in order to see the dynamic plasma behavior in SOL. In order to treat the transport from the core (peripheral) region, to SOL, and finally to the divertor region, a Core-SOL-Divertor model has been proposed. The results of model are compared with those of B2-EIRENE and show reasonable agreement. The peripheral (edge) plasma structure in the 3D magnetic configurations like LHD is so complicated that an averaged model, namely, stellarator-equivalent tokamak (SET) model has been introduced to simplify

the 3D plasma edge as a 2D edge. using UEDGLHD has a Local Island Divertor (LID), which consists of $m/n=1/1$ magnetic island. operation. To estimate the strike point pattern on LID, the Monte Carlo simulation has been carried out.

Laser fusion research is an alternative of the magnetic fusion research. For FIREX-I experiments, the construction of heating laser; named LFEX (Laser for Fusion Experiment), has been started. simulations by The target fabrication and irradiation system are also under development as the collaboration program between Osaka University and NIFS. A Fast Ignition Interconnected Integrated (FI³) code is continuously being developed for transport of relativistic electrons in a dense plasma. In FI³ code, a radiation hydrodynamic simulation with PINOCO code has been combined with a collective PIC simulation and a Fokker-Planck simulation by using the internet protocol DCCP. 3-D Rayleigh-Taylor instability in spherically stagnating systems has been successfully analyzed by using IMPACT-3D code.

Flows in the plasma make various phenomena. Driven magnetic reconnection is a typical example of such flow-magnetic field coupling system. Moreover, the magnetic reconnection is one of the basic plasma physics.

Structure of the current layer of the driven reconnection has been investigated in the two-dimensional open system with an explicit electromagnetic particle simulation. It is found that the current layer has two-scale structure, and that the larger (smaller) scale corresponds to ion (electron) meandering scale. The similar simulations have been done in the three-dimensional open system. It is found that both Drift-Kink Instability (DKI) and meandering ion motions can act to violate the frozen-in condition, and also that after the Lower Hybrid Drift Instability (LHDI) saturates, DKI is excited. It has been shown by using the two-dimensional open system simulation that the Hall term effects are suppressed by the gyroviscous cancellation in the range between ion meandering orbit scale and ion skin depth. On the other hand, in the framework of the Hall-MHD model, the fast reconnection is discussed, where ion skin depth acts as the mesoscale producing the chaos-induced resistivity. The simulations on the formation mechanism of sigmoidal structure in the solar corona have been performed, where it is found that the sigmoidal structure is created by the tearing instability and the explosive eruption is followed. In this case, as well as the fundamental magnetic reconnection process, the convective motion (flow) is quite important. Other flow-related problems are MHD turbulence with shear flows in the duct and the excitation of the low-frequency instabil-

ities by the flow in the magnetized plasma.

Simulations related to positron acceleration by a shock wave propagating obliquely to a magnetic field in an electron-positron-ion plasma are also presented, where three types particle acceleration behaviors are obtained. A trail connecting macroscopic process to microscopic process, a simple holistic simulation has been done in quiet aurora arc formation. The macroscopic (microscopic) process is treated by MHD fluid (particle) model.

NS and MHD turbulence simulations have been performed to investigate which scaling appears, Iroshnikov-Kraichnan scaling or Kolmogorov scaling. However, it might be difficult to definitely determine the scaling in the width of the used wave number range. Orthonormal divergence-free wavelet analysis is used to investigate the correlation between coherent structures and nonlinear interactions. The results quantitatively indicate that the coherent structures in turbulence play a principal role in the nonlinear transfer process of kinetic energy.

A new overset grid system, Yin-Yang grid has been proposed for numerical simulations in the spherical geometry. This grid system suits to massively parallel computations for spherical shell geometry. Particle-In-Cell (PIC) simulation code with exact charge conservation has been developed, where HPF is used. An Electromagnetic particle code is being developed for application to space propulsion using ECR discharge. In this code, PIC method and finite-difference-time-domain (FDTD) method is used to solve the Maxwell's equation of microwave.

Molecular Dynamics simulations might become one of key simulations for NINS collaborations. The dissipative particle dynamics simulation has been done for self-assembly of amphiphilic molecules. Depending on the coefficient of the interaction potential among hydrophilic beads, hydrophobic ones and water molecules, the effective microscopic molecular structure changes. Molecular dynamics simulation of collision between graphite and hydrogen is also done. The molecular dynamics simulations of coarse-grained amphiphilic molecules with explicit solvent molecules have been performed to understand detail molecular mechanisms of micelle formation in amphiphilic solution.

Construction of collaborative and seamless virtual environment for numerical simulation is reported, where integrated virtual environment for numerical simulation and visualization is prepared. In this system, the users can use the computers seamlessly without recognizing calculation and visualization computer.

(Okamoto, M.)

§1. Boundary Modulation by the Finite β Free Boundary Equilibrium Motion in Heliotrons

Nakajima, N., Nakamura, Y. (Kyoto Univ.)

In three-dimensional configurations, the confinement region is surrounded by the stochastic magnetic field lines related to magnetic islands or separatrix, leading to the fact that the plasma-vacuum boundary is not so definite compared with tokamaks that the various modulations of the plasma-vacuum boundary will be induced around the stochastic region by a large Shafranov shift of the whole plasma, in especially high- β operations. To examine such the modulation effects of the plasma boundary on MHD instabilities, high- β plasmas allowing a large Shafranov shift or a large Pfirsch-Schlüter current are considered in the inward-shifted LHD configurations with the vacuum magnetic axis R_{ax} of 3.6m [1], for which previous theoretical analyses based on the fixed boundary MHD equilibria indicate that pressure-driven modes are significantly more unstable compared with experimental observations. Since 1) the used pressure profiles have essential properties of experimentally observed pressure profiles and 2) the currentless condition is a good approximation, it is natural to consider that the discrepancy between theoretical results and the experimental ones might come from the boundary condition of the used MHD equilibria.

In order to understand the effects of the boundary modulation induced by the free boundary MHD equilibria, the dependence of the Fourier modes of the boundary on the β value has been investigated. Figure 1(a) shows how the dominant Fourier components change according to the β value or a Shafranov shift of a whole plasma. Most significant changes appear in bumpy components denoted by blue symbols in Fig. 1(a). Dominant boundary spectra of vacuum configurations with different vacuum magnetic axis position R_{va} are drawn in Fig. 1(b). Changes of the boundary spectrum by vacuum magnetic axis shift mainly appear in bumpy components with $(m, n) = (0, \neq 0)$, as well as those by a large Shafranov shift shown in Fig. 1(a). In the inward-shifted LHD configurations, the vacuum flux surfaces are so compressed into the helical coils inner side of torus by the external coil current that the bumpy deformation of

the plasma boundary is strongly enhanced. As β increases, the whole plasma moves from inner side of the torus to the outer side. Through this Shafranov shift, the enforced boundary shaping by external coil current will be so reduced that the bumpy deformation of the plasma boundary will diminish. The boundary modulation mainly appears as a large Shafranov shift of whole plasma.

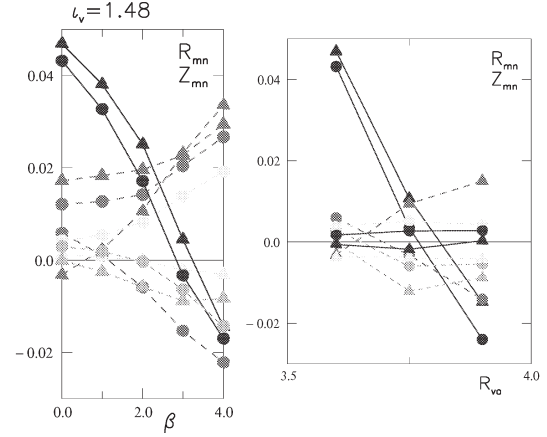


FIG. 1:(a) (the first column) β -dependence of dominant boundary spectra, except for $(m, n) = (0, 0)$ and $(m, n) = (1, 0)$, for MHD equilibrium with $l_v = 1.48$ at the boundary. Triangles and circles indicate Z_{mn} and R_{mn} components, respectively. Blue, red, green and yellow symbols denote bumpy components with $(m, n) = (0, \neq 0)$, components with $(m, n) = (\neq 0, 10)$, axisymmetric components with $(m, n) = (\neq 0, 0)$, and components with $(m, n) = (\neq 0, 20)$, respectively. In MHD equilibria with the fixed boundary, the boundary spectra correspond to the case of $\beta = 0$. (b) (the second column) Vacuum magnetic axis R_{va} dependence of dominant boundary Fourier spectra, except for $(m, n) = (0, 0)$ and $(m, n) = (1, 0)$, in the inward-shifted with $R_{va} = 3.6$ m, standard with $R_{va} = 3.75$ m, and outward-shifted with $R_{va} = 3.9$ m vacuum configurations.

In the case of the planar axis Heliotron configurations with a large Shafranov shift or a large internal current (Pfirsch-Schlüter current), not only the external coil current, but also the an internal plasma current change the boundary shape so much that the resultant MHD stability might significantly depend on the induced boundary modulation.

[1]Nakajima.N,et al.,in Fusion Energy 2004 (Proc. 20th Int.Conf.Vilamoura,2004)IAEA,Vienna,TH/6.

§2. Significant Stabilization of Ideal MHD Instabilities by the Boundary Modulation in Heliotrons

Nakajima, N.

The boundary modulation induced by the free boundary motion of MHD equilibrium mainly appears as a large Shafranov shift of the whole plasma. Thus, it might be expected that the MHD stability is improved by the boundary modulation. Figure 1 shows the comparison of global mode stability analyses between fixed (the first and the second columns) and free (the third and the fourth columns) boundary currentless MHD equilibria with $\beta = 3\%$ for three different plasma-vacuum boundaries denoted by ι_v in the inward-shifted LHD configuration. The pressure profile is assumed to be $P(s) = P(0)(1-s)(1-s^9)$ with the normalized toroidal flux s . This pressure profile is considered to be similar to that in experiments.

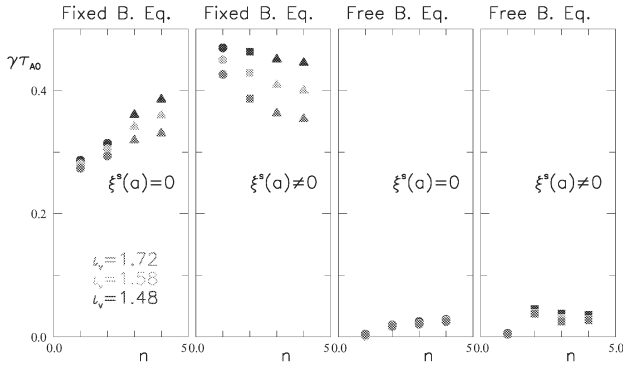


FIG. 1: Normalized growth rate $\gamma\tau_{A0}$ vs toroidal mode number n for MHD equilibria ($\beta = 3\%$) with fixed boundary (the first and the second columns) and with free boundary (the third and the fourth columns). Global mode stability analyses are performed for fixed boundary condition with $\xi^s(a) = 0$ (the first and the third columns) and for free boundary condition with $\xi^s(a) \neq 0$ (the second and the fourth columns). Blue, green, and red colors correspond to the MHD equilibria with the vacuum rotational transform at the plasma boundary being $\iota_v = 1.48$, $\iota_v = 1.58$, and $\iota_v = 1.72$, respectively. Circles (triangles) denote interchange (tokamak-like ballooning) modes. The squares indicate the ballooning-like structure induced by the free boundary motion with $\xi^s(a) \neq 0$.

The global mode stability analyses are performed for

fixed boundary condition with $\xi^s(a) = 0$ (the first and the third columns) and free boundary condition with $\xi^s(a) \neq 0$ (the second and the fourth columns), where the growth rates of the most unstable modes normalized by the Alfvén transit time on the magnetic axis $\gamma\tau_{A0}$ are drawn with respect to the toroidal mode number n , where $\tau \equiv \sqrt{\mu_0\rho_m}/(2\pi\epsilon)dV/d\Phi_T$ with the toroidal flux Φ_T and the permeability in the vacuum μ_0 . For typical high- β LHD operation parameters with the field strength $B \sim 0.5\text{T}$ and proton density $n_e \sim 3 \times 10^{19}\text{m}^{-3}$, $\gamma\tau_{A0} = 0.1$ corresponds to around $40\mu\text{sec}$. It is very clear that the significant MHD stabilization is brought by the boundary modulation induced by the free boundary equilibria.

The β -dependences of the growth rates of the free boundary perturbations $\xi^s(a) \neq 0$ are shown in Fig. 2 for 4 mode families, in three free boundary MHD equilibria with different vacuum boundary. For $\beta < 3\%$, the behavior of the growth rates of free boundary perturbations with respect to β value are similar to those of the fixed boundary perturbations. All the most unstable modes are interchange modes, and the normalized growth rates $\gamma\tau_{A0}$ decrease as β increases independent of plasma vacuum boundary reflecting the change of the rotational transform ι and the improvement of the Mercier criterion D_I induced by the boundary modulation. The significant stabilizing effects are produced by the boundary modulation as β increases.

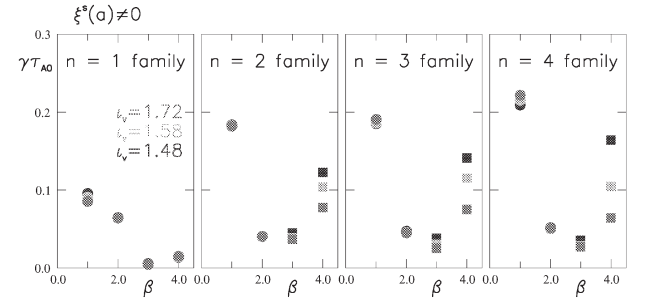


FIG. 2: β -dependences of the growth rates for 4 mode families under the free boundary stability condition with $\xi^s(a) \neq 0$. Blue, green, and red symbols correspond to free boundary MHD equilibria with $\iota_v = 1.48$, $\iota_v = 1.58$, and $\iota_v = 1.72$, respectively. Circles (squares) indicate interchange (free boundary induced ballooning) modes.

[1] Nakajima.N, et al., in Fusion Energy 2004 (Proc. 20th Int.Conf.Vilamoura,2004)IAEA,Vienna,TH/6.

§3. The Second Stability of the High- n Ballooning Modes in Heliotrons

Hudson, S.R. (PPPL), Nakajima, N.,
Hegna, C.C. (Univ. Wisconsin)

The boundary modulation induced by the free boundary motion of MHD equilibrium mainly appears as a large Shafranov shift of the whole plasma. Thus, it might be expected that the MHD stability is improved by the boundary modulation. In order to see how much the equilibrium is stable or unstable against high- n ballooning modes, high- n ballooning stability or $\epsilon' - P'$ stability diagram corresponding to $s - \alpha$ stability diagram in tokamak plasma are evaluated [1] by using the method of profile variations [2], where $\epsilon' = d\epsilon/d\psi$ and $P' = dP/d\psi$, respectively. Free boundary currentless MHD equilibria with $P(s) = P(0)(1 - s)(1 - s^9)$ (s is the normalized toroidal flux) are used for various vacuum plasma boundary in the inward-shifted LHD vacuum configuration. It has been found out that all the free boundary MHD equilibria with $\beta = 3\%$ or $\beta = 4\%$ are in the second stable region or strongly stable in the plasma core region, and near the marginally stable states in the plasma periphery against the high- n ballooning modes. Figure 1 shows the example of the $\epsilon' - P'$ stability diagrams in the plasma core region (the first row) and in the plasma periphery (the second row) for MHD equilibrium with vacuum boundary of $\epsilon_v = 1.48$. In those analyses, the radial wave number θ_k is set 0 and the most dangerous magnetic field line is selected in each flux surface. In Fig. 1, solid (dotted) lines indicate the marginally stability boundaries for MHD equilibrium with $\beta = 3\%$ ($\beta = 4\%$). Two rectangles in each graph indicate the location of the original surfaces for two β values, and the location moves along the direction of arrow as β increases. It is quite clear that the plasma core region is strongly stable against high- n ballooning modes, and that these properties do not change as β increases, namely, the core region has a tendency to move to the second stability region as β increases. On contrast to it, it is also clear that in the plasma periphery, the MHD equilibrium exists around the marginally stable state against the high- n ballooning modes. This tendency does not change in the

range of β value used in stability analyses. Moreover, it might be expected that the MHD equilibria with higher β values still exist near the marginally stable states against high- n ballooning modes near the plasma periphery.

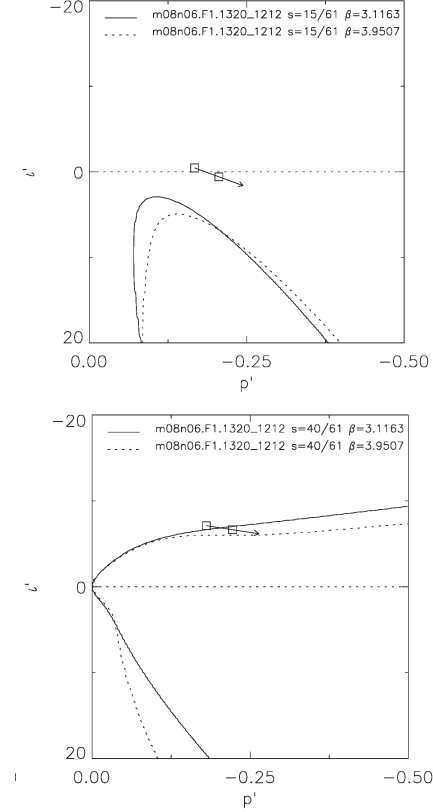


FIG. 1: Stability diagram of high- n ballooning modes in $\epsilon' - P'$ plane at two flux surfaces in the plasma core ($\rho = \sqrt{s} \sim 0.29$, the first row) and in the plasma periphery ($\rho \sim 0.82$, the second row) for MHD equilibrium with vacuum boundary of $\epsilon_v = 1.48$. Note that since ϵ is negative in these analyses, the vertical axis has opposite sign to standard usage and ϵ' is positive (negative) in plasma core (periphery). Solid (dotted) lines indicate the marginally stable lines for $\beta = 3\%$ ($\beta = 4\%$). Rectangles denote the location of the original flux surfaces, and arrows show the direction of the change of the location with increasing β .

- [1] Nakajima, N., et al., in Fusion Energy 2004 (Proc. 20th Int. Conf. Vilamoura, 2004) IAEA, Vienna, TH/6.
- [2] Hegna, C.C. and Nakajima, N., Phys. Plasmas **5** (1998) 1336.

§4. Fourier Mode Analysis of Numerical Results Obtained by Direct Numerical Simulation of MHD Under LHD Inward-shifted Configuration

Miura, H., Nakajima, N., Hayashi, T., Okamoto, M.

Direct numerical simulation (DNS) of three-dimensional (3D), compressible and nonlinear magnetohydrodynamic (MHD) equations are carried out to study plasma stability in the LHD under inward-shifted configuration. For the purpose of the analysis of DNS results in the framework of linear analysis, the Boozer coordinate is constructed by making use of VMEC2000 code. We show below that the full 3D natures of the MHD equations are vital to investigate the plasma stability, while some portions of the linear growth may look similar to the pictures obtained by the reduced set of MHD equations.

Our DNS starts from an initial equilibrium obtained by the HINT computation.¹⁾ Position of the vacuum magnetic axis is set to 3.6m. The pressure profile is sharp around the magnetic axis, having the central beta=4%. Because of the peaked profile, the initial equilibrium has $D_I > 0$ for wide range of the toroidal magnetic flux Ψ . Thus it is expected that the dynamical evolution of MHD equations shows strongly unstable behaviors. Below, we see numerical results of one run, in which the heat conductivity, resistivity and viscosity are set to 10^{-6} , 10^{-6} and 2×10^{-3} , respectively. The number of grid points are 97×97 in the poloidal section and 640 in the toroidal direction.

In Fig. 1, the mean pressure profile ($m/n=0/0$) and rotational transform of the initial equilibrium are shown, where m and n are poloidal and toroidal Fourier wave numbers, respectively. The abscissa is normalized so that it represents the beta value at the origin.

In Fig. 2, the growth of the power spectrum of the pressure, $|P_{mn}(\Psi)|^2$. The exponential growth of $m/n=1/1$ and $2/1$ Fourier modes are observed. The growth of $m/n=2/1$ mode is consistent with the observation in Fig.2. Because of the residue in the HINT computation, $m/n=0/1$ mode has a small but finite amplitude. Consequently, $m/n=1/1$ mode grows as the side band of $m/n=2/1$ mode. The growth of the Fourier modes are saturated after the multiple number of modes grow sufficiently.

In the saturated state, toroidal flow is as strong as poloidal flow. We observe that the toroidal flow and compressibility consist of essence of the dynamical evolution of the plasma in LHD. The numerical results were reported in the IAEA Fusion Energy Conference, Villamoura, Portugal, November 2004.¹⁾

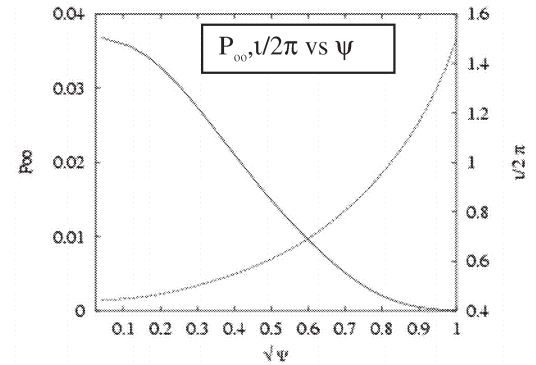


Fig. 1. Mean pressure profile ($m/n=0/0$) and the rotational transform of the initial equilibrium.

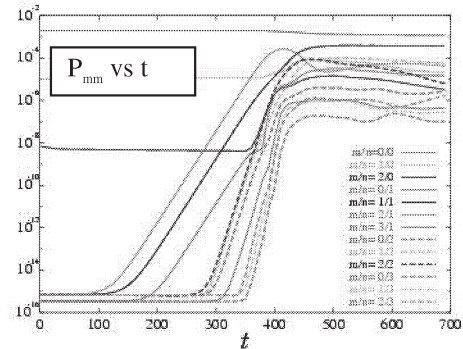


Fig. 2. Time evolutions of the Fourier power spectra of the pressure.

1) H. Miura, K. Ichiguchi, N. Nakajima, T. Hayashi and B. Carreras, *Non-disruptive MHD Dynamics in Inward-shifted LHD Configurations*, (20th IAEA Fusion Energy Conference, Villamoura, Portugal, 1-6 November 2004, IAEA-CSP-25/CD/TH/2-3, ISBN 92-0-100405-2)

§5. Nonlocal Energetic Particle Mode in a JT-60U Plasma

Todo, Y.

Shinohara, K., Takechi, M., Ishikawa, M. (JAERI)

Three types of frequency chirping instabilities, slow frequency sweeping (slow FS) mode, fast frequency sweeping (fast FS) mode, and abrupt large event (ALE) have been observed in the Japan Atomic Energy Research Institute Tokamak-60 Upgrade (JT-60U) plasmas heated with negative ion based neutral beam (NNB) injection. Frequencies of the three instabilities are in the range of shear Alfvén eigenmodes. Frequency sweeping of slow FS mode has a good correlation with equilibrium parameter evolution with time scale ~ 200 ms. On the other hand, time scales of the fast FS mode and the ALE are respectively 1-5 ms and 200-400 μ s, much shorter than the equilibrium time scale. Frequency of the fast FS mode shifts rapidly by 10-20 kHz in 1-5ms both upward and downward. The starting frequency of the fast FS mode changes in the time scale of the equilibrium parameter evolution and follows the toroidal Alfvén eigenmode (TAE) gap frequency.

We have previously investigated the fast FS mode in a JT-60U plasma using a simulation code for magnetohydrodynamics (MHD) and energetic particles, MEGA. We reported that there is an unstable mode near the plasma center and frequency sweeping close to that of the fast FS mode takes place¹⁾. The ratio of the linear damping rate (γ_d) to the linear growth rate (γ_L) in the simulation is consistent with hole-clump pair creation which takes place when is greater than 0.4^{2,3)}.

In this work⁴⁾, we focused on the linear properties of the energetic-ion driven instability in a JT-60U plasma where the fast FS mode was observed. The spatial profile of the unstable mode peaks near the plasma center where the safety factor profile is flat. The unstable mode is not a TAE because the spatial profile deviates from the expected location of TAE and the spatial profile consists of a single primary harmonic $m/n=2/1$ where m , n are poloidal and toroidal mode numbers. The real frequency of the unstable mode is close to the experimental starting frequency of the fast FS mode.

Simulations for various energetic ion orbit widths and energetic ion pressures were carried out to investigate energetic ion effects on the unstable mode spatial profile. Both energetic ion orbit width and energetic ion pressure broaden radial profile of the unstable mode. Energetic ion orbit width has significant effects on the mode spatial profile as is shown in Fig. 1. For the smallest orbit width, the spatial profile is extremely localized near the plasma center where the safety factor profile is rather flat at $0 < r/a < 0.2$. For larger orbit width, the peak location moves radially outward and the radial width is broadened. The radial width of mode spatial profile differs by a factor of 3 between the smallest and the largest (=experimental) orbit width. The radial restoring force, which is a force component in the minor radius coordinate and contributes

to real frequency of the oscillation, was analyzed. The MHD force and the energetic ion force were analyzed for various radial locations and converted to the real frequency. For the largest orbit width, the total frequency which is the sum of the MHD frequency and the energetic ion frequency takes roughly a constant value in the region $0 < r/a < 0.5$ where the unstable mode has substantial intensity. The total frequency is close to the frequency of the unstable mode. What is important is that the MHD force alone cannot keep the frequency spatially constant. The energetic ion frequency amounts to $-0.15 \omega_A$, which is about 60% of the unstable mode frequency. The energetic ions have significant effects on the unstable mode oscillation for the largest orbit width. For the smallest orbit width, the energetic ion frequency is only 10% of the total frequency near the plasma center. This might suggest the existence of a purely MHD eigenmode. However, if such a purely MHD eigenmode does exist without the presence of energetic ions, the spatial profiles of the unstable mode must be independent of the energetic ion parameters. We cannot find such a parameter region. Since we cannot investigate instabilities of low growth rate with the initial value approach, theoretical investigations are needed to clarify the existence of a purely MHD eigenmode near the plasma center with low magnetic shear.

The spatial width of the unstable mode with the smallest orbit width gives an upper limit of the spatial width which the MHD effects alone can induce. For the experimental condition of the JT-60U plasma, the energetic ions broaden the spatial profile of the unstable mode by a factor of 3. The major part of the spatial profile of the unstable mode is induced by the energetic ions. We conclude that the unstable mode is primarily induced by the energetic particles and the name "nonlocal EPM" can be justified.

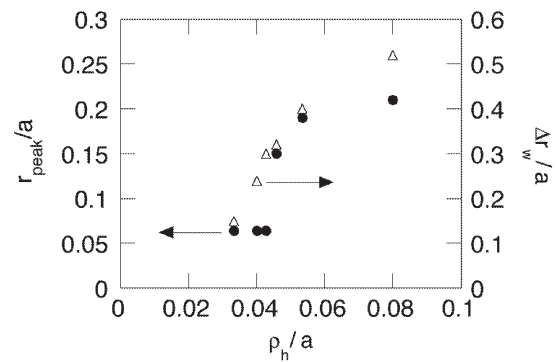


Fig. 1. Peak location (r_{peak}) and radial width (Δr_w) of the unstable mode spatial profile versus energetic ion parallel Larmor radius normalized by the minor radius.

References

- 1) Todo, Y. et al., J. Plasma Fusion Res. **79**, 1107 (2003), <http://jpsf.nifs.ac.jp/Journal/2003.html>.
- 2) Berk, H. L. et al., Phys. Lett. A **234**, 213 (1997); **238**, 408(E) (1998).
- 3) Berk, H. L. et al., Phys. Plasmas **6**, 3102 (1999).
- 4) Todo, Y. et al., Phys. Plasmas **12**, 012503 (2005).

§6. Simulation of Alfvén Eigenmodes and Energetic Particles in an LHD Plasma

Todo, Y., Nakajima, N.

The interesting experimental results of Alfvén eigenmodes in the LHD and CHS plasmas motivated us to extend the MEGA code^{1,2)} for helical plasmas. In the MEGA code, the MHD equations are coupled with the energetic ions through the energetic ion perpendicular current. The MEGA code has been extended to the helical coordinate system (u^1, u^2, u^3) ³⁾ which is used in the MHD equilibrium code, HINT. Relations between the helical coordinates and the cylindrical coordinates (R, ϕ, z) for LHD are

$$h = -1/2,$$

$$M = 10,$$

$$R = R_0 + u^1 \cos(hMu^3) + u^2 \sin(hMu^3),$$

$$z = -[u^1 \sin(hMu^3) - u^2 \cos(hMu^3)],$$

$$\phi = -u^3.$$

The vector calculations are expressed using the metric tensor as follows:

$$(\nabla \phi)^i = g^{ij} \frac{\partial}{\partial x^j} \phi,$$

$$\nabla \cdot \mathbf{v} = \frac{1}{\sqrt{g}} \frac{\partial}{\partial x^j} \sqrt{g} v^j,$$

$$\mathbf{j} \cdot \mathbf{E} = g_{ij} j^i E^j,$$

$$(\mathbf{j} \times \mathbf{B})^i = \sqrt{g} g^{ij} e_{jkl} j^k B^l,$$

$$(\nabla \times \mathbf{B})^i = \frac{1}{\sqrt{g}} e^{ijk} \frac{\partial}{\partial x^j} g_{kl} B^l.$$

The numerical methods are the 4th order finite difference for the MHD equations and the 4th order Runge-Kutta method for the time integration. The numbers of grid points are (91, 115, 1000) for (u_1, u_2, u_3) coordinates. The \mathcal{O} particle simulation is applied to the energetic ions. The number of marker particles is $N=4 \times 10^6$.

The MHD equilibrium of the LHD plasma was calculated using the HINT code. The rotational transform and the pressure in the equilibrium are shown in the left panel of Fig.1. The Alfvén continuous spectra for the toroidal mode number $n=2$ are shown in the right panel of Fig. 1. An example of passing particle orbit is shown in Fig. 2. In this calculation, the magnetic field intensity is $B=1.5\text{T}$, the energy of the particle is $E=150\text{keV}$, the major radius is $R_0=3.75\text{m}$, and the rotational transform is $\iota/2\pi=0.35$ at the plasma center. We see that the envelope of the particle trajectory is closed in the left panel of Fig. 2, which suggests a good particle confinement although the effects of the helical field are seen in both the panels of Fig. 2.

Alfvén eigenmodes were investigated in the LHD plasma. The beam ions with high beta value $\beta_{h/0}=P_{h/0}/(B^2/2\mu_0)=3.9\%$ are employed to destabilize Alfvén

eigenmodes. The beam ions have only the parallel velocity. A toroidal Alfvén eigenmode (TAE) with $n=2$ is destabilized. The real frequency and the growth rate are $\omega/\omega_A \sim 0.31$, $\gamma/\omega_A \sim 0.028$, respectively. The time evolution of a radial velocity harmonic with $m/n=4/2$ and the spatial profile of the TAE are shown in Fig. 3.

The high $\beta_{h/0}$, 3.9% is needed to destabilize the TAE. We can attribute the stability of the TAE to the narrow gap of the Alfvén continuous spectra shown in the right panel of Fig. 1. The narrow gap enhances the continuum damping and the stability of TAEs. It would be interesting to investigate the LHD plasmas with low magnetic shear where the continuum damping is not effective.

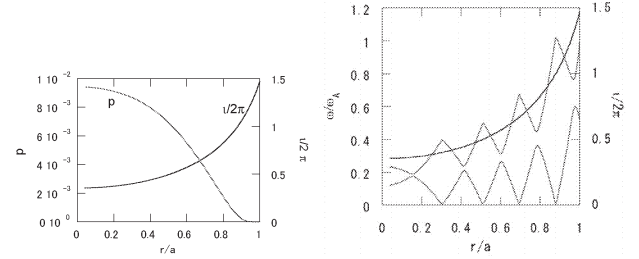


Fig. 1. Rotational transform and pressure in the LHD equilibrium (left panel) and Alfvén continuous spectra for the toroidal mode number $n=2$ (right panel).

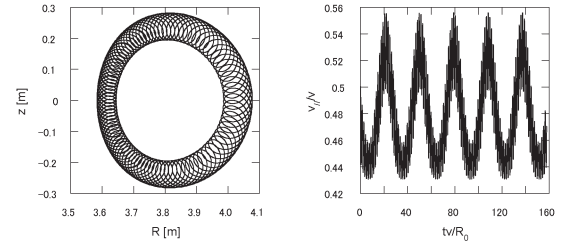


Fig. 2. An example of passing particle orbit. In this calculation, the magnetic field intensity is $B=1.5\text{T}$, the energy of the particle is $E=150\text{keV}$, the major radius is $R_0=3.75\text{m}$, and the rotational transform is $\iota/2\pi=0.35$ at the plasma center.

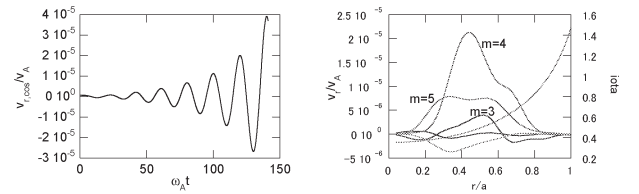


Fig. 3. Time evolution of a radial velocity harmonic with $m/n=4/2$ (left panel) and spatial profile of the TAE destabilized by the beam ions (right panel).

References

- 1) Todo, Y. and Sato, T., Phys. Plasmas **5**, 1321 (1998).
- 2) Todo, Y. et al., Phys. Plasmas **12**, 012503 (2005).
- 3) Todo, Y. et al., in Fusion Energy 2004 (Proc. 20th Int. Conf. Vilamoura, 2004) IAEA, Vienna, TH/3-1Ra.

§7. Nonlinear Evolution of the Fishbone Instability

Shiozaki, Y. (Graduate Univ. Advanced Studies)
Todo, Y.

The fishbone instability is a magnetohydrodynamic (MHD) instability driven by energetic particles. In tokamak plasmas, the primary harmonic of the fishbone spatial profile, which is located inside the $q=1$ magnetic surface, is $m/n=1/1$. Here, q is the safety factor, and m and n are the poloidal and toroidal mode numbers, respectively. Two theoretical explanations of the fishbone instability, the thermal ion diamagnetic drift fishbone and the precessional drift fishbone, were proposed. The frequency of the former is the thermal ion diamagnetic drift frequency, while that of the latter is close to the precessional drift frequency of the energetic ions. Although many theoretical researches have been made on the linear properties of the fishbone instability, the self-consistent nonlinear evolution of the fishbone instability has not been clarified yet. The finite resistivity and the MHD nonlinearity have not been taken into account in the previous nonlinear simulation study of the fishbone instability. We have investigated the nonlinear evolution of the precessional drift fishbone instability using a simulation code for MHD and energetic particles, MEGA.

We investigated the linear properties of the fishbone instability using the MEGA code¹⁾. The plasma parameters used are similar to those of the PDX tokamak where the fishbone instability was first observed. The MHD equilibria consistent with the energetic ion distributions where the trapped particles are dominant were constructed for the initial conditions of the simulations. In the initial conditions, the radius of the $q=1$ magnetic surface is 0.3 of the minor radius. When the energetic particles are absent, the kink instability takes place. We have carried out simulations for various energetic ion beta values. At a critical beta value of the energetic ions we see a transition in frequency from the kink instability to the fishbone instability. The frequency of the fishbone instability is close to 16 kHz for relatively high energetic ion beta values, while the kink instability has no rotation and the frequency is nearly zero for relatively low energetic ion beta values. Time evolutions of the MHD energy and the transferred energy were investigated. We have found that the instability is primarily driven by the energetic ions for relatively high energetic ion beta values. Moreover, the frequency of the instability is proportional to the beam injection energy. Thus, we can conclude that this instability is the precessional drift fishbone instability.

We have carried out five nonlinear simulation runs of the precessional drift fishbone instability with different parameters¹⁾. We can summarize the saturation process of the precessional drift fishbone instability.

1. At the linear growth phase, the energy transfer due to the Joule heating increases in proportion to the energy transfer from the energetic ions to the MHD fluid. The

former is smaller than the latter by one order of magnitude. At the nonlinear phase, the increase in the energy transfer from the energetic ions to the MHD fluid stops, while the energy transfer due to the Joule heating increases to the level of the energy transfer from the energetic ions to the MHD fluid. The balance between the two energy transfers leads to the saturation of the instability.

2. As the instability grows, the magnetic reconnection takes place leading to a magnetic island formation. The overlap of the $m/n=1/1$ and $2/1$ harmonics in the magnetic field fluctuation of the linearly unstable mode and the harmonics created by the nonlinear coupling, such as the $m/n=3/2$ harmonic, generates the stochastic regions of the magnetic lines of force.

3. The energetic ion orbit in the magnetic island and the stochastic regions of the magnetic lines of force is completely different from that in the initial equilibrium configuration. This reduces the number of the energetic ions that drive the fishbone instability, and also reduces the energetic ion pressure gradient. These stop the increase in the energy transfer from the energetic ions to the MHD fluid.

4. At the saturation of the fishbone instability, the energy transfer from the energetic ions to the MHD fluid keeps roughly a constant level. For the TAE instability, the energy transfer stops at the saturation due to the wave-particle trapping. Thus, we conclude that the wave-particle trapping is not important for the fishbone instability.

5. The estimated saturation level of the plasma displacement is the same order of magnitude as the radius of the $q=1$ magnetic surface ($r_{q=1}$). This is different from the previous simulation result of the diamagnetic drift fishbone instability where the saturation level of the plasma displacement is less than 10% of $r_{q=1}$ ²⁾. In the previous simulation, the magnetic reconnection does not take place because neither the MHD nonlinearity nor the finite resistivity was considered. This leads to the difference from the results of the present work. Thus, we conclude that the MHD nonlinearity and the finite resistivity are needed to take account in the nonlinear evolution of the fishbone instability.

6. At the saturation of the instability the frequency shifts downward. The frequency downshift is accompanied by the radial transport of the energetic ions.

7. In all of the cases the safety factor q is below unity at the magnetic axis. Then, the fishbone instability investigated in this work is driven not only by the energetic particles but also by the plasma current. As the safety factor q at the magnetic axis is closer to unity, the properties of the current-driven instability becomes weaker. The estimated saturation level of the plasma displacement is the same order of magnitude as $r_{q=1}$.

References

- 1) Shiozaki, Y., Ph.D. Thesis (2005, Graduate Univ. Advanced Studies, in Japanese).
- 2) Candy, J. et al., Phys. Plasmas **6**, 1822 (1999).

§8. Velocity-Space Structures of Distribution Function in Toroidal Ion Temperature Gradient Turbulence

Watanabe, T.-H., Sugama, H.

We have studied detailed velocity-space structures of ion distribution functions and related entropy balance in the toroidal ion temperature gradient (ITG) turbulence with the anomalous ion thermal transport, by means of the newly developed toroidal gyrokinetic-Vlasov simulation code for the flux tube geometry [1]. The kinetic simulations with high velocity-space resolution enable us to quantitatively discuss the entropy balance which has rarely been evaluated in conventional studies.

Simulation results of the the toroidal ITG turbulent transport clearly show generation of the fine velocity-space structures of the distribution function and their collisional dissipation. Detailed calculation of the entropy balance confirms the statistically steady state of turbulence, where the anomalous transport balances with the dissipation given by the weak collisionality. The above results obtained by simulations with high velocity-space resolution are also understood in terms of generation, transfer, and dissipation processes of the entropy variable in the phase space.

The statistically steady toroidal ITG turbulence is observed in terms of the saturated states of the entropy variable, the potential energy, the ion heat transport flux, and the collisional dissipation. Detailed calculation of the entropy balance for the toroidal flux tube geometry confirms the steady state of the turbulence where the transport balances with the collisional dissipation in the same way as found in the slab ITG system [2]. Fine velocity-space structures of the perturbed ion distribution function clearly appear in fluctuations with large wavenumbers as shown in Fig.1, while the heat transport flux is mainly produced by vortices with long wavelengths. Accordingly, the entropy variable produced by the unstable modes with a macro velocity-scale is transferred in the wave number and velocity spaces, and is finally dissipated in the micro scale by the finite collision. Thus, the statistically steady toroidal ITG turbulence can be sustained, as we have seen in the slab case.

Introduction of the finite collisionality also makes the long-time simulation of the turbulent transport possible by smoothing out the fine-scale structures of the distribution function. According to our

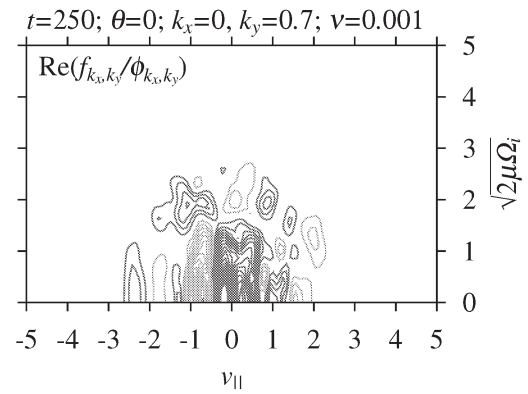


Figure 1: Velocity-space profile of real part of the perturbed distribution function observed in the toroidal ITG turbulence simulation at $t = 250L_n/v_{ti}$ for $k_y = 0.7\rho_i^{-1}$ where $\theta = z = 0$ and $k_x = 0$. The horizontal and vertical axes are defined by $v_{||}$ and $\sqrt{2\mu\Omega_i}$, respectively.

previous studies [2] on the slab ITG turbulence, the collision frequency used in the present study ($\nu_{ii} = 10^{-3}v_{ti}/L_n$) is in a regime where the transport flux has a logarithmic dependence on ν_{ii} . Even if one employs numerically-enhanced diffusivity instead of the collision term with coarser phase-space resolution so as to carry out a *collisionless* turbulence simulation for the same parameters as used here, the transport coefficient may deviate from that in the true collisionless limit. Therefore, in order to quantitatively study the collisionality dependence of the velocity-space structures of the distribution function, one needs to perform numerical simulations with higher phase-space resolution for a lower collision frequency, which remains for future works.

References

- [1] T.-H. Watanabe and H. Sugama, in “Proceedings of the 20th IAEA Fusion Energy Conference” (IAEA, Vienna, 2005).
- [2] Watanabe, T.-H., Sugama, H., Phys. Plasmas **11**, 1476 (2004).

§9. Linear Analysis of Resistive Wall Mode with Poloidal Rotation

Sato, M., Nakajima, N.

Linear dispersion relation of resistive wall mode with poloidal rotation has been derived using the well known reduced MHD equation in a cylindrical tokamak. For simplicity, we use a step function model. The plasma density for $r \leq a$ and for $r > a$ are set to be ρ_0 and ρ_v , respectively. A resistive wall is located at $r = r_w$ and a perfect conducting wall is located at $r = d$. The resistivity of the plasma for $r > a$ is extremely high so that the current is almost zero in the region.

Using the above assumption, the following dispersion relation is derived;

$$\begin{aligned} & -(\omega - m\Omega)^2 \{1 + \alpha\} \\ & = \frac{\gamma_d^2 - i\tau_w^* \gamma_w^2 \omega}{1 - i\tau_w^* \omega} + (1 - \rho_v/\rho_0)(2\omega - m\Omega)\Omega, \end{aligned} \quad (1)$$

where Ω is poloidal rotation frequency, m is poloidal mode number, γ_d is linear growth rate of ideal kink mode defined by

$$\gamma_d^2 = -2(m/q - n)^2 / (1 - (a/d)^{2m}) + 2(m/q - n)/q,$$

and

$$\begin{aligned} \tau_w^* &= \frac{1 - (r_w/d)^{2m}}{1 - (a/d)^{2m}} (1 - (a/r_w)^{2m}) \frac{\tau_w}{2m}, \\ \alpha &= \frac{\rho_v}{\rho_0} \frac{1 + (a/r_w)^{2m}}{1 - (a/r_w)^{2m}} \end{aligned}$$

Here, $\tau_w = \nu_0 r_w \delta / \eta_w$ is the diffusion time of the resistive wall, where δ is a thickness of the resistive wall and η_w is resistivity of the resistive wall.

For low poloidal rotation frequency, the *wall mode* which is locked to the resistive wall is destabilized;

$$\gamma = \frac{1}{\tau_w^*} \frac{\gamma_d^2 + [(1 + \alpha\rho)m - (1 - \rho)]m\Omega^2}{-\gamma_w^2 - [(1 + \alpha\rho)m - (1 - \rho)]m\Omega^2}, \quad (2)$$

$$\omega_r = 0, \quad (3)$$

where $\rho = \rho_v/\rho_0$.

When the poloidal rotation frequency satisfies

$$\Omega^2 \gtrsim \Omega_{c1}^2 = -\frac{r_w^2}{m(m - \frac{1-\rho_v}{1+\alpha\rho_v})(1 + \alpha\rho_v)}, \quad (4)$$

the *plasma mode* which rotates with respect to the resistive wall becomes destabilized;

$$\gamma = \frac{1}{\tau_w^*} \frac{\gamma_d^2 - \gamma_w^2}{2\omega_r \{ [m - 1 + (m\alpha + 1)\rho] \Omega - (1 + \alpha\rho)\omega_r \}} \quad (5)$$

$$\omega_r = (m - f)\Omega - \sqrt{-\frac{\gamma_w^2}{1 + \alpha\rho} - f(m - f)\Omega^2}, \quad (6)$$

where $f = (1 - \rho)/(1 + \alpha\rho)$.

For $\rho_v = \rho_0$, the linear growth rate decreases when the poloidal rotation frequency increases for $\Omega \gtrsim \Omega_{c1}$. For $\rho_v < \rho_0$, however, the linear growth rate increases again for $\Omega \gtrsim \Omega_{c2}$, because the poloidal rotation plays an effective gravity, where

$$\Omega_{c2}^2 = -\frac{r_w^2}{f(m - f)(1 + \alpha\rho_v)}. \quad (7)$$

For $\Omega \gtrsim \Omega_{c2}$, the mode driven by gradient of density appears;

$$\gamma = \sqrt{\frac{f [m - 1 + (m\alpha + 1)\rho_v] \Omega^2 + \gamma_w^2}{1 + \alpha\rho_v}}, \quad (8)$$

$$\omega_r = \frac{m - 1 + (m\alpha + 1)\rho_v}{1 + \alpha\rho_v} \Omega. \quad (9)$$

This mode grows using kinetic energy rather than magnetic energy.

Figure 1 shows dependence of linear growth rates on poloidal rotation frequency. The solution of the dispersion relation almost agrees with the numerical results from the initial value code. For $\rho_v/\rho_0 \leq 10^{-3}$, linear growth rates do not depend on ρ_v . Thus, high resistive plasma can be regarded as a vacuum for $\rho_v/\rho_0 \leq 10^{-3}$.

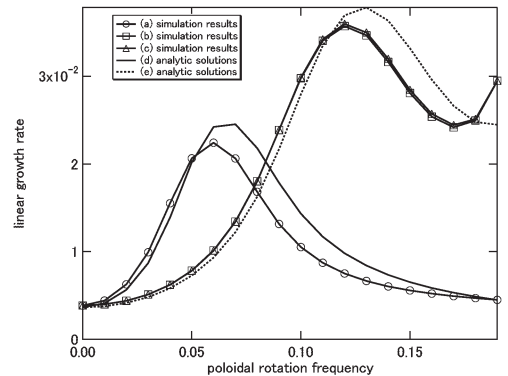


Figure 1: Dependence of linear growth rates on poloidal rotation frequency. (a) $\rho_v/\rho_0 = 1$, (b) $\rho_v/\rho_0 = 10^{-3}$, (c) $\rho_v/\rho_0 = 10^{-4}$, (d) $\rho_v/\rho_0 = 1$, and (e) $\rho_v/\rho_0 = 0$.

§10. Effect of Poloidal Rotation on Nonlinear Resistive Wall Mode

Sato, M., Nakajima, N.

Effect of poloidal rotation on nonlinear behavior and saturation level of resistive wall modes has been studied by means of nonlinear simulation. The nonlinear simulation code is based on reduced MHD equations in a low beta cylindrical tokamak. The code also solves time evolution of temperature and density. There is a high resistive plasma around a hot plasma to use the pseudo-vacuum model. The current is almost zero in the high resistive plasma so that linear growth rate of external mode does not depend on the resistivity at the rational surface of the mode.

Figure 1 shows time evolution of magnetic energy of $(m, n) = (3, 1)$ mode for $\rho_v = \rho_0$, where ρ_0 and ρ_v are plasma density at the plasma center and in the high resistive plasma, respectively. For $\Omega < 0.04$, the *wall mode* which is nearly locked to the resistive wall, is destabilized and the linear growth rate increases when the initial poloidal rotation frequency increases. In this case, the final saturation level does not depend on the initial poloidal rotation frequency. Figure 2 shows time evolution of magnetic energy of $(m, n) = (3, 1)$ mode for $\rho_v/\rho_0 = 10^{-3}$. In this case, the *wall mode* is unstable for $\Omega \leq 0.14$ and the final saturation level dose not depend on the initial poloidal rotation frequency. These results come from slowing down of the poloidal rotation near the plasma edge. The electromagnetic torque damps the poloidal rotation. For *wall mode*, the torque increases due to the effect of twisted mode structure when the initial poloidal rotation frequency increases .

When the poloidal rotation is sufficiently large, the *plasma mode*, which is rotates with respect to the resistive wall, becomes unstable. For the *plasma mode*, the torque decreases due to the effect of preventing magnetic field from diffusing in the resistive wall, when the initial poloidal rotation frequency increases. In this case, the poloidal rotation remains in the nonlinear phase as shown in Fig.3. Therefore, when the initial rotation frequency increases, the final saturation level decreases as

shown in Fig.1 for $\Omega \geq 0.04$.

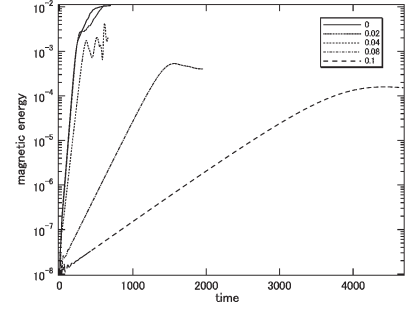


Figure 1: Time evolution of magnetic energy of $(m, n) = (3, 1)$ mode for $\rho_v = \rho_0$. For $\Omega < 0.04$, *wall mode* is unstable, for $\Omega \geq 0.04$, *plasma mode* is unstable.

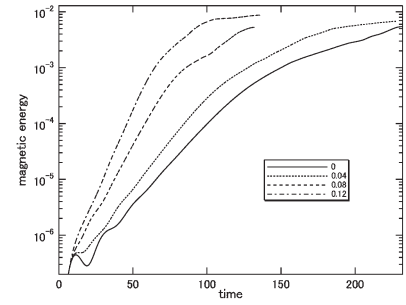


Figure 2: Time evolution of magnetic energy of $(m, n) = (3, 1)$ mode for $\rho_v/\rho_0 = 10^{-3}$. *wall mode* is unstable for $\Omega \leq 0.12$.

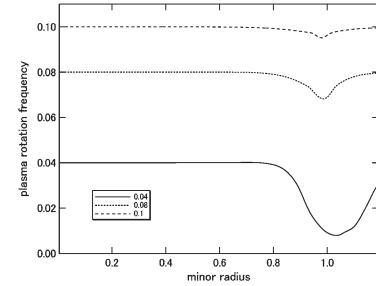


Figure 3: Radial profiles of poloidal rotation frequency at the final saturation for $\rho_v = \rho_0$.

§11. Study of Energy Transport of External MHD Modes in a Cylindrical Tokamak

Sato, M., Nakajima, N.

In this work, we studied nonlinear behavior of ideal external kink mode and resistive wall mode from the point of view of energy conservation using the reduced MHD equations. From the reduced MHD equations, the energy conservation law is derived as

$$\Delta E_m + \Delta E_k + Q_j + Q_\nu = 0, \quad (1)$$

where ΔE_m is a change of magnetic energy, ΔE_k is a change of kinetic energy, Q_j is dissipative energy due to joule heating, and Q_ν is dissipative energy due to viscosity. Figure 1 shows time evolution of energy for an ideal external kink mode. In the linear phase, magnetic energy decreases and most of the released magnetic energy is converted into kinetic energy. This shows that the ideal external kink mode is a current driven mode. In the nonlinear phase, the variation of the kinetic energy decreases and the released magnetic energy dissipates due to joule heating.

Figure 2 shows time evolution of energy for resistive wall mode without rotation. The resistive wall mode grows slowly so that the inertia term can be neglected. Thus, most of the released magnetic energy dissipates due to joule heating in the liner and the nonlinear phase. In the linear phase, the energy dissipates at the resistive wall. However, as the amplitude of the mode become close to the saturation level, the energy dissipates at the plasma rather than resistive wall

When rotation is added to the plasma, the rotation frequency of the mode is smaller than the rotation frequency of the plasma, so that the mode grows using kinetic energy according to the mechanism of Kelvin-Helmholtz instability. In this work, the mode grows using both magnetic energy and kinetic energy when rotation is added. Figure 3 shows time evolution of energy of resistive wall mode with poloidal rotation. In this case, the magnetic energy increases and the kinetic energy decreases in the linear phase, because the mode grows using kinetic energy rather than magnetic energy.

At $t = 80\tau_a$, the poloidal rotation reduces to zero near the plasma edge due to electromagnetic torque, and the increase of magnetic energy stops. After that, the magnetic energy decreases because the mode grows using magnetic energy rather than kinetic energy. Finally, the mode grows up to the saturation level without rotation.

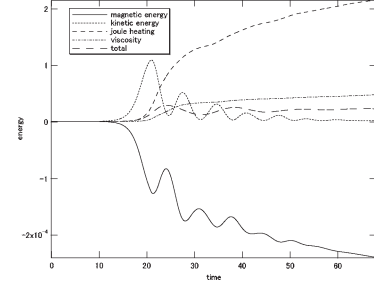


Figure 1: Time evolution of energy of ideal external kink mode.

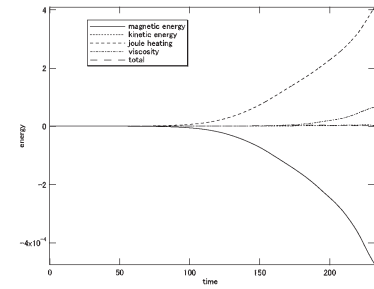


Figure 2: Time evolution of energy of resistive wall mode without rotation. Here, the resistive wall is located at $r = 1.2a$, where a is the plasma minor radius.

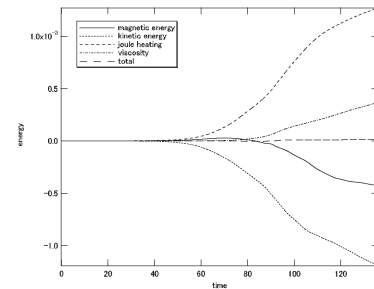


Figure 3: Time evolution of energy of resistive wall mode with poloidal rotation. Here, the poloidal rotation frequency is $\Omega\tau_a = 0.12$ and the resistive wall is located at $r = 1.2$.

§12. Motion of Ablation Cloud in Torus Plasmas

Ishizaki, R., Nakajima, N., Okamoto, M., Parks, P.B.
(General Atomics)

Injecting small pellets of frozen hydrogen into torus plasmas is a proven method of fueling. Experimentally, it is known that the density distribution, after the pellet ablates by encountering the high temperature in plasmas, is not consistent with the distribution inferred from assuming that the ablated material remains on the flux surfaces where the ablation occurred. The subsequent redistribution of mass is considered to be due to $E \times B$ drift induced by toroidal drift [1] It is this phenomenon which we seek to investigate.

In this research, the basic equations are MHD equations. They are solved in a cylindrical geometry (R, ϕ, z) with a rectangular cross-section as shown in Fig. 1, where R and ϕ are a major radius and toroidal angle, respectively. R - z plane is a poloidal surface. The cubic interpolated pseudo-particle (CIP) method is used in the code [2]. An initial magnetic field is a vacuum one proportional to $1/R$. An initial pressure and mass density are assumed to be uniform. In this paper, all variables are expressed in a normalized form. The particle supplement due to a pellet ablation is expressed by an artificial point source located at $(R, \phi, z) = (1, 0, 0)$. Those conditions are not realistic, but the results obtained give some useful understanding on drift of the ablation cloud across the flux surfaces.

Temporal evolutions are obtained by using ideal MHD equations here. Figure 2(a) and (b) show density contours on the mid-plane $z = 0$ at $t = 1$ and 10, respectively, where the time is normalized by an Alfvén transit time. A high density cloud is found to be quickly expanded along B-field compared with the displacement perpendicular to B-field. Figure 3 shows vertical electric field E_z . Dashed and solid lines show E_z at $t = 1$ and 10,

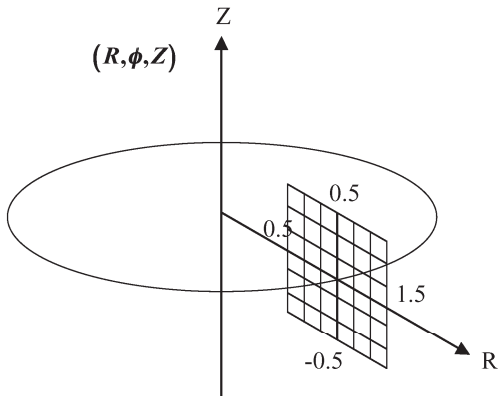


FIG. 1: Coordinate system of numerical code.

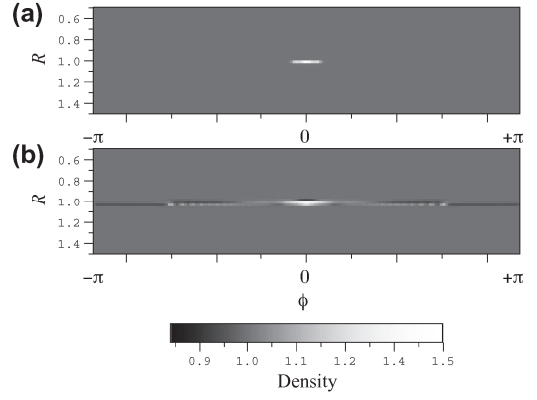


FIG. 2: Density contours on the mid-plane $z = 0$. A horizontal line is a toroidal angle ϕ and a vertical line is a major radius R . (a) and (b) show those at $t = 1$ and 10, respectively.

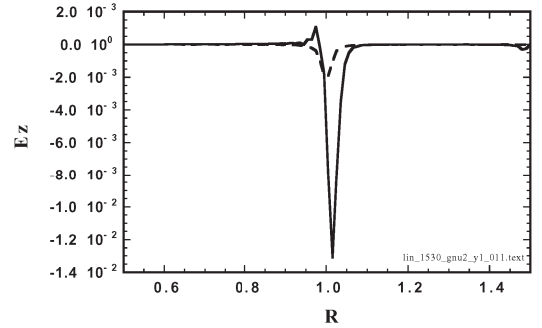


FIG. 3: Major radial profiles of E_z at $\phi = 0$ and $z = 0$. Dashed and solid lines show those at $t = 1$ and 10, respectively.

respectively. That is a negative value within the cloud due to the opposite ∇B and curvature drifts of the ions and electrons. Then, it is clear that the cloud is moved to the low field side due to $E \times B$ drift. A peak value of the drift velocity becomes 3×10^4 m/s at $5 \mu\text{s}$ corresponding to $t = 10$. Actually, the drift velocity is considered to be less than that peak value because a parallel current flowing along the field lines reduces the electric charge developing the vertical electric field E_z .

The motion of the ablation cloud in a vacuum field is investigated by solving the ideal MHD equations. A vertical electric field is induced due to a poloidal drift in the cloud and in result the cloud has a $E \times B$ drift velocity toward the low field side across the flux surfaces.

REFERENCES

- [1] P. B. Parks et al., Phys. Plasmas **7**, 1968 (2000).
- [2] T. Yabe and P. Y. Wang, J. Phys. Soc. Jpn **60**, 2105 (1991).

§13. Three-Dimensional Particle-In-Cell Simulation of Scrape-off-Layer Plasmas

Ishiguro, S.

There is a growing interest in investigation of three-dimensional kinetic effects of scrape off layer plasmas in magnetic fusion devices. For example, charged particle dynamics not only along a magnetic field but also across a magnetic field plays an important role in a blob transport across a magnetic field in a scrape off layer¹⁻⁵⁾. Plasma behavior in the helical diverter in Large Helical Device (LHD) also may cast an importance of three dimensional kinetic treatments. With this situation in mind, we have developed three dimensional Particle-In-Cell (PIC) simulation code for investigation of dynamic plasma behavior in a scrape-off-layer.

Figure 1 shows simulation configuration. Particle absorbing boundaries corresponding to diverter plates are placed in the ends of z-direction. Particle absorbing boundary is also placed at one end of the x-direction. This corresponds to a first wall. A particle impinging to particle absorbing boundaries is removed from the system. The particle absorbing boundaries are grounded. On the other hand, periodic boundary condition is applied in the y-direction. A uniform external magnetic field is pointing into the z-direction.

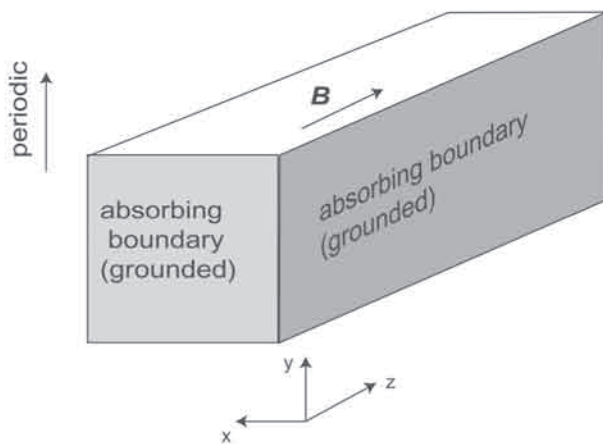


Fig. 1. Configuration of three dimensional Particle-In-Cell simulation for investigation of scrape off layer plasmas.

In order to investigate physics of plasmas in a scrape-off layer, large spatial scale and long time scale simulations are necessary. So we have to make use of a large number of CPUs and Large distributed memories.

The simulation code is constructed by using High Performance FORTRAN (HPF) and is arranged to have a good performance at the National Institute for Fusion Science (NIFS) "Plasma Simulator" NEC SX-7/160M5 system which consists of five nodes, 160 processor

elements, 1.28TBytes memory, vector parallel super computer. The peak peak performance is 1.44 TFlops. The parallelization in each node is done by auto-parallelization and the parallelization among multi nodes is done by using HPF. The base code with periodic boundary condition has attained 224GFlops.

We have made some preliminary runs to check the basic property of plasma surrounded by particle absorbing boundaries. Initially, Maxwellian electrons and ions are uniformly distributed in the system. Simulation parameters are following: the system lengths $L_x=L_y=128\lambda_{De}$, and $L_z=1024\lambda_{De}$, the grid cell number $128 \times 128 \times 1024$, the temperature ratio $T_i/T_e=1$, the ion to electron mass ratio $m_i/m_e=400$, the electron cyclotron frequency to electron plasma frequency $\omega_{ce}/\omega_{pe}=2$, the number of simulation particles $N_i=N_e=1,073,741,824$. Since escape of electrons from the system to the boundaries is faster than that of ions, plasma region is positively charged. Ion sheaths are created in front of the boundaries at the ends of z-direction. These features are clearly shown in Fig. 2, which is a potential profile in the x-z plane.

This simulation model will be extended to include non-uniform magnetic field and the transport of blobs will be investigated.

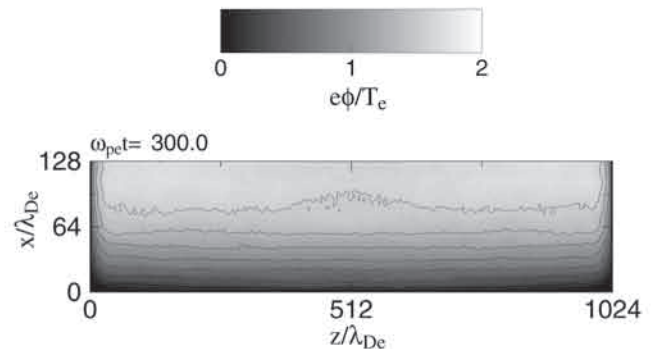


Figure 2: Potential profile in x-z plane.

References

- [1] M. Umansky, S. I. Krashennnikov, B. LaBombard, J. L. Terry, Phys. Plasmas **5**, 3373 (1998).
- [2] R. Schneider et al., in: 17th International Conference on Plasma Physics and Controlled Fusion Research, Yokohama, Japan, 19-24 October, 1998, paper FI-CN-69/THP2/05.
- [3] B. Lipschultz et al. in: 18th IAEA Fusion Energy Conference, Sorrento, Italy, 4-10 October, 2000, paper IAEA-CN-77/EX5/6.
- [4] S. J. Zweben, R. J. Maqueda, D. P. Stotler et al., Nucl. Fusion **44**, 134 (2004).
- [5] S. I. Krashennnikov, Phys. Lett. A **283**, 368 (2001).

§14. Core-SOL-Divertor Model and Application to Operation Space of EAST

Hiwatari, R. (CRIEPI: Central Research Institute of Electric Power Industry), Hatayama, A. (Keio Univ.), Okano, K. (CRIEPI), Asaoka, Y. (CRIEPI), Zhu, S. (Institute of Plasma Physics, China), Tomita, Y. (NIFS)

The transport models applied to Core-SOL-Divertor (C-S-D) model are a 0D core plasma model based on ITER physics guidelines and a usual two-point model for SOL-divertor region. The key issue of this C-S-D model is how to combine the two-point model with the 0D core plasma model. Usually, the upstream SOL density is a given parameter in the two-point model. In the C-S-D model, the particle balance for SOL-divertor region including the neutral transport is solved to evaluate the upstream SOL density n_s . We assume that all neutral particles are originated at the divertor plate. Its generation rate is supposed to be proportional to the particle flux to the divertor plate. Consequently, the following definition of the total neutral source rate N_n including gas puff N_{puff} at the edge region is applied;

$$N_n = n_d M_d C_s 2\pi R h \Delta_n \sin(\psi) + N_{\text{puff}}, \quad (1)$$

where n_d , M_d , C_s , R and ψ are density, mach number and sound velocity, major radius and the angle of the magnetic field at the divertor plate, respectively. The density decay length Δ_n is assumed to be twice of temperature decay length of SOL. By using this simple neutral model and the particle flux across the separatrix Γ_{core} from the 0D core plasma calculation, the particle balance equation for the SOL-divertor region becomes

$$\Gamma_{\text{core}} S_{\text{core}} + N_n^{\text{sol}} + N_n^{\text{div}} = n_d M_d C_s \sin(\psi) S_{\text{div}}, \quad (2)$$

where N_n^{sol} (N_n^{div}) is the total number of ionized

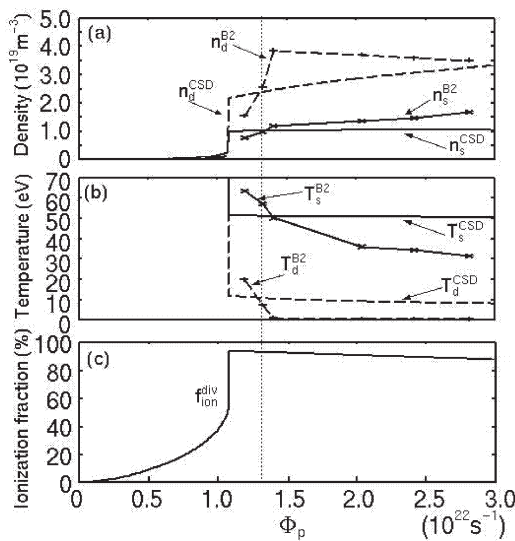


Fig.1 SOL-divertor parameters v.s. Φ_p (a) density, (b) temperature by the C-S-D model and the B2EIRENE, and (c) is the ionization fraction in the divertor region by C-S-D model

particles in the SOL (divertor) region, and S_{core} and S_{div} are the areas for the core and divertor region normal to the particle flux. The ionized particle numbers are defined by the ionization fraction in the SOL and the divertor region ($f_{\text{ion}}^{\text{sol}}$ and $f_{\text{ion}}^{\text{div}}$). Their definitions are $N_n^{\text{sol}} = f_{\text{ion}}^{\text{sol}} (1 - f_{\text{ion}}^{\text{div}}) N_n$ and $N_n^{\text{div}} = f_{\text{ion}}^{\text{div}} N_n$. The ionization fraction in the divertor region is modeled by $f_{\text{ion}}^{\text{div}} = 1 - \exp(-(L_d \sin(\psi))/\lambda_{\text{ion}}^{\text{div}})$, where L_d and $\lambda_{\text{ion}}^{\text{div}}$ are the length of the divertor region and the mean free path of the neutral particle, respectively. The ionization fraction in the SOL region is defined by $f_{\text{ion}}^{\text{sol}} = A_{\text{sol}} / (A_{\text{core}} + A_{\text{sol}} + A_{\text{pump}})$, where A_j denotes the effective area for core plasma, SOL and pumping effect, respectively.

To check the validity of this C-S-D model, comparison with the edge transport code (B2-EIRENE) is carried out on JT-60U plasma configuration¹⁾, and it is shown that the result by the C-S-D model is reasonable (Fig.1), however, other validation for the neutral transport should be carried out because of the simple neutral model.

By using this C-S-D model, we explore the possible operation space of EAST in the space of the total particle flux Φ_p and the total heat flux Q_{in} across the separatrix. The operational space is painted in Figure 2¹⁾, and each boundary is the operation condition as for (1) max. heat load to the divertor $q_{\text{div}} < 3.5 \text{ MW/m}^2$, (2) LH transition condition $Q_{\text{in}} > P_{\text{thr}}$, (3) available LHCD power $P_{\text{LHCD}} < 3.5 \text{ MW}$, and (4) power balance condition $P_{\text{LHCD}} < Q_{\text{in}}$.

Figure 2 indicates that the allowable heat flux to the divertor plate is a key parameter to extend the possible operation space. The upper boundary of Q_{in} is limited to 3.0~3.5MW by $q_{\text{div}} < 3.5 \text{ MW/m}^2$. The boundary of $q_{\text{div}} < 3.5 \text{ MW/m}^2$ for $Q_{\text{in}} < 3.0 \text{ MW}$ region implies the low recycling state. The upper boundary of the particle flux Φ_p is dominated by the power balance requirement for the low Q_{in} region, while it is limited by the available LHCD power for higher Q_{in} . In other words, the available power for the LHCD tends to be a key parameter to extend the operation density of the core plasma in this high Q_{in} regime. In this exploration, no gas puffing in the divertor region is assumed. The sudden changes of the curve for the required LHCD power and the power balance around $Q_{\text{in}} \sim 1.7 \text{ MW}$ are caused by the LH transition.

This work is partly supported by JSPS-CAS Core-University Program on Plasma and Nuclear Fusion.

Reference

- 1) Hiwatari, R. et al.: J. Nucl. Mater. **337-339**, (2005) 386-390

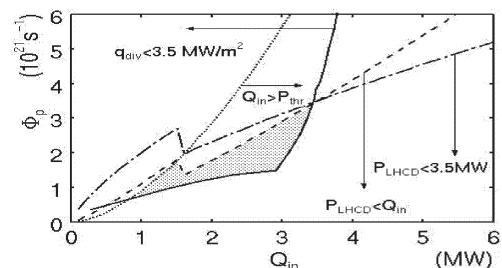


Fig. 2. Qualitative features of EAST operational space.

\$15. Edge Plasma Simulation of Stellarator System with UEDGE

Takayama, A., Tomita, Y., Ishiguro, S.,
Pigarov, A.Yu., Krashenninnikov (UCSD), Rognlien,
T.D. (LLNL)

Magnetic configuration at the edge of a stellarator is very complex and contains a mixture of closed flux surfaces and stochastic field lines. At present, there is no plasma transport code that can handle highly complicated case. Moreover, it is even not very clear what kind of set of transport equations can be used for these purposes. At the same time, it is feasible that due to a strong anomalous cross-field plasma transport and convective plasma flows, rather detailed features of stellarator magnetic topology do not matter much for averaged plasma parameters. Therefore, it is worth to try a simple approach to the modeling of stellarator edge plasma based on “averaging” of edge plasma parameters along the magnetic axis and introducing effective two-dimensional flux surfaces. In this sense, we substitute the stellarator edge with that what can be called a stellarator-equivalent tokamak (SET) edge. We apply this approach to edge plasma modeling for Large Helical Device (LHD). We simulate the LHD-stellarator-equivalent tokamak with 2D edge plasma transport code UEDGE¹⁾.

This method has following properties:

- Double null (bottom and top X-points) configuration,
- Same large aspect ratio,
- Same plasma cross-section elongation,
- Similar position of X-points, strike points at divertor plates, and plasma axis,
- Same radial gradient of magnetic flux in the core region adjacent to separatrix, and
- Similar compression factor for the edge magnetic flux tube, that is, the relation between the characteristic width of magnetic tube at the SOL mid-plane and its width in the divertor near strike points.

In the SET configuration, the characteristic connection length L_{SOL} of magnetic field lines from the SOL mid-plane to the divertor plates is typically set equal to the characteristic connection length in the real stellarator configuration calculated with 3D magnetic field line tracing code and averaged over a certain part of the “SOL”.

The UEDGE code solves in 2D the fluid equations for plasma transport and reduced set of Navier-Stokes equations for neutral particle transport. The plasma sources are the ionization of recycling atoms and flux from NBI-fuelled core plasma. Plasma is neutralized at the divertor plates and walls and the corresponding boundary

conditions are similar to that in tokamaks¹⁾. The combined effect of small-scale magnetic islands, stochastic magnetic field layers as well as of intermittency (infrequent but large-scale transport events) on cross-field plasma transport is modeled in UEDGE by prescribing the 2D profiles anomalous convective velocity V_{conv} and anomalous diffusivities (D_{\perp} , χ_{\perp}) and by adjusting these profiles in order to match the experimental plasma profiles and recycling data²⁾.

Figure is a simulation result (ion density) of the case with the following conditions: $B_T=3[\text{T}]$, $R_0=3.75[\text{m}]$, $n_{\text{ex}}=4.0 \times 10^{19}[\text{m}^{-3}]$, $P_e = \gamma_{\text{ei}} W_0$, $P_i = (1 - \gamma_{\text{ei}}) W_0$, $\gamma_{\text{ei}}=0.4$, $W_0=W_{\text{NBI}}-W_{\text{rec}}$, $W_{\text{NBI}}=3.5[\text{MW}]$, $W_{\text{rec}}=0.5[\text{MW}]$. In the obtained steady-state solutions, the plasma flux through core interface is equal to the neutral flux plus the NBI fuelling rate F_{NBI} . Anomalous diffusivity for this case is $D_{\perp}=0.20[\text{m}^2/\text{s}]$, $\chi_{\perp}=0.40[\text{m}^2/\text{s}]$.

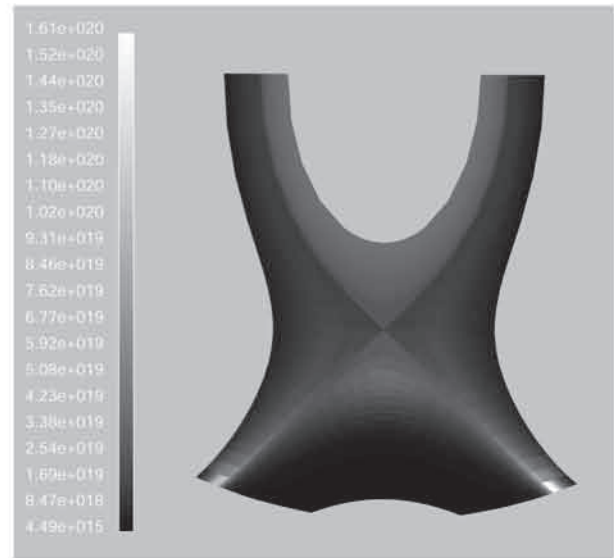


Figure Ion density n_i profile

References

- 1) Rognlien, T.D. *et al.*, J.Nucl.Mater. **196** (1992) 345.
- 2) Pigarov, A..Yu. *et al.*, J.Nucl.Mater. **313** (2003) 1076.

\$16. The Strike Point Pattern on Local Island Divertor in LHD

Jimbo, S. (Grad. Univ. Adv. Studies)
Takamaru, H. (Chubu Univ.)
Kanno, R., Satake, S., Okamoto, M.

The Local Island Divertor (LID) is one of the divertor concepts [1] involved in the Large Helical Device (LHD) configuration and it utilizes an $m/n=1/1$ island formed at the edge region of the LHD. The LID has been proposed to control the edge plasma of the LHD. Control of the edge plasma by means of the LID aims to achieve high temperature divertor operation (HT-operation). It is important to investigate whether or not the particle flux cross the island separatrix is successfully guided to the rear side of the island where the target plates are placed to receive the particle load. If the particles strike on the front part of the LID head, then the particles neutralized on the front part cannot be pumped out, because the front part is not covered by the pumping duct. Thus, optimization of the particle orbits in the island region is the key to realize HT-operation by means of the LID.

Assuming HT-operation is achieved it is expected that the neoclassical effect on the edge transport becomes important. Since the edge plasma in HT-operation is collisionless, the orbits of charged particles become complex compared to the field lines; i.e. the effect of the Coulomb collision causes the transition between a passing particle orbit in the 3D field line structure and a trapped particle orbit in toroidal and helical ripples (localized and/or blocked particle orbits). Thus, according to the ratio of the mean free path to the connection length, the pitch angles of the particles which contribute the particle flux to the LID head is expected to vary; in the present study it is called the neoclassical effect on the edge transport phenomena. Here, the connection length is given as a length along a field line connecting the core region to the LID head estimated as $L_c=100$ m. Monte Carlo simulation based on test particle representation is carried out in order to investigate on strike point patterns of ions on the LID head in the 3D field line structure, the edge plasma transport under HT-operation.

The strike point patterns on the LID head have been numerically observed by tracing the orbits of the guiding centers in the fixed magnetic field under the effects of the Coulomb collisions and the anomalous diffusion.

The change in strike point pattern was seen according to the change in l/L_c . When the mean free path l is estimated as $l/L_c=3$, the strike point pattern becomes almost symmetric, and peak of strike point pattern corresponds to the intersection of the island separatrix on the LID head. In this case, the passing particles mainly contribute the particle flux to the head, thus the particles contributing the transport follow the orbits along field lines of the island separatrix. When the mean free path l is estimated as $l/L_c=0.03$, the particles escaping into the island region suffer the pitch angle scattering sufficiently and are carried to a far region from the island separatrix. In this case the particles strike mainly the inside in front of the LID head and decrease the number of particles that reach rear side

separatrix. When the mean free path l is estimated as $l/L_c=0.3$ as shown in Fig1, the strike point pattern becomes not symmetric, and peak of the strike point pattern is located at the edge of the head. In this case, the particles transit between a passing particle orbit and a trapped particle orbit in toroidal and helical ripples. So trapped particle orbits escaping into the island region suffer the pitch angle scattering and are carried to inside of region from the island separatrix. Passing particle orbits move along field lines of the island. Around the head, $B \times \nabla B$ motion of particles are downward as shown in Fig.2. Therefore, the particle that approaches the head from the upper part reaches the head easily, and the particle that approaches from the lower side doesn't reach the head easily. Broken symmetry of strike point pattern is caused by this effect.

The neoclassical effect plays the important role in determining the strike point patterns on the LID head. The performance is improved according to the rise of l/L_c . The above results are not easily treated in fluid representation.

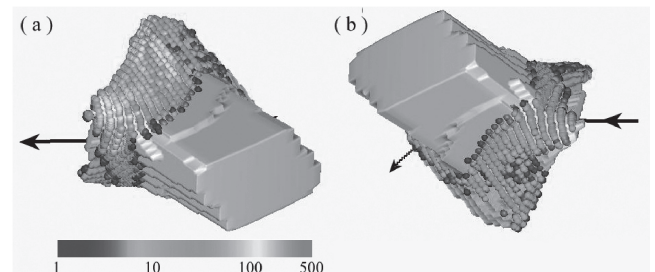


Fig. 1. The strike point pattern on the LID head for the Case of $R_{ax}=3.6$ m, $E=300$ eV and $l/L_c=0.3$: (a) the rear-view of the pattern, (b) the opposite-side-view of the figure (a). The color of the pattern indicates strength (A.U.) of the number of test particles striking the head.

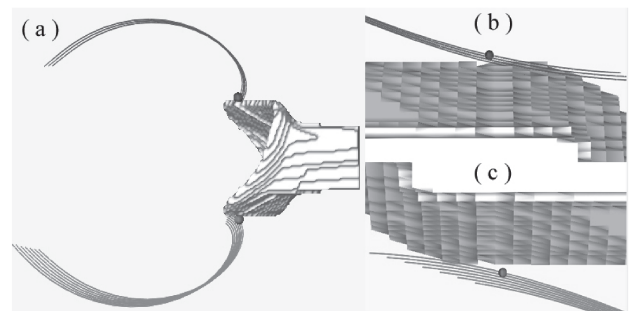


Fig. 2. Illustration of guiding center orbit; (a) side view, (b) closeup of back view (upper part), (c) closeup of back view (lower part), spheres are the initial positions of particle.

Reference

- 1) N. Ohya, et al, J.Nucl. Mater. **145-147** (1987) 844

\$17. 3-D Rayleigh-Taylor Instability in Spherically Stagnating Systems

Sakagami, H.

Okamoto, T. (Sanyo Electric Co. Ltd.)

Horikoshi, M., Nishihara, K. (Institute of Laser Engineering, Osaka University)

In inertial confinement fusion, the Rayleigh-Taylor instability is unavoidable during the implosion and can destroy spherical symmetry of a fusion target. It is, therefore, one of important research topics in this field to investigate this instability. At the Rayleigh-Taylor instability in 3-D systems, dynamics of vertical vortex pairs that are associated with mode coupling plays an important role unlike 2-D systems.¹⁾ On the other hand, the Rayleigh-Taylor instability in spherical geometry is quite different from that in planar geometry, because acceleration and wavelength vary in space and time. Thus we have been investigating nonlinear features of the fully 3-D Rayleigh-Taylor instability in spherically stagnating systems through numerical simulations.

As a Rayleigh-Taylor unstable interface is shrunk during the implosion and a radius of the interface is minimized at the maximum compression, we must set up the simulation system to capture the minimized interface with enough number of meshes. Recently advanced laser systems can be highly aligned and irradiate fusion targets more uniformly than ever, and the highly evolved fabrication technology can produce more precise spherical targets. So inspecting experimental results requires more precise simulations that calculate not only lower mode but also higher mode phenomena. Thus large-scale simulations are essential to analyze those experimental results with enough precision, and they will be accomplished only with parallel supercomputers. We have parallelized a three-dimensional fluid code, IMPACT-3D with High Performance Fortran on the Earth Simulator.²⁾

We have introduced a self-similar analysis to describe the stagnation dynamics, which includes the effects of spherical geometry, acceleration and wavelength varying in space and time.³⁾ At the start of each simulation, a small perturbation was applied to the density profile of the self-similar solution at the contact surface. We have performed large-scale simulations with initial perturbations, which are given by superimposing of two spherical harmonics function modes (6,3) and (12,6). The nonlinear structure is shown in Fig.1 (a). Actually an initial perturbation mainly comes from the fact that fusion targets are irradiated with a finite number of laser beams. This laser irradiation system induces the perturbation with the shape of not the spherical harmonics function but geometrical pattern related to the irradiation symmetry. We have also been investigating the Rayleigh-Taylor instability for initial perturbations based on an icosahedron, which was associated with GEKKO XII at ILE, Osaka University. Small perturbations with various amplitudes were applied to density profile at each vortex and face's incenter of

icosahedron, including randomly arranged bubbles/spikes with 32 levels of initial amplitudes, randomly arranged only bubbles with 16 levels, randomly arranged only spikes with 16 levels, a specific bubble surrounded by bubbles or spikes with different levels, and a specific spike surrounded by bubbles or spikes with different levels. The nonlinear structure for randomly arranged bubbles/spikes with 32 levels is shown in Fig.1 (b). From all simulation results, we plotted nonlinear growth rates of the Rayleigh-Taylor instability near the maximum compression as a function of initial perturbation amplitudes in Fig. 2. We found that all data were fallen onto a universal curve. Namely, the nonlinear growth rate is depended only on the initial perturbation amplitude regardless of many other conditions, and this characteristic is similar to that of the Richtmyer-Meshkov instability.

It is noted that the Earth Simulator Center claims more than 95% of vectorization ratio and more than 50% of parallelization efficiency to run the simulation code on the Earth Simulator, and we have cleared these severe criteria on using 1024x1024x1024 meshes and 128 nodes (1024 processors). Jobs can be easily submitted to the Earth Simulator through commonly used NQS-II system and typical runs can be done within 3 hours on 128 nodes of the Earth Simulator.

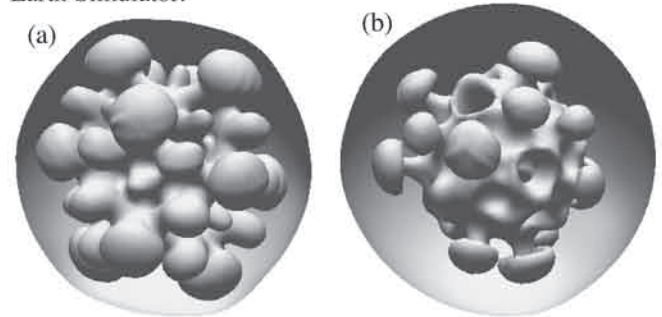


Fig.1. Three-dimensional structures for (a) double modes of spherical harmonics function and (b) randomly arranged bubbles/spikes with 32 levels.

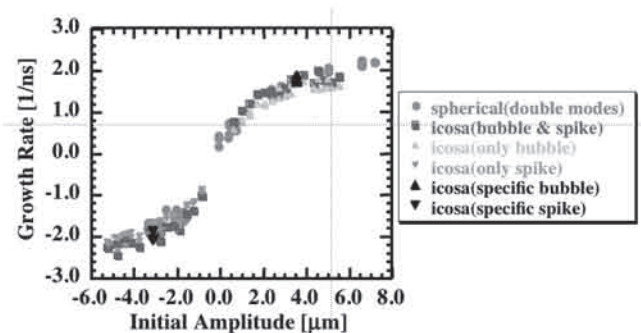


Fig.2. Nonlinear growth rates as a function of the initial perturbation amplitude for various conditions.

References

- 1) Horikoshi, M., et al., Phys. Plasma **9**, (2002) 3536.
- 2) Sakagami, H., et al., Proc. IEEE/ACM SC2002, (2002) pap147. (Gordon Bell Awards)
- 3) Hattori, F., et al., Phys. Fluids **29**, (1986)1719.

§18. Laser Fusion Research

Mima, K. (Institute of Laser Engineering, Osaka University)

Since April, 2003, we started the construction of heating laser of 10kJ/10ps/1.06 mm ; named LFEX (Laser for Fusion Experiment), for FIREX-I. The LFEX will be completed before the end of 2007. The expected rise time of the short pulse LFEX is less than 1ps and the focus diameter is smaller than 30 mm. As the front end of the laser, OPCPA is introduced to improve the contrast ratio to less than 10^{-8} . For pulse compression, segmented dielectric gratings will be used. The R&D for the coherent combining of the pulse compressed segmented beam has started [1]. After the completion of LFEX, we will start the foam cryogenic cone shell target experiment in late 2007.

Cone shell target implosion is studied by experiments and simulations for the FIREX-I target design. The detail of implosion hydrodynamics has been explored with a new implosion code PINOCO. The recent implosion simulations for FIREX targets show that a core plasma density is as high as the maximum density of spherical implosion and the area density can be higher than the spherical implosion.

By the peta watt laser heating simulation researches , we found that the cone top is heated up to a few 100 keV by electrostatic and electromagnetic collective interactions between relativistic electrons and back ground electrons. This reduces the laser relativistic electron energy to enhance the stopping power and the delayed energy transport from the heated cone top to the core keep core heating for a long time after the laser pulse. We believe that those processes related to the core heated should be controlled in the FIREX experiments. The scalability of these processes will be verified in the FIREX-I experiment and related theory and simulation research. From those understanding on the heating physics and the cone shell implosion hydrodynamics, we believe that the hot spark $(rR)_h$ and the temperature will reach 0.45 g/cm², and 5keV respectively in the FIREX-I.

The target fabrication and irradiation system with characterization of DT cryogenic foam layer are also under development as the collaboration program between Osaka University and NIFS(National Institute for Fusion Science). The DT fuel will be fed to the foam shell layer through a capillary and then, frozen to a solid layer. Then , The integrated FIREX-I experiment will start before the end of 2007. If the gain of the order of 0.1 and the temperature higher than 5keV are achieved in FIREX-I before the end of 2008, we plan to proceed to the FIREX-II in 2009. "Recent results and future prospects on fast ignition research: theory and experiment

Reference

- 1) N.Miyanaga, et al, Proceedings of IFSA2002, Monterey, Ca., US.
- 2) H.Nagatomo, Prodeedings of the IFSA2002, Monterey, Ca., US

§19. Research on High Energy Density Laser Plasma Physics

Mima, K., Theory and Simulation Group (Institute of Laser Engineering, Osaka University)

Since 2003, we continued to develop an Fast Ignition Interconnected Integrated code (FI3 code) to include appropriate physics in transport of relativistic electron in dense plasmas. A radiation hydrodynamic simulation with PINOCO [1] has been combined with a collective PIC simulation [2] and a Fokker Planck simulation [3] by using the inter net proto call DCCP [4]. As the demonstration of the FI3, we analyzed the imploded plasma heating processes in the cone target experiment [5]. We found in the analysis that an Au solid layer irradiated by a peta watt laser is highly biased to confine high density hot electron which is generated by strong two stream instability in relatively low density plasmas contacting the Au layer. As shown in Figs. 1 and 2, the heat flux from the cone tip to the imploded plasma continues at high level for a long time after the laser pulse and the main part of the heat flux is carried by sub-MeV electrons. We found that the plasma heating after the laser pulse is significant for a few pico second.

In a PIC simulation, it was also discovered that laser produced relativistic electrons are well confined on the plasma-vacuum interface when the laser incident angle is greater than 60 deg. This means that the relativistic electron heat transport is strongly inhibited on the solid target surface. This phenomena have been observed in a recent experiment at University Michigan[6]. By hybrid simulations, Weibel instability is further investigated. We found that the merging process of relativistic electron filaments is sensitive to electron beam cross section and total current. When the total current is much larger than the Alfven limit current, multi stationary filaments co-exist for a long time which means ion time scale. On the other hand, when the total current is not much larger than the Alfven limit current, filaments merge into a single filament. The detail of this result is shown by Matumoto in this Annual report.

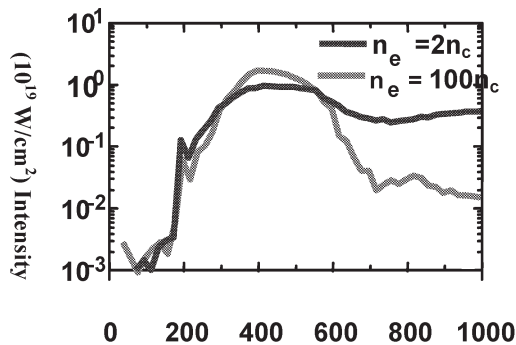


Fig. 1. Time dependent relativistic electron heat flux and heated core temperature

Reference

- 1) H. Nagatomo, et al., *Inertial Fusion Science and Applications 2001*, (Proc. of IFSA 2001, Kyoto), Elsevier, 140 (2001).
- 2) H. Sakagami, et al., *Inertial Fusion Science and Applications 2001*, (Proc. of IFSA 2001, Kyoto), Elsevier, 380 (2001).
- 3) T. Johzaki, et al., Ann. Prog. Rep. 2002, ILE, Osaka Univ., 95 (2003); T. Johzaki, et al., "Integrated Simulations for Fast Ignition Targets", to be published in Proc. of ITC-13.
- 4) H. Sakagami, et al., *Inertial Fusion Science and Applications 2003*, (Proc. of IFSA 2003, Monterey), ANS, 434 (2004).
- 5) R. Kodama, et al., *Nature*, **412**, 798 (2001); R. Kodama, et al., *Nature*, **418**, 933 (2002).
- 6) T. Lin et al, Private communication and poster session of APS DPP meeting 2004

§20. Structure of Thin Current Layer in Two-dimensional Open System

Horiuchi, R., Kawakita, T. (Nagoya U.), Ohtani, H., Ishizawa, A.

Magnetic reconnection is an important bridging process between microscopic physics, which leads to the generation of electric resistivity, and macroscopic physics which determines global plasma transport and global change of field topology. Thus, the spatial structure of current layer, which is a typical measure of microscopic physics, is not independent of macroscopic physics such as external driving field. In order to clarify relationship between microscopic physics and macroscopic physics controlling magnetic reconnection, we have examined the dependence of current layer structure on external driving electric field by using two-dimensional particle simulation code developed for an open boundary system.

The previous simulation study [1] have revealed that dynamical behavior of collisionless driven reconnection is strongly dependent on the spatial scale of driving field E_d , but insensitive to the amplitude of the field E_d . In order to clarify physical meaning of this result, we have carried out particle simulation of collisionless driven reconnection for larger mass ratio and wider parameter range of the driving field E_d . The simulation parameters are as follows; mass ratio $M_i/M_e=100$, total number of particles is 12000000, and the spatial scale of E_d is fixed to the same value in the previous simulation when the steady reconnection was realized [1].

The steady reconnection is realized in the same way as the previous simulation for each case. As is shown in Fig. 1, two-scale structure is formed in the current density profile at the steady state, except for the smallest driving field case. Figure 2 shows the temporal evolution of spatial scales of current layer for the amplitude of the driving field $E_{z0}=-0.05$. The larger scale is equal to ion meandering scale, while the smaller scale corresponds to the electron meandering scale. This result is in good agreement with the recent simulation result [2] that the reconnection electric field is sustained by the pressure tensor term originating from the ion stochastic motion near the neutral sheet. It is interesting to point out that a threshold value of the driving field may exist in forming the two-scale structure.

Reference

- 1) W. Pei, R. Horiuchi and T. Sato, Phys. Plasmas, **8** (2001), pp. 3251-3257.
- 2) A. Ishizawa, R. Horiuchi, and H. Ohtani, Phys. Plasmas, **11** (2004) 3579-3585.

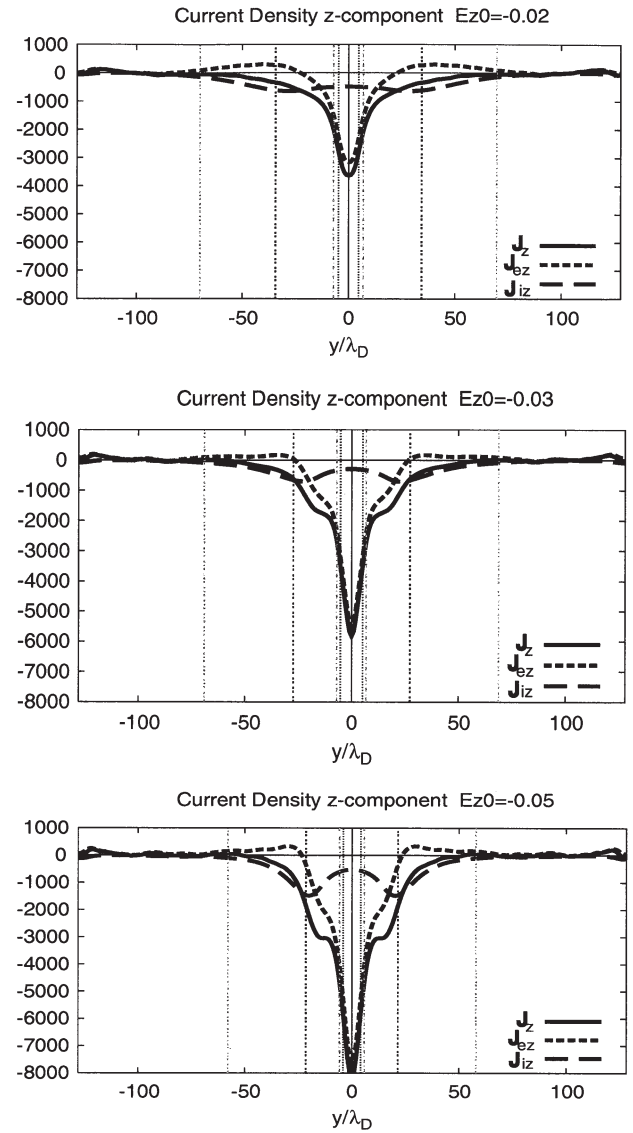


Fig. 1. Spatial profiles of current density profile for the driving field $E_{z0}=-0.02$ (top), 0.03 (middle), 0.05 (bottom).

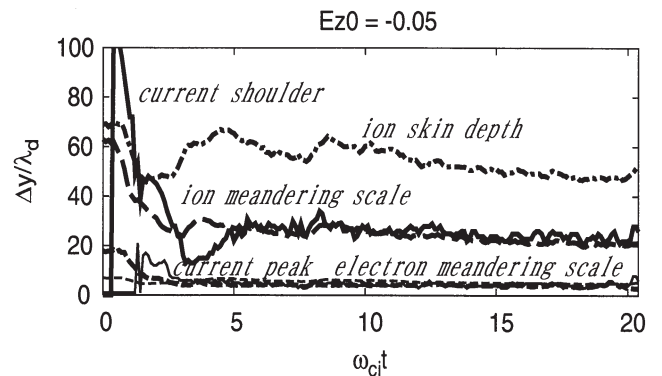


Fig. 2. Temporal evolution of spatial scales of current layer for the driving field $E_{z0}=-0.05$.

§21. Collisionless Driven Reconnection in Three-dimensional Thin Current Sheet

Horiuchi, R., Ohtani, H., Ishizawa, A.

Magnetic reconnection is controlled by multi-scale physics from microscopic physics, which leads to the generation of electric resistivity, through macroscopic physics which determines global plasma transport and global change of field topology. In order to clarify magnetic reconnection as multi-scale physics we have developed an open boundary model for particle simulation [1,2]. In this model the interaction between macro system and micro system is expressed by the plasma inflow and outflow through the system boundary.

A microscopic reconnection process is solved by means of an explicit electromagnetic particle simulation. A macroscopic process is introduced into this model as boundary conditions. A floating condition is used at the downstream boundary so that the plasma flow can move in and out freely through the boundary. The frozen-in condition, $\mathbf{E} + \mathbf{v}_s \times \mathbf{B} = 0$ ($s = i, e$), is assumed at the upstream boundary [1,2,3]. Thus, the plasma inflows can be symmetrically driven from two upstream boundaries by imposing the external electric field in the z direction. The ion and electron number fluxes are assumed to be always the same at the upstream and downstream boundaries so as to keep the total charge neutrality.

Triggering mechanism of collisionless driven reconnection and its dynamical behavior in an open system are examined by using the developed EM particle simulation code. It is found that there are two causes to violate frozen-in constraint and trigger collisionless reconnection. One is anomalous resistivity created by the DKI, and the other is originated by stochastic particle motion near the neutral sheet, which is expressed by off-diagonal components of pressure tensor term in two-fluid MHD as

$$n_j(\mathbf{E} + \mathbf{V}_j \times \mathbf{B}) = \frac{m_j}{q_j} \cdot n_j \left(\frac{\partial}{\partial t} \mathbf{V}_j + (\mathbf{V}_j \cdot \nabla) \mathbf{V}_j \right) + \frac{1}{q_j} \nabla \cdot \tilde{\mathbf{P}} + \frac{1}{q_j} \nabla p$$

By expanding each term into the DC and wavy components, we examine the roles of plasma instabilities and particle kinetic effects in Collisionless reconnection.

Figures 1 and 2 show the spatial profiles of non-ideal terms for electrons and ions when a low-frequency electromagnetic instability, called drift-kink instability (DKI), develops fully at the central region of current sheet. The reconnection point is located at the position $y=0$. The electric field becomes almost uniform in the quasi-steady state.

The reconnection electric field (solid line) is sustained by the ion pressure tensor originating from stochastic particle orbit (dashed line) in the ion current layer (Fig. 2). On the other hand, the wavy component

has a strong peak near the reconnection point, and balanced with the reconnection electric field in the electron case. In other words, anomalous resistivity created by the DKI is a main cause of the reconnection electric field in the electron current layer (Fig. 1). This result corresponds to the fact that the growth of the DKI is suppressed by three-dimensional effect and it grows just inside an electron current layer.

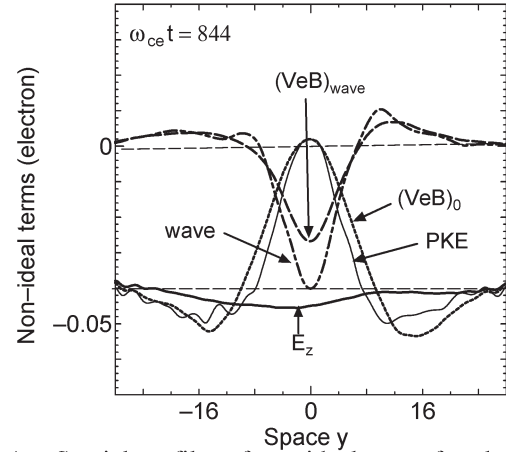


Fig. 1. Spatial profiles of non-ideal terms for electrons in the DKI phase.

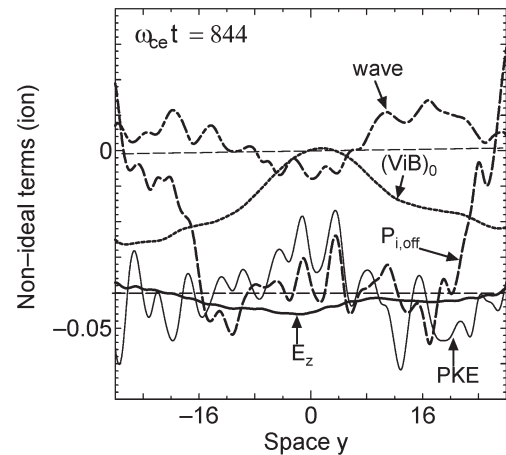


Fig. 2. Spatial profiles of non-ideal terms for ions in the DKI phase.

Reference

- 1) W. Pei, R. Horiuchi and T. Sato, Phys. Rev. Lett., **87** (2001) 235003-1-235003-4.
- 2) R. Horiuchi, H. Ohtani, and A. Ishizawa, Comp. Phys. Comm., **164** (2004) 17-22.
- 3) A. Ishizawa, R. Horiuchi, and H. Ohtani, Phys. Plasmas, **11** (2004) 3579-3585.

§22. Three Dimensional Particle Simulation on Collisionless Driven Reconnection

Ohtani, H., Horiuchi, R., Ishizawa, A.

Magnetic reconnection plays an important role in plasmas, and leads to the fast energy release from magnetic field to plasmas and the change of magnetic field topology [1]. To clarify the relationship between particle kinetic effects and anomalous resistivity due to plasma instabilities, we develop a three-dimensional particle simulation code for an open system [2,3]. From last year on, we develop the simulation code in a distributed parallel algorithm for a distributed memory and multi-processor computer system [4]. In this paper, we show simulation results of collisionless driven reconnection.

The number of initial particles is 72 million at the initial time, the simulation box size is $252\lambda_D \times 63\lambda_D \times 192\lambda_D$, the scale length of current layer is $25.2\lambda_D$ at the initial time, the thermal velocities of electron and ion are $0.25c$ and $0.025c$, respectively. λ_D is Debye length. The mass ratio m_i/m_e is 100 and the driving field E_z is $-0.04B_0$.

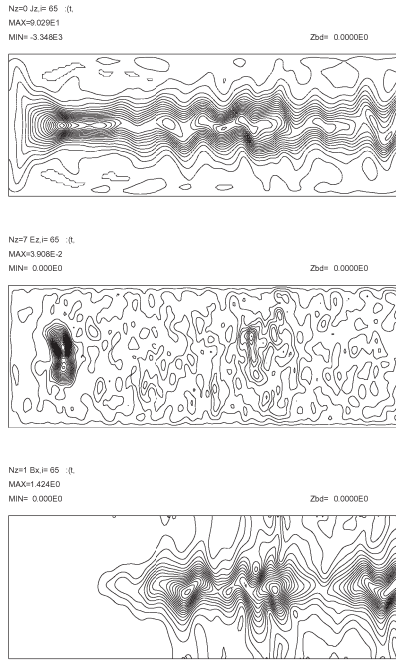
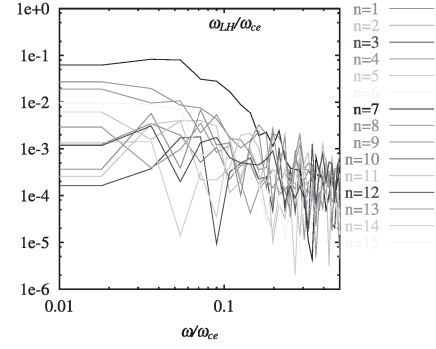
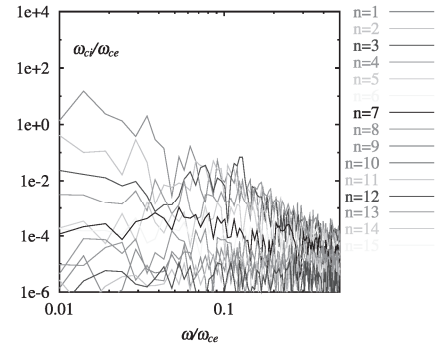


Fig. 1. Contour plot of spatiotemporal evolution (y - t) of Fourier mode of the current density $J_z(n=0)$ (top), the electric field $E_z(n=7)$ (middle) and the magnetic field $B_x(n=1)$ (bottom).

Figure 1 shows the contour plot of spatiotemporal evolution (y - t) of Fourier mode of the out-of-plane current density $J_z(n=0)$ (top), the electric field $E_z(n=7)$ (middle), and the magnetic field $B_x(n=1)$ (bottom), where n is the Fourier mode number in the z -direction



(a) E_z at the periphery of current layer.



(b) B_x at the center of current layer.

Fig. 2. Spectrum.

and the neutral sheet is located at the mid-point of y -axis. Figure 2 shows the spectrum of (a) E_z at the periphery of current layer and (b) B_x at the central region.

In the early period, the mode $E_z(n=7)$ grows in the periphery of the current layer, where the gradient of the current density is large. This mode $E_z(n=7)$ is identified as the lower hybrid drift mode (LHD mode) from the spectrum analysis (Fig. 2(a)). As LHD mode grows, the current density in the central region becomes peaked and then a low-frequency electromagnetic instability is excited near the central region (See the bottom figure of Fig. 1). This low-frequency instability, which has a frequency comparable to the ion gyration frequency (Fig. 2(b)), is considered to be the drift kink instability (DKI) and be a possible candidate for anomalous resistivity in the neutral sheet [2,3].

Reference

- 1) D. Biskamp: *Magnetic Reconnection in Plasmas* (Cambridge University Press, Cambridge, 2000).
- 2) R. Horiuchi *et al.*: Phys. Plasmas **6** 4565 (1999).
- 3) R. Horiuchi *et al.*: J. Plasma Fusion Res. SERIES, **6** 614 (2004).
- 4) H. Ohtani *et al.*: submitted to LNCL (2005).

§23. Suppression of Hall Term Effects by Gyroviscous Cancellation in Collisionless Magnetic Reconnection

Ishizawa, A., Horiuchi, R.

Collisionless magnetic reconnection is a fundamental mechanism for the rapid release of magnetic energy in space plasmas and laboratory plasmas. Recent computer simulation studies have revealed that the rate of reconnection by collisionless processes is very large compared to those obtained by using resistive MHD. Rapid reconnection is demonstrated to occur when the motions of electrons and ions decouple in a narrow region around the reconnection point. This decoupling is explained in terms of two-fluid effects and particle orbit effects, which are not included in the MHD model, and which form an ion-dissipation region. In this region the ion frozen-in condition is broken, while the electrons are tied to the field. This difference between the ion flow and electron flow causes fast magnetic reconnection.

We demonstrate the formation of an ion-dissipation region, in which motions of electrons and ions decouple and fast magnetic reconnection occurs during a steady state of two-dimensional collisionless driven reconnection without guide field by means of full-particle simulations. The Hall term effect is suppressed due to the gyroviscous cancellation at scales between the ion-skin depth and ion-meandering-orbit scale, and thus ions are tied to the magnetic field. The ion-frozen-in constraint is strongly broken by nongyrotropic pressure tensor effects due to ion-meandering motion, and thus the ion-dissipation region is formed at scales below the ion-meandering-orbit scale. A similar process is observed in the formation of an electron-dissipation region.

Figure 1 shows the spatial profiles of various terms measuring the violation of the frozen-in condition along the vertical line passing through the X-point in the steady state. Figure 1 (a) shows that the ions are tied to the field at the outside of the region indicated by ion scales. The ion frozen-in condition is strongly broken within the ion meandering orbit scale l_{mi} . On the other hand the ions are almost tied to the field and correspondingly the Hall term is small between ion skin depth and ion meandering orbit scale ($l_{mi} < y < d_i$). Figure 1 (b) shows that the electrons are still tied to the field in the ion-dissipation region where the ion frozen-in condition is broken. This electron frozen-in condition implies the violation of the ion frozen-in condition within ion skin depth. Figures 1 (c) and (d) show the spatial profiles of out-of-plane component of the terms in the ion and electron momentum equations. The ion pressure tensor term cancels out the ion inertia term in the two-fluid region ($l_{mi} < y < d_i$) where the ion inertia term is large and works toward breaking the frozen-in condition as shown in Fig. 1 (c). Therefore, this cancellation leads to the suppression of the Hall term effects and to the maintenance of the ion frozen-in constraint within d_i . The ion frozen-in condition is strongly broken in the full kinetic region within l_{mi} where the pressure tensor term is dominant. This large pressure tensor term is originated from the nongyrotropic ion-meandering motion. Figure 1 (d) shows that the electron pressure tensor

term and the electron inertia term break the electron frozen-in constraint near the X-point. The electron inertia term vanishes at the X-point, while the electron pressure tensor term has a sharp peak and it balances the electric field there. Thus, the reconnection electric field is generated by the nongyrotropic pressure tensor originating from the electron-meandering motion at the X-point. The electron pressure tensor seems to cancel out the electron inertia effect in the region between d_e and l_{me} .

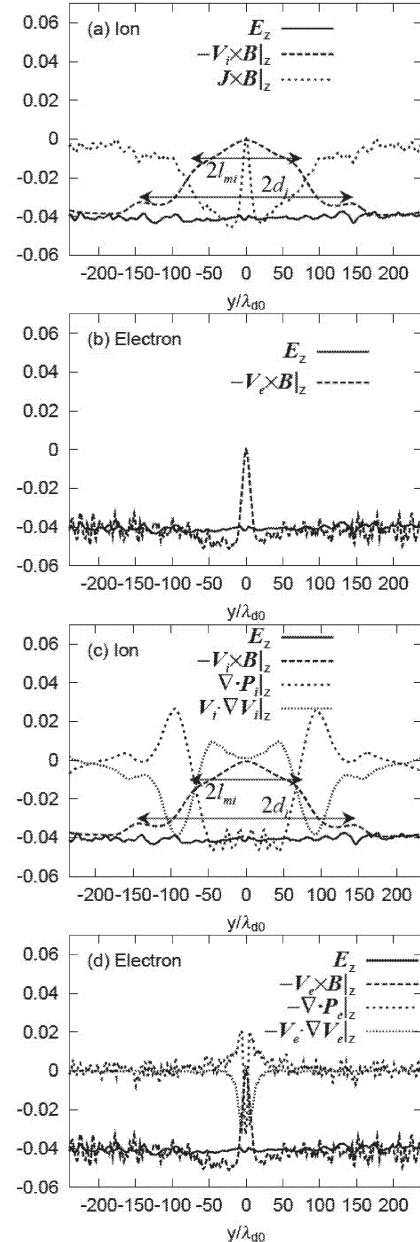


Fig. 1. The spatial profile of each term in the out-of-plane component of the ion momentum equation and of the electron momentum equation along the vertical line passing the X-point in the steady state

Reference

1) Ishizawa, A. and Horiuchi, R: to be published in Physical Review Letters (2005).

§24. Plasma Instabilities and Anomalous Resistivity in the Current Sheet

Moritaka, T. (Nagoya Univ.), Horiuchi, R., Ohtani, H., Ishizawa, A.

Magnetic reconnection can lead to topological change of magnetic field and fast energy conversion from magnetic field to particles and is widely believed as a fundamental process of the energetically active phenomena observed in the solar corona, the geomagnetic tail and fusion plasma. Instead of binary collisions, microscopic nonideal effect can dissipate magnetic field energy and cause collisionless magnetic reconnection in these systems.

A variety of microscopic plasma instabilities which can excite in the current sheet have so far been studied by linear analyses. It is important to clarify how the excitation of these instability causes non-ideal effect and collisionless magnetic reconnection. In this paper we investigate microscopic effect in collisionless magnetic reconnection by examining the force balance equation when these instabilities grow.

The simulation is carried out by using 2+1/2 dimensional explicit electromagnetic particle simulation code. We adopt the Harris type equilibrium with the antiparallel magnetic field configuration. Periodic and fixed boundary conditions are imposed in equilibrium current direction and along the gradient of magnetic field. The force balance expressed by two-fluid equation is examined using the particle simulation result. The relationship between non-ideal effect created by microscopic plasma instabilities and the generation of electric field is investigated based on this force balance equation.

In the early phase of the development of current sheet, the electromagnetic wave is excited at the periphery of the current sheet. The spectrum of this wave agrees with the linear analysis of LHDI¹⁾. Fig.1(top) shows the structure of magnetic field and the force balance at the phase of LHDI. The nonlinear coupling of the perturbations of the electric field and particle density $\tilde{n}\tilde{\mathbf{E}}$ contributes the outward flow of particle $\langle \mathbf{v} \rangle$ in the periphery of the current sheet. This outward flow results in the deformation of the equilibrium current sheet profile such as the localization of current density and magnetic flux. The change of the meandering orbit across the neutral sheet by this particle transport leads to the particle acceleration by the pressure tensor term in neutral sheet. But average electric field in the neutral sheet or magnetic flux reduction are not found in this phase.

After the saturation of LHDI, the growth of the longer electromagnetic wave is observed at the

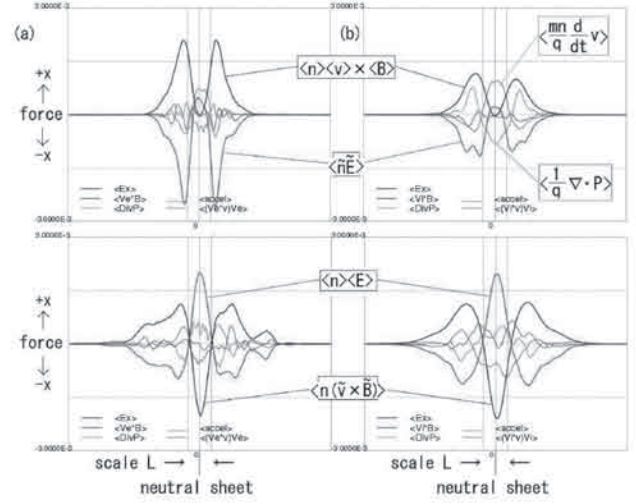


Figure 1: The spatial profile of force balance of electron (a) and ion (b) ; LHDI phase (top) and DKI phase (bottom)

neutral sheet²⁾³⁾. This wave has good agreement with linear analysis of DKI⁴⁾. The average electric field $\langle \mathbf{E} \rangle$ appears and current density dissipates at neutral sheet. The reduction of total magnetic flux consistent with the DC electric field is found in this phase. Fig.1(bottom) shows the magnetic field and the force balance at the phase of DKI. The force balance at the neutral sheet is changed by the excitation of DKI at the center of current sheet. The fluctuations of magnetic field and current density form the finite wavy component $\langle \tilde{\mathbf{u}}_j \times \tilde{\mathbf{B}} \rangle$ in Lorentz force term, and this term balances the average electric field. The anomalous resistivity examined from the damping rate of equilibrium current is the same order of the effective resistivity examined from DC electric field. The interaction between the fluctuation of magnetic field and microscopic plasma flow dissipates the momentum of particles and creates anomalous resistivity.

While the magnetic flux is re-distributed in the phase of LHDI, anomalous resistivity and magnetic flux reduction are generated through the nonlinear wave-particle interaction in the DKI phase. It is concluded that the DKI play an important role in creating anomalous resistivity and triggering collisionless magnetic reconnection.

References

- 1) R.C.Davidson, N.T.Gladd, C.S.Wu and J.D.Huba Phys.Fluids, **20**, 301(1977)
- 2) Z.Zhu and R.M.Winglee, J.Geophys.Res, **101**, 4885(1996)
- 3) R.Horiuchi and T.sato, Phys.Plasmas, **6**, 4565(1999)
- 4) W.Daughton, Phys.Plasmas, **6**,1329(1999)

§25. Simulation Study of Nonlinear Dynamics in Plasmas with Flows

Yoshida, Z., Numata, R., Furukawa, M., Hori, D., Ohsaki, S. (Graduate School of Frontier Sciences, The University of Tokyo), Hayashi, T.

Flows, which universally exist in plasmas, couple with magnetic fields and create various fascinating structures. Driven magnetic reconnection is a typical example of such flow-magnetic field coupled system.

In a high-temperature collisionless plasma, such as the solar corona, the rate of magnetic reconnection (diffusion) is so small that the ideal magnetohydrodynamics (MHD) model applies in a macroscopic scale. The reconnection speed, however, is much higher if a small scale structure is created. In a small scale, dissipation due to ion chaotic motion plays an important role. A theory of fast reconnection requires self-consistent explanations of the structure bridging the macro and micro scale hierarchies. The Hall-MHD model can describe such a “mesoscopic” hierarchy. The Hall term added to the Ohm’s law as a singular perturbation introduces an intrinsic length scale, viz., the ion skin depth ℓ_i . The ℓ_i is the scale where ion exhibits chaotic motion. The chaos of particle orbit yields a collisionless resistivity (referred to as the chaos-induced resistivity) when the system of particles are viewed as a plasma.

In this study, we consider the Hall-MHD model including the chaos-induced resistivity. The Ohm’s law is generalized as follows,

$$\mathbf{E} + \left(\mathbf{V} - \frac{\epsilon}{n} \nabla \times \mathbf{B} \right) \times \mathbf{B} = \frac{\eta}{R_m} \nabla \times \mathbf{B} \quad (1)$$

$$\eta(\mathbf{x}, t) := 1 + \sum_j \alpha \exp \left(-\frac{1}{\epsilon^2} |\mathbf{x} - \mathbf{x}_j(t)|^2 \right), \quad (2)$$

where ϵ is the ratio of the ion skin depth to the system size, R_m is the magnetic Reynolds number, α is the magnitude of the chaos-induced resistivity, and $\mathbf{x}_j(t)$ is the position of the magnetic nulls. Because the magnetic nulls move as the field changes, the resistivity has dynamic inhomogeneous distribution.

We have performed simulations using the code developed in ¹⁾ to study the effect of the Hall term and the chaos-induced resistivity. The parameters for the simulations are summarized in Table. I. Figure 1 shows the reconnection rate at the center of the dissipation region. The reconnection rate for $\alpha \neq 0$ is significantly large compared with that for $\alpha = 0$.²⁾ We also observe that intermittent bursts of the reconnection rate occur corresponding to the sudden enhancement of the resistivity. Figure 2 shows the out-of-plane current distribution obtained by the Hall-MHD model with the chaos-induced resistivity. We see that the X-type structure is formed. The current sheet is formed in other cases. Only the Hall term or the chaos-induced resistivity does not lead the X-shaped configuration. We conclude that the Hall effect co-

Table 1: Parameters for simulation. Taking $\alpha > 0$, the resistivity is enhanced (η_{\max} is the maximum of the enhancement factor.)

Run	A	B	C	D	E	F
ϵ	0	0.1	0.1	0.1	0.05	0.05
α	0	0	1	0.1	0	1
(η_{\max})	1	1	3	1.2	1	3

operates with the chaos-induced resistivity to yield such an X-type structure and leads the fast magnetic reconnection.

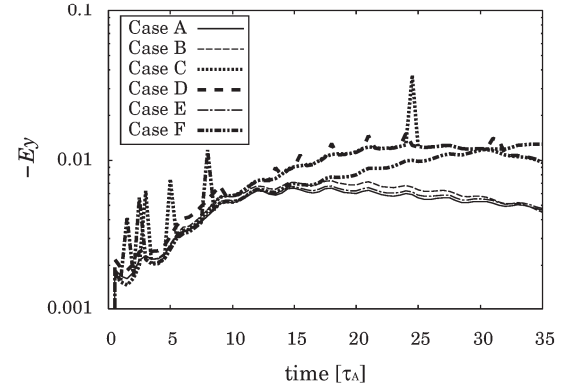


Fig. 1: Reconnection rate measured by the electric field at the center of the dissipation region.

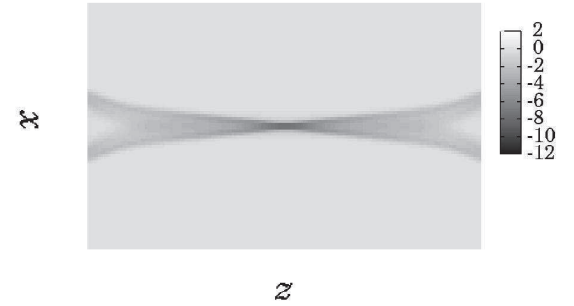


Fig. 2: X-type structure is obtained by using the Hall-MHD model with the chaos-induced resistivity.

References

- 1) Numata, R., Yoshida, Z., Hayashi, T. : J. Plasma and Fusion Res. SERIES 6 (2004) 130 ; Numata, R., Yoshida, Z., Hayashi, T. : Comput. Phys. Commun. 160 (2004) 291.
- 2) Numata, R., Furukawa, M., Yoshida, Z. and Hayashi, T. : submitted to Phys. Rev. Lett.

§26. Simulation Study of the Formation Mechanism of Sigmoidal Structure in the Solar Corona

Kusano, K. (The Earth Simulator Center, JAMSTEC)

The observations by the soft X-ray telescope (SXT) onboard Yohkoh satellite found that typical structure of forward-S or inverse-S shape often appears in the soft X-ray images of the solar corona.¹⁾ These typical morphology was named *sigmoid*.²⁾ Because sigmoids tend to appear associated with several eruptive events,³⁾ they are widely believed to be some precursor phenomena for eruptive flares.

Although several models have been proposed for the formation mechanism of sigmoid, they still remain as open questions how and why sigmoids are formed in prior to eruptive events. A widely believed idea is that the ideal kink instability of twisted field flux may cause the sigmoidal field. However, the observation indicates that there is no evidence of eruption for values of large-scale total twist approaching the threshold for the kink instability, though they sought 191 X-ray sigmoids.⁴⁾

On the other hand, we revealed, using the new methodology based on vector magnetogram observations and the induction equation,⁵⁾ that the helicity injection process in flare productive active regions was highly complicated both in time and space, and that even the sign of the helicity injection often changed. Furthermore, it is also clarified that the soft X-ray radiance from the active regions is almost proportional to the probability of sign reversal of the magnetic shear on the photosphere.⁶⁾ These results imply that the solar coronal activity is sensitive to the complexity in the magnetic structure, particularly to the reversal of the magnetic shear.

Motivated by the observations of magnetic helicity, we investigated the nonlinear dynamics of a magnetic arcade, which is subject to reversal of the magnetic shear, in terms of the three-dimensional numerical simulations. The simulation model is constituted by the finite difference approximation and the Runge-Kutta-Gill method. The simulation results clearly show that sigmoidal structure can be formed as a consequence of the tearing mode instability, which grows on the shear inversion layer, as seen in Fig.1. The detail analysis of the geometrical relationship between the sigmoid and the shear inversion layer reveals that the field twist parameter of sigmoid is consistent with the Taylor's minimum energy state. It indicates that the sigmoidal formation is a sort of the magnetohydrodynamic relaxation process like the reversed-field pinch experiments.

The simulation also indicates that the tearing mode instability, which gradually proceeds on the boundary between the sigmoid and the environmental field, is followed by an explosive eruption. It is caused by magnetic reconnection of the cusp shape field lines, as shown in Fig.2. The cusp field can be created by the collapsing of magnetic arcade, which results from the annihilation of magnetic flux through the tearing mode reconnection. The mutual excitation of the two

reconnections of the tearing instability and the cusp field plays a crucial role to trigger the eruption.

These results are consistent with the reversed-shear flare model^{6,7)} and well account for the causal relationship between the formation of sigmoid and the onset of flares.⁸⁾

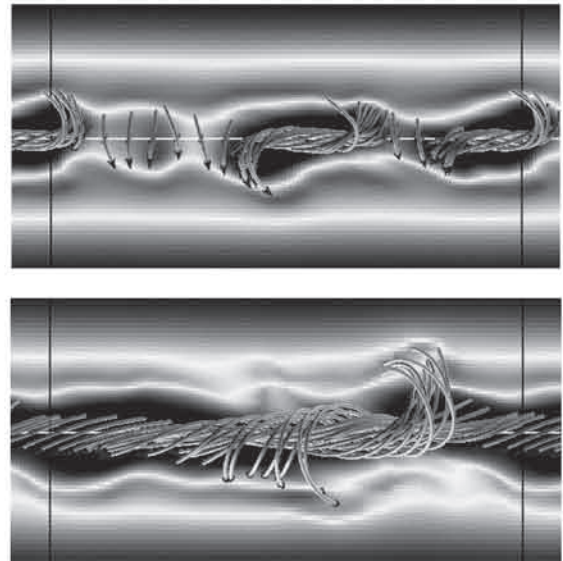


Fig. 1. Top view of the sigmoidal field lines in cases that the shear inversion layer is small (top) and large (bottom), respectively.

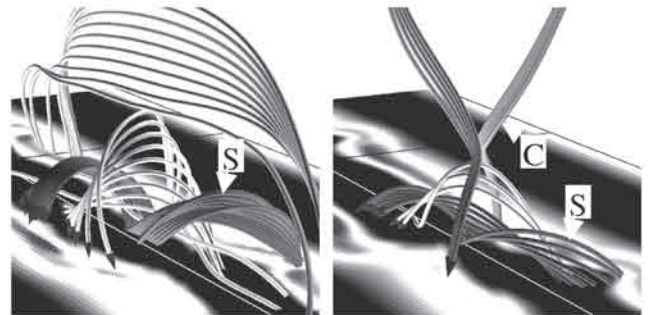


Fig. 2. Three-dimensional structure of the magnetic field lines in the formation phase of sigmoid (*left*) and the onset phase of eruption (*right*). Sigmoidal field and cusp field are denoted by S and C, respectively.

Reference

- 1) Tsuneta, S., et al., Solar Phys. **136**, (1991) 37
- 2) Rust, D.M., and Kumar, A., The Astrophys. J. Lett. **464**, (1996) L199
- 3) Canfield, R.C., et al., Geophys. Res. Lett. **26**, (1999) 627
- 4) Leamon, R.J., Canfield, R.C., Blehm, Z., and Pevtsov, A.A., The Astrophys. J. Lett. **596**, (2003) L255
- 5) Kusano, K., Maeshiro, T., Yokoyama, T., and Sakurai, T., The Astrophysical Journal **577**, (2002) 5011
- 6) Kusano, K., Maeshiro, T., Yokoyama, T., and Sakurai, T., Advances in Space Research **32**, (2003) 1917
- 7) Kusano, K., Maeshiro, T., Yokoyama, T., and Sakurai, T., The Astrophys. Journal **610**, (2004) 537
- 8) Kusano, K., The Astrophys. Journal (2005) in press

§27. Study on MHD Wall Shear Turbulent Flow on High Reynolds Number via Paralleled Direct Numerical Simulation

Satake, S. (Tokyo University of Science)

1. Objectives

Turbulent simulation is possible to apply to the large Reynolds number via developing large scale computer, and the computation is close to the realized engineering facilities. In the high Reynolds number computation, the large scale structures must be understood by not local structures but that of whole region in computational domain. Therefore, we need large memory for not only main computer but also visualization computer. On the other hand, the large scale computation under a magnetic field have not been carried out, the previous studies is limited for low magnetic number and low Reynolds number computations. In this study, the objective is to calculate the large scale turbulent structures with the large Reynolds and Hartmann number by SX-7 at NIFS. In this study, it is important to understand the turbulence suppression the turbulent channel flow in a transverse magnetic field and to reveal the mechanism of disappearance of large scale turbulence structures.

2. Numerical method for direct numerical simulations

Our DNS code is hybrid spectral finite difference methods (Satake and Kunugi (2003) and Satake et al.(2003)). The number of grid points, the Reynolds number and grid resolutions summarized in Table 1. The periodic boundary conditions are applied to the streamwise (x) and the spanwise (z) directions. As for the wall normal direction (y), non-uniform mesh spacing specified by a hyperbolic tangent function is employed. The all velocity components imposed the non-slip condition at the wall. The non-slip condition is used at the wall. A uniform magnetic field \mathbf{B}_0 defines that the y -axis lies along the axis of the streamwise direction in Fig.1. The Neumann condition for the electrical potential is adopted at the wall: Insulation wall assumption. The Hartmann numbers ($Ha = \mathbf{B}_0 2\delta / (\sigma/\rho\nu)^{1/2}$) based on the magnetic field \mathbf{B}_0 , the kinematic viscosity ν , the electrical conductivity σ and the channel width 2δ are set to 65.

Table 1

Re_τ	Ha	Region	Grid number	Δx^+	Δy^+	Δz^+
1100	0	$5\pi\delta \times 2\delta \times 2\pi\delta$	1024x1024x768	16.8	0.16-4.18	8.9
1194	65	$5\pi\delta \times 2\delta \times 2\pi\delta$	1024x1024x768	18.2	0.17-4.54	9.6

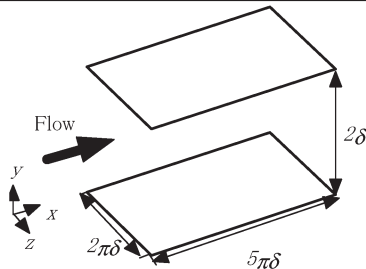


Figure 1 Computational domain.

3. Results

Mean velocity profiles are shown in Fig. 2. Satake & Kunugi (2003) and Satake et al. (2003) found that the logarithmic profile exits and elongated to the channel center. The logarithmic profile at $Ha=65$ shifted to the channel center, and wake region disappears clearly. The profile is good agreement with the experimental profile by Brouillette & Lykoudis (1967). To investigate this phenomenon for the change of the dominant scales, the streaky structures are visualized in Fig. 3. It is normalized by ν and $u\tau$. The volume visualized obtained as full volume ($L_x^+=17278$, $L_y^+=2200$, $L_z^+=6911$). The many small streaky structures exist in large streaky structures. The width of the large streaky structures are larger than 1000, located at away from the wall. Without MHD case, a few merged large streaks elongated to the channel center away from the wall. A characteristic size of the large streaky structures to the streamwise direction is even larger than the half of the channel width. Almost large structures located in $y^+ > 200$, correspond to the wake region in the mean velocity profile. On the other hand, the large scale motion at the channel center disappeared in Fig. 3. It is evident as the reason that the turbulent intensities are decrease at the channel center owing to the applied magnetic field. Moreover, the streaky structures are elongated to the streamwise direction.

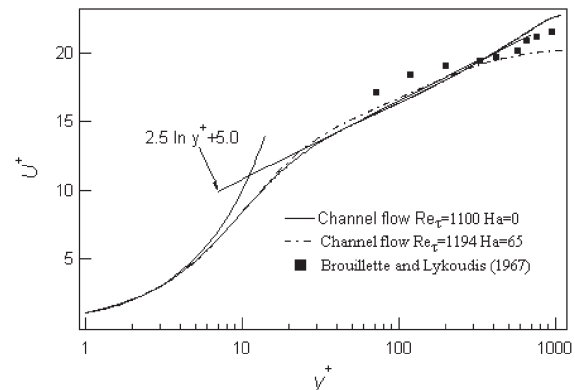


Figure 2 Mean velocity profiles

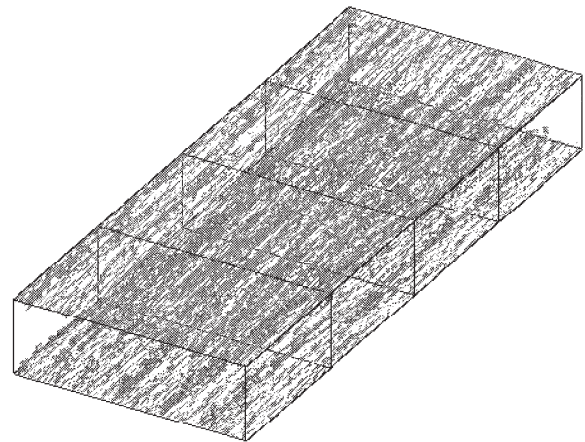


Figure 3 The contour of streaky structure; $u^+ < -3$

§28. Low-Frequency Instabilities Due to Flow Velocity Shear in Magnetized Plasmas

Kaneko, T., Saito, H., Hatakeyama, R. (Dept. Electronic Eng., Tohoku Univ.)
Ishiguro, S.

Field-aligned (parallel) plasma flow velocity shears play an important role in the generation of low frequency plasma instabilities. Recent theoretical works using kinetic treatment have predicted that the parallel flow velocity shear causes electrostatic ion-cyclotron and ion acoustic instabilities.¹⁾ According to the experimental results, on the other hand, it is demonstrated that the ion-acoustic, ion-cyclotron, and drift-wave instabilities are excited and suppressed by the parallel velocity shear, where the destabilizing and stabilizing mechanisms are well explained by the kinetic theory.²⁾ In the experimental investigation, however, it is difficult to change the shape and the location of the velocity shear, and the plasma parameters such as the ratio of the ion to electron temperature, which are very effective in the growth rate of the shear driven instabilities.

In this sense, a particle simulation is very useful method to clarify the effects of the velocity shear, because the simulation can easily set these parameters. From the viewpoint of investigating the general properties of the velocity shear driven instabilities, the simulation should be performed in the three dimensional (3D) system because in most cases waves propagate obliquely or perpendicularly to the direction of the flow velocity gradient under the influence of the velocity shear.

In our work, a three dimensional electrostatic particle simulation with a periodic boundary model is performed,³⁾ where an external uniform magnetic field directs to the positive z direction. Electrons and ions are uniformly loaded in the system at $t=0$. The system sizes L_x , L_y and L_z are $128\lambda_{De}$, $128\lambda_{De}$ and $512\lambda_{De}$, respectively. Here, λ_{De} is the Debye length. The number of electrons and ions per unit cell is 64. The ion to electron mass ratio m_i/m_e is fixed at 400. The ratio of the electron cyclotron to electron plasma frequency is $\omega_{ce}/\omega_{pe} = 5$ and the ion to electron temperature ratio is $T_i/T_e=0.5$. The time step width Δt is $0.1\omega_{pe}^{-1}$. The parallel ion flow velocity shear is introduced by means of changing the ion flow velocity v_{di} spatially in the x direction as shown in Fig. 1, where v_{te} is the electron thermal speed.

Figure 2 shows time evolutions of the real (solid line) and the imaginary (dashed line) parts of the spatial Fourier mode of the ion density fluctuation \tilde{n}_i/\bar{n}_i corresponding to the ion-cyclotron wave. This mode is measured in the uniform ion flow velocity region ($60 < x/\lambda_{De} < 64$) and in the velocity shear region ($32 < x/\lambda_{De} < 36$), which are indicated in Fig. 1 as "A" and "B", respectively.

The ion-cyclotron wave is destabilized in the Region A, when the ion drift speed exceeds a certain threshold. The spiky fluctuations in the time domain are locally observed in the Region B, i.e., in the velocity shear region, which are caused by the simultaneous existence of several coherent ion-cyclotron harmonics. Based on these results, the flow velocity shear is found to enhance not only the fundamental mode but also the high harmonic modes locally in the large velocity shear region.

In conclusion, it is clarified that the parallel ion flow velocity shear can excite the ion-cyclotron wave locally in the velocity shear region. These results are consistent with the analysis based on the local theory.

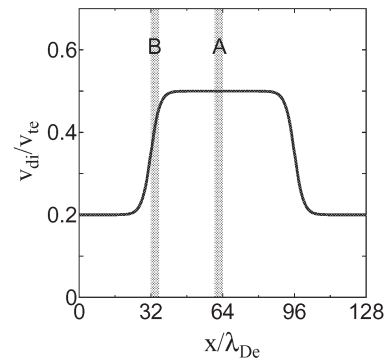


Fig. 1. Profile of ion flow velocity v_{di} in the x direction.

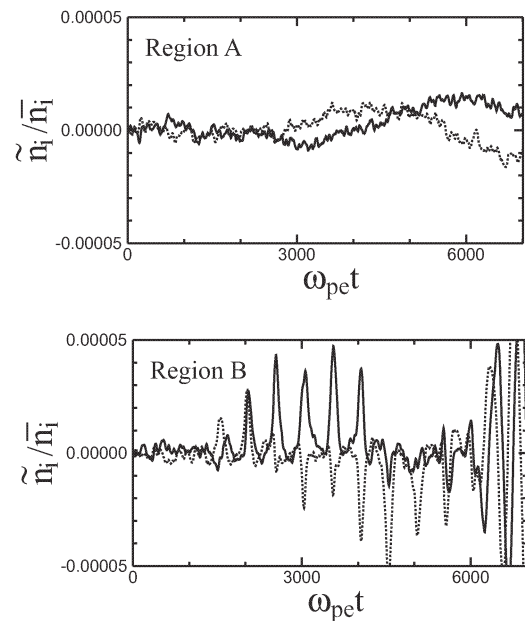


Fig. 2. Time evolutions of the real (solid line) and the imaginary (dashed line) parts of the spatial Fourier mode of the ion density fluctuation \tilde{n}_i/\bar{n}_i .

Reference

- 1) Ganguli, G. *et al.* : Phys. Plasmas **9** (2002) 2321.
- 2) Kaneko, T. *et al.* : Phys. Rev. Lett. **90** (2003) 125001.
- 3) Matsumoto, N. *et al.* : J. Plasma Fusion Res. SERIES, **6** (2004) 707.

§29. Self-Organization of Large-Amplitude Waves and Associated Particle Acceleration

Ohsawa, Y., Toida, M., Kato, K., Sato, M. (Nagoya Univ.)

Ishiguro, S., Hasegawa, H., Usami, S.

We have studied the nonlinear evolution of shock waves in a magnetized plasma and the acceleration of positrons, energetic ions, and electrons in those waves with relativistic electromagnetic particle simulations [1-7]. Also, we have investigated the effect of the presence of multiple ion species on the development of current-driven instabilities and energy transport and on the propagation and damping of perpendicular Bernstein waves and magnetosonic waves [8-10].

Here, we describe the results of relativistic particle simulations of positron acceleration by a shock wave propagating obliquely to a magnetic field in an electron-positron-ion plasma [2,3]. After the encounter with a shock wave, some positrons are accelerated along the magnetic field. The acceleration can become plateau owing to the deformation of the wave profile, which arises from the nonstationarity of the wave propagation. After the recovery of the wave profile, however, the acceleration can start again. By the end of the simulation, $\omega_{pe}t = 5000$, the Lorentz factors of accelerated positrons reach $\gamma \sim 2000$. Further, in this second stage acceleration, we find three different types of particle motions.

Figures 1-3 show time variations of γ for three different acceleration types. Here, γ represents the simulation result, γ_{HUC} is the energy increase calculated by use of the theory of parallel acceleration [2,5], and W_{\perp} is the work done by perpendicular electric fields. The acceleration is stagnant for $1000 < \omega_{pe}t < 2000$. The first type particle (Fig. 1) is accelerated nearly parallel to the magnetic field for $\omega_{pe}t > 2000$ as in the early phase ($\omega_{pe}t < 1000$); thus, γ and γ_{HUC} have similar profiles. The second type particle (Fig. 2) absorbs energy mainly from perpendicular electric fields in association with large-radius gyromotion; thus, γ and W_{\perp} are similar. In the third type (Fig. 3), particle orbits resemble

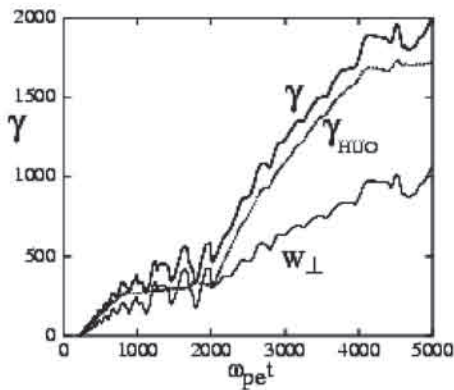


Fig. 1. Time variations of γ , γ_{HUC} , and W_{\perp} of a positron accelerated nearly parallel to the magnetic field. W_{\perp} is normalized to $m_e c^2$.

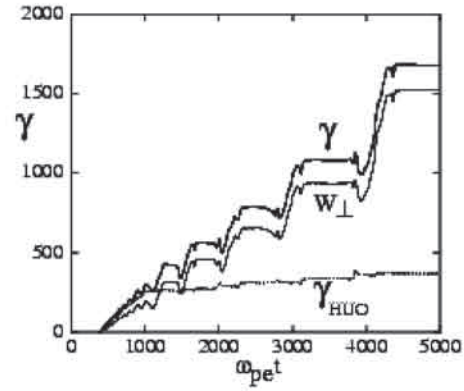


Fig. 2. Time variations of γ , γ_{HUC} , and W_{\perp} of a positron accelerated by perpendicular electric field in association with large-radius gyromotion.

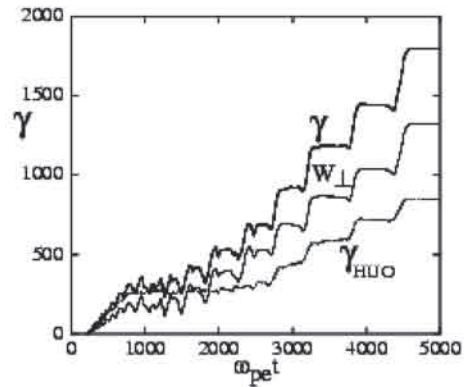


Fig. 3. Time variations of γ , γ_{HUC} , and W_{\perp} of a positron with an orbit similar to a curtate cycloid.

curtate cycloids. The energy jumps occur when the particle is reflected by the wave. Theoretical estimates for these three types of acceleration have been given. They quantitatively explain the simulation results.

References

- 1) Y. Ohsawa: *Physica Scripta* **T107** (2004) 32.
- 2) H. Hasegawa and Y. Ohsawa: *Phys. Plasmas* **12**, 012312 (2005).
- 3) H. Hasegawa and Y. Ohsawa: *J. Phys. Soc. Jpn.* **73** (2004) 1764.
- 4) S. Usami and Y. Ohsawa: *Phys. Plasmas* **11** (2004) 918.
- 5) S. Usami and Y. Ohsawa: *Phys. Plasmas* **11** (2004) 3203.
- 6) M. Sato, S. Miyahara, and Y. Ohsawa: *Phys. Plasmas* **12**, 052308 (2005).
- 7) A. Zindo, Y. Ohsawa, N. Bessho, and R. Sydora: *Phys. Plasmas* **12**, 052321 (2005).
- 8) M. Toida and H. Okumura: *Phys. Plasmas* **11** (2004) 1622.
- 9) M. Toida, T. Suzuki, and Y. Ohsawa: *Phys. Plasmas* **11** (2004) 3028.
- 10) T. Yoshiya, M. Toida, and Y. Ohsawa: *J. Plasma Fusion Res. Series*, **6** (2004) 383.

§30. Holistic Simulation – Auroral Arc Formation as the First Trial –

Kageyama, A., Sugiyama, T., Kusano, K., Ohno, N., Watanabe, K., Sato, T. (Earth Simulator Center)

The organizing system of the nature including industrial products are governed by the plural physical processes which are weakly but firmly interacting to each other. The “Holistic Simulation” can deal with such the organizing system

Suppose, for simplicity, a system that two processes, microscopic and macroscopic processes, are mutually interacting to each other. Weakness of the mutual interaction allows us to make simulations of both processes rather independently. Therefore, we need to exchange the information (data) between macroscopic and microscopic processes for the weak interaction. From the standpoint of the macroscopic process, data are not necessary at every microscopic unit time step to be transferred from the microscopic part, because there would be no appreciable macroscopic change of state in such a tiny time scale. On the other hand, from the microscopic standpoint, data are not necessary to be transferred at every macroscopic unit time step from the macroscopic part, because in such a short time scale the macroscopic state would not suffer any meaningful change at all. A reasonably small macroscopic time would be a reasonable data exchange period, because the microscopic process could be appreciably influenced by an appreciable change in the macroscopic state in a small macroscopic time step and also the macroscopic process could be influenced by an appreciable change in the microscopic state in that time step. By this way one can drastically reduce the data transfer rate.

Generally, an interesting phenomenon where the microscopic process plays an important role in macroscopic evolution is when the macroscopic (environmental) state is changed drastically at local regions, consequently the microscopic process also being strongly activated. We do not have to make microscopic simulations at all grid points, but that it would be enough to pick up several featuring grid points of the macroscopic grid system. Thus, we can reduce drastically the number of grid points that should be subjected to microscopic simulation.

As the first trial of the holistic simulation, we started by the quiet auroral arc formation. The fundamental origin of the quiet auroral arc is the feedback interaction between the magnetosphere and ionosphere, of which scale is of the order of 100,000 km. Due to the macroscopic interaction, the striated structure of the electric current is formed in the ionosphere. When the electric current exceeds some critical value in somewhere near the ionosphere, the large potential gap, in other words, the large electric field along the geomagnetic field line is created by the microscopic instability through the particle interaction among electrons and ions of which scale is 10 cm. Such large electric field accelerates the low energy

(100 eV) electrons up to 1 keV, which collide with the neutral atoms in the atmosphere to make auroral green(oxygen) or red(nitrogen) light. And also, such accelerated electrons ionized neutral atoms in the ionosphere, so that the ionospheric condition, therefore, the condition of the macroscopic interaction would be changed.

We employed MHD simulation for the macroscopic interaction between the magnetosphere and ionosphere, and the particle simulation in the open boundary condition for the microscopic interaction. Here, we also developed a new coordinate system, the dipole coordinate system, for the MHD simulation to get more realistic configuration of the magnetosphere.

As the boundary condition of the MHD simulation, we employed the fixed magnetospheric equatorial plane with a Heppner-type twin vortex plasma flow that works for the driving force of the feedback coupling between the magnetosphere and ionosphere. The ionosphere is described by the height-integrated ionospheric equations in which the Pedersen and Hall conductivities are taken into account. For the particle simulation, the open boundary condition is employed, where ions and electrons can freely flow into the simulation box and go out.

Starting the MHD simulation, we observed the striated structure of the electric current in the ionosphere as the time goes by, and the electron beam velocity exceeded the critical value that corresponds to 70% of the electron thermal speed. Then, using the information of the electron beam velocity, we made a shifted Maxwellian distribution function as an initial electron velocity distribution as well as the boundary condition on the upstream side, and started the particle simulation. During the execution of the microscopic (particle) simulation, we continued the macroscopic (MHD) simulation, because the macroscopic data is changed in the macroscopic time scale, in other words, the microscopic boundary condition on the upstream side is not changed in the microscopic time scale. After the electrostatic potential was formed due to the microscopic interaction and saturated, the information of the accelerated electrons was transferred to the macroscopic simulation, and was put into the ionospheric equation of the macroscopic simulation. Such simulation procedure was repeated, and thus, the simulation of the auroral arc formation was done self-consistently from both macroscopic and microscopic viewpoints.

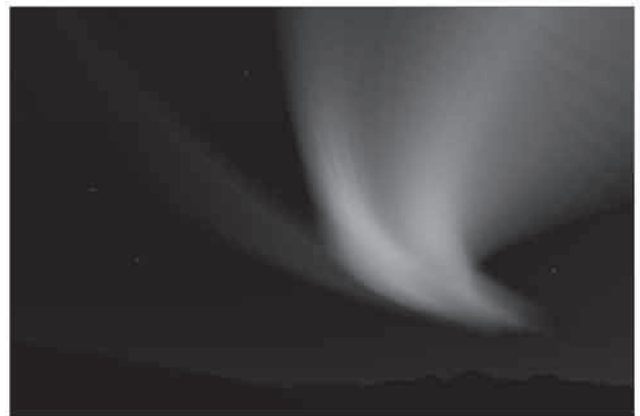


Fig. 1 The simulation results of auroral arc formation

§31. Intermittency and Transfer Phenomena in NS and MHD Turbulence

Gotoh, T. (Nagoya Inst. of Tech.)

It has been widely considered that when the Reynolds and magnetic Reynolds numbers are very large, spectrum of the total (kinetic plus magnetic) energy obeys Iroshnikov-Kraichnan(IK) scaling, $E^T(k) = C_{IK}(\epsilon v_A)^{1/2} k^{-3/2}$, where C_{IK} is a nondimensional constant, ϵ the average rate of the total energy dissipation, and $v_A \propto \sqrt{\langle b^2 \rangle}$ the Alfvén velocity. However, recent studies have claimed that the Kolmogorov(K) scaling $E^T = C_K \epsilon^{2/3} k^{-5/3}$ holds. We have numerically studied this scaling of the spectrum by direct numerical simulation of turbulence. Also high order statistics of the fields and their scaling exponents have been examined.

The equation for the Elsässer variable $z^\pm = u \pm b$ was integrated. The random force was applied at low wavenumber bands for the momentum equation alone, and statistical average was taken over time. The number of grid points was 128^3 and 256^3 . The magnetic Prandtl number is unity and Taylor microscale Reynolds numbers were 92 and 160.

Figures 1 and 2 show the energy spectra compensated by multiplying $k^{3/2}$ or $k^{5/3}$ and by normalizing in terms of IK or Kolmogorov scaling variables, respectively. It is difficult to definitely determine which scaling is preferred in the inertial range because of insufficient width of the range, but the IK scaling looks to work better in the dissipation range.

In MHD turbulence, a 4/3 law, counterpart to the 4/5 law in NS turbulence, is known to hold in the inertial range;

$$\left\langle \delta z_{\parallel}^\mp \delta z_i^\pm \delta z_i^\pm \right\rangle = -\frac{4}{3} \epsilon^\pm r. \quad (1)$$

This equation implies that δz^\pm would obey the Kolmogorov scaling if the intermittency is ignored. It was found that the third order moment of δz^\pm gradually approached the 4/3 law when the Reynolds number was increased (figure not shown). The structure functions of δz^\pm at low to moderate order were also computed, and their scaling exponents in the inertial range are shown in Fig. 3. Values of the scaling exponents are closer to the Kolmogorov scaling than to those by the IK scaling. However, it should be noted that the magnetic energy is about a quarter of the kinetic energy, which means that the characteristic time related to the Alfvén velocity is premature to dominate the energy transfer towards high wavenumbers. This might be a

reason for nearly Kolmogorov scaling. Certainly further examination would be required.

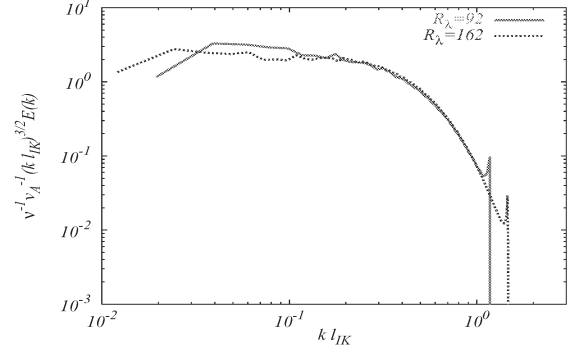


FIG. 1: Iroshnikov-Kraichnan(IK) scaling of the energy spectrum $(\nu v_A)^{-1} (k l_{IK})^{3/2} E^T(k)$

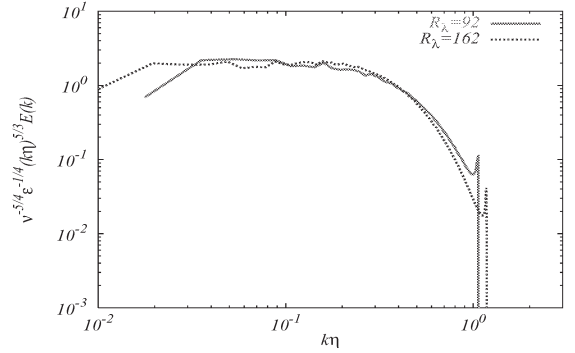


FIG. 2: The Kolmogorov scaling of the energy spectrum $\nu^{-5/4} \epsilon^{-1/4} (k \eta)^{5/3} E^T(k)$

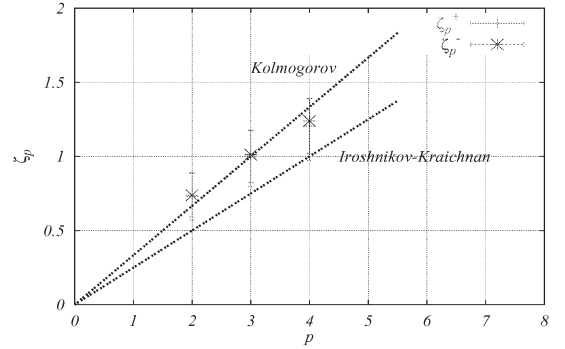


FIG. 3: Scaling exponents ζ_p^\pm of the structure functions of the Elsässer variable increment.

References

- 1). Gotoh T. and Mori K.: *Energy spectrum and transfer flux in Hydrodynamic and MHD turbulence* Proceedings of Workshop on Interdisciplinary Aspects of turbulence, Max Planck Institute for Astrophysics, (2005).

§32. Orthonormal Divergence-free Wavelet Analysis of Nonlinear Interactions between Coherent Structures

Araki, K. (Okayama Univ. Sci.)
Miura, H. (TCSC, NIFS)

Scale localness of nonlinear interactions in fully developed turbulence is one of the principal assumptions of Kolmogorov's phenomenology[1]. Many attempts and analyses have been made to relate this assumption to the dynamics of the Navier-Stokes equations (NSE)

$$\frac{\partial \mathbf{u}}{\partial t} + (\mathbf{u} \cdot \nabla) \mathbf{u} = -\nabla P + \nu \Delta \mathbf{u}. \quad (1)$$

Fourier analysis of nonlinear transfer $T(k, p, q)$ suggest the predominance of nonlocal interactions[2]. On the other hand, Fourier analysis of energy flux $\Pi(k, s)$ appeals the importance of *local* interactions[3]. Orthonormal divergence-free wavelet analysis of the counterpart of $T(k, p, q)$ reveals the localness of interactions[4]

More detailed divergence-free wavelet analysis of the nonlinear interaction is carried out. We evaluate the nonlinear interaction defined by the formula

$$\langle j, \vec{l} | \mathbf{u} | k, \vec{l}' \rangle = \int \mathbf{u}_{j, \vec{l}} \cdot (\mathbf{u} \cdot \nabla) \mathbf{u}_{k, \vec{l}'} d^3 \vec{x} \quad (2)$$

where $\mathbf{u}_{j, \vec{l}}$'s are wavelet decomposed velocity field and the indices j and \vec{l} imply the spatial scale and location of the analysing wavelet.

Numerical result is shown in the figures 1 and 2. Correlation between coherent structures and nonlinear interactions are qualitatively verified. This suggests that coherent structures in turbulence plays a principal role in the nonlinear transfer process of kinetic energy. Quantitative evaluation of statistics of nonlinear interaction is now undergoing.

- [1]. U. Frisch, *Turbulence*, (Cambridge Univ. Press, Cambridge, 1995).
- [2]. J. A. Domaradzki, R. S. Rogallo, Phys. Fluids A, **2**, p.413 (1990); P. K. Yeung, J. G. Brasseur, Phys. Fluids A, **3**, p.884 (1991); K. Ohkitani, S. Kida, Phys. Fluids A, **4**, p.794 (1992).

- [3]. Y. Zhou, Phys. Fluids A, **5**, p.2511 (1993);
- [4]. K. Kishida, K. Araki, S. Kishiba, K. Suzuki, Phys. Rev. Lett., **83**, p.5487 (1999).

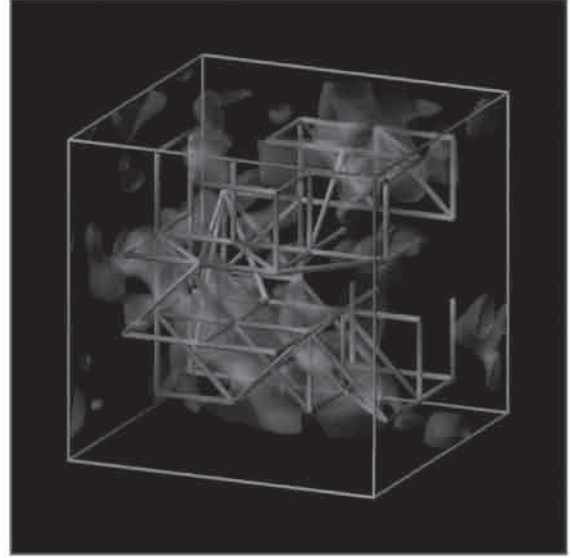


Figure 1: spatial distribution of “sweeping” type nonlinear interactions $\langle 4, \vec{l} | \mathbf{u} | 4, \vec{l}' \rangle$. The largest 200 interactions are displayed by tubes connecting the wavelet sites, \vec{l}' to \vec{l} . Transparent blobs are isosurfaces of the filtered velocity field \mathbf{u}_4 .

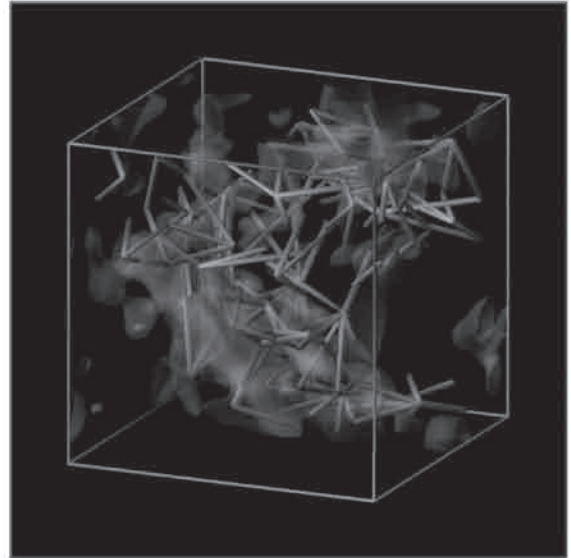


Figure 2: spatial distribution of “cascading” type nonlinear interactions $\langle 5, \vec{l} | \mathbf{u} | 4, \vec{l}' \rangle$.

§33. Yin-Yang Grid and Geodynamo Simulation

Kageyama, A. (Earth Simulator Center, JAMSTEC)

Recently, we proposed a new overset grid system, “Yin-Yang grid”, for numerical simulations in the spherical geometry [1]. The Yin-Yang grid is composed of two identical component grids—yin grid and yang grid—that are combined in a complementary way to cover a spherical surface with partial overlap on their borders. An example of the Yin-Yang grid is shown in Figure 1, whose component grids are shown in Figure 2.

Since yin grid and yang grid are identical in the shape, geometry, and metric tensors, subroutines for the basic solver and boundary conditions are recycled twice—once for yin and another for yang. This fact makes the Yin-Yang-based computer code very concise and efficient. Another advantage of the Yin-Yang grid comes from that the component grid (yin or yang) is nothing but a (part of) latitude-longitude grid. We can directly deal with the equations to be solved with the vector form in the usual spherical polar coordinates. We can make use of various resources of mathematical formulas, program libraries, and tools that have been developed in the spherical polar coordinates.

We have applied the Yin-Yang grid to a geodynamo simulation in which time development the thermal convection of a magnetohydrodynamic (MHD) fluid is solved in the spherical shell geometry. We have developed this Yin-Yang geodynamo code by converting our previous geodynamo code which was based on the traditional latitude-longitude grid. The code conversion was easy because most of the Yin-Yang code shares source lines with the latitude-longitude code: Our previous geodynamo code was basically a finite-difference MHD solver on spherical coordinates with a full span of colatitude ($0 \leq \theta \leq \pi$) and longitude ($-\pi < \phi \leq \pi$); on the other hand, the Yin-Yang grid code is also a finite-difference MHD solver on the spherical coordinates, but with just the smaller span of colatitude ($\pi/4 \leq \theta \leq 3\pi/4$) and longitude ($-3\pi/4 \leq \phi \leq 3\pi/4$). The major difference is the new boundary condition (mutual interpolation) for the communication between Yin grid and Yang grid.

The best performance achieved so far by our Yin-Yang dynamo code is 15.2 Tflops with 4096 processors of the Earth Simulator. This is 46% of the theoretical peak performance. With the total grid size of $511(\text{radial}) \times$

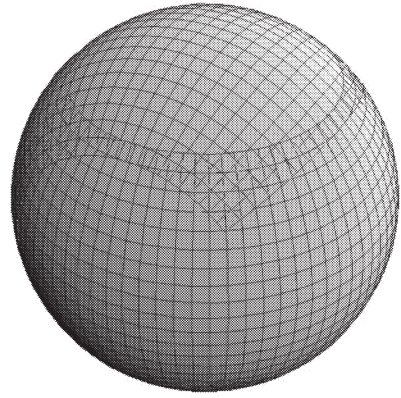


Figure 1: Comparison of azimuthal flow profiles obtained by simulation and experiment.

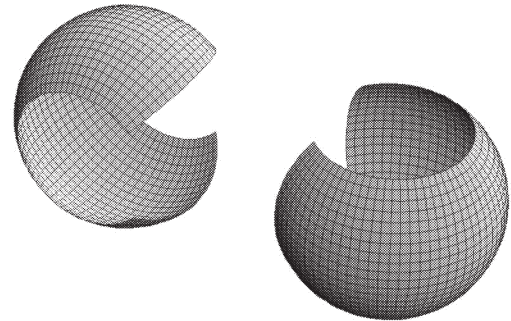


Figure 2: Comparison of azimuthal flow profiles obtained by simulation and experiment.

$514(\text{latitudinal}) \times 1538(\text{longitudinal}) \times 2(\text{Yin and Yang})$, the average vector length is 251.6, and the vector operation ratio is 99%. This performance demonstrates that the Yin-Yang grid suits to massively parallel computations for the spherical shell geometry [2].

We have also applied the Yin-Yang grid to the mantle convection simulation in the spherical shell geometry [3].

References

- [1] Akira Kageyama and Tetsuya Sato. *Geochem. Geophys. Geosyst.* 2004, 5(9):1–15, doi:10.1029/2004GC000734.
- [2] Akira Kageyama et al. *Proc. of the ACM/IEEE Supercomputing SC'2004 conference*, 2004.
- [3] Masaki Yoshida and Akira Kageyama. *Geophys. Res. Lett.* 2004, 31(12), doi:10.1029/2004GL019970.

§34. Development of Exact Charge Conservative Particle Simulation Code with High Performance Fortran

Hasegawa, H., Ishiguro, S., Okamoto, M.

In the Particle-in-Cell (PIC) method, which is a conventional scheme on plasma computer simulations (mainly, laser plasmas, space plasmas, and so on), dynamics of full particles (usually, ions and electrons) and time evolutions of self-consistent fields are calculated alternately. Although there are several methods for calculating time evolutions of the fields, finite-difference Ampere's and Faraday's laws are often used. In this case, however, one has to correct the electric field by the Gauss law (Poisson equation). Therefore, using the "Exact Charge Conservation Scheme¹⁾," we develop the three-dimensional, relativistic, electromagnetic PIC code^{2,3)}. In this scheme, current densities are computed with rigorous satisfaction of the finite-difference continuity equation. Thus, applying this algorithm, one needs no correction process. Further, because of the accuracy of current densities, in an open system simulation code, which is often used to investigate the behavior of magnetic reconnection, consistent boundary conditions can be given.

In the development, we also parallelize and vectorize the code. To make it adequate at multi-node jobs, we use not only an automatic parallelization in shared memory on each node by FORTRAN90/SX, which is a Fortran90 compiler for the SX supercomputer, but also manual parallelization in distributed memories among nodes with High Performance Fortran (HPF), which is a distributed parallel processing language.

In PIC simulation, the required memory size for particle data (positions, momenta) is usually more than 100 times as large as the one for field data. And then, the total calculation for particles needs more expensive costs of computing time than one for fields. In our code, subroutines for calculating current densities (subroutine CURRENT) and advancing particle momenta (subroutine PUSH) include the computations about particles. Hence, we especially optimize these subroutines.

First, inserting DISTRIBUTE HPF directive, arrays for particle data are distributed to each HPF process. Also, writing INDEPENDENT HPF directive immediately before the outermost DO statements, these loops are parallelized in each HPF process.

On the other hand, to use the "Exact Charge Conservation Scheme," the outermost loop in subroutine CURRENT contains complex multiple loops. Hence, it is not automatically parallelized by the FORTRAN90/SX. Thus, we inserted PARALLEL DO compiler directive to force parallelization. Further, using LISTVEC compiler directive⁴⁾, the loop for assigning process is vectorized without work arrays.

We then make examinations of the accuracy and

the performance of this code on the plasma simulator. The test simulation parameters are as follows. The total number of cells in system is $64 \times 64 \times 64$. Both the numbers of electrons and ions per cell are 216. The test calculations have been done for 100 time steps.

Figure 1 presents a time variation of the quantity dQ , where dQ is defined as

$$dQ = \int dV \left(\frac{\partial \rho}{\partial t} + \nabla \cdot \mathbf{J} \right)^2. \quad (1)$$

It is found that the continuity equation have been held over simulation time in a range of round-off error. We show, in Fig. 2, the dependence of the computing performance (GFLOPS) on the total number of processor elements (PE). The value of FLOPS linearly increases with the total number of PE. This fact indicates that parallelization is very successful.

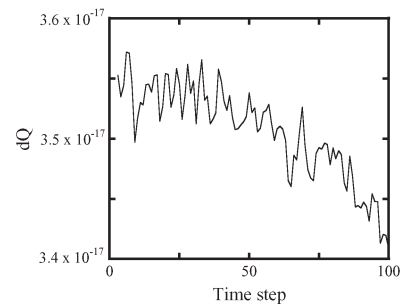


Fig. 1. Time variations of the quantity dQ .

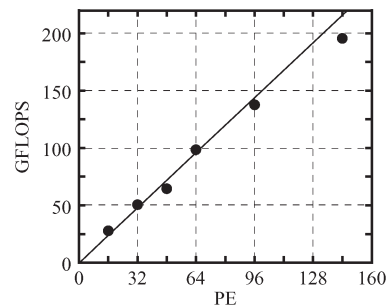


Fig. 2. Dependence of the computing performance (GFLOPS) on the total number of processor elements (PE). Here, the closed circles are the observed values, and the solid line denotes the value of 17% of theoretical peak performance.

References

- 1) Esirkepov, T. Zh.: *Comput. Phys. Comm.* **135** (2001) 144.
- 2) Hasegawa, H., Ishiguro, S., and Okamoto, M.: Submitted to *IPSJ Trans. on ACS*.
- 3) Hasegawa, H., Ishiguro, S., and Okamoto, M.: Submitted to *Lect. Not. Comput. Sci.*
- 4) Sugiyama, T. *et al.*: *IPSJ Trans. on ACS* (in Japanese) **45** (2004) 171.

§35. Development of an Electromagnetic Particle Code for Space Propulsion Application Using ECR Discharge

Nakashima, H., Masui, M. (Kyushu University)

The electric propulsion was adopted as thruster for a stationary satellite and a planetary explorer because of its high efficiency. Among the electric propulsion systems, an ion engine electrostatically extracts an ion from plasma. An ion engine with microwave discharge could extend lifetime as compared with DC discharge. In sample return mission MUSES-C of The Institute of Space and Astronautical Science (ISAS), 10cm class microwave discharge ion engine (8mN/400W) is adopted as a main thruster. In addition, this ion engine system has the neutralizer with the microwave discharge.¹⁾

Due to improvement of performances for ion engine with the microwave discharge, codes adopting various assumptions are being developed to analyze the plasma behavior and microwave propagation in the ion engine with the microwave discharge.²⁾ The purpose of the present study is to analyze plasma behavior and microwave propagation in the 10cm class ion engine and neutralizer. For this purpose, we have developed an electromagnetic particle code. This code is constituted of particle-in-cell (PIC) method to solve the equation of motion for electron and of finite-difference-time-domain (FDTD) method to solve the Maxwell's equation of microwave³⁾. The coupling code can solve the plasma behavior and microwave propagation in a self-consistent manner without complex assumptions. The coupling code is available not only to solve time evolution of the plasma but also to obtain collision and energy distribution function.

Analysis of the microwave propagation has been conducted under boundary conditions as given below:

1) Absorption boundary condition

An absorption condition is imposed at the end of the discharge chamber. Here, Mur's first absorption condition is adopted⁴⁾.

2) Reflection boundary condition

Perfect conductor (grid) was assumed at the end of the discharge chamber, so that the electric field which

parallel to the boundary plane is set equal to be zero. In each condition, plasma is not placed in the discharge chamber.

The following results are obtained:

1) In analysis of microwave propagation with altered boundary condition, the traveling wave exists for the absorption boundary. In the reflection condition assuming a perfect conductor, the reflection wave was confirmed in the discharge chamber. But the discharge chamber did not work as resonance cavity. Efficiency of plasma generation is increased when the discharge chamber imposed the reflection boundary condition is optimized to operate as the resonance cavity.

2) In the calculation including plasma, increase of the electron energy was larger for reflection boundary condition than absorption one. Existence of the grid in the microwave ion engine is important in term of reflecting the microwave.

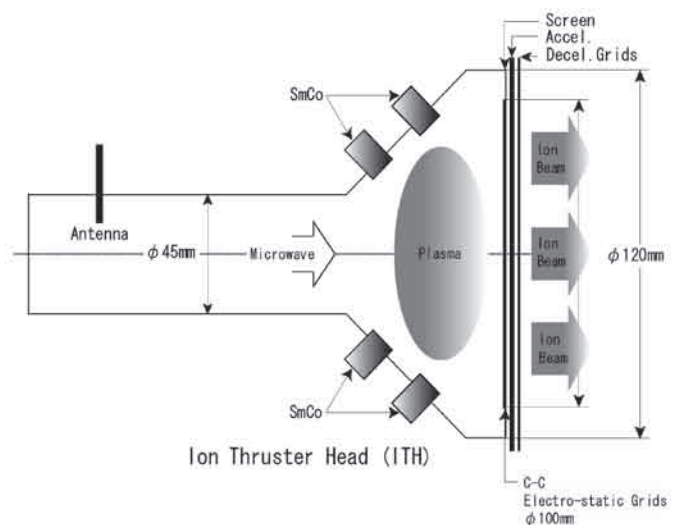


Fig. 1 10cm microwave discharge ion

Reference

- 1) Toki, K. et al.: "Technological Readiness of Microwave Ion Engine System for MUSES-C Mission", 27th Int. Electric Propulsion Conf, IEPC-01-174 (2001)
- 2) Hirakawa, M. and Nakakita, M. : "Simulation of Electron Cyclotron Resonance in a Microwave Discharge Ion Thruster", Trans. Japan Aero. Space Sci. 47 (1999) 267
- 3) Grotjohn, T. A. : "Numerical Modeling of a Compact ECR Ion Source", Rev. Sci. Instrum. 63 (1992) 2535
- 4) Mur, G., "Total-field Absorbing Boundary Conditions for the Time-Domain Electromagnetic Field Equations", IEEE Trans. Electromagnetic Compat., 40 (1998)100

§36. Dissipative Particle Dynamics Simulation on Self-assembly of Amphiphilic Molecules

Nakamura, H.

We studied self-assembled structure of particles with short-range interaction to compare with the long-range interaction by molecular simulation. Amphiphilic molecule was adopted as one of typical examples of particles with short-range interaction. It is known that the amphiphilic molecules have miscellaneous self-assembled structures. It is, therefore, difficult to make phase diagrams of the structure definite.

By Dissipative Particle Dynamics(DPD) simulation [1–6] which is one of “course-grained” molecular dynamics simulation methods and was developed to reveal the dynamics of a large number of particle, we obtained [7, 8] the phase diagram of a typical amphiphilic molecule, i.e. hexaoxyethylene n-dodecyl ether ($C_{12}E_6$) which is familiar to us as a nonionic surfactant.

At a room temperature, the phase diagram of $C_{12}E_6$ and water system exhibits the following phases: a hexagonal structure (H_1) are observed at 50 weight percent (50 wt %) of $C_{12}E_6$, a lamellar structure L_a at 75 wt % and so on. We showed [7,8] that the various phase structures of C12E6 are represented by the modified Jury model that is composed of one hydrophilic and one hydrophobic particle. From the simulation of the modified Jury model, we could show [7,8] H_1 phase near 50 wt % and L_a phase near 75 wt %. Moreover, we showed [7,8] the dependence of phase structure on packing parameter by effectively changing the coefficients of interaction potentials among different kinds of particles.

Israelachvili proposed the packing parameter as a means of clarifying the relationship between macroscopic self-assembled structure and microscopic molecular shape [9, 10]. The packing parameter p is the ratio of the volume V occupied by the hydrophobic tail to the product of the sectional area of a hydrophilic group S and the “maximum effective length (l)” of the hydrophobic. tail The concept of the packing parameter is intuitive and acceptable. However, calculating the packing parameter is very difficult, even by computer simulation, because it is almost impossible to derive macroscopic phase structure at the microscopic level by simulation, using techniques such as molecular dynamics (MD) simulation, for example.

In order to reveal the relation between macroscopic and microscopic structure, we studied both hydrophilicity and hydrophobicity dependence of the phase structure was clarified qualitatively by varying the interaction potential among hydrophilic, hydrophobic and water molecules in a DPD simulation using the modified Jury model. By varying the coefficient of the interaction potential between hydrophilic beads, hydrophobic ones and water molecules, the effective microscopic molecule structure can be changed. The macroscopic structure, therefore, also vary according to the packing parameter of the amphiphilic molecules. In Fig. 1, we show the hydrophilicity dependence of the self-assembled structure.

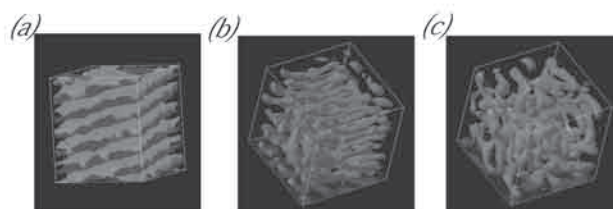


Figure 1: Self-assembly structures of amphiphilic molecule. The structure depends on the hydrophilicity of bead A and water W. We simulated three cases of the hydrophilicity coupling constant. In the most hydrophilic case(a), the amphiphilic molecules form the lamellar phase. The hexagonal and micelles phases are composed in the middle case(b) and the least case(c), respectively.

References

- [1] P. J. Hoogerbrugge and J. M. V. A. Koelman: Europhys. Lett. **19** (1992) 155.
- [2] J. M. V. A. Koelman and P. J. Hoogerbrugge: Europhys. Lett. **21** (1993) 363.
- [3] R. D. Groot and P. B. Warren: J. Chem. Phys. **107** (1997) 4423.
- [4] R. D. Groot and T. J. Madden: J. Chem. Phys. **108** (1998) 8713.
- [5] R. D. Groot and K. L. Rabone: Biophys. J. **81** (2001) 725.
- [6] S. Jury, P. Bladon, M. Cates, S. Krishna, M. Hagen, N. Ruddock, and P. Warren: Phys. Chem. Chem. Phys. **1** (1999) 2051.
- [7] H. Nakamura: Molecular Simulation **30** (2004) 941.
- [8] H. Nakamura and Y. Tamura: Comp. Phys. Com. (2005) (in press).
- [9] D. J. M. J. Israelachvili and B. W. Ninham: J. Chem. Soc. Faraday Trans. I **72** (1976) 1525.
- [10] J. Israelachvili: *Intermolecular and Surface Forces* (Academi Press, London, 1992) 2nd

§37. Molecular Dynamics Simulation of Collision between Graphite and Hydrogen

Ito, A. (Nagoya Univ.)
Nakamura, H.

1. Introduction

The interaction between wall and plasma, such as the divert of the nuclear fusion device, has been researched. When ions, electrons, or neutral atoms of plasma hit against the wall with low energy, chemical sputtering process becomes one of dominant reactions between the wall and plasma. In the experiment, it is reported that some molecules, such as hydrogens and methanes, are generated on the carbon wall[1]. Typical scale length of these processes is the order of a few nanometer. However, it is difficult to reveal the dynamics of plasma particles in the “nanoscale” structure of the carbon molecules by experiments. Therefore, in this paper, we try to reveal these dynamics by molecular dynamics(MD) simulation.

Before reporting the details of our simulations, we explain the experimental situation of wall and plasma interaction. A graphite is used as the carbon wall in the experiments. The graphite is composed of a graphene sheet, and graphene sheets forms a “layer” structure. The distance between graphene layers is about 3.348 ° Å. These layer structures aggregates and forms multicrystal.

The binding energy between layers is weaker than the bonding energy of carbon atoms in the same layer. The dominant process of the wall-plasma interaction, therefore, can be regarded as scattering of one graphene with one incoming particle. When the plasma particle is trapped by the carbon wall, the above scattering process must be repeated until kinetic energy becomes less than binding energy. Therefore, the question “How far do plasma particles penetrate the carbon wall?” fascinates experimentalists and designer of nuclear fusion reactor.

In this work, we reported the dependence of the penetration depth on the angle between an incoming particle and crystallographic direction of graphene sheets by the MD simulation.

2. Model

We used Brenner’s REBO potential[2] that is experimentally fixed to be able to treat the chemical reaction even by the classical theory.

The REBO potential is regarded as one of the Morse type

potentials[3]. Each coefficient depends on the binding state of the atoms and are continuously changed. To use this potential, we must restrict incoming hydrogen to be neutral.

We comment here about the reason to use the classical MD simulation for the chemical reaction. We, of course, know that chemical reaction behaves according to quantum effect. If we simulate the chemical reaction by quantum MD simulation, it will takes such a long time that existing computer cannot treat. We, therefore, used classical MD simulation with empirical interaction potential to get qualitative information of scattering process.

3. Result

We showed the dependence of the probability of the trapped particles on incoming particle energy in Fig. 1. During this simulation, we set the direction of the incidence particle to be vertical graphene sheet. It was found that some of incoming particles lose their kinetic energy by penetrating through several graphene, and then they are trapped by the carbon atom somewhere. On the other hand, it is also shown that some of incoming particles are reflected and come out again outside of a graphite wall. The trapping ratio of particles increases as energy of incoming particle becomes large. However, about 20 % of the incoming particles come out of the surface of the graphite even if their incoming kinetic energies are more than 150eV.

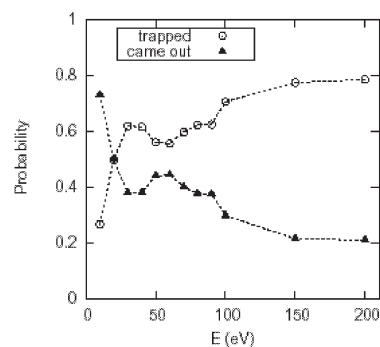


Figure 1: The probability that particles was trapped and came out of the graphite. Parameter E denotes the kinetic energy of incoming particle.

References

- [1] T. Nakano, et al. Nucl. Fusion 42, 689 (2002)
- [2] D. W. Brenner, et.al. J. Phys. Condens. Matter 14, 783 (2002)
- [3] P. M. Morse, Phys. Rev. 34, 57 (1929)
- [4] H.Yamada and S.Hamaguchi: Proc. Symp. Dry Process, (2002) 189

§38. Molecular Dynamics Simulation of Micelle Formation in Amphiphilic Solution

Fujiwara, S., Hashimoto, M., Itoh, T. (Kyoto Inst. Tech.)

Amphiphilic molecules such as lipid molecules and surfactant molecules contain both a hydrophilic “head” and a hydrophobic “tail”. In aqueous or organic solvents, these molecules often spontaneously self-assemble into various structures such as spherical and cylindrical micelles, bilayer membranes and bicontinuous cubic structure¹⁾. Self-assembly of amphiphilic molecules plays an important role in many biological and industrial processes. For example, surfactants have been successfully used to render quantum dots biocompatible. Although numerous computer simulation studies have so far been carried out on amphiphilic solutions, little is known about the detailed molecular mechanisms of micelle formation in amphiphilic solution. With a view to investigating micelle formation in amphiphilic solution at the molecular level, we perform the molecular dynamics (MD) simulations of coarse-grained amphiphilic molecules with explicit solvent molecules and analyze the micelle formation process.

The computational model is based on those used in the work by Goetz *et al.*²⁾ and by Noguchi *et al.*³⁾. An amphiphilic molecule consists of one hydrophilic particle and two hydrophobic particles which are fixed on a line and spaced equally. A solvent molecule is modeled as a hydrophilic particle. The interaction between a hydrophilic particle and a hydrophobic particle is modeled by a repulsive soft core potential and all other interactions are modeled by a Lennard-Jones potential. The equations of motion for all particles are solved numerically using the leap-frog algorithm at constant temperature with a time step of $\Delta t^* = 0.0025$. We apply the periodic boundary conditions. The amphiphilic concentration is set to 0.05. Initially, we provide a randomly distributed configuration of 97 amphiphilic molecules in solution at high temperature ($T^* = 10$) for various number densities ($\rho^* = 0.6, 0.65, 0.7, 0.75, 0.8, 0.85$). The number of solvent molecules is 5541. The system is then quenched to $T^* = 1.3$ and MD simulations of $t^* = 2.0 \times 10^4$ (8.0×10^6 time steps) are carried out for each number density.

We show, in Fig. 1, the snapshots of micelles formed at $\rho^* = 0.7$ and 0.75. Our simulations indicate that cylindrical micelles are formed at lower densities ($\rho^* \leq 0.7$) whereas planar bilayers are obtained at higher densities ($\rho^* \geq 0.75$). The time evolution of the potential energy at $\rho^* = 0.7$ and 0.75 is shown in Fig. 2. We find from this figure that the potential energy relaxes in a stepwise manner at $\rho^* = 0.75$. This kind of stepwise behavior is found at $\rho^* \geq 0.75$. It is also found that the energy relaxation proceeds in a gradual manner at $\rho^* = 0.7$. The similar gradual behavior is found at $\rho^* \leq 0.7$. These simulation results indicate that the number density has a major effect not only on the micelle shape but also on the micelle formation process.

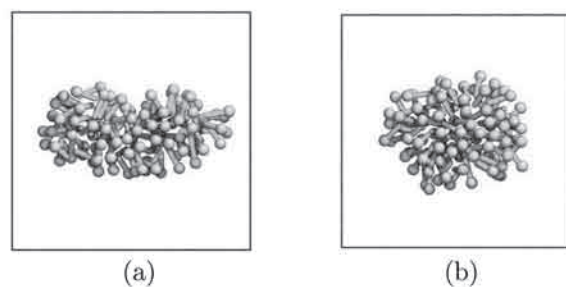


Fig. 1. Snapshots of micelles formed by amphiphilic molecules in solution: (a) cylindrical micelle ($\rho^* = 0.7$) and (b) planar bilayer ($\rho^* = 0.75$). Hydrophilic and hydrophobic groups are represented by spheres and cylinders, respectively. Solvent molecules are not shown for clarity.

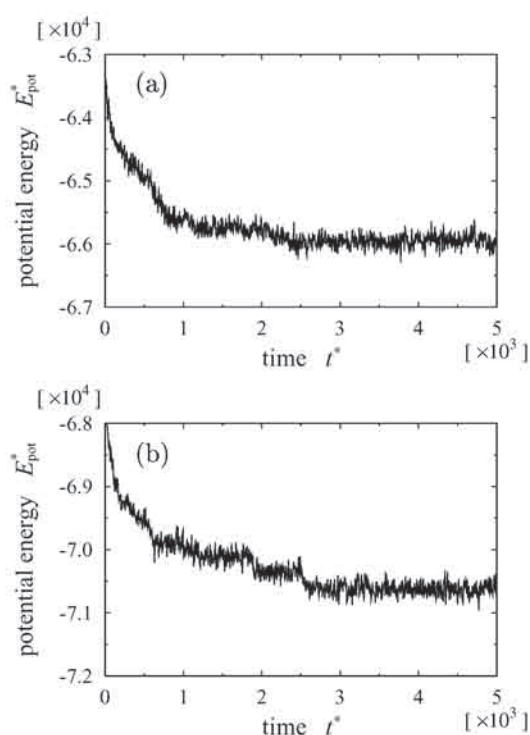


Fig. 2. Time evolution of the potential energy (a) at $\rho^* = 0.7$ and (b) at $\rho^* = 0.75$.

References

- 1) *Structure and Dynamics of Membranes*, edited by Lipowsky, R. and Sackmann, E. (Elsevier Science, Amsterdam, 1995).
- 2) Goetz, R. and Lipowsky, R., *J. Chem. Phys.* **108**, (1998) 7397.
- 3) Noguchi, H. and Takasu, M., *Phys. Rev. E* **64**, (2001) 041913.

§39. Construction of Collaborative and Seamless Virtual Environment for Numerical Simulation

Tamura, Y., Nakamura, H.,
Kageyama, A. (Earth Simulator Center),
Sato, S. (Earth Simulator Center)

In numerical simulation research, visualization is indispensable method, and virtual reality (VR) technology is also very effective for visualizing numerical data.

We have been developing an immersive VR system, called CompeXcope [1-2], which can represent real 3D visual and aural environment. But VR is not friendly for simulation researchers, since computer for simulation is different from visualization computer in general. So we constructed integrated virtual environment for numerical simulation and visualization. In this system, the user can use these computers seamlessly without recognizing calculation and visualization computer. Also it is very important issue to construct a multilateral communication network system where any researcher in any remote site can equally observe simulation result from any point.

In this research, we propose collaborative and seamless virtual environment for numerical simulation by network communication.

The users of the immersive VR systems can watch their own numerical simulation data or visualized something interesting, but they cannot discuss their data with partners in remote site if they have VR systems.

Since products from the immersive VR system are real 3D movies, images and sounds, they cannot be shared perfectly. So if they want to discuss these data, they must meet together in spite of using same VR systems. To improve these issues, connecting each VR systems through a public network is very effective.

In our system, virtual reality network is accomplished by socket communication (client-server model). In this system, not only numerical simulation result and simulation model, but also the position of observers and actions (e.g. drawing new isosurface, changing magnification) in remote sites, are shared. This system is very simple, but very effective since we cannot communicate with any researcher in any remote site without recognizing what he looks at and is interested in.

Generally, the researcher calculates in calculating server, and visualizes the output data in graphic workstation or his PC. But when he uses VR system for visualization of large-scale simulation result, there are some obstacles. A VR, especially immersive VR system, is generally situated in a location away from researcher's office. In addition, in immersive VR system, observers enter the VR space and

control visualized objects, but for changing simulation parameters, he needs to exit VR space, calculates by calculating server again and transfers the output data from the calculating server to the graphic workstation. It is serious problem for practical use. So we introduced real time simulation and visualization system to the CompeXcope system. The simulation result is shared between calculating server and graphic workstation. If the observer, in the CompeXcope system, changes some simulation parameters (such as temperature, arrangement of simulation model and so on), these information is sent to the server, which controls all shared data, and this server sends information to the calculating server. Finally the result from this calculating server is sent to the graphic workstation. By this system, the observer can simulate interactively without getting out. Figure 1 shows an example of this system.

We developed collaborative and seamless virtual environment. This system enables user of virtual reality system to visualize in the immersive projection display (virtual reality system), calculating with remote computer. In addition to this, the result of numerical simulation can be shared among remote sites, and the user can visualize and communicate in real time by network communication.

[1] A. Kageyama, Y. Tamura and T. Sato, Prog. Theo. Phys. Supplement 138 (2000).

[2] Y. Tamura, et al., Comput. Phys. Communications 142 (2001).

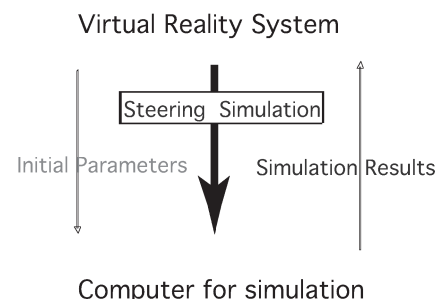
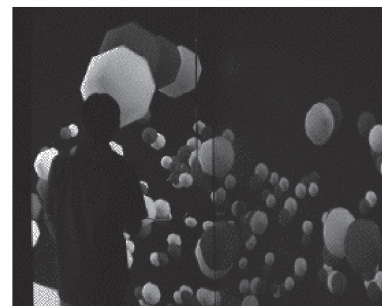


Fig. 1 Example of seamless numerical simulation environment

6. Personal Interchange Joint Research Program

Different from other collaboration programs of NIFS, where the university researchers come and join the research activities held at NIFS, this "personal interchange joint research program" supports financially that the staff of NIFS goes out to join the collaboration research in universities. Although NIFS provides many types of joint research programs that cover a variety of researches on nuclear fusion or plasma physics, many original ideas and the extensive studies are also carried out in university laboratories and other institutes. Sometimes, they are complementary to the specific projects of NIFS, and worth to be supported by NIFS. This program is for this purpose.

Two categories are prepared for collaboration; one is "project type" where the collaboration is made between two facilities; one is at NIFS and the other is at the university. A systematic research on the common subjects is done at both facilities by the researchers of both organizations to obtain a comprehensive knowledge on the subjects. The other is "detach type" where the researchers of NIFS take part in the study using the facility or experimental device at the university with a new idea or with an expert knowledge to explore a new field.

In this year, six subjects were carried out as "project (P) type" and five for "dispatch (D) type". All the programs have been done successfully, and brief summary of each subject are listed below.

[P 1]: *"Theoretical study of plasma turbulence"*

This subject has been carried out between NIFS theory group and the group of Kyushu University. A method of statistical analysis on the transition between two turbulent states has been developed. An example is an onset of neoclassical tearing mode in the L-mode plasma, the life time of which is shown to be strongly related to the plasma beta, and the life time reduces much when the beta value increases.

[P 2]: *"Higher-harmonic oscillation of Peniotron"*

This subject was carried out between NIFS ECH group and the group of Tohoku University on the development of high frequency microwave power source for plasma diagnostics. In order to develop a THz-range power source, they study a peniotron oscillator that has good conversion efficiency for higher harmonic waves. Then it is possible to produce high frequency wave using low magnetic field. An oscillator with 18 vanes was designed and set up this year, and will be tested next year. A simulation of output power and efficiency of this system was also done.

[P 3]: *"Investigation of refrigeration mechanism for the Stirling type pulse tube cryocooler"*

This collaboration was carried out between NIFS cryogenic group and the Institute of Quantum Science of Nihon University. The purpose of this project is to clarify the mechanism of Stirling type pulse tube cryocooler which is expected to be reliable due to its low level mechanical vibration. In this year, the relation between the phase controller and the pressure oscillator has been widely studied experimentally, and the results are explained well by numerical calculations.

[P 4]: *"Ion heating in a supersonic plasma flowing through a magnetic nozzle"*

This is a collaboration research program between NIFS HYPER-I group and Tohoku Univ. on studying fast plasma flow. The present study is on efficient heating of MPD arcjet plasma. When the RF of 15kW, 236 kHz is applied by a right-handed helically-wounded antenna, which is located downstream along plasma flow, the stored energy and ion temperature of plasma are clearly increased. Since hot plasma flow is obtained, next step will be a conversion experiment from thermal energy to flow energy by using a magnetic nozzle to realize fast plasma flow.

[P 5]: *"Electron Bernstein wave heating by long wavelength microwave"*

This program is the collaboration between Kyoto university LATE group and the NIFS CHS group on developing electron Bernstein wave (EBW) heating, which is crucial to produce high density plasma in both devices. The main purpose of the study is to study the coupling processes and to develop the effective launching method for efficient coupling. In LATE spherical tokamak, plasma and toroidal current are initiated successfully by ECH, which is considered to be heated by mode-converted EBW. In CHS, over-dense plasma is successfully generated using various working gas, and the results suggests that ECH is mode converted to EBW near the upper hybrid resonance layer.

[P 6]: *"Assessment on fusion reactors from the socio-economic viewpoint"*

This subject was carried out between Univ. of Tokyo and NIFS on the assessment of nuclear fusion as a future energy source. This assessment was done from the view point of socio-economics. The evaluation was carried out on which characteristics people require for future energy source. For example, people are asked which is better, A: the source has an inexhaustible but localized, B: the source is widely distributed but the amount is limited. The questionnaires are prepared for ordinary people and for specialists, and Delphi method is applied.

[D 1]: *"Proof-of-Principle experiments on the concept of moving-surface plasma-facing component"*

In this program, a researcher of NIFS visited the Osaka University and carried out the experiment using the MS-PFC (Moving-Surface Plasma-Facing Component) test unit integrated in Vehicle facility there. The effect of Li coating on the recycling of the surface was studied. It is found that a thin coating of Li reduces hydrogen recycling level. It is noticed that helium plasmas also exhibit noticeable reduction in recycling, although it apparently require higher Li deposition rate.

[D 2]: *"Magnetic island effect on radial particle flux in TU-Heliac"*

This is a program that was carried out in the small helical axis stellerator of Tohoku University (TU-Heliac). In TU-Heliac magnetic islands of $(n,m) = (3,2), (5,3)$ can be produced by adding vertical field externally, and the effect of magnetic island on the radial particle flux was studied. In TU-Heliac, the improved mode appears when the hot cathode is inserted into the plasma and the current is induced. It is found that the threshold amount of current depends on the width of magnetic island.

[D 3]: *"Heating and current drive experiments on the TST-2 Spherical Tokamak"*

This research program is on developing methods of current startup and sustainment in small spherical tokamak of university of Tokyo (TST-2). In order to carry out the experiment, TST-2 was temporally moved to Kyushu University to integrate their high power RF system in 2003. The data were analyzed this year, while TST-2 moved to Kashiwa Campus. The obtained results are (1) electron Bernstein wave heating and current drive were observed, (2) current startup by ramping poloidal field was successfully carried out, and (3) current ramp-up and sustainment by RF alone was also demonstrated.

[D 4]: *"Development and plasma experiments of an internal ring device with HTS coil"*

Mini-RT is a magnetically levitated internal coil device in university of Tokyo, where the magnetic dipole field is utilized for plasma confinement. For internal coil, an advanced high temperature super conducting wire is adopted. NIFS cryogenic group supported technically to realize this unique device. In this year, the plasma was

produced with inner coil levitating, and it is found that the electron density becomes high and that the plasma is located around the inner coil compared with the case the inner coil is mechanically supported, which may show that a separatrix is made.

[D 5]: *"Experimental and theoretical studies of CS-less startup for spherical tokamaks"*

In this program, the optimum startup method of spherical tokamak (ST) without central solenoid was studied experimentally and theoretically. Using TS-3 of University of Tokyo, merging experiments of two ST plasmas were carried out. Two ST plasmas were made by four PF coils separately, and they were merged in axial direction successfully. A two-dimensional MHD simulation of this process was also carried out.

LIST OF REPORT

1. Life time of plasma states near transition, Itoh S-I, et al., Kyushu Univ.
2. Higher-Harmonic Oscillation of Peniotron, Ando A. et al., Tohoku Univ.
3. Clarification on cooling mechanism of Stirling type pulse cryocooler, Yasohama K. et al., Nihon Univ.
4. Ion heating in a supersonic plasma flowing through a magnetic nozzle, Inutake M. et al., Tohoku Univ.
5. Electron Bernstein wave heating by long wavelength microwave in a spherical tokamak and a helical device, Maekawa T. et al., Kyoto Univ.
6. Assessment on Fusion Energy Development from the Socio-Economic Viewpoint, Ogawa Y. et al., Univ. Tokyo.
7. Magnetic Island Effect on Radial Particle Flux in TU-Heliac, Kitajima S. et al., Tohoku Univ.
8. Heating and Current Drive Experiments on the TST-2 Spherical Tokamak, Takase Y. et al., Univ. Tokyo.
9. ECH Plasma Experiments of an Internal Ring Device with HTS Coil, Ogawa Y. et al., Univ. Tokyo.
10. Experimental and Theoretical Studies of Startup Methods for Spherical Tokamak Plasmas, Ono Y. et al., Univ. Tokyo.

(Kaneko, O.)

§1. Life Time of Plasma States Near Transition Boundary

Itoh, S.-I., Yagi, M. (RIAM, Kyushu Univ.)
Itoh, K.

A stochastic equation for the amplitude of the neoclassical tearing mode (NTM) has been derived, and the life time of a state free of the onset of NTM is obtained. The model and basis are explained in refs.1 and 2. One has an explicit form of the life time as [3]

$$t_{\text{life}} = \frac{2\pi}{\eta \sqrt{\Lambda_0 \Lambda_m}} \exp(S(A_m)), \quad (1)$$

where the time rates $\Lambda_{m,0}$ are given as

$\Lambda_m = 2A \left| \partial \Lambda / \partial A \right|$ at $A = A_m$ and $\Lambda_0 = \Lambda(\langle A_0 \rangle)$, and the nonlinear dissipation function was given as

$$\begin{aligned} S(A) = & \Gamma_0 \frac{r_s^2}{\rho_b^2} \left(-\frac{4}{3} \Delta'_0 A^{3/2} + h A^2 \right) \\ & + \Gamma_0 \frac{r_s^2}{\rho_b^2} \frac{\rho_b^2}{2r_s^2} \frac{L_q}{L_p} \frac{\beta_p}{\beta_{pn}} \ln \left(1 + \frac{r_s^4 A^2}{\rho_b^4} \right) \\ & - \Gamma_0 \frac{r_s^2}{\rho_b^2} \frac{\beta_p}{\beta_{pn}} \left(A - \frac{w_{\text{cut}}^2}{r_s^2} \ln \left(1 + \frac{r_s^2}{w_{\text{cut}}^2} A \right) \right) \end{aligned} \quad (2)$$

with $\beta_{pn} = L_p / 2a_{bs} \epsilon^{1/2} L_q$ and

$$\Gamma_0 = \frac{2\ell}{R_M k^3 k_h^4 C^2 A_h^4 \tau_{ac}} \frac{\rho_b^2}{r_s^2}. \quad (3)$$

An explicit value of the transition rate was examined by specifying a micro mode for typical experimental parameters. For the L-mode plasmas, when one employs the current-diffusive ballooning mode (CDBM) as the micro mode, one has Γ_0 as

$$\begin{aligned} \Gamma_0 = & \frac{2 \times 10^{-4} \ell}{k^3 \left(-\alpha^{-1/2} (1 + \alpha) + s \sqrt{\beta m_i / m_e} \right)^2 s^4 R_M} \\ & \times \frac{r_s^6 \rho_b^2}{\delta^8} \alpha^{-11/2} \end{aligned} \quad (7)$$

where δ is the collisionless skin depth and $\alpha = \epsilon r_s \beta_p / L_p$ is the normalized pressure gradient.

For a set of typical parameters, $r_s / \rho_b \simeq 10$, $r_s / \delta \simeq 10^2$, $R_M \simeq 10^8$, $\beta m_i / m_e \sim 10$, $kr_s = 3$, $s = 1$, $\alpha \sim \beta_p / \beta_{pn}$, one has $\Gamma_0 \sim 3 \left(\beta_p / \beta_{pn} \right)^{-11/2}$. The life time of the state $A = 0$ (i.e., free from the NTM) is

shown in Fig.1. The unit of the life time is $2\pi / \eta \sqrt{\Lambda_0 \Lambda_m}$, which is of the order of Rutherford growth time. The dependence on plasma beta is shown. (Other parameters are fixed, $\Delta'_0 = 0$ and $h \rho_b^2 r_s^{-2} = 1/40$.) The life time strongly decreases as the plasma beta increases. And if it exceeds the effective phase limit β_p^* , the life time becomes of the order of the magnetic diffusion time. The contour of the life time is shown in Fig.2.

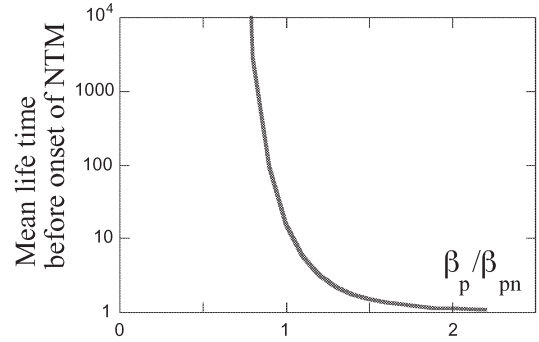


Fig.1 Mean life time before the onset of the NTM as a function of the plasma beta value. ($\Delta'_0 = 0$) Other parameters are $h \rho_b^2 r_s^{-2} = 1/40$, $w_{\text{cut}} = \rho_b$ and $L_q / L_p = 2$.

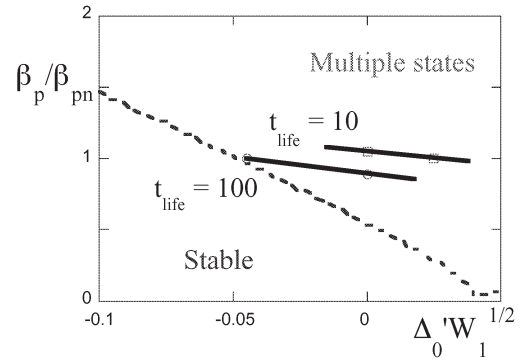


Fig.2 Contour of life time on the (Δ'_0, β_p) plane.

Cusp for the multiple solution is also shown by the dotted line. Above the dotted line, multiple solutions are allowed and stochastic transition takes place. (Other parameters are $h \rho_b^2 r_s^{-2} = 1/40$, $w_{\text{cut}} = \rho_b$ and $L_q / L_p = 2$.)

Reference

- [1] S.-I. Itoh and K. Itoh: J. Phys. Soc. Jpn. **69** (2000) 427
- [2] S.-I. Itoh, K. Itoh, M. Yagi: Phys. Rev. Lett. **91** (2003) 045003.
- [3] S.-I. Itoh, K. Itoh, M. Yagi: J. Phys. Soc. Jpn. **74** (2005) 947

§2. Higher-Harmonic Oscillation of Peniotron

Ando, A. (Dept. Electrical Eng., Tohoku Univ.),
Sato, N. (RIEC, Tohoku Univ.), Shimozuma, T.,
Inutake, M., Hattori, K. (Dept. Electrical Eng., Tohoku Univ.)

It is urgently required to develop a power source which can generate stably an electromagnetic wave in the frequency region of THz for the scattering diagnostics in large fusion devices. A gyrotron is a powerful source in the frequency region of millimeter and sub-millimeter and has been utilized in many devices not only for an electron cyclotron heating/current drive but for the scattering diagnostics. Though it can deliver a millimeter wave efficiently, a strong magnetic field is necessary in the high-frequency operation. As the oscillation frequency of this cyclotron maser device depends on an electron cyclotron frequency in a magnetic field, a strong magnetic field of more than 36 Tesla is necessary to generate 1 THz electromagnetic wave in a fundamental cyclotron harmonic oscillation. A higher-harmonic operation is feasible to reduce the strength of the magnetic field. However, gyrotrons are usually operated at 1st or 2nd harmonic condition because the efficiency becomes worse in a higher harmonic operation.

Peniotrons has been theoretically and experimentally recognized to generate an electromagnetic wave with very high conversion efficiency at cyclotron higher-harmonics, as well as cyclotron fundamental. Experiments of higher-harmonic operation with 3rd and 10th harmonic were successfully demonstrated in Tohoku University and 30 GHz and 100 GHz oscillations were obtained [1-4]. A slotted waveguide resonator was used for the peniotron interaction between an axis encircling electron beam and the space harmonic wave. An electron beam encircling with a large orbit interacts with the electromagnetic field near the resonator wall, where the vane structure enhances

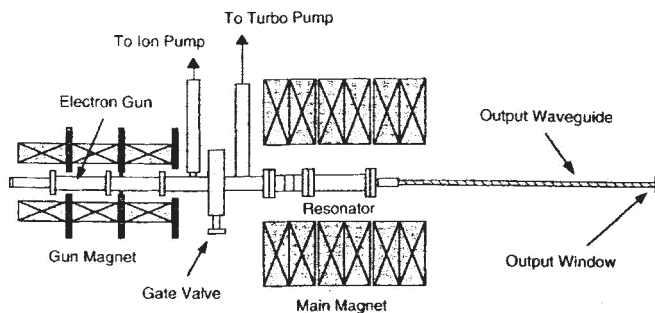


Fig.1 Experimental setup of the demountable peniotron device.

the intensity of electromagnetic field near the wall. The field intensity varies periodically along the beam orbit and electrons experience acceleration and deceleration during one Larmor motion. Owing to the peniotron interaction, electrons are gradually concentrated in the deceleration region, resulting that the electron kinetic energy converts to the electromagnetic wave energy. The n -th harmonic operation is possible by using $(n+1)$ -vane slotted waveguide resonator.

In this research, we are going to develop a higher-harmonic peniotron power source, which can be utilized in the scattering diagnostics in larger fusion devices. Resonators with a vane-number of 18 and 28 are designed and fabricated for 17th and 27th harmonic oscillation.

The experimental setup is shown in Fig. 1. The experimental tubes are demountable in an electron gun region. All of the sub-assemblies of the electron gun to the output circuit are aligned along the axis. An axially rotating electron beam is formed by passing through a cusp magnetic field. The electron beam interacts with electromagnetic field at a resonator immersed in a normal conducting magnet. The magnetic field can be applied up to 0.5 Tesla. Figure 2 shows simulated results of output power and electronic efficiency for 17th harmonic tube using a resonator with 18 vanes. Experiments of the peniotron oscillation are in preparation.

Reference

- 1) N.Sato, et.al., IEEE Trans. Plasma Science, **30** (2002) 859.
- 2) K.Yokoo, Inst. Electronics, Inform. and comm. Eng., ED2002-241 (2002) 43.
- 3) T.Ishihara, et.al., IEEE Trans. Electron Devices, **43** (1996) 827.
- 4) T.Ishihara, IEEE Trans. Electron Devices, **46** (1999) 798.

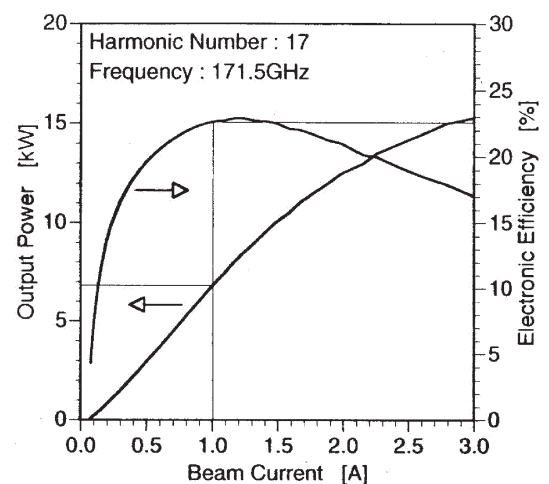


Fig.2 Simulated results of output power and electronic efficiency obtained for 17th harmonic tubes.

§3. Clarification on Cooling Mechanism of Stirling Type Pulse Tube Cryocooler

Yasohama, K. (Nihon Univ., Inst. Quantum Sci.)
Yamamoto, H. (Nihon Univ., Sci. Tech.)
Matsubara, Y. (Musashi Inst. Tech.)
Mito, T., Iwamoto, A., Hamaguchi, S., Maekawa, R.

The Stirling type pulse tube cryocooler features a high reliability and a low level of mechanical vibration because it has no solid displacer in its cooling section. In this type of cryocooler, the cooling power is determined almost by an internal construction and work-flow in a regenerator. The work-flow is brought to be set into an optimum state by a phase controlling. Therefore, clarifying on characteristics of the phase controlling mechanism is required for improving the cooling power of the pulse tube cryocooler.

In this study, using a numerical calculation we have investigated on the possibility of a prediction of characteristics for phase controlling mechanism, which is composed of an inertance tube and a buffer tank.

In general, the Stirling pulse tube cryocooler is made up of three main sections, which are a pressure oscillation generator, a pulse tube cooler and a phase controlling mechanism, and these sections are arranged in this order, and for a working gas, helium is used. In this study, of which an intention is to examine the behavior of the phase controlling mechanism, the experiment has been carried using an arrangement without a pulse tube cooler, that is, a phase controlling mechanism being connected in direct to a pressure oscillation generator.

The pressure oscillation generator employed in our experiment is a type of twin-piston driving and has a gas expulsion volume rate of 400 cc/cycle, a driving frequency range of 40 to 60 Hz. We prepared several kinds of inertance tubes, of which a diameter of 3/8, 4/8 and 5/8 inch and a length of 1.0 to 17.0 m. Volumes of the buffer tanks are 2500 and 3750 cc, and a pressure of helium working gas is 2.0 MPa.

For many combinations of frequencies, inertance tube diameters and lengths, and buffer tank volumes, measurements are made on an amplitude of the piston displacement, a pressure amplitude of helium gas at the input of the inertance tube (input pressure), and a phase difference between these piston displacement amplitude and input pressure amplitude.

A numerical calculation including fluid viscosity was performed for the phase difference between the input gas pressure and velocity, which make an important phase characteristic in the Stirling type pulse tube cryocooler. In this case, we made use of viscosity and

volume compressibility of helium gas as adjustable parameters. Those parameters were determined by adjusting the calculated phase of piston displacement and entrance pressure, to the measured one. In addition, we made a calculation on the phase characteristic when a orifice valve was placed at the input of the inertance tube.

For the phase difference between the input pressure and the piston displacement vs. driving frequency, the calculated one was found to agree well with the measured, on the all combinations of the inertance tube and the buffer tank. In particular, the agreement increases with diameter of the inertance tube. This indicates that selection of equation of calculation and adjustable parameters are appropriate.

Furthermore, it has been cleared that the phase is almost independent of the inertance tube diameter and the buffer tank volume, and the length of the inertance tube is a determining factor for the phase, which varies nearly periodically with the tube length.

The phase change is very large when the length is short, it varies from -90 to $+70$ deg under a length up to 1 m. It is supposed that this large phase change in a short length of the inertance tube makes it impossible to control the phase precisely by adjusting tube length. The phase variation decreases with an increase in inertance tube length. In order to enable the fine phase control by tube length adjustment, a length of 4-5 m at least is thought to be necessary.

When the inertance tube has the orifice valve at its input, the dependence of phase on the tube length is reduced and the phase is mainly determined by gas flow rate set by the orifice valve. In this case, phase can be finely controlled due to precise flow adjustment of a orifice valve

In conclusions, it has been possible to estimate the phase properties by a numerical calculation for the Stirling type pulse tube cryocooler having the phase control mechanism composed of the inertance tube and the buffer tank. This is supposed to be one of the methods effective to clarify the cooling mechanism and to improve the cooling power of the pulse tube cryocooler.

In the future, we are intending to introduce a displacer to measure the gas flow velocity and phase at the input of the inertance tube, and from direct comparison of the measured phase with the calculated one, the numerical calculation will be modified and its accuracy will be raised furthermore.

§4. Ion Heating in a Supersonic Plasma Flowing Through a Magnetic Nozzle

Inutake, M., Ando, A., Hattori, K., Tobari, H., Hatanaka, M., Shibata, M. (Dept. Electrical Eng., Tohoku Univ.)

Recently a plasma flow has been recognized to play an important role in space and fusion plasmas. Intensive researches to develop a fast flowing plasma with high particle and heat fluxes are required for the purpose of basic plasma researches as well as various wall material researches and space applications.

A magnetic nozzle acceleration and ion heating in a fast flowing plasma attracts much attention in an advanced electric propulsion system. In the Variable Specific Impulse Magnetoplasma Rocket (VASIMR) project, it is proposed to control a ratio of specific impulse to thrust at constant power.[1] This is a combined system of an ion cyclotron heating and a magnetic nozzle, where a flowing plasma is heated by ICRF (ion cyclotron range of frequency) power and the plasma thermal energy is converted to flow energy via a magnetic nozzle.

The purpose of this research is to investigate effective methods of wave excitation and to establish an ion heating technology in a fast flowing plasma for the advanced plasma thruster and other applications.

We have performed an ion heating experiment in a supersonic plasma flow produced in the HITOP device.[2,3] RF waves are launched by a right-handed helically-wound antenna in a helium plasma. This antenna is set at $Z=0.6\text{m}$ downstream of the Magneto-Plasma-dynamic Arcjet (MPDA) and excite RF waves with an azimuthal mode number of $m = -1$. The RF frequency can be changed from 100kHz to 500kHz with an input power up to 15kW.

When RF waves excited in a flowing plasma with a density around $1 \times 10^{13} \text{cm}^{-3}$, we observed an increase of plasma stored energy W_{\perp} measured by a diamagnetic coil located at $Z=2.23\text{m}$ downstream from the MPDA. Ion temperature T_i also increased during the RF pulse. However, no clear indication of the cyclotron resonance is observed, because the ion-ion collision frequency ν_{ii} is larger than the ion cyclotron frequency f_{ci} in the high density region and the waves are damped not by cyclotron resonance but by collisional damping. We decreased a plasma density from $1 \times 10^{13} \text{cm}^{-3}$ to $5 \times 10^{11} \text{cm}^{-3}$ so that the cyclotron heating phenomena appeared and a diamagnetic coil signal W_{\perp} increases drastically as shown in Fig.1. It is also observed that the peak position is shifted to lower magnetic field than that corresponding to $\omega/\omega_{ci}=1$, i.e. ω/ω_{ci} higher than 1. This is due to the Doppler effect caused by the fast plasma flow.[4]

Figure 2 shows a dependence of W_{\perp} on the RF input power P_{RF} . It linearly increases with P_{RF} . We have also measured ion temperature by an electrostatic energy analyzer, of which collection surface faces to perpendicular direction to the plasma flow. The perpendicular component of ion temperature $T_{i\perp}$ can be obtained. When P_{RF} increases, $T_{i\perp}$ increases almost linearly as shown in Fig.3.

Experimental researches on the energy conversion from thermal energy to flow energy by a magnetic nozzle should be pursued further.

Reference

- 1) F.R.ChangDiaz, et al.: Proc. of 36th Joint Propulsion Conf., (Huntsville,2000), AIAA-2000-3756.
- 2) M.Inutake, et al.: Proc. of 26th ICPIG, Vol.1, (2003). p.127.
- 3) A.Ando, et al.: Advances in Applied Plasma Science, 4 (2003) 193.
- 4) A.Ando, et al.: Proc. the 7th APCPST, (Fukuoka, 2004), A2 (2004) 45.

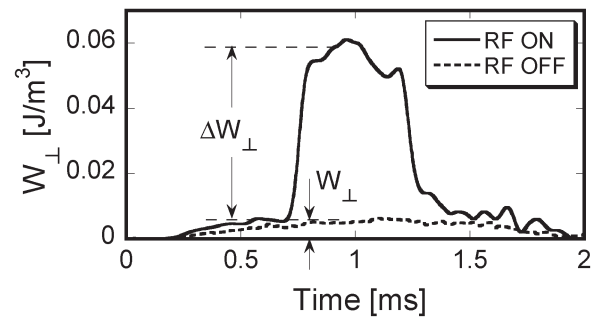


Fig.1 Time evolutions of diamagnetic coil signal W_{\perp} . $f_{\text{RF}}=236\text{kHz}$, $P_{\text{RF}}=15\text{kW}$.

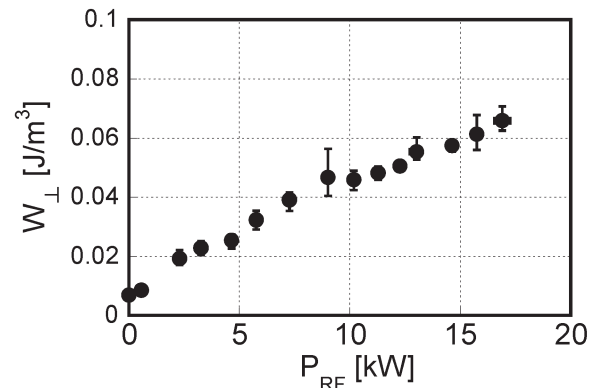


Fig.2 Dependence of diamagnetic coil signal W_{\perp} on input RF power P_{RF} . $f_{\text{RF}}=236\text{kHz}$.

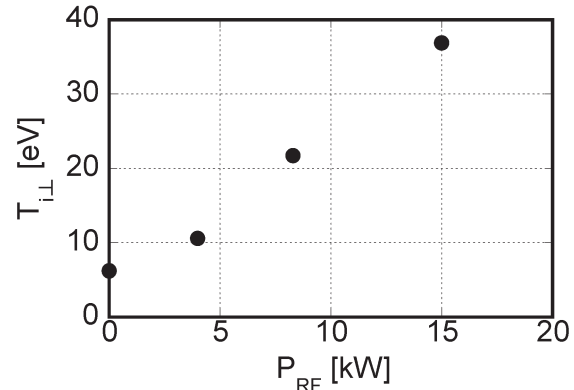


Fig.3 Dependence of perpendicular component of ion temperature $T_{i\perp}$ on input RF power P_{RF} . $f_{\text{RF}}=236\text{kHz}$.

§5. Electron Bernstein Wave Heating by Long Wavelength Microwave in a Spherical Tokamak and a Helical Device

Maekawa, T., Tanaka, H., Uchida, M., Yoshinaga, T. (Kyoto Univ.)

Ikeda, R., Takeuchi, M., Ito, T. (Nagoya Univ.)

Toi, K., Suzuki, C.

On the LATE device at Kyoto University, formation of Spherical Tokamak by ECRH without center solenoid have been conducted [1], while on the CHS device at NIFS, experiments for transport study based on the “non-dimensionally similar approach” have been conducted to simulate various transport processes in high temperature plasmas[2]. In both cases, the plasmas are generated and maintained by ECRH in over-dense regime via mode-converted electron Bernstein waves (EBW) from long wavelength microwaves and efficient coupling from external microwaves to EBW is crucial for experiments. The main purpose of the present study is to study coupling processes and to develop the effective launching method for efficient coupling.

Main objective of the LATE (Low Aspect ratio Torus Experiment) device is to demonstrate formation of ST plasmas by electron cyclotron heating (ECH) alone without center solenoid and establish its physical bases. By injecting a 2.45 GHz microwave pulse for 4 seconds, a plasma current of 1.2 kA is spontaneously initiated by $P=5$ kW under a weak steady vertical field of $B_v=12$ Gauss, and then ramped up with slow ramp-up of B_v for the equilibrium of the plasma loop and finally reaches 6.3 kA at $B_v=70$ Gauss. This currents amount 10 percents of the total coil currents of 60 kA for the toroidal field. Magnetic measurements show that an ST equilibrium, having the last closed flux surface with an aspect ratio of $R_0/a=20.4$ cm/14.5 cm=1.4, an elongation of $K=1.5$ and $q_{edge}=37$, has been produced and maintained for 0.5 s at the final stage of discharge. Spontaneous formation of ST equilibria under steady B_v fields, where plasma current increases rapidly in the time scale of a few milliseconds, is also effective and a plasma current of 6.8 kA is spontaneously generated and maintained at $B_v=85$ Gauss by a 5 GHz microwave pulse (130 kW, 60 ms). In both cases the plasma center locates near the second or third harmonic EC resonance layer and the line averaged electron density significantly exceeds the plasma cutoff density, suggesting that harmonic EC heating by the mode-converted EBW supports the plasma.

The mode conversion rate is estimated based on the plasma slab model [3]. In the case of 2.45 GHz experiments, free space wavelength (12.2 cm) is comparable to the plasma radius (20 cm), where maximum mode-conversion rate after optimization of injection angles and polarizations is only 60 %. On the other hand, in the case of 5GHz, oblique injection with left-handed circular polarization can give 90 % mode-conversion rate.

In CHS, 2.45 GHz microwaves up to 45 kW are injected perpendicularly to the toroidal field, into hydrogen, helium or neon gas. Most experiments were carried out in the so-called outward shifted configuration

of $R_{ax}=0.974m$, where R_{ax} is the magnetic axis position in the vacuum field. This magnetic configuration was chosen from a point of view of convenience for Langmuir probe measurements. The toroidal field strength at the plasma center B_t was scanned from $\sim 1000G$ to $\sim 600G$. The line averaged electron density reached to the maximum at $B_t=613G$, which was about three times, five times and 10 times higher than the O-mode cutoff density for hydrogen, helium and neon fuel gas, respectively. The dependence of the achieved electron density on fuel gas seems to be determined by plasma transport rather than RF physics. Note that the fundamental cyclotron layer at $B_t=613$ G is placed near the plasma boundary ($\rho\sim 0.9$) and the upper hybrid resonance layer is in the edge region with steep density gradient. The power deposition was measured using a power step technique, and concentrated in high density region inside the left hand cutoff [4]. These results suggest that launched electron cyclotron waves are mode-converted at the upper hybrid resonance layer to EBW, and damped through collisional damping. However, cyclotron damping cannot be ruled out in these experiments because polarization and directivity of the launched long wave-length waves cannot be specified definitely.

References

- [1] T. Maekawa *et al.* Proc. Of 20th IAEA Fusion Energy Conference, IAEA-CN-116/EX/P4-27
- [2] K. Toi *et al.*, 29th EPS on Plasma Physics and Controlled Fusion, Montereux, 2002, paper No.P4-06.
- [3] H. Igami *et al.*, Plasma Phys. and Control. Fusion, **46** (2004) 261
- [4] R. Ikeda *et al.*, to be published in J. Plasma Fusion Res. 2005.

§6. Assessment on Fusion Energy Development from the Socio-Economic Viewpoint

Ogawa, Y. (The University of Tokyo)
Okano, K., Asaoka, Y., Hiwatari, R. (CRIEPI)
Konishi, S. (Kyoto University)
Tobita, K. (JAERI)
Norimatsu, T. (Osaka University)
Sagara, A.

In the 21 century global environment and energy issues becomes very important, and this is characterized by the long-term (in the scale of a few tens years) and world-wide issue. In addition, future prospect of these issues might be quite uncertain, and scientific prediction could be very difficult. For these issues vigorous researches and various efforts have been carried out from various aspects; e.g., world-wide discussion such as COP3 in Kyoto, promotion of the energy-saving technology and so on.

Development of environment-friendly energy has been promoted, and new innovative technologies are explored. Nuclear fusion is, of course, a promising candidate. While, there might be some criticism for nuclear fusion from the socio-economic aspect, because it would take long time and huge cost for the fusion reactor development. Here we have started to assess the fusion energy development, comparing with other innovative energy technologies.

At first, we have considered to evaluate the characteristics which the people requires for future energy resources, based on questionnaire research from ordinary people. Several items are selected, and issues to be compared are defined. For each issue a social weight and scientific score are estimated. A social weight is determined by the public questionnaire, and a scientific score is by the scientific data for each energy technology. Here we have selected five items and related issues, as shown in Table 1, where a social weight and a scientific score are denoted by W_{ij} and P_{ij} , respectively.

Table 1. Items and issues to be compared.

Item	Issue	Social weight	Scientific score
Energy resource	1) total amount	W_{11}	P_{11}
	2) distribution	W_{12}	P_{12}
Environmental load	1) CO2 emission	W_{21}	P_{21}
	2) waste disposal	W_{22}	P_{22}
Economics	1) construction cost	W_{31}	P_{31}
	2) operation cost	W_{32}	P_{32}
Reliability and stability	1) natural vulnerability	W_{41}	P_{41}
	2) social vulnerability	W_{42}	P_{42}
Safety and security	1) hazard potential	W_{51}	P_{51}
	2) military application	W_{52}	P_{52}

Here we have planned three questionnaires as follows;

- 1) Screening questionnaire for more than thousand ordinary people,
- 2) Evaluation of the social weight in each issue for more than one hundred ordinary people,
- 3) Evaluation of the scientific score in various energy technologies for a few tens specialists.

At the screening questionnaire, interest and recognition for environment and energy issues are inquired. Through the screening questionnaire, about one hundred people are selected, where distribution on men-women, generation is paid much attention.

In the questionnaire research on the social weight, two issues for each item, shown in Table 1, are compared, and weight is inquired between two issues. For example in the case of the energy resource, the inquiry is as follows;

[There are two energy resources A and B. The resource A has an inexhaustible amount, but is localized in the earth. The resource B is widely distributed in the earth, but the amount is limited. Which resource do you select?]

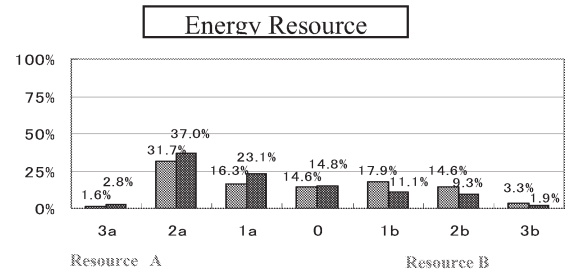


Fig. 1 Population of questionnaire for the energy resource.

Figure 1 shows the results of the questionnaire, where the left side such as “3a” means that a people supports the resource A strongly; i.e., the total amount is important. A people who supports both issues equally has voted at the middle point “0”. The results of Fig. 1 would indicate that people might support the total amount rather than distribution as an energy resource.

The same questionnaire has been carried out in two times, where in the second time the questionnaire results of the first time are presented for each people. This is usually called “Delphi” method. The right column denotes the result of the second questionnaire.

Next we are planning to evaluate a scientific score for several new energy technologies. Here we have selected following technologies;

- 1) Advanced coal technology with CO2 recovery system
- 2) SOFC top combined cycle (natural gas)
- 3) Solar power
- 4) Wind power
- 5) Space solar power station
- 6) Advanced fission
- 7) Fusion

At first we have to compile scientific data on each item listed in Table 1(i.e., energy resource, environmental load, economics, reliability and tolerance, and safety and security). A first version of the scientific data has been published from the CRIEPI group¹⁾, and a preliminary questionnaire for evaluating scientific scores in Table 1 has been carried out.

Reference

- 1) Hiwatari, R., CRIEPI internal report (2005).

§7. Magnetic Island Effect on Radial Particle Flux in TU-Heliac

Kitajima, S., Sasao, M., Shinto, K., Takahashi, H., Tanaka, Y., Utoh, H., Takenaga, M., Shinde, J., Ogawa, M., Aoyama, H., Iwazaki, K. (Dept. Eng., Tohoku Univ.)
Takayama, M. (Akita Prefectural Univ.)
Komori, A., Nishimura, K., Inagaki, S., Suzuki, Y.

It is important to study the effect of magnetic islands for the designing helical reactors. Recently the healing of magnetic islands was observed experimentally, which provides good prospects in the design for helical reactors, and many ideas, in which magnetic islands are actively applied to control/improve confinement modes, are proposed. In LHD it is also important to study the $m = 1$ island effect on the transport mechanism for the advanced control method of a plasma periphery. In the Tohoku University Heliac (TU-Heliac), a helical axis stellarator, the profile of a rotational angle can be changeable by selecting ratios of coil currents. TU-Heliac has local vertical field coils (auxiliary coils) which produce external perturbation fields to resonate the magnetic Fourier components of $(n, m) = (3, 2)$, $(5, 3)$ and to grow $m = 2$ and 3 magnetic islands. These islands were observed experimentally by the fluorescent mesh method. Furthermore the improved mode transition has been triggered by electrode biasing experiments using a hot cathode made of LaB_6 . The driving force $\mathbf{J} \times \mathbf{B}$ for a plasma poloidal rotation was externally controlled and the poloidal viscosity was successfully estimated from the driving force¹⁻²⁾. The purposes of our island experiments in TU-Heliac are, (1) to estimate the ion viscosity from the driving force for the poloidal rotation by the electrode biasing in configurations containing magnetic islands, and (2) to study the magnetic island effect on radial particle flux.

Preliminary biasing experiments in configurations containing magnetic islands were carried out in TU-Heliac. The LaB_6 hot cathode (diameter, 10 mm; length, 17 mm) was inserted horizontally into the plasma inside the $m = 3$ magnetic islands located along the plasma periphery as shown in Fig. 1. The hot cathode was heated by a floating power supply and negative current source was applied against the vacuum vessel by a *current-control* power supply (Fig. 1). In Fig. 2 increasing the magnetic island width which was proportional to the root of the auxiliary coil current I_{aux} , the electrode current I_E^* required for the improved mode transition was increasing. It suggested that the ion viscosity increased according to the increase of the magnetic island width. The experiment will be extended to biasing experiments in limiter configurations in order to clarify the effect of the target plasma volume on the transition. In order to estimate precisely poloidal Mach numbers in the biased plasmas ion temperature

measurements were tried out by a high-resolution spectrometer.

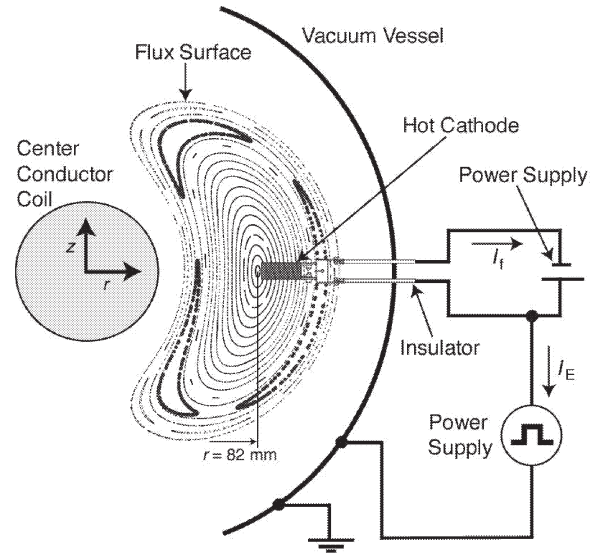


Fig. 1. The experimental set up of the hot cathode inserted horizontally into the plasma inside the $m = 3$ magnetic islands.

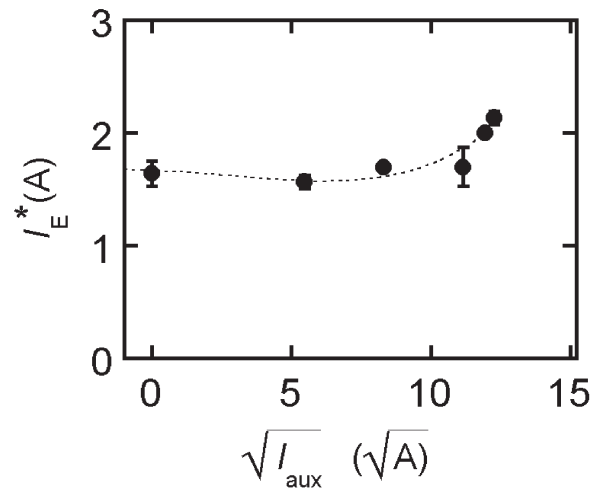


Fig. 2. Dependence of the electrode current I_E^* required for the improved mode transition on the root of the auxiliary coil current I_{aux} which is proportional to the magnetic island width.

Reference

- 1) Takahashi, H. *et al.*: Comparison of Bifurcation Phenomena During LH/HL Transition Observed in Biasing Experiment in Tohoku University Heliac, presented at ICPP2004 [Nice, Oct., 2004] D1-5.
- 2) S. Kitajima, *et al.*: LH Transition by a Biased Hot Cathode in the Tohoku University Heliac, presented at 20th IAEA FEC [Vilamoura, November 2004] IAEA-CN-116/EX/9-3.

§8. Heating and Current Drive Experiments on the TST-2 Spherical Tokamak

Takase, Y., Ejiri, A., Shiraiwa, S. (Frontier Sci., U. Tokyo)

Zushi, H., Hanada, K. (RIAM, Kyushu U.)

Sasaki, K., Hoshika, H. (Eng. Sci., Kyushu U.)

Mitarai, O. (IISTR, Kyushu Tokai U.)

Nishino, N. (Eng., Hiroshima U.)

Watari, T., Kumazawa, R., Seki, T.

This research is carried out as collaboration among several universities and NIFS. The purpose of this collaborative research is to perform heating and current drive experiments using radiofrequency (RF) waves on a spherical tokamak (ST) plasma, with the eventual objective of developing innovative methods for plasma start-up and steady-state sustainment. The TST-2 spherical tokamak at the University of Tokyo is presently the largest ST device in Japan, with $R = 0.38$ m and $a = 0.25$ m (aspect ratio $R/a = 1.5$). It has already achieved toroidal magnetic fields of up to 0.3 T and plasma currents of up to 0.14 MA. RF power of up to 400 kW in the frequency range 10–30 MHz is available for this experiment. In addition, transmitters at 200 MHz, previously used on the JFT-2M tokamak, have been transferred from JAERI during this fiscal year.

TST-2 was temporarily relocated to Kyushu University to take advantage of the high power microwave facility for TRIAM-1M. Eight klystrons operating at 25 kW each at 8.2 GHz were used for plasma start-up, heating, and current drive studies in the electron cyclotron frequency range. This work was carried out collaboratively among the University of Tokyo, Kyushu University, Kyushu Tokai University, Hiroshima University, and NIFS. Detailed analyses of data from these experiments were performed under this collaboration. Main results are summarized below:

(1) Electron heating and current drive by the electron Bernstein wave (EBW):

ST plasmas are characterized by very high dielectric constants. Therefore, the usual electromagnetic electron cyclotron waves (both O-mode and X-mode) are not accessible to the plasma core. EBW is a short-wavelength mode in this frequency range which can propagate in high dielectric constant plasmas and is absorbed strongly by electrons. A novel heating scenario using the X-B mode conversion process was attempted on TST-2. This scenario has the advantage of simple wave launching geometry. Although electron heating was not confirmed directly because of lack of electron temperature measurement, a clear increase of plasma stored energy by 10–20% was observed. The profile measurement of emission in the visible to soft X-ray energy range indicated absorption in the plasma core. However, the absorption efficiency deduced from the time rate of change of the stored energy was only 10–20%, indicating a power loss mechanism at the plasma periphery. In addition, a small increase of the plasma current was observed, suggesting current drive by EBW.

(2) Plasma current start-up by poloidal field coils, without the central solenoid (CS):

A large improvement in the economic competitiveness of a tokamak reactor can be realized if CS could be eliminated. Demonstration of tokamak operation without CS is indispensable to justify such a design. A successful plasma current start-up to 10 kA by induction from poloidal field (PF) coils (but without CS) was demonstrated on TST-2. This is the first demonstration of this start-up method in ST. In this scenario, the vertical field is ramped from the reverse direction in order to provide an adequate vertical field for equilibrium at the end of the formation phase. This means the plasma current must be started with the vertical field in the direction opposite to that required for equilibrium. Because the plasma is lost to the outboard side quickly, it is necessary to replenish plasma at a sufficiently fast rate during the ramp-up phase. This was provided by 100 kW of RF power in this experiment.

(3) Plasma formation, plasma current ramp-up and sustainment by RF power alone:

A quasi-steady-state plasma current of 4 kA was sustained for 0.28 s with 100 kW of RF power at a toroidal field of 0.16 T and a steady-state vertical field of 0.002T. No induction was used, either from the CS or other PF coils. The electron temperature measured by soft X-ray pulse height analysis was 180 eV. The electron density was less than 10^{18} m^{-3} , suggesting that the current was probably driven by ECW (not by EBW). Reconstruction of the magnetic configuration based on magnetic measurements indicate that there is substantial current flowing outside the last closed flux surface.

TST-2 was moved to the Kashiwa Campus of the University of Tokyo at the end of FY2003 (Fig. 1). Upgrades to power supplies and RF systems were performed in FY2004, providing capabilities for higher current and longer pulse operation. TST-2 is now back in operation, and RF heating experiments will resume in FY2005.

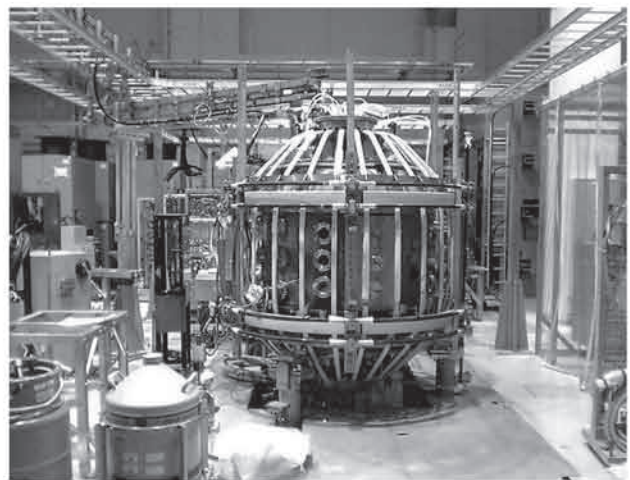


Fig. 1. TST-2 at the University of Tokyo Kashiwa Campus.

§9. ECH Plasma Experiments of an Internal Ring Device with HTS Coil

Ogawa, Y., Morikawa, J. (The University of Tokyo)
Iwakuma, M. (Kyushu University)
Mito, T., Yanagi, N.

The internal coil device Mini-RT, in which the high temperature superconductor coil is levitated, has been constructed, and the levitation experiments have been carried out¹⁻³⁾. Here we have focused on studying to clarify the effect of the removal of the supporting structure by the levitation of the internal coil. So experiments with the supported and levitated internal coil have been carried out in order to investigate the difference in plasma properties.

Figure 1 shows the dependence of electron density measured by the electrostatic probe as a function of the neutral gas pressure. When the internal coil is levitated, plasma production at the neutral gas pressure of 10^{-3} Pa was successfully carried out. In addition, it can be seen that the electron density increases as the increase of gap length between the internal coil and the supporting structure.

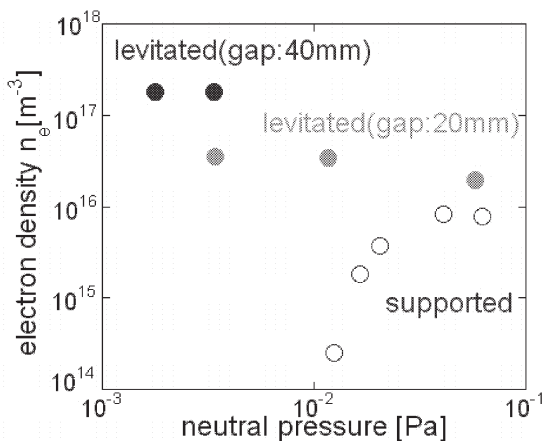


Fig. 1 Plasma density for cases of supported and levitated internal coil.

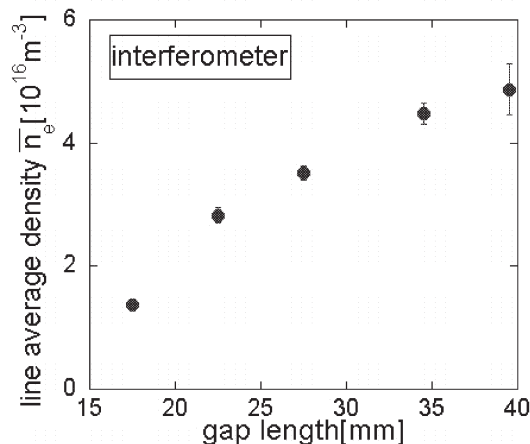


Fig. 2 Line-averaged density as a function of the gap length between the floating coil and the supporting structure.

The relation between the gap length and electron density at the constant neutral gas pressure was also measured. Figure 2 shows the results measured by the 4mm interferometer system. The neutral gas pressure was 3×10^{-3} Pa. It is apparent that the line-averaged density increases as the increase of the gap length.

Figure 3 shows the density profiles measured by electrostatic probe, when the internal coil is levitated. In this measurement, the neutral gas pressure was 1.5×10^{-3} Pa, and the injected ECH power was around 2.5 kW. The result obtained by the experiment with supported internal coil is also plotted for comparison, where the neutral gas pressure is in the range of 10^{-2} Pa. Notice that the neutral gas pressure is different in both cases. It is apparent that the plasma region becomes to be localized around the internal coil, when the internal coil is levitated. So the density gradient becomes much steeper, compared with the supported case. This is because that a separatrix is produced, when the current is applied in the levitation coil. The calculated position of the magnetic surface which passes the separatrix on the equatorial plane is around $R = 0.28$ m, which is in good agreement with the position of the density drop.

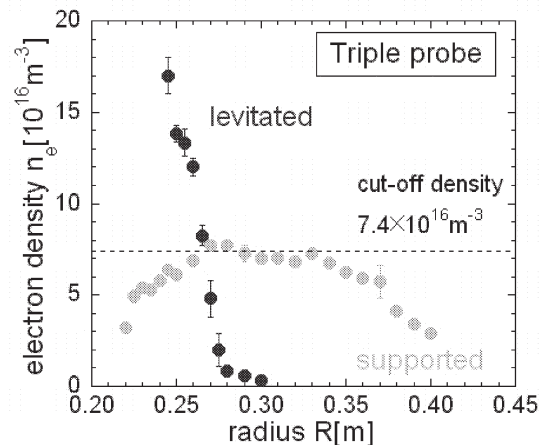


Fig. 3 Density profiles of supported and levitated coil cases.

More important difference lies in the absolute value of the density. Although the peak value is unknown in the levitated case, the maximum measured electron density ($1.6 \times 10^{17} \text{ m}^{-3}$) is much higher than the supported case, which is about twice of the cutoff density of the 2.45GHz microwave ($7.4 \times 10^{16} \text{ m}^{-3}$), resulting in the increase of the ionization degree to 50%. The electron temperature also increases in most region, and the value is about twice of the one obtained in the supported case.

References

- 1) Ogawa, Y., J. Cryog. Soc. Japan, **39** (2004), 175.
- 2) Mito, T., J. of Cryog. Of Japan, **39**, (2004) 182.
- 3) Yanagi, N., J. of Cryog. Soc. Japan, **39** (2004) 201.

\$10. Experimental and Theoretical Studies of Startup Methods for Spherical Tokamak Plasmas

Ono, Y., Nagayama, Y., Takase, Y., Mekawa, T., Nishio, S., Nagata, M. (Univ. Tokyo, NIFS, Kyoto Univ., JAERI, Hyogo State Univ.)

The spherical tokamak (ST) is expected to attain both of high-beta and long confinement time. Its key issue is how effectively we can startup high-beta ST without using the center solenoid coil whose space is limited in the center of ST. The University of Tokyo have three key ST devices for ST startup but a few plasma diagnostics. On the other hand, NIFS has a variety of plasma diagnostics, especially high special resolution measurements of plasma temperature and density useful for the ST startup measurements but not ST device. Because of these reasons, we have been collaborating with the ST group in NIFS using ST committees in JSFS and IEEJ. In this program, we made for the first time the all-Japan type joint study of ST startup by collaborating not only with NFS but also with all ST groups in Japan: Kyoto Univ., Hyogo State Univ., Kyusyu Univ. and Kyusyu-Tokai University.

A final goal of our project is to optimize the ST startup methods both from theoretical and experimental points of view. In 2004, the joint group made the high beta ST startup in TS-3 and 4, by combining PF coil induction and complete merging/ reconnection of two STs and also solenoid coil-less ST startup in TST-2, using RF and PF coil induction. We also made the corresponding Magnetohydrodynamic (MHD) simulation to verify these experimental results. Consequently, our proposal of large scale merging experiment was accepted by NSTX, Princeton Univ. as a new extension of merging startup experiment. We will start the first merging / reconnection experiment of NSTX in this summer season.

Figure 1 show the 2-D MHD simulation result of the ST merging startup and Fig. 2 shows the corresponding experimental result in TS-3. They indicate that two STs can be produced by the induction of two or four PF coils and they are merged successfully in the axial direction. The high power heating of reconnection is observed to suppress the strong paramagnetic toroidal field of initial low-beta STs.

A series of ST startup activities in four universities and two institutes were summarized in the joint meeting / experiment at Univ. Tokyo in Feb.. We compared the four

major ST startup methods: PF coil induction, RF, CHI, EF rampup and merging startup and finally refined their several key subjects especially from the view point of ST reactor requirements. These subjects will be tested in UTST, a new ST startup project in Univ. Tokyo and those ST groups will join it using a new remote experiment system by Super SINET in next fiscal year.

References

- [1] Y. Ono et al., Fusion Energy 2004, IC/P6-44, (2005).

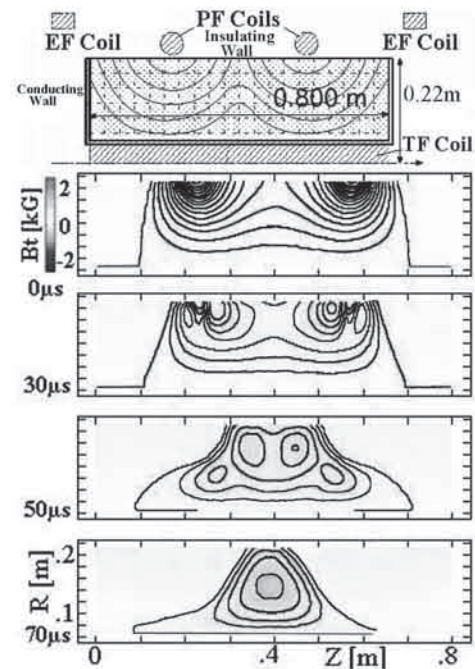


Fig. 1 Poloidal flux contours with internal B_t amplitude (color) during the merging startup (2-D MHD Simulation).

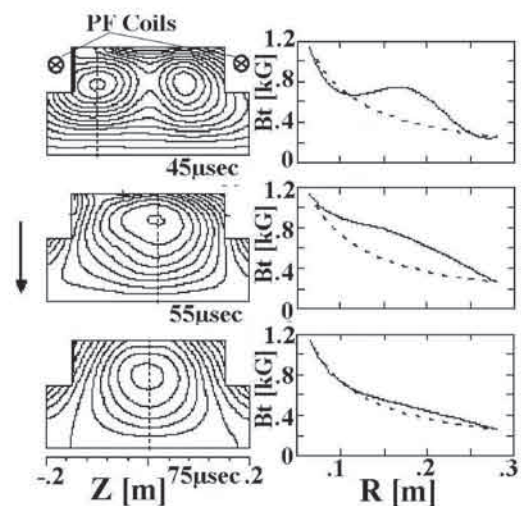


Fig. 2 Poloidal flux contours and radial B_t profiles during the merging startup. The dotted lines represent vacuum B_t (TS-3 Experiment).

7. Collaborations Using Super SINET

The remote access enables the users to use computers as if they are directly connected to the LHD-LAN. This is established using Super SINET, which is a fast network operated by National Institute of Information (NII) for scientific research. SuperSINET consists of the 10 Gbps back-bone and 1 Gbps branches. Remote stations and NIFS are connected with the SuperSINET. Using the multi protocol label switching-virtual private network (MPLS-VPN) technology on SuperSINET, LHD-LAN is extended to the remote stations. This extension is named “SNET”. In a SNET remote station, they can manipulate diagnostic devices in LHD.

Since SNET is a part of LHD-LAN, it is prohibited to connect to the other network. SNET is connected to the Internet passing through the firewall of NIFS-LAN. SNET is taken care of by the SNET manager. SNET users can ask him by E-mail (snet@nifs.ac.jp) in order to solve

problems on SNET.

A remote station is equivalent to the LHD control room. TV conference system is a useful item in the remote participation system. It is also connected to SNET. Since SNET is a fast local network, response is fast and no termination is caused when using TV conference system. Using the multi connection system, they can watch the LHD plasma in a remote station. Since LHD is continuous experiments and it lasts several hours in a day. The researches have to recognize how the experiment is going during the experiment. For this purpose, the TV conference system is also utilized in SNET.

Remote stations of LHD are spreading in Japan. Figure 1 shows locations of remote stations of LHD in Japan. In 2004, two remote sites, University of Tokyo (Hongo: Main Campus) and Kyoto University (Yoshida: Main Campus) joined to the SNET.

(Nagayama, Y.)

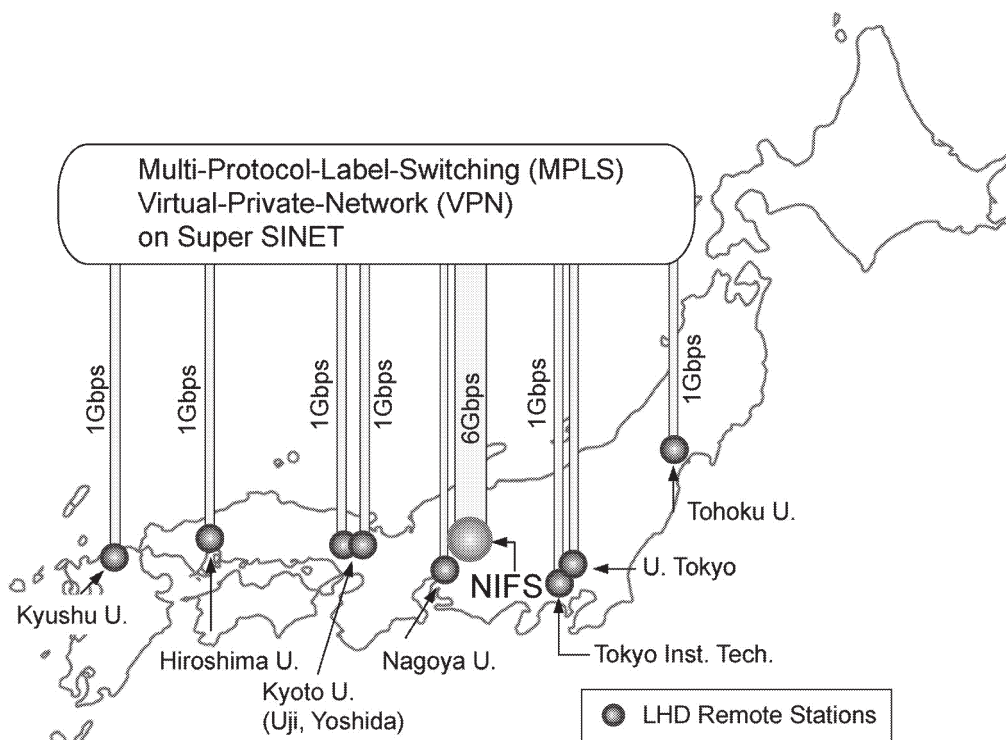


Fig.1 Remote stations of LHD in Japan.

§1. Network Reconstruction of LHD Experiment Remote Participation System

Tsuda, K., Nagayama, Y., Yamamoto, T.,
Hasegawa, H. (INTEC Solution Power Inc.)

The remote experiment participation system using high-speed network, Super-SINET, has been built since 2002. The High Temperature Plasma Center, University of Tokyo was connected to NIFS-LAN to perform collaboration for superconductivity study by MPLS (Multi-Protocol Label Switching) at the speed of 1Gbps in March 2002. In order to perform collaboration for LHD experiment, many remote stations in universities were connected to LHD experiment LAN by MPLS at the speed of 1Gbps, since 2002. The Dep. of Energy Engineering & Science of Nagoya University in April 2002, the Institute of Advanced Energy of Kyoto University in October 2002, the Art, Science and Technology Center of Kyushu University in April 2003, the Research Laboratory for Nuclear Reactors of Tokyo Institute of Technology in February 2004, the Dep. of Mechanical System Engineering of Hiroshima University in February 2004 and the Dep. of Quantum Science and Energy Engineering of Tohoku University in March 2004 were connected. The network for connecting a remote station and the LHD experiment LAN was reconstructed, and network environment of a remote station was made the same as the control building of NIFS in the 2003 fiscal year [1].

Using limited resources, two remote stations (in Kyoto University Yoshida campus and University of Tokyo) were newly economically connected in the 2004 fiscal year.

In the NIFS side, we designed and constructed as follows;

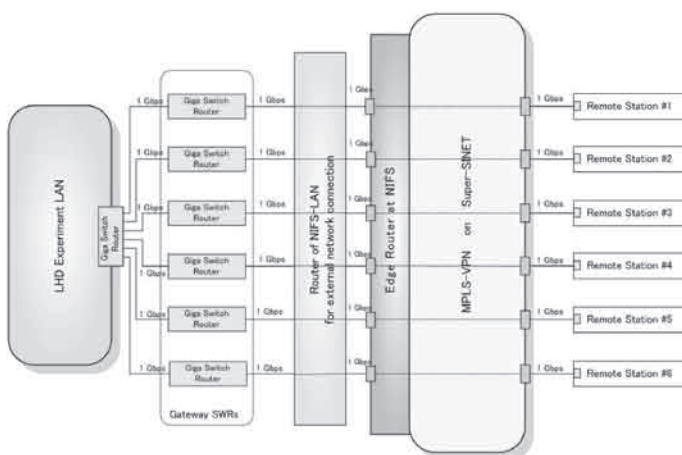


Fig.1 Block diagram of before reconstruction

1) In order to connect with new remote stations, we designed so that one interface port could communicate to two remote stations in MPLS space, because all interface ports of Super-SINET router at NIFS have been used.

2) The LHD-experiment-LAN was directly connected to the Super-SINET router, not through the router of NIFS-LAN for external connection.

3) We designed so that one gateway router can connect with two or more remote stations, and the number of gateway routers was decreased.

In the remote station side;

4) The gateway router which became free was used to establish in the new remote stations.

5) In the Kyoto University campus, VLAN was created on the Kyoto University campus LAN, for there was no optical fiber for connecting with a Super-SINET router at Kyoto University. And the Kyoto University remote station was connected to the LHD experiment LAN through the VLAN.

Since the remote station was combined in consideration of the amount of data which each remote station deals with, the user of a remote station can participate in LHD experiment with reasonable response time.

The block diagram of before and after reconstructing are shown in Fig. 1 and 2.

Reference

1) Tsuda, K., Nagayama, Y., Yamamoto, T., Hasegawa, H. :
Ann. Rep. NIFS (1993-1994) 400.

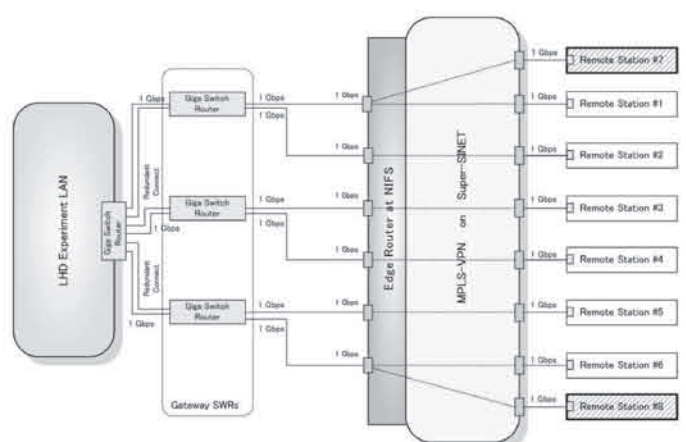


Fig. 2 Block diagram of after reconstruction

\$2. Millimeter-Wave Remote Experiment System Using Super-SINET

Mase, A., Kogi, Y., Uchida, K. (KASTEC, Kyushu Univ.)
Nagayama, Y., Kawahata, K.

In the end of FY 2002, the remote experiment system using super science information network (super-SINET) has been introduced to electron cyclotron emission imaging (ECEI) and ultra-short pulse reflectometry (USRM) systems installed in LHD as collaborating research programs. Bandwidth of the main backbone and branch line is 10 Gbps and 1 Gbps, respectively. We can now participate in the LHD experiment via remote control system and transfer the experimental data for online data processing from NIFS to Kyushu. In this paper, the present state of the system is reported.

In FY 2004, we have concentrated in the fabrication of the USRM remote experiment system. The schematic of the USRM system is shown in Fig. 1. The output of an impulse generator is fed to a 30 cm WRD-750 waveguide to obtain a chirped pulse with frequency range of 7-20 GHz. The chirped pulse is fed to an active doubler after passing through a 15 m low-loss coaxial cable in order to double the frequency range into 26-40 GHz, and amplified by a power amplifier. The transmitter and receiver are identical conical horn antennas with collimating lens. The reflected wave is amplified by low noise amplifiers to compensate the transmission loss of another coaxial cable. The signal is then digitized by a sampling scope with equivalent sampling frequency of 250 GHz.

The remote experiment system is as follows. The control client can operate the control server by using the super-SINET. The general-purpose interface bus (GPIB) card is installed in the control server. The remote console, which has graphical user interface (GUI) is prepared to control the instruments of the USRM via GPIB. The operations such as adjustment of supply voltage fed to amplifiers and the doubler, timing control of the impulse, data acquisition and monitoring can be performed from the remote site (Kyushu University). The monitor can display the current view of sampling scope for various times and

their analyzed data such as the frequency spectra as well as the machine parameters as shown in Fig. 2.

In FY 2004, the position control of the transmitter and receiver horn antennas has been installed as shown in Fig. 3. The angle between the two antennas can be adjusted depending on the various plasma conditions even between the plasma shot.

By using this system, the reflected signal from the cutoff layer has been obtained, and the electron density profiles have been reconstructed using the signal record analysis.

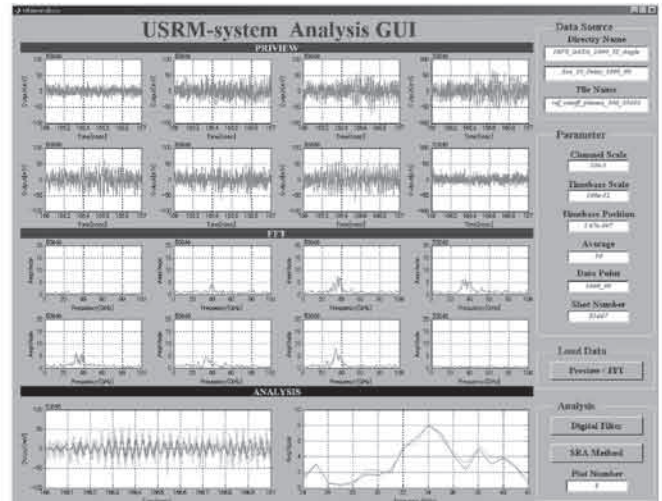


Fig. 2 Graphical user interface (MATLAB-GUI).

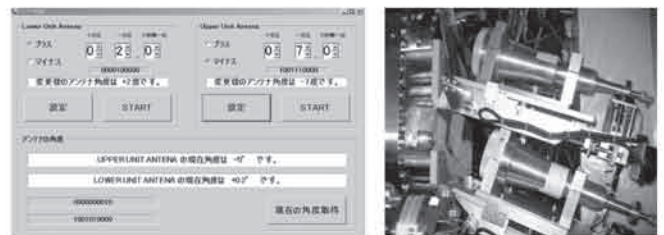


Fig. 3 Remote control system of the USRM antennas.

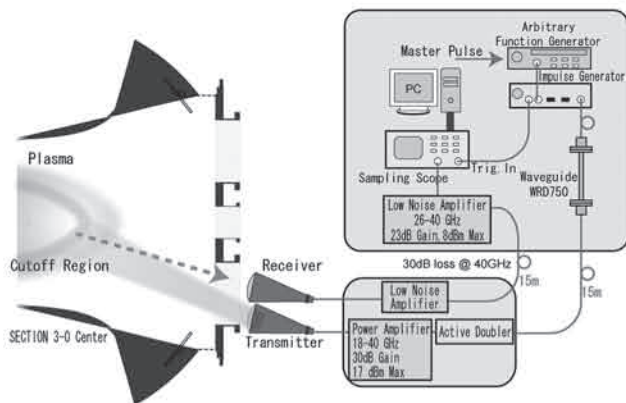


Fig. 1 Schematic of the USRM system.

§3. Statistical Analysis of Density Fluctuation in SOL/Divertor Plasmas of the LHD with Super-SINET

Takamura, S., Ohno, N., Miyoshi, H. (Nagoya Univ.),
Budaev, V. (Kurchatov Institute)
Masuzaki, S., Komori, A.

In the edge plasma of several types of fusion devices, experimental measurements have shown a spiky rather than random behavior of plasma fluctuations[1-5]. The fluctuations are self-similar, the self-similarity parameter varies little from one device to another. Discrepancies with classic heat diffusive scaling led to the searching of evidence of ballistic transport in fusion devices, suggesting the universality of self-similarity properties in edge of magnetically confined plasmas.

To describe long-term dynamic behavior of a stochastic system, the suitable statistical description is needed. Traditional methods like spectral ones have shown deviation from simple self-similarity (monofractality). Kolmogorov (1962) [6] formulated hypothesis invoking some statistical independence in the cascading process, which led to the log-normal model for the rate of dissipation of turbulent kinetic energy. To describe distinguish between absolute and weighted curdling of stochastic physical system, the statistical description by multifractal formalism was proposed by Mandelbrot [7]. The multifractal formalism relies on the fact that the highly nonuniform probability distribution arises from the nonuniformity of the system possessing rich scaling properties and self-similarity.

Plasma density fluctuations observed with divertor probes in LHD [8] were analyzed in terms of multifractal formalism revisited with wavelets. When $I(t)$ is the time evolution of ion saturation current, a trajectory in a q -dimensional space can be reconstructed with embedding method. Then, we can obtain a series of q -dimensional vectors \vec{r}_i , representing the phase portrait of the dynamical system:

$$\vec{r}_i = \{I[t_i], I[t_i + \tau], \dots, I[t_i + (q-1)\tau]\} \quad (1)$$

$$i = 1, 2, 3, \dots, m$$

where τ is appropriate delay time.

The multifractality can be described by following formula:

$$M(r) = \langle |\vec{r}_i - \vec{r}_j|^q \rangle \approx r^{\zeta(q)}, \quad (2)$$

$$\zeta(q) = qH - \lambda^2 q^2. \quad (3)$$

λ^2 means multifractality parameter. When $\lambda^2 = 0$, the system is mono-fractal,

Figure 1(a) and (b) show the typical time evolution of ion saturation currents measured at different positions. By using Eqs. (1) and (2), we can obtain $\zeta(q)$ and λ^2 is determined by Eq. (3). Apparently, both λ^2 's are finite value, which means that the fluctuation in the edge plasma of LHD can be characterized by multifractality. Multifractality factor defined in multiplicative cascade model, could be relevant parameter to characterize the edge plasma turbulence. To find whether the parameters of multifractality observed in this analysis, have a more universal validity, it would be interesting to extend multifractal analysis to a broader set of turbulent data from edge plasmas.

We also investigated bursts waiting-time statistics to examine the SOC model. From data of Figs. 1(a) and (b), it is found that the waiting time statistics is not a Poisson process.

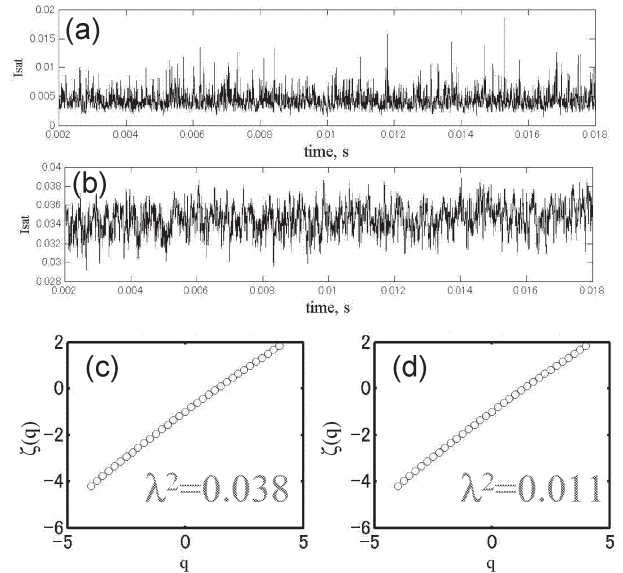


Fig. 1 (a),(b):typical time evolution of ion saturation currents measured with divertor probes in LHD, (c),(d): determination of multifractal parameter corresponding to (a) and (b) respectively.

References

- 1) B.A.Carreras e.a , Phys. Plasmas **3** , 2664 (1996).
- 2) LaBombard e.a. Nucl. Fusion **40** , 2041 (2000).
- 3) R.A.Moyer e.a., Plasma Phys. Controlled Fusion **38** , 1273(1996).
- 4) G.Y.Antar e.a , Phys. Rev. Lett. **87** , 065001 (2001).
- 5) V.Budaev e.a., Plasma Physics and Controlled Fusion **3** , 429 (1993).
- 6) A.N. Kolmogorov. J. Fluid Mech. **13** , 82, (1962).
- 7) B.B. Mandelbrot, J. Fluid Mech. **62** ,331 (1974).
- 8) S. Masuzaki e.a. Nuclear Fusion **42**, 750(2002).

§4. Emission Locations and Influx of Hydrogen Atoms on the Basis of Zeeman Profile

Iwamae, A., Atake, M., Sakaue, A., Fujimoto, T.* (Dept. Mech. Eng. Sci., Kyoto Univ.) Katai, R. (The Grad. Univ. for Advanced Studies) Goto, M., Morita, S.

In the magnetically confined plasmas oriented nuclear fusion reactor, determination of neutral particle influx from the plasma edge region to the main plasma is important for the purpose of studying H-mode, and the formation of the radial density profile. The Zeeman splitting of the spectral lines in He I is enable to determine the emission locations in the Large Helical Device (LHD)[1]. Polarization resolved Zeeman spectroscopy successfully enable us to deduce the emission location and the influx at a line of sight on the equatorial plane[2].

Ten lines of sight were equipped to cover the poloidal cross section at #1-O port for the polarization resolved observation as shown in Fig. 1. The emission from the plasmas was resolved into orthogonally polarized components with the polarization separation optics (PSO). Two types of the PSO were used. One consisted of a polarization separation Glan-Thompson prism and a pair of lens couplers. The other consisted of two Glan-Taylor prisms and a pair of lens couplers. The each image of the optical fiber cores of 400 μm diameter for the orthogonal polarization components was coaxially overlapped. Each PSO collects the plasma emission within 50 mm diameter cylindrical region.

An example of the polarization separation spectra are shown in Fig. 2. The observed spectra are fitted with assumptions that the emission locations are localized at

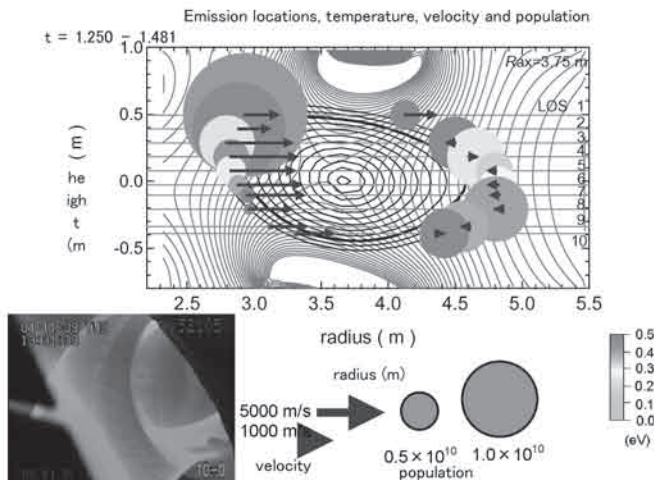


Fig. 0. Ten lines of sight cover the poloidal cross section at #1-O port. The emission locations on the LOS are indicated with the center position of the circles. The radius of circles is proportional to the upper level population $n(p=3)$. The length of the arrow represents the velocity component projected to the LOS. The plasma image taken at #10-O was shown at the left bottom. (#52105). [Tentative analysis]

* Professor emeritus

inner and outer points on a LOS, the magnetic field strength and direction are well represented with a calculated vacuum magnetic field. The orthogonal polarized components are fitted simultaneously and the results are shown in Fig. 2. The π components are parallel to the magnetic field direction. In the upper panels in Fig. 2, the π component is shifted to the longer wavelength direction and the

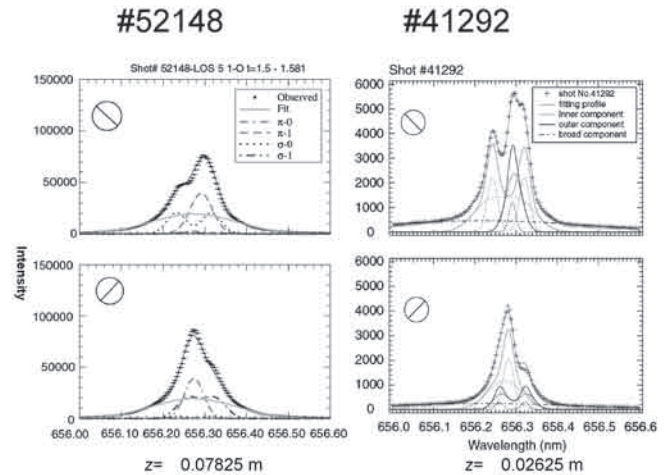


Fig. 2. The polarization separation spectra of hydrogen Balmer α for different discharges at LOS5 of #52105 and #41292. The circle with an oblique line indicates the direction of the polarized component.

π component in the lower panel indicates that the line center shifts to the shorter wavelength direction. The both ensemble of atoms contributed these parts of the spectral line profiles have inward velocity components to the main plasma. The summary of the least-squared fit is shown in Fig. 1. The inward velocity components from the inner side are higher than that from the outer side.

The Doppler width of H α in the discharge #52148 is broader than that in #41292. The difference in atom velocity distributions may reflect the change of the plasma-wall interaction such as recycling rate or inward neutral velocity driven by the radial neutral pressure gradient.

SNET was laid down to Yoshida campus of Kyoto University. We are able to control the spectrographs and the CCDs in the LHD machine room through KUINS 3 VLAN and SNET from the plasma lab in Kyoto.

- [1] M. Goto and S. Morita, Phys. Rev. E **65** 026401 (2002)
- [2] A. Iwamae, M. Hayakawa, M. Atake, T. Fujimoto, M. Goto and S. Morita, Phys. Plasmas, **12** 042501 (2005)

§5. Two Dimensional Ion Temperature and Velocity Measurements by Use of Visible Light Tomography System and Super SINET

Ono, Y., Balandin, A.L., Imazawa, R., Kawamori, E., Murata, Y., Itagaki, T., Yamanoue, T., Sato, K., Arimoto, K., Timura, T., Tawara, T. (Univ. Tokyo, High Temperature Plasma Cent./Dept. Electr. Eng.), Narushima, Y., Nagayama, Y., Yamazaki, K.

For the past four years, we have been developing a new visible-light tomography system for two dimensional (2-D) measurements of ion temperature and velocity. It is now is used for TS-4 device, and will be for LHD together with a well-controlled compact toroid (CT) injection system and the Super SINET. The coaxial plasma gun will deposit impurity plasma at an arbitrary spatial position of the Large Helical Device (LHD) plasma at an arbitrary time. Its injection time is much shorter than the conventional pellet injection, leading us to a new fast particle diffusion measurement in MHD time scale. The 2-D visible light tomography system was designed to measure directly 2-D profiles of its ion diffusion, temperature and velocity.

In 2004, the Super SINET system was installed for the visible light tomography diagnostics that will be used by both groups of LHD and TS-4. The tomography diagnostics is composed of 120 channel optical fibers and three polychromators with three ICCD cameras. Its major problem is that the measured Doppler shift and width for ion velocity and temperature measurements are integrated along the viewing line. The conventional reconstruction for the local data is to solve the inverse problem at each wave length and to fit a Gaussian profile to the obtained local spectrum.. However, the reconstructed local data have no relation with each other, though their spectrum are close to the Gaussian profile, so that we observed a significant increase in S/N ratio especially around the tail (short and long wavelength) regime of line spectrum.

We demonstrated for the first time, a new spectrum reconstruction method based on assumptions of Gaussian profile of line spectrum. Unlike the conventional MEM (Maximum Entropy Method) tomography only for the spatial profile, the MEM was applied not only to the spatial profile but also to wavelength profiles. This double

assumption, causes a significant reduction of reconstruction error, especially around the edge regions whose S/N are low. The measured spectrums are obtained by integrating the local line spectrum with the Gaussian profiles over the viewing lines, as shown in the following equations:

$$\tilde{f}(y, k) = 2 \sum_{r_i=y}^{r_i=R} a_{0i} \exp\left\{-\frac{k^2}{a_{2i}}\right\} \frac{r_i \delta r}{\sqrt{r_i^2 - y^2}},$$

$$L = \sum_{i=1}^M \sum_k g_{ik} \log g_{ik} + \gamma \sum_{i=1}^M \sum_k (f_{ik} - \tilde{f}_{ik})^2,$$

$$(g_{ik} = a_{0i} \exp\left\{-\frac{k^2}{a_{2i}}\right\})$$

where M and N are number of radial positions for reconstruction, an number of measurement channels, respectively. We determined the parameters λ , a_0 , a_1 , a_2 ($i=1 \cdots M$) by minimizing the L parameter mentioned above. The Akaike parameter was used for optimization of those parameters that strongly depend on γ parameter. Figures 1 (a) and (b) show the radial profiles of light emmisivity and ion temperature: the assumed profiles, profiles reconstructed by the conventional Abel inversion and profiles reconstructed by the new method mentioned above. The 10% and 20% noise components were added to the signals in cases (a) and (b), respectively. These data indicates that the new method is more robust against the noise component, especially in case (b).

References

- [1] A. Balandin and Y. Ono, J. Comp. Phys., **202**, (2005), 52.
- [2] Y. Ono et al., Fusion Energy 2004, IC/P6-44, (2005).

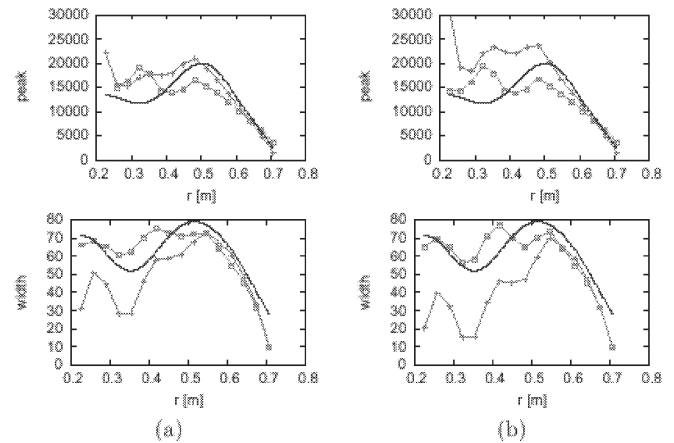


Fig. 1 Radial profiles of light emmisivity and ion temperature : assumed profiles, reconstructed profiles by the conventional Abel inversion (+) and the new inversion method (*). The 10% and 20% noise components were added to the signals in cases (a), and (b), respectively.

§6. Remote Participation for Plasma Experiments on the Mini-RT Device by Use of SuperSINET System

Ogawa, Y., Morikawa, J., Goto, T., Yatsuka, E. (The University of Tokyo)
Yanagi, N., Mito, T.

The internal coil device Mini-RT has been developed and constructed in the collaboration with the University of Tokyo, National Institute for Fusion Science and Kyushu University. The Bi-2223 High-Temperature Superconducting (HTS) wire is employed for the internal coil, and the device is operated in a persistent current mode. The levitation of the HTS coil is a first time in the world.

SuperSINET system is connecting between the University of Tokyo and NIFS for remote experiments. Remote system is shown in Fig. 1.

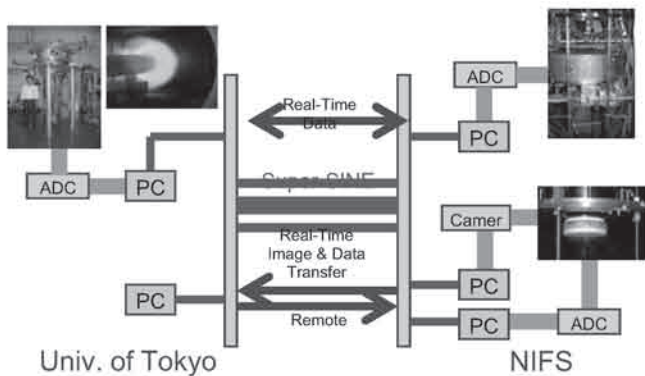


Fig. 1 Remote experimental system with the SuperSINET between the University of Tokyo and NIFS.

We have several R&D equipments in NIFS; e.g., cryogenic chamber for testing HTS wire, levitation system for HTS miniature coil and so on. While, in the University of Tokyo the Mini-RT device is operating for plasma experiments. The cooling and excitation of the Mini-RT HTS coil is not so reliable, because several new techniques are introduced. Sometimes we need further development of these components in collaborating the University of Tokyo and NIFS. Almost all of the data for cooling and excitation are transferred to the NIFS in the real-time by use of SuperSINET system, and the condition of the HTS coil can be monitored at the NIFS laboratory room.

The internal coil in the Mini-RT device should be levitated during a long time for plasma experiments. Preliminary experiments have been carried out in the NIFS with a small device called FB-RT. The miniature of the HTS coil is cooled with liquid nitrogen. The levitation experiment has been demonstrated in the atmosphere. The feedback control of the floating coil has been studied through the University of Tokyo by use of the SuperSINET system.

Figure 2 shows the photograph of the internal coil which is floating in the vacuum vessel of the Mini-RT device. Figure 3 shows the time history of the coil position during the coil levitation. We have succeeded to levitate the HTS

coil during one hour with an accuracy of a few tens micrometers.

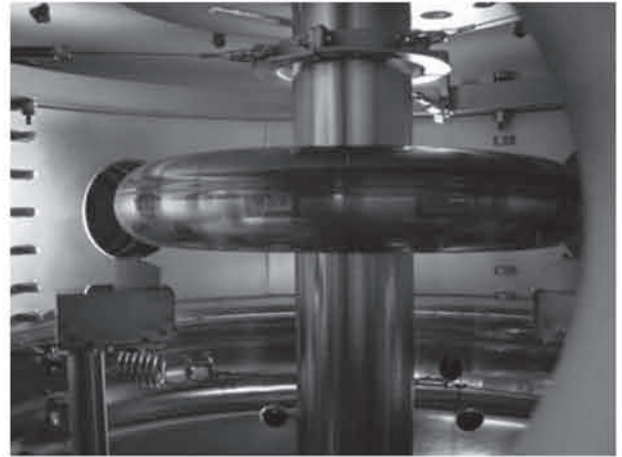


Fig. 2 Photograph of the floating HTS coil at the Mini-RT device.

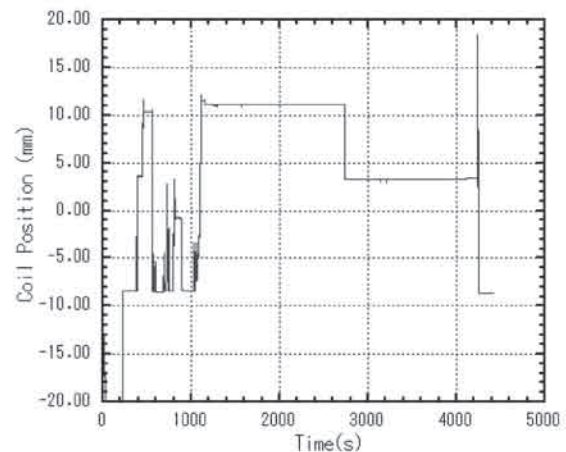


Fig. 3 Time history of the floating coil position.

Plasma experiments with the floating HTS coil has been carried out. Figure 4 shows the photograph of the plasma. The internal coil is pulled up with the levitation coil located at the upper region of the vacuum vessel. The magnetic surface is a combination of the HTS and levitation coils. That is a reason why the plasma cross section in Fig. 4 is deformed.

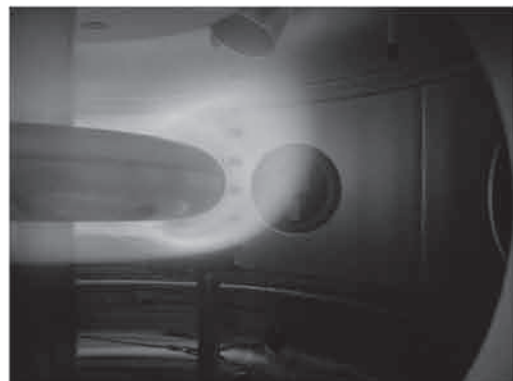


Fig. 4 Photograph of the plasma with the levitated HTS coil.

8. Coordination Research Center

In April 2004, the former Data and Planning Center was reorganized to establish a new center, “Coordination Research Center” to promote the cooperation research works to the external laboratories, universities and industries both for domestic and internationals.

The center consists of three divisions;

1. Division of Academic Research Coordination
 - *International Research Collaboration Group
 - *ITER Research Coordination Group
 - *Laser Research Coordination Group
 - *Inter-Institutional Research Coordination Group
2. Division of Industrial-Academic Research Coordination
3. Atomic and Molecular Data Research Center

Division of Academic research coordination has the function to bridge NIFS to the other academia including the administrative works.

The ITER research coordinating group, first of all, organized a coordinating committee on ITER collaboration, which consists of our specialists in various physics and technology fields. We have been discussing about a general plan of activity on ITER collaboration. We are strongly promoting to attend the ITPA (International Tokamak Physics Activity) meetings. In 2004, the total participants amounts to 34 persons and there were as many as 11 presentations, which drew much attention in terms of comparison between tokamak and helical plasmas. We have arranged for the periodical meeting with the domestic ITER team to discuss the collaboration items. We are also closely connecting with the Fusion Forum and Fusion Network including fusion engineering and plasma science. Furthermore, we have made up a WEB page on ITER collaboration to report our activities.

On April 1, 2004, 5 major leading inter-university research institutes in the natural sciences, i.e., the National Astronomical Observatory, the Institute for Molecular Science, the National Institute for Basic Biology, the National Institute for Physiological Sciences and NIFS (the National Institute for Fusion Science) were consolidated and realigned into the National Institutes for Natural Sciences (NINS). The Inter-Institutional Research Coordination Group has cooperated with the Research Cooperation and Liaison Office of NINS in promoting interdisciplinary integration of natural sciences towards development of new scientific fields. Imaging science and holistic science have

been chosen as joint projects of 5 institutions.

Division of Industrial-Academic Research Coordination serves to the industries in applying the technologies developed during the research works for the fusion experiments. Microwaves and cryogenics are major items. NIFS, in collaboration with Gifu Prefectural Institute of Ceramics and with Penn State University in the USA, has successful in transformation technology to industry. New technology is required in the field of industrial heating for reducing the green house effect. Microwave heating is the most exciting answer to the problem. The so called “microwave effect” shows rapid processing under lower temperatures compared to conventional heating. Another example is the applied superconducting technology, namely a Superconducting Magnetic Energy Storage (SMES) system, which would take over a conventional uninterruptible power supply system utilization of batteries and/or capacitors.

In the Atomic and Molecular Data Research Center, we develop the NIFS databases of atomic and molecular data for fusion and other plasma applications organizing the Japanese scientists in the universities and other institutes. The data include cross-sections for electron collisions (AMDIS), heavy particle collisions (CHART) and others as shown in Table 1. This year we specially worked on the evaluation of C data and molecular targets such as H₂, O₂ and hydrocarbon molecules. Our database has more than 900 registered users, about half outside Japan. As applications of atomic process data, we interpreted LHD spectra of xenon EUV emission, important to EUV Source (collaboration with Osaka ILE) and other impurities such as carbon and neon ions. We developed numerical databases of plasma EOS and radiative properties and used these for hydrodynamic simulations of Sn plasmas and pellets in LHD. Excited states in hydrogen atom from metal surface were also studies. As a new program we started to collaborate with National Astronomical Observatory for SolarB.

For international collaboration, we hosted the following visitors who stayed more than one month; Dr. Y. Ralchenko (NIFS), Dr. J. Rhee (KAERI), Prof. R. Janev (Juelich), Prof. U. Safronova (Nevada Univ.), W. Eckstein (Max Plank Ins.). Japan- Korea and Japan- China collaboration under CUP were continued on atomic processes in plasmas.

Table 1. Databases served through Web (<http://dbshino.nifs.ac.jp>)

Name	Records	Period	Contents
AMDIS	101,481	1961-2005	Excitation, Ionization and Recombination Data by Electron Impact
CHART	4,686	1957-2003	Numerical Data on Charge Exchange Cross Sections
MOL	3,175	1956-2004	(AMOL&CMOL) Numerical Data on Molecular Collision Processes
SPUTY	1,243	1931-2003	Numerical Data on Sputtering Yields for Mono-atomic Solids
BACKS	396	1976-1998	Numerical Data on Reflection Coefficients of Ions onto Surface
FUSION	1,269,374	1975-2004	Bibliography on Fusion Research extracted from INSPEC
PLASMA	80,032	1970-1986	Bibliography on Plasma Science extracted from INSPEC
AM	920,167	1970-2004	Bibliography on Atomic and Molecular Physics extracted from INSPEC
ORNL	75,625	1959-2003	Bibliography on Atomic Collisions collected at ORNL, USA

Archival studies on the nuclear fusion research at universities in Japan have been continued as a collaborative program of the center since 1999. The total number of items registered in “NIFS Nuclear Fusion Archives Database” is over 10,000. Along with collection of historical documents, an interview was held with Mr. Morino, S., who played an important role in fusion developments at Japanese industry. Activities were presented in various scientific meetings such as annual meeting of the Japan Society of Plasma Science and Nuclear Fusion Research, as well as at the KEK-UCLA workshop on KEK archives held at UCLA. On the basis of these activities, “Fusion Science Archives” was established in NIFS in January 2005 to promote archival activities for fusion research.

We held the 14th International Toki Conference as the joint meeting with the 4th International Conference on Atomic and

Molecular Data and Their Applications (ITC14 & ICAMDATA2004) in October 5-8, 2004, in Toki, Japan. Topics of the conference included atomic and molecular data production, collection, assessment, and dissemination, inertial and magnetic fusion, laboratory data needs and applications, astrophysics and atmospheric applications, lighting, plasma processing, plasma display panels, and other similar applications relying on understanding of atomic and molecular processes and needing atomic and molecular data. This was the first ICAMDATA in Asia. 180 participants from 23 countries attended the conference. 37 invited talks and 116 contributed poster papers were presented. We should mention the special lecture by Prof. R. B. Laughlin, the 1998 Nobel prize laureate for physics, on the fundamental aspects of physical basis of computability.

(Sato, M.)

§1. Particle Control by Moving-surface PFCs

Hirooka, Y. (NIFS), Hosaka, S., Ohgaki, H.,
Nishikawa, M. (Osaka Univ.)

It is widely recognized that particle control is a critical issue affecting the overall plasma confinement performance in steady state fusion devices. However, this technical issue has not experimentally been addressed because of the fact that essentially all major confinement devices are operating in the pulse mode.

Interestingly, reported at the most recent IAEA-TCM on "Steady State Operation" held in India in February 2005 were a number of observations indicative of the effects of particle recycling from the walls, saturated during extended pulse operation, which led to the termination of plasma confinement. These observations are from the major devices including JT-60U, LHD, HT-7, etc. The common problem pointed out with these cases is that wall recycling exceeds 100%, meaning that the core plasma density can not be controlled with external fueling.

As opposed to these, the effect of continuous wall pumping due to codeposition was also reported to help maintain long-pulse discharges conducted in TORE SUPRA and TRIAM-1M. For fusion power reactors, codeposition will result in a build-up of tritium, generating a safety issue.

These arguments clearly point to a need enabling wall concept development. For this purpose, the concept of moving-surface plasma-facing component (MS-PFC) has been evaluated over the past several years as part of NIFS collaborative programs with universities [1].

Used in this work is the MS-PFC test unit integrated in the Vehicle facility [2], shown in Fig. 1. In this test unit, a rotating drum made of copper and held at the floating potential, can be deposited with lithium simultaneously with steady state hydrogen or helium plasma bombardment. This is so that the plasma always sees freshly deposited lithium surface. Deposition rate measurements were conducted using a separate setup not.

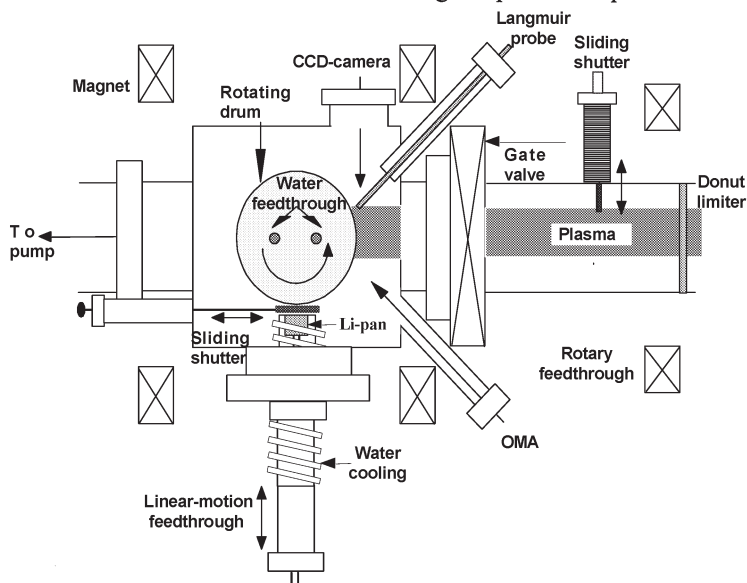


Fig. 1 A schematic diagram of the MS-PFC test unit.

Results of particle recycling measurements are shown in Fig. 2-(a) and (b), respectively, taken from hydrogen and helium plasma bombardment. The deposition of lithium in these data was initiated after steady respective state recycling conditions were established.

Notice that, as soon as lithium deposition starts, steady state hydrogen and helium recycling levels decrease significantly. In the case of hydrogen plasma, the two deposition rates of approximately 7 and 9 Å/s were examined and the degrees of H_α intensity reduction have been found to be nearly proportional to the deposition rate. The detailed particle balance modeling has recently been published [1]. As opposed to hydrogen plasmas, apparently helium plasmas require higher lithium deposition rates to exhibit noticeable reduction in recycling. The data shown in Fig. 2-(b) were taken at the lithium deposition rate of 50 Å/s.

Lithium is known to form a hydride in the form of LiH, whereas there is no such chemical affinity for helium. Using the molecular dynamics simulation method, it has been shown that helium can be trapped due to a three dimensional electrostatic potential "cage" effect, associated with lattice imperfections of lithium. Details on this will be published elsewhere [3].

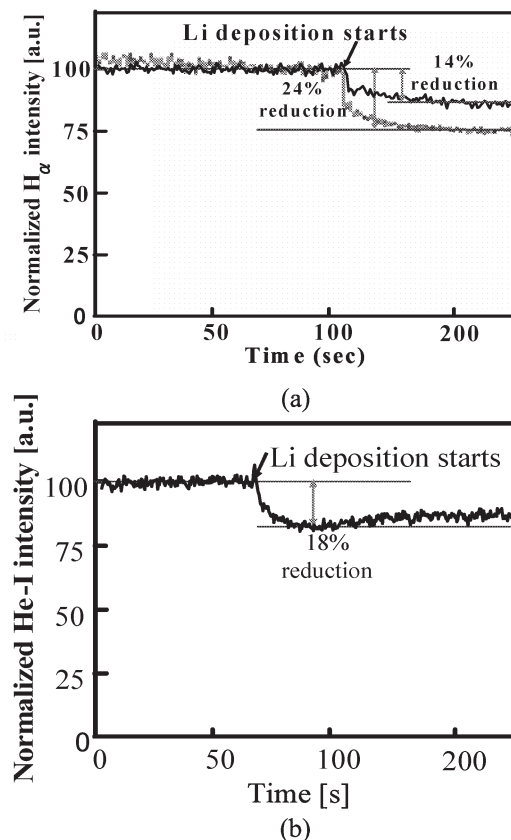


Fig. 2 Reduced steady state hydrogen and helium recycling from a lithium-deposited rotating drum.

Reference

- 1) Hirooka, Y. et al, Fusion Sci. Technol, **47**(2005)703.
- 2) Hirooka, Y. et al., Nucl. Mater. **337-339**(2005)585.
- 3) Hirooka, Y. et al., Submitted to Nucl. Fusion.

§2. Activities on ITER Collaboration

Nakamura, Y., Tohdo, Y., Seo, K.

Our activities on ITER collaboration have already started from one year before our institute was regenerated as the Inter-University Research Institute, National Institute of Natural Science on April 1st, 2004. On the basis of discussion about the supporting method for ITER project, the ITER research coordinating group with three persons was organized under the Academic Research Coordination Laboratory in the Coordination Research Center, which was newly formed in our institute. Our important work is to make a structure which enables us to participate in ITER project with ease and with high evaluation.

First of all, in order to discuss the broader issues on ITER project, we organized a coordinating committee on ITER collaboration, which consists of our specialists in various physics and technology fields including visiting professors from JAERI. The first meeting was held on 25 June and discussed about a general plan of activity on ITER collaboration in this year. Main items are indicated as follows:

- (1) promotion for active research on ITER project
- (2) exploitation of budgets for ITER relating researches
- (3) advertisement of ITER collaboration activities
- (4) enhancement of evaluation for ITER researches

Secondly, in order to understand our potentiality for ITER collaboration, we listed up the relating researches including general tokamak research issues and found that there were many issues connected with the ITER research in the view point of plasma confinement in toroidal system and development for future fusion reactor system. The International Tokamak Physics Activity (ITPA) is a very important task for making the ITER project successful. Therefore, we are strongly promoting to attend the ITPA meetings, which are divided into seven groups (MHD, Disruption and Control; Confinement Database and Modeling; Transport Physics; Pedestal and Edge; SOL and Divertor; Steady State Operation; Diagnostics). Each group meeting is planned to hold two times every year and a large number of our colleagues attended to the meetings as shown in Table 1 and Table 2. In 2004, the total participants amounts to 34 persons and there were as many as 11 presentations, which drew much attention in terms of comparison between tokamak and helical plasmas. This collaboration is also very important for understanding a toroidal plasma comprehensively.

To build up a closer connection with the Japan Participant Team for ITER Transitional Arrangements is one of important works in our group. We have arranged for the periodical meeting with the domestic ITER team and the meeting has been held two times in 2004. We have been discussing the collaboration items and how to execute,

taking into account each situation before the establishment of ITER organization. We are also closely connecting with the Fusion Forum, which is promoting a nuclear fusion research including the ITER project in Japan. On the other hand, in order to ask university researchers the opinions for ITER collaboration, we presented our activities in the coordinating meeting of Fusion Network including fusion engineering and plasma science.

Another important work is to enhance the evaluation for ITER researches. Our activities in 2004 were reported in the main meetings (LHD experimental results, large scale computer simulation results, etc.) in our institute. In addition, We have made up a WEB page on ITER collaboration activities including the outline of ITER project, the plans and reports of our activities.

Topical Group	Date (Place)	Participants (Presentations)
Sol and Divertor	13-16 Jan. (Naka)	2 (0)
Diagnostics	18-21 Feb. (Naka)	3 (0)
	23-24 Apr. (San Diego)	1 (0)
MHD, Disruption and Control	5-6 Feb. (Naka)	6 (0)
Confinement Database and Modelling	8-11 Mar. (Naka)	2 (1)
Transport Physics	8-12 Mar. (Naka)	5 (3)
Steady State Operation and Energetic Particles	8-12 Mar. (Naka)	8 (2)

Table. 1. ITPA Meeting in Spring 2004

Topical Group	Date (Place)	Participants (Presentations)
MHD, Disruption and Control	8-10 Nov. (Lisbon)	1 (1)
Confinement Database and Modelling	8-10 Nov. (Lisbon)	0
Transport Physics	8-11 Nov. (Lisbon)	2 (2)
Pedestal and Edge	8-10 Nov. (Lisbon)	2 (1)
Sol and Divertor	8-11 Nov. (Lisbon)	1 (1)
Steady State Operation	8-10 Nov. (Lisbon)	1 (0)

Table. 2. ITPA Meeting in Fall 2004

§3. Theoretical Investigation of Molecular Dynamics in Intense Laser Fields

Kono, H., Nakai, K. (Dept. of Chem., Graduate School of Sci., Tohoku Univ.), Tanaka, M.

We investigated dynamical processes of molecules in various phases induced by intense laser fields of $I < 10^{16}$ W/cm². First, we developed a quantum mechanical method to theoretically investigate the nuclear dynamics of polyatomic molecules in intense laser fields by using time-dependent adiabatic states defined as the eigenfunctions of the instantaneous electronic Hamiltonian including the interaction with a laser electric field. The properties of the adiabatic states of polyatomic molecules can be calculated by *ab initio* molecular orbital methods. We have already applied the proposed approach to dynamics of CO₂ in near-infrared intense fields and revealed that in the dication stage, simultaneous symmetric two-bond stretching followed by the occurrence of a large-amplitude bending motion is induced by an intense field [1]. We have also investigated [2] experimentally observed selective cleavage of C-O and C-C bonds of ethanol in intense laser fields of light intensity $I \sim 10^{15}$ W/cm² [3]. The calculated ratio of the probability of C-O bond cleavage to that of C-C bond cleavage becomes smaller with decreases in the pulse length, as was observed in the experiment [3]. This example is the first demonstration that field-induced nonadiabatic transition plays a decisive role in the reaction dynamics of molecules in intense laser field.

Competition between ionization and fragmentation of a large molecule in intense laser fields has attracted much attention. A spectacular production of stable, highly charged C₆₀ by intense short laser pulses of $\lambda \sim 1600$ nm, reaching up to C₆₀¹²⁺ without any fragmentation, has been reported in the literature [4]. We have theoretically studied the stability of selected C₆₀ cations, ranging from C₆₀⁺ to C₆₀¹⁸⁺. To investigate the unusual stability of highly charged cations of C₆₀, we calculated the geometries and vibrational frequencies of C₆₀ cations. All calculations have been carried out using DFT/ B3LYP implemented in the Gaussian 03 suites of program.

It is well known that the neutral C₆₀ has the *I_h* point group which is highly symmetric and the removal of an electron causes a change in the structure. Except C₆₀¹⁰⁺ and C₆₀¹⁸⁺ cations which possess *I_h* point group (the HOMO is fivefold degenerate and the HOMO-1 is fourfold degenerate), the *I_h* symmetry will be broken. In fact, structural optimization indicates that the structure of C₆₀^{z+} is nearly of *I_h* symmetry with a *small* prolate/oblate distortion. The C-C bond lengths increase

by only 0.03 Å as *z* increases to +12. Using vibrational frequency analysis, we have concluded that the C₆₀^{z+} cation is stable up to *z*=14. No imaginary vibrational frequencies appear. The vibrational frequencies of C₆₀¹²⁺ are as high as those of the neutral C₆₀.

More interesting is the surprisingly small difference between the vertical ionization potential and adiabatic ionization potential upon ionization to a charge state of C₆₀, which reflects the small structural change between cations. The difference is only 0.9 eV for the ionization step from C₆₀ to C₆₀¹⁰⁺. This leads to a small excess vibrational energy upon ionization. We believe that the small excess vibrational energy upon ionization is the main reason why no fragmentation is observed up to C₆₀¹²⁺ in the excitation case of 1600 nm ultrashort pulses. Using a method of first-principle molecular dynamics simulation, we are also examining how C₆₀ cations dissociate when a sufficient excess vibrational energy is supplied. C₂ elimination pathways of dissociation energy of ~ 30 eV are found in the simulation.

We have also carried out molecular dynamics (MD) simulations for a dilute aqueous solution of pyrimidine in order to investigate the mechanisms of field-induced molecular alignment in a liquid phase [5]. An anisotropically polarizable molecule can be aligned in a liquid phase by the interaction with a nonresonant intense laser field. We derived the effective forces induced by a nonresonant field on the basis of the concept of the average of the total potential over one optical cycle. The results of MD simulations show that a pyrimidine molecule is aligned in an aqueous solution by a linearly polarized field of light intensity $I \sim 10^{13}$ W/cm² and wavelength $\lambda = 800$ nm. The temporal behavior of field-induced alignment is adequately reproduced by the solution of the Fokker-Planck equation for a model system in which environmental fluctuations are represented by Gaussian white noise. From this analysis, we have revealed that the time required for alignment in a liquid phase is in the order of the reciprocals of rotational diffusion coefficients of a solute molecule. The degree of alignment is determined by the anisotropy of the polarizability of a molecule, light intensity, and temperature. We also discuss differences between the mechanisms of optical alignment in a gas phase and a liquid phase.

References

- [1] Y. Sato, H. Kono, S. Koseki, and Y. Fujimura, J. Am. Chem. Soc. **125** (2003) 8019.
- [2] H. Kono *et al.* Chem. Phys. **304** (2004) 203.
- [3] R. Itakura *et al.*, J. Chem. Phys. **119** (2003) 4179.
- [4] V.R. Bhardwaj *et al.*, Phys. Rev. Lett., **91** (2003) 203004.
- [5] J. Ohkubo, T. Kato, H. Kono, and Y. Fujimura, J. Chem. Phys. **120** (2004) 9123.

§4. First-Principles Molecular Dynamics Studies of Plasma-Surface Interactions

Koga, T., Tanaka, M.

Over the last several decades, carbon or carbon-based materials have been extensively used for plasma-facing components in magnetic confinement fusion devices[1]. It is therefore of great importance to have a thorough understanding of processes involved in the interactions (chemical or physical sputterings, etc.) between carbon and the plasma species (mainly hydrogen or isotopes)[1]. However, it is difficult to investigate such phenomena by the experiments because these phenomena are of the atomic level. So we are trying to investigate them by computer simulation.

We are currently studying the hydrogen storage phenomena in graphite by using the first-principles molecular dynamics simulation in the framework of the local density functional theory [2]. We adopt the tight-binding method and the norm-conserving pseudopotentials by Troullier and Martins [3]. The self-consistent electrons density is calculated with the Kohn-Sham equation, while atoms are moved by the classical molecular dynamics

Through adsorption, the bonded hydrogen atom changes the local electronic states of graphite from sp^2 -like to sp^3 -like orbitals[4]. Thus, this may break the C-C bonds formed between the hydrogen-adsorbed carbon and other carbon. However, an energy maximum (barrier) occurs at the CH_2 molecule when the number of adsorbed hydrogen atoms on one carbon atom is increased. Thus, some special mechanism including physical sputtering is expected to overcome the barrier and help to create the hydrocarbon molecules like CH_3 and CH_4 .

Then, we have simulated the phenomenon of graphite that happens after the saturation state. In these calculations, the graphite in the unit cell consists of 5 layers with each layers containing 24 carbon atoms ($7.41 \times 8.56 \times 31.19 \text{ \AA}^3$). We do both geometry optimization and molecular dynamics calculations by adding hydrogen atoms successively. The hydrogen atoms penetrate through the graphite surface, modify the internal graphite layers while reducing velocities, and are finally adsorbed to graphite. After having reached the saturated condition, we keep adding the hydrogen atom.

Figure 1 shows the collapse of graphite by the

hydrogen adsorption. It is said that the hydrogen adsorption becomes saturated at about 40% [5]. We have shown that after the saturation of hydrogen atoms the hydrocarbon molecules are generated, and that at the same time graphite layers are destroyed at the hydrogen adsorbing sites.

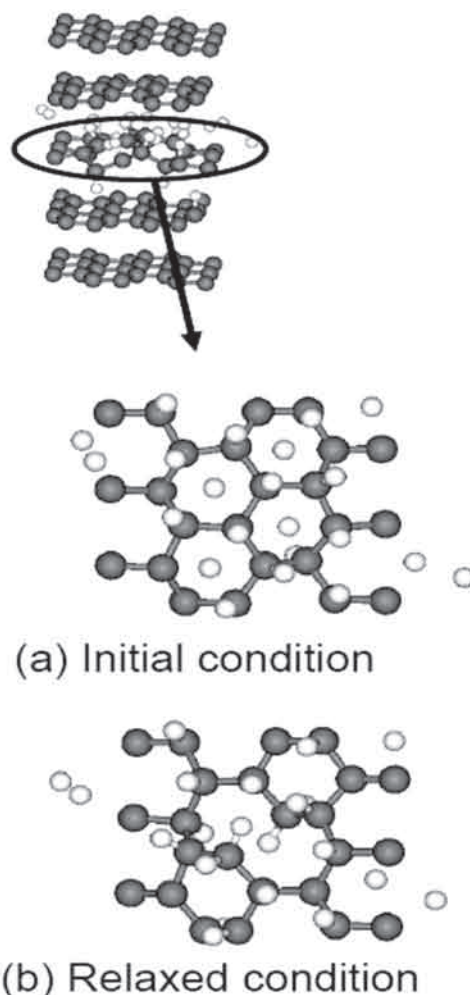


Fig. 1. Appearance of collapse of graphite. (a) initial condition and (b) relaxed condition by the first-principle molecular dynamics. White and black balls denote hydrogen and carbon atoms, respectively.

References

- [1] A.A.Haasz *et al.*, J.Appl.Phys. **77**, 66(1995)
- [2] J.Perdew and A.Zunger, Phys.Rev.**B23**, 5048(1981)
- [3] L.Kleinman and D.M.Bylander, Phys.Rev.Lett. **48**, 1425(1982)
- [4] Y.Zempo and M.Tanaka, Newsletter of National Institute for Fusion Science (February, 2004).
- [5] J.Roth and J.Bohdansky, Appl.Phys.Lett. **51**, 964(1987)

§5. DNA in Nanopores: Strong Electrostatic Interactions in Cellular Dynamics Processes

Tanaka, M.
Rabin, Y. (Bar Ilan University, Israel)

DNA that carries genetic information in living cells is a charged polymer with a unit charge in every 3~4 Angstroms along its thread. When this DNA migrates from cellular liquid of the dielectric constant $\epsilon_w = 80$ into a nano-size pore embedded in the cell membrane, the pore both geometrically and electrostatically affect the DNA. The membrane has the low dielectric constant $\epsilon_m = 2-3$, and roughly speaking, the electrostatic energy is enhanced by ϵ_w / ϵ_m times. In this respect, the electrostatic interactions are very important in the life processes [1].

In order to study the DNA and ion distributions in the nano-size pore, we perform molecular dynamics simulations. We take a rectangular box which is separated to upper and lower compartments by the membrane in the middle. The membrane is pierced by a cylindrical pore extending along the vertical axis, and the pore and compartments are filled with cellular liquid of large dielectric constant ϵ_w . Salt ions and neutral solvent particles that emulate water are put in these space. As mentioned, the electrostatic interactions are important due to large inhomogeneity of the dielectric constant, thus the Poisson equation must be solved for charges $\rho(r)$ and dielectric constant $\epsilon(r)$.

$$\nabla \cdot (\epsilon \nabla \phi) = -4\pi\rho$$

This equation is solved in real space using the conjugate gradient method (this takes up more than 90% of all the computation times). The DNA is modeled by connected charged and neutral beads of different sizes that correspond to the phosphate group, neutral sugar ring and base. These particles move under the Coulombic and Lennard-Jones forces [1].

Fig.1 shows the time histories of the number of (positive) counterions, (negative) coions, and the net charge in the pore for the empty pore (a) and DNA-stuffed pore (b). When the DNA is absent from the pore, a few pairs of counterions and coions reside in the pore, but isolate ions are not present because of the electrostatic repulsion from the membrane.

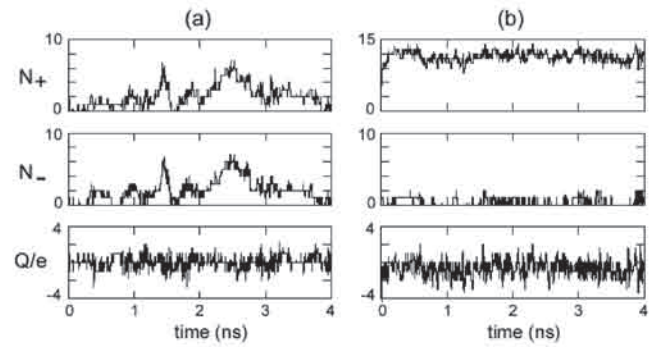


Fig.1 Time histories of the number of counterions and coions and net charge in the pore for (a) the empty pore and (b) DNA-stuffed pore.

With the DNA in the pore, counterions condense on the DNA to reduce the electrostatic energy as depicted in Fig.1(b). On the other hand, coions are repelled from the negatively charged DNA and are depleted from the pore. The DNA is elongated in the pore due to electrostatic repulsion from the membrane.

The effects of the electrostatic interactions are best shown in Fig.2 where the dielectric constant of the membrane is set to the normal value $\epsilon_m = 2$ in (a), and is $\epsilon_m = 80$ in (b). In the figure only charged phosphate beads are plotted for the DNA (for clarity). Coions (red sphere) are depleted by repulsion from the pore in (a), but there are a few of them in (b). This clearly proves the importance of the electrostatic effects in the life process.

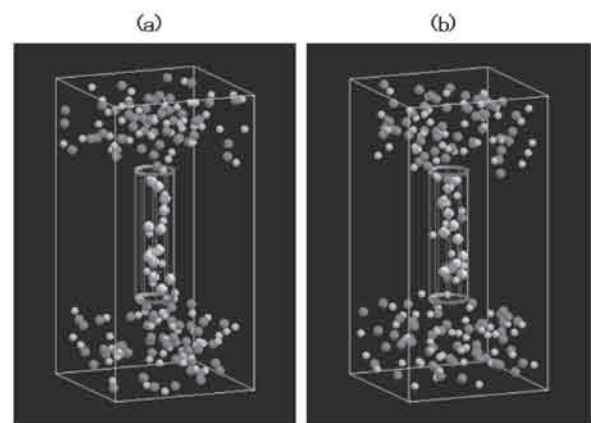


Fig.2 Snapshots of DNA (only charged phosphate groups are plotted), counterions [green spheres] and coions [red spheres] for (a) $\epsilon_m = 2$ and (b) $\epsilon_m = 80$ cases.

Reference

- [1] Y.Rabin and M.Tanaka, Phys.Rev.Lett., 94, 148103 (2005)

§6. High-Performance Cluster Computer by means of Linux PCs and Low-Latency (GAMMA) Communication Software

Tanaka, M.

A high-performance PC cluster machine using the Linux operating system and MPI (Message Passing Interface) for inter-processor communications has been constructed using the Gigabit Ethernet and the communication software GAMMA (Genoa Active Message Machine), in place of the standard TCP/IP protocol. Fast C/Fortran compilers are adopted with the GAMMA communication libraries. This method has eliminated large communication overhead characteristic of the TCP/IP protocol, and resulted in significant increase in the computational speed of real application programs at nominal additional costs, including the first-principle molecular dynamics simulations. The cost performance is by one order of magnitude better than the Itanium2 based cluster computer [1], and even more than that of conventional supercomputers.

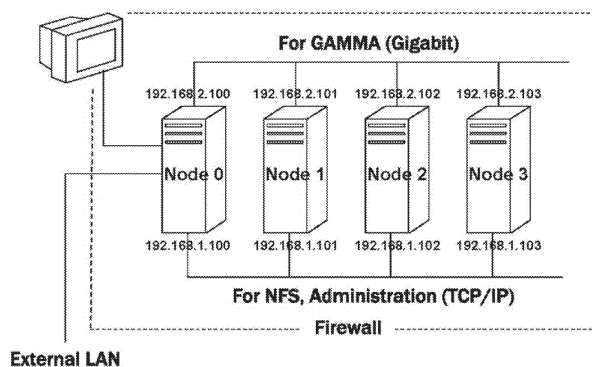


Fig.1 Typical network configuration of a PC cluster computer.

To realize fast computation of actual programs using parallel computers, it is necessary to reduce the massive communication overhead. This is done by means of low-latency communication methods in place of the TCP/IP protocol, which is usually done using expensive hardware [2]. However, its cost is higher than the computational units when the Intel-based IA-32 architecture machines (standard Windows PCs) are adopted. Here, we use a free software GAMMA which does

similar functions through direct interactions between the network device and the application program [3]. Fig.1 shows the typical configuration of the PC cluster computer where dual network is used to separate data and administrative communications. Fig.2 depicts the relation between the transmitted data size and the transmission speed for the GAMMA's point-to-point data transmission (Pentium 4 /3.0GHz and 3Com996 NICs are used). Table I summarizes the computational speed of the TCP/IP and GAMMA protocols for the PC cluster machine, together with the RISC cluster machine of the same size which is 10 times more expensive than the PC cluster machine.

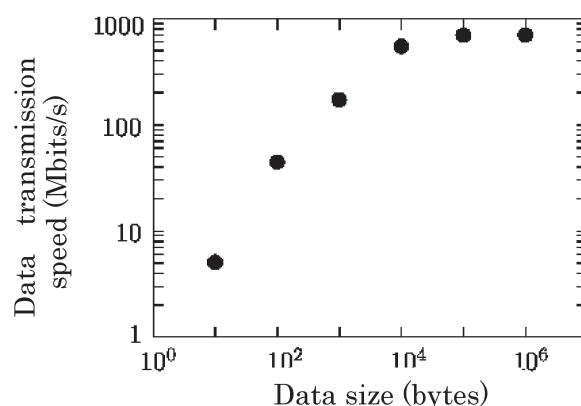


Fig.2 The relation between the transmitted data size and the transmission speed for the GAMMA communications

Table I. Comparison of TCP/IP and GAMMA communication methods for the PC cluster, and that for the same size RISC cluster [1].

	Wallclock	Overhead	Ratio
PC TCP/IP	93 sec	26sec	1.39
<u>PC GAMMA</u>	<u>66 sec</u>	<u>0.1sec</u>	1.00
RISC cluster	64 sec	0.1 sec	1.00

References

- [1] M.Tanaka, Butsuri (Japan Phys. Soc.) 59, 898-902 (2005); Los Alamos Archive, physics/0407152 (2004).
- [2] Myrinet as add-on network devices, and high-speed network for Itanium2 clusters.
- [3] G.Chiola and G.Ciaccio, <http://www.disi.unige.it/project/gamma/>

§7. Microwave Heating of Liquid Water and Ice: Molecular Dynamics Study

Tanaka, M., Sato, M.

By molecular dynamics simulations we have shown that water is heated by applied microwave through excitation of rotational alignment and subsequent relaxation of electrical dipoles. Crystal ice is much less heated due to hydrogen-bonded molecular network.

Electromagnetic waves heat solid, liquid and gaseous matters such as engineering materials, laboratory plasmas and biological matters including living cells. A microwave ovens used in daily food processing is one of such examples. The purpose of this study is to investigate the heating process of water and salt solutions by applied microwaves in terms of classical molecular dynamics simulation.

We use the microwaves of 10GHz whose wavelength is 3cm. Since the molecular scale is much less than this length, and since all the involved velocities are much less than the speed of light ($v/c \ll 1$), we can safely assume that the waves are spatially uniform, time varying electric field of the form $E(t) = E_0 \cos(\omega t)$. Water molecules are represented by the rotating rigid body known as the SPC water model [1]. We adopt crystal ice for the initial conditions with randomized O-H directions [2]. These molecules move under the Coulomb and Lennard-Jones forces which are exerted by surrounding molecules [3].

Fig.1 shows the time history of the applied microwave field, the potential energy (Coulombic + Lennard-Jones), and the total energy of the system. The observed heating is attributed to the increase in the

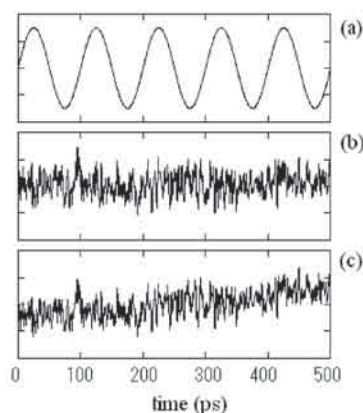


Fig.1: The time history of (a) the applied microwave field, (b) potential energy and (c) total energy of the system for water.

translational energy resulting from rotation excitation and relaxation of water molecules. Distributions of the water dipoles in terms of the directional cosine of their angles with the x-axis $\cos\Theta$ are shown in Fig.2. For room temperature water, the molecular dipoles distribute randomly. However, with the finite microwave field the dipoles align along the electric field direction and follow at each instant the statistical (Boltzmann) distribution $\exp(-E d \cos\Theta / kT)$ [d is the dipole moment of H_2O].

By contrast, the water in ice state is hardly heated by microwave. This is due to the formation of hydrogen-bonded network in crystal ice. The bird's-eye view of H_2O molecules for the ice state in Fig.3 reveals this situation.

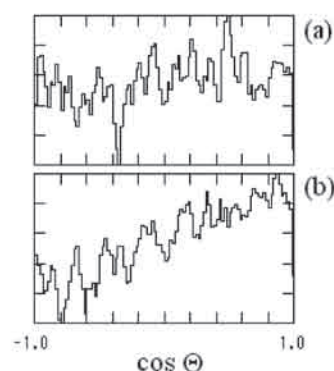


Fig.2. The distribution of water dipoles (logarithmic scale) in terms of the angles Θ with the x-axis for water of 300K. The microwave electric field is null in (a) and points to the x direction in (b).



Fig.3 Bird's-eye view of 2700 H_2O molecules in ice state.

References

- [1] H.Berendsen, J.Grignera, T.Straatsma, J.Phys. Chem. 91, 6269 (1987)
- [2] Courtesy of Dr. M.Matsumoto
- [3] Y.Rabin and M.Tanaka, Phys.Rev.Lett., 94, 148103 (2005)

§8. Microscopically In-situ Investigation for Microwave Processing of Metals

Sato, M., Motojima, O., Agrawal, D. (The Pennsylvania State University), Roy, R. (The Pennsylvania State University)

New innovative technologies are required in the field of industrial heating for reducing green house effects. Microwave heating is one of the most promising answers to the problem. So called “microwave effect” is believed to cause the rapid processing at lower temperature as compared to the conventional heating. Microwave processing is not only to reduce energy consumption, it also leads to innovations in new materials. The mechanism of microwave–matter interaction has not been fully understood yet. However, it could be explained by the concept regarding the nature of microwave interactions with materials, which is “**microscopically thermal non-equilibrium** by **selective** heating of the components”.

R. Roy et al. (MRL the Penn State Univ.) reported sintering of powder metals by microwave in 1999 and de-crystallization of ferrite magnetic materials by microwave heating ⁽¹⁾ in 2002.

In 2003–4, in order to investigate the mechanism(s) of these processes, National Institute for Fusion Science (NIFS) has focused its attention to the necessity of making in-situ observations of micro-structure transformations during sintering process, and developed a microscope using a long focal length object lens and a high resolution CCD imaging camera with digital zooming feature. Observation of microstructure transformation was attempted during the de-crystallization phenomena of ferrite precursor material consisting of $4\text{Fe}_3\text{O}_4 + \text{BaCO}_3$. Within seconds of microwave H-field exposure, many “localized hot cores” in the order of 100 micron in length and huge temperature gradients of 200~400°C in 100 micron, were observed. Therefore, temperature gradients of few thousands of degrees Celsius/mm, were maintained for a significant period of time. This clearly shows that “microscopic thermal non-equilibrium” can exist (Fig. 1). So far, it was believed that such a thermal non-equilibrium could not exist because, even with the existence of selective heating, immediate scattering of heat by thermal conduction and radiation to the periphery will make temperature uniform throughout.

This phenomenon of de-crystallization is observed when the sample is placed at the magnetic flux maxima in a single mode cavity, and is not observed at the electric field maxima. These suggest that the mechanism of microwave

absorptions is not explained simply by the dielectric loss.

Energy Input to local spot >>
Energy loss from spot



Fig.1 Microscopic Non-thermal State

The small non-equilibrium hot spots rise, move and dissipate occasionally in the body..

Reference:

- 1) R.Roy, R.Peelamedu, L.Hutt, J.Cheng, D, Agrawal: Definitive experimental evidence for microwave effects: radically new effects of separated E and H fields, Mat Res Innovation 6 (2002) p128-14

\$9. Time Dependent Electron Temperature and C^{2+} Ion Density Derived from CIII Spectra

Kato, T., Goto, M., Morita, S., Sato, K., Funaba, H., Murakami, I., Peterson, B.

Time dependent VUV spectra in the wavelength range $\lambda = 90 - 130$ nm have been measured and CIII, OVI, H Ly α , NeVII, NeVI and NeV lines are observed. We constructed a collisional radiative model for C^{2+} ions including the levels up to $n = 5$. We included the contribution of dielectronic recombination (DR) rate to each excited state. Since the contribution of highly excited states larger than $n = 5$ is important to DR rate, we included the contribution of DR rate between $5 < n < 500$ to the level $n = 5$ considering the density dependence of DR rate. With this collisional radiative model, we study temperature and density dependence of CIII line intensities. The population density of excited states can be expressed by the sum of the ionizing component and the recombining component. The ionizing component is proportional to the ground state ($1s^2 2s^2$) and the recombining component is proportional to the ground state of the next ionized ions ($1s^2 2s$). We study the intensity ratio of the resonance line ($2s2 1S - 2s2p 1P$, 97.7 nm) and a triplet line ($2s2p 3P - 2p2 3P$, 117.5nm) of CIII. The intensity ratio in ionizing plasma is smaller than unity and that in recombining plasma is larger than unity as shown in Fig.1. We can distinguish ionizing and recombining phase by the intensity ratio $I((2s2p 3P - 2p2 3P, 117.5nm)/(2s2 1S - 2s2p 1P, 97.7 nm))$.

Time dependent spectra from plasma heated by ECH (#15080) showed the line intensity ratios of the ionizing phase during the heating and the recombining phase after the heating. The derived electron temperature from CIII line intensity ratios during the heating is 30 - 40 eV, decreases to 2 - 3 eV after the heating stops and drops to 0.1 eV. On the contrary for the plasma heated by NBI (#28967), the CIII spectra indicate always ionizing plasma. The time dependent plasma parameters for #28967 are shown in Fig.2. Neon gas was puffed in this shot and the plasma collapse due to the radiation of neon ions at around 1.3 sec [1]. The derived electron temperatures from CIII are $T_e = 40$ eV during 0.2 - 0.8 sec, 20 eV at 0.8 - 1.1 sec and drops to 3 eV at 1.3 sec when the radiation is maximum as shown in Fig.3. After the radiation collapse CIII line intensities decay slowly and the electron temperature continues to be constant about 2 eV until 1.7 sec as shown in Fig.3. From i) the derived electron temperature, ii) the intensity of CIII resonance line and iii) the averaged electron density shown in Fig.3, we derived the time variation of the density of C^{2+} ions. The derived density of C^{2+} is almost constant during the plasma temperature is high and increases rapidly according to the decrease of the electron temperature and become constant again after the radiation collapse as shown in Fig.3. The electron temperature drops due to the radiation of neon L-shell ions.

The problem remains is what is the mechanism of the decrease of the electron temperature during the radiation collapse. We would like to study on this problem using the spectroscopic measurement of impurities.

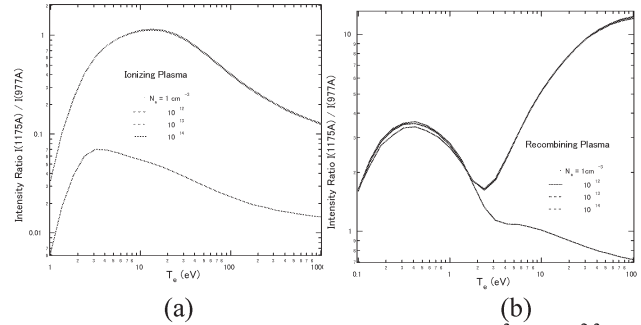


Fig.1 Intensity ratio of CIII lines I ($(2s2p 3P - 2p2 3P, 117.5nm)/(2s2 1S - 2s2p 1P, 97.7 nm)$) in ionizing plasma (a) and recombining plasma (b).

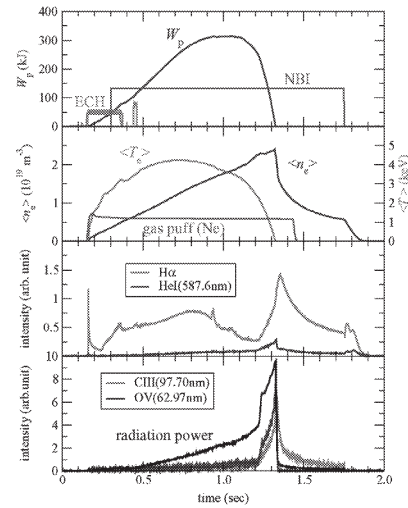


Fig. 2. The shot summary for #28967 heated by NBI.

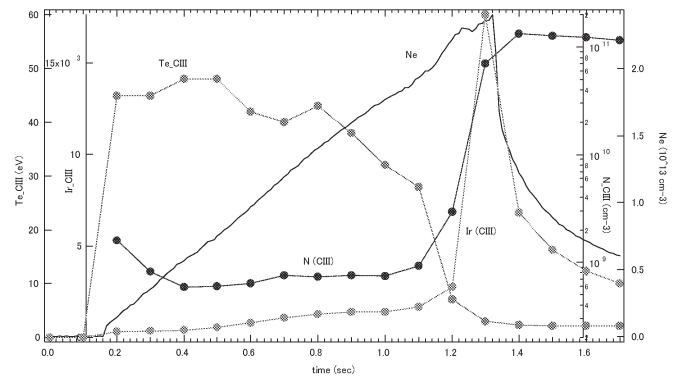


Fig. 3. The derived time dependent carbon ion density $N(C^{2+})$ from the intensity CIII lines and the averaged electron density.

1) T. Kato et al, Annual report of NIFS, 372 (2002)

\$10. EUV Spectra of Xe Ions Measured from LHD

Kato, T., Obara, T., Sato, K., Funaba, H., Suzuki, C.
Yamamoto, N. (Nagoya Univ.)
Nishimura, H., Nishihara, K. (Osaka Univ.)

EUV spectra from Xenon ions in LHD have been measured in the wavelength range 10 – 17 nm. We analyze the spectral lines near 13 nm. We compare the spectra with theoretical calculations and identify the spectral lines from Xe¹⁰⁺ ions.

We can make a bench mark test of computer codes using the observed spectral lines. This is important because the theory has not been extensively tested for such high- Z low charge ions. We will study plasma conditions which give the best EUV emission and will make a collisional radiative model for high-Z many-electron ions.

Xe gas was puffed into LHD plasma in NIFS and the EUV spectra from Xe ions were measured. The electron temperature at the center of LHD is about 3keV while the periphery is about 10 - 30 eV. Generally Xe emission is weak in the beginning of the plasma and strong during or after radiation collapse. A 2m grazing incidence multichannel spectrometer SOXMOS[1] with 600 grooves/mm grating was used for measurement. The measured line-width (FWHM) is $\delta\lambda = 0.023\text{nm}$ for the 13.2830nm Fe XXIII line.

We used the spectra before Xe gas puffing for wavelength calibration. Spectra with and without Xe gas puffing are shown in Fig.1. Iron FeXXIII 13.283, FeXXI 12.873, FeXXII 13.577, CVI 13.49, Cr XXI 14.987 nm lines were used as references. We used a calibration by least square fit to several measured reference lines which are shown in Fig.1.

We could observe the spectra without radiation collapse in 2004; the spectra when the plasma was heated by NBI. The spectra during the heating have strong lines and are quite different from those in radiation collapse as shown in Fig.2. The spectra during the heating are simpler than those in radiation collapse. We also observed the spectra from the edge separated 24 cm from the center by tilting the spectrometer by 1 degree from the center. The comparison of the spectra from center and edge are shown in Fig.3. The FeXXIII and FeXXII lines are strong only from the center but most of the lines from Xe ions are the same intensities from center and edge. From this measurement we could know the most of the Xe spectra emitted from the edge but not from the center. This means that Xe ions are lower charged ions than Fe XXIII and Fe XXII ions which have ionization potential 1.8 - 1.9 keV. Comparing spectra from hot and cold regions helps us decide which line comes from which ions charge state. We identify the lines of Xe ions in the spectra during the heating using the measurement by Berlin EBIT [1]. The Xe ion species are identified from Xe 19+ to Xe 25+ as shown in Fig.1. During the radiation collapse at least three new prominent lines appear among many lines as noted by a box in Fig.2. The line No.12 is identified as a line from Xe 8+ [2]. Therefore we think that the spectra

during the radiation collapse are mainly emitted from the Xe ions of 18+ to 8+. When we compare the charge exchange spectroscopy by Tanuma [3], the spectra during the radiation collapse looks like those from Xe17+ and Xe 16+. However it is difficult to identify these lines because these lines have not been studied yet.

We will study the spectra during the radiation collapse more carefully for identification using theoretical calculations. We will also study the phenomena of radiation collapse using the time history of the intensities of different Xe ions.

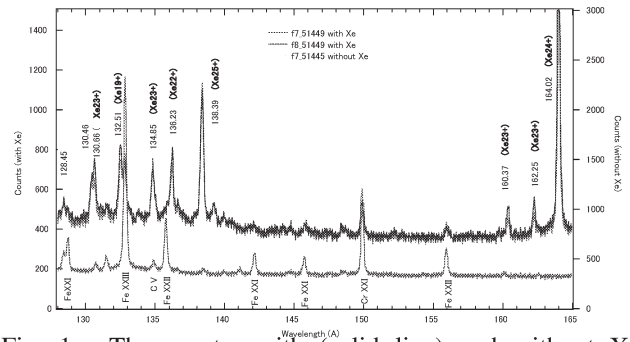


Fig. 1. The spectra with (solid line) and without Xe (dotted line) gas during the heating of NBI.

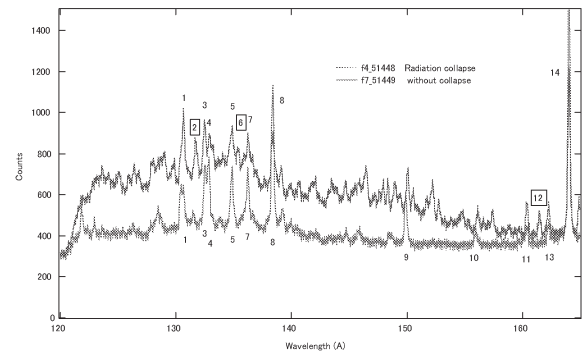


Fig. 2. The comparison of the spectra during the heating with those in the radiation collapse.

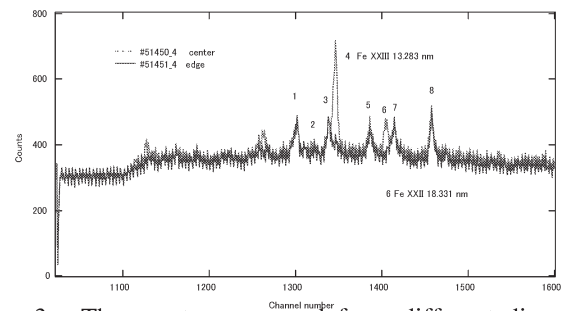


Fig. 3. The spectra measured from different directions; center (solid line) and edge (dashed line).

- 1) R. Radtke, C. Biedemann et al, PEARL conference (2005)
- 2) E.B. Saloman, J. Phys. Chem. Ref. Data, Vol. 33, 765 (2004)
- 3) H. Tanuma, private communication (2004)

§11. X-ray Spectral Analysis on Electron Interaction with Highly-Charged Xe Ions

Kato, D., Nakamura, N. (Univ. of Electro-Commun.),
Ohtani, S. (Univ. of Electro-Commun.)

Charge state distribution of Xe ions in an electron-beam-ion-trap (EBIT) was studied based on coupled rate equations for ion population density and temperature. A synthetic X-ray spectrum of highly charged Xe ions was compared with an experimental spectrum measured at the Tokyo-EBIT. Observed lines have been identified and the wavelengths have been determined experimentally for elements of $Z=50-56^{1)}$.

The X-ray transition excited by a 60 μm -diam electron beam was measured at the Tokyo-EBIT with a flat crystal spectrometer²⁾. Two types of crystal were used according to objective wavelength; one was LiF(200) with an area of 120x50 mm² and another was Si(111) with an area of 120x70 mm². The spectrometer was operated in vacuo (10^{-7} torr) to avoid absorption by air. Fig. 1 shows an example of the experimental and synthetic X-ray spectra for Xe ions.

The synthetic spectrum was obtained using atomic data of the HULLAC code and a given charge state distribution. The charge state distribution was predicted using a set of coupled rate equations for ion population densities and temperatures. The ion-loss rate was approximated by a formula for the magnetic-mirror configuration of a uniform magnetic field³⁾. In the present calculation, we assumed that neutral Xe gas was injected continuously into the trap so that the neutral density was maintained at 10^5 cm^{-3} . Charge exchange (CX) with the neutral Xe atoms may affect the charge state distribution to some extent. However, it was neglected in the present calculations, since the CX rate was estimated to be several orders of magnitudes smaller than the ion-loss rate for the neutral density of 10^5 cm^{-3} . In Fig. 1(b), four electric-dipole lines of the Ne-like ions are indicated as 3D, 3E, 3F, 3G, E2M, E2L, and M2 lines.

3E, 3F, and 3G. Their upper levels are $(2p_{3/2}^{-1}3d_{5/2})_{J=1}$, $(2p_{3/2}^{-1}3d_{3/2})_{J=1}$, $(2p_{1/2}^{-1}3s)_{J=1}$, and $(2p_{3/2}^{-1}3s)_{J=1}$, respectively. Two electric-quadrupole lines E2M and E2L and one magnetic-quadrupole line M2 have upper levels of $(2p_{3/2}^{-1}3p_{1/2})_{J=2}$, $(2p_{3/2}^{-1}3p_{1/2})_{J=2}$, and $(2p_{3/2}^{-1}3s)_{J=2}$, respectively. Lower levels for those lines are of the ground state $(2p^6)_{J=0}$.

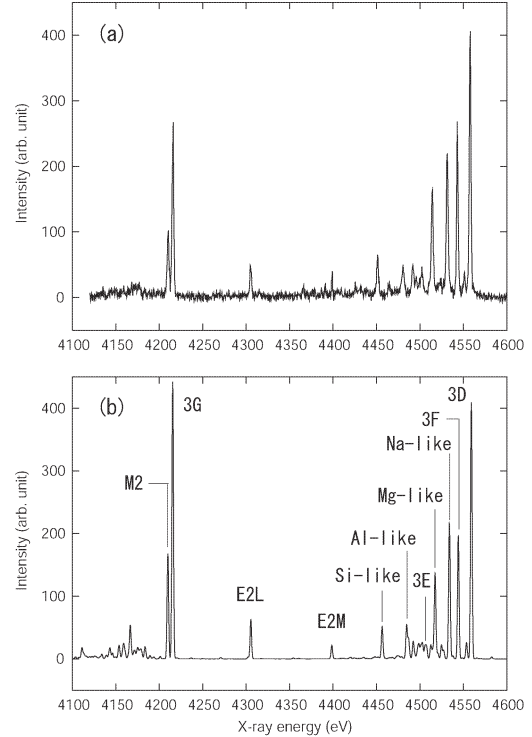


Fig. 1: (a) Experimental X-ray spectrum of Xe ions measured at the Tokyo-EBIT. Electron beam energy ≈ 5540 eV (below the ionization energy of the Ne-like Xe ion), electric current ≈ 97 mA, magnetic field strength in the drift tubes ≈ 4 T, and axial potential well ≈ 100 eV. (b) Synthetic spectrum convoluted using the Gaussian distribution function with a full-width-at-half-maximum of 2 eV. 3D, 3E, 3F, 3G, E2M, E2L, and M2 lines are of Ne-like ions.

References

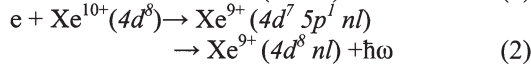
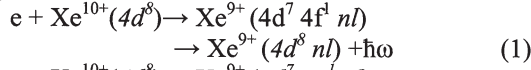
- 1) Kato, D., Nakamura, N. and Ohtani, S.: submitted to Journal of Plasma and Fusion Research.
- 2) Nakamura, N.: Rev. Sci. Instrum. 71 (2000) 4065.
- 3) Marrs, R.E.: Nucl. Instrum. Methods Phys. Res. B 149 (1999) 182.

§12. Dielectronic Recombination of Xe¹⁰⁺ Ions

Mi-Young Song, Kato, T.

Dielectronic recombination is the dominant electron-ion recombination process in high-temperature plasmas and therefore, is very important in determining the ionization balance. Another very important role of DR is connected with the presence of so-called satellite lines arisen due to the radiative decay of autoionizing states of an ion. As the interest about Xenon ions grows recently for EUV sources, many people are working on the research about Xenon ions. We need data about atomic collision processes of Xenon ion to analyze Xenon spectra. However, as long as we know, there are few papers which give us enough data of the dielectronic recombination rate coefficient to each final bound state. These data are necessary to estimate the population of the excited states by a collisional radiative model. In this report, we calculated the data for the dielectronic recombination from Xe¹⁰⁺(4d⁸) to the excited states of ions Xe⁹⁺. We investigate the Xe⁹⁺(4d⁷ 4f¹ nl) and Xe⁹⁺(4d⁷ 5p¹ nl) states as autoionizing states, which are important for the dielectronic recombination process. We use the Flexible Atomic Code (FAC) [3] for calculating the data of dielectronic recombination rate coefficient.

The dielectronic recombination[1] is a resonant, two step processes in which a multicharged ion captures a free electron with simultaneous excitation of the target electron and creates a doubly excited ion, which then decays by a radiative transition.



The DR rate coefficients, $\alpha_{\text{DR}}(i_0, f; T_e)$, for electrons in the Maxwellian distribution can be expressed as

$$\alpha_{\text{DR}}(i_0, f; T_e) = \left(\frac{h^3}{2\pi m k_B T_e} \right)^{3/2} \sum_i \frac{1}{2g_0} Qd(i_0, i, f) \exp\left(-\frac{E_{i,i_0}}{k_B T_e}\right) \quad (3)$$

where T_e is the electron temperature, m is the electron mass, h is the Planck constant, k_B is the Boltzmann constant, g_i and g_0 are the statistical weights of the autoionizing state (i) formed by dielectronic capture and the target state (i_0) before dielectronic capture, E_{i,i_0} is the resonance energy. The intensity factor (Qd) for the dielectronic satellite lines are given by

$$Qd(i_0, i, f) = \frac{g_i A_a(i, i_0) \text{Ar}(i \rightarrow f)}{\sum_{\text{all } i_0} A_a(i, i_0) + \sum_{\text{all } f'} \text{Ar}(i \rightarrow f')} \quad (4)$$

where $\text{Ar}(i \rightarrow f)$ is the radiative decay rate from level i to level f , $A_a(i, i_0)$ is the autoionization rate from level i to level i_0 . The sum over i_0 runs over all levels in the next higher ion reachable from level i by autoionization, and the sum over f' runs over all bound levels reachable from i by

radiative decay. The autoionizing states formed by dielectronic capture may either autoionize, or radiatively decay. The radiative decay to the states below the ionization limit completes the recombination process.

We calculated the data $n \leq 15$ and $l \leq n-1$ by FAC code. We use empirical scaling laws ($A_a \propto n^{-3}$) for estimating contributions from autoionizing states with higher n for the $n > 15$.

$$\begin{aligned} & \text{Ar}(4d^7 4f^1 nl, 4d^7 5p^1 nl \rightarrow 4d^8 nl) \\ & \approx \text{Ar}(4d^7 4f^1 15l \rightarrow 4d^8 15l), \\ & A_a(4d^7 4f^1 nl, 4d^7 5p^1 nl, 4d^8) \\ & \approx A_a(4d^7 4f^1 15l, 4d^7 5p^1 15l, 4d^8) (15/n)^3 \quad (5) \end{aligned}$$

Figure 1 shows the total dielectronic recombination rate coefficient calculated for the following processes of I [$\text{Xe}^{10+}(4d^8) + e \rightarrow \text{Xe}^{9+}(4d^7 4f^1 nl) \rightarrow \text{Xe}^{9+}(4d^8 nl) + \hbar\omega$] and II [$\text{Xe}^{10+}(4d^8) + e \rightarrow \text{Xe}^{9+}(4d^7 5p^1 nl) \rightarrow \text{Xe}^{9+}(4d^8 nl) + \hbar\omega$] processes. Curves I and II represent the DR process including $n = 4-100$. Curves I' and II' represent the DR process including $n = 1-15$ and $l = n-1$. For the level higher than $n=15$, we included $l=0-6$. The values of the total dielectronic recombination rate coefficient have the maximum values between 10eV and 100eV and the maximum position of dielectronic recombination rate coefficient increase towards high electron temperature for larger n and l .

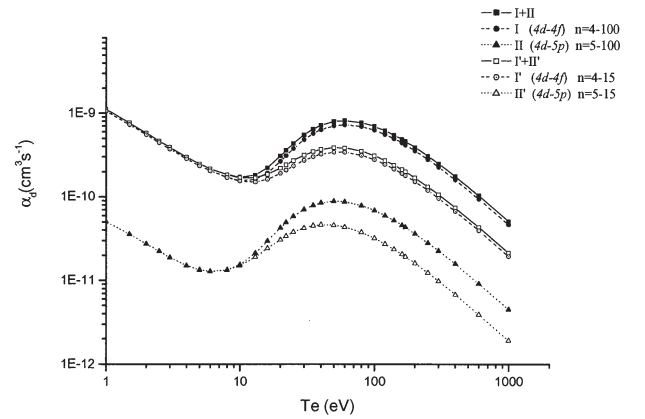


Fig. 1. Total dielectronic recombination rate coefficient obtained by summation of each dielectronic recombination rate coefficient for these autoionizing states of I (4fnl) and II (5pnl).

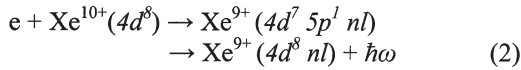
Reference

- 1) A. Burgess, *Astrophys. J.* **139** (1964) 776
- 2) J. N. Gau, Y. Hahn and J. A Retter, *J. Quant. Spectrosc. Radiat. Transfer* **23** (1980) 131
- 3) M. F. Gu, *Astrophys. J.* **590** (2003) 1131

§13. Satellite line of Xe⁹⁺ Ions

Mi-Young Song, Kato, T.

Recently EUV light sources from compact plasmas are now intensively studied for the next generation of lithography. The multicharged Xe ions emit EUV emission and are now investigated extensively. However we do not know the detailed atomic processes for there Xe ions. The satelliteline [1-2] transitions for parent emission of the types Xe¹⁰⁺ (4d⁷ 5p¹ → 4d⁸) ion are emitted by the radiative stabilization of doubly excited states in the Xe⁹⁺ (4d⁷ 5p¹ nl → 4d⁸ nl). The doubly excited states are populated by the processes of dielectronic capture:



The dielectronic recombination processes is resonated by the incident electron energy, the required being equal to the energy of the doubly excited state relative to the ionization energy of the Xe⁹⁺ ion. The autoionization takes place only when the energy of the doubly excited states is above the threshold energy.

The emissivity of a dielectronic satellite transition from the autoionizing state i to a final state f is proportional to a Qd (i_0, i, f) factor which expresses the rate of dielectronic capture into the autoionizing state followed by radiative decay to the final state. Thus, the emissivity of a satellite lines produced by dielectronic recombination can be expressed as

$$I_s = n_e n_z \left(\frac{h^3}{2\pi m k_B T_e} \right)^{3/2} \frac{e^{-E_{i,i_0}/k_B T_e}}{2} \times \langle Qd(i_0) / g_0 \rangle \quad (3)$$

$$Qd(i_0, i, f) = \frac{g_i Aa(i, i_0) Ar(i \rightarrow f)}{\sum_{all i_0} Aa(i, i_0) + \sum_{all f'} Ar(i \rightarrow f')} \quad (4)$$

where n_e is the electron density, n_z is the ion density, h is the Plank constant, k_B is the Boltzmann constant, g_i and g_0 are the statistical weights of the autoionizing state (i) formed by dielectronic capture and the target state (i_0) before dielectronic capture, E_{i,i_0} is the resonance energy, and $\langle Qd(i_0) / g_0 \rangle$ represent the average value over all initial state the Xe¹⁰⁺ (4d⁸).

To understand the relation of the satellite lines and the radiative decay lines of Xe¹⁰⁺ ions, we need to calculation of the emissivity of a lines produced by collisional excitation rate coefficient from level i_0 to level i' using the Mewe empirical formula based on the Bethe approximation of parent ions can be expressed as

$$I_s = n_e n_z C_{i_0, i'}(T_e) \quad (5)$$

$$\begin{aligned} C_{i_0, i'}(T_e) = 3.69 \times 10^{-12} \frac{1}{\sqrt{T_e}} \frac{1}{E_{i_0, i'}} P(E_{i_0, i'} / T_e) e^{-E_{i_0, i'} / T_e} \\ \times \langle Ar_{i', i_0} g_{i'} / g_0 \rangle \end{aligned} \quad (6)$$

where $g_{i'}$ and g_0 are the statistical weights of the excited state i' and ground states i_0 of Xe¹⁰⁺, E_{i', i_0} is the energy difference between i_0 level to i' level and $\langle Ar_{i', i_0} * g_{i'} / g_0 \rangle$ represent the average value over all initial state the Xe¹⁰⁺ (4d⁸). Figure 1 shows the sum of the intensity factor ($\langle Qd(i_0) / g_0 \rangle$) for the satellite transitions from states of the 4d⁷ 5p¹ 5l to 4d⁸ 5l of the Xe⁹⁺ ions about different l , at $n=5$.

Figure 2 shows the $\langle Ar_{i', i_0} * g_{i'} / g_0 \rangle$ values of the line from radiative decay from Xe¹⁰⁺ (4d⁷ 5p¹) to Xe¹⁰⁺ (4d⁸).

Through figures, we know that the dielectronic satellite lines of Xe⁹⁺ ions appear near the radiative decay lines of Xe¹⁰⁺ ions and the dielectronic satellite lines have values that can not ignore at low temperate. For identification of the spectrum from the highly charged ions, we will study more detailed about the direct excitation of the parent ions.

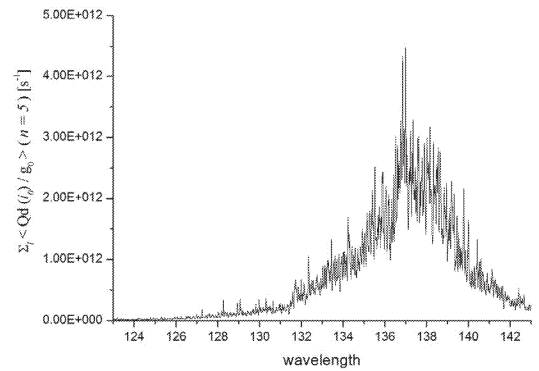


Fig. 1. Satellite line of the transition
[Xe⁹⁺ (4d⁷ 5p¹ nl) → Xe⁹⁺ (4d⁸ nl) + $\hbar\omega$]

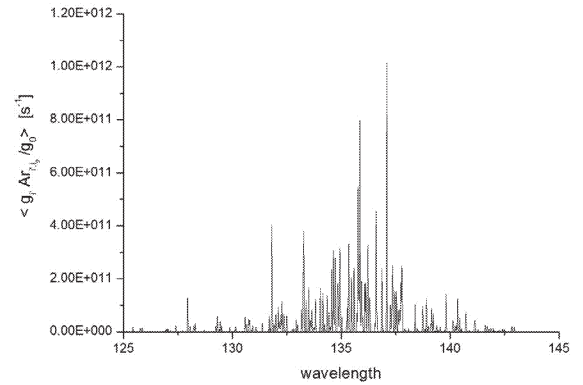


Fig. 2. Radiative line of the transition
[Xe¹⁰⁺ (4d⁷ 5p¹) → Xe¹⁰⁺ (4d⁸) + $\hbar\omega$]

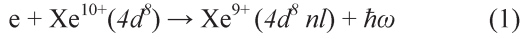
Reference

- 1) R. D. Cowan, "The Theory of Atomic Structure and Spectra", (University of California Press, Berkeley 1981)
- 2) H. R. Griem, "Principles of Plasma Spectroscopy" (Cambridge University Press, New York, 1997)

§14. Radiative Recombination of Xe¹⁰⁺ Ions

Mi-Young Song, Kato, T.

In radiative recombination, a free electron is directly captured by a target, releasing its kinetic energy and binding energy of the final bound state to the emitted photon. Radiative recombination is an important contributor to the total recombination rate coefficients at least in some temperature ranges.



Radiative recombination is obtained from the photoionization cross sections through the Milne relation.

The photoionization cross sections for the $n < 10$ shell are calculated in the distorted-wave approximation, taking into account the electronic dipole operator. The atomic code (FAC) used in the computation is developed by the M. F. Gu [1]. Photoionization cross sections are computed at six photon-electron energies of $E_e < 10E_{th}$, where the E_{th} values are the ionization thresholds for corresponding shells and for $E_e > 10E_{th}$, we used a simplified version of the formula suggested by Verner et al.[2] until 10000eV,

$$\sigma_{PI}(E_e) = \sigma_0 x^{-3.5-l+p/2} \left(\frac{1+b}{\sqrt{x+b}} \right)^p, \quad (2)$$

where $x = (E_0 + E_e)/E_0$, l is the orbital angular momentum of the photoionized shell, and σ_0 , E_0 , p , and b are fit parameters. For the photoionization of the particular nl shell, we obtained the radiative recombination to the excited state nl .

The radiative recombination cross section from FAC code are fitted by series of terms containing various powers of $u = E_e/E_{th}$ for $u \leq 10$. For higher energies we need different fitting formula as Eq. (4).

$$\sigma_n^l(u) = \frac{1}{u(u+1)} \times \sum_{i=0}^3 a_i u^i, \quad (u \leq 10) [cm^2] \quad (3)$$

$$\sigma_n^h(u) = \frac{1}{u(u+1)} \times 10^{\sum_{i=0}^6 a_i u^i}, \quad (10 < u < 1000) [cm^2] \quad (4)$$

Here a_n is the fitting parameter. This cross section fitting formula is used until $n \leq 10$ shell. Radiative recombination for $n > 10$ shells are estimated using the semiclassical Kramers formula

$$\sigma_n(x) = 2.1 \times 10^{-22} \cdot \frac{n}{x(x+1)}, \quad x = E_e/E_0 [cm^2] \quad (5)$$

where n is the principle quantum number, $E_0 = z^2 \text{Ry}/n^2$, Ry is the Rydberg energy, and z is the residual charge of the ion. Contributions up to $n = 1000$ are taken into account.

The Maxwellian averaged rate coefficients of the partial n shells are calculated numerically using the cross sections in the temperature range $10^{-3} - 10^3$ eV

$$K_{rr}^n(T_e) = 6.6941 \times 10^{-14} \sqrt{E_{th}^n} \beta^{3/2} \times \left(\int_0^1 u \sigma_n^l(u) e^{-\beta u} + \int_0^\infty u \sigma_n^h(u) e^{-\beta u} \right) \quad (6)$$

where $\beta = E_{th}^n/kT_e$. Thus, the total radiative recombination rate coefficient into all states of the Xe⁹⁺ ions can be written in the form

$$K_{rr}^{tot}(T_e) = \sum_{n=4}^{10} K_{rr}^n(T_e) + \sum_{n=11}^{1000} 5.18 \times 10^{-14} \times z \beta^{3/2} e^{-\beta'} E_1(\beta') \quad (7)$$

where $\beta' = z^2 \text{Ry}/n^2 kT_e$.

Figure 1 show the l -distribution of radiative recombination rate coefficient at $n=5$. Figure 2 show the total radiative recombination rate coefficient represented by the solid line and the total dielectronic recombination rate coefficient represented by the dotted lines. Through figures, we know that the values of the radiative recombination rate coefficient are smaller than the values of the dielectronic recombination processes in our interest temperature region at $T_e = 1\text{eV} - 1000\text{eV}$.

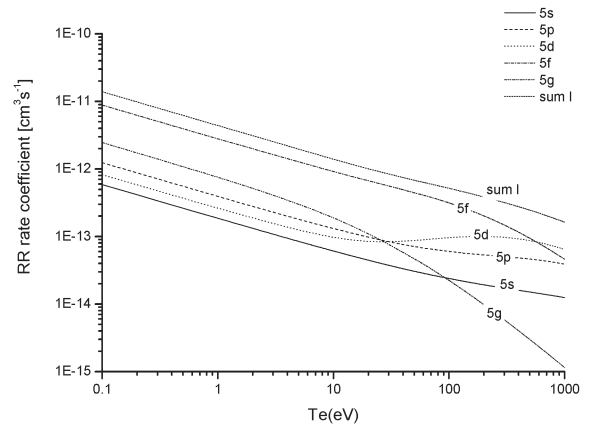


Fig. 1. l -distribution of radiative recombination rate coefficient at $n=5$.

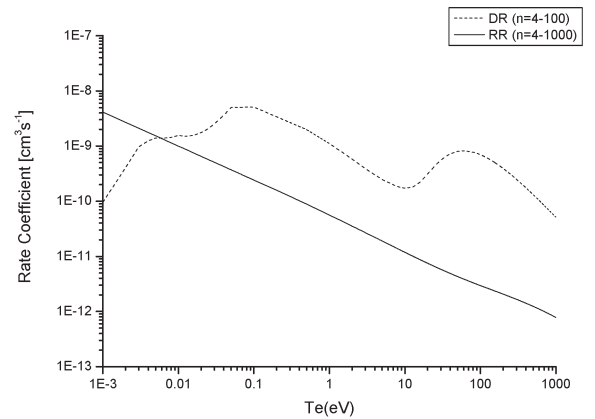


Fig. 2. Comparison of radiative recombination rate coefficient (the dotted line) and dielectronic recombination rate coefficient (the solid line) of Xe¹⁰⁺ ions.

Reference

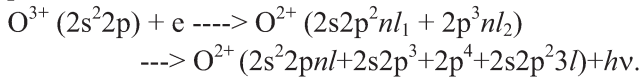
- 1) M. F. Gu, *Astrophys. J.* **590** (2003) 1131
- 2) D. A. Verner, D. G. Yakovlev, I. M. Band, and M. B. Trzhaskovskaya, *At. Data Nucl. Data Table*, **55** (1993) 233

§15. Dielectronic Recombination Rate Coefficients to Excited States of Carbonlike Oxygen and Dielectronic Satellite Lines

Safronova, U.I. (Univ. of Nevada, Reno, USA)
 Ralchenko, Yu (NIST, USA)
 Murakami, I., Kato, T., Kato, D.

Energy levels, radiative transition probabilities, and autoionization rates for C-like oxygen (O^{2+}) including $1s^2 2s^2 2pnl$, $1s^2 2s2p^2 nl$, and $1s^2 2p^3 nl$ ($n=2-8$, $l \leq n-1$) states are calculated by the Hartree-Fock-Relativistic method (Cowan code). Autoionizing levels above the thresholds $1s^2 2s^2 2p^2 P$, $1s^2 2s2p^2 ^4P$, 2S , 2S , 2P , and $1s^2 2p^3 ^4S$, 2D are considered. Configuration mixing $2s^2 2pnl + 2p^3 nl$ plays an important role for all atomic characteristics. Branching ratios relative to the first threshold and intensity factors are calculated for satellite lines, and dielectronic recombination rate coefficients are presented for the excited 218 odd-parity and 218 even-parity states. The dielectronic recombination (DR) rate coefficients are calculated including $1s^2 2s^2 2pnl$, $1s^2 2s2p^2 nl$, estimated by extrapolation of all atomic characteristics to derive the total DR rate coefficient. It is found that the orbital angular momentum quantum number l distribution of the rate coefficients shows a peak at $l=4$. The total DR rate coefficient is derived as a function of electron temperature. The state-selective DR rate coefficients to excited states of C-like oxygen, which are useful for modeling O III spectral lines in a recombining plasma, are calculated as well.

Dielectronic recombination from O^{3+} to the excited states of O^{2+} is defined by the following sequence of processes:



As an initial state we consider the ground state of O^{3+} , $2s^2 2p$. The doubly excited states, $2s2p^2 nl$ and $2p^3 nl$, are taken into account as intermediate states.

The DR rate coefficients $\alpha(\gamma' | \alpha_0)$ to the excited state of O^{2+} are obtained by summing up the intensity factor $Q_d(\gamma, \gamma' | \alpha_0)$ multiplied by the exponential factor, over the autoionization levels γ as follows:

$$\alpha_d(\gamma' | \alpha_0) = 3.3 \times 10^{-24} \left(\frac{I_H}{T_e} \right)^{3/2} \sum_{\gamma} e^{\frac{E_s}{T_e}} Q_d(\gamma, \gamma' | \alpha_0) / g(\alpha_0)$$

where

$$Q_d(\gamma, \gamma' | \alpha_0) = g_{\gamma} A_r(\gamma, \gamma') K(\gamma, \alpha_0),$$

$$K(\gamma, \alpha_0) = \frac{A_a(\gamma, \alpha_0)}{(A_r(\gamma) + A_a(\gamma))},$$

$$A_r(\gamma) = \sum_{\gamma'} A_r(\gamma, \gamma'),$$

$$A_a(\gamma) = \sum_{\alpha'} A_a(\gamma, \alpha').$$

Here $A_r(\gamma, \gamma')$ are radiative transition probabilities and $A_a(\gamma, \alpha_0)$ are autoionization rates.

The total DR rate coefficient is obtained by summation of the rate coefficients of DR processes through all possible intermediate singly and doubly excited states. For the total DR rate coefficient we need to consider contribution from doubly excited states $2p^3 nl$ with high n levels and also the contribution from singly excited states with high n , $2s^2 2p nl$ states.

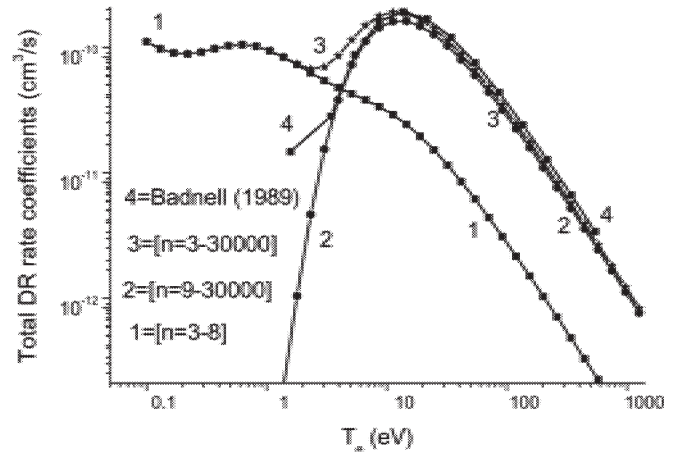


Fig.1 Total DR rate coefficient as a function of electron temperature (no. 3), compared with rate coefficient obtained by Badnell and Pindzola ¹⁾ (no.4). Line with no. 2 is the sum of the state selective DR rate coefficients with $2s^2 2pnl - 2s2p^2 nl$ transitions, which agrees with the result of Badnell and Pindzola.

References

- 1) N. R. Badnell and M. S. Pindzola, Phys. Rev. **39**, 1685 (1989).

§16. Ion Source Development for the Research of High Z Impurity Ions

Ohtani, S., Nakamura, N.
(Univ. Electro-Communications)
Sakaue, H.A., Kato, D.

A systematic research on atomic processes of highly charged impurity ions started as the NICE project in Institute of Plasma Physics. It has contributed to initiate an international research trend, and to deepen understandings of this field. These activities were succeeded to the NIFS, where experimental studies of highly charged ions (HCIs) and systematic collection of the atomic data on HCIs are currently on going. However, the HCI research is now faced with a new phase with the development of a new ionization source such as Electron Beam Ion Trap (EBIT). Using these ion sources, new types of atomic data which could not be obtained with ordinal ion sources are being accumulated. The purpose of this collaborative research is to collect such new atomic data and to build it as a data base.

On 15-17 April 2004, the ninth International Symposium on Electron Beam Ion Sources and Traps and Their Applications – EBIS/T 2004 was held at the Tokyo Metropolitan University. There were about 40 participants and about 30 papers presented. The meeting has shown a remarkable progress in science and technology with the EBIS/T machines. We also attend the symposium to know the recent trend of ion source technologies and found that various kind of new atomic data has been accumulated using new types of HCI sources based on Electron Cyclotron Resonance Ion Source (ECRIS) and Electron Beam Ion Source / Trap (EBIS/T).

After the symposium we had two meetings in order to collect and evaluate new data of HCIs. Especially, we concentrated on the data for HCI-surface collision

processes. In the collisions of HCI with surfaces, a huge number of secondary particles are emitted. However, data base of yield of such particles are not enough. Thus, we planned to construct a new data base for secondary particle emission in the collisions of HCIs and surfaces.

In the interaction with solid surfaces, a variety of experimental parameters exist such as energy, incident angle, and charge state of HCIs as well as energy, emission angle and species of secondary particles. Thus we concentrated on the integral yield of secondary particle including electrons, positive and negative ions, and neutrals. Moreover, it is considered to be useful for researchers to provide bibliographic data table classified according to the species of ions and the target materials. We have collected and evaluated the data from this point of view.

In these studies, new types of an ion source developed in recent years are found to be very useful for the highly charged impurity ion research. It has been understood that atomic data for the collisions of HCIs and surfaces is still insufficient because the experiment parameter and the ionic species include many things. Thus we concluded that it is very effective to establish collaborative experimental research using the Tokyo-EBIT at the University of Electro-Communications.

In principle, the Tokyo-EBIT can produce any ion (any charge state of any element). It is equipped with a beam line for extracted HCIs. Through collaborations using the Tokyo-EBIT, it is expected that many new data will be accumulated for the interactions of HCIs and surfaces.

§17. Time-dependent Density Functional Study on Excited Hydrogen Atom Formation via Non-resonant Electron Capture by a Proton from Refractory Metal Surfaces

Kato, D., Suno, H.* , Kimura, M. (Kyushu Univ.), Tanabe, T. (Kyushu Univ.), Kato, T.

Excited state abundance in neutrals reflected at refractory metals has been an issue of study concerning the plasma-wall interaction in nuclear fusion devices. D α emission has been observed from the reflected neutrals of a deuteron beam at a molybdenum surface¹⁾. However, the mechanism of the excited state formation has been little understood. Excited levels of the atomic hydrogen are above the Fermi level of the molybdenum by a few eV. Surface electrons hardly transfer to such the shallow levels via tunneling or classical-over-the-barrier, unless some surface impurities decrease the effective work function substantially. The effect of the surface impurities has not been studied in the present work; we have investigated other (non-trivial) mechanism first²⁾.

In the present work, the non-resonant single-electron capture by an outgoing proton from metal surfaces was studied by means of the semi-classical theory (electronic transition was treated quantum mechanically, while proton motion was represented by classical trajectories). Early studies on the electron transfer have been undertaken with the aid of simplified interaction matrix elements and/or the adiabatic approximation, e. g. Brako and Newns³⁾ and Burgdörfer et al.⁴⁾. The present study is based upon direct numerical solutions of the time-dependent Schrödinger equation including accurate interaction potentials.

Present calculations were performed for tungsten and molybdenum slabs whose widths are about 100 a. u. (about 5 nm). At low proton velocities, the occupation probability of

the ground level ($n=1$) is almost unity, whereas those of the excited levels are vanishingly small as expected in the adiabatic approximation. As the velocity increases, the probabilities of the excited levels grow, while that of the ground level declines. A hump was found in the $n=2$ occupation probability at low velocities. It may be attributed to the oscillatory transition between quasi-resonant states of the $n=2$ level and a discrete conduction level of the metal slab. With the larger slab width (the higher number density of the conduction levels), the hump becomes less significant. For the semi-infinite metal, the hump should disappear after the transition amplitude is integrated over the continuous conduction band in which the atomic levels are embedded (bandwidth effect).

It is noted that the present model is based upon the dispersion relation of the quasi-free electron-gas. However, transition metals like tungsten have substantially different density of states from that of the free electron-gas. An improved model taking account of a correct density of states is under development. The Auger deexcitation might depopulate the excited levels, while it is left for future studies.

References

- 1) Tanabe, T., Ohya, K., and Otsuki, N.: J. Nucl. Mater. 220-222 (1995) 841.
- 2) Kato, D. et al.: submitted to Journal of Plasma and Fusion Research.
- 3) Brako, R. and Newns, D.M.: Rep. Prog. Phys. 52 (1989) 655.
- 4) Burgdörfer, J., Kupfer, E., and Gabriel, H.: Phys. Rev. A 35 (1987) 466.

* present address: Erath Simulator Center

§18. Charged and Neutral Particle Behavior at and near Plasma Facing Material Surfaces

Ohya, K. (Tokushima Univ.),
Tanabe, T. (Kyushu Univ.),
Asakura, N., Kubo, H., Simizu, K., Takizuka, T.,
Takenaga, H., Nakano, T., Higashijima, S. (JAERI),
Itoh, A., Imai, M. (Kyoto Univ.),
Ohno, N., Chen, A. (Nagoya Univ.),
Kado, S., Tsuneyuki, S., Yoshimoto, Y. (Tokyo Univ.),
Ono, T. (Okayama Univ. Sci.),
Kawata, J. (Takuma National College of Tech.),
Hatakeyama, A. (Keio Univ.),
Sawada, K. (Shinshu Univ.),
Shouji, M., Tomita, Y., Nakamura, H., Masuzaki, S.,
Kato, D., Kato, T.

In this working group, we investigate electronic excitation, ionization, electron capture, and electron emission at plasma facing material surfaces exposed to plasmas. It aims to understand energy and particle transport under abnormal circumstances such as arcing, hotspot etc. Theoretical methods and simulation codes which were developed in this project would be available for nuclear fusion researches at the NIFS.

One of research topics is excited state abundance in neutrals reflected at refractory metals. The excitation probabilities are expected to be important for spectroscopic diagnostics of high-energy hydrogen component reflected at the plasma facing wall. To estimate the excitation probabilities, a semi-classical theoretical method (electronic transition was treated quantum mechanically, while proton motion was represented by classical trajectories) is being developed. The method enables to calculate single-electron capture by a proton outgoing from metal surfaces. The calculations are being performed for tungsten, molybdenum, beryllium, etc. Preliminary results were presented at the 14th International Toki Conference joined with the 4th International Conference on Atomic and Molecular Data and

Their Applications (Toki, Oct. 5-8, 2004)¹⁾.

Monte Carlo program code of electron backscattering and secondary electron emission from solids has been published in NIFS-DATA series²⁾. The program code was developed by the collaborator (Ohya), and is available for researchers on their request. The code is applicable to mono-atomic metals, semi-conductors and insulators for electron impact energies of 0.1 – 10 keV. It provides information on energy and angular distributions of backscattered electrons and secondary electrons, as well as total yield.

A quantum molecular dynamics code (VASP) has been introduced in this working group. The code is applicable to calculating accurate impurity transport coefficients in fusion reactor materials.

Two group meetings were held in January and March 2005 to discuss about each research topic. One of the meetings was held as a joint meeting with “theoretical and simulation study on boundary layer plasma” working group. Studies on secondary and backscattered electron emission from solid targets by charged particle impact were reviewed, and an effect of the electron emission on the ion sheath profile was examined at the meeting. In the other meeting, Prof. M. Tanaka (NIFS) was invited to present his quantum molecular dynamics study on chemical sputtering of graphite by hydrogen. Measurements of the chemical sputtering rate at the JT-60 were presented by the collaborator (Nakano). Current understandings on mechanisms of the chemical sputtering were reviewed at the meeting. It was suggested that transport coefficients of methane molecules in the graphite should be studied by using the quantum molecular dynamics.

References

- 1) Kato, D. et al.: submitted to Journal of Plasma and Fusion Research.
- 2) Ohya, K. et al.: NIFS-DATA 84 (2004).

§19. Cross Section Database for Carbon Ions: Electron-impact Excitation, Ionization, and Charge Exchange in Collisions with Hydrogen Atoms

Suno, H. (Earth Simulator Center, JAMSTEC)
Kato, T.

diagnostics and energy-loss calculations in fusion plasmas. Charge-exchange process of carbon ions with hydrogen atoms also provides a useful plasma diagnostics. In this work, we have constructed a set of cross sections for such processes. As a basis for this cross section set we have used the available experimental and theoretical data from the literature and critically assessed their accuracy.

There exist numerous theoretical cross section data for electron-impact excitation of carbon ions. Previously, Itikawa et al. [1] compiled cross sections reported before 1985, assessed them for carbon ions (C^+-C^{5+}) as well as oxygen ions (O^+-O^{8+}), and fitted their recommended values to an analytical formula. Except for optically allowed transitions, all electron-impact excitation cross sections are scattered, and it has been sometimes difficult to determine the recommended data. We have carefully chosen reliable electron-impact data from references. Once the recommended cross sections were determined, a fit was made, which facilitates their applications. In most cases, we fitted the collision strength Ω into the analytical formula:

$$\Omega_{if} = A + B/X + C/X^2 + D/X^3 + E \ln X,$$

where A, B, C, D, and E are the fit coefficients, X the electron energy scaled by the transition energy, that is $X = E/V_{if}$. Figure 1 shows an example of our results, where we present the case of the $C^{5+} 1s \rightarrow 2s$ transition.

Electron-impact ionization of carbon ions has been extensively studied both experimentally and theoretically. The experimental measurements and theoretical calculations agree fairly well with each other. The recommended cross section for electron-impact ionization is parametrized by the expression

$$\sigma[cm^2] = \frac{10^{-13}}{IE} \left\{ A_1 \ln(E/I) + \sum_{i=2}^N A_i \left(1 - \frac{I}{E} \right)^{i-1} \right\},$$

where the collision energy E and ionization potential I are expressed in eV units and A_i are fitting coefficients. An example is shown in Fig. 2, where we present the ionization of C^{5+} .

There also exist numerous theoretical and experimental results for charge exchange processes in collisions of carbon ions with hydrogen atoms. Particularly the $C^{6+}+H$ collisions are the most studied processes. The recommended cross sections are fitted to analytic fit functions such as

$$\sigma[cm^2] = 10^{-16} \times \frac{a_1 \exp[-(a_2/E)^{a_3}]}{1 + (E/a_4)^{a_5} + (E/a_6)^{a_7}},$$

where the collision energy E is expressed in eV/amu units and a_i are fitting parameters. An example is shown in Fig. 3.

In summary, we have studied electron-impact excitation, ionization of atomic carbon ions, and charge exchange for carbon ions. More than 100 processes have been treated. Although we have shown only examples of our results, all our results will be published in Atomic Data and Nuclear Data Tables.

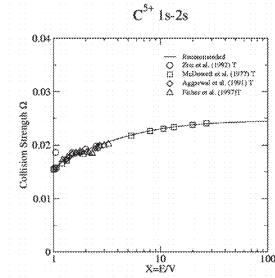


Fig. 1. Recommended electron-impact collision strength for the $C^{5+} 1s \rightarrow 2s$ transition with the original collision strengths from the literature.

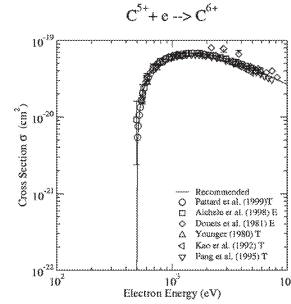


Fig. 2. Recommended cross section for the electron-impact ionization of C^{5+} as well as the original data from the literature.

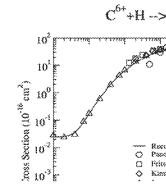


Fig. 3. Recommended cross section for the charge exchange between C^{6+} and H, as well as the original data from the literature.

Reference

- 1) Y. Itikawa et al., Atomic Data Nucl. Data Tables **33**, (1985) 149

§20. Network of Atomic and Molecular Database Related to the Processing Plasmas

Iinuma, K. (Tohoku Univ.),
Samukawa, S. (Tohoku Univ.),
Ito, H. (Chiba Inst. Tech.),
Sugai, H. (Nagoya Univ.),
Nakamura, Y. (Keio Univ.),
Hatano, Y. (Tokyo Inst. Tech.),
Kono, A. (Nagoya Univ.),
Sato, T. (Muroran Inst. Tech.),
Tanaka, M. (Pegasus Soft),
Tanaka, H. (Sophia Univ.),
Tsumori, K., Kato, T., Kato, D.

Up to now the National Institute for Fusion Science (NIFS) has compiled and evaluated databases for fusion science. A globe spanning information network has been setup involving the academic and energy science networks in the USA. This network enables individuals, universities and other institutions all over the world to access the computers and data services of NIFS, enabling effective joint research. As a challenge for the 21st century compilation and evaluation of these databases, so invaluable for science development and the industry, needs to be enlarged to include data from other areas of science and engineering. In this project, we search for reliable atomic and molecular databases for further development of the plasma processing technology (e.g. vertical integrated computer-aided design for device processing), and aim at establishing a network of such databases. Through the database network, an effective trinity symbiotic relation among the NIFS, universities, and industries would be formed. From this viewpoint, consultative meetings were held at NIFS in December 2004 and March 2005.

This project seeks to know the currently available data gathered by individuals, universities and other research centers. In the US, the group led by L. G. Christophorou, at the National Institute for Science and Technology (NIST)¹⁾, had devoted itself to data compilation and evaluation for some important molecules related to plasma processing. However the project has since ended. Other related works include those carried out by individuals for companies (e.g. W. L. Morgan, for Kinema Research & Software)²⁾ and universities in conjunction with companies (e.g. V. McKoy

and C. Winstead, for Intel)³⁾. In the EU, some French group has privately compiled databases for plasma processing gases. In Japan, the Investigation Committee on “Discharge Plasma Electron Collision Cross-Sections”, in the IEE Japan⁴⁾, started the similar project about 5 years ago. They tried to compile swarm experiments databases related to plasma processing at Hokkaido Univ., Kitami Inst. of Tech., Muroran Inst. of Tech., Chiba Inst. of Tech. and Keio Univ. They evaluated relevant data from all over Japan, with some international references, and made recommended databases, e.g. CF₄. After discussion on some technical and copyright issues, we have obtained their consent to have a link to their database from the NIFS database.

A meeting with some companies (PEGASUS Software Inc., WaveFront Co. Ltd., ULVAC Inc., and Hitachi Ltd.) was held to listen to current status of industrial applications of A&M data to the plasma processing. The data needs are high and include variety of processes, but available data is limited. For application to plasma processing by using atmospheric discharge, Prof. Y. Ichikawa (ISAS, emeritus Professor) was invited at the meeting to present his work on new data compilation and evaluation for electron collision cross sections of N₂ target.

Prof. M. Hayashi (Gaseous Electronics Institute, past away on Dec. 7, 2004) did extensive work in compiling references for various molecules, in a series of publications called the “Bibliography of Electron and Photon Cross Sections with Atoms and Molecules, NIFS-DATA Series”. However, there are still many bibliographic data compiled by him remained unpublished. These data are being prepared for publication in the NIFS-DATA series by Prof. Y. Nakamura (Keio Univ.).

References

- 1) Christophorou, L.G. and Olthoff, J.K.: Adv. Mol. Opt. Phys. **44** (2001) 59.
- 2) Morgan, W.L.: Adv. Mol. Opt. Phys. **43** (2001) 97.
- 3) Winstead, C. and McKoy, V.: ICAMDATA, (Gatlingburg, Tennessee, AIP Conference Proceedings 636, 2002) p. 241.
- 4) Sakai, Y.: Appl. Surf. Sci. **192** (2002) 327.

§21. Study of Evolutional Data Collecting System for the Atomic and Molecular Databases

Sasaki, A., Kubo, H. (Japan Atomic Energy Research Institute)

Joe, K. (Nara Women's University)

Pichl, Lukas (The Aizu University)

Ohishi, M. (National Astronomical Observatory)

Kato, D., Kato, M., Murakami, I., Kato, T. (National Institute for Fusion Science)

We study atomic and molecular database based on computer and internet technology to collect and evaluate a large amount of data required for scientific as well as industrial applications [1]. The project has been started since FY2003, and during FY2004 we have developed several trial codes for the unified search over online journals [2] to find scientific abstracts concerning to the atomic data, and to identify and collect information on the atomic and molecular states in the abstracts [3].

We had a working group meeting on 17-Jun-2004 to understand the present status and direction of the project, as well as programming and network infrastructure applicable to the project.

In addition, we had a hearing from Prof. Itikawa for the experience of collecting articles concerning to the atomic data based on the analysis of titles, abstracts, and figures and figure captions in the articles, to learn the selection is rather made using limited information.

In order to find a scientific article on the atomic and molecular data using a computer program, we need to model articles to be understood by a computer. As a data mining systems in a variety of fields, we firstly used frequency of keywords appeared in abstracts of the papers. Abstracts are chosen because we learn after investigations of the conventional procedure of searching articles that they contain sufficient information of the content. More specifically TF/IDF (term frequency/inverse document frequency) of each keyword is calculated [3]. Using the TF/IDF, any abstract is represented by a point in the n -dimensional document space, having n determined from the total number keywords contained in the test collection.

The model allows us to evaluate similarity between two abstracts by calculating the Euclid distance in the n -dimensional space. Moreover, having a set of reference abstracts concerning to the atomic and molecular data, it may be possible to classify whether the data is likely to be contained or not in test abstract by calculating similarity to the reference set. Although, mathematical representation of the reference set in the document space is not clear, having a sufficient number of reliable positive and negative examples as training data [3], machine language algorithms such as LVQ (Learning Vector Quantization) can be applied to find the criteria for the decision [4].

The accuracy of the text classification is represented by two quantities, precision and recall. In the present system, recall, which corresponds to the fraction of the articles

classified by the system as the atomic and molecular data is contained, to the total articles in the sample set, which contain the atomic and molecular data, is more important. Because, we estimate the number of articles, which contain atomic and molecular data is small ($<100/\text{year}$) compared to the total number of articles published in the field of physics and physical chemistry ($>10^4/\text{year}$).

Accuracy of the classification depends on the quality of the keywords. Useful keywords are those appear in the articles concerning to the atomic and molecular data, and do not appear in other articles, thus usefulness of each keywords can be estimated by measuring the probability of appearance in the positive and negative examples.

Using machine learning algorithms, pairs of keywords which frequently appear together can also be recognized. In particular, technical terms are sometimes represented by two or more consecutive nouns, such as "cross section" and "impact ionization". We analyze such technical terms used in the field of physics from the abstracts of articles in Phys. Rev. A-E statistically to find keywords appear frequently in the articles concerning to the atomic and molecular data.

Furthermore, we investigate methods which can recognize and extract expressions of atomic and molecular states in the abstracts, which should appear frequently in the articles concerning to the atomic and molecular data.

For instance, an atomic state is represented hierarchically from the atomic and ionic species (Al XI, Li^{3+} , H-like Al etc.), electron configuration ($1s^2 2s^2 2p^2$), and to fine structure (1S_0). In electronic documents, these representations of the atomic states are written according to the syntax rules such as using html as ¹S₀ for the fine structure level. These rules can be generalized and formulated using the regular expression, and the information of atomic states can be recognized and extracted from articles automatically. Interestingly, expression of atomic species can easily be extended to simple molecules by accepting the repetition of the rule for atoms.

The present project will be continued to FY2005. We are going to combine techniques to find good keywords for the text classification. Precision and recall of the system will be evaluated quantitatively using a larger set of reference and test sets to improve the accuracy.

References

- [1] <http://dpc.nifs.ac.jp/amdrc/index-j.html>
- [2] L. Pichl, et al., Proceedings of DNIS 2005, LNCS 3433, pp. 159, Springer, 2005.
- [3] A. Sasaki et al., paper presented at Joint ITC14 / IAMDATA 2004, October 5-8, 2004
- [4] Y. Itikawa, ADANDT, **63**, 315 (1996).
- [5] Salton, G. and McGill, M.J. : Introduction to Modern Information Retrieval, McGraw-Hill Book Company, 1983.
- [6] Kohonen, T.; The Self-Organizing Maps (3rd edition), Springer, 2001.

§22. LAMP Prototype Bibliography Databases

Pichl, L., Suzuki, M. (Univ. of Aizu)
Kimura, M. (Grad. Sch. of Sci., Kyushu Univ.)
Kato, D., Kato, T. (Nat. Inst. Fusion Sci.)

LAMP is a free-software open-source solution for databases with on-line access. Unlike from commercial database system, it is available at zero software (SW) cost. We have therefore developed a prototype bibliography database for electron-molecule collision data (list of relevant articles was provided by Prof. Y. Itikawa) using LAMP SW technology, and a server PC donated to the Coordination Research Center. The present database differs from the ORACLE *bibliography* system used by NIFS in the following two points: (1) more general search fields (category; type of collision process and target molecule) and (2) inclusion of abstract text (in HTML format) and full text links in the bibliography database. This particular work is a part of a broader study on the applicability of Linux database systems to Data Centers, involving various subprojects in computer sciences and physics, with the ultimate goal of database cost reduction.

Data in the present electron-molecule scattering bibliography database are classified into the following fields: author, year, journal, volume, page, title, category, and molecule/process [1-2]. Abstract text and link to full text in pdf format is also available [2]. The online search interface and data format is shown in Fig. 1.

The screenshot shows a web browser window with the address bar displaying 'http://webhome.crk.ubc.ca/~fap/bib/'. The page title is 'Bibliography Database'. The search results are as follows:

author	year	journal	volume	page	title	category	index/abstracts
F. A. Boulton	1994	Ann. Phys.	33	4157	Carbon isotope section data for carboniferous	3	CT4bis, CT4bis, CT4bis, CT4bis, CT4bis

Fig. 1. Bibliography database for electron-molecular collisions: search interface and data format.

The database in Fig. 1 is useful in two aspects: it provides well-organized references to electron-molecule scattering collected by Prof. Y. Itikawa, but also demonstrates that free-software open-source databases are enough secure and inexpensive (honorarium for programming work by college students is safely bound to 5% of the commercial cost).

Next, we proceeded to develop a more advanced bibliography database system, which *retrieves articles* from online publishers and *inputs data* into the database *automatically* as shown in Fig. 2, saving much labor cost of part-time workers, who usually **handle** data manually.

[illegible]

Fig. 2. Robot system for retrieval, extraction and data input of journal articles, their abstracts and full text URLs.

The above electronic robot (with working name "Evolutionary database") [3] retrieves journal articles from databases of APS and IOP according to predefined queries, processes and extracts cataloguing strings, and inputs html abstracts and links to full text articles. On the basis of this system, we also developed a joint search tool, which bridges APS and IOP databases [4]. Future work in progress covers databases of numerical data, differential cross-section databases and a database builder.

References (URLs)

- 1) <http://crdb.nifs.ac.jp/bib/iti/top.php>
- 2) http://crdb.nifs.ac.jp/iti/list/list_top.php
- 3) http://crdb.nifs.ac.jp/evodb/evodb_top.php
- 4) http://crdb.nifs.ac.jp/j_search/is_top.php

§23. Simulation Experiment of Confinement Improvement of Plasmas for Super Science Highschool (SSH) Program (Fluid Dynamics Experiment in Kitchen)

Ida, K., Yoshinuma, M., Nagaoka, K.

Super Science Highschool (SSH) program is physics education program for highschool students. An experiment simulating the improved confinement of plasma magnetically confined is invented using simple instruments one can prepare in the kitchen[1]. Figure 1 shows very simple experimental setup for the understanding of the Ekman flow using an electric hot plate (1400W), an aluminum pot (30cm diameter, 10cm depth, 7000cc), a spoon and water (with 6cm height) that are usually available in the kitchen. The temperature of the water is measured at the center and edge of the pot near the bottom (10mm above the bottom of pot) with thermometers. The region of the pot bottom heated by the electric hot plate is localized near the center with a diameter half of the pot diameter (15cm diameter). To have better localization of the heated region, an aluminum pot is recommended rather than a steel pot, because the smaller heat capacity results in a larger difference between the temperatures at the center and at the edge.

Figure 2(a) shows the time evolution of the water temperatures measured at the center and edge of the pot. The hot plate is turned on at 60 seconds and the water is stirred by a spoon only during the period from 360 to 420 seconds with a rotation speed of 90 rpm. Both the temperatures in the edge and center increase linearly after the hot plate is turned on. Because of the convective flow of water in the pot, there is no difference in the temperatures at the center and edge of the pot. While stirring the water ($t = 360 - 420$ second) there is a small difference in the temperatures because the convective flow maintaining the uniformity of the temperature is distorted by the rotation of the water. After stopping the stirring, the water keeps rotating inertially for several minutes. Just after stopping stirring, the central temperature increases rapidly with a rate of increase of 30 degree per minute, which is more than ten times faster than the rate of increase before stirring (2.5 degree per minute). This sharp increase stops after 20 second and the difference in temperature between the edge and center reaches 10 degrees. The differences in temperature are kept for one and a half minutes, then the difference becomes small with the decrease of the central temperature.

The mechanism of sharp increase of central temperature can be explained as follows. The centrifugal force produces higher pressure near the edge then a downstream flow along the barrier and a flow toward the center along the base of the pot is driven by the non-uniformity of the pressure. Because the flow toward the center along the base is localized in a thin layer, the water in this flow continues to be heated when it travels from the edge to the center without rising up. As seen in Fig.3(a), the central temperature near the bottom of the pot is higher than that near the water surface. In general, the reversal of the temperature gradient (higher temperature at

lower part of the water) is unstable, however, it can be sustained with rotation of the water. This phenomena contradicts common sense that hotter water rises to the top. During the steady state phase after the rapid increase of the central temperature, the flow in the thin layer along the bottom is damped and the upper temperature becomes identical to the lower temperature, which indicates that normal convective flow appears central region ($r < 6$ cm) as seen in Fig.3(b). The rotational flow still exists in the outer region ($r > 6$ cm) and the upper part of the water is at a higher temperature than normally predicted. In this phase, the central region is governed by convective flow, while the outer region is governed by the rigid rotation.

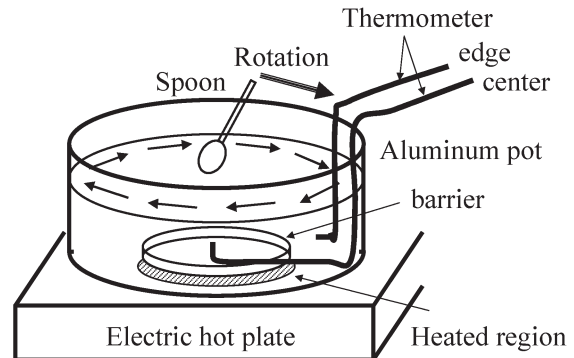


Fig. 1. Experimental setup in the kitchen.

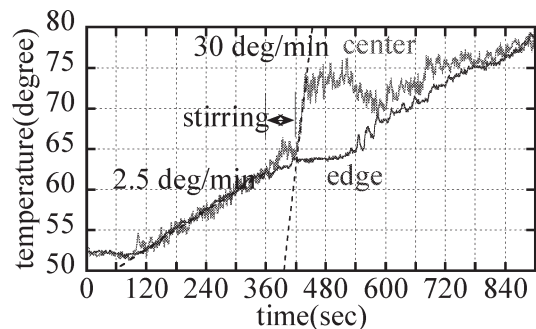


Fig. 2. Time evolution of water temperature measured at the edge and center in the pot near the bottom (10mm from the bottom of pot), when there is no barrier.

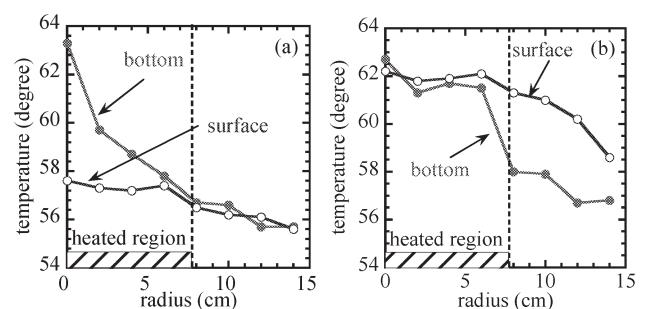


Fig. 3. Radial distribution of temperature (a) at the end of the rapid increase of temperature and (b) during the steady state phase after the rapid increase of temperature when there is no barrier.

Reference

- Ida, K., et.al., American J. Phys. 73 (2005) 635

§24. Evaluation of Fusion R&D — Cost Reduction of Fusion Plants —

Tazima, T., Iguchi, H.

The most important issue in realization of a commercial fusion power plant is the reduction of the capital cost. In the case of a fission power plant, the capital cost of one GWe power plant is about 4000×10^8 yen (gross weight of power plant is about 15,000 ton). The power plant consists of a core reactor and surrounding facilities such as buildings and electric power generator. The former costs about 1500×10^8 yen (5,000 ton in weight), and the latter costs about 2500×10^8 yen (10,000 ton in weight). Since the energy density of the magnetic fusion power plant is extremely low, the core volume of the fusion reactor is bigger than that of the fission reactor by about 20 times, and its weight is heavier by about 10 times. The cost of the power plant is in proportion to weight. Therefore the cost of a fusion reactor might be 1500×10^8 yen, which is 10 times more expensive than that of the fission reactor.

On the other hand, a driver system is most expensive in an inertial fusion power plant. For example, the cost of a future semiconductor laser is estimated to be 3000×10^8 yen /MJ. Since the required output of the laser driver is 4 MJ in a commercial power plant, the cost of the driver might be 12000×10^8 yen, which is also extremely expensive. Recent proposals for cost reduction of nuclear fusion reactors are as follows.

○Magnetic fusion reactor

Recently current start-up by radio-frequency has been experimentally realized in tokamaks. If CS coils can be removed, the aspect-ratio of the tokamak can be reduced. An inner wall blanket can be removed in a low-aspect-ratio system, because its effective area as a tritium breeder is small. In addition, the current density of the toroidal coil can be increased by the re-examination of coil support structures without CS coils. Then the total magnetic stored energy becomes smaller than that in a standard tokamak reactor by more than 10 times. In a low-aspect-ratio tori, the ratio of the surface area of plasma facing wall and the plasma volume can be increased with elongation. Then a compact reactor can be designed without increasing neutron wall loading

○ An inertial fusion reactor

Since a laser system is expensive, the cost of inertial fusion power plant is also high. Therefore required driver output should be reduced to attain a reasonable cost. On the other hand, even if a laser system raises the number of the repetition, the cost may not be influenced very

much. In other words, the cost of 1MJx 16Hz becomes about one fourth of that of 4MJx 4Hz. Expected pellet gain is 200 at maximum, and possible repetition rate for one chamber is several Hz at maximum. Therefore in the case of a driver of one MJ, we can expect only a small output reactor with one chamber system. Then a set of several reactor chambers and one laser system might give a reasonable cost.

In late years an idea of the fast ignition gives excellent experimental results. The most attractive advantage of the fast ignition is that we can expect a small output reactor chamber. Today's estimation gives a reasonable cost of power plant of 1GWe as 5500×10^8 yen. In this case, the cost of the laser system of 1MJx 16Hz and 4chambers is estimated to be about 3000×10^8 yen.

A fusion power plant can be a future alternative of energy source, if its capital cost is around 5×10^8 yen, because the fuel expense is very cheap.

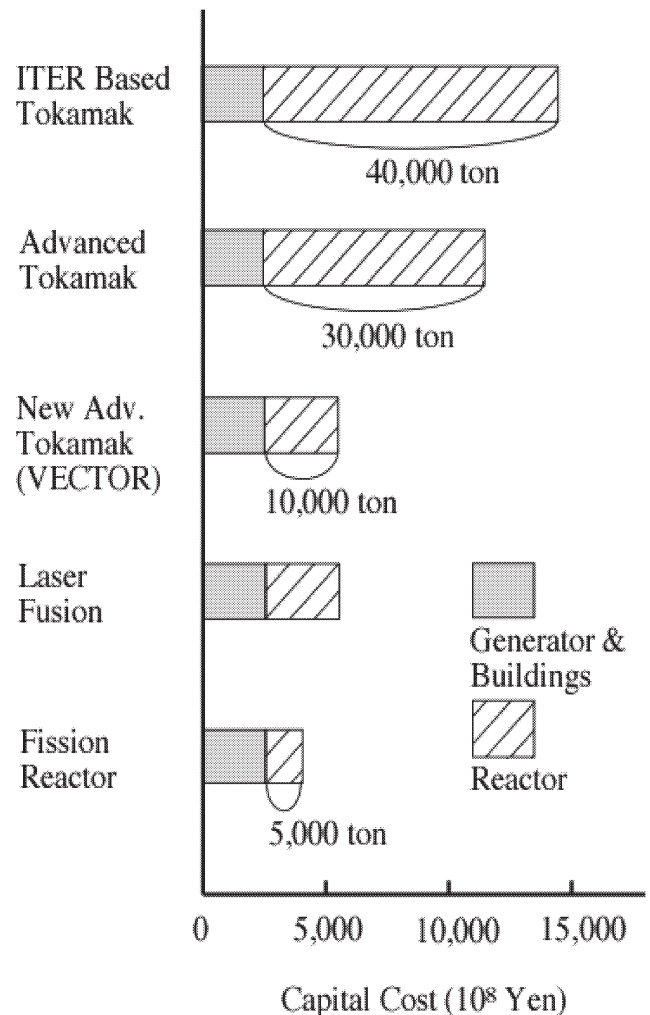


Fig.1 Capital costs of various power plants.

§25. Archival Studies on the Nuclear Fusion Research at Universities in Japan — Inter-University Collaboration System in Early Days of Fusion Science —

Nisio, S., Uematsu, E. (Nihon Univ., College of Science & Technology),
Kawakami, I. (Nihon Univ., Professor Emeritus),
Kojima, C. (Nihon Univ., College of Commerce),
Takaiwa, Y. (KEK),
Takeda, T. (Univ. Electro-Communications),
Sato, N. (Tohoku Univ., Professor Emeritus),
Sato, K.N. (Kyushu Univ., RIAM),
Terashima, Y. (Nagoya Univ., Professor Emeritus),
Fujita, J., Obayashi, H. (NIFS, Professor Emeritus),
Kitsunezaki, A. (Research Organization for Information Science, RIST),
Matsuoka, K., Namba, C., Kimura, K.

Based on the documents included in NIFS Nuclear Fusion Archives Database, we observed some characteristic features of the Institute of Plasma Physics (IPP, 1961-1989), Nagoya University, particularly in early days of fusion research in Japan.

As is given in earlier report ¹⁾, IPP was established after the intensive discussions of so-called “AB-dispute”, which resulted in A-plan, to start with the basic research of plasma science, in 1959. Kakuyuugo-Kondankai (Nuclear Fusion Research Group, researchers’ forum founded in 1958) requested Science Council of Japan (SCJ) to organize the Special Committee for Nuclear Fusion (SCNF), where the institution for A-plan (eventually IPP) was discussed in detail. In 1959 SCJ made a Recommendation to the Government for establishing IPP as a university-attached collaborative institute. As the host university, Nagoya University accepted, and IPP was established in 1961.

According to the discussions summarized at SCNF, IPP should have the following characters:

- to promote the general studies of plasma physics and technology for fusion research
- to give a center of nation-wide collaborative work
- to be operated under researchers’ autonomy
- to behave as a university-attached organization adjusted to inter-university nature
- to set up a system fit for official management
- to get cooperative understandings of the host university, including future possibility for the institute to leave the university

These conditions were well fulfilled between IPP and Nagoya University.

One of the most important agreements was so-called “Mutual Respect and Mutual Independence”, by which the Institute and University recognized the autonomy of each other side. Although belonging to Nagoya University, IPP did not participate University Council. The IPP members did not use the right to vote at the election of University President. On the other hand, the operation of IPP was decided by the Steering Committee, more than half members of which were elected from Kakuyuugou-Kondankai and the rest from the IPP staff. The Steering Committee was in a sense acted for the Faculty Meeting of the Institute. This gave the autonomy of fusion research community in Japan. The research program plans of IPP were discussed and proposed by the Scientific Committees, whose members were also based on Kakuyuugou-Kondankai. IPP budget was treated separately from University. Just on education side IPP staff and facilities contributed for the graduate school course of the University.

Generally speaking, these systems functioned effectively and successfully until the final period of IPP, though the schemes of Kakuyuugou-Kondankai and SCJ had largely changed in the middle of 1980’s. It should also be taken into consideration that the growth in fusion research fields to include high temperature plasma physics and reactor technology and engineering. IPP itself should grow into a larger system. In 1989 the main part of Institute of Plasma Physics, Nagoya University was together with two other institutions (Plasma Physics Laboratory, Kyoto University, and Institute for Fusion Theory, Hiroshima University) reorganized to give a new institute NIFS. In this way IPP left Nagoya University the rest part as Plasma Science Center.

The present study was carried out as a part of “The Archival Studies on Establishments of Inter-University Collaborative Institutes in Japan” organized by Sokendai (The Graduate University for Advanced Studies). Comparing with similar collaborating institutes, for instance KEK, IPP had kept quite unique relations with the host university in the agreement of Mutual Respect and Mutual Independence, and this might be further investigated through archives.

Reference:

- ¹⁾ Terashima, Y., et al. Annual Report of NIFS 1999-2000, 398(2000)

§26. Complementary Study of Nuclear Fusion Archiving by Means of Oral History

Fujita, J. (Professor-Emeritus, NIFS),
Terashima, Y. (Professor-Emeritus, Nagoya Univ.),
Obayashi, H. (Professor-Emeritus, NIFS),
Namba, C., Kimura, K.,
Sato, N. (Professor-Emeritus, Tohoku Univ.),
Matsuoka, K.

Introduction

Archival studies have been carried out on early day's nuclear fusion research, by collecting historical documents, and constructing the database for them, as described in the previous section of this annual report. Some of the documents, however, are missing, and the base-line stories are not always clear due to the incompleteness of the materials. It is an urgent task to complement the archives with interviews with senior scientists who played important role in those days, by means of oral history, which is one of important method in archival studies. So far interviews with Prof. Sekiguchi on the topics of the nuclear fusion research in early day's Japan, and with Prof. Matsuura on the R-Project were carried out.

Interview

The interview was conducted with Dr. N. Morino as the interviewee with the subject of participation of industrial society in the fusion research in Japan.

Since there was the limitation of the written sources, we made an interview to understand the fusion research circumstances and background and the relations among industries of those days.

1. Interview subject: "On the Participation of the Industries in the Nuclear Fusion Research in Japan."
2. Interviewee: Dr. Morino Nobuyuki,
3. Interviewer: Terashima Y., Obayashi H., Fujita J., Namba C., Kimura K.
4. Date and place: 2004.11.18, 1:30-5:00 pm, at the Office of the Japan Society of Plasma Science and Nuclear Fusion Research.
5. Transcription. To be published in 2005.

Procedure of the Interview

(1) Questions in advance

Questions from interviewers were first gathered and summarized as follows: The questions in outline were handed to the interviewee in advance.

- Motivations for Japanese Industries to participate in the nuclear fusion research development
- Role of the Japan Atomic Industrial Forum on the nuclear fusion research development
- Comparison of Japanese industries with those in other countries on the commitment to the nuclear fusion research
- Archives in Japanese industries
- Industries' own research and development for nuclear

fusion studies

- Role of the Japan Society of Plasma Science and Nuclear Fusion Research on the enrichment of nuclear fusion archives from the viewpoint of former administrator of the society
- The others.

(2) Response from the interviewee in advance

The response from the interviewee to the questions above mentioned was obtained. The summary of the response in length of 5 pages was distributed to the interviewers prior to the interview.

(3) Talk given by interviewee

The interviewee gave a talk toward the plural interviewers under the moderator of Fujita, J.

(4) Questions and answers

Questions and answers were given in the course of interviewee's talk.

(5) Discussions

Discussions were held to understand the historical facts in the interviewing group

(6) Transcription and record making

After preparing a rough transcript, all the interviewers checked and edited it for accuracy and clarity. The response given in advance by the interviewee was also checked and confirmed for authenticity. The edited transcript then went on to the interviewee for corrections or additions.

(7) Publication

The question outline, the response by interviewee and the interview record will be published in NIFS-MEMO after corrected by the interviewee.

Outcome of the interview

The interview was very successful, mainly due to the cooperative manner of the interviewee. We could not only experience the days with the speaker but also get many access points to further studies.

Following points have come up to us through the interview:

(1) Pre-interview preparation

- Prepare enough materials concerning the subject or topics to be explored
- Define the focal points of the interview and to formulate them into detailed and significant questions
- Keep the general direction given in the question outline

(2) To make sure whether the interviewee preserves any materials that ought to be deposited.

(3) To treat sensitive personal information or what the interviewee wants to be kept confidential with care because of ethical considerations.

Future plan

We are planning to extend the interview toward more persons and subjects including those in the field of industry.

§27. Foundation of Fusion Science Archives

Matsuoka, K., Namba, C., Kimura, K.,
Terashima, Y. (Professor-Emeritus, Nagoya Univ.),
Obayashi, H., Fujita, J. (Professor-Emeritus, NIFS)

Foundation of Fusion Science Archives in NIFS and fusion archives in general are described here.

Archival activities in NIFS have been continued since 1999 under the nationwide collaboration that includes Nihon Univ., Tohoku Univ., Kyushu Univ., Nagoya Univ., KEK, Sokendai (The graduate University for Advanced Studies) etc. These activities have been presented at the annual meeting of Plasma and Fusion Research and described in the series of annual review of NIFS.

Fusion Science Archives started on January 1, 2005 as the formal organization in NIFS, which reflects the increased understanding of importance of archives thanks to the above mentioned activities. Another factor surrounding NIFS is originated in the increased importance of archival activity on natural and social sciences among the 18 inter-university research institutes consisting of Sokendai.

The organization, being independent of research divisions and centers of NIFS, belongs directly to the deputy director-general and consists of two permanent scientists of NIFS staff and one archivist from a company.

The primary purposes of fusion archives, already well-known, are repeated in the followings: 1) collection and preservation of historical materials on fusion research at universities in Japan to make its organization and history clear, 2) establishing the standards to make the database open to public, 3) editing chronological tables, 4) interviewing senior scientists who played important roles at the early stage of the research, 5) circulating the database through INTERNET, and so on. Because it is becoming more important than before to provide scientists and citizen with database of historical documents for evaluation and accountability of nuclear fusion research, and because we could get lessons on the strategy of research in the future from old archives, archives on nuclear fusion should be further promoted by achieving above-mentioned objectives.

On February 15 the mini-workshop that commemorated the foundation was held at NIFS. About 70 scientists nationwide took part in and three review talks were given by Dr. H. Sugawara, Professor-emeritus of KEK and a board member of directors of Sokendai, Prof. S. Nishio of Nihon University, and Prof. C. Namba of NIFS. These talks covered importance of archives, activities on fusion research at the very beginning phase of Japan, and activities in NIFS so far, respectively. Sokendai has his own projects on archives and has a close relation with activities in NIFS. The workshop was reported in

two local newspapers, being effective to make archives known to citizen.

On January 25, before the foundation, the workshop was held at KEK with the topics of foundation of inter-university research institutes. Dr. H. Obayashi presented archival activities in NIFS focusing on the subjects of WS.

On March 2 and 3 big workshop was held at Hayama-campus of Sokendai. Scientists took part in WS from 18 inter-university research institutes. Those from the institute of social sciences gave us basic knowledge on archives and oral history, which were very useful for all participants. Total number of 7 people participated from the field of fusion archives, and K. Matsuoka introduced the Fusion Archives recently founded and Mrs. K. Kimura presented the archival studies on the early phase of fusion research in Japan. NIFS and KEK, at present, are institutes that have formal organizations of archives among inter-university institutes on natural sciences. Two institutes are expected to play a key role to organize archival networks on natural sciences among inter-university research institutes.

Collection and preservation of historical materials were continued in this fiscal year and ??? materials were newly registered in NIFS archives. Along with these activities interview was conducted with Dr. N. Morino as the interviewee with the subject of participation of industrial society in the fusion research in Japan.

Making a survey of the activity of the next fiscal year we could expect progresses in the followings.

1) The number of staff is to be increased by one. The budget and the area for the office work will be augmented, too. These will enhance our activities more effectively.

2) The category of collaboration research on fusion archives in NIFS had been independent of any research categories. This increased the number of research programs to be six, which was more than usual. Research subjects will be enlarged as follows: criteria of opening database, oral history, history of inter-university institutes, history of confinement devices, and chronological tables.

3) The relation between NIFS archives and Sokendai's archival study is to be strengthened. This is because the 4-year project on the history of inter-university research institutes will start in the next year in Sokendai.

4) US-Japan collaboration is to be started on fusion archives and workshop is to be scheduled in the US.

9. Fusion Engineering Research Center

Activities in the Fusion Engineering Research Center (FERC) are summarized as follows;

- (1) key-technology development for advanced blanket systems,
- (2) development of advanced low activation materials,
- (3) key technology verification study for development of the intense neutron source for material irradiation tests,
- (4) development of an advanced superconducting magnetic system for fusion.

Based on successful production of large-scale vanadium alloys, such as NIFS-HEAT1 and 2 (V-4Cr-4Ti), with very low impurities, various kinds of specimens have been manufactured for its characterization with liquid Li /fusion-neutron environments, for studies on processes of welding or machining *etc.* Tensile parameters have been obtained for specimens exposed with liquid Li as a function of temperature. It has been found that ultimate strength is not degraded up to 773 K, but softening happens at 1073 K. Fabrication of creep test tubes was successful and creep tests in Li without irradiation was carried out. Samples are now under neutron irradiation.

Liquid Li is the primary candidate as breeding/coolant materials for vanadium-based blanket concepts. Insulating coating against MHD effects of metal lithium coolant is one of critical issues in this concept. Detail studies on in-situ coating are in progress. Thickness of Er_2O_3 coating layer was obtained as a function of temperature, exposure time to Er-doped Li *etc.* and growth kinetics has been discussed. Irradiation effects have been studied in collaboration programs.

Study on deuterium and helium retentions of NIFS-HEATs have been continued. Total amount of retained He was saturated at a fluence of $\sim 5 \times 10^{21}/\text{m}^2$ and the saturation level was $2.75 \times 10^{21} \text{ He}/\text{m}^2$. Precipitates of Ti-O-C complex in V-4Cr-4Ti alloy have been discussed as a possible He sink.

Low cycle fatigue behaviors of JLF-1 steel have been studied using engineering size specimens. Relationships between fatigue life, total strain range, plastic strain range and stress range were obtained experimentally and discussed.

Neutronics investigation have been carried out for self-cooled liquid blanket systems for modified FFHR2 design and possible test blanket module with Li and V alloys. Results indicate that both of the lithium and Flibe self-cooled blanket systems without solid neutron multiplier are feasible concept enhancing the performance of the FFHR. The primary purpose of the test blanket module (TBM) in ITER is defined as validation of the tritium production rate predicted based on the neutron transport calculation. Spectral control is necessary for the module to simulate fusion DEMO blanket conditions. For this purpose, the module is covered with a B_4C layer to shield thermal neutrons in the calculation. It is found that the impact of the

B_4C layer is significant and more detail consideration will be required in designing the TBM.

Installation of a cryogenic irradiation system has been completed in the fusion neutron source (FNS) facility in JAERI. Total neutron production of $5.35 \times 10^{17} \text{ n}$ during the first irradiation test. Change in resistance of copper wires was measured. Two Nb_3Al wires were prepared. One was rapid heated and quenched (RHQ). The other was annealed at 1073 K for 10 hours after RHQ. Critical temperature of these wires has been under investigation.

Development of V-based superconductor is continued. A multifilamentary wire was prepared with (Hf, Zr)/V/Ta 55 cored by applying a rapidly-heating and quenching (RHQ) process to the powder-in-tube processed simple precursors (Hf-Zr metal powder mixture/V tube composite). It has been found that optimum post-annealing temperature after the RHQ is drastically lower in this study than that of temperature on the conventional diffusion process.

Development of RHQT processed Nb_3Al superconductors is carried out with a reduced Nb configuration utilizing tantalum matrix instead Nb matrix. All the Ta matrix JR precursors could be extruded and drawn down to 0.8 mm ϕ without any breaking, where Al layer thickness is adjusted to the same value of the conventional Nb matrix precursor.

The collaboration program on material irradiation test facility has been completed in this fiscal year. The program continued for five years after started in 2000. The main results are summarized as follows.

- (1) Stable liquid lithium flow is confirmed with the flow velocities up to 15 m/s. Thickness variation of the flow is carefully measured and the amplitude is 2 mm at the velocity of 15 m/s.
- (2) It is confirmed that Fe-Ti alloy is effective to control nitrogen concentration in liquid lithium and that Y metal is promising to remove tritium from the lithium flow.
- (3) An alternate design of high flux test module is proposed for optimization of temperature control in the test cell. Specimens are set in cast-like capsules and precise measurement of specimen temperature is possible in this design. A stepwise approach by comparing calculation and experiment results in improvements in temperature uniformity and controllability in the cell.
- (4) DBTT shift of a ferritic steel is successfully measured by Master Curve Method with use of 1/2 size and standard size CT specimens. Further efforts are necessary to develop small specimen test technology utilizing smaller CT specimens.
- (5) Experimental study has been carried out on the neutron emission spectra and activation cross-section in accelerator structure elements. The data base for designing the irradiation facility is much improved.

(Noda, N.)

§1. Neutronics Investigation into a Test Blanket Module with Li and V alloys

Muroga, T., Tanaka, T.

Technical discussion on ITER-Test Blanket Modules (TBM) has been made in Test Blanket Working Group (TBWG)[1]. The discussion is based on the concepts of breeding blankets to be developed for DEMO. The present concepts of lithium self-cooled blanket for DEMO are categorized into “No beryllium (Li/V)” and “With beryllium (Li/Be/V)” concepts. The former and the latter systems use neutron reaction of ${}^7\text{Li}$ ($n, n\alpha$)T and ${}^9\text{Be}$ ($n, 2n$) ${}^2\text{He}$ for enhancing the Tritium Breeding Ratio, respectively. A Design Description Document was presented from Russia based on Li/Be/V blanket concept. However, the document based on Li/V concept has not been presented to TBWG yet.

The Li/V concept has some advantages over Li/Be/V concept; (1) the blanket structure can be simplified, (2) the system is free from the issues of natural resource limit and handling safety concerning beryllium, (3) no periodic replacement of blanket because of the lifetime of Be is necessary. The present study is the initial effort of investigating Li/V TBM from the neutronics aspects. In this report, the neutron energy spectrum and tritium production rate have been calculated using MCNP code with JENDL-3.2 database to characterize the Li/V test modules to be installed as ITER-TBM.

The primary purpose of the module test was defined as validation of the tritium production rate predicted based on the neutron transport calculation. For this purpose the module was designed to be composed of sectioned thick boxes which accommodate slow Li flow. The schematic view and cross section of the module is given in figure 1. This system enables to measure the tritium production rate as a function of the distance from the first wall. The size of the four boxes was limited ($\sim 0.027\text{m}^3$) so as to satisfy the introduction limit of liquid lithium into the ITER test port. In Figure 1, there is a thin Li layer behind the first wall where Li is flowing with relatively high rate. The purpose of the layer is to cool the first wall and test MHD effect. The use of Li in this layer is, however, optional.

Spectral control is necessary for the module to simulate fusion DEMO blanket conditions. For this purpose, the module is covered with a B_4C layer to shield thermal neutrons. Figure 2 shows the result of calculation for tritium production in the module for the cases with and without the B_4C cover of 7.5 mm thick. With the cover, tritium production rate decreases but the contribution of ${}^7\text{Li}$ reaction to the overall tritium production increases significantly.

The contribution of ${}^7\text{Li}$ reaction to overall tritium production can be a parameter showing the spectral effects in the blanket area. The calculation implies that with coverage of B_4C layer of 2~5mm, the tritium production reaction from Li in the module is similar to that in the Li/V blanket. In the module experiment, the thickness of the B_4C

cover can be a parameter for verifying the neutron transportation calculation.

Reference

- 1) V.A. Chuyanov, “ITER Test Blanket Working Group activities: a summary, recommendation and conclusions”, *Fus. Eng. and Design* **61-62**, 273 (2002).

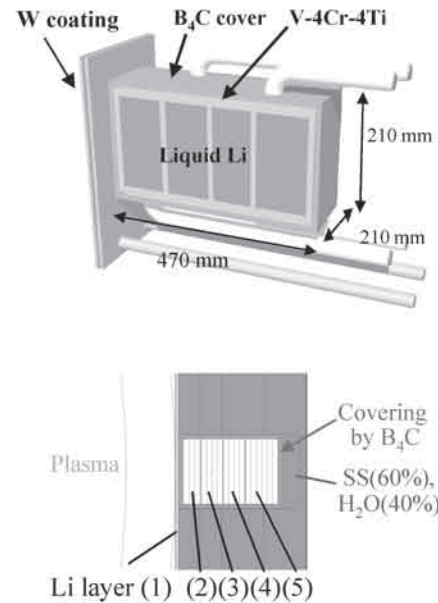


Fig. 1 The schematic view and cross section of the Li/V test module.

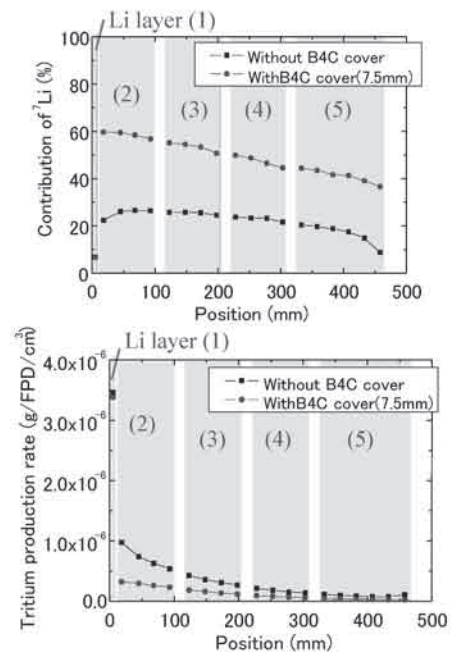


Fig. 2 Tritium production rate (upper Fig.) and contribution of ${}^7\text{Li}$ ($n, n\alpha$)T reaction to overall tritium production (lower Fig.) as a function of the position in the Li/V test module.

§2. Development of 14 MeV Neutron Irradiation Test System for Superconducting Magnet Materials

Nishimura, A.

Since neutron would come out of plasma vacuum vessel through ports, importance of evaluation of neutron irradiation effect on superconducting magnet increases on a design process of ITER. A new test facility using a GM refrigerator was installed to evaluate the effects of pure 14 MeV neutron irradiation on the superconducting magnet materials at FNS in JAERI under collaborations among Universities, National Institutes and JAERI. The first irradiation test was carried out for three weeks on September, 2004, and the second was done for one week in March, 2005. This report will describe the test facility and some typical results obtained in these irradiation tests.

The test facility was designed and assembled at FNS as shown in Fig.1. To keep samples at 4.5 K during the irradiation without liquid helium, a GM refrigerator was adopted. The refrigeration capacity is 0.5 W and the helium compressor was placed at the basement of the other experimental hall. FNS has a rotating target system which can produce 14 MeV neutron at the rate of 3×10^{12} n/s. Samples are set-up on the cold target and the neutron irradiation can be carried out keeping the sample temperature at 4.5 K. On the cold stage, the following five samples were attached. (1) Tough pitch copper wire. (0.28 mm ϕ) (2) Oxygen free copper wire. (0.299 mm ϕ) (3) Nb₃Al wire. (As-RHQ. 0.79 mm ϕ) (4) Nb₃Al wire. (RHQ + annealed. 0.79 mm ϕ) (5) Nb₃Sn wire. (0.70 mm ϕ)

Change in resistance of copper wires was measured. Two Nb₃Al wires were prepared. One was rapid heated and quenched (RHQ). The other was annealed at 1073 K for 10 hours after RHQ. Critical temperature of these wires was investigated. The cold stage temperature was measured with Cernox sensor and temperature was kept at 4.5 K. Two sensors were prepared to compare the irradiation damage.

At the top of cryostat, the following samples are attached. (1) Glass fiber reinforced plastic. (GFRP, G10-CR) (2) Polystyrene powder. (Molecular size was selected) (3) TEM samples of Nb₃Sn and NbTi wires. (4) Nb foils.

GFRP samples are three-point tested after irradiation and interlaminar share strength (ILSS) is evaluated. A newly developed mechanical testing machine is shown in Fig.2. Polystyrene powder, of which molecular size was adjusted, was irradiated and change in size was investigated.

During the first irradiation test, total neutron production of 5.35×10^{17} n was achieved and neutron fluence at the center of the cold stage was 1.47×10^{20} n/m². At the second irradiation test, the total neutron production was 2.54×10^{17} n and neutron fluence at the center of the cold stage was 0.70×10^{20} n/m². Therefore, the total neutron fluence at the center of the cold stage was 2.17×10^{20} n/m².

Results of change in resistance of copper wires are shown in Fig.3. By using a parameter of dpa, the data can be plotted on a linear relation on a log-log diagram. The irradiation test continues to a fiscal year of 2005.

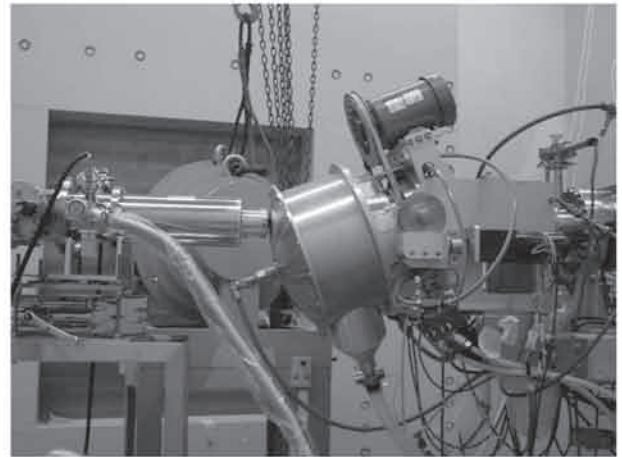


Fig. 1 Set up of cryogenic target with GM refrigerator. (March 7, 2005)

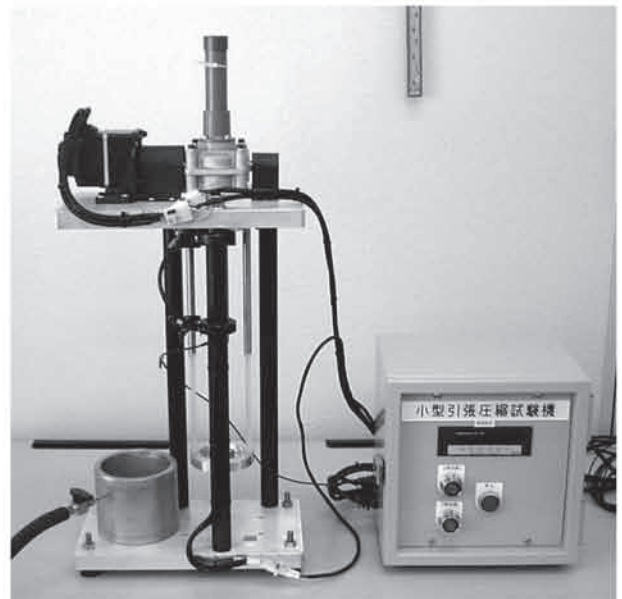


Fig. 2. A three-point bending test facility for evaluating interlaminar shear strength.

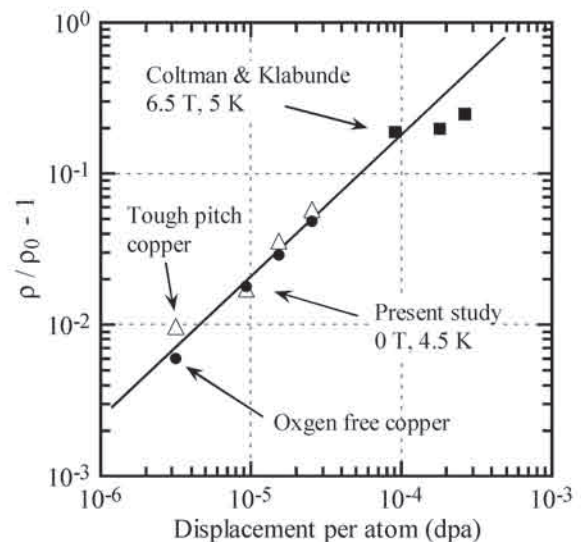


Fig. 3 Change in resistance of copper wires after neutron irradiation.

§3. Tensile Properties of Low Activation Vanadium Alloy after Liquid Lithium Exposure

Nagasaka, T., Muroga, T.
Li, M., Hoelzer, D.T., Zinkle, S.J. (ORNL)
Grossbeck, M.L. (Univ. Tennessee, USA)
Matsui, H. (IMR, Tohoku Univ.)

Vanadium alloys are recognized as attractive candidate structural materials for liquid Li cooled blanket for fusion reactor. Transfer of impurities occurs between V alloy and liquid Li. Generally, C and N migrate to V alloy from Li, while O is removed from V alloy by Li. However, the mechanisms of the transfer, distribution of the impurities after Li exposure and the effects on mechanical properties have not been clarified. In the present study, a candidate V-4Cr-4Ti alloy, designated as NIFS-HEAT-2, was exposed to liquid Li for up to 1963 hr. The impurity transfer, impurity distribution and its effect on tensile properties were investigated.

The reference low activation V-4Cr-4Ti alloy, designated as NIFS-HEAT-2, was cold-rolled into 0.25 mm-thick sheets, followed by annealing at 1273 K for 2 hr. The sheets were cut into coupon specimens with the size of 0.25 X 5 X 25 mm. The exposure temperature to Li (T_{Li}) was 973 K and 1073 K. The exposure time was 255 to 1963 hr. After the exposure, Li was chemically removed by liquid ammonia. From the coupons, miniature tensile specimens with a size of 0.25 X 4 X 16 mm (gauge: 0.25 X 1.2 X 5 mm) were punched out. The residual punched-coupons were chemically analyzed for C, N and O.

Table 1 lists the results of chemical analysis after the Li exposure. C and N impurity levels were increased with exposure time by contamination from the Li, while O was decreased by scavenging by the Li.

Figure 1 and 2 present the tensile parameters obtained for specimens exposed with liquid Li at 1073 K (T_{Li}). From the data at room temperature (943 hr), miniature tensile tests show data scattering of about 40 MPa in strength (YS, UTS) and 10 % in elongation (UE, TE). Considering these scattering, change in UTS was small until 773 K ($T_{Tensile}$) after Li exposure at 1073 K (T_{Li}) for 428 and 943 hr., while degradation of UTS at 973 and 1073 K ($T_{Tensile}$), such as 50 and 80 MPa, respectively, was considerable. On the other hand, elongation decrease by Li exposure was observed at RT and 773 K ($T_{Tensile}$), but not at higher temperature. However, all the specimens still keep higher ductility than 6.5 % in UE and 13 % in TE.

Thousands wppm of C and N contamination indicated in Table 1 did not introduce significant hardening in both hardness and tensile tests. From microstructural observations, the contaminated C and N were thought not to induce solid solution hardening, since they were absorbed by the Ti-C-N type precipitates.

Possible mechanisms of 80 MPa softening at 1073 K ($T_{Tensile}$) with impurity reduction are (1) loss of precipitation hardening by Ti-C-O type precipitates existing before the lithium exposure and (2) loss of solid solution hardening by O. Another mechanism independent of O reduction is (3) change

Table 1 Impurity concentrations in NIFS-HEAT-2 (V-4Cr-4Ti) before ($t_{Li} = 0$) and after ($t_{Li} > 0$) liquid Li exposure

Exposure temperature, T_{Li} / K	Exposure time, t_{Li} / hr	C, C_C / wppm	N, C_N / wppm	O, C_O / wppm
	0	62	84	158
973	255	142	342	142
	499	280	1000	171
1073	260	238	884	51
	428	130	143	66
	943	477	2273	29
	1443	505	2317	79
	1963	797	3420	47

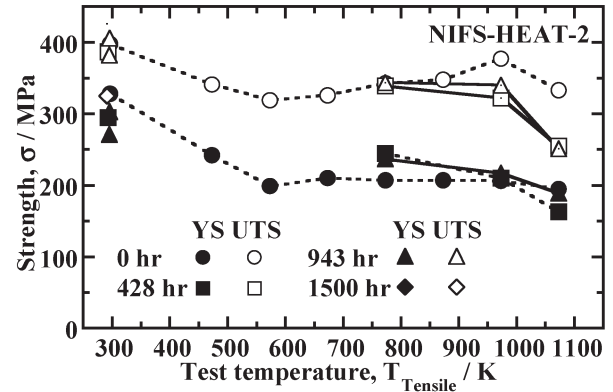


Fig. 1 Tensile test temperature ($T_{Tensile}$) dependence of yield strength (YS, 0.2 % proof stress) and ultimate tensile strength (UTS) of NIFS-HEAT-2 before and after the Li exposures at 1073 K (T_{Li}).

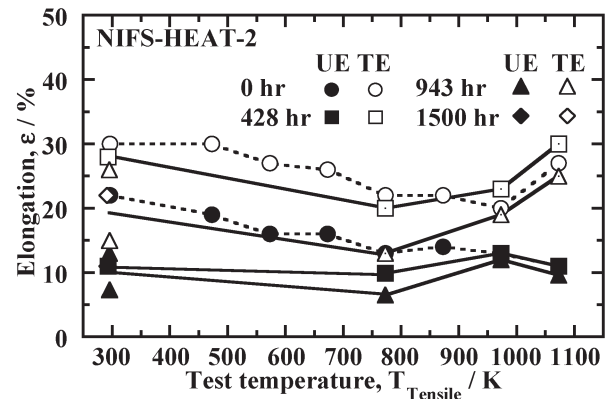


Fig. 2 Tensile test temperature ($T_{Tensile}$) dependence of uniform elongation (UE) and total elongation (TE) of NIFS-HEAT-2 before and after the Li exposures at 1073 K (T_{Li}).

of grain boundary condition. Assuming Orowan type strengthening for (1) case, the contribution of Ti-C-O precipitates is estimated as less than 5 MPa. For (2) case, the strength drop of 16 MPa would be explained, if Ti-C-O precipitates release O into the matrix during tensile tests at 1073 K ($T_{Tensile}$). (3) case is the effect of the precipitates covering grain boundaries. Enhancement of grain boundary slip and local fracture of the precipitates are possible. Investigation on the grain boundary effects are undergoing to complete the mechanism analysis of impurity transfer and change in tensile properties at high temperature.

§4. Fabrication and Superconductivity of V-based Laves Phase Compound Multifilamentary Wires Synthesized by a RHQ Process to PIT Precursors Using a V Tube

Hishinuma, Y., Nishimura, A.
Kikuchi, A., Iijima, Y., Takeuchi, T. (NIMS)
Inoue, K. (Dept. Electrical and Electronic Eng.,
Tokushima Univ.)

V-based Laves phase compounds, $V_2(\text{Hf,Zr})$, show very attractive superconducting properties a maximum $T_c = 10.1$ K, maximum H_{c2} above 20 T and a insensitivity to mechanical strain. In addition, V-based Laves phase compound shows much higher radiation resistance than that of Nb-based A15 compound wires and tapes. Therefore we thought that Laves phase compound superconductors were promising as low activation and high field conductors for advanced fusion reactors. However, $V_2(\text{Hf,Zr})$ precursor (Hf-Zr alloy/V matrix) is very hardness and low workability, so we thought that it needed a new process which does not pass through the conventional diffusion reaction between Hf-Zr alloy and V matrix in order to improve workability and superconducting properties. Then, we fabricated the Laves phase compound multifilamentary wire by applying a rapidly-heating and quenching (RHQ) process to the powder-in-tube processed simple precursors (Hf-Zr metal powder mixture/V tube composite) and its microstructures and superconducting properties was investigated.

First, high purity metal hafnium (Hf) and zirconium (Zr) powders were adjusted to have equal molar ratio. This powder was well ground by hand, and then wet ball-mill processing was carried out for 3 hours to homogenise the mixed metal powder. After the ball-mill processing, mixed powder was packed into V tubes. This composite ($(\text{Hf}_{0.5}\text{Zr}_{0.5})/\text{V}$) was cold-rolled with a grooved roller and the wire drawn a diameter of about 1.20 mm. Intermediate annealing was carried out several times at

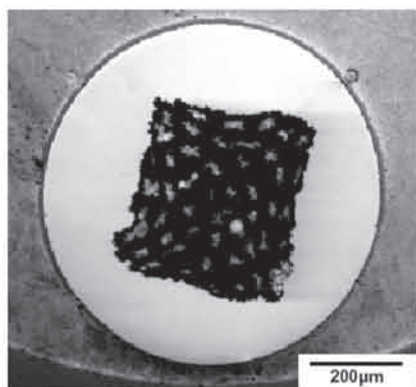


Fig. 1. Typical SEM photograph of the cross-sectional structure on the prepared (Hf, Zr)/V-Ta 55 cored multifilamentary wire.

1173 K for 1 hour to soften this composite during this deformation. The (Hf,Zr)/V composite was cut into short pieces, and they were stacked into a tantalum (Ta) tube. The number of stacked (Hf,Zr)/V composite was 55 pieces. This composite ($(\text{Hf,Zr})/\text{V}/\text{Ta}$) was cold-rolled with a grooved roller and drawing machine to wire of about 0.754 mm diameter as well as (Hf,Zr)/V composite. Fig.1 shows a typical SEM photograph of the cross-sectional structure of the prepared (Hf, Zr)/V-Ta 55 cored multifilamentary wire. The precursor wire was set into RHQ apparatus, and it was applied to the RHQ treatment in a dynamic vacuum chamber. The precursor wire was continuously heated up to the several temperatures with moving at 1.0 m/sec of velocity. The precursor wire was heat treated by resistive-heating during 0.1 sec using dc current. Subsequently, the wire was continuously quenched into the Ga bath at about 320 K from above 2500 K. Then, some of the as-RHQ wires were additionally post-annealed at several temperatures for 10 hours in the vacuum.

J_c value of sample post-annealed at 873 K was estimated to be about 100 A/mm² at 4.2 K and 10 T. J_c dependence of magnetic field on the sample post-annealed at 873 K was higher than for the as-quenched sample, and then the H_{c2} value calculated by Kramer's formula was 16 T for the sample post-annealed at 873 K was also improved compared to the as-quenched sample. On the other hand, the J_c dependence on magnetic field for the sample post-annealed at 1173 K was lower than for the as-quenched sample as well as its H_{c2} value. We found that optimum post-annealing temperature in this study was drastically lower than that of temperature on the conventional diffusion process.

ACKNOWLEDGEMENT

We would like to thank for Tsukuba Magnet Laboratory of NIMS for providing us with using high magnetic field magnet facilities for the I_c measurement.

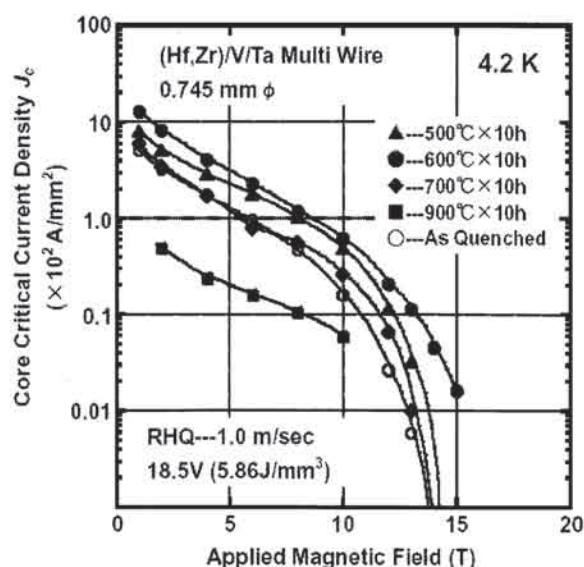


Fig. 2. Typical J_c - B curves of RHQ samples

\$5. Neutronics Investigation of Self-cooled Liquid Blanket Systems for Modified FFHR2 Design

Tanaka, T., Muroga, T., Sagara, A.

The original design of the FFHR2 [1] adopted self-cooled Flibe blanket system of 90 cm in thickness with a structural material of ferritic steel, JLF-1, and solid beryllium neutron multiplier. Recently, modified FFHR2 design with increased blanket space of 120 cm has been proposed to improve the radiation shielding performance [2]. This modification of the dimensions provides the possibility for other types of simple and attractive self-cooled liquid blanket systems without using solid neutron multiplier. The concept of liquid lithium cooled blanket system with a structural material of vanadium alloy has been studied for the preferable compatibility, mechanical property at high temperature and high efficiency operation at up to $\sim 700^\circ\text{C}$. Coolant of Flibe also could be used with vanadium alloy for high temperature operation by REDOX control with MoF_6 or WF_6 . In the present study, the compatibility of tritium self-sufficiency and neutron shielding ability of the lithium and Flibe self-cooled blanket systems without solid neutron multiplier was investigated for application to the modified FFHR2 design.

Neutronics calculation was performed with the MCNP-4C Monte Carlo code and JENDL 3.2 nuclear data library. Local tritium breeding ratio (local TBR) and fast neutron flux at outside of radiation shield were calculated for the simple geometry shown in Fig. 1. The torus was fully covered with the uniform tritium breeding channels and radiation shield. The breeding channels consisted of lithium or Flibe coolant (~ 83 vol.%) and a structural material of V-4Cr-4Ti (~ 17 vol.%). To enhance the tritium production, the ratio of ^6Li in both of lithium and Flibe coolant was enriched to 35 %. Radiations were shielded with a layer of JLF-1 (~ 70 vol.%) and B_4C (~ 30 vol.%) to avoid critical damage on super-conducting magnets. For the compatibility of tritium self-sufficiency and neutron shielding, the local TBR of $> \sim 1.3$ and fast neutron flux (> 0.1 MeV) of $< 1.0 \times 10^{10}$ n/cm 2 /s at outside of the radiation shield should be satisfied simultaneously. The balance of thickness for the breeding channels and radiation shield was examined under the constant total thickness of 120 cm and the neutron wall load of 1.5 MW/m^2 .

Figure 2 shows the achievable local TBR and neutron shielding performance by the present calculation. In the lithium blanket system, the local TBR increased with the thickness of the breeding channels exceeding 1.3. In parallel, the fast neutron flux at outside of the radiation shield also increased and exceeded 1.0×10^{10} n/cm 2 /s. Therefore, the thickness of the lithium breeding channels was decided to ~ 55 cm due to the limitation of the shielding ability. In contrast, the fast neutron flux for the Flibe blanket system never exceeded the limitation of 1.0×10^{10} n/cm 2 /s even for much thicker breeding channels, i.e. much thinner radiation shield. This indicated that the Flibe coolant itself has

superior shielding ability compared with the lithium coolant. However, the local TBR weakly increased with the thickness of the breeding channels. Since the increase of the local TBR was within $\sim 1\%$ for thicker channels and close to 1.3, the thickness of the breeding channels was decided to 60 cm. The TBR and shielding ability of the two blanket systems may be improved further with design efforts.

The present results of neutronics investigation indicated that both of the lithium and Flibe self-cooled blanket systems without solid neutron multiplier are feasible concept enhancing the performance of the FFHR. The FFHR design with these two blanket systems are designated as FFHR-LV and FFHR-FV [3]. Further neutronics investigation will be carried out focusing on three-dimensional effect of the helical blanket structure.

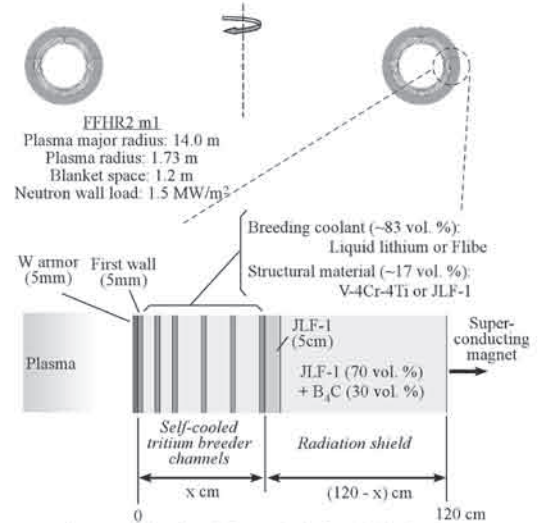


Fig. 1. Geometric model of self-cooled liquid blanket system for nuclear calculation.

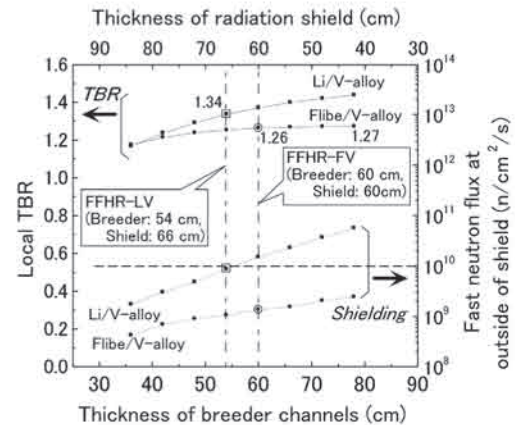


Fig. 2. Local TBR and neutron shielding performance calculated for the lithium and Flibe blanket systems with ^6Li enrichment to 35 %

References

- [1] A. Sagara *et al.*, Fusion Engineering and Design, 49-50(2000)661-666.
- [2] A. Sagara *et al.*, Nuclear Fusion, 45(2005)258-263.
- [3] T. Tanaka *et al.*, Fusion Science and Technology, 47(2005)530-534.

§6. Development of Tantalum Matrix RHQT Processed Nb₃Al Superconductors

Takeuchi, T., Banno, N., Kikuchi, A., Iijima, Y.,
Noda, T. (Nat. Inst. Mater. Sci.)
Nishimura, A., Hishinuma, Y.

In a tokamak-type fusion reactor, magnet systems are composed of a toroidal field (TF), a poloidal field (PF), and central solenoid (CS) coils. Among these, the TF coils are placed at the nearest position from the plasma, and their structure and composition are affected by neutron irradiation depending on the spectrum and the fluence. The CS coils next to the TF coils are also possibly affected by the neutron irradiation. Superconducting materials, such as NbTi, Nb₃Sn and Nb₃Al, are considered for use in ITER and commercial reactors. However, Nb produces long half-life radioactive nuclide-like ⁹⁴Nb ($T_{1/2} = 2 \times 10^4$ y) under heavy irradiation conditions. It is therefore important to suppress the excess use of Nb in these conductors; diffusion barrier and matrix materials, except for superconducting filament materials.¹⁾

Since Nb₃Al shows much better strain tolerance than Nb₃Sn does, many attempts have been made to fabricate the multifilamentary and stoichiometric Nb₃Al conductor, of which aspects are key issues to be solved for its commercialization. Such a Nb₃Al conductor can be fabricated by the so-called RHQT technique; the multifilamentary Nb/Al precursor is subjected to joule heating at 1900-2000°C, quenching to a molten Ga bath around 50-100°C to form the metastable supersaturated-solid solution Nb(Al)_s filaments embedded in a Nb matrix, and then transformation annealing at 800°C to form the stoichiometric Nb₃Al filaments in a Nb matrix.

In the present study, we have replaced Nb matrix with Ta which has an advantage of a shorter half-time of induced-radioactivity when irradiated with neutrons. Ta seems to have additional advantages²⁾: (1) excellent tolerance to uniaxial and transverse stresses at a low temperature to be caused by a huge electromagnetic force, (2) higher mechanical strength at elevated temperature to suppresses undesirable creep deformation in the reel-to-reel joule-heating of the wire, (3) less reactivity with Ga to suppress the formation of Ga-rich compound on the surface of wire, like a chain of islands, during RHQ operation, (4) non-superconductive matrix in fields to suppress the magnetic instability like flux jumps of wire.

In order to examine the drawability of such Ta matrix precursors, we have prepared three kinds of Ta matrix JR Nb/Al precursors that have different volume ratios of Ta as substitution for Nb. Fig. 1 shows schematic illustrations of the three designs of Ta matrix JR precursors manufactured. The cross-sectional structure of a Ta sheath and Ta dummy filaments in the multi-strand is common to all cases, but, according to the Ta matrix design, we have changed the material species of the inter-filament barrier and the intra-filament core from Nb to Ta. Both of the barrier and the core are changed to Ta for the 1st design, only the core for the 2nd design, and neither of them for the 3rd design. The 0.2% yield stress of Ta at room temperature (170 MPa) is much larger than that of Nb (45 MPa),

the extrusion ratio was consequent as adjusted so that it was smaller than that used for conventional Nb matrix precursors. Contrary to our expectations, all the Ta matrix JR precursors could be extruded and drawn down to 0.8 mmφ without any breaking, where Al layer thickness is adjusted to the same value of the conventional Nb matrix precursor.

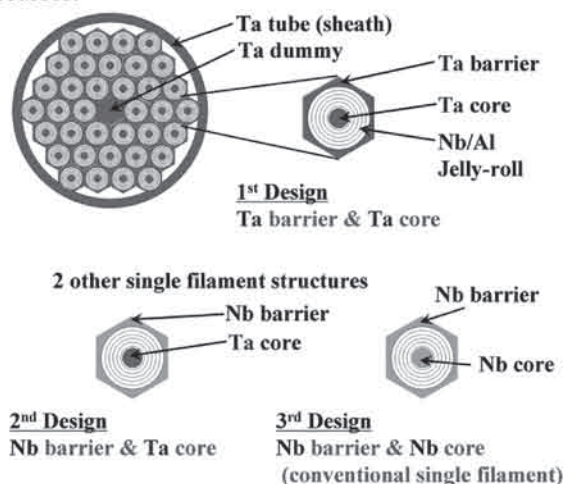


Fig. 1. Schematic illustrations of the three designs of Ta matrix JR precursor manufactured.

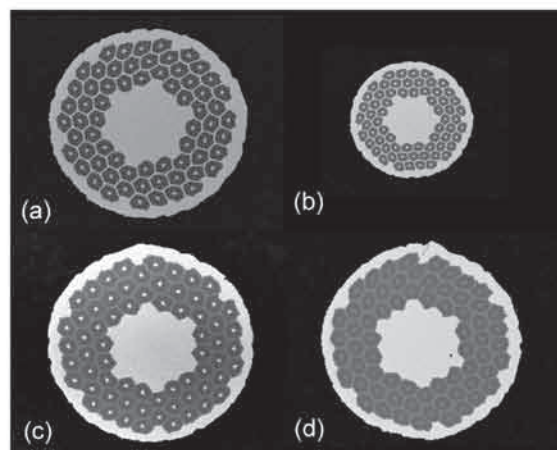


Fig. 2. Finished cross-sections of (a) the Design 1 precursors (0.8 mmφ), (b) the Design 1 at 0.5 mmφ, (c) the Design 2 at 0.8 mmφ, and (d) the Design 3 at 0.8 mmφ.

Fig. 2 shows the finished cross sections of the Ta matrix precursors manufactured. Since the 1st design Ta matrix precursors (all Ta) exhibited the best workability at least until 0.8 mm in diameter, we have further drawn it down to 0.5 mm in diameter. The JR filament diameter is reduced to about 40 μm for this 0.5 mmφ wire as shown in Fig. 2 (b).

Reference

- 1) Noda, T. et al, J. Nuc. Mat., **329-333** (2004) 1590
- 2) Takeuchi, T. et al, IEEE Trans. Appl. Supercond. **15** (2005) 3372

§7. Helium Retention and Thermal Desorption Properties of V-4Cr-4Ti Alloy (NIFS-HEAT2)

Hirohata, Y., Yamauchi, Y., Hino, T. (Hokkaido Univ.), Nagasaka, T., Muroga, T. (NIFS)

Vanadium alloy is an attractive structural material used for fusion reactor because of its low induced radioactivity and good thermal and mechanical properties at high temperatures. The vanadium alloy, V-4Cr-4Ti, may be a promising material because it shows excellent mechanical tolerance to neutron damage and low helium and hydrogen production rate during 14 MeV neutron irradiation. The first wall of V-alloy is exposed to helium ions with different energies during helium glow discharge cleaning and helium ash resulting from fusion reactions. Therefore, it is important to investigate the He retention property of the V-alloy after He ion irradiation. In this study, the helium retention property of V-4Cr-4Ti alloy (NIFS HEAT2) was examined by using an ECR ion irradiation apparatus. Ion energy of helium was taken at 5 keV, which the projected range of He ion in the sample is ~27 nm. Helium ions were irradiated in the V-alloy after annealing at 1373 K for 1 hr at room temperature with high flux ($\sim 10^{18}$ He/m²/s) and high fluences (up to 1×10^{22} He/m²), i.e. this fluence corresponds to ~90 dpa, which is comparable with that of α -particles of the operating condition of DEMO reactor. Subsequently, the retained deuterium or helium was measured by thermal desorption spectroscopy, TDS.

From SEM observation, it was found that a lot of blisters with the size of 0.1~0.5 μ m were observed on the irradiated sample, and after heating at 673 K, no significant changes were observed on the surface, but after heating at 1473 K, many blisters ruptured and pinholes were observed. Thermal desorption spectra of helium after helium ion irradiation are shown in Fig.1. Many desorption peaks were observed in the TDS spectra. These peaks were divided into three groups, i.e. Peak I was the desorption around 500K, Peak II at 826~896 K, and Peak III at temperature higher than 1100 K. The activation energies of Peak I, II, and III were obtained as 1.50, 2.35~2.59, and 3.59~4.16 eV, respectively. From these activation energies, it was found that the He desorption of Peak I, II, and III corresponded to the dissociation energies of He_nVX type defect cluster, that of He_nV₅X cluster, and the rupture of the blister and internal bubbles [1]. Here, n denoted the number of helium atom (n>1), V vacancy, and X impurity atoms, such as C, N, or O. The total amount and amounts corresponding to Peak I, II, and III are shown in Fig. 2. The amount of retained helium of Peak III and II was saturated at low fluence, while that of Peak I was gradually saturated at higher fluence. The total amount of retained He was saturated at the fluence of $\sim 5 \times 10^{21}$ He/m² and the value was 2.75×10^{21} He/m², corresponding to the concentration of 1.4 (He/V). Distribution of fine precipitates consisted of Ti-O-C complex in V-4Cr-4Ti alloy was drastically changed by the final annealing temperature [3,4]. These precipitates might act as a sink for He. Additional

experiments were conducted to investigate the effect of final annealing temperature on the He retention. Smallest retention of He was observed in the sample with annealing at 1373 K after polishing.

It is reported that the origin of the bubble and blister was He_nVX [1]. Therefore, if the V-alloy would be kept at operational temperature (V-alloy blanket; 673~923 K [2]) during both discharge cleaning and ion implantation, the amount of desorbed He for the Peak I would significantly decrease and the amount of retained He would be small.

Desorption and retention behaviors of He examined in this study could be useful for wall conditionings of first wall of the V-alloy for the blanket

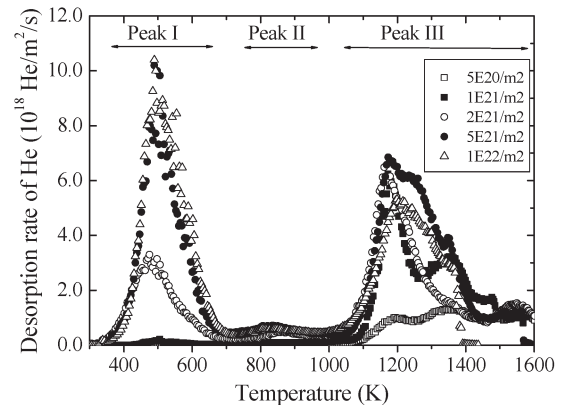


Fig.1 Thermal desorption spectra of helium after helium ion irradiation at room temperature. Ramp rate is 1 K/s.

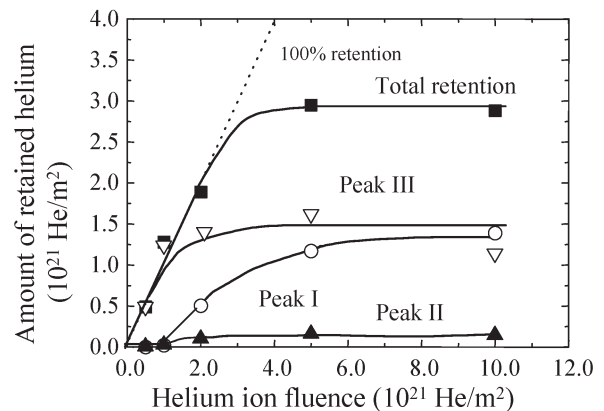


Fig.2 Amount of retained helium in the V-alloy (NIFS HEAT2) as a function of helium ion fluence

Reference

- 1) A.V. Fedorov, A.van Veen, A.I. Ryazanov, J.Nucl.Mater. 233-237 (1996) 385-389.
- 2) S.J. Zinkle, N.M. Ghoniem, Fusion Eng. and Design. 51-52 (2000) 55-77.
- 3) A. Nishimura, A. Iwahori, et.al., J.Nucl.Mater. 329-333 (2004) 438-441.
- 4) N.J.Heo, T.Nagasaka, T.Muroga, H.Matsui, J.Nucl.Mater. 307-311 (2002) 620-624.

§8. The Growth and Resistivity of In-situ Er_2O_3 Coating on V-4Cr-4Ti

Yao, Z. (Grad. Univ. Advanced Studies)
Suzuki, A. (Univ. Tokyo)
Muroga, T., Tanaka, T.

One of the critical issues for the self-cooled Li/V-alloy blanket is the magneto-hydrodynamic (MHD) pressure drop. The insulating coatings on the inner wall of components for mitigating the pressure drop are under development. An in-situ coating in liquid Li is very attractive. The previous studies [1, 2] showed the in-situ formation and stability of Er_2O_3 coating by exposing oxygen-charged V-4Cr-4Ti in liquid Li doped with Er at high temperature. In this report, the results on the growth and resistivity of the coating were shown.

V-4Cr-4Ti sheets were oxidized in flowing argon, annealed in vacuum and exposed in liquid Li doped with Er.

Fig. 1 shows the thickness of the Er_2O_3 coating with exposure time at temperature of 500-700°C. The Er_2O_3 coating was not formed at 500°C, perhaps owing to slow diffusion of Er and O, or weak reaction between Er and O at 500°C. The thickness of the Er_2O_3 coating is a function of the exposure time. The figure indicates that the Er_2O_3 coating is stable at 600°C up to 750h of exposure to liquid Li, and stable at 650°C or 700°C up to 300h. The thickness seems to saturate at $\sim 0.1\mu\text{m}$ at 600°C, $\sim 0.6\mu\text{m}$ at 650°C and $\sim 1.3\mu\text{m}$ at 700°C.

Fig. 2 shows the thickness (T) of Er_2O_3 coating formed on the V-4Cr-4Ti substrate (oxidized for 6h at 700°C, annealed for 16h at 700°C and finally exposed in liquid Li doped with Er) at 600°C, 650°C and 700°C as a function of the exposure time (t), $T^n = k \cdot t + a$. Here $a=0$ was assumed, corresponding to a negligible nucleation duration observed. The figure shows the growth kinetics of Er_2O_3 coating obey a logarithmic law with high exponent ($n \approx 3$ or 4) at 600°C, and 650°C, suggesting that the rate of growth to Er_2O_3 coating should be significantly low. The solubility of erbium is very low (0.15 wt%) in liquid lithium at 600°C. Thus slow delivery of either oxygen from substrate or erbium from Li to the interface is thought to be responsible for the slow growth of the coating. The growth process was expedited suddenly at 700°C exhibiting a low exponent ($n \approx 2$) that almost obeys a parabolic law resulting in the quick growth of the coating.

Fig. 3 shows the resistivity \times thickness of V-4Cr-4Ti coated by Er_2O_3 in vacuum ($\sim 10^{-3}\text{Pa}$) during heating comparing with a minimum requirement for design of fusion blanket. Up to $\sim 550^\circ\text{C}$, the in-situ measured resistivity was over the minimum requirement. However over 550°C , resistivity starts to drop below the minimum requirement, because the electrode degraded or disconnected owing to melting or vaporization of Ag paste as a linker. Therefore, resistivity of coating is expected still over the minimum requirement up to 700°C , by improving linking of electrodes.

The study showed the growth kinetics of in-situ Er_2O_3 coating. The coating has resistivity over the minimum requirement for insulator for fusion blanket.

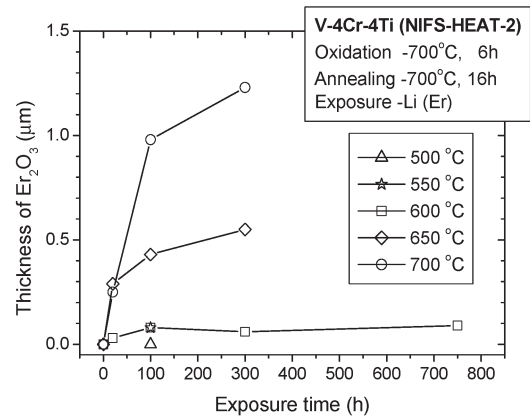


Fig.1 Thickness of Er_2O_3 coating on V-4Cr-4Ti as a function of exposure time in Li doped with Er

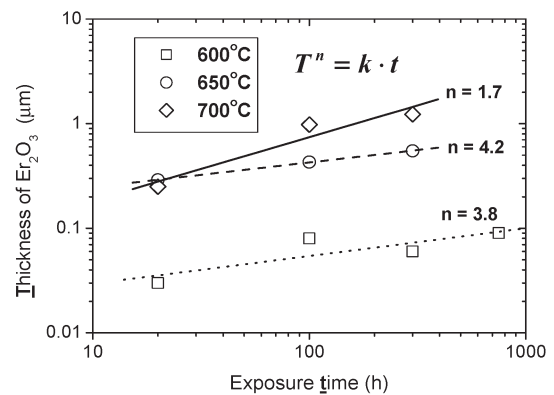


Fig.2 Thickness of Er_2O_3 coating on V-4Cr-4Ti substrate as a function of the time of exposure to liquid Li doped with Er.

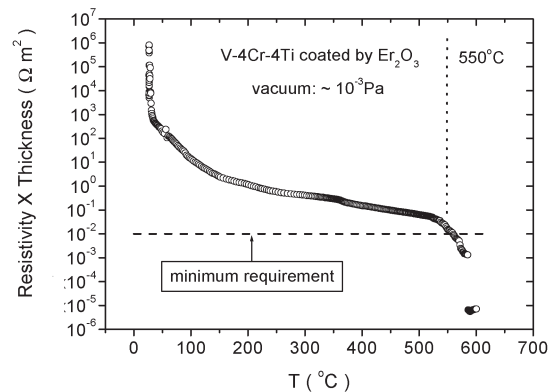


Fig.3 Temperature dependences of resistivity of V-4Cr-4Ti coated by Er_2O_3 in vacuum during heating

Reference

- 1) Yao, Z. et al.: Ann. Rep. NIFS (2002-2003) 404.
- 2) Yao, Z. et al.: Ann. Rep. NIFS (2003-2004) 436.

§9. Study on Low Cycle Fatigue Behaviors of JLF-1 Steel

Li, H. (Grad. Univ. Advanced Studies)
Nishimura, A., Nagasaka, T., Muroga, T.

Reduced activation ferritic/martensitic (RAF/M) steels are considered for structural application in potential fusion energy systems. The cyclic thermal and mechanical loading of ITER and DEMO-blankets poses the problem of fatigue at different temperature.

In this work, the low cycle fatigue (LCF) behaviors of JLF-1 RAF/M steel at 673K in vacuum condition were studied using engineering size specimens.

RAF/M steel, JLF-1 was machined to cylindrical specimens with 18 mm in parallel and 8 mm in diameter and polished along the longitudinal direction with #1500 paper to erase the circumferential machining marks. LCF tests were carried out in 5×10^{-3} Pa at RT and 673K under fully reversed axial strain control using a Shimazu Servo Pulser with a dynamic load capacity of ± 98 kN. The axial strain was measured by an extensometer (Shinko 1501-93-20, G.L. is: 12.5mm).

The relationships between fatigue life (N_f) vs. total strain range ($\Delta \epsilon_t$), plastic strain range ($\Delta \epsilon_p$) and stress range ($\Delta \sigma$) are shown from Fig. 1 to Fig.3 (the data of “RT, 0.4 %/s, Air” were taken from [1]). The total strain range, plastic strain range and stress range are obtained from hysteresis curves at around half of fatigue life ($N_f/2$). The fatigue life at 673 K is almost same as that at RT when the life is plotted against the total strain range. The regression curve at 673 K is expressed as the following equation:

$$\Delta \epsilon_t = \Delta \epsilon_p + \Delta \epsilon_e = 20.09 N_f^{(-0.4091)} + 0.5758 N_f^{(-0.06187)}$$

which at RT [1] is:

$$\Delta \epsilon_t = \Delta \epsilon_p + \Delta \epsilon_e = 91.02 N_f^{(-0.5956)} + 1.023 N_f^{(-0.09462)}$$

On the other hand, when the life is plotted against the stress range (Fig. 3), the temperature effect is clear. With increasing the temperature, the stress level is decreased.

From Fig. 1 to Fig 3, the effects of the strain rate and vacuum are very small at RT. There is no obvious difference between the data of 0.1%/s and 0.4%/s.

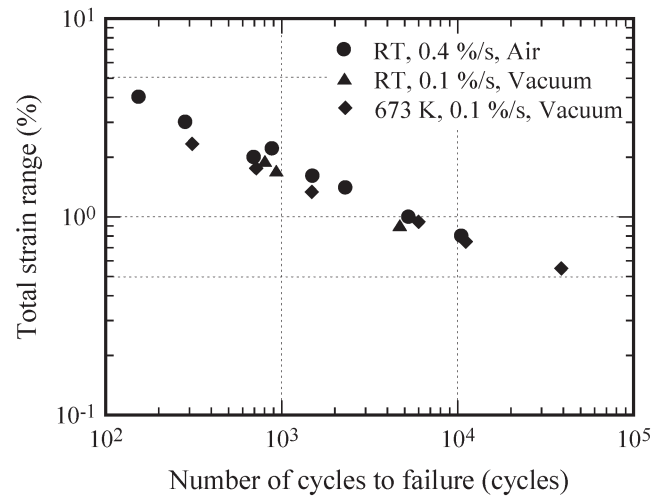


Fig.1. Total strain range vs fatigue life

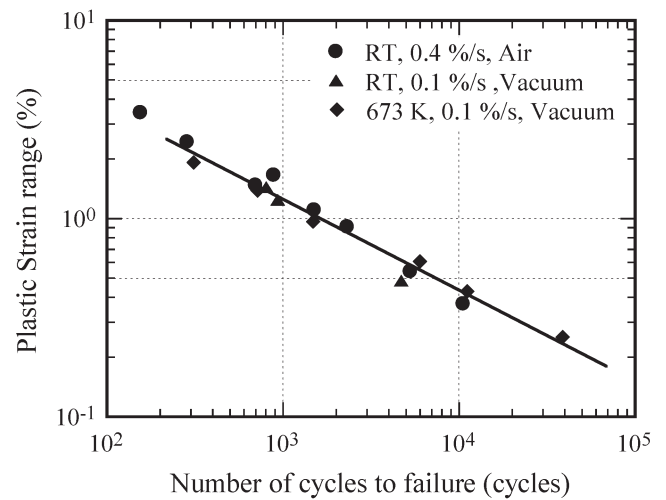


Fig. 2 Plastic strain range vs fatigue life

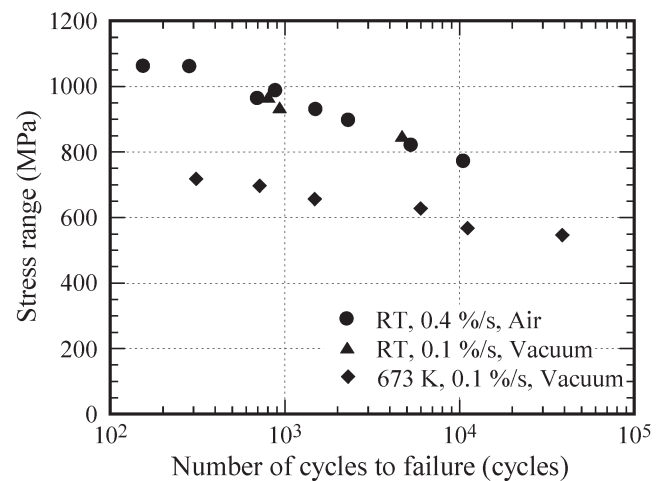


Fig. 3 Stress range vs fatigue life.

Reference:

[1] A. Nishimura, et al, J. Nucl. Mater. 283-287 (2000) 677.

\$10. Experimental Study on Liquid Lithium Flow for IFMIF Target

Horiike, H., Kondo, H., Ida, M.^{*}, Iida, T., Inoue, S., Kukita, Y.^{**}, Miyamoto, S., Muroga, T.⁺, Nakamura, Hideo^{*}, Nakamura, Hiroo^{*}, Sato, H., Suzuki, A.⁺⁺, Tanaka, T.⁺, Yamanaka, S., Yamaoka, N.
Graduate School of Osaka Univ., ^{*}JAERI,
^{**}Graduate School of Nagoya Univ., ⁺NIFS,
⁺⁺Graduate School of Tokyo Univ.

1. Introduction

To develop high flux 14MeV neutron source for study on fusion reactor materials, IFMIF (International Fusion Materials Irradiation Facility) has been designed under international collaboration. In present design of IFMIF, liquid metal lithium is employed to be D⁺ beam target, and neutrons are generated by D⁺-Li nuclear stripping reaction. The lithium flows down along a concave back wall at a velocity of approximately 15 m/s. This flow is irradiated by deuteron beams of 40 MeV, whose center is located 175 mm downstream from the nozzle

To predict variation of neutron flux in time and space, it is necessary to have knowledge of lithium target flow behavior, especially, generation and growth of surface perturbations and thickness variation.

2. Experimental facility

The present experiment was carried out with the lithium loop at Osaka University. A test section of free surface flow is mainly consisted of a two staged nozzle and a 70mm wide straight flow channel. The nozzle geometry is almost the same as the JAERI design. By the nozzle, rectangular flow of 10 mm height and 70 mm width is formed. Flow velocity can be up to 15m/s under pressure, and 5 m/s under vacuum.

3. Results and Summary

Figure 1 show pictures of lithium free surface taken by a CCD camera with a strobe which half width of emission is approximately 20 micro seconds. Flow directions are right to left in the pictures. In the pictures, longitudinal disturbances with slightly angle to flow direction, that is called surface wake, were observed.

The surface wake is generated at corners between the nozzle and side walls of the flow channel, and at the nozzle edge probably because chemical compounds attached at the edge. The wake shape was compared with analytical study of Lamb[1], and showed good agreement. By the analysis, wakes from the corners have less affect to beam irradiation region.

On the flow surface, small waves that wavelength is around 1 mm were also observed. The waves were not observed in the velocity region of less than 3m/s, and have periodicity to flow direction in the velocity region of around 5 to 9 m/s. the periodic waves was compared with a liner stability theory on a free surface shear layer underneath of free surface around the nozzle edge[2]. The results show good agreement. In the velocity region of more than 10m/s, waves have no periodicity and were consider being turbulent flow.

Surface height variation was measured by a contact probe. When the probe contacts with the lithium flow surface, an electrical circuit between the probe, lithium flow and the flow channel is closed. And the contact with the flow surface can be detected. Figure 2 shows results of the measurements. The measurement position was at the center

of the beam region that is 175 mm downstream from the nozzle. The figure shows average thickness of the flow by the plots, and thickness variation by the bars against mean flow velocity. The average thickness increases as the velocity increase in the velocity region of 2 to 8m/s. And the thickness decreases to the initial thickness of 10mm in the velocity region of more than 8 m/s. The thickness variation is probably caused by surface wakes. The amplitude of the height variation increases monotonically, and it is approximately 2 mm at the velocity of 15 m/s. The variation is considered to be caused by the surface waves and wakes from the edge. In present experiment, the nozzle edge is fouled by the chemical compounds, and that compounds seem to increase the surface variation as surface wake. Further experiment with cleaner nozzle is planned to be conducted and the results will be reported soon.

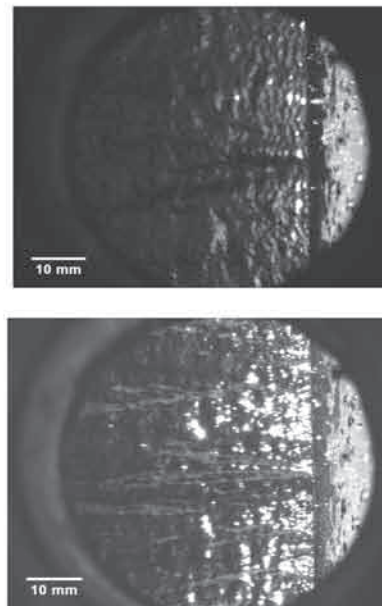


Fig.1. Pictures of lithium flow surface
Upper : Mean velocity is 7 m/s
Bottom : 13 m/s

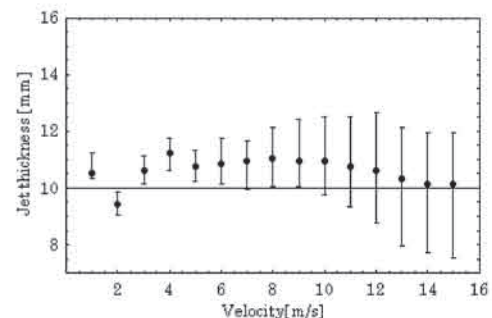


Fig.2. Thickness variation of the flow against the mean velocity at the beam center

Reference

- [1] H.Lamb, Hydrodynamics, article 256 and 272, sixth ed 1932, Cambridge University Press
- [2] K. ITOH, H. NAKAMURA and Y. KUKITA, "Free-surface Shear Layer Instabilities on a High-speed Liquid Jet" Fusion Technol., Vol.37, pp.74-88, (2000)

§11. Control of Nitrogen Concentration in Liquid Lithium by Iron-Titanium Alloy

Tanaka, S., Hirakane, S., Yoneoka, T. (Univ. of Tokyo), Muroga, T.

Reducing the nitrogen concentration in liquid lithium is one of the most important steps in creating a liquid lithium blanket system. In this study, in order to verify the nitrogen gettering performance of Fe-Ti alloy, the variation in the nitrogen concentration in liquid lithium, into which Fe-10at.%Ti or Fe-5at.%Ti getter was immersed, was examined. In the experiments, the alloys were cut into plates of 1 x 10 x 40 mm³. The mass of the lithium was 25 g. The initial nitrogen concentration in liquid lithium was adjusted to 90-280 wtppm by contacting N₂ gas with the liquid lithium (Sieverts' method). The experiment was conducted by using a molybdenum crucible in a stainless-steel pot in the glove box filled with argon gas. The nitrogen concentration in the sampled lithium was measured using the ammonia method.

Figure 1 shows the variation in the nitrogen concentration in liquid lithium at 873 K under different immersion conditions. Based on the results, it was concluded that Fe-Ti alloy absorbs the nitrogen in the liquid lithium, although the effect is not durable, and that Fe-5at.%Ti possesses a better gettering performance than Fe-10at.%Ti. The total quantities of absorbed nitrogen for initial nitrogen concentration of 280 wtppm are comparable to the amount of titanium existing between the surface and a depth of several μm , provided that the absorbed nitrogen is trapped by titanium as TiN. Based on the fact that the nitrogen concentration in liquid lithium decreased from the initial 100 wtppm to 30 wtppm due to both Fe-10at.%Ti and Fe-5at.%Ti, Fe-Ti alloy was determined to be effective even when the nitrogen concentration is low. Note that the value of 30 wtppm is almost equal to the measurement limit. In order to clarify the effect of temperature on the gettering performance, the nitrogen concentration in liquid lithium with the Fe-Ti alloys at 723 K was measured until the variation stopped. Then, the temperature was changed to 873 K and the concentration was measured again until the variation stopped. The result of this experiment is given in Fig. 2. The nitrogen concentration at which the variation stopped at 873 K was lower than that at 723 K in both Fe-Ti alloys. This temperature dependence indicated that some absorbed nitrogen can migrate easily between the liquid lithium and the Fe-Ti alloy.

XRD spectra were obtained of the Fe-Ti alloys before and after the immersion test at 873 K with the initial nitrogen concentration of 250 wtppm. Before the immersion, $\alpha\text{-Fe}$ and Fe₂Ti peaks were detected for Fe-10at.%Ti, while only $\alpha\text{-Fe}$ peaks were observed for Fe-5at.%Ti. After immersion, TiN peaks emerged for both Fe-10at.%Ti and Fe-5at.%Ti. In addition, a decrease in the Fe₂Ti peaks was noticed for Fe-10at.%Ti. These

observation suggest that some of the absorbed nitrogen formed TiN by consuming the titanium in the Fe₂Ti of Fe-10at.%Ti, and by combining with the titanium dissolved in the $\alpha\text{-Fe}$ matrix of Fe-5at.%Ti.

XMA images of the sample were also studied. For Fe-10at.%Ti sample after the immersion test, a zone considered to be TiN was detected only near the surface, at a depth less than several μm . The distribution of titanium on the surface was determined by XMA before and after the immersion. The localization of titanium was also determined. This localization could have been caused by the gathering of the TiN generated by the nitriding of Fe₂Ti in the surface region. Since some regions of the surface did not contain TiN, it is reasonable to assume that something other than TiN coverage of the surface impeded the nitrogen absorption.

XPS spectra were taken after the immersion test during the surface sputtering for Fe-10at.%Ti. TiN peak at 396.7eV was observed at a depth of 200-4000nm. The concentration of the TiN peak was smaller at 0-200nm than that at 200-4000nm.

Temperature dependence of the attained nitrogen concentration (Fig. 2) and the limit of nitrogen concentration in the case of initial nitrogen concentration of 280 wtppm were discussed from these results and an internal diffusion barrier was thought to exist in the bulk of the alloy to impede nitrogen diffusion.

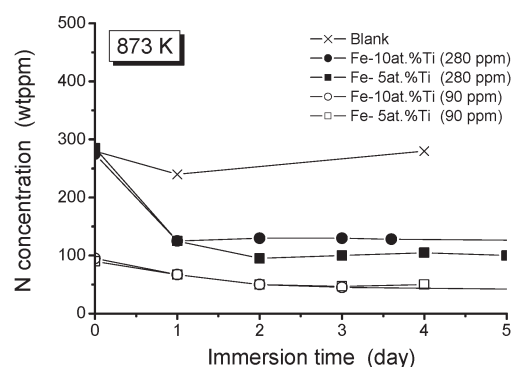


Fig. 1 Variations in the nitrogen concentration in liquid lithium at 873K.

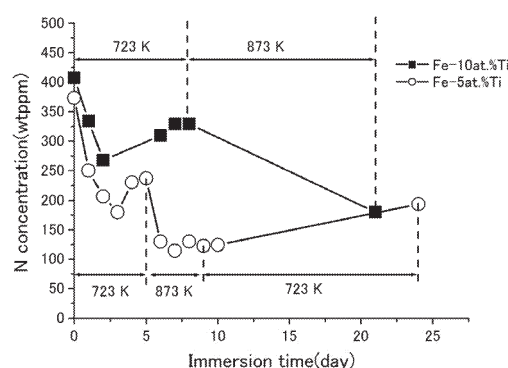


Fig. 2 Temperature dependence of the nitrogen concentration in liquid lithium.

§12. An Experimental Study to Recover Tritium by Yttrium from IFMIF Li Loop

Fukada, S. (Kyushu University)
Muroga, T.

Liquid Li is proposed as a flowing target to generate neutron for the International Fusion Materials Irradiation Facility (IFMIF). Fast D^+ ion beam hits the flowing Li target to generate fast neutrons by a D-Li stripping reaction. At the same time, tritium is generated in the Li target, and its rate is estimated 7g/year. In order to operate IFMIF continuously and safely, tritium should be recovered from the flowing Li. Yttrium is considered the most effective material to remove tritium from Li. The target concentration for the tritium recovery is 1 ppm in Li.

Fig. 1 shows a comparison in equilibrium H_2 pressure among the Li hydride (a chain line), the Y hydride (an upper solid line), the α -phase Y (a lower solid line) and the α -phase Li (a dashed line). As seen in the figure, the dissociation plateau pressure of the Y hydride is lower than that of the Li hydride. The tritium recovery in IFMIF will be performed under the condition where Y particles are in the hydride phase and the tritium concentration in Li is 1 wppm. Then, we need to operate the Y bed at 250 °C from the crossover between the equilibrium pressure of YH_2 and that of the α -phase Li. This operation temperature of 250 °C was targeted at the previous design for the IFMIF Y trap.

We experimented the recovery of H_2 from Li by Y plates in the present NIFS collaboration study. **Fig. 2** shows examples of the H_2 absorption rate for the Y- H_2 system and the Li-Y- H_2 system. The H_2 absorption rate for the Li-Y- H_2 system is almost the same as that for the Y- H_2 system at 400 °C. Therefore, the Y plate at temperatures higher than 400 °C assures us to recover H_2 from liquid Li as well as from a gaseous Ar- H_2 mixture. However, the absorption rate heavily dropped at temperatures lower than 350 °C. Therefore, we cannot expect sufficient H_2 absorption there.

In the actual Y hot trap, it will be operated at flowing conditions. Then liquid Li flows through an Y particle bed. Since the tritium mass transfer rate is limited by diffusion through the Li boundary layer or the Y inside, the hydrogen concentration inside the Y bed changes from the Y hydride to the α -phase. The region where the concentration changes from the lower concentration to the higher one is called a breakthrough curve in the terminology of the chemical engineering field. Then, the H_2 absorption temperature can be relieved (can be raised). If the α -phase condition is equal to $YH_{0.006}$, the absorption temperature can be operated even at 500 °C as seen in Fig. 1. In this temperature, most of the Y particle bed is in the hydride phase and the rest in the mass-transfer zone is the α -phase region.

In order to improve the H_2 absorption performance at lower temperatures, we tested HF acid treatment. Usually, Y surfaces are covered with an Y oxide.

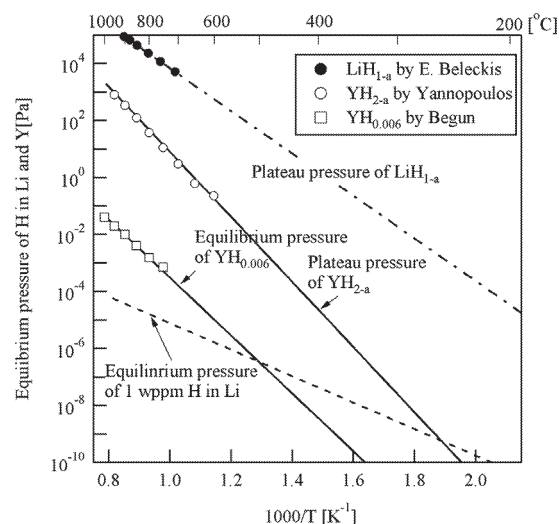


Fig. 1 Tritium recovery condition for INMIF Li loop

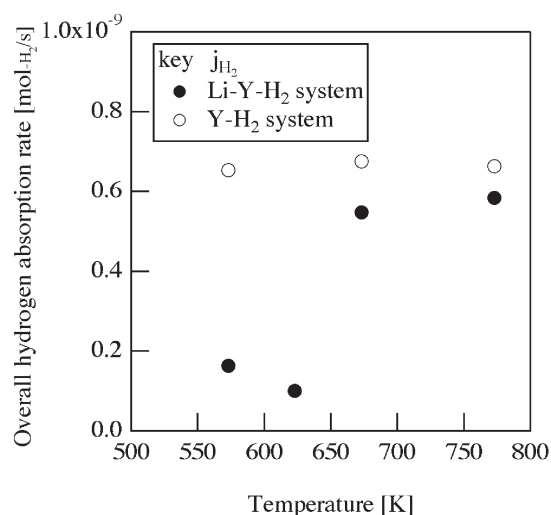
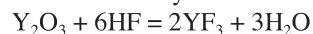


Fig. 2 Hydrogen recovery rate for Li-Y- H_2 system

Thermodynamic consideration predicts that the oxide can be removed by the HF treatment as follows:



We can also expect that YF_3 formed on the surfaces is resolved in liquid Li. Therefore a fresh metal layer will be disposed on the Y surfaces. Thus we expect hydrogen recovery by an Y bed down to 1 ppm at 500 °C. Now, we initiated the HF treatment experiment.

Another problem is to desorb tritium from Y. We need to heat it up until at least 850 °C to recover tritium from the Y bed. This temperature is not so low. We need to develop another effective desorption method for tritium recovery from Y.

References

- [1] S. Fukada, M. Kinoshita, K. Kuroki, T. Muroga, J. Nucl. Mater., in printing.
- [2] M. Kinoshita, S. Fukada, T. Muroga, M. Nishikawa, Proc. ISFNT-7, (2005).
- [3] S. Fukada, M. Kinoshita, *et al.*, Proc. Intern. WS on Tritium Management and Corrosion Activities for Liquid Breeder Blanket, ENEA-Brasimone, Italy, (2004).

§13. Design Activity of High Flux Irradiation Test Module of IFMIF

Shimizu, A., Yokomine, T., Ebara, S. (Kyushu Univ.), Nakamura, H., Yutani, Y. (JAERI), Muroga, T., Noda, N. (NIFS)

During irradiation test in IFMIF, accurate temperature control and monitoring of specimens are required since irradiation characteristics of materials have a strong dependency on temperature. In the high flux test module (HFTM) of IFMIF, temperature control using cooling by gas and heating by electric heaters are supposed to be used. A severe restriction is imposed on the temperature control in HFTM because available space for heaters, insulations, cooling channels and so on is very restricted (about 0.5 l for the specimens) while different irradiation temperature must coexist within it. From these reasons, the temperature control for specimens in the HFTM is one of the most challenging issues of the IFMIF design activities.

The authors have proposed an alternative design concept of HFTM with high cooling performance in which specimens are set in cast-like capsules and precise measurement of specimen temperature is possible [1,2]. In Kyushu University, a series of studies on the HFTM has been developed so far based on the assumption of a constant nuclear heating, taking no account into the spatial distribution of nuclear heating. It is, however, envisaged that the produced neutron flux has a spatial distribution in a plane normal to the beam direction and it was reported that it was attenuated by about 1 % as it traveled for 1 mm toward the beam direction [3]. Since nuclear heating is considered to have a similar distribution to that of neutron flux, it is feared that a warp or buckling of capsule, that is the irradiation unit in the HFTM, occurs due to the temperature difference between the front and rear side of the beam direction. For the advanced design, it is indispensable to investigate thermal behaviors with the non-uniform heating. Here, we performed heat transfer experiments taking the non-uniform power density distribution into account. Moreover, thermal-hydraulic analysis was performed numerically to investigate basic heat transfer performances such as a relation between capsule temperature and coolant velocity and to estimate the heater power required to even temperature profile and to achieve a certain temperature level in a capsule.

The spatial distribution of the heat generation in the irradiation volume in the HFTM assumed in this study is an approximate estimation obtained by referring to [4]. In the experiment, mica heaters with power density variations are used in order to simulate the non-uniform nuclear heating while ceramic heaters are used for the temperature control mainly to homogenize the temperature profile in the capsule. The gas loop system and the test section used for the present investigation are the same as those described by previous work [1], gaseous nitrogen is similarly used as imitation gas and Reynolds number is varied within the range from 7000 to 22000. It is found from the experimental results that the temperature difference in the capsule of 37.1 °C without heating of

ceramic heaters can be mitigated to 28.7 °C with the maximum heating of ceramics heater. This is due to relatively small power of the ceramic heaters compared to the mica heaters. Additionally, despite the temperature control of the ceramic heaters, temperature at the end of the capsule does not rise sufficiently. It was concluded that other heaters which compensate the low volumetric heat generation rate at the end of the capsule have to be added in order to realize more uniform temperature distribution in the capsule in addition to the ceramic heaters with higher power.

Following this, simulations were performed taking one typical capsule as the standard configuration and keeping the similarity to the experiment. Based on the experimental results, an additional heater was introduced to the end of the capsule. In the calculations, four kind of fully developed flows with mean flow velocity of 43.7, 78.9, 87.6 and 263 m/s at the inlet are provided as the inlet conditions of coolant flow. The corresponding Reynolds numbers at the inlet, based on the channel width of 1 mm, are 939.3, 1691, 1880 and 5636, respectively. The flow is laminar at $Re=939.3$ and 1691 while turbulent at $Re=1880$ and 5636. All calculations are presented for the capsule at the most heavily loaded location. Obtained temperature profile in the beam direction indicates almost symmetric profile against the geometrical center in the beam direction although it is envisaged that the heat production profile in the beam direction may make a large temperature difference between the front and the rear side of the capsule. Temperature profiles in the span-wise direction for both cases, one with nuclear heating only and the other with nuclear as well as heater heating to aim at uniform temperature, show that temperature distributions are well improved by heaters for temperature control. It should be noted that the effect of the end heater is prominent and it remarkably contributes to the realization of the uniform temperature profile in the capsule. From results of the relation between supplied heater power and the maximum temperature in the capsule, it is found that the capsule temperature doesn't rise so much for large Reynolds number cases even if a huge power is supplied. Moreover we derived the conclusion from the relation between the maximum temperature and the temperature difference in the capsule that a high capsule temperature causes a large temperature difference and small Re leads to a small temperature difference in the capsule compared with large Re case at the same temperature level. These results indicate that small Re number is preferable to be used.

References

- [1] Y. Yonemoto, et al., Feasibly study of gas-cooled test cell for material testing in IFMIF, Fusion Eng. Des. 63-64 (2002) 443-447.
- [2] S. Ebara, et al., Structural analysis for the gas-cooled high flux test module of IFMIF, 23rd SOFT 2004.
- [3] V. Heinzel, et al., Lay-out activities for the IFMIF high flux test module, Fusion Eng. Des. 63-64 (2002) 47-52.
- [4] S. Gordeev, et al., Optimized design and thermal-hydraulic analysis of the IFMIF/HFTM test section, FZKA 6895, Oct. 2003.

§14. Evaluation of Validity of Master Curve Method to Measure the DBTT Shift of Ferritic Steels for Blanket Structural Components

Kimura, A., Kasada, R., Ono, T. (Inst. of Advanced Energy, Kyoto University)

The shift of the ductile-brittle transition temperature (DBTT) has been considered to be critical for blanket structure components which were made of reduced activation ferritic steels. The evaluation of the DBTT shift under the synergistic effects of high dose of neutron irradiation and transmutation helium generation is one of the most important missions of high energy neutron sources for fusion materials development.

In this research, the feasibility of Master Curve Method (MCM) to evaluate DBTT shift of ferritic steels was investigated with use of miniaturized compact tension (CT) specimens.

The material used was a reduced activation ferritic steel, JLF-1LN, whose nitrogen concentration was reduced to 150wt.ppm. The CT specimens with different geometries with keeping similarity were produced, as shown in Fig. 1 that describes the 1/4, 1/2 and standard size specimens. Fracture toughness was measured by following the ASTM standard E813 (E1820-99a). The master curve was expressed by the following equation:

$$K_{Jc(med)} = 31 + 77 \exp[0.019(T - T_0)] \quad (1)$$

where T_0 is the reference temperature. As for the normalization of the fracture toughness obtained by miniaturized specimens to that of standard specimens, the equation (2) was adopted with an assumption that the fracture was governed by the weakest link model.

$$K_{Jc(1T)} = K_{min} + [K_{Jc(xT)} - K_{min}](B_{xT}/B_{1T})^{1/4} \quad (2)$$

where B_{xT} and B_{1T} is the specimen thickness of the miniaturized specimen and the standard specimen, respectively. In order to simulate irradiation hardening, a part of the steels was heat-treated at a different condition to increase the hardness of the steel. The difference in the DBTT between the steels measured by impact test was 84K.

The master curves of the steels with different hardness are shown in Fig. 2(a) and (b). The fracture toughness was measured with 1/2 size specimen for the normalized and tempered steel, and the standard specimens for normalized specimens. Well-defined master curves were obtained for both the standard and 1/2 size specimens, and the DBTT shift was estimated to be 78K that is rather close to the value obtained by impact test.

As for the 1/4 specimens, however, it was very difficult to get the fracture toughness values around 100 MPa·m^{1/2}. Finally, no master curve was obtained for both the steels with use of 1/4 size specimens. This is considered to be due to an abrupt transition behavior from brittle to ductile fracture in the miniaturized specimens, especially for 1/4 size CT specimens.

The DBTT shift of a ferritic steel was successfully measured by MCM with use of 1/2 size and standard size CT specimens. Further efforts are necessary to develop small specimen test technology utilizing smaller CT specimens, such as 1/4 size specimens.

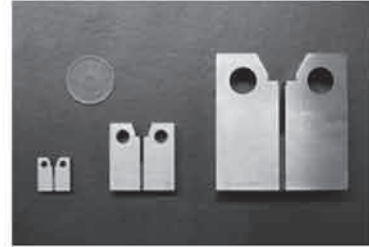


Fig. 1. The CT specimens used to evaluate the validity of the Master Curve Method to evaluate the DBTT shift of ferritic steels.

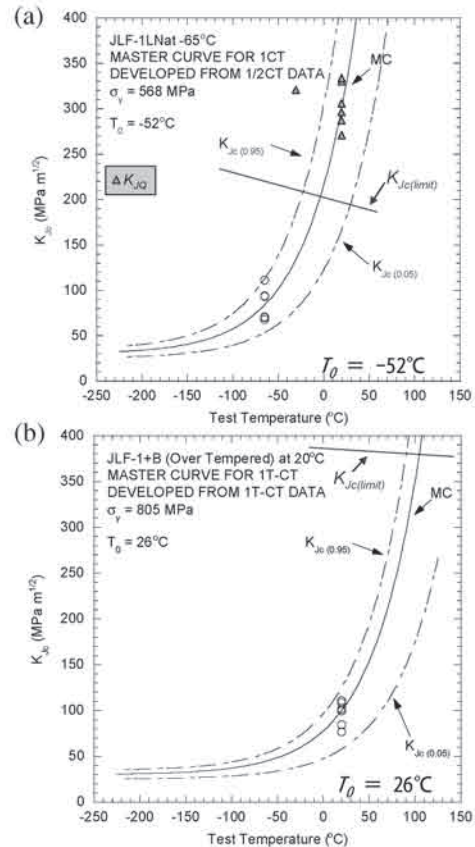


Fig. 2. The master curve of: a) normalized and tempered ferritic steel with use of 1/2 size specimens, and b) normalized steel with use of standard specimens.

Reference

- 1) Ono, H., Kasada, R., Kimura, A., J. Nucl. Mater., 329-333 (2004) 1117-1121.

§15. Experimental Studies on the Neutron Emission Spectra and Activation Cross-section in IFMIF Accelerator Structural Elements

Itoga, T., Hagiwara, M., Baba, M., Oishi, T., Kamata, S. (Cyclotron and Radioisotope Center, Tohoku Univ.), Sugimoto, M. (JAERI), Muroga, T.

We have been conducting systematic experiments on the neutron emission spectrum and radioactivity accumulation in IFMIF structural elements in order to establish the data base for the design of IFMIF1,2). The experiments are carried out at the Tohoku University AVF cyclotron (K=110 MeV) facility. We measured neutron spectrum with the TOF method using a beam swinger system, and activation using a stack target technique.

Last year, we carried out new experiments for 40 MeV deuterons on Fe and Ta, and obtained the results of

- 1) neutron emission spectrum from a thick Fe, Ta target and
- 2) activation cross-sections of the $^{nat}\text{Fe}(d,x)^{51}\text{Cr}$, ^{52}Mn , ^{56}Co , ^{57}Co , and ^{58}Co reactions.

- 3) neutron emission spectrum from a thin lithium target bombarded with 25 MeV deuterons, were also measured.

The experimental method was almost the same with previous experiments1,2) and described only briefly here.

A deuteron beam from the Tohoku University cyclotron was transported to the target chamber at the center of the beam swinger system in the No.5 target room. The neutron spectrum was obtained by using two NE213 scintillators, 14-cm-diam and 10-cm-thick, and 5-cm-diam and 5-cm-thick equipped with n- γ discriminators. The smaller one measured low energy region, and the larger one higher energy region. The data were accumulated as three-parameter data for TOF, n- γ spectra and pulse-height of the NE213 detector. The detection efficiency was obtained by calculation using the code SCINFUL-R.

We measured the activities in the targets after irradiation using high-pure Ge detectors by detecting the corresponding gamma-rays due to the decay of radioactive nuclides accumulated by the deuteron bombardment.

Thirty thin targets of carbon and aluminum with natural composition and 200- μm -thick were stacked to stop the incident beam in the targets. The targets were set on a remotely-controlled target changer together with a beam viewer.

The beam current was around a few nano-amperes or less. A secondary electron suppressor was placed around the target. The beam charge on the target was measured with an ORTEC current digitizer and a multi-channel scaler to record the time history of the beam.

Figures 1 and 2 show thick target neutron emission spectrum from iron and tantalum, respectively, as a function of emission angle. Neutron spectra are measured over the almost entire range of secondary energies. They consist of two components: one is due to breakup of incident deuterons around 15 MeV with very strong angular dependence, and a

low energy component due to the evaporation and almost isotropic. The intensity of low energy component seems increasing with the target mass compared with the data on carbon and aluminum. Inversely, the breakup neutrons around 15 MeV looks to become less with the target mass. This result suggests that the breakup of incident deuterons is more dominant in light nuclides. Experimental neutron emission data covering the low energy region as the present data are very few and then the present can be used for the model development of the neutron emission.

In Fig.3-6, the results of the activation cross-sections are shown, together with other experiments. The present values for iron are consistent with other data. The present data can be directly used for estimation of radioactivity induced in the target and structural elements in IFMIF accelerator system.

Reference

- 1) T. Aoki et al., *J. Nucl. Sci. Technol.*, **41** (2004), 399-405
- 2) M., Hagiwara, et al., *J. Nucl. Materials*, **329-333**, (2004) 218-222

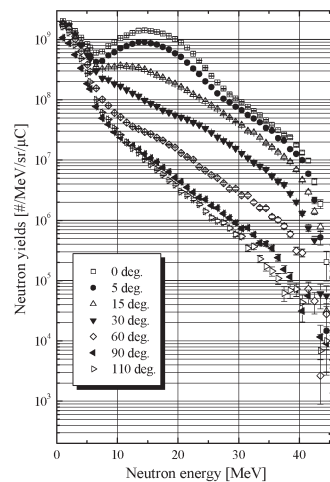


Fig.1 Thick target Fe(d,n) spectrum.

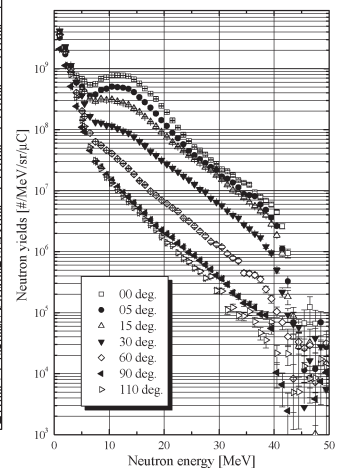


Fig.2 Thick target Ta(d,n) spectrum.

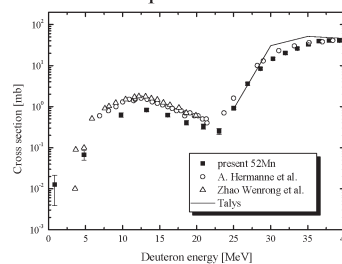


Fig.3 Fe(d,x) ^{52}Mn cross section

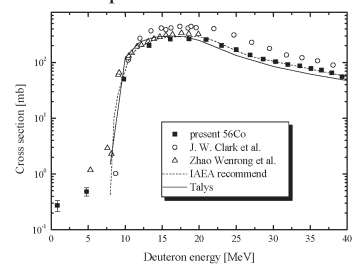


Fig.4 Fe(d,x) ^{56}Co cross section

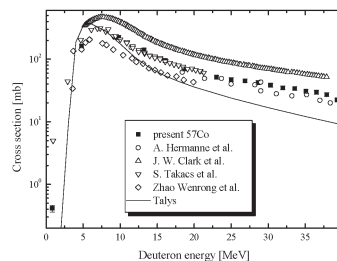


Fig.5 Fe(d,x) ^{57}Co cross section

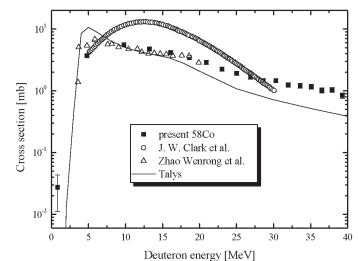


Fig.6 Fe(d,x) ^{58}Co cross section

10. Safety and Environmental Research Center

The Safety and Environmental Research Center (SERC) has been studied to promote and to implement radiation safety issues in NIFS. Major contribution of the SERC is radiation safety management of X-ray emission devices, which are LHD, CHS, and their plasma heating devices like NBI and ECH. The accelerator device of Heavy Ion Beam Probe (HIBP) for plasma diagnostic began to operation in the LHD. For safety operation of LHD and related devices, radiation management system and access-control system were well integrated. Radiation monitoring by the Radiation Monitoring System Applicable to Fusion Experiments (RMSAFE) continued successfully. The other radiation safety issues are considering the safety management plan for the deuterium (D) plasma experiments, especially neutron and tritium. The SERC is responsible to the research and development studies concerning fusion safety, so that variety of issues should be surveyed in the field of safety science and technology, such as radiation protection, environmental science. It would be pointed out that some of these scientific investigations have been successfully carried out as collaboration with researchers of many universities, research institutes and companies. Topics of the activities of the SERC during FY 2004 are summarized as follows:

(1) Radiation management system

For the occupational workers in radiation control area, educational training and registration system have been established. At the same time access control system which includes several entrance/exit gates, identity cards and registration rule to the radiation control area, was sophisticated, and its software system was improved. Also much information of the management system became accessible from the web site of NIFS.

(2) Radiation monitoring system

It is required that the annual exposure dose caused by operation of some radiation emission devices should not exceed 50 μSv on the site boundary. To ensure the limit, a monitoring system RMSAFE has been installed. The RMSAFE is capable to detect burst X-ray and to discriminate the radiation caused by plasma experiment from the natural radiation and to accumulate the exposure dose. The annual radiation dose level caused by experiments of LHD and CHS at the site boundary was less than 1 μSv in FY 2004. Major radiation was caused by the CHS operation. Also the environmental radiation has been measured every three months using TLD (Thermo-Luminescence Dosimeter) sensor in Toki and Tajimi area. To develop a neutron monitor, a portable directional neutron source finder has been proposed and designed. As a result it was confirmed that the portable instrument is useful for specifying the direction of a remote existing neutron source on great angular resolution.

(3) Environmental tritium measurements

It is important to grasp tendency of the environmental

tritium concentration level in water and atmosphere before start out the DD experiment. Simple and accurate tritium measurement method in the environmental water with liquid scintillation counting system has been developed. Some water samples of extremely low level of tritium in the environmental have been measured. Also the atmospheric tritium gases have been measured with separating chemical forms of water, hydrogen and methane respectively. For the isotopic hydrogen gas trapping, an automatic instrument was made and operated in good performance. High sensitive tritium monitor has been developed using an improved proportional counter. These studies were performed as collaboration with Nagoya University, Toyama University, Kumamoto University, Kyushu University and Niigata University.

(5) Development of tritium safety treatment system

From view point of radiation safety, the tritium and neutron which will be generated by DD nuclear fusion reaction are key issues. Developments of tritium safety treatment technologies are important to successfully perform the DD plasma experiment. The key technologies are removing and isotopic separation of rare tritium from the vacuum pumping exhaust gas and exhaust air from the LHD vacuum vessel. Major topics are (a) proton conducting cell to extract tritium as hydrogen gas form, (b) pressure swing adsorption (PSA) method to separate hydrogen isotopes, (c) a high polymer membrane dehumidifier for vacuum vessel purge gas treatment unit to cleanup, (d) advanced Combined Electrolysis Catalytic Exchange (CECE) method to enrich tritium in liquid waste and to reduce its volume, (e) advanced honeycombs intend to high volumetric gas treatment under less flow resistance. These studies were performed as collaboration with Kyushu University, Nagoya University, Shizuoka University, Toyama University, University of Tokyo, Japan Atomic Energy Research Institute and some companies.

(6) Nonionizing radiation measurement and management

Leakage of static magnetic field and variable frequencies of electromagnetic fields are concerned in a magnetic fusion plasma experimental facility. The static magnetic leakage has been measured continuously outside of the LHD hall, and it was found that its strength was less than 1 mT. The continuous measurement system of electro magnetic field around the ICRF wave source was installed. Though each of the electromagnetic field is no problem for workers' safety, multiple exposure dose level should be estimated considering from a static field to band of high frequency field. To study about the comprehensive frequency band of electromagnetic fields would be required in the large plasma experimental facility. These researches have been performed as collaboration with Utsunomiya University and Nagoya Institute of Technology.

(Uda, T.)

§1. Design of a Portable Directional Neutron Source Finder

Yamanishi, H.

An instrument that determines the direction of a remote existing neutron source has been designed. The instrument's configuration is shown in Fig. 1. This instrument combines a polyethylene block and four ^3He counter tubes. The advantages of the instrument are portability and good angular resolution. The count from the detector was varied with the neutron incident angle due to the moderator. Using this characteristic, the direction of the neutron source can be measured precisely by revising the axis of the instrument so that the difference between the four detectors measurements is minimized. Consequently, the direction of the central axis of the instrument in which the response difference of the four detectors reaches a minimum indicates the direction of the neutron source. The directional response of the ^3He counter tube was calculated using the Monte Carlo calculation code MCNP, and the possible use of the newly configured instrument as a directional neutron source finder was discussed.

In order to demonstrate the application of the instrument, an experiment on ^{252}Cf irradiation was carried out. The activity of the neutron source was 0.23 MBq. The neutron source was fixed at 1 m above the floor, and the center of the instrument was set at the same height. The distance between the source and the center of the instrument was 1.5 m. The change in the count difference between the two detectors is shown in Fig. 2. This change forms a point symmetry around the zero point. In order to derive the angle at which the count difference is zero, the curve was fitted by cubic polynomial. Accordingly, the derived value was 0.118 degrees. This angle corresponds to the measured direction of the source. As a result, the instrument was able to specify the direction of a neutron source with high precision when a $\pm 1^\circ$ angle error of the turntable is taken into account. In order to compare the experiment result with the calculated value, the calculation was done using MCNP for this experimental arrangement. The spectrum from the ^{252}Cf neutron source (ISO8529) was used. The comparison result is also shown in Fig. 2. As a consequence, the experimental results agreed well with the simulation results.

As a result, it was confirmed that the portable instrument is useful for specifying the direction of a remote existing neutron source on great angular resolution.

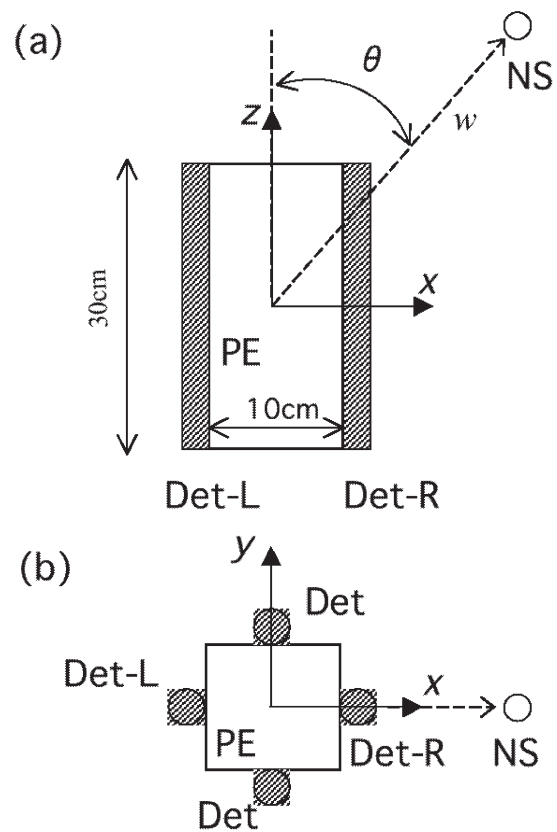


Fig. 1. Configuration of the instrument and calculation model. (a) Cross section of x-z plane. (b) Cross section of x-y plane. PE, polyethylene block, 10 cm x 10 cm x 30 cm; Det, Det-R, Det-L, ^3He counter tube; NS, neutron source; θ , angle of incidence.

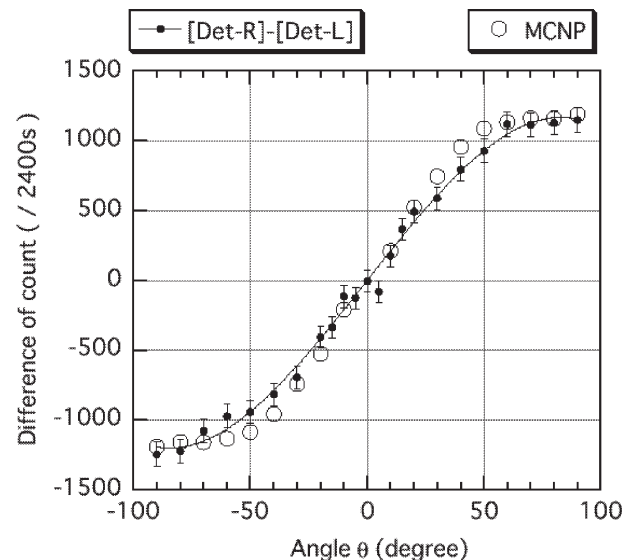


Fig. 2. Measured count difference between Det-R and Det-L in regard to angle of incidence. Comparison the measured value with the calculated value.

§2. Environmental Atmospheric Tritium Monitoring with Automatic Discriminate Sampling of Different Chemical Forms

Sugiyama, T., Uda, T.,
Momoshima, N. (Kumamoto Univ.),
Munakata, K. (Kyushu Univ.),
Tanaka, M., Tsuji, N. (Nippon Kucho Service Co. Ltd.)

As an environmental radiation safety issue an atmospheric tritium monitoring system is necessary for the experiments of the LHD deuterium plasma discharges. The detailed variation of background tritium level must be known before the experiments start and the tritium level must be monitored after the experiments start.

Atmospheric tritium mainly consists of three different chemical forms, that is, HTO, HT and CH_3T . The quality factors of these species vary significantly in the Japanese law for radiation protection. Hence, it is desired that these tritium species should be monitored distinctively.

Conventional technique of atmospheric tritium sampling is discriminate oxidization of tritiated species followed by collection of water with sieve beds. The technique has been confirmed as reasonable and proper though it was manually operated and rather complex. For the practical use of this technique, we have developed the automatic system for the sampling in last fiscal year. In this report we show the results of the environmental atmospheric tritium monitoring.

i) Radiation measurements

Radioactivity of tritium was counted by a low background liquid scintillation counter (LB-III, Aloka). The stocked water samples (65 g for HTO, 10 g for HT and CH_3T) were mixed with the same amount of liquid scintillator (Ultima Gold LLT, Perkin Elmer). Twenty ml of plastic vials were used for counting the HT and CH_3T fractions while the HTO fractions were measured in 135 ml plastic vials. Counting time was 1500 minutes for each sample, where measurements of 50 minutes were replicated for 15 times and the cycle was repeated twice.

ii) Results of measurements

The measured values of tritium concentrations in the air

are plotted in Fig. 1 with respect to each species. The early data before 2004 were obtained with the manual sampling system, and the data after 2004 were obtained with the present automatic system. Although some fluctuations are observed almost the same trend was obtained in comparison with both methods. The value for HTO varies according to seasons because environmental moisture varies. Average tritium concentrations of HTO, HT and CH_3T are obtained as 4.37, 10.0 and 2.42 mBq/m^3 , respectively.

The automatic system enables us to increase the sampling frequency. We now perform the measurement once a month steadily. Temporal change and regional difference of the tritium concentrations will be investigated in future research.

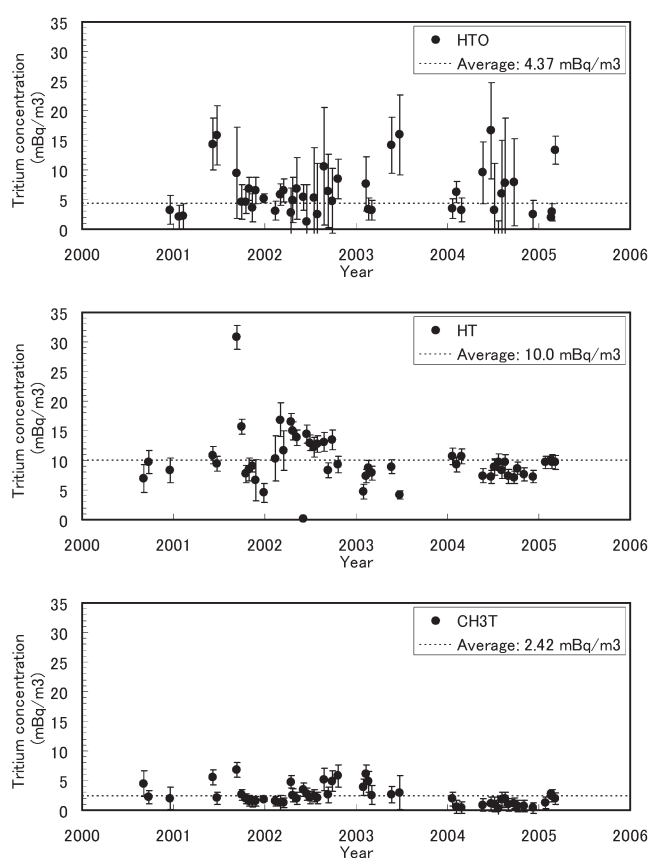


Fig. 1: Atmospheric tritium concentration in Toki area

Reference

- 1) Uda, T., Sugiyama, *et al.*: *ISFNT-7*, P3-21, Tokyo, May (2005).

§3. A Simplified Method for Tritium Measurement in the Environmental Water Samples

Sakuma, Y.

Iida, T. (Graduate School of Eng., Nagoya Univ.)

Ogata, Y. (School of Health Sciences, Nagoya Univ.)

Kakiuchi, M. (Faculty of Science, Gakushuin Univ.)

Torikai, Y. (HRC, Toyama-Univ.)

Satake, H. (Faculty of Science, Toyama-Univ.)

1. Abstract

Liquid scintillation counting is the most popular method to measure the tritium concentration in the low-level water samples, such as environmental water samples. Lately in Japan, the tritium concentration has become very low, and the value is within the detective limit by the low background liquid scintillation counter. Then, we have developed a simplified and accurate procedure with the electrolysis enrichment¹⁾²⁾³⁾. By means of this procedure, we have been measuring tritium concentration of several samples for two years.

2. Experimental and Results

The measurement was carried out as follows;

**SAMPLING⇒RO FILTRATION⇒ENRICHMENT⇒
LS COCKTAIL MIXING⇒LS COUNTING**

To determine the tritium enrichment factor, the heavy water concentration was also measured before and after the enrichment using a mass spectrometer. The results were shown in Fig. 1. All most all of the measured values were between 0.1 and 0.5 Bq/kg. The values of the vapor samples in the air were significantly higher than the others.

3. Conclusion

(1) The tritium concentration in the environmental water samples was successfully measured by the new measurement procedure.

(2) The values were 0.1-0.5 Bq/kg-water except vapor samples.

References

- 1) Y. SAKUMA et al., Proc. 10th ICRP, P-4a-248 (2000).
- 2) T. KOGANEZAWA et al., Radioisotopes, Vol.53, No.5 (2004) 277.
- 3) Y. SAKUMA et al., J. Radioanalytical and Nuclear Chemistry, Vol.255, No.2 (2003) 325.

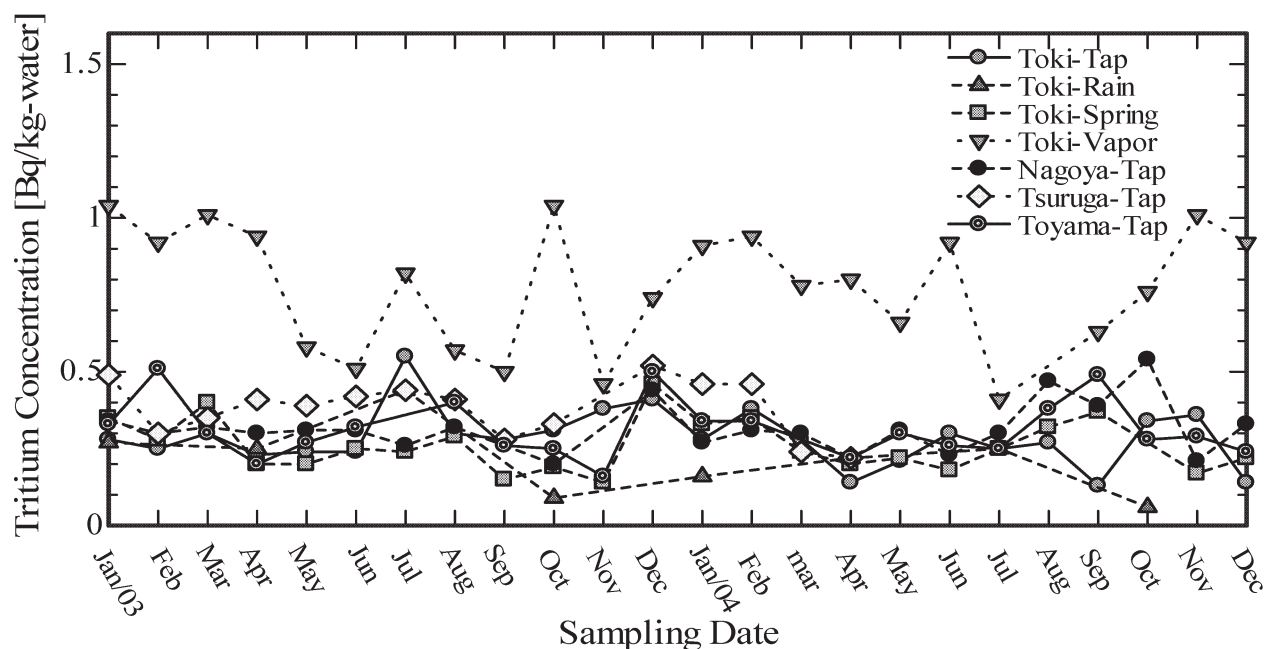
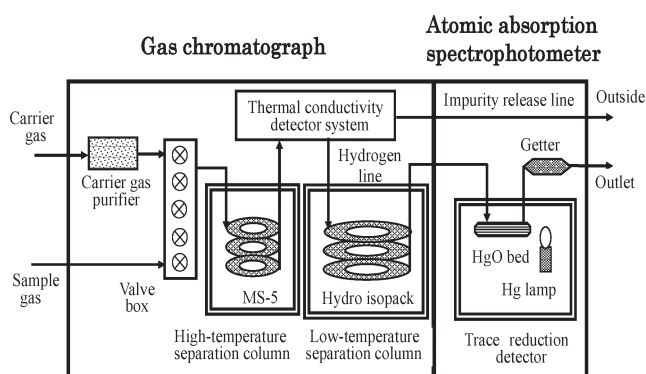


Fig. 1 Results of measurement.

§4. Isotopic Separation Analysis Using Improved Hydrogen Analyzer

Kawano, T., Yamato, A., Uda, T.
Tuboi, N., Tsuji, H. (GTR Tec)

We previously developed an analyzer that used a trace reduction detector to measure infinitesimal concentrations of hydrogen in air. The detector detects extremely small amounts of hydrogen by using the reduction reaction of mercuric oxide with hydrogen. Experiments demonstrated that the analyzer can measure concentrations as low as $5 \text{ cm}^3/1000 \text{ m}^3$. The analyzer is equipped with a carrier gas purifier, high- and low-temperature separation columns, and an “after-cut method” is used to remove impurities,

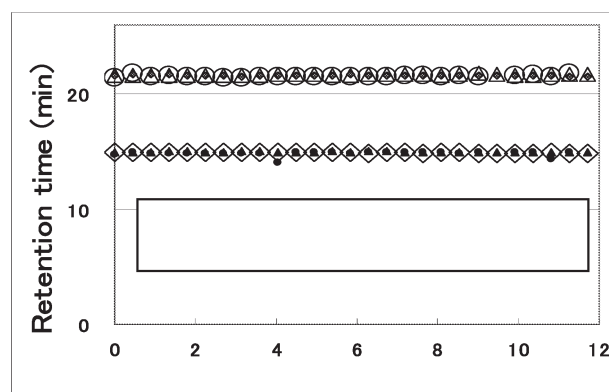


including nitrogen, contained in the sample gas. Experiments using protium and deuterium separately demonstrated that the analyzer works well regardless of differences in the hydrogen isotope. We have used the analyzer to distinguish hydrogen isotopes in three gas mixture test samples (protium and deuterium with almost equal concentrations in nitrogen). Nitrogen gas was used as the dilution gas to simulate an air sample.

We repeatedly measured the concentrations of protium and deuterium in each sample for about 12 hours and obtained more than 30 chromatograms for each. Then we examined these chromatograms from the viewpoints of retention time stability and peak area stability.

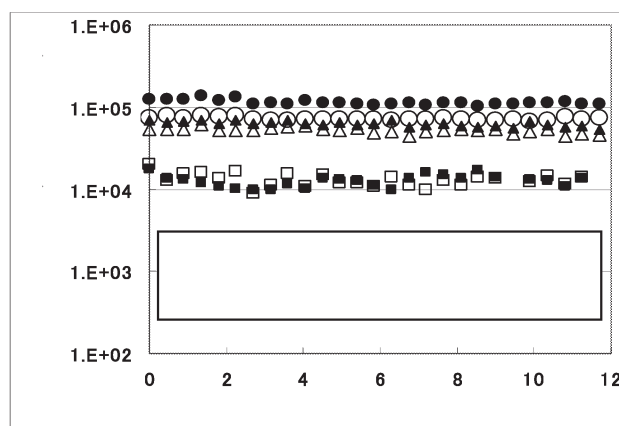
The retention times obtained for the three test sample gases are shown in Fig. 2. The elapsed time in hours, shown on the X axis, indirectly represents the repetition time of the measurements. Because each measurement took about 27 minutes, the total elapsed time divided by 27 equals the repetition time. The Y axis shows the retention time in minutes.

As shown in Fig. 2, all the data for the three sample gases are distributed closely along one of two horizontal lines, although the lines themselves are not actually drawn. The upper line corresponds to the retention time obtained for deuterium (D_2), and the lower corresponds to that for protium (H_2). The retention times clearly differ between the two. Moreover, the two times are constant and virtually



indistinguishable, independent of the concentration and repetition time. The average retention times (and relative standard deviations) were 14.8 min (1.45%), 15.0 min (0.26%), and 14.9 min (0.25%) for the protium in the 5-, 20-, and 50- $\text{cm}^3/1000 \text{ m}^3$ sample gases, respectively. For deuterium they were 21.6 min (0.47%), 21.7 min (0.17%), and 21.6 min (0.22%). The difference between the protium and deuterium was about 6.5 minutes. The retention times were thus distinguishable and very stable.

The changes in the peak areas in the chromatograms obtained for the three test sample gases are shown in Fig. 3. While they fluctuated from trial to trial, the lines connecting them are still horizontal. The relative standard deviations derived for the protium and deuterium in the 5-, 20-, and 50- $\text{cm}^3/1000 \text{ m}^3$ sample gases were about 17.3, 8.3, and 7.3%, and 18.3, 8.8, and 4.6%, respectively. It seems reasonable that the deviation increased as the concentration was reduced for both the protium and deuterium.



These results indicate that the peak areas obtained at the same time for both elements were stable, independent of the elapsed time and repetition time. This means that the analyzer can detect concentrations of protium and deuterium as low as about $5 \text{ cm}^3/1000 \text{ m}^3$.

§5. Development of Exhaust Gas and Effluent Liquid Treatment System for LHD

Asakura, Y., Kawano, T., Sugiyama, T., Uda, T.

In order to carry out deuterium plasma experiments on the Large Helical Device (LHD), NIFS is planning to install a system for the recovery of tritium from exhaust gas and effluent liquid. As well as adopting proven conventional systems, NIFS is planning to apply the latest technologies. The following specific methods have been selected for final evaluation for actual applications.[1]

(A) Membrane Dehumidifier for Vacuum Vessel Purge Gas Treatment Unit

Oxidized tritium (tritiated water vapor) contained in the purge gas is usually removed using an absorbent column. However, if a dew point of less than -60°C could be obtained using a polymer membrane dehumidifier, the equipment could be reduced in size and a more stable dehumidifying performance could be expected.

(B) High Sensitivity Tritium Monitor for Online Gas Phase Tritium Monitoring Unit

A real-time monitor has not been commercially available for concentrations under $5 \times 10^{-4} \text{ Bq/cm}^3$, which is 1/10 of the regulation value for tritiated water vapor in the exhaust gas. Using the hydrogen pump described, it is possible to lower the effective detection limit by greater than an order of magnitude, by concentrating the hydrogen-isotope gas (including tritium) and by removing the radon gas which is mixed in at the monitoring stage.

In order to make efficient developments, two collaborated researches have been carried out.

- 1) Development of hydrogen gas pumping apparatus applying proton conducting ceramics [TYK]
- 2) Study on polymer membrane type dehumidifier for tritium removal [Shizuoka Univ.]

Development status are summarized as follows.[2]

① Membrane dehumidifier [Photo.1]

In order to elucidate the performances under atmospheric pressure at the permeate side, we carried out experiments using a commercially available polyimide hollow-fiber filter module (Ube Industries, UM-C10HF, O.D.: 90 mm, L: 1160 mm). The polyimide hollow-fiber filter module can achieve a very low dew point of less than -70°C under the dry state of the polymer membrane. However, the dew point shows a sharp increase followed by the decrease in the permeated flow rate. These data suggest that the targeted dew point can be sustained by optimizing the dry state of the polymer membrane. As shown in Photo.1, we

have just constructed the mock-up test dehumidifier, in which the permeated flow rate is kept to the constant value necessary to achieve the targeted dew point by regulating the purge gas flow rate automatically.

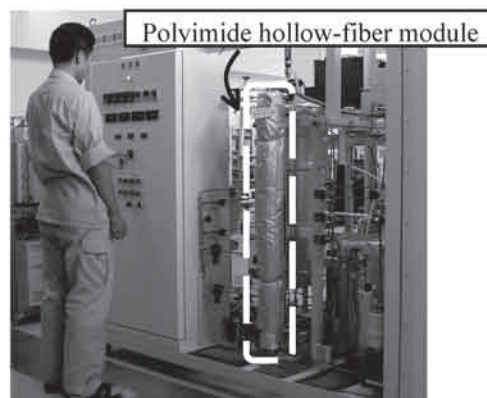


Photo.1 Outward of the mock-up test dehumidifier

② High sensitivity tritium monitor [Photo.2]

We have performed water-vapor electrolysis experiments in an atmosphere containing 20 % oxygen. In terms of stability during long-term operation, we have used a commercially available $\text{CaZr}_{0.9}\text{In}_{0.1}\text{O}_{3-\alpha}$ tube with one end closed and with platinum electrodes (O.D.: 15 mm, I.D.: 12 mm, L: 200 mm, effective electrode area: 47 cm^2). These estimated results indicate that the hydrogen extraction performances of the present proton-conducting ceramic are adequate for application in the high sensitivity in-line tritium monitor. Based on the experimental results, trial manufacturing of the actual hydrogen pump having the capacity of 1 cc/min , which is necessary to the high sensitivity tritium monitor for concentration under $5 \times 10^{-4} \text{ Bq/cm}^3$ has just completed as shown in Photo.2.

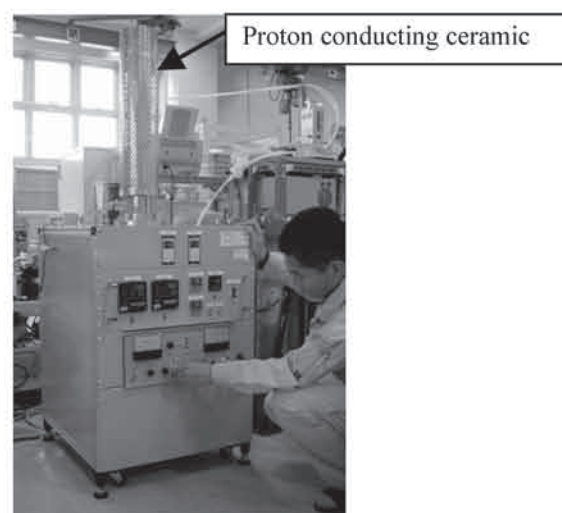


Fig.2 Outward of the mock-up test hydrogen pump

References

- [1] Y. Asakura, et al., J.Nucl.Sci.Technol., 41 (2004) 863
- [2] Y. Asakura, et al., Fusion Sci.Technol., 48 (2005) 401

§6. Water-Vapor Decomposition by Using Zirconium-Nickel Alloy

Kawano, T.

A decomposition-processing vessel was developed for hydride compounds like methane and water vapor. The vessel can be installed in a tritium cleanup system for application to exhaust gases discharged from fusion facilities. The system is distinguished from conventional ones from the viewpoint that all tritium in various chemical forms in the exhaust gas is removed as tritiated hydrogen molecules. The developed decomposition-processing vessel can be used to make hydrogenated compounds decompose into their respective elements so as to extract the tritium only in the form of hydrogen molecules, and other elements are fixed within the vessel.

In my previous studies, to develop a decomposition-processing vessel for tritiated compounds, zirconium-nickel alloy was examined using methane, because methane is one of typical tritiated constituents in exhaust gas discharged from facilities for handling or producing (or both) tritium like a fusion experimental laboratory. In the present study, I used water vapor as a target constituent to be decomposed instead of methane, because water vapor is also another one of the main tritiated compounds. I carried out an experiment to examine how water-vapor was decomposed by zirconium-nickel alloy.

Performance tests were carried out using helium gas mixed with about 1.1% water vapor by using an in-house humidifier, in which water vapor was added to the helium carrier gas through the humidifier. The flow rate of the humidified helium gas was 35 standard cm^3/min and the gas temperature in the vessel was 873 K during the entire experiment. This decomposition condition is exactly the same as those assumed in the methane decomposition carried out in previous studies.

The present experiment is the first trial of water-vapor decomposition using zirconium-nickel alloy. I performed the experiment of water vapor decomposition on ZrNi alloy three times. For each measurement, concentrations of both water vapor and hydrogen, generated from water-vapor decomposition, were observed at the inlet and outlet of the decomposition-processing vessel by using a gas-chromatograph system. Consequently, I obtained exactly same results for three time measurements. Typical one of those measurements is shown in Fig. 1, in which the horizontal solid line indicates the initial concentration of water vapor (about 1.1%) before undergoing the decomposition process. The changes in the concentration of the flowing gas just after the decomposition process are plotted as a function of the elapsed time by open circles and open squares for water vapor and hydrogen, respectively. As

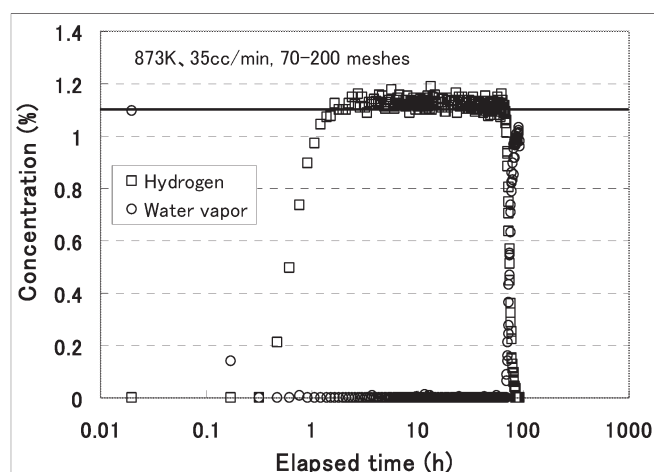


Fig.1 Change in water vapor and hydrogen concentrations in the flowing gas just after the decomposition process

shown in Fig. 1, the water-vapor concentration decreased immediately first. Hydrogen (which should be generated by the water-vapor decomposition) was not detected in this stage (0.3-0.5 hours elapsed time). The hydrogen peak was found first at an elapsed time of about 0.5 hours, after which the hydrogen concentration gradually increases. It must need a proper time delay for development of decomposing absorbed water vapor in ZrNi alloy.

After that, the increase in hydrogen concentration led to a full-scale decomposition reaction. The fastest decomposition of water vapor and generation of hydrogen were first observed at about one hour after the start of the process, and then a briskest reaction was maintained for about seventy hours. At the bottom of the curve for water vapor about 1.1% hydrogen was observed, but water vapor was not detected at all, which meant almost 100% of the water vapor was decomposed. After that, it subsequently weakened gradually, and approximately 85 hours later, the water-vapor decomposition ceased.

The experimental results show that zirconium-nickel alloy can easily decompose water vapor, in particular, hydrogen can be extracted in the form of hydrogen molecules under the same decomposition condition suitable for methane decomposition (temperature: 873 K; gas flow rate: 35 standard cm^3/min ; material size: 70-200 meshes).

§7. Performance of Honeycomb Type Catalysts for Oxidation of Tritiated Hydrogen and Methane Gases

Uda, T., Sugiyama, T., Asakura, Y.
Munakata, K. (Interdisciplinary Graduate School of Engineering Sciences, Kyushu University)
Tanaka, M. (Nippon Kucho Service Co. Ltd)

Recovery of tritium released into a tritium processing room in a nuclear fusion plant is a key issue of safety. The catalytic oxidation of isotopic hydrogen including tritium is a conventional method for removing tritium that is released accidentally into the working area. If tritium release occurs in the fusion plant, large volume of air should be treated by an air cleanup system. Thus, the cleanup system would be designed by considering the high volumetric velocity of the process gas. Such high throughput of air causes pressure drop in the catalysis bed, which results in high loads to pumping systems or compressors. The present study dealt with honeycomb catalysts, which are generally used in the automotive industry, and examined their feasibility to the tritium recovery system operated under higher volumetric gas rates. At first the pressure drop was estimated for particle-packed beds (3 mm ϕ particles) and a small-diameter (1 mm) tube modeled for honeycomb catalysts. Comparison of the two cases shows that the pressure drop of honeycomb catalyst is smaller than that of the packed bed by one order of magnitude. Therefore, the honeycomb catalyst is apparently suitable for the high throughput of air. The next attention is to obtain the oxidizing properties of honeycomb catalysts whether it is suitable for application to the fusion tritium cleanup system. The catalytic oxidizing experiments of honeycomb catalysts have been performed using hydrogen and methane mixture gas. It was performed using two honeycomb substrates which are cordierite and Al-Cr-Fe metal alloy with cell density of 400 CPSI (cells per square inches). In the experiments, the gas flow rate and temperature were varied to obtain more detailed engineering data. Figure 1 shows the example of oxidation of H₂ and CH₄ over the Pt/cordierite catalyst Pd/cordierite catalyst. As seen in this figure, H₂ is almost completely converted to water at 100 °C even at the space velocity of 3800 h⁻¹, which indicates that the performance of the Pt/cordierite catalyst is higher than that of conventional Pd/cordierite catalyst. Thus, it was found that the Pt/cordierite catalyst is effective for oxidation of hydrogen isotopes gases with high throughput.

It was also examined about the conversions of H₂ and CH₄ over the Pt/20%Cr-5%Al-Fe catalyst with the cell density of 400 CPSI. In comparison with the results for the cordierite and metal honeycomb catalysts considerable well catalytic oxidizing performance was observed.

As the results, it was found that honeycomb catalysts are useful; especially the cordierite honeycomb possesses better oxidizing property than the metal honeycomb.

Whereas the metal honeycomb has an advantage for oxidation of hydrogen gas under room temperature, because it does not have structural water molecule that would cause memory effects via tritium contamination. Based on the database obtained, the catalyst volume was estimated for a volumetric velocity of 1000 Nm³/hour. The volume estimation results are shown in table 1 and 2. Here DASH-520 is conventional particle type catalyst. It was found that these honeycomb catalysts can be used for the high-performance removal system of tritium from tritiated gases. They are also applicable to the collection of tritiated gases for tritium measurement in atmospheric air around the fusion facility and the environment.

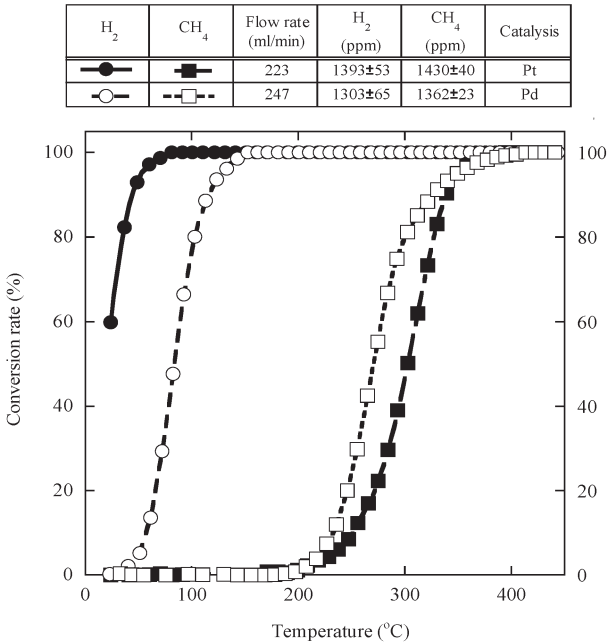


Fig. 1 Efficiency of oxidizing catalysts for cordierite honeycombs.

Table I Volume estimation of catalytic reactor for H₂

Catalysis metal	Operation temperature (°C)	Catalyst volume for H ₂ (m ³)		
		Metal honeycomb	Cordierite honeycomb	DASH-520
Pt	60	2.3	0.5	0.7
Pd	60	6.6	11.3	1.9

Table II Volume estimation of catalytic reactor for CH₄

Catalysis metal	Operation temperature (°C)	Catalyst volume for CH ₄ (m ³)		
		Metal honeycomb	Cordierite honeycomb	DASH-520
Pt	300	2.0	2.8	3.7
Pd	300	0.4	1.0	0.4**

**at 290°C

§8. Field Measurement in Hi-Level Multiple Source EM Environment

Kamimura, Y. (Dept. Engin., Utsunomiya Univ.)

In the nuclear fusion experiment facilities, there are the strong static magnetic fields, the ELF magnetic fields generated from the power supply equipments, and the leakage electromagnetic radiation such as various plasma heating devices of 10 MHz-168 GHz. The electromagnetic radiations for the plasma heating are generated attended with the burst, and they show the spectra with wide frequency-range. These irregular electromagnetic fields cause a potential error in the measurement result of the electromagnetic field measuring instrument. The purpose of this study is to establish the measurement technique whose reliability is higher than the employed safety evaluations under such a special, high-level, electromagnetic environment. Moreover, the problem of an electromagnetic, environmental measurement is dug up, arranged, and the countermeasure method is examined.

Method

Electromagnetic field strength is measured with two or more measuring instruments such as wideband electromagnetic field probe (HI-3604), portable electromagnetic field dosimeter (ESM-20), ELF electromagnetic field meter (EFA-3) and portable accumulative magnetic field meter (EMDEX-II), and it makes comparative study. The environment where two or more high-level electromagnetic fields exist is confirmed, and the evaluation method is examined according to the frequency.

Result

As a result of the investigation, it is found that the static magnetic field in the room that the employee entered is 0.12 mT or less when plasma magnetic field strength is 3 T. The static magnetic field at this level doesn't provide the disturbance to the electromagnetic field measuring instruments used.

The ELF magnetic field in the neighborhood of the electric motor-generator for NBI changes widely between 5 Hz and 60 Hz. By comparing with ELF electromagnetic field meter (EFA-3) that can be measured in frequency 5 Hz-30 kHz, it is found that the error is caused in magnetic field meter (EMDEX-II) of the portable accumulation type because the frequency 40 Hz or less is cut. Moreover, the exposure evaluation method for a multi frequency is needed because there is a possibility of existing together to the magnetic field of power frequency (60 Hz). Therefore, it is necessary to measure the shape of waves.

The leakage electromagnetic radiations of the plasma heating devices are evaluated by converting it into the power density. However, a remarkable error can be likely to lead by depending on the characteristic of the measurement meter when they have wide spectra.

Moreover, though it differs from the purpose for which it was originally intended, it is found that the IC card reader of the entrance management system is generated of an unexpectedly strong electromagnetic field. For example, the magnetic field of about 1 A/m has been generated in the distance 35 cm. There is a possibility of the mis-measurement by the use of the cellular phone, too. When an individual exposure is evaluated with the magnetic field measurement meter of the portable accumulation type, it is necessary to note it especially.

Discussion

Though a stationary magnetic field is no problem, it is necessary to estimate the influence by the rapid change magnetic field with quenching of the superconducting coil.

It is necessary to refer to the statement of ICNIRP in 2003 to evaluate the magnetic field exposure of a multiple frequency in the frequency band up to 100 kHz [1]. Electromagnetic environment of the neighborhood of the electric motor-generator for NBI (5 Hz-60 Hz) corresponds to that case. It is necessary to evaluate it by the peak value of the differentiation of the magnetic field, and the analog output of the magnetic field measuring instrument is passed through the differentiation filter, or the shape of waves of it is taken into the computer and calculates. If it is a pickup coil output, it is possible to evaluate as it is.

The measuring instrument used to measure the electromagnetic high frequency field with a wide spectrum that leaks from the plasma heating device should evaluate and check the response characteristic to the amplitude change.

It is necessary to investigate the electromagnetic interference generated by the card reader of the entrance management system and by the cellular phone.

Reference

- 1) ICNIRP Statement: "Guidance on determining compliance of exposure to pulsed and complex non-sinusoidal waveforms below 100 kHz with ICNIRP guidelines," Health Physics **84**, 3 (2003) 383-387

§9. Measurements of Static and Variable Magnetic Fields in a Large Plasma Experimental Facility

Uda, T., Obayashi, H.
Kamimura, Y. (Utsunomiya University)

Although the LHD is plasma confinement device with strong static magnetic field, not less magnetic field is leak out around the device. Except the superconducting magnetic systems, many electromagnetic devices are applied for fusion plasma experiments. Various frequencies of electromagnetic devices are used like NBI and its electric power source of a motor generator (60Hz), heating systems of ICRF (25-100 MHz), and ECH (84-168 GHz). Also for discharge cleaning, resonance frequency (2.45 GHz) system is used. As above mentioned, static magnetic field and wide spectrum of frequencies electromagnetic waves are concerned. Safety issues seem to be not only strong electromagnetic field but also complex of static magnetic field and variable frequencies of magnetic fields, which are from extremely low frequency (ELF) of 60 Hz to high frequency of 168 GHz. Considering the safety and health effects for workers in the plasma experimental facility, leakage of magnetic field strength around the LHD and related devices have been measured.(1) Static magnetic field has been measured since the first plasma experiment of the LHD in 1998. The fixed monitoring point is 23 m far from the center of LHD in south direction. The measurement instrument is Gauss Meter 9900 (F.W. Bell Co) and three axial probe ZOA99-3208. The magnetic field strength measured in the period of 8th cycle of LHD operation, 9/1(2004)-1/31(2005) is shown in Fig.1. Background on not-operation is about 0.06 mT, which is a double of terrestrial magnetic field. It caused by magnetization of steel materials in the monitoring room. The data shown in Fig. 1 is already subtracted the back ground. When the LHD plasma magnetic field is 3 T, it increased to 0.1 -0.2 mT.

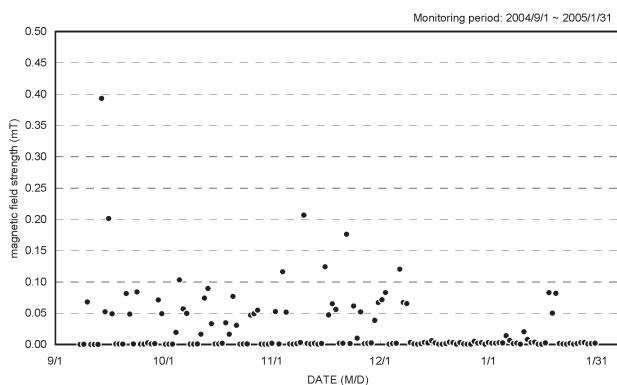


Fig.1 Result of magnetic leakage monitoring in 9/1(2004)-1/31(2005) outside of the LHD hall.

As major issues of the super conducting magnetic coil system, it decreases quickly for protection of the coil system

on quenching or on abnormal event occurrence. According to our experiences magnetic field strength at the fixed point was spontaneously increased to about 0.5 mT on such a coil protection mode. Small variation of magnetic field strength less than 0.01 mT was observed according to the local island divertor (LID) operation.

Except the coil system of the LHD, there are some kinds of static magnetic field producing devices. For example a gyrotron, of ECH has a super conducting magnet coil, of which strength is 7 T at the center of coil. Leakage of magnetic field strength is measured with the gauss meter. Although entrance of workers in the ECH device is regulated by the leakage of magnetic field, high electric voltage and X-ray radiation is more important safety issues.

There are many kinds of ELF related devices in the laboratory. Major devices are electric power source for super conducting magnetic coils system and a motor generator for power supply to the NBI device. The ELF magnetic field strength around the electric equipments in the laboratory was distributed between 0.2-40 μ T. The average ELF level in office is about 0.1 μ T.

There are many types of microwave generator for plasma heating such as ICRF and ECH and for discharge cleaning of plasma facing walls. We begin continuous monitoring around the ICRF wave generator using a data logging system. The measurement instrument is EMC-300 and three axes electric field probe Type 18 (Narda Co.). Result is shown in Fig. 2. The maximum electric field was 8 V/m that is about 1/10 of the occupational regulation level proposed as guide line by the International Conference for Non-Ionizing Radiation Protection (ICNIRP). Exposure dose measurement and estimation to such high frequencies of electromagnetic fields is an important issue. So we have studied in collaboration with Nagoya Institute of Technology and Utsunomiya University.

Reference

- 1) Uda, T. et al., EMC'04 Sendai, 2(2004) 853

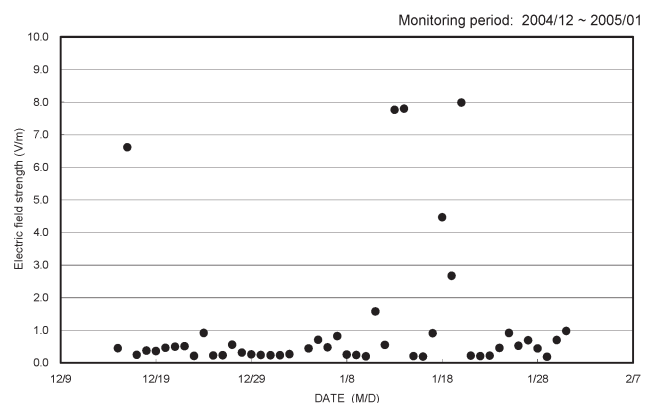


Fig. 2 Electric field strength monitored around the ICRF electromagnetic wave generator.

11. Computer and Information Network Center

The Computer and Information Network Center was established in order to meet the various computational needs for numerical computations, simulation studies, data processing, and data access in the area of plasma physics, nuclear fusion research, and their related fields. Furthermore, the Center provides the network environment suitable for research life.

The Center has been mainly supporting the Large Helical Device (LHD) Experiment Project and its related Simulation Project, and the Research Collaboration with worldwide universities and institutes.

NIFS has two computer systems. One is the general purpose computer system which serves mainly for the LHD Experiment project and is operated by the Center.

The other is the supercomputer system, NEC SX-7/160M5, which serves mainly for the Advanced Simulation Project and is primarily operated by Theory and Computer Simulation Center.

The main part of the general purpose computer system consists of NEC SX-5 with 6 CPU elements, whose schematic view is shown in Figure 1.

Since the establishment of NIFS, the Center has also made significant improvements in the LAN and WAN. And now, the campus information network of NIFS serves as an infrastructure of information, and is becoming indispensable to the research life.

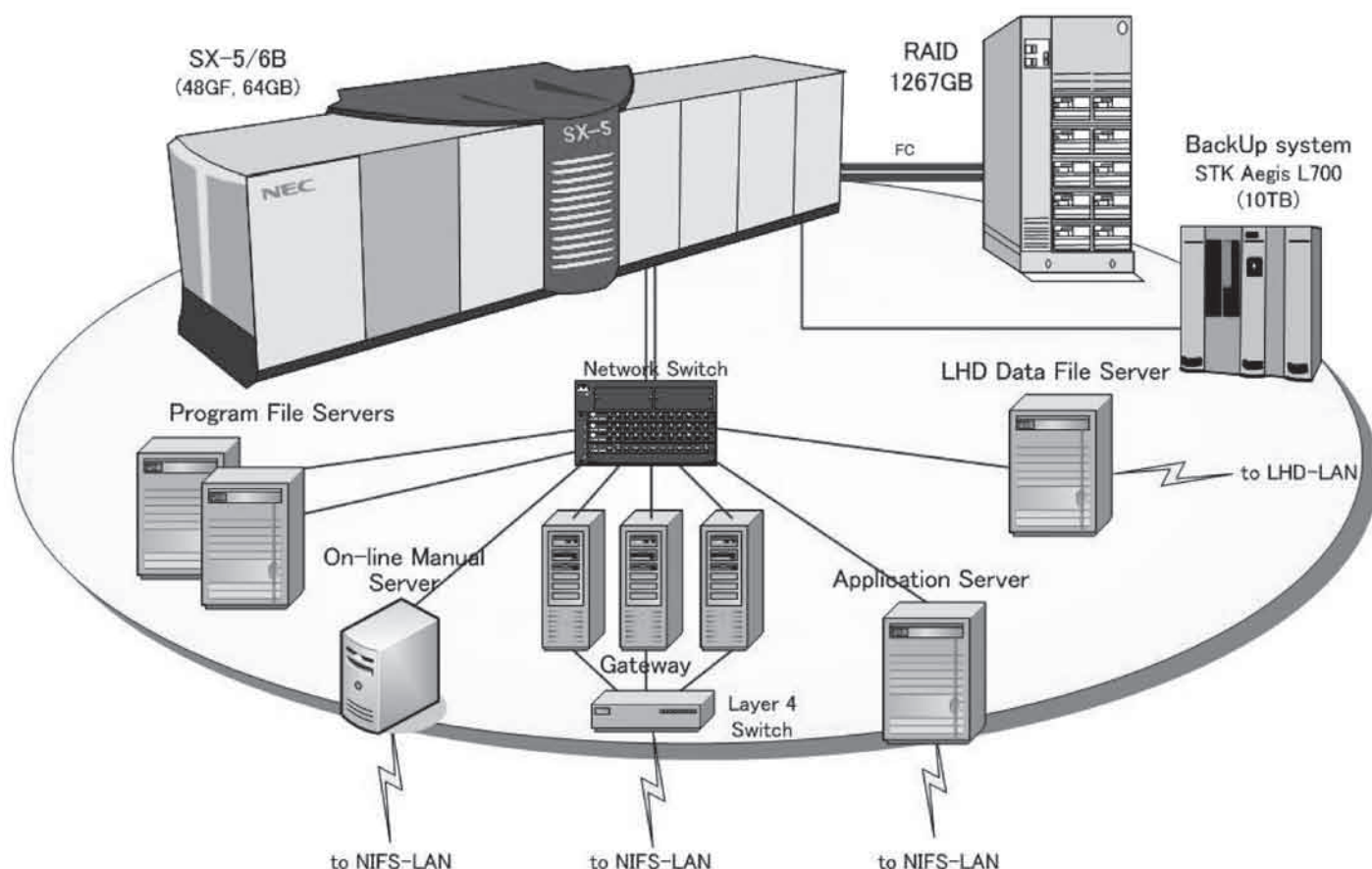


Fig. 1 : Schematic View of General Purpose Computer System

1. General Purpose Computer System

The CPU server consisting of six vector processing elements of NEC SX-5, are working cooperatively as the main part of the system. The amount of the main memory and processing speed are 64GB and 48GFLOPS, respectively. The CPU server is available only for the batch jobs. In current job queuing system, 9 job queue classes are available according to required CPU time and memory size, in which user can use up to 30GB memory.

The CPU server is connected by Fiber Channel to the high-speed magnetic disk system (RAID) with 1267GB storage. There is also equipped the 10TB mass storage system, STK Aegis L700 for the back-up of the high-speed magnetic disk system. The mass storage system is also used for the migration/recall of the files of the magnetic disk system. By adopting this migration/recall system, the magnetic disk system can maintain capacity required to run jobs. Now, a threshold value is set up to 70% and the system is continuing stable operation.

Three gateways as the front end processor are provided so that the users can submit their batch jobs using NQS through the NIFS-LAN from all over the world. In order to keep users' programs, the program file server which consists of two independent processing units is introduced for high reliability. All the system is operated by UNIX OS.

There are also the application server and the LHD data file server which are used for the scalar processing of the small-scale calculations and for the data processing of LHD experiment, respectively.

The computer system has been operated all-day-long except for the periods of the system maintenance which were less than 3days long in total, and for the period of the power outage of NIFS. The monthly used CPU time of the computer system are shown in Figure 2. The total operation time, the total used CPU time, the ratio of CPU time to the operation time, and the numbers of executed jobs are summarized in Table 1.

The numbers of the collaboration projects and registered users in the 2004 FY are 63 and 195, respectively.

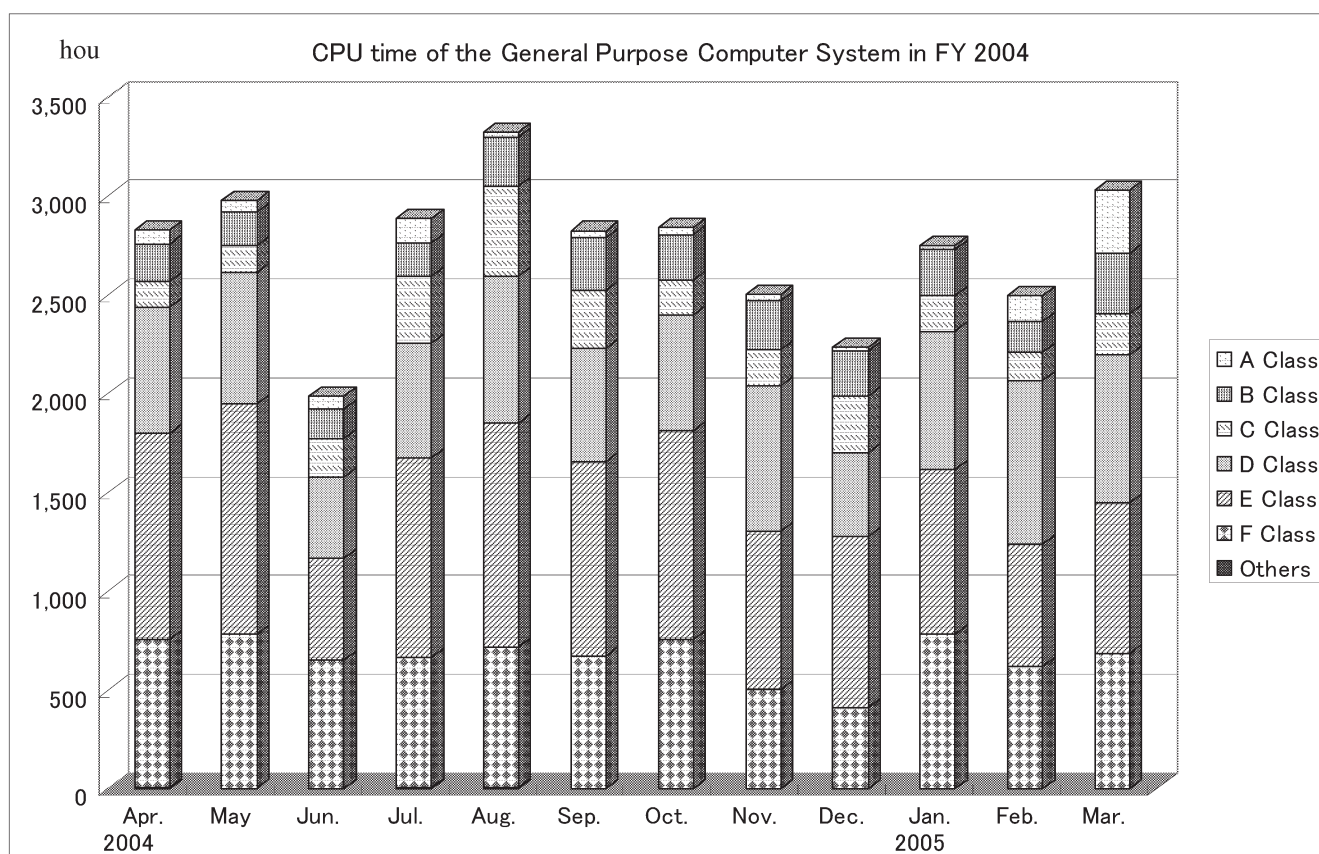


Fig. 2 : Operation Overview of SX-5 in FY

A: operation	B: cpu time	Ratio: B/6A	Number of jobs
8,663:32 hrs	33,147:45	63.8 %	80,325

Table 1 : Summary of SX-5 Operation in FY 2004

(Operation time is multiplied by 6 for reason SX-5 has 6

2. NIFS Campus Information Network

The advanced NIFS campus network of information called "NIFS-LAN" has been contributed to development of nuclear fusion research as the information infrastructure.

NIFS-LAN consists of three autonomous clusters which have the different purpose and usage as follows;

- 1) Research Information Cluster is the network of general use, and covers the campus whole region.
- 2) LHD (Large Helical Device) Experiment Cluster is offered for LHD experiment, and covers the building relevant to LHD experiment.
- 3) Large-scale Computer Simulation Research Cluster is offered in order to promote large-scale computer simulation research efficiently.

NIFS-LAN was built using ATM (Asynchronous Mode) Switches and a large number of Switching Hubs in the 1995, the 1996 and the 1998 FY. Introducing the Gigabit system in the 2001 FY, NIFS-LAN was shifted to the Gigabit system from ATM switching system. The gigabit network system has the speed of 1Gbps in the basic portion, and hosts for users are connected by 100Mbps, respectively.

NIFS-LAN is connected to Super-SINET, for the campus LAN and for the remote experiment participation. As shown below, NIFS-LAN with high-performance and high-security provides the user with comfortable and safe network environment.

1) Reinforcement of Internet connection

NIFS-LAN is connected to Super-SINET (Super Science Information Network, managed by National Institute for Informatics) by nine 1Gbps circuits. One circuit is used for campus LAN, the eight remaining circuits are used for LHD remote experiment participation.

2) Improvement in security

NIFS-LAN is working Fire-Wall, and IDS (Intrusion Detection System) and VPN (Virtual Private Network), in order to keep high-level security. The One-time-password system is also worked, in order to make LHD experiment data access from external researchers. Moreover, in order to protect of the attack from the outside, the mail server with an anti-computer virus function and a spam mail removal function is worked.

In 2004 FY, the following security measures started, according to the NIFS security policy which was defined in March 2004.

- a) A room for detecting and quarantining computer-virus was equipped;

It is confirmed in a quarantine room whether the PC is infected with the computer-virus, and whether the PC has any security holes, before the PC is connected to NIFS-LAN.

- b) Development of the MAC Address Certification System for receiving DHCP service;

This system permits DHCP (Dynamic Host Configuration Protocol) service only to the hosts registered into the database. Host's MAC (Media Access Control) Address are registered into a database and all DHCP servers within NIFS-LAN can control access with reference to the database. The limited registrant performs the host's security check, when the MAC address of the host is registered.

- c) Improvement in security of a wireless LAN access server;

The security setting parameters of a wireless LAN access server was made severe.

- d) Establishment of the network only for external connection;

The network was established for those who stay during a short period in our institute.

3) Reconstruction of the remote participating system for a LHD experiment

The LHD remote experiment participating system via Super-SINET was started in the 2001 FY. The remote station was installed in Tohoku University, University of Tokyo, Tokyo Institute of Technology, Nagoya University, Kyoto University, Hiroshima University and Kyushu University. Those remote stations were connected to LHD-LAN by 1Gbps MPLS-VPN(Multi-Protocol Label Switching - Virtual Private Network) on Super-SINET, respectively. In order to newly connect two remote stations (in University of Tokyo and Kyoto University), the network by the side of NIFS was reconstructed in the 2004 FY.

The connection between NIFS-LAN and the external networks is shown in Fig. 3.

The block diagram of NIFS campus information network is shown in Fig. 4.

(Horiuchi, R.)

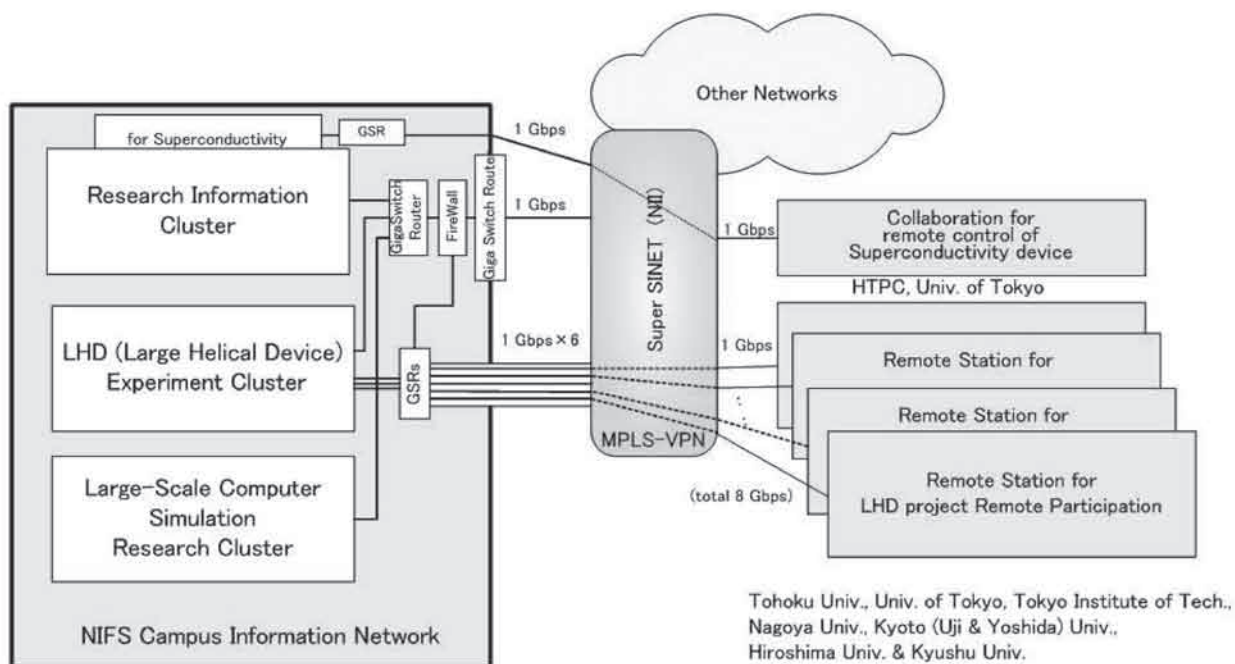


Fig. 3: External Connection of NIFS-LAN

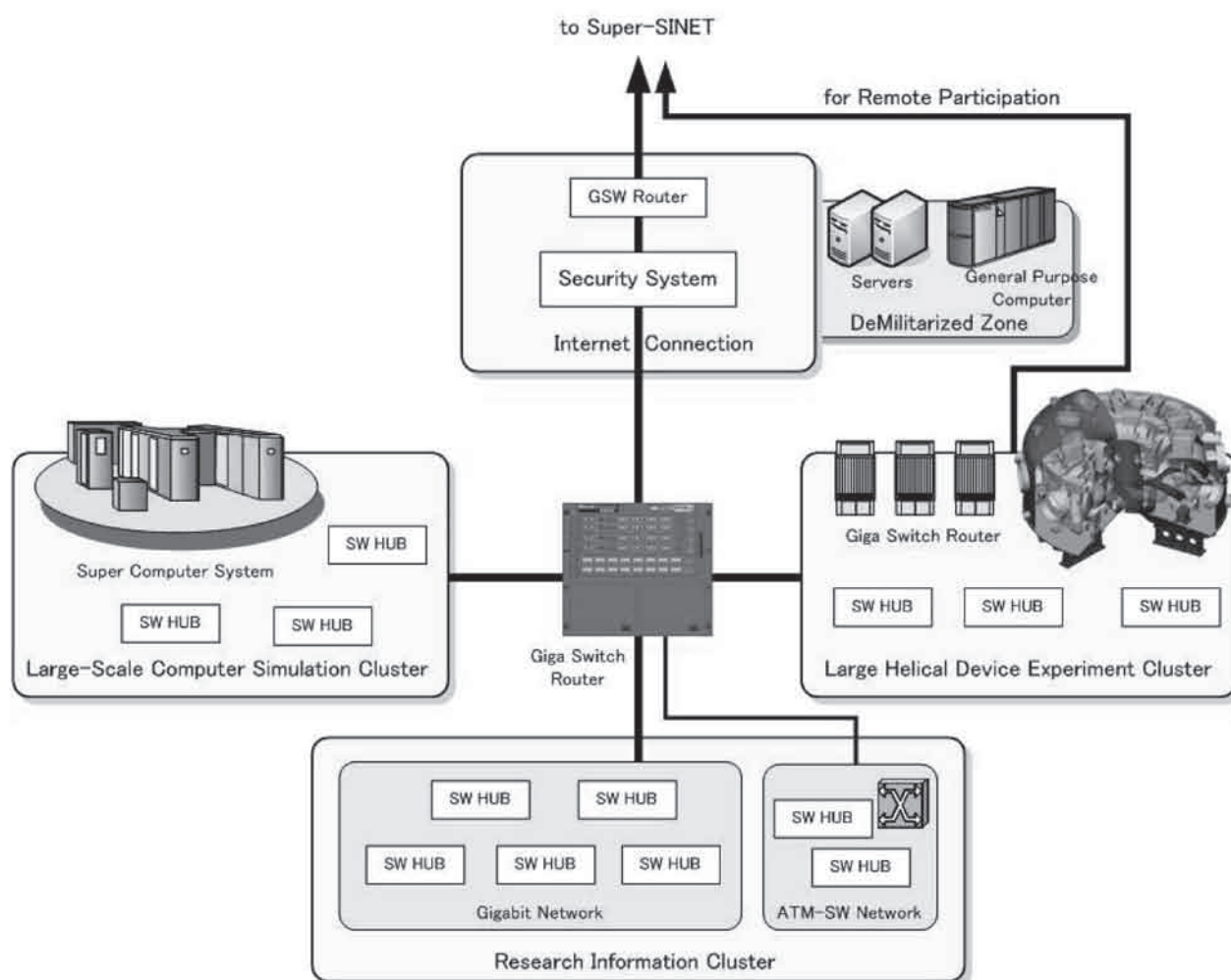


Fig.4: Block Diagram of NIFS Campus Information Network (NIFS-LAN)

12. Bidirectional Collaborative Research Program

The nuclear fusion research in universities including the National Institute for Fusion Science (NIFS) had been carried out by making use of different types of devices in order to prove the scientific viability as fusion reactor of various plasma confining concepts, which was thought to be the superior way from the viewpoints of developing the best fusion reactor and also of training a variety of specialists in this research field. With this policy, nuclear fusion research in the Japanese universities has produced many fruitful results. However, in order to push the fusion research activity further, it is considered to be more efficient to emphasize the principal device by rearranging and integrating multiple experimental devices which nevertheless have supported fusion research activity in Japan in this decade. This idea was proposed by the Committee of the Science Subdivision under the Council for Science and Technology, and the execution of this plan promoting collaborative research was given a high priority. The new policy of the committee is summarized in the report “Policy for executing Japanese nuclear fusion research”.

In the report, it is pointed out that continuous scientific research activity is necessary for a comprehensive understanding of toroidal plasma physics under the parameters which can be extrapolated to the fusion reactor. Therefore the Large Helical Device (LHD) has been selected as one of four principal fusion research programs in Japan, and NIFS is expected to expedite collaborating research. It is also noted in the report that the universities must contribute to the study of important issues in nuclear fusion research, such as the function of electrostatic potential on plasma confinement, high beta plasma physics, optimum magnetic configuration for plasma transport, steady state plasma generation, and so on. NIFS is requested to play a leading role in the execution of these studies among universities as an inter-university research institute.

A bidirectional collaborative research program has been newly set up so as to accomplish the role of NIFS proposed above. In past collaborative programs, university researchers went to NIFS and joined the research activity at NIFS. But in this program, the opposite movement of

researchers is enabled, so that NIFS researchers can go to the universities and join the activities at the universities. Hence a more efficient use of resources in both facilities becomes possible and the synergetic effect is expected.

This new collaborative research program started in this year under the support of the Ministry of Education, Culture, Sports and Technology. It involves four major university research centers; the Plasma Research Center, University of Tsukuba / The Laboratory of Complex Energy Process, Institute of Advanced Energy, Kyoto University / the Laser Fusion Research Center, Osaka University / Advanced Fusion Research Center, Research Institute for Applied Mechanics, Kyushu University. In this collaborative program, the researchers of NIFS and of those four research centers can move back and forth to each other to collaborate on the same research subject. In addition to this, each research center can have its own programs for using its major facility so that the researchers of other universities can come and join. It is unique and important that all these activities are supported financially as function of the NIFS bidirectional collaborative research program. The subjects of the bidirectional research program are subscribed from all over Japan every year as one of the three categories of the collaboration research program of NIFS, and the collaboration committee, which is organized under the administrative board of NIFS, adjudicates and selects the subjects.

In this year, forty three subjects were adopted in this category, among which were 14 at Tsukuba University, 7 at Kyoto University, 15 at Osaka University, and 7 at Kyushu University. All of these collaborations were carried out successfully, and the new program is proceeding well.

(Komori, A.)

§1. ICRF Wave Excitation and Propagation in the Axisymmetrized Tandem Mirror GAMMA 10

Fukuyama, A. (Kyoto University)
Yamaguchi, Y., Ichimura, M., Higaki, H. (University of Tsukuba)

At present, the realization of high-density operation with potential confinement is one of the most important issues on the tandem mirror research. Up to $4 \times 10^{12} \text{ cm}^{-3}$, the density increase with the potential formation has been observed in the GAMMA 10 tandem mirror. The plasma production with ion-cyclotron-range of frequency (ICRF) waves is commonly used in both fusion research and plasma applications. In plasmas with a relatively low density (order of 10^{12} cm^{-3}) and a small radius (a few tens cm), the wavelength is in the same order of the plasma size and eigenmodes are formed in both radial and axial directions. Because the wavelength depends strongly on the density, the density is likely to be clamped at the optimum value for the eigenmode formation. The saturation of the density increase is sometimes observed in GAMMA 10. To investigate the eigenmode formation, a two-dimensional wave calculation code has been introduced [1]. The spatial structures of the excited waves are obtained in the axisymmetric mirror field of the GAMMA 10 central cell.

To raise the limit for the density clamping, higher frequency ICRF source (high harmonic fast wave: HHFW), of which frequency is from 6 to 10 times ion cyclotron frequency at the midplane of the central cell, has been used. When HHFW is applied, several eigenmodes with different radial structures will be possibly excited [2] and the restriction of the density clamping will become moderate. The increase of the density from the saturation level has been clearly observed in the experiment [3]. In Fig.1, the amplitude of the wave field measured with a magnetic probe is plotted as a function of the line density. Before applying HHFW, initial plasmas with relatively low density are produced by ICRF waves near the fundamental cyclotron frequency. As shown in the figure, the amplitude of the wave field at $5 \times 10^{13} \text{ cm}^{-2}$ becomes small. In the

experiment, the density clamping is sometimes observed around this value. When the additional HHFW is applied, the density increases continuously above the value and the amplitude of the wave field starts to increase again from the value of $5 \times 10^{13} \text{ cm}^{-2}$. A solid line in the figure indicates the calculated amplitude of the wave field in the GAMMA 10 configuration. The eigenmode formation in the axial direction is clearly indicated on both experiment and calculation.

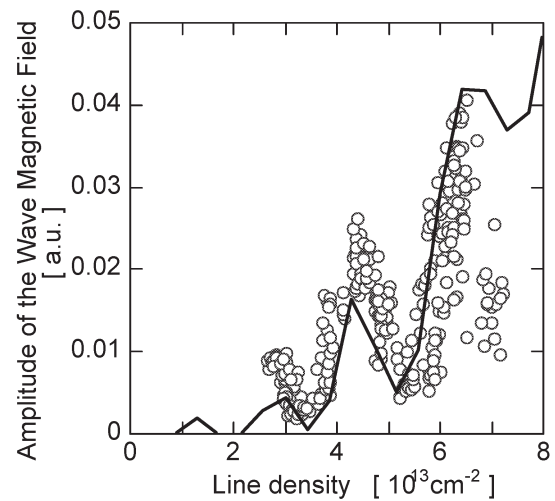


Fig.1 The amplitude of the wave field, measured with a magnetic probe, as a function of the line density. A solid line indicates the calculated amplitude in the GAMMA 10 configuration.

- [1] Fukuyama, A. and Ichida, A., Proc. of 1996 Int. Conf. On Plasma Phys., Vol.2, p.1342 (1997).
- [2] Yamaguchi, Y., et al., Trans. Fusion Sci. and Tech., **47**, 1536 (2005).
- [3] Ichimura, M., et al., Phys. Plasmas, **8**, 2066 (2001).

§2. Study of Impurity Ion Radiation Intensity in the GAMMA 10 Plasma

Yoshikawa, M., Kubota, Y., Kobayashi, T., Saito, M., Nakashima, Y. (Univ. Tsukuba, PRC)
Kato, T., Murakami, I., Goto, M.

Time and space resolved spectroscopic measurements of radiation spectra from a plasma give us a lot of important information, such as time and space variations of plasma density, electron and ion temperatures, etc. After comparing the collisional-radiative model (CR-model)¹⁾ calculation results for impurity ion line radiation and neutral hydrogen line emission intensities and those measured by spectroscopic method, we can obtain the impurity ion densities, electron density and electron temperature. The aim of this study is to construct the database of the absolute impurity ion and neutral hydrogen emissions and the CR-model for plasma spectroscopic diagnostics in the fusion plasmas.²⁻³⁾ Moreover, the neutral particle behavior is studied by using CR-model and multi-channel H_α line emission detection systems in GAMMA 10.⁴⁾

We have constructed the H_α line emission detection systems in each cells of GAMMA 10. In this year, the 5-channel H_α line emission detection systems are newly installed in the central throat and the barrier cell. Figure 1 shows the time dependence of H_α line emission radial profile in the barrier cell of GAMMA 10. Then the absolute H_α line emission radial profiles in each cell of GAMMA 10 are obtained in order to study the neutral particle behaviors and particle balances in the GAMMA 10

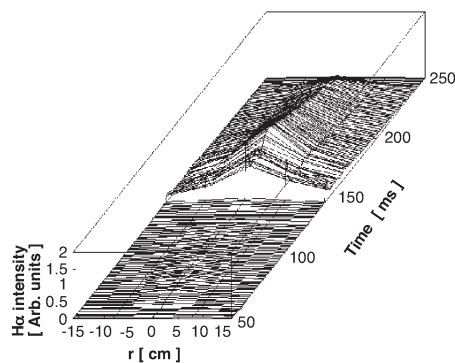


Fig. 1: Time dependence of H_α line emission radial profile in the barrier cell of the GAMMA 10.

plasma.

CR-model calculation codes for carbon and oxygen ions developed in NIFS were used in this study.¹⁾ We applied CR-model calculation results to observed impurity spectra in the GAMMA 10 tandem mirror to evaluate the impurity density profile and the particle balance of each charge state of carbon ion. We obtained CII and CIII density profiles by measured spectra and effective population rate coefficients. Moreover, we considered particle balance of each charge state of carbon ion, and estimate carbon ions density profiles with ionizing plasma approximation with considering the mirror confinement time. We calculated the effective ionization rate for each charge state of carbon ion and obtained the density profile of each ion. Figure 2 shows the density profiles of electron and each charge state of carbon ion estimated by the particle balance. Moreover, we calculated absolute emission intensities from all carbon ions. The result of our estimation showed that CV is dominant in the center of plasma and CIV is comparable to CIII in edge region. Then CIV spectrum (154.8 nm) is expected to emit the strongest in all carbon spectra.

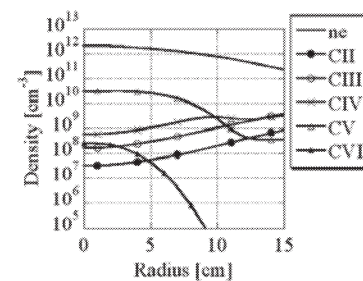


Fig. 2: Density profiles of electron and each charge state of carbon ion estimated by the particle balance.

Reference

- 1) Kato, T., et al.; Fusion Eng. Des, **34-35** (1997) 789.
- 2) Yoshikawa, M., et al.; Annual Report of NIFS, April 2001-March 2002 (2002) 374.
- 3) Yoshikawa, M., et al.; Annual Report of NIFS, April 2003-March 2004 (2001) 415.
- 4) Yoshikawa, M., et al.; Transactions of Fusion Science and Technology, **43** (2003) 189.

§3. Anisotropic Electron Velocity Distribution Function in GAMMA10 Tandem Mirror Plasma Analyzed by Means of Plasma Polarization Spectroscopy

Iwamae, A., Atake, M., Fujimoto, T.* (Dept. Mech. Eng. Sci., Kyoto Univ.)
Kobayashi, T., Kubota, Y., Matama, K., Yoshikawa, M. (Plasma Research Center, Univ. of Tsukuba)

The electron velocity distribution function (EVDF) in a plasma is one of the most important attribute of the plasma. When the EVDF is isotropic and Maxwellian, the determination of the EVDF is equivalent to measuring the electron temperature. However, a plateau-shaped electron energy distribution function is observed in the plug region of GAMMA 10 tandem mirror, in the case the electron cyclotron resonance heating (ECRH) is adopted for formation of a plug potential with a thermal barrier [1]. A departure from the Maxwellian velocity distribution is inferred. Since the electrons are accelerated in the direction perpendicular to the magnetic field, the non-Maxwell characteristics may indicate that the electron by ECR microwave in the plasma.

The emission from the plasma in the plug-barrier region was resolved into orthogonally polarized components, π and σ lights, with the polarization separation optics (PSO) schematically shown in Fig 1. The PSO consisted of a lens and a polarization separation Glan-Thompson prism made of calcite. The π light is the linearly polarized component parallel to the quantization axis i.e. magnetic field direction, and the σ light perpendicular to the magnetic field direction. These polarized light components were transmitted through a bundle of twenty optical fibers to the entrance slit of a one-meter focus spectrometer. The dispersed spectra were recorded with a charge coupled device (CCD) of $7.4 \times 7.4 \mu\text{m}$ 2048×2048 pixels equipped with a fast mechanical shutter. The dispersion was 0.296 nm/mm . The CCD was cooled and the temperature was kept constant at 275 K .

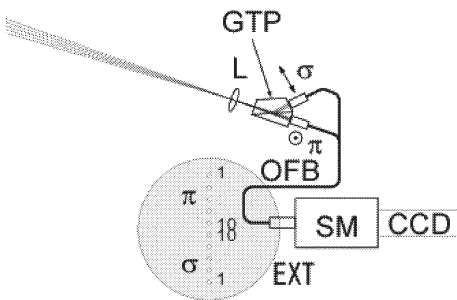


Fig. 1. Polarization Separation Optics.
GTP : Glan-Thompson Prism. OFB : Optical Fiber Bundle. SM : Spectrometer. CCD. Charge coupled device.

Figure 2 shows an example of the polarization separation spectra emitted from neutral helium atoms in the plasma during ECR discharge cleaning. Since the upper level of the line of $\lambda 504.8 \text{ nm}$ is a ^1S state, this line emission is never polarized and can be used as the reference for the polarization determination for other lines. The intensity of the π component I_π of the line $\lambda 501.6 \text{ nm}$ is higher than that of the σ component I_σ . After averaging over the twelve exposures, the observed polarization degrees $P = (I_\pi - I_\sigma)/(I_\pi + I_\sigma)$ of the lines $\lambda 504.8 \text{ nm}$ and $\lambda 501.6 \text{ nm}$ are $0.000(19)$ and $0.155(9)$, respectively. The numbers in the parentheses represents statistic errors.

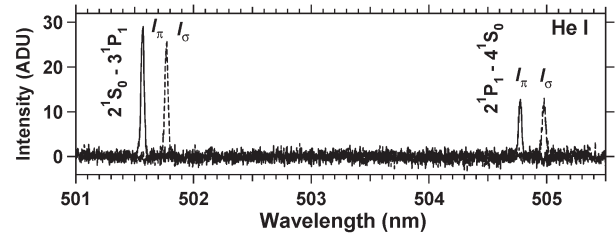


Fig. 2. Polarization separation spectra of HeI lines at $\lambda 504.8 \text{ nm}$ and $\lambda 501.6 \text{ nm}$. The σ component is displaced by 0.2 nm for easier comparison.

The magnetic field direction is perpendicular to the line of sight. Thus the longitudinal alignment $A_L = (I_\pi - I_\sigma)/(I_\pi + 2I_\sigma) = 2P/(3 - P)$ for 501.6 nm is $0.109(7)$.

Population-alignment collisional-radiative (PACR) model [2] for He I is used to estimate the anisotropic electron velocity distribution function (EVDF). We assumed that the EVDF is represented by a model function of two orthogonal temperature parameters

$$f(v, \theta) = 2\pi \left(\frac{m}{2\pi k_B} \right)^{3/2} \left(\frac{1}{T_{rd}^2 T_{ax}} \right)^{1/2} \exp \left[-\frac{m}{2k_B} \left(\frac{\sin^2 \theta}{T_{rd}} + \frac{\cos^2 \theta}{T_{ax}} \right) \right]$$

where T_{ax} and T_{rd} are axial and radial temperature parameters, respectively.

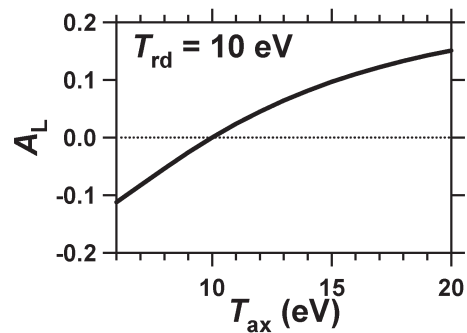


Fig. 3. A_L dependence on T_{ax} of two temperature parameter EVDF. T_{rd} is constant at 10 eV

A_L dependence on T_{ax} is shown in Fig. 3. When the shape of the EVDF is prolate spheroid, A_L is negative. When the shape of the EVDF is oblate spheroid, A_L is positive. $A_L = -0.11$ is obtained at the parameters $T_{rd}, T_{ax} = 10, 16 \text{ eV}$.
[1] T. Cho, *et al.*, Phys. Rev. Lett. **64**, 1373 (1990).
[2] A. Iwamae, *et al.*, in press

* Professor emeritus

\$4. Development of High Performance Antennas for Electron Heating in GAMMA 10

Saito, T., Tatematsu, Y., Hojo, H. (Univ. Tsukuba, PRC)
Ohkubo, K., Kubo, S., Shimozuma, T., Yoshimura, Y.
Saigusa, M. (Faculty of Engineering, Ibaraki Univ.)
Notake, T. (Graduate School of Engineering, Nagoya Univ.)
Nagai, D., Nozaki, K. (Graduate School of Pure and Appl. Sci. Univ. Tsukuba)

i) Objective

The role of electron cyclotron resonance heating (ECRH) in the GAMMA 10 tandem mirror is creating the plasma confining potential and heating of electrons in the central cell. Present important issues are high potential creation with high power microwave injection and controlling the radial potential profile. For central cell electron heating, is anticipated reduction of electron drag on hot ions. To achieve the above issues, it is necessary to radiate microwave power efficiently to the resonance surface. It is particularly important in a mirror device to control the radiation profile from an antenna, because the cyclotron resonance layer exists at a given position along the machine axis. The key issue is the design of mirrors for the transport of the microwave beam. The objective of the present study is development of the mirrors with necessary performance and application to the GAMMA 10 experiment.

ii) Method and procedure

A computer code was newly developed for calculation of electromagnetic (EM) field of the radiated microwave with a rather long wavelength corresponding to the frequency of 28 GHz. This code has been verified by low power tests. The EM field on the reflecting mirror is calculated from the field distribution over the open end of the power transmitting waveguide and that on the resonance layer is evaluated from the current induced on the reflecting mirror. The shape of the mirror is determined so that the EM field is to be axi-symmetric on the resonance layer through iterative calculation.

iii) Results

A new gyrotron of 28 GHz, 500kW was installed for high power electron heating at the plug position. Then a new antenna system was developed corresponding to HE11 mode transmission of the microwave power. A record value of an ion confining potential of 2.1 kV, which is three times as high as that in the experiment in the previous experiment, has been generated with the new antenna.

For electron heating in the central cell, the TE02 mode delivered from a 200 kW gyrotron was converted to the TE11 mode and radiated off the reflecting mirror installed just at the open end of the waveguide. Then, the distribution of the radiated field on the resonance layer has been optimized. Fig. 1 shows the distribution of the power density transmitted to the resonance layer along the vertical (x-axis of GAMMA 10 coordinates) direction. Its peak value is twelve times as high as that in two years ago and two times as high as that in the last year experiment. The new antenna system has been installed in March 2005.

iv) Next task

We will develop a new design technique of an antenna radiating EM field with an arbitrary power distribution for control of the radial potential profile in the next year. Experiments of central cell electron heating will be carried out and an antenna with further high performance will be developed. Application of the present technique to LHD will be considered.

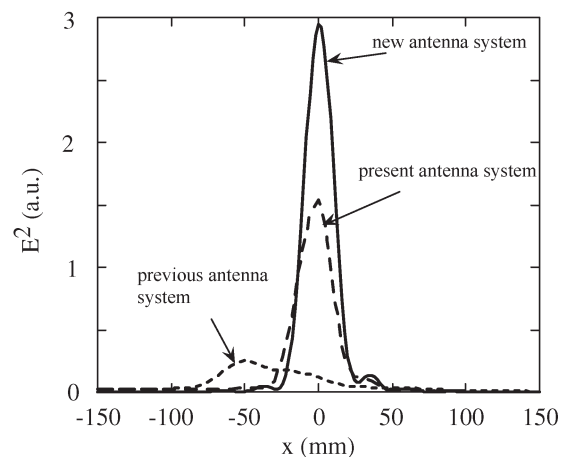


Fig. 1. The power distribution on the resonance layer in the central cell radiated from the new antenna is shown along with those from previous antennas.

References

- 1) Tatematsu, Y. et al.: in "US-Japan Workshop on Applications of RF Physics for Plasma Heating and Current Drive"
- 2) Tatematsu, Y. et al.: Trans. Fusion. Sci. Tech. **47** (2005) 257.

§5. Investigation on Applicability of a CUSPDEC to the GAMMA 10 Tandem Mirror

Yasaka, Y., Takeno, H. (Kobe Univ.)

Tomita, Y.

Ishikawa, M., Nakashima, Y., Saito, T., Hirata, M.,
Cho, T. (Univ. Tsukuba)

A cusp-type direct energy converter (CUSPDEC) for thermal ions produced in a D-³He fusion reactor¹⁾ has been investigated using a small-scale experimental device with a low-energy plasma source. The cusp magnetic field is used to separate ions from electrons, and a dc-biased plane collector decelerates and collects ions as a one-stage direct energy converter. Experimental results have revealed that the slanted cusp field has better capability of the charge separation than the normal cusp field. It is also found that the efficiency of energy conversion depends on the shape of the energy distribution function of incoming ions. Based on these experimental findings as well as theoretical and numerical studies, we here investigate applicability of the experimental device as a test direct energy converter for the GAMMA10 tandem mirror.

The CUSPDEC device consists of a plasma source, a guide field section, a cusp magnetic field section, and electron and ion collectors. The cusp field is created by two magnetic coils, A and B as shown in Fig.1. By adjusting the current in the two coils, I_A and I_B , the field line curvature can be varied. Typical values are $I_A = 30$ A and $I_B = 40$ A. A plasma beam with ions accelerated up to 0.3 keV is injected into the cusp field. We measured the ion and electron fluxes with changing I_B for a fixed $I_A = 30$ A. We define the transmission ratio of the particles as the ratio of the flux at the point cusp to that at the entrance. When the cusp field is formed, most of the electron flux flows into the line cusp and most of the ion flux into the point cusp, yielding the

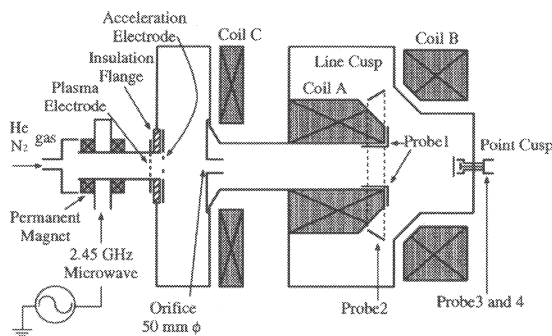


Fig. 1. Schematic diagram of CUSPDEC experimental device.

transmission ratio of electrons to about 0.1 and that of ion to 0.7~0.8.

The CUSPDEC device is assumed to be connected to an end flange of the GAMMA10 device, after removing the plasma source section, to accept end loss flux from the

plasma. The axial length between an end plate of the GAMMA10 device and the entrance of the CUSPDEC is about 2.5 m. Among several operation modes in the GAMMA10 device, we choose the hot ion mode and the ECRH plug mode²⁾ as shot examples. The data from an end loss analyzer for these particular shots show that the electron temperature for the hot ion mode is ~0.1 keV and that for the ECRH plug mode is ~ 0.7 keV with 2.9-keV tail component. The parallel ion temperature is 0.3~0.5 keV.

When the end loss flux is introduced to the CUSPDEC device, it is expected that electrons are deflected toward the line cusp region along the field lines and ions pass through the null point flowing into the point cusp region. We here

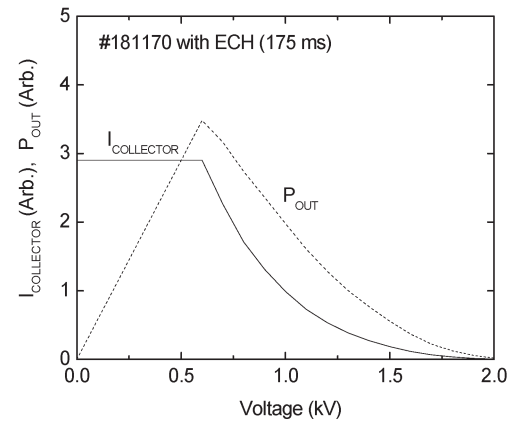


Fig. 2. Estimated current-voltage characteristics of the ion collector (solid line) and dc power output (dotted line) from the CUSPDEC..

assume that the transmission ratio of electrons is 0.

The solid curve in Fig. 2 is the current-voltage characteristics of the ion collector operating as the one-stage direct energy converter, which is located at the point cusp region of the CUSPDEC device. This curve is obtained from the measured ion energy distribution function for the ECRH plug mode in the GAMMA10 device. The dotted curve in Fig. 2 shows the output dc power P available for an external load. The conversion efficiency is defined as

$$\eta = \frac{P(V = V_{\text{opt}})}{I_0 \cdot E},$$

where V_{opt} is the voltage that gives a maximum P , I_0 is the collector current at low voltage, and E is the average energy of incoming ions. The value of η in this case is calculated to be 0.67. We will proceed to perform an experiment on the direct energy conversion in the GAMMA10 device.

References

- 1) Momota, H., Ishida, A., Kohzaki, Y., Miley, G., et al.: Fusion Technol., **21**, 2307 (1992).
- 2) Saito, T., Tatamatsu, Y., Kiwamoto, Y., et al.: Trans. Fusion Technol., **35**, 233 (1999).

§6. Magnetic Configuration of Kobe-Cusp DEC in GAMMA 10

Tomita, Y.,
Yasaka, Y., Takeno, H. (Kobe Univ.),
Ishikawa, M. (Univ. Tsukuba),
Nakashima, Y., Katanuma, I., Saito, T., Hirata, M.,
Cho, T. (PRC, Univ. Tsukuba)

The single slanted cusp direct energy converter (Kobe-Cusp DEC) [1] has been installed in Kobe University to investigate the proof of principle of the direct energy conversion, where several interesting results were pointed in respect to the charge separation between ions and electrons and energy discrimination of injected ion beams [2]. Now we have a plan to connect the Kobe-Cusp DEC in the GAMMA 10 tandem mirror device in order to investigate the high performance of the direct energy conversion. The Kobe-Cusp DEC will be attached obliquely on the end plate in GAMMA 10 device.

The magnetic field lines due to the Kobe-Cusp DEC without the GAMMA 10 device are shown in Fig.1, where the currents of the coils A, B, and C are 13.6, 15.4, 5.8 kAT, respectively. The stagnation point appears at the position of $\zeta = 0$ cm.

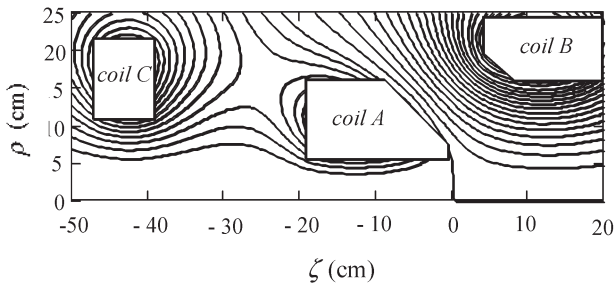


Fig.1 Magnetic field lines in the Kobe-Cusp DEC without the GAMMA 10 tandem mirror, where the currents of coils A, B, and C are 13.6, 15.4, 5.8 kAT, respectively.

In this configuration the GAMMA 10 mirror device makes the axial magnetic field of around 50 G along the symmetric axis of the Kobe-Cusp DEC ζ . This axial magnetic field slides the stagnation position to $\zeta = 2$ cm and makes sharp the slope of the line cusp separatrix (Fig.2). The slope angle of the line cusp is able to be changed by controlling the coil currents. The whole magnetic field lines from the attached position to the GAMMA 10 ($\zeta = -150$ cm) is shown in Fig.3. In these configuration the radial magnetic field produced by the Gamma 10 mirror field is quite small compared to the axial magnetic field, for example, radial magnetic field $B_\rho < 10$ G at $\rho = 0$ cm, $\zeta = -100$ cm, which is compared to the axial component $B_\zeta = 600$ G.

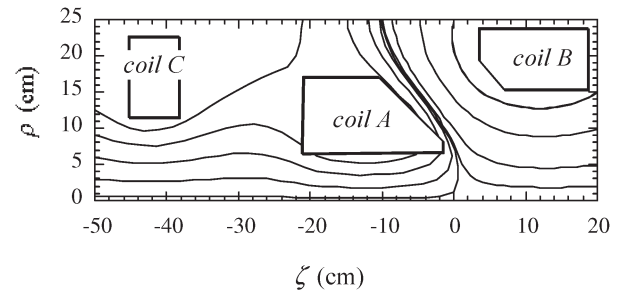


Fig.2 Magnetic field lines in the Kobe-Cusp DEC and the GAMMA 10 tandem mirror device. The coil currents are the same in Fig.1 and the GAMMA 10 device makes the axial magnetic field of around 50 G.

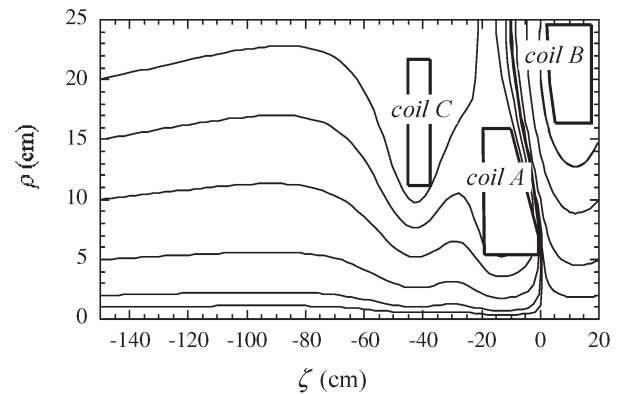


Fig.3 Magnetic field lines in the Kobe-Cusp DEC and the GAMMA 10 mirror device. The Kobe-Cusp DEC is attached at the end plate of the GAMMA 10 device, where the axial position of $\zeta = -150$ cm.

The quasi flux surface with a radius 3.6 cm at the axial position of $\zeta = -150$ cm crosses the right-lower corner of the coil A ($\rho = 5$ cm, $\zeta = 0$ cm). This means the injected GAMMA 10 plasma, especially electrons, outer than the radius of 3.6 cm has a possibility to contact to the coil can of the coil A. In order to study the performance of the Kobe-Cusp DEC the particle simulation in this configuration is necessary.

Reference

- 1) Tomita, Y., Yasaka, Y., Ishikawa, M., and Nemoto, T.: Trans. Fusion Science and Technol., **47** (2005) 43.
- 2) Takeno, H. and Yasaka, Y.: Trans. Fusion Technol. **39**, (2001).386.

§7. Excitation of RF Waves in GAMMA 10 and in the Local Magnetic Mirror Configuration on LHD

Ichimura, M., Higaki, H., Kakimoto, S., Yamaguchi, Y., Inoue, D., Ide, K., Nakagome, K., Nemoto, K. (University of Tsukuba)
Watari, T., Kumazawa, R., Mutoh, T., Seki, T., Saito, K.

In the GAMMA 10 tandem mirror, the ion cyclotron range of frequency (ICRF) heating is used not only for producing initial plasma but also for sustaining MHD stability and heating of the central cell ions. A hot-ion mode of operation has been realized and plasmas with a strong temperature anisotropy (which is defined as the temperature ratio of perpendicular to parallel to the magnetic field line) are formed. In the typical discharges, the anisotropy becomes more than 10 and Alfvén ion cyclotron (AIC) modes are spontaneously excited due to the anisotropy [1]. The AIC mode is one of the micro-instabilities and is observed as an eigenmode in the axial direction.

On the while, in fusion-oriented devices with a toroidal configuration, a high power ICRF heating and a high power neutral beam injection (NBI) heating are commonly used to create the high performance plasmas. Resultant high-energy ions are trapped in the local magnetic mirror configuration and form the velocity distribution with the strong anisotropy. In LHD, the measurement of fluctuations in the ion cyclotron frequency range has been started. In burning plasmas, the ion cyclotron emission (ICE) has been observed in the ion cyclotron frequency and its higher harmonic regions [2].

In this research, the mechanism of the excitation of those micro-instabilities in the ion cyclotron frequency range is investigated and the relation among the AIC mode, ICE and other instabilities. On 2004, the experimental observation is focused to the excitation of the higher harmonic AIC waves in GAMMA 10. Figure 1 shows the temporal evolution of the frequency of excited modes and the wave amplitude is represented by a shade of brightness. The fundamental AIC waves are shown in Fig.1(a) and the fluctuations in the 2nd harmonic region in Fig.1(b). The frequency changes depending on the plasma parameters are clearly observed in both signals.

To evaluate the excitation of the higher harmonic waves,

the dispersion relation of the electromagnetic waves in hot plasmas with the temperature anisotropy has been solved. It is verified the waves in a fast Alfvén wave branch become unstable due to the temperature anisotropy. As shown in Fig.1, the frequency band of the 2nd harmonic waves is narrower than that of the fundamental waves. In Fig.2, the growth rate of the 2nd harmonics is plotted as a function of the ion temperature. The growth rate of the 2nd harmonic waves is indicated to be quite small in the present plasma parameters.

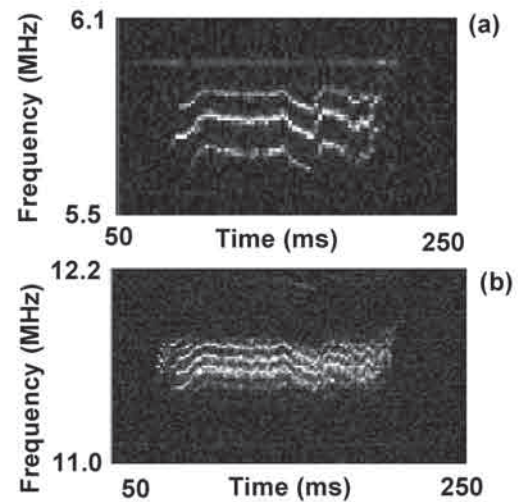


Fig.1 Temporal evolution of the frequency of excited modes (a) AIC modes and (b) 2nd harmonic waves. The wave amplitude is represented by a shade of brightness.

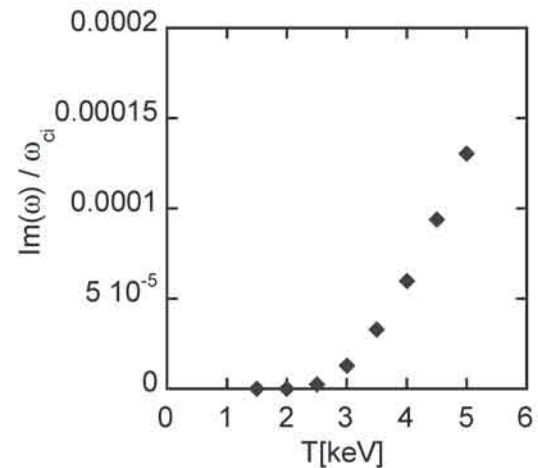


Fig.2 The growth rate of the 2nd harmonic waves are plotted as a function of ion temperature

- [1] Ichimura, M., et al., Phys. Rev. Lett. **70**, 2734 (1993).
- [2] Cottrell, G.A. and Dendy, R.O., Phys. Rev. Lett. **60**, 33 (1988).

§8. ICRF Heating and Ion Acceleration at the Open End in GAMMA 10

Ando, A., Tobari, H., Shibata, M., Hattori, K., Inutake, M. (Dept. Electrical Eng., Tohoku Univ.)
Ichimura, M., Higaki, H. (Plasma Research Center, Tsukuba Univ.)

Recently, it is expected that many plasma technologies developed in the long-running fusion researches should be utilized in other research fields. Near-future space exploration missions need further investigation of advanced electric propulsion systems which use high density plasma production and acceleration technique. A magnetic nozzle acceleration and ion heating in a fast flowing plasma attracts much attention in such an advanced electric propulsion system. In the Variable Specific Impulse Magnetoplasma Rocket (VASIMR) project, proceeded in NASA as a main engine in manned Mars missions, it is proposed to control a ratio of specific impulse to thrust at constant power.[1] This is a combined system of an ion cyclotron heating and a magnetic nozzle, where a flowing plasma is heated by ICRF (ion cyclotron range of frequency) power and the plasma thermal energy is converted to flow energy via a magnetic nozzle. ICRF heating to a fast-flowing plasma has been demonstrated with an input RF power up to 15kW in the HITOP device, and Doppler effect due to the plasma flow was observed.[2] For the further development of the thruster, experimental investigation with higher RF power is inevitable.

The concept of the thruster well suites an open-ended mirror device, where intensive researches of plasma confinement and RF heating has been progressed. A well-organized large-scale linear magnetic device, GAMMA10, has a number of useful diagnostics and high-power RF systems.

The purpose of this research is to investigate effective methods of wave excitation and to establish a high-power ion heating technology in a fast-flowing plasma for the advanced plasma thruster.

Firstly, we have performed experiments to measure ion Mach numbers in the open-end section. In the GAMMA10, there observed an increase of ion temperature in the open-end section under the high ion temperature mode operated with central ion beach heating. An ion Mach number was measured by up-down type Mach probe located at 30cm downstream from the central cell in order to investigate a relationship between central ion heating and an ion flow toward the end cell.

Here, M_i is represented as a ratio of ion flow velocity U to ion acoustic velocity C_s . It is related to a ratio of the plasma flow energy E to its thermal energy W .

$$M_i = \frac{U}{C_s} = \frac{U}{\sqrt{\frac{k_B(\gamma_e T_e + \gamma_i T_i)}{m_i}}} = \sqrt{\frac{\frac{1}{2} m_i U^2}{\frac{1}{2} k_B(\gamma_e T_e + \gamma_i T_i)}} = \sqrt{\frac{E}{W}}$$

Efficient plasma acceleration can be realized by converting plasma thermal energy to flow energy. M_i is one of the good indicators of plasma flow properties.

Figure 1 shows ion saturation currents detected by one of collection tips of the Mach probe as a function of an angle between plasma flow direction and that normal to the collection surface. The collection surface faces to the central cell at the angle of 180°. Though the magnetic field at measurement position is 1T, the Mach probe still under the unmagnetized condition because of the high ion temperature more than 100eV.

Figure 2 shows a radial profile of M_i at the Mach probe position. The axis of abscissas is an equivalent radius of the central cell. It is found that M_i at $r=0$ is more than 2, namely a super sonic flow is formed in the end-cell region.

Experimental researches on the effect of high-power RF heating on the plasma flow and energy conversion by a magnetic nozzle should be pursued further.

Reference

- 1) F.R.ChangDiaz, et al.: Proc. of 36th Joint Propulsion Conf., (Huntsville,2000), AIAA-2000-3756.
- 2) A.Ando, et al.: Proc. the 7th APCPST, (Fukuoka, 2004), A2 (2004) 45.

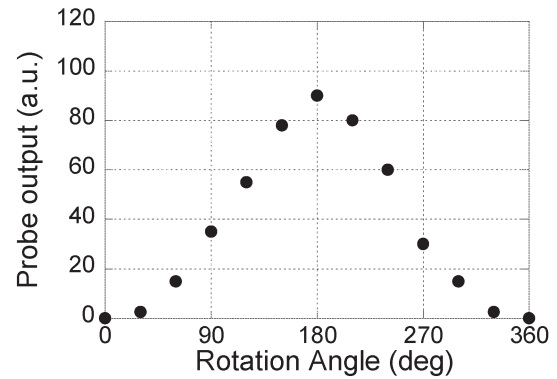


Fig.1 Ion saturation currents detected by the directional probe as a function of an angle between plasma flow direction and normal to probe surface.

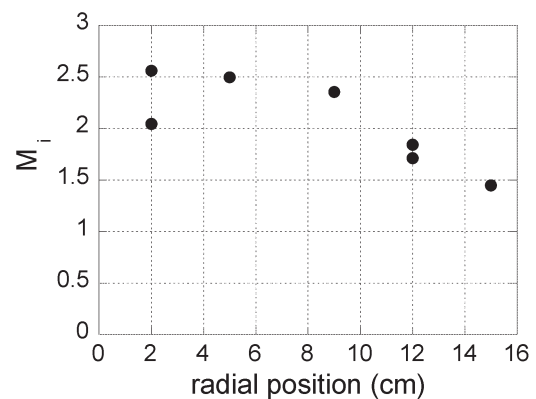


Fig.2 Radial profile of an ion Mach number M_i at end-mirror cell in Gamma 10. (an equivalent radius to the center cell region)

§9. Propagation and Radiation of Cyclotron Waves and Excitation of Fluctuations Due to High Power Plug ECRH

Hatakeyama, R., Kaneko, T., Takahashi, K.
(Dept. Electronic Eng., Tohoku Univ.)
Saito, T., Tatematsu, Y., Itakura, A.
(Plasma Res. Center, Univ. Tsukuba)

The electron cyclotron wave (ECW) is an important plasma wave in the fields of basic plasma physics, thermonuclear fusion, and some applications. Especially, high power electron cyclotron resonance heating (ECRH) is hoped to be the most effective method for the formation of thermal transport barrier in tandem-mirror devices,¹⁾ where localized strong electron heating in the perpendicular direction against the magnetic-field lines is demanded. Although the localized wave absorption is necessary for efficient and strong electron heating as mentioned above, the Doppler shift effect by high energy electrons expands the cyclotron resonance region, namely, broadens the wave absorption region.

In Tohoku University, on the other hand, it was reported that a left-hand polarized wave (LHPW), which has been believed not to be related to electron cyclotron resonance (ECR), is also unexpectedly and sharply absorbed near the ECR point.^{2,3)} In addition, the experimental results demonstrated that the damping region of the LHPW is more localized than that of the right-hand polarized wave (RHPW). Although the mechanism has not been entirely clarified, we believe that the localized LHPW absorption can lead to the localized and strong electron heating. When this new damping mechanism of the ECW is applied to the efficient electron heating in large fusion devices such as the tandem-mirror device using the high power ECRH, it is necessary to clarify the nonlinear effects of the strong wave field on the propagation and radiation of the ECW.

Based on these backgrounds, the purpose of the present work is to clarify the propagation and radiation characteristics of the ECW, including the nonlinear effects such as parametric decay which can cause the degradation of the heating efficiency.

Experiments are carried out with a plasma in the west plug/barrier cell of the GAMMA10 tandem mirror. This cell is an axisymmetric mirror that is connected to the central solenoid through a quadrupole mirror cell along the magnetic-field lines. The plasma is produced in the central solenoid by radio-frequency (RF) wave heating, and a potential barrier created by ECRH in the plug/barrier cells at the machine ends prevents the plasma from flowing out along the field lines. The ECRH power at 28 GHz is delivered to the fundamental resonance layer of 1 T for the plug and to the second harmonic layer of 0.5 T near the

mid-plane for the thermal barrier. The heating power, variable up to 500 kW, is generated in a newly developed gyrotron, transmitted through a cylindrical corrugated wave-guide system in HE_{11} mode and radiated to the resonance layer with newly designed mirrors. We have set up a measurement system for receiving and analyzing electromagnetic radiation in the electron cyclotron range of frequencies, which consists of a movable receiver antenna, a heterodyne mixer with a Gunn oscillator (28 GHz, 13 dBm), and a spectrum analyzer.

Figure 1 shows the observed frequency spectrum of radiated electromagnetic waves from the plug region, where the launched plug ($\omega_1/2\pi = 28.06$ GHz) and barrier ($\omega_2/2\pi = 28.0$ GHz) ECRH powers are 240 kW and 100 kW, respectively. A continuum radiation is observed extending over several hundred MHz above the fundamental electron cyclotron frequency. Moreover, a sharp peak is observed below the frequency $\omega_2/2\pi$ of the second harmonic heating wave by the difference $(\omega_1 - \omega_2)/2\pi$, possibly due to a nonlinear effect of the strong wave field, such as the parametric instability.

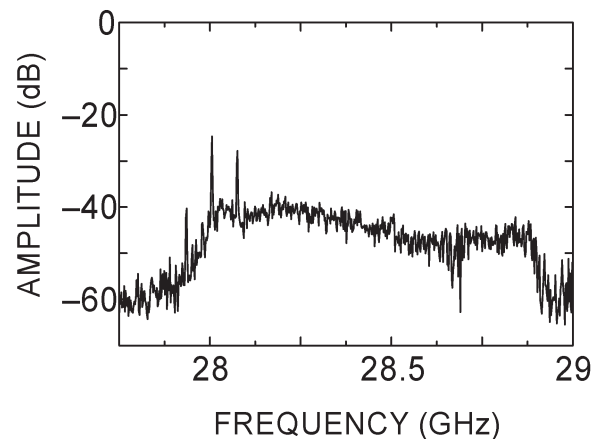


Fig. 1. Frequency spectrum of radiated electromagnetic waves at the plug region, where the plug and barrier ECRH powers are 240 kW and 100 kW, respectively.

Reference

- 1) Saito, T., Ishii, K., Itakura, A., Ichimura, M., Islam, M.K., *et al.* : J. Plasma Fusion. Res. **81** (2005) 288.
- 2) Kaneko, T., Murai, H., Hatakeyama, R., and Sato, N. : Phys. Plasmas **8** (2001) 1455.
- 3) Takahashi, K., Kaneko, T., and Hatakeyama, R. : Phys. Rev. Lett. **94** (2005) 215001.

§10. Study of Radial Transport of Bounce Ions by Means of Control of Radial Potential Profile of Core Plasma

Ishii, K., Saito, T., Katanuma, I., Yoshikawa, M., Kojima, A., Miyata, Y., Yamaguchi, T., Fujimoto, S. (Tsukuba Univ.)
Iguichi, H.

In order to measure the density profile of the periphery plasma, the lithium beam probe method is applied successfully in National Institute for Fusion Science. The beam probe method is also suitable for the measurement of the density profile at the inner mirror throat of the plug/barrier cell in the tandem mirror.

The bounced ion by the electrostatic plug potentials plays an important role in the improvement of the confinement time in the tandem mirror.

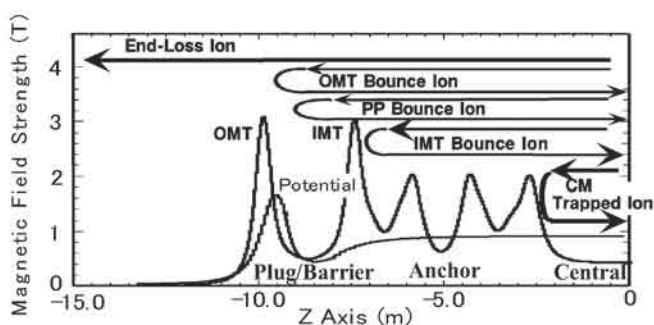


Fig.1. Bounce ions and axial magnetic field and potential profiles

The transport of the plug potential bounce ion was investigated numerically, and the moderate radial potential profile was useful to suppress the ion transport into the loss region due to the slight discrepancy between the magnetic flux tube and the equi-potential surface. 1) The bounce ions were also measured directly by using a charge exchange bounce ion analyzer located near the inner mirror throat of the plug/barrier cell. We selected both pitch angle and energy of the charge exchange neutral particle caused by the bounce ion, and identified the plug potential (PP) bounce ion, the outer mirror throat (OMT) bounce ion and the inner mirror throat (IMT) bounce ion as shown in Fig.2. The density profile of the plasma is required to estimate the quantity of the bounce ion.

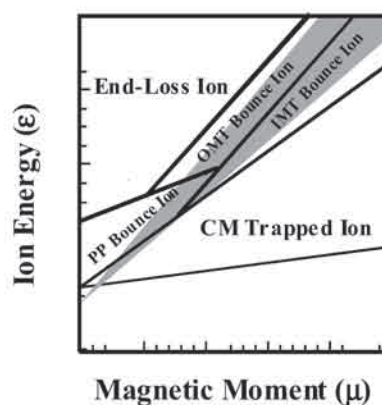


Fig.2. Measurable region of the bounce ions

The plug potential bounce ion and the outer mirror throat bounce ion were measured as shown in Fig. 3.

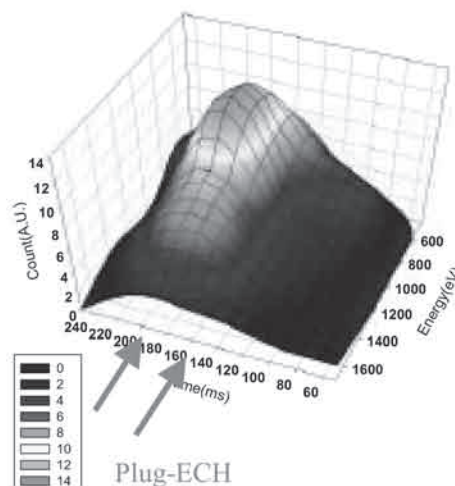


Fig.3. PP bounce ion and OMT bounce ion are created during plugging

The bounce ion was investigated with the radial potential profile of the central solenoid measured by the gold neutral beam probe. The neutral particle density and the plasma density profiles are required in order to estimate the quantity of the bounce ion. We try to set the lithium beam probe at the IMT region for measurement of the plasma density profile.

Reference

- 1) Ishii, K., et al., Transactions of Fusion Science and Technology **47**, No.1T (2005) 78

§11. Study of Potential Confinement Mechanism via Plasma Visualization Technology

Mase, A., Kogi, Y., Ignatenko, M. (KASTEC, Kyushu Univ.)
Yoshikawa, M., Itakura, A., Nakahara, A., Hojo, H.,
Cho, T. (PRC, Univ. Tsukuba)
Nagayama, Y.

In tandem mirrors, an electrostatic potential is created in order to improve axial confinement. The radial electric field E_r due to this potential causes a $E_r \times B$ plasma rotation in the direction of the ion diamagnetic drift velocity. The verification of the effect of E_r is one of the most critical issues to understand the physics basis for recent confinement improvement. Understanding the mechanism of this effect requires the use of sophisticated diagnostic tools for measurement of plasma profiles and their fluctuations. Recently, numerous studies have stressed the need for high resolution imaging diagnostics, which will permit the visualization of 2D and 3D structures of plasma parameters such as electron density and temperature. Significant advances in microwave and millimeter wave technology have enabled the development of a new generation of imaging diagnostics as visualization tool in this frequency range. This report describes the development of millimeter wave imaging diagnostics applied to the GAMMA 10 tandem mirror.

In this fiscal year, we have operated a phase-imaging interferometer (PII) installed in the plug region. The PII consists of a quasi-optical transmission line with parabolic and ellipsoidal mirrors and heterodyne receiver with a frequency of 70 GHz and is comprised of a 4×4 hybrid detector array with the 16 elements of beam-lead GaAs Schottky barrier diodes bonded to bow-tie antennas on a fused-quartz substrate. A scalar-feed horn produces a symmetric radiation pattern with low side lobes, which is well fitted by a Gaussian distribution. The cross section of the probe beam is 200 mm × 200 mm at the plasma center. The receiving optics, an ellipsoidal mirror, a flat mirror, and polyethylene lenses, are designed by using a ray-tracing method to focus radiation signals onto a 2D detector array. The quadrature-type detection system provides the phase difference between two intermediate frequency (IF) signals obtained by mixing the transmitted signal (RF) and the local oscillator signal (LO). The phase difference is proportional to line density of plasma.

Since the number of the quadrature phase detector is limited to 4 in the present stage, at least 4 plasma shots with good reproducibility are needed to obtain a full 2D profile. The time evolution of the line density obtained by one of the channels is shown in Fig. 1(a). The changes of the 2D line-density profiles during the plasma shot are shown in Fig. 1 (b) and (c). When the ECRH power is applied to the plug cell plasma at $t=180$ ms, the confining potential is created near the position of $z=962$ cm where the magnetic field strength equals to 1 T. At the region of $z=971$ cm where the imaging system is installed, the loss particles

decrease due to the formation of the confining potential. When the ECRH is turned off at $t=200$ ms, the confining potential disappears, and a short burst appears in the line-density signal corresponding to the axial drain of the plasmas. The variation of the profile in the axial direction is caused by the change of the magnetic field.

We are developing a new type of imaging antenna named double balanced mixer antenna (DBMA). The DBMA has electrically similar structure to doubly balanced mixer. Two sets of baluns in the DBM act as two dipole antennas in DBMA. Each antenna is arranged perpendicularly in order to detect RF and LO waves with different polarization. The IF signals generated in ring quad diodes are combined directly outside of the DBMA via RF rejection choke coils. The characteristics of the antenna is have been tested at the frequency of 70 GHz. We plan to replace present imaging antenna, bow-tie antenna, to DBMA in FY2005.

In order to upgrade the imaging system to imaging reflectometer, the numerical study of microwave imaging reflectometry (MIR) has been started. The parameter of focusing optics, such as lens aperture size and the effect of misalignment has determined for the central cell MIR system.¹⁾

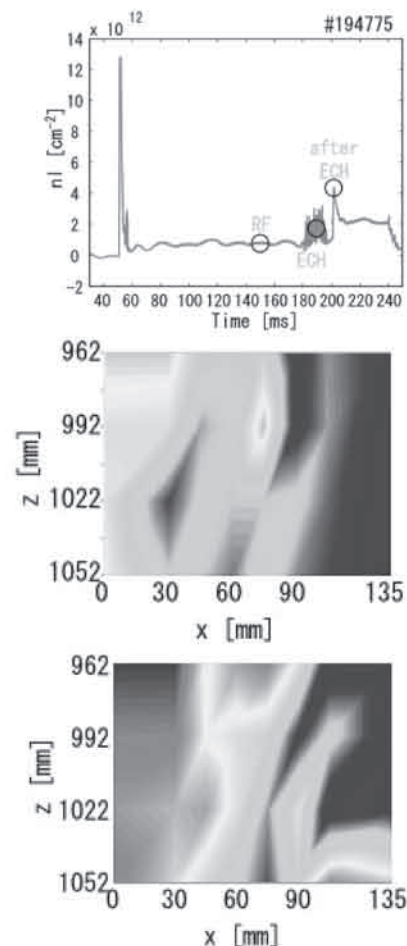


Fig.1 Time evolution of 2D line density profiles.

Reference

1) Ignatenko, M., Mase, A., Bruskin, L., Kogi, Y., and Hojo, H., Trans. Fusion Sci. Tech. **47**, 183 (2005).

§12. Analysis of Neutral Particle Transport and Recycling Behavior in Open Magnetic Field Configuration Plasmas

Nakashima, Y., Yoshikawa, M., Islam, Md. K. (Univ. Tsukuba, P.R.C.)
 Nishino, N. (Hiroshima Univ., Eng.)
 Kobayashi, S. (Kyoto Univ., I.A.E.)
 Shoji, M.,
 Sawada, K. (Shinshu Univ., Eng.)
 Ishimoto, Y. (JAERI, Naka)
 Kubota, Y., Higashizono, Y. (Univ. Tsukuba, Graduate School of Pure and Appl. Sci.)
 Tomita, Y., Sagara, A., Masuzaki, T., Morisaki, T.

Investigation of edge plasma behavior and neutral particle transport is important subject for open magnetic field configuration plasmas as well as toroidal configuration plasmas. Particularly in tandem mirror plasmas, penetration of neutrals into the core plasma region plays an important role in formation of the neutral density profile, since the plasma density is lower than that of tokamaks. Neutral particle transport simulations based on the Monte-Carlo methods have been widely used as a standard way to approach neutral behavior in the complicated systems of fusion devices. In this study, we develop three-dimensional neutral transport analyses in open magnetic field region such as in GAMMA 10 plasmas using the Monte-Carlo neutral particle code DEGAS. In order to investigate precise behavior of edge plasmas, a high-speed camera is applied to the GAMMA 10 central-cell for the first time.

Figure 1 shows the mesh model of the wall surface of the vacuum chamber in the central and anchor cells, together with the grid structure of the plasma surface and the components installed in the vacuum chamber used in the present calculation. In this model, as shown in the figure, an up-down symmetry is introduced and the simulation space is divided into 11 segments radially and 8 segments azimuthally. In the axial direction, 69 segments are defined, which extend from the central midplane to the outer-transition of the anchor-cell. In order to apply the geometrical structure precisely into the simulation space, additional structures, "second wall", are defined. In the present simulation, a gasbox and two ICRF antennas are treated as isolated walls in addition to the 3-dimensional mesh structure of the central-cell vacuum vessel wall. The components defined as the second wall are shown in Fig.1 (c). After introducing this boundary condition, a modification of the algorithm has been made in the code, which preserves the consistency in particle tracking with interactions between test particles and the "second wall". Thus the use of a "second wall" was successfully applied in addition to the usual vacuum chamber wall. It enabled us to realize a detailed three-dimensional particle simulation including complicated structures in the simulation space.

In the GAMMA 10 central-cell, visible imaging measurement was tried by a fast camera (Ultima-SE, Photron Inc.) for the very first time. Gas puff in the central region was used to visualize mainly plasma periphery and

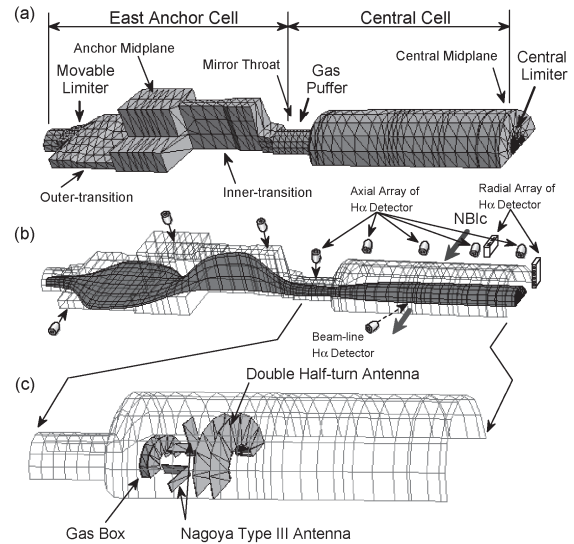


Fig. 1. Mesh model used for the 3D-DEGAS simulation. (a) surface structure of the vessel wall, (b) grid shape of the plasma surface, (c) structure of the "second wall" introduced into the code.

it is expected that plasma turbulence will be visualized. Figure 2 shows one of the digital video output images of gas puff imaging with 40500 FPS and 64x64 pixels. The right side in Fig.2 is limited by port duct. During gas puff, localization of plasma light and the vibration of plasma periphery were observed clearly by the fast camera.

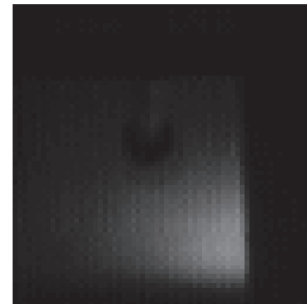


Fig. 2. Video output image during gas-puff imaging. Gas puffing is carried out at the right side of the picture from the bottom.

Reference

- 1) Nakashima, Y. *et al.*: Proc.16th PSI meeting (May 24-28, 2004, Portland Maine, USA)
- 2) Nakashima, Y. *et al.*: Trans. Fusion Technol. **47** No.1T (2005) 155.
- 3) Nakashima, Y. *et al.*: J. Nucl. Mater. **337-339** (2005) 461.
- 4) Nishino, N., Nakashima, Y. *et al.*: submitted to J. Plasma and Fusion Research.

§13. Analysis of Edge Fluctuation with ICRF in a Tandem Mirror for the Purpose of Radial Transport Control

Takeo, H., Yasaka, Y. (Kobe Univ.), Hojo, H., Ichimura, M., Higaki, H., Cho, T. (Univ. Tsukuba)

A study on formation of DC electric field and flow shear by an application of ICRF is important irrespective of confinement magnetic configuration¹⁾. Present study has a purpose of clarification of physical mechanism of the relation among ICRF, DC field, and flow shear, and transport control based on the phenomena. As a fundamental study, edge fluctuation varying with ICRF non-linearly is analyzed in GAMMA10 tandem mirror.

In GAMMA10, low frequency fluctuations in the scrape-off layer plasma are observed by application of RF2 which is for central cell ion heating. Frequency spectrum measured by probes shows a fundamental oscillation of 5 kHz, and 2~4th order harmonic oscillations exist during whole period of a shot.

Macroscopic parameters of line density and diamagnetic signal increase as RF power increases as shown in Fig. 1. The increasing rates, however, vary at around net power of 50 kW.

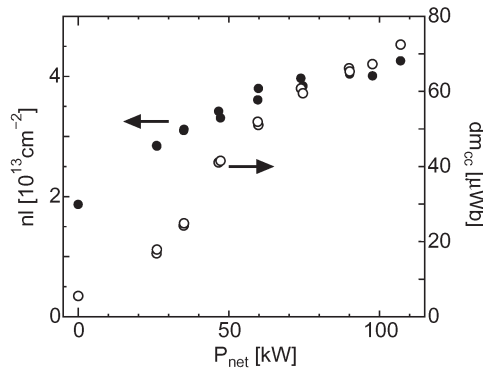


Fig. 1 Line density and diamagnetic signal versus RF net power.

Low frequency fluctuations also vary at the same threshold power. Figure 2 indicates samples of spectrum. Here, (a) and (b) are for relatively higher RF net power(90 kW) and for lower one(35 kW), respectively. As shown in the figure, the fluctuation consists of plural number of frequencies for (a). On one hand, it consists of a single frequency for (b).

Dispersion relation of the fluctuation also measured by an axially aligned probe array. Figure 3 shows frequency versus phase difference between probe signals for highly correlated components. In the relatively higher RF net power case(a), fluctuation has a constant velocity from center to throat, although it has almost

no phase difference in the lower one(b). The former one is considered to be an electron drift wave, and the latter one is a flute wave.

The characteristics of edge fluctuation were observed, which varied non-linearly with ICRF power and had correlation with macroscopic parameters.

Reference

- 1) O. Sakai and Y. Yasaka: Phys. Plasmas **2**, 3249 (1995).

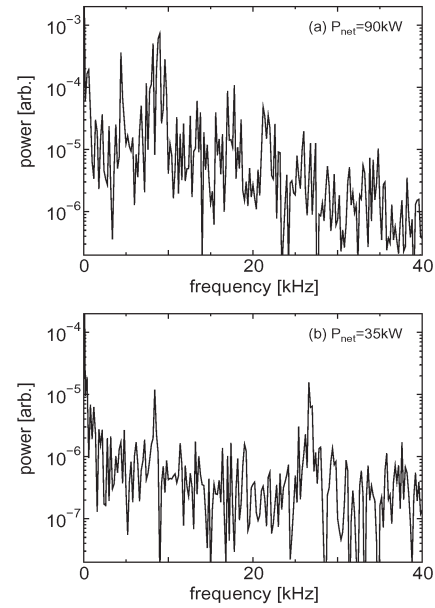


Fig. 2 Samples of spectrum of fluctuation: higher RF net power(a) and lower one(b).

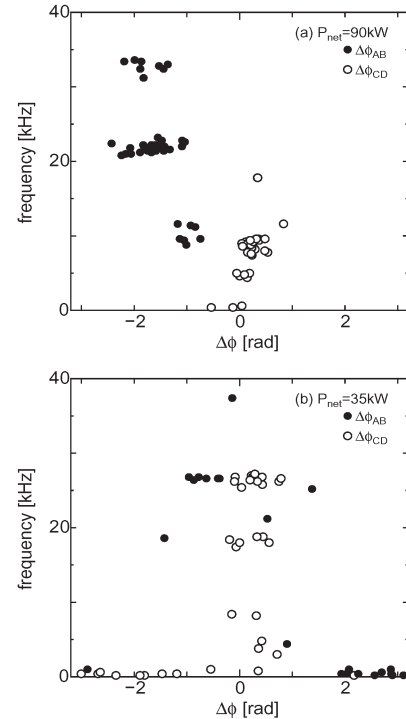


Fig. 3 Dispersion relations of fluctuation: higher RF net power(a) and lower one(b).

§14. Progress in Potential Formation and Findings in the Associated Radially Sheared Electric-Field Effects on the Suppression of Intermittent Turbulent Vortex-like Fluctuations and Transverse Losses

Cho, T., GAMMA 10 Group (Plasma Research Center, University of Tsukuba),
 Pastukhov, V.P. (Russian Research Center “Kurchatov Institute”, Moscow, Russia),
 61 Collaborators from Japanese Universities and Institutes

(1) *Three-time progress up to 2.1 kV in the formation of ion-confining potential heights in comparison to those attained 1992-2002 is achieved (Fig. 1) for tandem-mirror plasmas in the hot-ion mode with ion temperatures of several keV.*^{1,2)}

(2) The advance in the potential formation gives bases for a *finding of the remarkable effects of radially produced shear of electric fields E_r or non-uniform sheared plasma rotation $\Omega_r = E_r / (r_c B)$ on the suppression of turbulent fluctuations for the first time in GAMMA 10.*^{1,2)} (Here, r_c denotes a radius mapped to the central-cell.) (2-i) Such a shear effect on the central-cell plasmas is highlighted visually by x-ray tomography diagnostics (Fig. 2); that is, spatially and temporally *fluctuated vortex-like structures are clearly observed* in plasmas produced by ICH alone [having a quite *weak shear*]. (2-ii) However, during the application of plug ECH into the ICH plasmas, an associated potential rise produces a *stronger shear* [$E_r = \text{several } 10 \text{ kV/m}^2$]. In this case, *the disappearance of the turbulent vortices* on the basis of such a high-potential formation due to ECH is found in association with *plasma confinement improvement*. In fact, *the associated temperature rise and transverse loss suppression are observed.*^{1,2)}

(3) From the viewpoints of both (i) a *conventional idea of higher and better potential confinement in the axial direction* [i.e., E_z effects] and (ii) the *present new finding of a turbulent vortex disappearance due to a strong radial electric shear* [i.e., E_r effects] in the transverse direction, simultaneously, such a high potential formation is found to play an essential role in providing stably improved plasma confinement both radially and axially.^{1,2)}

(4) *For the physics interpretations and control of such potential [or the associated E_r or Ω_r shear] formation, the validity of our proposed theory of the potential formation is extendedly tested under the conditions with auxiliary heatings. The data described above well fit to the extended surfaces calculated from our proposed consolidated theory of the strong ECH theory (plateau*

formation) with Pastukhov’s theory on energy confinement. The validity of the extension of our proposed physics mechanism encourages the future extendable scalability of potential formation having prospective *simultaneous E_z and E_r (or Ω_r) shear effects on confinement improvements.*

References

- 1) Cho, T. et al. Phys. Rev. Lett. **94** (2005) 085002.
- 2) Cho, T. et al. Plenary Invited Talk in the 5th International Conference on Open Magnetic Systems for Plasma Confinement (Novosibirsk, 2004).

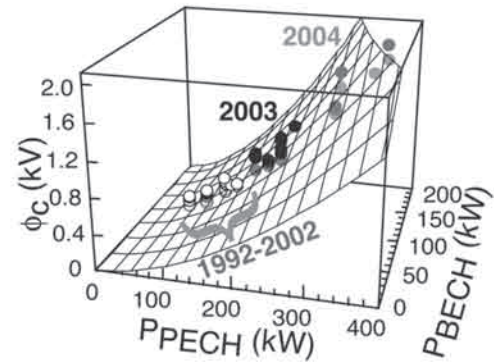


Fig. 1. Three-times advance in ion-confining potential (ϕ_c) formation including a record of 2.1 kV (filled circles), in comparison to ϕ_c attained 1992-2002 (open circles), is achieved. These extended data fit well to the scaling surface of ϕ_c with plug (P_{PECH}) and barrier (P_{BECH}) ECH powers. Here, a tandem mirror potential configuration with $n_p/n_c=0.1$ having $T_i=\text{several keV}$ is employed.

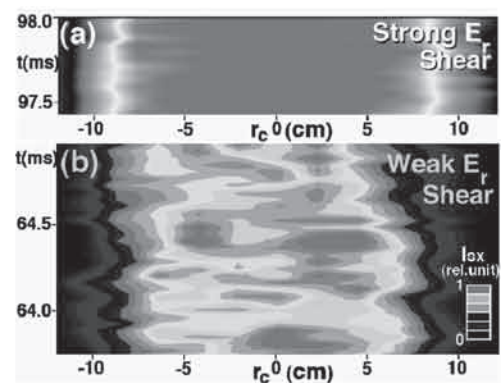


Fig. 2. Contours of central-cell x-ray brightness in the cases with (a) strong and (b) weak E_r shear formation. “Hot-colored areas” show higher plasma-pressure locations. Vortex-like structures are found in (b). The data are obtained by the use of our developed x-ray tomography systems. ($I \propto n_e n_i T_e^{2.3}$.)

§15. Study of Relations between the Spatial Structure of Potential-Trapped Electron Distribution Functions and the Physics Scaling Law of Plasma Confining Potentials

Hirata, M., Cho, T., Kohagura, J., Numakura, T., Fukai, T., Yokoyama, N., Tokioka, S., Tomii, Y., Miyake, Y. (Plasma Research Center, University of Tsukuba)
Ogura, K., Suzuki, Y., Komiyama, K., Saito, H. (Niigata Univ.)

In tandem-mirror devices, the second-harmonic ECH in the barrier region is utilized for the formation of a thermal-barrier potential, which reduces the electron heat flow between the central cell and the plug region. The fundamental ECH is employed for the formation of an ion-confining potential in the plug region. Scaling laws of potential formation and associated effects along with their physical interpretations are consolidated on the basis of experimental verification using the GAMMA10 tandem mirror. A proposal of extended consolidation and generalization of the two major theories—(i) Cohen's strong ECH theory for the formation physics of plasma confining potentials and (ii) the generalized Pastukhov theory for the effectiveness of the produced potentials on plasma confinement is made through the use of the energy balance equation.

Therefore, it is important to investigate electron-velocity distribution functions using x-ray diagnostics in these thermally isolated regions (i.e., the plug, the central-cell, and the barrier regions), since these electron distribution functions are directly affected by electrostatic potentials in the kilovolt range, although these regions are connected through magnetic-field lines. These kilovolt-range potentials may form various shapes of distribution functions in the thermally separated regions. Several types of x-ray diagnostics, such as x-ray energy spectrum analyses, x-ray absorption methods, and x-ray tomographic reconstructions using various types of x-ray detectors have been employed for obtaining various shapes of electron-velocity distribution functions as well as their spatial profiles.

This report is described the electron behavior of the potential confined electrons in the central-cell and plug region. In particular, the energy spectra, from pulse height analysis ranging from 1-keV down to a few hundred eV, are measured with a newly developed "ultra-low-energy measurable" pure-Ge (ULE Ge) detector (see Fig. 1). A ULE Ge detector has been characterized using synchrotron radiation from the storage ring at the National Institute of Advanced Industrial Science and Technology (AIST) (see Fig. 2). As a result, it is confirmed that this detector is able to be employed for less than 1-keV x-ray measurement, and therefore this detector makes it possible to observe simultaneously the electron velocity distribution function that consisted of the lower-energy bulk electron component

and also the high-energy electron component in the central cell and the plug region of the GAMMA10 tandem-mirror. For the x-ray spectrum analyses, the relativistic Born approximation corrected by the Elwert factor is used for the values of the x-ray cross section. The analysis code is made under this collaboration between Niigata Univ. and Plasma Research Center, University of Tsukuba.

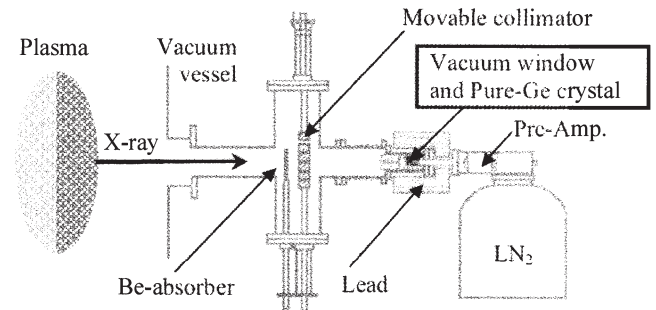


Fig. 1. Schematic view of soft-x-ray pulse-height analysis system with an ultra-low energy pure germanium (ULE Ge) detector for less than 1-keV x-ray measurement,.

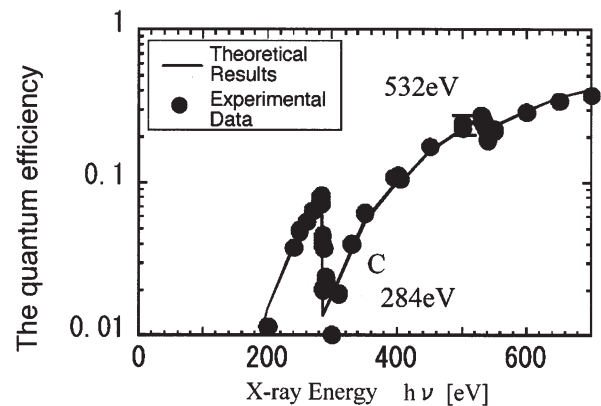


Fig. 2. The quantum efficiency of the ULE Ge detector normalized by the incident x-ray energy. The solid curve is calculated using the x-ray absorptions by the special polymer window and a 0.12- m thick Be. The data points with the Be filter are plotted. In general, the obtained data tend to fit the calculated curve, having some reasonable discrepancies near the absorption edges of O and C are found.

References

- 1) Hirata, M., *et. al.*, , Rev. Sci. Instrum. **75** (2004) 3631.
- 2) Ogura, K., *et. al.*, , Trans. on Fundamentals and Mater. **124** (2004) 456.
- 3) Cho, T., *et. al.*, , Phys. Rev.Lett. **94** (2005) 085002.
- 4) Hirata, M., *et. al.*, , Nucl.Fusion **31** (1991) 752.

§16. Study of Heliotron J Peripheral Plasma Using Fast Camera

Nishino, N. (Hiroshima Univ.), Takahashi, K., Fukagawa, Y., Kawazome, H., Mizuuchi, T., Sano, F., Kondo, K., Nagasaki, K., Okada, H., Kobayashi, S., Yamamoto, S. (Kyoto Univ.)

1. Aim

The technique of plasma measurement using fast camera is widely applied on many tokamaks and STs, and this method is very powerful two-dimensional tool for analysis of peripheral plasma behavior. The turbulence in peripheral region becomes the center of attention to relate the confinement recently. Mostly this turbulence looks like filament in tokamak and ST, and this filament like behavior is also seen in LHD plasma. Therefore, it is very interesting that this phenomenon generally exist in helical system. Heliotron J [1] has $I=1$ helical magnetic field and ∇B can be small to expect good particle confinement, and the bumpiness can be also change by varying the toroidal magnetic field. In 2004 the movable limiter (cannon ball type) was installed in Heliotron J to study the peripheral plasma and plasma-wall interaction.

Our aim is to study the peripheral plasma using the combination of the movable limiter, Langmuir probe and fast camera.

2. Instrumental set up

The camera was installed at one of the corner section in Heliotron J. Using fiber optics the camera was controlled remotely by PC in control room.

3. Summary

The low frequency harmonic oscillation in peripheral region was found in H-mode[2]. The density is rather high ($1.5\text{-}3\times 10^{19}\text{m}^{-3}$). The low frequency oscillation were reported in several tokamaks already, however, this is first observation in the helical systems. This result was reported in [3-6].

Fig.1 and 2 show the movable limiter and harmonic oscillation in H-mode plasma. This oscillation is 5.7kHz by Fast Fourier Transform. This oscillation occurred the beginning of the H-mode and lasts 10-20ms. The further study will be investigated soon.

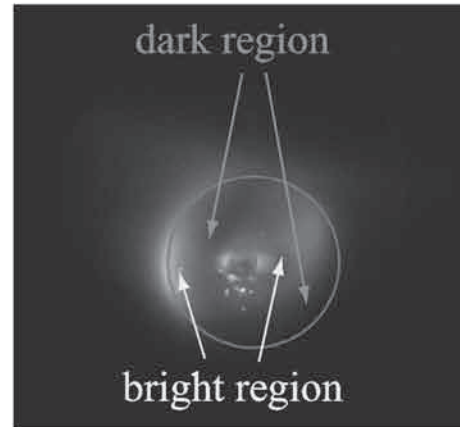


Fig.1 Typical field of view using fast camera
Red circle shows the outline of the movable limiter.

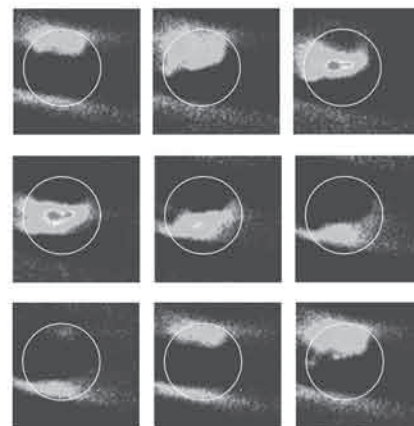


Fig. 2 Harmonic oscillation in H-mode plasma
Only 5.7kHz component is shown

References

- 1). T. Obiki, et al.: Plasma Phys. Control. Fusion **4** 1151 (2000)
- 2). F. Sano, et al.: J. plasma Fusion Res. **79**, No.11 1111(2003)
- 3). T.Mizuuchi, et al.: J Nucl. Mater. **337-339** 332(2005)
- 4). N.Nishino, et al.: J. Plasma Fusion Res. **1278** 179 (2004)
- 5). N. Nishino, et al.: J Nucl. Mater. **337-339** 1073(2005)
- 6). Kawazome, et al.: J Nucl. Mater. **337-339** 490(2005)

§17. ICRF Heating Experiment in Heliotron-J

Mutoh, T., Kumazawa, R., Seki, T., Saito, K. (NIFS)
Okada, H., Torii, Y., Sano, F., Hanatani, K.,
Mizuuchi, T., Kobayashi, S., Nagasaki, K. (IAE,
Kyoto Univ.)
Kondo, K., Nakamura, Y. (Grad. School, Energy Sci.,
Kyoto Univ.)

The high energy particle confinement and MHD stability are key issues of a helical-axis heliotron device, Heliotron J as an advanced helical device. High energy ions generated by ion cyclotron range of frequencies (ICRF) heating are utilized for the investigation of energetic ion confinement in Heliotron J. A charge exchange neutral particle energy analyzer (CX-NPA) is scanned in the toroidal direction in order to observe ions in the wide range of the velocity distribution.

The ICRF heating is performed with minority heating mode for the investigation of energetic ions using a loop antenna. The high energy flux up to 10 keV is observed during ICRF pulse imposed on ECH target plasmas with $T_i = 0.2$ keV. The ICRF pulse is launched from the low field side at the corner section of the plasma. In this cross section, the mod-B has tokamak-like structure. The measured hydrogen-minority flux decreases as increasing the toroidal angle (becoming far from the pitch angle = 90 degrees) because of the perpendicular acceleration of protons by ICRF heating as shown in Fig.1.

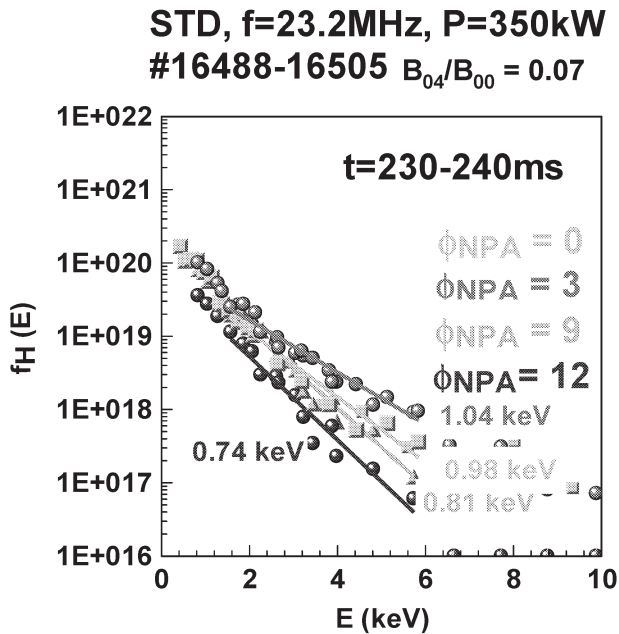


Fig.1. Energy spectra of hydrogen flux for various toroidal angles of CX-NPA. The effective temperature of the tail component is estimated.

It is noted that the loss region along the NPA's line of sight increases when the toroidal angle decreases from the result of the orbit calculation. Therefore, the flux peak located near the toroidal angle = 3 degrees (corresponding pitch angle = 117°). When the direction of the magnetic field is reversed, the difference of the observed fluxes is also found. The flux with the anti-parallel velocity is larger than that

with parallel velocity. This is supposed to be due to the smaller loss region along the line of sight of NPA.

High energy ion confinement is studied in relation to the magnetic configurations. It is predicted that one of the magnetic Fourier components, toroidal mirror ripple component (B_{04}) plays a key role on the collisionless particle confinement in the Heliotron J configuration. Three configurations are selected; the mirror ripples (B_{04}/B_{00} , where B_{00} is the averaged magnetic field strength) are 0.02, 0.07 and 0.16 at the normalized minor radius $\rho = 0.5$. The case of 0.07 corresponds to the standard configuration (STD) of Heliotron J. This experiment has been performed in the low density deuterium plasmas ($<1 \times 10^{19} \text{ m}^{-3}$) since the plasma should be collisionless. The ICRF frequency is adjusted so that the cyclotron resonance layer may be positioned within $\rho = 0.2$. The observed high energy flux is largest in the case of the highest mirror ripple and the smallest for the lowest mirror although the loss region along the NPA's chord is largest in the case of 0.16 among the three configurations. The estimated tail temperature is 1.04 keV for 0.16 of B_{04}/B_{00} , 0.87 keV for 0.07, and 0.47 keV for 0.02, respectively. This result suggests that the configuration with larger mirror ripple in this experimental range has an effect to improve the confinement of high energy ions.

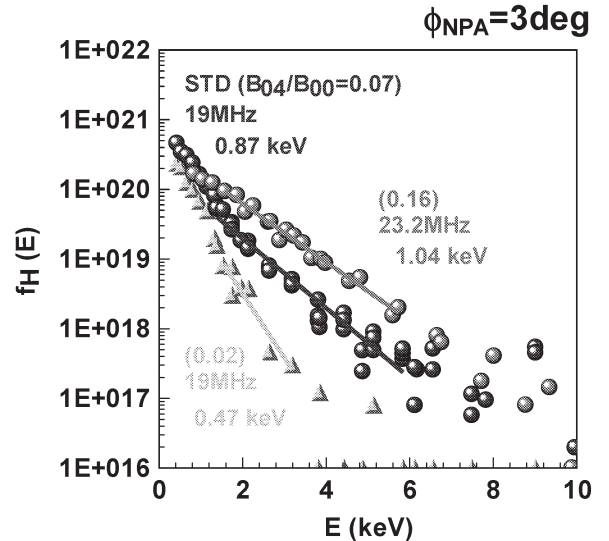


Fig. 2. Energy spectra of hydrogen flux in three configurations by changing bumpy component.

In this campaign, the high energy ion confinement is investigated using ICRF minority heating. As a result of the experiment, the velocity distribution of accelerated ions and the dependency of toroidal mirror ripple on the high energy formation and confinement are qualitatively understood. In the next campaign, the quantitative estimation of the high energy ion confinement is planned with power modulation method. The bulk heating experiment will be performed with a newly installed loop antenna in addition to the first one.

§18. Study on Neutral Hydrogen and Impurity Behavior in Heliotron J Plasmas

Kondo, K. (G. School of Energy Science, Kyoto Univ.), Arimoto, H. (G. School of Energy Science, Kyoto Univ.), Mizuuchi, T. (IAE, Kyoto Univ.), Sano, F. (IAE, Kyoto Univ.), Nishino, N. (Hiroshima Univ.), Nagasaki, K. (IAE, Kyoto Univ.), Okada, H. (IAE, Kyoto Univ.), Kobayashi, S. (IAE, Kyoto Univ.)

In order to investigate the velocity distribution function of deuterium atoms, which gives information about the recycling process, in the Heliotron J edge plasma region, spectral line shapes of $D\alpha$ emitted in front of a carbon limiter have been measured with a high resolution spectrometer. Measured spectral profiles have an asymmetric structure and are decomposed into the broad and narrow Gaussian components. The central wavelengths of each component shift toward the blue side. The intensity distribution is similar to the footprint of the magnetic field lines on the limiter surface. The reflected atoms affects the intensity distribution of the broad component.

The $D\alpha$ spectral profiles emitted in front of the carbon limiter are measured in 70 GHz ECH plasmas. The plasmas are produced in the standard configuration and pulse duration is 100 ms. The gas puffing is controlled to keep the electron density almost constant during the discharge. Figure 1 shows the $D\alpha$ spectral profile measured from the top port. The spectral profile has an asymmetric structure and can be decomposed into three Gaussian components. Since deuterium atoms have two components, cold and warm, at the edge plasma region, it is necessary to consider the sum of two components. But as can be seen in the figure, the intensity of $H\alpha$ line is smaller than that of $D\alpha$ line and too weak to be treated as a composition of two components. In the $D\alpha$ spectral profile, the central wavelengths of each component shift toward the blue side. The flow velocities corresponding to the shifts are 4.6×10^4 m/s and 6.2×10^3 m/s in the broad and narrow components, respectively. The errors caused by the fitting process are less than 1.8×10^3 m/s. The energy of clearly distinguished shoulder in the blue wing ranges from 26 eV to 147 eV. The half widths of the broad and narrow components are equal to the Doppler widths of deuterium atoms at the temperatures of 19.6 eV and 3.5 eV, respectively. It seems that the broad component is due to the emission from charge exchanged and reflected atoms and that the narrow component is due to the emission from dissociated atoms.

Most of the emission attributed to the reflected atoms is distributed in the blue side because the reflected atoms move away from the limiter surface and most of them move towards the spectrometer. Figure 2 shows the dependence of the intensity of the broad component on the edge electron density for the sightline #2-3, #2-5 and #2-8. The intensities increase with the edge electron density. The intensity measured at the sightline #2-5 has a maximum value and largest rate of increase. The sightline #2-5 is viewing strike points of the divertor legs. The connection length of the divertor legs is about 80 m. on the other hand, intensities of the sightline #2-3 and #2-8 have similar rate

of increase. Since the emission due to reflected atoms has a large contribution to the intensity of the broad component, it is our expectation that the broad component intensity will increase with the particle flux coming to the limiter surface. In the measurement, the edge electron temperature is almost constant ($T_{\text{edge}} \approx 20$ eV) with changes in the edge electron density. Thus incident energies of the deuterium ion flux caused by the sheath acceleration also remain constant. The ion flux estimated from the ion saturation current linearly increases with the edge electron density. In Fig.2, the intensities of the broad component are in proportion to the edge electron density. This result indicates that the intensity of the broad component is caused by an increase of the incident ion flux.

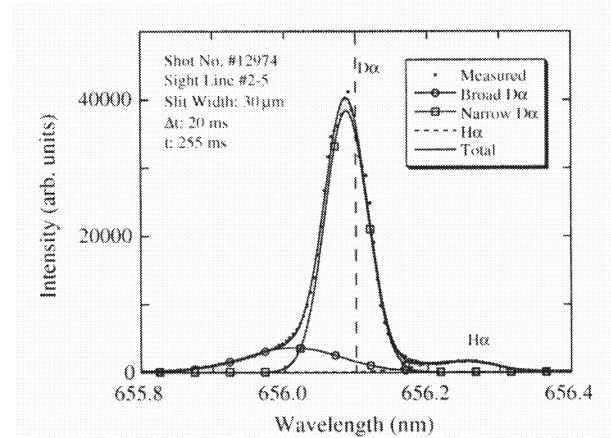


Fig.1 The $D\alpha$ spectral profile emitted in front of the carbon limiter. The spectral profile has an asymmetric structure and can be decomposed into three Gaussian components. The $D\alpha$ line is fitted a sum of two components, broad and narrow. The $H\alpha$ line is fitted by a single component.

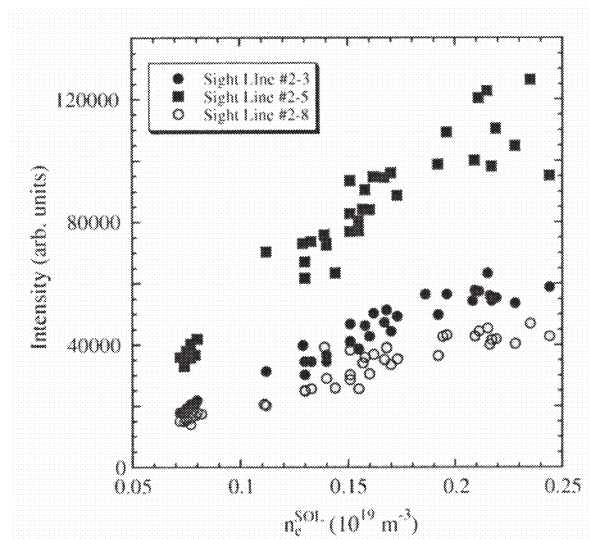


Fig.2 Dependence of the broad component intensity on the edge electron density for the sight lines #2-3, #2-5 and #2-8.

References

- [1] H.Kawazome et al., J. Nucl. Mater. 337-339, 490 2005

§19. Hard X-ray Diagnostic System Intended to Study Effect of Bumpy Ripple Control on Plasma Confinement in Heliotron J

Isobe, M., Okamura, S., Yoshimura, Y., Matsushita, H. (NIFS)

Kobayashi, S., Kaneko, M., Okada, H., Sano, F. (Kyoto Univ.)

In the Heliotron J device based on the quasi-omnigeneous concept, the bumpy ripples plays an important role in neoclassical confinement [1,2]. In order to explore optimized configuration from experimental approach, the Heliotron J is designed to be flexible in changing the magnetic field configuration. The purpose of this work is to investigate dependence of confinement property on magnetic field configuration through measuring pulse height spectra of X-rays, i.e. energy distribution of electrons in low density ECRH plasmas.

Aiming at detection of X-rays originating from electrons, a hard X-ray detector based on a cadmium telluride (CdTe) diode (Amptek inc. /XR -100T- CdTe) is chosen because a silicon (Si) semiconductor detector suitable for measuring relatively low energy X-rays is being employed in the Heliotron J. Because of higher Z than that of the Si detector, the CdTe detector is favorable for high energy X-ray measurement. The thickness of beryllium (Be) window installed in front is 4mil. Figure 1 shows detection efficiency as a function of photon energy. This was calculated by use of the linear attenuation coefficients for Be given in Ref. 3. It is seen that the detector has uniform efficiency in the energy range from 7 keV to 50 keV. On the other hand, the Si detector used in Heliotron J significantly loses efficiency in energy range above 10 keV. Hence this detector can cover for the Si detector for high energy range. We need to know the relation between pulse height and photon energy before we use it. The detector was therefore exposed by radioactive γ -ray sources to perform energy calibration. Figure 2 shows pulse height spectra due to exposure of γ -rays from ^{133}Ba and ^{241}Am . The sharp peaks are so-called photo peaks which can be used for the calibration. From this figure, we confirmed that there exists linearity between the γ -ray's energy and pulse height from the detector. Also this figure gave us a conversion coefficient from pulse height in V to photon energy in keV.

Next, we installed this detector on CHS to find the aperture diameter suitable for actual use in Heliotron J because plasma parameter of Heliotron J is similar to that of CHS. Figure 3 shows X-ray energy distribution from CHS plasma in B_t of 0.95 T. The diameter of circular aperture is fixed to be $100\mu\text{m}$ and currently the aperture can not be changed from the outside of vacuum. The ECR wave of 53.2 GHz is perpendicularly injected in this case. In comparison with higher n_e case, total photon flux is larger and effective temperature looks higher in lower n_e case as expected. However, it is obvious that the aperture diameter of $100\mu\text{m}$ is too small to obtain good statistical

photon counts in this case. In next fiscal year, we are going to improve the aperture system to make change of aperture size possible from the outside of vacuum and install this detector system on Heliotron J device.

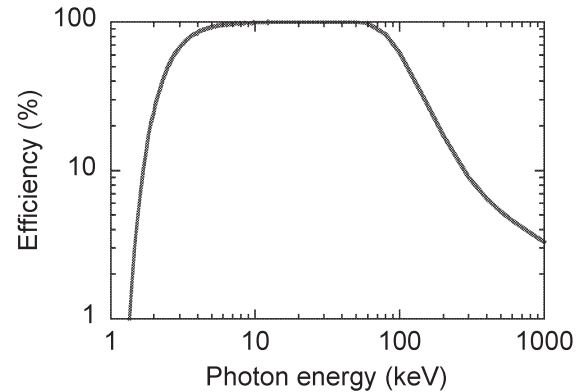


Fig. 1 Detection efficiency as a function of photon energy for the CdTe X-ray detector.

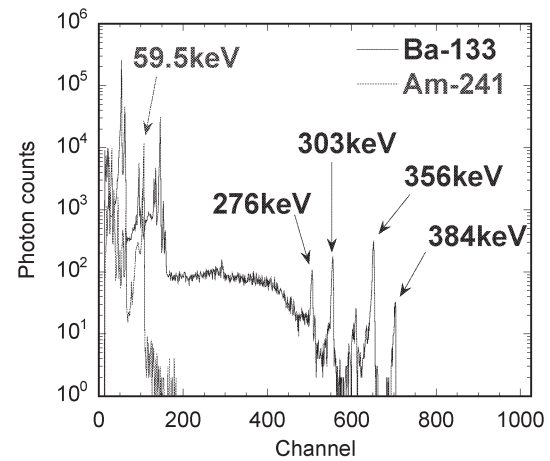


Fig. 2 Pulse height spectra due to γ -ray exposure.

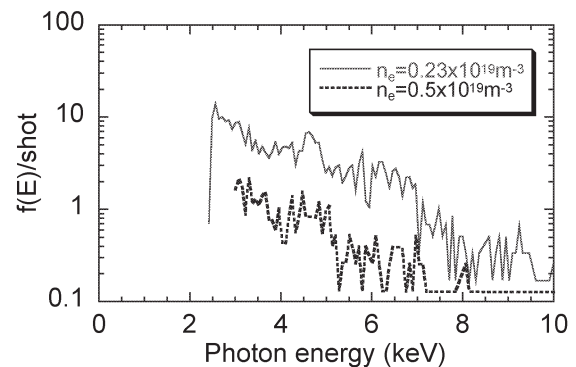


Fig. 3 Energy distribution of X-ray from ECRH plasmas of CHS in B_t of 0.95T.

References

- 1) Obiki, T. *et al.*, Nuclear Fusion **41**, (2001)833.
- 2) Mizuuchi, T. *et al.*, Plasma Science & Technology **6**, (2004)2372.
- 3) Hubbell, J.H., Int. J. Appl. Radiat. Isot., **33**, (1982)1296.

§20. Dependence of Poloidal Viscosity on Magnetic Configuration in Heliotron J and its Implication to H-Mode Quality

Yokoyama, M., Suzuki, Y.,
Nakamura, Y., Mizuuchi, T., Sano, F., Heliotron J
Experimental Team (Kyoto Univ.)

The dependence of the confinement quality of H-mode on magnetic configuration has been observed in Heliotron J (HJ) based on the rotational transform scan experiment 1). The experimental edge rotational transform dependence of the confinement enhancement factor, $H_{ISS95}(= \tau_E^{exp}/\tau_E^{ISS95})$ over the L-mode confinement has revealed that there exist the specific configurations for which the high quality H-mode ($1.3 < H_{ISS95} < 1.8$) are attained, where τ_E^{exp} is the experimental global energy confinement time and τ_E^{ISS95} is the confinement time scaling so called ISS95 2) from the international stellarator database.

As an attempt to understand this configuration dependence, the geometrical neoclassical poloidal viscous damping rate coefficient, $C_p = \langle \mathbf{e}_p \cdot \mathbf{B} / B \rangle$, 3) has been estimated. Here, \mathbf{B} is the magnetic field vector, \mathbf{e}_p the poloidal base vector in the Hamada coordinates and bracket indicates the flux surface average. VMEC2000 has been utilized to enhance the convergence property of MHD equilibria to feature the corrugated surface shapes, especially close to the plasma periphery, as much accurate as possible since such a corrugated surface might affect the poloidal flow through enhancing the poloidal viscosity. However, it has been rather difficult to reconstruct corrugated surface regions fully even with the VMEC2000, which is the future subject to resolve.

The poloidal viscous damping rate coefficients are plotted in Fig. 1 as a function of plasma radius for the series of four magnetic configurations with different edge rotational transform ranging from 0.493 to 0.64. The H_{ISS95} has been evaluated for these four cases as, $H_{ISS95} \sim 1.8$ (0.493), 1.4 (0.56), 1 (0.597) and 0.8 (0.64). From the configuration

dependence of C_p , there seems to be some coincidence between the H_{ISS95} and the reduction of C_p in the inner region. However, this result still remains inconclusive due to the lack of more comprehensive and accurate equilibrium information such as the magnetic island chain anticipated at the plasma periphery (related to the corrugates flux surfaces as pointed above). The construction of Boozer coordinates by following magnetic field lines (then transformation to Hamada coordinates) is one of candidates to overcome this problem. In addition, more investigation is required to include the dependence of the viscous damping rate on edge pressure and collision time. In order to examine the relevance of such a theoretical analysis, measurements of edge impurity ion poloidal rotation by means of charge-exchange recombination spectroscopy is under preparation.

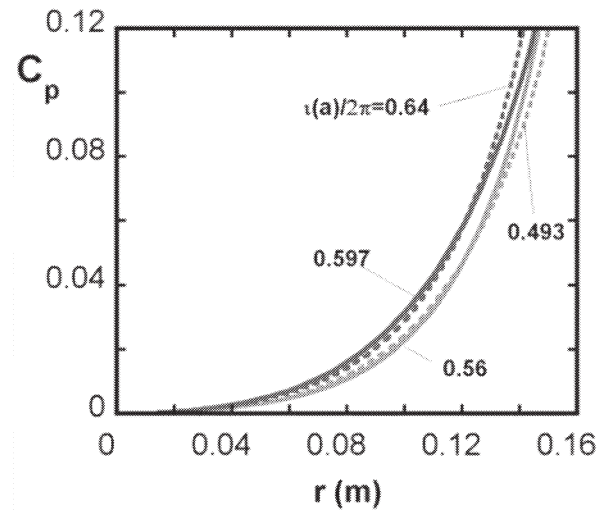


Fig. 1 The radial profile of C_p for four magnetic configurations with different edge rotational transform.

References

- 1) F.Sano et al., 20th IAEA Fusion Energy Conf., EX_2-2, submitted to Nucl. Fusion (2004).
- 2) U.Stroth et al., Nucl. Fusion 36(1996)1963.
- 3) H.Wobig et al., Plasma Phys. Contrroll. Fusion, 37(1995)893.

§21. Optimization of Helical System Concept

Sano, F. (Institute of Advanced Energy, Kyoto University)

The collaboration research between the Heliotron J group and the CHS group has started since the last fiscal year, which is aimed at understanding the common confinement physics independent of the device characteristics through joining the plasma experiment mutually and discussing the experimental results. Especially we have been exploring the control of the confinement and transport of helical plasmas by investigating the confinement improved modes^{1,2)}, which is closely related to the optimization of advanced helical configuration. The collaboration research will continue next year, and the following five themes are chosen; (1) the construction for confinement database, (2) the structure formation accompanying with the confinement transition, (3) ECCD, EBWH and EBCD, (4) the production and confinement of high energy particles and (5) the theoretical analysis of helical configuration optimization. Each group joined the plasma experiment for one week in the first and second term year, and we have been using internet for data analysis. This fiscal year we put emphasis on the themes, ECCD and production and confinement of high energy particles. The results are as follows:

In the ECH/ECCD plasmas, high energy tail ion has been observed in several toroidal devices such as TCV, FT and W7-A. The physics of the high energy ion production has not been clarified yet, although some explanations has been proposed such as the mode conversion of EC waves to the lower hybrid waves and the effect of non-isotropic Maxwellian distribution of electron. The high energy ions with the energy of more than $6 \times T_i$ has been observed in Heliotron J ECH plasmas in the conditions where the electron density was lower than $1 \times 10^{19} \text{ m}^{-3}$. In the last year, an existence of the high energy tail ion has been confirmed in the ECH/ECCD plasmas of CHS under some conditions. In order to ascertain the cause of the production of ion tail, we focused on the dependence of the ion tail on the direction of the driven current by ECCD and characteristics of magnetic fluctuations.

The direction of the toroidal current of ECCD was varied by controlling the injection angle of ECH from -9 deg. to $+9$ deg. in toroidal direction. Accordingly, the toroidal current was changed to be from 3 kA in CTR-direction to 4 kA in Co-direction. The effect of the bootstrap current is considered to be negligible, since the toroidal current was measured to be less than 1 kA in the case of perpendicular injection of ECH angle (Perp). Figure 1 shows the ion energy distribution obtained in the three injection angles of ECH, which is measured with Fast Neutral Particles Analysis (FNA) system. No clear dependence on the direction of the driven current is observed. Note that when FNA set tangentially in the toroidal direction the charge exchange neutral flux was higher than that in the perpendicularly case.

The magnetic fluctuations in the frequency range of 50-250 kHz are observed only in the case that the ion tail

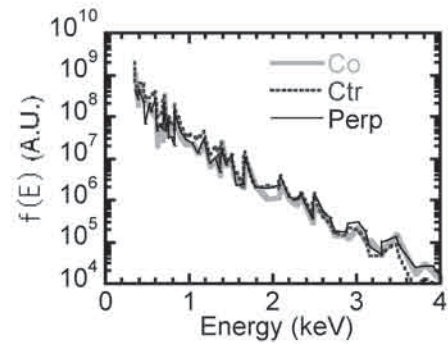


Fig. 1. Ion Energy distribution obtained in ECH/ECCD plasmas of CHS.

is measured. Figure 2 shows the time evolution of the toroidal mode number of the magnetic fluctuations in the CTR-CD case ($I_p = 4$ kA) with the magnetic probe array. Modes of $m/n = 4/1, 3/1, 5/2$ and $2/1$ are observed, where m/n are the poloidal/toroidal mode numbers, respectively. The modes propagate in the ion diamagnetic drift direction and in the counter direction of the magnetic field. In the perpendicular injection case, on the other hand, the modes of $m/n = 4/1$ disappeared. Moreover, only $2/1$ mode can be seen in the Co-CD plasma. The rotational transform in the CHS vacuum magnetic field is 0.3 in the core region and 1.1 at the edge. The equilibrium calculation of VMEC with taking into account of the effect of toroidal current predicts that the peaked current profile by 4 kA in the CTR direction has a capability to decrease the rotational transform to be less than 0.25 at the core. The core rotational transform in the Co-CD case, on the other hand, increases to be more than 0.4. Therefore, the change in the mode numbers of the magnetic fluctuation due to the ECCD directions (Co, CTR) is consistent with the profile change of rotational transform. Such a magnetic fluctuation has not observed yet in the standard configuration of Heliotron J because of its low magnetic shear avoiding rational surfaces, and it will be tested in the relatively high shear configuration acrossing a rational surface.

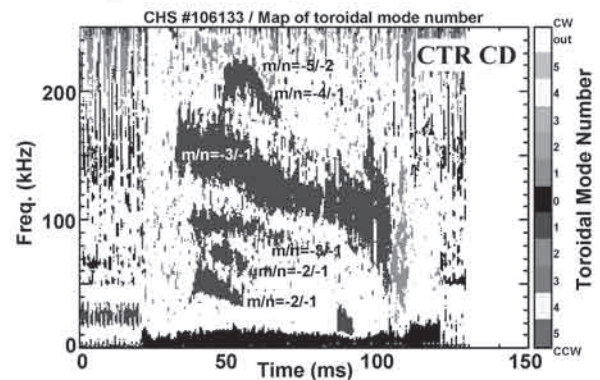


Fig. 2. Map of the toroidal mode numbers in the case ion tail appears in CTR-CD plasma.

References

- 1) S. Okamura, et al., 14th Int. Stellarator Workshop, Greifswald, Germany, 21-26 September 2003.
- 2) S. Kobayashi, M. Isobe, et al., JSPF Annual Meeting, 25A40P, Mito, Nov. 25-28, 2003

§22. Study of the Driving Mechanism of Toroidal Current in Heliotron-J

Watanabe, K.Y.
Motojima, G., Okada, H., Nakamura, Y., Sano, F.
(Kyoto Univ.)

In helical devices, net toroidal currents are not required to produce magnetic field for plasma confinement, while theoretical prediction suggests that there are several kinds of net toroidal currents, that is, bootstrap current, beam driven current and microwave driven current. Even if these toroidal currents are sufficiently small to activate current driven instabilities, they can affect the characteristics of the magnetic configurations. In the low magnetic shear devices, appearance of the low order rational magnetic surface due to the toroidal current might lead to a big island structure and/or the degradation of the confinement. Even in the devices with a finite magnetic shear, the net toroidal currents with direction increasing the rotational transform lead to the decrease in the magnetic shear and the suppression of Shafranov shift, which restrains the formation of magnetic well. Then, the study of the driving mechanism of toroidal current in helical devices is important.

The Heliotron-J device (H-J) is quit suitable to study the driving mechanism of toroidal current in helical devices because there we can make the operation with various magnetic configurations more easily comparing with other helical devices. Table.1 shows the advantage of the H-J from viewpoint of study on the driving mechanism of toroidal current. Here we show an experimental result on the bootstrap current in H-J.

Figure 1 shows the dependence of the bumpy component of magnetic field strength on the observed toroidal current in the NBI+ECH plasmas. Here the electron densities are almost same. Circles and squares denote the observation and the bootstrap current of the theoretical prediction, respectively. Here the bumpiness of the magnetic field changes by 5 times, but the toroidal ripple and helical ripple of the magnetic field are almost same within less than 5%. The theoretical prediction is calculated by the SPBSC code [1], which is based on a momentum approach proposed by Shing et al [2]. The increase of the current with the bumpiness is observed in both the experiment and the prediction. However, the current value itself in the experiment is larger than the prediction. The reason is why the Ohkawa current exits in the experiments. The estimation of the Ohkawa current is one of the future subjects.

According to the neoclassical transport theory in the asymmetrical devices, the existence of the neoclassical current proportional to the radial electric field is predicted when the ion collisionality is different from the electron one. The above current exists only in asymmetrical devices like H-J. In ECH discharges, the electrons and the ions are expected to belong to the $1/\nu$ and the plateau collisional regimes, respectively, and the radial electric field becomes the positive [1,3]. There the negative neoclassical current is expected. Figure 2 shows the time trace of the observed toroidal current and the electron density in ECH discharges. In the latter phase of the discharges, the electron density

rapidly decreases and the observed toroidal current becomes negative. This behavior is consistent with the theoretical prediction based on the neoclassical current proportional to the radial electric field. In the low density, the super-thermal effect of ECHD cannot be ignored yet. The qualitative estimation of the neoclassical current proportional to the radial electric field is under the consideration.

Reference

- 1) K.Y.Watanabe et al, Nucl.Fusion 35(1995)335.
- 2) K.C.Shaing and J.D.Callen, Phys. Fluids 26(1983)3315.
- 3) N.Nakajima et al, J.Phys.Soc.Jpn 61(1992)833.

H-J	LHD
1. Easy to change the bumpiness of B 2. L/R period is shorter than a typical discharge time, (especially in ECH)	1. Ion collisionality becomes low. 2. Existence of powerful profile measurement 3. Because magnetic structure is simpler than H-J, it is easy to analyze it.

Table.1 Characteristics of H-J and LHD from viewpoint of study on the driving mechanism of toroidal current

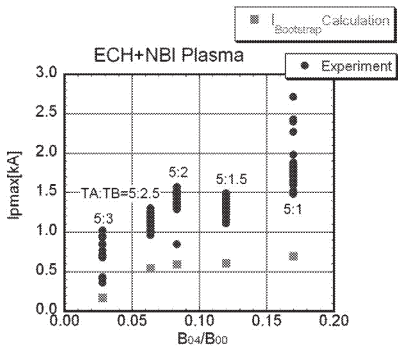


Fig.1 The observed toroidal current dependence on the bumpiness of B (NBI+ECH discharge).

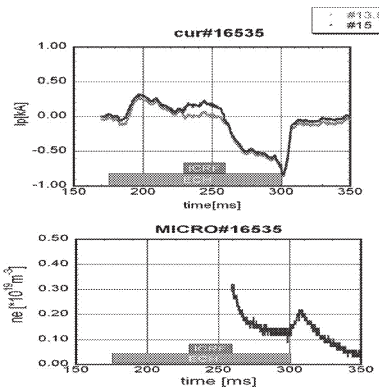


Fig.2 Time trace of observed toroidal current (top) and the electron density (bottom) (ECH, $B_{04}/B_{00} \sim 0.03$)

§23. Interaction of Intense Femtosecond Laser Pulses with Clusters

Sakabe, S., Hashida, M., Shimizu, S. (Kyoto Univ. ICR)
Iida, T., Sato, F. (Grad. Sch. Eng., Osaka Univ.)

Femtosecond laser-matter interaction is briefly reviewed comparing with nanosecond laser-plasma interactions. And first the intense laser-molecule interaction in the relatively low intensity range of 10^{12} - 10^{16} W/cm², that is parent ion generation applicable to femtosecond laser mass spectrometry, are briefly reviewed, and second in the intensity region above 10^{16} W/cm² we have studied the energy distributions of ions generated by the Coulomb explosion in a cluster and a low-density plastic foam.

Recent progress in ultraintense femtosecond lasers has enabled the production of ionic radiation energetic enough to induce nuclear reactions, such as fusion, photofission, and electron-positron pair production. The generation of high-energy ion radiation by intense femtosecond laser plasma interactions can be effected by two mechanisms. One is by acceleration in an electrostatic field induced by high-energy electrons driven by a ponderomotive force in an overdense plasma in thin foils [1], and the other is by Coulomb explosion in a gas or underdense plasma [2]. The ion energy distributions resulting from the two mechanisms are quite different. Ions accelerated by the laser accelerated electron-induced electrostatic field generally exhibit a broad Boltzmann energy distribution. Ions generated by Coulomb explosion, however, exhibit an energy distribution of $dN/dE \sim E^{-1/2}$ having a finite maximum E_{\max} . The Coulomb explosion thus produces a much greater fraction of high-energy ions. However, due to the low density of the gases used, interaction rates are quite low, and so the overall efficiency of high-energy ion generation is much less than in the ejected electron method which takes place in over-dense plasmas. Although the Coulomb explosion is generally only induced in low-density gases by intense femtosecond lasers, it may be possible to induce the effect more efficiently in foam-structured material in which local

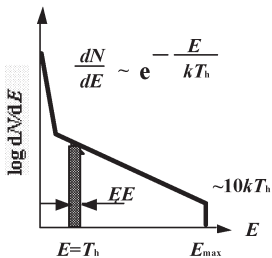
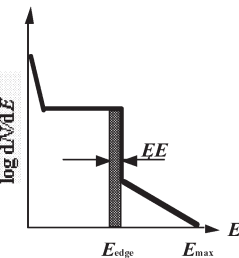
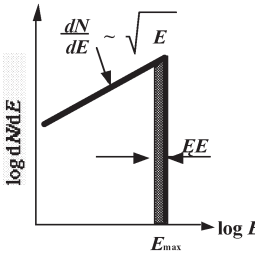
density is high enough to support the Coulomb explosion, but average density is low enough to allow laser propagation. [3]

The energy distributions of protons emitted from the Coulomb explosion of hydrogen clusters by an intense femtosecond laser have been experimentally obtained. Ten thousand hydrogen clusters were exploded, emitting 8.1 keV protons under laser irradiation of intensity 6×10^{16} W/cm². The energy distributions are interpreted well by a spherical uniform cluster analytical model. The maximum energy of the emitted protons can be characterized by cluster size and laser intensity. The laser intensity scale for the maximum proton energy, given by a spherical cluster Coulomb-explosion model, is in fairly good agreement with the experimental results obtained at a laser intensity of 10^{16} – 10^{17} W/cm² and also when extrapolated with the results of three-dimensional particle simulations at 10^{20} – 10^{21} W/cm².

Energetic proton generation in low-density plastic (C₃H₁₀) foam by intense femtosecond laser pulse irradiation has been studied experimentally and numerically. Plastic foam was successfully produced by a sol-gel method, achieving an average density of 10 mg/cm³. The foam target was irradiated by 100-fs pulses of a laser intensity 1×10^{18} W/cm². A plateau structure extending up to 200 keV was observed in the energy distribution of protons generated from the foam target, with the plateau shape well explained by Coulomb explosion of lamella in the foam. The laser-foam interaction and ion generation were studied qualitatively by two-dimensional particle-in-cell simulations, which indicated that energetic protons are mainly generated by the Coulomb explosion. From the results, the efficiency of energetic ion generation in a low-density foam target by Coulomb explosion is expected to be higher than in a gas-cluster target.

REFERENCES

[1] S. Okihara, *et al.*, J. Nucl. Sci. Tech. **39** (2002), 1.
[2] S. Sakabe, *et al.*, Phys. Rev. A **69**(2004), 023203, M. Hirokane *et al.*, Phys. Rev. A **69**, 063201(2004).
[3] S. Okihara, *et al.*, Phys. Rev. E **69**(2004), 026401.

	Thin film	Foam	Cluster
Reference	(1)	(2)	(3)
Average target electron density (cm ⁻³)	<1x10 ²³	8x10 ²⁰	10 ¹⁸ ~10 ²⁰
Laser intensity(W/cm ²)	1.2x10 ¹⁸	7x10 ¹⁷	6x10 ¹⁶
Energy distribution			
Yield of protons	1.9x10 ⁵	8.7x10 ⁶	1.6x10 ⁶
Proton energy (keV)	180~200	180~200	3.8~4.2

§24. X-ray Imaging in Fast Ignition Fusion Experiments
— Poisson Noise Reduction by ICA Filter —

Chen, Y.-W. (Ritsumeikan Univ.)
Han, X. (Univ. of the Ryukyus)

Penumbral imaging is a technique which uses the fact that spatial information can be recovered from the shadow or penumbra that an unknown source casts through a simple large circular aperture.¹ Since such an aperture can be “drilled” through a substrate of almost any thickness, the technique can be easily applied to highly penetrating radiation such as neutrons and γ rays. To date, the penumbral imaging technique has been successfully applied to image the high-energy x rays, protons, and neutrons in laser fusion experiments. The limitation of penumbral imaging is that the straightforward deconvolution is very sensitive to noise contained in the penumbral image. The penumbral images are always degraded by Poisson noise.

In this paper, we proposed a Poisson noise filtering method based on independent component analysis (ICA) for penumbral imaging. The goal of ICA is to perform a linear transformation which makes the resulting variables as statistically independent from each other as possible. In image decomposition by ICA, most independent components have super-Gaussian distribution and the corresponding basis functions are similar to localized and oriented human visual response (receptive field). In the proposed filtering, the penumbral image is first transformed by using ICA basis functions and then the noise components are removed by a soft thresholding technique, which is known as Shrinkage. Compared with other methods such as wavelet-based filtering, the ICA-based filtering is determined by data alone and adaptive to the data. The filter is used as a preprocessing of reconstructions of penumbral images.

The penumbral image (\mathbf{P}) can be expressed as a linear combination of basis functions as Eq.(1).

$$\mathbf{P} = \sum_{i=0}^{N-1} s_i \mathbf{a}_i = s_0 \mathbf{a}_0 + s_1 \mathbf{a}_1 + \cdots + s_{N-1} \mathbf{a}_{N-1} \quad (1)$$

$$= \mathbf{A} \mathbf{s}$$

where \mathbf{a}_i is the basis functions which is learned by ICA and s_i is its coefficient. The shrinkage function is shown in Eq.(2).

$$\hat{\mathbf{s}} = g(\mathbf{s}) = \frac{\mathbf{s}^2 + \theta^2}{\mathbf{s}^2} \quad (2)$$

where θ is the power of Poisson noise. The filtering is performed as:

$$\hat{\mathbf{P}} = \mathbf{A} \hat{\mathbf{s}} = \sum_{i=0}^{N-1} \hat{s}_i \mathbf{a}_i = \hat{s}_0 \mathbf{a}_0 + \hat{s}_1 \mathbf{a}_1 + \cdots + \hat{s}_{N-1} \mathbf{a}_{N-1} \quad (3)$$

The experimentally obtained penumbral image and its profile are shown in Figs. 1(a). The penumbral image was divided into 240×240 pixels. The size of one pixel is about $22.5 \times 22.5 \mu\text{m}$ corresponding to a pixel resolution on the source plane of $2.6 \mu\text{m}$. Fig. 1(b) shows the image after the ICA-domain filtering and its profile. The reconstructed images of Fig.1(a) and 1(b) are shown in Fig.2(a) and 2(b), respectively. As shown in Fig.2, the source image has been reconstructed with a high SNR, while if we do not use the filter, the reconstructed image is not clear.

In conclusion, we proposed an ICA-domain filtering for Poisson noise reduction. The proposed filter was used as a preprocessing of penumbral image reconstructions. Both simulation and experimental results showed that the reconstructed image was dramatically improved in comparison to that without the noise-removing filters.

Reference:

(1) Y.W. Chen, X.Han and S.Nozaiki, *Rev. Sci. Instrum.*, Vol.75, pp.3977-3878(2004)

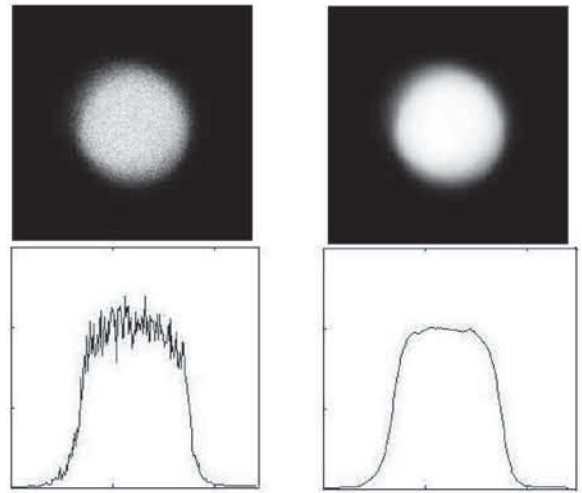


Fig.1 Penumbral images and its profiles. (a) without and (b) with filtering

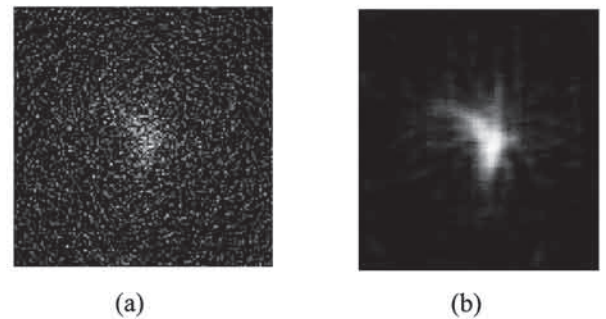


Fig.2 Reconstructed images. (a) without filtering; (b) with ICA filtering .

§25. X-ray Penumbral Imaging for Laser-produced Plasma
— Uniformly Redundant Penumbral Array —

Chen, Y.-W. (Ritsumeikan Univ.)
Nozaki, S. (Okinawa National College of Technology)

Penumbral imaging is a technique which uses the fact that spatial information can be recovered from the shadow or penumbra that an unknown source casts through a simple large circular aperture. Since such an aperture can be “drilled” through a substrate of almost any thickness, the technique can be easily applied to highly penetrating radiation such as neutrons and γ rays. The limitation of penumbral imaging is that the straightforward deconvolution is very sensitive to noise contained in the penumbral image. In this paper, in order to increase the SN ratio of the penumbral image, we propose a new imaging technique of uniformly redundant penumbral array (URPA), which combines the advantages of URA to the penumbral imaging. In URPA, multi penumbral apertures are used instead of single penumbral aperture, which are arranged in *m*-sequence as shown in Fig.1(b). The reconstruction process contains two steps: one is to use a decoding operator to obtain the real penumbral image and the second step is to use a wiener filter to reconstruct the source image like conventional penumbral imaging.

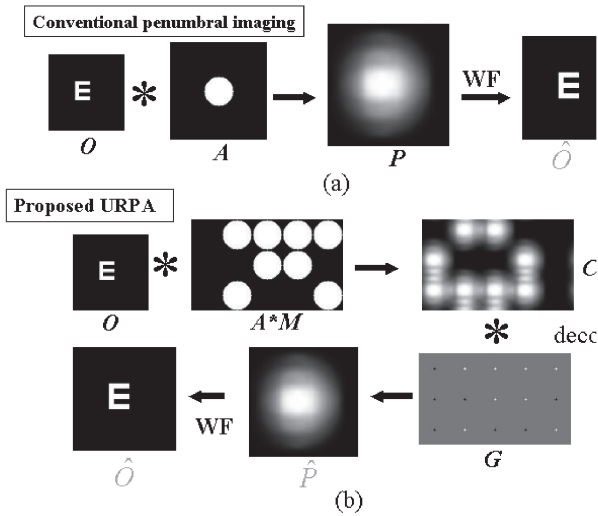


Fig.1 The basic concept of URPA; (a) conventional penumbral imaging; (b) URPA

The coded penumbral image can be expressed as:

$$C = M * A * O \quad (1)$$

where A is the aperture function and M is the uniformly redundant array (2D m-sequence) which is used as a coding operator. O is the source image.

The penumbral image can be obtained by using decoding operator (G) as:

$$\hat{P} = G * C = (G * M) * A * O \quad (2)$$

where

$$M * M = \begin{cases} (r \times s + 1) / 2; & \text{mod}(i, s) = 0 \text{ and } \text{mod}(j, r) = 0 \\ (r \times s + 1) / 4; & \text{others} \end{cases} \quad (3)$$

And

$$G * M = \begin{cases} (r \times s + 1) / 2; & \text{mod}(i, s) = 0 \text{ and } \text{mod}(j, r) = 0 \\ 0; & \text{others} \end{cases} \quad (4)$$

Thus the penumbral image is given by:

$$\hat{P} = \frac{r \times s + 1}{2} A * O \quad (5)$$

As shown in Eq.(3), we can obtain a perfect enhanced penumbral image with a factor of $(r \times s + 1)$.

The simulation results are shown in Fig.2. It can be seen that The SNR of penumbral images can be significantly improved by URPA. The larger the URPA size, the higher the SNR. By using a penumbral image with higher SNR, we can easily obtain a reconstructed image with high resolution and high SNR. The SNR of the reconstructed image using 15x17 URPA is improved by a factor of 500 compared with the conventional penumbral imaging for the case of $\sigma^2=13.8$

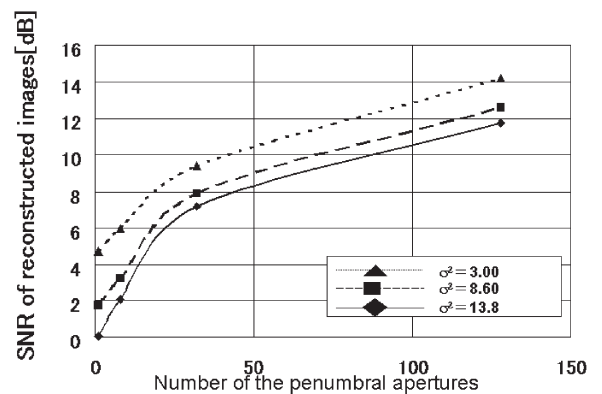


Fig.2 Improvements of reconstructed image by URPA.

Reference:

(1) Y.W. Chen, H.Yamamoto and S.Nozaiki, *Rev. Sci. Instrum.*, Vol.75, pp.4017-4019(2004).

§26. Compression and Fast Heating of Liquid Deuterium Targets and Related Research

Azechi, H., Shiraga, H., Shigemori, K., Tanaka, K.A., Kodama, R., Norimatsu, T., Mima, K. (ILE, Osaka University)
Okamoto, M.

A new project FIREX (Fast Ignition Realization Experiment) has started aiming at proof-of-principle demonstration of an advanced concept called fast ignition, in which a highly-compressed fuel plasma is heated to achieve ignition and burn with an ultra-short laser pulse before it expands with the sound speed. In the first phase of the project, a dense fuel created by the current GXII laser will be heated with a new 10-kJ PW laser to 'the ignition temperature'.

In 2004, remarkable progress has been made in construction of LFEX laser and development of cryogenic foam target with reentrant cone for the heating laser.

A new heating laser system LFEX has been constructed and demonstrated the first light at kJ output level. This laser is designed to integrate advanced laser technologies developed at ILE to maximize the outcome for both EUV and FIREX at a minimum cost. The EUV experiment was carried out in May 2005.

Good understanding and control of non-spherical implosion of cone targets are one of the most critical elements for the success of the FIREX program.

Under the collaboration with University of Rochester, we have successfully observed the dynamics of a compressed core at the cone tip. The result was compared with unified computer code PINOCO-2D and we found that high-density compression is possible in non-spherical implosion with existence of a cone.

Development of a cryogenic target for FIREX-1 has been conducted under the collaboration between the National Institute of Fusion Science (NIFS) and the Institute of Laser Engineering, Osaka University (ILE).

The cryogenic target for FIREX-I consists of a transparent foam shell coated with a gas barrier and the reentrant gold cone that is guiding the heating laser to the compressed core. A vibration-free cryostat was constructed at NIFS to demonstrate the proof of principle of foam method and the low density RF foam shell was developed at ILE.

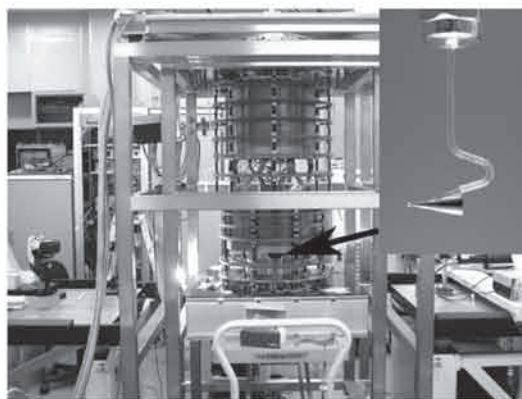


Fig. 1 Cryostat and the target to demonstrate foam method.

§27. Simulation Study of Chamber Evacuation Dynamics of Laser Fusion Reactor

Furukawa, H., Norimatsu, T., Kozaki, Y., Azechi, H., Mima, K. (ILE, Osaka University)
Ishizaki, R., Sagara, A.

One of the critical issues of a laser fusion reactor with a wet wall is the chamber clearance. After micro explosion with 100 MJ nuclear yield, 10 kg of liquid metal evaporates from the surface due to heating by α particles, ions and debris from the target. Contribution of x-ray on the ablation is negligible in the case of direct drive implosion[1]. The evaporated plume makes, then, mist and clusters after expansion cooling. Such clusters would attach on the injected target surface and degrade the target performance through RT instabilities and preheat of the fuel. Another concern is the influence on the propagation of laser beams.

To experimentally simulate the ablation process, laser irradiation is often used. We, however, found that ablation process by ions is quite different from that by lasers. The range of α particles in liquid Pb is about 10 μm . As the result, superficial liquid Pb evaporates as a high density, low temperature, plasma with low ionization rate. In our preliminary estimation, the plume becomes clusters within a few cm flight after ablation. Formation of clusters in a laser-ablated plume is studied extensively by Yabe and Luk'yanchuk through simulation and experiment [2, 3]. They found that the experimental result agreed well with simulation.

In this study we numerically evaluated the formation of clusters in the ablated plume in a laser fusion reactor basing on Luk'yanchuk, Zeldovich-Raizer model[3].

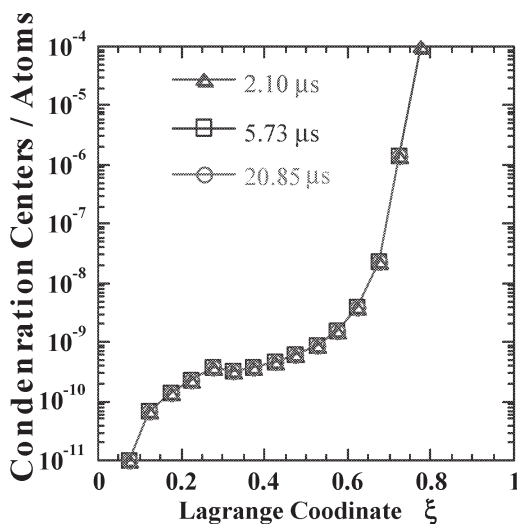


Fig. 1 Condensation centers per atoms of vapor.

The simulation code is written for spherically symmetric, isothermally expanding plasma including physics of 1) condensation, 2) kinetic equation, 3) kinetics of cluster growth, 4) adiabatic equation, 5) size distribution

function for nano clusters. Figure 1 shows condensation centers per atoms of vapor.

Figure 2 shows temporal change of clusters in the plume. Figure 2 indicates that nano clusters less than 250 nm diameter are formed in the plume.

In order to discuss the influence of these clusters on the target performance and beam propagation, we had to consider whole dynamics of ablated vapor. Since the initial velocity of the ablated vapor is 140 m/s. If there is no collisions with ablated vapor from the other inner surface, these clusters would directly condense on the other inner surface and disappear before the next laser irradiation. Numerical evaluation on these process is the next work.

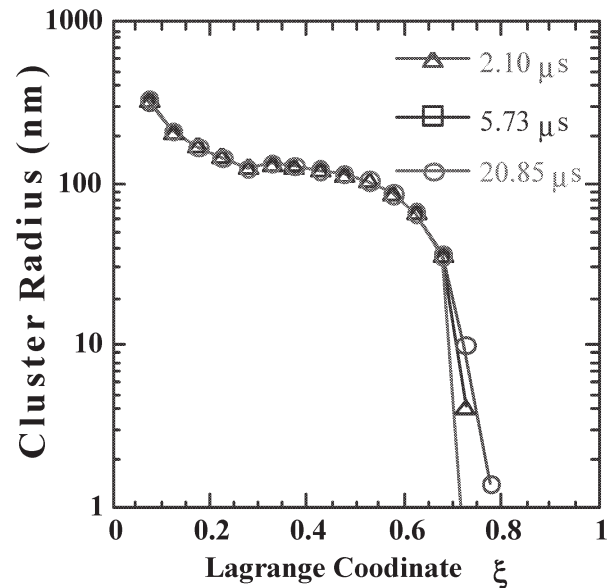


Fig. 2 Temporal change of clusters in the plume.

References

- 1) H. Furukawa, Y. Kozaki, K. Yamamoto, T. Johzaki, and K. Mima ; submitted to Fusion Engineering and Design(2004).
- 2) Masahiro Kuwata, B.S. Luk'yanchuk, and T. Yabe ; Jpn J. Appl. Phys. 40 (2001) 4262 – 4268.
- 3) B. S. Luk'yanchuk, W. Marine, S. I. Anisimov, and G. A. Simakina, SPIE **3618** (1999) 434-452.

§28. Evaluation of the Stability of SiC/SiC Composites for Inertial Fusion Dry Wall Chamber to High Temperature Irradiation and Design Study Based on the Material Properties

Kohyama, A. (Institute of Advanced Energy, Kyoto University), Hinoki, T. (Institute of Advanced Energy, Kyoto University), Kondo, S. (Graduate School of Energy Science, Kyoto University), Norimatsu, T. (Institute of Laser Engineering, Osaka University), Kozaki, Y. (Institute of Laser Engineering, Osaka University)

INTRODUCTION

The first wall of an Inertial Fusion Energy (IFE) chamber will suffer serious damage from intense pulsed neutrons and other energetic particles. Due to excellent mechanical properties at high temperatures, chemical stability and low activation following neutron irradiation, SiC/SiC composites is attractive for Tokamak fusion reactors. The knowledge about irradiation resistance at high temperature over 1773 K is indispensable, in particular for designing dry wall chamber of IFE in spite of technical difficulty.

The objective of this work is to understand the stability of SiC/SiC composites to high temperature irradiation over 1500 °C to establish design window for IFE dry wall chamber.

EXPERIMENTAL PROCEDURE

A high purity polycrystalline 3C-SiC produced through chemical vapor deposition process were irradiated with 5.1MeV Si²⁺ for inducing displacement damage at DuET facility, Kyoto University. The damage level was up to 3 dpa (displacement per atom), and irradiation temperature was up to 1873 K. The magnitude of swelling and microstructure were examined at MUSTER (Multi-scale testing and evaluation research) facility. The surface height change as a consequence of irradiation-induced swelling was measured with MicromapTM interferometric optical surface profiling system. For a microstructural examination, the irradiated specimens were subjected to a thin-foil processing using a focused ion beam (FIB) micro-processing device. The microstructural was examined with cross-sectional transmission electron microscopy (XTEM).

RESULTS AND DISCUSSION

In figure 1, the swelling of SiC irradiated at 3dpa is plotted as a function of irradiation temperature, along with reported neutron irradiation data [1]. Considering the outstanding controllability of irradiation conditions in the present ion irradiation experiment, we suspect that part of neutron data have been affected by irradiation

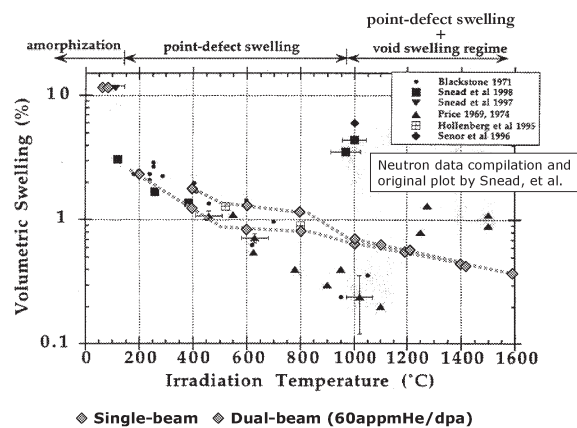


Figure 1. Temperature dependence of swelling of SiC induced by irradiation.

temperature uncertainty and/or unintentional transient low temperature neutron exposure that is peculiar to the irradiation in fission reactor cores [2]. In addition, some of the neutron data might have been affected by transmutation of boron, which had been added as a sintering aid to produce dense materials.

Void formation at high temperature ($T_{irr} > 1273$ K) has been concerned about severe increase in swelling. The trend curve of swelling shown in figure 1 indicates that the void formation have little influence on the swelling value below 1873 K. It was also confirmed by TEM examination.

Nano-powder Infiltration and Transient Eutectic Phase (NITE) Process developed at Kyoto Univ. is the most promising process to fabricate SiC/SiC composites for nuclear application [3]. The NITE-SiC/SiC composites consist of high purity 3C-SiC fiber and 3C-SiC matrix. The dimensional stability in the NITE-SiC/SiC composites is expected to be close to monolithic SiC studied here. The results in the present study indicate that the NITE-SiC/SiC is applicable to the first wall without severe swelling at high temperature.

REFERENCES

- [1] S.J.Zinkle and L.L.Snead: Fusion Materials, DOE/ER-0313/24 (1998) 93-114.
- [2] M. Kiritani: J. Nucl. Mater. 160 (1988) 135-141.
- [3] A. Kohyama, Mater. Trans., 46[3] (2005) 384-393.

§29. Study on Tritium Behavior in Liquid Blanket System of Laser Inertial Fusion Reactor

Nishikawa, M. (Graduate School of Eng. Sci., Kyushu U.)
Fukada, S. (Graduate School of Eng., Kyushu U.)
Katayama, K. (Graduate School of Eng. Sci., Kyushu U.)

In designing of the liquid blanket system for a laser inertial fusion reactor, it is necessary to have the efficient tritium recovery system for assurance of tritium self-supply and to have the tritium safety confinement system for certification of the tritium radiation safety.

It is required to know the tritium transfer properties in liquid breeder materials because the wetted wall system is considered to protect the first wall in design of the inertial fusion reactor of Osaka University. At present, use of Lithium Lead is considered as the breeder material though only a small amount of reports have been made on tritium transfer properties. It is anticipated that a large part of the bred tritium may permeate to the outer circumstances because the solubility of hydrogen in lithium lead is considered to be so small. Accordingly, the object of the present researchers is to make the measurement of tritium diffusivity and solubility in lithium lead and lithium as a part of the cooperative research program lead by the Institute of Laser Engineering, Osaka University.

The following advancements are made in this year.

- 1) Tritium diffusivity and solubility in lithium are preparatory measured using a U type tube reactor and the data in this study are compared with data reported by Alire or Moriyama et al. The diffusivity in this study agrees with the tendency of equation reported by Alire.
- 2) The experimental apparatus as shown in Fig. 1 is made in a glove box so that the experiment using tritium is also capable. In experiment, temperature, gas flow rate to the both gas flow channel, concentration of hydrogen isotopes added to the both channel, thickness of liquid breeder are variable parameters.
- 3) Solubility and diffusivity of hydrogen in FLiNaK are preparatory observed in this year and it is concluded that the apparatus shown in Fig. 1 can give a reliable results. The similar apparatus is made by the present researchers in the Idaho National Environmental Laboratory to measure the tritium transfer properties in FLiBe, and good results are obtained so far.
- 4) The tritium release behavior from solid breeder blanket materials are also performed as a part of this cooperative research works because use of a solid breeder in a inertial confinement is not fully abandoned yet. It is assured in this study that not a little amount of bred tritium is released as the chemical form of HTO from most solid breeder materials even when hydrogen is mixed to the blanket purge gas. The fact that both HT and HTO are released

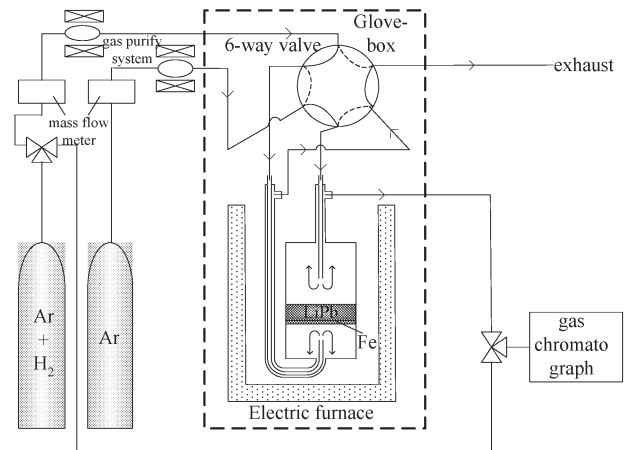


Fig. 1. Experimental apparatus made by present researchers for measurement of tritium transfer properties in liquid breeder materials.

makes it difficult to recover whole bred tritium. It is also anticipated that a part of tritium in HT form will be transferred to the cooling water for electricity after permeation through the wall material of cooling devices.

Therefore, more research is required to understand the tritium behavior to assure tritium self-supply together with certification of tritium safety for liquid and solid blanket system.

References

- 1) M. Kinoshita, Y. Yamashita, K. Kuroki, S. Fukada and M. Nishikawa, "Diffusion of hydrogen isotope in liquid lithium", 6th Cross Straits Symposium, Pohang (Korea), Nov. 18-20, 2004
- 2) M. Nishikawa, "Behavior of bred tritium in blanket system, 12th CBBI, Karlsruhe, Sept. 16-17, 2004
- 3) M. Nishikawa, T. Kinjyo and Y. Nishida, "Chemical form of tritium released from solid breeder materials", J. Nucl. Mater., Vol. 325, pp. 87-93(2004)
- 4) S. Fukada, R.A. Anderl, T. Terai, A. Sagara, and M. Nishikawa, "Diffusion coefficient of tritium through a molten salt FLiBe blanket and evaluation of tritium leak from fusion reactor", 7th International Conference on Tritium Science and Technology, Baden-Baden (Germany) Sept. 21-24, 2004

§30. Design Study on Foam-cryogenic Targets by Integrated Simulations

Nakao, Y. (Kyushu Univ.), Mima, K., Nagatomo, H., Johzaki, T., Sunahara, A. (Osaka Univ.), Sakagami, H. (Univ. of Hyogo), Taguchi, T. (Setsunan Univ.), Nishiguchi, A. (Osaka Inst. Technol.), Okamoto, M., Horiuchi, R., Ishiguro, S.

In fast ignition (FI) laser fusion, an ultra-intense short-pulse laser is focused on pre-compressed plasma to heat it to ignition temperature. One of the most critical issues is the clarification of the mechanism of the effective fast heating. In the recent FI experiments with cone-guided targets, an imploded core was heated up to $\sim 800\text{eV}$ with a high coupling efficiency. For analysis of this experiment, we carried out integrated simulations.

First, using 2D hydro code PINOCO¹⁾, we simulated the implosion dynamics of a cone-guided target to obtain the compressed core profiles. Initially a target shell of polystyrene ($\rho=1.06\text{g/cm}^3$) has a uniform thickness of $8\mu\text{m}$ and an inner radius of $250\mu\text{m}$. The target is uniformly irradiated by 6kJ Gaussian-pulse-shaped laser with the wave length of $\lambda_L=0.5\mu\text{m}$.

Then, the profiles of fast electrons generated in the interaction of ignition laser with compressed plasma were evaluated with 1D PIC code FISCOF 1²⁾. The Au cone tip was modeled by $10\mu\text{m}$ -thickness plasma with the electron density $n_e = 100n_c$, where n_c is the critical density. The $50\mu\text{m}$ -thickness imploded plasma was putted behind the cone tip. The simulation was carried out by assuming that the electron density in the rear of the cone tip is $n_{e,\text{rear}} = 100n_c$ and/or $2n_c$. The 150fs Gaussian pulse ($\lambda_L=1.06\mu\text{m}$, $I_L=10^{20}\text{W/cm}^2$) was assumed as ignition laser. It was found that if there exists a density gap at the contact surface between the cone tip and the imploded plasma (i.e. if $n_{e,\text{rear}} = 2n_c$), the energy of forward-directed fast electrons becomes lower and the pulse duration becomes longer, which leads to high coupling efficiency from the fast electrons to the dense core, compared with case without the density gap³⁾.

Using both profiles, i.e. time-dependent “source” electron profile and the imploded core profile, as initial and boundary conditions, we carried out Fokker-Planck / hydro simulation of core heating process.^{4), 5)} To this end we coupled relativistic Fokker-Planck code RFP-2D with a 1D radiation hydro code. **Figure 1** shows the temporal evolutions of core heating rate by fast electrons and temperatures averaged over dense core region ($\rho > 50\text{g/cm}^3$). In the early stage the core heating rate is lower in the case neglecting the density gap, and the core temperatures rise more slowly. However, the duration of core heating is longer in the case with density gap. This is because a portion of the fast electrons confined inside the cone tip are continuously delivered to the core even after finishing the laser irradiation. Consequently the fuel core is more heated up. In our simulation, the core was finally heated up to

0.5keV , which is still lower than the temperatures measured in the experiments.

Even though the density gap effect was included, in the present simulations we could not obtain core heating as observed ($\sim 0.8\text{keV}$) in the experiment. To fit more with realistic situations, each of the simulation codes is required model improvement, e.g. considerations of a) magnetic field generation during implosion, multi-dimensional effect in the fast electron generation, and c) re-circulation fast electrons due to a sheath field generated around the core.

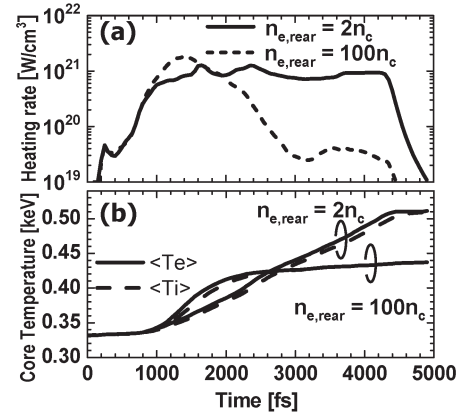


Fig. 1. Temporal evolutions of (a) core heating rate and (b) ion and electron temperatures averaged over dense core region.

References

- 1) H. Nagatomo, *et al.*, *Proc. of 2nd Int. Conf. on Inertial Fusion Sciences and Applications* (Kyoto, 2001), Elsevier, 140 (2001).
- 2) H. Sakagami, *et al.*, *Proc. of 3rd Int. Conf. on Inertial Fusion Sciences and Applications* (Monterey, 2003), ANS, 434 (2004).
- 3) H. Sakagami, *et al.*, “Integrated Fast Ignition Simulation of Cone-Guided Target with Three Codes”, to be published in *Proc. of ICPP 2004*.
- 4) Y. Nakao, *et al.*, *Proc. of 20th IAEA Fusion Energy Conf.* (Vilamoura, 2004), IAEA-CSP-25/CD, IF/1-5 (2005).
- 5) T. Johzaki, *et al.*, “Integrated Simulations for Core Heating of Cone-Guided Targets in Fast ignition”, submitted to *Phys. Rev. Lett.*

§31. Innovative Concepts of Free Surface Cooling System on First Wall of Fusion Reactor

Kunugi, T., Kino, C. (Kyoto Univ.)
Sagara, A.

As for the application of the free surface concept to the FFHR (Force-Free Helical Reactor) design conducted by the National Institute for Fusion Science (NIFS) [1], it is necessary to consider the helical configuration, that is, at a certain position the free surface would be at the ceiling. In this case, the liquid might fall down into the plasma. So, we proposed the innovative free-surface cooling concept (Kunugi-Sagara type Free-surface Blanket, KSFB-I) for a magnetic confinement fusion reactor such as the FFHR design [2]. In this concept, if we can make many micro-channels on the first wall as a flow passage, we will expect a capillary force to withstand the gravity force and the wall shear stress. In the case of FFHR, the candidate working liquid is a Flibe. In general, a high Prandtl number ($Pr = \nu/\alpha$, here ν is viscosity and α is thermal diffusivity) fluid like Flibe ($Pr \sim 30$) has relatively lower heat transport capability than that of liquid metal ($Pr \sim 0.03$ for Li). However, the surface heat flux at the first wall is about 0.1 MW/m^2 : it is quite low compared to the usual magnetic fusion reactors. Therefore, the Flibe can be used as working fluid of the liquid wall.

Lithium lead (^{17}Li - ^{83}Pb) is selected as a working liquid in the present study because LiPb is extremely low Prandtl number ($Pr \sim 0.003$). Additionally LiPb eutectic permits the use of moderately enriched or natural Li and has a relatively low cost in comparison with other tritium generating and multiplier materials. Since LiPb has five times higher density than that of Flibe, it might be a problem to keep the fluid in the channel of first wall with reticular grids.

In the present study, the numerical simulation to evaluate its feasibility has been carried out as shown in Fig. 1. For the wall material, a tungsten is chosen as one of candidates because of high temperature resistance and low activation property, and furthermore, a good neutron multiplier to increase tritium breeding ratio (TBR).

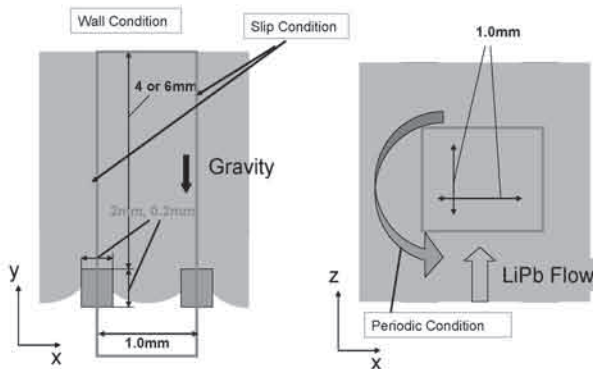


Fig. 1 Computational domain

We performed the numerical simulations in order to evaluate the feasibility of this innovative cooling

concept proposed here. In the case of $10\text{mm} \times 10\text{mm}$, the numerical results indicate that the LiPb flow is kept stably in the flow passage because of the low-pressure region induced as shown in Fig. 2. Moreover, this concept shows enough heat transport potential as shown in Fig. 3. This is because we can find the deformation of the free surface and the circulation flows in the flow passage in the case of $1\text{mm} \times 1\text{mm}$. It is considered that these circulation flows could enhance the heat transfer for LiPb flows.

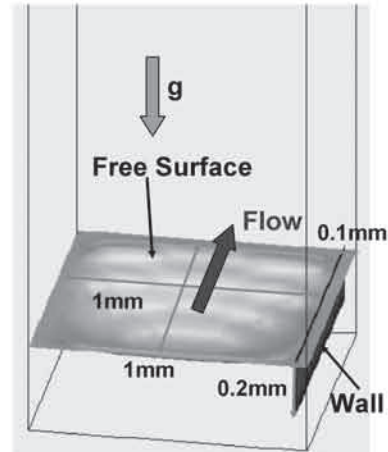


Fig. 2 Free-surface deformation due to shear flow/gravity

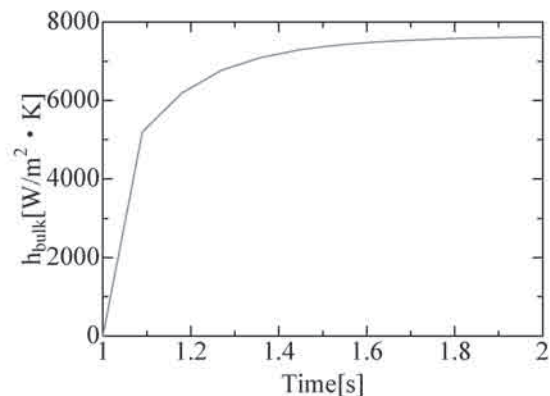


Fig. 3 Trend of the bulk heat transfer coefficient (example)

The following results were obtained:

- 1) LiPb free-surface flow can be kept stably in the grid-typed flow passage if the physical properties are correct.
- 2) Large secondary flow appear in the grid-typed flow passage.
- 3) These secondary flows would enhance the heat transfer for LiPb flows.
- 4) New KSFB wall concept might be one of the candidates of liquid wall concept for fusion reactors. However, the results obtained here were very preliminary. Further investigation would be necessary in the future.

Reference

- [1] A. Sagara, et al, Proc. of 17th IAEA Fus. Energy Conf., Yokohama, (1998) FTP-3,.
- [2] T. Kunugi et al., Fus. Eng. and Des. **65** (2003) 381

§32. Measurement of Particles Ablated by Intense Laser Irradiation

Konishi, S., Yamamoto, Y. (Kyoto Univ.)
Nishimura, H., Norimatsu, T. (ILE, Osaka Univ.)

For the development of laser fusion reactor, feasibility of the chamber that is anticipated to be exposed to several Hz or more frequent pulse irradiation will be a major technical issue. One of the possible difficulty is the evacuation of chamber that will be filled with vapor, mist or particles of chamber wall, regardless of it is made of liquid or solid. Particularly with fast-ignition target, lead from cone attached to the fuel is anticipated to be plated on the wall. Chamber wall will be ablated by energetic particles and the resulted vapor will recombine to form mist, cluster or particles that are suspected to stay in the chamber. This collaborative research will investigate the basic behavior of the ablated particles from the surface simulating laser fusion chamber.

Figure 1 (a) illustrate the setup of the experimental apparatus. In this study, plastic target simulating debris and ions from laser fusion target is irradiated with YAG laser. Ablated particles are observed with Thomson parabola for ion energy and for species with quadrupole mass spectrometer and the charge collector. Figure a (b) shows the configuration between plastic primary target, metal secondary target and the charge collector. Plastic target is first irradiated with YAG laser and secondary ablation by debris from plastic target as well as primary ions are analyzed. Ablation of metals by debris are important, both for EUV generation with tin and laser fusion chamber with lead metal. It is expected both phenomena would be described with a very similar model.

In the fiscal year 2004, two experimental campaigns of two 2 weeks each were performed to verify the performance of the apparatus. Thomson parabola detected Carbon ions of 1 to 3 charges. Figure 2 shows the example of the mass spectroscopy obtained from the irradiation of plastic target. As seen in the figure, $14n+1,2$ peaks were observed that are considered to correspond clusters of ethylene (CH_2) $_n$. Such clusters were either formed by direct ablation or reactions between ablated particles. Charge collector detected the secondary ablation of tin and lead. However the results were unstable and further improvement in the experiment is considered to be needed.

In the fiscal year 2005, we plan to install broad range mass spectrometer of up to ca. 1000 to detect larger size particles. At the same time, laser intensity and pulse length will be changed to better simulate the laser fusion and EUV conditions.

Acknowledgement

The authors appreciate Prof. Sakawa of Nagoya University and Dr. Fujioka of Osaka University for their supports on the experiments.

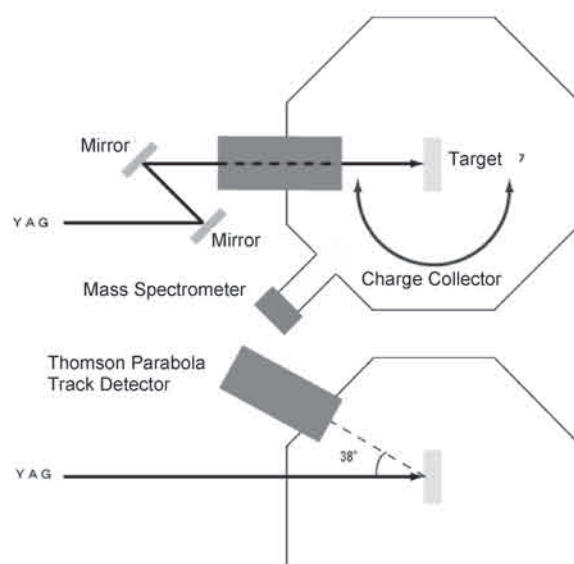


Fig.1 (a) Experimental Apparatus

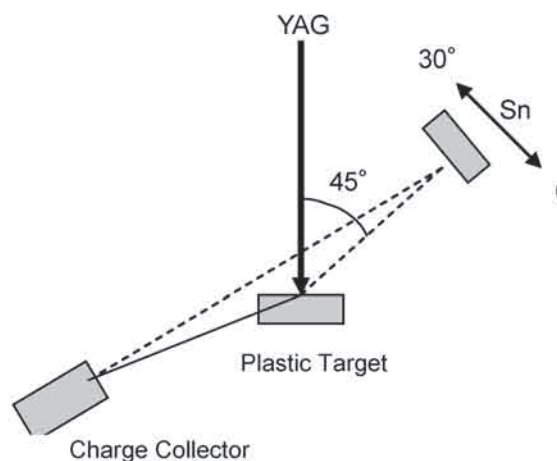


Fig.1 (b) Configuration of plastic target, metal target and charge collector

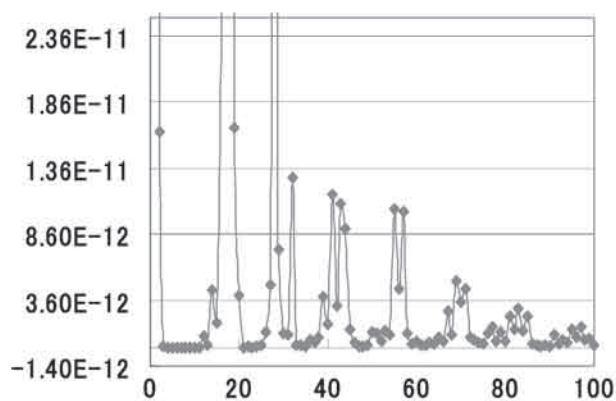


Fig.2 mass analysis of ablated particles

§33. Research on Target Heating Processes Using PW-Laser-Driven Intense Proton Beams

Ogawa, M., Hasegawa, J., Oguri, Y., Nakajima, M., Horioka, K. (Tokyo Institute of Technology)

Stopping power of hot and dense matter for heavy ions is predicted to be larger than that of cold equivalent, resulting in the range shortening of projectiles. This effect, called as “plasma effect”, is very important for target design of heavy-ion-driven inertial confinement fusion. By using z-pinch-discharge plasmas or laser-produced plasmas as targets for beam-plasma interaction experiments, many scientists have so far examined the enhancement of stopping power due to the plasma effect. However, no experiment using beam-heated plasma has been conducted. Thus, the purpose of this study is to examine the feasibility of the interaction experiments using plasma targets heated by PW-laser-driven intense proton beams. We estimate the energy loss of the protons in a carbon foil using a simple simulation code and survey the optimum experimental parameters.

Kodama *et al.* have measured the energy spectra of converging proton beams from a concave thin foil target backward irradiated by a PW laser at ILE. We used one of the spectra obtained by them for our estimation, which was integrated with incident angles from 0° to 30° . By neglecting space charge effects, here we assumed that the front surface of the carbon foil was located at the geometrical focal point of the converging proton beam. Because the incident protons penetrate the foil with diverging, the beam-heated volume in the foil had a conical shape as shown in Fig. 1. We evaluated the amount of beam energy deposition on this volume by integrating the total energy loss of protons. The energy loss calculation used the Bethe's stopping formula extended to plasma media. To obtain temperature from the internal energy of the target, we used a SESAME equation-of-state library. By assuming that high-energy protons were generated at the moment of PW-laser irradiation, the arriving time of each proton was determined from its velocity and the distance between the foils ($300\ \mu\text{m}$). Figure 2 shows the time evolution of foil temperature for various foil thicknesses from $10\ \mu\text{m}$ to $500\ \mu\text{m}$. From the figure one can see rapid increases in the foil temperature due to the energy deposition by penetrating protons. Here, we neglected the expansion of the plasma and assumed that the plasma had the same density as solid because the heating time ($\sim 10\ \text{ps}$) was much smaller than the time scale of hydrodynamic motion. For the case of a $100\text{-}\mu\text{m}$ foil, a plasma with a temperature of $100\ \text{eV}$ and a mean ion charge of 4 was finally obtained after heating, which means that the condition for measuring the plasma effects on the stopping power is satisfied. In Fig. 2 we plotted the energy spectra of incident and outgoing protons. Solid lines for outgoing protons are in the case of plasma target with beam heating, while dashed lines are in the case of cold target without beam heating. For high-energy protons with kinetic energies above $10\ \text{MeV}$, spectrum shifts to lower energy were very small because of low stopping power for such high-energy protons. No plasma effect was detectable because the foil target was not heated enough when the

high-energy protons interacted with the target. On the other hand, because relatively low-energy protons with energies around $1\ \text{MeV}$ lost large amount of their energy in the foil, spectrum shifts to lower energy were observable. In addition, the enhancement of energy loss due to the plasma effect could be observed, particularly in the cases using a foil of $50\ \mu\text{m}$ and $100\ \mu\text{m}$.

In conclusion, to observe plasma effects in actual experiments, a novel method for high-resolution energy spectrum measurement will be needed.

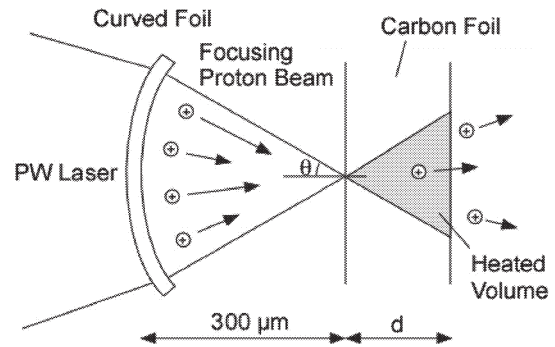


Fig. 1. A schematic of beam-heated foil plasma interacting with intense protons.

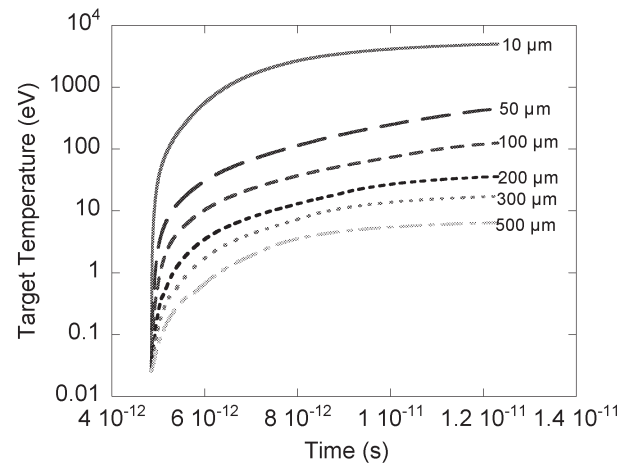


Fig. 2 Time evolutions of target temperature for various foil thickness.

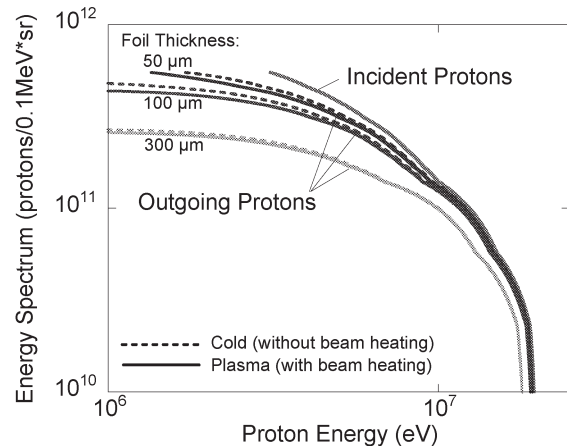


Fig. 3. Energy spectra of protons outgoing from carbon foils of $50\ \mu\text{m}$, $100\ \mu\text{m}$, and $300\ \mu\text{m}$ thick.

§34. Physics of High Energy Density Plasma driven by Fast Pulse Power Discharges

Horioka, K., Nakajima, M., Sasaki, T. (Tokyo Institute of Technology)
Mima, K. (Osaka University)

Hot dense matters naturally observed in Jovian planets, white dwarfs and also in a fuel plasma of inertial confinement fusion, are of primary concern in this study. The plasma in a strongly coupled state is produced by a wire explosion driven by a fast pulse power generator composed of a water-filled test chamber, a low inductance discharge section and a cylindrically arranged capacitor bank. The electrical energy powered into the plasma is estimated by integration of voltage-current characteristics of the pulsed discharge. In order to estimate the plasma density, the boundary of the plasma evolution is observed with a fast framing photography. The cylindrical shock wave in water is measured by the schlieren method and the history of pressure evolution is evaluated by comparing the shock wave trajectory with numerical estimation based on a quotidian equation of state (QEOS)[1]. Evolutions of electrical conductivity, corresponding coupling parameters and the equation of state of the plasma are discussed.

In this study, thin wires are exploded in water by coaxially arranged low inductance capacitors [2]. The fast discharge is insulated and tamped by the surrounding water, and can make a dense symmetric plasma in the water filled test chamber. In contrast to previous experiment, our study is intended to make a semi-empirical scaling of the equation of state and transport coefficient. We observe the time history of the shock wave to estimate the temporal evolution of plasma pressure. The behavior of shock waves in the surrounding water is used as an indicator of the pressure history.

A schematic diagram of the experimental arrangement is shown in Fig.1. We use a capacitor bank consisted of cylindrically arranged $8 \times 0.4 \times 10^{-6} \text{F}$ low inductance capacitors. To avoid the skin effect on the exploding plasma, thin wires made of Al or Cu are used. The electrical resistivity is evaluated from values of the inductively corrected voltage and the discharge current using a voltage divider and a Rogowski coil. We also estimate the history of input power to the plasma with the discharge characteristics. The evolution of wire plasma is observed by a fast streak camera with microscopic attachment. The conductivity is evaluated directly from the electrical characteristics and effective diameter of the exploding-wire plasma. We measured the behavior and electric characteristics of plasma evolution at least three times. The results showed that the plasma is sufficiently reproducible to estimate parameters of the transient plasma.

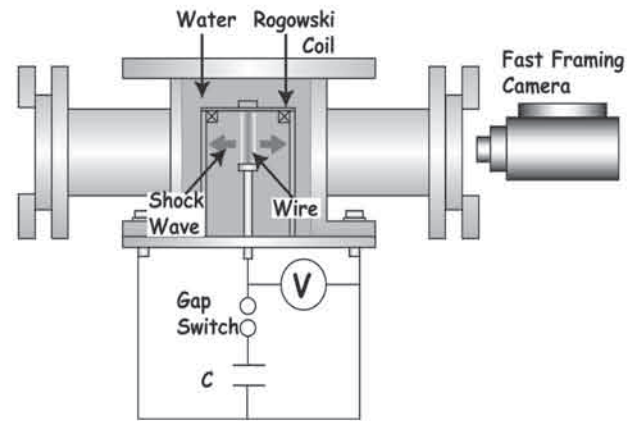


Fig.1 Schematic diagram of experimental arrangement for exploding wire experiments.

The experimentally estimated conductivity evolved from a value corresponding to a solid state with room temperature to a highly ionized state with intermediate stage. The regime which provides minimum conductivity is considered to be a phase transition region of the wires. In fact, we could observe visible image of wires only after around 500nsec from the start of discharge.

We have made a two-temperature 1D-MHD model coupled with a circuit model to calculate the behavior of wire explosion in water. Here, a quotidian equation of state (QEOS) [1] and the time history of experimentally obtained energy input to the plasma are used in the hydrodynamic simulation. Our goal is to make a semi-empirical modeling, using the numerical calculation and experimental values [3].

In order to study the physics of strongly-coupled, high-energy density plasma, a preliminary experiment and a numerical simulation were performed. The experimental results show that wire plasmas exploded in water are sufficiently reproducible to evaluate the evolutions of the plasma, especially the conductivity at phase transition regime. Results indicate that the evolution of the average electric conductivity of wire plasma after the phase transition region and the discrepancy of the numerical results from the experimental observation can be attributed to the conductivity model and the EOS model [4]. We are going to measure the trajectory of shock wave to estimate the time history of pressure and derive a more detailed semi-empirical modeling of the conductivity and the EOS for the strongly coupled plasma.

References

- 1). More, R.M., Warren, K.H., Youn, D.A., and Zimmerman, G.B., *Phys. Fluid*, **31**, 3059 (1988).
- 2). Desilva, A.W., and Katsouras, J.D., *Phys. Rev.*, **57**, 5945 (1998)
- 3). Horioka, K., Nakajima, M., Sasaki, T., Mizoguchi, T., *Proc. 15th High Power Particle Beams*, St. Petersburg (2004)
- 4). Sasaki, T., Mizoguchi, T., Kikuchi, T., Nakajima, M., and Horioka, K., *Proc. Jap. Soc. Fusion Sci.*, Sendai, (2004)

§35. Measurement of Bremsstrahlung Emission Using SX-CCD Camera

Ida, K., Kobuchi, T., Shiraga, H. (Osaka Univ.),
Azechi, H. (Osaka Univ.)

In the plasma compressed by the laser, the electron density and temperature can be derived by the intensity of bremsstrahlung emission from the plasma compressed by laser. The energy range measured should be 10 – 30keV to avoid the absorption of bremsstrahlung in the plasma, because the density of the plasma can be few hundred times of solid density. The bremsstrahlung emission from the plasma, J_ν , is given by

$$J_\nu d\nu = \frac{32\pi}{3} \left(\frac{2\pi}{3mkT} \right)^{1/2} \frac{Z^2 e^6}{mc^3} N_+ N_e \exp\left(\frac{-h\nu}{kT}\right) d\nu$$

where m , k , T , Z , N_+ , N_e are electron mass, Boltzman constant, electron temperature, atomic charge, ion density, electron density, respectively.

Soft X-ray CCD cameras with photon counting capability have been widely used in space X-ray observatory in astronomy. The amount of charge in each pixel of the CCD created by the individual X-ray photon is proportional to the energy of X-ray. Therefore the xray energy spectra can be obtained by counting the number of photons at a given intensity (photon counting mode). The soft x-ray CCD camera used in this diagnostic is a Andor DO432 with a full frame front illumination CCD detector. The imaging area has 1250(H)x1152(V) pixels and each pixel of the CCD detector is fabricated on special silicon with a size of 22.5 μ m x 22.5 μ m. The readout noise is 15 electrons for 1MHz ADC. The resolution of the ADC is 7 electrons/ADC-count and the dark current is only 0.01 electron/pixel second at the cooling temperature of -70°C using multistage Peltier devices.

Figure 1 shows the spectrum of Mn K α (5.89keV), Np L α (13.93keV) and Ag L α and K α (2.98keV and 22.16keV) in the soft X-ray range emitted from the radioisotope of Fe⁵⁵, Am²⁴¹, Cd¹⁰⁹, respectively measured with SX-CCD detector with 50 μ Be filter. The peak of the dark charge gives the offset level of intensity as zero energy. The relation between the intensity and the energy of the photon is plotted in Fig.2. The slope gives the conversion ratio from the counts to energy of 28.8eV/counts. The Fe K- α line is fitted by a Gaussian plus linear and the full width at half maximum (FWHM) is 0.22keV at 5.89keV as shown in Fig.3.

The energy resolution of the soft X-ray camera is good enough to distinguish the line radiation of impurities in the plasma and continuum contribution due to the bremsstrahlung emission. Therefore the electron density and temperature of the plasma compressed by laser are expected to be measured from the absolute level and slope of the bremsstrahlung emission using soft X-ray CCD camera.

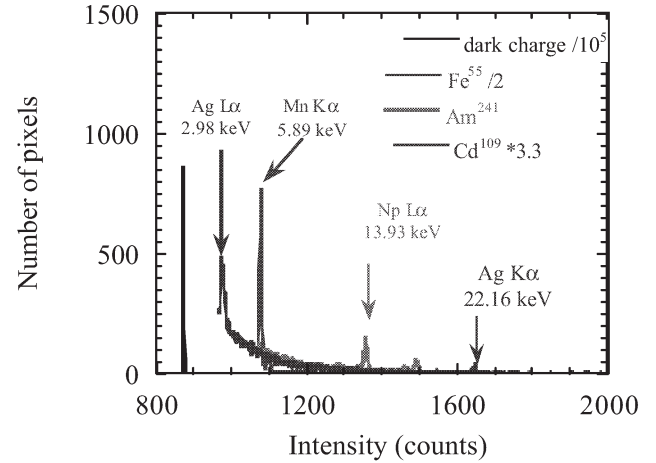


Fig. 1. Energy spectrum of soft X-ray emitted from the radioisotope of Fe⁵⁵, Am²⁴¹, Cd¹⁰⁹.

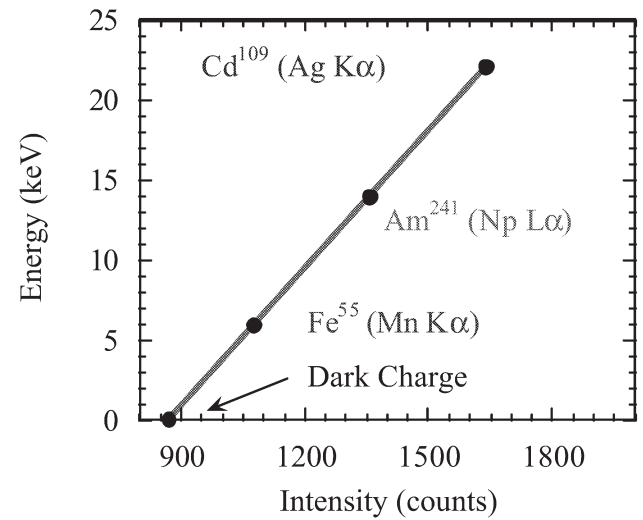


Fig. 2. Photon energy of soft X-ray as a function of intensity (count of ADC).

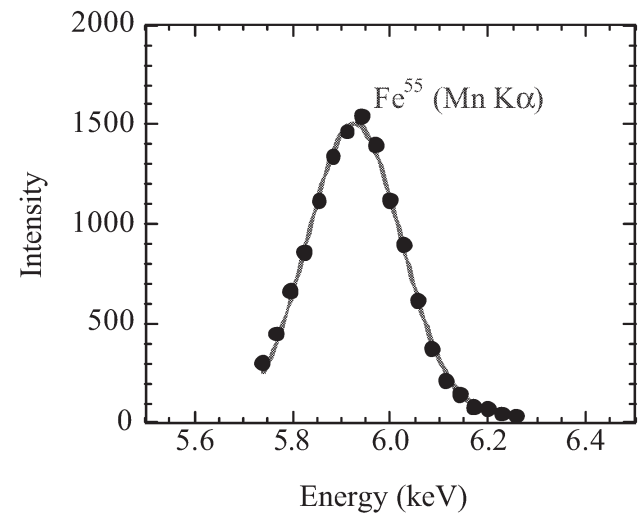


Fig.3. The spectrum of Fe K- α line is fitted by a Gaussian plus linear

§36. Natural Diamond Detector for Neutron and γ -ray Measurements in Laser Fusion Experiments

Isobe, M. (NIFS)
Azechi, H., Kodama, R. (I.L.E., Osaka Univ.)
Krasilnikov, A.V. (TRINITI, Russia)

1. Introduction

Natural diamond detectors (NDD) have been applied to the Large Helical Device to diagnose energy distribution of fast neutral particles originating from neutral beam heating and ion cyclotron resonance heating [1,2]. Because the diamond detector is known to be fast in time response, it may be applicable to neutron and γ -ray measurements in laser fusion experiments based on time of flight technique. In this report, NDD we have developed and electronics planned for laser fusion experiments are briefly described.

2. Operation and properties of NDD

Figure 1 shows a NDD prepared for this work. NDD with ohmic Au contacts and a DC bias can serve as a radiation detector. Two different NDDs have been prepared. Both detectors have the sensing area of $\phi 2$ mm. One and another have the thickness of 0.1 mm and 0.2 mm, respectively. The signal generation process is basically similar to that of a Si semiconductor detector. In the case of the high energy photons, electron-hole pairs are created by photoelectric events. In the case of neutrons, a variety of nuclear processes such as elastic and inelastic scattering $^{12}\text{C}(n,n')^{12}\text{C}$, nuclear reaction $^{12}\text{C}(n,\alpha)^9\text{Be}$ and so on are involved [3]. The important properties of NDD in comparison with a Si detector include a high band gap of 5.5 eV, short mean free drift time of ~ 10 ns, large saturation carrier velocity of 2.2×10^7 cm/s for E of 10^4 V/cm, high breakdown voltage of 10^7 V/cm. Further detailed descriptions of NDD's properties are available in Ref. 3 and 4.

3. Electronics

Figure 2a) shows the electronic circuit used for neutral particle measurement in LHD. This system is suitable for measurement of energy spectrum of detected particles through pulse height analysis but it is slow in time response. Because the time response of GHz range is required in the laser fusion experiment, the circuit used in LHD can not be used for this purpose. In order to enhance time response as much as possible, we will use a circuit shown in Figure 2b). A high voltage bias-T (Picoseconds Pulse Lab./Model : 5531) resistively couples the signal cable to a high voltage power supply and capacitively couples the signal cable to a GHz sampling oscilloscope.

4. Plan in next fiscal year

We have so far developed thin NDD in anticipation of ultra fast response and have prepared necessary electronics used for this experiment. In next,

first we will check total bandwidth of this system by use of ultraviolet laser with pulse width less than 1 ns. After this check, NDDs will be applied to laser fusion experiments in I.L.E. Osaka University.

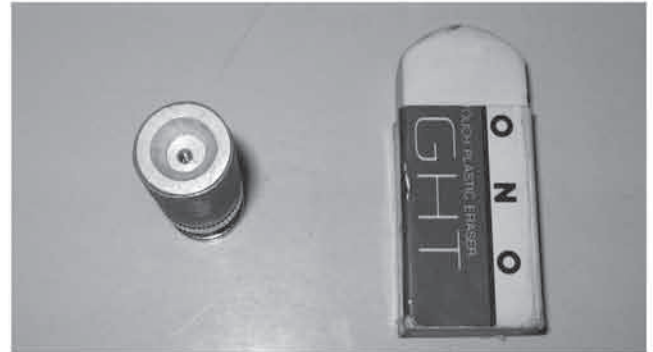


Fig. 1. Photograph of natural diamond detector. It has a size of $\phi 2$ mm and 0.1 mm thickness. Surface electrode is made from Au.

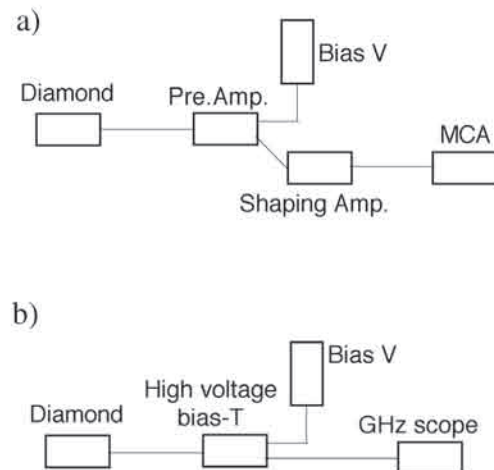


Fig.2 a) Electronic circuit used for fast neutral particle measurements in LHD [1]. b) Circuit planned for laser fusion experiment in ILE Osaka University.

References

- 1) Isobe, M., *et al.*, Rev. Sci. Instrum. **72**, (2001) 611.
- 2) Saida, T., *et al.*, Nucl. Fusion, **44**, (2002) 488.
- 3) Pillon, M., *et al.*, Nucl. Instrum. Methods **B101**, (1995) 473.
- 4) Krasilnikov, A.V., *et al.*, Rev. Sci. Instrum. **68**, (1997) 1721.

§37. Aerosol Formation and Its Effects on the Chamber Wall Lifetime and Operation of IFE Power Reactors

Hirooka, Y. (NIFS)
Tanaka, K.A. (Osaka Univ.)

It is well known that in IFE reactors chamber wall components will be exposed to repeated short pulses of 14 MeV neutrons, X-ray, unburned DT fuel particles and pellet debris such as CD complex ions. As a result, chamber wall surfaces will be subject to evaporation and ablation but at the same time to condensation and deposition of materials.

These processes will no doubt affect the lifetime of wall components, particularly if they are solid, and also the laser pulse frequency, i.e. reactor power output, if they are protected by some flowing liquid. Whether the wall surface is solid or liquid, one predicts the aerosol formation in the periphery of chambers where the ejected materials density would be extremely high.

However, it is also true that aerosol formation is likely in the middle of chambers. This is because most of the current IFE reactor studies employ either a cylindrical or spherical chamber, which has the axis and point of symmetry. Therefore, evaporated or ablated materials will be transported to focus due to these symmetries, leading to the formation of aerosol.

Under some conditions, the aerosol particle size will increase, losing its density though, whereas the opposite may be true under other conditions. As such, the formation of aerosol will occur in yet-to-be-explored manners though one can speculate that important parameters are the species, density, velocity, angle, etc.

The present work is intended to investigate the behavior of aerosol formation from materials ejected due to pulse power radiation. Fundamental discussions on the pulsed power beam and materials interactions have been continued since 2004. Shown in Fig. 1-(a) and (b) are diagrams illustrating the materials behavior and the pulsed ion beam power conditions and the pulsed laser beam conditions, respectively. As can be seen in these diagrams, there is no significant difference between ion and laser beam cases if under identical power conditions.

Thus, a laboratory-scale experimental setup, employing a high-power YAG laser, has been carefully designed and will be constructed to operation within the fiscal year of 2005. In this setup, the laser is optically split into two beams to irradiate two LiPb-alloy targets from which plume plasmas will be emitted, leading to the formation of aerosol. A schematic diagram is shown in Fig. 2.

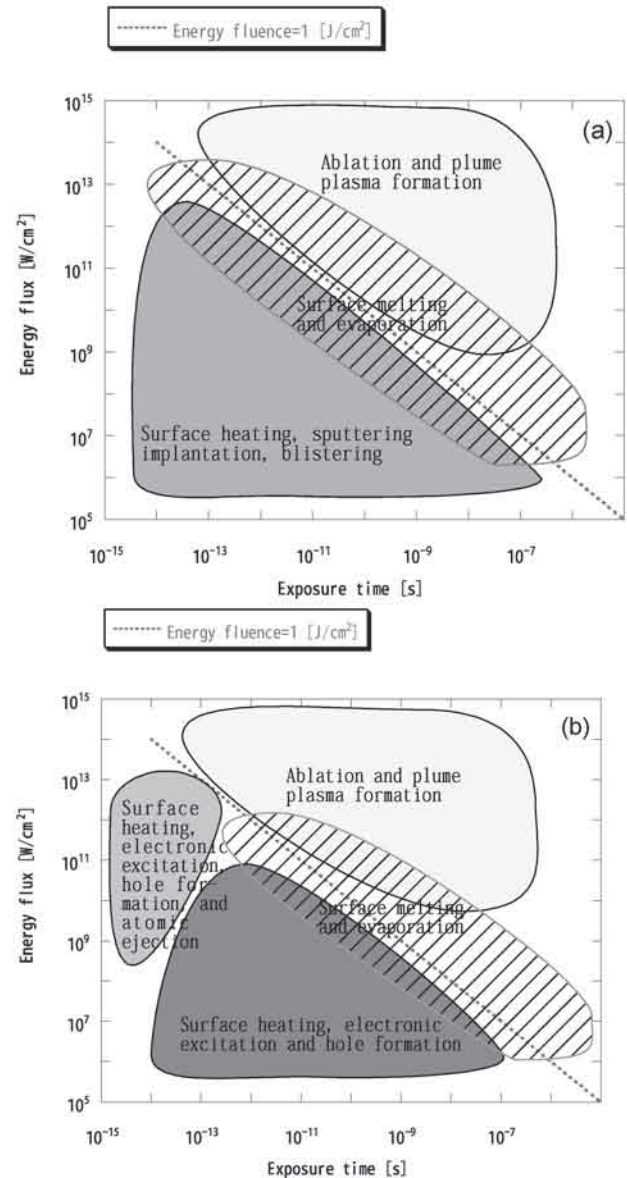


Fig. 1 Pulsed power beam and materials interaction diagrams for (a) ion beam and (b) laser beam cases.

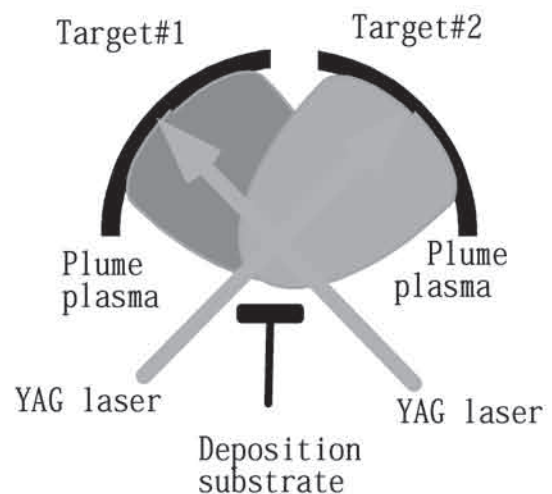


Fig. 2 Dual beam-target setup for aerosol formation.

§38. Application of a Fast Video Camera for Study on Triam-2M Peripheral Plasma and Plasma-surface Interactions

Nishino, N. (Grad. Sch. Mec. Eng., Hiroshima Univ.)
Zushi, H., Hanada, K., Sasaki, K., Sato, K. (Dept.,
Kyushu Univ.)

Dust in plasma is produced as a result of the plasma-wall interaction. Therefore, the generation of dust suggests the degradation of the first wall. Also, dust behavior affects impurity content in the main and SOL/divertor plasma. Moreover, for nuclear fusion reactor dust affects tritium inventory. Thus, dust study is very important for future nuclear fusion reactor and this is ITER relevant.

Triam-1M is suitable machine for dust study, because of limiter discharge and long pulse discharge (>2hr world record). Plasma-wall interaction mainly occurs at the limiter surface. Therefore, it is very easy to observe the in-situ plasma-wall interaction. Long pulse discharge enables us to heat up the wall surface such as fusion experimental reactor.

In this study dust behavior measurement using fast video camera is proposed and first results are reported. This study is very fruitful now, and the similar attempt is proceeding in the other machine (e.g. NSTX). Hiroshima Univ. provides fast camera and it is installed at the small horizontal port for a far-infrared camera. Fig. 1 shows the schematic of camera setting. The distance between plasma and fast camera is around 2400mm. Fig.2 shows the typical view from this port. The camera view has 256x256 pixels, and recording speed is 4500 frames per second (FPS). In this view the horizontal direction is horizontal (normal view). The bright region in the center is main plasma, and the both sides are the port. The left hand side of plasma is the edge of the limiter. During long pulse discharge (more than 30 s) the obvious number of dust are found by fast camera. The white arrows in Fig.2 indicate small bright region due to dust. The camera image is two-dimensional (2-D). The movement of dust along the line of sight is unknown, however, the parallel movement along the image plane can be calculated. The parallel velocity of this dust is around 10m/s. If we get 3-D view, it will enable us to get the real velocity and we can compare the dust velocity and theory prediction. This is the future plan.

As far as numbers of dust generated in single discharge, the degree of the plasma-wall interaction or first wall degradation can be estimated. The fast camera images show the dust particle one by one. Then, the numbers of dust can be counted by manual. When dust results from the limiter surface, the limiter is brighter than usual. Fig.3 shows the relationship between discharge time and the number of dust found by fast camera. The recording time of fast camera is shorter than the discharge, therefore, the trigger fired by the light monitor signal of the limiter surface from the bottom port. Unfortunately the limiter temperature is not measured precisely this time. Therefore,

the relationship between the discharge time and the limiter temperature is unknown.

In the near future we will try to get 3-D information for dust behavior measurement. The idea is very simple. If dust can be seen from two different lines of sight such as human eyes, it is not so hard to identify the position of dust.

This study was held under Bi-directional collaboration between Hiroshima Univ. and Kyushu Univ. The author deeply appreciates the support of NIFS.

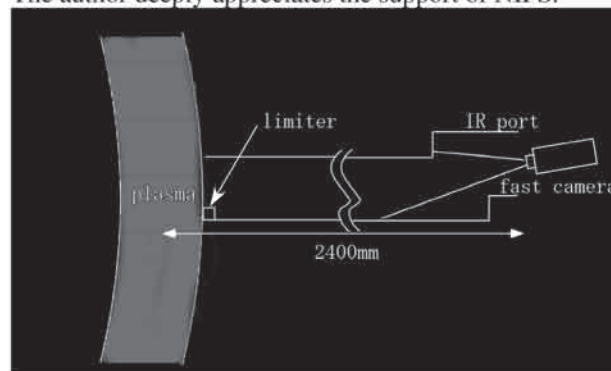


Fig. 1. Schematic of the camera setting in Triam-1M

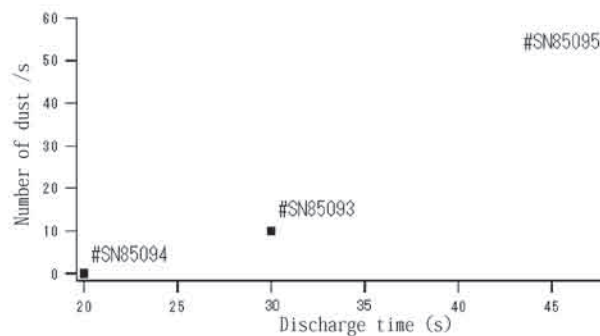
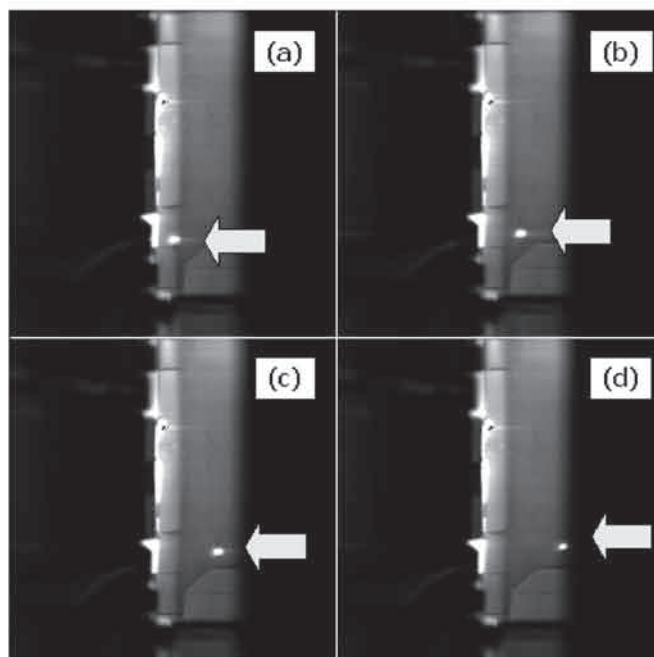


Fig.3 Relationship between the number of dust and discharge time

§39. Application of the Zeeman Patterns to the Local Plasma Diagnostics in the TRIAM-1M Tokamak (NIFS04KUTR001)

Kado, S., Shikama, T. (The Univ. of Tokyo)
Zushi, H. (RIAM, Kyushu Univ.)

Standard passive spectroscopy yields only a line-integrated emission along the viewing chord. In order to obtain the local plasma parameters, active methods such as the charge exchange spectroscopy, which makes use of a neutral beam injection, have been applied for highly-charged (usually hydrogenic) ions in core region.

We have been developed a method in which local information can be obtained from the Zeeman patterns even in the device without NBI.1) In principle, this method can be applied both to the core and the boundary region. We have shown that the radial position of emission, temperature and the flow velocity in the position can be determined from the best-fit of the spectral line shape calculated by taking into account the Zeeman profile, the Doppler broadening and the Doppler shift. 2)

The experiments are performed in the TRIAM-1M super-conducting tokamak under the condition of 8.2 GHz lower hybrid current driven discharge. The magnetic field strength of about 7 T at the plasma center is generated using 16 Nb₃Sn super-conducting toroidal field coils. The plasma boundary shape is restricted by three D-shaped poloidal limiters and one vertically movable limiter installed in the upper port of the vacuum vessel. All plasma-facing components are made of molybdenum.

The emission from the plasma is observed using fan-shaped 25 viewing chords in the poloidal section. In front of the object lenses, a linear polarizer is attached with its polarization axis perpendicular to the toroidal field direction for the observation of the σ components. The collected emission is dispersed using a spectrometer (Acton Research AM-510) having a focal length of 1 m and equipped with a 1800 grooves/mm ruled grating. This fiscal year, we replaced the image-intensified CCD (ICCD) detectors 62 μ m in the MCP resolution with the electrically cooled back-illuminated CCD (Andor DU440-BU2). The dimension of the CCD chip is 2048 x 512 pixels and each pixel size is 13.5 x 13.5 μ m². This replacement improved the effective image resolution and lowered the noise to a great extent.

The H α spectrum consists of seven transitions due to the fine structure splitting. In the external magnetic field, these seven components split into totally eighteen π and thirty σ components. When analyzing the emission from low temperature neutrals, one should estimate the shape of H α spectrum containing these transitions, because the shape of the spectrum is strongly affected by the fine structure. In the fitting procedure, the thirty σ components are calculated based on the quantum mechanical method. 2) In addition, three temperature components: cold (<1eV), warm (1~10eV),

and hot (~100eV) are assumed for the fitting procedure, since hydrogen atoms usually have multi-temperature components originated in the production processes, such as dissociations or charge-exchanges.

Fig.1(a) shows the separated positions of the emission. One can see that the spatial resolution of the measurement is much improved by installing the cooled-CCD detector compared to the former ICCD detector shown in Fig.1(b). Filled circles indicate the separated position of emission along the viewing chords and marker size represents the relative intensity of the cold components. The horizontal bar shown with the marker is the standard deviation of the fitting procedure. Filled triangles denote the positions obtained on the peripheral viewing chords assuming single magnetic field for checking the results. Emissions in the high-field side originate from the region between the vacuum vessel and the D-shaped poloidal limiter surface, namely so-called limiter shadow. The obtained positions of the emission are consistent with the bright positions in the visible image measured with the TV camera installed for the purpose of monitoring the plasma position. 3)

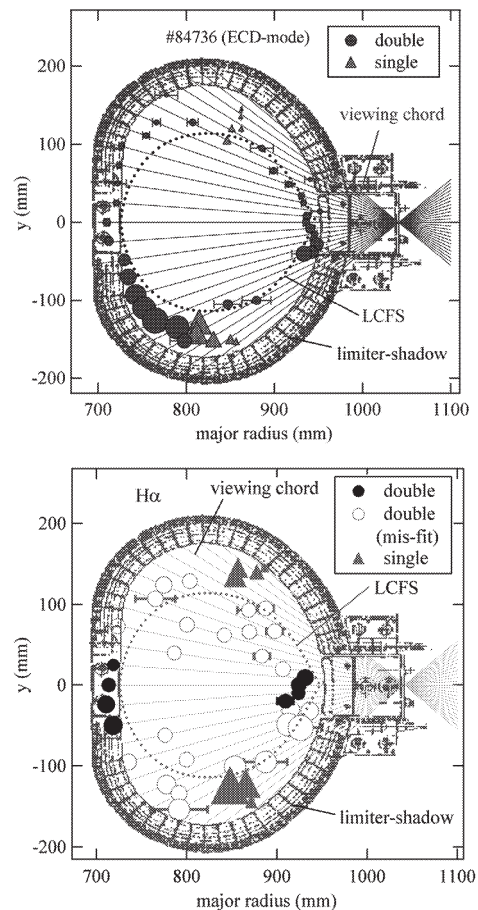


Fig.1: The measured position of H α emission. (a: upper) The measured position using back-illuminated CCD detector (b : lower) The position measured using ICCD . 2)

Reference

- 1) J. Weaver, et al. : Rev. Sci. Instrum. **71** (2001) 1664.
- 2) T. Shikama, et al. : Phys. Plasmas **11** (2004) 4701.
- 3) H. Zushi, et al. : Nucl. Fusion **43** (2003) 1600.

\$40. Design and Fabrication of Compact Plasma Wall Interaction Experimental Device (CDP)

Hanada, K., Sato, K.N., Zushi, H., Yoshida, N.
(Kyushu University)

Mitarai, O. (Kyushu Tokai University)

Maekawa, T. (Kyoto University)

Takase, Y., Ejiri, A., Shiraiwa, S. (University of Tokyo)

Nagata, M. (University of Hyogo)

Nagayama, Y.

1. Introduction

Spherical tokamak (ST) is a candidate for cost-effective fusion reactor and the improvement of the plasma performance of ST has been tried in many institutes, which is including in the experimental groups of University of Tokyo by use of TST-2 devices. The experimental group of Kyoto University has been done the development of the plasma start up without ohmic heating coil by RF current drive on LATE devices. One of the effective technique to provide fuel into plasma is compact toroid (CT) injection, which has been proceeded in University of Hyogo. Steady state operation is also a key issue to realize a fusion reactor. In the research of tokamaks, steady state operation will become crucial point and the trials to do long pulse operations in a large tokamak, JT-60U started. The experimental group of Kyushu University has many experiences to sustain the plasma current by use of RF current drive.

The cooperation of these experimental groups under the assistance with NIFS has the possibility to make a new way to realize the fusion reactor using steady state operation of ST. In 2003, we executed the collaboration, which TST-2 moved tentatively to Kyushu University and the RF injection experiment to TST-2 were done successfully[1,2]. On March, 2004, TST-2 moved to Kashiwa campus in University of Tokyo and this experimental program was completed. After this experimental program, the researchers feel the necessity of compact experimental platform of ST and we construct new compact ST called compact plasma wall interaction experimental device (CPD) under the framework in by-directional collaboration program organized by NIFS. The purposes of CPD are 1) confirmation of the effect of EBWCD, 2) investigation of the effect of wall temperature to PWI, 3) CT injection to ST, 4) study of the active control of PWI, 5) confinement study of energetic particles in ST, 6) role in the platform of innovative concept.

2. Specification of CPD

The schematic views of CPD are shown in Fig. 1. The major and minor radii are 0.3 and 0.2 m, respectively. The toroidal magnetic field is 0.25 T at $R=0.25\text{m}$. The features of CPD are 1) four toroidal return coils to investigate the confinement of the energetic particles in ST, 2) four F570 flanges to install the vacuum pump, heating sources, diagnostics and so on. A heating source is RF in frequency of 8.2 GHz up to 200kW. The waveguides to inject RF into plasma are available in the previous TST-2 experiment in Kyushu University. Three pairs of poloidal field coils and center solenoid are installed on CPD. The center solenoid is

able to provide the magnetic flux up to 100mVs. All of magnetic coils are driven by the power supplies for the magnetic coils of TRIAM-1M. Capability of these power supplies is enough to operate their coils and as the result, it is possible to do the feedback control of the plasma position.

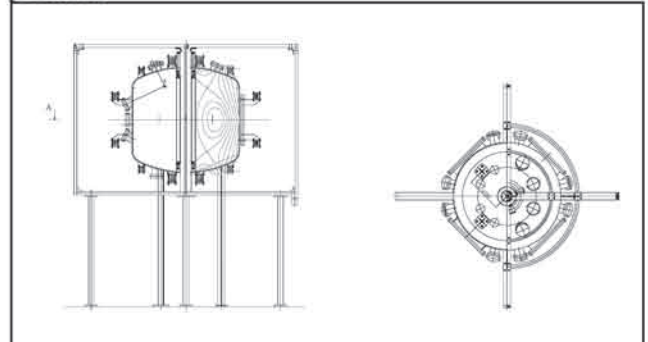


Fig. 1 Schematic side cross-sectional and Top views of CDP. The magnetic surfaces of standard configuration are overwriting on the side cross-sectional view.

3. Fabrication and check

Figure 2 shows the photograph of CDP just after the installation at the experimental hall of TRIAM-1M. The position is the same of previous TST-2. The check of vacuum leak and the energization of the magnetic coils are carried out and the results are well. After the installation of the RF heating system and diagnostics, the plasma experiment will be started.

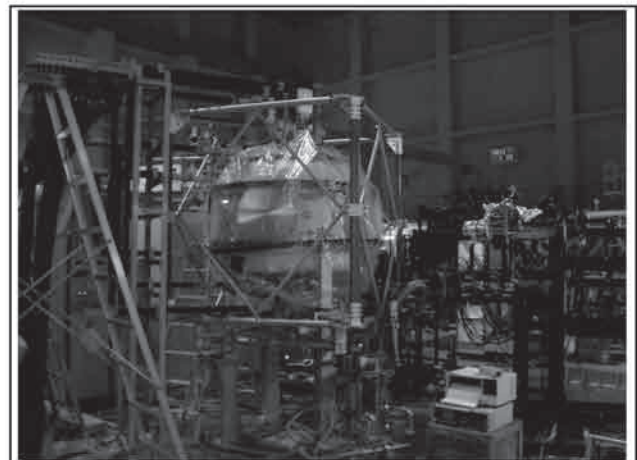


Fig. 2 The photograph of the CPD during vacuum leak check at the experimental hall of TRIAM-1M.

References

- [1] Mitarai, O, et al., Rapid communication J. Plasma and Fusion res. Vol. 80, No.7 (2004)
- [2] Kasahara, H., et al., Proc. the 31th EPS meeting (London) (2004).

§41. Current Startup/Current Drive and Heating Experiments Using RF/mm-Waves on the TRIAM-1M Tokamak

Idei, H. (Research Institute for Applied Mechanics, Kyushu Univ.)

In a framework of the bi-directional collaboration organized by NIFS, new collaboration program was begun in the field of the RF heating and current drive in the TRIAM-1M tokamak. The TRIAM-1M tokamak has super-conducting magnetic coils to generate the high field up to 8T. It is an object of the collaboration to promote research activities in the subjects, specially related to the high-field tokamak experiments. In use of full characteristics of the super-conducting magnet tokamak, the steady-state operation in the lower hybrid current drive (LHCD) plasmas has been demonstrated. The Enhanced Current Drive (ECD) efficiency mode was found in the LHCD plasma, and has studied on its characteristics and relation to the transport phenomena. The start-up of the plasma current by only using radio frequency (RF) [electron cyclotron (EC) and lower hybrid (LH)] waves has been executed in the tokamak. A remote-steering antenna system for electron cyclotron heating and current drive (ECH/ECCD) has been newly developed for the experiments in the tokamak. Fundamental ECH and ECCD at the ITER frequency from the low field can be experimentally tested using the developed antenna system.

Obtained main experimental results are as the followings.

1) ECD-mode LHCD plasma experiments

Electron internal transport barrier (eITB) has been obtained in the ECD-mode LHCD plasmas. The plasma with eITB can be maintained up to 25 sec, which corresponds to more than 100 times of current diffusion time, $\tau_{L/R}$, as shown in Fig.1[1]. Self-organized slow sawtooth oscillations of plasma current, density, temperature, and so on with the period comparable to the current diffusion time have been also observed in the long duration discharges[1]. The oscillation, which has no helical structure, appears only in the high performance plasma with eITB and it seems to be induced by the variation of the transport coefficient which has relation to the current density profile estimated by the radiation from energetic electrons. In the ECD-mode LHCD plasma, ion temperature profiles became peaked. Ion internal transport barrier has been also formed in the intermediate state of the ECD mode, as shown in Fig.2[2]. Physics of the transition associated with ITB formations and current profile effects on the sustainment of ECD/ITB modes has been investigated.

2) ECH/ECCD experiments

The ECH/ECCD experiments using the remote steering antenna have started on the TRIAM-1M tokamak for the first in the world. In the O-mode experiments, the dependence of the increased current on the steering angle in the oblique injection was observed. However, the heating effect in an improvement of the LHCD efficiency, compared to the ECCD effect, was dominant. In the X-mode experiment, there was clear difference of the plasma current in the co- and counter-steering cases, as shown in Fig.3, due to the ECCD effect on the coupling for the forward fast electrons in the energy range of 10-60keV[3]. The resonant energy range is consistent with that of the fast electrons generated by LHCD. In the off-axis ECCD experiment, the hollow profile of the hard X intensity increased by ECH/ECCD was observed. Developed antenna system has been successfully used for the ECH/ECCD experiments in the tokamak.

The other experiments on the side-band structure in the LH wave and this disruption control by using ECH/ECCD were also carried out. More than 15 members who are specialist in the field of the RF heating and current drive experiments joined to this collaboration program. The obtained experimental results were introduced and discussed at the 19th TRIAM Workshop that was held 4-5th October. At the workshop, experimental subjects and machine time schedule in the winter experimental campaign were also discussed.

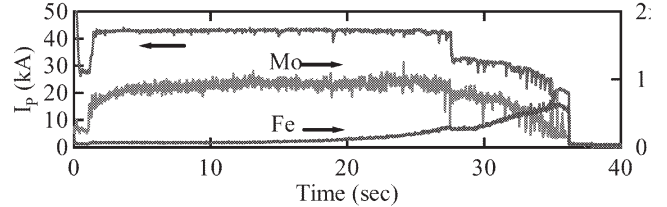


Fig. 1: Sustainment of eITB formation for 25 second in the ECD-mode LHCD plasma .

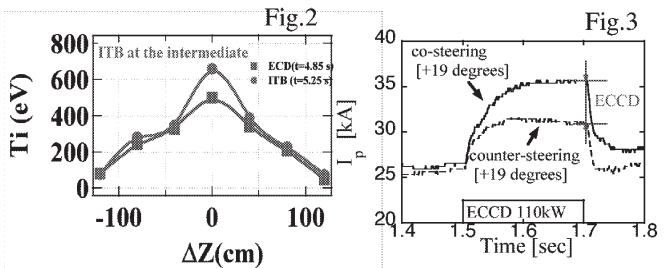


Fig. 2: Ion temperature profiles in the ECD-mode.

Fig. 3: Time evolution of plasma current in the co- and counter steering ECCD experiments.

References

- [1] K. Hanada et al., IAEA-CN-116-EX/P4-25(2004).
- [2] H. Zushi et al., IAEA-CN-116-OV/5-2(2004).
- [3] H. Idei et al., IAEA-CN-116-PD/1-2(2004).

§42. Modeling of Particle Balance in Steady State Plasma Confinement Device: TRIAM-1M

Hirooka, Y. (NIFS)
Zushi, H. (Kyushu Univ.)

Over the past two decades most of the “sub-critical, i.e., $Q < 1$ ” fusion experiments have been successfully conducted using large tokamaks such as TFTR and JET. Also, the construction site for ITER (for the International Thermonuclear Experimental Reactor), intended to exceed the energy breakeven, i.e., $Q = 1$, has recently been decided to be Cadarache. Although ITER is planned to be operated in the long pulse mode, the pulse duration is limited to ~ 500 seconds due to the OH capacity. Interestingly in this regard, recent operation experiences with the TRIAM-1M tokamak have demonstrated that it often takes hours of continuous plasma interactions for wall components to reach their respective thermal equilibria [2]. Therefore, one predicts that the ITER pulse length is not sufficiently long for all the in-vessel components to reach steady state temperatures, in which case gas recycling dynamics unavoidably affect edge characteristics, and hence the core plasma performance during the course of pulse discharge. Clearly, not all the technical issues associated with steady state operation will be resolved by the ITER program as it is planned.

Among these remaining issues, particle balance and its control are critical in achieving true steady state because they can affect the overall reactor performance significantly as to fuel economy and related on-site radiation safety, lifetime of the plasma-facing components and core plasma stability. Though it has not been addressed until now, well-regulated fusion power generation probably would require solomonic control over particle balance because local plasma behavior is not quite at steady state due to the facts that core fueling tends to be discontinuous, particularly if it is done by pellet injection, and edge energy bursts due to ELMs is generally high-frequency but not truly continuous, etc. Responses to these operation “kick-backs” from plasma-facing components are yet to be explored in ITER and fusion devices beyond it towards the end of the 21st century.

To understand the particle balance behavior in steady state devices, a zero-dimension, four-reservoir (core, SOL, gas, wall) particle balance model has been applied to analyze the data taken from TRIAM-1M with the emphasis on interpretation of the wall pumping effects observed in long-pulse limiter discharges heated by LHCD.

The particle balance model equations used are:

$$\frac{dN_{core}}{dt} = \frac{N_{core}}{\tau_{core}} + \alpha_1 \frac{\langle \sigma v \rangle_{cl}}{2V_{gs}} N_{gs} N_{SOL} - \alpha_2 \frac{\langle \sigma v \rangle_{cl}}{V_{gs}} N_{gs} N_{core} + \left(\frac{N_{SOL}}{\tau_{SOL}} + \alpha_1 \frac{\langle \sigma v \rangle_{cl}}{2V_{gs}} N_{gs} N_{SOL} + \alpha_2 \frac{\langle \sigma v \rangle_{cl}}{V_{gs}} N_{gs} N_{core} \right) (R_e^r f_{core} + R_f^{ref} f_{core}) + f_{core} \Phi_{ext} \quad (1)$$

$$\frac{dN_{SOL}}{dt} = \frac{N_{SOL}}{\tau_{SOL}} + \frac{N_{core}}{\tau_{core}} - \alpha_1 \frac{\langle \sigma v \rangle_{cl}}{V_{gs}} N_{gs} N_{SOL} + \beta \frac{\langle \sigma v \rangle_{cl}}{V_{SOL}} N_{gs} N_{SOL} + \left(\frac{N_{SOL}}{\tau_{SOL}} + \alpha_1 \frac{\langle \sigma v \rangle_{cl}}{2V_{gs}} N_{gs} N_{SOL} + \alpha_2 \frac{\langle \sigma v \rangle_{cl}}{V_{gs}} N_{gs} N_{core} \right) \{ R_e^r f_{SOL} + R_f (1 - f_{core}^{ref}) \} + f_{SOL} \Phi_{ext} \quad (2)$$

$$\frac{dN_{gs}}{dt} = -S_{pump} N_{gs} - \beta \frac{\langle \sigma v \rangle_{cl}}{V_{SOL}} N_{gs} N_{SOL} + \left(\frac{N_{SOL}}{\tau_{SOL}} + \alpha_1 \frac{\langle \sigma v \rangle_{cl}}{2V_{gs}} N_{gs} N_{SOL} + \alpha_2 \frac{\langle \sigma v \rangle_{cl}}{V_{gs}} N_{gs} N_{core} \right) (R_e^r (1 - f_{SOL} - f_{core}^{ref}) - \gamma(Y_{spu} \frac{N_{SOL}}{\tau_{SOL}} + Y_{spu-1} \alpha_1 \frac{\langle \sigma v \rangle_{cl}}{2V_{gs}} N_{gs} N_{SOL} + Y_{spu-2} \alpha_2 \frac{\langle \sigma v \rangle_{cl}}{V_{gs}} N_{gs} N_{core})) + (1 - f_{core} - f_{SOL}) \Phi_{ext} \quad (3)$$

$$\frac{dN_{wall}}{dt} = \left(\frac{N_{SOL}}{\tau_{SOL}} + \alpha_1 \frac{\langle \sigma v \rangle_{cl}}{2V_{gs}} N_{gs} N_{SOL} + \alpha_2 \frac{\langle \sigma v \rangle_{cl}}{V_{gs}} N_{gs} N_{core} \right) (1 - R_e - R_f) + \gamma(Y_{spu} \frac{N_{SOL}}{\tau_{SOL}} + Y_{spu-1} \alpha_1 \frac{\langle \sigma v \rangle_{cl}}{2V_{gs}} N_{gs} N_{SOL} + Y_{spu-2} \alpha_2 \frac{\langle \sigma v \rangle_{cl}}{V_{gs}} N_{gs} N_{core}) \quad (4)$$

,where N_{core} , N_{SOL} , N_{gs} , N_{wall} are the particle inventories in the core, SOL, gas, and wall, respectively, α_1 , α_2 , β , are adjusting parameters to express degrees of separation between the SOL and gas regions. All other symbols have their usual meanings. Results obtained are shown in Fig. 1, showing reasonably good agreement between the experimental data and model predictions.

The next step is to apply this particle balance model to analyze the data taken from experiments in which some of the wall components are acting as neutral gas sources due to the thermal degassing effect in addition to the usual gas-puff fueling.

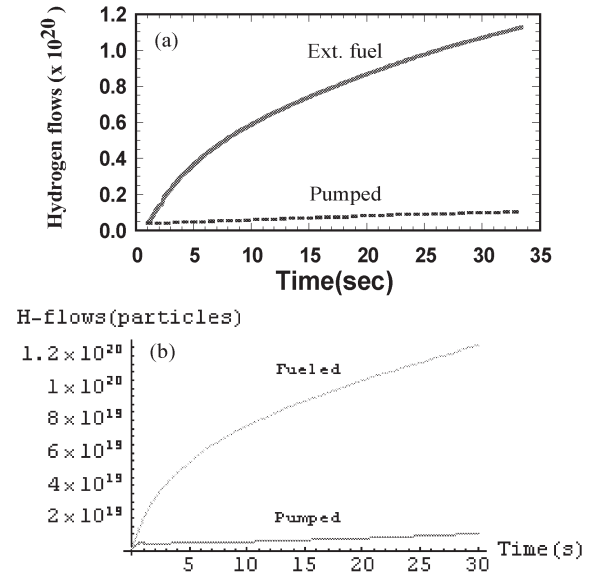


Fig. 1 A comparison between the experimental data (a) and model predictions (b) for the particles gain by external fueling and the loss due to active pumping.

§43. Measurement of Two Dimensional Image of Hard X-ray in TRIAM-1M

Ida, K., Kobuchi, T., Zushi, H. (Kyushu Univ.),
Hanada, K. (Kyushu Univ.)

In tokamak, the lower hybrid current drive (LHCD) is useful tool to realize a long pulse discharge and also control toroidal current profiles to stabilize MHD instabilities and hence to improve plasma confinements. The current profile can be estimated from the radial profile of the hard X-ray radiated from the fast electrons carrying the toroidal current. The radial profile of X-ray is measured with hard X-ray CCD camera installed in the tangential port. Before installing the X-ray CCD camera into TRIAM-1M, the X-ray CCD camera system has been installed in CHS to test the possibility to measure the toroidal current profile.

Figure 1 shows the experimental setup for X-ray CCD camera system installed in CHS. The flux of hard x-rays can be adjusted by changing the size of the pinhole (0.03mm, 0.1mm and 0.3mm). The pinhole disks are made of tungsten and the thickness is 0.5mm. A 12-mm-thick tantalum mask with V-shape hole is installed in front of the pinhole disk to prevent x-rays above 30keV. A carbon collar is mounted between the pinhole and filter disk to avoid the reflection of visible light from the plasma through the pinhole.

Between the pinhole and the CCD detector, a rotating filter disk is arranged and six Be filters, with different thicknesses of 10 μ m, 30 μ m, 70 μ m, 140 μ m, 300 μ m and 800 μ m, respectively, are mounted on the disk. The x-ray flux is adjusted to a level good for photon counting mode by choosing appropriate combinations of pinhole and Be filter. The hard x-ray CCD camera used in this diagnostic is a Princeton Instruments SX-TE/CCD-1024SB with a TEK 1024x1024D frame transfer back illumination CCD detector. Since half of the pixels are devoted to storage area, the imaging area has 1024x512 pixels. Each pixel of the CCD detector is fabricated on special silicon with a size of 24 μ m x 24 μ m. The readout noise is 32 electrons for 100kHz ADC. The resolution of the ADC is 5 electrons/ADC-count and the dark current is only 5-10 electron/pixel second at the cooling temperature of -40°C using multistage Peltier devices.

Figure 2 shows the spectrum of Ti K α (4.76keV), Cr K α (5.46-5.71keV) and Fe K α (6.54-6.70keV) in the X-ray range emitted from the plasma, respectively measured with X-ray CCD detector. The energy resolution of the hard X-ray camera is good enough to distinguish the line radiation of impurities in the plasma and continuum contribution emitted from the fast electrons carrying current. As seen in Fig.3, the energy spectrum can be measured up to 20 keV

According to the results of test of the X-ray CCD camera system in CHS, the current density profile of the plasma driven by LHCD in TRIAM-1M is expected to be measured from the hard X-ray emission using the X-ray CCD camera system.

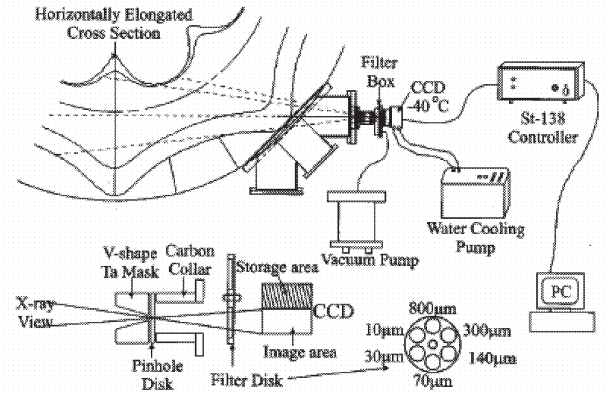


Fig.1 Top view of experimental setup for X-ray CCD camera system in CHS.

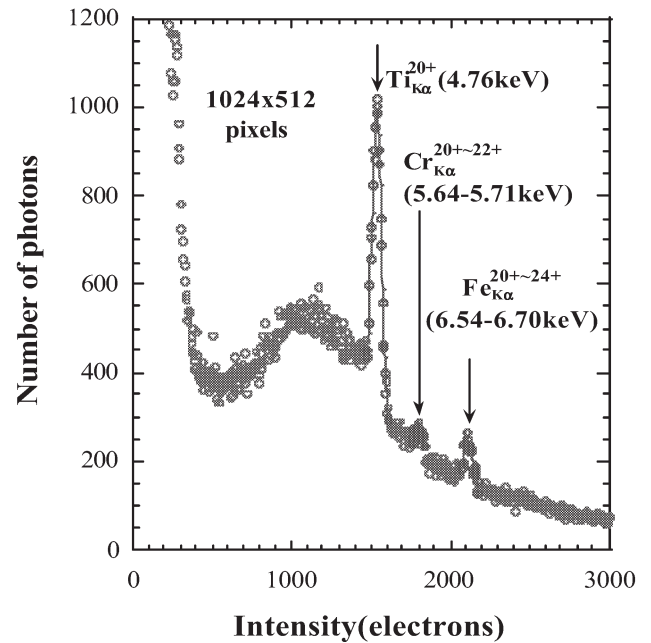


Fig. 2. Energy spectrum of X-ray emitted from the CHS plasma measured with the X-ray CCD camera system.

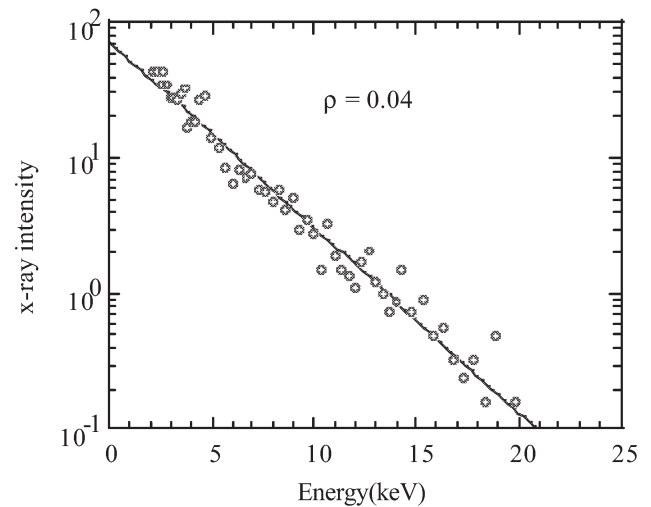


Fig. 3. Energy spectra of hard X-ray measured in CHS plasma with the X-ray CCD camera system.

§44. Integration of PWI Experiments, Diagnostics, Simulation and Modeling in Steady State Plasma

Sakamoto, M. (RIAM, Kyushu Univ.) on behalf of collaborators

Understanding of the global wall recycling is one of the most critical issues from the viewpoints of density control and tritium inventory for the steady state operation of the fusion plasma. It is necessary to investigate comprehensively from macroscopic and microscopic viewpoints. In this study, we have utilized the superconducting tokamak TRIAM-1M, in which a long pulse operation can be carried out, as a platform of the study under Interactive Coordinated Researches of NIFS.

In this year, we carried out the plasma experiments for nine weeks. Many collaborators joined the experiments and multi-directional studies could be promoted. As the macroscopic approach, the following measurements have been carried out; the recycling structure of the long duration discharges with profile measurements of H_α intensity, DEGAS simulation, spectroscopic measurement of the boundary plasma, Langmuir probe measurement of the scrape of layer (SOL), heat load profile on the plasma facing components, global particle balance and development of the particle balance modelling including the change in the wall temperature [1-10]. As the microscopic approach, the following measurements have been carried out; analysis of the radiation damage process using the surface probe system, analysis of the structure of the deposition layer, quantitative estimation of the retention inside the deposits, real time measurement of the growth of the deposition layer using the optical method and dust measurement [11,12].

The co-deposition is a key for the understanding of the global wall recycling from the macroscopic and microscopic points of view as shown in Fig.1. The surface probe experiments have revealed that the deposit on the plasma facing side (P-side) consists of fine grains of which diameter is $\sim 1\text{nm}$ and it has no distinct structure, and the deposit on the electron drift side (E-side) is bcc polycrystalline of a lattice constant 0.31nm . Mo deposition rates on the P-side and the E-side of the material probe are $6.4 \times 10^{16} \text{ Mo atoms m}^{-2} \text{ s}^{-1}$ and $3.9 \times 10^{17} \text{ Mo atoms m}^{-2} \text{ s}^{-1}$, respectively. The wall pumping rate which is evaluated from the hydrogen retention of the Mo deposit and the discharge duration is $6.4 \times 10^{15} \text{ H atoms m}^{-2} \text{ s}^{-1}$ for the P-side and $1.3 \times 10^{16} \text{ H atoms m}^{-2} \text{ s}^{-1}$ for the E-side. These values are consistent with the wall pumping rate ($8.6 \times 10^{16} \text{ H atoms m}^{-2} \text{ s}^{-1}$) which is evaluated from the global particle balance inside the vacuum chamber.

The influence of the local structure of the first wall on the global wall recycling has been studied using the ML with good cooling capability. No wall saturation was observed in the 5 h 16 min discharge with the ML, since particle release was suppressed by less temperature rise of the main chamber. The global wall pumping rate without

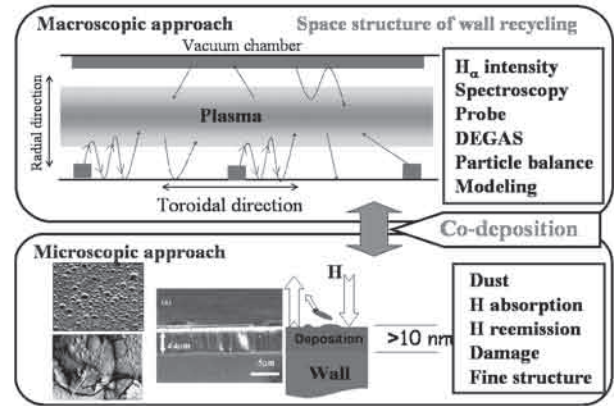


Fig. 1 Schematic diagram of a strategy of the wall recycling study. It is important to understand the multi-scale phenomena.

the ML, $\sim 8.6 \times 10^{16} \text{ atoms m}^{-2} \text{ s}^{-1}$, is 3.6 times higher than that of the long duration discharge without the ML. The temperature rise in the wall is attributed to the transition of the wall role from the particle sink to the source. The co-deposition of hydrogen with Mo is a key for the wall role of the particle sink. No clear difference of the growth rate of Mo deposits on the viewing window located from the limiter surface between with and without the ML. The growth rate is from $\sim 2 \times 10^{-4} \text{ nm/s}$ to $\sim 8 \times 10^{-4} \text{ nm/s}$. The toroidal structure of hydrogen recycling changes significantly near at the ML. The characteristic length of localization of the neutral particles, which are produced due to the plasma-wall interaction, is about 30 cm. It is consistent with the result of the DEGAS simulation [4]. Integration of H_α intensity with and without the ML over the whole toroidal length is the same within 3%, which is less than the error, i.e. 15%.

Reference

- 1) Zushi, H. et al., Proc. of Fusion Energy Conference (Vilamoura, 2004) OV/5-2.
- 2) Sakamoto, M. et al., Proc. of Fusion Energy Conference (Vilamoura, 2004) EX/P5-30.
- 3) Sakamoto, M. et al., Proc. of conference on JSPF (2004) 23aA30P.
- 4) Higashizono, Y. et al., Proc. of conference on JSPF (2004) 23aA31P.
- 5) Nakashima, K. et al., Proc. of conference on JSPF (2004) 23aA32P.
- 6) Sakamoto, M. Proc. of PSS-2005/SPP-22 (2005) S4-4.
- 7) Ogawa, M. et al., Proc. of PSS-2005/SPP-22 (2005) P3-101.
- 8) Nakashima, K. et al., Proc. of 60th conference on JSP (2005) 25aXB-11.
- 9) Zushi, H. et al., Proc. of 60th conference on JSP (2005) 25aXB-12.
- 10) Uehara, K. et al., Proc. of 60th conference on JSP (2005) 27aXB-1.
- 11) Miyamoto, M. et al., Proc. of conference on JSPF (2004) 23aB06P.
- 12) Miyamoto, M. et al., J. Nucl. Mater. 337-339 (2005) 436.

13. Research Information Office

1. Introduction

Research Information Office was established in October 2004 by enlarging functions of "Research Information Center". Its mission is to construct the database system of the research activity that must be useful for improving the quality of education and research at NIFS. Another important role is to report the newest research outputs by publishing the annual report and series of NIFS Report.

2. Research activity database

The purposes of the research activity database are to (1) help improve and individualize the quality of education and research at NIFS, (2) help reduce the administrative burden of evaluations, and (3) help the researchers reduce the amount of work for reporting their results.

The database of research activity is indispensable for the evaluation of the mid-term plan. The evaluation database will consist of the research activity database and the administrative database. The latter database includes organization, joint researches, education, students, human affairs, facilities, equipment, and so on that are managed by the administrative office. The research activity database will include mainly the individual research results that are known by the researchers themselves, as shown in table 1.

The relational database management system (DBMS) that can use standard retrieval language (SQL) is adopted for the NIFS research activity database. PostgreSQL is selected as the database application, and it works on Linux. Individual's information is updated by Web input. The access to the database is limited by an individual account and the password. The data of a domestic and foreign joint research will be managed uniformly in this database system including the acceptance. The procedure of application for paper submission will be integrated in this system including the paper submission system of the LHD group. Furthermore, co-authors will be identified for evaluation of the joint research. As a rule, the data is opening in the place to the public. It needs the approval the evaluation committee at NIFS to edit of the data and to disclose the edited data to the outside.

As the first stage, we are working on the construction of the publication database that will be compatible with the ReaD database and a university information database of the National Institution for Academic Degrees and University Evaluation (NIAD-UE).

ReaD is database service managed by Japan Science and Technology Agency (JST) due to promote cooperation among industry, academia, and government. ReaD provides scientific information on research institutes, researchers, research projects, and research resources in Japan.

NIAD-UE was established based on the Law concerning the General Rules of Independent Administrative Institutions and the National Institution for Academic Degrees and University Evaluation Law. The institution's mission is to contribute to further development

of higher education in Japan. In order to raise the quality of education and research, NIAD-UE conducts evaluations of teaching conditions and research activities at higher education institutions (universities, junior colleges and colleges of technology) and inter-university research institutes. NIAD-UE is currently proceeding with specific steps for creation of a university information database that not only helps improve the quality of education and research and reduce the administrative burden of the evaluations but also responds to the international context of higher education quality assurance. The database is expected to be an information source that helps improve international society's understanding of the education and research activities at higher education institutions in Japan.

Table 1 Items of the research activity database.

1. Name
2. Affiliation
3. Belonging academic society
4. Class at universities
5. Publication (book, paper, proceedings, etc.)
6. Patent
7. Prize
8. Conference presentation
9. Conference management
10. Activities at outside committee
11. Public lecture, exhibition, and visitor receipt
12. Press release
13. Other social activity

3. Publication of NIFS reports

Publication of the annual report and series of NIFS Report is also important task of the Research Information Office. The number of publication from April 2004 to March 2005 is shown in Table 2 with the past total. The office also collects laboratory reports and other literatures concerning to nuclear fusion and related fields. Total number of collected reports in this fiscal year was about 600, and approximately 35,100 reports have been collected so far.

Table 2 Number of Published NIFS Reports

	FY 1989-2003	FY 2004	TOTAL
NIFS	796	13	809
NIFS-DATA	84	8	92
NIFS-TECH	11	1	12
NIFS-PROC	54	5	59
NIFS-MEMO	45	0	45
Annual Report	15	1	16

(Imagawa, S.)

III. International Collaboration

The international collaboration is one of the four major activities of the institute. The collaboration covers multilateral institutional ones, bilateral ones, other governmental or inter-institutional agreements and personal exchanges. They are mostly supported by Grant-in-Aid of Scientific Research of Ministry of Education, Culture, Sports, Science and Technology (MEXT), or JSPS (Japan Society for Promotion of Science) program. A detailed description of activities is given in the following tables. The multilateral collaborations are those under the US-Japan Fusion Cooperation Program, the IEA TEXTOR Collaboration and IEA Stellarator Agreement. In order to promote scientific exchanges between NIFS and foreign leading institutes, the following agreements on academic exchange and cooperation shown in Table 1 have been

signed up. Grant-in Aid for International Scientific Research programs and individual travel grants for participating overseas international symposia (both being supported by MEXT) have effectively functioned to promote international activities of NIFS (shown in Table 2). List of guest professors (supported by MEXT), who stayed for more than three months, and research fellows (JSPS research fellowship) are listed in Tables 3 and 4, respectively. The 14th International Toki Conference on Plasma Physics and Controlled Nuclear Controlled Fusion was held in October 2004, NIFS being as the host institute. Statistics of visitors and visit by NIFS staff in FY 2004 are as follows; foreign scientists from 24 countries visited NIFS 167 person-times and NIFS staff went abroad 199 person-times (to more than 12 countries).

(Matsuoka, K.)

Table 1. List of Academic Exchange and Cooperation Agreement with NIFS

<i>Organization</i>	<i>Country</i>	<i>Effective from</i>
UCLA, Plasma and Fusion C.	USA	3 July '90
Institute of Plasma Physics, Academia Sinica	China	27 June '92
Max-Planck Institute for Plasmaphysics	Germany	11 May '93
Kurchatov Institute of Nuclear Fusion	Russia	15 May '93
Kharkov Institute of Physics and Technology	Ukraine	7 Oct. '94
The Australian National University	Australia	8 May '95
Korea Basic Science Institute	Korea	6 March '96

Table 2. Joint Study by Grant-in-Aid for Scientific Research in FY 2004

<i>Research subject</i>	
Advanced Physics and Technology for Steady-state Fusion Reactor	Director-General O. Motojima

Table 3 List of guest professors in FY 2004

<i>Name</i>	<i>Organization</i>	<i>Country</i>	<i>Term</i>
Dolan Thomas James	Idaho National Engineering & Environmental Laboratory	USA	6 Oct.'03 ~ 30 Apr.'04
Chutov Yuri Ivanovich	Taras Shevchenko Kiev University	Ukraine	9 Jan.'04 ~ 14 Apr.'04
Horacek Jiri	Institute of Theoretical Physics, Charles University Prague	Czech	10 Jan.'04 ~ 10 Apr.'04
Vyacheslavov Leonid Nikolaevich	Budker Institute of Nuclear Physics	Russia	12 Jan.'04 ~ 12 May.'04 10 Jan.'05 ~ 10 May.'05
Vranjes Jovo	Center for Plasma Astrophysics	Bosnia and Herzegovina	2 Mar.'04 ~ 1 Jun.'04
Gao Zhe.	Tsinghua University	China	13 Apr.'04 ~ 16 Jul.'04
Hameiri Eliezer	New York University	USA	2 Jun.'04 ~ 2 Sep.'04
Ralchenko Yuri	Maryland University, College Park	Israel	24 Jul.'04 ~ 24 Oct.'04
Yeliseyeva Olha	Karpenko Physico-Mechanical Institute, National Academy of Science Ukraine	Ukraine	2 Aug.'04 ~ 2 Nov.'04
Eckstein Wolfgang	Max-Planck Institute for Plasmaphysics	Germany	26 Aug.'04 ~ 2 Dec.'04
Chu Ming-Sheng	General Atomics	USA	1 Sep.'04 ~ 30 Nov.'04
Yu Wei	Shanghai Institute of Optics and Fine Mechanism	China	1 Sep.'04 ~ 28 Dec.'04
Kleiber Ralf Armin	Max-Planck Institute for Plasmaphysics	Germany	3 Sep.'04 ~ 6 Dec.'04
Rhee Yong-Joo	Korea Atomic Energy Research Institute	Korea	1 Oct.'04 ~ 31 Dec.'04
Livshits Alexander Iosifovich	Bonch-Bruевич University of Electrotechnical Communications	Russia	1 Dec.'04 ~ 31 Mar.'05
Kharchev Nikolay Konstantinovich	General Physics Institute of Russian Academy of Science	Russia	1 Dec.'04 ~ 28 Feb.'05
Weller Arthur	Max-Planck Institute for Plasmaphysics	Germany	5 Jan.'05 ~ 4 Apr.'05
Tshakaya David	Institute of Theoretical Physics, University of Innsbruck	Georgia	6 Jan.'05 ~ 15 Apr.'05
Neudatchin Sergei	Russian Research Center "Kurchatov Institute"	Russia	12 Jan.'05 ~ 15 Apr.'05

Table 4 List of JSPS invited fellows for NIFS in FY 2004

○Postdoctoral Fellowships for Foreign Researchers

<i>Name</i>	<i>Organization</i>	<i>Country</i>	<i>Term</i>
Pavlichenko Rostyslav Olegovich	Fukui University	Ukraine	1 Apr.'03 ~ 31 Mar.'05

○Invitation Fellowship Programs for Research in Japan

<i>Name</i>	<i>Organization</i>	<i>Country</i>	<i>Term</i>
McCormick Kent Gerald	Max-Planck Institute for Plasmaphysics	Germany	17 Nov.'04 ~ 3 Dec.'04

1. US - Japan (Universities) Fusion Cooperation Program

The recent most important subject for the fusion world is the decision about the ITER project. Among parties: Japan, Europe, USA, Russia, China and Korea, the site for ITER is decided as Cadarache, France.

In Japan, since NIFS became a member of "Inter-University Research Institute, National Institutes of Natural Sciences" on April 1st, 2004, the new organization of the LHD experimental groups adequate for the experimental phase started, and the LHD experiments were carried out quite successfully together with collaborators from Universities, JAERI and the international institutions.

One of the main activities of the Japanese university researchers participating in the US-Japan collaboration is the research in the national spherical torus experiment (NSTX) in Princeton University, while many US researchers participated in the LHD experiments just as in the last year.

Fusion Physics Planning Committee (FPPC)

In the FPPC, out of 71 exchanges 45 were completed. This completion rate is almost the same as in the previous year. The workshops were successfully held, and the exchanges continue to be productive and beneficial to both sides. The annual meeting of the FPPC was held by a televideo communication on March 4, 2005. Participants were from Universities, NIFS, JAERI, and DOE to summarize the 2004 activity and formulate the 2005 activity.

Joint Institute for Fusion Theory (JIFT)

Almost all of the activities in the three categories - workshops, personal exchanges, and joint computational projects were carried

out during the past year, although more U.S. scientists are encouraged to visit Japan.

All four workshops were successfully held, in addition to the JIFT Steering Committee meeting. In the category of personal exchanges, three Visiting Professors (one more than the usual number) and six Visiting Scientists made exchange visits, while two other exchange visits were deferred. The JIFT joint computational projects were also active.

Fusion Technology Planning Committee

The US/Japan collaboration on fusion technology completed another productive and successful year in JFuY 2004. Of the 39 planned cooperative items related to the two Annexes, 28 were completed as follows: 2 committee meetings, 18 participations, and 8 workshops/technical meetings including 7 JUPITER-II workshops. Of the 22 planned cooperative items related to the general technology joint planning categories, 16 were completed as follows: 9 workshops/technical meetings and 7 participations. Activities of the 4th year of the JUPITER-II collaboration are developing. Programs are subdivided to 9 tasks and significant results have been obtained.

The 23rd Executive Secretary Meeting (ESM) was held by a televideo communication on April 14, 2005. It was noted that both sides have developed a significant and mutually valuable collaboration involving all technical elements of the fusion energy sciences program.

General Secretary for US-Japan
Collaboration Planning Committee
Shigeru Sudo

STATISTICAL REVIEW OF FUY 2004 EXCHANGE PROGRAM (NIFS)

Grand Total

		US → J	J → US	Total
Proposed	Man	113	165	278
	Item	46	80	126
Performed	Man	91	141	232
	Item	31	65	96

Personnal Exchange Program

(Including Overall Planning)

		US → J	J → US	Total
Proposed	Man	0	1	1
	Item	0	1	1
Performed	Man	0	1	1
	Item	0	1	1

Fusion Technology

(1) Superconducting Magnets

		US → J	J → US	Total
Proposed	Man	0	4	4
	Item	0	1	1
Performed	Man	0	4	4
	Item	0	1	1

(2) Structural Materials

		US → J	J → US	Total
Proposed	Man	1	7	8
	Item	1	2	3
Performed	Man	1	7	8
	Item	1	2	3

(3) Plasma Heating Related Technologies

		US → J	J → US	Total
Proposed	Man	2	7	9
	Item	2	2	4
Performed	Man	0	0	0
	Item	0	0	0

(4) Blankets

		US → J	J → US	Total
Proposed	Man	0	5	5
	Item	0	1	1
Performed	Man	0	5	5
	Item	0	1	1

(5) In-Vessel/High Flux Materials and Components

		US → J	J → US	Total
Proposed	Man	11	0	11
	Item	4	0	4
Performed	Man	9	0	9
	Item	2	0	2

(6) Others

		US → J	J → US	Total
Proposed	Man	4	1	5
	Item	1	1	2
Performed	Man	4	1	5
	Item	1	1	2

Fusion Physics

(1) Planning

		US → J	J → US	Total
Proposed	Man	3	0	3
	Item	1	0	1
Performed	Man	3	0	3
	Item	1	0	1

(2) Plasma Core Phenomena

		US → J	J → US	Total
Proposed	Man	17	8	25
	Item	6	5	11
Performed	Man	14	8	22
	Item	4	5	9

(3) Plasma Edge Behavior and Control

		US → J	J → US	Total
Proposed	Man	5	7	12
	Item	1	4	5
Performed	Man	0	7	7
	Item	0	4	4

(4) Heating and Current Drive

		US → J	J → US	Total
Proposed	Man	7	3	10
	Item	2	3	5
Performed	Man	7	3	10
	Item	2	3	5

(5) New Approach and Diagnostics

		US → J	J → US	Total
Proposed	Man	32	56	88
	Item	15	24	39
Performed	Man	25	48	73
	Item	10	20	30

Joint Institute of Fusion Theory

		US → J	J → US	Total
Proposed	Man	14	19	33
	Item	6	10	16
Performed	Man	13	18	31
	Item	5	9	14

DOE/MEXT Materials (Annex I)

		US → J	J → US	Total
Proposed	Man	17	47	64
	Item	7	26	33
Performed	Man	15	39	54
	Item	5	18	23

(Sudo, S.)

2. TEXTOR Collaboration

In collaboration experiments with Dynamic Ergodic Divertor (DED), modified schemes with $m/n=3/1$, $12/4$ were mainly applied. Either static modification and dynamic application were investigated. It has been found that a toroidal rotation is excited by a rotational DED field with $m/n=3/1$, but that the rotational direction is opposite to the applied field rotation. With a tangential X-ray camera, $m=2$ fluctuations have been observed above a certain threshold coil current. An experiment on AE excitation with utilizing the DED coils is proposed from Japan and a preliminary experiment has been carried out. All the activities in this fiscal year are summarized in the following table. Highlights in some of individual programs are described in this report.

PSI studies related with test limiters

Pure W and K doped W were exposed to TEXTOR edge plasma to examine whether blistering takes place or not. Sample temperature was carefully controlled less than 500 deg. C, in which blistering was observed in ion beam experiments. The samples were exposed to 12 OH shots and 8 NBI shots. Total fluence was an order of 10^{24} m^{-2} ,

enough fluence for blistering to appear in ion beam experiments. But no blistering was observed.

In the previous W and Ta twin limiter experiments, carbon deposition pattern was different between Ta and W. But in this case, W and Ta sides were not exposed in the same edge plasmas, so the experimental results were unreliable. In 2004, W and Ta were placed on the same side of a graphite roof limiter to expose the same plasma. After exposure to 12 OH shots and 8 NBI shots, different carbon deposition pattern was observed. Detailed analysis is in progress.

In the CVD-W limiter and ferrite limiter experiments last year, surface melting took place. The detailed observation of solidified layers and discussion on possible mechanism to dominate melt layer motion were performed.

The erosion and deposition patterns on W and Ta test limiters exposed to the TEXTOR deuterium plasma containing a small amount of C impurity are simulated with the modified EDDY code. The EDDY code was modified to be able to simulate erosion and deposition pattern under actual test limiter conditions. In addition,

Japanese Participation in 2004 – 2005

Subjects	Participants	Term	Key Persons <i>etc.</i>
1. PSI studies with test limiters	T. Tanabe (Nagoya Univ.) Y. Ueda (Osaka Univ.) Y. Sakawa (Nagoya Univ.)	04. 9. 11 - 9. 25 04. 11. 28 - 12. 5 04. 11. 29 - 12.22	T. Tanabe / V. Philipps
2. Tangential X-ray Camera	S. Ohdachi (NIFS) S. Ohdachi (NIFS) K. Toi	04. 6.23 - 7.3 05. 3.14 - 3.20 05. 3.14 - 3.20	K. Toi / G. Fuchs
3. Tritium Measurement	M. Matsuyama (Toyama Univ.)	04. 9.11 – 9.19	M. Matsuyama /V. Philipps (visit to F. Z. Karlsruhe)
4. Helicon-wave plasma production, DED experiments	T. Shoji (Nagoya Univ.) T. Shoji (Nagoya Univ.) M. Okamoto (Nagoya Univ.)	04. 6. 6- 6. 21 05. 1.6 - 1.9 05. 3. 14 - 3. 22	T. Shoji / K. H. Finken
5. Millimeter-Wave Imaging			A. Mase/ A. J. H. Donne
6. H recycling	M. Sakamoto (Kyushu Univ.)	05. 2.27 - 3. 6	
7. Edge Plasma Diagnostics	A. Tsushima (Yokohama National Univ.)	05. 1. 15 - 1. 24	A. Tsushima / S. Jachmich
8. He measurement in LHD	M. Lehnen (IPP, FZJ) B. Hiller (IPP, FZJ)	04.11.7 - 11.20 (visit to NIFS)	H. Funaba/M. Lehnen
9. PSI with ferritic steel	K. Tsuzuki (JAERI)		Joint work with item 1 (Key person from JAERI Y. Kusama)

ionization and dissociation processes of hydrocarbon molecules other than methane were included in the codes. similar to the observation in surface measurements. In the erosion zone, the re-deposited C forms a W (Ta)-C mixed layer with small C concentration. Assumptions for chemical erosion yields of 0.01 for W and <0.005 for Ta fit the calculated widths of the deposition zone to the experimentally determined values. Possible reasons for the difference between W and Ta are discussed.

X-Ray Tangential Camera

In order to study the images, e.g., those obtained at DED experiments, tomographic reconstruction codes have been developed. From one tangential view of the plasma, it is not possible to reconstruct a three-dimensional (3D) radiation profile. Assuming that radiation along the magnetic field lines is constant, reconstruction of a two-dimensional (2D) profile on a poloidal plane is tried. First, video image is decomposed to one stationary component and fluctuating components using singular value decomposition method. Then, equilibrium magnetic field is determined by the stationary image; we select an equilibrium by which the best reconstruction can be made. Using this equilibrium magnetic field, the lines of sights are interpreted as the curved lines on the target poloidal plane. Thereby, 3D-reconstruction problem is reduced to the well-known 2D problem. The standard techniques widely used in solving 2D reconstruction are used. A successful reconstruction has been made with 2D images on a poloidal plane. This code using flux coordinate I is extended so that use in the 3D equilibrium field of the Large Helical Device is possible.

After the measurement on the TEXTOR tokamak on 2003, the camera system was moved to Japan and mounted on the LHD again with refinements. The fast framing video camera (KODAK 4540MX) was replaced with a new one (Vision Research: PhantomV7.0). About 10bit of the dynamic range is expected now. Time for the data transfer is reduced to 5 min. (Data every two discharges in the LHD are taken). With improved dynamic range, images at the minor internal disruption events have been obtained when the local magnetic shear reduced in the 8th experimental campaign. Pre/post cursors having $m=1,2,3$ structures are observed. Comparing the events to the off-axis sawtooth in tokamak devices is now going on.

Application of the BIXS system to ITER

To evaluate the amount and depth profile of tritium retained in plasma-facing materials (PFMs) of ITER that accompanies the strong radiation fields, the applicability of BIXS was examined using γ -emitters and carbon tiles contaminated with tritium. Measurements of the tiles with a γ -emitter showed that the presence of the γ -field has no influence in the shape of the β -ray-induced X-ray spectra, although the whole intensity was dependent on radioactivity of a γ -emitter. To simulate more accurately the in-vessel environment of PFMs, one of the carbon tiles having still its metallic part activated by DT fusion experiments in JET was

subjected to BIXS measurements. Although the increase in a radiation level due to the Compton effects appeared in the spectrum, there was not any significant effect on the shape of a spectrum. The effects of such radiations from PFMs can be basically reduced shielding a detector with lead materials and/or decreasing the thickness of a detector element. It was concluded, therefore, that BIXS is applicable for *in-situ* measurements of tritium retention by PFMs with a simple shielding of the X-ray detector even in presence of strong X- and γ -fields.

Other Collaborations

The system of superimposing RF current (50kHz-1MHz, <2A) on DED coil (12/4 mode) is installed and tested. Impedance measurement system on DED coil are installed and tested. Perform the calibration of RF voltage and current detectors and analyse the frequency spectrum in vacuum. Measure the change in the spectrum of RF voltage and current for few NBI heated plasma shots. Calculate the DED coil impedance spectrum for AEs excitations.

The experiment of ECE imaging (ECEI) is in progress. Notch filter with rejection frequency of 140 GHz has been designed at UC Davis (UCD), and fabricated using electro fine forming (EF2) technique in Kyushu Hitachi Maxell, Ltd. The rejection of -32.5 dB at $f=140$ GHz and less than 1 dB transmission loss at the pass band are obtained, which are better than those values fabricated by conventional etching process. The filter has been attached to the microwave imaging reflectometer (MIR) system in TEXTOR-94 tokamak operated by UCD-PPPL and FOM group. Simulation study of microwave imaging reflectometry has been performed. The numerical model consists of analytical and FDTD (Finite-Difference Time-Domain) solution of 2D Maxwell's equations. Tests of the imaging concept for the case of tokamak have shown its feasibility and high potential to visualize the long-scale turbulence of tokamak plasmas. Both conventional and imaging reflectometers can measure small amplitude fluctuations (up to $\delta n/n=4\%$). But only large aperture MIR system can measure density fluctuations with larger amplitude ($\delta n/n\sim 7\%$).

Penning type gauges have been applied to LHD for helium partial pressure measurement as a collaboration work. The penning gauge spectroscopy was operated during the main discharges of LHD. The visible light from 580 to 730nm was observed. The optical alignment was carried out by using the glow discharge. Temporal development of the line intensity of H and HeI (668nm) was obtained. The time resolution was 250ms, which is dependent on the integration time of the CCD camera. The line intensity showed similar behavior of the neutral pressure which was measured by the fast ion gauge located at the 7.5U port. The ratio of the HeI intensity to the H intensity was evaluated. It showed different value during and after the main discharge.

(Noda, N.)

3. International Collaboration on Helical Fusion Research — IEA Stellarator Agreement —

1. Background and overview

Since 1985 the world stellarator research community has been continuing to promote international collaborations under the IEA Implementing Agreement referred to as “Cooperation in Development of the Stellarator Concept”. Based on the approval by the FPCC, this agreement has been extended for the next five years till July 2005, and will be extended for a further five years until July 2010. Participating countries in this agreement are Japan, U.S.A., Australia, Germany, Spain, Ukraine, and Russia.

In order to discuss technical and administrative issues associated with the collaborations, the Stellarator Executive Committee was put together in 1985 under the IEA implementing agreement and has been playing the key role in the world stellarator research community. The first Chairman of the committee was Dr. G. Greiger, former Director of IPP-Garching. Prof. A. Iiyoshi of Chubu Univ. served as the second Chairman from 1998 to 2004. In 2004, Dr. C. Alejandre of CIEMAT in Spain took over from Prof. Iiyoshi as the third Chairman, and at the same time, Prof. O. Motojima, Director General of NIFS, became the vice-Chairman of the committee.

The Stellarator Executive Committee meeting was held on November 2nd, 2004, during the 20th IAEA Fusion Energy Conference in Vilamoura, Portugal. The next meeting will be held in conjunction with the 15th International Stellarator Workshop in Madrid, Spain, in October 3rd – 7th, 2005.

Prof. O. Motojima presented the 2004 summary talk on the international stellarator collaborations at the FPCC annual meeting held in Paris in March 2005. This summary includes the contents to be described in the following sections.

2. Japan

2-1. LHD team at NIFS.

The main goal of this year's campaign (Sept. 2004-Jan. 2005) is to achieve long pulsed discharges with temperature greater than 1 keV. In December 2004, a steady-state plasma was successfully sustained for 31 min and 45 sec. The average input power was 680 kW (ICRF [38.47MHz] 520 kW, ECH 100 kW and NBI60 kW). The central temperature was around 2 keV and the line-averaged density was around $0.7\sim0.8 \times 10^{19} \text{ m}^{-3}$. Before the 2003 campaign, the plasma duration time of the ICRF long-pulse experiment was limited by local temperature rises of the diverter carbon plates near the

ICRF antenna section, and gradual increase of out-gassing from the wall finally terminated the plasma operation. Since then, the new mechanical structure and new carbon material sheets were added to suppress the temperature rise and the out-gassing rate. The hardware of ICRF heating was also improved. The LHD vacuum chamber was conditioned by boronization, which seemed to be effective in suppressing the impurity influx to low levels during steady-state operations. The long-duration operation was made possible by introducing swing technique for the magnetic axis position around 3.6 m and 3.7 m for diversing the heat loads.

In the LHD discharges, it is difficult to maintain the detached plasma state. The plasma either becomes attached or shrinks and subsequently collapses. Under the certain conditions with $R_{ax} = 3.65\text{m}$, however, detached state of the plasma is triggered by massive gas puff and maintained for 2 seconds.

Attempts to achieve higher beta plasma have been made. Capability to change the current center of the helical coil, the effective coil pitch allows us to change the minor radius and the iota profile. We find that the optimum coil pitch for high beta is around 1.2. (1.254 for the standard configuration). With increasing beta, the mode number ratio (n/m) of the observed magnetic fluctuation mode with highest amplitude increases.

The basic divertor functions of the LID have been confirmed. e.g. the particle pumping is so effective that the required gas puffing rate is an order of magnitude higher compared with non-LID discharge with the same density. One of the major objectives is to achieve the confinement improvement. There are a few promising observations. e.g., the LID discharges exhibits the very peaked density profile even though transiently when the pellet fuelling is used. We also find that at $n = 2 \times 10^{19} \text{ m}^{-3}$, the temperature profile is fairly steep in the edge ($0.7 < \rho < 1.0$), unfortunately low gradient in the core ($0 < \rho < 0.7$).

We observed bifurcation between equilibrium with a large island ($n/m = 1/1$) and without. For the fixed plasma, a large island appears suddenly when the external resonant perturbation field exceeds a critical value. Conversely, for the fixed resonant field, the island suddenly disappears when the beta at the rational surface ($\tilde{\iota} \approx \pi = 1$) exceeds a critical value, which is proportional to the applied resonant field.

Collaboration with Germany

1) Dr. Norbert Rust from IPP-Garching collaborated with

M.Osakabe (NIFS) to develop an experimental technique to evaluate the NB-power heating profile of LHD-plasmas experimentally.

2) W. Kasperek (IPF Stuttgart) collaborated with K. Ohkubo (NIFS) in order to measure the characteristic of radiation for symmetric direction in a remote steering waveguide antenna for ECH/ECCD, which is proposed by NIFS. K. Ohkubo (NIFS) calculated the directivity on the radiation of the above-mentioned antenna and compared with their results.

3) M. Lehnen and A. Hiller (Forschungszentrum Juelich) visited NIFS (N. Noda and H. Funaba) in order to measure the hydrogen and helium partial pressure by the penning gauge spectroscopy on LHD.

4) M. Kobayashi visited MaxPlanck Institut fuer Plasmaphysik (Germany) to collaborate with Prof. F. Sardei and Dr. Y. Feng for the implementation of the 3D edge transport code, EMC3-EIRENE, in the LID configuration of LHD. He visited MaxPlanck Institut at April 2004 to take over the codes for the application, and analyzed the edge transport physics of LID. The results were partly presented at 14th Toki conf. at 2004.

5) R. Ishizaki (NIFS) visited Max-Planck Plasma Physics Laboratory (IPP) in Garching from Mar. 4 to Mar. 19 for joint work with Dr. P. Lang on "Theoretical study on pellet ablation" in revealing a new physics that the life time of the pellet is dominated by deformation of the pellet.

Collaboration with USA

1) G. Rewoldt (PPPL) visited NIFS from May 13 to 14 as a JIFT exchange researcher in order to discuss results from numerical analysis of microinstabilities in helical plasmas based on a linear gyrokinetic simulation code.

2) J. H. Schultz (MIT) and T. Mito (NIFS) jointly held the US-Japan Workshops on "Application of high temperature superconductor coil for fusion plasma experimental devices" from December 11th to 12th, 2004 at MIT (US).

3) L. Grisham (PPPL) visited NIFS (Y. Oka) for a week to continue the systematic observation of the Doppler-shifted velocity distribution of the negative ion beam as a function of operating conditions, especially first spectrum of slotted accelerator in N-NBI Beam Line-1, and the observation for long pulse ($> 100\text{sec}$) beam.

4) E. Hameiri (New York Univ.) stayed at NIFS from Jun. 2 to Sept. 2 as a NIFS Guest professor for collaboration research on "Hall-MHD Stability Theory".

5) S. Ishiguro (NIFS) visited Institute for Fusion Studies (IFS), The University of Texas at Austin from Nov. 8 to Dec. 2 for the collaboration research in "Particle simulation in open systems."

6) H. Ohtani (NIFS) visited PPPL from Nov. 13 to Dec.

12 for collaboration on "Simulation Study of Collisionless Driven Reconnection" with Dr. Yamada and Dr. Ji.

Collaboration with Russia

1) L. N. Vyacheslavov (Budker Institute of Nuclear Physics) visited NIFS (K. Tanaka) for 4 months, continued developing CO_2 laser imaging interferometer for density profile and fluctuation measurements on LHD.

2) V. A. V. Krasilnikov (Troitsk Institute for Innovating and Fusion Research, Russia) visited NIFS (M. Isobe) from Jan. 4 to Jan. 24, 2004, in order to study confinement property of neutral beam-injected energetic ions by use of natural diamond detectors in LHD. The results were presented in 31th EPS conference held at London 2004.

Collaboration with EU

1) S. Yamada (NIFS) visited national laboratories in EU from Feb.3 to Feb.11 for exchange novel knowledge on new superconductors and liquefied hydrogen applications, and for discussion of cryogenics and superconducting key technology for advanced fusion reactor with Drs. L. Decker (Linde AG), Tom Taylor (CERN) and P. Komarek, W. Feitz, K-P. Juengst and R. Heller in FZK-ITP.

2-2. CHS team at NIFS.

Collaborations with US

1) M. Isobe (NIFS) visited D. A. Spong (ORNL) from 22 Nov. to 24 Nov. to discuss on the analysis of the experimental data for ripple-induced fast ion loss measurement in CHS plasmas.

2) D. A. Spong (ORNL) visited NIFS from 1st to 5th of Mar. to discuss with M. Isobe about the method of modelling beam ion trajectories in CHS with Monte Carlo simulation.

3) Ed Lazarus (GA) visited NIFS to discuss the plan of the experiment in CHS to check the correctness of the 3-D magnetic equilibrium reconstruction code developed for NCSX project.

4) G. Tynan (UCSD) visited NIFS for the discussion of the experimental observation of zonal flow in CHS and Reynolds stress.

Collaborations with Spain

1) S. Okamura (NIFS) visited CIEMAT (Spain) from 9th to 12th of Nov. to join TJ-II experiment and discuss about the HIBP potential measurement and ITB formation.

2) L. Macarena CIEMAT visited CHS from 8th to 10th of Mar. to join CHS experiment and discuss NBI system

of CHS and LHD.

3) K. Nagaoka (NIFS) visited L. Macarena (CIEMAT) from 6th to 7th of July to discuss on NBI system of TJ-II and probe experiments in CHS.

Collaboration with Germany

1) C. Suzuki (NIFS) visited IPP Greifswald for 2 weeks and worked with J. Nuehrenberg and A. Subbotin for the stellarator configuration optimizer including the evaluation of the contour of second adiabatic invariant.

Collaboration with Switzerland

1) C. Suzuki (NIFS) visited CRPP Lausanne for a week and worked with W. A. Cooper for ideal MHD stability calculations of the optimized stellarator.

Collaboration with Ukraine

1) O. S. Pavlichenko (IPP Kharkov) visited NIFS for a week and worked with C. Suzuki for the preparation of fluctuation measurement of edge H alpha intensity in CHS plasma.

Collaboration with China

1) A. Fujisawa visited to Tsinghua University in Beijing, ASIPP in Hefei, and SWIP in Chengdu for the discussion of experiments on transport barrier and zonal flow.

2-3. Heliotron-J team at Kyoto University

International collaborations by the Heliotron-J team

1) D. Anderson (U. Wisconsin), M. Liniers (CIEMAT), B. Blackwell (ANU), R. Burhenn (IPP, Greifswald), R. Brakel (IPP, Greifswald), S. Gerhardt (U. Wisconsin), E. Sorokovoy (Kharkov Inst.), A. Chechkin (Kharkov Inst.), D. Mikkelsen (PPPL), S. Knowlton (Auburn Univ.), D. Spong (ORNL), M. Mikhailov (Kurchatov Inst.), and T. Dolan (NIFS) attended the Joint Meeting of US-Japan Workshop and Kyoto University 21st COE Symposium on "NEW APPROACH IN PLASMA CONFINEMENT EXPERIMENT IN HELICAL SYSTEMS" which was held at Kyoto University on March, 2-4, 2004. The meeting was organized by The Institute of Advanced Energy of Kyoto University in the frame of the 2003 US-Japan Cooperation Programs in Fusion Physics Area and the Kyoto University 21COE Program, "Establishment of COE on Sustainable Energy System". The meeting covered the topics and areas of the new approach in plasma confinement experiment in helical systems, especially, in advanced helical systems such as quasi-axial, quasi-helical, quasi-poloidal symmetry and quasi-omnigeneous (quasi-isodynamic) devices and in heliotron/torsatron devices. Recent progress of the related experiments, theories, engineering and design studies was discussed.

2) S. Benkadda (University of Provence, Marseille) visited Kyoto Univ. as a guest professor from Nov. 9 to Mar. 31. He studied transport and complexity in magnetic fusion plasmas.

3) The development of ray tracing calculation code, "TRECE" for ECH/ECCD for Heliotron J configuration was continued with V. Tribaldos (CIEMAT) along the same line as in 2003.

4) Discussions with H-1NF team (ANU) were kept along the same line as in 2003.

5) Discussions with U-3M team (Kharkov) were kept along the same line as in 2003.

3. EU

3-1. GERMANY

3-1-1. Wendelstein 7-X

In 2004, the project Wendelstein 7-X has entered into the transition from the design and construction phase towards the assembly phase. Design and manufacturing of the different machine components of the basic device has progressed considerably. This was accompanied by a strong engineering effort from the newly established subdivision System Engineering. In parallel to the development of the basic components, assembly of the stellarator has been prepared with respect to the assembly technology and the assembly procedures and with trials using dummy parts or the first components delivered to Greifswald.

By the end of 2004, 38 winding packages of the non-planar coils have been delivered for coil assembly and additional eight are in different stages of production. The manufacture of the 20 planar coils at Tesla Engineering was continued. By the end of 2004, all twenty winding packages have been produced and nine were embedded in the casings and finished. After production all superconducting coils are tested under operational conditions at the Low Temperature Laboratory of Commissariat à l'Énergie Atomique (CEA) in Saclay. Meanwhile, four non-planar and five planar coils were tested. The electromagnetic tests have been passed without problems. Quenches occurred at slightly higher temperatures than predicted giving some additional margin. During operation, the coils could experience a situation where high voltage develops (rapid shut-down) during a simultaneous loss of the insulation vacuum. In the worst case the coil would pass the Paschen minimum. Therefore an additional high-voltage test of the coils at reduced pressure is carried out. Tests with the first coil showed partial discharges. As a consequence, the connections of the coils to the support structure as well as the interfaces between the coils and the inter-coil support elements had to be modified.

The coil support structure consists of ten identical

sectors with a total weight of 72 t which span a central pentagon. Ten cylindrical supports carry the weight of the support structure and provide the thermal barrier between the cold structure and the machine base. The first module shall be delivered to Greifswald mid of next year which is still compatible with the assembly schedule.

An extensive R&D program has been performed to develop the inter-coil supports. The supports between the planar and non-planar coils have been re-designed to allow mechanical attachment and removal during assembly and to allow precise machining of the matching parts after the coils are adjusted. The design is in its final stage and the procurement contracts are planned for the beginning of 2005.

The co-operation with the FZ Jülich was extended. The qualification of the 170 bar joint-housing (prototyping) and of the bus-bar rounding was completed successfully. The qualification of the bus-bar insulation and of the joint-insulation started.

The five types of non-planar and two types of planar coils are energised by power supplies providing direct currents of up to 20 kA at voltages of less than 30 V. In 2004, all seven power supply units were installed and individually commissioned and accepted. The concept of the quench detection electronic was further worked out in co-operation with experts from FZ Karlsruhe.

The plasma vessel is composed of ten half-modules. Each half-module is cut into two sectors to allow stringing of the innermost coil during assembly. The complex shape of the plasma vessel follows the 3D shape of the plasma boundary and is manufactured from 200 precisely bent and welded steel rings. By the end of 2004, all 200 steel rings have been produced, the main bodies of four half-modules are ready and the four sectors of the first two modules have been delivered for assembly.

Efficient insulation of the cold magnet system requires careful protection against heat conduction and radiation for which high vacuum, actively cooled thermal shields, and multi-layers of reflecting metallic foils are used. The basic concept consists of 20 layers of multi-layer insulation (MLI) which are covered by an actively cooled thermal shield. The shields were manufactured from glass epoxy resin panels instead of conventional metal sheet. This novel design allows much easier production and better shape accuracy. Three layers of copper meshes inside the laminated glass epoxy resin panels ensure sufficient thermal conductivity. The first insulation segment was mounted to the first sector of the half module of the plasma vessel in summer 2004.

The in-vessel components comprise divertor target plates and baffles for energy and particle control, panels and heat shields to protect the wall against plasma radiation, control coils to modify the magnetic

configuration at the plasma boundary, water supply lines for heat removal and cryo-pumps to control the neutral gas density during high-density plasma operation. In order to protect the cryo-pumps behind the target plates protective shields are required. The first target elements were subjected to an electron beam with a power density of 10 MW/m² without damage in the Jülich facility Judith. Characterisation of the target plate material by FZ Jülich revealed that the mechanical strength fell short and reached only 60 % of the specified value.

The refrigeration system has an equivalent capacity of 7 kW at 4.5 K to supply the magnet system with supercritical helium at different temperatures and provide liquid helium to the current leads and to the divertor cryo-pumps. The contract runs according to schedule.

Assembly tools for the handling and transportation of coils and plasma vessel sectors were commissioned. The design of a large, extensive and very complex lifting structure for half-modules and modules (100 t) was completed, the manufacturing was launched. Several coil threading tests were done in 2004. Two pieces of the PV of the former DEMO-cryostat have been prepared for welding trials such that they correspond to the real geometry of the W7-X sectors. It was shown, that the shrink-accuracy of about 2 mm was within the expected range. For the welding of intra-coil support elements a development program was established together with FZ Jülich.

According to the present planning, it is expected to start the commissioning of W7-X in 2010. Due to the delivery delay of components, the assembly could not start as planned in the first half of 2004.

The full set of diagnostics proposed for W7-X and assigned to the 140 diagnostic ports has been reduced to the subset of start-up diagnostics which comprises the diagnostics necessary for the safe operation and the control of the machine and those diagnostics adapted to and being indispensable during the start-up phases of the experiment. The charge exchange injector is being developed in collaboration with FZ Jülich and the Budker-Institute, Novosibirsk. The 2 MeV accelerator provided by Text-U Austin, Texas which is foreseen as an energetic thallium ion source in a heavy ion beam probe diagnostic has been installed.

The diagnostics are being developed in close collaboration with FZ Jülich. Agreements on collaboration covering particular problems were made with the Budker Institute, Novosibirsk, the PTB-Brunswick, IFP-CNR Milano, the Kharkov-Institute of Physics and Technology and the University of Helsinki. Other European institutions from Denmark, Hungary, Spain, Sweden, Portugal and Poland expressed their interest to collaborate. Closer contacts

are being established.

The Electron Cyclotron Resonance Heating (ECRH) system is being developed and built by FZ Karlsruhe as a joint project with IPP and IPF Stuttgart. The 'Projekt Mikrowellenheizung für W7-X' (PMW) co-ordinates all engineering and scientific activities in the collaborating laboratories and in industry. It is responsible for the realisation and installation of the ECRH system for W7-X. The whole system is designed to provide the W7-X experiment with a microwave power of 10 MW at a frequency of 140 GHz for 30 minutes. It will consist of ten gyrotrons with 1 MW power each, a low loss continuous wave (CW) capable transmission line and flexible in-vessel launch antennas, which are also designed for a continuous wave full power operation in a microwave and plasma environment.

The development of the gyrotron within the framework of an European R&D program (FZ Karlsruhe, CRPP Lausanne, TED Thales Electron Devices, IPF Stuttgart and IPP Greifswald/Garching) has been successfully finished now. Two prototype tubes were manufactured within this program. The first pre-prototype gyrotron "Maquette" was already installed in Greifswald and operates routinely for high power test of the W7-X transmission line elements, as well as for high power, long-pulse tests of an ITER remote-steering launcher mock-up within the frame of an EFDA contract (see JB2004 IPF-Stuttgart).

3-1-2. W7-AS

After the shutdown of the experiments on W7-AS in 2002, vacuum magnetic flux surfaces measurements have been repeated after the initial measurements in 1988. The new measurements have been extended to high magnetic field strengths and to the standard divertor configuration. Furthermore, new methods also intended for W7-X to make magnetic field lines visible and to measure the absolute field strength have been successfully applied.

During the plasma experiments on W7-AS, a discrepancy was quite often found between B_0 , calculated from the coil currents, and the "necessary" B_0 for the interpretation of diagnostic signals where an electron cyclotron resonance was involved. Therefore, it was desired to calibrate the calculation of B_0 independently. A nuclear magnetic resonance (NMR) sensor with maximum detectable field strength of 1.05 T was used. It is found that the measured value of B_0 was about 0.5% smaller than the calculated one.

Dedicated 3D EMC3-EIRENE simulation results show poor neutral screening efficiencies for the divertor radiation case, i.e. for small plasma-to-target distances or large connection lengths in the ranges consistent with the experimentally observed unstable detachment. This link

between poor neutral screening and unstable detachment has been investigated by a linear stability analysis using the 3D simulation results. This study identifies an instability driven by the recycling neutrals penetrating into the core as being responsible for the observed unstable detachment.

High power ECCD experiments at W7-AS were analyzed and compared with predictions from linear theory (adjoint approach) as well as with non-linear (bounce-averaged) Fokker-Planck simulations. Only at low densities, both approaches overestimate the ECCD efficiency compared to the current balance of bootstrap and inductive current.

On-axis co- and counter-ECCD experiments in W7-AS led to rather large positive or negative central current densities leading to extreme deformations of the usually flat profile of the rotational transform. In order to understand and interpret the findings in these experiments - strong low- m mode activity for co-ECCD and strongly degraded central confinement visible in flat Te-profiles for counter-ECCD-high resolution equilibrium calculations with the new VMEC-version were carried out.

3-1-3. WEGA

On the WEGA stellarator the studies of the properties of ECR heated plasmas at 2.45 GHz have been continued. Using an additional magnetron with a power of 20kW, in total 26kW microwave power, is installed at WEGA. In order to interpret the measured over dense plasmas an OXB mode conversion process is suggested. This was supported by calculations of the full-wave equation by E. Holzhauer, University of Stuttgart. For global plasma characterisation an analysis of the global particle and power balance was performed. By solving the particle balance equation, the particle confinement time and diffusion coefficient could be determined and compared with theoretical estimates. The existence of a two-temperature electron energy distribution could be verified by first soft X-ray measurements. With the help of a new kind of 2D imaging modulated optical solid state (MOSS) spectrometer, measurements of the ion temperature and the poloidal flow velocity in helium plasmas were carried out.

In preparation of the magnetic flux surface diagnostic on W7-X, a modified electron beam technique with the aim to make magnetic field lines visible has been applied. The method is based on the collisional interaction of an electron beam with a highly diluted gas.

3-1-4. Stellarator Theory

In 2004, the work of the Stellarator Theory Division was concentrated on widening the scope of the theoretical work at the Greifswald Branch Institute and

on further development of the stellarator concept, notably for quasi-isodynamic configurations.

The collaboration with NFI (Kurchatov) continued within a WTZ agreement. With a confinement system with qualitatively new confinement properties the emphasis in 2004 was on integrated optimizations. With a further extension of the CAS3D stability code in 2004, a tool is available for the determination of general toroidal plasma equilibria by perturbation theory now. The influence on MHD modes of fast particles whose confinement in burning plasmas is essential, has been investigated experimentally not only for tokamaks, but also for stellarators, as e.g., in W7-AS. Recently, the parameter space for the excitation of toroidal Alfvén eigen modes (TAE's) and energetic particle modes (EPM's) has been explored at LHD. A drift-kinetic extension of the ideal magneto-hydrodynamic (MHD) stability code CAS3D has been calculated for realistic 3D conditions (W7-AS shot No. 39042) considering the contribution of circulating particles.

Global ITG turbulence in the geometry of a straight cylinder as a first simplified model of the W7-X stellarator has been investigated. For this purpose, the gyrokinetic global non-linear particle-in-cell code TORB (CRPP/IPP) was started to be modified. In 2004, TORB8 was further extended to include the influence of a finite rotational transform in zero- β straight-cylinder geometry.

Using the DALF-Ti code for turbulence calculations of the boundary plasma, the influence of shear and rotational transform on the strength of zonal flows in axisymmetric configurations has been investigated. Turbulence calculations for W7-X showed that finite- β effects of the equilibrium lead to only a slight decrease in the particle and heat fluxes which are already small at zero- β . The 3D global linear gyrokinetic code EUTERPE has been extended in order to allow computations of electrostatic ITG modes for finite- β equilibria. In an application to the vacuum W7-X equilibrium only slab-like modes (with finite parallel wave number) but not the curvature driven mode found before in the gyrokinetic calculations with EUTERPE could be identified.

The 3D fluid transport code BoRiS simplified the adaption procedure to arbitrary geometries by introducing the complete metric tensor in the algorithm. Changing geometries reduces then to pre-processing of the grid and the metrics. An automatic time stepping control was prepared in order to minimize computational effort and to improve numerical stability.

3-1-5. W7-X Applied Theory

Within a comprehensive international collaboration a revision of the ISS95 confinement data base was continued (NIFS, CIEMAT, U-Kyoto, ANU,

U-Wisconsin, U-Stuttgart, and IPP). An update resulting in ISS04 was proposed.

The development of predictive and analysis transport code for stellarators has been continued. The preliminary agreement with Princeton Plasma Physics Laboratory and Oak Ridge National Laboratory on the collaborative development of a transport code was concluded.

Benchmarking of the bootstrap-current coefficient was initiated using the Drift Kinetic Equation Solver (DKES) and a δf Monte Carlo code to calculate the neoclassical transport coefficients in the standard configurations of W7-X and LHD.

For a database of tokamak configurations in an extended "standard model" (different i , r/R and elongation), the 3 mono-energetic transport coefficients (radial transport, bootstrap current and electric conductivity) were calculated using DKES for all collisionalities. Based on the flux-friction relations (due to symmetry), only the bootstrap current coefficient is fitted (and the other Pfirsch-Schlüter contributions) for a good and consistent representation of all coefficients (EURATOM collaboration with TU-Graz).

The work to provide a fast coordinate transformation from real to magnetic space based on the method of Function Parametrization (FP) has been carried on (EURATOM collaboration with UCC).

A new Fokker-Planck/Monte-Carlo hybrid technique was developed and applied for the NBI power deposition in W7-X. In this technique, the slowing-down of the fast NBI ions on flux-surfaces (without radial diffusion) is calculated with a fast FP solver, and this solution is used in the δf MC technique for the marker equation (collaboration with CIEMAT and NIFS).

Self-consistent 3D plasma and neutral gas transport simulations for W7-X with realistic divertor plates and baffles have been obtained for three typical island-divertor configurations. The plasma parameter distributions in the divertor region and the particle and energy depositions on the divertor plates are shown to strongly depend on the position and size of the islands.

Numerical efforts to understand and describe neoclassical transport of impurities in stellarator plasmas have been undertaken. A new code solves the radial continuity equations for each ionization stage of the impurity ions for given background plasma profiles and magnetic configuration. It is shown that the spatial distribution results from the competition between the radial electric field and the thermal force (which construct a convective flux), and the diffusive term, which flattens the radial impurity distribution. It is also shown that for typical stellarator discharges there is no pronounced temperature screening effect as in tokamak plasmas.

3-1-6. Stellarator System Studies

A power supply system for feeding the superconducting coils of the Helias reactor has been investigated. This multiconverter supply system has been optimized, in view of low losses in the components and minimal negative impact to the power grid. A significant improvement of the power factor and thereby reduction of the power factor was found.

3-2. SPAIN

3-2-1. International collaborations in 2004 using TJ-II at CIEMAT

Collaboration with Russia

- 1) K. Sarkisyan (and the ECRH IOFAN team) was participating in the operation of the ECRH system of TJ-II and in the Bernstein Waves heating project, theoretical calculations (TRUBA code) and design of the system. GUP-VEI (Moscu) was involved in the power supply for Bernstein modes heating system.
- 2) M. Tereshchenko (as a member of ECRH IOFAN team) was participating in the Bernstein Waves heating project, adapting the ray tracing code TRUBA to the geometry of TJ-II. He has also cooperated in the further improvements of the code, namely, performing the mode conversion automatically and introducing a relativistic absorption model.
- 3) S. Petrov (IOFFE) visited Ciemat (October–November 2004) to install a new neutral particle analyzer in TJ-II. Dr. D. Makarin (St.Petersburgo University) was involved in the development of new code for charge-exchanged interpretation measurements.
- 4) A. Fernández (CIEMAT) visited the Institute Applied Physics Institute (Nizhny Novgorod) in May 2004 to study the possibility of frequency control of the gyrotrons.
- 5) B. N. Skvortsova (IOFAN) was participating in experiments with 2 mm scattering in TJ-II (Nov-2004).
- 6) A. Melnikov and L. Eliseev (Kurchatov Institute) were visiting Ciemat to participate in the characterization of radial electric fields in the TJ-II stellarator.

Collaborations in Europe

Germany

- 1) IPP-Greifswald. Bernstein experiments. H. Laqua visited Ciemat in November 2004.
- 2) IPF (Stuttgart). G. Müller participated in the improvement of some components of the ECRH system in 2004.

France

- 1) E. Blanco has visited the university of Nancy (one week) and S. Heuraux was in Ciemat to study the

Doppler reflectometer viability in the TJ-II stellarator using a 2-D full-wave code.

Portugal

- 1) A broadband heterodyne reflectometer has been designed and built in collaboration with IST (Lisboa) and was installed in TJ-II in January 2004.
- 2) L. Cupido and C. Silva were visiting Ciemat and E. Blanco was in IST-Lisbon during 2004.

Collaboration with USA

- 1) Visit of D. Rasmussen (ORNL) and P. Ryan to Ciemat, from the 19th to 23d July. Discussions were focused on three topics: NBI, Electron Bernstein waves and Pellet injection. The NBI discussions were organized around the general status of NBI into TJ-II, NBI Electrical System, Ion Source and beam transmission. ORNL expresses the interest in the participation in the Electron Bernstein Waves heating experiments in the TJ-II stellarator. Physics issues and hardware required to install a (ORNL) pellet diagnostic in the TJ-II were discussed. K. McCarthy (CIEMAT) was visiting ORNL in October 2004 to discuss the pellet diagnostic for TJ-II.
- 2) G. Barber and D. Sparks (ORNL) visited Ciemat (Autumn 2004) to check NBI tetrode behavior and to discuss upgrades of NBI system.
- 3) PPPL: S. Zweben was visiting Ciemat to set a 2-D visualization of transport in the TJ-II stellarator. A Princeton Scientific Instruments intensified camera with CCD sensor (PSI-5) was used. Bright, long-living structures are frequently seen with a spatial extent of few centimeters has been observed in TJ-II.
- 4) B. Carreras was visiting Ciemat in October 2004 to continue our long-standing collaboration between the CIEMAT, the University of Carlos III and Oak Ridge National Laboratory in the statistical description of turbulent transport in fusion plasmas.
- 5) D. Spong was collaborating in the investigation of Alfvén modes appearing NBI heated plasmas in TJ-II stellarator.
- 6) J. A. Jiménez was visiting ORNL (S.P. Hirshman) to participate in stellarator equilibrium studies.

Collaboration with Ukraine

- 1) The Heavy Ion Beam Probe team (headed by L. Krupnik, Institute of Plasma Physics, National Science Center “Kharkov Institute of Physics and Technology”, Kharkov) has been fully involved in the characterization of radial electric fields in ECRH and NBI plasmas in the TJ-II stellarator during 2004 experimental campaign.
- 2) F. Castejón (CIEMAT) was collaborating with S. Pavlov in theory of plasma rf-heating. He visited CIEMAT during November and December 2004 to work in a fully relativistic dispersion relation for electrons.

Collaboration with Japan

- 1) S. Okamura (NIFS) stayed in CIEMAT (9–12 Nov, 2004), being involved in TJ-II operation and discussing the physics of transport barrier formation.
- 2) M. Liniers visited Japan (March and July, 2004) to discuss NBI system and plasma confinement in helical systems.
- 3) The collaboration in the development of ray tracing calculation code (with V. Tribaldos, CIEMAT) has continued for Heliotron J configurations.

3-2-2. International collaborations: Stellarator Implementing agreement

During 2004 we continued with the participation in the "International Collaboration on Neoclassical Transport" (ICNT), whose main goal is to provide a comprehensive description of the neoclassical transport processes relevant to plasma performance in stellarator experiments. Results were discussed during the third edition of the Kinetic Theory Workshop held in Graz, Austria. Members of this Collaboration are: C.D. Beidler, H. Maaßberg and M. Schmidt from IPP, S. Murakami and A. Wakasa from NIFS, D. Mikkelsen and R.B. White from PPPL, D. Spong from Oak Ridge, and W. Kernbichler, V.V. Nemov, S.K. Kasilov from Gratz University and V. Tribaldos (Ciemat, Spain).

3-2-3. International Stellarator Confinement Database

During 2004, CIEMAT has continued participating in the activities of the International Stellarator Confinement Database, aiming to revise the previous ISS95 database, including the stellarator experiments launched since 1995, and to address the requirements for a reactor assessment. The members of this collaboration are: Chairman: J. Harris, ANU (Australia), H. Yamada and S. Okamura, NIFS (Japan) (Physics Coordination), E. Ascasibar, CIEMAT (Spain), A. Dinklage, IPP Greifswald (Germany), F. Sano, Kyoto University (Japan), U. Stroth, CAU, Kiel (Germany), J.N. Talmadge, University of Wisconsin-Madison, (USA).

4. Russia

Collaboration between General Physics Institute (GPI) and CIEMAT (Spain)

- 1) Six persons participated in the exploitation and modernization of the TJ-II gyrotron complex (total duration of visits: 12.5 months-person).
- 2) 4 persons participated in numerical calculation and preparation of system for plasma heating by Bernstein waves (total duration: 6 months-persons).
- 3) One person (for two months) participated in the

measurements of plasma density fluctuations on TJ-II by using 2-mm scattering diagnostic.

- 4) One person (for one month) participated in the test measurement of modulation of TJ-II gyrotron radiation on ultrasonic frequency with the using of special magnetostriction transformer.
- 5) One person (for two months) participated in analysis and interpretation of magnetic diagnostics for TJ-II.
- 6) Two person participated in the measurements of the power density distribution in the different cross-sections along the transmission lines of the TJ-II gyatron system (total duration: 3 months-persons).

Collaboration between GPI and NIFS (Japan)

- 1) Two persons participated in the analysis of experimental data of plasma fluctuations in LHD with the aide of the new statistical method (total duration: 2.5 months-persons).

Collaboration between Kurchatov Institute and NIFS (Japan)

- 1) Two short visits for discussions on plasma instabilities and near-wall turbulence in LHD.

Collaboration between Kurchatov Institute and Keldysh Institute with IPP (Greiswald, Germany) and CRPP (Switzerland)

- 1) Four persons from Kurchatov Institute (for one month) participated in the development of the numerical optimization of advanced stellarators.

5. Ukraine

5-1. Institute of Plasma Physics of the National Science Center "Kharkov Institute of Physics and Technology" of the NAS of Ukraine (IPP NSC KIPT)

Collaborations by the plasma theory division

- 1) Applying the fast field line tracing NEO code to investigate the $1/\nu$ regime neoclassical transport for URAGAN-2M (V.V.Nemov and S.V.Kasilov visited Institut für Theoretische Physik, Technische universität Graz (Austria) and worked with B.Seiwald and W.Kernbichler).
- 2) Analytical and numerical studies of the optimized Quasi-isodynamic stellarator configurations (V.V.Nemov, S.V.Kasilov and V.N.Kalyuzhnyj continued collaboration with J.Nührenberg, C.Nührenberg and R.Zille (Max-Planck-Institut für Plasmaphysik, Germany), V.D.Shafranov, M.I.Mikhailov, M.Yu.Isaev, M.A.Samitov, A.A.Skovoroda and A.A.Subbotin (Kurchatov Institute, Russia), W.Kernbichler and M.F.Heyn (Institut für Theoretische Physik, Technische universität Graz, Austria), W.A.Cooper (Ecole Polytechnique and Centre de Recherches en Physique de

Plasmas, Switzerland) and K.Yamazaki (National Institute for Fusion Science, Japan).

3) Analysis of the magnetic configurations of the HELIAS Reactor with the different magnetic field period number and, particularly, the effect of the different configurations on the removal of cold alpha-particles (A.A.Shishkin in collaboration with T.Andreeva, C.B.Beidler, E.Harmeyer, Yu.Igitkhanov, F.Herrnegger, J.Kisslinger and H.Wobig (Max-Planck-Institut für Plasmaphysik, Germany), Ya.Kolesnichenko and V.Lutsenko (Institute of Nuclear Research, Kyiv).

4) Analysis of the possibility of the impurity ions accumulation in the region of the magnetic islands for the geometry of stellarator NCSX, PPPL, USA (A.A.Shishkin in collaboration with H.Mynick (Princeton Plasma Physics Laboratory, USA).

5) Effects of magnetic system coils misalignments on magnetic field configuration of the NCSX stellarator were studied (V.A.Rudakov continued collaboration with A.V.Georgiyevskiy, E.Fredrickson and M.Zarnstorff (Princeton Plasma Physics Laboratory, USA).

Collaborations by the plasma experiment divisions

Collaboration with NIFS (Japan)

1) Prospect of glow discharge in Ar+H₂ in an increase of conditioning efficiency (V.Voitsenya and D.Naidenkova in collaboration with J.Kubota, S.Masuzaki, A.Sagava, K.Yamazaki).

2) Environment effect on mirrors exposed inside LHD (V.S.Voitsenya, V.Konovalov in collaboration with A.Sagava).

3) Comparative studies of edge plasma density fluctuations for RF, ECH and NBI plasmas (O.Pavlichenko in collaboration with K.Matsuoka, S.Okamura and CHS team).

4) In the frames of the LIME program: Investigations of electrostatic turbulence in the edge plasma were carried out under conditions of transition to the improved confinement mode in the U-3M torsatron (V.Chechkin and E.Volkov in collaboration with S.Masuzaki and K.Yamazaki).

Collaboration with Kyoto University (Japan)

1) Analysis of the edge fluctuations in Heliotron J (V.Chechkin, E.Sorokovoj and A.V.Chechkin in collaboration with T.Mizuuchi and Heliotron-J team).

Collaboration with CIEMAT (Spain)

1) Exact relativistic plasma dispersion functions (S.Pavlov in collaboration with F.Costejon).

2) Evaluation and compact form of Trubnikov's plasma dielectric tensor (S.Pavlov in collaboration with F.Costejon).

3) Studies of the radial electric field end confinement in the TJ-II stellarator for large variety of magnetic

configurations, plasma parameters and heating scenarios (L.I.Krupnik and HIBP team in collaboration with C.Hidalgo and TJ-II team).

Collaboration with IPP, Greifswald, Germany

1) Conceptual design study for a Heavy Ion Beam Probing (HIBP) diagnostic for W7-X Stellarator (L.I.Krupnik and HIBP team in collaboration with Hartfuss, Wendelstein-7X team and A.Melnikov, L.Eliseev, RNC "Kurchatov Institute", Moscow, Russia).

2) Development and manufacturing of the system of Heavy Ion Beam Probe (HIBP) diagnostic for WEGA Stellarator (L.I.Krupnik and HIBP team in collaboration with Wega team).

5-2. Institute for Nuclear Research of the NAS of Ukraine, Kyiv.

Collaboration with Max-Planck-Institut für Plasmaphysik Germany

1) The development of theory of Alfvén instabilities caused by the energetic ions in stellarators, interpretation of observations of Alfvénic activity in Wendelstein 7-AS, and the study of the influence of the radial electric field on the confinement of energetic ions in Wendelstein 7-X (Ya. I. Kolesnichenko, V. V. Lutsenko, V.S. Marchenko, Yu.V. Yakovenko, O.S. Burdo, O. P. Fesenyuk (all from KINR) and A. Weller, A. Werner, H. Wobig, J. Geiger, A. Koenies, S. Zegenhagen (all from IPP)).

Collaboration with PPPL (USA)

1) Analysis of Alfvén continuum and Alfvén eigenmodes in NCSX (Ya.I. Kolesnichenko, Yu.Yakovenko, V.V. Lutsenko, O.P. Fesenyuk (all from KINR) collaborated with R. White (PPPL).

5-3. Karazin National University, Kharkov

Collaboration with Max-Planck-Institut für Plasmaphysik, Greifswald, Germany

1) The development of new transport code (Oleg Shishkin jointly with collaborators: Dr. R. Schneider, Dr. Yu. Igitkhanov, Dr. C. Beidler and Dr. H. Wobig from Max-Planck Institut fuer Plasmaphysik, Greifswald, Germany, in particular, during the staying of Oleg Shyshkin in Greifswald since 01.02.2004 till 31.05.2004 in the framework of the Sandwich Fellowship Program (i.e. he was common Ukrainian-German PhD student).

2) Impurity transport and electromagnetic waves in the plasma periphery of a HELIAS reactor configuration and WENDELSTEIN 7-X (I.Girka, O.Shishkin (National University) and A Shishkin (NSC KIPT) in collaboration with German Scientists).

6. United States

Collaborations with Japan

- 1) D. Anderson, S. Gerhardt (UW), S. Knowlton (Auburn), and D. Spong (ORNL) participated in a US-Japan Workshop on New Approaches in Plasma Confinement Experiments in Helical Systems in Kyoto.
- 2) F. Najmabadi and R. Raffray (UCSD), L-P Ku (PPPL), and J. Lyon (ORNL) participated in a US-Japan workshop with EU participation in Tokyo on Fusion Power Plants in Tokyo.
- 3) D. Anderson and S. Gerhardt (UW) visited the Heliotron-J (H-J) facility and had discussions on H-mode studies in H-J and on future experiments of mutual interest in both H-J and the Helically Symmetric Experiment (HSX) in Madison.
- 4) J. Lyon (ORNL) visited the National Institute for Fusion Science in Toki to (1) collaborate with P. Goncharov on neutral particle analysis on the Large Helical Device (LHD), which resulted in two conference papers, (2) and develop a joint US-Japan-Germany paper on stellarator reactor studies with A. Sagara and K. Yamazaki.
- 5) B. Carreras (ORNL) collaborated with K. Ichiguchi on MHD studies for LHD.
- 6) M. Isobe visited ORNL to discuss incorporating fluctuating fields from instabilities into the ORNL DELTA5D code and applying it to Alfvén instabilities and fishbone modes in CHS.

Collaborations with Spain

- 1) B. Carreras (ORNL) worked with B. van Milligen and the TJ-II team on transport modeling and on transitions triggered by the edge density, and with L. Garcia and R. Sanchez from the University Carlos III in Madrid. R. Sanchez visited ORNL.
- 2) D. Rasmussen and P. Ryan (ORNL) visited the TJ-II team to develop detailed plans for a TJ-II/ORNL collaboration in the areas of NBI, EBW emission and pellet fueling. ORNL neutral beam injectors are being used for plasma heating on TJ-II. ORNL provided assistance in diagnosing and optimizing neutral beam operation in order to increase the injection voltage. ORNL and the TJ-II team are planning a collaboration on high power EBW heating at 28 GHz. As part of the collaboration ORNL will provide a horn, focusing lens and holder for collecting EBW emission and compare code predictions and the TJ-II team will provide the rest of the receiver and model the emission results.
- 3) K. McCarthy from TJ-II visited ORNL to discuss physics and technology issues related to installing an ORNL pellet injector on the TJ-II stellarator in order to raise the plasma beta and to do transport experiments.
- 4) S. Zweben (PPPL) visited the TJ-II team to work on edge turbulence imaging in TJ-II in collaboration with C. Hidalgo. PPPL has loaned to TJ-II an ultra-fast camera

that was used for edge turbulence imaging on Alcator C-Mod and on NSTX. The collaboration group has imaged fluctuations during the formation of spontaneous sheared flows using the fast camera leading to the first 2-D visualization of turbulence during the speed up of plasma rotation and spontaneous shear flow development in TJ-II.

5) D. Spong (ORNL) visited the TJ-II group to discuss collaboration on Alfvén mode studies.

6) J. Jimenez visited ORNL to learn the use of the ORNL STELLGAP code for Alfvén modes in TJ-II.

Collaborations with Germany

1) MHD equilibria and stability in high-beta plasmas in W7-AS were explored and a paper and oral presentation were given at the IAEA Fusion Energy Conference by M. Zarnstorff (PPPL). A key result of the analysis is that the observed soft beta limit in W7-AS may be due to the onset of magnetic stochasticity in the equilibrium as determined using the PPPL PIES code. The MHD stability calculations indicate that edge kink modes should be excited at high beta. These predictions are consistent with observed MHD activity, however the modes saturate at low amplitude and fortuitously do not affect the beta limit.

2) A. Grossman (UCSD) and H. McGuinness (RPI) worked with E. Strumberger on divertor code calculations.

3) D. Mikkelsen (PPPL) visited IPP Greifswald to work on semi-analytic fits to ORNL DKES diffusivities for NCSX.

4) D. Spong (ORNL) and D. Mikkelsen participated in a Kinetic Theory Workshop in Graz, Austria organized by IPP Greifswald on neoclassical transport, ECCD, ECH deposition and fast ion modeling.

(Komori, A.)

4. JSPS-CAS Core-University Program on Plasma and Fusion

A bilateral international collaboration program “*JSPS-CAS Core-University Program (CUP) on Plasma and Fusion*” was started in FY2001, which is supported by Japan Society for the Promotion of Science (JSPS) for Japanese side and by Chinese Academy of Science (CAS) for Chinese side. National Institute for Fusion Science (NIFS) and Institute of Plasma Physics Chinese Academy of Science (ASIPP) serve as the core institutes for this program in each country and assist the collaborations between all universities in Japan and China.

These two institutes have been establishing collaboration relationship in the previous decade. Based on the achievements in the past and following the progresses of the nuclear fusion research both in Japan and China, this program was established to ensure the further development of the collaboration. And, coverage of the subjects is also expanded to include fusion technologies to meet the new stage of the nuclear fusion research.

General review of collaboration in FY 2004

FY2004 is the 4th year since the core university program started. Knowing each other and getting well acquainted with available facilities in other countries, researchers conducted practical and significant collaborations: 69 Japanese researchers visited China and worked at ASIPP and other institutes (421 person-days). 52 persons visited Japan and worked at NIFS and other universities and institutes (778 person-days).

At ASIPP, physics experiments toward the improvement of energy confinement were conducted by using HT-7 tokamak. In the steady-state-oriented experiments, a 4 minute shot was achieved.

In the LHD device at NIFS, 30-minute shots were obtained using ICRF heating.

Japanese and Chinese researchers took part in experiments in each other's countries and shared the results of investigations. The newly launched HL-2A device is furnished with diverters as is JT-60 and SWIP researchers have started collaborations with JAERI. In the framework of Seminar, a workshop “Laser Physics and High Density Plasma Physics” was held. Inertial

fusion is showing rapid progress in laser technology, in the physics of ultra-high-density plasmas, and in simulations. The core university program has made a substantial contribution to this progress.

I-1A Development of advanced plasma heating for high performance plasma

Zhao Yanping (ASIPP) visited NIFS hosted by T. Seki, and conducted a long pulse experiment with ICRF group members. At the end of his visit, he conducted an experiment on de-hydrogenization from the wall with N. Ashikawa and S. Masuzaki. The following five persons visited NIFS and joined Zhao Yanping in working on the design of an ICRF system for the EAST and HT-7 device. Wang Lei (ASIPP) made a comparison of the ASIPP liquid stub tuner with the one at NIFS, the latter is the prototype of the former. Ji Zhilin (Beijing Broad Cast Machinery Factory) designed a DC power supply for a driver amplifier (100kW power level). Zhang Wei (Beijing Broad Cast Machinery Factory) improved the design of the anode cavity.

Hu Liqun (ASIPP) visited JAERI hosted by Y. Sakamoto, and investigated NBI-related technologies. ASIPP plans to have two NBI system of parallel injection for the EAST tokamak under construction; his visit was a preparation for this move. H. Idei (Kyushu Univ.) visited ASIPP, hosted by Zhao Yanping. He analyzed the ECH system of EAST/HT-7 at ASIPP in comparison with that of TRIAM-1M. He worked on the optimization of the mirror size of the EAST device and its effect on beam propagation characteristics. His suggestion was to use a tapered waveguide.

T. Suzuki (JAERI) visited SWIP invited by Liu Yong and analyzed the data obtained on HL-2A. Analyzing the data with various combinations of the currents in three poloidal coils, he compared it with Neo-Alcator Scaling. Though the experimental data is limited to Ohmic plasmas, investigation on energy confinement has begun.

T. Shimozuma (NIFS) visited SWIP, hosted by Rao Jun and Zhou Jun. He analyzed the ECH system of the HL-2A tokamak and gave advice from experiences with the LHD. He gave a seminar “Transport Barriers

Created by ECH and Millimeter Technologies in LHD”.

T. Seki (NIFS) visited ASIPP and held discussions with Zhao Yanping on increasing the power of Ion Bernstein Heating and possible collaboration in applying global code for the prediction of experimental results of the EAST device.

I-1B Development of diagnostics and control methods for high performance plasma

T. Morisaki (NIFS) visited ASIPP and introduced the method of imaging the magnetic flux surface developed for the LHD, discussing details of: 1)electron gun, 2)fluorescent screen, 3)adaptation to a tokamak which does not have rotational transport, and 4)comparison with the ripple measurement by use of the hall element. His visit was in order to transfer these technologies in the coming commissioning phase of the EAST device.

K. Tanaka (NIFS) visited ASIPP and conducted an experiment related to particle transport by use of density modulation. He also transferred a code for analyses, and gave advice on the detector of the interferometer based on the knowledge gained on the LHD.

R. Sakamoto (NIFS) visited ASIPP and gave a seminar on the pellet injector of the LHD and the experiments using it. He also discussed the diagnostics necessary to make pellet injection experiments efficient.

H. Tamai (JAERI) visited ASIPP and gave a seminar titled “Present Design Activity of National Centralized Tokamak Facility for the Demonstration of Steady State High Beta Operation” During his stay, discussions were made on 1)wall conditioning and 2)flux saving on plasma ignition phase of the EAST device.

Jie Yinxian (ASIPP)visited NIFS, invited by K. Tanaka and conducted an experiment on particle transport on the LHD device by means of density modulation.

Xie Jinlin (USTC) visited NIFS, hosted by K. Toi, and conducted an experiment on so-called “dimensionally similar plasma”.

Cui Zhengying (SWIP) visited NIFS, hosted by S. Morita, and discussed the diagnostics for the HL2-A device, which is now in operation at SWIP. Special discussion was made on 1)the improvement of the normal-incidence impurity spectrometer and 2) on the benefits of using a grazing angle type spectrometer. She also made a comparative study of the conditioning of the LHD and HL2-A devices.

Yan Longwen (SWIP) visited NIFS and analyzed the characteristics of H-mode with K. Toi and S. Ohdachi. He also visited JAERI and discussed with H. Kamada, N. Oyama, and K. Kamiya H-modes observed on JT-60 and JFT-2M and left a report.

Li Yadong (ASIPP) visited JAERI invited by Y. Kawano. He learned from design of CO₂ laser interferometer and laser Thomson scattering system. A detector system developed in JAERI will be introduced in ASIPP.

Luo Jialong (ASIPP) visited Kyushu University hosted by K. Nakamura. He worked with K. Nakamura for the data acquisition system for long time discharges in TRIAM tokamak, particularly for the development of real time display.

Liu Yi (SWIP) visited Kyoto Univ.(Institute of Advanced Energy) and worked with K. Nagasaki for the improvement of reconstruction from X-ray signals. Liu Yi has worked at NIFS on the development of reconstruction techniques of a bolometer array.

He Yexi (Tsinghua Univ.), Wang Wenhao (Tsinghua Univ.), and Wang Long (Inst. Physics) visited Kyoto Univ. and attended an international workshop (“The 10th International workshop on Spherical Tokamak”) and presented papers: 1) “The Improvement of operational conditions on the SUNIST spherical Tokamak”, 2) “Edge Plasma Electrostatic Fluctuation and Anomalous Transport Characteristics in the Sino-United Spherical Tokamak”, and “Non-inductive current startup with electron cyclotron wave pre-ionization in the SUNIST”. They also held discussions with the group of T. Maekawa on the plasma production for the LATE and SUNIST tokamaks. LATE has achieved 8 kA of non- inductive current, which became one of topical subject. They also visited The Univ. of Tokyo and discussed with the group of Y. Takase the possible theme of collaborations on the TST tokamak.

I-2A Study on plasma surface interactions and plasma facing materials

K.Okuno (Shizuoka Univ.) and M. Matsuyama (Toyama Univ.) visited SWIP, invited by Xu Zengyu and gave the presentations “Behavior of Hydrogen in Reactor Materials” and “Tritium Science in Fusion Reactors” respectively. Xu Zengyu introduced research related to blankets. They also made a plan to invite Wang Mingxu at Shizuoka University to research on the

behavior of hydrogen in boron coated layers.

N. Noda (NIFS), N. Yoshida (Kyushu Univ.) and T. Hino (Hokkaido Univ.), visited (NIN), invited by Li Zhengxian, and held a work shop on plasma wall interaction and plasma-facing component materials. The titles of their presentations were “Plasma-Surface Interactions and Plasma Facing Materials in the Large Helical Device”, “Recent Studies on Fusion Reactor Materials and Plasma Wall Interaction at Kyushu University”, and “Laboratory Plasma Physics and Engineering”. Guo Quanguai (Inst. of Coal Chem.), Hu Jiansheng (ASIPP), Liu Shenghong (NIN), Li Hua (ASIPP), and Li ZhengXian (NIN) attended on the Chinese side and made presentations on “Research Activities and the Primary Results of Carbon- Based Materials for HT-7 and EAST”, “The Primary Results of Oxygen Experiments to Remove Co-Deposition Layers in the LHD”, “Development of Super-Conducting Materials”, “Experiments on Plasma Facing Components in HT-7” and “Studies on Cu-W Materials” respectively.

Hu Jiansheng (ASIPP) visited NIFS, invited by N. Noda. On the HT-7 device, long -pulse shots of 3 minutes were achieved in 2004. Here, doped graphite GBST1308(1%B,2.5%Si,7.5%Ti) is used as the limiter material. He investigated a limiter tile of this material (used in long-pulse operation) in erosion and sublimation by using SEM combined with EDS.

Wang Mingxu (SWIP) visited Shizuoka University, invited by K. Okuno. He injected an ion beam to a thin film of boron having oxygen as an impurity, and investigated the effect of oxygen impurity on chemical- and desorption- behavior. Photoelectric spectroscopy and thermal desorption spectroscopy (TDS) were used.

Li ZhengXian (NIN) prepared specimens of tungsten-coated high-density carbon and copper and did research using TDS. In addition, he investigated heat deposition characteristics.

Guo Quanguai (Inst. of Coal Chem.) visited NIFS, hosted by N. Noda, and Kyushu Univ., hosted by N. Yoshida. He gave a talk on “the microscopic structure of doped Graphite, which is a candidate material for the EAST device”. He discussed with K. Tokunaga the following subjects: 1) the microscopic structure change of materials under glow discharge irradiation in the LHD, 2) the effects of co-deposition on recycling in TRIAM-1M, and 3) Microscopic structure change of diverter materials in the LHD.

I-3A Atomic and molecular processes in plasma

S. Ohtani (Univ. of Electro communication) visited Fudan University, hosted by Zou Yaming, and cooperated on the start-up of a new highly-charged ion source and confirmed the specifications. He also discussed new subjects of collaboration using the TOKYO EBIT.

H. Suno, T. Kato, and Mi-young Song (NIFS) attended the conference “Physics at EBIT and Advanced Research Light Sources” held at Sanya and presented papers with the following titles: “Recommended Cross Section Data for Carbon Ions and Atoms: Electron Impact Excitation, Ionization and Charge Exchange”, “Impurity Emissions Measured from Large Helical Device”, and “Dielectric Recombination Processes for Xenon Ions”. This conference was organized by researchers of Fudan Univ., represented by Yang Fujia.

F. Koike (Kitasato Univ.) visited Northwest Normal University, hosted by Dong Chenzhong, and discussed the Auger process of Neon. He wrote a paper based on this discussion and presented it at “Physics at EBIT and Advanced Research Light Source” held in Sanya.

Yuan Zhensheng (USTC) visited the Univ. of Electro communication, hosted by S. Ohtani, and conducted a collaborative experiment on the electron-atom processes, specifically the ones which play an important role in plasma. An important result was obtained with regard to the excitation to auto-ionization state of Xenon.

Dong Chenzhong (Northwest Normal Univ.) visited NIFS, hosted by T. Kato, attended the conference ICAMDATA04 held at Toki, and presented a paper “Life Time and Branching Fractions of High Angular Momentum States for the Iron Group”, which is based on results obtained under CUP. In addition, he worked to summarize the workshop held in Lanzhou under CUP in 2003.

I-4C Development of high pressure plasmas for environmental application and materials processing

M. Kogoma (Sophia Univ.) visited Fudan University, hosted by Liang Rongqing, and visited Donghua Univ. (Surface Engineering Center), hosted by Jing Zhang. He gave a seminar “The Basic Knowledge of Atomic Pressure Glow Discharge Plasma and its Application” and held discussions. He also visited Dalian Univ. of Technology hosted by Wang Dezhen, and discussed the

future main subjects of research at the some university. R. Hatakeyama (Tohoku Univ.) visited Taiyuan Univ. of Technology, Tsinghua Univ., Inst. of Physics, and Dalian Univ. of Technology hosted by Liu Xuguang, Pu Yi-Kang, Nan Jiang, and Qiu Jieshan, and introduced his experiences with methods of controlling micro-carbon structure, applications of which to environment technology and microstructural surface industry are expected. These will be helpful for the future development of application of low temperature plasma in China.

Liu Xuguang (Taiyuan Univ. of Technology) visited Tohoku University hosted by R. Hatakeyama, and learned about methods of producing carbon nano-tubes, and carbon onions.

I-4D Heating Behavior of Blast Furnace Slag Bearing High Ti Under Microwave

N. Yoshikawa (Tohoku Univ.) visited Chongqing University, hosted by Bai Chenguang. He discussed the new subject of at extracting Ti from iron ore to make the ore usable as a resource for cement, while using the extracted Ti as industrial material. He also visited Anhui University and gave a talk on the some subject and introduced research, which is being carried out at Tohoku University.

I-5A Study of ultra-high density plasma (Inertial confinement fusion)

R. Kodama (Osaka Univ.) visited the Institute of Physics in Beijing, hosted by Zhang Jie, and made a plans about ultra-high-intensity laser experiment, scheduled in 2005 and specified the subject to be the investigation of the high-energy electron.

K. Nagai (Osaka Univ.) visited Southeast University, hosted by Gu Zhongze. He took part in the first collaboration aimed at developing millimeter-sized capsules coated with tin, which are needed for laser-inertial fusion and at developing such micro-particles filling poly-ethyl capsules, which are used as biosensors in medicine

Gu Yuqiu (Nat. Key Labo. for Laser Fusion) visited the Laser Fusion Research Center in Mianyang and measured the angular distribution function of high-energy electrons and the magnetic field in interaction between lasers and solids.

Li Yutong (Inst. of Physics) attended the “International

Workshop on Fast Ignition and High Field Physics” held in Kyoto and discussed plasma-foam interaction with R. Kodama. Sheng Zhengming (Inst. of Physics) discussed with K. Mima and R. Kodama the radiation in the Tera-Hertz frequency range in the interaction between the laser and inhomogeneous plasma.

Zheng Jian (Inst. of Physics) considered the possibility of using coherent transitive radiations obtained in the interaction with an ultra-intense laser for diagnostics of high -energy electrons.

I-5B Theory and simulation on inertial fusion plasmas

The following 5 researchers participated in the workshop “JSPS-CAS Core University Program Seminar on Laser Fusion Science and High Energy Density Plasma Physics”, which was held in the framework of a seminar: H. Takabe (Osaka Univ.), H. Nagatomo (Osaka Univ.), Y. Kishimoto (Kyoto Univ.), K. Nishihara (Osaka Univ.) and T. Johzaki (Osaka Univ.). They presented their works under CUP, these are published in the proceedings “JSPS-CAS Core University Program Seminar on Laser Fusion Science and High Energy Density Plasma Physics”.

H. Takabe (Osaka Univ.) visited the Institute of Physics, hosted by Zhang Jie. He discussed the details of the experiment to be held in Osaka in June involving the Institute of Physics and the National Astronomical Observatories.

Xu Yan (IAPCM) visited Osaka university and NIFS and discussed the dynamics of radiative fluid, especially target design and data analyses. Ye Wenhua (IAPCM) visited Osaka University and NIFS, hosted by K. Mima. He made simulation in collaboration with K. Nishihara, of Rayleigh-Taylor instability including ablation and wrote a paper. Wang Feilu (NAOC) visited Osaka university, hosted by H. Takabe and discussed the opacity on the evolution of space. The collaboration to improve this opacity code will be continued.

Chen Min (Inst. of Physics) visited Osaka university, hosted by H. Takabe, and presented his work “Rear Side Harmonics of a Target and Laser Ionization fronts” and studied “Astrophysics in Laboratory”. Presently, he is developing a particle code to predict the outcome of experiments on collisionless shock and particle acceleration. Z.M. Sheng who was in Osaka at that time, took part in this discussion. He Feng (SIOFM)

visited Osaka university, hosted by K. Mima, and discussed the interaction between relativistic laser beams and electron plasmas.

Zhu Shaoping (IAPCM) visited Osaka university and NIFS, hosted by K. Mima, and discussed 1) evolution of laser plasma interaction by use of particle simulation code and 2) general computational mathematics.

II-A Study on reduced activation materials for fusion

A. Kohyama and T. Konishi (Kyoto Univ.) visited ASIPP and discussed with Wu Yican the possibility of collaboration in the development of a low -activation SiC/SiC composite material and the design of breeding blankets using the composite. They also discussed the preliminary design of the test blanket modules which China is proposing. In addition, they visited the Shanghai Institute of Ceramics and discussed with Dong Shaoming the control of the manufacturing process of the SiC/SiC composite currently being developed through collaboration.

H. Takahashi (Hokkaido Univ.) visited the University of Science and Technology, Beijing, hosted by Hu Benhu, and investigated the effects of helium on the creation of voids and bubbles in low activation Fe-Cr-Mn austenite stainless steels under irradiation. Prof. Hu presented the results at the Fifth Pacific International Conference on Advanced Materials and Processing (PRICM-5).

Jiang Dongling (Shanghai Inst. of Ceramics) visited Kyoto University, hosted by A. Kohyama. He investigated the temperature dependence of residual impurity content and bond strength for a Carbon fiber SiC Composite material produced by use of the fiber chemical vapor infiltration method.

Dong Shaoming (Shanghai Inst. of Ceramics) visited Kyoto University, hosted by A. Kohyama, and investigated the relation between the sintering temperature and the strength of Carbon-fiber SiC Composite materials produced by use of the reactive sintering method.

II-B Study on CTR blanket and tritium

K. Okuno (Shizuoka Univ.) and Y. Ohya (The Univ. of Tokyo) visited SWIP, hosted by Feng Kaiming and Zhang Guoshu, and exchanged information on the progress of research in their institutes. They also visited ASIPP and held discussions with Xiao Bingjia, Wu Yican, and Wang Xiangke. The subjects of these

discussions were: 1) absorption/desorption characteristics of hydrogen and its isotopes in structural SiC materials. 2) behavior of hydrogen isotopes in blanket materials such as Li_2O and Li_2TiO_3 . 3) Tritium desorption under neutron irradiation for blanket material Li_4Si_4 . 4) The HC-SB TBM module which has been proposed by China for the ITER test module(LiSi_4).

Feng Kaiming (SWIP) visited NIFS, hosted by T. Muroga, and reported on the preliminary design of the ITER test module. He also visited JAERI and The Univ. of Tokyo and attended “8th China/Japan Symposium on Advanced Materials”. Wang Weihua (ASIPP) attended “The 8th China/Japan Symposium on Advanced Materials” and presented a paper titled “Preliminary Design and Analysis for the FDS-II Demo Reactor and DLL blanket”.

II-C Design integration of advanced reactors and key technology evaluation

T. Muroga and A. Sagara (NIFS) visited SWIP and ASIPP and held discussions with Feng Kaiming and Wu Yican on the following subjects: 1) a tritium breeding blanket made using ($\text{Li}_4\text{Si}_4, \text{Li}_2\text{TiO}_3$), which has been proposed for the ITER TEST blanket in SWIP, 2) the NIFS proposal for a Flibe-based blanket, which has a specially-designed solid moderator as the first wall. 3) a helium cooled liquid (LiPb) blanket, which has been proposed by ASIPP for the ITER TEST module. H. Watanabe (Kyushu Univ.) visited Beijing and presented the results of collaboration at the Fifth Pacific International Conference on Advanced Materials and Processing (PRICM-5). The contents of the presentation were: 1) the irradiation effects of a laser-welded low-activation vanadium alloy and 2) the effects of temperature variation during irradiation for pure copper.

S. Nishio (JAERI) visited SWIP and ASIPP and introduced in his lecture the blanket system for tokamak-type DEMO reactors under discussion at JAERI. One of his emphases is that the shell effect of the blanket has an indispensable function in economically feasible reactors. He discussed with Feng Kaiming and Wu Yican the design philosophy for their own blankets (solid and liquid). A. Hasegawa (Tohoku Univ.) attended PRICAM-5 and presented a paper titled “the Irradiation Behavior of Advanced SiC/SiC Composites for Fusion Application”. He reported on the microstructure of SiC/SiC irradiated with ion accelerators.

Wang Hongyan (ASIPP) and Pan Chuanjie (SWIP) attended “the 8th China/Japan Symposium on Advanced Materials” and submitted a paper titled “Free Surface Flow through a Gradient Magnetic Field”. They visited JAERI, the University of Tokyo, and NIFS to see laboratories for reactor technology. Pan Chuanjie gave lectures on “the MHD effects of Liquid Metal” at the two institutes.

II-D Development of superconducting key technology for advanced fusion reactor

T. Ishigohka (Seikei Univ.), T. Hamajima (Tohoku Univ.), and S. Yamada (NIFS) visited the Institute of Electric Engineering, hosted by Xiao Liye, Tsinghua Univ. hosted by Han Zhenghe, Technical Inst. of Physics and Chemistry, and ASIPP, hosted by Li Jiangang and Wu Songtao. They gave lectures on cryogenic technologies and discussed the targets of collaboration. The titles of their talk were “The Monitoring of Large Superconducting Magnet Using the AE Technique”, “Irregular AC Losses with Long Time Constants in CIC”, and “NIFS, the LHD and the Current Feeder System”.

S. Tanahashi and H. Chikaraishi (NIFS) visited SWIP, hosted by Wan Shujin, and gave advice on the improvement of the flywheel generator which is used in the power supply for the poloidal coils in the HL-2A device.

Hou Yu (Xian Jiaotong Univ.) visited NIFS, hosted by A. Nishimura, and studied the the cryogenic system of the LHD. He also attended the “Asian Conference on Applied Superconductivity and Cryogenics”.

Wu Jiefeng (ASIPP) visited NIFS hosted by S. Yamada and studied the cryogenic technologies developed at NIFS. He gave a seminar titled “The Manufacture and Tests on the TF/PF Magnet System for EAST” and “The Converter System of the Poloidal Field Power Supply of the EAST Tokamak” and held detailed discussions on these matters.

Li Laifeng (Technical Inst. of Physics and Chemistry) visited NIFS, hosted by A. Nishimura, and attended the “Asian Conference on Applied Superconductivity and Cryogenics”. At NIFS, he studied the cryogenic system of the LHD.

Gao Ge (ASIPP) visited NIFS, hosted by S. Yamada. He made comparative studies of the cryogenic systems designed by ASIPP and NIFS the practical operation, and

of the protection systems.

III-A Study on theoretical analyses of MHD and micro-instability in plasmas

H. Sanuki (NIFS), H. Naito (Yamaguchi Univ.), and A. Fujisawa (NIFS) visited Tsinghua Univ., ASIPP, and SWIP and held seminars to spread their knowledge of their own special fields. They held discussions with 12 persons of theoretical group members at ASIPP, and discussed with 36 members of theorists and experiments at SWIP.

H. Sanuki gave a lecture on drift wave and the formation of electric fields in plasmas titled “Non-local Analysis of Temperature Gradient Driven Short Wave length Modes in Plasmas”.

H. Naito gave a seminar talk titled “The Simulation Study of Kineic MHD mode”. He explained the principle of simulation by use of gyro-kinetic reduced MHD model and gave an interpretation of the results.

A. Fujisawa visited Tsinghua Univ., ASIPP, and SWIP and gave seminars on “The Zonal flow observed on the CHS device” and discussed this subject with the audience.

Hu Yemin (ASIPP) visited NIFS, hosted by H. Sanuki, discussed the effect of the electric field on plasma confinement, gave a talk titled “Axial shock in a Z-pinch” and improved the model.

III-B Study on transport theory code development of numerical analysis and confinement improvement

Dong Jiaqi (SWIP) visited NIFS on the invitation of H. Sanuki and K. Itoh (NIFS) and engaged in the improvement of the analyses code of the ion temperature gradient mode and electron drift wave instability. Full kinetic responses were incorporated instead of adiabatic response. He also discussed with H. Sugama the general formulation of ITG type drift wave and discussed GAM oscillation with A. Fujisawa and T. Watari.

III-C Physics of self-organization in complex plasmas

M. Okamoto and S. Ishiguro (NIFS) visited IAPCM, hosted by Zhu Shaoping. They gave a seminar entitled “Particle Simulation Research Activities at Theory and Computer Simulation Center, National Institute for Fusion Science”, and discussed possible collaboration in this field. They also offered the possibility of receiving Chinese students at the Graduate University for

Advanced Studies. Cao Lihua (IAPCM) visited NIFS, hosted by R. Horiuchi, and conducted a collaboration on nonlinear phenomena in laser plasma interaction and structure formation using particle simulation.

30-D Modeling of edge and diverter plasma and control of impurities and recycling particles

Zhu Sizheng (ASIPP) visited NIFS, hosted by Y. Tomita. He analyzed the diverter structure of the EAST device at ASIPP by use of B2-EIRENE code and showed that a double null structure has better performance than a single null structure. He presented this result as a paper entitled “The Present Status of HT-7U Tokamak and Modeling Studies for the EAST Diverter”.

SEMINAR: JSPS-CAS Core University Program Seminar on Laser Fusion Science and High Density Plasma Physics

The seminar in FY 2004, entitled “JSPS-CAS Core University Program Seminar on Laser Fusion Science and High Energy Density Plasma Physics” was held at the International Asia Pacific Convention Center at

Sanya. Representatives of the organizers were K. Mima (Osaka Univ.) from Japan and Zhu Shaoping (IAPCM) from China. On organization, there was the support of the National Hi-Tech Inertial Confinement Fusion Committee of China and the Institute of Applied Physics and Computational Mathematics. From Japan, Osaka University and NIFS took the role of the local organizing committee. The participants from Japan were: 1)K. Mima, 2)Y. Izawa, 3)N. Miyanaga, 4)J. Kawanaka, 5)K. Nagai, 6)H. Habara, 7)S. Fujioka, 8)R. Horiuchi, 9)M. Kado, and 10)K. Ueda. There were 4 other participants in this workshop in the category of 15B, making the number of submitted papers from Japan 19. From China 18 papers were presented. In China, there are two peta-watt lasers under construction: Shenguang-III (Shanghai) and FIREX-I (Mianyang). Collaboration under CUP is important in order to obtain the largest possible output from these devices. Research on ultra-high-dense plasma is progressing rapidly in China and collaboration will benefit research in both countries.

(Watari, T., Namba, C.)

JSPS-CAS Core-University Program on Plasma and Fusion STATISTICAL REVIEW OF FY2004

Title		J→C person (person-day)	C→J person (person-day)	Total person (person-day)
I-1A	Development of advanced plasma heating for high-performance plasma confinement	4 (42)	5(79)	9(121)
I-1B	Development of diagnostic and control methods for high-performance plasma confinement	5(31)	10(160)	15 (191)
I-2A	Study on plasma-surface interactions and plasma facing materials	5(23)	4(82)	9(105)
I-3A	Atomic and molecular processes in plasma	6(37)	2(78)	8(115)
I-4C	Development of high pressure plasmas for environmental application and materials processing	2(18)	1(15)	3(33)
I-4D	Heating behavior of blast furnace slag bearing high Ti under microwave	1(5)	0(0)	1(5)
I-5A	Study of ultrahigh density plasma (Inertial confinement fusion)	2(18)	4(22)	6 (40)
I-5B	Theory and simulation on inertial fusion plasmas	6 (29)	6(74)	12(103)
II-A	Study on reduced activation materials for fusion	4(24)	3(45)	7(69)
II-B	Study on CTR blanket and Tritium	2(14)	2(32)	4(46)
II-C	Design integration of advanced reactors and key technology evaluation	5(28)	2(32)	7(60)
II-D	Development of superconducting key technology for advanced fusion reactor	5(36)	4(50)	9(86)
III-A	Study on theoretical analysis of MHD and micro-instabilities in plasmas	2 (15)	1 (22)	3 (37)
III-B	Study on transport theory: Code development of numerical analysis and confinement improved mode in torus plasmas	1 (8)	1 (32)	2 (40)
III-C	Physics of self-organization in complex plasmas	2(6)	1 (10)	3 (26)
III-D	Modeling of edge and divertor plasma and control of impurities and recycling particles	0 (0)	1 (15)	1 (15)
	Scientist Exchange	7 (29)	5 (30)	12 (59)
	Seminar	10 (58)	0 (0)	10 (58)
Grand Total		69(421)	52(778)	121 (1,199)

IV. Department of Engineering and Technical Services

The Department of Engineering and Technical Services is involved in all kinds of work on the design, fabrication, construction and operation of experimental devices in the fields of software and hardware.

This department is composed of engineers, and their tasks fall under the following five goals:

To develop advanced and systematic engineering capabilities on the basis of basic engineering results which have been obtained thus far.

To educate excellent engineers with responsible administration.

To cultivate creative engineering abilities.

To improve the documentation of and the transfer of engineering knowledge to the next generation.

To perform tasks with systematic responsibility.

The department consists of the following five divisions: the Fabrication Technology Division takes care of the construction of small devices and the quality control of parts for all Divisions. The Device Technology Division is responsible for LHD and LHD peripheral devices except for the heating devices and the diagnostic devices. The Plasma Heating Technology Division has responsibility for the ECH system, ICRF system and NBI system. The Diagnostic Technology Division develops, operates and maintains all diagnostic devices and the Control Technology Division has responsibility for the central control system, the current control system and the LHD network. The number of staff is 46 engineers and several part-time workers. We take care of the development, the operation and the maintenance of LHD and the LHD peripheral devices with about 47 operators.

1. Fabrication Technology Division

The main tasks are the fabrication of experimental equipment, technical consultation, research development of apparatus, technical cooperation and supply of experimental parts and materials. The division also administers all the office work of the department. The staff of our division is mainly working in the central workshop. In our division, we received about 400 jobs for the fabrication of devices in this fiscal year. 95% of them could be fabricated in our central workshop. We support the construction of devices and their control systems as requested from each research division.

(1) Phase detection circuit.

We designed and manufactured the high-phase resolution phase detection circuit. The 3ch digital phase comparator parts of this circuit are integrated in a one chip FPGA (Field Programmable Gate Array) device. With the FPGA, it is possible to program the inner logic circuit flexibly and the volume of this circuit can be downsized. As for the specification of this circuit, the input signal is 1 MHz, the phase detection range is the 15 fringes with a phase

resolution of $1/180$ of a fringe, and a response speed of 1msec. This circuit has been used on the 3ch FIR laser interferometer on CHS.

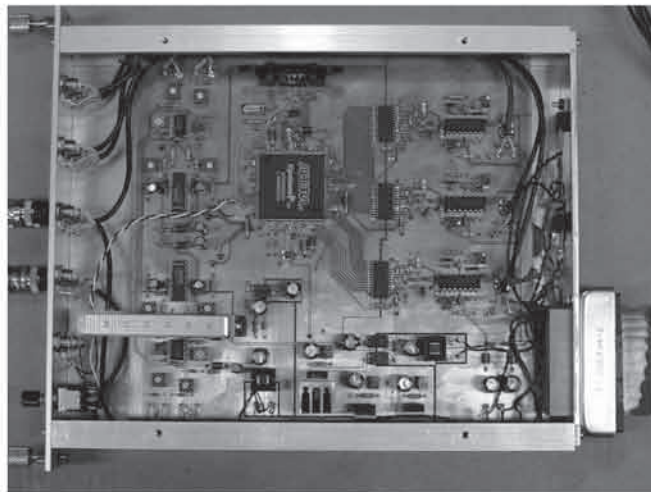


Fig.1 3ch phase detection circuit

(2) Gated integrator.

This circuit processes an output signal from a photomultiplier used for a laser Doppler spectrometer. The signal is gated by the analog switch controlled trigger signal, and the gated signal is output through an integrator. As for the specifications of this circuit, the minimum gate delay time is 200 ns, the minimum gate width is 40 ns, the input time constant is $200\text{ ns} \sim 160\mu\text{s}$, the output time constant is $10\text{ ms} \sim 10\text{ s}$ and the signal gain is 30. Rev. Sci. Instrum. 66(8) p4395 1995 is referred to manufacture this circuit.



Fig.2 Gated integrator

(3) The hydrogen gas shield for the cryogenic target of the FIREX project

In a cryogenic target used for the FIREX project, we have manufactured a prototype hydrogen gas shield. The apparatus is constructed of oxygen-free copper and an aluminum alloy. The hydrogen gas shield is welded by Electron Beam Welding (EBW).

a) EBW of oxygen-free copper.

In the case of oxygen-free copper, the fusion zone depth of the EBW is shallow and rough. In order to deepen the fusion zone, the distance from the EBW system to the base metal was set at 150mm.

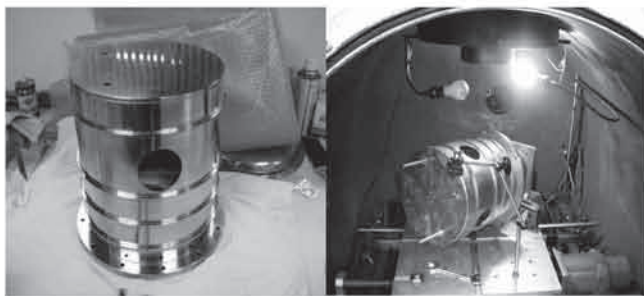


Fig.3 EBW of oxygen-free copper.

b) EBW of aluminum alloy.

In the case of an aluminum alloy in EBW, a deep melting zone can be obtained, but sputtering loss often occurred at the weld zone. By setting the distance from the EBW system to the base metal at less than 150mm, we improved the condition of the welding zone.

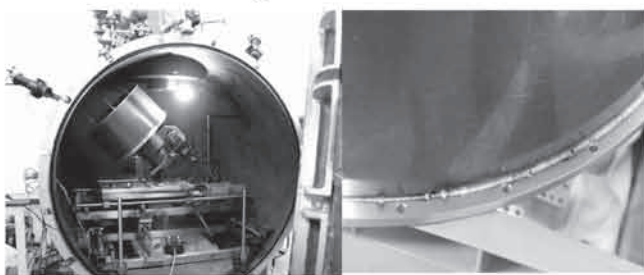


Fig.4 EBW of aluminum alloy.

(4) Gate valve control system

In order to maintain ultra-high vacuum in LHD, the gate valve control system controls on the gate valves on LHD. The plasma vacuum vessel of LHD has about 550 ports and this system controls about 100 gate valves. This system had been operating from the second-experimental campaign, and has worked without a major leak accident for six years. In order to respond to added and relocated instruments with gate valves every campaign, we had to alter wiring and rebuild the control program. To resolve these problems, after the seventh-experimental campaign, we improved two aspects of the system as follows. (1) To get the control signals of the gate valve, the main terminal box was installed at a distance of more than 20m from LHD. In the modification of the gate valve location, long cabling is required. So, 10 relay terminal boxes were installed at each main port on LHD. The installation of these terminal boxes allows easy cabling for system modification. (2) The construction of the gate valve control program for the common use. There are various operation types of the instruments, whose major examples are as follows; a) The instrument is inserted into the plasma vacuum vessel of LHD. b) The gate valve is controlled by the instrument side at the plasma shot timing. c) The gate valve is always opened to the experiment. A common control program was implemented, which does not require reprogramming after

system modification and which improved the reliability of the system. As a result, the improved system has operated from the eighth-experimental campaign without trouble.

2. Device Technology Division

The Division supports the operation, the improvement and the maintenance of LHD, the peripheral devices for LHD, cryogenic and super conducting R&D devices,

(1) Operation and Maintenance of LHD

LHD operation started on July 26 in the eighth-experimental campaign, the cryostat was evacuated as usual. The evacuation of the plasma vacuum vessel began on July 27. We found four vacuum leaks; three CF-flanges of the plasma vacuum vessel, and an NBI gate-valve had a seat leak. The vacuum leaks were fixed on Aug. 7, and the coil cool-down was started at Aug. 11. The cooling down was completed on Sep. 9. These 4 leaks are our new record in all previous vacuum-leak tests.

The first energizing of LHD in the eighth-campaign was on Sep. 10. The number of operation days of the SC-coils was 56 days. The number of days of the plasma experimental period was 132 days. The warm up of the S.C.-coils was started on Jan. 21.

During this period, the interruption of commercial power occurred four times due to thunderstorms and one time due to an accident at a power plant. They were June 28, July 20, 27, Aug. 7 and Aug.26.

The LHD cryogenic system did not have any major problems during the 8th operation.

(2) C-stage design

For the installing a new NBI (BL-4) at the 5-O port, It was necessary to reconstruct the C-stage.

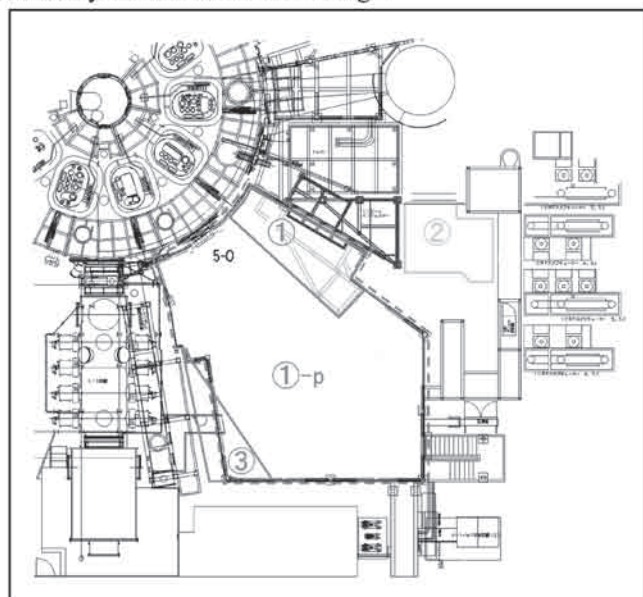


Fig. 5 C-stage reconstruction design

Figure 5 shows C-stage design for the BL-4. 1p is the previous C-stage. 1 is the new C-stage, 2 and 3 are new additional stages.

First of all, equipment, pipes and wires that had been installed above and below the stage must be removed. Next, the stage will be reconstructed. At the same time, it is necessary to select the equipment that would be reinstalled and to design the new stage for those. In addition, the routing for the piping and wiring that connected those instruments must be designed and carried out. To perform this smoothly, it is important to arrange the work schedule and area in the laboratory and among sub contractors.

(3) Dynamic simulator development for the Helium Refrigerator/Liquefier for LHD

The model of the Helium Refrigerator/Liquefier was modified for the Dynamic Simulator. The cool-down sequence programs of the simulation model used the same program as the Helium Refrigerator/Liquefier for LHD.

This year the helical-coils and poloidal-coils and bus-lines were modeled. The coil model was not a standard program. So, we made the calculation program for the coils and the bus-lines.

The coil models were used for the cool-down operation in the dynamic simulator. The coil parameters were adjusted by comparing between the calculation result and the cool-down data from the LHD. The result is shown in Figure 6.

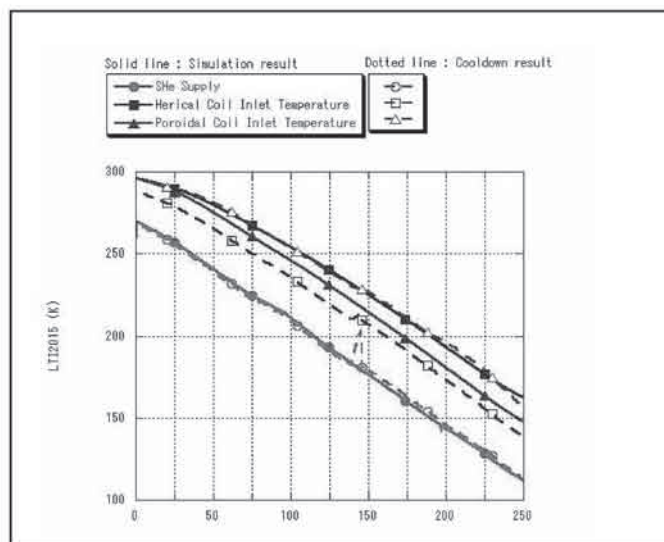


Fig. 6 Cool-down simulation data compared with the actual cool-down data in the 7th operation

The solid lines show the simulation results, the broken lines show the cooling result of the seventh experimental campaign.

(4) Gate Valve Control System

There are many diagnostic devices attached to the LHD. The gate valve control system controls the gate valves installed between the LHD and the accompanying equipment. It is partially responsible for preserving the vacuum in the plasma vacuum vessel.

More than seven years had elapsed since the system was

established and this control terminal had become obsolete.

Therefore, we developed a new control program for the Gate Valve Control System with the general-purpose software LabVIEW ver7.1 (figure 7).

(LabVIEW delivers a "graphical" development environment for signal acquisition, measurement analysis, and data presentation.)

With a fully functional control terminal, we can efficiently maintain the system.

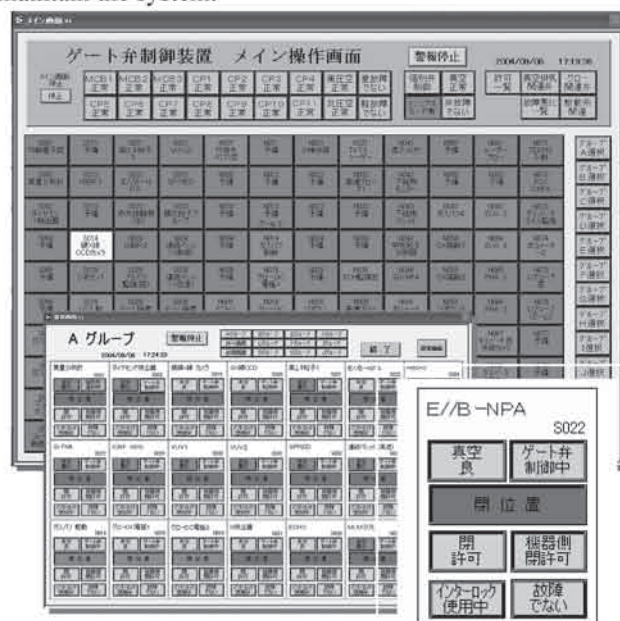


Fig.7 Gate valve control panels

(5) Saving consumed electric power of the Helium Refrigerator/Liquefier

The helium refrigerator for LHD has an equivalent refrigeration capacity of 9.1 kW at 4.4K, it includes eight sets of the oil injected screw-type compressors. The in total consumed electric power is 3.49 MW with 1100 g/s mass flow rate in winter. The steady-state cooling has been maintained for more than four months in every experimental campaign. So, the reduction of a consumed power is one of the most important issues.

The characteristic of the unloaded operation of this system was investigated for power reduction. The mass flow rate of the main circulation to the cold-box was controlled to 700 g/s, and the other of 400 g/s was bypassed. We tried the reduction of this bypass flow by the unload-operation of the low-pressure compressor.

As a result, the maximum power consumption reduction was 520kW during steady-state cooling operation, at that time the reduced mass flow rate was 220 g/s.

15% of the consumed electric power was saved with this operation.

(6) Technical Support for Cryogenics and Superconductivity Laboratories (CSL)

A cryogenic system with a capacity of 200 l/h (500 W at 4.2 K) and a high dc current supply of 75 kA at 21 V,

including a cooling water system with an 800 kW heat exchanger, was installed at the CSL. Operation of these test facilities and daily inspection of them are carried out by the members of the Device Technology Division. In particular, we are responsible for the annual duty inspection of the cryogenic system, regular maintenance of the cooling water system and preparation for the experiments.

3. Plasma Heating Technology Division

The main works of this division are the operation and maintenance of plasma heating devices and common facilities. We have also performed technical support for the improvement and the development of these devices, and the installation of new devices.

In the 8th experimental campaign, the ICRF system with six reinstalled antennas was used for steady state plasma experiments as a main plasma heating device. The high temperature plasmas with $T_{i0} \sim 2$ keV were maintained for 1905 seconds. In this case, the total injection energy of all the heating devices was about 1.3 GJ. In the case of plasma sustained only by ECH, the duration time was drastically extended to 3900 seconds from the record of 756 seconds achieved in the previous experimental campaign. This extension in the operation time owes to several improvements in the heating system. The details of the activities are as follows.

(1) ECH

(a) Gyrotron Operation & LHD experiment

During the 8th experimental campaign, we could inject millimeter waves with a total power level of over 2MW into LHD by using 8 Gyrotrons for pulsed operation. In the steady state experiment, the injected millimeter wave duration was 3900sec by a continuous wave (CW) Gyrotron. The time history of the injection power is shown in Figure 8. The reliability of the ECH operation for the experimental shots was 90%. The average of the transmission efficiency of all waveguide lines was about 68%.

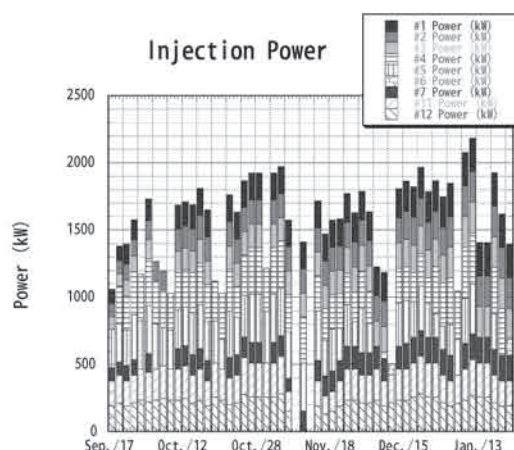


Fig. 8 The history of ECH injection power during the 8th experimental campaign

One of the important missions in this experimental campaign was the sustainment of the steady state plasma with the ICRF power as a main heating source. It requires a CW ECH power source for plasma heating. In the steady state experiment, the plasma sustainment time was successfully extended up to 3900 seconds.

(b) Improvement of CW waveguide transmission system

We have improved two key components of the vacuum waveguide system with an inner diameter of 31.75mm for long pulse plasma experiments. One is the pump out tee and another is the DC-break. Both components were damaged in previous long pulse experiments. In order to increase the pumping efficiency, the wall of the waveguide in this tee had many holes that made the heat conduction of this part worse and the mechanical strength weak, resulting in a strong deformation of the waveguide wall after the long pulse operation. The improved pump out tee has a small gap (1mm) in the waveguide and a water-cooling path through the housing block. As for the DC-break, ceramic insulator covering the waveguide gap was heated up due to leakage power or heat conduction from the waveguide and was broken during long pulse operation. We have replaced this ceramic part by an aluminum disk coated by an oxidation capsule ($50 \mu\text{m}$) for electrical insulation. These components are manufactured in the workshop of NIFS. Nine pump out tees and two DC-breaks (Figure 9) are installed on the waveguide system of 60 m length.

We used this upgraded CW waveguide system and succeeded in transmitting a power of 120 kW for more than one hour to LHD during the 8th cycle experiment. The problems with the pump out tee and DC-break were solved up to the 120 kW level in the real CW system.

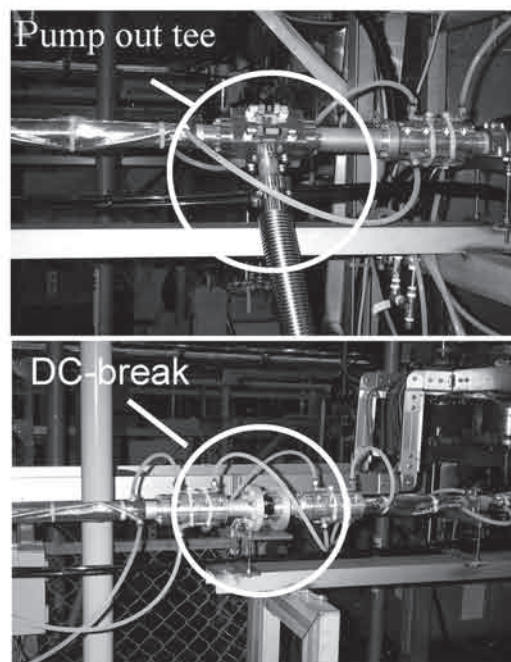


Fig. 9. Set up of pump out tee and DC break installed on the CW transmission system.

(c) Improvement of a polarizer

In ECH, it is the most important aim to increase the absorption power. The injection power has been increased step by step in every experimental campaign, but arcing on the polarizer became a serious problem. Arcing occurs due to a concentrated electric field. We can reduce the concentration of the electric field by broadening the beam width with the same beam power. In the transmission line, we built in the quasi-optical units so that the polarizer was placed 1 m away from the wave-guide (Fig 10). The beam width at the mirror surface, which was about 25mm, became about 50mm. We could transmit a more high-power beam during the 8th experiment campaign.

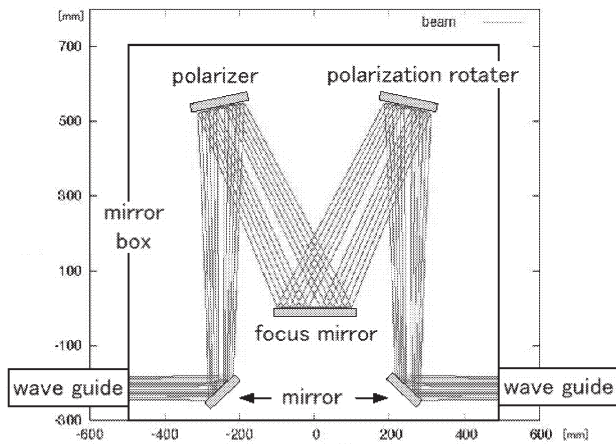


Fig 10. Beam profile in the polarizer mirror box. This figure shows the cross section of the beam expressed by the contour lines of a spot size normalized by the $1/e$ radius at each propagating position.

(2) ICRF

(a) Modification of the triggering sequence

In the 8th experimental campaign, a triggering sequence for the start-up of the ICRF heating was set up for a steady state plasma discharge. The ICRF heating was started simultaneously just after the neutral beam injection (NBI) was terminated. An electric circuit was fabricated for that purpose. The voltage of the plasma arc for the plasma production in NBI was used as the signal of the end of the pulse of the NBI and the trigger signal for the start-up of the ICRF heating was produced. However the voltage signal includes noise and several triggering pulses were formed in the circuit. This problem was solved employing a logic circuit as shown in the block diagram, in figure 11.

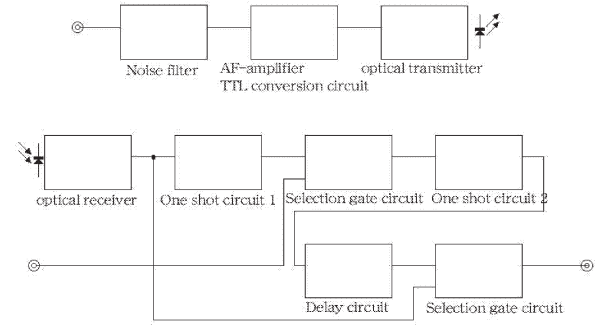


Fig. 11 block diagram of the trigger signal for the start-up of ICRF

(b) Water-cooled jacket for the outer conductor of transmission lines

In the transmission line of the ICRF heating system, the temperature rises by the RF dissipation loss. And the impedance shifts because of the expansion of the transmission line due to this temperature rise. The 240D coaxial tubes were cooled by water flow in the inner conductor. But the cooling for the outer conductor was only both free convection heat transfer to the inner conductor and to the atmosphere. Therefore, we put water-cooled jackets on the outer conductors of the transmission lines. The jackets consist of several copper $40 \times 20 \text{ mm}^2$ rectangle pipes of 2mm thickness placed parallel to the coaxial tube and surrounding the outer conductor. The inner side of these pipes is shaped so as to have better contact to the curved surface of the outer conductor. These pipes are connected in series as a water channel, therefore in the 8th experimental campaign, the flow rate of water was only 5l/min. In order to increase the flow rate of water to improve the cooling efficiency, a change in the connection of each pipe of the water channel from series to parallel is planned.

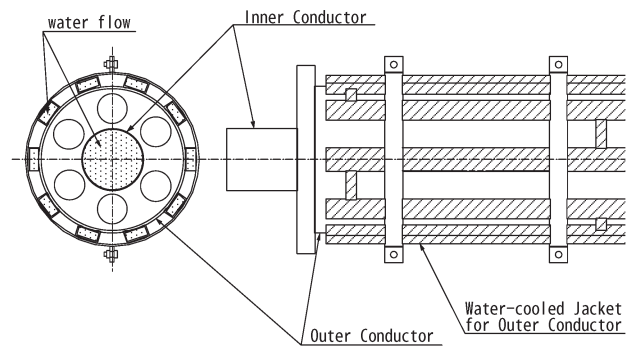


Fig. 12 Layout of a water-cooling jacket on a 240D coaxial tube

(3) NBI

(a) The Operation and Maintenance of NBI Devices

(BL-1, 2, 3) in the 8th experimental campaign of LHD

During the 8th experimental campaign, three beam-lines have performed the operation for the neutral beam injector. The number of the beam shots injected into LHD amounts to about 15,000. The time history of the injection power is shown in Figure 13. On BL-2 we made a minor change to improve the electrode, conditioned the electrode increase the beam power and then started the beam line conditioning. The power drops and the lack of columns on the chart is due to some troubles occurring in the beam-lines. They are the cooling-water leaks at the electrode, or in the flexible tube connected to the beam dump and the breakdown of the semiconductor elements for the rectification in the power supply. The beam-lines made a quick recovery by the exchange of reserve stock parts and by repairs done within a short time.

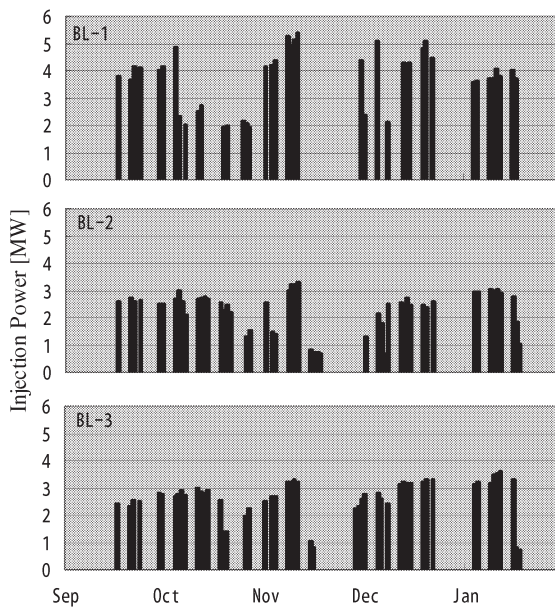


Fig. History of injection power during the 8th experimental campaign

Fig. 13 The time history of the NBI injection power

(b) Development of P-NBI data acquisition system

For the positive-NBI system, which is planned to start its operation in LHD from the 9th experimental campaign, we have been developing a data acquisition system. The system covers all of the data required for operation. The vacuum pressures along the beam-line are continuously monitored, the voltage and the current data of the power supplies are acquired by the sequence trigger at every shot and the beam profile is deduced from the heat load on the calorimeter. The data summary is also created from the acquired data for every shot. The data acquisition system is also equipped with an alert function, in which the interlock signals are sent to the control system at the detection of an excessive temperature rise of the beam-line components. Now we are assembling the hardware system and making the control and

GUI programs. The whole system will be operated successfully in the 9th campaign after test operations at the NBI test-stand.

(c) New NBI plan

We made the plan as follows about the construction of the new NBI (40keV-6 MW by 4 Positive ion sources). (Fig. 14)

A beam line vacuum vessel is installed at the 5-O port, and the C stage is removed. The power supply for the plasma production (for a filament and an arc) is installed in the LHD hall, and the other power supply is installed in the basement of the LHD hall or the trans-yard of the heating power supply building. All utilities (gas, cooling water, electric power, etc.) branch from existing NBIs and are connected in the basement of the LHD hall. The LN2 buffer tank for the cryo-pump will be replaced by a larger sized one. The same design as for the existing beam line apparatus (vacuum vessel, beam dump, calorie meter, vacuum pump, etc.) is applied to the new system, as well as the control system. But for the power supply, a part of the apparatus was re-designed using a different part because of the production stoppage of the parts used in the existing design. The measurement system with PC is used with the newest OS, maintaining compatibility with the existing one. This construction plan will surely be helpful also to the maintenance of the existing NBI, for example, by reservation of the service parts, and by renewal testing of various systems, etc.

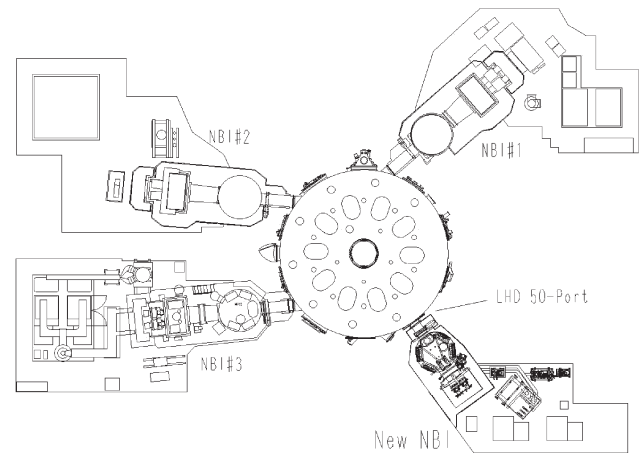


Fig. 14 The layout Plane of New NBI

(4) Motor-Generator (MG)

The MG is used to supply the pulsed power to the NBI for LHD and the CHS magnetic coils. The MG had generated 53,238 shots in this fiscal year and 302,377 shots since its construction. The operation time counted 2,163 hours in this fiscal year and 13,681 hours in a total.

Under the annual inspection in this fiscal year, the following components were checked: oil in the MG, a diesel engine generator, a rectifier for excitation, a transformer, a circuit breaker, two air-break switches, a liquid resistor, 3 condensers and 13 vacuum circuit-breakers. In another case,

the CPU of the MG control computer was replaced by a new one since the old one suffered from communication errors. A 24 V power unit for the velocity control board was found to be damaged and was replaced. The network printer for the MG control computer was upgraded. During the next LHD experimental campaign, the length of the brushes due to wear would be below the critical level. So, new brushes should be installed before the start of the LHD experiment.

4. Diagnostics Technology Division

This division supports utility construction and device installation work for LHD diagnostics, and the development, operation and maintenance of the diagnostic devices and of the data acquisition system for LHD and the plasma experiment. For the 8th experimental campaign, some diagnostics were newly installed and reconstructed on the LHD: the compact NPA, etc. After this experimental campaign some diagnostics were removed from the 5-O and the 10-O ports of LHD for the NBI (BL-4) construction.

In this experimental campaign, the first diagnosis of the LHD plasma by the HIBP was achieved, and the diagnosis of the electron density of the LHD plasma by the Thomson Scattering Diagnostic Systems was also achieved. Some troubles were caused by some diagnostic systems, for example, by the FIR laser system, by the Thomson laser system, and so on, but the plasma experiment was not stopped by those troubles in this experimental campaign.

Our principal tasks in this fiscal year are described as follows.

(1) Development, Operation and Maintenance of the Radiation Monitoring System

An area radiation monitoring network system named RMSAFE has been developed at NIFS for application to the LHD fusion plasma experiment.

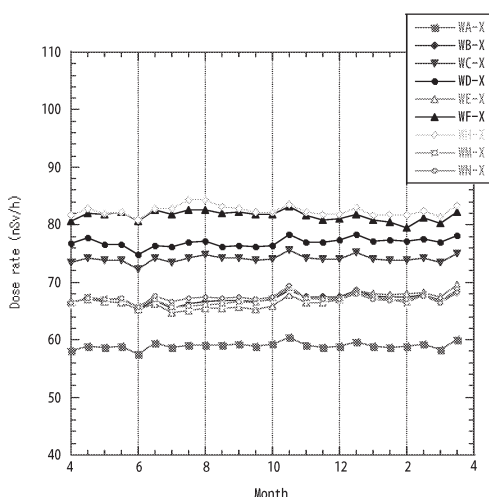


Fig. 15 The monthly average data of the $X(\gamma)$ radiation monitors on the site boundary in this fiscal year.

The RMSAFE is capable of accumulating burst-like exposure due to plasma experiments as well as observing the continuous background radiation level. The system was brought into operation in 1992. A total of 47 radiation detectors are now installed at 36 points in the Toki site and the experimental buildings. Figure 15 shows the monthly average data of the $X(\gamma)$ radiation monitors on the site boundary in this fiscal year. These data show that the levels of the radiation exposure at these monitoring posts are maintained at the environmental back ground level.

(2) Thomson Scattering Diagnostics

In the LHD Thomson scattering diagnostic, a sliding cover glass system is set in front of the diagnostic window to protect the window from being darkened and broken by thermal stress. After each experimental campaign, a cover glass is removed from the system and its transmittance is measured to check the influence of the cover glass on the analyzed data. The result of the error analysis is shown in Figure 16. The relative errors before the 7th campaign are much smaller than statistical and systematic errors (a few percents). Thus, they were negligible. However, in the 8th campaign the error was not negligible. Therefore, we are developing a diagnostic system to measure the transmittance during the experimental period.

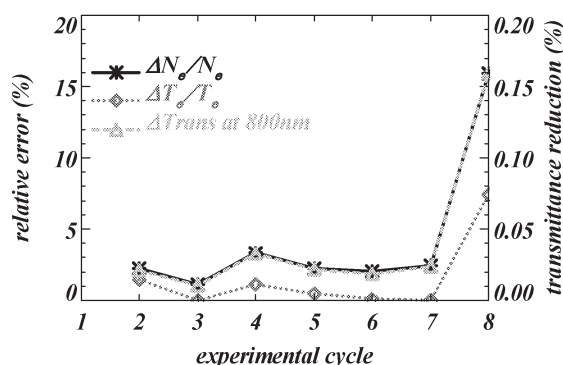


Fig. 16 The transmittance reduction of a cover glass and relative error of electron temperature (T_e) and density (N_e)

(3) Operation and Maintenance of FIR Diagnostics and Microwave Reflectometer

The operation and maintenance (for example, high voltage power supply, vacuum system, supplied gas system, phase detection circuit, dehydrator, water cooling system etc.) were responsibly executed. Therefore in this 8th experimental campaign, in almost all shots, the electron density data was completely acquired. So it contributed greatly to the plasma experiment.

(4) Micro channel plate (MCP) set up in the second beam line of the HIBP

Three highly sensitive MCPs were set up in the second beam line of the HIBP as a beam detector, because the second beam was weak. Two movable MCPs were set up

instead of the Faraday Cup type detector as a Beam Profile Monitor (BPM) in the path of the beam line. Figure 17 shows the MCP made as a movable type. The MCP is driven from the atmospheric side by a pneumatic system through a bellows. The beam detector in the final stage was changed to a MCP.

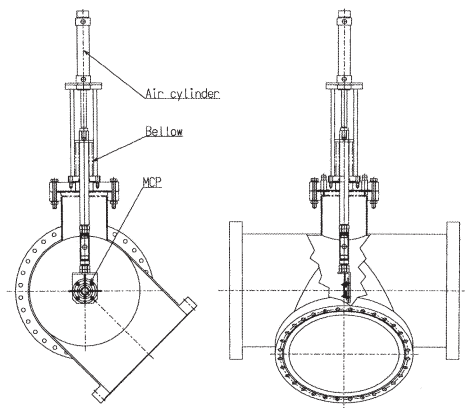


Fig.17 Structure of the MCP made as a movable type for the HIBP beam detection.

(5) Vacuum leak test with the test chamber in the Plasma Diagnostics Laboratories

Preliminary vacuum leak tests were carried out on diagnostic devices to be used for the LHD plasma experiment and the parts to be used in these diagnostic devices using the leak test chamber in the Plasma Diagnostics Laboratories. For example, the beam dump and some parts of the Thomson Scattering Diagnostics System, some parts of the Charge Exchange spectroscopic System, the window of the Boronization System, some parts of the HIBP system, some parts of the TESPEL Diagnostics System, etc. We carefully tested these devices and parts to be used in this experimental campaign, therefore in this experimental campaign the LHD plasma experiment was not stopped by vacuum leakage of the diagnostic devices.

(6) Technical support to diagnostic devices to prepare for measurement of plasma parameters.

The technical support has been performed to prepare for the measurement of plasma parameters by each diagnostic device starting a few months before the LHD plasma experiment every year. For the 8th experimental campaign, we prepared more developed diagnostic devices and managed to obtain plasma parameters. As for the main parts of each diagnostic device, researchers in charge control them directly, but as for most of the peripheral parts, technical staffs control them mainly. After checking the diagnostic device is installed for the measurement of the plasma parameter. For example, the Compact Neutral Particle

Analyzer (CNPA) had a minute air leak in the vacuum chamber for the signal detector at first and it took much time for us to find the leak and seal it. As a result, the CNPA was allowed to be used for the LHD experiment in the second half of this campaign and original useful plasma parameters could be obtained.

(7) Development of a Data Acquisition System

In the data management system for the LHD plasma experiment, the number of diagnostics using WE7000 and the Compact PCI digitizer has been increased very much. And in the Compact PCI diagnostic, the image data acquisition using the camera module has been achieved. Therefore, the acquired data size has been increased extremely. To backup and serve these expanded data, the huge storage RAIDs and DVD changers were introduced. And the plan to construct the SAN (Storage Area Network) system using the Fiber-Channel RAIDs is advancing now.

The data size per 1 channel has been increased dramatically (especially in the camera image diagnostics), and the new data retrieving method that can retrieve a part of the data is being developed.

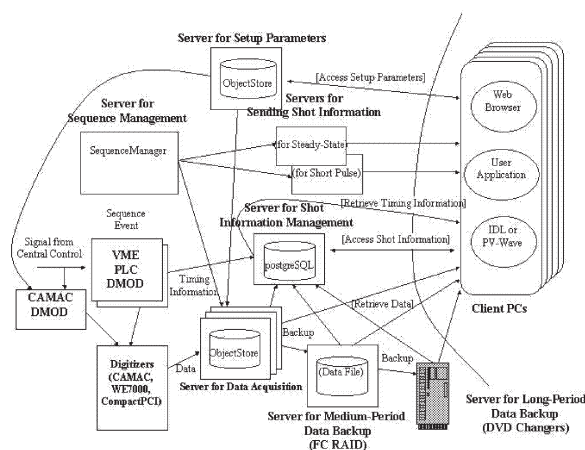


Fig. 18 Summary of LHD Data Management System

5. Control Technology Division

The missions of this division are to contribute to the LHD, to the CHS experiments and to Computer and Information Network Center in the following technical assignments; the central control system and its man-machine interface system, the SC coil current control system, the LAN system and the data acquisition system. In FY 2004, on these subjects, not only the operation and the maintenance were completed, but also many developments were continued for each technical theme. The activities of this division are as follows.

(1) Development of the function of real-time magnetic axis shift in the coil parameter setting

The main mission of the 8th experimental campaign was long pulse operation with ICRF heating. During a long discharge, the temperatures of the diverter plates suddenly

rise because the plates are exposed to the heat flux from the diverter legs. In this case, the magnetic axis should be shifted in a real-time to control the local rise of the plate temperature.

We have developed the function which enables the specification of the coil parameters to be done not only before the discharge but also at an arbitrary timing. After the currents parameter setting of the initial magnetic axis value, the final magnetic axis position value and the transfer time value to the coil power supply system, the magnetic axis starts to shift and the current axis position is informed to the experiment coordinator by computer voice.

Finally, the rapid rise of the plate temperature was controlled and it improves the cooling efficiency by dispersing the heat on the diverter plate.



Fig.19 Console window of the magnetic axis shift

(2) Liquid stub tuner control by multi computer system

The world record input heating energy of 1.29GJ was achieved in a long-pulse plasma discharge in the 8th experimental campaign of LHD. In order to always reduce the reflected RF power during a long-pulse plasma discharge, a multiple channel Feed Forward / Feed Back control method using a multi-computer system was developed for setting the 10 liquid stub tuners to the proper positions. The liquid stub tuner control system is composed of a Multi-computer system, Owner LAN and Unix server. Figure.20 shows the block diagram of this control system, and the system is composed of 8 computers. This system controls the start/stop and CCW/CW directions of the pulse-motors of the 10 liquid stub tuners monitoring the reflected and the forward RF powers. It was one of the keys to achieve the long-pulse plasma discharge. The LAN is not usually used in the feedback control system because of traffic and collisions. In this case noise is often introduced in the measurement of the liquid surface level because of the liquid bubble and the turbulence. This liquid stub tuner control system can ignore a dead time of several hundred milliseconds. Considering these phenomena, a system using

LAN was used. The plasma discharge could be maintained for a long time by optimizing the various functions for the liquid surface level controlled by this system. Control could be achieved using a PI control employing the LTIS law of Cinos. As a result, the ratio of the reflected to the forward RF power could be kept to less than 4% during the long-pulse plasma discharge of 31 minutes 45 seconds.

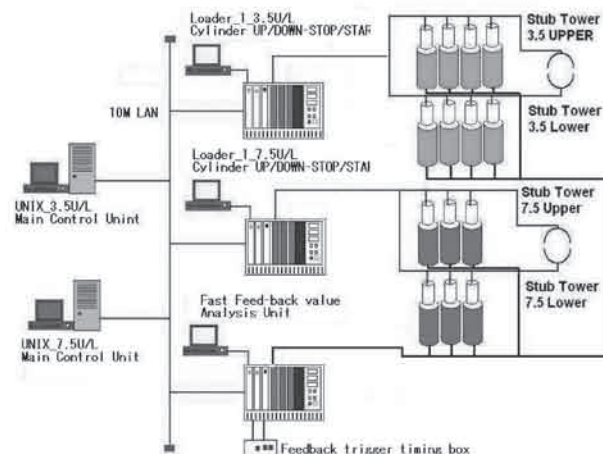


Fig. 20 Liquid stub Feedback computer control system

(3) Data Acquisition and Analysis system for CHS

The total operating time of the Cinos computer system was about 1500 hours in this fiscal year. There was no shutdown time caused by hardware or software trouble. The Cinos system was improved both in the core computer and the periphery modules as well as software resources. The new VME computer module has a faster processing speed than the old one. The number of AD/c input channels increased as well.

The main purpose of the improvement is to keep the data acquisition time short and to cope with the increase in the experimental data. More details about the new equipment are as follows:

- [1] The VME computer module board for the data acquisition was changed, because the amount of data to be processed becomes now five times of the initial design. The computer clock speed is now 700 MHz instead of 60 MHz. The VME memory size was extended from 768 M byte to 1Gbyte, because the speed of the computer can not be improved without increasing memory size simultaneously.
- [2] Six CAMAC fast AD/C modules (25 MHz, 12 bit, 4 CH) are installed.
- [3] Experimental data are stored in the RAID system (Level. 5) of one computer system. The RAID system is sensitive to vibration from the outside and has a risk of crashing, because it contains a mechanically rotating structure. Therefore, an additional computer has been prepared for back-up, which can store the data of about 5000 CHS shots. When the data overflow, the old data are transferred and stored in a digital linear tape (DLT) device.

(4) Development of a DHCP operating system by MAC address administration

The necessity for strict security management has risen with the spread of note-PCs. In the current year, we developed the DHCP operating system by the MAC address administration in collaboration with the computer and the information network center. In this system, the MAC address and user information are related and managed. The database of the MAC address is offered to all DHCP servers in the institute, and the user cannot connect without permission.

This system is composed of four parts; the registration part, the output part to DHCP server, the inspection part and the administration part, and all processing is run on a UNIX machine. The DHCP service user registers the MAC address and user information by the Web browser. When the registration is completed, the MAC address information is sent to the DHCP server and the user can use the network at once.

This system has operated since September, 2004 without trouble. We were able to promptly identify the source terminal using this registered information when a virus infection occurred.

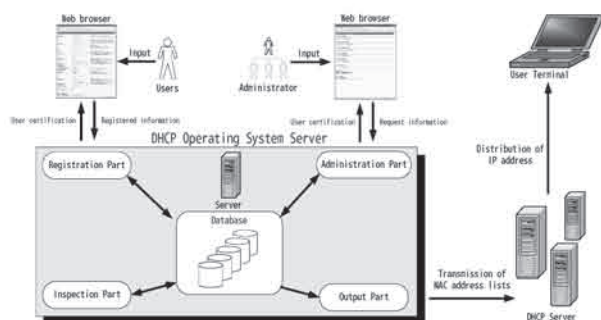


Fig. 21 Block diagram of the DHCP operating system using MAC address administration

(5) Shutter control for Charge Exchange Spectroscopy

In LHD, since the view windows must be protected from titanium gettering reliable shutter systems are very important. Each shutter is moved by compressed air or a super sonic wave motor and it is controlled by a PLC (Programmable Logic Controller) shutter control system. A new idea for shutter operation was presented for the charge exchange spectroscopy system. The shutter will be moved by the reciprocal action of a control current and the magnetic field in LHD to protect an optical mirror of the system. Figure 22 shows the principle of the shutter and its control system. The PLC controls a power supply and a SSR (Solid State Relay) circuit. The SSR circuit controls the current directions to 4 shutters.

In this experimental campaign, this new shutter failed. The failure will be corrected by the next experimental campaign.

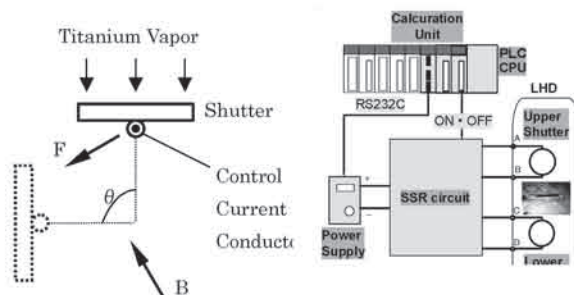


Fig. 22 Principle of the shutter and the control system

(6) Construction of the Network Quarantine room

Recently, computer virus infections are big problem in the network system. Our institute has ordered the installation of vaccine software for all PC. Also the NIFS mail server detects viruses and rejects mail or doubtful appended files.

This year, many virus infections were introduced by the laptop PCs brought on from the outside. No PC that was infected by a virus outside the institute should be connected to the campus LAN directly. The network quarantine room was constructed in the institute, that was connected to an outside Firewall. The person who brings a laptop PC must install the newest vaccine software, and he must scan the disk of the PC in the room. Many viruses have been detected in the network quarantine room. This room is important as a countermeasure against viruses. Figure 23 shows a snapshot of the network quarantine room.



Fig. 23 Snapshot of the network quarantine room.

(7) Management and maintenance of the LHD-LAN

The LHD-LAN has been provided for LHD experiments. As the LHD experiment progresses, a large number of computers have been connected to the LHD-LAN, a large amount of data has been stored in them and a high-performance data transfer environment has been required. The Gigabit network system with high-performance was installed in the LHD-LAN in FY 2000 and it is working. In FY 2004, our contributions are as follows in addition to the regular management and maintenance;

- 1) Adaptation of the new DHCP system with the MAC Address Certification.
- 2) Increase of SNET nodes.
- 3)

Increase of Optical Fiber Cables.

1) The following work was carried out so that the MAC Address Certification System was running in LHD-LAN. The MAC Address Certification System was a new security standard of DHCP service proposed by the NIFS Information Security Committee.

a) Because the MAC address certification could not be constructed with the DHCP service originally included in the Windows Operating System which had been used in the LHD-LAN, an ISC DHCP server program which enabled the MAC address certification was installed into UNIX servers in LHD-LAN, and the new service was started.

b) The environment to forward the database made by the MAC Address Certification System developed by the NIFS MAC Address Certification System Project to DHCP servers of LHD-LAN was built. The environment is based on the following application software; Openssh, rsync, sudo and others.

c) The new DHCP system was running on servers in the LHD experiment analysis LAN. In order to provide the new DHCP service in another LHD subnet, LHD diagnosis client LAN, the DHCP Relay Agent was defined in a router of the LHD-LAN.

2) The remote participation system of LHD experiments via Super-SINET called SNET was established in FY 2000. By FY 2003, 7 nodes of SNET were installed at University of Tokyo, Nagoya University, Kyoto University (Uji Campus), Kyushu University, Tohoku University, Tokyo Institute of Technology and Hiroshima University. In this FY, 2 nodes of SNET were newly installed at Kyoto University (Yoshida Campus) and University of Tokyo (Depart. of Technology).

3) Many Optical Fiber Cables have been provided for the LHD experiment. They are used for networking or transmission of the LHD operational information. In FY 2004, 80 Optical Fiber Cables were laid in the LHD building. The latest block diagram of LHD-LAN is shown in Figure 24.

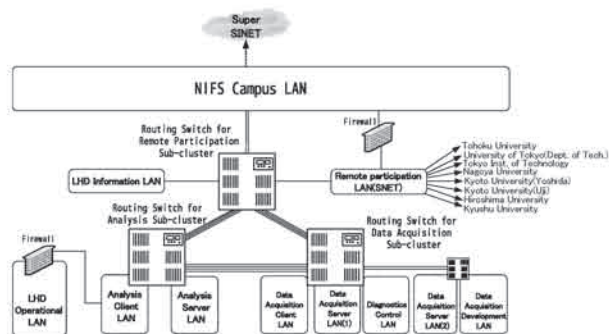


Fig. 24 Block diagram of LHD-LAN

(8) Programming lecture on Visual Basic(VB)

We have held a training course of the computer programming of the GUI(graphical user interface) using VB for other universities and institutes technical staffs as a technical exchanges. Also in our institute, there was a request for a VB training course. Therefore we held the course 6 times during the period from June to August 2004.

There were 11 participants. In this course, we lectured on the following contents; the foundation of VB, the foundation of socket communication, the control of a sequencer with socket communication, the control of a device with RS-232C communication and the development of an application by DLL(Dynamic Link Library). We think that they improved their skills in VB by this course.

Figure 25 shows a view of the training course.



Fig. 25 Snapshot of Visual Basic Lecture

6. Symposium on Technology and Technical Exchange

(1)The Symposium on Technology

The Symposium on Technology was held on March 3 and 4, 2005 in the Suita campus of Osaka University. There were 650 participants from many Japanese universities, national laboratories, technical colleges and some industries. In this symposium 242 papers were presented in 8 oral sessions and a poster session. Technical experience and new techniques were reported and discussed. Ten papers were presented from our department. The titles of the presentations were as follows; Transmittance Reduction of the Cover Glasses Installed on the LHD Thomson Scattering Diagnostic View Window, Analysis of Induced Errors, Construction of Real Time Simulation device and Dynamic Simulation of a Helium Refrigerator/Liquefier for LHD, Failure investigation during the LHD experiments, Development of DHCP operating system by MAC address administration, The operating of the gate valve control system for Large Helical Device (LHD), Introduction of 250MVA Motor-Generator driving control system at NIFS, Development of Interlock Systems and AGC System for ICRF Heating on the LHD and Safety interlock system of HIBP etc.

In the steering committee held during the symposium, Institute for Molecular Science was adopted as a next host organization and we exchanged our views frankly about symposium as it ought to be. Figure26 shows a snapshot of the poster session.

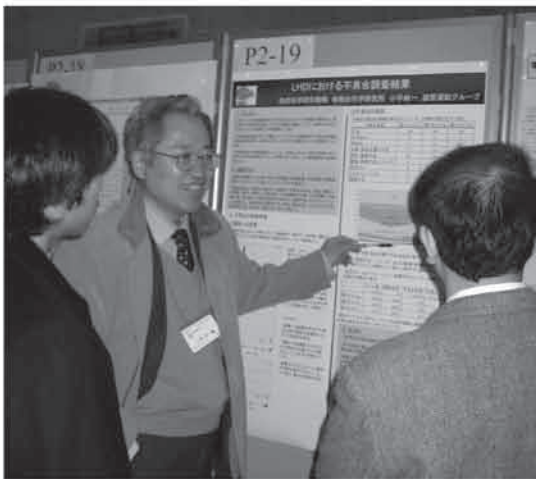


Fig.26 Snapshot of the poster session

(2) Technical exchanges

Technical exchanges between our department and other institutes or universities were held in order to improve the technical skill of the staff. Thirty-five technical officials of other laboratories participated in our 8 exchange programs in this fiscal year. The program names and participants were as follows; “Symposium on Safety and Health Management in the Laboratory” from 25 universities and 4 institutes, “Electronics technology” and “Vacuum technology” from Chubu University, “Radiation detection technology”, and “Cryogenic technology” from Institute for Molecular Science, “Structure analytic simulation technology” from Kyoto University, and “Machining process technology” from Mie University.

V. Department of Administration

The Department of Administration principally handles general affairs and accounting work. In the very first fiscal year of the new institute, the effort has been made on the establishment of its organization and the preparation of facilities. Especially, intensive work has been done for the planning of construction in the new site which is urgently needed for promoting the Large Helical Device Project.

The Department consists of 4 divisions, namely, General Affairs, Joint Research, Financial Affairs, and Facilities, details of which will be described in the following.

General Affairs Division

The General Affairs Division consists of 4 units: General Affairs, Documents and Legal Affairs, Personnel, and Science Information and Library. Major responsibilities of this division are to provide administrative support for the activities of the Board of Councilors and the Advisory Council for Research and Management, preparation of various ceremonies and events, documents and public information services, enactment of rules and regulations, general personnel administration and library services.

Staff Members

(2004 Fiscal Year)

Director-General	1
Professors	42
Associate Professors	36
Research Associates	59
Administrative Staff	43
Technical & Engineering Staff	47
Visiting Scientists	22
Total	251

Books and Journals

(2004 Fiscal Year)

Japanese Books	13,160
Books in Other Languages	43,211
Total (vols)	56,371
Japanese Journals	270
Journals in Other Languages	775
Total (titles)	1,045

Financial Affairs Division

The Financial Affairs Division has 3 sections and 2 special members: Financial Affairs, Accounting, Contract, and 2 expert staff members in charge of Budget and Government Procurement. The sections and expert staff members are responsible for the office work relating to budget, revenue/ expenditure, settlement of accounts, payment of allowance, supply of articles, national property, official residence, and guard of government office building.

Settlement

(2004 Fiscal Year)
(in million of Yen)

Salaried Wages	2,081
Operating Cost	8,792
Equipment	0
Site & Buildings	23
Grant-in-Aid for Scientific Research	226
Total	11,122

Facilities Division

The Facilities Division consists of 4 units: General Affairs Section of Facilities Division, Planning Section of Facilities Division, Control and Maintenance Section of Facilities Division and The Building and Repairs Section of Facilities Division. They are responsible for the office work relating to the budget, planning and designing, contract, supervision of the work of construction and maintenance for office building, campus road, equipment of lighting, telephone, power station, air conditioning, water service, gas service, elevator, crane etc. Recently, they have promoted Facility Management. (Facility Management combines proven management practices with most current technical knowledge to provide human and effective work environments. It is the business practice of planning, providing and managing productive work environments.)

Research stuff Building, Administration Building, the Library, the Guest House, the Central Work-shops, and six main laboratories; Cryogenics and Superconductivity Laboratories, the Plasma Heating Laboratories, the Plasma Diagnostics Laboratories, the Computer Center and Simulation Laboratories, the R & D Laboratories and Large Helical Devices Building, were constructed from 1990 to 2000.

Site and Buildings

(2004 Fiscal Year)

Toki	
Site	464,445 m ²
Buildings	
Total Building Area	39,235 m ²
Total Floor Space	69,759 m ²

Research Cooperation Division

The Research Cooperation Division consists of three units, #I, #II and #III, which are in charge of arranging international cooperation, and inter university coordination, respectively. The latter deals with subsidy for scientific research and support the graduate school program.

Joint Research

(2004 Fiscal Year)

LHD Joint Planning Research			Joint Research			Joint Research Using Computer			Workshop			Total		
Applications	Applications Accepted	Researchers Accepted	Applications	Applications Accepted	Researchers Accepted	Applications	Applications Accepted	Researchers Accepted	Applications	Applications Accepted	Researchers Accepted	Applications	Applications Accepted	Researchers Accepted
36	3	221	234	234	1,892	53	52	136	16	16	444	339	333	2693

Number of Graduate School Students

(Research Students)

(2004 Fiscal Year)

Affiliation	Degree/Year	Master's Course	Doctor' s Course	Total
Nagoya Univ. Graduate School		6	3	9
Tokyo Univ. Graduate School		0	4	4
Others		9	9	18
Total		15	16	31

(The Graduate University for Advanced Studies Students)

(2004 Fiscal Year)

Doctor's Course			
Grade 1	Grade 2	Grade 3	Total
5	8	11	24

International Exchange

Number of Foreign Researchers

(2004 Fiscal Year)

Invited by Ministry of Education, Science, Sports and Culture	Joint Research	Workshop Participants	Visitors	Invited by Japan Society for the Promotion of Science	Others	Total
20	68	73	3	0	3	167

Foreign Researchers to NIFS

(2004 Fiscal Year)

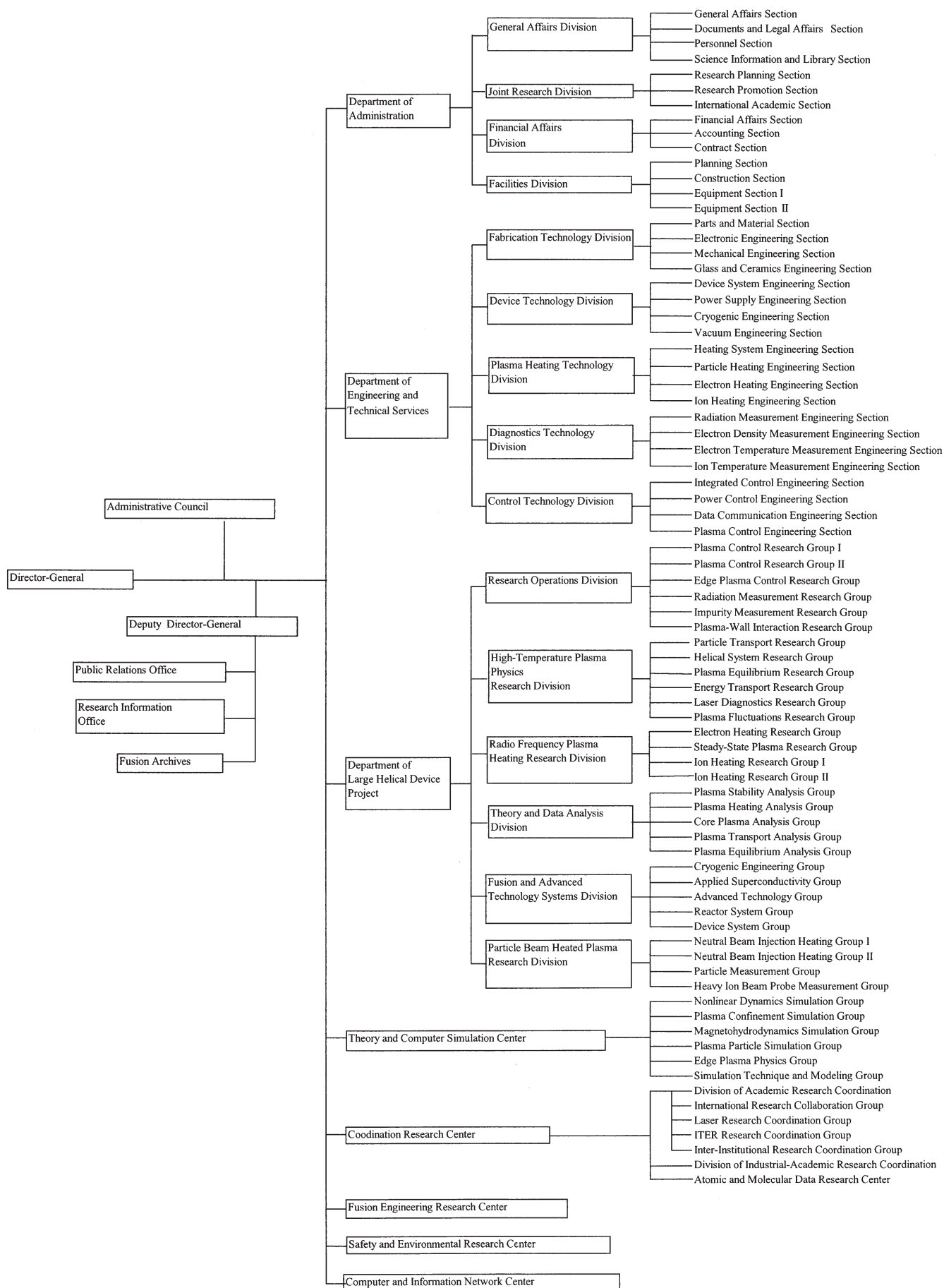
P.R.China	U.S.A.	Russia	India	F.R.G.	Ukraina	R.Korea	Spain	Others	Total
44	31	27	4	15	3	11	0	32	167

NIFS Researchers to Overseas

(2004 Fiscal Year)

U.S.A.	F.R.G	P.R.China	Russia	France	R.Korea	Italy	Switzerland	U.K.	Others	Total
60	14	25	3	9	17	8	1	4	58	199

APPENDIX 1. Organization of the Institute



APPENDIX 2. Members of Committees

Advisory Council for Research and Management

IZAWA, Yasukazu	Director, Institute of Laser Engineering, Osaka University	NODA, Nobuaki	Director of Fusion Engineering Research Center, NIFS
OHSAWA, Yukiharu	Professor, Graduate School of Science, Nagoya University	UDA, Tatsuhiko	Director of Safty and Environmental Research Center, NIFS
OKAJIMA, Shigeki	Professor, School of Engineering, Chubu University		
OGAWA, Yuichi	Director, High Temperature Plasma Center, The University of Tokyo		
SASAO, Mamiko	Professor, Graduate School of Engineering, Tohoku University		
CHO, Teruji	Director, Plasma Research Center, University of Tsukuba		
HINO, Tomoaki	Professor, Graduate School of Engineering, Hokkaido University		
FUKUYAMA, Atsushi	Professor, Graduate School of Engineering, Kyoto University		
MATSUDA, Shinzaburo	Executive Director, Japan Atomic Energy Research Institute (JAERI)		
YOSHIDA, Naoaki	Professor, Research Institute for Applied Mechanics, Kyusyu University		
SUDO, Shigeru	Deputy Director-General, NIFS		
KOMORI, Akio	Director of Department of Large Helical Device Project, NIFS		
OKAMOTO, Masao	Director of Theory and Computer Simulation Center, NIFS		
OHYABU, Nobuyoshi	Director of Research Operations Division, NIFS		
KAWAHATA, Kazuo	Director of High-Temperature Plasma Physics Research Division, NIFS		
OHKUBO, Kunizo	Director of Radio Frequency Plasma Heating Research Division, NIFS		
HAYASHI, Takaya	Director of Theory and Data Analysis Division, NIFS		
MITO, Toshiyuki	Director of Fusion and Advanced Technology Systems Division, NIFS		
SATO, Motoyasu	Director of Coordination Research Center, NIFS		

APPENDIX 3. List of Staff

Director-General

MOTOJIMA, Osamu

Deputy Director-General

SUDO, Shigeru

Department of Large Helical Device Project

Prof. KOMORI, Akio (Executive Director)

(Research Operations Division)

Prof. OHYABU, Nobuyoshi (Director)

Prof. KOMORI, Akio

Prof. YAMAZAKI, Kozo

Prof. OKAMURA, Shoichi

Prof. NAGAYAMA, Yoshio

Assoc. Prof. IGUCHI, Harukazu

Assoc. Prof. PETERSON, Byron Jay

Assoc. Prof. MORISAKI, Tomohiro

Assoc. Prof. KUBOTA, Yusuke

Assoc. Prof. MORITA, Shigeru

Res. Assoc. SAKAMOTO, Ryuichi

Res. Assoc. ISOBE, Mitsutaka

Res. Assoc. MASUZAKI, Suguru

Res. Assoc. KOBAYASHI, Masahiro

Res. Assoc. SHOJI, Mamoru

Res. Assoc. GOTO, Motoshi

Res. Assoc. MIYAZAWA, Jun-ichi

Res. Assoc. SUZUKI, Chihiro

Res. Assoc. ASHIKAWA, Naoko

Res. Assoc. INAGAKI, Shigeru

Res. Assoc. YOSHIMURA, Shinji

(High-Temperature Plasma Physics Research Division)

Prof. KAWAHATA, Kazuo (Director)

Prof. SUDO, Shigeru

Prof. YAMADA, Hiroshi

Prof. NARIHARA, Kazumichi

Prof. TOI, Kazuo

Assoc. Prof. TANAKA, Kenji

Assoc. Prof. SAKAKIBARA, Satoru

Assoc. Prof. WATANABE, Kiyomasa

Assoc. Prof. SATO, Kuninori

Assoc. Prof. TANAKA, Masayoshi

Res. Assoc. TOKUZAWA, Tokihiko

Res. Assoc. AKIYAMA, Tsuyoshi

Res. Assoc. EMOTO, Masahiko

Res. Assoc. NARUSHIMA, Yoshiro

Res. Assoc. NAKANISHI, Hideya

Res. Assoc. NISHIMURA, Shin

Res. Assoc. MUTO, Sadatsugu

Res. Assoc. TAMURA, Naoki

Res. Assoc. YAMADA, Ichihiko

Res. Assoc. MINAMI, Takashi

Res. Assoc. FUNABA, Hisamichi

Res. Assoc. OHDACHI, Satoshi

(Radio Frequency Plasma Heating Research Division)

Prof. OHKUBO, Kunizo (Director)

Prof. MUTOH, Takashi

Prof. NAKAMURA, Yukio

Prof. KUMAZAWA, Ryuhei

Assoc. Prof. KUBO, Shin

Assoc. Prof. SIMOZUMA, Takashi

Res. Assoc. YOSHIMURA, Yasuo

Res. Assoc. IGAMI, Hiroe

Res. Assoc. NISHIURA, Masaki

Res. Assoc. SEKI, Tetsuo

Res. Assoc. SAITO, Kenji

(Theory and Data Analysis Division)

Prof. HAYASHI, Takaya (Director)

Prof. SANUKI, Heiji

Prof. ITOH, Kimitaka

Prof. SUGAMA, Hideo

Prof. NAKAJIMA, Noriyoshi (Additional Post)

Assoc. Prof. KANNO, Ryutaro

Assoc. Prof. ICHIGUCHI, Katsuji

Res. Assoc. YOKOYAMA, Masayuki

Res. Assoc. MIZUGUCHI, Naoki

Res. Assoc. SATAKE, Shinsuke

Res. Assoc. SUZUKI, Yasuhiro

Res. Assoc. TODA, Shin-ichiro

Res. Assoc. YAMAGISHI, Osamu

※ This list was made up as of March 31, 2005.

(Fusion and Advanced Technology Systems Division)

Prof. MITO, Toshiyuki (Director)
Prof. SATO, Motoyasu
Prof. IMAGAWA, Shinsaku
Prof. SAGARA, Akio
Prof. NODA, Nobuaki (Additional Post)
Assoc. Prof. TAKAHATA, Kazuya
Assoc. Prof. YANAGI, Nagato

Assoc. Prof. CHIKARAISHI, Hirotaka
Assoc. Prof. YAMADA, Syuichi
Assoc. Prof. MAEKAWA, Ryuji
Res. Assoc. HAMAGUCHI, Shinji
Res. Assoc. TAMURA, Hitoshi
Res. Assoc. IWAMOTO, Akifumi
Res. Assoc. SEO, Kazutaka

(Particle Beam Heated Plasma Research Division)

Prof. KANEKO, Osamu (Director)
Prof. IDA, Katsumi
Prof. TAKEIRI, Yasuhiko
Prof. HAMADA, Yasuji
Assoc. Prof. OKA, Yoshihide
Assoc. Prof. OZAKI, Tetsuo
Assoc. Prof. FUJISAWA, Akihiko
Res. Assoc. OSAKABE, Masaki

Res. Assoc. NAGAOKA, Ken-ichi
Res. Assoc. TSUMORI, Katsuyoshi
Res. Assoc. YOSHINUMA, Mikiro
Res. Assoc. IKEDA, Katsunori
Res. Assoc. SHIMIZU, Akihiro
Res. Assoc. NISHIZAWA, Akimitsu
Res. Assoc. IDO, Takeshi

Theory and Computer Simulation Center

Prof. OKAMOTO, Masao (Director)
Prof. HORIUCHI, Ritoku
Prof. NAKAJIMA, Noriyoshi
Prof. ISHIGURO, Seiji
Prof. SAKAGAMI, Hitoshi
Assoc. Prof. TODO, Yasushi
Assoc. Prof. TOMITA, Yukihiro
Assoc. Prof. WATANABE, Tomohiko

Assoc. Prof. NAKAMURA, Hiroaki
Assoc. Prof. MIURA, Hideaki
Res. Assoc. ISHIZAWA, Akihiro
Res. Assoc. OHTANI, Hiroaki
Res. Assoc. ITO, Atsushi
Res. Assoc. TAKAYAMA, Arimichi
Res. Assoc. ISHIZAKI, Ryuichi
Res. Assoc. TAMURA, Yuichi

Coordination Research Center

Prof. SATO, Motoyasu (Director, Additional Post)

(Division of Academic Research Coordination)

Prof. SUDO, Shigeru (Chief, Additional Post)

[International Research Collaboration Group]

Prof. MATSUOKA, Keisuke (Group Chief)
Prof. YAMAZAKI, Kozo (Additional Post)
Prof. WATARI, Tetsuo

Prof. NODA, Nobuaki (Additional Post)
Assoc. Prof. NAMBA, Chusei
Assoc. Prof. HIROOKA, Yoshihiko

[Laser Research Coordination Group]

Prof. OKAMOTO, Masao (Group Chief, Additional Post)
Prof. SAKAGAMI, Hitoshi (Additional Post)
Assoc. Prof. TAJIMA, Teruhiko

Assoc. Prof. OZAKI, Tetsuo (Additional Post)
Res. Assoc. IWAMOTO, Akifumi
(Additional Post)

[ITER Research Coordination Group]

Prof. NAKAMURA, Yukio (Group Chief, Additional Post)
Assoc. Prof. TODO, Yasushi (Additional Post)
Res. Assoc. SEO, Kazutaka (Additional Post)

[Inter-Institutional Research Coordination Group]

Prof. YAMADA, Hiroshi (Group Chief, Additional Post)
Prof. SUGAMA, Hideo (Additional Post)
Assoc. Prof. TANAKA, Motohiko

(Division of Industrial-Academic Research Coordination)

Prof. SATO, Motoyasu (Director, Additional Post)
Prof. MITO, Toshiyuki (Additional Post)
Assoc. Prof. YANAGI, Nagato (Additional Post)
Assoc. Prof. SHIMOZUMA, Takashi (Additional Post)

Assoc. Prof. CHIKARAISHI, Hirotaka
(Additional Post)
Assoc. Prof. YAMADA, Shuichi
(Additional Post)
Assoc. Prof. MAEKAWA, Ryuji
(Additional Post)

(Atomic and Molecular Data Research Center)

Prof. KATO, Takako (Chief)
Prof. MORE, Richard
Assoc. Prof. MURAKAMI, Izumi

Res. Assoc. SAKAUE, Hiroyuki
Res. Assoc. KATO, Daiji

Fusion Engineering Research Center

Prof. NODA, Nobuaki (Director)
Prof. NISHIMURA, Arata
Prof. MUROGA, Takeo
Prof. SAGARA, Akio (Additional Post)
Prof. IMAGAWA, Shinsaku (Additional Post)

Assoc. Prof. NAGASAKA, Takuya
Assoc. Prof. KUBOTA, Yusuke
(Additional Post)
Res. Assoc. HISHINUMA, Yoshimitsu
Res. Assoc. TANAKA, Teruya
Res. Assoc. KATO, Daiji (Additional Post)

Safety and Environmental Research Center

Prof. UDA, Tatsuhiko (Director)
Prof. ASAKURA, Yamato
Prof. NISHIMURA, Kiyohiko
Assoc. Prof. SAKUMA, Yoichi

Assoc. Prof. KAWANO, Takao
Res. Assoc. YAMANISHI, Hirokuni
Res. Assoc. SUGIYAMA, Takahiko

Computer and Information Network Center

Prof. HORIUCHI, Ritoku (Director, Additional Post)
Prof. DEN, Mitsue

Assoc. Prof. TSUDA, Kenzo
Res. Assoc. YAMAMOTO, Takashi

Guest Professor

Prof. KUSAMA, Yoshinori (Japan Atomic Energy Research Institute (JAERI))	(Apr. 1, '04–Mar. 31, '05)
Prof. SASAO, Mamiko (Tohoku University)	(Apr. 1, '04–Mar. 31, '05)
Prof. MATSUBARA, Youichi (Musashi Institute of Technology)	(Apr. 1, '04–Mar. 31, '05)
Prof. MATSUOKA, Mamoru (Mie University)	(Apr. 1, '04–Mar. 31, '05)
Prof. YOSHIZAWA, Akira (The University of Tokyo)	(Apr. 1, '04–Mar. 31, '05)
Prof. MIMA, Kunioki (Osaka University)	(Apr. 1, '04–Mar. 31, '05)
Prof. WATANABE, Kunihiro (Japan Agency for Marine - Earth Science and Technology)	(Apr. 1, '04–Mar. 31, '05)
Prof. OHSAWA, Yukiharu (Nagoya University)	(Apr. 1, '04–Mar. 31, '05)
Prof. NISHIHARA, Motohisa (Hitach Ltd.(retired))	(Apr. 1, '04–Mar. 31, '05)
Prof. IKEDA, Tetsuo (Nagoya Institute of Technology)	(Apr. 1, '04–Mar. 31, '05)
Prof. OKUNO, Kenji (Shizuoka University)	(Apr. 1, '04–Mar. 31, '05)
Prof. OGAWA, Yuichi (The University of Tokyo)	(Apr. 1, '04–Mar. 31, '05)
Prof. TAKEUCHI, Takao (Superconducting Materials Center, National Institute for Materials Science)	(Apr. 1, '04–Mar. 31, '05)
Assoc. Prof. MURAKAMI, Sadayoshi (Kyoto University)	(Apr. 1, '04–Mar. 31, '05)
Assoc. Prof. ISHII, Kameo (University of Tsukuba)	(Apr. 1, '04–Mar. 31, '05)
Assoc. Prof. IWAKUMA, Masataka (Kyushu University)	(Apr. 1, '04–Mar. 31, '05)
Assoc. Prof. KOIZUMI, Norikiyo (Japan Atomic Energy Research Institute (JAERI))	(Apr. 1, '04–Mar. 31, '05)
Assoc. Prof. OIKAWA, Shun-ichi (Hokkaido University)	(Apr. 1, '04–Mar. 31, '05)
Assoc. Prof. TAKAMARU, Hisanori (Chubu University)	(Apr. 1, '04–Mar. 31, '05)

Assoc. Prof. KOHNO, Hirohiko (Tohoku University)	(Apr. 1, '04–Mar. 31, '05)
Assoc. Prof. SHIRAGA, Hiroyuki (Osaka University)	(Apr. 1, '04–Mar. 31, '05)
Assoc.Prof. HIROHATA, Yuko (Hokkaido University)	(Apr. 1, '04–Mar. 31, '05)
Prof. DOLAN, Thomas J. (Idaho National Engineering & Environmental Laboratory)	(Oct. 6, '03–Apr. 30, '04)
Prof. HORACEK, Jiri (Charles University)	(Jan. 10, '04–Apr. 10, '04)
Prof. CHUTOV, Yuri. (Taras Shevchenko Kiev University)	(Jan. 9, '04–Apr 14, '04)
Prof. VYACHWSLAVOV, Leonid N. (Budker Institute of Nuclear Physics)	(Jan. 12, '04–May. 12, '04& Jan.10, '05–May. 10, '05)
Prof. HAMEIRI, Eliezer (New York University)	(June 2, '04–Sept. 2, '04)
Prof. YELISEYEVA, Olha (Karpenko Physico- Mechanical Institute, National Academy of science Ukraine)	(Aug. 2, '04–Nov. 2, '04)
Prof. ECKSTEIN, Wolfgang (Max-Planck-Institute for Plasma Physics)	(Aug. 26, '04–Dec.2 '04)
Prof. CHU, Ming-Sheng (General Atomics)	(Sept 1, '04–Nov. 30, '04)
Prof. YU, Wei (Shanghai Institute of Optics and Fine Mechanism)	(Sept 1, '04–Dec. 28, '04)
Prof. RHEE, Yong-Joo (Korea Atomic Energy Research Institute)	(Oct 1, '04–Dec. 31, '04)
Prof. LIVSHITS, Alexander I. (Bonch-Bruevich University of Electrotechnical Communications)	(Dec. 1, '04–Mar. 31, '05)
Prof. WELLER, Arthur (Max-Planck-Institute for Plasma Physics)	(Jan. 5, '05–Apr. 4, '05)
Prof. TSKHAKAYA, David (Institute of Theoretical Physics, University of Innsbruck)	(Jan. 6, '05–Apr. 15, '05)
Assoc. Prof. VRANJES, Jovo (Centre for Plasma Astrophysics(CPA))	(Mar. 2, '04–Jun. 1, '04)
Assoc. Prof. GAO, Zhe (Tsinghua University)	(Apr. 13, '04–July 16, '04)
Assoc. Prof. RALCHENKO, Yuri (Maryland University, College Park)	(July 24, '04–Oct. 24, '04)
Assoc. Prof. KLEIBER, Ralf A. (Max-Planck-Institute for Plasma Physics)	(Sep. 3, '04–Dec. 6, '04)
Assoc. Prof. KHARCHEV, Nikolay K (General Physics Institute of Russian Academy of Sciences)	(Dec. 1, '04–Feb. 28, '05)
Assoc. Prof. NEUDATCHIN, Sergei (Kurchatov Institute)	(Jan. 12, '05–Apr. 15, '05)

COE Research Fellow

HASEGAWA, Hiroki	(Apr. 1, '04–Mar. 31, '05)
TAKAGI, Shoji	(Apr. 1, '04–Oct. 30, '04)
GONCHAROV, Pavel	(Oct 1, '04– Mar. 31, '05)
KASUYA, Naohiro	(Apr. 1, '04–Mar. 31, '05)
MATSUMOTO, Yoshikatsu	(Apr. 1, '04–Mar. 31, '05)
ISHIZAWA, Akihiro	(Apr. 1, '04–Sep. 30, '04)
ISHIHARA, Norio	(Apr. 1, '04–Apr. 30, '04)
SUNO, Hiroya	(Apr. 16, '04–Mar. 31, '05)
SONG, Mi-yong	(Jun. 2, '04–Mar. 31, '05)
NAKAMURA, Ki-ichiro	(Jun. 16, '04–Mar. 31, '05)
MICHAEL, Clive Alvin	(July 1, '04–Mar. 31, '05)
NUNAMI, Masanori	(Dec. 1, '04–Mar. 31, '05)

Research Fellow (Science research)

MATSUBARA, Akihiro	(Apr. 1, '04–Mar. 31, '05)
KOBUCHI, Takashi	(Apr. 1, '04–Mar. 31, '05)
GONCHAROV, Pavel	(Apr. 1, '04–Sep. 30, '04)
NAGASHIMA, Yoshihiko	(Apr. 16, '04–Mar. 31, '05)
TAKAGI, Shoji	(Nov. 1, '04–Mar. 15, '05)

JSPS Research Fellow

KOBAYASHI, Masahiro	(Apr. 1, '02–Sep. 30, '04)
SATO, Masahiko	(Apr. 1, '04–Mar. 31, '05)
YAMAGISHI, Osamu	(Apr. 1, '03–Dec. 31, '04)
<i>(Postdoctoral Fellowships for Foreign Researchers)</i>	
PAVLICHENKO, R.O.	(Apr. 1, '03–Mar. 31, '05)
LENNAERT, V.V.	(Apr. 10, '03–Jan. 9, '04)
<i>(Invitation Fellowship Programs for Research in Japan)</i>	
McCORMICK, G.K	(Nov. 17, '04–Dec. 3, '04)

Department of Administration

ARAI, Akio	(Department Director)
------------	-----------------------

General Affairs Division

YAMAMOTO, Yoshio	Director
DEGUCHI, Hidenori	Deputy Director
General Affairs Section	
MUTO, Hideyuki	Chief
Documents and Legal Affairs Section	
HIRANO, Keiji	Chief
Personnel Section	
ICHIOKA, Akihiro	Chief
Science Information and Library Section	
HIRANO, Keiji	Chief, Additinal Post

Financial Affairs Division

FUJINAMI, Toyohiko	Director
TAKEDA, Minoru	Deputy Director
DOHMAE, Hiroki	Chief
SHIROSHIMA, Toshiaki	Chief
Financial Affairs Section	
MORIKAWA, Harunori	Chief
Accounting Section	
YAMADA, Kenji	Chief
Contract Section	
KITOH, Yumiko	Chief

Joint Research Division

KOKUDAI, Masatoshi	Director
MIYAKE, Ryouichi	Deputy Director
Research Planning Section	
TAKEUCHI, Shoji	Chief
Research Promotion Section	
TAKEICHI, Masahiro	Chief
International Academic Section	
MATSUURA, Katsunori	Chief

Facilities Division

ARAKI, Kazuo	Director
WATANABE, Yasuo	Deputy Director
Planning Section	
AKAGAWA, Yasuhiro	Chief
Construction Section	
NAKAGAWA, Shin-ichi	Chief
Equipments Section I	
HAYASHI, Hidenori	Chief
Equipments Section II	
OHTA, Tsuyoshi	Chief

Department of Engineering and Technical Services

YAMAUCHI, Kenji Department Director

(Fabrication Technology Division)

TANIGUCHI, Yoshiyuki Director

Parts and Material Section

BABA, Tomosumi Chief

Electronic Engineering Section

ITO, Yasuhiko Chief

Mechanical Engineering Section

SUGITO, Syoji Chief

Glass and Ceramics Engineering Section

OKADA, Kohji Chief

(Plasma Heating Technology Division)

TAKITA, Yasuyuki Director

Heating System Engineering Section

KATOH, Akemi Chief

Particle Heating Engineering Section

ASANO, Eiji Chief

Electron Heating Engineering Section

KOBAYASHI, Sakuji Chief

Ion Heating Engineering Section

SHIMPO, Fujio Chief

(Control Technology Division)

KODAIRA, Jun-ichi Director

Integrated Control Technology Section

TSUKADA, Kiwamu Chief

Power Control Engineering Section

TAKAHASHI, Chihiro Chief

Data Communication Engineering Section

YOKOTA, Mitsuhiro Chief

Plasma Control Engineering Section

KATOH, Takeo Chief

(Device Technology Division)

IIMA, Masashi Director

Device System Engineering Section

YONEZU, Hiroaki Chief

Power Supply Engineering Section

YASUI, Koji Chief

Cryogenic Engineering Section

MORIUCHI, Sadatomo Chief

Vacuum Engineering Section

HAYASHI, Hiromi Chief

(Diagnostics Technology Division)

MIYAKE, Hitoshi Director

Radiation Measurement Engineering Section

KONDO, Tomoki Chief

Electron Density Measurement Engineering
Section

KATOH, Shinji Chief

Electron Temperature Measurement Engineering
Section

KOJIMA, Mamoru Chief

Ion Temperature Measurement Engineering
Section

KOMOTO, Takeo Chief

This list was made up as of March 31,2005

APPENDIX 4. List of Publications I (NIFS Series)

- NIFS-797 M.I. Mikhailov, K. Yamazaki
Fast Particles Confinement in Stellarators with Both Poloidal-Pseudo-Symmetry and Quasi-Isodynamicity
Apr. 2004
- NIFS-798 T. Takahashi, T. Kato, N. Iwasawa and Y. Kondoh
Power Deposition by Neutral Beam Injected Fast Ions in Field-Reversed Configurations
Apr. 2004
- NIFS-799 V.S. Voitsenya, D.I. Naidenkova, Y. Kubota, S. Masuzaki, A. Sagara, K. Yamazaki
On the Possibility to Increase Efficiency of Conditioning of Vacuum Surfaces by Using a Discharge in a Hydrogen-noble Gas Mixture
Apr. 2004
- NIFS-800 S.-I. Itoh, K. Itoh, A. Yoshizawa and N. Yokoi
Periodic Change of Solar Differential Rotation
May 2004
- NIFS-801 V.S. Voitsenya, A. Sagara, A.I. Belyaeva
Effect of Exposure inside the LHD Vessel on Optical Properties of Stainless Steel Mirrors
Jun 2004
- NIFS-802 T.J. Dolan and K. Yamazaki
Upgrade and Benchmarking of the NIFS Physics-Engineering-Cost Code
July 2004
- NIFS-803 Contributions to 31st European Physical Society Conference on Plasma Physics (London, UK, 28 June to 2 July, 2004) from NIFS
Aug. 2004
- NIFS-804 M. Tanaka
A Cluster of Personal Computers Equipped with Low-Latency Communication Software
Aug. 2004
- NIFS-805 P.H. Diamond, S.-I. Itoh, K. Itoh and T.S. Hahm
Review of Zonal Flows
Oct. 2004
- NIFS-806 H. Nakamura, N. Hatano and R. Shirasaki
Quantum Nernst Effect
Jan. 2005
- NIFS-807 H. Sugama and T.-H. Watanabe
Dynamics of Zonal Flows in Helical Systems
Jan. 2005
- NIFS-808 Collection of Contributions from NIFS to 20th IAEA Fusion Energy Conference (Vilamoura, Portugal, 1-6 Nov. 2004)
Jan. 2005
- NIFS-809 K. Itoh, S.-I. Itoh, M. Yagi
Self-annihilation of Magnetic Islands in Helical Plasmas
Feb. 2005
- NIFS-810 M. Yokoyama, L. Hedrick, K.Y. Watanabe and N. Nakajima
The Configuration Dependence of Ripple Transport in LHD by the Application of the GIOTA Code
Feb. 2005
- NIFS-811 K. Itoh, K. Hallatschek, S.-I. Itoh, P.H. Diamond, S. Toda
Coherent Structure of Zonal Flow and Onset of Turbulent Transport
Feb. 2005

- NIFS-DATA-85 I. Murakami, T. Kato, U.I. Safronova and A.A. Vasilyev
Dielectronic Recombination Rate Coefficients to Excited States of Boronlike Oxygen and Dielectronic
Satellite Lines
May 2004
- NIFS-PROC-55 Text of Simulation Science Open Lecture 2003
Apr. 2004
- NIFS-PROC-56 Proceedings of the Meeting on Large Scale Computer Simulation Research
Apr. 2004
- NIFS-PROC-57 (Eds.) T. Fujimoto, P. Beiersdorfer
Proceedings of The Japan-US Workshop on Plasma Polarization Spectroscopy and The Fourth
International Symposium on Plasma Polarization Spectroscopy
July 2004
- NIFS-PROC-58 Proceedings of the 7th Simulation Science Symposium
July 2004
- NIFS-PROC-59 F. Koike and D. Chenzhong (Eds.)
JSPS-CAS Core University Program Seminar Proceedings of Japan-China Joint Seminar on Atomic and
Molecular Processes in Plasma, March 6-11, 2004, Lanzhou, China
Feb. 2005
- NIFS-TECH-12 M. Tanaka
Beowulf Cluster Equipped with High-Speed Communication Software
May 2004

APPENDIX 5. List of Publications II (Journals, etc.)

- (1) Adachi, Y., Ninomiya, A., Uriu, Y., Ishigohka, T., Mito, T., Imagawa, S., Yanagi, N., Sekiguchi, H., Yamada, S.
Introduction of Fuzzy Logic Theorem for Quench Detection in Superconducting Coil System of the Large Helical Device
J. Cryo. Soc. Jpn. Vol.40, No.3 (Mar. 2004) pp.93-99
- (2) Aiba, N., Tokuda, S., Hayashi, T., Wakatani, M.
Simulation Study on the Motion of the Pressure Perturbation in an Axisymmetric Toroidal System
J. Phys. Soc. Jpn. Vol.73 (2004) pp.364-373
- (3) Aiba, N., Tokuda, S., Ishizawa, T., Okamoto, M.
Application of the Two-dimensional Newcomb Problem to Compute the Stability Matrix of External MHD Modes in a Tokamak
Plasma Phys. control. Fusion Vol.46, (Sep. 2004) pp.1699-1721
- (4) Aoki, J., Kiwamoto, Y., Soga, Y., Sanpei, A.
High-Fidelity Optical Transfer System for Two Dimensional Imaging of Density Distribution of a Pure Electron Plasma
Jpn. J. Appl. Phys Vol.43, No.10 (2004) pp.7267 - 7270
- (5) Aoki, J., Kiwamoto, Y., Soga, Y., Sanpei, A.
Novel Application of Electron Vortex Dynamics to the Alignment of Magnetic and Cylinder Axes
Jpn. J. Appl. Phys Vol.43, No.11 (2004) pp.7777 - 7781
- (6) Aramaki, M., Kato, K., Goto, M., Muto, S., Morita, S., Sasaki, K.
Development of a compact divertor simulator excited by helicon-wave discharge
Jpn. J. Appl. Phys. Vol.43, No.3 (Apr. 2004) pp.1164-1165
- (7) Asakura, Y., Sugiyama, T., Kawano, T., Uda, T., Tanaka, M., Tsuji, N., Katahira, K., Iwahara, H.
Application of Proton-conducting Ceramics and Polymer Permeable Membranes for Gaseous Tritium Recovery
J. Nucl. Sci. Technol. Vol.41, No.8(Aug. 2004) pp.863-870
- (8) Azechi, H., Shiraga, H., Nakai, M., Shigemori, K., Fujioka, S., Sakaiya, T., Tamari, Y., Ohtani, K., Murakami, M., Sunahara, A., Nagatomo, H., Nishihara, K., Miyanaga, N., Izawa, Y.
Suppression of the Rayleigh-Taylor Instability and its implication for the impact ignition
Plasma Phys. Control. Fusion Vol.46 (Dec. 2004) pp.B245-B254
- (9) Chen, J.M., Muroga, T., Nagasaka, T., Xu, Y., Li, C., Qiu, S.Y., Chen, Y.
Precipitation behavior in V-6W-4Ti, V-4Ti and V-4Cr-4Ti alloy
J. Nucl. Mater. Vol. 334, Issues 2-3(Sep.2004) pp.159-165
- (10) Chikaraishi, H., Sato, Y., Shimada, R.
Basic study on conductive characteristics of SiC power device for its application to AC/DC converter
IEEE Trans. Appl. Supercond. Vol.14, No.2, (June 2004) pp.690-692
- (11) Dolan, T. J., Yamazaki, K., Sagara, A.
Helical Fusion Power Plant Economics Studies
Fusion Sci. Technol. Vol.47, No.1(Jan. 2005) pp.60-72
- (12) Donne, A.J.H., de Bock, M.F.M., Classen, I.G.J., von Hellermann, M.G., Jakubowska, K., Jaspers, R., Barth, C.J., van der Meiden, H.J., Oyevaar, T., van de Pol, M. J., Varshney, S.K., Bertschinger, G., Biel, W., Busch, C., Finken, K.H., Koslowski, H.R., Kramer-Flecken, A., Kreter, A., Liang, Y., Oosterbeek, H., Zimmermann, O., Telesca, G., Verdoolaege, G., Domier, C.W., Luhmann, N.C. Jr., Mazzucato, E., Munsat, T., Park, H., Kantor, M., Kouprienko, D., Alexeev, A., Ohdachi, S., Korsholm, S., Woskov, P., Bindslev, H., Meo, F., Michelsen, P.K., Michelsen, S., Nielsen, S.K., Tsakadze, E., Shmaenok, L.
Overview of Core Diagnostics for TEXTOR
Fusion Sci. Technol. Vol.47, No.2 (Feb. 2005) pp.220-245
- (13) Finken, K.H., Abdullaev, S.S., de Bock, M.F.M., von Hellermann, M., Jakubowski, M., Jaspers, R., Koslowski, H.R., Kramer-Flecken, A., Lehnen, M., Liang, Y., Nicolai, A., Wolf, R.C., Zimmermann, O., de Baar, M., Bertschinger, G., Biel, W., Brezinsek, S., Busch, C., Doone, A.J.H., Esser, H.G., Farshi, E., Gerhauser, H., Giesen, B., Harting, D., Hoekzema, J.A., Hogewij, G.M.D., Huttemann, P.W., Jachmich, S., Jakubowska, K., Kalupin, D., Kelly, F., Kikuchi, Y., Kirschner, A., Koch, R., Korten, M., Kreter, A., Krom, J., Kruezi, U., Lazaros, A., Litnovsky, A., Loozen, X., Lopes Cardozo, N.J., Lyssoivan, A., Marchuk, O., Matsunaga, G., Mertens, Ph., Messiaen, A., Neubauer, O., Noda, N., Philipps, V., Pospieszczyk, A., Reiser, D., Reiter, D., Rogister, A.L., Sakamoto, M., Savtchikov, A., Samm, U., Schmitz, O., Schorn, R.P., Schweer, B., Schller, F.C., Sergienko, G., Spatschek, K.H., Telesca, G., Tokar, M., Uhlemann, R., Unterberg, B., Van Oost, G., Van Rompuy, T., Van Wassenhove, G., Westerhof, E., Weynants, R., Wiesen, S., Xu, Y.H.,
Toroidal Plasma Rotation Induced by the Dynamic Ergodic Divertor in the TEXTOR Tokamak
Phys. Rev. Lett. Vol.94 (Jan. 2005) pp.015003 1-5
- (14) Finken, K. H. , Reiter, D., Denner, T., Dippel, K. H., Hobirk, J., Mank, G., Kever, H., Wolf, G. H., Noda, N., Miyahara, A., Shoji, T., Sato, K. N., Akishi, K., Boedo, J. A., Brooks, J. N., Conn, R. W., Corbett, W. J., Doerner, R. P., Goebel, D., Gray, D. S., Hillis, D. L., Hogan, J., McGrath, R. T., Matsuyama, M., Moyer, R., Nygren, R. E., Watkins, J.
The Toroidal Pump Limiter ALT-II in TEXTOR
Fusion Sci. Technol. Vol.47 (Feb. 2005) pp.126-137
- (15) Fujioka, S., Shiraga, H., Azechi, H., Nishimura, H., Izawa, Y., Nozaki, S., Chen, Y.
Temporal resolved x-ray penumbral imaging technique using heuristic image reconstruction procedure and wide dynamic range x-ray streak camera
Rev. Sci. Instrum. Vol.75, No.10 (Oct. 2004) pp.4010-4012

- (16) Fujioka, S., Sunahara, A., Nishihara, K., Ohnishi, N., Johzaki, T., Shiraga, H., Shigemori, K., Nakai, M., Ikegawa, T., Murakami, M., Nagai, K., Norimatsu, T., Azechi, H., Yamanaka, T.
Suppression of the Rayleigh-Taylor instability due to Self-Radiation in a Multiablation Target
Phys. Rev. Lett. Vol.92, No.19 (May 2004) pp.195001-1~195001-4
- (17) Fujioka, S., Sunahara, A., Ohnishi, N., Azechi, H., Shiraga, H., Nakai, M., Shigemori, K., Murakami, M., Nagai, K., Nishimura, H., Norimatsu, T., Nishihara, K., Izawa, Y., Nozaki, S., Chen, Y.
Suppression of Rayleigh-Taylor Instability Using High-Z Doped Plastic Targets for Inertial Fusion Energy
J. Plasma Fusion Res. Vol.80, No.7 (July 2004) pp.597-604
- (18) Fujioka, S., Sunahara, A., Ohnishi, N., Tamari, Y., Nishihara, K., Azechi, H., Shiraga, H., Nakai, M., Shigemori, K., Sakaiya, T., Tanaka, M., Ohtani, K., Okuno, K., Watari, T., Yamada, T., Murakami, M., Nagai, K., Norimatsu, T., Izawa, Y., Nozaki, S., Chen, Y.
Suppression of Rayleigh-Taylor instability due to radiative ablation in brominated plastic targets
Phys. Plasmas Vol.11, No.5 (May 2004) pp.2814-2822
- (19) Fujisawa, A.
Internal Transport Barrier and Bifurcation Phenomena in Stellarators
Fusion Sci. Technol. Vol.46, No.1 (2004) pp.91-100
- (20) Fujisawa, A.
Structural Bifurcation in a Toroidal Plasma: A Brief Review of Bifurcation Phenomena in CHS Stellarator
Recent Res. Devel. Physics Vol.5 (Dec. 2004) pp.1147-1164
- (21) Fujisawa, A., Itoh, K., Iguchi, H., Matsuoka, K., Okamura, S., Shimizu, A., Minami, T., Yoshimura, Y., Nagaoka, K., Takahashi, C., Kojima, M., Nakano, H., Oshima, S., Nishimura, S., Isobe, M., Suzuki, C., Akiyama, T., Ida, K., Toi, K., Itoh, S.-I., Diamond, P.H.
Identification of Zonal Flows in a Toroidal Plasma
Phys. Rev. Lett. Vol.93, No.16 (Oct.2004) pp.165002-1~165002-4
- (22) Fukumoto, K., Matsui, H., Muroga, T., Zinkle, S. J., Hoelzer, D. T., Snead, L. L.
Varying temperature effects on mechanical properties of vanadium alloys during neutron irradiation
J. Nucl. Mater. Vol.329-333 (Aug. 2004) pp.472-476
- (23) Fukumoto, K., Matsui, H., Narui, M., Nagasaka, T., Muroga, T.
Manufacturing pressurized creep tubes from highly purified V-4Cr-4Ti alloys, NIFS-Heat2
J. Nucl. Mater. Vol.335, No.1 (Dec. 2004) pp.103-107
- (24) Fukumoto, K., Takahashi, K., Anma, Y., Matsui, H.
Effect of Impurities on Microstructural Evolution and Deformation Process of Ion-Irradiated V-Cr-Ti alloys
Materials Transaction Vol.46, No.3 (Mar. 2005) pp.503-510
- (25) Funaba, H., Ohyabu, N., Takeiri, Y., Watanabe, K., Kubo, S., Shimozuma, T., Ida, K., Miyazawa, J., Sakamoto, R., Nagaoka, K., Tanaka, K., Peterson, B.J., Osakabe, M., Nagayama, Y., Inagaki, S., Narushima, Y., Sakakibara, S., LHD Experimental Group
Difference in Electron Transport between Co- and Counter-NBI-Heated Plasmas in the Inward-Shifted Configurations on LHD
Fusion Sci. Technol. Vol.46 (Sep. 2004) pp.262-270
- (26) Gao, Z., Sanuki, H., Itoh, K., Dong, J.Q.
Short Wavelength Electron Temperature Gradient Instability in Toroidal Plasmas
Phys. Plasmas Vol.12, No.2 (Feb. 2005) pp.022503-1~022503-7
- (27) Gao, Zhe, Dong, J. Q., Sanuki, H.
Effect of flow shear on temperature gradient short wavelength modes
Phys. Plasmas Vol.11, No.6 (June 2004) pp.3053-3059
- (28) Gao Zhe, Sanuki, H., Itoh, K., Dong, J. Q.
Short Wavelength Ion Temperature Gradient Instability in Toroidal Plasmas
Phys. Plasmas Vol.12, No.2 (Feb. 2005) pp.022502-1~022502-10
- (29) Garner, F., Gelles, D., Greenwood, L., Okita, T., Sekimura, N., Wolfer, W.
Synergistic Influence of Displacement Rate and Helium/dpa Ratio on Swelling of Fe-(9, 12)Cr Binary Alloys in FFTF at ~400°C
J. Nucl. Mater. Vol.329-333 (2004) pp.1008-1012
- (30) Goncharov, P.R., Lyon, J.F., Ozaki, T., Sudo, S.
A Numerical Approach to the Localization of Passive Line Integrated Neutral Particle Measurements on LHD
J. Plasma Fusion Res. Series Vol.6 (2004) pp. 314-317
- (31) Goncharov, P.R., Lyon, J.F., Ozaki, T., Sudo, S., Tamura, N., Sasao, M., Krasilnikov, A., Isobe, M., Saida, T., LHD Experimental Group
Local and Multi-Chord Neutral Particle Diagnostics of Complex 3D Shaped LHD Plasma
Proc of 31st EPS conf. Vol.P5, No.112 (July 2004)
- (32) Goncharov, P.R., Ozaki, T., Sudo, S., Tamura, N., Isobe, M., TESPEL Group, LHD Experimental Group, Sasao, M., Saida, T., Krasilnikov, A.V., Sergeev, V.Yu.
Digital Processing of Solid State Detector Signals in Pellet Charge Exchange Measurements on LHD
Rev. Sci. Instrum. Vol.75, No.10 (Oct. 2004) pp.3613-3615
- (33) Hahm, T.S., Diamond, P.H., Lin, Z., Itoh, K., Itoh, S.-I.
Turbulence Spreading into Linearly Stable Zone and Transport Scaling
Plasma Phys. Control. Fusion Vol.46, No.5A (2004) pp.A323-A334

- (34) Hamaguchi, S., Imagawa, S., Yanagi, N., Hishinuma, Y., Mito, T., Takahata, K., Chikaraishi, H., Tamura, H., Iwamoto, A., Yamada, S., Nishimura, A.
Thermal Hydraulic Characteristics of Superconducting Coil Cooled by Subcooled He I
IEEE Trans. Appl. Supercond. Vol. 14, No. 2 (2004) 1439-1442
- (35) Hasegawa, H., Ohsawa, Y.
Low-Frequency Oblique Waves in Magnetized Electron-Positron-Ion Plasmas
J. Phys. Soc. Jpn. Vol.73, No.7(July 2004) pp.1764-1774
- (36) Hasegawa, H., Ohsawa, Y.
Positron Acceleration to Ultrarelativistic Energies by an Oblique Magnetosonic Shock Wave in an Electron-Positron-Ion Plasma
Phys. Plasmas Vol.12, No.1 (Jan. 2005) pp.012312-1~012312-7
- (37) Hashizume, H., Ito, S., Takami, S., Sagara, A.
Joint Performance of HTc Superconductor for Remountable Magnet System
Fusion Sci. Technol. Vol.47 (2005) pp.901-905
- (38) Hatano, Y., Hayakawa, R., Nishino, K., Ikeno, S., Nagasaka, T., Muroga, T., Watanabe, K.
Surface Segregation of Ti in a V-4Cr-4Ti Alloy and Its Influence on the Surface Reaction Rates of Hydrogen Isotopes
Materials Transactions Vol.46, No.3 (Mar. 2005) pp.511-516
- (39) Hattori, Y., Rubinstein, R., Ishizawa, A.
Shell Model for Rotating Turbulence
Phys. Rev. E Vol.70 (2004) pp. 046311
- (40) Hayashi, K., Mito, T., Okumura, K., Abe, R.
Line voltage detector for SMES system designed to protect from momentary voltage drop
IEEE Trans. Appl. Supercond. Vol.14, No.2 (June 2004) pp.754-757
- (41) Hemmi, T., Takahata, K., Mito, T., Iwamoto, A., Tamura, H., Yanagi, N.
Experimental Apparatus for Measuring the Characteristics of HTS Coils under Controllable Magnetic Field, Orientation and Temperature
IEEE Trans. Appl. Supercond Vol. 14, No. 2 (2004), pp. 1806-1809
- (42) Higuchi, A., Ohya, M., Shirai, Y., Shiotsu, M., Imagawa, S.
Cooling Stability Test of He II Cooled LHD Conductor (I)-Current Supply and Measuring Method
IEEE Trans. Appl. Supercond. Vol.4, No.2 (2004) pp.1443-1446
- (43) Himura, H., Wakabayashi, H., Fukao, M., Isobe, M., Okamura, S., Yamada, H.
Experiments on Injecting Electrons Helical magnetic Field Configuration
IEEE Trans. Plasma Sci. Vol.32, No.2 (Apr. 2004) pp.510
- (44) Hino, T., Sagara, A., Nobuta, Y., Inoue, N., Hirohata, Y., Yamauchi, Y., Masuzaki, ., Noda, N., Suzuki, H., Komori, A., Ohyabu, N., Motojima, O., LHD Experimental Group
Material probe analysis for plasma facing surface in the large helical device
Nucl. Fusion Vol.44, No.4 (2004) pp.496-502
- (45) Hirooka, Y., Fukushima, H., Ohno, N., Takamura, S., Nishikawa, M.
Moving-Surface Plasma-Facing Components for Particle Control in Steady State Magnetic Fusion Devices
Fusion Sci. Technol. Vol.45, No. Jan-issue (Jan. 2004) pp.60-64
- (46) Hirooka, Y., Ohgaki, H., Ohtsuka, Y., Nishikawa, M.
A New Versatile Facility: Vehicle-I for Innovative PFC concepts Evaluation and its First Experiments on Hydrogen Recycling from Solid and Liquid Lithium
J. Nucl. Mater. Vol.337-339 (Mar. 2005) pp.585-589
- (47) Hishinuma, Y., Imagawa, S., Yanagi, N., Mito, T., Nishimura, A., Ymada, S., Takahata, K., Chikaraishi, H., Tamura, H., Iwamoto, A., Hamaguchi, S., Seo, K., Honda, T., Shinba, T., Yoshinaga, S., Satoh, H., Kakui, H., Motojima, O.
Design and Operation of the Sub-cooled Helium Test Facility for the LHD Helical Coils
IEEE Trans. Appl. Supercond. Vol.14, No.2 (2004) pp. 1435-1438
- (48) Hishinuma, Y., Kikuchi, A., Iijima, Y., Yoshida, Y., Nishimura, A., Takeuchi, T., Inoue, K.
Microstructure and superconductivity of V-based Laves phase compound superconductor synthesized rapidly-heating/quenching process
J. Nucl. Mater. Vol.329-333 (2004) pp.1580-1584
- (49) Hiwatari, R., Kuzuyama, Y., Hatayama, A., Okano, K., Asaoka, Y., Zhu, S., Tomita, Y.
Simple Core-SOL-Divertor Model to Investigate Plasma Operation Space
Plasma Phys. Vol.44, No.1-3 (2004) pp. 76 - 82
- (50) Horiuchi, R., Ohtani, H., Ishizawa, A.
Structure formation and dynamical behavior of kinetic plasmas controlled by magnetic reconnection
Compt. Phys. Commun. Vol.164 (2004) pp.17-22
- (51) Horiuchi, R., Ohtani, H., Ishizawa, A.
Dynamical Evolution of Thin Current Sheets in a Three-Dimensional Open System
J. Plasma Fusion Res. SERIES Vol.6 (2004) pp.614-617

- (52) Ichiguchi, K., Carreras, B.A.
Effects of Self-Consistent Flow on Island Generation in Interchange Mode
J. Plasma Fusion Res. SERIES Vol.6 (2004) pp.589-592
- (53) Ichiguchi, K., Nakajima, N., Carreras, B.A.
Nonlinear Analysis for Stabilization of Interchange Mode in LHD Plasmas
Fusion Sci. Technol. Vol.46, No.1 (2004) pp.34-43
- (54) Ida, K., Inagaki, S., Shimozuma, T., Tamura, N., Funaba, H., Narihara, K., Kubo, S., Murakami, S., Wakasa, A., Yokoyama, M., Takeiri, Y., Watanabe, K.Y., Tanaka, K., Yoshinuma, M., Liang, Y., Ohyabu, N., Akiyama, T., Ashikawa, N., Emoto, M., Fujita, T., Fukuda, T., Goncharov, P., Goto, M., Idei, H., Ikeda, K., Isayama, A., Isobe, M., Kaneko, O., Kawahata, K., Kawazome, H., Kobuchi, T., Komori, A., Kumazawa, R., Masuzaki, S., Minami, T., Miyazawa, J., Morisaki, T., Morita, S., Muto, S., Mutoh, T., Nagayama, Y., Nakamura, Y., Nakanishi, H., Narushima, Y., Nishimura, K., Noda, N., Notake, T., Nozato, H., Ohdachi, S., Oka, Y., Okajima, S., Osakabe, M., Ozaki, T., Peterson, B.J., Sagara, A., Saida, T., Saito, K., Sakakibara, S., Sakamoto, R., Sakamoto, Y., Sasao, M., Sato, K., Sato, M., Seki, T., Shoji, M., Suzuki, H., Takeuchi, N., Toi, K., Tokuzawa, T., Torii, Y., Tsumori, K., Watari, T., Yamada, H., Yamada, I., Yamamoto, S., Yamamoto, T., Yoshimura, Y., Itoh, K., Matsuoka, K., Ohkubo, K., Sudo, S., Uda, T., Yam, K.
Characteristics of Transport in Electron Internal Transport Barriers and in the Vicinity of Rational Surfaces in the Large Helical Device
Phys. Plasmas Vol.11, No.5bv (May 2004) pp.2551-2557
- (55) Ido, T., Miura, Y., Hoshino, K., Hamada, Y., Nagashima, Y., Ogawa, H., Shinohara, K., Kamiya, K., Nishizawa, A., Kawasumi, Y., Kusama, Y., JFT-2M group
Electrostatic fluctuation and fluctuation-induced particle flux during formation of the edge transport barrier in the JFT-2M tokamak
Proc. 20th Int. Conf. of Fusion Energy (IAEA) EX/4-6Rb (Nov. 2004)
- (56) Ignatenko, M., Mase, A., Bruskin, L., Kogi, Y., Hojo, H.
Effects of Asymmetry and Target Location on Microwave Imaging Reflectometry
Rev. Sci. Instrum. Vol.75, No.10 (Oct. 2004) pp.3810-3812
- (57) Ignatenko, M., Mase, A., Bruskin, L., Kogi, Y., Hojo, H.
Numerical Study of Microwave Imaging Reflectometer for a Tandem Mirror Device
Trans. Fusion Sci. Tech. Vol.47, No.1T (2005) pp.183-186
- (58) Ikeda, K., Takeiri, Y., Kaneko, O., Nagaoka, K., Oka, Y., Osakabe, M., Tsumori, K., Sato, M., Asano, E., Kawamoto, T.
Control of Negative Ion Beam Uniformity by Using Multipower Supplies for Arc Discharge
Rev. Sci. Instrum. Vol.75, No.5 (May 2004) pp.1744-1746
- (59) Ikeda, K., Takeiri, Y., Kaneko, O., Nagaoka, K., Oka, Y., Osakabe, M., Tsumori, K., Sato, M., Asano, E., Kawamoto, T.
Control of negative ion beam uniformity by using multi-power supplies for arc discharge
Review of Scientific Instruments Vol.75, No.5 (May 2004) pp.1744-1746
- (60) Imagawa, S., Hishinuma, Y., Seo, K., Takahata, K., Hamaguchi, S., Iwamoto, A., Chikaraishi, H., Tamura, H., Moriuchi, S., Yamada, S., Nishimura, A., Mito, T., Motojima, O.
Asymmetrical Normal-zone Propagation Observed in the Aluminum-stabilized Superconductor for the LHD Helical Coils
IEEE Trans. Appl. Supercond. Vol.14, No.2 (June 2004) pp.1507-1510
- (61) Imagawa, S., Sagara, A.
Scale Effects on Magnet Systems of Heliotron-Type Reactors
Plasma Sci. Technol. Vol.7, No.1 (Feb. 2005) pp.2626-2628
- (62) Imagawa, S., Yanagi, N., Hishinuma, Y., Mito, T., Takahata, K., Chikaraishi, H., Tamura, H., Iwamoto, A., Hamaguchi, S., Seo, K., Yamada, S., Nishimura, A., Motojima, O.
Results of Stability Test in Subcooled Helium for the R&D Coil of the LHD Helical Coil
IEEE Trans. Appl. Supercond. Vol.14 (June 2004) pp.1511-1514
- (63) Imagawa, S., Yanagi, N., Sekiguchi, H., Mito, T., Motojima, O.
Performance of the Helical Coils for the Large Helical Device in Six Years' Operation
IEEE Trans. Appl. Supercond. Vol.14 (June 2004) pp.1388-1393
- (64) Inagaki, S., Ida, K., Tamura, N., Shimozuma, T., Kubo, S., Nagayama, Y., Kawahata, K., Sudo, S., Ohkubo, K., LHD Experimental Group
Cold Pulse Experiments in Plasma with an Electron Internal Transport Barrier on LHD
Plasma Phys. Control. Fusion 46 (2004) pp.A71-A76
- (65) Inagaki, S., Tamura, N., Ida, K., Nagayama, Y., Kawahata, K., Sudo, S., Morisaki, T., Tanaka, K., Tokuzawa, T., the LHD Experimental Group
Observation of Reduced Heat Transport Inside the Magnetic Island 0 Point in the Large Helical Device
Phys. Rev. Lett. Vol.92, No.5(Feb. 2004) pp.055002-1~055002-4
- (66) Ishiguro, S., Nikolic Lj., Skoric, M. M., Li, B.
Intense Reflection of a Relativistic Laser Pulse in Subcritical Plasmas
J. Plasma and Fusion Res. Vol.6 (2004) pp.279-282
- (67) Ishikawa, H., Itoh, T., Hashimoto, M., Fujiwara, S.
Phase Transition in Even-Even Nylon Crystals
J. Phys. Soc. Jpn. Vol.73, No.2 (Feb. 2004) pp.303-306
- (68) Ishizaki, R., Nakajima, N., Parks, P.B.
Analysis of pellet ablation with atomic processes
J. Plasma Fusion Res. Series Vol.6 (2004) pp.353-356

- (69) Ishizaki, R., Parks, P.B., Nakajima, N., Okamoto, M.
Two-dimensional Simulation of Pellet Ablation with Atomic Processes
Phys. Plasmas Vol.11, No.8 (Aug. 2004) pp.4064-4080
- (70) Ishizawa, A., Horiuchi, R., Ohtani, H.
Mass ratio dependence of current layer structure in collisionless driven reconnection
J. Plasma Fusion Res. SERIES Vol.6 (2004) pp.287-290
- (71) Isobe, M., Nakajima, N., Shimizu, A., Suzuki, C., Akiyama, T., Nishimura, S., Okamura, S., Matsuoka, K., Spong, D.A.
Orbit Topology and Confinement of Energetic Ions in the CHS-qa Quasi-Axisymmetric Stellarator
J. Plasma Fusion Res. SERIES Vol.6 (2004) pp.622-625
- (72) Itagaki, M., Kamisawada, J., Oikawa, S.
Boundary-only integral equation approach based on polynomial expansion of plasma current profile to solve the Grad-Shafranov equation
Nucl. Fusion Vol.44 (2004) pp.427-437
- (73) Ito, T., Aaramaki, T., Otsuka, S., Suzuki, T., Togawa, O., Kobayashi, T., Kawamura, H., Amano, H., Senjyu, T., Chaykovskaya, E.L., Lishavskaya, T.S., Karasev, E.V., Novichkov, V.P., Scherbinin, A.F., Tkalin A.V., Volkov, Y.N.
Anthropogenic Radionuclides in Seawater of the Japan Sea: The Results of Recent Observations and the Temporal Change of Concentrations
J. Nucl. Sci. Tech. Vol.42, No.1 (2005) pp.99-100
- (74) Itoh, K., Hallatschek, K., Itoh, S-I.
Excitation of Geodesic Acoustic Mode in Toroidal Plasmas
Plasma Phys. Control. Fusion Vol.47 (2005) pp.451-458
- (75) Itoh, K., Hallatschek, K., Toda, S., Itoh, S-I, Diamond, P.H., Yagi, M., Sanuki, H.
Collisional Effects on Coherent Structures of Zonal Flows and Turbulent Transport
Plasma Phys. Control Fusion Vol.46, No.5A (May 2004) pp.A335-A340
- (76) Itoh, K., Hallatschek, K., Toda, S., Sanuki, H., Itoh, S-I.
Coherent Structure of Zonal Flow and Nonlinear Saturation
J.Phys. Soc. Jpn. Vol.73, No.11 (Oct. 2004) pp.2921-2923
- (77) Itoh, S-I., Itoh, K., Yoshizawa, A., Yokoi, N.
Periodic Change of Solar Differential Rotation
Astrophys. J. Vol.618 (Jan. 2005) pp.1044-1048
- (78) Itoh, S-I., Itoh, K., Yagi, M., Toda, S.
Statistical Theory for Transition and Sustainment of the Improved Confinement State
Plasma Phys. Control. Fusion 46 (2004) pp.A341-A346
- (79) Itoh, Sanae-I., Itoh, K., Yagi, M.
Life Time of Plasma States Near Transition Boundary
J.Phys. Soc. Jpn. Vol.74, No.3 (Mar. 2005) pp.947-950
- (80) Iwamoto, A., Maekawa, R., Mito, T.
Development of evaluation technique on thermal impedance between dissimilar solids
Adv. Cryog. Eng. Vol.49 (2004) pp.643-650
- (81) Jain, R., Browning, P., Kusano, K.
Solar Coronal Heating by Forced Magnetic Reconnection: Multiple Reconnection Events
Phys. Plasmas Vol.12 (Jan. 2005) pp.012904-012915
- (82) Jimbo, S., Kanno, R., Takamaru, H., Okamoto, M.
Strike Point Pattern on Local Island Divertor Head
J.Plasma Fusion Res.SERIES Vol.80, No.8 (2004) pp.649-650
- (83) Kaneba, T., Tokuzawa, T., Kawahata, K., Ito,Y., Nagayama, Y., LHD Experimental Group
Electron density profile measurement using an ultrashort-pulsed radar reflectometer on large helical device
Rev. Sci. Instrum. Vol.75, No.10 (Oct. 2004) pp.3846-3848
- (84) Kanno, R.
Stochastic representation of fluid equations
J. Plasma Phys. Vol.70 (June 2004) pp.359-367
- (85) Kanno, R., Jimbo, S., Takamaru, H., Okamoto, M.
Monte Carlo Simulation of Particle Transport in the LID Configuration
J. Plasma Fusion Res. SERIES Vol.6 (2004) pp.527-530
- (86) Kanno, R., Toi, K., Watanabe, K., Hayashi, T., Miura, H., Nakajima, N., Okamoto, M.
HINT Computation of LHD Equilibrium with Zero Rotational Transform Surface
J. Plasma Fusion Res. SERIES Vol.6 (2004) pp.227-229
- (87) Kasahara, H., Sumiyoshi, F., Kawagoe, A., Kubota, K. and Akita, S.
AC Losses in Long Bi-2223 Tapes Wound Into a Solenoidal-Coil
IEEE Trans. Appl. Supercond Vol.14, No.2 (June 2004) pp.1078-1081

- (88) Kasuya, N., Itoh, K., Takase Y.
Structural Formation Induced by Electrode Biasing in Tokamaks: Accessibility to a Double-Peaked Er Shear Layer
Plasma Phys. Control. Fusion Vol.46, 5A (May 2004) pp.A235-A240
- (89) Kasuya, N., Itoh, K., Takase, Y.
Radial and Poloidal Structure Coupled with Shear Viscosity under the Existence of a Large Flow Shear in Tokamaks
J. Plasma Fusion Res. SERIES Vol.6 (2004) pp.283-286
- (90) Katagiri, K., Murakami, A., Shoji, Y., Teshima, H., Sawamura, M., Iwamoto, A., Mito, T., Murakami, M.
Tensile and bending mechanical properties of bulk superconductors at room temperature
Physica C Vol.412-414 (2004) pp.633-637
- (91) Katagiri, K., Takaya, R., Tachikawa, K., Yamada, Y., Iwamaot, A., Watanabe, K.
Stress/Strain Characteristics of PIT MgB₂ Tapes with Ni Sheath
J. Japan Inst. Metals Vol.68, No.9 (2004) pp.642-647
- (92) Katayama, T., Tanabe, T., Syresin, E., Watanabe, I.
Simulation studies of the electron cooler for MUSUES at RIKEN
Nucl. Instrum. Methods Phys. Res. Vol.A532 (2004) pp.408-412
- (93) Kato, H., Miyazaki, T., Hase, T., Hamada, M., Tachikawa, K.
Improved Fabrication Process for Nb₃Sn Conductors with Ta-Sn Powder Core
IEEE Trans. Appl. Supercond. Vol.14 (June 2004) pp.987-990
- (94) Kato, T., More, R., Yamamoto, N., Nishimura H., Rosmej, F.B.
X-ray satellite spectra of H-like ions
Inertial Fusion Sciences and Application 2003, Editors, B.A. Hammel, D.D. Meyerhofer, J. Meyer-ter-Vehn and H. Azechi, ISBN (2004) pp.992-996
0-89448-686-1
- (95) Kato, T., Murakami, I.
NIFS DATABASE and Cooperations with IAEA DCN
Springer Series in Chemical Physics Vol.78 (2004) pp.371-383
- (96) Kato, T., Yamamoto, N., Rosmej F.B.
X-ray spectral diagnostics for satellite lines of H-like Mg ions measured by a high resolution spectrometer
Laser and Particle Beams Vol.22 (2004) pp.245-251
- (97) Kawagoe, A., Sumiyoshi, F., Mito, T., Chikaraishi, H., Baba, T., Okumura, K., Iwakuma, M., Henmi, T., Hayashi, K., Abe, R., Ushiku, T., Miyoshi, K.
Winding Techniques for Conduction Cooled LTS Pulse Coils for 100 kJ Class UPS-SMES as a Protection from Momentary Voltage Drops
IEEE Trans. Appl. Supercond Vol. 14, No. 2 (2004) pp. 727-730
- (98) Kawagoe, A., Sumiyoshi, F., Mito, T., Kawashima, T.
Compact stranded superconducting conductors with both low ac loss and high stability. II. Experiments to confirm fundamental performance
Cryogenics Vol.44, No.9 (Sep. 2004) pp.623-630
- (99) Kawagoe, A., Sumiyoshi, F., Mito, T., Kawashima, T. and Hirano, N.
Compact stranded superconducting conductors with both low ac loss and high stability. I. Proposal of a new design
Cryogenics Vol.44, No.9 (Sep. 2004) pp.617-622
- (100) Kawahata, K., Tanaka, K., Tokuzawa, T., Akiyama, T., Ito, Y., Okajima, S., Nakayama, K., Wylde, R.J.
Development of a new two color far infrared laser interferometer for future fusion devices
Rev. Sci. Instrum. Vol.75, No.10 (Oct. 2004) pp.3508-3510
- (101) Kawahata, K., Tanaka, K., Tokuzawa, T., Ito, Y., Akiyama, T., Sanin, A., Okajima, S., Tsuji-Iio, S., Vyacheslavov, L., the LHD Group
Electron Density Profile Measurements on LHD
IEEE Trans. Plasma Sci. Vol.32, No.2 (Feb.2004) pp.519-524
- (102) Kawano, T.
Water-Vapor Decomposition Using Zirconium-Nickel Alloy
J.J.A.P Vol.43, No.9A/B (2004) pp.L1127-L1129
- (103) Kawano, T.
On possibility of monitoring tritium concentration in air using gas chromatograph method
Proceedings of the Fifth Workshop on Environmental Radioactivity (2004.10) pp.62-66
- (104) Kiwamoto, Y., Aoki, J., Soga, Y.
Potential distribution of nonuniformly charged ellipsoid
Phys. Plasmas Vol.11, No.10 (2004) pp.4868 - 4870
- (105) Kiwamoto, Y., Aoki, J., Soga, Y., Sanpei, A.
Controlled experiments on self-organization of ordered structures in a pure electron plasma
Plasma Phys. Control. Fusion Vol.47 (2005) pp.A41-A51

- (106) Kobayashi, T., Yoshikawa, M., Kubota, Y., Saito, M., Numada, N., Ishii, K., Cho, T.
Measurement technique of electric field using ultraviolet/visible spectroscopy in cylindrical plasmas
Review of Scientific Instruments Vol.75 (2004) pp.4121-4123
- (107) Kodama, H. Oyaidzu, M., Sasaki, M., Kimura, H., Morimoto, Y., Oya, Y., Matsuyama, M., Sagara, A.
Studies on structural and chemical characterization for boron coating films deposited by PCVD
J. Nucl. Mater. Vol.329, No.333 (Aug. 2004) pp.889-893
- (108) Koganezawa, T., Iida, T., Ogata, Y., Tsuji, N., Kakiuchi, M., Satake, H., Yamanishi, H., Sakuma, Y.
Development of a Simplified Treatment for Measuring Tritium Concentration in the Environmental Water-Removal of Dissolved Ions by Reverse Osmosis Membrane for Electrolysis Enrichment-
Radioisotopes Vol.53, No.5 (May 2004) pp.277-285
- (109) Kogi, Y., Uchida, K., Mase, A., Bruskin, L., Ignatenko, M., Tokuzawa, T., Nagayama, Y., Kawahata, K.
Ultrashort-Pulse Reflectometer on LHD
Rev. Sci. Instrum. Vol.75, No.10 (Oct. 2004) pp.3837-3839
- (110) Kolesnichenko, Ya.I., Yamazaki, K., Yamamoto, S., Lutsenko, V.V., Nakajima, N., Narushima, Y., Toi, K., Yakovenko, Yu.V.
Interplay of Energetic Ions and Alfvén Modes in Helical Plasmas
Phys. Plasmas Vol.11, No.1 (2004) pp.158-170.
- (111) Komori, A., Morisaki, T., Masuzaki, S., Shoji, M., Ohyabu, N., Yamada, H., Tanaka, K., Kawahata, K., Narihara, K., Morita, S., Peterson, B.J., Sakamoto, R., Sakakibara, S., Motojima, O., LHD Experimental Group
Initial Results of Local Island Divertor Experiments in the Large Helical Device
Fusion Sci. Technol. Vol.46, No.1 (July 2004) pp.167-174
- (112) Konishi, S., Fujita, K., Okamura, T., Shirai, Y., Shiotsu, M.
Effect of orifice location on heat transfer in a duct filled with pressurized He II
IEEE Transactions on Applied Superconductivity Vol.14, No.2 (June 2004) pp.1762-1765
- (113) Koyama, M., Fukumoto, K., Matsui, H.
Effects of purity on high temperature mechanical properties of vanadium alloys
J. Nucl. Mater. Vol.329-333 (Aug. 2004) pp.442-446
- (114) Krashenninnikov, S.I., Tomita, Y., Smirnov, E.D., Janev, R.K.
On Dust Dynamics in Tokamak Edge Plasmas
Phys. Plasmas Vol.11, No.6 (2004) pp.3141-3150
- (115) Kubota, Y., Yoshikawa, M., Nakashima, Y., Kobayashi, T., Saito, M., Ohki, T., Higashizono, Y., Itakura, A., Tsunoda, S., Cho, T.
Temporal Behavior of Electron and Neutral Hydrogen Density Profiles during NBI in the GAMMA 10
J. Plasma Fusion Res. SERIES Vol.6, No.1T (June 2004) pp.673-676
- (116) Kubota, Y., Yoshikawa, M., Nakashima, Y., Yamada, H., Sakamoto, R.
Development of an integrated pellet diagnostic system for fueling pellets
Review of Scientific Instruments Vol.75 (2004) pp.4228-4230
- (117) Kuramoto, E., Hiratani, M., Okita, T., Morishita K., Sekimura, N., Soneda, N.
How can we bridge the multiple length scale models of radiation damage processes?
Vol.80, No.6 (June 2004) pp.492-499
- (118) Kusakabe, T., Pichl, L., Buenker, R. J., Kimura, M., Tawara, H.
Isotope Effect in Charge-Transfer Collisions of Slow H⁺ and D⁺ Ions with H₂, HD, and D₂ Molecules
Phys. Rev. A Vol.70, No.5(Nov. 2004) pp.052710 1-7
- (119) Kusano, K., Maeshiro, T., Mii, H., Yokoyama, T., Sakurai, T.
Study of Magnetic Helicity and Magnetohydrodynamic Relaxation in Solar Flare Processes
J. Plasma Fusion Res. SERIES Vol.6 (2004) pp.115-118
- (120) Kusano, K., Maeshiro, T., Yokoyama, T., Sakurai, T.
The Trigger Mechanism of Solar Flares in a Coronal Arcade with Reversed Magnetic Shear
The Astrophysical Journal Vol.610, No.1 (July 2004) pp.537-549
- (121) Li, B., Ishiguro, S., Skoric, M. M., Takamaru, H.
Stimulated Raman Scattering, Cascade-into-Condensate and Acceleration of Large Relativistic Electromagnetic Solitons in Intense Laser Interaction with an Underdense Plasma
J. Plasma Fusion Res. SERIES Vol.6 (2004) pp.275-278
- (122) Li, B., Ishiguro, S., Skoric, M.M., Takamaru, H., Sato, T.
Acceleration of high-quality, well-collimated return beam of relativistic electrons by intense laser pulse in a low-density plasma
Laser and Particle Beams Vol.22, Issue3 (2004) pp.307-314.
- (123) Liu, X., Yamada, T., Yamauchi, Y., Hirohata, Y., Hino T., Noda, N.
Helium retention of vanadium alloy after energetic helium ion irradiation
Fusion Eng. Des. Vol.70 No.4 (Oct. 2004) pp.329-334

- (124) Liu, X., Yang, L., Tamura, S., Tokunaga, K., Yoshida, N., Noda, N., Xu, Z.
Thermal response of plasma sprayed tungsten coating to high heat flux
Fusion Eng. Des. Vol.70, No.4 (Oct. 2004) pp.341-349
- (125) Maehata, K., Iwamoto, A., Iwamoto, Y., Maekawa, R., Mito, T., Ishibashi, K., Shintomi, T., Takeo, M., Tachikawa, K., Yamada, Y., Yamada, S.
Development of 1.8 K HTS Current Feedthrough using Large-Sized YBCO Bulk Conductors
IEEE Trans. Appl. Supercond Vol. 14, No. 2 (2004) pp. 1782-1785
- (126) Maekawa, R., Iwamoto, A., Hamaguchi, S.
Transient heat transport in subcooled He II associated with JT effect
Adv. Cryog. Eng. vol. 49B (2004) pp. 991-998
- (127) Maekawa, R., Ooba, K., Nobutoki, M., Mito, T.
Dynamic simulation of helium liquefier
Adv. Cryog. Eng. vol. 49A (2004) pp. 192-199
- (128) Maekawa, R., Ooba, K., Nobutoki, M., Mito, T.
Dynamic simulation of a helium refrigerator/liquefier for LHD
Cryogenics vol. 45 (2005) pp.199-211
- (129) Maekawa, T., Tanaka, H., Uchida, M., Yoshinaga, T., Yamaguchi, S., Igami, H., Konno, M., Katsuura, K., Hayashi, K., Abe, Y., Yamada, J., Maebara, S., Imai, T.
Formation of Spherical Tokamak Equilibria by ECH in the LATE Device
Proc. 20th Int. Conf. of Fusion Energy (IAEA) IAEA-CN-116/EX/P4-27(Nov. 2004)
- (130) Masuda, K., Yoshikawa, K., Toku, H., Nagasaki, K., Mizutani, T., Takamatsu, T. and Imoto, M.
Performance Characteristics of an Inertial-Electrostatic Confinement Fusion Device with Magnetron
Proc. of 20th IEEE/NPSS Symposium on Fusion Engineering (2004) pp.628-631
- (131) Matsubara, A., Watanabe, T., Sugimoto, T., Sudo, S., Sato, K.
Effect of Plasma Flow on the Gas Conductance in a Simulated Closed-Divertor
J. Plasma Fusion Res. SERIES Vol.6 (2004) pp.433-436
- (132) Matsumoto, N., Kaneko, T., Ishiguro, S., Hatakeyama, R.
Three-Dimensional Electrostatic Particle Simulation of Parallel-Flow-Shear Driven Low-Frequency Plasma Instabilities
J. Plasma Fusion Res. SERIES Vol.6 (2004) pp.707-710
- (133) Matsumoto, Y., Nagaura, T., Oikawa, S., Watanabe, T.
Particle Orbit Analysis under ICRF Heating in the LHD
Jpn. J. Appl. Phys. Vol.43 (2004) pp.332-341
- (134) Matsumoto, Y., Nishiura, M., Matsuoka, K., Sasao, M., Wada, M., Yamaoka, H.
Contribution of Local H^- Density to Extracted H^- Beam Current in a Cesium Seeded Hydrogen Plasma
Rev. Sci. Instrum. Vol.75, No.5 (2004) pp.1757-1759
- (135) Matsuoka, K., Okamura, S., Nishimura, S., Isobe, M., Suzuki, C., Shimizu, A., Tanaka, N., Hasegawa, M., Naito, H., Urata, K., Suzuki, Y., Tsukamoto, T.
Engineering Design Study of Quasi-Axisymmetric Stellarator with Low-Aspect Ratio
Fusion Sci. Technol. Vol.46, No.2 (2004) pp.378-387
- (136) Matsushita, H., Ida, K., Okamura, S., Isobe, M., Akiyama, R., Yoshimura, Y., the CHS Group
Loss Cone Boundary Measurement Using Diagnostic Neutral Beam and Neutral Particle Analyzer in a Compact Helical System
Rev. Sci. Instrum. Vol.75, No.10 (Oct. 2004) pp.3607-3609
- (137) Matsuura, H., Iguchi, S., Morisaki, T., Tanaka, K., Komori, A., Motojima, O., LHD experimental Group
Relationship between Magnetic Field Structure and Plasma Density Profile in LHD Edge Region
J. Plasma Fusion Res. SERIES Vol.6 (2004) pp.662-664
- (138) Mihaila, I., Ohtsu, Y and Fujita, H.
Measurement of ion temperature in magnetized inductively coupled plasma with external helical antenna
Phys. Lett. A Vol.327 (July 2004) pp.327-331
- (139) Minami, T., Fujisawa, A., Iguchi, H., Liang, Y., Ida, K., Nishimura, S., Yokoyama, M., Murakami, S., Yoshimura, Y., Isobe, M., Suzuki, C., Nomura, I., Toi, K., Yoshimura, M., Shimizu, A., Takahashi, C., Matsuoka, K., Okamura, S., CHS Group
Increased Understanding of Neoclassical Internal Transport Barrier on CHS
Nucl. Fusion Vol.44, Issue2 (Feb. 2004) pp.342-349
- (140) Mitarai, O., Oda, A., Sagara, A., Yamazaki, K., Motojima, O.
Pellet injection algorithm for the FFHR helical reactor
Fusion Eng. Des. Vol.70, No.3 (July 2004) pp.247-267
- (141) Mitarai, O., Sagara, A., Imagawa, S., Tomita, Y., Watanabe, KY., Watanabe, T.
Parameter Requirements for D-3He Helical Reactors
J. Plasma Fusion Res. SERIES Vol.6 (2004) pp.303-305

- (142) Mito, T., Kawagoe, A., Chikaraishi, H., Okumura, K., Abe, R., Baba, T., Yamauchi, K., Yokota, M., Henmi, T., Seo, K., Hayashi, K., Iwakuma, M., Sumiyoshi, F.
Development of UPS-SMES as a Protection from Momentary Voltage Drop
IEEE Trans. Appl. Supercond Vol. 14, No. 2 (2004) pp. 721-726
- (143) Mito, T., Morikawa, J., Ogawa, Y., Ohkuni, K., Hori, D., Yamakoshi, S., Iwakuma, M., Uede, T., Itoh, I., Fukagawa, M., Fukui, S.
Experiments of the HTS Floating Coil System in the Mini-RT Project
IEEE Trans. Appl. Supercond. Vol.14, No.2 (June 2004) pp.1539-1542
- (144) Mito, T., Yanagi, N., Ogawa, Y., Morikawa, J., Ohkuni, K., Iwakuma, M., Uede, T., Nose, S., Itoh, I., Fukui, S., Nagayama, T., Okuno, J.
Design and Construction of a Mini-RT Device
J. Cryo. Soc. Jpn. Vol.39, No.5(2004) pp.182-192
- (145) Miura, H.
Excitations of acoustic waves in compressible isotropic turbulence
Journal of Turbulence vol.5(2004) pp.010
- (146) Miura, H., Hayashi, T.
Low m/n Mode Behavior of MHD Plasma in LHD
J. Plasma Fusion Res. SERIES Vol.6 (2004) pp.349-352
- (147) Miyamoto, M., Tokitani, M., Tokunaga, K., Fujiwara, T., Yoshida, N., Masuzaki, S., Komori, A.
Microscopic damage of materials exposed to glow discharge cleanings in LHD
J. Nucl. Mater. Vol. 329-333, No.1 (Aug. 2004) pp.742-746
- (148) Mizuguchi, N., Hayashi, T.
MHD Equilibrium and Stability of Spherical Tokamak Plasma with Current Hole
J. Plasma Fusion Res. SERIES Vol.6 (2004) pp.362-365
- (149) Momoshima, N., Takamura, M., Nagao, Y., Toyoshima, T., Okai, T., Uda, T.
Development of sampling apparatus for atmospheric tritium
Radioecology and Environmental Dosimetry (IES) (2004) pp.416-420
- (150) Morita, S., Goto, M., Masuzaki, S., Suzuki, H., Tanaka, K., Nozato, H., Takeiri, Y., Miyazawa, J., LHD experimental group
Effect of Ne glow discharge on ion density control in LHD
Plasma Sci. Technol. Vol.6, No.5 (Oct. 2004) pp.2440-2444
- (151) Morita S., Morisaki T., Tanaka K., Goto M., Masuzaki S., Osakabe M., Sakakibara S., Sakamoto R., Toi K., Ashikawa N., Funaba H., Ikeda K., Kaneko O., Kawahata K., Kubo S., Muto S., Nagaoka K., Nishimura K., Nozato H., Oka Y., Shimozuma T., Takeiri Y., Tokuzawa T., Tsumori K., LHD experimental group
H-mode-like discharges under the presence of 1/1 rational surface at ergodic layer in LHD
J. Plasma Fusion Res. Vol.80, No.4 (Apr. 2004) pp.279-280
- (152) Motojima, O., Hamada, Y., Komoro, A., Watanabe, K.Y., Mutoh, T., Takeiri, Y., Ida, K., Akiyama, T., Asakura, N., Ashikawa, N., Chikaraishi, H., Cooper, W.A., Emoto, M., Fujita, T., Fujiwara, M., Funaba, H., Goncharov, P., Goto, M., Hamada, Y., Higashijima, S., Hino, T., Hoshino, M., Ichimura, M., Idei, H., Ido, T., Ikeda, K., Imagawa, S., Inagaki, S., Isayama, A., Isobe, M., Itoh, T., Itoh, K., Kado, S., Kalinina, D., Kaneba, T., Kaneko, O., Kato, D., Kato, T., Kawahata, K., Kawashima, H., Kawazome, H., Kobuchi, T., Kondo, K., Kubo, S., Kumazawa, R., Lyon, J.F., Maekawa, R., Mase, A., Masuzaki, S., Mito, T., Matsuoka, K., Miura, Y., Miyazawa, J., More, R., Morisaki, T., Morita, S., Murakami, I., Murakami, S., Mutoh, S., Nagaoka, K., Nagasaki, K., Nagayama, Y., Nakamura, Y., Nakanishi, H., Narihara, K., Narushima, Y., Nishimura, H., Nishimura, K., Nishiura, M., Nishizawa, A., Noda, N., Notake, T., Nozato, H., Ohdachi, S., Ohkubo, K., Ohyabu, N., Oyama, N., Oka, Y., Okada, H., Osakabe, M., Ozaki, T., Peterson, B.J., Sagara, A., Saida, T., Saito, K., Sakakibara, S., Sakamoto, M., Sakamoto, R., Sasao, M., Sato, K., Seki, T., Shimozuma, T., Shoji, M., Sudo, S.,
Review on the Progress of the LHD Experiment
Fusion Sci. Technol. Stellarator Issue Vol.46 (July 2004) pp.1-12
- (153) Murakami, S., Nakajima, N., Yamada, I., Kawahata, K., Tokuzawa, T., Komori, A., LHD experimental group
Effects of global MHD instability on operational high beta-regime in LHD
Proc. 20th Int. Conf. Vilamoura 2004 (Vienna: IAEA) CD-ROM file EX/3-3
- (154) Muroga, T.
Vanadium Alloys for Fusion Blanket Applications
Mater. Trans. Vol.46, No.3 (Mar. 2005) pp.405-411
- (155) Muroga, T., Nagasaka, T., Chen, J.M., Xu, Z.Y., Huang, Q.Y., Wu, Y.C.
Characterization for Fusion Candidate Vanadium Alloys
Plasma Sci. Technol. Vol. 6, No. 4 (2004) pp. 2395-2399
- (156) Muroga, T., Nagasaka, T., Nishimura, A., Chen, J.M.
Improvement of Vanadium Alloys by Precipitate Control for Structural Components of Fusion Reactors
Mater. Sci. Forum Vols.475-479 (2005) pp.1449-1454
- (157) Muroga, T., Watanabe, H.
Microstructure Response in Copper and Copper Alloys Irradiated with Fission Neutrons with Controlled temperature Variations
J. ASTM Int. Vol.1, No.9 (Oct. 2004) pp.753-762

- (158) Mutoh, T., Kumazawa, R., Seki, T., Saito, K., Watari, T., Torii, Y., Takeuchi, N., Shimpō, F., Nomura, G., Yokota, M., Watanabe, T., Osakabe, M., Sasao, M., Murakami, S., Saida, T., Okada, H., Takase, Y., Fukuyama, A., Ashikawa, N., Emoto, M., Funaba, H., Goncharov, P.R., Goto, M., Hamada, Y., Ida, K., Idei, H., Ikeda, K., Imagawa, S., Inagaki, S., Isobe, M., Kobuchi, T., Kubo, S., Masuzaki, S., Matsuoka, K., Minami, T., Mito, T., Miyazawa, J., Morisaki, T., Morita, S., Muto, S., Nagayama, Y., Nakamura, Y., Nakanishi, H., Narihara, K., Narushima, Y., Nishimura, K., Noda, N., Notake, T., Ohdachi, S., Oka, Y., Ozaki, T., Peterson, B.J., Sagara, A., Sakakibara, S., Sakamoto, R., Sato, K., Sato, M., Shimozuma, T., Shoji, M., Suzuki, H., Takeiri, Y., Tamura, N., Tanaka, K., Toi, K., Tokuzawa, T., Tsumori, K., Watanabe, K., Yamada, H., Yamada, I., Yamazaki, K., Yokoyama, M., Yoshimura, Y., Yoshinuma, M., Kaneko, O., Kawahata, K., Ohyabu, N., Ohkubo, K., Komori, A., Sudo, S., Motojima, O.
- Long -Pulse Operation High-Energy Particle Confinement Study in ICRF Heating of LHD*
Fusion Sci. Technol. Vol.46 (July 2004) pp.175-182
- (159) Nagasaka, T., Heo, N.-J., Muroga, T., Nishimura, A., Watanabe, H., Narui, M., Shinozaki, K.
- Impact properties of NIFS-HEAT-2 (V-4Cr-4Ti) after YAG laser welding and neutron irradiation at 563 K*
J. Nucl. Mater. Vol.329-333, Part 2 (Aug. 2004) pp. 1539-1543
- (160) Nagayama, Y., Kawahata, K., Inagaki, S., Morisaki, T., Narihara, K.
- Electron Cyclotron Emission Diagnostics for Helical Plasma in the Large Helical Device*
IEEE Trans. Plasma Sci. Vol.32, No.4-3 (Aug. 2004) pp.1716-1720
- (161) Nagayama, Y., Tomita, Y., Mitarai, O.
- Feasibility of Advanced Fuel Fusion Reactor*
J. Plasma Fusion Res. Vol.80, No.11 (Nov. 2004) pp.962-964
- (162) Nakagawa, S., Matsuyama, M., Kodama, H., Oya, Y., Okuno, K., Sagara, A., Noda, N., Watanabe, K.
- Behavior of tritium release from thin boron films deposited on SS316*
J. Nucl. Mater. Vol.329, No.333 (Aug. 2004) pp.904-908
- (163) Nakamura, H.
- Supramolecule Structure for Amphiphilic Molecule by Dissipative Particle Dynamics Simulation*
Mol. Simul. Vol. 30 (2004) pp.941-945
- (164) Nakamura, K., Iguchi, H., Ueda, M., Narihiro, Z., Shimizu, A., Morisaki, T., Isobe, M., Takahashi, C., Nishimura, S., Suzuki, C., Yoshimura, Y., Nagaoka, K., Minami, T., Yoshinuma, M., Ida, K., Okamura, S., Matsuoka, K.
- Two-dimensional diagnostic of edge plasma structure using a lithium beam probe in a compact helical system*
Rev. Sci. Instrum. Vol. 76, No.1 (2005) pp.013504-1~013504-9
- (165) Nakamura, Y., Livshits, A.I., Nakahara, Y., Hatano, Y., Busnyuk, A., Ohyabu, N.
- Hydrogen absorption capability of a niobium panel for pumping neutral atoms in divertor region*
J. Nucl. Mater. Vol.337-339 (Mar. 2005) pp.461-465
- (166) Nakamura, Y., Suzuki, Y., Yamagishi, O., Kondo, K., Nakajima, N., Hayashi, T., Monticello, D.A., Reiman, A.H.
- MHD equilibrium and pressure driven instability in $L = 1$ heliotron plasmas*
Nucl. Fusion Vol.44, No.3 (2004) pp.387-394
- (167) Nakanishi, H., Hochin, T., Kojima, M., LABCOM group
- Search and Retrieval Method of Similar Plasma Waveforms*
Fusion Eng. Des. Vol.71 No.1-4 (June 2004)pp.189-193
- (168) Nakano, H., Fujisawa, A., Shimizu, A., Ohshima S., Minami, T., Yoshimura, Y., Okamura, S., Matsuoka, K.
- Simultaneous Measurements of Density and Potential Fluctuation with Heavy Ion Beam Probe in the Compact Helical System*
Rev. Sci. Instrum. Vol.75, No.10 (Oct. 2004) pp.3505-3507
- (169) Narihara, K., Yamada, I., Hayashi, H., Ikeda, K., Kaneko, O., Nagaoka, K., Oka, Y., Osakabe, M., Sakakibara, S., Takeiri, Y., Tanaka, K., Tokuzawa, T., Tsumori, K., LHD Experimental Group
- Observation of Electron Temperature Profiles with Bulged Regions around the $i=1$ Magnetic Surfaces of the Large Helical Device*
J. Plasma Fusion Res. Vol.80, No.4 (2004) pp.277-278
- (170) Narihara, K., Yamada, I., Hayashi, H., Yamauchi, K.
- Design, Construction, and Performance of a Composite Mirror for Collecting Thomson Scattered Light from the Large Helical Device Plasma*
Rev. Sci. Instrum. Vol.75, No.10 (Oct. 2004) pp.3878-3880
- (171) Narushima, Y., Watanabe, K.Y., Sakakibara, S., Nakajima, N., Nishimura, K., Yamada, H., Yamazaki, K., LHD Experimental Group, Cooper, W.A.
- MHD Stability of Low- n Ideal External Mode in Large Helical Device Plasma*
J. Plasma Fusion Res. SERIES Vol.6 (2004) pp.214-217
- (172) Nemov, V., Shimizu, A., Okamura, S., Isobe, M., Suzuki, C., Nishimura, S., Akiyama, T., Matsuoka, K.
- The Effect of Coil Misalignment on Particle Transport in Quasi-Axisymmetric Systems*
J. Plasma Fusion Res. Series Vol.6 (2004) pp.508-511
- (173) Nishimura, A., Iwahori, A., Heo, N.J., Nagasaka, T., Muroga, T., Tanaka, S.-I.
- Effect of precipitation and solution behavior of impurities on mechanical properties of low activation vanadium alloy*
J. Nucl. Mater. Vol. 329-333, Part 1 (Aug. 2004) pp. 438-441.
- (174) Nishimura, A., Iwahori, A., Heo, N. J., Nagasaka, T., Muroga, T., Tanaka, S. -I.
- Effect of Precipitation and Solution Behavior of Impurities on Mechanical Properties of Low Activation*
J.Nucl. Mater. Vol.329-333 (2004) pp.438-441

- (175) Nishimura, A., Kakeshita, T
Microstructural Stability of 316 Stainless Steel during Long Term Exposure to High Magnetic Fields at Cryogenic Temperatures
Adv. Cryog. Eng. Vol.50 (2004) pp.98-105
- (176) Nishimura, A., Mito, T., Yamada, S., Imagawa, S., Takahata, K., Yanagi, N., Chikaraishi, H., Tamura, H., Iwamoto, A., Hamaguchi, S., Y. Hishinuma, Y., Nyilas, A.
Measurement of Superconductor Motion in R&D Coil for Supercooling of the LHD Helical Coil
IEEE Trans. Appl. Supercond. Vol. 14, No.2 (2004) pp. 1515-1518.
- (177) Nishimura, K., Ashikawa, N., Masuzaki, S., Miyazawa, J., Sagara, A., Goto, M., Peterson, B.J., Komori, A., Noda, N., Ida, K., Kaneko, O., Kawahata, K., Kobuchi, T., Kubo, S., Morita, S., Osakabe, M., Sakakibara, S., Sakamoto, R., Sato, K., Shimozuma, T., Takeiri, Y., Tanaka, K., Motojima, O., LHD Experimental Group
Development of the plasma operational regime in the large helical device by the various wall conditioning methods
J. Nucl. Mater. Vol.337-339 (2004) pp.431-435
- (178) Nishimura, K., Ashikawa, N., Sagara, A., Noda, N., Kawahata, K., Morita, S., Peterson, B.J., Sakakibara, S., Takeiri, Y., Tanaka, K., Sato, K., Komori, A., LHD Experimental Group
Effects of Boronization in LHD
J. Plasma Fusion Res. Vol.79, No.12 (Dec. 2003)pp.1216-1217
- (179) Nishimura, S., Sugama, H.
Bootstrap Current Coefficients in Stellarators
J. Plasma Fusion Res. SERIES Vol.6 (2004) pp.437-441
- (180) Nishimura, S., Sugama, H., CHS Group
Neoclassical Transport Including Impurities and the Bootstrap Current in Advanced Helical Systems
Fusion Sci. Technol. Vol.46 (Jul. 2004) pp.77-81
- (181) Nishiura, M., Isobe, M., Saida, T., Sasao, M., Darrow, D.S.
Scintillator Probe Diagnostic for High Energy Particles Escaped from Large Helical Device
Rev. Sci. Instrum. Vol.75, No.10 (Oct. 2004) pp.3646-3648
- (182) Nobuta, Y., Yamauchi, Y., Hirohata, Y., Hino, T., Sagara, A., Masuzaki, S., Ashikawa, N., Noda, N., Motojima, O., LHD Experimental Group
Material probe study for plasma facing wall of LHD
J. Nucl. Mater. Vol.329-333 (2004) pp.800-803
- (183) Nozato, H., Morita, S., Goto, M., Takase, Y., Ejiri, A., Amano, T., Tanaka, K., Inagaki, S., LHD Experimental Group
A Study of Charge Dependence of Particle Transport Using Impurity Pellet Injection and High-Spatial Resolution Bremsstrahlung Measurement on the Large Helical Device
Phys. Plasmas Vol.11, No.5 (2004) pp.1920-1930
- (184) Nozawa, M., Murakami, M., Zhang, P., Kimura, N.
Variation of the film boiling mode in He II from the vicinity of the lambda pressure down to the saturated state
J. Cryo. Soc. Jpn. Vol.39, No.6 (June 2004) pp.277-284
- (185) Nozawa, N., Kimura, N., Murakami, M., Yamamoto, I.
Variation of Subcooled Film Boiling State in HeII with the Pressure
Adv. Cryog. Eng. Vol.49(2004) pp.968-975
- (186) Numata, R., Yoshida, Z., Hayashi, T.
Two-Fluid Nonlinear Simulation of Self-Organization of Plasmas with Flows
J. Plasma Fusion Res. SERIES Vol.6 (2004) pp.130-133
- (187) Numata, R., Yoshida, Z., Hayashi, T.
Nonlinear three-dimensional simulation for self-organization and flow generation in two-fluid plasmas
Compt. Phys. Commun. Vol.164 (2004) pp.291-296
- (188) Ogawa, H., Kumita, K., Ono, M., Tonegawa, A., Shibuya, T., Kawamura, K.
Spatial profiles of Molecular Assisted Recombination for the formation of the detached plasma
J. Plasma Fusion Res. SERIES Vol.6 (Apr. 2004) pp.453-456
- (189) Ohtsu, Y and Fujita, H.
Production of high-density capacitively coupled radio-frequency discharge plasma by high-secondary-electron-emission oxide
Appl. Phys. Lett. Vol.85, No.21 (Nov. 2004) pp.4875-4877
- (190) Ohya, K., Nakayama, Y., Hamada, Y., Tanabe, T., Kirschner, A., Phillips, V., Noda, N.
Modeling of Material Mixing Effects on Plasma Surface Interactions in Magnetic Fusion Devices
Physica Scripta Vol.T111 (May 2004) pp.138-144
- (191) Ohya, K., Tanabe, T., Kirschner, A., Hirai, T., Philipps, V., Wada, M., Ohgo, T., Noda, N.
Dynamic transition between erosion and deposition on a tungsten surface exposed to edge plasmas containing carbon impurities
J. Nucl. Mater. Vol.337-339 (Mar. 2005) pp.882-886
- (192) Ohya, K., Tanabe, T., Rubel, M., Wada, M., Ohgo, T., Hirai, T., Philipps, V., Kirschner, A., Pospieszczyk, A., Huber, A., Sergienko, G., Brezinsek, S., Noda, N.
Modeling of erosion and deposition patterns on C-W and W-Ta twin limiters exposed to the TEXTOR edge plasmas
J. Nucl. Mater. Vol.329-333 (Aug. 2004)pp.732-736

- (193) Ohya, M., Higuchi, A., Shirai, Y., Shiotsu, M., Imagawa, S.
Cooling Stability Test of He II Cooled LHD Conductor (2)-Experimental Results
IEEE Trans. Appl. Supercond. Vol.14, No.2 (2004) pp. 1447-1450
- (194) Oka, Y., Shoji, T., Hamabe, M., Sakawa, Y., Suzuki, C., Ikeda, K., Kaneko, O., Nagaoka, K., Osakabe, M., Takeiri, Y., Tsumori, K., Asano, E., Kawamoto, T., Kondo, T., Sato, M.
Characteristics of multiantenna rf ion source
Rev. Sci. Instrum. Vol.75, No.5 (May 2004) pp.1841-1843
- (195) Oka, Y., Tsumori, K., Takeiri, Y., Ikeda, K., Kaneko, O., Nagaoka, K., Osakabe, M., Asano, E., Kawamoto, T., Kondo, T., Sato, M., Grisham, L., Honda, A., Umeda, N., Yamamoto, T.
Studies of H⁻ source for large helical device-neutral beam
Rev. Sci. Instrum. Vol.75, No.5 (May 2004) pp.1803-1808
- (196) Okamoto, A., Nagaoka, K., Yoshimura, S., Vranjes J., Kono, M., Kado, S., Tanaka, M.Y.
Anti-ExB flow field associated with a vortex formation in a partially ionized plasma
Proceedings of 12th International Congress on Plasma Physics (Oct. 2004) <http://hal.ccsd.cnrs.fr/ccsd-00001987>
- (197) Okamoto, A., Yoshimura, S., Kado, S., Tanaka, M.Y.
Measurement of Azimuthal Flow Velocity Using Laser-induced Fluorescence Spectroscopy in a HYPER-I Plasma
J. Plasma Fusion Res. Vol.80, No.12 (Dec. 2004) pp.1003-1004
- (198) Okamoto, A., Yoshimura, S., Tanaka, M.Y.
Measurement of Supersonic Rotation Accompanied with a Plasma Hole
J. Plasma Fusion Res. SERIES Vol.6(2004) pp.606-609
- (199) Okamura, S., Matsuoka, K., Nishimura, S., Isobe, M., Suzuki, C., Shimizu, A., Ida, K., Fujisawa, A., S. Murakami, S., Yokoyama, M., Itoh, K., Hayashi, T., Nakajima, N., Sugama, H., Wakatani, M., Nakamura, Y., Anthony Cooper, W.
Confinement Characteristics of Quasi-Axisymmetric Stellarator CHS-qa
Nucl. Fusion Vol.44, No.5(2004) pp.575-581
- (200) Okamura, S., Minami, T., Oishi, T., Suzuki, C., Ida, K., Isobe, M., Yoshimura, Y., Nagaoka, K., Toi, K., Fujisawa, A., Akiyama, T., Iguchi, H., Ikeda, R., Kado, S., Matsuoka, K., Matsushita, H., Nakamura, K., Nakano, H., Nishimura, S., Nishiura, M., Ohshima, S., Shimizu, A., Takagi, S., Takahashi, C., Takeuchi, M., Yoshinuma, M.
Edge Transport Barrier Formation in Compact Helical System (CHS)
Plasma Phys. Control. Fusion Vol.46, No.5A (May 2004) pp.A113-A119
- (201) Okamura, T., Saeki, M., Shiotsu, M.
Numerical analysis on forced convection heat transfer in pressurized He II
IEEE Transactions on Applied Superconductivity Vol.14 No.2 (June 2004) pp.1758-1761
- (202) Okita, T., Wolfer, W.G.
A Critical Test of the Classical Rate Theory for Void Swelling
J. Nucl. Mater. Vol.327 (2004) pp.130-139
- (203) Okita, T., Wolfer, W.G., Barnett, D.
Motion and Rotation of Small Glissile Dislocation Loops in Stress Fields
Phys. Rev. Lett. Vol.92, No.8 (Feb. 2004) pp.085507 1-4
- (204) Ono, H., Kasada, R., Kimura, A.
Specimen Size Effects on Fracture Toughness of JLF-1 Reduced-Activation Ferritic Steel
J. Nucl. Mater. Vol.329-333(Dec. 2004)pp.1117-1121
- (205) Ono, M., Kumita, K., Tonegawa, A., Shibuya, T., Kawamura, K.
Control of H⁻ ion density in the sheet plasma by an electron emitter
J. Plasma Fusion Res.SERIES Vol.6 (Apr. 2004) pp.457-460
- (206) Ono, M., Tonegawa, A., Kumita, K., Shibuya, H., Kawamura, K.
Detached plasma control by negative ion in divertor simulator
J.Nucl.Mater. Vol.337-339 (Mar. 2005) pp.261-265
- (207) Osakabe, M., Seki, T., Takeiri, Y., Tanaka, K., Narihara, K., LHD- experimental Group, Murakami, S., Sasao, M.
Evaluation of Energetic Particle Confinement Using CXNPA with NB-blip Experiments on Large Helical Device
Rev. Sci. Instrum. Vol.75, No.10 (Oct. 2004) pp.3601-3603
- (208) Oya, Y., Kodama, H., Oyaidzu, M., Morimoto, Y., Matsuyama, M., Sagara, A., Noda, N., Okuno, K.
Implanted hydrogen isotope retention and chemical behavior in boron thin films for wall conditioning
J. Nucl. Mater. Vol.329-333 (Aug. 2004) pp.870-873
- (209) Ozaki, T., Goncharov, P., Murakami, S., Sanuki, H., Okamura, S., Sudo, S., Kubo, S., Shimoizuma, T., Ohkubo, K., Notake, T., Ida, K., Tanaka, K., Oka, Y., Osakabe, M., Takeiri, Y., Tsumori, K., Ikeda, K., Kaneko, O., Narihara, K., Nagayama, Y., Sakakibara, S., Shoji, M., Nakanishi, H., Kojima, M., Yamauchi, K., Kawahata, K., Komori, A., Motojima, O., LHD Experimental Group
Temperature, Density, Magnetic Field and Pitch Angle Dependence of Neutral Particle Spectrum in Large Helical Device
J. Plasma Fusion Res. SERIES Vol.6 (2004) pp.310-313
- (210) Ozaki, T., Goncharov, P., Sudo, S., Shoji, M., Kawahata, K., Kaneko, O., the LHD Experimental Group, Murakami, S.
Two dimensional scanning high-energy particle diagnostic system in Large Helical Device
Rev. Sci. Instrum. Vol.75, No.10 (Oct. 2004) pp.3604-3606

- (211) Parks, P.B., Baylor, L.R., Ishizaki, R., Jardin, S.C., Samtaney, R.
Recent advances in the theory and simulation of pellet ablation and fast fuel relocation in tokamaks
Proc. 20th Int. Conf. of Fusion Energy (IAEA) IAEA-CN-116/TH/P3-9(Nov. 2004)
- (212) Peterson, B. J., Sagara, A., Noda, N., Sato, K., Kato, T., Nakamura, Y., Masuzaki, S., Morisaki, T., Xu, Y., Goto, M., Morita, S., Shoji, M., Nishimura, K., Ashikawa, N., Kawahata, K., Ohyabu, N., Komori, A., the LHD Experiment Group
Experiences with carbon divertor operation in LHD
Physica Scripta Vol.T111 (2004) pp.29-33
- (213) Sagara, A., Imagawa, S., Mitarai, O., Dolan, T., Tanaka, T., Kubota, Y., Yamazaki, K., Watanabe, K.Y., Mizuguchi, N., Muroga, T., Noda, N., Kaneko, O., Yamada, H., Ohyabu, N., Uda, T., Komori, A., Sudo, S., Motojima, O.
Improved Structure and Long-life Blanket Concepts for Heliotron Reactors
Nucl. Fusion Vol.45 (Mar.2005) pp.258-263
- (214) Saida, T., Sasao, M., Isobe, M., Krasilnikov, A.V., Kumazawa, R., Mutoh, T., Watari, T., Seki, T., Saito, K., Murakami, S., Matsuoka, K., LHD experimental group
Study of Ripple-trapped Proton Behaviour in LHD by Two Line-of-sight Measurements of Fast Neutrals
Nucl. Fusion Vol.44, No.4 (Apr.2004) pp.488-495
- (215) Sakamoto, R., Yamada, H., Tanaka, K., Tokuzawa, T., Murakami, S., Goto, M., Morita, S., Ohyabu, N., Kawahata, K., Motojima, O., LHD experimental group
Observation of pellet ablation behaviour on the Large Helical Device
Nuclear Fusion Vol.44, No.5 (May 2004) pp.624-630
- (216) Sanin, A., Tanaka, K., Vyacheslavov, L., Kawahata, K., Akiyama, T.
Two-dimensional Phase Contrast Interferometer For Fluctuation Study on LHD
Rev. Sci. Instrum. Vol.75, No.10 (Oct. 2004) pp.3439-3441
- (217) Sanuki, H., Itoh, K., Fujisawa, A., Dong, J.Q.
Effect of Sheared Flow on Microinstabilities and Transport in Plasmas
Plasma Sci. Technol. Vol.7, No.1 (2005) pp.2610-2614
- (218) Sanuki, H., Todoroki, J.
Effect of Magnetic Axis Shift on Neoclassical Transport in Helical Torus
J. Plasma Fusion Res. SERIES Vol.6 (2004) pp.233-236
- (219) Satake, S., Okamoto, M.
Study of Finite-Orbit-Width Effect on Neoclassical Transport in Tokamak Core Region
J. Plasma Fusion Res. SERIES Vol.6 (2004) pp.144-147
- (220) Sato, M., Wakatani, M.
Study of neoclassical tearing modes based on a reduced MHD model in cylindrical geometry
Nucl. Fusion Vol.45, No 2 pp.143-149
- (221) Sawada, K., Kohashi, Y., Sakai, M., Saiki, T., Nakamura, H.
Finite-Difference Time-Domain Simulation of Polarization Near-Field Scanning Optical Microscope
HPCS2005 (June 2005) pp.123-129
- (222) Seki, M., Yamamoto, I., Sagara, A.
Overview of Recent Japanese Activities in Fusion Technology
Fusion Sci. Technol. Vol.47 (2005) pp.300-307
- (223) Sekimura, N., Morishita, K., Kuramoto, E., Soneda, N., Okita, T., Hiratani, M.
Theory and Modeling of Radiation Damage Processes in Materials
J. Plasma Fusion Res. Vol.80, No.3 (Mar. 2004) pp.228-235
- (224) Sheng Zheng-Ming, Mima, K., Zhang Jie, Sanuki, H.
Emission of Electromagnetic Pulses from a Laser Wakefield through Mode Conversion
Phys. Rev. Lett. Vol.94, No.11 (Mar. 2005) pp.950031-950034
- (225) Shimozuma, T., Idei, H., Shapiro, M., Temkin, R., Ito, S., Notake, T., Kubo, S., Yoshimura, Y., Kobayashi, S., Mizuno, Y., Takita, Y., Ohkubo, K.
Alignment Method of ECH Transmission Lines Based on the Moment and Phase Retrieval Method Using IR Images
J. Plasma Fusion Res. Vol.81, No.3 (2005) pp.191-196
- (226) Shinohara, K., Takechi, M., Ishikawa, M., Kusama, Y., Tsuzuki, K., Urata, K., Kawashima, H., Tobita, K., Fukuyama, A., Cheng, C.Z., Darrow, D.S., Kramer, G.J., Gorelenkov, N.N., Nazikian, R., Todo, Y., Miura, Y., Ozeki, T.
Energetic particle physics in JT-60U and JFT-2M
Plasma Phys. Control. Fusion Vol.46, No.7 (2004) pp.S31-S45
- (227) Shiozaki, Y., Todo Y.
Computer simulation of fishbone oscillation
J. Plasma Fusion Res. SERIES Vol.6 (2004) pp.618-621
- (228) Shiraga, H
High-Density Implosion of Fuel Target for Laser Fusion
The Review of Laser Engineering Vol.32, No.5 (May 2004) pp.306-312

- (229) Shiraga, H., Fujioka, S., A. Jaanimagi, P., Stoeckl, C., Stephens, R. B., Nagatomo, H., Tanaka, K. A., Kodama, R., Azechi, H.
Multi-imaging x-ray streak camera for ultrahigh-speed two-dimensional x-ray imaging of imploded core plasmas
Rev. Sci. Instrum. Vol.70, No.10 (Oct. 2004) pp.3921-3925
- (230) Shoji, M., Kumazawa, R., Saito, K., Watanabe, T., Nakamura, Y., Masuzaki, S., Morita, S., Goto, M., Noda, N., Ohyabu, N., LHD Experimental Groups
Three-dimensional proton trajectory analyses and simulation of neutral particle transport in an ICRF heated long pulse discharge on the large helical device
J. Nucl. Mater. Vol.337-339 (Mar. 2005) pp.186-190
- (231) Shoji, M., Morisaki, T., Masuzaki, S., Goto, M., LHD Experimental Groups
Fully-three Dimensional Simulation of Neutral Particle Transport in the Plasma Periphery on the Large Helical Device
J. Plasma Fusion Res. SERIES Vol.6 (2004) pp.512-515
- (232) Smirnov, R., Tomita, Y., Takizuka, T., Takayama, A., Chutov, Y.
Dynamics of Dust Particles Coming off a Wall in Sheath and Presheath
J. Plasma Fusion Res. SERIES Vol.6 (2004) pp.752-755
- (233) Smirnov, R., Tomita, Y., Takizuka, T., Takayama, A., Chutov, Yu.
Particle Simulation Study of Dust Particle Dynamics in Sheaths
Plasma Phys. Vol.44, No.1-3 (2004) pp.150 - 156.
- (234) Soneda, N., Okita, T., Morishita K., Kuramoto E., Hiratani, M., Sekimura, N.
How can we bridge the multiple timescale models of radiation damage processes?
J. Plasma Fusion Res. Vol.80, No.4 (Apr. 2004) pp.318-324
- (235) Spineanu, F., Vlad, M., Itoh, K., Sanuki, H., Itoh, S-I.
Polo Dynamics for the Flierl-Petviashvili Equation and Zonal Flow
Phys. Rev. Lett. Vol.93, No.2(July 2004)pp.025001-1~025001-4
- (236) Sudo, S., Kalinina, D., Stutman, D., Finkenthal, M., Tamura, N., Sato, K., Matsubara, A., LHD Experimental Group
Development of the Ultrasoft X-ray Diagnostic for Impurity Transport Studies with a Tracer-Encapsulated Solid Pellet Injection on LHD
J. Plasma Fusion Res. Vol.80, No.7(2004) pp.545-546
- (237) Sudo, S., Peterson, P.J., Kawahata, K., Nagayama, Y., Narihara, K., Hamada, Y., Toi, K., Ida, K., Iguchi, H., Sato, K., Morita, S., Ozaki, T., Nishizawa, A., Tanaka, K., Minami, T., Yamada, I., Mutoh, S., Emoto, M., Nakanishi, H., Goto, M., Ohdachi, S., Tokuzawa, T., Inagaki, S., Ido, T., Yoshinuma, M., Sakakibara, S., Masuzaki, S., Morisaki, T., Shoji, M., Osakabe, M., Ashikawa, N.
LHD Diagnostics Toward Steady-State Operation
IEEE Trans. Plasma Sci. Vol.32, No.1 (Feb.2004) pp.167-176
- (238) Sugama, H., Watanabe, T.-H.
Study of Electromagnetic Microinstabilities in Helical Systems with the Stellarator Expansion Method
Phys. Plasmas Vol.11, No.6 (June 2004) pp.3068-3077
- (239) Sugama, H., Watanabe, T.-H.
Dynamics of Zonal Flows in Helical Systems
Phys. Rev. Lett. Vol.94, No.11 (Mar. 2005) pp.115001 1-4
- (240) Sugama, H., Watanabe, T.-H.
Spectrum of the Velocity Distribution Function in the Slab Ion Temperature Gradient Driven Turbulence
J. Plasma Fusion Res. SERIES Vol.6 (2004) pp.271-274
- (241) Sugiyama, T., Asakura, Y., Uda, T., Abe, Y., Shiozaki T., Enokida, Y., Yamamoto, I.
Preliminary Experiments on Hydrogen Isotope Separation by Water-Hydrogen Chemical Exchange under Reduced Pressure
J. Nucl. Sci. Technol. Vol.41, No.6 (June 2004) pp.696-701
- (242) Suzuki, C., Okamura, S., Isobe, M., Nishimura, S., Shimizu, A., Akiyama, T., Matsuoka, K., Nakajima, N., Cooper, W.A., Nuhrenberg, C.
Effects of Current Profile on Global Ideal MHD Stability in a Compact Quasi-Axisymmetric Stellarator
J. Plasma Fusion Res. SERIES Vol.6 (2004) pp.519-522
- (243) Suzuki, C., Peterson, B.J., Ida, K.
Measurement of Impurity Emission Profiles in CHS Plasma Using AXUV Photodiode Arrays and VUV Bandpass Filters
Rev. Sci. Instrum. Vol.75, No.10 (Oct. 2004) pp.4142-4144
- (244) Suzuki, Y., Nakamura, Y., Kondo, K., Nakajima N., Hayashi, T.
Magnetohydrodynamic Equilibrium of Heliotron J Plasmas
Fusion Sci. Technol. vol.46, (2004) pp.234-240
- (245) Tachikawa, K.
Development of Nb3Sn Conductors
J. Cryo. Soc. Japan Vol.39, No.9 (2004) pp.377-382
- (246) Tachikawa, K., Ikeda, Y., Koyata, Y., Izawa, H., Takeuchi, T.
Structure and High-Field Performance of (Nb,Ta)3Sn Superconducting Wires Prepared from Sn-Ta sheets
J. Japan Inst. Metals Vol.68, No.9 (2004) pp.624-628

- (247) Tachikawa, K., Izawa, H., Ikeda, Y., Koyata, Y., Takeuchi, T.
Structure and High-Field Performance of (Nb,Ta)3Sn Wires Prepared from Sn-Ta Matrix
Progress of Nb-Based Superconductors (Apr. 2004) pp.9-16
- (248) Tachikawa, K., Izawa, H., Ikeda, Y., Koyata, Y., Takeuchi, T.
New High-Field (Nb,Ta)3Sn Superconductors Prepared from Sn-Ta Matrix
IEEE Trans. Appl. Supercond. Vol.14 (June 2004) pp.979-982
- (249) Tachikawa, K., Izawa, H., Ikeda, Y., Koyata, Y., Takeuchi, T. Watanabe, K.
Fabrication of High-Field (Nb,Ta)3Sn Conductors through a Jelly Roll Process
Adv. Cryog. Eng. Vol.50 (2004) pp.387-394
- (250) Tachikawa, K., Yamada, Y., Katagiri, K., Kumakura, H., Iwamoto, A., Watanabe, K.
Effect of metal powder addition in Ni-sheathed PIT MgB2 tapes
Adv. Cryogenic Mater. Eng. Vol.50 (2004) pp.561-568
- (251) Takagi, S., Toi, K., Takechi, M., Murakami, S., Tanaka, K., Nishimura, S., Isobe, M., Matsuoka, K., Minami, T., Okamura, S., Osakabe, M., Takahashi, C., Yoshimura, Y., CHS Experimental Group
Characteristics of Sawtooth Oscillations Observed in the Compact Helical System
Phys. Plasmas Vol.11, No.4 (2004) pp.1537-1544
- (252) Takahata, K.
Reduction of Hotspot Temperature in Cable-in-Conduit Conductors
J. Cryog. Soc. J. Vol.39, No.4 (2004) pp.161-165
- (253) Takahata, K., Mito T., Nishijima, S.
Numerical Analyses of Non-uniform Current Distribution within the Multi-strand Superconducting Cable for the Fusion Apparatus
IEEE Trans. Appl. Supercond. Vol.14, No.2 (June 2004) pp.1360-1364
- (254) Takahata, K., Tamura, H., Mito, T.
Thermal Contact Conductance between the Bundle and the Conduit in Cable-in-Conduit Conductors
IEEE Trans. Appl. Supercond. Vol. 14, No. 2 (2004) pp. 1477-1479
- (255) Takami, S., Inoue, T., Sakakibara, S., Matsuoka, K., Ise, T., Eto, D., Haga, T.
Current control system of the power supplies for LHD superconducting coils
IEEE Trans. Appl. Supercond. Vol.14, No.2 (June 2004) pp.1431-1434
- (256) Takeiri, Y.
Chapter 16 "Giant Ion Sources for Neutral Beams"
The physics and Technology of Ion Sources (Edited by Ian G. Brown), Second, Revised and Extended Edition (2004) pp.341-371
- (257) Takeiri, Y., Kubo, S., Shimozuma, T., Yokoyama, M., Osakabe, M., Ikeda, K., Nagaoka, K., Yoshimura, Y., Ida, K., Funaba, H., Tanaka, K., Peterson, B.J., Yamada, I., Ohyabu, N., Ohkubo, K., Kaneko, O., Komori, A., LHD Experimental Group, Murakami, S.
Electron ITB Formation with Combination of NBI and ECH in LHD
Fusion Sci. Technol. Vol.46 (July 2004) pp.106-114
- (258) Takeuchi, N., Seki, T., Torii, Y., Saito, K., Watari, T., Takase, Y., Kumazawa, R., Mutoh, T., Watanabe, T., Zhao, Y
Variation of N// and its effect on fast wave electron heating on LHD
J. Plasma Fusion Res. SERIES Vol.6 2004) pp.642-646
- (259) Tamura, H., Mito, T., Iwamoto, A., Yamada, Y., Tachikawa, K.
Mechanical Properties and Reinforcement of Bi-2212 Tubular Bulk Superconductor for Current Lead
IEEE Trans. Appl. Supercond. Vol.14, No.2 (June 2004) pp.1319-1322
- (260) Tamura, H., Mito, T., Yamada, Y., Tachikawa, K., Heller, R.
Design Study of HTS Current Lead Using Reinforced Bi-2212 Tubular Bulk
IEEE Transactions on Applied Superconductivity Vol. 14, No. 2 (2004) pp. 686-689
- (261) Tamura, S., Liu, X., Tokunaga, K., Tsunekawa, Y., Okumiya, M., Noda, N., Yoshida, N
High-temperature properties of joint interface of VPS-tungsten coated CFC
J. Nucl. Mater. Vol.329-333 (Aug. 2004) pp.711-716
- (262) Tamura, S., Liu, X., Tokunaga, K., Tsunekawa, Y., Okumiya, M., Noda, N., Yoshida, N.
High heat flux properties of pure tungsten and plasma sprayed tungsten coatings
J. Nucl. Mater. Vol.329-333 (Aug. 2004) pp.687-691
- (263) Tanaka, K., Morita, S., Sanin, A., Vyacheslavov, L., Michael, C., Kawahata, K., Murakami, S., Wakasa, A., Yamada, H., Miyazawa, J., Tokuzawa, T., Akiyama, T., Goto, M., Ida, K., Yoshinuma, M., Yamada, I., Yokoyama, M., Masuzaki, S., Morisaki, T., Sakamoto, R., Funaba, H., Komori, A.
Particle transports and related turbulent fluctuations on LHD
Proc. 20th Int. Conf. of Fusion Energy (IAEA) EX/P6-28 (Nov. 2004)
- (264) Tanaka, K., Sanin, A., Vyacheslavov, L., Akiyama, T., Kawahata, K., Tokuzawa, T., Ito, Y., Okajima, S.
Precise Density Profile Measurements by using a Two Color YAG/CO2 Laser Imaging Interferometer on LHD
Rev. Sci. Instrum. Vol.75, No.10 (Oct. 2004) pp.3429-3432

- (265) Tanaka, M.
Electrophoresis of a Rod Macroion under Polyelectrolyte salt: Is Mobility Reversed for DNA ?
Journal of Physics:Condensed Matters 16 (2004), pp.S2127-S2134
- (266) Tanaka, M.
A Personal Supercomputer Equipped with High-Speed Communication Software
Bulletin Phys. Soc. Jpn. Vol.59, No.12 (2004) pp.898-902
- (267) Tanaka, T., Suzuki, A., Muroga, T., Sato, F., Iida, T., Nishitani, T.
Radiation induced conductivity of ceramic coating materials under 14 MeV neutron irradiation
J. Nucl. Mater. Vol. 329-333, Part 2 (Aug. 2004) pp. 1434- 1437
- (268) Toda, S., Itoh, K.
Theoretical Study of the Hysteresis Characteristic of Electric Fields in Helical Plasmas
Plasma Phys. Control. Fusion Vol.46 (2004) pp.1039-1050
- (269) Todo, Y., Berk, H. L., Breizman, B. N.
Energetic ion transport due to Alfvén eigenmode bursts
J. Plasma Fusion Res. SERIES Vol.6 (2004) pp.69-73
- (270) Todo, Y., Nakajima, N., Shinohara, K., Takechi, M., Ishikawa, M., Yamamoto, S.
Nonperturbative effects of energetic ions on Alfvén eigenmodes
Fusion Energy 2004 (2004) TH/3-1 Ra
- (271) Todo, Y., Shinohara, K., Takechi, M., Ishikawa, M.
Nonlocal Energetic Particle Mode in a JT-60U Plasma
Phys. Plasmas Vol.12, No.1 (Jan. 2005) pp.012503-1~012503-7
- (272) Todoroki, J.
Integration Formula of the Magnetic Field Produced by the Finite Size Helical Coil with Arbitrary Polygonal Cross Section
J. J. A. P. Vol.43, No.3 (2004) pp.1209-1213
- (273) Todoroki, J., Sanuki, H., Yokoyama, M.
A New Method Constructing Magnetic Flux Coordinates
J. Plasma Fusion Res. Series Vol.6 (2004) pp.230-232
- (274) Toi, K., Ikeda, R., Takeuchi, M., Ito, T., Suzuki, C., Matsunaga, G., Shoji, T., Okamura, S., CHS Experimental Group
Experimental Simulation of High Temperature Plasma Transport Using Almost Dimensionally Similar Cold Plasmas in the Compact Helical System
J. Plasma Fusion Res. SERIES Vol.6 (2004) pp.516-518
- (275) Toi, K., Ohdachi, S., Yamamoto, S., Nakajima, N., Sakakibara, S., Watanabe, K.Y., Inagaki, S., Nagayama, Y., Narushima, Y., Yamada, H., Narihara, K., Morita, S., Akiyama, T., Ashikawa, N., Ding, X., Emoto, M., Funaba, H., Goto, M., Ida, K., Idei, H., Ido, T., Ikeda, K., Imagawa, S., Isobe, M., Itoh, K., Kaneko, O., Kawahata, K., Kobuchi, T., Komori, A., Kubo, S., Kumazawa, R., Li, J., Y. Liang, Y., Masuzaki, S., Mito, T., Miyazawa, J., Morisaki, T., Murakami, S., Muto, S., Mutoh, T., Nagaoka, K., Nakamura, Y., Nakanishi, H., Nishimura, K., Nishizawa, A., Noda, N., Notake, T., Ohkubo, K., Ohtake, I., Ohyabu, N., Oka, Y., Okamura, S., Ozaki, T., Peterson, B.J., Sagara, A., Saida, T., Saito, K., Sakamoto, R., Sasao, M., Sato, K., Sato, M., Satow, T., Seki, T., Shimozuma, T., Shoji, M., Sudo, S., Tanaka, M.Y., Tamura, N., Tanaka, K., Tsumori, K., Uda, T., Watari, T., Weller, A., Xu, Y., Yamada, I., Yokoyama, M., Yoshimura, S., Yoshimura, Y., Yamazaki, K., Matsuoka, K., Motojima, O., Hamada Y., Fujiwara, M.
MHD Instabilities and Their Effects on Plasma Confinement in Large Helical Device Plasmas
Nucl. Fusion Vol.44, No.2 (Feb. 2004) pp.217-225
- (276) Toi, K., Ohdachi, S., Yamamoto, S., Sakakibara, S., Narihara, K., Tanaka, K., Morita, S., Morisaki, T., Goto, M., Takagi, S., Watanabe, F., Nakajima, N., Watanabe, K.Y., Ida, K., Ikeda, K., Inagaki, S., Kaneko, O., Kawahata, K., Komori, A., Masuzaki, S., Matsuoka, K., Miyazawa, J., Nagaoka, K., Nagayama, Y., Oka, Y., Osakabe, M., Ohyabu, N., Takeiri, Y., Tokuzawa, T., Tsumori, K., Yamada, H., Yamada, Y., Yoshinuma, K., LHD Experimental Group
Observation of the Low to High Confinement Transition in the Large Helical Device
Phys. Plasmas Vol.12, No.2 (Feb. 2005) pp.020701-1~020701-4
- (277) Toi, K., Yamamoto, S., Nakajima, N., Ohdachi, S., Sakakibara, S., Osakabe, M., Murakami, S., Watanabe, K.Y., Goto, M., Kawahata, K., Kolesnichenko, Ya.I., Masuzaki, S., Morita, S., Narihara, K., Narushima, Y., Takeiri, Y., Tanaka, K., Tokuzawa, T., Yamada, H., Yamada, I., Yamazaki, K., LHD Experimental Group
Energetic Ion Driven Alfvén Eigenmodes in Large Helical Device Plasma with Three-dimensional Magnetic Structure and Their Impact on Energetic Ion Transport
Plasma Phys. Control. Fusion Vol.46 No.7 (July 2004) pp.S1-S13
- (278) Tokitani, M., Miyamoto, M., Koga, D., Tokunaga, K., Fujiwara, T., Yoshida, N., Masuzaki, S., Ashikawa, N., Morisaki, T., Shoji, M., Komori, A., LHD Experimental Group
Microscopic and macroscopic damage in metals exposed to LHD divertor plasmas
J. Nucl. Mater. Vol.337-339, No.1 (Mar. 2005) pp.937-941
- (279) Tokitani, M., Miyamoto, M., Tokunaga, K., Fujiwara, T., Yoshida, N., Komori, A., Masuzaki, S., Ashikawa, N., Inagaki, S., Kobuchi, T., Goto, M., Miyazawa, J., Nishimura, K., Noda, N., Peterson, B.J., Sagara, A., LHD experimental group
Microscopic Modification of Wall Surface by Glow Discharge Cleaning and its Impact on Vacuum Properties of LHD
Proc. 20th Int. Conf. of Fusion Energy (IAEA) IAEA-CSP-25/CD, No.1(Nov. 2004.) EX/P5-34
- (280) Tokunaga, K., Baldwin, M. J., Doerner, R. P., Noda, N., Kubota, Y., Yoshida, N., Sogabe, T., Kato, T., Schedler, B.
Blister formation and deuterium retention on tungsten exposed to low energy and high flux deuterium plasma
J. Nucl. Mater. Vol.337-339(Mar. 2005) pp.887-891

- (281) Tolstikhin, O, Namba, C.
Quantum-mechanical and semiclassical study of the collinear three-body Coulomb problem: Inelastic collisions below the three-body disintegration threshold
Phys. Rev. A Vol.70, No.6 (Dec. 2004) pp.062721-1~062721-21
- (282) Tomita, Y., Smirnov, R., Chutov, Y., Takayama, A., Takizuka, T.
Reduction of Sheath Potential and Dust Ion-Acoustic Wave by Negatively Charged Dust Particles
J. Plasma Fusion Res. SERIES Vol.6 (2004) pp.429-432
- (283) Tomita, Y., Smirnov, R., Chutov, Yu., Takayama, A., Takizuka, T.
Reduction of Sheath Potential and Particle Flux at a Target Plate by Negatively Charged Dust Particles
Plasma Phys. Vol.44, No.1-3 (2004) pp.138 - 143
- (284) Tomita, Y., Smirnov, R., Zhu, S.
Stationary Potential Formation and Oscillations in Plasma with Immovable Dust Particles
Plasma Sci. Technol. Vol.17, No.1 (June 2005) pp.2657-2659
- (285) Torikai, Y., Tokunaga, K., Baldwin, M. J., Doerner, R. P., Noda, N., Kubota, Y., Yoshida, N., Sogabe, T., Kato, T., Schedler, B.
Tritium distribution in JET Mark IIA type divertor tiles analysed by BIXS
J. Nucl. Mater. Vol.337-339 (Mar. 2005) pp.575-579
- (286) Toyofuku, M., Ohtsu, Y and Fujita, H.
High ozone generation with a high-dielectric constant material
J. J. A. P. Vol.43, No.7 (July 2004) pp.4368-4372
- (287) Tsuchiya, T., Noguchi, S., Yamashita, H., Ishiyama, A., Yanagi, N., Mito, T.
Transient Stability Analysis of Large Aluminum Stabilized Superconductor by 2D and 3D Finite Element Analysis
IEEE Trans. Appl. Supercond Vol. 14, No. 2 (2004) pp. 1330-1333
- (288) Tsumori, K., Nagaoka, K., Osakabe, M., Takeiri, Y., Ikeda, K., Kaneko, O., Oka, Y., Kawamoto, T., Asano, E., Sato, M., Kondo, T., Asano, S., Suzuki, Y., Okuyama, T., and Ichihashi, K.
High power beam injection using an improved negative ion source for the large helical device
Rev. Sci. Instrum. Vol.75, No.5 (May 2004) pp.1847-1850
- (289) Vlad, M., Spineanu, F., Misguich, J.H., Reuss, J-D., Balescu, R., Itoh K., Itoh, S-I.
Lagrangian versus Eulerian correlations and transport scaling
Plasma Phys. Control. Fusion volume 46, issue 7 (2004) 1051 - 1063
- (290) Vranjes, J., Tanaka, M.Y., Kono, M., Poedts, S.
Electrostatic Perturbations in Partially Ionized Plasma with the Effects of Ionization and Recombination
Phys. Plasmas Vol.11, No.9(Sep. 2004)pp.4188-4195
- (291) Wang, A. K., Sanuki, H., Dong, J. Q., Zonca, F., Itoh, K.
Magnetic field gradient and curvature driven drift modes in the toroidal plasmas
Chinese Physics Letter Vol.21, No.8 (2004) pp.1575-1577
- (292) Wang, A., Sanuki, H., Dong, J., Zonca, F., Itoh, K.
Interaction Between the Trapped Electrons and Magnetic Field Gradient and Curvature-Driven Drift Waves in the Toroidal Plasma
J. Plasma Fusion Res. SERIES Vol.6 (2004) pp.237-240
- (293) Watanabe, K.Y., Narushima, Y., Sakakibara, S., Ohdachi, S., Toi, K., Cooper, A.W., Nakajima, N., Narihara, K., Tanaka, K.
Relationships between the Prediction of Linear MHD Stability Criteria and the Experiment in LHD
J. Plasma Fusion Res. Series Vol.6 (2004) pp.523-526
- (294) Watanabe, K.Y., Weller, A., Sakakibara, S., Narushima, Y., Ohdachi, S., Narihara, K., Tanaka, K., Ida, K., Toi, K., Yamada, H., Suzuki, Y., Kaneko, O., Large Helical Device Experimental Group, Wendelstein 7-AS Experimental Group
Progress of High-Beta Experiments in Stellarator/Heliotron
Fusion Sci. Technol. Vol.46, No.1 (July 2004) pp.24-33
- (295) Watanabe, T., Choyal, Y., Minami, K.
Microwave Excitation by Constrained Large Orbit Electron Beam-Aunified Dispersion Relation for Slow and Fast -Wave Devices
IEEE Trans. Plasma Sci. Vol.32, No.3(June 2004) pp.1298-1309
- (296) Watanabe T., Gotoh T.
Statistics of a Passive Scalar in Homogeneous Turbulence
New Journal of Physics 6 (2004) 40
- (297) Watanabe, T.-H., Sugama, H.
Kinetic Simulation of Steady States of Ion Temperature Gradient Driven Turbulence with Weak Collisionality
Phys. Plasmas Vol.11, No.4 (Apr. 2004) pp.1476-1483
- (298) Watanabe, T.-H., Sugama, H.
Plasma turbulent transport and fine-scale structures of phase space distribution function
J. Plasma Fusion Res. SERIES Vol.6 (2004) pp.23-27
- (299) Watanabe, T.-H., Sugama, H.
Velocity-space structures of distribution function in toroidal ion temperature gradient turbulence
Proc. 20th Int. Conf. of Fusion Energy (IAEA) IAEA TH/8-3Rb(Nov. 2004)

- (300) Watanabe, T., Matsumoto, Y., Hishiki, M., Oikawa, S., Hojo, H.
Ignition Condition for p-11B Reactor with LHD Type Magnetic Field Configuration
J. Plasma Fusion Res. SERIES Vol.6 (2004) pp.630-633
- (301) Watanabe, T., Matsumoto, Y., Hishiki, M., Oikawa, S., Hojo, H., Shoji, M., Masuzaki, S., Kumazawa, R., Saito, K., Seki, T., Mutoh, T., Komori, A., LHD Experimental Group
Magnetic Field Structure and Confinement of Energetic Particles in the LHD
Proc. 20th Int. Conf. of Fusion Energy (IAEA) IAEA-CN-116/EX/P4-47(Nov. 2004)
- (302) Watari, T., Hamada, Y., Fujisawa, A., Toi, K., Itoh, K.
Extension of Geometric Acoustic Mode Theory to Helical Systems
Phys Plasmas Vol.12, No.6 (June 2005) pp.062304 1-8
- (303) Yamada, H., Ida, K., Murakami, S., Watanabe, K.Y., Ascasibar, E., Brakel, R., Dinklage, A., Harris, J.H., Okamura, S., Sano, F., Stroth, U., Inagaki, S., Tanaka, K., Goto, M., Nishimura, K., Narihara, K., Morita, S., Sakakibara, S., Peterson, B.J., Sakamoto, R., Miyazawa, J., Morisaki, T., Osakabe, M., Toi, K., Tamura, N., Ikeda, K., Yamazaki, K., Kawahata, K., Kaneko, O., Ohyabu, N., Komori, A., Motojima, O.
Configuration Effect on Energy Confinement and Local Transport in LHD and Contribution to the International Stellarator Database
Fusion Sci. Technol. Vol.46, No.1 (July 2004) pp.82-90
- (304) Yamada, H., Ida, K., Watanabe, K.Y., Sakakibara, S., Inagaki, S., Ohyabu, N., Yokoyama, M., Yoshinuma, M., Cooper, W.A., Kobuchi, T., Osakabe, M., Toi, K., Suzuki, Y., Akiyama, T., Asakura, N., Ashikawa, N., Emoto, M., Fujita, T., Fujiwara, M., Funaba, H., Goncharov, P., Goto, M., Hamada, Y., Higashijima, S., Hino, T., Hoshino, M., Ichimura, M., Idei, H., Ido, T., Ikeda, K., Isayama, A., Isobe, M., Itoh, T., Itoh, K., Kado, S., Kalinina, D., Kaneba, T., Kaneko, O., Kawahata, K., Kawazome, H., Kondo, K., Lyon, J.F., Mase, A., Masuzaki, S., Matsuoka, K., Miura, Y., Miyazawa, J., Morisaki, T., Morita, S., Muto, S., Mutoh, T., Nagaoka, K., Nagasaki, K., Nagayama, Y., Nakamura, Y., Nakanishi, H., Narihara, K., Nishimura, K., Nishiura, M., Nishizawa, A., Noda, N., Notake, T., Nozato, H., Ohadachi, S., Ohkubo, K., Ohyama, N., Oka, Y., Okada, H., Ozaki, T., Peterson, B.J., Sagara, A., Saida, T., Saito, K., Sakamoto, M., Sakamoto, R., Sasao, M., Sato, K., Seki, T., Shimozuma, T., Shoji, M., Sudo, S., Takagi, S., Takahashi, Y., Takase, Y., Takeiri, Y., Takenaga, H., Takeuchi, N., Tamura, N., Tanaka, K., Tanaka, M., Tokuzawa, T., Torii, Y., Tsumori, K., Watanabe, F.,
Recent Results from LHD Experiment with Emphasis on Relation to Theory from Experimentalist's View
J. Plasma Fusion Res. SERIES Vol.6 (2004) pp.51-59
- (305) Yamada, I., Narihara, K., Funaba, H., Hayashi, H., LHD Experimental Group
Design and Development of the Large Helical Device TV Thomson Scattering
Rev. Sci. Instrum. Vol.75, No.10, PartII (Oct 2004) pp.3912-3914
- (306) Yamada, Y., Chikai, S., Watanabe, M., Tachikawa, K., Tamura, H., Iwamoto, A., Mito, T.
Transport Performance in Bi2212 Cylinders Prepared by the Diffusion Process for Current Lead Application
IEEE Trans. Appl. Supercond. Vol.14, No.2 (June 2004) pp.638-641
- (307) Yamamoto, S., Toi, K., Nakajima, N., Ohdachi, S., Sakakibara, S., Watanabe, K.Y., Goto, M., Ikeda, K., Kaneko, O., Kawahata, K., Masuzaki, S., Morisaki, T., Morita, S., Murakami, S., Narihara, K., Oka, Y., Osakabe, M., Takeiri, Y., Tanaka, K., Tokuzawa, T., Tsumori, K., Yamada, H., Yamada, I., Yamazaki, K., and LHD experimental group
Observation of Helicity-Induced Alfvén Eigenmodes in Large-Helical-Device Plasmas Heated by Neutral-Beam Injection
Phys. Rev. Lett. Vol.91, No.24 (Dec.2003) pp.(245001-1)-(245001-4)
- (308) Yamanishi, H., Miyake, H., Yamazaki, T., Komura, K.
Sensitivity of TLD and RPLD to Cosmic Ray Hard Component Measured in Ogoya Tunnel
Jpn. J. Health Pys. Vol.39, No.2(June2004) PP.108-112
- (309) Yamaoka, H., Matsumoto, Y., Nishiura, M., Sasao, M., Wada, M.
Angular resolved energy distributions of low energy light ions reflected from a polycrystalline Mo surface
J. Nucl. Mater. Vol.337-339 (Mar. 2005) pp.942-945
- (310) Yamauchi, Y., Yamada, T., Hirohata, Y., Hino, T., Muroga, T.
Deuterium retention in V-4Cr-4Ti alloy after deuterium ion irradiation
J. Nucl. Mater. Vol. 329-333, Part 1 (Aug. 2004) pp.397-400
- (311) Yamazaki, K., Mikhailov, M., Sakakibara, S., Okamura, S., Garcia, J., Dies, J., Funaba, H., Amano, T.
Neoclassical and Anomalous Transport Analysis of Helical Reactor Plasmas
J. Plasma Fusion Res. SERIES Vol.6 (2004) pp.357-361
- (312) Yanagi, N., Mito, T., Morikawa, J., Ogawa, Y., Hamaguchi, S., Hishinuma, Y., Ohkuni, K., Hori, D., Iwakuma, M., Uede, T.
Engineering Development of an HTS Floating Coil for the Mini-RT Project
J. Cryog. Soc. J. Vol.39, No.5 2004 pp.193-200
- (313) Yanagi, N., Morikawa, J., Mito, T., Ogawa, Y., Ohkuni, K., Hori, D., Yamakoshi, S., Iwakuma, M., Uede, T.
Cool-down and Excitation Tests of the HTS Floating Coil in the Mini-RT Project
J. Cryog. Soc. J. Vol.39, No.5 (2004) pp.201-208
- (314) Yanagisawa, T., Itoh, T., Saruyama, Y., Fujiwara, S.
Thermal, Structural and Ferroelectric Properties of Amorphous Phases in Quenched Nylon 6 Film
J. Phys. Soc. Jpn. Vol.73, No.10 (Oct. 2004) pp.2763-2767
- (315) Yao, Z., Suzuki, A., Muroga, T., Katahira, K.
Chemical formation of erbium oxide layer on V-4Cr-4Ti during exposure to liquid lithium doped with erbium
J. Nucl. Mater. Vol. 329-333 (2004) pp.1414-1418

- (316) Yao, Z., Suzuki, A., Nagasaka, T., Muroga, T.
Behavior of Oxygen in Fusion Candidate Vanadium Alloys during Oxidation and Annealing
 Materials Science Forum 475-479 (2005) pp.1445-1448
- (317) Yatsuyanagi, Y., Kiwamoto, Y., Tomita, H., Sano, M. M., Yoshida, T., Ebisuzaki, T.
Dynamics of Two-Sign Point Vortices in Positive and Negative Temperature States
 Phys. Rev. Lett. Vol.94 (2005) pp.054502 (1-4)
- (318) Yokoi, N., Yoshizawa, A., Itoh, K., Itoh, S.-I.
A variational analysis of flow-reversal condition in a turbulent swirling pipe flow using the bulk-helicity concept
 Phys. Fluids Vol.16, No. 5 (2004) 1186
- (319) Yokoyama, M., Ida, K., Yoshinuma, M., Shimoizuma, T., Watanabe, K.Y., Murakami, S., Wakasa, A., Kubo, S., Takeiri, Y., Narihara, K., Morita, S., Tanaka, K., Yoshimura, Y., Notake, T., Osakabe, M., Itoh, K., Komori, A., Motojima, O., LHD experimental G
The Effect of Non-Axisymmetry of Magnetic Configurations on Radial Electric Field Transition Properties in the LHD
 J. Plasma Fusion Res. SERIES Vol.6 (2004) pp.218-221
- (320) Yokoyama, M., Watanabe, K.Y., Nakajima, N
The Configuration Dependence of Ripple Transport in LHD
 J. Plasma Fusion Res. Vol.81, No.2 (Feb. 2005) pp.83-84
- (321) Yoshikawa, K., Masuda, K., Yamamoto, Y., Takamatsu, T., Toku, H., Nagasaki, K., Hotta, E., Yamauchi, K., Ohnishi, M., Osawa, H.
Research and Development of a Compact Fusion Neutron Source for Humanitarian Landmine Detection
 Proc. 20th Int. Conf. of Fusion Energy (IAEA) IC/P6-54(Nov. 2004)
- (322) Yoshikawa, M., Kubota, Y., Kobayashi, T., Saito, M., Numada, N., Nakashima, Y., Cho, T., Koguchi, H., Yagi, Y., Yamaguchi, N.
Absolute calibration for vacuum ultraviolet spectrograph system for plasma diagnostics
 Review of Scientific Instruments Vol.75 (2004) pp.4088-4090
- (323) Yoshikawa, M., Saito, M., Kubota, Y., Kobayashi, T., Nakashima, Y., Higashizono, H., Itakura, A., Hirata, M., Miyake, Y., Kohagura, J., Cho, T.
H Measurements in the PLUG/BARRIER Cells of the Tandem Mirror GAMMA 10
 Transactions of Fusion Science and Technology Vol.47, No.1T (June 2005) pp.339-341
- (324) Yoshikawa, M., Sedo, K., Kubota, Y., Kobayashi, T., Itakura, A., Kohagura, J., Murakami, I., Kato, T., Cho, T.
Study of Impurity Ion radiation intensities using collisional-radiative model in the GAMMA 10 plasma
 J. Plasma Fusion Res. SERIES Vol.6 (2004) pp.685-688
- (325) Yoshimura, S., Okamoto, A., Tanaka, M.Y
Observation of Plasma Hole in an ECR Ar Plasma
 J. Plasma Fusion Res. SERIES Vol.6 (2004) pp.610-613
- (326) Yoshimura, Y., Akiyama, T., Isobe, M., Shimizu, A., Suzuki, C., Takahashi, C., Nagaoka, K., Nishimura, S., Minami, T., Okamura, S., Matsuoka, K., Kubo, S., Shimoizuma, T., Notake, T., Ohkubo, K.
Variation of Heating Efficiency of Magnetically Sheared CHS Plasmas by Polarization Control of 106GHz EC-Wave
 J. Plasma Fusion Res. SERIES Vol.6 (2004) pp.651-654
- (327) Yoshinuma, M., Ida, K., Baldzuhn, J.
Charge Exchange Spectroscopy by Fabry-Perot Spectrometer in W7-AS
 Rev. Sci. Instrum. Vol.75, No.10 (Oct. 2004) pp.4136-4138
- (328) Yoshizawa, A., Itoh, S.-I., Itoh, K., Yokoi, N.
Dynamos and MHD Theory of Turbulence Suppression
 Plasma Phys. Control. Fusion Vol.46, No.3 (Mar. 2004) R25-R94

Author Index

A

Abe, H.	233
Abe, K.	238
Abe, R.	114, 119
Adachi, Y.	90
Agrawal, D.	398
Akiyama, R.	279
Akiyama, T.	158, 161, 207, 268, 269, 270, 271, 272, 273, 276, 277, 278, 285, 286, 323, 325, 326
Amano, H.	223
Ando, A.	315, 373, 375, 456
Ando, T.	213
Aoki, A.	206
Aoki, J.	316
Aoyama, H.	295, 378
Araki, K.	362
Aramaki, M.	205, 302, 304
Arimoto, H.	34, 466
Arimoto, K.	159, 387
Arita, K.	249
Asakura, N.	408
Asakura, Y.	260, 262, 263, 264, 265, 266, 439, 441
Asano, E.	73, 136, 137, 138, 140
Asano, S.	137
Asaoka, Y.	344, 377
Ascasibar, E.	11
Ashikawa, N.	28, 78, 79, 80, 81, 82, 83, 84, 85, 217, 219
Atake, M.	208, 386, 451
Atarashi, M.	223
Azechi, H.	474, 475, 483, 484
Azumi, M.	183

B

Baba, M.	433
Baba, T.	114
Balandin, A.L.	159, 387
Banno, N.	424
Beidler, C.D.	11, 22, 171
Belchenko, Yu.	140
Budaev, V.	385

C

Carreras, B.A.	165
Chen, A.	408
Chiba, S.	257
Chikaraishi, H.	8, 93, 107, 114, 119
Cho, T.	194, 195, 453, 454, 459, 461, 462, 463
CHS Experimental Group.....	268, 292
CHS Group	276, 277, 278, 279, 280, 281, 283, 286, 297
Chu, M.S.	166
Cooper, W.A.	41

D

Darrow, D.S.	134
Davydenko, V.	140
Dinklage, A.	11
Dong, J.Q.	187, 188, 189

F

Ebara, S.	258, 431
Eiza, N.	242
Ejiri, A.	153, 379, 488
Emoto, M.	157

Enokida, Y.	263
Ezumi, N.	63

F

Feng, Y.	49
Fujimoto, S.	458
Fujimoto, T.	208, 386, 451
Fujisawa, A.	268, 273, 280, 281, 282, 283, 286, 295, 300, 317, 322
Fujita, H.	206, 318
Fujita, J.	415, 416, 417
Fujita, T.	17
Fujiwara, S.	368
Fujiwara, T.	98
Fukada, S.	255, 430, 477
Fukagawa, Y.	464
Fukai, T.	463
Fukumasa, O.	204
Fukumoto, K.	246
Fukuyama, A.	70, 86, 200, 449
Funaba, H.	12, 13, 38, 86, 145, 399, 400
Furukawa, H.	259, 475
Furukawa, M.	355
Furuya, Y.	311
Furuzawa, A.	210

G

GAMMA 10 Group	462
Gao, Zh.	187, 188, 189
Goncharov, P.	25
Goncharov, P.R.	75
Goto, M.	16, 28, 33, 52, 53, 205, 208, 210, 386, 399, 450
Goto, T.	388
Gotoh, T.	361
Grisham, L.	73, 138
Grossbeck, M.L.	421

H

Hagita, T.	101
Hagiwara, M.	433
Hallatschek, K.	179, 180
Hamabe, M.	204, 247
Hamada, Y.	147, 148, 149
Hamaguchi, S.	103, 115, 123, 374
Hamajima, T.	88, 100, 106
Hamasaki, S.	105
Han, X.	472
Hanada, K.	379, 486, 488, 491
Hanatani, K.	465
Hara, M.	102, 112, 219
Harris, J.H.	11
Haruyama, T.	103
Hasegawa, H.	359, 364, 383
Hasegawa, J.	481
Hasegawa, M.	324
Hashiba, Y.	217
Hashida, M.	471
Hashimoto, M.	368
Hashizume, H.	220, 234, 254, 257
Hashizume, K.	219
Hata, K.	103, 226
Hata, S.	284
Hatakeyama, A.	408
Hatakeyama, R.	358, 457
Hatanaka, M.	315, 375
Hatano, Y.	96, 219, 410

Hatayama, A.	344
Hattori, K.	315, 373, 375, 456
Hayashi, H.	144, 145
Hayashi, K.	119
Hayashi, T.	164, 168, 175, 176, 334, 355
Hegna, C.C.	333
Heliotron J Experimental Team	468
Heller, R.	121
Hemmi, T.	118, 125
Henmi, T.	114
Higaki, H.	77, 449, 455, 456, 461
Higashijima, S.	408
Higashizono, Y.	460
High-Density Theme Group	54
Himura, H.	297
Hino, T.	84, 217, 238, 425
Hinoki, T.	242, 476
Hirakane, S.	429
Hirano, K.	322
Hirata, M.	453, 454, 463
Hirayama, T.	309
Hirohata, Y.	219, 425
Hirooka, Y.	391, 485, 490
Hishinuma, Y.	213, 227, 422, 424
Hiwatari, R.	344, 377
Hochin, T.	163
Hoelzer, D.T.	421
Hojo, H.	169, 452, 459, 461
Homma, H.	219
Honda, A.	73, 138
Hori, D.	355
Horiguchi, K.	228
Horii, S.	317
Horiike, H.	428
Horikoshi, M.	347
Horioka, K.	481, 482
Horiuchi, R.	350, 351, 352, 353, 354, 444, 478
Hosaka, S.	391
Hoshika, H.	379
Hoshino, M.	31
Hosoda, Y.	160
Hozumi, N.	112
Hudson, S.R.	333

I

Ichiguchi, K.	165, 166
Ichihashi, K.	137
Ichimasa, Y.	222
Ichimura, M.	77, 449, 455, 456, 461
Ichizono, K.	206
Ida, K.	16, 19, 22, 23, 25, 34, 45, 51, 150, 271, 272, 273, 274, 279, 288, 300, 317, 413, 483, 491
Ida, M.	428
Ide, K.	455
Idei, H.	67, 203, 489
Ido, T.	147, 148, 149
Igami, H.	9, 21, 24, 65, 66, 67, 68, 69, 127, 128, 278, 286
Ignatenko, M.	152, 154, 459
Iguchi, H.	281, 284, 289, 290, 295, 299, 300, 317, 414
Iguchi, S.	291
Iguichi, H.	458
Iida, T.	240, 428, 437, 471
Iijima, Y.	227, 422, 424
Iinuma, K.	410
Iio-Tsuji, S.	285
Ikeda, K.	25, 26, 27, 72, 73, 136, 137, 138, 140
Ikeda, R.	292, 293, 295, 296, 376
Ikeda, T.	240
Ikeda, Y.	73, 138

Imagawa, S.	87, 88, 89, 90, 91, 115, 123, 216, 250, 252, 253, 258, 493
Imai, M.	408
Imamura, Y.	237
Imazawa, R.	159, 387
Imazu, S.	156
Inagaki, S.	9, 14, 15, 24, 43, 66, 201, 286, 378
Inamoto, A.	228
Inoue, D.	455
Inoue, K.	422
Inoue, S.	428
Inoue, T.	147, 148
Inutake, M.	315, 373, 375, 456
Isaev, M. Yu.	325
Isayama, A.	43, 67
Ise, T.	93
Ishibashi, K.	105
Ishida, M.	107
Ishigohka, T.	90, 91
Ishiguro, S.	343, 345, 358, 359, 364, 478
Ishii, K.	299, 458
Ishii, N.	70, 200
Ishikawa, M.	194, 195, 196, 197, 198, 199, 335, 453, 454
Ishimoto, Y.	83, 460
Ishiyama, A.	106
Ishizaki, R.	342, 475
Ishizawa, A.	350, 351, 352, 353, 354
Islam, Md. K.	460
Isobe, M.	134, 201, 268, 269, 270, 271, 272, 273, 276, 277, 278, 279, 286, 287, 288, 294, 295, 297, 300, 323, 324, 325, 326, 467, 484
Itagaki, T.	159, 387
Itakura, A.	457, 459
Ito, A.	367
Ito, H.	410
Ito, S.	9, 65, 68, 127, 128, 254
Ito, T.	376
Ito, Y.	207
Itoga, T.	433
Itoh, A.	408
Itoh, K.	172, 177, 178, 179, 180, 181, 182, 183, 186, 188, 189, 280, 372
Itoh, S.	69
Itoh, S.-I.	172, 179, 180, 181, 182, 183, 186, 372
Itoh, T.	368
Iwakiri, H.	79
Iwakuma, M.	110, 114, 380
Iwama, N.	160
Iwamae, A.	208, 386, 451
Iwamoto, A.	103, 104, 106, 122, 374
Iwazaki, K.	295, 378

J

Jimbo, S.	175, 176, 346
Jin, W.G.	308
Jitsukawa, S.	230
Joe, K.	411
Johzaki, T.	478
Jozaki, T.	259

K

Kado, S.	211, 212, 274, 305, 408, 487
Kageyama, A.	363, 369
Kajita, S.	212
Kakimoto, S.	455
Kakiuchi, M.	437
Kalinina, D.	51
Kalinina, D.V.	50
Kamada, Y.	70, 200

Kamata, S.	433
Kamimura, Y.	442, 443
Kamiya, K.	222
Kaneko, M.	467
Kaneko, O.	25, 26, 73, 135, 136, 137, 138, 140, 142, 370
Kaneko, T.	358, 457
Kanno, R.	175, 176, 346
Kasaba, K.	104, 229
Kasada, R.	432
Kasahara, H.	70, 200
Kasuya, N.	177, 178
Katagiri, K.	104, 229
Katai, R.	53, 208, 386
Katanuma, I.	454, 458
Katayama, K.	477
Kato, D.	401, 405, 406, 407, 408, 410, 411, 412
Kato, K.	359
Kato, M.	411
Kato, S.	149
Kato, T.	98, 399, 400, 402, 403, 404, 405, 407, 408, 409, 410, 411, 412, 450
Katoh, S.	147, 148
Kawabata, S.	109, 124
Kawagoe, A.	109, 114
Kawahara, Z.	256
Kawahata, K.	14, 15, 18, 19, 20, 29, 143, 146, 152, 153, 154, 158, 161, 207, 268, 285, 384
Kawakami, I.	415
Kawakita, T.	350
Kawamori, E.	159, 321, 387
Kawamoto, T.	140
Kawamura, K.	218, 311, 312
Kawano, T.	262, 264, 266, 438, 439, 440
Kawara, Z.	220
Kawasaki, S.	206
Kawashima, T.	109
Kawata, J.	408
Kawazome, H.	464
Khan, R.	168
Kharchev, N.	21
Kikuchi, A.	227, 422, 424
Kim, S.W.	243
Kimura, A.	230, 432
Kimura, K.	415, 416, 417
Kimura, M.	310, 407, 412
Kimura, N.	103, 108
Kimura, T.	311
Kino, C.	479
Kitajima, S.	201, 294, 295, 378
Kitaura, Y.	80
Kitsunozaki, A.	415
Kiwamoto, Y.	316
Kizu, K.	83, 213
Kobayashi, H.	111
Kobayashi, M.	34, 48, 49
Kobayashi, S.	9, 65, 68, 69, 127, 128, 232, 460, 464, 465, 466, 467
Kobayashi, T.	202, 450, 451
Kobuchi, T.	45, 150, 483, 491
Kodama, R.	474, 484
Koga, K.	80
Koga, T.	394
Kogi, Y.	152, 153, 154, 384, 459
Kogoshi, S.	206
Kohagura, J.	463
Kohyama, A.	243, 476
Koizumi, N.	213
Kojima, A.	299, 458
Kojima, C.	415
Kojima, M.	9, 156, 163
Komada, S.	136, 157

Komatsu, K.	222
Komatsu, T.	228
Komiyama, K.	463
Komori, A.	3, 15, 48, 49, 79, 84, 217, 378, 385, 448, 501
Kondo, H.	428
Kondo, K.	34, 464, 465, 466
Kondo, S.	476
Kondo, T.	73, 136, 137, 138, 140
Konishi, S.	377, 480
Kono, A.	205, 304, 410
Kono, H.	393
Konoshima, S.	17
Kosaki, M.	112
Kotoh, K.	264
Koyata, Y.	215
Kozaki, Y.	259, 475, 476
Krashennniko.	345
Krasilnikov, A.V.	484
Kubo, H.	408, 411
Kubo, N.	134, 201
Kubo, S.	9, 15, 21, 24, 65, 66, 67, 68, 69, 127, 128, 203, 278, 286, 452
Kubota, Y.	97, 98, 202, 237, 450, 451, 460
Kudo, K.	154, 264
Kukita, Y.	428
Kumagai, S.	228
Kumazawa, R.	5, 6, 7, 8, 31, 70, 77, 200, 379, 455, 465
Kunugi, T.	220, 256, 479
Kurishita, H.	230, 232, 237, 248
Kurumada, A.	237
Kus, A.	11
Kusakabe, T.	310
Kusano, K.	356, 360

L

LABCOM Group.....	156
Leboeuf, J.-N.	183
LHD Experimental Group.....	7, 8, 10, 16, 38, 49, 50, 51, 84, 145
Li, H.	427
Li, M.	421
Livshits, A.I.	96

M

Maeda, M.	103
Maehata, K.	105
Maekawa, R.	103, 105, 114, 120, 122, 374
Maekawa, T.	67, 129, 376, 488
Mase, A.	152, 153, 154, 384, 459
Masuda, K.	162
Masui, M.	365
Masuzaki, S.	8, 34, 48, 49, 55, 56, 57, 60, 62, 63, 78, 79, 81, 84, 85, 217, 385, 408
Masuzaki, T.	28, 218, 460
Matama, K.	451
Matsubara, A.	50, 51, 311, 312
Matsubara, Y.	105, 120, 374
Matsuda, W.	308
Matsui, H.	230, 232, 236, 246, 421
Matsukawa, M.	213
Matsukawa, T.	107
Matsumoto, C.	210
Matsumoto, T.	183
Matsumoto, Y.	139, 149, 252, 313
Matsunaga, G.	293
Matsuo, K.	284
Matsuoka, K.	268, 273, 276, 277, 278, 280, 281, 282, 284, 286, 300, 323, 324, 325, 326, 415, 416, 417, 494

Matsushita, H. 279, 288, 467
 Matsuura, H. 291
 Mekawa, T. 381
 Mendenilla, A. 149
 Michael, C.A. 18, 19, 29
 Mima, K. 190, 259, 348, 349, 474, 475, 478, 482
 Minami, T. 268, 269, 270, 271, 272, 273,
 276, 277, 278, 282, 286, 300
 Minoda, A. 112
 Misawa, T. 206, 318
 Mitarai, O. 28, 250, 252, 379, 488
 Mito, T. 91, 99, 103, 104, 105, 106, 109, 110,
 113, 114, 115, 118, 119, 121, 122,
 123, 124, 125, 215, 374, 380, 388
 Miura, H. 334, 362
 Miura, Y.M. 213
 Miya, N. 83
 Miyake, Y. 463
 Miyamoto, K. 223
 Miyamoto, M. 78
 Miyamoto, S. 428
 Miyamoto, Y. 98
 Miyata, Y. 299, 458
 Miyauchi, H. 82
 Miyauchi, N. 308
 Miyawaki, K. 236
 Miyazawa, J. 9, 12, 17, 34, 54, 56, 57
 Miyoshi, H. 385
 Mi-Young Song 402, 403, 404
 Mizokoshi, H. 142
 Mizuguchi, N. 168
 Mizuno, Y. 9, 65, 68, 69, 112, 127, 128
 Mizuuchi, T. 464, 465, 466, 468
 Momoshima, N. 223, 436
 Mori, S. 204
 Moriguchi, M. 97
 Morikawa, J. 380, 388
 Morisaki, T. 15, 16, 28, 34, 48, 49, 64, 460
 Morishita, K. 233
 Morita, S. 16, 25, 26, 27, 33, 34, 39, 52, 53,
 151, 205, 208, 210, 386, 399
 Morita, Y. 114
 Moritaka, T. 354
 Motojima, G. 470
 Motojima, O. 1, 49, 84, 398
 Munakata, K. 266, 436, 441
 Murakami, S. 12
 Murakami, I. 399, 405, 411, 450
 Murakami, M. 67
 Murakami, S. 11, 27, 86, 134
 Murakami, Y. 112
 Muramoto, Y. 112
 Muraoka, K. 17
 Murata, Y. 159, 387
 Muroga, T. 219, 230, 232, 233, 234, 238, 239,
 240, 241, 242, 243, 245, 246, 419, 421,
 423, 425, 426, 427, 428, 429, 430, 431, 433
 Muto, S. 51, 151, 205
 Mutoh, S. 68
 Mutoh, T. 7, 8, 9, 25, 65, 70, 77,
 126, 193, 200, 455, 465

N

Nagahara, H. 183
 Nagai, D. 452
 Nagai, K. 122
 Nagao, M. 112
 Nagaoka, K. 25, 26, 71, 73, 136, 137, 138,
 140, 150, 268, 269, 270, 271, 272, 273,
 275, 276, 277, 278, 286, 287, 300, 413
 Nagasaka, T. 219, 232, 236, 238, 239,
 246, 421, 425, 427

Nagasaki, K. 66, 67, 464, 465, 466
 Nagashima, Y. 288
 Nagata, M. 381, 488
 Nagata, S. 241
 Nagatomo, H. 478
 Nagayama, Y. 14, 15, 47, 152, 154, 157, 159, 201,
 249, 286, 381, 382, 383, 384, 387, 459, 488
 Naito, H. 324
 Naitou, H. 183, 204
 Nakagome, K. 455
 Nakahara, A. 459
 Nakai, H. 103
 Nakai, K. 232, 393
 Nakai, M. 122
 Nakajima, M. 481, 482
 Nakajima, N. 86, 167, 170, 173, 331, 332,
 333, 334, 336, 339, 340, 341, 342
 Nakamura, H. 366, 367, 369, 408, 431
 Nakamura, Hideo 428
 Nakamura, Hiroo 428
 Nakamura, K. 97, 231, 289, 290
 Nakamura, N. 401, 406
 Nakamura, S. 100
 Nakamura, Y. 7, 8, 9, 25, 86, 96, 192, 219,
 327, 328, 331, 392, 410, 465, 468, 470
 Nakanishi, H. 9, 156, 163
 Nakano, H. 280, 281, 282, 283, 286
 Nakano, T. 83, 408
 Nakao, Y. 478
 Nakashima, H. 365
 Nakashima, Y. 194, 195, 202, 450, 453, 454, 460
 Nakayama, K. 158, 207
 Nakaze, T. 215
 Namba, C. 415, 416, 417, 511
 Namba, S. 314
 Narihara, K. 16, 39, 46, 47, 144, 145
 Narihiro, Z. 290
 Narita, F. 228
 Narui, M. 246
 Narushima, Y. 36, 41, 42, 44, 47, 159, 387
 Nejoh, Y.N. 192
 Nemoto, K. 455
 Nemoto, T. 196
 Ninomiya, A. 91
 Nishida, T. 264
 Nishiguchi, A. 478
 Nishihara, K. 347, 400
 Nishijima, S. 214
 Nishikawa, M. 391, 477
 Nishimura, A. 92, 213, 227, 228, 244,
 420, 422, 424, 427
 Nishimura, H. 201, 209, 298, 400, 480
 Nishimura, K. 17, 80, 81, 82, 83, 84, 85,
 201, 217, 378
 Nishimura, S. 268, 271, 272, 273, 276, 277, 278,
 286, 300, 323, 324, 325, 326, 327, 328
 Nishino, N. 379, 460, 464, 466, 486
 Nishio, S. 381
 Nishiura, M. 134, 139, 147, 148, 149, 201, 313
 Nishizawa, A. 147, 148, 149
 Nita, N. 219, 236
 Nobuta, Y. 84
 Noda, N. 34, 84, 98, 217, 224, 226,
 232, 237, 248, 418, 431, 499
 Noda, T. 424
 Noguchi, S. 106
 Nomura, S. 101
 Nonomura, M. 156
 Norimatsu, T. 122, 259, 377, 474, 475, 476, 480
 Norimura, T. 222
 Notake, T. 9, 21, 24, 65, 66, 67, 68, 69,
 127, 128, 203, 278, 286, 452

Nozaki, K.	452
Nozaki, S.	473
Nozato, H.	52
Numakura, T.	463
Numata, R.	355
Nunami, M.	175, 176

O

Obara, T.	400
Obayashi, H.	415, 416, 417, 443
Oda, A.	252
Oda, S.	232
Oda, T.	34, 314
Ogata, Y.	437
Ogawa, H.	60, 114, 147, 148, 201
Ogawa, M.	295, 378, 481
Ogawa, Y.	377, 380, 388
Ogiwara, H.	243
Ogura, K.	463
Oguri, Y.	481
Ohdachi, S.	16, 39, 40
Ohgaki, H.	391
Ohgo, T.	34
Ohishi, M.	411
Ohkubo, J.	113
Ohkubo, K.	9, 21, 24, 65, 66, 67, 69, 127, 128, 278, 286, 452
Ohkuma, H.	207
Ohnishi, M.	194, 195
Ohno, N.	63, 319, 320, 360, 385, 408
Ohsaki, S.	355
Ohsawa, Y.	359
Ohshima, S.	280, 281, 282, 283, 286
Ohsuna, M.	156
Ohta, Y.	101
Ohtani, H.	350, 351, 352, 354
Ohtani, S.	309, 401, 406
Ohtsu, Y.	318
Ohya, K.	408
Ohya, M.	216
Ohyabu, N.	34, 47, 48, 49, 60, 84, 94, 96, 217, 218
Oikawa, S.	174
Oishi, T.	274, 433
Oka, Y.	25, 26, 73, 136, 137, 138, 140, 141
Okabe, Y.	266
Okada, H.	464, 465, 466, 467, 470
Okai, T.	223
Okajima, S.	158, 161, 207, 268, 285
Okamoto, A.	211, 302, 304, 305
Okamoto, M.	173, 175, 176, 329, 334, 342, 346, 364, 474, 478
Okamoto, T.	347
Okamoto, Y.	220
Okamura, S.	267, 268, 269, 270, 271, 272, 273, 274, 276, 277, 278, 279, 280, 281, 282, 284, 285, 286, 288, 291, 294, 295, 297, 300, 323, 324, 325, 326, 467
Okano, K.	344, 377
Okita, T.	233
Oku, T.	237
Okumura, K.	114, 119
Okuno, K.	82, 213, 262, 265
Okuyama, T.	137
Onishi, Y.	262
Ono, K.	78
Ono, M.	311
Ono, T.	222, 408, 432
Ono, Y.	159, 381, 387
Oosako, T.	70, 200
Osakabe, M.	26, 73, 76, 136, 137, 138, 140
Oya, Y.	82, 262, 265
Oyaidzu, M.	82, 265

Oyama, N.	17
Ozaki, T.	25, 74, 75

P

Parks, P.B.	342
Pastukhov, V.P.	462
Pavlichenko, R.	152
Peterson, B.	399
Peterson, B.J.	17, 56, 57, 160, 273
Pichl, L.	310, 412
Pichl, Lukas	411
Pigarov, A.Yu.	345
Pshenichnikov, A.	21

R

Rabin, Y.	395
Ralchenko, Yu.	405
Razzak, M.A.	320
Reiter, D.	49
Rognlien, T.D.	345
Roy, R.	398

S

Saeki, K.	191
Safronova, U.I.	405
Sagara, A.	82, 83, 84, 85, 193, 217, 218, 219, 220, 234, 249, 250, 251, 252, 253, 254, 255, 256, 257, 258, 259, 377, 423, 460, 475, 479
Saigusa, M.	452
Saito, H.	219, 358, 463
Saito, K.	70, 77, 130, 131, 132, 200, 455, 465
Saito, M.	202, 450
Saito, T.	452, 453, 454, 457, 458
Saitou, Y.	302, 306
Sakabe, S.	471
Sakagami, H.	347, 478
Sakai, Y.	308
Sakakibara, S.	16, 20, 35, 36, 37, 38, 39, 41, 42, 44, 65, 68, 86
Sakakita, H.	206
Sakamoto, M.	10, 492
Sakamoto, R.	17, 23, 30, 31, 47, 56, 202, 206
Sakaue, A.	208, 386
Sakaue, H.A.	308, 309, 310, 406
Sakawa, Y.	296
Sakuma, Y.	223, 437
Sakurai, I.	210
Sakurai, M.	309
Samukawa, S.	410
Sanada, K.	228
Sanin, A.L.	18, 19
Sano, F.	11, 464, 465, 466, 467, 468, 469, 470
Sanuki, H.	179, 187, 188, 189, 191, 192,
Sardei, F.	49
Sasaki, A.	411
Sasaki, K.	205, 379, 486
Sasaki, T.	482
Sasao, M.	134, 139, 201, 294, 295, 313, 378
Satake, H.	437
Satake, M.	234
Satake, S.	173, 175, 176, 220, 256, 346, 357
Sato, A.	103
Sato, F.	240, 471
Sato, H.	428
Sato, K.	7, 34, 50, 51, 159, 194, 311, 312, 314, 387, 399, 400, 486
Sato, K.N.	206, 318, 415, 488
Sato, M.	73, 136, 137, 138, 140, 247, 339, 340, 341, 359, 389, 397, 398
Sato, N.	373, 415, 416

Sato, S.	369
Sato, T.	360, 410
Sato, Y.	107
Satou, M.	238
Sawada, A.	241, 245
Sawada, K.	33, 204, 263, 408, 460
Schedler, B.	98
Seki, T.	32, 70, 77, 85, 133, 200, 379, 455, 465
Sekiguchi, H.	90, 91
Sekimura, N.	233
Seo, K.	90, 118, 124, 125, 213, 392
Sheng Zheng-Min.	190
Shibagaki, K.	205
Shibahara, M.	220
Shibata, M.	315, 375, 456
Shibuya, M.	73, 136, 137, 138
Shibuya, T.	218, 311, 312
Shidara, H.	67
Shigemori, K.	474
Shikama, T.	241, 487
Shimada, K.	213
Shimada, R.	101, 285
Shimizu, A.	147, 148, 149, 252, 258, 273, 276, 277, 278, 280, 281, 282, 283, 286, 323, 324, 325, 326, 431
Shimizu, S.	471
Shimizu, Y.	112
Shimozuma, T.	9, 15, 21, 24, 65, 66, 67, 68, 69, 127, 128, 129, 203, 278, 286, 373, 452
Shinde, J.	295, 378
Shindo, Y.	228
Shinohara, K.	335
Shinohara, S.	142, 317
Shinto, K.	201, 295, 378
Shintomi, T.	103
Shiotsu, M.	103, 216, 226
Shiozaki, T.	263
Shiozaki, Y.	337
Shiraga, H.	474, 483
Shirai, Y.	103, 216
Shiraiwa, S.	379, 488
Shiratani, M.	80
Shoji, M.	34, 58, 59, 61, 460
Shoji, T.	141, 296
Shoji, Y.	104, 229
Shouji, M.	408
Simizu, K.	408
Soga, Y.	316
Sogabe, T.	98
Spong, D.A.	323
Sudo, S.	34, 50, 51, 155, 162, 496
Suehiro, J.	102, 112
Sugai, H.	410
Sugama, H.	173, 184, 185, 327, 328, 338
Sugimoto, M.	433
Sugimoto, T.	311, 312
Sugiyama, T.	223, 263, 264, 360, 436, 439, 441
Sumi, T.	311
Sumiyoshi, F.	109, 114
Sunahara, A.	478
Suno, H.	407, 409
Suzuki, A.	219, 241, 245, 426, 428
Suzuki, C.	268, 271, 272, 273, 276, 277, 278, 286, 292, 293, 295, 296, 300, 323, 324, 325, 326, 376, 400
Suzuki, M.	412
Suzuki, Y.	11, 46, 86, 137, 324, 378, 463, 468

T

Tachikawa, K.	113, 121, 215
Tada, S.	311
Taguchi, T.	478

Takagi, S.	39
Takahashi, C.	132, 268, 273, 276, 278, 286, 300
Takahashi, H.	201, 294, 295, 378
Takahashi, K.	457, 464
Takahashi, T.	223
Takahashi, Y.	64
Takahata, K.	88, 89, 100, 117, 118, 125, 213
Takaiwa, Y.	415
Takamaru, H.	175, 176, 346
Takamura, S.	63, 320, 385
Takano, S.	228
Takao, T.	231
Takase, Y.	70, 133, 200, 379, 381, 488
Takayama, A.	345
Takayama, M.	201, 295, 378
Takayanagi, T.	309
Takechi, M.	335
Takeda, H.	222
Takeda, T.	228, 415
Takeiri, Y.	25, 26, 27, 73, 76, 136, 137, 138, 140, 204
Takenaga, H.	17, 408
Takenaga, M.	295, 378
Takeno, H.	194, 195, 196, 197, 198, 199, 453, 454, 461
Takeuchi, M.	276, 292, 293, 295, 296, 376
Takeuchi, N.	70, 133, 200
Takeuchi, T.	227, 422, 424
Takita, Y.	9, 65, 68, 69, 127, 128
Takiyama, K.	34, 314
Takizuka, T.	17, 408
Tamai, H.	213
Tamura, H.	113, 117, 121, 228
Tamura, N.	50, 51, 56, 155
Tamura, Y.	369
Tanabe, T.	221, 248, 261, 407, 408
Tanaka, H.	67, 376, 410
Tanaka, K.	16, 17, 18, 19, 29, 39, 158, 207, 285
Tanaka, K.A.	474, 485
Tanaka, M.	266, 393, 394, 395, 396, 397, 410, 436, 441
Tanaka, M.Y.	301, 302, 303, 304, 305, 306, 307, 316
Tanaka, N.	324
Tanaka, S.	262, 429
Tanaka, T.	240, 241, 251, 419, 423, 426, 428
Tanaka, Y.	201, 249, 295, 319, 320, 378
Taniguchi, S.	192
Taniguchi, T.	70, 200
Tatematsu, Y.	452, 457
Tauchi, H.	222
Tauchi, Y.	204
Tawara, T.	159, 387
Tawara, Y.	210
Terai, T.	245
Terashima, Y.	415, 416, 417
Theory and Simulation Group.....	349
Timura, T.	159, 387
Tobari, H.	315, 375, 456
Tobita, K.	377
Toda, S.	172, 179
Todo, Y.	335, 336, 337
Toh, K.	241
Tohdo, Y.	392
Toi, K.	16, 20, 39, 40, 64, 76, 272, 273, 276, 292, 293, 295, 296, 376
Toida, M.	359
Tojo, H.	70, 200
Tokioka, S.	463
Tokitani, M.	78, 79
Toku, H.	162
Tokuda, S.	183
Tokunaga, K.	98
Tokunaga, T.	79

Tokuzawa, T.9, 20, 146, 153, 158, 207, 321
Tomida, A.302, 303
Tomii, Y.463
Tomita, Y.162, 194, 195, 196, 197, 198, 199,
252, 344, 345, 408, 453, 454, 460
Tomota, Y.237
Tonegawa, A.218, 311, 312
Torii, Y.465
Torikai, Y.437
TRIAM Exp. G.206
Tribaldos, V.11
Tsuchiya, B.241
Tsuchiya, K.213
Tsuda, K.383
Tsuda, M.88, 100, 106
Tsuiji, H.438
Tsuiji, N.436
Tsuiji-Iio, S.101, 161, 268
Tsukada, K.147, 148, 149
Tsumori, K.25, 26, 73, 136, 137, 138,
139, 140, 142, 204, 410
Tsuneyuki, S.408
Tsushima, A.191, 302, 306, 307
Tsushima, S.263
Tsutsui, H.101, 285
Tsuzuki, K.83
Tuboi, N.438

U

Uchida, K.153, 384
Uchida, M.67, 376
Uchida, T.319
Uda, T.222, 223, 262, 263, 264, 266,
434, 436, 438, 439, 441, 443
Uematsu, E.415
Uesugi, Y.319, 320
Umeda, N.73, 138
Urata, K.324
Uriu, Y.91
Usami, S.359
Uto, H.201, 295, 378

V

Veshchev, E.50
Viniar, I.155
Vyacheslavov, L.N.18, 19

W

Wada, M.139, 149, 313
Wakabayashi, H.297
Wakaki, M.311
Watanabe, A.231
Watanabe, F.16, 39
Watanabe, H.239
Watanabe, J.137
Watanabe, K.68, 252, 360
Watanabe, K.Y.11, 13, 35, 36, 37, 38, 39, 41,
42, 44, 46, 71, 86, 150, 170, 470
Watanabe, M.113
Watanabe, T.169, 252
Watanabe, T.-H.184, 185, 338
Watanabe, Y.80
Watari, T.31, 70, 77, 133, 200, 379, 455, 511

Y

Yagai, T.100
Yagi, M.172, 179, 182, 183, 372
Yagyu, J.83
Yakovlev, M.15

Yamada, H.11, 12, 13, 17, 30, 31,
35, 37, 86, 202, 206
Yamada, I.144, 145, 308, 309
Yamada, S.91, 102, 112, 116, 213
Yamada, Y.113, 121
Yamagishi, O.19
Yamaguchi, H.302, 303
Yamaguchi, S.247
Yamaguchi, T.44, 46, 68, 299, 458
Yamaguchi, Y.449, 455
Yamamoto, H.374
Yamamoto, I.263
Yamamoto, N.400
Yamamoto, S.20, 76, 464
Yamamoto, T.73, 138, 194, 383
Yamamoto, Y.162, 254, 480
Yamanaka, S.428
Yamanashi, H.223, 435
Yamanoue, T.159, 387
Yamaoka, H.139, 313
Yamaoka, N.428
Yamasaki, K.239
Yamato, A.438
Yamauchi, K.114
Yamauchi, Y.425
Yamazaki, K.27, 39, 159, 206, 252, 326, 387
Yanagi, N.67, 90, 91, 103, 106, 115,
118, 123, 125, 380, 388
Yao, Z.426
Yasaka, Y.194, 195, 196, 197, 198,
199, 453, 454, 461
Yasohama, K.374
Yatsuka, E.388
Yokoi, N.181, 186
Yokomine, T.95, 256, 258, 431
Yokota, M.114, 132, 147, 148
Yokoyama, M.11, 19, 22, 27, 86, 170,
171, 173, 201, 295, 468
Yokoyama, N.463
Yonenaga, I.247
Yoneoka, T.429
Yoshida, M.157
Yoshida, N.78, 79, 98, 239, 248, 488
Yoshida, S.183
Yoshida, Z.355
Yoshikawa, A.82, 262, 265
Yoshikawa, K.162
Yoshikawa, M.202, 450, 451, 458, 459, 460
Yoshimoto, Y.408
Yoshimura, S.302, 303, 304, 305, 306, 307, 316, 318
Yoshimura, Y.9, 21, 24, 65, 66, 67, 68, 69,
127, 128, 268, 271, 272, 273, 276,
277, 278, 282, 286, 288, 300, 452, 467
Yoshinaga, T.376
Yoshinuma, M.16, 22, 23, 150, 274, 413
Yoshizawa, A.181, 186
Yoshizawa, S.235
Yuki, K.220, 234, 256, 257
Yutani, Y.431
Yuyama, M.103

Z

Zhang, Jie.....190
Zhu, S.344
Zinkle, S.J.421
Zushi, H.203, 379, 486, 487, 488, 490, 491

How to Reach National Institute for Fusion Science



ACCESS

When you use the public transportation facility

from Centrair

• **Centrair** — (L-sky) — **Meitetsu Kanayama Sta.** (36km)

about 25min

JR Kanayama Sta. — (Chuo Expressway) — **JR Tajimi Sta.** (33km)

about 33min (express)

JR Tajimi Sta. — (Toutetu Bus) — **Kenkyuugakuentoshi** (7km)

about 15min

from JR Nagoya Sta.

• **JR Nagoya Sta.** — (Chuo Expressway) — **JR Tajimi Sta.** (36km)

about 22min (super express)

about 30min (express)

about 40min (local)

JR Tajimi Sta. — (Toutetu Bus) — **Kenkyuugakuentoshi** (7km)

about 15min

◇ **from Nagoya Airport** (Obihiro-Akita-Yamagata-Niigata-Kouchi-Matsuyama-Kumamoto)

• **Nagoya Airport** — (taxi) — **JR Kachigawa Sta.** (4km)

about 10min

• **Nagoya Airport** — (Meitetsu Bus) — **JR Kachigawa Sta.** (4km)

about 19min

JR Kachigawa Sta. — (Chuo Expressway) — **JR Tajimi Sta.** (21km)

about 20min

JR Tajimi Sta. — (Toutetu Bus) — **Kenkyuugakuentoshi** (7km)

about 15min

When you use a car

• **from Chuo Expressway Toki I.C. or Tajimi I.C.** (8km)

about 20min

• **from Tokai-Kanjo Expressway Tokiminami Tajimi I.C.** (2km)

about 5min

National Institute for Fusion Science

Building Arrangement



NIFS plot plan

- | | |
|---|------------------------------------|
| ① Cryogenics and Superconductivity Laboratories | ⑭ Auditorium |
| ② Large Helical Device Building | ⑮ Guest Housing |
| ③ Computer Center and Simulation Laboratories | ⑯ High-Voltage Transformer Station |
| ④ Heating Power Supply Building | ⑰ Cooling Water Pump House |
| ⑤ LHD Control Building | ⑱ Helium Compressor House |
| ⑥ Plasma Heating Laboratories | ⑲ Cooling Tower |
| ⑦ Plasma Diagnostics Laboratories | ⑳ Warehouse |
| ⑧ R & D Laboratories | ㉑ Helium Tank Yard |
| ⑨ Motor-Generator Building | ㉒ Power Station |
| ⑩ Central Workshops | ㉓ Recreation Facilities |
| ⑪ Research Staff Building | ㉔ Gymnasium |
| ⑫ Library | ㉕ Club House |
| ⑬ Administration Building | ㉖ Guard Of ce |